



Kyoji Sassa · Binod Tiwari
Ko-Fei Liu · Mauri McSaveney
Alexander Strom
Hendy Setiawan *Editors*

Landslide Dynamics

ISDR-ICL Landslide

Interactive Teaching Tools

Volume 2

Testing, Risk Management and Country Practices



A Programme of
the ICL for ISDR



EXTRAS ONLINE

 Springer

Landslide Dynamics:
ISDR-ICL Landslide Interactive Teaching
Tools

Kyoji Sassa · Binod Tiwari
Ko-Fei Liu · Mauri McSaveney
Alexander Strom · Hendy Setiawan
Editors

Landslide Dynamics: ISDR-ICL Landslide Interactive Teaching Tools

Volume 2: Testing, Risk Management
and Country Practices



A Programme of
the ICL for ISDR



Springer

Editors

Kyoji Sassa
International Consortium on Landslides
Kyoto
Japan

Mauri McSaveney
GNS Science
Lower Hutt
New Zealand

Binod Tiwari
Civil and Environmental Engineering
California State University
Fullerton, CA
USA

Alexander Strom
Geodynamics Research Center—branch
of JSC “Hydroproject Institute”
Moscow
Russia

Ko-Fei Liu
Department of Civil Engineering
National Taiwan University
Taipei
Taiwan

Hendy Setiawan
Disaster Prevention Research Institute
Kyoto University
Uji, Kyoto
Japan

Additional material to this book can be downloaded from <http://extras.springer.com>.

ISBN 978-3-319-57776-0 ISBN 978-3-319-57777-7 (eBook)

<https://doi.org/10.1007/978-3-319-57777-7>

Library of Congress Control Number: 2017946030

© Springer International Publishing AG 2018

This work is subject to copyright. All rights are reserved by the Publisher, whether the whole or part of the material is concerned, specifically the rights of translation, reprinting, reuse of illustrations, recitation, broadcasting, reproduction on microfilms or in any other physical way, and transmission or information storage and retrieval, electronic adaptation, computer software, or by similar or dissimilar methodology now known or hereafter developed.

The use of general descriptive names, registered names, trademarks, service marks, etc. in this publication does not imply, even in the absence of a specific statement, that such names are exempt from the relevant protective laws and regulations and therefore free for general use.

The publisher, the authors and the editors are safe to assume that the advice and information in this book are believed to be true and accurate at the date of publication. Neither the publisher nor the authors or the editors give a warranty, express or implied, with respect to the material contained herein or for any errors or omissions that may have been made. The publisher remains neutral with regard to jurisdictional claims in published maps and institutional affiliations.

Cover illustration: Bird’s-eye view which based on the geomorphological map by photo interpretation around Mt. Unzen-Fugendake and Mt. Mayu-Yama (Inoue, 1999, Unzen Restoration Office, 2002) Inoue K (1999) Shimabara-Shigatsusaku Earthquake and topographic changes by Shimabara catastrophe. *Journal of the Japan Society of Erosion Control Engineering* 52(4):45–54 (in Japanese) Unzen Restoration Office of the Ministry of Land, Infrastructure and Transport of Japan (2002) *The Catastrophe in Shimabara—1791–92 eruption of Unzen–Fugendake and the sector collapse of Mayu-Yama*. An English leaflet (23 pages)

Printed on acid-free paper

This Springer imprint is published by Springer Nature
The registered company is Springer International Publishing AG
The registered company address is: Gewerbestrasse 11, 6330 Cham, Switzerland

Foreword for the ISDR-ICL Landslide Interactive Teaching Tools

Disasters induced by natural hazards annually affect millions of people. Disasters may pose a serious threat to health, cultures, and development prospects. Disasters have been increasing in this period of climate change, urbanization, and overpopulation. Predictions are that several types of events arising from natural hazards will become more frequent; thus, impacts of resulting disasters could become more devastating. Among these potentially catastrophic hazards are landslides.

Two major milestones, 2030 Agenda for Sustainable Development and the Paris Agreement on climate change, were adopted in 2015. The same year in Sendai, Japan, Member States adopted the Sendai Framework for Disaster Risk Reduction 2015–2030. The Framework aims of assessing the global progress on disaster risk reduction, identifying its priority actions, and setting the role of stakeholders.

The key outcome relating to landslides from the Sendai Framework for Disaster Risk Reduction 2015–2030 is the *International Strategy for Disaster Risk Reduction—International Consortium on Landslides Sendai Partnerships 2015–2025 (ISDR-ICL Sendai Partnerships)*.

The *International Consortium on Landslides, ICL*, actively supported by UNESCO, is a vital organization for landslide disaster risk reduction. Through international scientific communities, it conducts advanced research and builds capacities in landslide prevention and mitigation.

In line with the objectives of Sendai Partnership, ISDR-ICL is launching the Landslide Interactive Teaching Tools (LITT). This interactive open-access teaching toolkit aims to help academia, leading engineers, and practitioners to formulate necessary capacities and technical training for landslide disaster risk reduction. The set of tools includes methodologies and case studies on how to map, monitor, and forecast such extreme events. This open-access teaching tool could be periodically revised and updated by the community of users based on the reviews, comments, and new research findings.

Nowadays, more than ever, we need stronger scientific cooperation and broader result dissemination. In this spirit, I thank all the contributors to this initiative and I pledge UNESCO's continuing support to deepening partnerships for education and resilience in societies across the world.



Flavia Schlegal
Assistant Director-General of UNESCO
for Natural Sciences

Preface: Aim and Outline of the ISDR-ICL Landslide Interactive Teaching Tools

Aim

The International Consortium on Landslides (ICL) proposed the ISDR-ICL Sendai Partnerships 2015–2025 for global promotion of understanding and reducing landslide disaster risk at a session of “Underlying risk factors” of the 3rd WCDRR on the morning of 16 March 2015. The partnership was proposed as a voluntary commitment to the World Conference on Disaster Risk Reduction, Sendai, Japan, 2015, and also as tools for implementing and monitoring the Post-2015 Framework for Disaster Risk Reduction and the Sustainable Development Goals. It was approved and signed by 16 global stakeholders in the afternoon of the same day in Sendai, Japan, and the Secretary-General Mr. Petteri Taalas of the World Meteorological Organization (WMO) signed it on 16 April 2016.

The Sendai partnerships acknowledge that

- At a higher level, social and financial investment is vital for understanding and reducing landslide disaster risk, in particular social and institutional vulnerability, through coordination of policies, planning, research, capacity development, and the production of publications and tools that are accessible, available free of charge and are easy to use for everyone in both developing and developed countries.

Landslide science and technologies have continuously been developed to be more reliable, precise or cost-effective for landslide disaster risk reduction over the world. However, this scientific and technological progress has not been shared equally over the world. The gap between the available level of science and technologies and the practical use of those in many countries, regions and communities is very wide. To fill this gap, ICL has created Landslide Interactive Teaching Tools, which are always updated and continuously improved, based on responses from users and lessons learned during their application. All text books gradually become outdated. To avoid this problem, ICL plans to upload the latest teaching tools in the WEB of Teaching Tools and print text tools periodically.

Landslide Dynamics

A landslide is a downslope movement of rock, soil or both. Landslide disasters are caused by exposure to **hazardous motions of soil and rock** that threaten vulnerable human settlement in mountains, cities, coasts, and islands, as stated in the Sendai Partnerships. Understanding “Landslide dynamics” is the very basis of landslide disaster risk reduction.

Organizations Contributing Teaching Tools

Each teaching tool will be submitted by the teaching tool contributing organization as shown in the list of contributing organizations. Each organization has its own Teaching Tool Identifying Number consisting of telephone number of the country and the registered number within the country. The involvement of organization as well as individual researcher is adopted to keep quality and updating of each tool.

Outline

The teaching tools are classified in two fundamentals for Landslide Dynamics and four major parts of tools.

The part number is included in each teaching tool identifier. Each part has 3–5 subparts.

Due to the requirement of book publication structure, the subparts do not appear in the content because of two levels of publication structure. Two fundamentals are splitted in Vol. 1 and Vol. 2 as shown in each content of Vol. 1 and Vol. 2. Please refer the following subparts, fundamentals and their pages.

Fundamentals

- (1) Landslide Types: Description, illustrations and photos which is included in Front Matters of Vol. 1 (page 1–38)
- (2) Landslide Dynamics for risk assessment which is included in Front Matters of Vol. 2 (page 1–79)

Part 1 Mapping and Site Prediction (which is included in Vol. 1)

- (1) Basic Mapping (Tool No.1–No.5: page 41–112)
- (2) Site Prediction Using GIS (Tool No.6–No.13: page 113–195)
- (3) Field Guidelines (Tool No.14–No.15: page 197–232)

Part 2 Monitoring and Early Warning (which is included in Vol. 1)

- (1) Remote Sensing Techniques for Landslide Monitoring (Tool No.16–No.19: page 235–295)
- (2) Monitoring System Instrumentation (Tool No.20–No.22: page 297–340)
- (3) Rainfall Threshold for Landslide Prediction (Tool No.23–No.32: page 341–447)
- (4) Landslide Time Prediction from Pre-failure Movement Monitoring (Tool No.33–No.38: page 449–551)

- (5) Guidelines for Landslide Monitoring and Early Warning Systems (Tool No.39–No.41: page 553–599)

Part 3 Risk Assessment (which is included in Vol. 2)

- (1) Numerical Modeling and Simulation (Tool No.1–No.12: page 83–275)
- (2) Physical and Mathematical Modeling (Tool No.13–No.16: page 277–319)
- (3) Laboratory Soil Testing for Landslide Analysis (Tool No.17–No.20: page 321–402)
- (4) Analysis and Assessment of Landslides (Tool No.21–No.24: page 403–443)

Part 4 Risk Management and Country Practices (which is included in Vol. 2)

- (1) Landslide Risk Management (Tool No.25–No.34: page 447–597)
- (2) Community Risk Management (Tool No.35–No.39: page 599–667)
- (3) Country Practices (Tool No.40–No.53: page 669–831)

The teaching tools consist of three types of tools.

1. The first type is TXT-tools consisting of original texts with figures. The first edition includes two volumes of books.
2. The second type is PPT-tools consisting of PowerPoint files and video tools made for visual lectures.
3. The third type is PDF-tools consisting of already published reference papers/reports, guidelines, and others.

The second and the third types of tools are supplementary tools of the text tools (text books).

Each teaching tool has its own identifier. The identifier of each tool consists of three parts:

1. the number of the part of the tools in which it appears (Parts 1–4);
2. the country telephone code and an assigned unique number for each contributing organization (for example 081-1 signifies Japan-ICL headquarters, and 081-3 signifies Japan—Erosion and Sediment Control Department, Ministry of Land, Infrastructure, Transport and Tourism);
3. the last part of the identifier is a consecutive number assigned to the teaching tool by its contributing organization.

Call for Contribution to the Interactive Teaching Tools

The International Consortium on Landslides calls for new tools to this Landslide Interactive Teaching tools.

New progress of Landslide Science and Technology, and case studies and country practices in the world are good information for practitioners and

engineers in other countries and other fields as well. We plans to establish a new Editorial Manager for Landslide Teaching Tools to promote the capacity building for the contribution of new tools. The authors of teaching tools in this publication are also requested to improve their contributed tooks and contribute new tools for other people in the world landslide community.

Those who are willing to contribute to the Landslide Teaching Tools are requested to contact ICL Secretariat and one of Editors of this teaching tools Vol. 1 and Vol. 2. All authors and editors of this teaching tools are highly appreciated for their useful contribution and editorial efforts.

Contacts

Editor-in-Chief

Kyoji Sassa: International Consortium on Landslides (ICL) (e-mail: sassa@iclhq.org)

Editorial Secretariat

- Kyoji Sassa: Secretary-Genearl in ICL Secretariat, Kyoto, Japan (e-mail: secretariat@ichhq.org)
- Khang Dang: Assistant to Editor-in-Chief (e-mail: khangdq@gmail.com)
- Hendy Setiawan: Assistant to Editor-in-Chief (e-mail: sethiawan.hendi.45w@kyoto-u.jp)

Editors of Parts

Fundamentals

- Kyoji Sassa: International Consortium on Landslides (ICL), Japan (e-mail: sassa@iclhq.org)

Part 1: Mapping and Site Prediction

- Fausto Guzzetti: CNR—Consiglio Nazionale delle Ricerche, Istituto di Ricerca per la Protezione Idrogeologica, Italy (e-mail: F.Guzzetti@irpi.cnr.it)
- Hiromitsu Yamagishi: Shin Engineering Consultant Co. Ltd, Japan (e-mail: hiromitsuyamagishi88@gmail.com)

Part 2: Monitoring and Early Warning

- Željko Arbanas: University of Rijeka, Faculty of Civil Engineering, Croatia (e-mail: zeljko.arbanas@gradri.uniri.hr)
- Nicola Casagli: University of Florence, Department of Earth Sciences, Italy (e-mail: nicola.casagli@unifi.it)

Part 3: Risk Assessment

- Kyoji Sassa: International Consortium on Landslides, Japan (e-mail: Sassa@iclhq.org)
- Binod Tiwari: Civil & Environmental Engineering Department, California State University, USA, (e-mail: btiwari@fullerton.edu)

Part 4: Risk Management and Country Practices

- Mauri McSaveney: GNS Science, New Zealand (e-mail: m.mcsaveney@gns.cri.nz)
- Ko-Fei Liu: National Taiwan University, Chinese Taipei (e-mail: kfliu@ntu.edu.tw)
- Alexander Strom: Geodynamics Research Centre—branch of JSC “Hydroproject Institute”, Russia (e-mail: strom.alexandr@yandex.ru)



Kyoji Sassa
Executive Director
International Consortium on Landslides

Contents

TXT-tool 0.081-1.1 Landslide Dynamics for Risk Assessment	1
Kyoji Sassa and Khang Dang	
Part III Risk Assessment	
TXT-tool 3.081-1.1 An Integrated Model Simulating the Initiation and Motion of Earthquake and Rain-Induced Rapid Landslides and Its Application to the 2006 Leyte Landslide	83
Pham Van Tien, Kyoji Sassa and Khang Dang	
TXT-tool 3.385-1.1 Application of Integrated Landslide Simulation Model LS-Rapid to the Kostanjek Landslide, Zagreb, Croatia	101
Karolina Gradiški, Kyoji Sassa, Bin He, Željko Arbanas, Snježana Mihalić Arbanas, Martin Krkač, Predrag Kvasnička and Maja Oštrić	
TXT-tool 3.081-1.2 Simulation of Landslide Induced Tsunami (LS-Tsunami) Based on the Landslide Motion Predicted by LS-RAPID	111
Khang Dang, Kyoji Sassa, Hideaki Yanagisawa and Bin He	
TXT-tool 3.081-1.3 A Hypothesis of the Senoumi Submarine Megaslide in Suruga Bay in Japan—Based on the Undrained Dynamic-Loading Ring Shear Tests and Computer Simulation	131
Hendy Setiawan, Kyoji Sassa and Bin He	
TXT-tool 3.081-1.4 Initiation Mechanism of Rapid and Long Run-Out Landslide and Simulation of Hiroshima Landslide Disasters Using the Integrated Simulation Model (LS-RAPID)	149
Loi Doan Huy, Kyoji Sassa, Hiroshi Fukuoka, Yuji Sato, Kaoru Takara, Hendy Setiawan, Tien Pham and Khang Dang	

TXT-tool 3.385-1.2	
Deterministic Landslide Susceptibility Analyses	
Using LS-Rapid Software	169
Sanja Dugonjić Jovančević, Osamu Nagai, Kyoji Sassa and Željko Arbanas	
TXT-tool 3.886-1.1	
Debris2D Tutorial	181
Ko-Fei Liu and Ying-Hsin Wu	
TXT-tool 3.081-1.5	
Manual for the LS-RAPID Software	191
Kyoji Sassa, Hendy Setiawan, Bin He, Karolina Gradiški and Khang Dang	
TXT-tool 3.034-2.1	
A Debris Flow Regional Fast Hazard Assessment Toolbox	225
Francesco Bregoli, Vicente Medina and Allen Bateman	
TXT-tool 3.386-1.1	
Two-Dimensional Debris-Flow Modelling	
and Topographic Data	235
Jošt Sodnik and Matjaž Mikoš	
TXT-tool 3.886-1.2	
Simulation for the Debris Flow and Sediment Transport	
in a Large-Scale Watershed	251
Ying-Hsin Wu, Ko-Fei Liu, Yi-Chin Chen, Yu-Jia Chiu and Shang-Shu Shih	
TXT-tool 3.385-1.3	
Landslide Occurrence Prediction in the Rječina River	
Valley as a Base for an Early Warning System	263
Martina Vivoda Prodan, Sanja Dugonjić Jovančević and Željko Arbanas	
TXT-tool 3.001-1.1	
Physical Modelling of Rain-Induced Landslides	277
Binod Tiwari and Beena Ajmera	
TXT-tool 3.001-1.2	
Physical Modelling of Earthquake-Induced Landslides	287
Beena Ajmera and Binod Tiwari	
TXT-tool 3.044-1.1	
The Runout of Chalk Cliff Collapses—Case Studies	
and Physical Model Experiments	297
Elisabeth T. Bowman and W. Andy Take	
TXT-tool 3.007-1.1	
Mechanical-Mathematical Modeling and Monitoring	
for Landslide Processes	315
Valentina Svalova	

TXT-tool 3.081-1.6	
Manual for the Undrained Dynamic-Loading Ring-Shear Apparatus	321
Hendy Setiawan, Kyoji Sassa, Khang Dang, Maja Ostric, Kaoru Takara and Martina Vivoda	
TXT-tool 3.081-1.7	
Undrained Dynamic-Loading Ring-Shear Apparatus and Its Application to Landslide Dynamics	351
Hendy Setiawan, Kyoji Sassa, Hiroshi Fukuoka, Gonghui Wang and Naohide Ishikawa	
TXT-tool 3.081-1.8	
A New High-Stress Undrained Ring-Shear Apparatus and Its Application to the 1792 Unzen–Mayuyama Megalide in Japan	371
Khang Dang, Kyoji Sassa, Bin He, Kaoru Takara, Kimio Inoue and Osamu Nagai	
TXT-tool 3.001-1.3	
Laboratory Measurement of Fully Softened Shear Strength and Its Application for Landslide Analysis	393
Binod Tiwari and Beena Ajmera	
TXT-tool 3.081-1.9	
Dynamic Properties of Earthquake-Induced Large-Scale Rapid Landslides Within Past Landslide Masses	403
Pham Van Tien and Kyoji Sassa	
TXT-tool 3.001-1.4	
Using Excel Tools for Slope Stability Analysis	413
Beena Ajmera and Binod Tiwari	
TXT-tool 3.034-1.1	
A Textural Classification of Argillaceous Rocks and Their Durability	421
Jordi Corominas, Joan Martinez-Bofill and Albert Soler	
TXT-tool 3.039-1.1	
Landslide-Related WPS Services	435
Ivan Marchesini, Massimiliano Alvioli and Mauro Rossi	
Part IV Risk Management and Country Practices	
TXT-tool 4.084-1.1	
Soil Slope Stability Analysis	447
Do Minh Duc	
TXT-tool 1.081-2.4	
Risk Evaluation Using the Analytic Hierarchy Process (AHP)—Introduction to the Process Concept	461
Eisaku Hamasaki and Toyohiko Miyagi	

TXT-tool 4.039-3.1	
Terrestrial Laser Scanner and Geomechanical Surveys for the Rapid Evaluation of Rock Fall Susceptibility Scenarios	477
Giovanni Gigli, Stefano Morelli, Simone Fornera and Nicola Casagli	
TXT-tool 4.039-3.2	
How to Assess Landslide Activity and Intensity with Persistent Scatterer Interferometry (PSI): The PSI-Based Matrix Approach	493
Francesca Cigna, Silvia Bianchini and Nicola Casagli	
TXT-tool 4.034-1.1	
Quantitative Rockfall Risk Assessment for Roadways and Railways	509
Olga Mavrouli and Jordi Corominas	
TXT-tool 4.084-1.2	
Landslide Vulnerability Assessment: A Case Study of Backan Town, Northeast Vietnam	521
Do Minh Duc, Mai Trong Nhuan, Tran Dang Quy and Tran Manh Lieu	
TXT-tool 4.086-1.1	
Landslide Investigations in the Northwest Section of the Lesser Khingan Range in China Using Combined HDR and GPR Methods	539
Zhaoguang Hu, Wei Shan and Hua Jiang	
TXT-tool 4.052-1.1	
Landslide Risk Perception	555
Irasema Alcántara-Ayala	
TXT-tool 4.886-1.1	
Taiwan Typhoon Loss Assessment System (TLAS Taiwan) Web Tool	569
Hsin-Chi Li, Yi-Chen Chen and Mei-Chun Kuo	
TXT-tool 4.385-1.1	
Method for Prediction of Landslide Movements Based on Random Forests	575
Martin Krkač, Drago Špoljarić, Sanja Bernat Gazibara and Snježana Mihalić Arbanas	
TXT-tool 4.062-1.1	
Community Hazard Maps for Landslide Risk Reduction	599
Dwikorita Karnawati, Teuku Faisal Fathani, Wahyu Wilopo and Budi Andayani	
TXT-tool 4.039-1.1	
Definition and Use of Empirical Rainfall Thresholds for Possible Landslide Occurrence	607
Silvia Peruccacci and Maria Teresa Brunetti	

TXT-tool 4.062-1.1 A Socio-technical Approach for Landslide Mitigation and Risk Reduction	621
Dwikorita Karnawati, Teuku Faisal Fathani, Wahyu Wilopo and Syamsul Maarif	
TXT-tool 4.066-1.1 Community-Based Landslide Risk Management Approaches	631
Asian Disaster Preparedness Centre (ADPC)	
TXT-tool 4.039-2.1 On the Protection of Cultural Heritages from Landslides	647
Claudio Margottini	
TXT-tool 4.886-1.2 Procedures for Constructing Disaster Evacuation Maps: Guidelines and Standards	669
Su-Chin Chen and Lien-Kuang Chen	
TXT-tool 4.886-1.3 Emergency Post-landslide Disaster Documentation	675
Lien-Kuang Chen	
TXT-tool 4.386-1.1 State-of-the-Art Overview on Landslide Disaster Risk Reduction in Slovenia	683
Matjaž Mikoš, Magda Čarman, Jože Papež and Jernej Jež	
TXT-tool 4.086-1.2 Shallow Landslides and Plant Protection in Seasonal Frozen Regions	693
Ying Guo, Wei Shan, Yuying Sun and Chengcheng Zhang	
TXT-tool 4.886-1.4 Ecological: Countermeasure Guidelines and Case Histories in Taiwan	703
Chia-Chun Ho, Jen-Yang Lin and Yi Wen Chiu	
TXT-Tool 4.086-1.3 The Impact of Climate Change on Landslides in Southeastern of High-Latitude Permafrost Regions of China	715
Wei Shan, Zhaoguang Hu and Ying Guo	
TXT-tool 4.052-1.2 Landslide Risk Communication	731
Irasema Alcántara-Ayala	
TXT-tool 4.504-1.1 How to Make a Database of Landslides in Tegucigalpa, Honduras	743
Lidia Torres Bernhard, Nelson Sevilla, Kiyoharu Hirota, Hiromitsu Yamagishi and Tsukamoto Satoru	

TXT-tool 4.039-3.3	
Debris Flows Modeling for Hazard Mapping	761
Massimiliano Nocentini, Veronica Tofani, Giovanni Gigli, Francesco Fidolini and Nicola Casagli	
TXT-tool 4.039-4.1	
Landslide Investigations and Risk Mitigation: The Sarno, Italy, Case	771
Giovanna Capparelli, Luciano Picarelli and Pasquale Versace	
TXT-tool 4.081-8.1	
Landslide Monitoring for Early Warning in the Hai Van Station Landslide in Vietnam	785
Shiho Asano, Hirotaka Ochiai and Huynh Dang Vinh	
TXT-tool 4.081-1.1	
Mechanism of Large-Scale Deep-Seated Landslides Induced by Rainfall on Gravitationally Deformed Slopes: A Case Study of the Kuridaira Landslide in the Kii Peninsula, Japan	793
Pham Van Tien, Kyoji Sassa, Kaoru Takara, Hiroshi Fukuoka, Khang Dang, Tatsuya Shibasaki, Hendy Setiawan, Nguyen Duc Ha and Le Hong Luong	
TXT-tool 4.081-9.1	
Rotary Sampling Drilling Technology to Extract High-Quality Cores Using a Sleeve-Incorporating Core Barrel and Polymer Mud in Landslide Areas of Japan and Vietnam	807
Shinro Abe, Norio Sato, Dinh Van Tien, Do Ngoc Ha, Le Ngoc An and Luu Xuan Khoat	
TXT-tool 4.081-1.2	
Mechanism of the Aratozawa Large-Scale Landslide Induced by the 2008 Iwate-Miyagi Earthquake	819
Hendy Setiawan, Kyoji Sassa, Kaoru Takara, Maja Ostric, Toyohiko Miyagi and Hiroshi Fukuoka	
List of PPT-tools and PDF-tools	833

TXT-tool 0.081-1.1

Landslide Dynamics for Risk Assessment

Kyoji Sassa and Khang Dang

Abstract

The study of landslide dynamics is a fundamental tool to aid in proactive responses to reduce landslide disaster risk, which has become intensified by the increasing development of mountain slopes due to economic and population growth in many developing countries. Landslide risk is also increasing due to extreme rainfalls caused by changing climate in many landslide-prone areas in the world. Natural landslide phenomena would have initially attracted attention through the observation of ground deformation/movement which changed the natural scenery in the mountains and sometimes affected people's living areas before the era of industrialization. Geological and geomorphic studies started at this stage. Civil engineering works to construct roads, bridges, dams and river banks, and engineering works to mine hard rocks, limestones, coals, valuable metal and minerals developed during the industrialization of human society. They caused artificial geomorphic changes and often triggered landslides. To avoid triggering landslides due to human activities and to stabilize landslide slopes, industry-centered landslide studies were developed. The main tool was slope stability analysis based on soil and rock mechanics. In the post-industrialization period, people-centered disaster risk reduction studies integrating natural sciences, social sciences and engineering to save people's lives have developed. The initial global scale initiative was the International Decade for Natural Disaster Reduction (IDNDR) from 1st January 1990 to the end of 1999. Peoples are rarely killed by either slow-speed or short-distance landslides. The landslides

K. Sassa (✉) · K. Dang
International Consortium on Landslides, Gokasho,
Uji, Kyoto 611-0011, Japan
e-mail: kyoji.sassa@gmail.com

K. Dang
e-mail: khangdq@gmail.com; khang@iclhq.org

K. Dang
VNU University of Science, Hanoi, Vietnam

affecting people's lives are rapid and long-runout landslides, which they cannot escape from. Landslide studies to assess the velocity and travel distance of landslides must be developed. This is topic is landslide dynamics. This paper describes the core concepts and the important aspects of landslide dynamics as the fundamentals of ISDR-ICL Landslide Teaching Tools, which aim to support landslide risk reduction efforts through reliable landslide risk assessment and the early warning and land-use changes.

Keywords

Landslide dynamics • Undrained ring shear test • Simulation model
Hazard assessment

Contents

1	Introduction	2
1.1	Introduction	3
1.2	Landslide Initiation Mechanism	6
1.3	A Sled Model for the Motion of Landslides ..	12
2	Undrained Dynamic-Loading Ring-Shear Apparatus (UDRA)	15
2.1	Introduction	16
2.2	Structure and Control System of the Undrained Dynamic-Loading Ring-Shear Apparatus (ICL-2)	17
2.3	Effects of the Rubber Edge and Its Correction.....	22
2.4	Types of Undrained Dynamic-Loading Ring-Shear Tests Using ICL-2	27
2.5	Three Types of Relationships Presented in UDRA Test Results.....	29
3	Landslide Simulation Model (LS-RAPID) and Landslide-Induced Tsunami Model (LS-Tsunami)	29
3.1	Landslide Simulation Model (LS-RAPID).....	32
3.2	Landslide-Induced Tsunami Model (LS-Tsunami)	39
4	Applications of UDRA, LS-RAPID and LS-Tsunami	46
4.1	Application to the 1792 Unzen-Mayuyama Megaslide-and-Tsunami Disaster.....	48
4.2	Application to the 2014 Hiroshima Rain-Induced Shallow-Landslide-Debris Flow Disaster	62
	References	77

outline of representative conventional soil tests used for landslide studies: direct shear tests, tri-axial tests and ring shear tests, and the basic concept of undrained dynamic loading ring-shear tests are explained in Sect. 1.1 Introduction. Section 1.2 describes the landslide initiation mechanisms and their triggering factors: static pore water pressure, the pore pressure increase due to rainfall and excess pore pressure changes during earthquakes as the very base of landslide dynamics. Section 1.3 introduces the basic sled model for the motion of landslide. The model assumes that shear resistance on the sliding surface is the cause of energy loss of potential energy during the motion of a landslide. The sled model is the basis of landslide dynamics, though there are two major differences described in Sect. 3.1.

1. While the sled model assumes a constant frictional coefficient, the integrated computer simulation model (LS-RAPID) introduces a function to calculate the changing frictional coefficient during motion using the landslide dynamics parameters measured and estimated by the undrained dynamic-loading ring-shear apparatus.
2. While the sled model does not include energy loss other than frictional energy, LS-RAPID automatically reduces a kinetic energy at a certain mesh point and a certain time period where/when a kinetic energy loss other than frictional energy loss by collision of the landslide mass to the valley walls or steps etc. occurs, and the calculation diverges and

1 Introduction

Abstract

Section 1 aims to explain the basic concept of landslide dynamics, which is concerned with the velocity and travel distance of landslides. The

unreasonable depth or velocity appears as its result.

Keywords

Landslide dynamics • Undrained ring shear test • Initiation mechanism • Sled model

1.1 Introduction

To design engineered slopes in civil engineering and mining engineering works, slope stability analysis has been developed to prevent the occurrence of slope instability. The triaxial test and the direct shear test are used for this purpose.

Figure 1 is a schematic figure showing a direct shear test. A soil specimen is put in two shear boxes with a split. Normal stress is loaded on the sample, then shear force is applied parallel to the splitting surface of the two boxes. Shearing will take place, and the shear strength of the sample will be measured. The test can create a sliding surface, but it has two weak points as a tool for studying landslides.

- The possible shear displacement is limited because the shear area is being reduced as shear displacement progresses. The test can measure the peak shear strength, but it is difficult to measure the post-failure shear resistance for the large shear displacements in landslides.

- The pore pressure generated during shearing will greatly change the shear resistance. Undrained shearing is not possible because of water leakage through the gap, so pore pressure mobilized during shearing cannot be investigated.

Figure 2 is a schematic figure of a triaxial test (Bishop and Henkel 1962). A soil specimen is set within a rubber membrane, and confining pressure (σ_c) is loaded by increasing the water pressure within the triaxial cell. The axial load is then increased until the specimen fails. The shear strength of specimen will be obtained from the maximum axial load.

The triaxial test can produce failure in an undrained state, so pore-water pressure mobilized during shearing can be monitored. However, it has two weak points as a tool to study landslides.

- It cannot create a clear sliding surface within the specimen, although the specimen is deformed and failure is caused within the specimen.
- Post-failure behavior in the progress of a large shear displacement cannot be reproduced, and pore pressure generation in this stage cannot be measured.

Figure 3 shows a schematic figure of a ring shear apparatus that was designed to investigate landslides by Bishop et al. (1971). The apparatus allows the formation of a sliding surface and

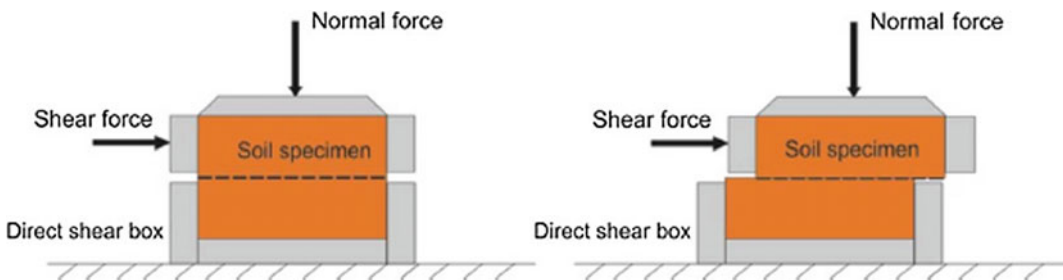


Fig. 1 Direct shear test

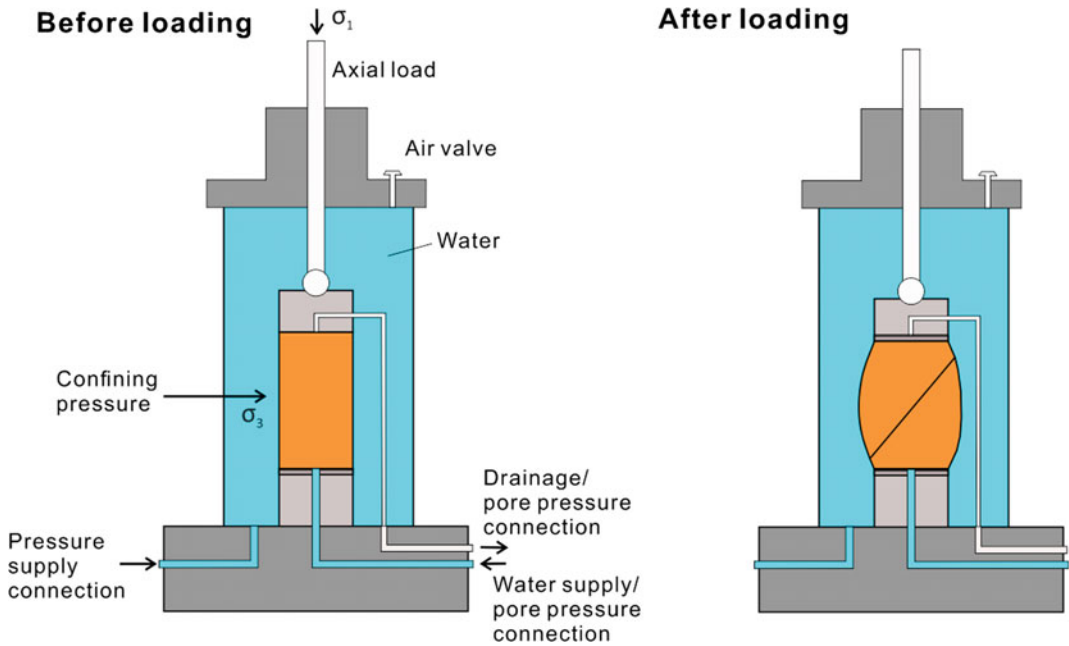


Fig. 2 Schematic figure of a triaxial test

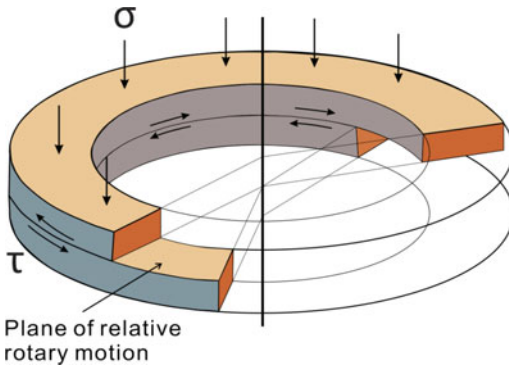


Fig. 3 Schematic figure of a ring shear apparatus by Bishop et al. (1971)

large shear displacement after failure and is thus suitable for studying landslide phenomena. However, it has two weak points as a tool to study landslides.

- The undrained state cannot be produced because of leakage of water through the gap between the two shear boxes. The pore pressure generated during shearing is not monitored.

- Seismic loading ring shear tests simulating earthquake-induced landslides and pore-pressure-controlled ring shear tests simulating rain-induced landslides and rapid post-failure motion cannot be carried out.

Figure 4 is a schematic figure of the undrained dynamic loading ring shear apparatus developed by Sassa et al. (2004, 2014a, b). This apparatus can maintain an undrained stage during 50 cm/s shear in the center of specimen (ICL-2 model), and 224 cm/s in the center of a specimen (DPRI-6 model).

Shear stress loading based on a record of seismic waves is possible using the servo-control system. To maintain the undrained state of the shear box during shearing, a rubber edge set in the lower shear box is pushed to the bottom of the upper shear box at a contact stress greater than the generated pore pressure inside the specimen. The contact pressure is maintained by controlling the distance between the upper box and the lower box using a servo-control system that can measure the distance to a precision of 1/1000 mm.

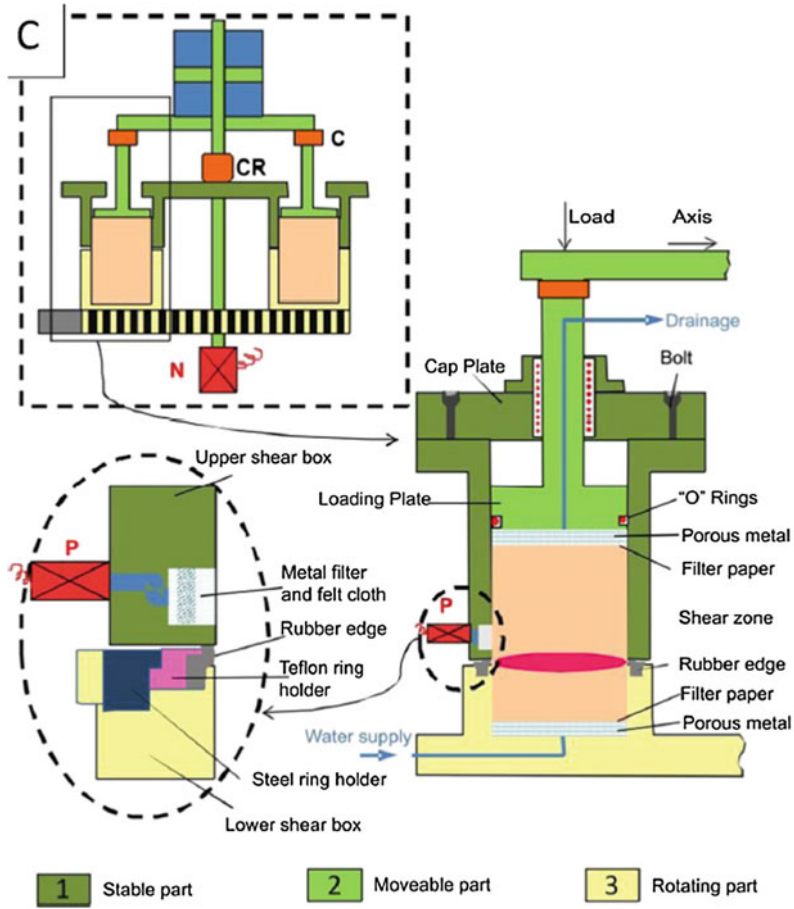


Fig. 4 Schematic figure of the undrained dynamic-loading ring shear apparatus (Sassa et al. 2014a)

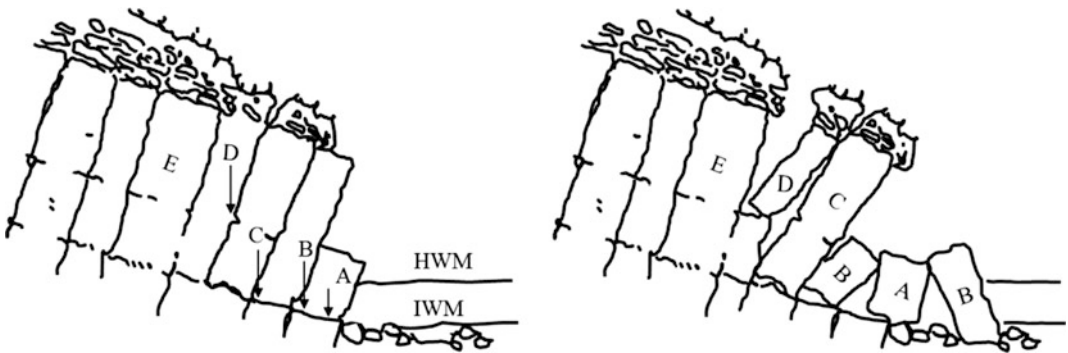


Fig. 5 Separation of an unstable mass from the stable part of slope by toppling failure (from Varnes 1978)

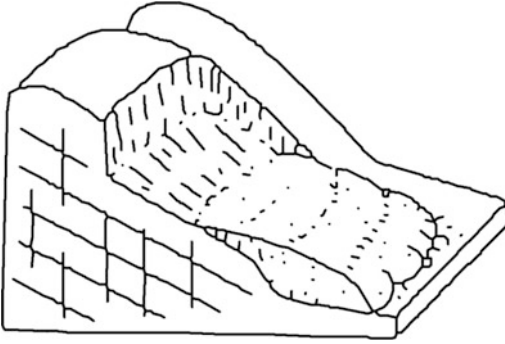


Fig. 6 Separation of an unstable mass from the stable part of slope by sliding failure (from Sassa 1984)

The successful development of an undrained dynamic-loading ring shear apparatus has enabled the development of *landslide dynamics* to study the initiation and motion of highly dangerous rapid landslides and to assess the landslide hazard created by rapid landslides.

1.2 Landslide Initiation Mechanism

1.2.1 Introduction

A landslide is a phenomenon in which a part of a mass of soil or rock will move out from its place in a layer on a slope. An unstable part of the mass will separate from the stable part by topping failure or sliding failure. The separation is caused by failure, namely a stress drop followed by movement.

An illustration of a separation by toppling failure is shown in Fig. 5 and separation by sliding failure in Fig. 6. Toppling of rock is a

major mechanism for rock falls causing disasters along roads and railways. Most disastrous landslides, however, occur by sliding. The initiation mechanism of landslides is discussed later.

1.2.2 Shear Strength of Soils/Rocks

Figure 7 presents the concept of initiation of motion between two blocks and the mobilized friction angle at failure. In this figure, T is shear force (shear stress multiplied by contact area), N is normal force (normal stress multiplied by contact area), and R is shear resistance.

Initially, the block is stable. The shear resistance R will take the same value as the shear force T until the initiation of motion at failure. Shear resistance R at failure is expressed as R_f . If the shear force T increases, the combined force ($T + N$) increases and the direction of action rotates clockwise, as shown in Fig. 7.

The angle between N and the combined force ($N + T$) at failure is called the friction angle (ϕ). In physics, R/N is called the coefficient of friction. However, in landslide science as well as soil mechanics, the coefficient of friction is more usually expressed as $\tan \phi$ using the friction angle.

In a manner similar to Fig. 7, however, with soils, shearing will occur within the soil mass (not at the border between two blocks). The friction angle within a soil mass is sometimes called the internal friction angle or internal angle of friction. Figure 8. shows shearing within a soil mass where force/unit area is expressed as stress, namely normal stress σ , shear stress τ and shear resistance.

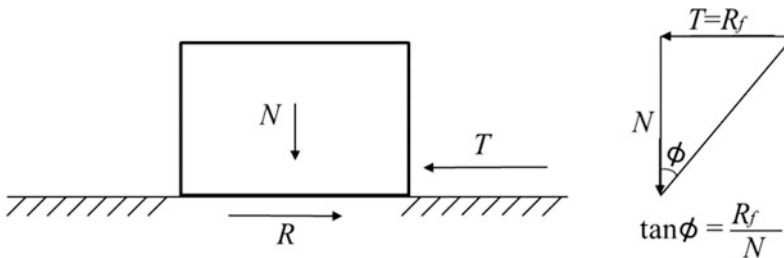


Fig. 7 Shear strength and friction angle

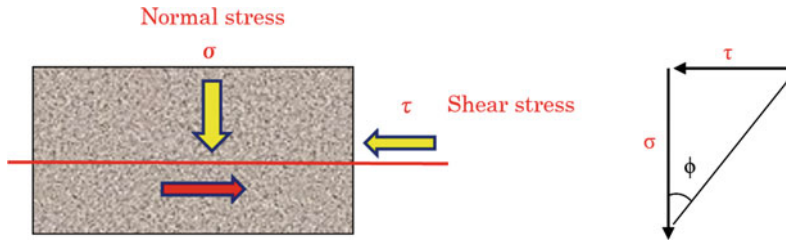


Fig. 8 The shearing within a soil mass with normal stress (σ), shear stress (τ) and shear resistance and the resulting internal friction angle (ϕ)

When a wet soil is dried, it becomes hard, like a brick. In this case, such a soil has a strong shear resistance, even without any normal stress. Such a shear-resistance factor that is independent of normal stress is expressed as cohesion (C).

In the case of soils, the shear stress at failure, τ_f is expressed by Eq. 1.

$$\tau_f = C + \sigma \cdot \tan \phi \quad (1)$$

Here,

τ_f Shear stress at failure (shear strength)

σ Normal stress

C Cohesion

ϕ Internal friction angle.

All friction angles dealt with in landslides are internal friction angles, and so it is simply called friction angle hereafter.

1.2.3 Effect of Pore Pressure

Landslides can be triggered by rainfall. Figure 9a illustrates the rainfall, and its infiltration into two types of slopes. The upper case is a slope with shallow landslides. The slope layer consists of two layers: a thin permeable soil layer overlies a

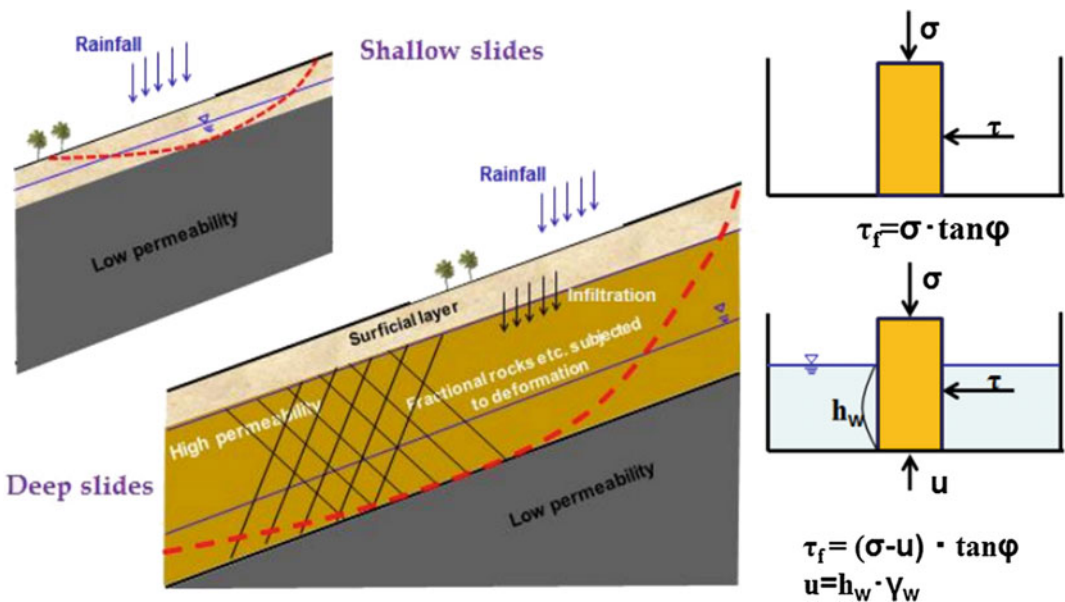


Fig. 9 Rainfall and groundwater formation and pore water pressure

less permeable layer such as bedrock. The lower case is a slope with deep landslides. The slope consists of three layers: a surficial soil layer, a fractured rock layer or weathered rock layer with high permeability, and a bedrock layer with low permeability. When rain water infiltrates into the slope, groundwater flow will appear above the layer with low permeability, at a shallow depth within a soil layer (A-top) and at a greater depth within the fractured/weathered rock (A-bottom). With continuous rain, the groundwater level gradually rises within the soil layer of the slope (A-top) or within the fractured rock layer (A-bottom). The groundwater rise will decrease the shear strength of the soils or fractured/weathered rocks and cause shallow landslides (A-top) or deep landslides (A-bottom). For the deep landslides, previous slope deformation or repeated small shear displacements during earlier rainfalls and earthquakes may decrease the shear strength at a potential sliding surface, such as at the base of the weathered rock.

Figure 9b illustrates the effect of a groundwater rise in a manner that most people can intuitively visualize. A yellow block stands on the floor of an empty pool. When a person wishes to move this block by pushing horizontally on it, the force necessary to move it is expressed in the units of stress (neglecting the component of cohesion) as

$$\tau_f = \sigma \cdot \tan \phi \quad (2)$$

As water fills the pool, water pressure (u) acts on the bottom of the block and its value is (water height) \times (unit weight of water). Water pressure acting on the sides of the block will be cancelled. Therefore, the stress acting on the floor of the pool below the block will be decreased from σ to $(\sigma - u)$. In this case, the shear stress at failure will be decreased by the value of the pore pressure,

$$\tau_f = (\sigma - u) \cdot \tan \phi \quad (3)$$

$(\sigma - u)$ is expressed as σ' which is called “effective normal stress”.

Water pressure inside the soil mass is called pore-water pressure because water exists in the pore spaces within the soil layer.

1.2.4 Pore-Water Pressure from Groundwater Flow Parallel to the Slope

Groundwater flows within the soil mass in a slope. So the pore-water pressure is not the same as in Fig. 9b. Figure 10 presents groundwater flow within a soil layer parallel to the bedrock. We will consider that the sliding surface of a landslide will be formed at the base of the soil layer. The value of water pressure acting on the soil base is NOT (water depth Z_w) \times (unit weight of water) as in Fig. 9. If stand pipes are installed at three different heights along the normal direction to the slope (shown in Fig. 10), the top of the water level in the three different

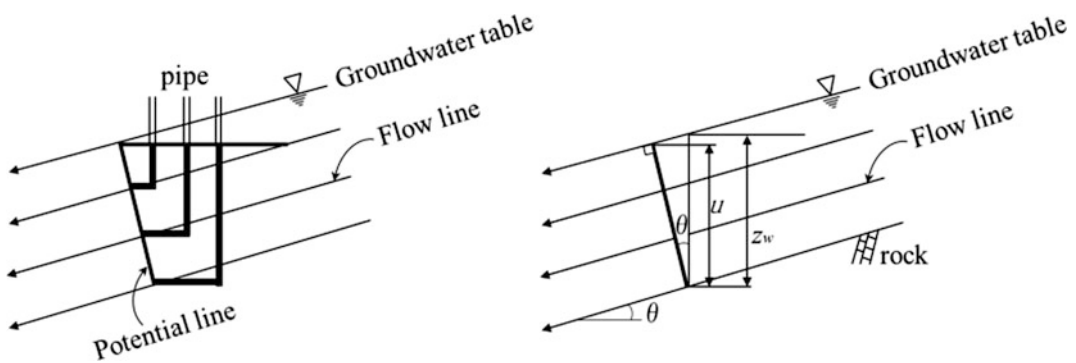


Fig. 10 Pore pressure in the groundwater flowing parallel to a slope

stand pipes must be the location of the surface of the groundwater. Water flows along the slope, and no water flows along the direction normal to the slope, which is called the equipotential line.

Therefore, the pore-water pressure (u) acting at the base of the soil layer is:

$$u = z_w \cdot \gamma_w \cdot \cos^2 \theta \tag{4}$$

Here, z_w is vertical depth of groundwater flow, γ_w is unit weight of water, θ is slope angle.

1.2.5 Pore-Water Pressure Acting on the Potential Sliding Surface from an Underlying Layer

Pore-pressure acting on the sliding surface can be supplied from an underlying layer (Fig. 11). The bedrock usually forms a less permeable layer. However, in a tectonically active area, such rock masses may be sheared by tectonic stress. Shear bands with large pores and high permeability may exist. When rain falls in these geological circumstances, usually dry channels passing across shear bands may carry water flows during rainfalls. The shear bands can become saturated by water. The elevation head may much higher than the elevation head at the base of a potential landslide mass (Fig. 11). If

the permeability of the potential landslide mass is much lower than the permeability of the shear bands, high water pressure may act on the base of the landslide-susceptible layer (potential sliding surface). This is one example of the mechanism by which pore-water pressure is supplied to a potential sliding surface.

1.2.6 Stress Acting on the Sliding Surface

We will consider the stress acting on a sliding surface which is assumed to be formed at the base of a soil layer (Fig. 12). Stress is the force acting on a unit area. So we will imagine a soil column with a unit length along the bed rock.

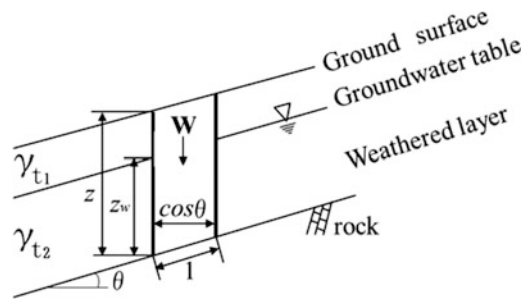
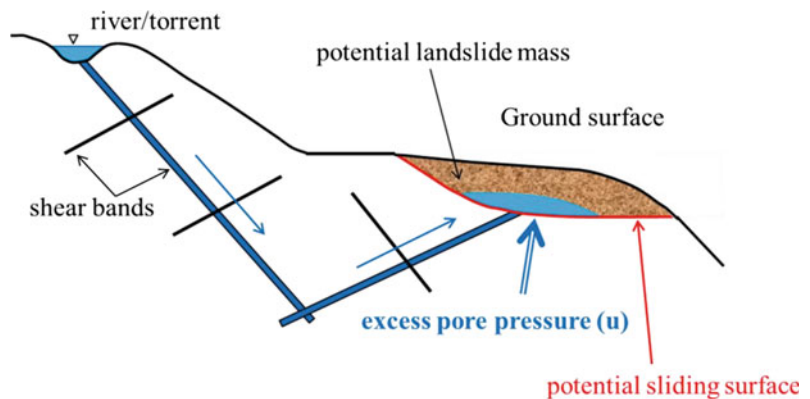


Fig. 12 Stress acting on the sliding surface within a simple slope

Fig. 11 Pore-water pressure acting on a potential sliding surface from an underlying layer. The excess pore-water pressure u in this example may be quite different from the example in Fig. 10



The self-weight of the soil column (W) is expressed as:

$$W = \{\gamma_{t1} \cdot (z - z_w) + \gamma_{t2} \cdot z_w\} \cos \theta \quad (5)$$

Here,

γ_{t1} wet unit weight of soil above the groundwater surface

γ_{t2} wet unit weight of soil below the groundwater surface.

Wet unit weight means unit weight of soils including the weight of pore water within the soil.

$$\begin{aligned} \tau &= W \cdot \sin \theta \\ &= \{\gamma_{t1} \cdot (z - z_w) + \gamma_{t2} \cdot z_w\} \cos \theta \cdot \sin \theta \\ &= \gamma_{t1} \cdot z \cdot \cos \theta \cdot \sin \theta + (\gamma_{t2} - \gamma_{t1}) \cdot \cos \theta \cdot \sin \theta \cdot z_w \end{aligned} \quad (6)$$

$$\begin{aligned} \sigma &= W \cdot \cos \theta \\ &= \{\gamma_{t1} \cdot (z - z_w) + \gamma_{t2} \cdot z_w\} \cdot \cos^2 \theta \\ &= \gamma_{t1} \cdot z \cdot \cos^2 \theta + (\gamma_{t2} - \gamma_{t1}) \cdot \cos^2 \theta \cdot z_w \end{aligned} \quad (7)$$

Equations 4 and 7 are combined to give Eq. 8.

$$\begin{aligned} \sigma' &= \sigma - u \\ &= \gamma_{t1} \cdot z \cdot \cos^2 \theta + (\gamma_{t2} - \gamma_{t1}) \cdot \cos^2 \theta \cdot z_w \\ &\quad - z_w \cdot \gamma_w \cdot \cos^2 \theta \\ &= \gamma_{t1} \cdot z \cdot \cos^2 \theta - \{\gamma_w - (\gamma_{t2} - \gamma_{t1})\} \cos^2 \theta \cdot z_w \end{aligned} \quad (8)$$

The difference between the wet unit weight above the groundwater surface and the unit weight below the groundwater surface is usually small, because soil and weathered rock layers usually include or retain water by capillary suction. In order to simplify the explanation and figure, we will ignore this effect in the following figures, and Eq. 8 may be simplified as Eq. 9.

$$\sigma' = \sigma - u = (\gamma_t \cdot z - \gamma_w \cdot z_w) \cos^2 \theta \quad (9)$$

1.2.7 Landslide Initiation Mechanism of Water/Pore Pressure Rise

Figure 13 illustrates the landslide initiation mechanism due to pore-water pressure in the case similar to Figs. 9 and 10. The upper figure shows the soil column with a unit length along the base of a soil (weathered rock) layer, assumed to be a layer susceptible to landsliding. The weight of the soil column (W in Fig. 12) is expressed as mg in Fig. 13.

Here, $m = \rho \cdot g \cdot Z \cdot \cos \theta$ (ρ : density of the soil layer).

The reason for the use of mass is that it is convenient for expressing the effect of earthquakes for earthquake-induced landslides. If no groundwater exists within the soil column (no pore-water pressure is acting), the initial stress at the bottom on this column is plotted as "I" in the stress-path figure of normal stress and shear stress (Fig. 13).

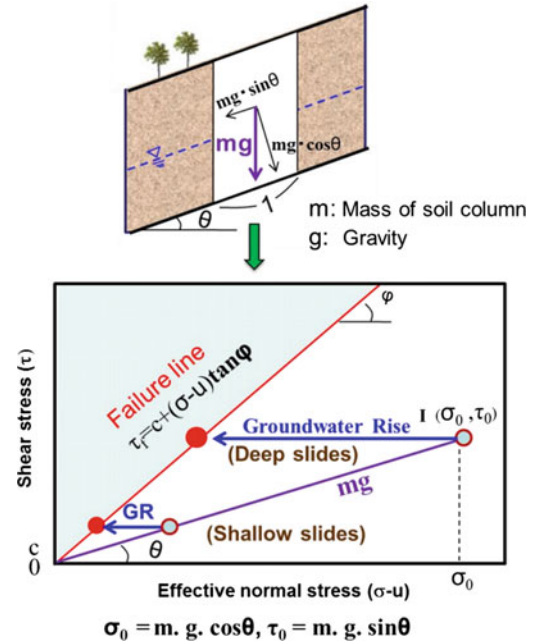


Fig. 13 Landslide-initiation mechanism due to groundwater rise/pore-water pressure rise

Normal stress at I is $\sigma_0 = mg \cos \theta$, Shear stress at I is $\tau_0 = mg \sin \theta$

Note:

- (1) The initial stress point is on the line with an inclination of slope angle θ .
- (2) The length between the origin and the stress point I represents $m \cdot g$ (weight of soil column W).

When the groundwater level increases, pore-water pressure (u) increases. The stress moves toward to the left.

When the stress reaches the failure line expressed by Eq. 1, shear failure will occur at the stress at failure (shown as red circle along the failure line).

$$\tau_f = C + \sigma \cdot \tan \phi \quad (10)$$

1.2.8 Landslide Initiation Mechanisms of Earthquakes

Earthquake-induced landslides may occur on both steep slopes and gentle slopes. Figure 14 presents the loaded stress in a slope (Fig. 14a) and the stress path during earthquakes (Fig. 14b). No pore-water pressure is considered in this figure before the earthquake. The initial stress

acting on the base of the landslide-susceptible layer ($m \cdot g$) in Fig. 14a, is plotted at I in Fig. 14b.

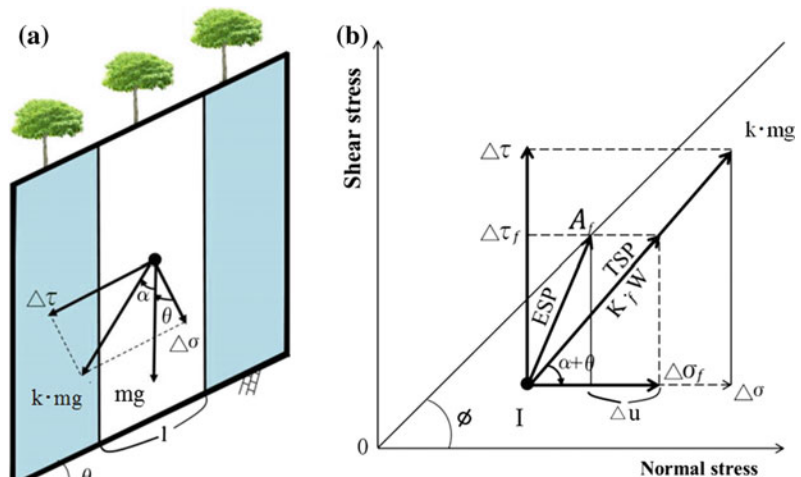
When an earthquake occurs and a seismic acceleration is loaded, the loaded stress is expressed by $k \cdot mg$; k is called the seismic coefficient, which is the ratio of the seismic acceleration (a) and gravity (g), namely $k = a/g$.

When expressing the direction of seismic force as α from the vertical direction, the direction of the seismic stress increment is expressed as $(\alpha+\theta)$. Here θ is slope angle.

The effective stress path during the earthquake is not the same direction as the total stress path. Figure 14 illustrates the case where the initial stress + the seismic stress reach the failure line. Pore-water pressure may be generated during seismic loading, then the effective stress path shifts from I to A_f .

Seismic stress is a dynamic stress, which is different from gravity (permanent) and pore-water pressure (relatively slow change). When the seismic stress reaches or even crosses the failure line, the difference between shear stress and shear resistance will be used to accelerate the soil column. When the time is vary (0.01–0.1 s or so) the shear displacement will be very limited and may stabilize after termination of ground shaking without becoming a rapid and

Fig. 14 Landslide-initiation mechanism – the initial stress + the seismic stress



TSP: Total Stress Path; ESP: Effective Stress Path

long-travelling landslide. However, the safety factor at the potential sliding surface has become less than 1.0. This is identified from the concept in static landslide (soil) mechanics that failure occurred at the potential sliding surface. Static landslide (soil) mechanics does not include the post-failure motion.

1.2.9 Landslide Initiation Mechanism by Seismic Loading in Addition to Water-Pore Pressure Rise

Earthquakes may occur during a very dry season, or in a wet season. Water pressure may increase even in a dry season, on slopes near reservoirs, rivers, lakes or under water, such as in submarine landslides. Figure 15 illustrates the stress path of landslide initiation for the effect of earthquakes and pore-water pressure (mostly rainfall).

Initial stress acting on the potential sliding surface will be located at I in Fig. 15. Pore pressure will act on the sliding surface by either groundwater rise in the landslide-susceptible layer or excess pore-pressure supply from the underlying layer, the stress point will move to A in Fig. 15, i.e. the distance between the stress in the slope and the failure line becomes closer. In this state, a smaller seismic stress (red arrow in

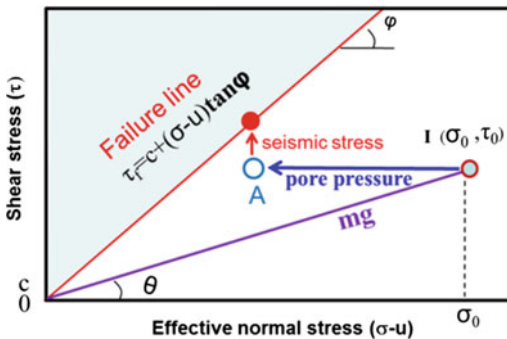


Fig. 15 Landslide-initiation mechanism by the combined effect of earthquake and pore pressure rise. Seismic stress in this figure is drawn in the vertical direction, with only a shear-stress increment. Seismic stress has both a shear-stress and a normal-stress component. However, the normal-stress increment will be nullified by the generated pore-water pressure when the sliding surface is fully saturated. In this case, the effective seismic stress increment is mostly vertical

Fig. 15) may cause failure of the soil layer. One possible example was the 2006 Leyte landslide in Philippines. It may have been triggered by a magnitude $M_s = 2.6$ earthquake after heavy rainfall. The landslide, which had a volume of around 20 million m^3 , killed over 1000 people.

1.3 A Sled Model for the Motion of Landslides

The basic model for landslide motion is the “Sled Model” which was originally proposed by Körner (1980). It is a model in which a sled moves down the slope and stops at the toe of the slope. During motion, the friction between the sled and the slope causes frictional energy loss. Energy losses other than friction are neglected in the sled model. (Note: The integrated computer simulation model (LS-RAPID) described in Sect. 3 is based on this sled model, but it has a function to consume a certain kinetic energy automatically when/where the kinetic energy loss is not neglected.) Figure 16 illustrates the concept of the sled model.

The motion of the landslide mass is viewed as the motion of a “point mass” at the center of gravity. We express the mass of this point mass (landslide mass) as “ m ”, and gravity of acceleration as “ g ” and the elevation of the center of gravity from a datum (elevation of the center of gravity of the landslide mass after deposition) as “ h ”, and slope angle “ θ ”, which is not constant, but varies along the slope.

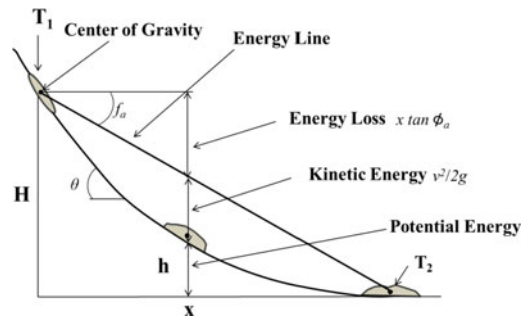


Fig. 16 The sled model for the motion of landslides

In this case, the landslide mass before motion has a potential energy $m \cdot g \cdot h$. The landslide mass after deposition has zero potential energy.

The energy at the location of X during motion is a sum of potential energy and kinetic energy $1/2 (m \cdot v^2)$.

Energy loss by friction from the starting point to X is calculated by Eq. 11.

$$E_f = \int_0^x mg \cdot \cos \theta \cdot \tan \phi_a \frac{dx}{\cos \theta} = mgx \cdot \tan \phi_a \quad (11)$$

Here:

E_f	Energy loss by friction
$\tan \phi_a$	coefficient of friction
ϕ_a	apparent friction angle
$m \cdot g \cdot \cos \theta$	normal stress acting on the slope per unit horizontal length
$dx/\cos \theta$	slope length corresponding unit horizontal length
$mg \cdot \cos \theta \cdot \tan \phi_a \cdot (dx/\cos \theta)$	frictional energy loss per unit horizontal length

The concept of the Sled Model assumes that the value of the coefficient of friction is constant during the whole travel distance.

The mass of landslide is “ m ” and the gravity of acceleration is “ g ”. All energies are divided by $m \cdot g$ and expressed by the unit of height (called “head”) in the manner of hydraulics.

Total energy is the same at the starting point, at the location x and at the deposition point.

Total energy at the starting point = potential energy (H).

Total energy at location x = energy loss ($x \cdot \tan \phi_a$) + kinetic energy ($v^2/2g$) + potential energy ($m \cdot g \cdot h$).

Total energy at the deposition point = energy loss ($X \cdot \tan \phi_a$).

In this figure (Fig.16), it is known that the apparent friction angle and the slope geometry will decide the velocity of the landslide mass.

The sled mode is used in back analysis. If the apparent friction angle is estimated from a previous similar case, the travel distance and average velocity will be known.

1.3.1 Apparent Friction Angle Mobilized during Motion

The sled model assumes that the coefficient of friction ($\tan \phi_a$) is constant during the whole travel distance, which is called the average coefficient of friction or equivalent coefficient of friction.

However, the real friction at the sliding surface during motion will be affected by the following three components, 1) pore-water pressure (u) acting in the shear zone, 2) normal stress (σ) acting on the sliding surface which is affected by the depth of landslide mass, and 3) the effective friction angle mobilized during motion (ϕ_m).

When considering the apparent friction angle mobilized during motion, Eq. 11 will be replaced by Eq. 12 based on (u), (σ) and (ϕ_m).

$$E_f = \int_0^x mg \cdot \cos \theta \cdot \tan \phi_a \frac{dx}{\cos \theta} = mgx \cdot \tan \phi_a \tan \phi_a \approx \frac{\sigma - u}{\sigma} \cdot \tan \phi_m \quad (12)$$

Here:

- ϕ_a apparent friction angle mobilized during motion
- ϕ_m effective friction angle mobilized during motion
- σ normal stress
- u pore water pressure.

Precisely expressing the right side of the second line of Eq. 12, cohesion during motion is usually negligible, however, viscosity or kinetic energy loss due to collision may not be negligible. Usually those values in landslides during motion are not so high when compared with frictional energy loss. Therefore, the equation is expressed by not an equal sign ($=$), but by nearly equal (\approx).

Though the sled model assumes that apparent friction angle is constant through the whole travel distance, the effective friction angle during motion (ϕ_m) will be different in soils in the shear zone, depending on its degree of saturation. Pore pressure mobilized during motion in the shear zone will change in sheared soils and with

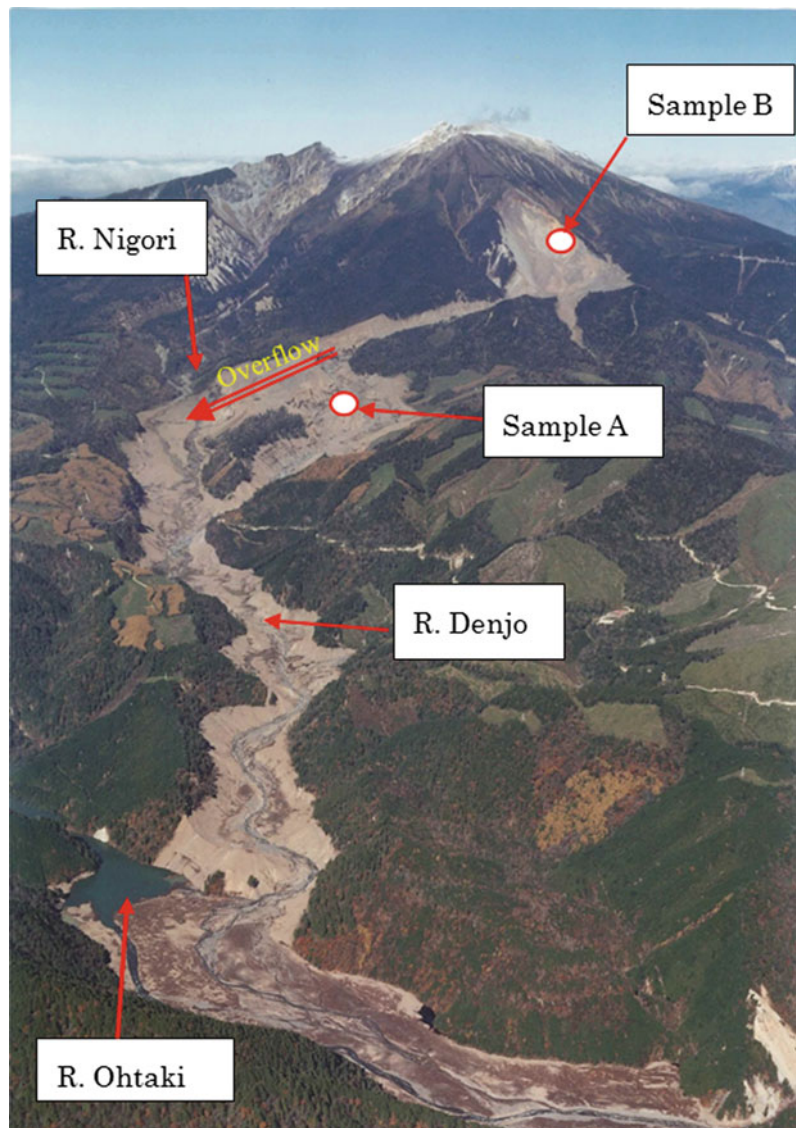
shearing conditions, saturation degrees and drainage conditions.

If apparent friction ϕ_a can be measured or estimated from geotechnical testing of the soils during shear in on the sliding surface, the motion of the landslide can be numerically calculated from the slope geometry. Accordingly, the prediction of landslide motion and landslide hazard assessment becomes theoretically possible.

Sassa (1988a) presented an application of the sled model to the motion of the 1984 Ontake landslide. Figure 17 shows an air photo of the

Ontake landslide. The traveling landslide mass produced undrained loading on the torrent deposit and generated pore water pressure. Pore pressure (u) that generated the undrained loading is affected by the pore pressure parameter B (Fig. 18 right). The torrent deposit is saturated at 95–100%, B -value for 0.6–0.9. The estimated apparent friction angle was 3.4° in the lower stream, 6.9° in the middle stream and 14° in the upper stream to the initial landslide. This study presented the effectiveness of applying the sled model to rapid and long-runout landslides.

Fig. 17 A large-scale landslide ($3.6 \times 10^7 \text{ m}^3$) was triggered by the 1984 Nagano-ken Seibu earthquake in the Ontake volcano. It travelled over 12 km at 80–100 km/h (22–28 m/s) through R. Denjo and R. Ohtaki. A part of landslide mass overflowed R. Denjo on the curve and crossed over the mountain ridge between R. Nigori and R. Denjo and entered into R. Nigori



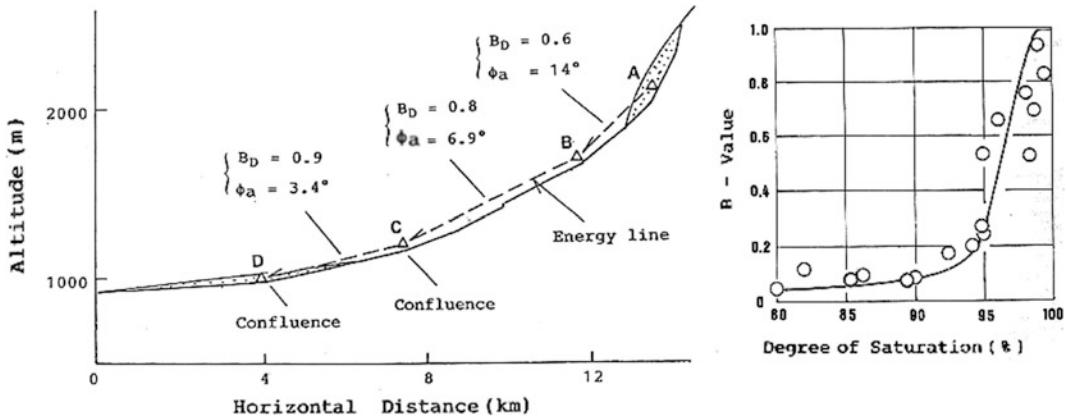


Fig. 18 Section of the Ontake landslide travel path and its energy line estimated from shear tests of the sample (A) taken from the deposit of R. Denjo (*left*). The

relationships of B-value and the degree of saturation of the sample (A) is from an isotropic triaxial compression test (*right*) (from Sassa 1988a)

The undrained dynamic-loading ring-shear apparatus (UDRA) had not yet been developed in 1988, and the direct measurement of shear resistance mobilized during the initiation and the motion of landslides was not measured at this stage. Thereafter, Sassa (1995), Sassa et al. (2004) developed a new dynamic-loading ring-shear apparatus. Then, shear resistance mobilized during the motion of landslides could be estimated from the developed undrained dynamic-loading ring-shear apparatus. This apparatus provided an effective tool in the progress of landslide dynamics.

2 Undrained Dynamic-Loading Ring-Shear Apparatus (UDRA)

Abstract

Section 2 describes the undrained dynamic-loading ring-shear apparatus (UDRA). It has enabled researchers to develop landslide dynamics by reproducing the processes from the initial stage of stress before landslide occurrence, and stress changes due to seismic loading or pore pressure increase or other types of stress loading, to the formation of a sliding surface and the

post-failure motion. This apparatus can maintain an undrained condition during failure and post-failure motion and can measure generated excess pore water pressure. To do this, a new technical development was needed.

Section 2.2 describes the mechanical structure of the apparatus and servo-control system in order to load any type of stress, including seismic stress, and to maintain an undrained state in the shear box during shearing. Section 2.3 explains the friction and the contact force of the rubber edge, which prevents water leakage between the upper shear box and the lower shear box and the correction of these two effects. Section 2.4 describes the various types of undrained dynamic-loading ring-shear tests and Sect. 2.5 presents examples of three basic types of figures of the ring shear tests; time series of data, and stress path, shear stress-shear displacement relationships.

Keywords

Landslide dynamics • Undrained ring shear test • Initiation mechanism • Sled model

2.1 Introduction

The development of landslide dynamics requires the measurement of shear resistance mobilized during the initiation of rain-induced and earthquake-induced landslides, and also the motion of landslides travelling onto the lower slope or an alluvial deposit.

Sassa et al. (2004) have developed a new undrained dynamic-loading ring-shear apparatus (UDRA) based on a series of developments of ring shear apparatuses from DPRI-1 (Sassa 1984), DPRI-2, 3, 4, 5, 6 and DPRI-7.

The UDRA was modified and improved to be used abroad without support from the producing companies. The first one was ICL-1 (a transportable UDRA) which was donated to the university of Rijeka in Croatia in 2012 by a SATREPS (Science and Technology Research Partnerships for Sustainable Development) funded by the Japan Science and Technology Agency (JST) and the Japan International Cooperation Agency (JICA). The second one is ICL-2 (a high-stress UDRA, maximum loading capacity and undrained capacity is 3000 kPa). ICL-2 is the latest version. Easy and low-cost maintenance for the most sensitive undrained rubber edge and also the loading system have been developed. Various safety systems have

been developed to prevent possible damage to the apparatus by mishandling based on the problems experienced by many trainees invited from Vietnam. The apparatus was donated to the Institute of Transport Science and Technology (ITST) of the Ministry of Transport, Vietnam in 2015. It operates well in Vietnam.

The series of dynamic-loading ring-shear apparatus is listed in Table 1 (Sassa et al. 2014a). This chapter describes mainly the latest version ICL-2 (Sassa et al. 2014b).

Figure 19 presents the concept of the undrained dynamic-loading ring-shear apparatus (UDRA). A sample is taken from the soil layer (left-top figure) where the sliding surface of the initial landslide formed within the slope to study the shear behavior and the pore pressure generation in the process of failure and the formation of the sliding surface. Another sample (right figure) is taken from the lower slope or torrent deposits or the alluvial deposit within which a sliding surface will be formed during the motion of the landslide. Those samples are set in the ring shear box (left-bottom) and a monotonic-shear stress or seismic shear-stress or pore pressure are loaded. When shear failure has occurred, the rotation will be started. The generated pore-pressure, mobilized shear-resistance and the resulting shear displacement are monitored. The basic concept of

Table 1 The series of the dynamic-loading ring-shear apparatus developed by Sassa et al. since Sassa (1992)

Version	(1992) DPRI-3	(1996) DPRI-4	(1997) DPRI-5	(1997) DPRI-6	(2004) DPRI-7	(2011) ICL-1	(2012) ICL-2
Inner diameter (cm)	21.0	21.0	12	25.0	27.0	10.0	10
Outer diameter (cm)	31.0	29.0	18	35.0	35.0	14.0	14.2
Max. height of sample (cm)	9.0	9.5	11.5	15.0	11.5	5.2	5.2
Shear area (cm ²)	408.41	314.16	141.37	471.24	389.56	75.36	79.79
Max. shear speed (cm/s)	30.0	18.0	10.0	224.0	300.0	5.4	50
Max. normal stress (kPa)	500	3000	2000	3000	500	1000	3000
Max. pore-water pressure (kPa)	–	490	400–600	400–600	400–600	1000	3000

DPRI-3 is the trial version of an undrained dynamic-loading ring shear apparatus. It could maintain some pore pressure within the shear box, and pore pressure was monitored to some extent. But it did not reach a practical undrained test level

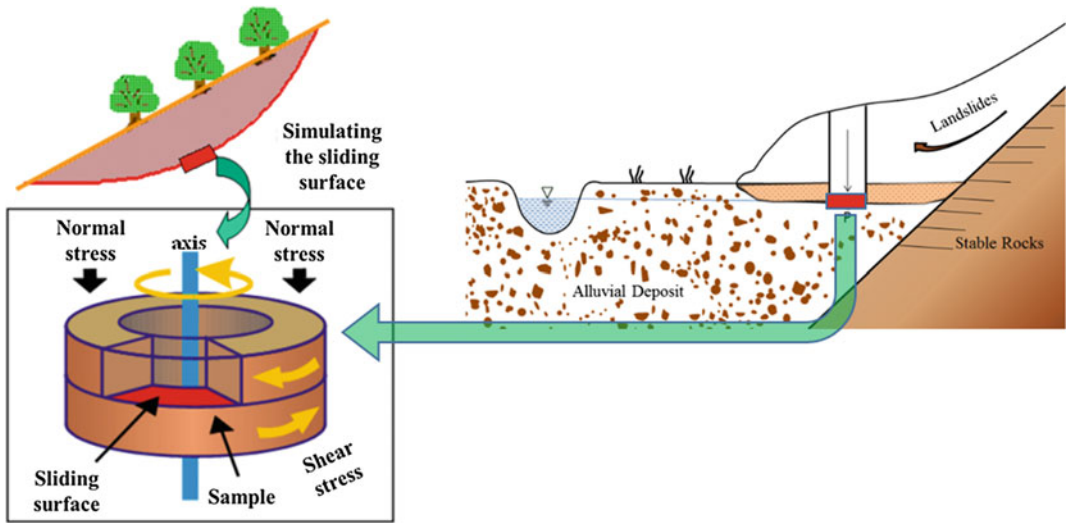


Fig. 19 Schematic figure of concept of an undrained dynamic-loading ring-shear apparatus (UDRA)

UDRA is the reproduction of landslide processes within the testing apparatus and the observation of the shear behavior, namely a physical simulation of landslides focusing on the sliding surface.

2.2 Structure and Control System of the Undrained Dynamic-Loading Ring-Shear Apparatus (ICL-2)

2.2.1 Outline and Mechanical Structure

Figure 20 presents a photo of the setup for the high-stress undrained dynamic-loading ring-shear apparatus (ICL-2), which was installed at the UNESCO-KU-ICL UNITWIN laboratory in Kyoto University. The system includes the following six units:

- (1) Computer system (the left screen is to set the testing and the recording conditions, the right screen is to monitor the stress path and the time series data of pore pressure, mobilized shear resistance, loaded normal stress, shear displacement etc.).
- (2) Main control unit for control and monitoring (amplifies of monitoring and servo-controllers of normal stress, shear stress and gap control).

- (3) Main ring shear apparatus consisting of the shear box, normal stress loading system and shear stress loading system.
- (4) Power supply box for normal stresses and shear stresses.
- (5) Pore-pressure supply unit for the servo-pore-pressure-control test.

Close-up photos of the shear box are shown in Fig. 21. The right photo includes the hanging frame of the upper shear box and the loading cap, plus the water supply pipe (I) and the drainage pipe (H).

The pipe (I) is disconnected during the test because the lower ring will be rotated. The drainage pipe (H) does not always need to be disconnected during tests because a valve can be closed, but often it is removed during the undrained test.

- A: Shear box
- B: Normal stress loading piston
- C: A pair of two shear stress sensors
- D: Loading cap
- E: Hanging frame to lifting the loading cap
- F: Pore pressure sensor
- G: Connection to the pore pressure control system

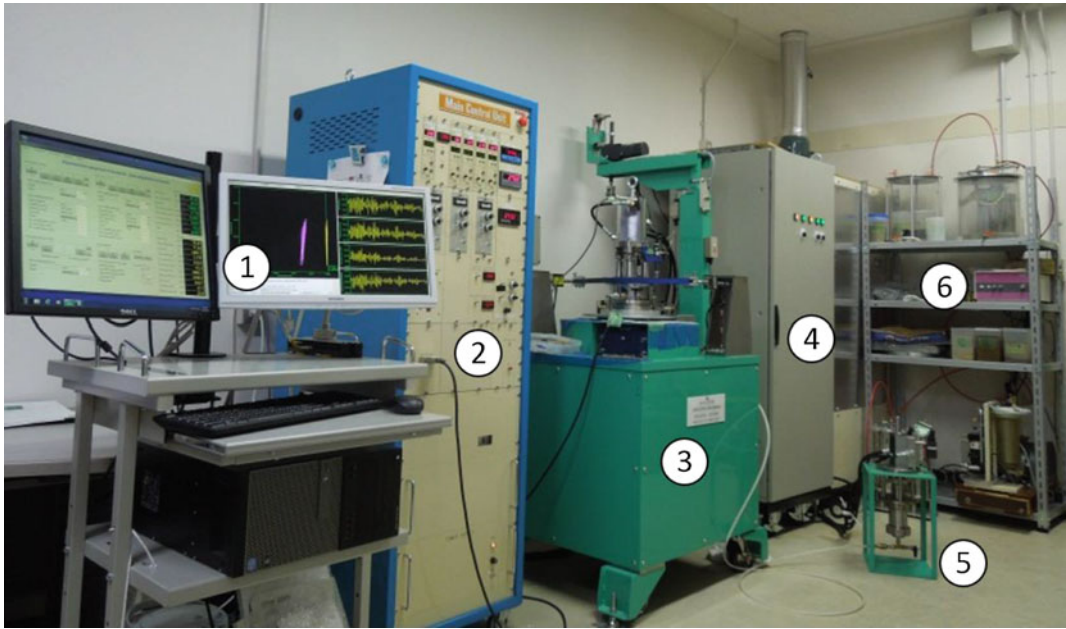


Fig. 20 Photo showing the setup of the ICL-2 apparatus



Fig. 21 Photo of shear box and normal stress loading piston and shear stress sensor. *Left photo* connecting the pipe (G) to the pore pressure control system. *Right photo* connecting the pipe for the de-aired water supply (I) and the pipe for drainage (H)

H: One-touch plug for the water drainage from the shear box

I: One-touch plug for the de-aired water supply from the bottom of the shear box

Figure 22 is a diagram of the mechanical structure of ICL-2. The parts of the apparatus are

coded with different colors in the figure as follows:

Part 1 (Gray color) is the stable part on the bottom.

Part 2 (Yellow color) is the lower shear box and the rotating table, and rotates horizontally for shearing.

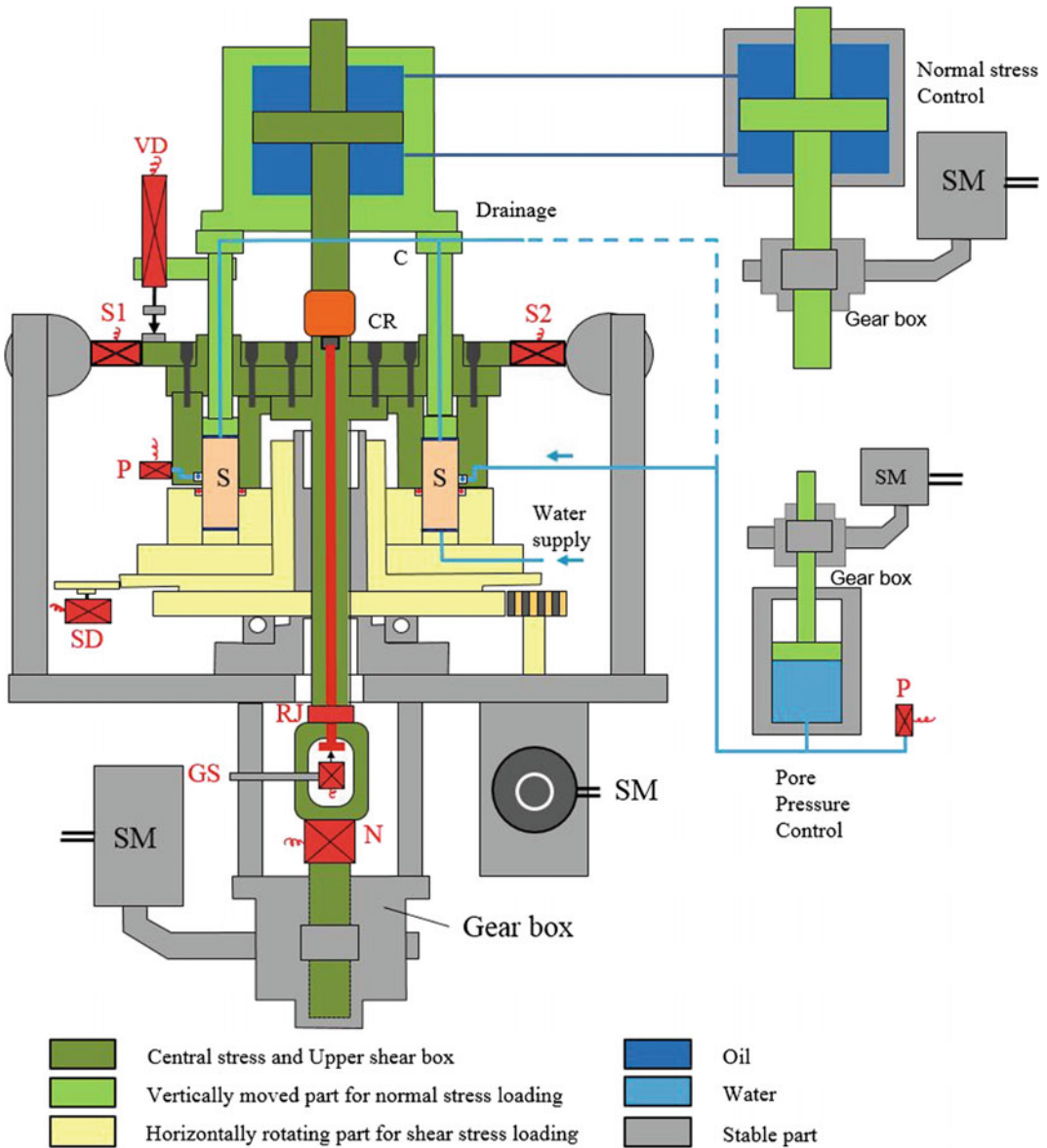


Fig. 22 Mechanical structure of ICL-2 (central section of the main body); S sample; CR connection ring; RJ rotary joint; C connection; N load cell for normal stress; S1, S2 load cell for shear resistance; GS gap sensor; SM servo-motor;

Part 3 (Dark green color) is the upper shear box, the loading cap and the central axis. This part can rotate horizontally and move vertically. This part is horizontally retained by a pair of load cells (S1 and S2) which monitor shear stress, and is vertically retained by the load cell, which monitors normal stress (N). Each load cell is very slightly extended or compressed as required to measure forces. The part below the rotary joint (RJ) is not rotatable, but is moved vertically by a servo-motor for gap control. The whole dark green part is moved to adjust the gap between the upper and lower shear boxes using the gap control servo-motor.

Part 4 (Light green color) is the loading piston to supply normal stress and the loading rods to the sample. When oil pressure is increased in the lower chamber (blue) of the loading piston, the central axis is pulled upward. In reaction, the housing of the loading piston and the loading rods are pushed down on the sample, thus a normal stress is loaded. The normal stress change is measured by the load cell (N), because the tensile stress is acting through the central axis during the process of oil pressure increase in the lower chamber of the piston.

2.2.2 Control System for the Undrained Dynamic-Loading Ring-Shear Apparatus (ICL-2)

The undrained dynamic-loading ring-shear apparatus has four servo-control systems for normal stress, shear stress/speed/shear displacement, pore pressure and gap. The system is outlined in Fig. 23.

1. Normal-stress servo-control system

Normal stress (static and seismic) is produced by two loading piston system (LP-1 and LP-2) controlled by a servo-motor (SM; gray color) (Fig. 23). Normal stress to the soil sample is transferred through three upright loading rods connected to the loading piston (LP-2). When a control signal (red line) is sent from the computer to increase normal stress, the servo-motor rotates and pulls the loading piston 1 (LP-1, dark blue)

down and increases the oil pressure in the lower chamber of LP-1, resulting in increment of oil pressure of the lower chamber of LP-2 (LP-1 and LP-2 are exactly same each other). It will pull up the central axis and push down the loading rods and plate. Therefore, normal stress to the sample will be increased. The normal stress acting on the sliding surface is measured by the vertical load cell for normal stress (N; red color). This measured value is used as the feedback signal (FS, black line) to the servo-amplifier (SA). The servo-amplifier (SA, red color) automatically controls the value of loaded normal stress to the predetermined value by sending a control signal to the servo-control motor (SM).

2. Shear (stress/speed/displacement) servo-control system

As shown in Fig. 23 (in the third column), shear stress is generated by a servo-control shear motor (SM, gray color). An electric signal of shear stress control is supplied by the computer through the servo amplifier (SA) to the servo motor. The servo-control shear motor rotates the lower shear box (yellow part) through a gear, while the upper shear box (dark green part) is retained to two pedestal pillars through the shear stress measuring sensors S1 and S2. The shear stress mobilized on the sliding surface is measured by $S1 + S2$, because the torque caused by the shear stress on the shear surface and the rubber edge shear resistance is balanced by the torque applied by the two shear load cells. The servo-control motor applies the planned shear load by instruction from the control signal given from the computer through the servo-amplifier. The third illustration in Fig. 23 presents the control signal (red line) to the servo-motor and the feedback signal (black line) from the shear load cell in the shear-stress control test. In the seismic loading tests, seismic shear stress is calculated from a seismic record and saved in the computer. This seismic shear stress is used as the control signal (Sassa et al. 2014b). Shear stress control is mostly used. However, shear speed control is possible in this servo-motor. But the feedback signal is not used. The servo-motor will

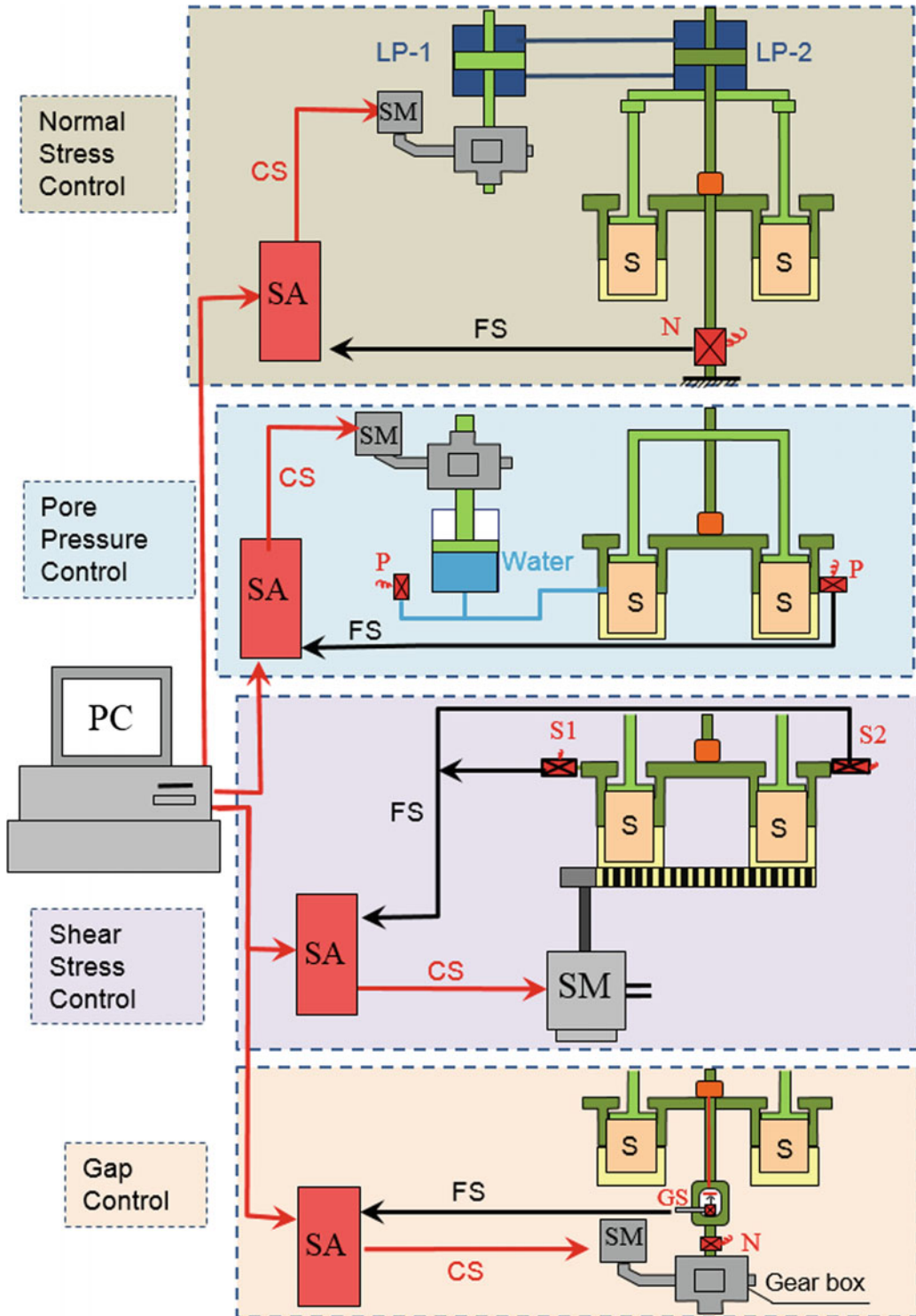


Fig. 23 Servo-control system of ICL-2; *PC* computer control system; *S* sample; *N* load cell for normal stress; *S1*, *S2* load cell for shear resistance; *GS* gap sensor; *FS* feedback signal; *CS* control signal; *SM* servo-controlling motor; *LP* loading piston; *SA* servo-amplifier

rotate exactly with the control signal. A shear displacement control test is sometime used as a very slow speed test, for example 200 cm shear displacement for 12 h during night. In this case, the monitored value of the shear displacement sensor is used as the feedback signal. The maximum speed of ICL-2 is 50 cm/s in the center of the sample. Any lower speed is possible in the shear displacement control mode.

3. *Pore-water pressure servo-control system*

To simulate rain-induced landslides, pore pressure control tests are conducted. The control system is shown in the second column of Fig. 23. Initially the pore pressure increase rate or program is saved in the computer. The control signal is given to the servo-amplifier (SA). It rotates the servo-motor (SM) and then water pressure is supplied to the shear box. The feedback signal is returned from the pore-pressure sensor (P: red color), thus automatically controlling the pore pressure.

4. *Gap servo-control system*

The gap control system (including gear box, servo-control motor and gap sensor, GS) is shown in the lowest column of Fig. 23. To maintain an undrained state during testing, the gap between the lower and upper shear box must be maintained to create a contact stress at the rubber edge that is greater than the pore water pressure generated within the shear box. The gap value is automatically kept constant by the gap control servo-amplifier (SA: red). SA sends a control signal to the servo-control motor (SM) for gap control and receiving a feedback signal from the gap sensor (GS). Then, it keeps the gap always the same, with a given value. The precision of the gap value in the ICL-2 apparatus is 1/1000 mm. The gap between the upper shear box and the lower shear box is precisely controlled, even when the samples dilate during shearing or during cyclic or seismic loading. When the sample dilates and tends to increase the

gap, the servo-motor immediately responds to maintain pressure to keep the gap constant.

2.3 Effects of the Rubber Edge and Its Correction

The undrained testing of ring shear tests in ICL-2 is very difficult task because a high-water pressure of up to 3 MPa must be maintained within the shear box without any water leakage. The contact force of the rubber edge on the bottom of the upper ring must be kept always greater than the generated pore water pressure inside the shear box. The gap between the upper shear box and the lower shear box is always kept same during any shear stress loading (even seismic loading) and any speed of shearing (50 cm/s in the center of sample) and any change in the total or the effective normal stress through the entire test using the feedback signal of gap sensor (GS) and control signal to the servo-motor (SM) for gap control (as shown in Fig. 23).

The contact force of the rubber edge to the bottom of the upper shear box necessarily causes the friction which increases the measured shear resistance, and the contact force between the rubber edge and the bottom of the upper shear box affects the measured normal stress. Those two effects must be corrected to obtain the shear stress and the normal stress acting on the sliding surface.

2.3.1 Structure of the Rubber Edge and Forces Acting on the Rubber Edge

The most important part of the undrained dynamic-loading ring-shear apparatus is the rubber edge installed between the upper ring shear box and the lower ring shear box to maintain an undrained state in the shear box.

Figure 24 is a close up of the rubber edge. A red color rubber edge is placed on the lower shear box, and a Teflon ring holder presses on the rubber edge and the stainless steel ring holder, which was fixed to the lower ring by screws, further presses on the Teflon ring holder. The

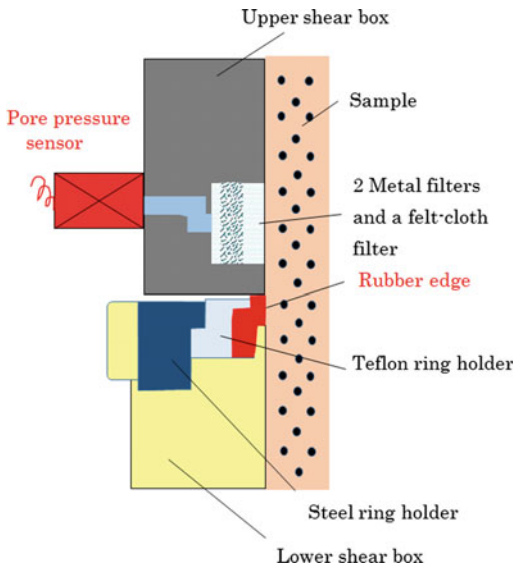


Fig. 24 Close up figure of the rubber edge and its holder components

rubber edge is not pasted by glue, only pressed by a Teflon holder. It can easily be changed by a new rubber edge without any processing. A Teflon holder has two roles; one is to support the rubber edge in a vertical position against a high horizontal pressure loaded from the saturated sample (up to 3 MPa at full liquefaction). Another role is protection from possible damage due to direct contact between the two shear boxes when the rubber edge thickness has been reduced after repeated and long shearing and also ensure possible minimal change between the gap distances in a rapid stress change.

A further close-up schematic figure of the rubber edge (red color) and its adjacent parts is shown in Fig. 25. The red color rubber edge is pushed to the left by a horizontal stress (yellow arrow) from the saturated sample. The Teflon ring holder pressed down by the steel ring holder provides the supporting force (blue arrow) to the right as the reaction. Accordingly, the rubber edge is horizontally pushed from both sides and tends to push up the upper shear box because the gap between two shear boxes is kept constant. Therefore, the vertical force (F_{rubber}) is produced vertically from the rubber edge to the upper shear box.

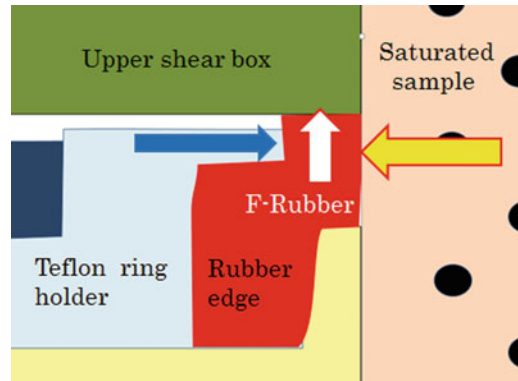


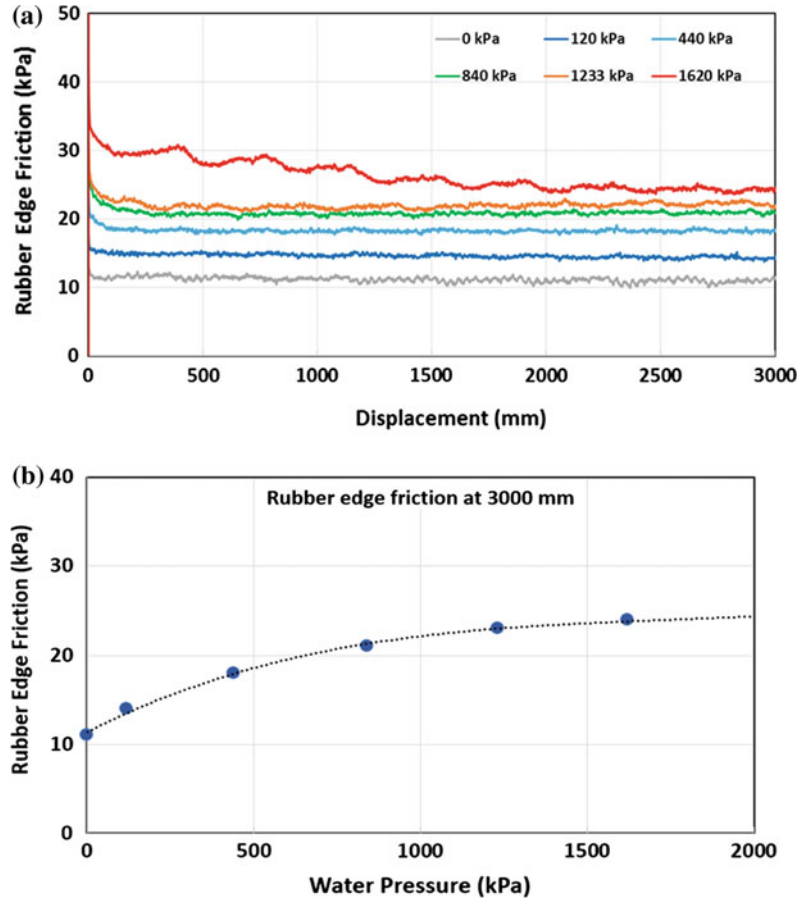
Fig. 25 The acting forces on the rubber edge

2.3.2 Rubber Edge Friction

The value of rubber edge friction must be changed by the rubber edge contact force (F_{Rubber}) with the upper shear box. F_{Rubber} is changed by the horizontal pressure. To investigate this friction, the shear box is filled with water, which is sheared at different water pressures. Figure 26a shows the measured shear resistance mobilized during shearing of water until 3000 mm shear displacement. Water has no shear resistance, so it is the effect of the rubber edge friction on the shear stress. As seen in this figure, rubber edge friction is between 10 and 33 kPa. The most important parameter in landslide dynamics is the steady-state shear resistance after a large shear displacement. To obtain this value, 2000–3000 mm shear displacement is carried out. The shear stress due to rubber edge friction is 12–24 kPa and converges to the higher water pressure as shown in Fig. 26b.

The rubber edge is coated by Teflon spray and further coated by vacuum silicon grease (high-vacuum sealing compound) before each test. The value is affected by the quality of this hand-made coating and also by the smoothness of the rubber edge. If the rubber edge height is not the same throughout the inner rubber edge and the outer rubber, initially a long shearing will be carried out to make it smooth. Therefore, it is not always the same. It must be measured and the value must be subtracted from the measured value of shear resistance to obtain the shear resistance working on the shear surface.

Fig. 26 Rubber edge friction measured by shearing water in the shear box under different water pressures. **a** Shear stress due to the rubber edge friction at six different water pressures from 0 to 1620 kPa. **b** Shear stress by the rubber edge friction at 3000 mm shear displacement. *Note* the steady-state shear resistance, which is the most important parameter to decide the landslide velocity and travel distance, is obtained and measured around 2–3 m shear displacement



2.3.3 Rubber Edge Contact Force

All vertical forces acting on the shear zone (F-sample) and the rubber edge (F-rubber) and in the central axis (F-axis) are shown in Fig. 27a. F-axis is measured by a vertical load cell (N). When the self-weight of the upper shear box and the loading piston is cancelled as the dead weight from the stress monitored by the vertical load cell (N), the following expression is obtained.

$$F\text{-sample} = F\text{-axis} - F\text{-rubber} \quad (13)$$

F-rubber should be proportional to the horizontal stress working at the rubber edge and the

horizontal stress should be proportional to the vertical stress. When approximating the relationships, F-rubber to be $\beta \cdot F\text{-axis}$,

$$F\text{-sample} = (1 - \beta) \cdot F\text{-axis} = \alpha \cdot F\text{-axis}$$

Dividing by the shear area of the ring shear box, the following relation will be obtained.

$$\sigma = \alpha \cdot \sigma_m \quad (14)$$

- σ_m Measured normal stress calculated by F-axis/shear area
- σ Normal stress working on the shear surface
- α Normal stress correction factor.

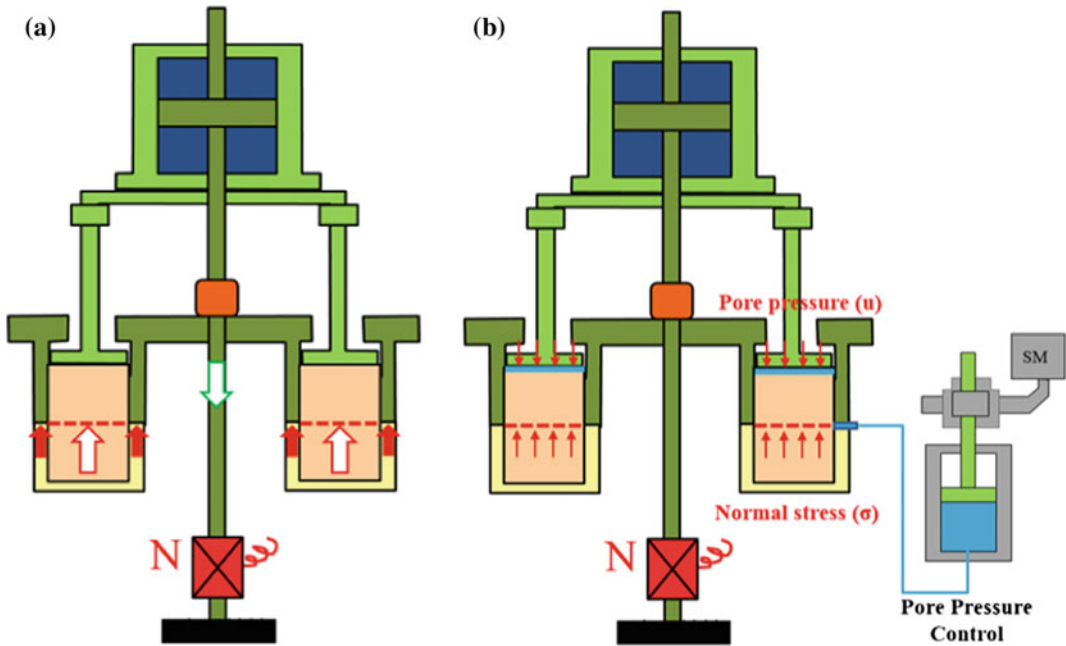


Fig. 27 Investigation of the normal stress that acts on the shear surface. **a** Balance of vertical forces. F-sample (normal stress on the shear surface: white arrow) + F-rubber (the rubber edge contact force: red arrow) +

F-axis (tensile force on the central axis: green arrow) = 0. **b** Measurement of the total normal stress acting on the shear surface of saturated soil samples after consolidation under a given normal stress

Investigation of the normal stress correction factor α

The normal stress working on the shear surface was experimentally investigated for saturated silica sands at different normal stress levels by the following test, shown in Fig. 27b.

1. Consolidate the saturated sample at a given normal stress, such as 0, 0.5, 1, 1.5, 2, 2.5 MPa.
2. Increase pore water pressure using the pore pressure control system until the loading plate starts to lift for each normal stress test, i.e. a water layer is formed between the loading plate and the sample.
3. Measure the pore water pressure at this stage. The side friction of the shear box should be negligible because no effective stress is working within the soil mass. In this condition, the water pressure (u) in the water layer below the loading plate and the normal stress (σ) working on the sliding surface must be the same.

Figure 28a presents the relationship between the measured normal stress (F-axis/shear area) and the pore water pressure at the instant when the loading plate starts to lift, namely a thin water layer is formed below the loading plate. The pore pressure, which is equal to the practically acting normal stress on the shear surface in the test (Fig. 27b) is smaller than the measured normal stress by F-axis/area.

Figure 28b shows the normal stress correction factor (α), which is the ratio between the measured normal stress ($\sigma_m = \text{F-axis/area}$) and the normal stress working on the shear surface (σ). Table 2 presents its numerical values of (σ_m), u (same with σ) and the normal stress correction factor (α). The value of the normal stress correction factor changes from 0.81 to 1.0. The rubber edge behaves almost as a rigid body in the low normal stress (100 kPa). The rubber edge contact forces will increase with the normal stress, but it will convert to around a certain value (0.81 in this case) in the higher stress range.

The hardness index of used rubber edges is around 90° or more. The rubber hardness index is

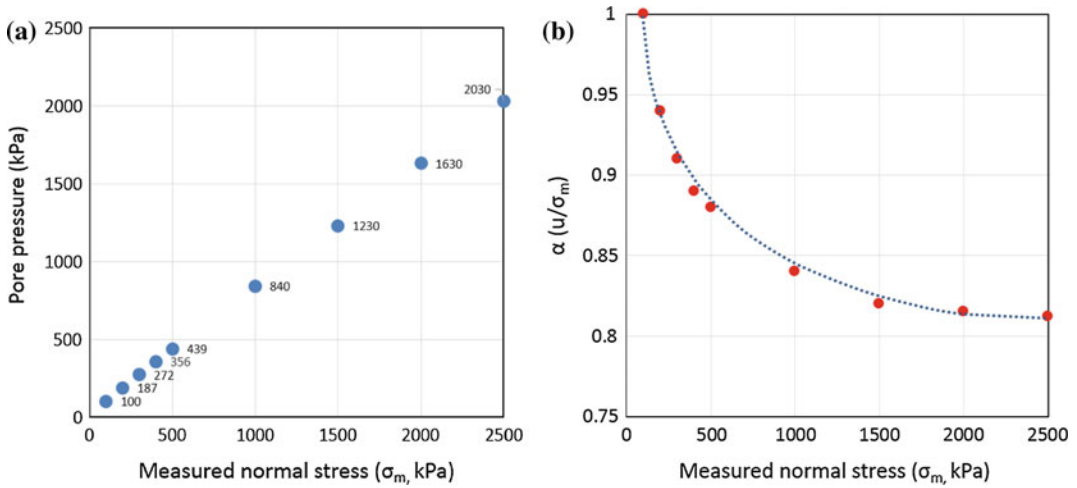


Fig. 28 Correlation between pore pressure (u) and normal stress (σ) in saturated and consolidated soils samples at different normal stress

Table 2 Values of measured normal stress (σ), pore pressure (u) and normal-stress correction factor (α)

Measured normal stress (kPa)	Pore pressure (kPa)	$\alpha (u/\sigma_m)$
2500	2030	0.812
2000	1630	0.815
1500	1230	0.82
1000	840	0.84
500	439	0.88
400	356	0.89
300	272	0.91
200	187	0.94
100	100	1.00

not precisely decided in its production. And the rubber edge hardness and deformation characteristics can be changed because of repeated stress loading during the use of the rubber edge. Therefore, it must be measured, referring to Fig. 28b and Table 2.

Sample: silica sand, $B_D = 0.96$

For setting $\alpha = 1.0$, the measured normal stress is not the same if there is pore water pressure in the water layer. For setting $\alpha = 0.81$, the measured normal stress is the same as the pore water pressure in the water layer, which equals the normal stress acting on the shear surface.

2.3.4 Correction of Two Effects of Rubber Edges on Shear Stress and Normal Stress

Granular materials such as sands and soils cannot maintain any cohesion after a large shear displacement. Interlocking and any chemical bonds should be lost during the large shear displacement. This assumption will be true for sands and other normal soils. This assumption is used for correction of normal stress.

ICL-2 has a function to input the normal stress correction factor in the normal stress control system. The stress path of Fig. 29a was obtained

by a monotonic shear-stress control test (shear-stress increasing rate is 2 kPa/s). The rubber edge correction factor (α) was set as 0.9 (around middle of Table 2) in the control computer before the test.

1. Correction of rubber edge friction

25 kPa was reduced from the graph of Fig. 29a, referring the rubber edge friction shown in Fig. 26b.

2. Correction of rubber edge effect on normal stress.

After the rubber edge correction, the extension of stress path crosses the negative shear stress at zero normal stress.

The stress path is controlled by the generated excess pore pressure, which is completely independent of rubber edge effects. So the shape of the stress path is the same. The change of normal stress correction factor will move the horizontal location of the stress path. When we give the value of 0.86 as the normal stress correction factor, the stress path of Fig. 29b will be obtained.

ICL-2 has a function for setting the rubber edge friction and the normal stress correction factor

before the test. For further tests in the same or similar conditions, the stress path of Fig. 29b will be obtained without any correction after the test. However, the correction procedure for 1 and 2 (above) after the test is not difficult. So we usually do not input the rubber edge friction in the computer. We input a value of the normal stress correction factor, referring to Fig. 28b or Table 2, and adjust this value after the test, as stated above, based on the zero cohesion after a large shear displacement.

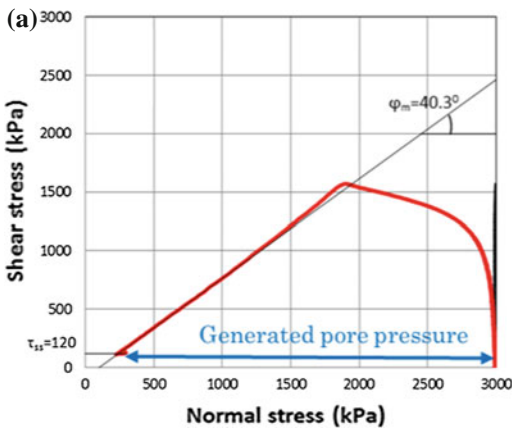
2.4 Types of Undrained Dynamic-Loading Ring-Shear Tests Using ICL-2

The undrained dynamic-loading ring-shear apparatus has the following different types of shearing for different purposes.

2.4.1 Basic Tests

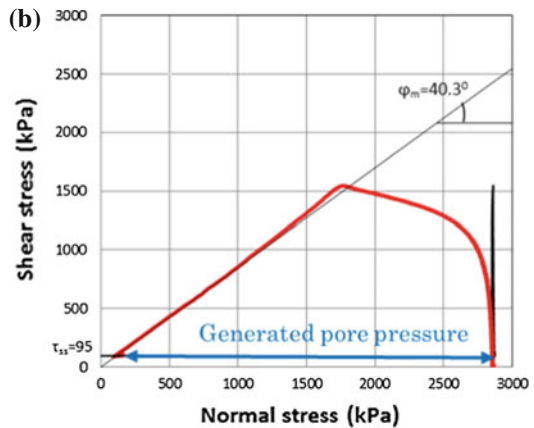
1.1 Constant shear-speed control test

The constant shear-speed control test typically is similar to the conventional ring shear testing and direct shear testing. The rubber edge friction measurement test in Fig. 26 is applied in this test.



Original test data:

$\alpha = 0.9$, Normal stress $\sigma = 3,000$ kPa,
 $B_D = 0.95$, shear-stress increasing rate = 2 kPa/s
 No reduction of Rubber edge friction



Corrected data:

$\alpha = 0.86$, Normal stress $\sigma = 2,867$ kPa,
 Reduced by Rubber edge friction = 25 kPa

Fig. 29 Test result of the monotonic shear-stress control undrained ring-shear test (a) and the correction of rubber edge effects (b)

1.2 Shear-displacement control test

The maximum shear speed of the servo-motor is 50 cm/s for ICL-2. Less than 0.1% speed (0.5 mm/s) is not able to be controlled in the speed-control mode. A shear-displacement control test is used for very slow shearing tests, such as 1–2 m shear displacement for 12 h during an overnight test, namely 0.023–0.046 mm/s.

Such slow speed testing is not necessary for the sandy soils which are involved in rapid landslides. But some researchers plan to test clayey soils drilled from the sliding surface of reactivated landslides.

1.3 Monotonic increasing shear-stress test (a basic shear stress control test)

This is the most basic test of undrained dynamic-loading ring-shear testing to measure the undrained steady-state shear resistance as a key parameter for landslide dynamics. Figure 29 is the monotonic increasing shear-stress test. All natural processes caused by the force of gravity proceed under the stress-control states such as the slope angle increment or during excavation in the lower slope. When the stress reaches the failure line, shear displacement is accelerated by the reduction of shear resistance after peak strength in most cases. Then, a rapid motion by the generation of excess pore pressure during the post-failure motion will occur. It will continue until it reaches an undrained steady-state shear resistance, as shown in Fig. 29. This phenomenon shown in Fig. 29 is called sliding-surface liquefaction (Sassa et al. 2004, 2010).

1.4 Cyclic-loading shear-stress control test

This is the basic preparatory test to investigate the behavior of earthquake-induced landslides. After the consolidation of the sample by a certain normal stress and shear stress loaded by gravity, additional shear stress is applied by a cyclic wave of shear stress (sine curve). The additional shear stress is increased step by step until it is sure to reach the failure line, which was already obtained

by the monotonic increasing shear stress test. From this test, we can estimate the seismic acceleration that can cause failure of soils for a given slope angle.

2.4.2 Landslide Ring-Shear Simulation Tests

Landslides are very complex phenomena. The most reliable tests to assess the dynamic behavior of landslides during an indoor experiment is to reproduce the phenomena by physically simulating the process. All processes cannot be reproduced by any indoor experiment. So the UDRA aims to reproduce the phenomenon of sliding surface formation and post-failure shear displacement by simulating all stresses acting on the sliding surface and the resulting pore pressure generation. Namely, UDRA can conduct a mechanical simulation using the undrained dynamic loading system.

This characteristic is quite different from triaxial tests and direct shear tests, and the capability of conducting undrained tests and the dynamic loading by a servo-control system is different from conventional ring shear tests (Sassa et al. 2004).

2.1 Rain-induced landslide simulation test

Many landslides are caused by rainfall, triggered by pore pressure increases. UDRA has a pore pressure control system as shown in Fig. 22. Any pattern of pore pressure change can be applied similar to the shear stress change corresponding to the seismic record. However, there is no need for such a pore pressure change, so we will conduct a monotonic increasing pore-pressure test. After the consolidation of normal stress and shear stress and reproducing the stress state on the sliding surface, pore pressure is increased by a constant rate of shear stress increment.

2.2 Earthquake-induced landslide simulation test

To simulate an earthquake-induced landslide, we will input a shear-stress curve calculated from the real earthquake record or a past earthquake

record in the computer. It is used as the control signal for the shear stress servo-motor. In the very initial stage, we input a normal-stress curve in the computer and used it as the control signal of the normal stress control servo-motor. However, we mostly test soils in a fully saturated state (pore pressure parameter B_D is greater than 0.95). In this case, the normal stress change will be cancelled out by the excess pore pressure generation and the effective normal stress will be a minimum. Then, in the later stage, we usually input the seismic shear-stress change, while keeping the total normal stress as the constant during the earthquake-induced landslide simulation test.

2.3 Ring shear simulation test of landslide loading onto deposits

When a landslide is initiated, the landslide mass travels onto the lower slope layer or onto torrent deposits or alluvial deposits, as illustrated in Fig. 19. To assess the movement of landslide mass over the deposits, which differ from the soil layer at the initial landslide, we have to simulate that condition using a sample taken from those layers/deposits. This is undrained dynamic-loading testing by simulating the loading of the moving landslide mass onto the deposit. This dynamic loading is different from cyclic loading and seismic loading, but is only a one-time loading. The loading is directly from the landslide mass onto the deposit. The given stress can be stronger than earthquake-loading for the deposit. In cases which the potential sliding surface of the deposit is saturated, the deposit is sheared and the sheared soil layer is entrained by the moving landslide mass. Sometimes an initial small landslide mass that began near the top of the mountains will increase its volume during motion over the lower slope and torrent beds and a large landslide mass strike urban settlements (Example of the 2014 Hiroshima disaster in Japan is introduced in Sect. 4.2. Application to the 2014 Hiroshima rain-induced shallow-landslide-debris flow disaster).

2.5 The Types of Relationships Presented in UDRA Test Results

The test result of UDRA is presented in the following three relationships.

1. Time series of parameters (Shear stress, normal stress, pore water pressure and shear displacement) to observe the behavior of the original data.
2. Stress path (relationship between the total normal stress and effective normal stress and shear stress) to understand the dynamic behavior of the sample.
3. Relationships between shear stress and the shear displacement. It is important to observe the shear stress reduction after failure to the steady state. When the shear displacement from the failure to the steady state is short and the strength reduction from the peak to the steady state is great, progressive failure development is rapid around the firstly failed local point.

Two sets of figures for a basic monotonic increasing shear-stress test and a seismic loading ring shear test are shown in Figs. 30 and 31.

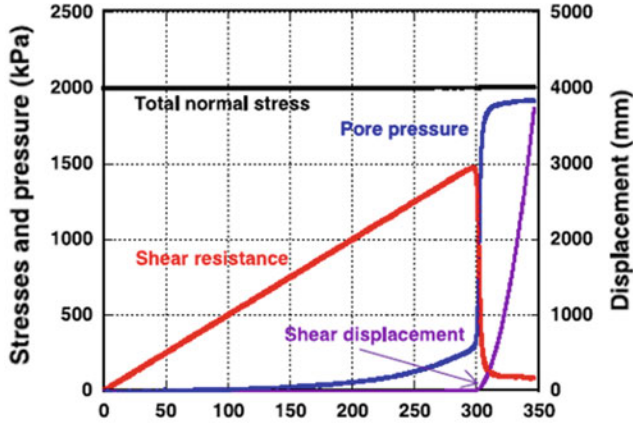
3 Landslide Simulation Model (LS-RAPID) and Landslide-Induced Tsunami Model (LS-Tsunami)

Abstract

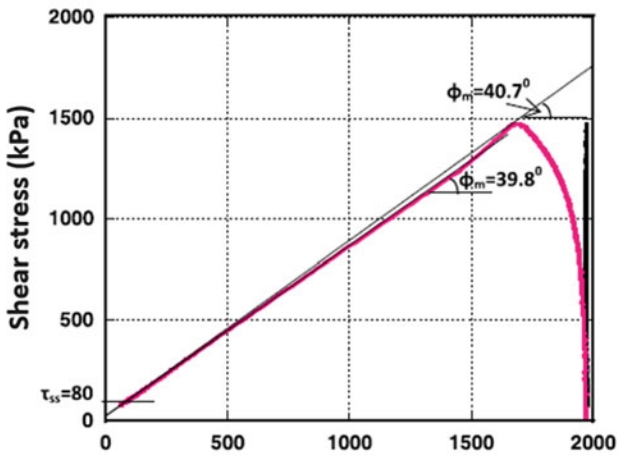
Section 3 aims to explain the basic theory of an integrated model to simulate the initiation and motion of landslides (LS-RAPID) and also an integrated model to simulate landslide-induced tsunami (LS-Tsunami).

The LS-RAPID simulation needs geotechnical parameters measured or estimated from the undrained dynamic-loading ring-shear testing. The theory of LS-RAPID, the geotechnical parameters necessary to simulate landslide initiation and motion, and their characteristics are described.

(a) Time series of Data



(b) Stress path



(c) Shear stress and shear displacement relationships

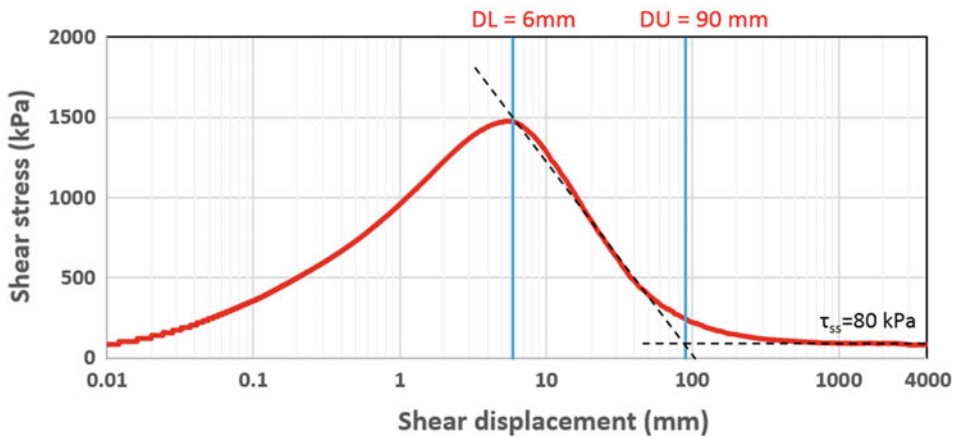
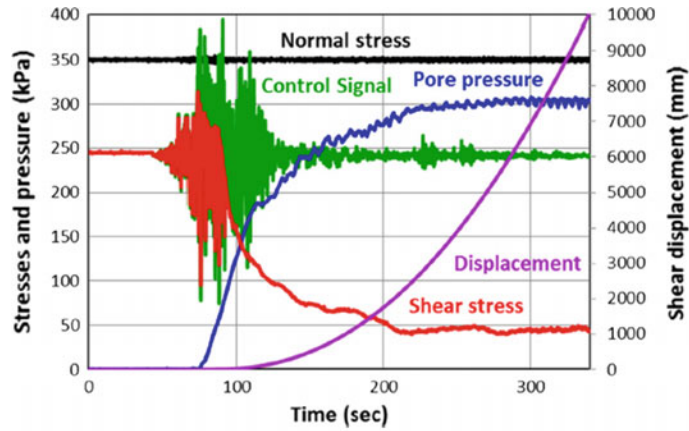


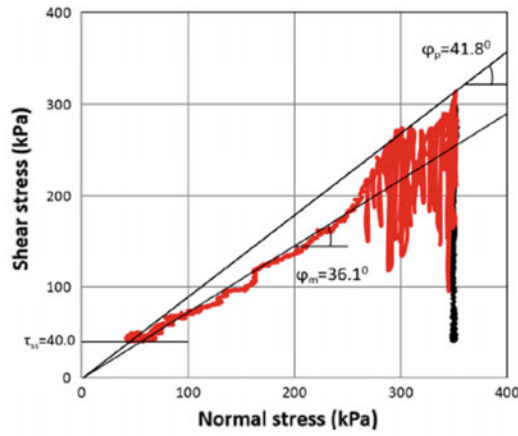
Fig. 30 Example data of a monotonic increasing shear-stress test. Sample: volcanic sands taken from 1792 Unzen Mayuyama landslide, $B_D = 0.96$

Fig. 31 Example data of a seismic-loading ring shear test. Sample: volcanic ash taken from the 2016 Kumamoto earthquake induced landslide. $B_D = 0.95$ (Dang et al. 2016)

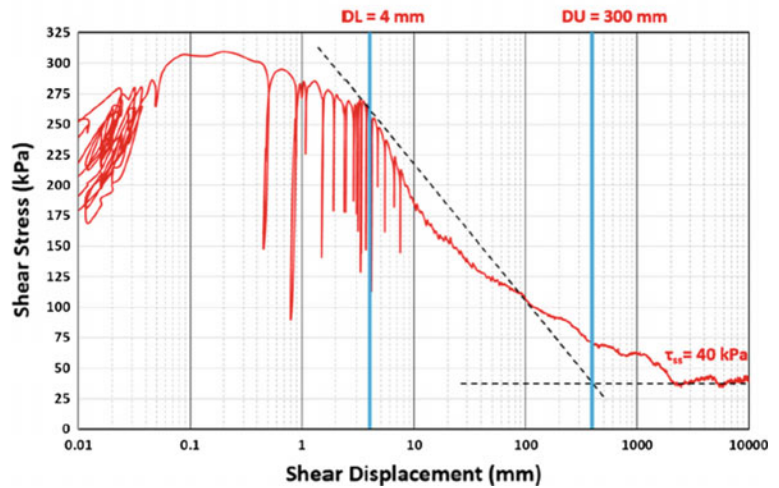
(a) Time series of Data



(b) Stress path



(c) Shear stress and shear displacement relationships



The LS-Tsunami model to simulate landslide-induced tsunami was developed under the following concept. The tsunami wave is caused by the vertical upheaval of the sea floor during the motion of a landslide under sea. The motion of the landslide mass under water is given by the LS-RAPID simulation as the trigger. The simulation of tsunami is the same as in the IOC Tsunami manual published by UNESCO in 1997.

Keywords

Landslide dynamics • Computer simulation • LS-RAPID • LS-Tsunami

3.1 Landslide Simulation Model (LS-RAPID)

3.1.1 Basic Theory of LS-RAPID

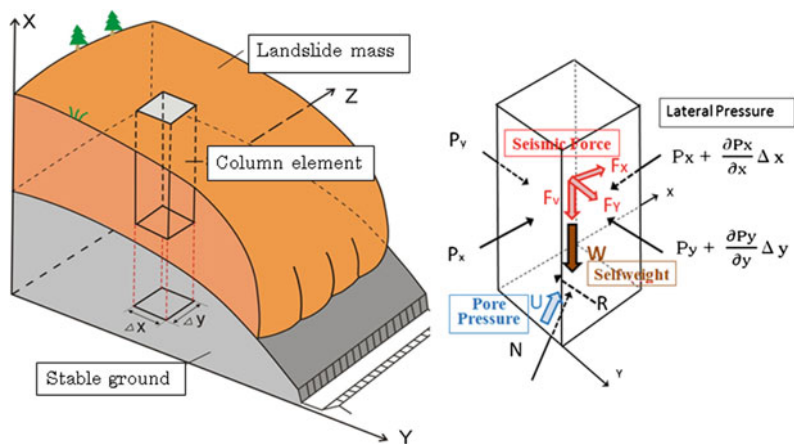
Shear resistance mobilized during motion is not as simple as static slope stability analysis, because it will be mostly determined by pore-water pressure generation in the shear zone during shear. The undrained dynamic-loading ring-shear test can simulate various cases of landslide initiation and motion, and measure the pore-water pressure generation and resulting shear resistance mobilized in the sliding surface. However, a hazard assessment needs the areal

distribution of a landslide mass. The areal distribution of the landslide mass is estimated though numerical simulation by inputting the key measured or estimated parameters obtained from the undrained dynamic-loading ring-shear apparatus (UDRA).

Sassa (1988b) proposed a numerical simulation model for the motion of landslides. It uses parameters that can be measured in geotechnical tests. However, it does not simulate the initiation process. Initiation of landsliding is done using slope stability analysis or FEM analysis, and there had been no computer simulation model for both initiation and motion of landslides. Sassa et al. (2010) proposed a model simulating both landslide initiation and motion within the same model. A computer programming company has modified it to include user-friendly input and output systems. This version of the model is called LS-RAPID and is commercially available to any user. The concept of this simulation is explained in Fig. 32.

A vertical imaginary column is considered within a moving landslide mass. The forces acting on the column are: (1) self-weight of the column (W); (2) seismic forces (vertical seismic force F_v , horizontal x - y direction seismic forces F_x and F_y); (3) lateral pressure acting on the side walls (P); (4) shear resistance acting on the base (R); (5) the normal stress acting on the base (N) given from the stable ground as a reaction to

Fig. 32 Basic concept of LS-RAPID



Driving force = (Self-weight + Seismic forces) + lateral pressure + shear resistance

$$am = (W + Fv + Fx + Fy) + \left(\frac{\partial P_x}{\partial x} \Delta x + \frac{\partial P_y}{\partial y} \Delta y \right) + R \quad (15)$$

the normal component of the self-weight; and (6) pore pressure acting on the base (U).

The landslide mass (m) will be accelerated by an acceleration (a) from the sum of these forces: where R includes the effects of forces of N (normal stress due to self-weight W) and U that works in the upward direction of the maximum slope line before motion and in the opposite direction of landslide movement during motion. All stresses and displacements are projected and calculated into the horizontal plane (Sassa 1988b).

Equation (15) can be expressed into x and y directions (Sassa et al. 2010) as shown in Eqs. 16 and 17. The assumption that the sum of landslide mass that flows into a column (M , N) is the same with the change or increase of height of the soil column will give the relationship of Eq. 18 (Table 3).

$$\begin{aligned} \frac{\partial M}{\partial t} + \frac{\partial}{\partial x}(u_o M) + \frac{\partial}{\partial y}(v_o M) \\ = gh \left\{ \frac{\tan \alpha}{q+1} (1 + Kv) + Kx \cos^2 \alpha \right\} \\ - (1 + Kv) kgh \frac{\partial h}{\partial x} - \frac{g}{(q+1)^{1/2}} \cdot \frac{u_o}{(u_o^2 + v_o^2 + w_o^2)^{1/2}} \\ \times \{h_c(q+1) + (1 - r_u)h \tan \phi_a\} \end{aligned} \quad (16)$$

$$\begin{aligned} \frac{\partial N}{\partial t} + \frac{\partial}{\partial x}(u_o N) + \frac{\partial}{\partial y}(v_o N) \\ = gh \left\{ \frac{\tan \beta}{q+1} (1 + Kv) + Ky \cos^2 \beta \right\} \\ - (1 + Kv) kgh \frac{\partial h}{\partial y} - \frac{g}{(q+1)^{1/2}} \\ \cdot \frac{v_o}{(u_o^2 + v_o^2 + w_o^2)^{1/2}} \\ \times \{h_c(q+1) + (1 - r_u)h \tan \phi_a\} \end{aligned} \quad (17)$$

$$\frac{\partial h}{\partial t} + \frac{\partial M}{\partial x} + \frac{\partial N}{\partial y} = 0 \quad (18)$$

Equations (16), (17) and (18) above were established for processes of both landslide initiation and motion. The value of ϕ_a , h_c , r_u varies in three states: (i) pre-failure state before shear displacement at failure (start of strength reduction), (ii) transient state between pre-failure state and steady state, and (iii) steady state after the end of strength reduction. The lateral pressure ratio (k) in Eq. (16) and (17) is expressed by using the Jakey's equation (Sassa 1988b) as follows,

$$k = 1 - \sin \phi_{ia}$$

$$\tan \phi_{ia} = \frac{(c + (\sigma - u) \tan \phi_i)}{\sigma} \quad (19)$$

where $\tan \phi_{ia}$ is the apparent friction coefficient within the landslide mass and $\tan \phi_i$ is the effective friction within the landslide mass, which is not always the same with the effective friction during motion on the sliding surface (ϕ_m). The value of $k = 1.0$ when the sample is in the liquefied state ($\sigma = u$ and $c = 0$), and $k = 0$ when in the rigid state. The apparent friction coefficient ($\tan \phi_{a(ss)}$) can be obtained by knowing the steady-state shear resistance (τ_{ss}) and the total normal stress (σ) from ring shear tests. A further detailed explanation of the conceptual model and other parameters of the LS-RAPID software can be found in Sassa (1988b) and Sassa et al. (2010).

Figure 33 presents the relationship of mobilized shear resistance and shear displacement

Table 3 Symbols and parameters of the LS RAPID model equations

Symbol/parameters	Description
h	Height of soil column within a mesh (depth of the moving mass)
g	Gravity (acceleration)
α, β	Angles of the ground surface to x-z plain and y-z plain
u_o, v_o, w_o	Velocity of a soil column to x, y, z directions (velocity distribution in z direction is neglected, regarded to be a constant)
M, N	Discharge of soil per unit width in x, y directions, respectively ($M = u_o h, N = v_o h$)
k	Lateral pressure ratio (ratio of lateral pressure and vertical pressure)
$\tan \phi_a$	Apparent friction coefficient mobilized at the sliding surface of landslide
h_c	Cohesion c expressed in the unit of height ($c = \rho g h_c, \rho$: density of soil)
q	$\tan^2 \alpha + \tan^2 \beta$
w_o	$-(u_o \tan \alpha + v_o \tan \beta)$
Kv, Kx, Ky	Seismic coefficients to the vertical, x and y directions
r_u	Pore pressure ratio (u/σ)

from the peak to the steady state in an undrained ring-shear test. The figure compares a cyclic loading ring-shear test (by 1 Hz) and a monotonic shear-stress loading test. In the figure, the thin line is the result of the monotonic shear stress loading test and the thick line is the result of the cyclic loading test. Both lines overlap. The relationship between shear stress and shear displacement during the undrained shearing is independent of the frequency of loading during rainfall or earthquakes.

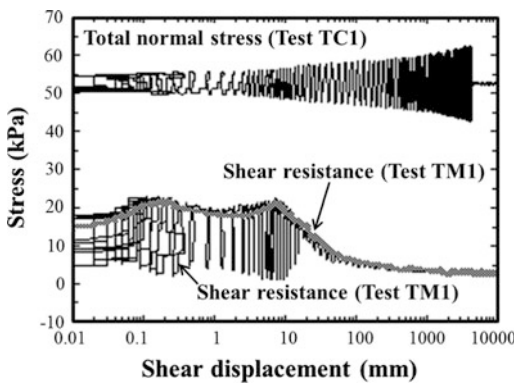


Fig. 33 The shear stress and shear displacement relationship in undrained ring-shear tests (Trandafir and Sassa 2006)

Figure 34 is the result of a cyclic loading ring-shear test on Tertiary-age sand in which a rapid landslide was triggered by the 2004 Mid-Niigata earthquake. The shear resistance started to decrease at a shear displacement (DL) of 5 mm, and it continued to decrease until it reached a steady state after some hundred millimeters of displacement. This relationship of reduction in shear resistance is approximated by a straight line (the purple line). In this case, the initiation of steady state appears to be at DU (240 mm). In the integrated simulation model, the shear displacement after DU is at a steady state. The steady-state shear resistance appears to

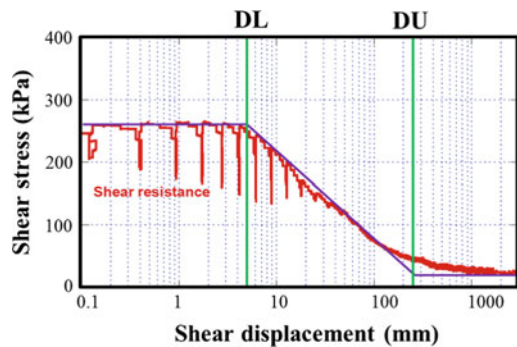


Fig. 34 The shear stress and shear displacement relationship of the undrained cyclic loading test on Tertiary sand

be determined by the large excess pore-water pressure that is generated.

Figure 35 presents the undrained monotonic increasing shear-stress tests under different consolidation pressures. The generated pore-water pressure will change at the loaded normal stress corresponding to the landslide depth, but the steady-state shear strength remains constant. It is considered that soil grains will be crushed during motion until a certain normal stress. Grain crushing necessarily reduces volume reduction and pore pressure generation in the normal stress range greater than this threshold value of each type of soil grains. The depth of landslide will change during motion, and is affected by the movement velocity, the ground topography on the travel course (wide plain or narrow valley etc.) and others.

Therefore, we use the steady-state shear resistance as the key parameter during motion. The initiation process is shear displacement until the situation at point DL (Fig. 34) is reached. This state will be the equivalent of conventional slope stability analysis, and so we use the peak friction angle, and pore-water pressure that acts on the potential sliding surface before motion.

Figure 36 illustrates the pore pressure acting on the sliding surface before failure (initial static pore water pressure due to the groundwater level) and the excess pore-water pressure generated by grain crushing and volume reduction in the post-failure process. The groundwater level is indicated in the figure. This groundwater will give the following pore-water pressure (u).

$$u = z_w \cdot \gamma_w \cdot \cos^2 \theta \quad (20)$$

Here,

- z_w vertical depth of ground water level,
- γ_w unit weight of water,
- θ slope angle.

When post-failure motion starts, pore-water pressure is generated in the shear zone. Illustrating the pore-water pressure generated inside the shear zone as a stand-pipe, it is possible for the water level inside the pipe to be higher than the ground surface, as shown in Fig. 36. Following these considerations, we have included

the following three stages in the integrated computer simulation model:

Stage 1 (before failure)

$$D < DL : \tan \phi_a = \tan \phi_p, c = c_p, \gamma_u = \gamma_u \quad (21)$$

Stage 2 (steady state)

$$D > DL : \tan \phi_{sa} = \tan \phi_{a(ss)}, c = 0, \gamma_u = 0 \quad (22)$$

Stage 3 (transient state)

$$DL \leq D \leq DU : \tan \phi_a = \tan \phi_p - \frac{\log D - \log DL}{\log DU - \log DL} \cdot (\tan \phi_p - \tan \phi_{a(ss)}) \quad (23)$$

$$c = c_p \left(1 - \frac{\log D - \log DL}{\log DU - \log DL} \right)$$

$$\gamma_u = \gamma_u \frac{\log DU - \log D}{\log DU - \log DL}$$

3.1.2 Remarks and Application of LS-RAPID

Steady-State Shear Resistance (τ_{ss}) and Pore-Pressure Generation Rate (B_{ss})

Figure 37 illustrates the summary on the stress path of the initiation and motion of landslides. The stresses on the potential sliding surface before the landslides (σ_0, τ_0) are located somewhere under the failure line at peak. Then, rain-fall, an earthquake or their combined effects shifts the stress path. If the effective stress path reaches the failure line at peak, a failure (landslide initiation) occurs. When the shear zone is saturated and the materials are those susceptible to grain crushing and volume reduction, a pore-water pressure is generated. In this case, the stress path in Fig. 37 moves down and leftward and reaches the failure line during motion and accelerates until reaching a steady state (σ_{ss}, τ_{ss}). The mobilized apparent friction angle in the

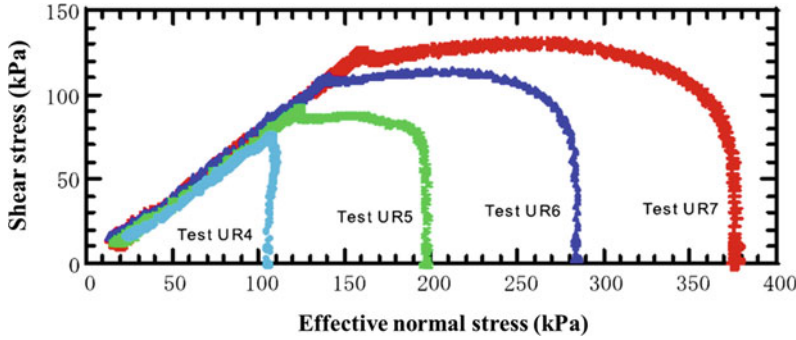


Fig. 35 Undrained ring-shear tests on the Osaka formation (granitic sandy soil) in which a disastrous rapid landslide was triggered by the 1995 Kobe earthquake (Okada et al. 2000)

steady state ($\phi_{a(ss)}$) is shown as the green line in Fig. 37. Landslide travel distance is much affected by this value and slope geometry.

If the material is the same, the steady-state shear resistance will be the same. As shown in Fig. 38, the apparent friction angle at steady state is different for different landslide depths. A deep landslide (Case A) has the lowest apparent friction angle and a medium landslide (Case B) has a medium friction angle.

In a shallow landslide (Case C), the acting normal stress is less than the steady-state normal stress (σ_{ss}). No pore-water pressure is generated, and so the apparent friction angle at steady state is the same as the effective friction angle during motion (ϕ_m).

When a deep landslide moves, such as Case A, the depth of the landslide mass will

change during the progress of travel. If the depth is greater, the mobilized apparent friction is smaller. If the depth becomes smaller during motion, the mobilized apparent friction becomes greater and the landslide becomes easy to stop.

We measure the steady-state shear resistance of a fully saturated soil through an undrained ring-shear test. However, the same soils may be somewhere dry, somewhere partially saturated, and somewhere fully saturated. The mobilized steady-state shear resistance changes with the degree of saturation. Figure 39 illustrated the effect of saturation. Sassa defined the pore-pressure generation rate (Bss) to be 1.0 in the fully saturated state, which is measured by ring-shear testing. Bss = 0 in the dry state (with no pore-water pressure). The steady-state shear resistance is the same as the shear resistance on the failure line during motion (yellow point in Fig. 39). If the soil is partially saturated, the steady-state stress point in Fig. 39 is at the blue point between the fully saturated case (red point) and the dry case (yellow point).

This simulation model was applied to the Leyte landslide, using the test results of the involved volcanoclastic debris and others.

Estimation of Landslide Block

In order to simulate LS-RAPID, we have to give two components within three topographical components; (1) the ground surface topography before landslide, (2) the topography of sliding surface or the stable ground, (3) the landslide

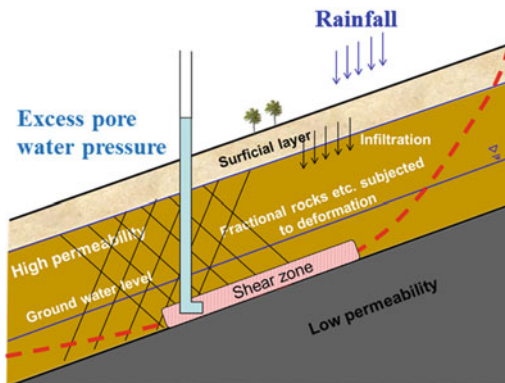
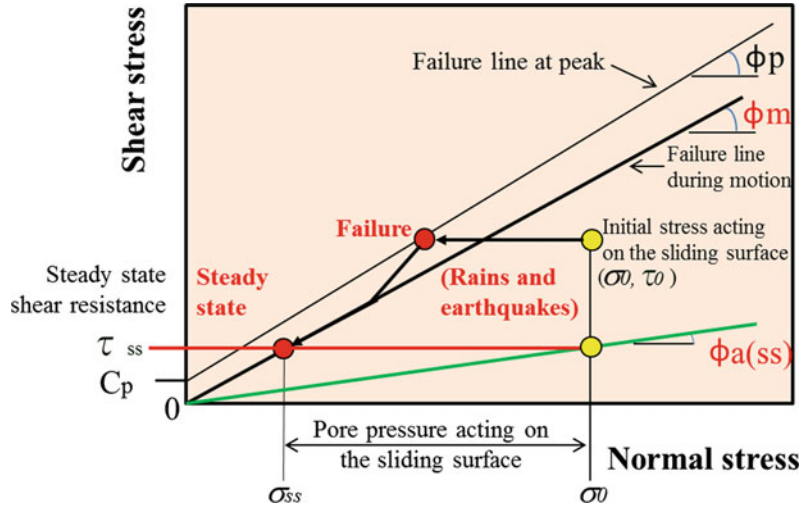


Fig. 36 Illustration of excess pore water pressure generated in the shear zone

Fig. 37 The steady state shear resistance and the apparent friction angle at the steady state



mass or unstable soil layer depth distribution. For the Leyte landslide, we could obtain the topographical map from the Philippine Institute of Volcanology and Seismology (PHIVOLCS). But no data of post-landslide topography was available. Our investigation team measured the central section and some of borders of the landslide by total station. Then, we made a landslide block using the function of LS-RAPID to create one or two ellipsoids. In this case, we made one

ellipsoid to pass the headscarp, possible the bottom of landslide and side borders (Sassa et al. 2010).

The application of LS-RAPID for the 1792 Unzen Mayuyama landslide (Sect. 4.1) used (1) the ground surface topography before landslide, and (2) the topography of the sliding surface. The application of LS-RAPID for the 2014 Hiroshima shallow landslide—debris flow disaster (Sect. 4.2) used (1) the ground surface topography before landslide, and (2) the unstable

Fig. 38 The steady-state shear resistance and the apparent friction angle at the steady state in different depths of landslide mass

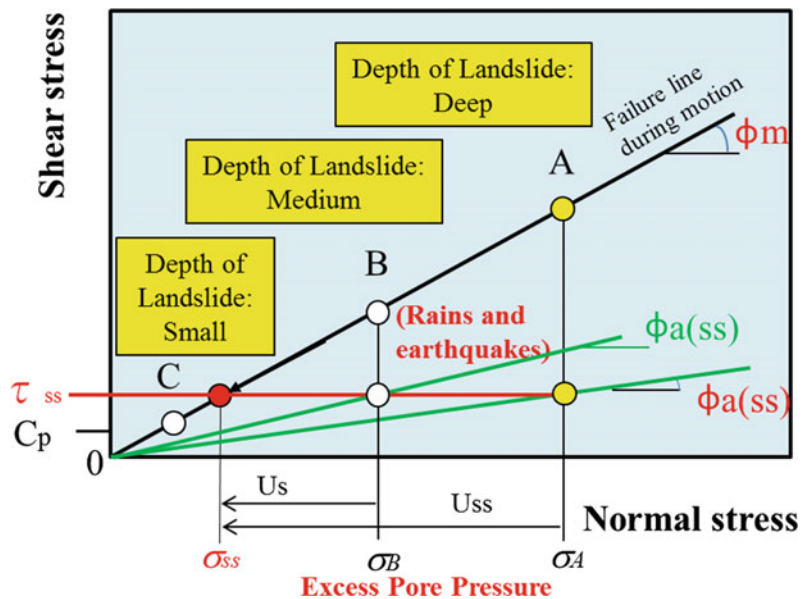
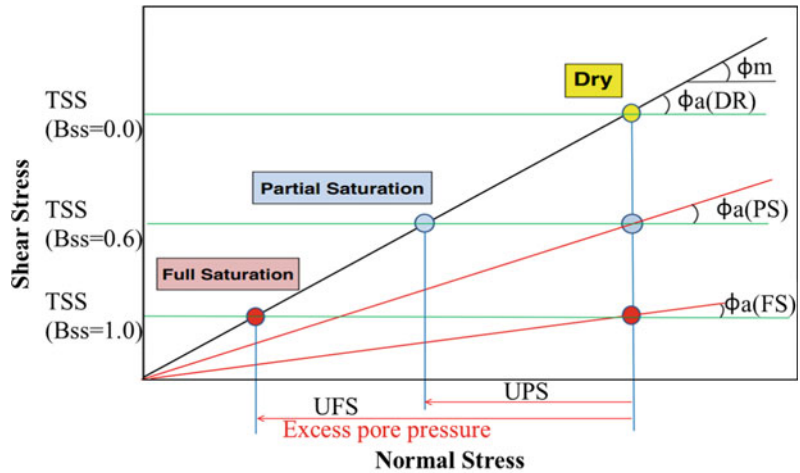


Fig. 39 Relationship between the pore-pressure generation rate (B_{ss}) and the apparent friction coefficient



soil layer depth distribution. The application of LS-RAPID for the hypothesis of the Senoumi submarine megaslide in Suruga Bay (Sassa et al. 2012) used (1) the ground surface topography before landslide, and (2) the topography of the stable ground (current sea floor). The unstable mass was widely distributed. A landslide occurred in a certain place within the unstable mass area above the stable ground. When the stronger earthquake struck, a further area slid. The shape of the unstable deposit cannot be an ellipsoid or one or two landslide blocks. Progressive failures were triggered and the liquefied landslide mass flowed into the Suruga Trough through a narrow gate (Sassa et al. 2012).

Measurement of Landslide-Dynamics Parameters and Triggering Factors of the Leyte Landslide

The Leyte landslide was initiated by a nearby small-scale earthquake after one week of rainfall. The heavy rainfall brought the stability of the slope close to near failure, but it did not fail. However, a small seismic acceleration triggered the landslide under the high pore-water pressure.

The failure line was obtained in the preliminary ring shear test, and the initial stress was created below the failure line. Then the estimated small earthquake-loading was input using the seismic wave record under the estimated

maximum acceleration. The undrained seismic loading ring shear tests, the seismic wave record, as well as the rainfall record can be referred to in Sassa et al. (2010).

The Leyte Landslide Simulation Results by LS-RAPID

A series of motions with an explanation for each step was presented for the case of $K_{EW} = 0.12$, $K_{NS} = K_{UD} = 0.061$, $r_u = 0.15$ (Fig. 40). The left figures of A and B show the assumed pore pressure ratio and the assumed seismic acceleration. The blue balls represent the unstable soil mass and red balls the moving soil masses. Deep soils are shown by larger balls, and shallow soils by smaller balls.

A progressive failure took place. Initially a small shear failure occurred in the top part of the landslide (the small red color area in B), the failed areas increased in C. The landslide mass travels to the flat area (residential area including school and church) at high speed in D. All buildings, including the school and church, were destroyed or buried. More than 1000 people were killed in this landslide.

An oblique air photo taken from a helicopter and the simulation results presented in the 3D view from a similar angle are shown in Fig. 41. The travel distance and the major part of the landslide distribution were well reproduced.

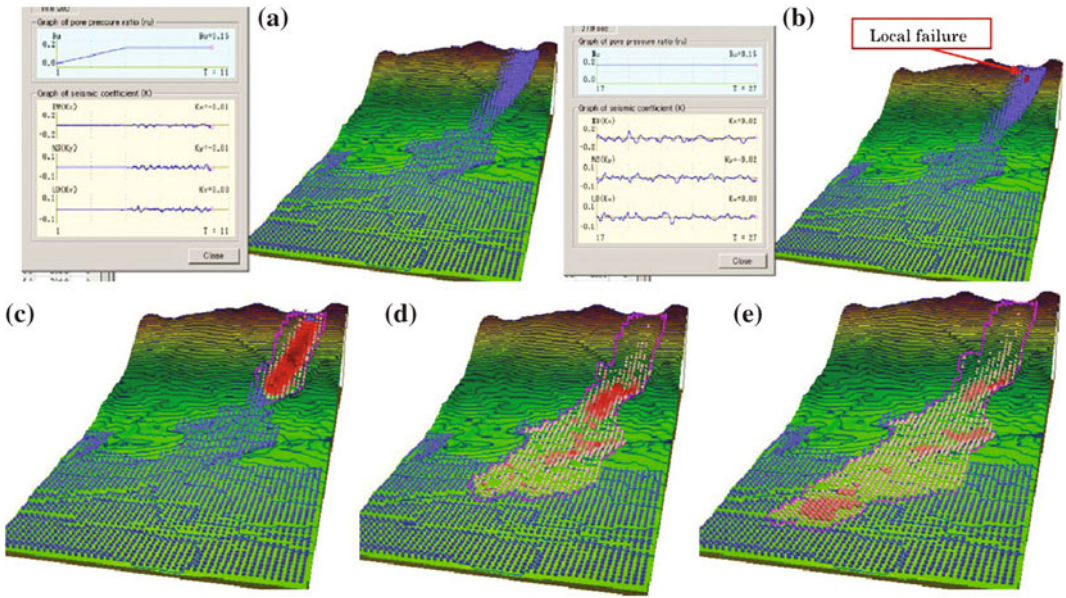


Fig. 40 Simulation result of the Leyte landslide. **a** r_u rises to 0.15 and the earthquake will start but no motion, **b** continued earthquake loading triggers a local failure, as presented in *red color mesh*, **c** an entire landslide block is

formed and moving, **d** the *top* of landslide mass moves onto alluvial deposits, **e** Deposition. Mesh size is 40 m; area is 1960×3760 m; contour interval is 20 m; 3 m unstable deposits on the alluvial deposit area (*blue balls*)

A secondary debris flow and muddy water spread to the left in the photo and from field observation. These are not represented in the numerical simulation. This application is introduced in detail in Sassa et al. (2010).

3.2 Landslide-Induced Tsunami Model (LS-Tsunami)

3.2.1 Introduction

When a large landslide mass rapidly enters the sea, or a rapid landslide occurs under the sea, a

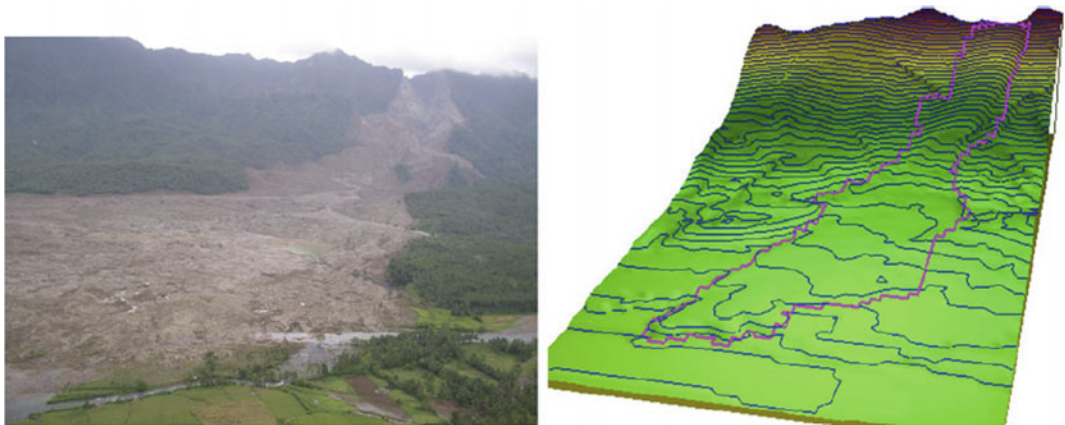


Fig. 41 Air photo and the result of computer simulation of the Leyte landslide. This application is introduced in the detail in PDF-tool 3.081-1.5

tsunami wave is generated in the water as the landslide mass moves beneath the water. Landslide-induced tsunami have been studied by researchers with different backgrounds and methods. Ataie-Ashtiani and Yavari-Ramshe (2011) and Biscarini (2010) developed a landslide-induced tsunami model based on physical small-scale model experiments, in which a solid block was placed on an inclined plate and the mass slides into water in a water-tank to generate waves. The former simplified the landslide mass as a rigid body and the later simplified the landslide as a fluid. Glimsdal et al. (2013) developed a model for a real submarine landslide in Norway. The landslide mass was simplified as a flexible box and the movement occurred as a deformable visco-plastic Bingham fluid.

Baba et al. (2012), based on the studies by Satake (2001) and Abe et al. (2008), simplified the real landslide movement as a vertical downward movement of a plate in the source area and a vertical upward movement of another plate in the deposition area. That is, the relative movements of the two plates simplified the real landslide movement in the sea floor. This method was applied to a small submarine landslide triggered by a 2009 M_w 6.4 earthquake in Suruga Bay, Japan. The tsunami heights were well monitored by tide gauges, ocean-bottom pressure gauges, ultra-sonic wave meters, and a GPS tsunami meter installed in and around the bay. 3-D bathymetric data around the landslide were obtained within the bay with a spatial resolution of 1.0 m grid using an autonomous underwater vehicle (AUV). The tsunami heights and wave forms which were obtained by integrating waves simulated the fault-only model (Aoi et al. 2010) and waves simulated by the submarine landslide-induced tsunami model reasonably matched the observed tsunami heights.

The authors were pleased by this case study that the vertical movement of the submarine ground surface due to a landslide can well simulate the landslide-induced tsunami. All previous studies of landslide-induced tsunami have not used the motions of landslides simulated by a landslide dynamics model.

We have decided to use the landslide motion simulated by LS-RAPID as the trigger of tsunami. The tsunami simulation model used in this study is a well established and widely used model (IOC 1997). We assumed that horizontal forces between the landslide mass and water can be neglected, and the tsunami is triggered only by the water mass on the submarine ground upheaved due to the moving landslide mass. This assumption is the same as that by Baba et al. (2012), Abe et al. (2008) and Satake (2001). The tsunami simulation code using the landslide motion data from LS-RAPID was developed (LS-Tsunami) for this study (Sassa et al. 2016).

3.2.2 Basic Principles of the Landslide-Induced Tsunami Model

The basic principles of the landslide-induced tsunami model used in this study are illustrated in Fig. 42. The left part of this figure is same as the principle of the integrated landslide simulation model (LS-RAPID), the only difference is that the landslide mass is located beneath a water surface. The right part of Fig. 42 illustrates the elevated water mass (which causes a tsunami wave) created by the upward displacement of the interface between the landslide and the water due to the movement of the landslide mass over the sea floor.

When the landslide mass enters or travels across the sea floor, the elevation of the submarine ground surface (which is the interface of landslide mass and submarine water) will be increased. The submarine ground surface elevated by the landslide mass will raise the water mass above the landslide-water interface by an amount, Δh , in a unit time, Δt . The shear resistance (τ_{sw}) between soil and water at this interface should be much smaller than the shear resistance within the soil. Hence, this resistance, τ_{sw} was ignored in the simulation. The effective stress acting on the surface between the bottom of the soil column and the top of the sea floor was regarded as being unaffected by the increase in water height for the following two reasons: (1) the surficial deposit on the sea floor is unconsolidated, and hence is expected to be

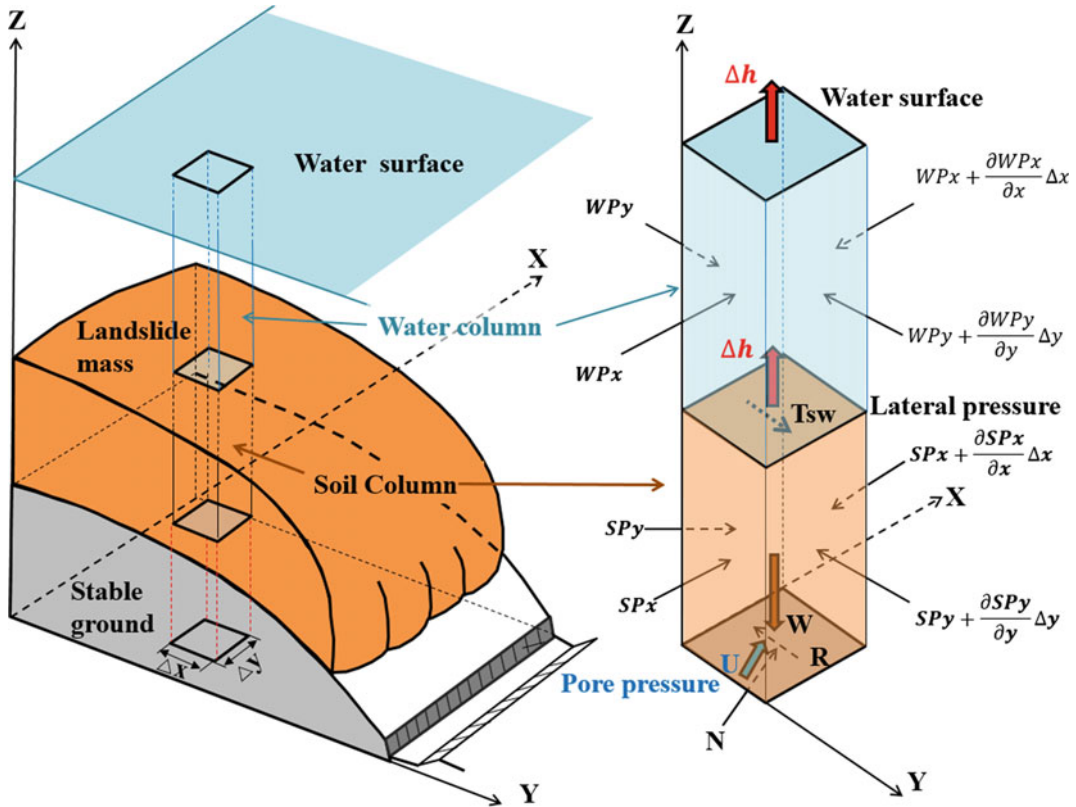


Fig. 42 Basic principles of the landslide-induced tsunami simulation model

permeable enough to transmit the water-pressure change due to water height change to the bottom of the soil column above the sea floor; and (2) the soil column of the moving mass is both unconsolidated and water saturated, hence the transmission of water-pressure change from the top to the bottom of the soil column is fast (elastic wave velocity of water is around 1.5 km/s) and can be regarded as instantaneous.

When a landslide mass enters into water, the buoyant force of the water will act on the soil mass. Namely the unit weight of the soil mass (γ_t) on land will change to the buoyant unit weight of the soil mass, the difference between γ_t and γ_w (unit weight of sea water) under water. In the case of partial submersion, the buoyant force of the water will act only on the part of soil mass below the water surface. No tangential force between soil and water is considered because the tangential force by water will be negligible

compared to the shear resistance mobilized in the shear surface of large-scale landslides.

Though we need many parameters to simulate landslide motion by LS-RAPID, additional new parameters used in tsunami simulation (LS-Tsunami) are the unit weight of sea water and Manning’s roughness coefficient for basal resistance between water and ground.

3.2.3 Equations to Simulate Landslide-Induced Tsunami

The calculation part of the landslide-induced tsunami model contains the following two steps.

- The first step: simulation of landslide mass by the integrated landslide simulation model “LS-RAPID” on land and on the sea floor. The equations of the first step are (1)–(4), which are the same as in LS-RAPID (Sassa et al. 2010).

- The second step: simulation of the tsunami by LS-Tsunami. The equations of the second step are (5)–(8), which is an established tsunami simulation model (IOC 1997).

The concept of LS-RAPID is that the acceleration (a) of the soil mass (m_s) is induced by the sum of forces of the self-weight of the soil mass, the seismic force acting on the soil column, the shear force acting on the bottom of the soil column, and lateral pressure acting on the sides of the soil column (Eq. 24).

The concept of the landslide-induced tsunami simulation (LS-Tsunami) is that the acceleration (a) of the water mass (m_w) is induced by the sum of forces of the lateral pressure acting on the sides of the water column and the Manning's basal shear resistance due to roughness of the ground (Eq. 28). Both sets of equations are shown from (1) to (8) below.

Basic Equations for the Motion of the Landslide (LS-RAPID)

This is explained in the previous Sect. 3.1 Landslide Simulation Model (LS-RAPID). The only difference is the mass of soils (m_s) in Eq. 24 and the mass of water (m_w) in Eq. 28.

$$am_s = (W + Fv + Fx + Fy) + \left(\frac{\partial P_x}{\partial x} \Delta x + \frac{\partial P_y}{\partial y} \Delta y \right) + R \quad (24)$$

$$\begin{aligned} & \frac{\partial M}{\partial t} + \frac{\partial}{\partial x}(u_o M) + \frac{\partial}{\partial y}(v_o M) \\ & = g h \left\{ \frac{\tan \alpha}{q+1} (1 + Kv) + Kx \cos^2 \alpha \right\} \\ & \quad - (1 + Kv) k g h \frac{\partial h}{\partial x} - \frac{g}{(q+1)^{1/2}} \\ & \quad \cdot \frac{u_o}{(u_o^2 + v_o^2 + w_o^2)^{1/2}} \\ & \quad \times \{ h_c(q+1) + (1 - r_u) h \tan \varphi_a \} \end{aligned} \quad (25)$$

$$\begin{aligned} & \frac{\partial N}{\partial t} + \frac{\partial}{\partial x}(u_o N) + \frac{\partial}{\partial y}(v_o N) \\ & = g h \left\{ \frac{\tan \beta}{q+1} (1 + Kv) + Ky \cos^2 \beta \right\} \\ & \quad - (1 + Kv) k g h \frac{\partial h}{\partial y} - \frac{g}{(q+1)^{1/2}} \\ & \quad \cdot \frac{v_o}{(u_o^2 + v_o^2 + w_o^2)^{1/2}} \\ & \quad \times \{ h_c(q+1) + (1 - r_u) h \tan \varphi_a \} \end{aligned} \quad (26)$$

$$\frac{\partial h}{\partial t} + \frac{\partial M}{\partial x} + \frac{\partial N}{\partial y} = 0 \quad (27)$$

Basic Equations for the Motion of Water (LS-Tsunami)

$$am_w = \frac{\partial P_x}{\partial x} \Delta x + \frac{\partial P_y}{\partial y} \Delta y + R(\text{Manning}) \quad (28)$$

where

a	Acceleration of a water column
m_w	Water mass in a column
$R(\text{Manning})$	Manning's basal resistance between water and ground
$\frac{\partial P_x}{\partial x} \Delta x, \frac{\partial P_y}{\partial y} \Delta y$	Lateral pressure acting on the side wall of column in x and y directions.

Equation 28 is expressed by Eqs. 29 and 30 in the x and y directions. The relationship that the sum of water mass that flow into a column (M , N) is the same with the change or increase of height of the water column is expressed in Eq. 31.

$$\frac{\partial M}{\partial t} + \frac{\partial}{\partial x}(u_o M) + \frac{\partial}{\partial y}(v_o M) = -gh \frac{\partial \eta}{\partial x} - \frac{\tau_x}{\rho} \quad (29)$$

$$\frac{\partial N}{\partial t} + \frac{\partial}{\partial x}(u_o N) + \frac{\partial}{\partial y}(v_o N) = -gh \frac{\partial \eta}{\partial y} - \frac{\tau_y}{\rho} \quad (30)$$

$$\frac{\partial h}{\partial t} + \frac{\partial M}{\partial x} + \frac{\partial N}{\partial y} = 0 \quad (31)$$

where

h	Height of water column within a mesh
η	Elevation of water surface above sea level datum
u_0, v_0	Velocity of a water column in X and Y directions, respectively (velocity distribution in Z direction is neglected, and assumed to be a constant)
M, N	Discharge of water per unit width in X and Y directions respectively ($M = u_0 h$, $N = v_0 h$)
g	Acceleration due to gravity.

Manning's basal resistance R (Manning) is expressed as below:

$$\text{X-component: } \frac{\tau_x}{\rho} = \frac{gn^2}{h^{7/3}} M \sqrt{M^2 + N^2}$$

$$\text{Y-component: } \frac{\tau_y}{\rho} = \frac{gn^2}{h^{7/3}} N \sqrt{M^2 + N^2}$$

ρ : Density of sea water, n : Manning's roughness coefficient.

3.2.4 Application of the Model to Two Hypothetical Simple Coastal Landslides

The new landslide-induced tsunami simulation was initially applied to two hypothetical landslides (A and B) on an imaginary slope.

- Case A: Maximum depth = 100 m. Maximum length = 500 m, Maximum width = 300 m, Volume = $5.8 \times 10^6 \text{ m}^3$
- Case B: Maximum depth = 313 m. Maximum length = 1230 m, Maximum width = 1000 m, Volume = $170 \times 10^6 \text{ m}^3$

The top of the slope was flat, the slope angle was 35° , and the bottom of the slope was a flat sea bed. The peak friction angle (ϕ_p) was 42° and the friction angle during motion (ϕ_m) was 40° . The heads of both landslides are at the top of the slope, and the toes of both landslides are at the water surface. In Figs. 43 and 44, the distance between the left end and the coast is 2000 m, and the distance from the coast to the bottom of the

figure is 100,000 m. Definitions of the maximum landslide velocity and the maximum tsunami height in Tables 4 and 5 are as follows:

- The *maximum landslide velocity* is the maximum velocity within the landslide mass when the front of the landslide mass reaches the flat sea/lake floor. Landslide velocity is one of indexes of triggering of tsunami as well as the landslide depth and the water depth.
- The *maximum tsunami height* is the maximum height in the tsunami profile (in Figs. 43 and 44) when the front of tsunami reaches 10 km from the coast. It is an index of tsunami effect over a sea/lake.

The motion of the tsunami is calculated at each 0.05 s, but the profiles in Figs. 43 and 44 in 2D views are outputted and saved as the figures at each 5 s.

Figure 43 and Table 4 shows the relation between the water depth and the tsunami behavior at a constant steady-state shear resistance (80 kPa), and different water depths (2, 20, 200 m).

The maximum tsunami heights are from 0.1 to 62.0 m. It increased with the depth of water and the landslide volume. As the depth of water increases, the maximum landslide velocity increases because the longer acceleration will increase landslide velocity on the longer steep slope below sea level. The larger volume of water at the deeper water depth is upheaved by the moving landslide mass and causes a greater tsunami height.

Figure 44 and Table 5 shows the relation between the steady-state shear strength and the tsunami behavior at a constant water depth (200 m), and different steady-state shear resistance. As the steady-state shear resistance increases, the maximum velocity decreases, and also the maximum tsunami height decreases. The relationship between the maximum tsunami height and the tsunami traveling time is inversely proportional in Table 4. However, the effect of steady-state shear resistance and the maximum landslide velocity on the tsunami traveling time is limited at the same water depth (Table 5).

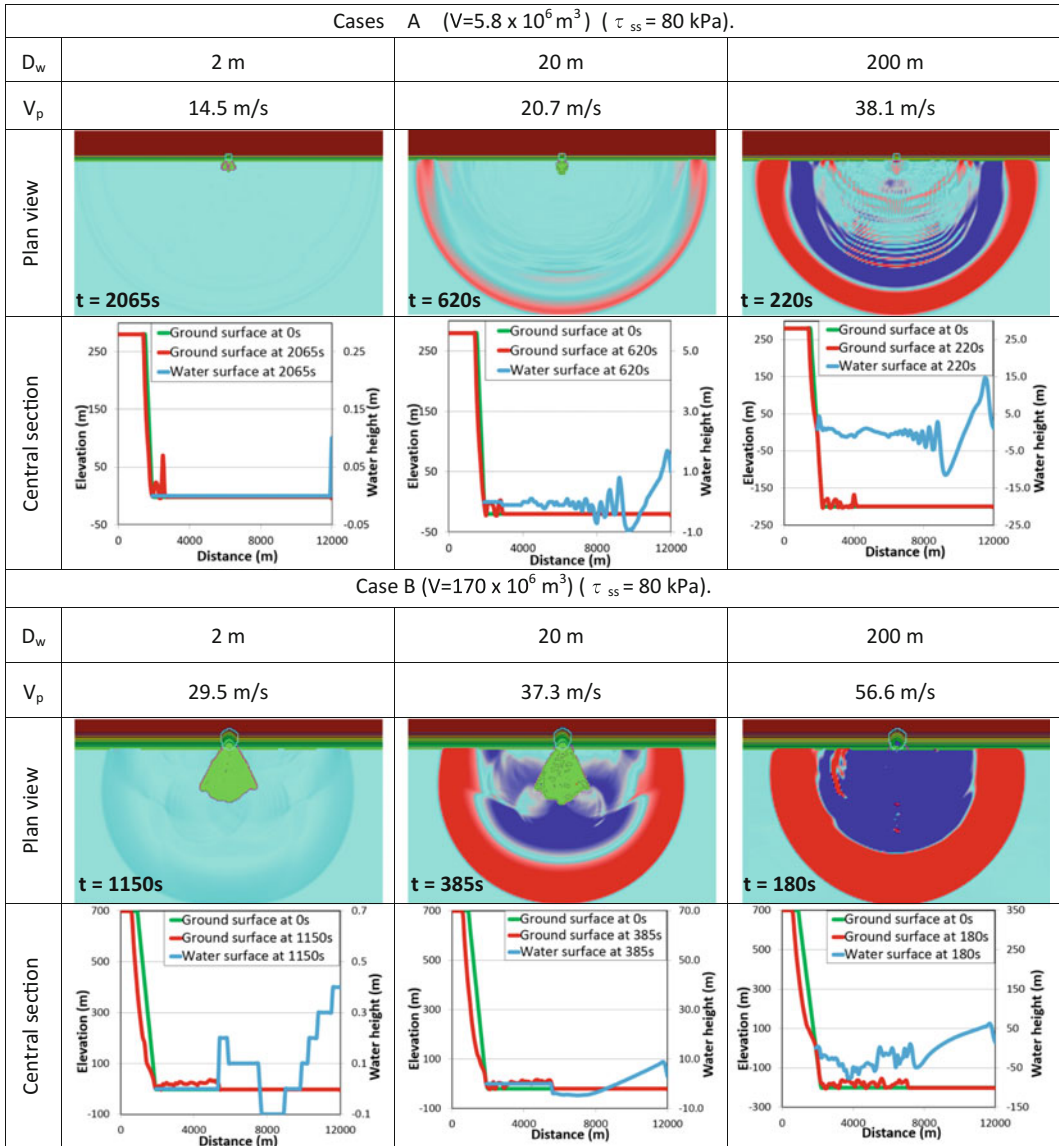


Fig. 43 Tsunami and landslide profiles when the tsunami front reached 12,000 m. The steady-state shear strength is constant ($\tau_{ss} = 80 \text{ kPa}$). Water depths vary from 2 to 200 m. D_w , depth of water in the sea/lake, V_p , maximum landslide velocity when the landslide front

reached the flat sea/lake floor. The *bright red color* presents waves more than 3 m above sea level and the *dark blue color* presents waves less than 3 m below sea level

Figure 45 presents the profiles of landslide and tsunami during motion in case B ($V = 170 \times 10^6$, $\tau_{ss} = 80 \text{ kPa}$) for the water depth = 200 m; 21 s after the initiation of simulation, the top of landslide mass reached the sea floor. The tsunami was generated. At 26.5 s, the

landslide mass started to move along the sea floor. A clear and high tsunami wave was formed. But the location of the tsunami head and the landslide head is almost same. At 57.5 s, the head of tsunami moved faster than the head of landslide. The landslide mass moved out from

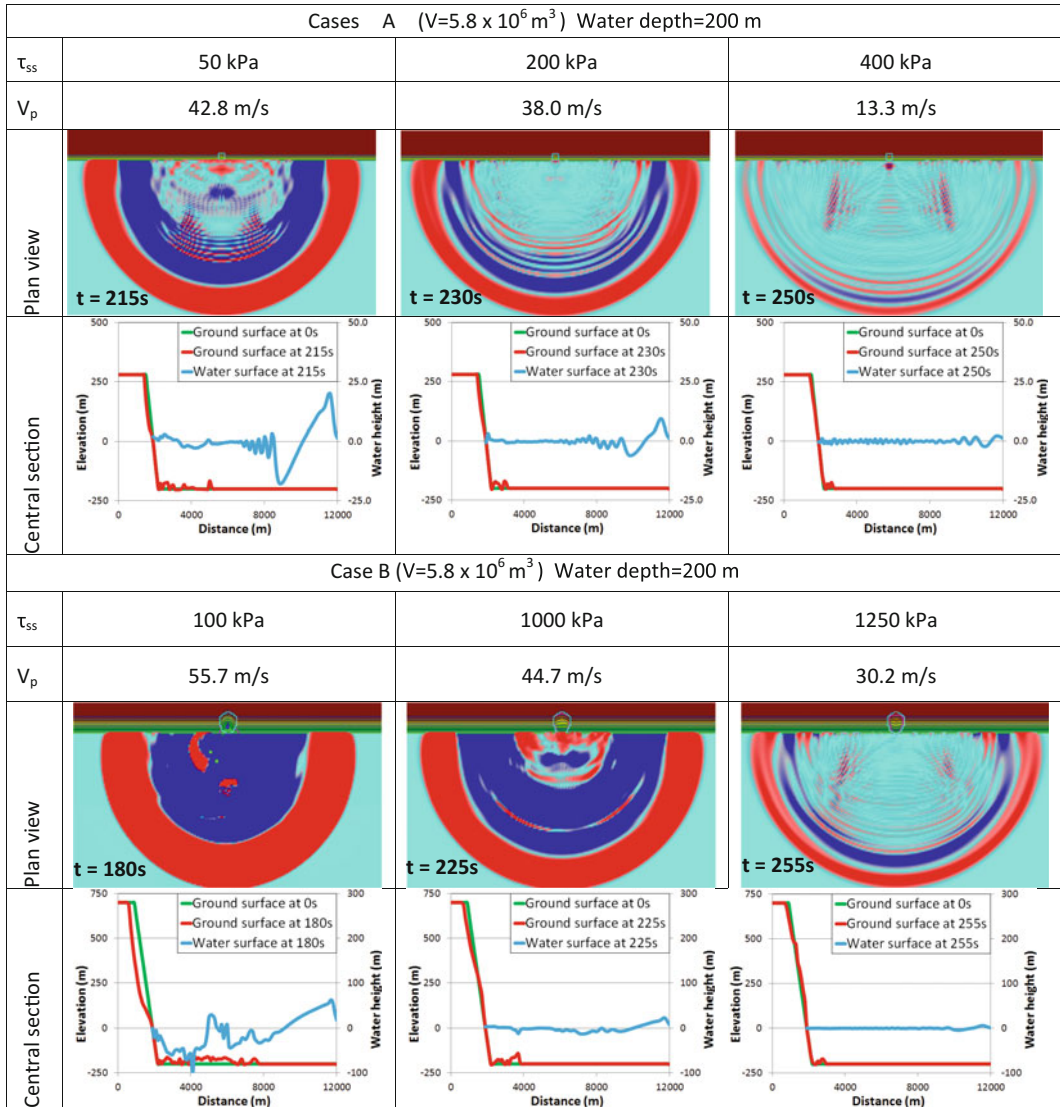


Fig. 44 Tsunami and landslide profiles when the tsunami front reached 12,000 m. The water depth is constant (200 m). Steady-state shear strengths are from 50 to 1250 kPa. τ_{ss} steady-state shear resistance of the landslide. V_p maximum landslide velocity when the landslide

front reached the flat sea/lake floor. The *bright red color* presents waves more than 3 m above sea level and the *dark blue color* presents waves less than 3 m below sea level

the source area at 139 s. The tsunami head reached 10 km from the coast at 180 s. Movement of the tsunami wave on the water surface is shown in the top-left corner. Red part is a tsunami wave higher than the sea level, and blue part is a tsunami wave lower than the sea level. The section of tsunami in Fig. 45 visualizes the motion of tsunami in its profile.

PDF Tools Related to Sect. 3

- PDF-tool 3.081-1.1 Manual of RSA Undrained Ring Shear Test
- PDF-tool 3.081-1.2 Manual of Model LS-RAPID
- PDF-tool 3.081-1.3 Landslide ring shear simulator (Landslides Vol. 1, No. 1)

Table 4 Relation between water depth and tsunami behavior (steady-state shear resistance = 80 kPa)

Landslide volume	Depth of water (m)	Maximum landslide velocity (m/s)	Tsunami traveling time(s) to 10 km from the coast	Maximum tsunami height (m) in Fig. 43
A: $5.8 \times 10^6 \text{ m}^3$	2	14.5	2065	0.1
	20	20.7	620	1.7
	200	38.1	220	14.7
B: $170 \times 10^6 \text{ m}^3$	2	29.5	1150	0.4
	20	37.3	385	8.7
	200	56.6	180	62.0

Table 5 Relation between the steady-state shear resistance and tsunami behavior (depth of water is 200 m)

Landslide volume (m^3)	Steady-state shear resistance (kPa)	Maximum landslide velocity (m/s)	Tsunami traveling time(s) to 10 km from the coast	Maximum tsunami height (m) in Fig. 44
A: 5.8×10^6	50	42.8	215	20.0
	200	38.0	230	9.2
	400	13.3	250	2.2
B: 170×10^6	100	55.7	180	62.0
	1000	44.7	225	23.4
	1250	30.2	255	5.9

PDF-tool 3.081-1.5 An integrated model simulating the initiation and motion of earthquake and rain induced rapid landslides and its application to the 2006 Leyte landslide (Landslides, Vol. 7–3)

PDF-tool 3.081-1.6 A hypothesis of the Senoumi submarine megaslide in Suruga Bay in Japan—based on the undrained dynamic-loading ring shear tests and computer simulation (Landslides, Vol. 9)

4 Applications of UDRA, LS-RAPID and LS-Tsunami

Abstract

Section 4 presents the practical application of the undrained dynamic-loading ring-shear apparatus (UDRA) and the integrated landslide simulation model (LS-RAPID) and the integrated landslide-induced tsunami model (LS-Tsunami) for two landslide disasters in Japan.

One example is 1792 Unzen-Mayuyama landslide and the resulting landslide-induced

tsunami disaster in Japan. Around 15,000 people were killed by this landslide and the landslide-induced tsunami. The Unzen-Mayuyama landslide took place in the Unzen volcano, Shimabara Peninsula, Kyushu Island, Japan. It is one of biggest landslides (maximum depth 400 m, total volume is $3.4 \times 10^8 \text{ m}^3$) and historically the biggest landslide disaster in Japan. The disaster was well documented and well investigated. It is the best example for the application of this LS-RAPID and LS-Tsunami as a megaslide, an earthquake-induced landslide, and a landslide-induced tsunami.

Another example is a swarm of rain-induced shallow landslides triggered by local heavy rainfalls on 20 August 2014 that killed 74 persons in an urban settlement in Hiroshima city, Japan. The depths of the landslides are 2–4 m; they are very shallow and small-scale. However, many landslides occurred near the top of mountains during rains, then travelled down to the lower slopes and torrent deposits. Those landslides entrained saturated unstable deposits on the slope and torrents deposits by

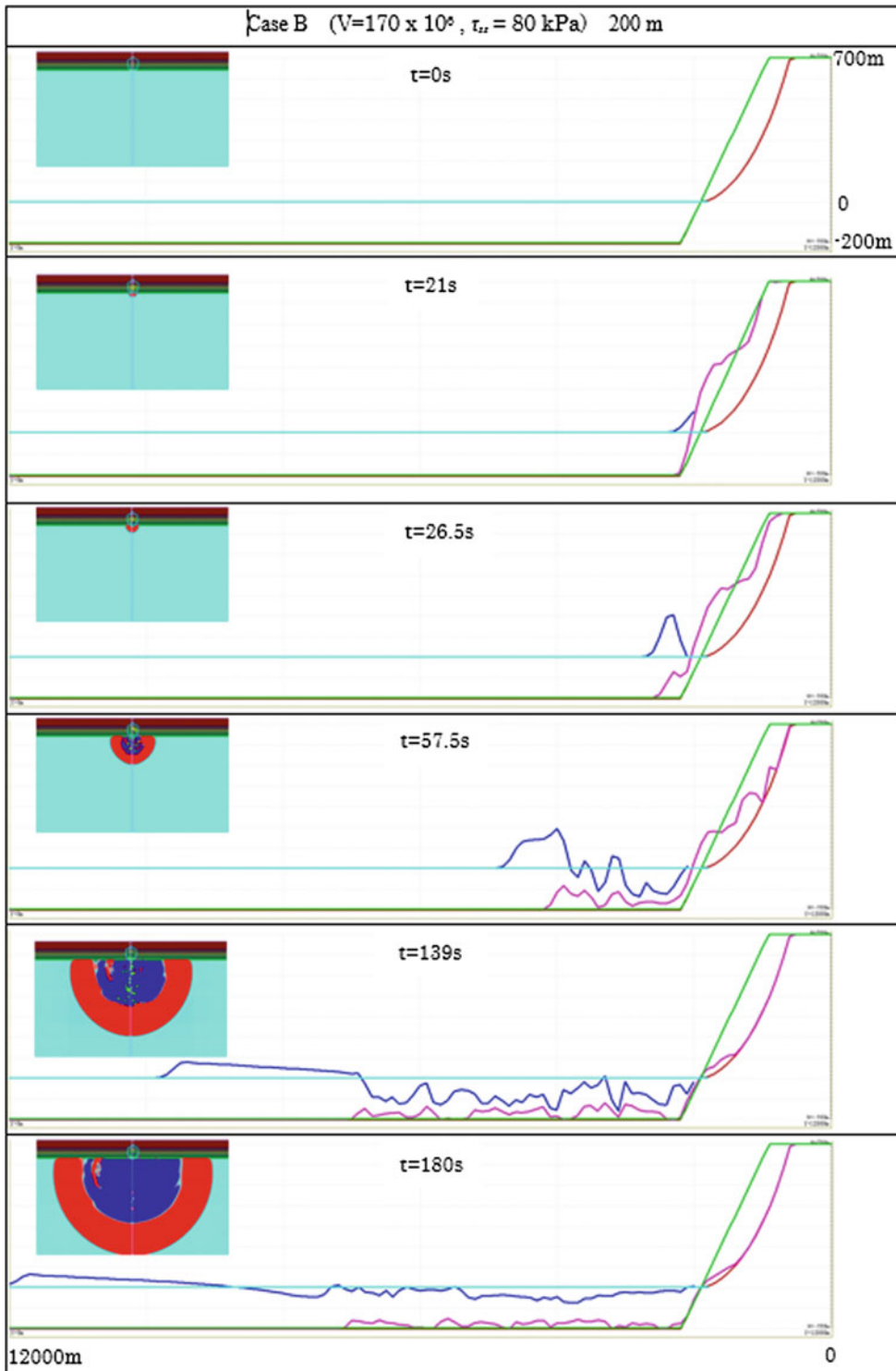


Fig. 45 Tsunami and landslide profiles during motion

undrained loading and increased their volume, and struck apartments and houses in an urban residential area. Each landslide was small and shallow, but this disaster was a shock to the society of Japan, because a new law to reduce landslide disasters had been established in 2000 and extensive efforts made to reduce further landslide disasters, based on lessons from an earlier Hiroshima landslide disaster in 1999. This case presents a good example of rain-induced small, shallow landslides which caused a major disaster.

Keywords

Landslide dynamics • LS-RAPID • LS-Tsunami • 1792 Unzen-Mayuyama landslide • 2014 Hiroshima landslide disaster • LS-RAPID • LS-Tsunami

4.1 Application to the 1792 Unzen-Mayuyama Megaslide-and-Tsunami Disaster

The undrained dynamic-loading ring-shear apparatus (UDRA), the integrated landslide simulation model (LS-RAPID) and the integrated landslide-induced tsunami simulation model were applied to the 1792 Unzen-Mayuyama megaslide initiation and motion, and also the motion of the tsunami induced by this rapid long-runout landslide. This landslide-and-tsunami disaster was both the largest landslide disaster in Japan and the largest volcanic disaster in Japan, and also one of largest tsunami disasters in Japan. This landslide disaster was well investigated by many people and the government. Therefore, the landslide topography before and after the failure, and the tsunami disasters on the Shimabara Peninsula and the Kumamoto and Amakusa coasts are recorded. The nearby earthquake which triggered the landslide was also investigated from the destruction of houses and the toppling of

tombstones (introduced in Sassa et al. 2014b). This is the best case study of the application of UDRA, LS-RAPID and LS-Tsunami.

4.1.1 Application of UDRA and LS-RAPID to the 1792 Unzen-Mayuyama Megaslide

Outline of the 1792 Unzen-Mayuyama Landslide

The 1792 Unzen Mayuyama megaslide is the largest landslide disaster and also the largest volcanic disaster in Japan. This landslide killed a total of 15,153 persons, of which 10,139 persons died in the Shimabara area. Other people were killed on the opposite banks by the landslide-induced tsunami wave: 4653 persons in the Kumamoto Prefecture, 343 persons in Amakusa Island and 18 persons in other areas (Usami 1996). The landside area is shown in Fig. 46, including the head scarp location, the direction of movement of this landslide, and also some islands in the sea which were part of the landslide mass that entered the sea.

Figure 47 shows the profile of this landslide. The section of the initial main landslide block is shown by a red dotted mass, and the secondary sliding block pushed forward by the motion of the initial landslide mass is shown by a black dotted soil layer. The original ground surface before the landslide and the sliding surface were estimated by Inoue (1999) and the MLIT Unzen Restoration Office (2002). The main sliding block and the secondary sliding block were interpreted by Sassa et al. (2014b). The lines of slope angles of 6.5° and 28.1° were drawn for the undrained dynamic-loading ring shear test to physically simulate the initiation of the landslide (red dotted area) and the movement of the secondary sliding block (black dotted area) due to the undrained loading from the displaced initial landslide mass.

For a series of initial tests of ICL-2, we took two samples from the 1792 Unzen Mayuyama landslide in Shimabara City of Kyushu Island of Japan.

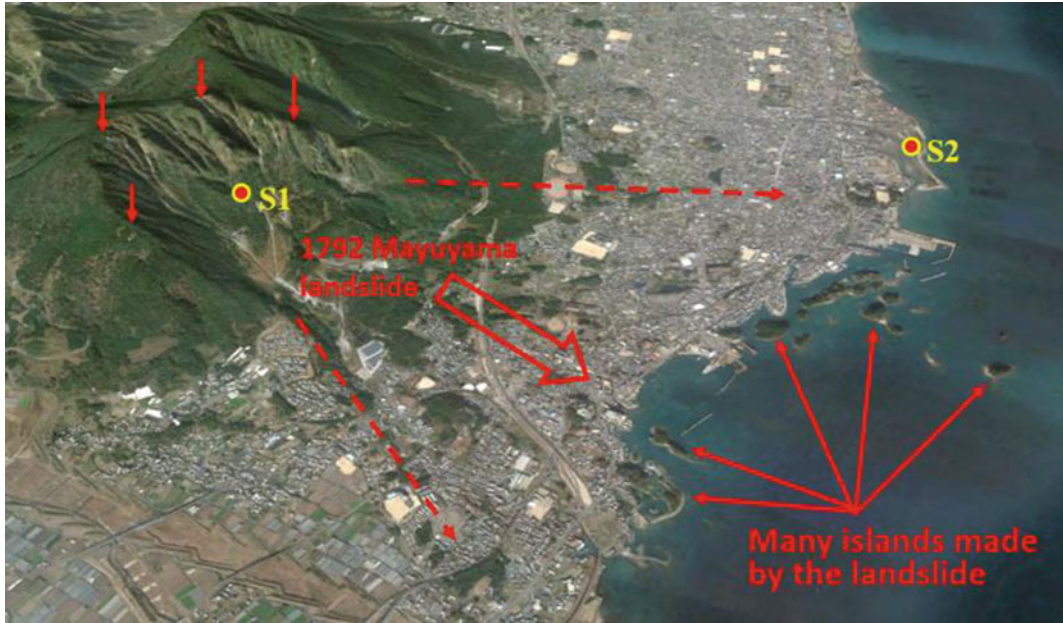


Fig. 46 Overview of the 1792 Unzen-Mayuyama landslide

Sampling from the 1792 Unzen-Mayuyama Landslide Site

The location of sampling is shown in Fig. 46. Mayuyama is a dome of the Unzen Volcano. The whole mountain consists of volcanic lava (rock) and eruption products (debris and sands). The sliding surface of landslides probably formed within a sandy layer to avoid strong intact lava

rocks and boulders. We took a sample (S1) from the sandy zone exposed along a torrent side slope in the source area. Sample state during sampling is shown in Fig. 48. Sample 2 (S2) was taken along the coastal area outside the landslide moving area as a representative soil before the landslide. The grain size distribution of both samples is shown in Fig. 49.

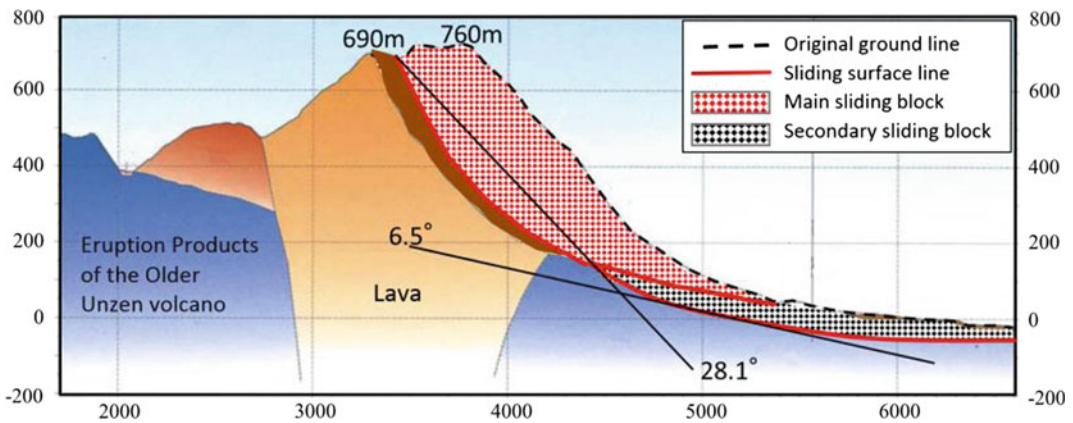


Fig. 47 Section of the 1792 Unzen-Mayuyama landslide and its interpretation

Results of UDRA Testing of the 1792 Unzen-Mayuyama Landslide

We performed four tests on the sample (S1) taken from the source area of Unzen Mayuyama to investigate the initiation of the landslide block in the upper slope (red dots block in Fig. 47) using the ICL-2 apparatus.

- (1) As a basic test, we performed a series of monotonic undrained increasing shear stress tests that were conducted at various consolidation pressures ranging from 300 to almost 3000 kPa. The result is shown in Fig. 50. The friction angle during motion is 39.8° . In all tests a large excess pore pressure generation during shearing was observed. These test results suggested the possibility of rapid landslide motion.
- (2) We performed the test with increasing pore pressure to check which level of pore water pressure can trigger the initiation of landslide.

In Fig. 51, pore water pressure was increased until the sample failed and caused a landslide. Firstly the sample was saturated, in which the B_D



Fig. 48 Photo of the sand layer from which sample (S1) was taken. It is an exposed slope along a torrent channel in the source area of the Unzen Mayuyama landslide

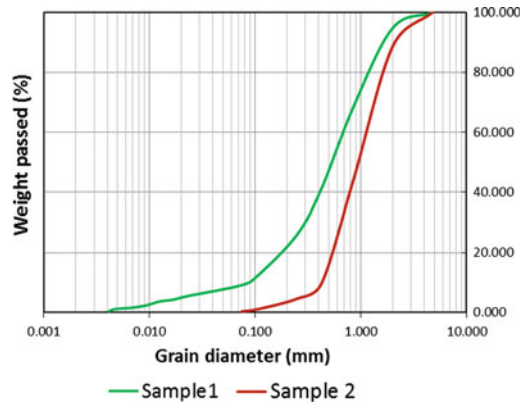


Fig. 49 Grain size distributions of Sample 1 (S1) and Sample 2 (S2)

value was 0.98. Then, it was consolidated until 3.0 MPa of normal stress and 1.5 MPa of shear stress in a drained condition. This preparation stage aims to reproduce the initial stress in the slope as shown by a black line in Fig. 51.

These initial stresses correspond to the slope of $\arctan(1.5/3.0) = 26.5^\circ$, a similar angle to the landslide block in Fig. 47. Then, in order to simulate the pore-pressure-induced landslide process, the pore water pressure was gradually increased at the speed of $\Delta\sigma = 5$ kPa/s. Failure occurred at a pore water pressure of 1.2 MPa,

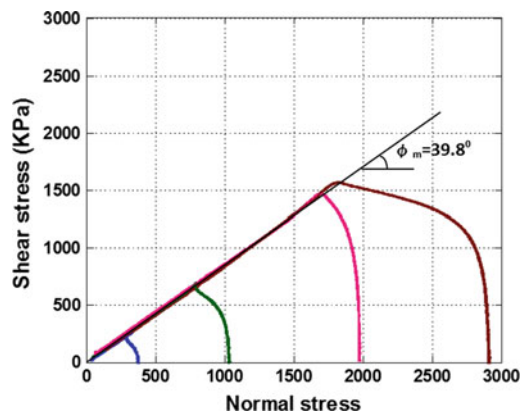


Fig. 50 Combined undrained monotonic stress control tests on Sample 1 (S1). Shear stress increment rate: $\Delta\tau = 1-5$ kPa/s, $B_D = 0.93-0.96$

namely a pore water pressure ratio $r_u = 1.2/3.0 = 0.4$. The friction angle at failure was 39.4° .

(3) In order to examine the shear behavior during the seismic-loading test to simulate the initiation of the earthquake-induced landslide, we performed an undrained cyclic loading test on the saturated Sample S1. The test result is shown in Fig. 52. Initially the saturated sample was consolidated at 2.0 MPa normal stress. Then, a 1.2 MPa shear stress was loaded in the drained state to create the initial stress state. The slope angle of this normal/shear stresses corresponds to $\arctan(1.2/2.0)$, namely 31.0° . The shear box was then switched to the undrained state for the undrained cyclic loading test. We have saved the control signal in the computer as follows: the initial cycle of shear stress increment ± 300 kPa will be loaded in a sine curve, the second, the third and the fourth cycle of shear stress will be loaded by increasing ± 300 kPa in each step. (Normal stress is 2 Mpa, so the soil should fail before the loading of the 4th cycle, where the total shear stress will be 2.4 MPa.) Thereafter, three cycles will be kept constant and decrease the cyclic shear stress to zero. This computer signal was given to the servo-amplifier for shear stress while the control signal for normal stress is kept

constant. Then, pore water pressure generation during the test, mobilised shear resistance, and shear displacement were monitored. The stress path and the time series data of this test are shown in Fig. 52. The shear stress reached the failure line at the second cycle and the shear stress dropped after the peak of the third cycle due to high pore water pressure generation. This is the sliding surface liquefaction. Then, the shear displacement (purple line) accelerated and reached more than 10 m. The peak friction angle was 40.5° , friction angle during motion was 39.6° . The steady-state shear resistance was 81 kPa.

Examination of Earthquake Loading at the Unzen Mayuyama Landslide

In April of 1792 a series of earthquakes struck the Shimabara area. The greatest earthquake hit the area on 21 May 1792. The magnitude of this nearby earthquake is estimated to have been $M = 6.4 \pm 0.2$ (Usami 1996).

Usami estimated that the seismic intensity at Shimabara was at least V and possibly VI. The Unzen Restoration Office, however, estimates that the seismic intensity which triggered the Unzen–Mayuyama landslide was VII, because more than 30% of the houses were destroyed in the Shimabara area. Exact seismic accelerations may never be known, but probably were around

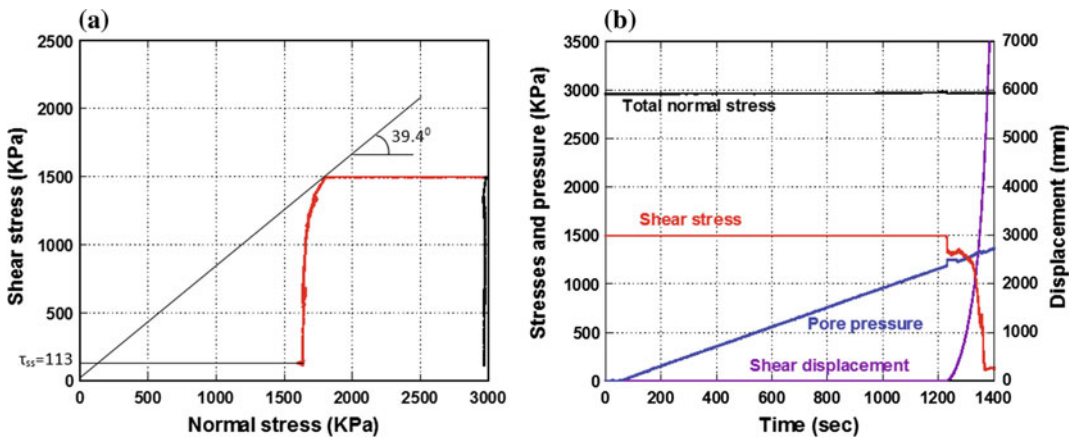


Fig. 51 Pore pressure control test on Sample 1 (S1) from Mayuyama source area. $B_D = 0.98$

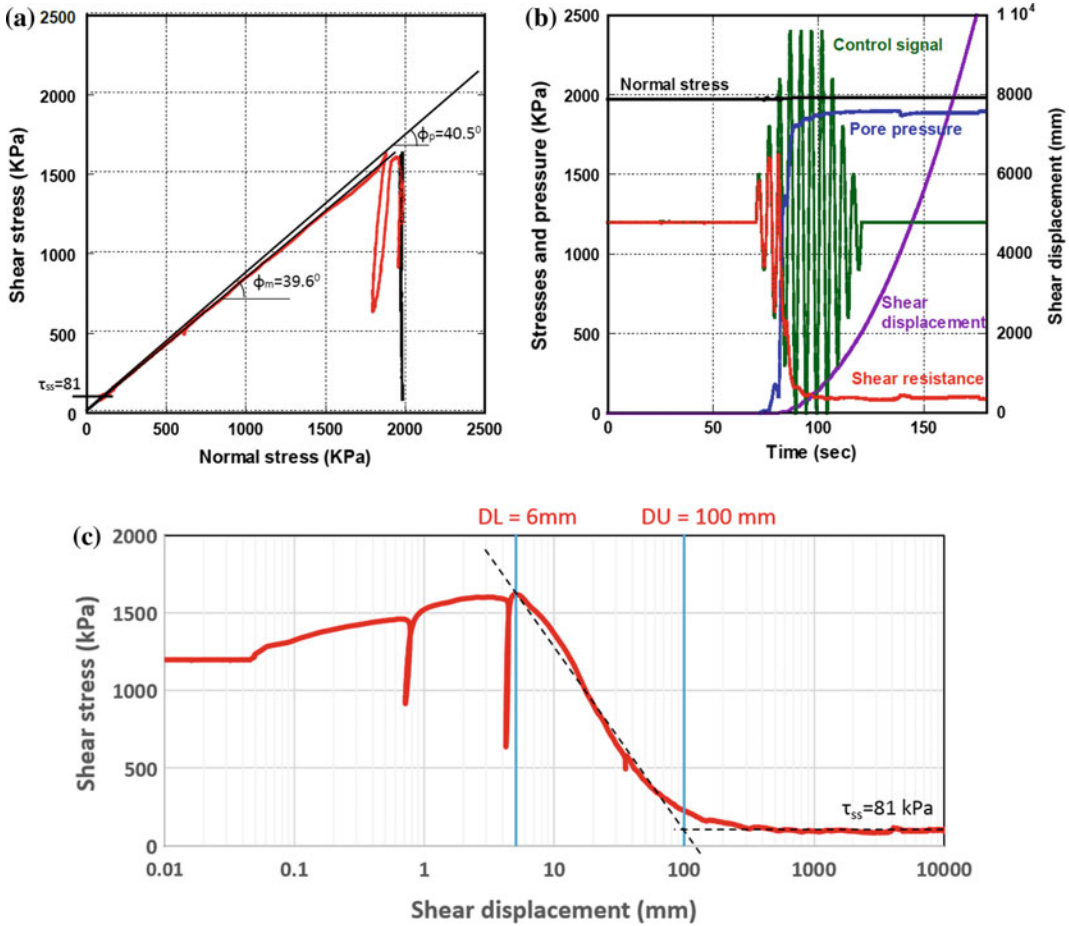


Fig. 52 Undrained cyclic loading test on Sample 1 (S1). B_D value: 0.98, cycle rate: 0.2 cycle/s, shear stress step: 300 kPa

400 cm/s^2 or greater. The Japanese seismic intensities (Usami 1996) are as follows:

- V: 80–250 cm/s^2 (where walls and fences are cracked, and Japanese gravestones fall down).
- VI: 250–400 cm/s^2 (where less than 30% of Japanese wooden houses are destroyed).
- VII: More than 400 cm/s^2 (where more than 30% of the houses are destroyed, landslides are triggered and surface fault rupture is seen).

The estimate of an acceleration of more than 400 cm/s^2 by the Restoration Office is probably correct, as it is based on a detailed study of house damage.

However, we do not have the seismic record of 1792 earthquake, so we have used a recent case. In recent years, the 2008 Iwate-Miyagi Nairiku Earthquake ($M = 7.2$) triggered the Aratozawa landslide (67 million m^3) in Miyagi Prefecture. The seismic record is presented in Fig. 53. The maximum recorded acceleration was 739.9 cm/s^2 at MYG004 (National Research Institute for Earth Science and Disaster, Prevention, NIED) in the NS component. It is of a similar scale and both triggered megaslides. We have decided to use the Iwate-Miyagi earthquake wave form recorded in Miyagi Prefecture (MYG004) for the ring-shear simulation test and also the computer simulation for 1792 Unzen Mayuyama landslide.

Estimation of the Unit Weight of Soils in the Slope from a Ring-Shear Consolidation Test

We have to estimate the unit weight for planning the ring-shear simulation test and also the integrated landslide simulation (LS-RAPID). The measurement of unit weight by sampling of an undisturbed soil layer from the ground surface may not give the correct value for the soil layer at a greater depth. To estimate it, we consolidated the sample (S1) in the ring shear apparatus in the saturated condition. The consolidation stress, sample height, dry unit weight and saturated unit weight are shown in Fig. 54. The saturated unit weight can reach 21 kN/m³ in 3 MPa, but the dry unit weight is 19 kN/m³ at 3 MPa. Values are smaller in shallower areas. Based on a range of values, we used one value for the whole area. We assumed this value as 19.5 kN/m³, as a value between the saturated unit weight and the dry unit weight, because the soil layer is not fully saturated, but not fully dry.

Ring-Shear Simulation Test of the Earthquake-Induced Unzen-Mayuyama Landslide

We conducted the ring shear simulation test of the Unzen-Mayuyama landslide (Fig. 55). It was a seismic-loading ring shear test to simulate the initiation of the Mayuyama landslide by the combined effect of pore water pressure and earthquake shaking. Initially the sample (S1) was saturated ($B_D = 0.94$) and consolidated to 3 MPa in normal stress and 1.5 MPa in shear stress; the corresponding slope angle is $\arctan(1.5/3.0) = 26.6^\circ$. Then pore water pressure was increased up to 800 kPa, namely a pore water pressure ratio of $r_u = 800/3000 = 0.27$ as the initial slope condition; although the exact value is not known, it must be smaller than 0.4. A preparatory test (Fig. 51) showed that $r_u = 1.2/3.0 = 0.4$ is the critical pore water pressure which causes a landslide without an earthquake. The earthquake which triggered the 1792 Unzen-Mayuyama landslide was estimated to be Magnitude $M = 6.4 \pm 0.2$ and seismic intensity as VII during the earthquake based on the Japanese standard, which corresponds to more than 400 cm/s², as explained above.

The Iwate-Miyagi earthquake triggered the large-scale Aratozawa landslide (67 million m³) in 2008. We loaded the NS component 2008 Iwate-Miyagi earthquake record (maximum acceleration is 739.9 cm/s²) at MYG004 as the

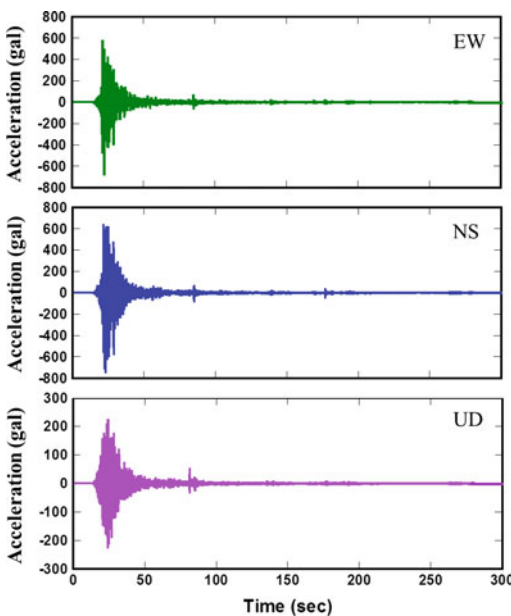


Fig. 53 The 2008 Iwate-Miyagi earthquake record (MYG004) from K-net of National Research Institute for Earth Science and Disaster Prevention (NIED)

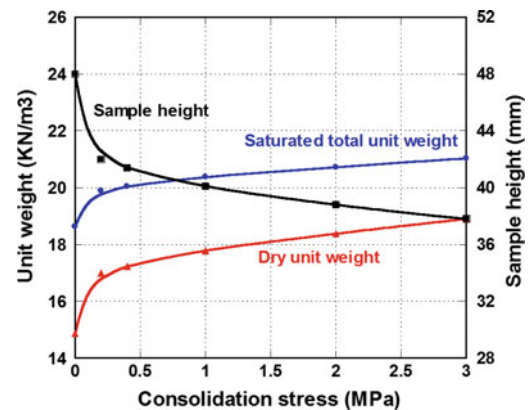


Fig. 54 Sample S1 was consolidated in the ring shear apparatus to obtain saturated and dry unit weight

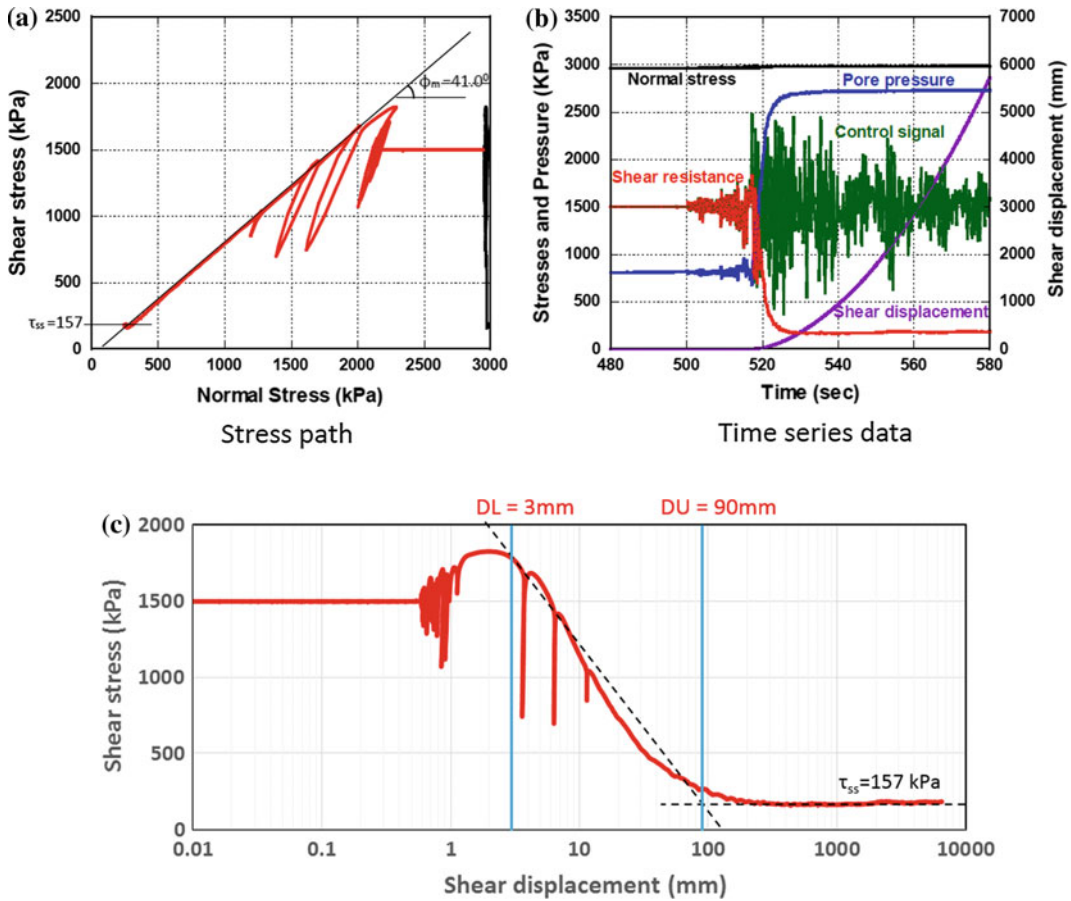


Fig. 55 Undrained seismic loading test on Sample 1 (S1). $B_D = 0.94$, seismic wave: 2008 Iwata-Miyagi earthquake record, 5 times slower speed

additional shear stress. For precise pore pressure monitoring as well as servo-stress control, a 5 times slower speed of seismic acceleration record was applied. The test result is shown in Fig. 55.

The green line represents the control signal. The maximum value is 2469 kPa (1500 + 969 kPa) and the minimum value is 369 kPa (1500 - 1131 kPa). The loaded acceleration (a) is calculated from the ratio of seismic acceleration and gravitational acceleration: $a/g = 969/1500$ or $a/g = 1131/1500$, because $ma = 969$ kPa and $mg = 1500$ kPa, expressing the landslide mass at unit area as m. The acceleration corresponds to +633 and -739 cm/s^2 . Therefore, the control signal for shear stress given to the ring shear apparatus exactly corresponded to the monitored acceleration record.

As shown in Fig. 55, failure occurred around 1825 kPa, namely $a/g = (1825 - 1500)/1500 = 0.22$, the acceleration needed for failure was 216 cm/s^2 . This test results suggested that around 1/3 smaller earthquake shaking (around $216/633 = 0.34$) than the Iwate-Miyagi earthquake should have caused failure under a slope condition with a pore pressure ratio of 0.27. The steady-state shear strength was 157 kPa.

LS-RAPID Landslide Simulation Based on the Parameters Obtained from UDRA

We conducted a LS-RAPID landslide simulation based on the landslide dynamics parameters measured and estimated by UDRA testing. All values used in the LS-RAPID and LS-Tsunami are written in Table 6.

Table 6 Parameters used in the computer simulation LS-RAPID for Unzen-Mayuyama landslide-and-tsunami disaster

Parameters used in simulation	Value	Source
<i>Parameters of soils in the source area (deeper area)</i>		
Steady-state shear resistance (τ_{ss})	120 kPa	Test data
Lateral pressure ratio ($k = \sigma_h/\sigma_v$)	0.7–0.8	Estimation (see text)
Friction angle at peak (ϕ_p)	42.0°	Test data
Cohesion at peak (c)	10 kPa	Assumed small
Friction angle during motion (ϕ_m)	40.0°	Test data
Shear displacement at the start of strength reduction (D_L)	6 mm	Test data
Shear displacement at the start of steady state (D_U)	90 mm	Test data
Pore pressure generation rate (B_{ss})	0.7–0.9	Estimated
Total unit weight of the mass (γ_t)	19.5 kN/m ³	From the test
Unit weight of sea water (γ_w)	10.1 kN/m ³	Average sea water density (1.026 kg/m ³)
<i>Parameters of soils in the moving area (shallower area)</i>		
Steady-state shear resistance (τ_{ss})	30–80 kPa	Test data
Lateral Pressure ratio ($k = \sigma_h/\sigma_v$)	0.8–0.9	Estimated
Friction angle at peak (ϕ_p)	40.0°	Test data
Cohesion at peak (c)	10 kPa	Assumed small
Friction angle during motion (ϕ_m)	40.0°	Test data
Shear displacement at the start of strength reduction (D_L)	6 mm	Test data
Shear displacement at the end of strength reduction (D_U)	90 mm	Test data
Pore pressure generation rate (B_{ss})	0.7–0.9	Estimated
Total unit weight of the mass (γ_t)	19.5 kN/m ³	From the test
<i>Triggering factor</i>		
Excess pore pressure ratio in the fractured zone (r_u)	0.21	Assumption
0.5 times of the 2008 Iwate-Miyagi earthquake	Max:370 cm/s ²	Wave form of the ground motion record at MYG004
<i>Parameters of the function for non-frictional energy consumption</i>		
Coefficient for non-frictional energy consumption	1.0	See Sassa et al. (2010)
Threshold value of velocity	100 m/s	A few times greater than maximum reported speed
Threshold value of soil height	400 m	Maximum depth of the initial source area
<i>Other factors</i>		
Steady-state shear resistance under sea	10 kPa	Data (Sassa et al. 2004)
Unit weight of sea water	10.1 kN/m ³	Average sea water density
Manning's roughness coefficient	0.025	Under water and vacant lots (MLIT Guideline 2012)

1. Steady-state shear resistance: 120 kPa in the landslide source area (deep soil layer), while 40–80 kPa in the landslide moving area (shallower soil layer) from monotonic increasing shear-stress tests in the lower normal stress test within the test results of Fig. 50 (detailed results of each test are reported in Sassa et al. 2014b)
2. Friction angle during motion: 40.0° from Fig. 50.
3. Peak friction angle: 42.0° . The maximum was 41.2° in a series of the monotonic increasing shear-stress tests (Fig. 50). However, the value in the field condition can be greater.
4. Critical shear displacements for start of strength reduction (DL) and the start of steady state (DU): 6 and 90 mm from Figs. 52c and 55c, and also Fig. 30c.
5. Pore pressure generation rate B_{ss} is 0.7–0.9 in the source area, and 0.99 under the sea (completely saturated). Outside of landslide it is 0.2, regarded as not saturated on the ground.
6. Lateral pressure ratio k : 0.7–0.9. We assumed this value to be 0.9 in the coastal area and under the sea because of the mobilization and the loss of initial structure of the landslide body and the high degrees of saturation. Outside of landslide it is 0.4, regarded as not saturated.
7. Unit weight of soils: 19.5 kN/m^3 estimated from Fig. 54.
8. Pore pressure ratio before earthquake: 0.21.
9. Seismic loading: 0.5 times of three components of the Miyagi-Iwate earthquake (maximum acceleration 370 cm/s^2).

Estimation of Landslide Block

As explained in Sect. 3.1 LS-RAPID, we have to input two components within the three topographical components; (1) the ground surface topography before the landslide, (2) the topography of sliding surface or the unmovable (stable) ground, (3) the landslide mass or movable (unstable) soil layer depth distribution. For the Leyte landslide (see Sect. 3.1), we could obtain the topographical map from the Philippine Institute of Volcanology and Seismology

(PHIVOLCS). But no data of post-landslide topography was available. We made a landslide block using the function of LS-RAPID to create one ellipsoid to give the landslide body. However, in the case of Unzen-Mayuyama, a previous researcher estimated the topography before the landslide and also the possible sliding surface close to the current digital map (Unzen Restoration Office of the Ministry of Land, Infrastructure and Transport, Japan 2002, 2003).

Figure 56 presents the ground surface topography before the landslide (left) and the sliding surface of the landslide (right) shown using LS-RAPID. When the sliding surface must be estimated, this method should be used.

Figure 57 presents the result of LS-RAPID simulation:

- At 11 s, the power water pressure reached 0.21 and the earthquake started, but no motion appeared.
- At 17 s, the main shock of earthquake struck the area and failure occurred within the slope. The failure started from the middle of the slope.
- At 26 s, the earthquake peak passed and was gradually terminating. The whole landslide mass was formed during the earthquake shaking.
- At 64 s, the landslide mass continued to move after the earthquake and entered into the sea.
- At 226 s, the landslide mass stopped moving and was deposited.

The landslide deposition area was compared to the figure (right-bottom of Fig. 57) made by the Unzen Restoration Office (2002). The travel distance and the moving area are similar. The section of line A in the right-bottom figure and the EW section (almost same with line A) of the computer simulation were compared and presented in Fig. 61, together with the maximum simulated landslide height and the maximum simulated tsunami height at each point of the section.

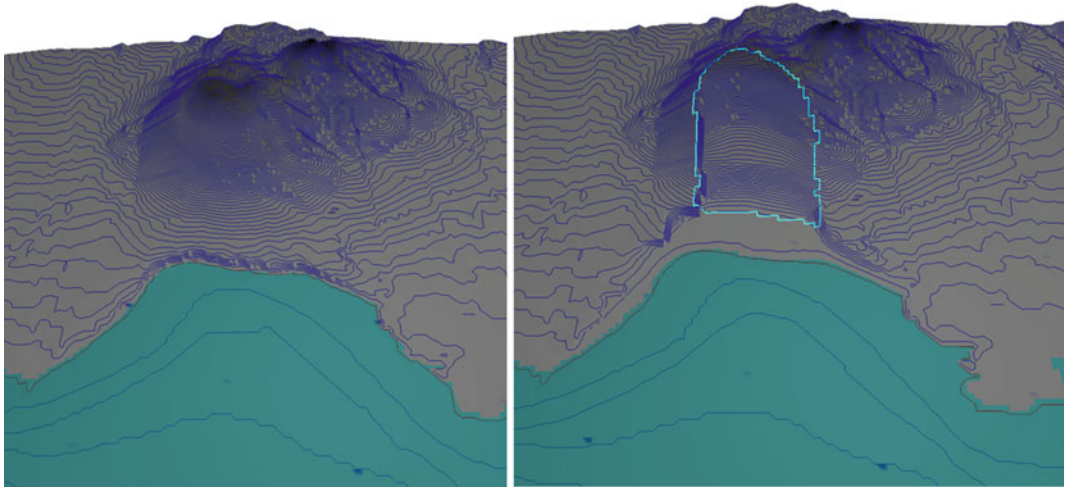


Fig. 56 Data saved in LS-RAPID for simulation. *Left* topography of the estimated ground surface of the Unzen-Mayuyama Mountain before the landslide. *Right*

topography of the sliding surface. *Blue line* is the estimated initial landslide source area

4.1.2 Application of LS-Tsunami to the 1792 Unzen-Mayuyama Landslide-Induced Tsunami Disaster

LS-Tsunami Simulation of the Unzen-Mayuyama Landslide-Induced Tsunami

The data set of landslide motion calculated by LS-RAPID at each 0.1 s was saved, and used as input to LS-Tsunami as the tsunami trigger. Additional parameters input in the LS-Tsunami are the unit weight of sea water and the Manning's roughness coefficient for basal resistance in the sea. The Manning's roughness coefficient is not a testing value, but an empirical value used for analysis of water movement such as tsunamis and floods. The most commonly used value of Manning's coefficient for tsunami simulation is $0.025 \text{ m}^{1/3} \text{ s}$ (MLIT 2002; Tinti and Tonini 2013; Imamura 2009). The tsunami motion generated by the landslide motion was calculated by LS-Tsunami. The result of simulated tsunami height at each mesh and at each 0.05 s was saved. The simulated result is presented in Fig. 58.

The first figure at the top of Fig. 58 shows that the initial landslide started to move at 0 min 20 s. The second figure on the top at 35 s shows the landslide mass reaching the coastal line. The third figure on the top at 1 min 25 s shows the landslide mass entering into the sea and triggering the tsunami wave. The left figure (5 min 55 s) in the center shows the expanding tsunami wave in the Ariake Sea, and the top parts of the moving landslide blocks (dark brown color dots) are seen above sea level, as shown by a white arrow. The yellow arrow shows the tsunami wave striking Futsu Town. The right figure in the center shows when the tsunami wave reached Kumamoto Prefecture on the opposite bank. The left figure (21 min 20 s) on the bottom shows that the tsunami wave was reflected from the opposite bank to strike the southern part of Shimabara Peninsula (around Futsu town) again as shown by the yellow arrow. Around 3500 persons were killed in the southern part of Shimabara Peninsula by the tsunami (Fig. 59). The right figure on the bottom at 29 min 55 s shows another reflected wave striking the northern side of the Mayuyama landslide area. In this figure, the bright red color presents the wave more than

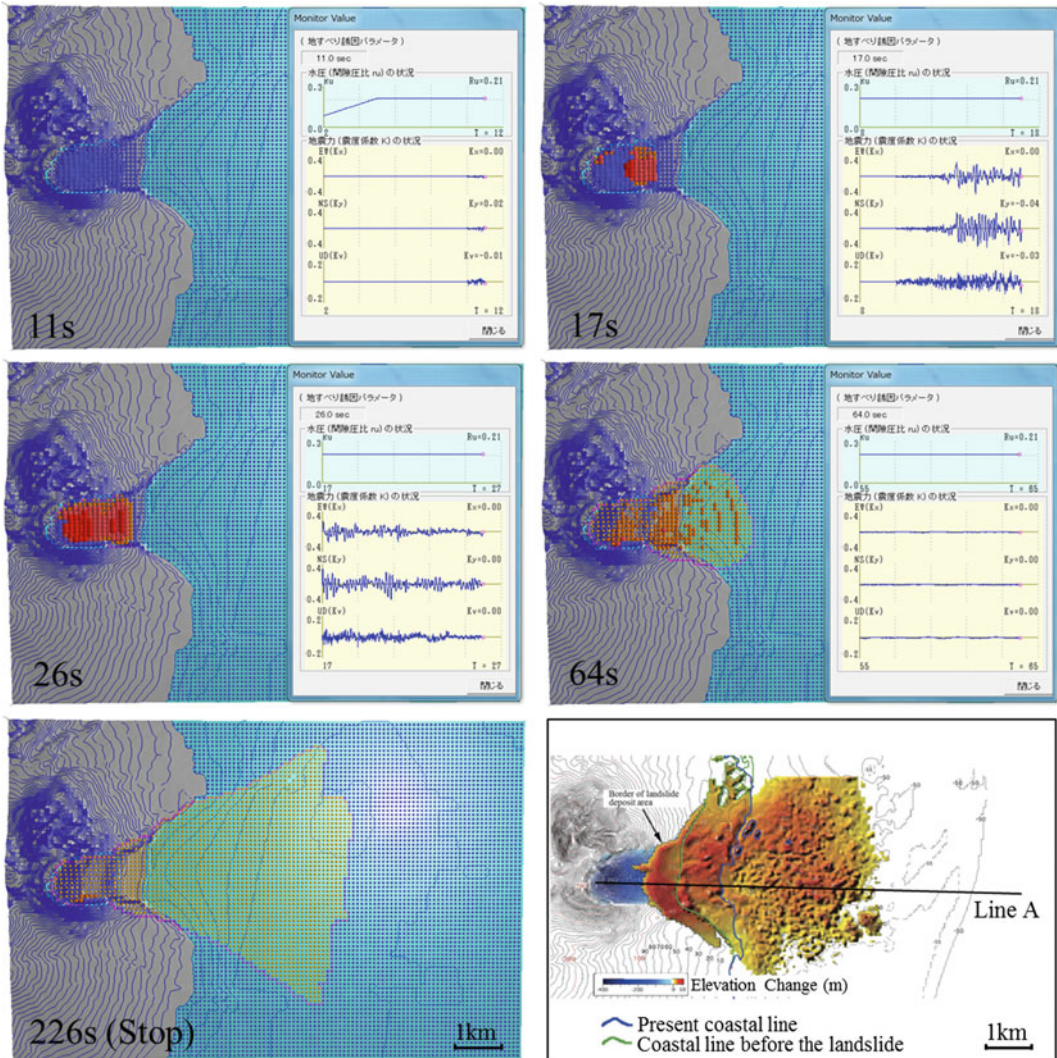


Fig. 57 LS-RAPID simulation result of the 1792 Unzen-Mayuyama landslide

5 m above sea level and the dark blue color presents the wave less than 5 m below sea level.

Comparison Between the LS-Tsunami Simulation Result and the Historical Record

The tsunami disaster investigated by the Unzen Restoration Office (2002, 2003) is shown in Fig. 59. The residents in the community erected Tsunami-Dome-Ishi (tsunami stopping stones) at the highest points where the tsunami reached. Tsunami-Dome-Ishi are found in Kyodomari, in Umedo and in Ohtao along the coast of

Kumamoto Prefecture, which were carefully investigated by Tsuji and Hino (1993). People in the Shimabara Peninsula built stone pillars in memory of the tsunami disasters. Tsuji and Murakami (1997) investigated tsunami heights in the Shimabara Peninsula. This figure was based on those investigations, including historical data as well as the stone pillars. The original image for Fig. 59 is a Japanese printed figure, which cannot be changed. English explanations have been added to the figure caption by adding A–I. The word of Shimabara-Taihen, Higo-Meiwaku

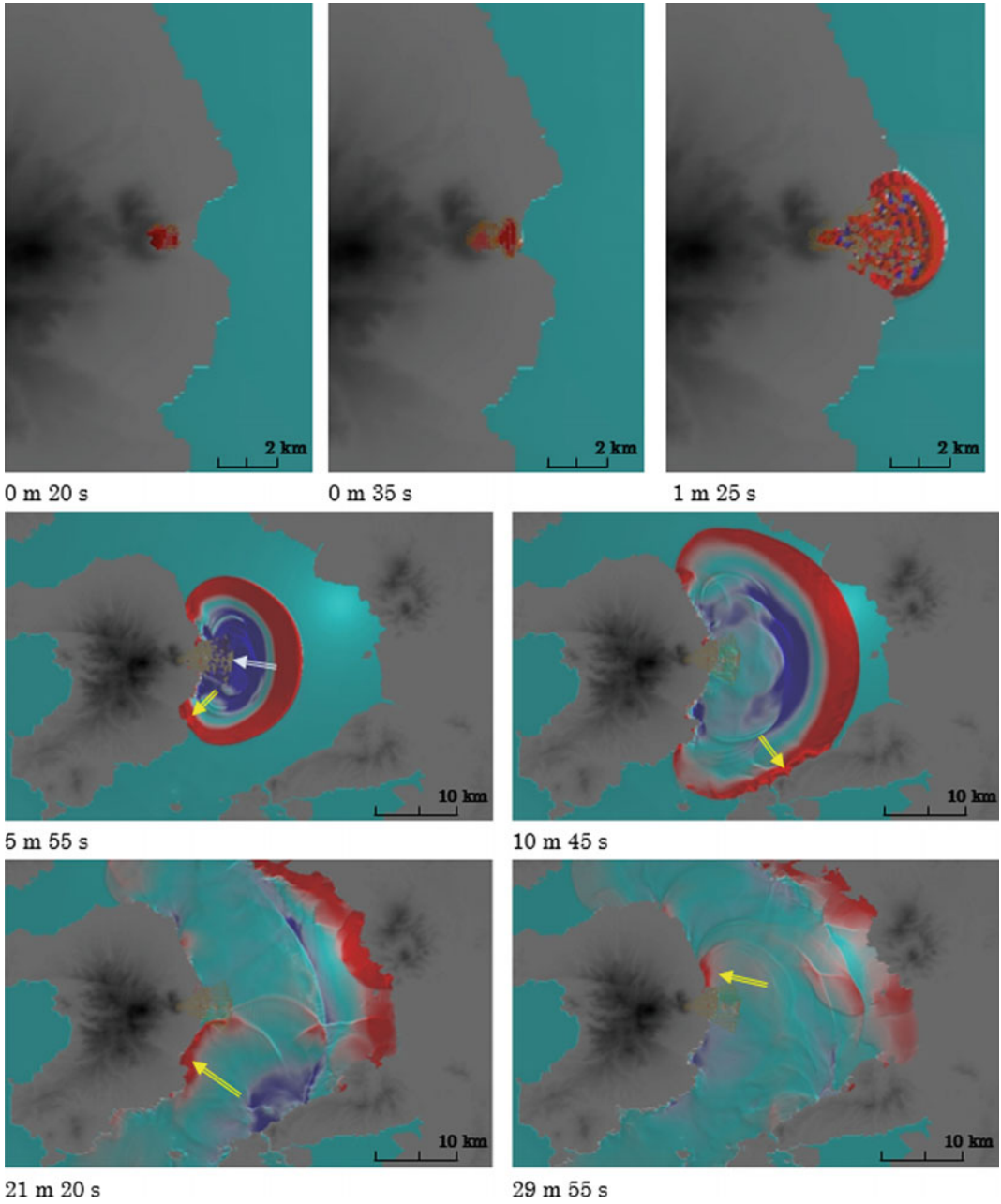


Fig. 58 LS-Tsunami simulation result for the 1792 Unzen-Mayuyama landslide-induced tsunami disaster

in A means the “Catastrophe” in Shimabara area and “Annoyance” or “adversely affected” in Higo (Kumamoto) region in the opposite coast. This word “Shimabara-Taihen, Higo-Meiwaku” is often used in Japan for the cases in which

something happens in the opposite half of the globe, and the adverse effects strike Japan.

Five sites (three sites from the Kumamoto coast and two sites from the Shimabara coast) with clearer evidences were selected to compare the results simulated by the LS-Tsunami based



Fig. 59 Records of disaster by the Unzen landslide-and-tsunami disaster (by Unzen Restauration Office 2003). Total number of death is 15,153 persons. The size of circles is proportional to the number of human fatalities in the area. The legend for the number of deaths is show in the right-top corner. A Disasters around Ariake Sea and monuments by the Shimabara-Taihen, Higo-Meiwaku. The “Catastrophe” in Shimabara Area and “Annoyance” or “adversely affected” in Higo (Kumamoto) region. B The numbers of deaths are shown in the circles (the largest is 500 persons). C The greatest deaths are Shimabara town around the castle (5251 persons). D The second largest deaths are the southern

part of Shimabara Peninsula (around 3500 persons). E–G Tsunami-Dome-Ishi (a stone showing the tsunami reaching that point) was set to record the tsunami by the communities in Kyodomari (E), Umedo (F) and Otao (G) of the Higo (Kumamoto) Han area. The Tsunami-Dome-Ishi in Kyodomari was moved for the construction of a road, but its former location is marked on the road retaining wall (by the regional education committee). The Tsunami-Dome-Ishi is limited in Higo (Kumamoto) Han area. These tsunami records are reliable. H, I Stone pillars for memorial services for deaths by tsunami in Futsu (H) and Mie (I) in Shimabara Han area

on LS-RAPID to the tsunami heights indicated by historical records for both coasts. The maximum tsunami heights at each 0.05 s for each mesh were plotted on the map and the contour map was made to visualize the tsunami wave (Fig. 60). Locations of these five sites are shown in this figure. The simulated tsunami wave reached more than 5 km inland on the Kumamoto coast.

Table 7 presents the reported and simulated tsunami heights at five sites along the Kumamoto and the Shimabara coasts. Differences between the computer simulation and the historical records for the five specific points are less than 5.7 m for Manning’s coefficient 0.025 m^{1/3} s. Manning’s coefficient is not a measured value, but a reference value. Thus, smaller Manning’s coefficient cases are also calculated. The difference was 4.6 m for

Manning's coefficient $0.020 \text{ m}^{1/3} \text{ s}$, and 5.2 m for Manning's coefficient $0.015 \text{ m}^{1/3} \text{ s}$, except the case at Futsu. The difference is smaller, but the effect is very limited.

Futsu is a special case where the first direct tsunami wave from the source of the tsunami hit the cliff of the Futsu terrace, and probably was amplified due to the gulf-shaped coast line. The tsunami wave flowed up to the terrace (Tsuji and Murakami 1997). The tsunami wave striking Futsu is seen at $5 \text{ m } 55 \text{ s}$ in Fig. 58 and the return wave also struck Futsu from a different direction at $21 \text{ m } 20 \text{ s}$. Many people were killed in this area. The simulation of LS-Tsunami used 100 m mesh data. It cannot include the effect of local amplification of tsunami height due to the sharp topography in this part of the coast.

LS-Tsunami uses the average elevation for each 100 m mesh. The elevation of Tsunami-Dome-Ishi on the slope is not always close to the average height of calculated mesh. In the case of a $15\text{--}20^\circ$ slope, 25 m ($1/4$ of one

mesh) difference in horizontal distance cause $6.7\text{--}9.1 \text{ m}$ elevation difference. The maximum 5.7 m difference in Table 7 is within the elevation difference on the slope. Considering these conditions, it can be reasonably said that the estimated tsunami hazard area and the tsunami heights along the coast by LS-Tsunami are well matched with the historical record.

Comparison of the Maximum Heights of the Landslide and the Maximum Heights of Tsunami Along the Central Section

The upper figure of Fig. 61 presents the maximum landslide movement height and the maximum tsunami height calculated by LS-RAPID and LS-Tsunami at each time step (0.1 s for the landslide, and 0.05 s for the tsunami wave) at each mesh along the central line of landslide. The ground surface before the landslide and the ground surface after the deposition of the landslide were investigated by Inoue (1999) and MLIT (2002, 2003). The lower figure of Fig. 61 shows the central section of the ground surface

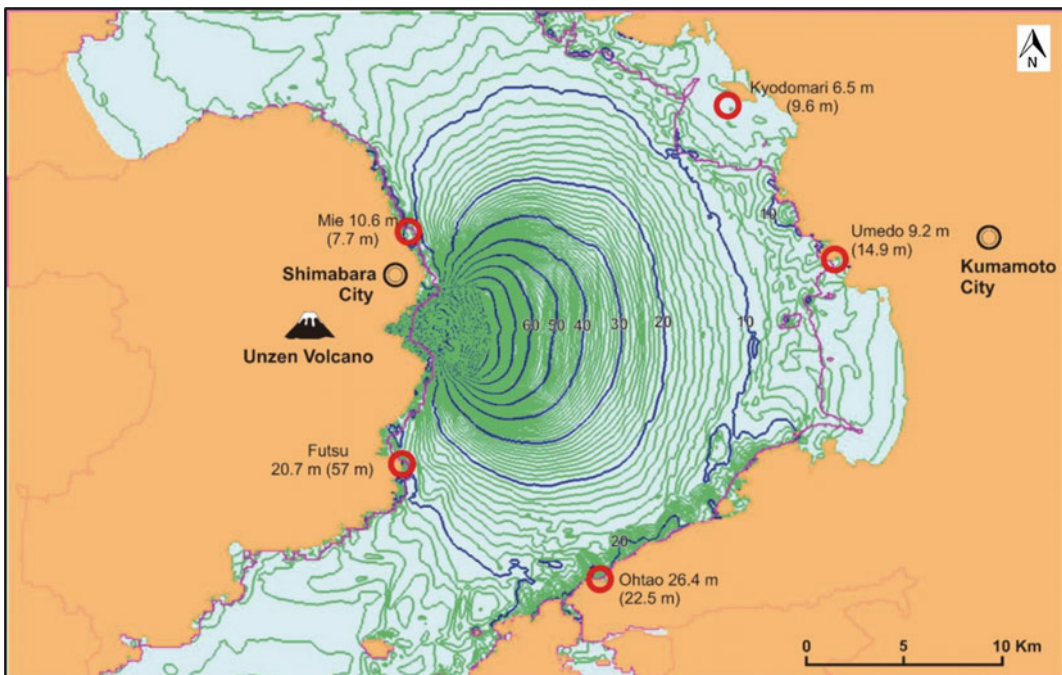


Fig. 60 Contour of the maximum tsunami height at each mesh with the tsunami height records in the Kumamoto side coast and in the Shimabara side coast. The coastline is shown in red where the tsunami wave moved up to the land

Table 7 Comparison of tsunami heights between simulation result and historical record

Location	Tsunami heights from Tsunami-Dome-Ishi and Memorial stone pillars (m)	Tsunami heights by LS-Tsunami Manning's coefficient = 0.025 ($m^{1/3} s$) (m)	Tsunami heights by LS-Tsunami Manning's coefficient = 0.020 ($m^{1/3} s$) (m)	Tsunami heights by LS-Tsunami Manning's coefficient = 0.015 ($m^{1/3} s$) (m)
Kumamoto coast	Kyodomari	9.6	6.5	9.7
	Urnedo	14.9	9.2	13.2
	Ohtao	22.5	26.4	27.7
Shimabara coast	Futsu	57	20.7	21.3
	Mie	7.7	10.6	11.0

before and after the landslide. The landslide travel distance estimated by LS-RAPID is a little longer than the real one. However, the horizontal distance from the head scarp to the landslide toe is around 10,000 m in both cases. The highest landslide mass above the original ground surface near the coast is 127 m at the time resolution of 0.1 s. The highest tsunami height near the coast is 70 m higher than the surface of the moving landslide mass at the time resolution of 0.05 s.

4.2 Application to the 2014 Hiroshima Rain-Induced Shallow-Landslide-Debris Flow Disaster

4.2.1 Outline of the Hiroshima Landslide Disaster

A swarm of small-scale shallow landslides were triggered by local heavy rain in Hiroshima City in the early morning of 20 August 2014. Those landslide masses moved down the slope and along the torrent deposits and entered urban settlements. This landslide-debris flow disaster claimed 74 dead, 255 houses damaged (MLIT-Ministry of Land, Infrastructure, Transport and Tourism). The cumulative rainfall from 20:30 PM of 19 August until 04:30 AM of 20 August reached 248 mm at Miiri rain gauge station in Hiroshima. This is main cause of the Hiroshima disasters.

66 persons were killed at Yagi and Midorii area, which is shown in Fig. 62. Each landslide is small, but 74 persons were killed in the Hiroshima urban area. This disaster was a shock to the Japanese society and a lesson that reliable hazard assessment technology for small scale-landslides is needed.

Figure 63 shows the distribution of the initial swarm of landslides in the upper part of the mountains and also their travel area, from the Geospatial Information Authority of Japan (GSI). The landslide mass should have increased during travel onto the lower slope and the torrent deposit. The increased volume of debris struck the human settlement; Fig. 64 illustrates the

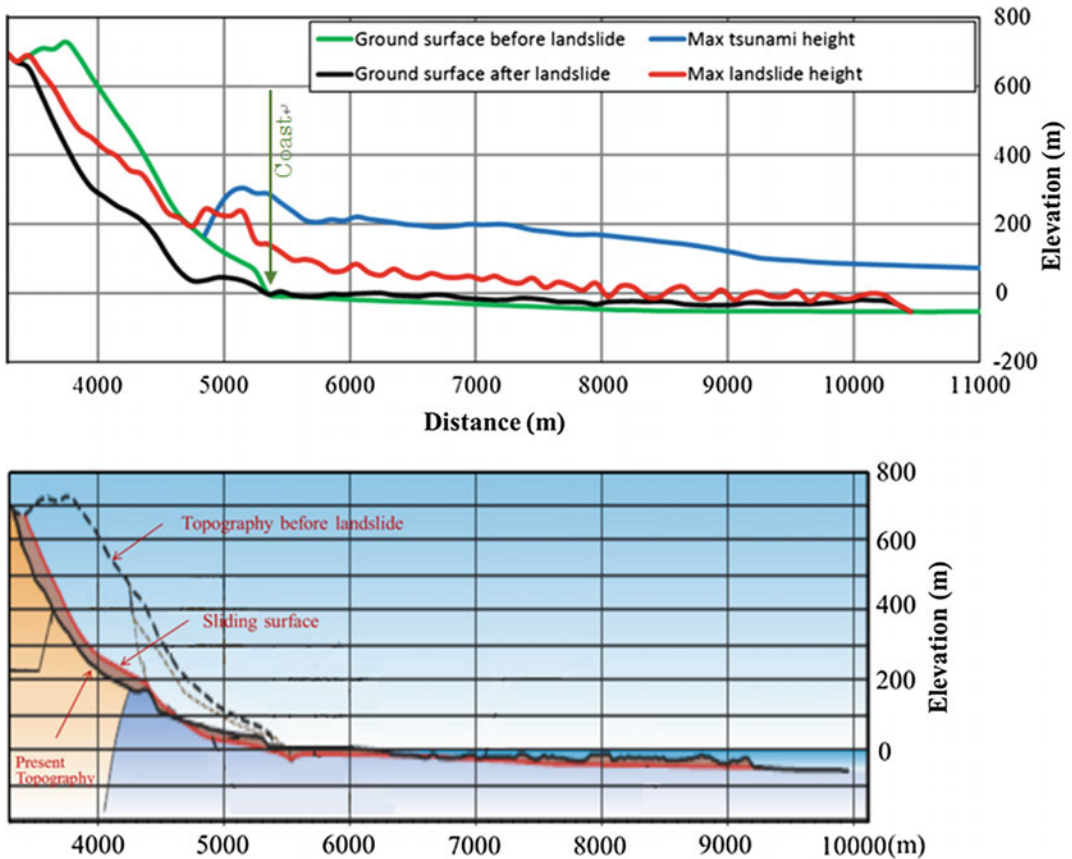


Fig. 61 The simulated maximum heights of tsunami wave and the landslide mass (*top*) and the central section of landslide reported by MLIT (*bottom*)

process. The initial landslide imposed an undrained loading to the lower slope. The lower slope had been saturated at the sliding surface, although the pore pressure is not enough to cause failure. Undrained loading contributed an additional dynamic shear stress to the lower slope layer. This is not seismic loading, but a single pulse loading. The acceleration given to the soil layer can be strongly similar to that of a nearby earthquake. In this case, the lower soil layer was entrained into the moving landslide mass. The increased volume of landslide mass then struck the houses and killed residents.

slope in weathered granitic sands (Sassa et al. 2014c). Figure 66 shows the grain size distributions of both samples. Soil samples were taken as disturbed samples. The weathered soil layer normally will be in a consolidated state. Then, both samples are normally consolidated to a given stress level in most cases. The consolidation tests were conducted by the ring shear apparatus from 0 to 200 kPa. The test result is shown in Fig. 67, where dry unit weight and saturated unit weight, together with sample height, change. This data is used for LS-RAPID simulation as the unit weight of the soil layer.

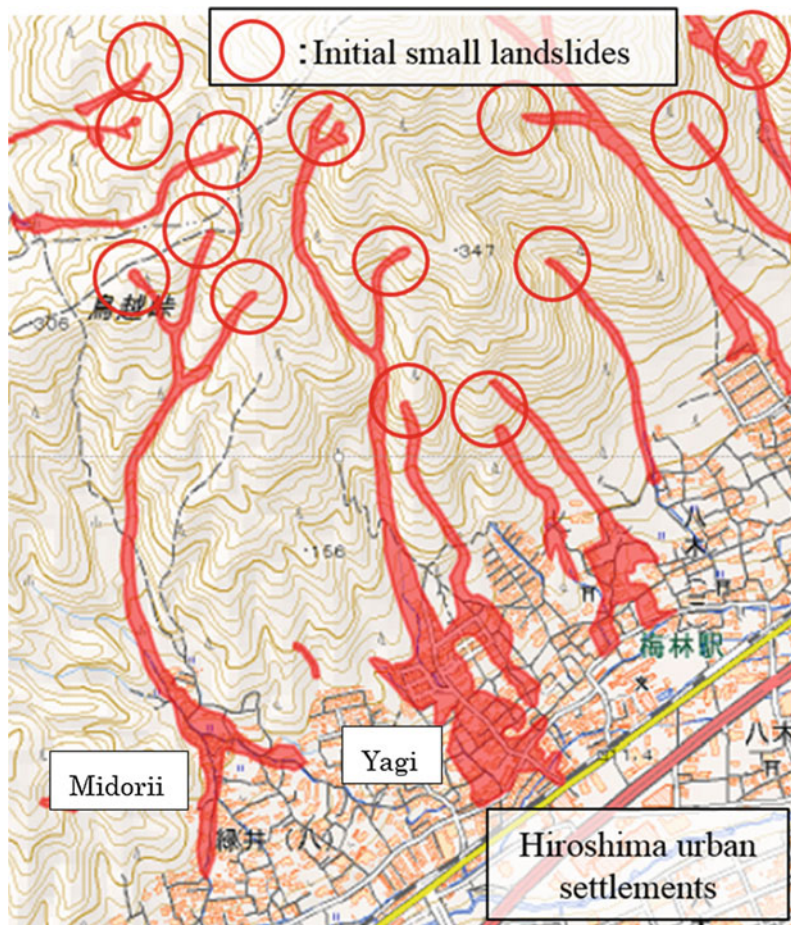
4.2.2 Sampling from the Initial Landslides

Figure 65 shows sampling of the initial landslide areas of Yagi and Midorii. Both are on a steep



Fig. 62 Photo of the Yagi-area and Midorii in 2014 Hiroshima landslide-debris flow disaster

Fig. 63 A swarm of small and shallow landslides on the upper slopes of settlements at Hiroshima. Their volume increased when landslide masses traveled over unstable deposits on the lower slope and along torrent deposits (modified from GSI WEB)



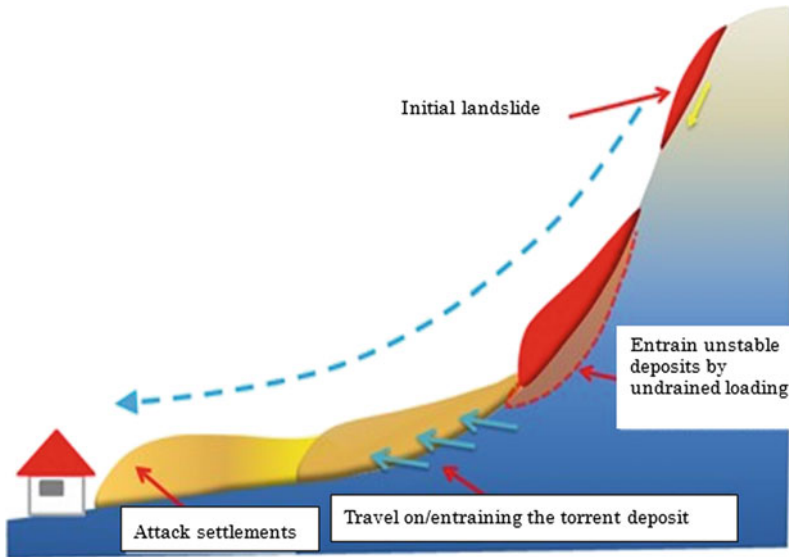


Fig. 64 Schematic figure of the motion of a shallow-landslide over unstable deposits on the lower slope and along torrent deposits to the human settlement (Ochiai and Sassa 2016, unpublished)

4.2.3 Ring Shear Testing of the Sample Taken from One of the Initial Landslides in Yagi Area

Using Ring Shear Apparatus (ICL-1)

The maximum depth of Unzen-Mayuyama landslide was around 400 m, while the initial landslides in Yagi and Midorii area are from 3 to 5 m (around 4 m) from data measured by Laser profiler (Ohta River Management Office of the Ministry of Land, Infrastructure, Transport and

Tourism), 1/10th of the depth of Unzen. The ICL-2 apparatus (designed for 3 MPa at maximum) cannot be used for this study, though shear stress sensors and pore pressure sensors can be switched for less than 1 MPa. We therefore used the ICL-1 portable apparatus. It was designed to be compact and transportable to three counterpart universities in Croatia. It is much smaller and lighter than ICL-2, but its maximum capacity of normal stress and undrained capability is 1 MPa. It has been donated to Croatia and is being used at the University of Rijeka. The shear stress sensors



Fig. 65 Photos of landslide and sampling in Yagi (left) and Midorii area (right)

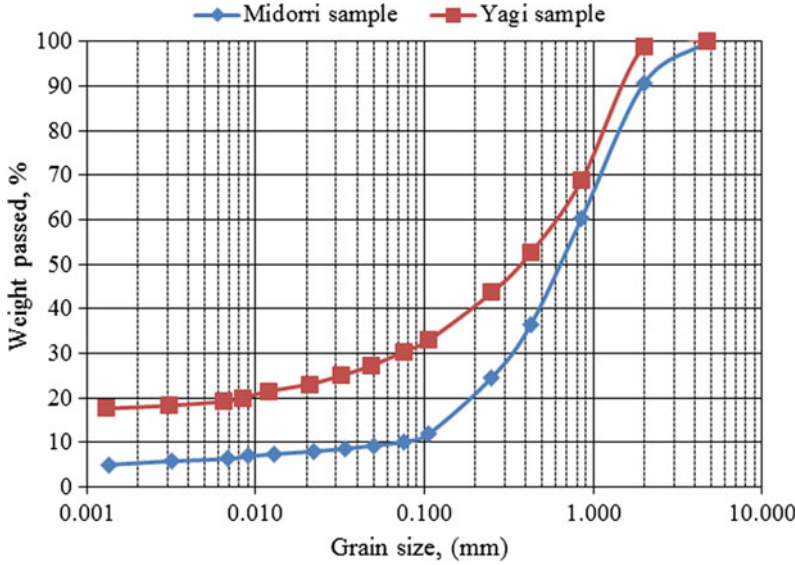


Fig. 66 Grain size distribution on Yagi and Midorri sample

and the pore water pressure transducers can be switched for 500 kPa. The structure of ICL-1 is practically same as for ICL-2. The main difference is the maximum speed of shearing. The maximum shear speed of ICL-2 is 50 cm/s, while the maximum shear speed of ICL-1 is 5.4 cm/s. This apparatus was used to study a hypothetical submarine megaslide in Suruga Bay, Japan (Sassa et al. 2012). Figure 68 presents the apparatus (left), amplifier for the sensors and servo-system (center), the monitoring and control-system, including the computer (right), and two monitor screens for control signals and recording of the stress path and time series data.

Results of the Undrained Increasing Shear-Stress Tests on Yagi Sample

A series of tests were conducted to investigate landslide initiation and the motion, as illustrated in Fig. 64. The first tests were the basic test “undrained increasing shear stress tests. The results are shown in four graphs in Fig. 69. Figure 69a shows the time series data for 100 kPa, and Fig. 69b presents the time series of data for 50 kPa. Both shear behaviors are very similar. During the approach to failure, the pore water pressure is rapidly increasing and decreasing due to dilatancy of grains during the initial shearing. Then, after the failure, rapid

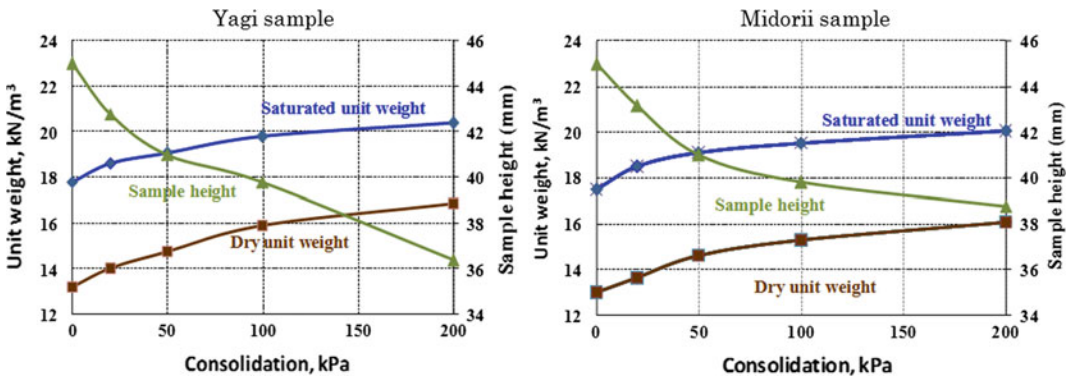


Fig. 67 Dry and saturated unit weight of Yagi and Midorri samples at different consolidation pressure

shearing causes grain crushing in the shear zone and generate a high pore-water pressure. This is a typical sliding surface liquefaction phenomena. Both data are presented in the stress path in Fig. 69c. Both stress paths reached a peak failure line of 41.5° once it moved up along the line. Then, grain crushing and pore pressure generation started and resistance went down to a low steady-state shear resistance (6.2 and 3.2 kPa). To connect the two peak failure points, the peak failure line (ϕ_p) crossed the shear stress at 4.2 kPa. This is cohesion at peak. Cohesion will be zero in the granular materials in the failure line during motion (ϕ_m), but the sand structure at the peak state still maintained an interlocking structure. This data (Fig. 69c) did not show a linear relation corresponding to the failure line during motion (ϕ_m). However, the pore pressure control test (Fig. 70) shows a linear stress path at 35.6° . This will be the friction during motion.

Result of the Increasing Pore-Pressure Test

The Hiroshima landslides were triggered by rainfalls. The initiation of landslides is caused by a pore pressure increase. On the steep slopes, a low pore-water pressure or even the loss of

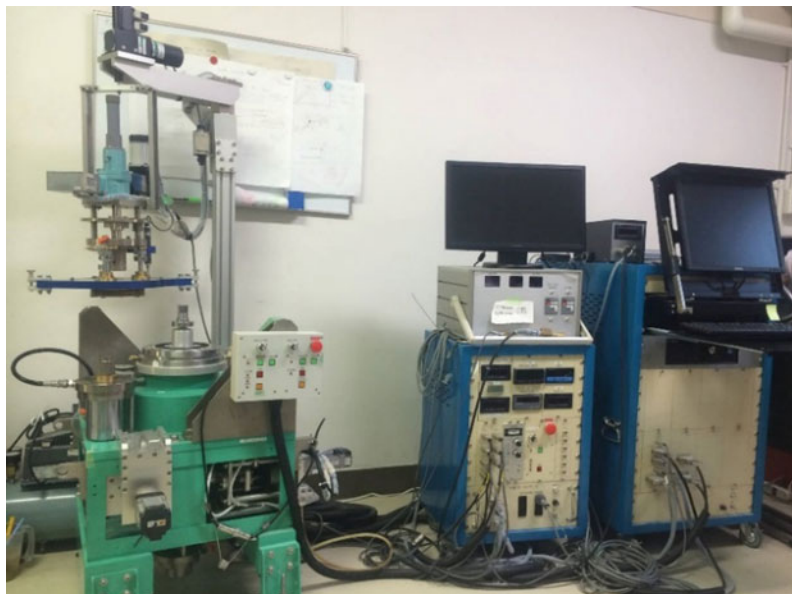
suction may trigger a landslide. On the gentle slopes, a higher pore pressure is necessary to cause landslides. In order to observe the effect of pore pressure generation carefully, the initiation on a gentle slope was simulated. The initial normal stress and shear stress (50 and 15 kPa, corresponding to a slope of 16.7°) was loaded in the drained condition to create a stress state before rainfalls. Then, pore pressure was increased up to 30 kPa, at a rate of 0.02 kPa/s.

The examiner expected that the failure would occur before the stress state ($\sigma' = 20$ kPa, $\tau = 15$ kPa, on the line of 36.9°). But it seems to almost start moving. After waiting for 200 s, the pore water pressure then started to increase at a rate of 0.02 kPa/s.

Then, the failure occurred and shearing suddenly proceeded. To monitor the pore water pressure during shearing, the examiner closed the pore pressure supply valve. Then, the monitored stress path went down the failure line during motion ($\phi_m = 35.6^\circ$).

The pore pressure control test is basically a drained test in which water can move out or in. When the valve of the pore pressure supply is not closed, the excess pore water pressure generated

Fig. 68 Photo of ICL-1 used for this investigation



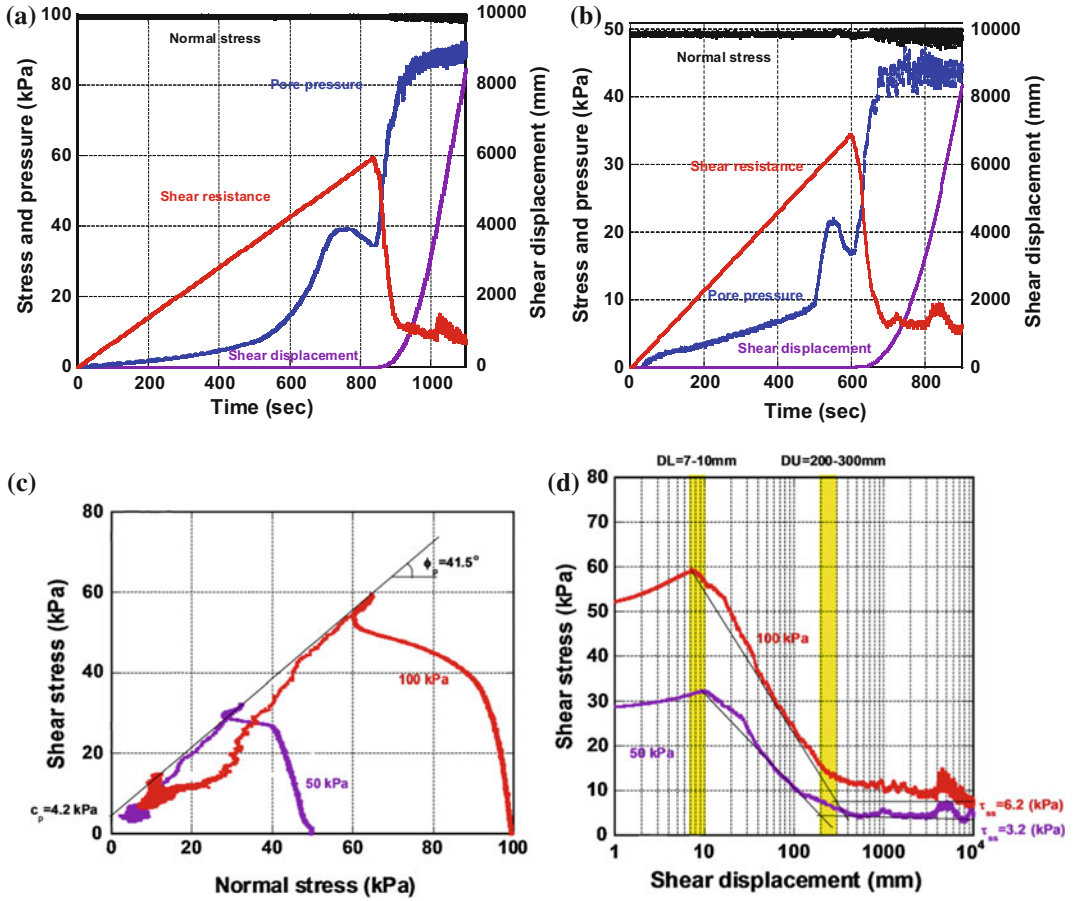


Fig. 69 Two monotonic shear stress loading tests of Yagi sample for 50 and 100 kPa

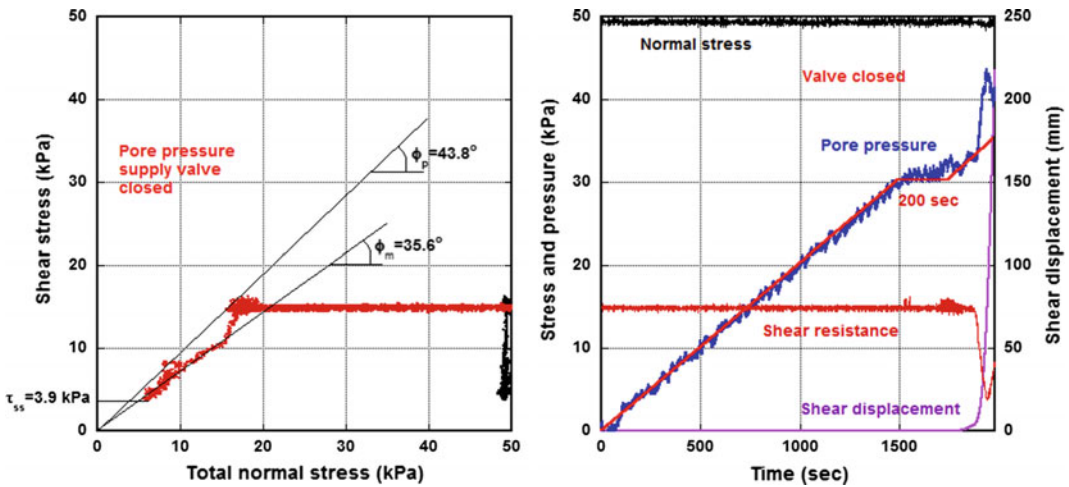


Fig. 70 Increasing pore water pressure test on the Yagi sample. BD = 0.99, pore pressure increment = 0.02 kPa/s

within the shear zone is not monitored by the pore pressure sensor, as shown in Fig. 51 (increasing pore pressure test for Mayuyama landslide).

Result of the Dynamic-Loading Test to Simulate the Entrainment of Torrent Deposit Material

When a small, rapid, and long-travelling landslide is generated on the upper slope, its landslide mass moves onto the lower slope and onto torrent deposits, as illustrated in Fig. 64, as well as Fig. 19. Figure 71 illustrates the moving landslide mass on the torrent deposit.

When the landslide mass moves onto the torrent deposit, the normal stress will increase the normal stress component of the loaded soil weight of the moving landslide mass. The shear stress will increase the shear stress component of the loaded soil weight of the moving landslide mass.

According to the data from a Laser Profiler by MLIT, the depth of initial landslides are around 2–4 m, and the depth of deposits of debris after the termination of movement is 3.7–7.4 m (Sassa et al. 2014c). Based on this information, we used the initial stress (56 kPa in normal stress and 15 kPa in shear stress) on the potential sliding surface within the deposit. We used 122 kPa in normal stress after loading. As for the additional shear stress, 110 kPa as dynamic shear stress and 35 kPa as static shear stress were applied after

the termination of dynamic force. The acting dynamic shear stress is not known, but the given value is less than the normal stress and will cause failure. The dynamic stress and the dynamic coefficient (ratio between dynamic force and loaded weight) were introduced by Sassa et al. (1997) and it was also used in Sassa et al. (2004).

The test results are presented in Fig. 72; Left: stress path and Right: time series data. Both data show the torrent deposit will be sheared by this undrained loading, and the steady-state shear resistance reached 2.9 kPa. Those parameters obtained from testing of samples taken from the site were used for the computer simulation.

Examination of the Triggering Factor of Landslides—10 min Rainfall Records and Estimation of Pore Water Pressure Ratio

The pore water pressure ratio acting on the potential sliding surface is needed to conduct the LS-RAPID simulation. The pore water pressure ratio in the slope layer is a function of rainfall, as a supply of water into the soil layer, and the water drainage from the soil layer. One of the simple models was introduced by Montrasio and Valentino (2008) and Liao et al. (2010). Figure 73 shows the concept of the SLIDE model proposed by Liao and Hong. In this model, pore water pressure is expressed in Eq. 32, and the ratio between the depth of soil

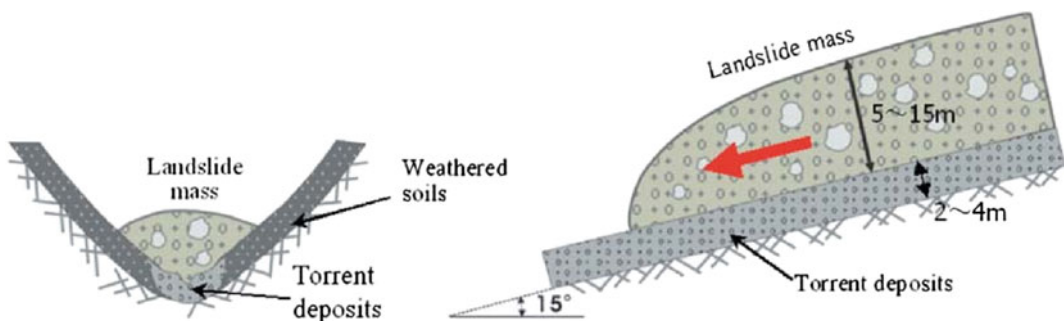


Fig. 71 Illustration of the undrained loading onto the torrent deposit

layer and the depth of groundwater layer (m) is calculated in Eq. 33. The assumption is simply that the water depth in a column in the infinite slope is changed by the balance of rainfall infiltration (assumed all rain will infiltrate into the ground) and the drainage flow from the column.

$$\Delta U = m.H.\gamma_n. \cos^2 \beta \tag{32}$$

And, changes in the ratio of groundwater layer to the soil layer pressure (m) is calculated by equation

$$\begin{cases} m_1 = 0 \\ O_t = K_t \cdot \sin \beta \cdot m_t \cdot H \cdot \cos \beta \cdot \Delta t \\ \Delta m_t = \frac{(I_t - O_t)}{n \cdot H \cdot (1 - S_r)} \\ m_{t+1} = m_t + \Delta m_t \end{cases} \tag{33}$$

where ΔU is pore-water pressure, m is the ratio between the depth of soil layer and the depth of ground water layer, t is the time, Δt is time interval, m_t is initial value of m , and m_t is calculated at each time-step. O_t represents the water outlet of a finite portion of a slope of finite length L . I_t is rainfall intensity, and K_t is the significance of a global drainage capability due to both the intrinsic soil permeability and the presence of numerous preferential down-flow pathways, H is the landslide depth, n is porosity; β is slope angle; and S_r is degree of saturation.

Figure 73 presents the result with the rainfall data from Miiri station in blue on the graph, and the calculated pore pressure is drawn as a red curve. The peak pore pressure is 21.5 kPa. The total unit weight of the nearly saturated soil layer is 18.5 kN/m^3 , $H = 4 \text{ m}$, and $\beta = 30^\circ$. Excess pore-water pressure ratio was expressed as: $r_u = u/\sigma$.

The total normal stress acting on the potential sliding surface in the 4-m deep soil layer, calculated using the almost saturated unit weigh of soils (18.5 kN/m^3) from Fig. 67, is 55.5 kPa. The maximum pore pressure ratio is estimated to be 0.39. The pore pressure ratio in each time unit is expressed by the value shown in Fig. 74

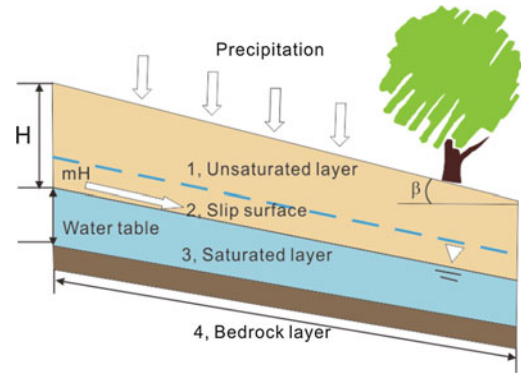


Fig. 73 Schematic illustration of water infiltration inside the infinite slope (SLIDE model by Liao et al. 2010)

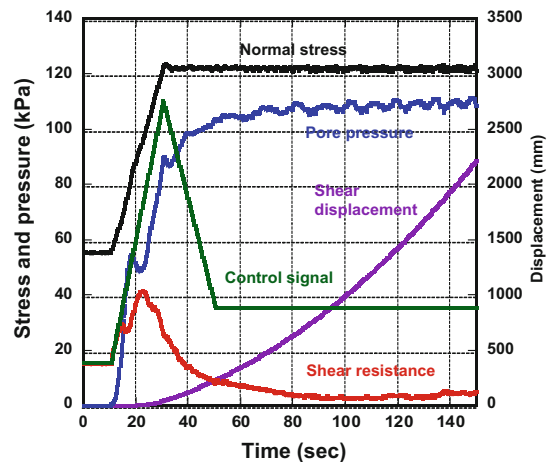
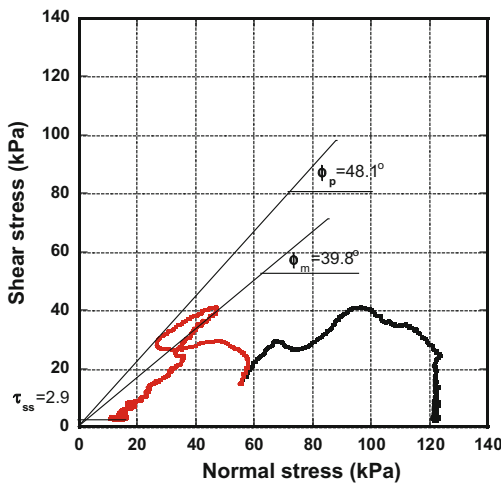


Fig. 72 Undrained loading test onto the torrent deposit using the Yagi sample

divided by 55.5 kPa. This pore pressure ratio is input to LS-RAPID as a graph of the triggering factor. It is similar to the seismic record in the earthquake-induced landslides. All parameters used in the LS-RAPID simulation of the Hiroshima landslide-debris flow disaster are listed in Table 8.

Ground Surface and Distribution of Movable Soil Depth

In order to simulate, we need to give two components of three topographic conditions as stated in Sect. 4.1 Estimation of landslide block: (1) the ground surface topography before landslide, (2) the topography of sliding surface or the unmovable (stable) ground, (3) the landslide mass or movable (unstable) soil layer depth distribution.

We input (1) and (2) for the Mayuyama landslide. For the Hiroshima landslides we have (1) a digital map before the landslide, but we did not have a detailed digital map after the landslide. Then, we used a depth distribution of movable soils from 2 to 4 m in the source area from field investigation and Laser profiler by MLIT in the places where landslides are identified from air photos and 1 m deposits through the

torrent and the alluvial deposit, although it can be deeper in some places, with no deposit in some places.

LS-RAPID Simulation Results for the 2014 Hiroshima Landslide Disaster

The simulation results of LS-RAPID are presented by video and PDF snapshots. Figure 76 presents eight snapshots of landslide movement. Red color balls represent the moving mass, while blue balls represent the stable mass (Fig. 75).

At 3h21m04s, landslides occurred in the top of Yagi district (Yagi-1)

At 3h21m53s, Yagi-1 and Yagi-2 flowed together to the residential areas.

At 3h23m03s, the displacement mass reached residential areas in Yagi district.

At 3h44m22s, failure occurred in the central of Midorii (Midorii-2).

At 3h54m45s, failure occurred in the other part of Midorii district (Midorii-3).

At 4h01m25s, two landslides in Midorii district (Midorii-2, -3) flowed into the residential area.

At 4h13m50s, Midorii-3 and Yagi-3 started to move.

Fig. 74 Pore water pressure calculated by SLIDE model from the 10 min rainfall record from 20.30 PM on 19 August 2014

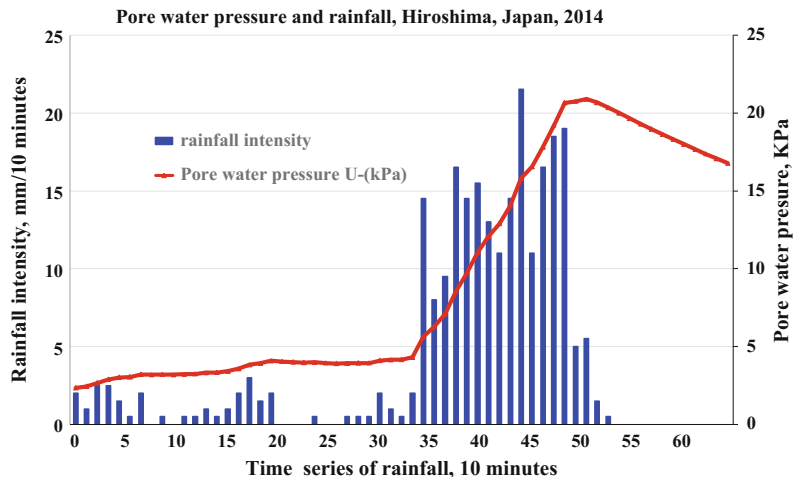


Table 8 Parameters used for LS-RAPID simulation

Parameters.	Value	Source
<i>Parameters of soils in the Yagi area</i>		
Steady state shear resistance (τ_{ss} , kPa)	3.2/2.9	Test data
Lateral pressure ratio ($k = \sigma_m/\sigma_v$)	0.5–0.95	Estimation
Friction angle at peak (φ_p , °)	44.0	Test data
Cohesion at peak (c , kPa)	0.5–1.0	Test data
Friction angle during motion (φ_m , °)	37.5	Test data
Shear displacement at the start of strength reduction (DL, mm)	5	Test data
Shear displacement at the start of steady state (DU, mm)	200	Test data
Pore pressure generation rate (Bss)	0.2–0.95	Estimated
Total unit weight of the mass (γ_t , kN/m ³)	18	Test data
Specific gravity (G_s , g/cm ³)	2.64	Test data
Porosity (n)	0.44	Test data
Degree of saturation (S_r , %)	0.82	Estimated
Permeability (K_t , m/s)	0.001	Estimated
<i>Parameters of soils in the Midorii area</i>		
Steady state shear resistance (τ_{ss} , kPa)	3.0	Test data
Lateral pressure ratio ($k = \sigma_m/\sigma_v$)	0.2–0.95	Estimated
Friction angle at peak (φ_p , %)	36.0–44.0	Test data
Cohesion at peak (c , kPa)	0.5–1.0	Test data
Friction angle during motion (φ_m , °)	37.5	Test data
Shear displacement at the start of strength reduction (DL, mm)	5	Test data
Shear displacement at the start of steady state (DU, mm)	200	Test data
Pore pressure generation rate (Bss)	0.2–0.95	Estimated
Total unit weight of the mass (γ_t , kN/m ³)	18	Test data
Specific gravity (G_s , g/cm ³)	2.68	Test data
Porosity (n)	0.44	Test data
Degree of saturation (S_r , %)	0.82	Estimated
Permeability (K_t , m/s)	0.001	Estimated
<i>Triggering factor</i>		
Excess pore pressure ratio in the fractured zone (r_u)	0.03–0.4	Calculated from SLIDE model
<i>Other parameters</i>		
Slope angle (θ , °)	30	Investigated
Landslide depth (H , m)	4	Investigated
Unit weight of water (γ_w , N/m ³)	9.8	Normal value
Rainfall intensity (I_r , mm/10 min)	0–21.5	Monitoring

At 4h15m29s, the landslide mass stopped moving.

In the left side, 10 mm rain falls and the pore pressure ratio is presented for each time snapshot.

Figure 76 presented the whole mountain in Yagi and Midorii, but it is difficult to see the movement of landslides at the top part of mountains. Then, Fig. 77 was made to visualize the landslide movement and development in the top part of slope.

At 3h18m00s, the pore-water pressure reached 15.2 kPa, and sliding started in the first landslide (Yagi-1)

At 3h21m21s, Yagi-1 reached near the second landslide (Yagi-2). The valley slope might have been excavated by the moving landslide mass.

The toe of Yagi-2 failed. The failure triggered the retrogressive failure of the whole Yagi-2.

At 3h21m25s, the whole Yagi-2 landslide mass had moved.

At 3h21m37s, the combined larger mass of Yagi-1 and Yagi-2 flowed down to residential areas. It is a typical example of the development of a landslide moving mass during the motion.

Comparison of the LS-RAPID Simulation and the Laser Profiler Data by MLIT

Ohtagawa River Management Office of MLIT used a Laser Profiler after the landslide disaster and compared the results to previous laser profiles (precision is not so high). We obtained this data, and Godai Develop Cooperation compared both datasets in detail. The result is shown in Fig. 78. It includes landslide volumes and land-

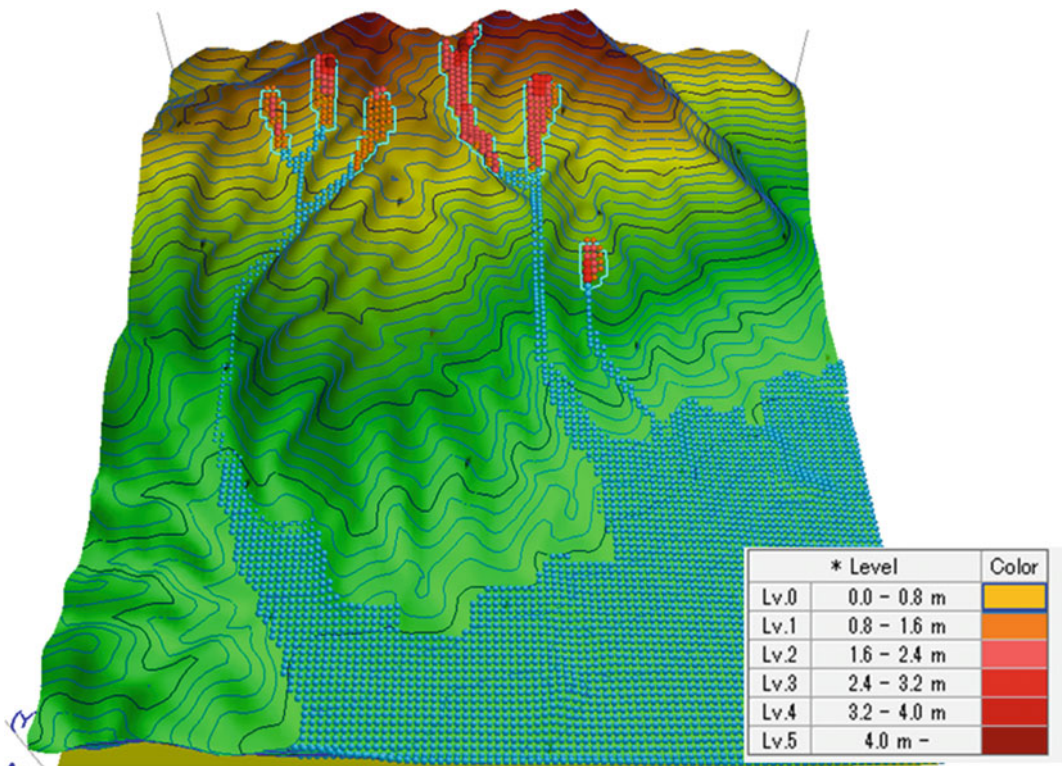


Fig. 75 The depth distribution of movable soils in the simulation. *Red color areas* landslide source area (depth is 2-4 m); *Blue areas* landslide moving area (depth is 1 m)

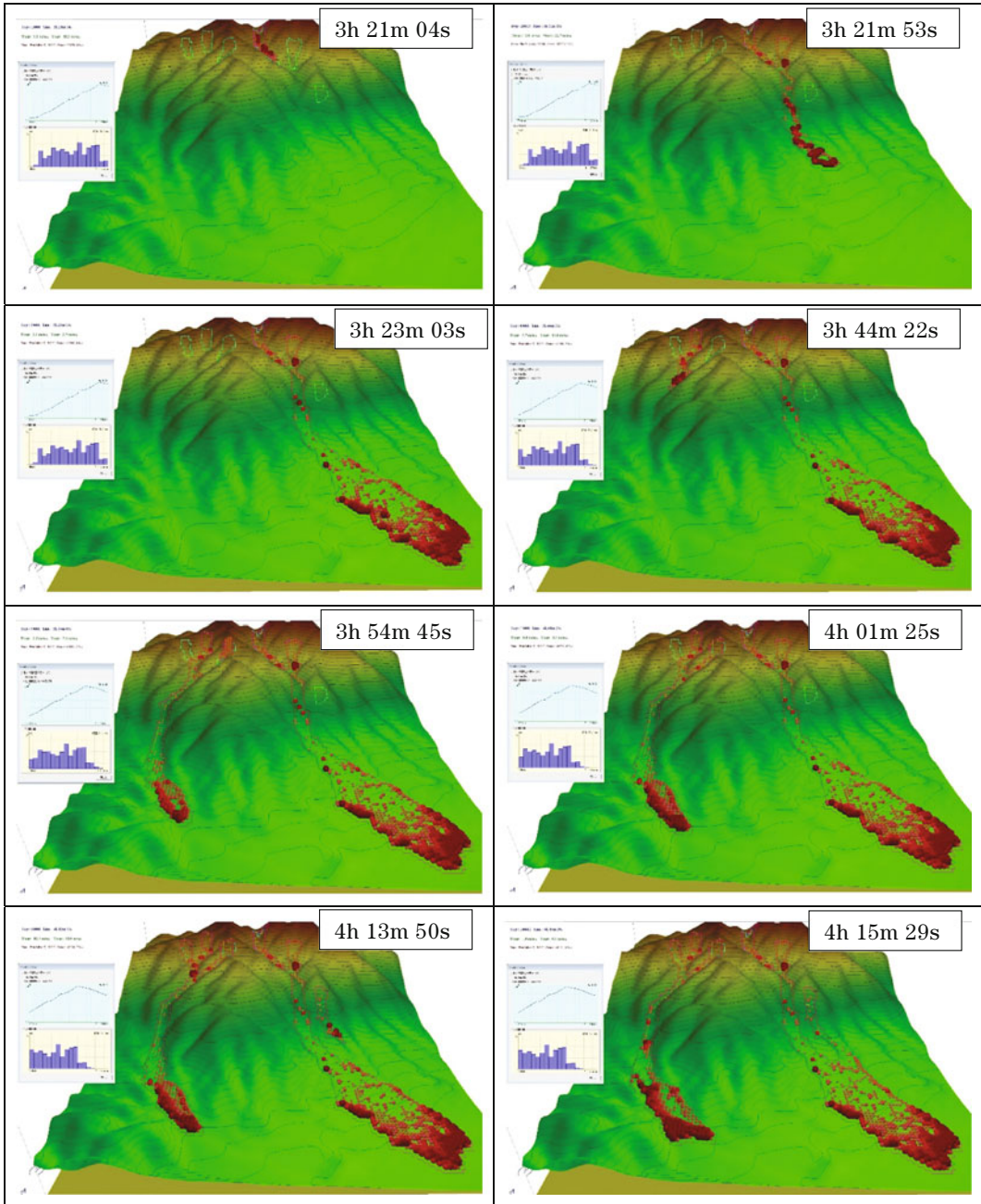


Fig. 76 Simulation result of the Hiroshima rain-induced landslide disaster by LS-RAPID

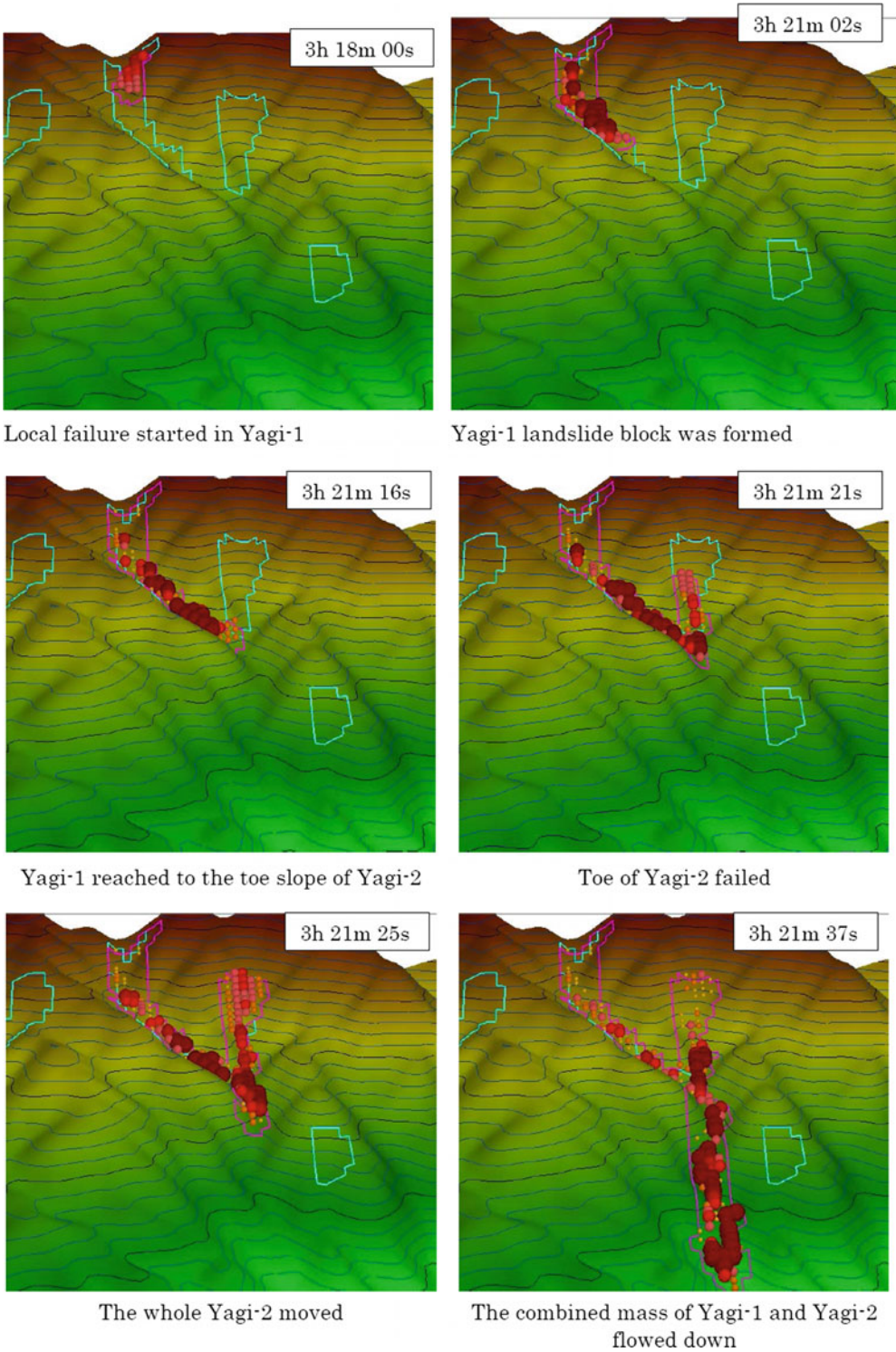
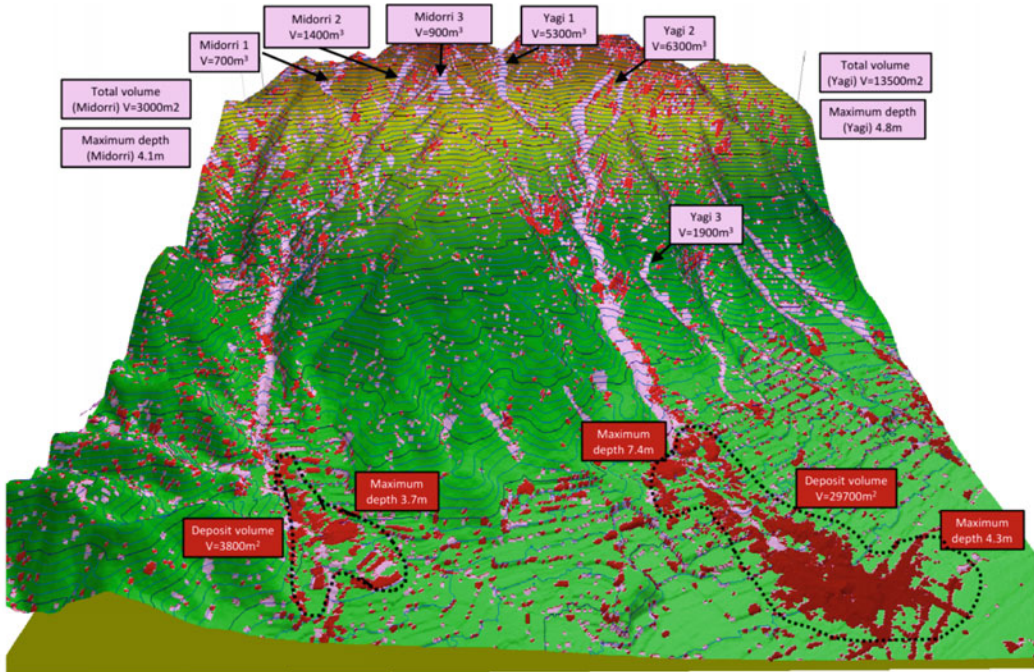
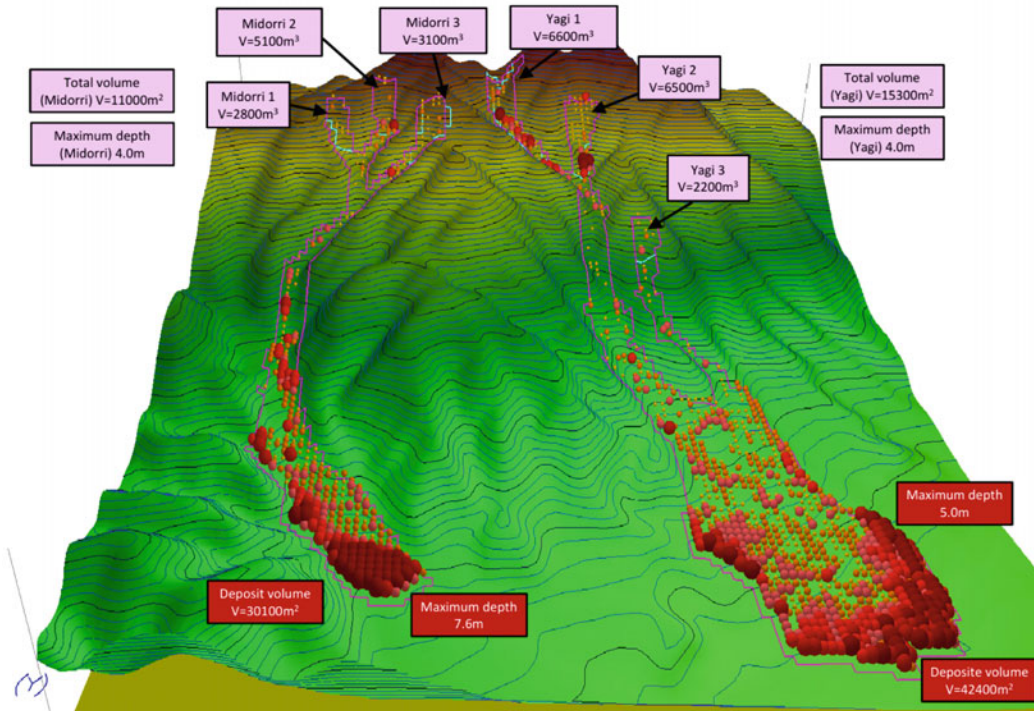


Fig. 77 Development of landslides increasing in volume during motion



Landside debris distribution made from the Laser Profiler data (Ohtagawa River Management Office of MLIT) (Sassa et al. 2014c). Pink: excavated part, Dark red: deposited part



Result of LS-RAPID simulation (Sassa et al. 2014c)

Fig. 78 Comparison between laser profiler data and LS-RAPID simulation results

slide depths for each small landslide and also volumes of deposit.

Laser Profiler:

The maximum depths of Yagi landslide and Midorii landslide in the source area is 4 m.

Total landslide volume in the source area of Yagi is 13,500 m³

Total landslide volume in the source area of Midorii is 3000 m³

Total landslide volume in the deposition area of Yagi is 29,700 m³

(2.2 times greater than that in the source)

Total landslide volume in the deposition area of Midorii is 3800 m³

(Almost the same volume as the source)

Maximum depths in the deposition area in Yagi is 7.4 m near the exit of the valley

(where an apartment was destroyed) and 4.3 m

Maximum depth in the deposition area in Midorii is 7.6 m.

LS-RAPID

The maximum depths of Yagi landslide and Midorii landslide in the source area is 4 m.

Total landslide volume in the source area of Yagi is 17,400 m³

Total landslide volume in the source area of Midorii is 11,000 m³

Total landslide volume in the deposition area of Yagi is 43,100 m³

(2.5 times greater than that in the source)

Total landslide volume in the deposition area of Midorii is 30,100 m³

(2.7 times greater than that in the source)

Maximum depth in the deposition area in Yagi is 5.6 m

Maximum depth in the deposition area in Midorii is 7.6 m

The LS-RAPID simulation was conducted before obtaining the Laser Profiler data (previous

measurements are rougher than that measured after the disaster). Yagi's result is rather similar, and Midorii's result is rather different. The landslide volume in the source area was different.

References

- Abe I, Goto K, Imamura F, Shimizu K (2008) Numerical simulation of the tsunami generated by the 2007 Noto Hanto earthquake and implications for unusual tidal surges observed in Toyama Bay. *Earth Planets Space* 60:133–138
- Aoi S, Enescu B, Suzuki W, Asano Y, Obara K, Kunugi T, Shiomi K (2010) Stress transfer in the Tokai subduction zone from the 2009 Suruga Bay earthquake in Japan. *Nat Geosci* 3:496–500
- Ataie-Ashtiani B, Yavari-Ramshe S (2011) Numerical simulation of wave generated by landslide incidents in dam reservoirs. *Landslides* 8(4):417–432
- Baba T, Matsumoto H, Kashiwase K, Hyakudome T, Kaneda Y, Sano M (2012) Microbathymetric evidence for the effect of submarine mass movement on tsunami generation during the 2009 Suruga Bay earthquake, Japan. In: Yamada Y et al (eds) *Submarine mass movements and their consequences*. *Advances in natural and technological hazards research*, vol 31. Springer, Berlin, pp 485–494
- Biscarini C (2010) Computational fluid dynamics modelling of landslide-generated water waves. *Landslides* 7(2):117–124
- Bishop AW, Henkel DJ (1962) The measurement of soil properties in the triaxial test. *English Language Book Society and Edward Arnold*
- Bishop AW, Green GE, Garga VK, Andersen A, Brown JD (1971) A new ring-shear apparatus and its application to the measurement of residual strength. *Geotechnique* 21(1):273–328
- Dang K, Sassa K, Fukuoka H, Sakai N, Sato Y, Takara K, Quang L, Doan L, Pham T, Nguyen H (2016) Mechanism of two rapid and long-runout landslides in the 16 April 2016 Kumamoto earthquake using a ring-shear apparatus and computer simulation (LS-RAPID). Published online first (doi:10.1007/s10346-016-0748-9)
- Glimsdal S, L'Heureux JS, Harbitz CB, Pedersen GK (2013) Modelling of the 1888 landslide tsunami, Trondheim, Norway. In: *Proceeding of the second world landslide forum "landslide science and practice"*, vol 5. Springer, Berlin, pp 73–79

- Imamura F (2009) Tsunami modeling: calculating inundation and hazard maps (chapter 10). In: Bernard EN, Robinson AR (eds) *The sea tsunamis*. Harvard University Press, London, pp 321–332
- Inoue K (1999) Shimabara-Shigatusaku earthquake and topographic changes by Shimabara catastrophe. *J Jpn Soc Eros Control Eng* 52(4):45–54
- Intergovernmental Oceanographic Commission (IOC) (1997) Numerical method of tsunami simulation with the leap-frog scheme. In: IUGG/IOC time project IOC manuals and guides, No. 3. UNESCO. 126 p
- Körner H (1980) Model conception for the rock slide and avalanche movement. In: *Proceedings of international symposium “INTEPRAEVENT” 1980*, vol 2, pp 15–55
- Liao Z, Hong Y, Wang J, Fukuoka H, Sassa K, Karnawati D, Fathani F (2010) Prototyping an experimental early warning system for rainfall-induced landslides in Indonesia using satellite remote sensing and geospatial datasets. *Landslides* 7(3):317–324
- Ministry of Land, Infrastructure, Transport and Tourism (MLIT) Water and Disaster Management Bureau, Coastal management office (2012) Guideline for the assessment for Tsunami inundation area. Ver. 1.00, http://www.mlit.go.jp/river/shishin_guideline/bousai/saigai/tsunami/shinsui_settei_ver100.pdf
- Montarasio L, Valentino R (2008) A model for triggering mechanisms of shallow landslides. *Nat Hazards Earth Sci* 8:1149–1159
- Okada Y, Sassa K, Fukuoka H (2000) Liquefaction and the steady state of weathered granite sands obtained by undrained ring shear tests: a fundamental study on the mechanism of liquidized landslides. *J Nat Disaster Sci* 22(2):75–85
- Sassa K (1984) The mechanism starting liquefied landslides and debrisflows. In: *Proceedings of 4th international symposium on landslides*, vol 2. pp 349–354
- Sassa K (1988a) Geotechnical model for the motion of landslides. In: *Proceedings of 5th ISL*, pp 37–55
- Sassa K (1988b) Geotechnical model for the motion of landslides. In: *Proceeding of 5th international symposium on landslides, “landslides”*, Balkema, Rotterdam, vol 1. pp 37–56
- Sassa K (1992) Access to the dynamics of landslides during earthquakes by a new cyclic loading high-speed ring shear apparatus. In: *Proceedings of 6th international symposium on landslides*, pp 1919–1937
- Sassa K (1995) Access to the dynamics of landslides during earthquakes by a new cyclic loading high-speed ring shear apparatus. In: *Proceedings of 6th ISL*, pp 1919–1937
- Sassa K, Fukuoka H, Wang G, Ishikawa N (2004) Undrained dynamic-loading ring-shear apparatus and its application to landslide dynamics. *Landslides* 1(1):7–19
- Sassa K, Nagai O, Solidum R, Yamazaki Y, Ohta H (2010) An integrated model simulating the initiation and motion of earthquake and rain induced rapid landslides and its application to the 2006 Leyte landslide. *Landslides* 7(3):219–236
- Sassa K, He B, Miyagi T, Strasser M, Konagai K, Ostric M, Setiawan H, Takara K, Nagai O, Yamashiki Y, Tutumi S (2012) A hypothesis of the Senoumi submarine megaslide in Suruga Bay in Japan—based on the undrained dynamic-loading ring shear tests and computer simulation. *Landslides* 9(4):439–455
- Sassa K, He B, Dang K, Nagai O, Takara K (2014a) Plenary: progress in landslide dynamics. In: *Landslide science for a safer geoenvironment*, vol 1. Springer, Berlin, pp 37–67
- Sassa K, Dang K, He B, Takara K, Inoue K, Nagai O (2014b) A new high-stress undrained ring-shear apparatus and its application to the 1792 Unzen-Mayuyama megaslide in Japan. *Landslides* 11(5):827–842
- Sassa K, Fukuoka H, Sato Y, Takara K, Huy L, Setiawan H, Pham T, Dang K (2014c) Initiation mechanism of rapid and long runout landslides and simulation of Hiroshima landslide disasters using the integrated simulation model (LS-RAPID). In: *Proceedings of the international forum “urbanization and landslide disaster”*, pp 85–112 (in Japanese)
- Sassa K, Dang K, Yanagisawa H et al (2016) A new landslide-induced tsunami simulation model and its application to the 1792 Unzen-Mayuyama landslide-and-tsunami disaster. *Landslides* 13(6):1405–1419
- Satake K (2001) Tsunami modeling from submarine landslides. In: *Proceedings of the international tsunami symposium*, pp 665–674
- Tinti S, Tonini R (2013) The UBO-TSUFDF tsunami inundation model: validation and application to a tsunami case study focused on the city of Catania, Italy. *Nat Hazards Earth Syst Sci* 13:1795–1816
- Trandafir A, Sassa K (2006) Performance-based assessment of earthquake induced catastrophic landslide hazard in liquefiable soils. *Geotech Geol Eng* 24:1627–1639
- Tsuji Y, Hino T (1993) Damage and Inundation height of the 1792 Shimabara landslide tsunami along the coast of Kumamoto prefecture. *Bull Earthquake Res Inst* 68:91–176 (University of Tokyo, in Japanese)
- Tsuji Y, Murakami Y (1997) Inundation height of the 1792 Mayuyama landslide tsunami in the Shimabara Peninsula side. In: *Historical earthquake*, No. 13. Society of Historical Earthquake Studies, pp 135–197
- Unzen Restoration Office of the Ministry of Land, Infrastructure and Transport of Japan (2002) *The Catastrophe in Shimabara: 1791–92 eruption of Unzen-Fugendake and the sector collapse of Mayu-Yama*. An english leaflet (23 p)
- Unzen Restoration Office of the Ministry of Land, Infrastructure and Transport of Japan (2003) *The Catastrophe in Shimabara: 1791–92 eruption of*

- Unzen-Fugendake and the sector collapse of Mayu-Yama. A Japanese leaflet (44 p)
- Usami T (1996) Materials for comprehensive list of destructive earthquakes in Japan. University of Tokyo Press (in Japanese)
- Varnes D (1978) Slope movement types and processes (Fig. 2.1 types of slope movement), landslides-analysis and control. Transportation Research Board, National Academy of Science, USA

Part III
Risk Assessment

TXT-tool 3.081-1.1

An Integrated Model Simulating the Initiation and Motion of Earthquake and Rain-Induced Rapid Landslides and Its Application to the 2006 Leyte Landslide

Pham Van Tien, Kyoji Sassa and Khang Dang

Abstract

An earthquake and rainfall induced rapid landslide claimed more than 1000 people in the province of Southern Leyte, the Philippines on 17 February 2006. Landslide hazard assessment based on the simulation of initiation and motion of landslides has a great significance in practice to prepare and mitigate such disasters in the future. This research presents a new integrated computer model (LS-RAPID) simulating the initiation and motion of landslides triggered by rainfalls and/or earthquakes using the landslide parameters obtained from the undrained dynamic loading ring shear apparatus. This model LS-RAPID was developed from the geotechnical model for the motion of landslides (Sassa in Proceedings of 5th international symposium on landslides, “Landslides”. Balkema, Rotterdam, vol 1, pp 37–56, 1988) and its improved simulation model (Sassa et al. in Landslides 1(3):221–235, 2004b) and new knowledge obtained from a new dynamic loading ring shear apparatus (Sassa et al. in Landslides 1(1):7–19, 2004a). The model well simulated the development process of progressive failure to a rapid motion and the entrainment of deposits in the runout path. The combination of field investigation and ring shear test’s results on the 2006 Leyte landslide suggested that this

P. Van Tien (✉)
Disaster Prevention Research Institute, Graduate
School of Engineering, Kyoto University, Kyoto,
Japan
e-mail: phamtiengtvt@gmail.com

K. Sassa · K. Dang
International Consortium on Landslides, Kyoto,
Japan
e-mail: sassa@iclhq.org

K. Dang
VNU University of Science, Hanoi, Vietnam

landslide was triggered by both effects of pore pressure increase due to rainfall and seismic forces due to a very small earthquake. The application of this simulation model could well reproduce the initiation and the rapid long runout motion of the Leyte landslide.

Keywords

Leyte landslides • Computer simulation • Rapid landslides
Ring shear test

Contents

1 Introduction	84
2 Basic Principle of Simulation	85
2.1 Apparent Friction Coefficient ($\tan \phi_a$)	85
2.2 Shear Resistance Reduction After Failure to the Steady State.....	86
2.3 Effect of Soil Depth on the Steady State Shear Resistance.....	87
2.4 Effect of Saturation on the Apparent Friction Coefficient and the Steady State Shear Resistance.....	88
2.5 Effect of Pore Pressure Ratio to Shear Resistance in the Initiation Process.....	88
3 Landslide Enlargement in the Entrainment Area	89
4 Resistance Due to Non-frictional Energy Consumption	90
5 Examination of the Performance of Each Process	90
5.1 Initiation Process.....	90
5.2 Safety Factors.....	91
5.3 Moving Process.....	92
5.4 Combined Effects of Earthquake and Pore Pressure Ratio	93
6 Application to the 2006 Leyte Landslide	94
6.1 Triggers of the Landslide.....	95
6.2 Dynamic-Loading Ring-Shear Test	96
6.3 Test Results.....	96
7 Computer Simulation for the Leyte Landslide	97
8 Conclusions	99
References	99

1 Introduction

Rapid landslides are often triggered by earthquakes or the combined effects of earthquakes and rains, which cause extensive damages to social properties and human lives, such as the Hattian Balla in Pakistan, the 2008 Wenchuan earthquake-induced landslides in China and rainfall-earthquake induced Leyte landslide in the Philippines. Due to a limited budget to implement expensive landslide prevention countermeasures, the most effective and economical way to reduce human loss from such disasters is landslide hazard assessment and disaster preparedness including early warning, evacuation and land use planning (Sassa et al. 2014). The development of a reliable and practical landslide risk assessment technology focusing the initiation and progressive motion of landslides at the post-failure stage and the resulting hazard area is currently required for the disaster preparedness. For this purpose, a new computer simulation model incorporating the initiation process of landslides triggered by earthquakes and rains in addition to the runout has been developed by Sassa since 1988. While all models so far are calibration-based using the appropriate rheological parameters without

obtaining from laboratory tests, the LS-RAPID model enables to conduct it based on the availability of laboratory experiments and monitored seismic records (Sassa et al. 2010). Basically, this model uses the geotechnical parameters of landslide samples measured from undrained dynamic loading ring shear tests such as mobilized friction angle from the initiation to the motion and shear resistance mobilized during post-failure and at the steady state. The computer simulation could perform well to simulate the process of progressive failure, the moving process and the development to a rapid landslide of a soil sample under the stresses including pore pressure increase due to rainfall and/or dynamic loading due to earthquakes in the field. The combination of landslide ring shear simulator and the integrated landslide simulation model has provided a new practical tool for landslide hazard assessment.

2 Basic Principle of Simulation

The fundamental concept of this simulation is illustrated in Fig. 1. A vertical imaginary column is considered within a moving landslide mass. The forces acting on the column consist of: (1) self-weight of column (W), (2) Seismic forces (vertical seismic force F_v , horizontal x - y

direction seismic forces F_x and F_y), (3) lateral pressure acting on the side walls (P), (4) shear resistance acting on the bottom (R), (5) the normal stress acting on the bottom (N) given from the stable ground as a reaction of normal component of the self-weight, and (6) pore pressure acting on the bottom (U). The forces including driving forces (Self-weight + Seismic forces), lateral pressure, and shear resistance acting on a massive body (m) will cause it to accelerate by acceleration (a) as shown in the following equation:

$$am = (W + F_v + F_x + F_y) + \left(\frac{\partial P_x}{\partial x} \Delta x + \frac{\partial P_y}{\partial y} \Delta y \right) + R \tag{1}$$

Here, R includes the effects of forces of N and U in Fig. 1 which works in the upslope direction of the maximum slope line before motion and in the opposite direction of landslide movement during motion. The angle of slope is different in the position of column within landslide mass. All stresses and displacements are projected to the horizontal plane and calculated on the plane (Sassa 1988; Sassa et al. 2010).

Some important parameters and their concepts are presented later in the following session whereas others are explained in detail by Sassa (1988) and Sassa et al. (2010).

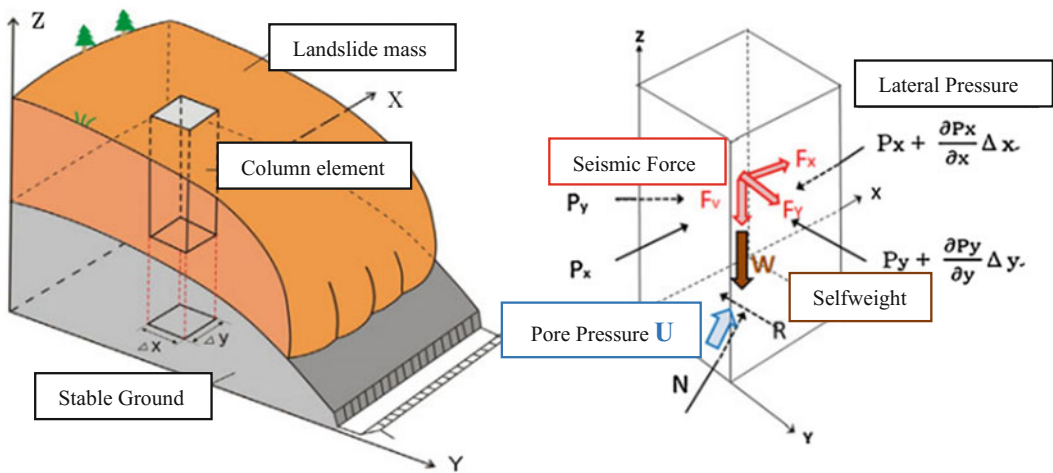


Fig. 1 Fundamental concept of landslide simulation model

2.1 Apparent Friction Coefficient ($\tan \phi_a$)

The initial stress point $I_0 (\sigma_0, \tau_0)$ acting on the sliding surface of the slope before rainfalls or earthquakes is shown in Fig. 2. When the effective stress path shifts from the initial point to failure line at peak (ϕ_p) under impacts of seismic loading and/or pore pressure generation, the landslide movement takes place. After failure, stress line continues to go down along with failure line and reach to steady state at large shear displacement. Pore pressure will be generated by volume reduction due to grain crushing/particle breakage while shear stress starts to reduce in progress of shear displacement. Below the steady state any further grain crushing and pore pressure reduction will not occur and only shear displacement will proceed under a constant shear resistance (τ_{ss}) corresponding to apparent friction angle ($\phi_{a(ss)}$) at the steady state (Sassa 1988). The apparent friction coefficient at the steady state in detail is expressed by the ratio of steady-state shear resistance (τ_{ss}) and the initial normal stress acting on the sliding surface (σ_0), which corresponds to the total normal stress (σ) by soil weight at the site in the simulation: $\tan(\phi_{a(ss)}) = \tau_{ss}/\sigma$.

2.2 Shear Resistance Reduction After Failure to the Steady State

The initiation and motion process of this model consists of the following four sub-processes. Firstly, landslide mass exists under an initial state in a stable condition with the friction coefficient at peak ($\tan \phi_p$). Next, failure takes place at sliding surface due to pore pressure generation during rainfalls and/or seismic loading during earthquakes, or their combined effects. Then, the landslide experiences a transient state from the failure to steady state in which pore pressure generation and resulting shear strength reduction will proceed in progress with shear displacement. Finally the landslide mass continues to move at the steady state without any further stress change.

The mentioned four stages from the pre-failure state to a steady state of motion through the transient state are denoted in the Fig. 3. As can be seen, the friction angle at peak (ϕ_p) remains unchanged until the shear displacement DL (Starting point of failure and strength reduction) in the pre-failure state. Shear strength will reduce from DL to DU (End of strength reduction) in progress with shear displacement along a line in the logarithmic axis. A steady-state landslide motion will start under the apparent friction

Fig. 2 Apparent friction coefficient ($\tan \phi_a$), steady-state shear resistance (τ_{ss}) and the friction coefficient during motion ($\tan \phi_m$)

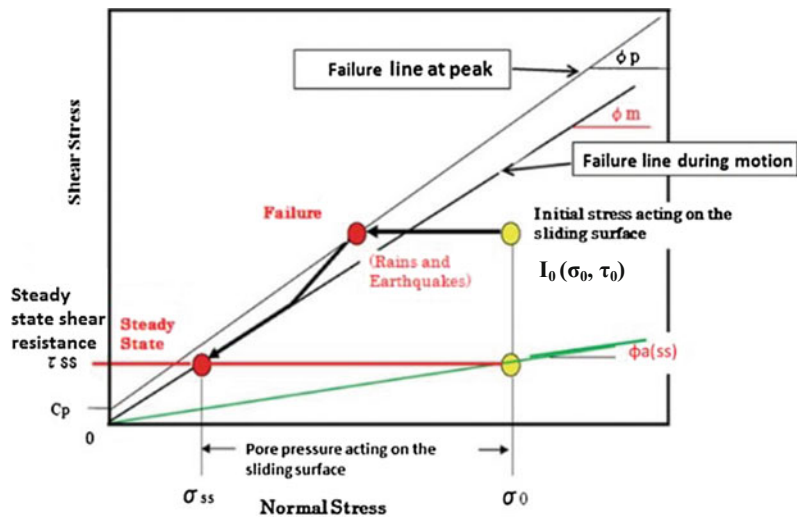
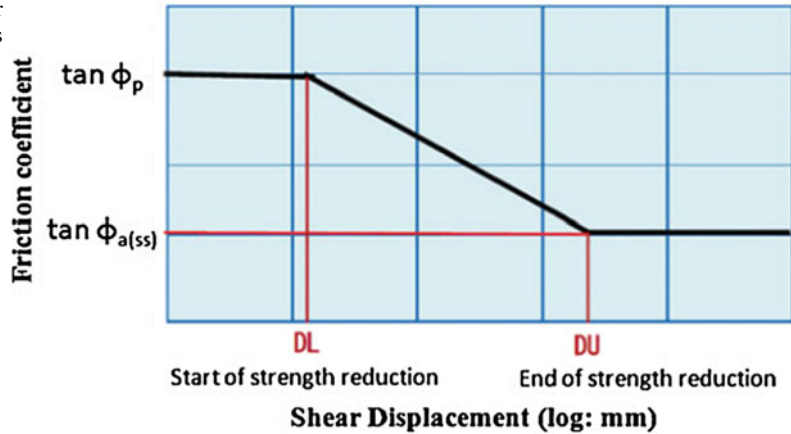


Fig. 3 Model of shear strength reduction in progress of shear displacement



coefficient at steady state ($\tan \phi_{a(ss)}$) after DU in the shear displacement. Expressing the shear displacement as D, the friction coefficient has three stages below.

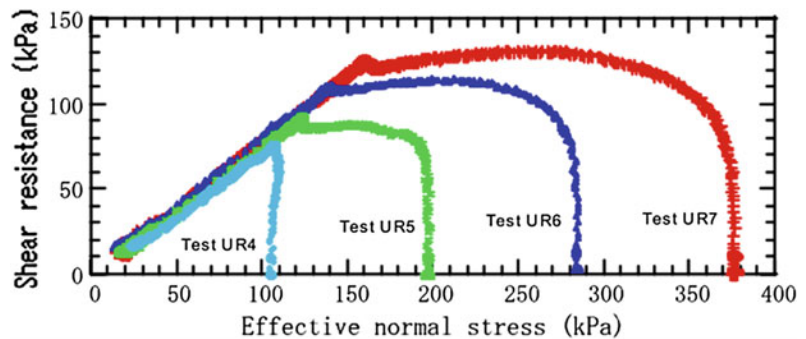
1. Initial deformation stage before failure ($D < DL$): $\tan \varphi_a = \tan \varphi_p$
2. Stage of steady-state motion ($D > DU$): $\tan \varphi_a = \tan \varphi_{a(ss)}$
3. Stage of transient state ($DL < D < DU$):

$$\tan \varphi_a = \tan \varphi_p - \frac{\log D - \log DL}{\log DU - \log DL} (\tan \varphi_p - \tan \varphi_{a(ss)})$$

2.3 Effect of Soil Depth on the Steady State Shear Resistance

The steady state shear resistance is one of the most important parameters to predict the motion of landslides. This stress is affected by the pore pressure generation in the shear zone, but it is independent of the level of loaded normal stress. In references to experimental results on weathered granitic soils taken from the Nikawa landslide in Nishinomiya city, Hyogo Prefecture, Japan (Okada et al. 2000), all of effective stress paths of undrained monotonic ring shear tests reached the same failure line and went down along the failure line and stopped at a steady state point (σ_{ss}, τ_{ss}) (Fig. 4). It means that although the total normal

Fig. 4 Undrained ring shear tests on the samples of the Nikawa landslide from Okada et al. (2000) (BD = 0.98)



stress acting on the sliding surface is changing in the process of a mass movement on the ground, the mobilized shear resistance at steady state is still constant. This relation is used for the integrated computer simulation model simulating the initiation and the motion of landslides.

2.4 Effect of Saturation on the Apparent Friction Coefficient and the Steady State Shear Resistance

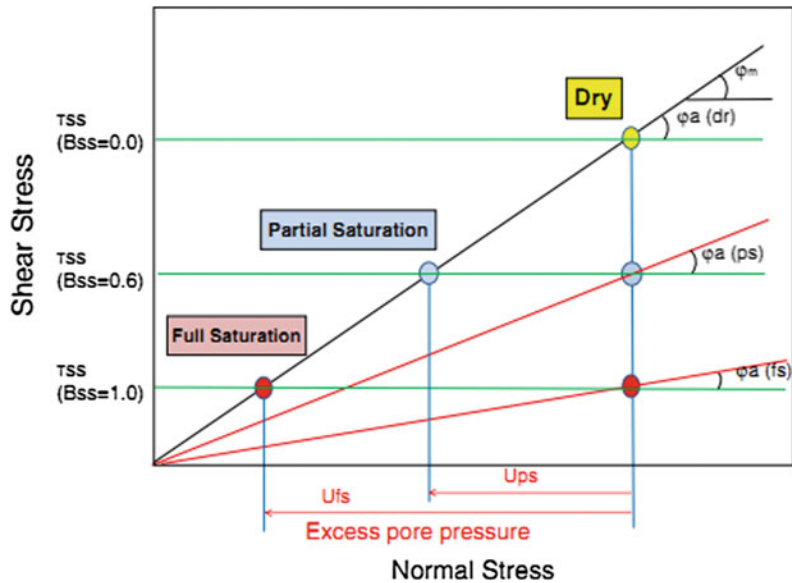
The apparent friction coefficient and the steady state shear resistance depend on how much pore water pressure will be generated in the shear zone during motion in which pore pressure value is much affected by the degree of saturation. Accordingly, the steady-state shear resistance will be changed by the degree of saturation of the soil. To express these relations, a parameter of pore pressure generation rate is used to define the effect of saturation to the steady state shear resistance and the apparent friction coefficient. This parameter is calculated as the ratio of excess pore pressure increment and normal stress increment in the

undrained ring shear test. As drawn in Fig. 5, the steady-state shear resistance at full saturation is τ_{ss} ($B_{ss} = 1.0$) and the steady state at dry state is τ_{ss} ($B_{ss} = 0.0$). If the percentage of pore pressure generation is 60% of the full saturation, the steady state is denoted as τ_{ss} ($B_{ss} = 0.6$). The apparent friction angle $\phi_a(dr) = \phi_m$ in the dry state while the angles at full saturation is the lowest ($\phi_a(fs)$) and at partial saturation $\phi_a(ps)$ are in between.

2.5 Effect of Pore Pressure Ratio to Shear Resistance in the Initiation Process

Effect of excess pore pressure generated during shear is included in the value of the apparent friction coefficient $\tan \phi_{a(ss)}$ in the steady state ($D > DU$). However, the effect of pore pressure due to ground water rise during rainfalls is not considered in the apparent friction coefficient in the range of $D < DL$. The transient phase in $DL < D < DU$ are both partly working. The effects of pore pressure ratio (r_u) together with the apparent friction coefficient ($\tan \phi_a$) in three stages are written as below.

Fig. 5 Relation between the pore pressure generation rate (B_{ss}) and the apparent friction coefficient



$$\begin{aligned}
 & D < DL : \tan \varphi_a = \tan \varphi_p, \\
 & c = c_p, r_u = r_u
 \end{aligned} \tag{2}$$

$$\begin{aligned}
 & D > DU : \tan \varphi_a = \tan \varphi_{a(ss)}, \\
 & c = 0, r_u = 0
 \end{aligned} \tag{3}$$

$$\begin{aligned}
 & DL \leq D \leq DU : \tan \varphi_a = \tan \varphi_p \\
 & - \frac{\log D - \log DL}{\log DU - \log DL} (\tan \varphi_p - \tan \varphi_{a(ss)})
 \end{aligned} \tag{3}$$

$$\begin{aligned}
 \%c &= c_p \left(1 - \frac{\log D - \log DL}{\log DU - \log DL} \right), r_u \\
 &= r_u \cdot \frac{\log DU - \log D}{\log DU - \log DL}
 \end{aligned} \tag{4}$$

Shear displacement (D) at each mesh is calculated from the sum of (velocity of each step) x (time step of each step) in the x-direction and the sum in the y-direction for a specific mesh (Sassa 1988; Sassa et al. 2010). When and where shear displacement reaches DU, the steady-state movement will start. The movement area will progressively enlarge because of shear strength reduction.

3 Landslide Enlargement in the Entrainment Area

When a landslide moves onto unstable alluvial or torrent deposits, the moving landslide volume will often be increased by excavating and entraining the deposits. For simulating, a

volume enlargement model was assumed by simplifying its formation process as follows: the sudden reduction of shear strength from the peak friction to the apparent friction at the steady state will occur when a landslide mass greater than a certain threshold height of soil thickness (Δh_{cr}) reaches a mesh containing unstable deposits. As shown in Fig. 6, when a landslide mass comes, the height of soil column in this entrainment area increases from h_d to $(h_d + \Delta h)$. If the height of landslide mass $\Delta h > \Delta h_{cr}$, the friction at the base of this column becomes that at the steady state.

Figure 6(left) illustrates the 1996 landslide-triggered debris-flow disaster in the Gamahara torrent, Otari village, Nagano Prefecture, Japan which claimed 14 human casualties, where I—a landslide moving from the upper slope, II—undrained loading the deposit, III—moving of debris flows along the torrent channel. The volume enlargement of this debris flow is due to excavating the torrent deposit during travel down the torrent channel. Figure 6(right) presents the result of a ring shear test to reproduce the process of the Gamahara torrent (Sassa et al. 2004a). In this simulation, the loading of shear stress and normal stress was rapidly increased within 5 s. After that, normal stress was kept constant while shear stress was reduced due to the increment of self-weight (corresponding to $\alpha = 0$ in the top figure). The variation of stresses mobilized shear resistance and monitored pore pressure generation in the progress of accelerated shear displacement were shown in the

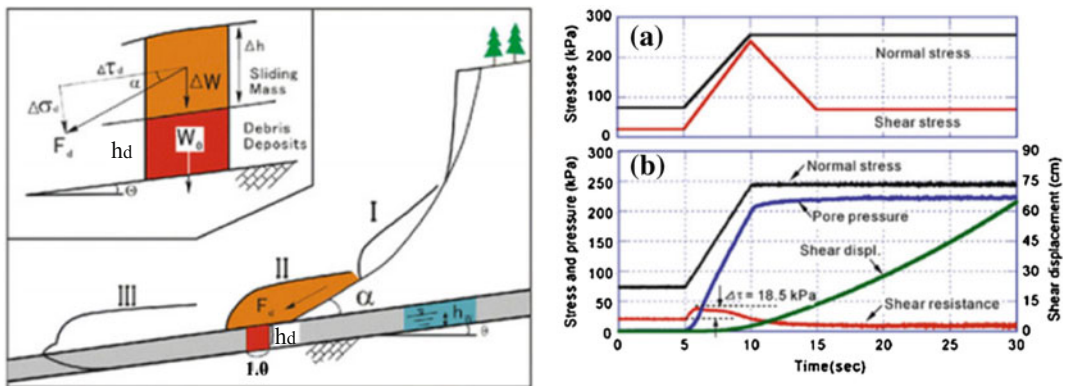


Fig. 6 Illustration of the landslide-induced debris flow (left) and the result of undrained ring shear test simulating this process (right) (Sassa et al. 2004a)

graph Fig. 6b. The failure occurred only with 18.5 kPa of shear stress increment.

4 Resistance Due to Non-frictional Energy Consumption

The basic equation of 1 is based on the assumption in which all potential energy is consumed as the frictional energy at the sliding surface during motion. However, the landslide mass may lose kinetic energy during a collision of sub-masses within a landslide mass, momentum transfer to engulfed materials and the movement passing over vertical gaps/falls, horizontal bent or other not smooth ground surface. To avoid a wrong simulation result due to this assumption automatically, the energy loss function is needed to incorporate for a specific mesh and a specific time step by the threshold values of extraordinary velocity or/and thickness. The major part of non-frictional energy consumption here will be the loss of kinetic energy. Thus, the non-frictional energy consumption in a column will be $\alpha(\frac{1}{2}mv^2)$. The Eq. (1) is rewritten as below:

$$am = (W + Fv + Fx + Fy) + \left(\frac{\partial P_x}{\partial x} \Delta x + \frac{\partial P_y}{\partial y} \Delta y \right) + R + \alpha \left(\frac{1}{2} mv^2 \right) \quad (5)$$

where m , soil mass within a column at the mesh; v , the velocity at the mesh; Coefficient for non-frictional energy consumption (constant with the dimension of a reciprocal of length).

5 Examination of the Performance of Each Process

The performance of simulating processes of LS-RAPID is examined by applying it to a simple imaginary slope and compared to the safety factors obtained from some conventional limit equilibrium slope stability analyses (such as Fellenius, Bishop, Janbu, Spenser, Morgenstern–Price) with an

enough large shear displacement for DL and DU within 2 and 5 m, respectively. The imaginary slope consists of three parts of slope: a flat ground in the top, a steep slope in the middle and a gentle slope in the bottom. The area of simulation is 350 m wide and 440 m long, the size of the mesh is 10 m, the maximum vertical depth of landslide is 40.53 m, the total landslide volume is 231,300 m³. The landslide body was created in a form of an ellipsoid which is explained in the application to the Leyte landslide (Sassa et al. 2010).

5.1 Initiation Process

The characteristic of LS-RAPID is the expression of strength reduction during deformation and the progressive failure, whereas the limit equilibrium slope stability analyses assumed the whole sliding surface of a landslide fails at once. In the model, a stable slope is considered to fail by a high pore pressure ratio supplied from the bedrock (Figs. 7 and 8) or a combined effect of seismic loading in addition to moderate pore pressure ratio (Fig. 9).

The initiation process of rapid landslides due to pore pressure increase was examined by inputting three different pore pressure ratios: $r_u = 0.4, 0.5, 0.6$. The values of $\tan \phi_p = 0.8$, $c_p = 50$ kPa, $\tau_{ss} = 50$ kPa, $k = 0.5$, $B_{ss} = 0.99$, $\tan \phi_m = 0.60$ were given to all simulation area. Next, different values of shear displacement in the progress of shear resistance reduction corresponding to the starting point of failure (DL) and shear resistance at the steady state were input to the model. The simulation results are shown in the form of 3D view in Fig. 7. The contour line is 2.0 m pitch. The red color line shows the area of moving landslide mass. The red color will appear when/where the velocity at a mesh will exceed 0.5 m/s.

DL = 10 mm, DL = 1000 mm

For $r_u = 0.4$ (Fig. 7a), only two small areas on the top of slope showed a slight movement and two red colored circles were observed, but no further progressive failure appeared. For $r_u = 0.5$ and 0.6 rapid landslide motion appeared as shown in Fig. 7c, e.

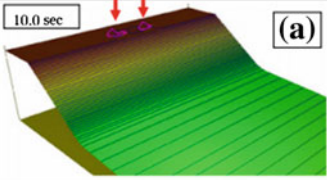
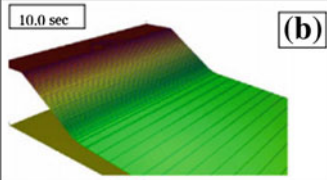
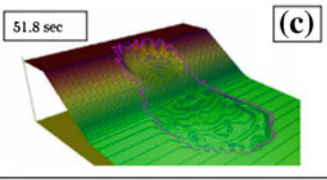
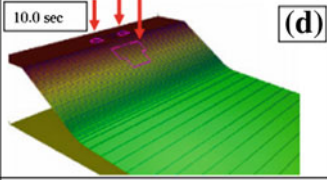
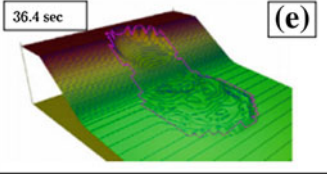
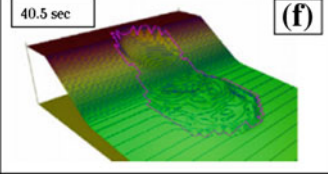
PP ratio r_u	Landslide simulation RAPID		Slope stability analysis				
	DL=10mm, DU=1000mm	DL=2000mm, DU=5000mm	Fel. (*1)	Bisp (*2)	Jan (*3)	Spn (*4)	M&P (*5)
0.4	 (a)	 (b)	1.545	1.443	1.381	1.433	1.431
0.5	 (c)	 (d)	1.351	1.207	1.151	1.200	1.199
0.6	 (e)	 (f)	1.155	0.973	0.923	0.970	0.970

Fig. 7 Comparison of the landslide initiation in LS-RAPID and in Slope Stability Analysis, $\tan \phi_p = 0.8$, $c_p = 50 \text{ kPa}$, $\tau_{ss} = 50 \text{ kPa}$, $k = 0.5$, $B_{ss} = 0.99$, $\tan \phi_m =$

0.60 , $\alpha = 0$, mesh, 10 m; area, $350 \times 440 \text{ m}$; contour line, 2 m. *1 Fellenius, *2 Bishop simplified, *3 Janbu simplified, *4 Spenser, *5 Morgenstern-Price

DL = 2000 mm, DU = 5000 mm

No motion appeared for $r_u = 0.4$, a limited deformation appeared for an instant in the case of $r_u = 0.5$ as shown Fig. 12b, d. A rapid landslide occurred for $r_u = 0.6$ (Fig. 7f). The border of landslide initiation is between $r_u = 0.4$ and 0.5 for smaller DL-DU, and it is between 0.5 and 0.6 for greater DL-DU.

Time

The simulation will stop when the zero velocity for all meshes appeared. Time in the figure shows the time from the start to the end of motion. Ten seconds for A, B, D is the pre-decided minimum calculation time, because the initial velocity is zero, and a certain time of calculation is necessary to know movement will start or not.

5.2 Safety Factors

For the central section of this landslide mass, two-dimensional slope stability analyses were implemented using the stability analysis software

“Slide version 5” by Rocscience. The same shear strength parameters at the peak and also the same pore pressure ratio ($\tan \phi_p = 0.8$, $c_p = 50 \text{ kPa}$, $r_u = 0.4, 0.5, 0.6$) were given for all stability analysis methods. The calculated safety factors for (1) Fellenius, (2) Bishop Simplified, (3) Janbu simplified, (4) Spenser, (5) Morgenstern-Price were shown in the right column of Fig. 7. The onset of landslide motion, namely the unit safety factor ($FS = 1.0$) appears when the value of r_u is between 0.5 and 0.6 for four models. For the Fellenius method, the factor of safety becomes unity when the value of r_u is between 0.6 and 0.7. Therefore, the border of stability ($FS = 1.0$) is same with the border by LS-RAPID in the case of long shear displacement (2 m) until the start of shear strength reduction except the Fellenius method. The difference between LS-RAPID and the Limit Equilibrium Slope stability Analysis comes mainly from the consideration of local shear and progressive failure or the overall shear for the whole landslide body at once. The difference between three-dimensional analysis (LS-RAPID)

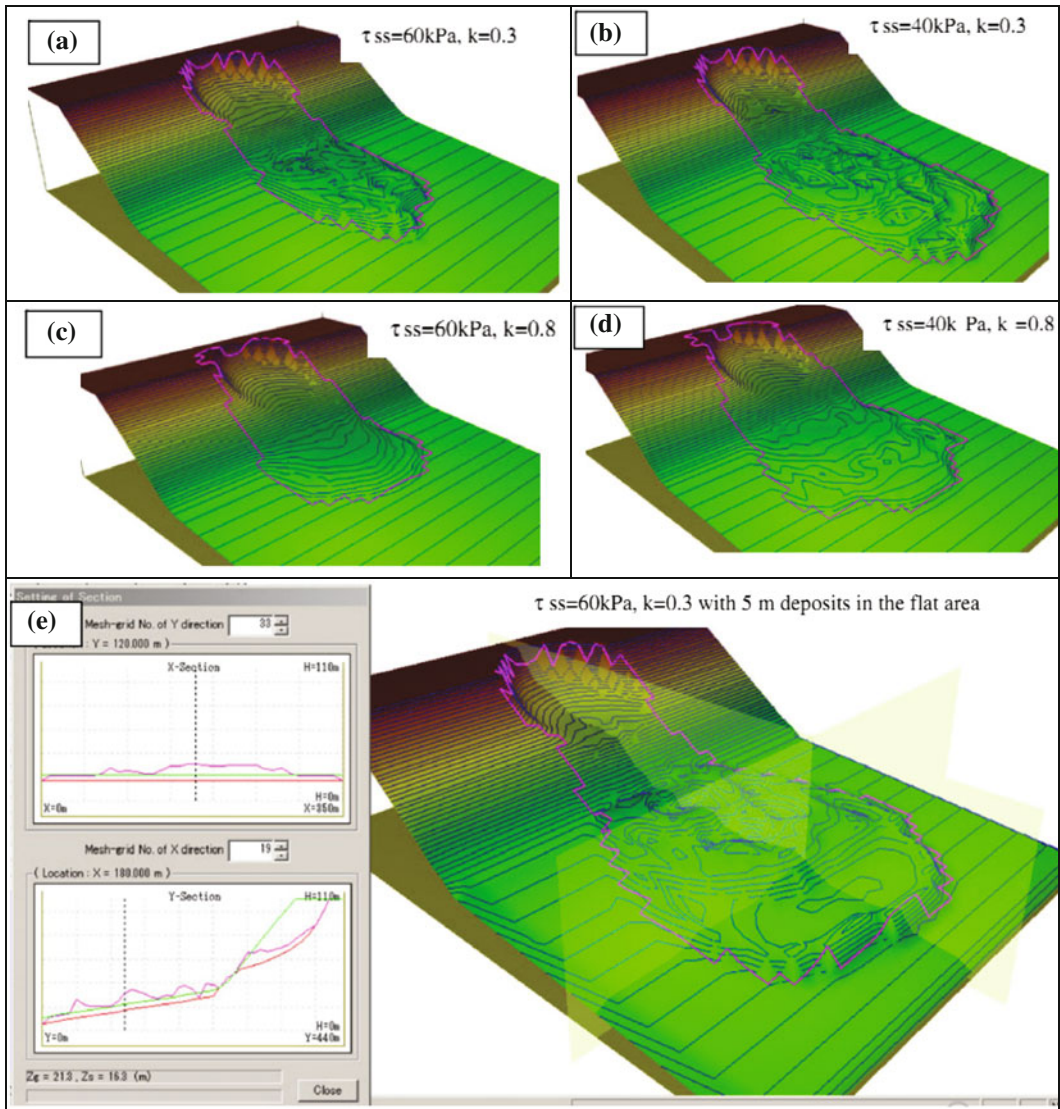


Fig. 8 Effects of steady-state, lateral pressure ratio, and unstable deposits in the traveling ground. $\tan\phi_p = 0.8$; $c_p = 50$ kPa; $\tau_{ss} = 40$ and 60 kPa; $k = 0.3$ and 0.8 ;

$r_u = 0.5$; $B_{ss} = 0.99$; $\tan\phi_m = 0.60$; $\alpha = 0$; $DL = 10$ mm; $DU = 1000$ mm; mesh, 10 m; area, 350×440 m

and two-dimensional analysis is not possible to be discussed in this examination.

5.3 Moving Process

Two key parameters for this simulation are steady-state shear resistance (τ_{ss}) and lateral pressure ratio (k). The τ_{ss} controls how far a landslide mass moves. The lateral pressure presents the

softness of soil mass. A–D of Fig. 8 visualized the results of motion for two different steady states ($\tau_{ss} = 40, 60$ kPa) and two different lateral pressure ratio ($k = 0.3$ and 0.8). Two cases (B and D) of smaller steady state ($\tau_{ss} = 40$ kPa) travelled longer than two cases (A and C) of greater steady state ($\tau_{ss} = 60$ kPa). While two cases (C and D) of greater lateral pressure ratio ($k = 0.8$) presented wider lateral movement than two cases (A and B) of

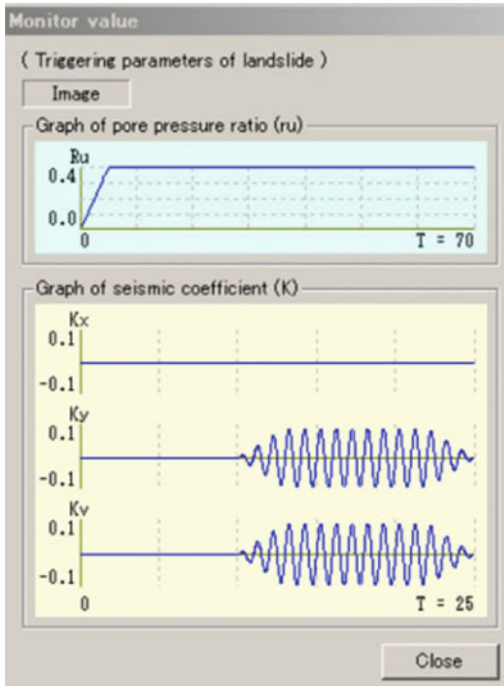


Fig. 9 Landslide triggering factors of rainfall and seismic coefficients

smaller lateral pressure ratio ($k = 0.3$). The deposit shape was more flat and smooth in cases with greater lateral pressure ratio.

When a landslide mass travels on unstable deposits in the traveling course, sometimes those deposits are entrained by shearing below materials as illustrated in Fig. 6. The effect was investigated by adding unstable deposits on the flat area in the case of Fig. 8e; 5 m deposits were located on the flat area (usually alluvial deposits). The results of movement and the longitudinal section and the cross section were also presented. Comparing to Case A (same steady-state shear resistance and lateral pressure ratio), the volume was increased and the movement area was increased. The transparent plates presented the location of longitudinal and crossing sections which are shown on the right side of Fig. 8e. The green color is the original ground surface. The difference of colors is not clear in this small figure. The dense red color presents the bottom of unstable mass (alluvial deposit) on the flat area and the landslide mass in the source area. The pink color presents the surface of landslide mass after motion.

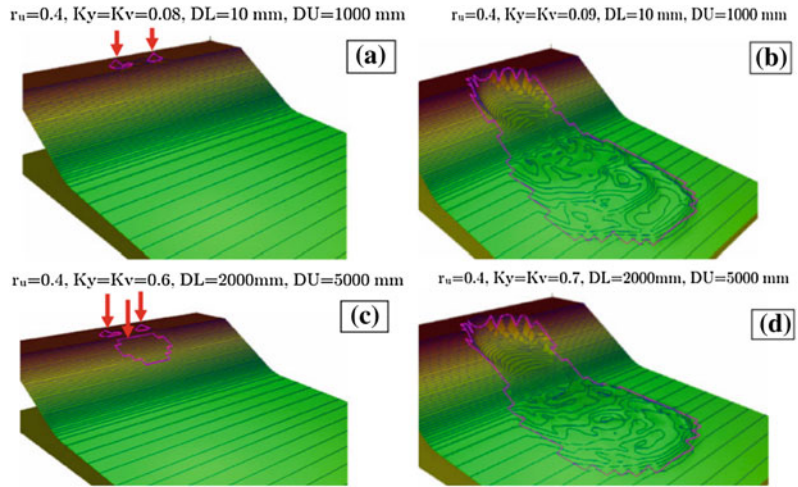
5.4 Combined Effects of Earthquake and Pore Pressure Ratio

Landslides may be triggered by seismic or pore water pressure or their combined impacts. In order to examine the combined effects of earthquake and pore pressure ratio, both triggering factors were loaded in the same imaginary slope with Figs. 7 and 8. Initially, the pore pressure ratio is increased from 0 to 0.4 during $T = 0-5$ s. Then, cyclic loading was loaded from $T = 10-25$ s with 1 Hz (as shown in Fig. 9). The magnitude reaches the pre-decided value for three cycles and keeps the same magnitude for nine cycles and decreases to zero for three cycles. The same magnitude of horizontal shaking (K_y -landslide direction) and vertical shaking (K_v) was loaded while horizontal shaking in the x-direction (crossing direction to the landslide) was kept zero. Four test results are presented in Fig. 10 for two seismic coefficients and two sets of DL and DU just above/below the occurrence of rapid landslides. Figure 10a, c presents the cases which local deformations are observed, but those stopped without further progressive failure. Figure 10b, d presented the motion of rapid landslides. In the case of DL = 10 mm, DU = 1000 mm, the critical seismic shaking was between $K_y = K_v = 0.08$ and 0.09. In the case of DL = 2000 mm and DU = 5000 mm, the critical seismic shaking was between $K_y = K_v = 0.6$ and 0.7. Therefore, landslide risk during earthquakes is much affected by the threshold value of shear displacement to start the shear strength reduction as well as the magnitude of seismic shaking (seismic coefficient).

6 Application to the 2006 Leyte Landslide

A frontal view of the Leyte landslide taken from a helicopter is presented in Fig. 11a. In Fig. 11, a plan of hard rock is seen at the left side of the head scarp. Other parts of the slope seem to be weathered volcanoclastic rocks or debris. The landslide mass moved from the slope and deposited on the flat area with a length about 4 km. Materials of volcanoclastic debris and strongly weathered

Fig. 10 Landslide simulations by combined effects of seismic loading and pore pressure ($\tan\phi_p = 0.8$, $c_p = 50$ kPa, $\tau_{ss} = 50$ kPa, $k = 0.5$, $B_{ss} = 0.99$, $\tan\phi_m = 0.60$)



volcanoclastic rocks (including sand and gravel) in many flow-mounds or hummocky structure were found by a site observation. The section of the central line after the landslide (Fig. 11b) was created by a site survey illustrated the initial landslide mass (the red-color part) and displaced landslide debris after deposition (the blue-color part). The inclination connecting the top of the initial landslide and the toe of the displaced landslide deposit is approximately 10° , which

indicates the average apparent friction angle mobilized during the whole travel distance. The value is much smaller than the usual friction angle of debris (sandy gravel) of $30^\circ\text{--}40^\circ$. Therefore, it suggests that high excess pore-water pressure was generated during motion. Figure 11c shows a flow mound that travelled from the initial slope to this flat area without much disturbance. Movement without much disturbance is possible when the shear resistance on the sliding surface became

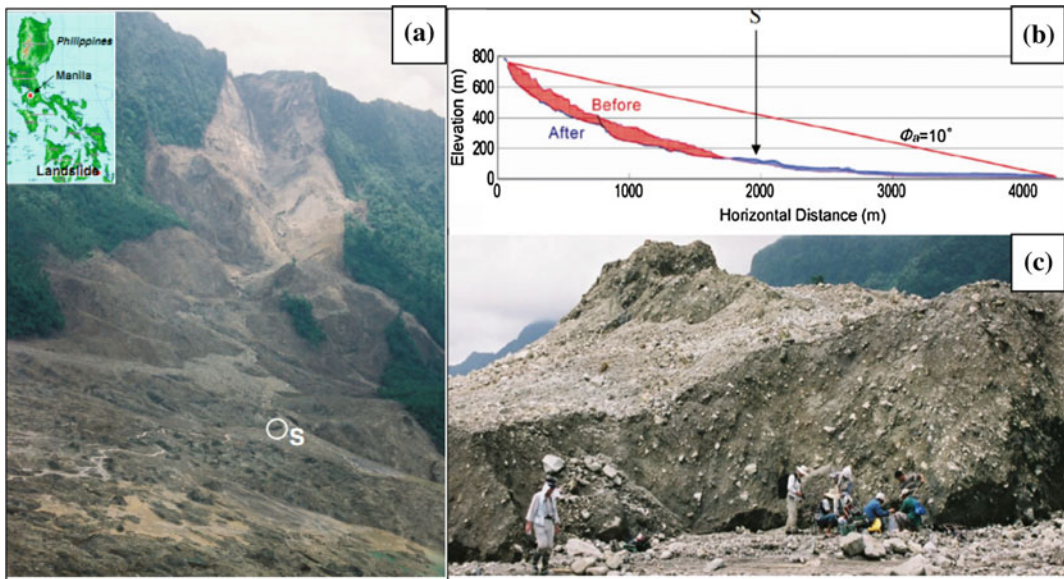


Fig. 11 The front view of the Leyte landslide on 17 February 2006 (a), a central section (b) and sampling point S (c) (Sassa et al. 2010)

very low; thus, movement of the material is like that of a sled. To perform undrained dynamic-loading ring-shear tests, a sample of about 100 kg from the base of the flow mound was taken as shown in the point “S” in the section of Fig. 11a and the photo of Fig. 11c.

6.1 Triggers of the Landslide

A heavy rainfall (459.2 mm for 3 days on 10–12 February and 571.2 mm for 5 days on 8–12 February 2006) occurred in this area before the day of the landslide as shown in Fig. 12(left) (PAGASA 2006). This rainfall should have increased the ground-water level and pore-water pressure inside the slope. However, the peak groundwater level had likely depleted before the occurrence of the landslide on 17 February because the rainfall on 13–17 February was small (total 99.0 mm for 5 days). Ground-water level increasing was simulated by using a tank model as the same in the Zentoku landslide, Japan (Hong et al. 2005), which had a depth and inclination similar to that of the Leyte landslide. When inputting 10 days’ precipitation records at the nearest monitoring station in Otikon (about 7 km west of the landslide) on 8–17 February, the peak ground-water level occurred on 13 February 2006. Because the peak groundwater level had already passed when the landslide

occurred on 17 February, we deduced that a small earthquake was the final trigger of the landslide.

A small earthquake occurred at the nearest location (10.30N, 124.90E) 22 km west of the source area of the landslide, 6 km deep, with magnitude M_s 2.6 (according to PHIVOLCS) was investigated as one of a triggering. The seismic record at Maasin is shown in Fig. 12 (right). E–W component in blue color was the major direction of seismic shaking; other two components are around a half magnitude. Using the standard attenuation function between peak ground acceleration and hypocentral distance (Fukushima and Tanaka 1990), the peak ground acceleration at the landslide site was estimated at 10 gal for this magnitude. The expected peak acceleration at the bottom of the landslide mass was estimated as about 60–200 gal.

6.2 Dynamic-Loading Ring-Shear Test

The undrained dynamic loading ring shear apparatus DPRI-6 (Sassa et al. 2004a) was used for this research, which can simulate the formation of the shear zone and its post-failure motion by reproducing the stress acting on the sliding zone and to observe pore pressure changes, mobilized shear resistance, possible liquefaction

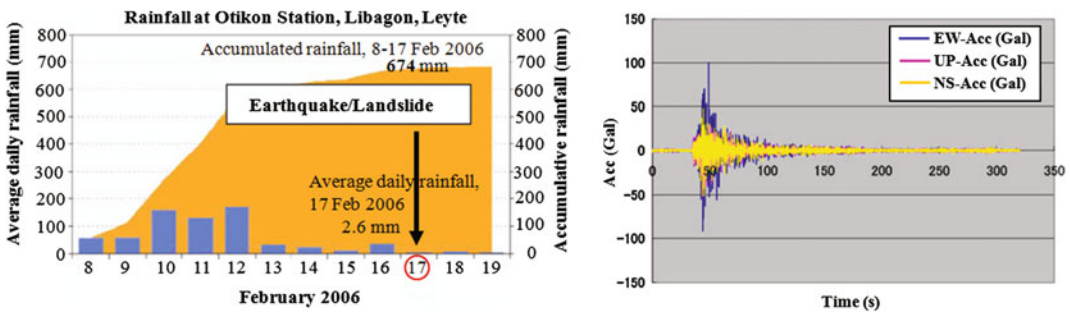


Fig. 12 Triggering factors of the Leyte landslide. Record of rainfalls monitored at Otikon and the earthquake monitored at Maasin, Leyte

and post-failure rapid motion at large displacement. It can provide seismic stress in addition to gravity and pore-water pressure as triggering factors. The capability of DPRI-6 is to do tests under dynamic loading up to 5 Hz and high-speed shearing up to 224 cm/s.

Doing ring shear test, the saturated sample (BD = 0.98) was firstly built in the shear box. The stress acting on the sliding surface of the deepest part (around 120–200 m) is very high. However, because of the capacity of this apparatus: the sliding surface was assumed for the test to be 35 m deep and at an inclination of 25°. The unit weight of the soil was assumed to be 20 kN/m³. In the preliminary test to increase pore-water pressure until failure, the failure line of this material was obtained. It was 39.4° in the friction angle and almost zero cohesion. In the simulation test of a rain- and earthquake-induced landslide, the normal stress corresponding to that of 5 m lower than the critical ground-water level (i.e., further 5 m rise of ground-water level shall trigger the landslide) was first loaded on the sample. Then, the shear stress due to the self-weight of the soil layer was loaded. It is the stress point shown by the white circle in Fig. 13a. Finally, three components of seismic record observed at Massin (PHIVOLCS, Code

number: MSLP, Latitude: 10.1340, Longitude: 124.8590, Elevation: 50.0) were calculated so that the peak seismic stress may correspond to the range of seismic acceleration of 60–200 gal, but as low as possible to avoid failure before seismic loading.

6.3 Test Results

The stress path of the test is presented in Fig. 13a. The effective stress path showed a complicated stress path like a cloud. The stress path reached the failure line repeatedly. Therefore, this small seismic stress triggered the failure of the soil sample and gave a repeated shear displacement during the period of stress reaching the failure line. Meanwhile, pore pressure generation (blue color line) due to grain crushing and volume reduction was accelerated in the progress of shear displacement (green color line). The sliding surface liquefaction phenomenon was observed. The value reached a very small steady state stress (red color line). This process is presented in the time series data around the failure in Fig. 13b. The mobilized apparent friction coefficient defined by steady-state shear resistance divided by the total normal stress was 0.016

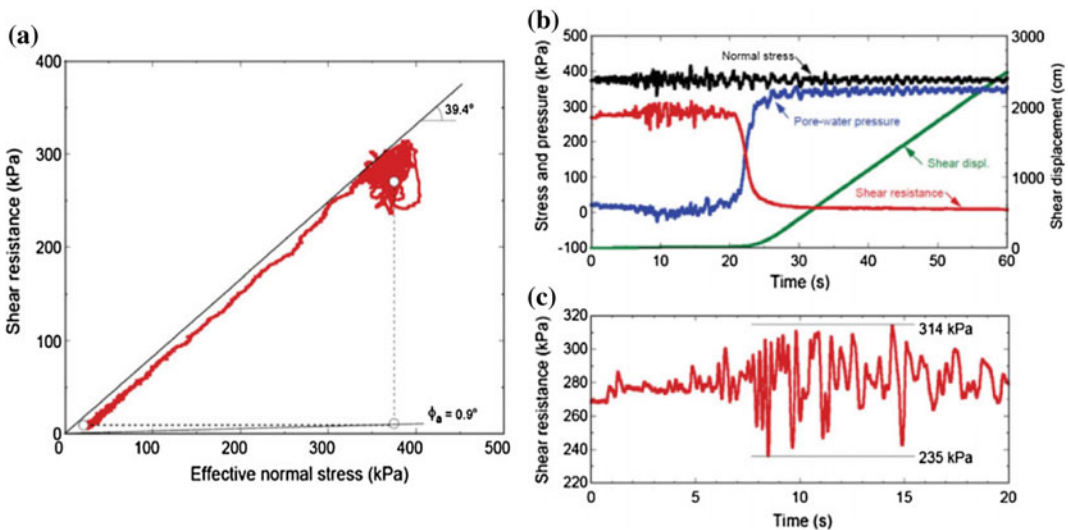


Fig. 13 Ring shear test results on the Leyte sample (BD = 0.98). **a** Stress path; **b** time series data of stresses, pore pressure, shear resistance and shear displacement; **c** enlarged shear resistance monitoring record

(0.9°). The monitored shear resistance is shown in Fig. 13c. When the stress reaches failure line, the balance of shear stress and shear resistance is manifested as acceleration. As seen in the figure, the magnitude of increment of shear resistance seems to be slightly smaller than the decrement. The level of seismic stress is around 40 kPa, the shear stress due to gravity is about 275 kPa. The ratio is 0.145. Namely the seismic coefficient $K = 0.145$. The estimated magnitude of stress is to load 60–200 gal, namely $K = 0.06–0.20$.

7 Computer Simulation for the Leyte Landslide

After creating a landslide body and its sliding surface on topographical map, key parameters obtained from ring shear tests were used for the landslide simulation. As shown in Fig. 14, the steady-state shear strength is very low as less than 10 kPa. However, the testing condition is 100%

full saturation and the loading stress corresponding to 35 m deep (much shallower) and the used sample may be more weathered than that in this deep landslide body. Therefore, a higher value of $\tau_{ss} = 40$ kPa was selected as a practical value for this landslide. The peak friction coefficient and peak cohesion before motion in the source area were estimated as $\tan\phi_p = 0.9$, $c_p = 100–300$ kPa, respectively. Next, the value of B_{ss} was estimated depending on the degree of saturation of different landslide parts as follows: $B_{ss} = 0.1–0.2$ was given in this area, and the middle part was probably more saturated ($B_{ss} = 0.4–0.6$) and the lower part in the patty field on the flat area was probably well saturated ($B_{ss} = 0.9–0.97$). The landslide body was stiff at the top, and moderate in the middle and much disturbed in the lower part and on the flat area (lateral pressure ratio $k = 0.2–0.7$). The shear displacement of shear strength reduction was estimated from the test as $DL = 100$ mm and $DU = 1000$ mm referring to the test of Fig. 14.

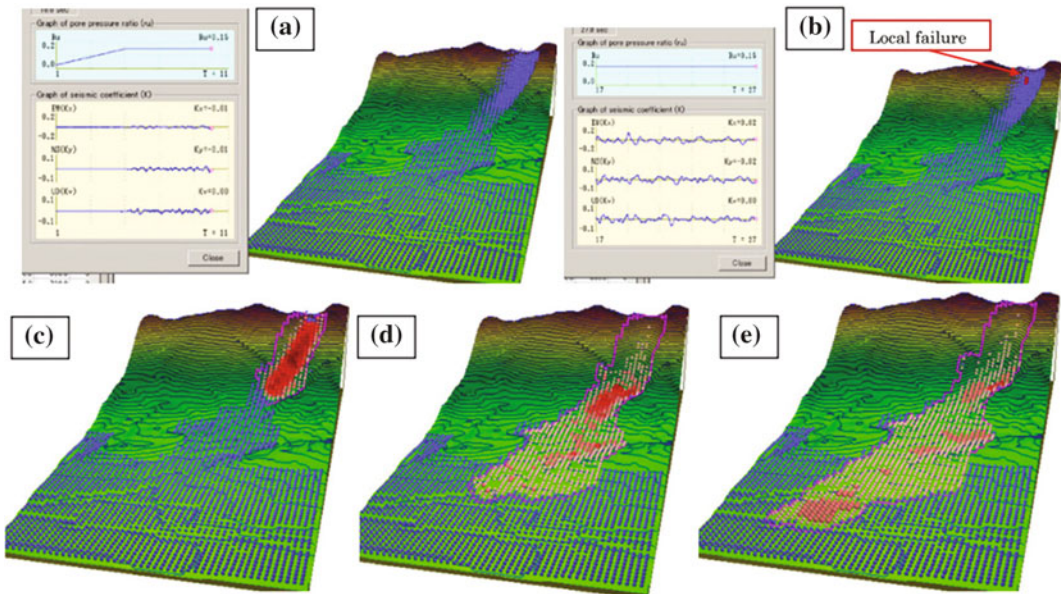


Fig. 14 Simulation result of the Leyte landslide, Pore pressure ration $r_u = 0.15$ and seismic coefficient by the earthquake $K_{EW} = 0.12$, $K_{NS} = K_{UD} = 0.061$

As for the non-frictional energy consumption, we set threshold values for velocity are 80 m/s in velocity, 200 m in soil height, and energy loss coefficient as $\alpha = 1.0$. As previously explained, almost same results were obtained for $\alpha = 0.2, 1.0, 2.0, 5.0, \text{ and } 10.0$ in the preliminary tests.

In the trial simulation, no landslide occurred at pore pressure ratio $r_u = 0.10, 0.15$. However, the case of $r_u = 0.16$ caused a rapid landslide. Around 30% saturation in this source area is the critical value to trigger a landslide without the earthquake. Then, a various magnitude of seismic shaking using the waveforms of EW, NS, and UD recorded at Maasin, Leyte was given in addition to pore pressure ratio of 0.15. The border to create a rapid landslide existed between $K_{EW} = 0.11$ and 0.12. Then, we gave $K_{EW} = 0.12$. Using the ratio of magnitudes of seismic records of EW, NS and UD, $K_{NS} = K_{UD} = 0.061$. The seismic shaking in three directions of EW, NS and UD were given in this simulation. 3 m unstable deposits are assumed in the alluvial deposit area. Blue balls shown in Fig. 14a are the unstable soil deposits (initial landslide body) in the source area and also unstable deposits in the alluvial flat area. The critical height ($\Delta h_{cr} = 0.5$ m) to reduce shear strength from peak to the steady state was given. The threshold values that trigger the function for non-frictional energy

consumption are 200 m in the soil height and 80 m/s in velocity. 200 m was set to be a bit greater than the maximum depth of the initial landslide body (188.7 m) because the height will decrease after the start of motion; 80 m was decided to be around 3–4 times greater than the velocity of 20–26 m/s observed in the 1984 Ontake rapid landslide in volcanoclastic debris which was a greater $3.6 \times 10^7 \text{ m}^3$ in volume and travelled over 9 km.

A series of motion with the explanation for each step was presented in the case of $K_{EW} = 0.12, K_{NS} = K_{UD} = 0.061, r_u = 0.15$ in Fig. 14. For validation of the simulation model, an air photo was taken from the helicopter and the simulation results presented in the 3D view from a similar angle are presented in Fig. 15. The travel distance and the major part of landslide distribution were well reproduced.

8 Conclusions

The following are very important outcomes achieved in this research:

1. A new computer simulation model (LS-RAPID) was developed successfully to integrate the stability analysis from a stable

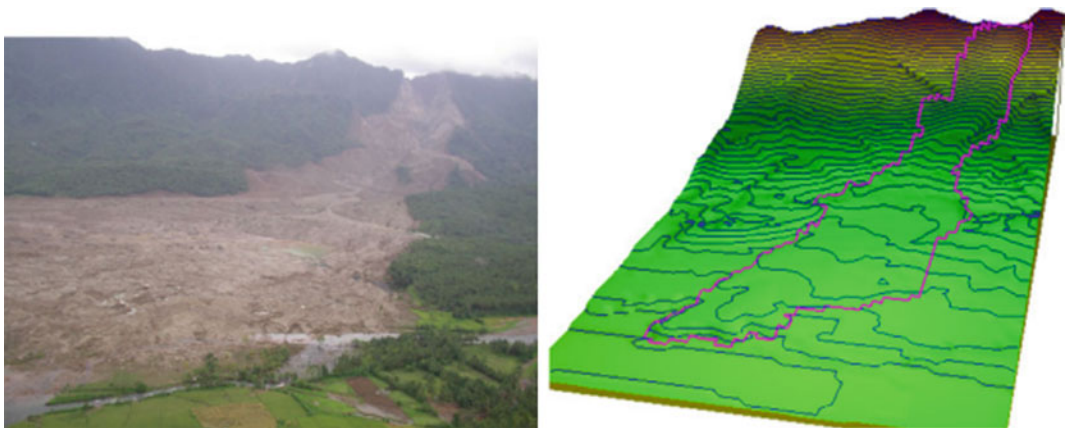


Fig. 15 Comparison of air and the computer simulation result of the Leyte landslide. *Photo* Taken by K. Araiba, Japan-Philippines investigation team member

state to the failure (initiation of the landslide) and the dynamic analysis for the post-failure motion under impacts of pore pressure increase and/or seismic loading. The model could produce progressive failure of the slope initiated at a threshold value of shear displacement when shear resistance starts to decrease from the peak to the steady state T.

2. Comparison of LS-RAPID and conventional limit equilibrium stability analyses of Bishop, Janbu, Spensor, Morgenstern and Price showed that landslides will be initiated in smaller pore water pressure ratio in LS-RAPID because of progressive failure. The threshold value of start of shear strength reduction was changed from 10 mm (estimated from experiments) to 2000 mm (a large value) to restrain the initiation of progressive failure. In this case, the border between motion and no motion in LS-RAPID was the same with the border by conventional limit equilibrium stability analyses.
3. The new computer simulation was applied to the 2006 Leyte landslide based on the key parameters measured in laboratory ring shear tests using rainfall data and monitored seismic records at the Maasin observatory. Even though, it was not completed because the loaded normal stress is different due to the limited capability of the apparatus. In the simulation model, a rapid landslide was reproduced with a similar travel distance and distribution area which was triggered by a pore water pressure ratio of 0.15 and a small seismic shaking of $K_{EW} = 0.12$ and K_{NS} and $K_{UD} = 0.061$. The simulation result almost corresponded that the rapid landslide triggered by a small nearby earthquake of $M_s = 2.6$ in 5 days after the consecutive heavy rains for 3 days intensity of over 100 mm/day.
4. In the computer simulation model developed, profiles of sections, values of triggering factors, the values of depth distribution, velocity distribution and mobilized apparent friction

(calculated from the steady-state shear resistance and the soil depth) at different site/time can be monitored during motion. Also a video and photos of motion can be recorded and extracted. Those are useful for analysis of the moving process and performance of simulation and further improvement through the application of various case studies.

Acknowledgements This research is a technical development activity for the computer simulation within the project titled as “Early Warning of Landslides”, one of the projects of the International Program on Landslides (IPL) jointly managed by ICL, UNESCO, WMO, FAO, UNISDR, ICSU, and WFEO. The project was financially supported by the Ministry of Education, Culture, Sports, Science and Technology of Japan (MEXT) in the framework of International Joint Research Promotion Fund. The project (leader: K. Sassa) was jointly conducted by the International Consortium on Landslides (ICL) and the Disaster Prevention Research Institute (DPRI) of Kyoto University, the China Geological Survey, the Korean Institute of Geoscience and Mineral Resources (KIGAM) and the National Institute for Disaster Prevention (NIDP) in Korea, University of Gadjah Mada (UGM) and the Bandung Institute of Technology (ITB) of Indonesia, Philippine Institute of Volcanology and Seismology (PHIVOLCS). The part of Leyte landslide investigation was conducted together with Assoc. Prof. Hiroshi Fukuoka, Prof. Hideaki Marui, Assoc. Prof. Fawu Wang and Dr. Wang Gonghui.

References

- Fukushima Y, Tanaka T (1990) A new attenuation relation for peak horizontal acceleration of strong earthquake ground motion in Japan. *Bull Seismol Soc Am* 84:757–783
- Hong Y, Hiura H, Shino K, Sassa K, Fukuoka H (2005) Quantitative assessment on the influence of heavy rainfall on the crystalline schist landslide by monitoring system—case study on Zentoku landslide in Japan. *Landslides* 2–1:31–41
- Okada Y, Sassa K, Fukuoka H (2000) Liquefaction and the steady state of weathered granite sands obtained by undrained ring shear tests: a fundamental study on the mechanism of liquidized landslides. *J Nat Disaster Sci* 22(2):75–85
- Philippine Atmospheric, Geophysical and Astronomical Services Agency (PAGASA) (2006)

- Sassa K (1988) Geotechnical model for the motion of landslides. In: Proceedings of 5th international symposium on landslides, "Landslides", Balkema, Rotterdam, vol 1, pp 37–56
- Sassa K, Fukuoka H, Wang G, Ishikawa N (2004a) Undrained dynamic-loading ring-shear apparatus and its application to landslide dynamics. *Landslides* 1(1):7–19
- Sassa K, Wang G, Fukuoka H, Wang FW, Ochiai T, Sugiyama Sekiguchi T (2004b) Landslide risk evaluation and hazard mapping for rapid and long-travel landslides in urban development areas. *Landslides* 1(3):221–235
- Sassa K, Nagai O, Solidum R, Yamazaki Y, Ohta H (2010) An integrated model simulating the initiation and motion of earthquake and rain induced rapid landslides and its application to the 2006 Leyte landslide. *Landslides* 7:219–236
- Sassa K, He B, Khang D, Nagai O, Takara K (2014) Progress in landside dynamics. In: Proceedings of world landslide forum 3, Beijing, vol 1, pp 37–70

TXT-tool 3.385-1.1

Application of Integrated Landslide Simulation Model LS-Rapid to the Kostanjek Landslide, Zagreb, Croatia

Karolina Gradiški, Kyoji Sassa, Bin He, Željko Arbanas, Snježana Mihalić Arbanas, Martin Krkač, Predrag Kvasnička and Maja Oštrić

Abstract

This paper describes numerical modeling of the Kostanjek landslide using the LS-Rapid software. The analyses using the LS-Rapid software were made for two different triggering factors i.e. excess of pore water pressure, and combination of pore excess water pressure and earthquake occurrence, and it was applied at two different landslide cases. In the first case, the LS-Rapid software was used to re-examine the landslide model for the Kostanjek landslide reported by Ortolan (Development of 3D engineering geological model of deep landslide with multiple sliding surfaces (example of the Kostanjek landslide). Faculty of Mining, Geology and Petroleum Engineering, University of Zagreb, Zagreb, 1996), Mihalinec and Stanić (Građevinar 43:441–447, 1991) and Stanić and Nonveiller (Eng Geol 42:269–283, 1996). In the second case, LS-Rapid was used to confirm the Kostanjek landslide model in which the sliding surfaces are initially developed through the soil mass. During the initial shearing, the excess pore pressure is often generated during the landslide activations by triggering factors and the post failure-motion of the landslide. The strength parameters used in these analyses were derived from tests in undrained ring shear apparatus carried out by Oštrić et al. (Proceeding of the 10th anniversary of ICL, Kyoto, Japan, 2012a, Disaster Prevent Res Inst Annu B 55:57–65, b). It is expected that the results of the Kostanjek Landslide simulation using LS-Rapid software and parameters obtained

K. Gradiški (✉) · S.M. Arbanas · M. Krkač ·
P. Kvasnička
Faculty of Mining, Geology and Petroleum
Engineering, University of Zagreb, Zagreb, Croatia
e-mail: karolina.gradiski@hotmail.com

K. Sassa
International Consortium on Landslides, Kyoto,
Japan
e-mail: kyoji.sassa@gmail.com

B. He
State Key Laboratory of Lake Science and
Environment, Nanjing Institute of Geography and
Limnology, Chinese Academy of Science, Nanjing,
China

Ž. Arbanas
Faculty of Civil Engineering, University of Rijeka,
Rijeka, Croatia

M. Oštrić
Croatian Waters, Rijeka, Croatia

from undrained tests carried out in ring shear apparatus would give realistic results and would help for better understanding of the Kostanjek landslide behavior.

Keywords

Kostanjek landslide · LS-RAPID · Slope stability

Contents

1	Introduction	102
2	Historical Landslide Model and Slope Stability Analysis	102
3	Stability Analysis Using LS-RAPID Software	105
4	Results	107
	References.....	108

1 Introduction

The Kostanjek Landslide is located in the western part of the City of Zagreb, in residential area at the base of the southwestern slope of the Medvednica Mt. It was initially activated in 1963 by mining and excavation in two open pit mines. Massive blasting and excavation in the foot of the slope caused slope movements in an area of 1.2 km². Landslide velocities have been changing in last 50 years, from landslide activation until today, in range from extremely slow to very slow.

2 Historical Landslide Model and Slope Stability Analysis

Engineering Geological Model According to Ortolan (1996)

Ortolan (1996) proposed engineering geological landslide model on the basis of geotechnical investigations mainly carried out in the period 1988–1989 and this landslide model is in use until today. According to this model there exist

three slip surfaces at different depths. The maximum depth of the deepest slip surface is about 90 m; the depth of the intermediate slip surface is 65 m, while the superficial slip surface is about 50 m deep (Fig. 1). The total volume of the displaced landslide mass amounts to approx. 32.6×10^6 m³, while it is about 12.8×10^6 m³ for the intermediate slip surface and about 7×10^6 m³ for the shallowest slip surface. Slip surfaces are subparallel; they are predisposed by the bedding planes in the rock mass (Ortolan and Pleško 1992).

The landslide geometry, the state of pore pressure on sliding surface and shear resistance parameters were determined from the results of field and laboratory investigations. The 3D engineering geological model of the Kostanjek landslide (Ortolan 1996) is presented on the Fig. 1.

Hydrogeological conditions at the area of the Kostanjek landslide were determined based on the data of permeability tests and piezometric level measurements in the exploration boreholes (KS-2, KS-2', KS-3, KS-4, KS-5, KS-6 and KS-7) from the period 1988–1994. In some piezometers (KS-6 and KS-7 placed on the east and south-east part of landslide body) the water pressure level is above the surface, and in all of them it is close to the ground surface. The yearly precipitation in the region averages 1000 mm, partly in the form of snow, which causes rising of ground water level in the spring, when soil becomes saturated to the surface (Stanić and Nonveiller 1996).

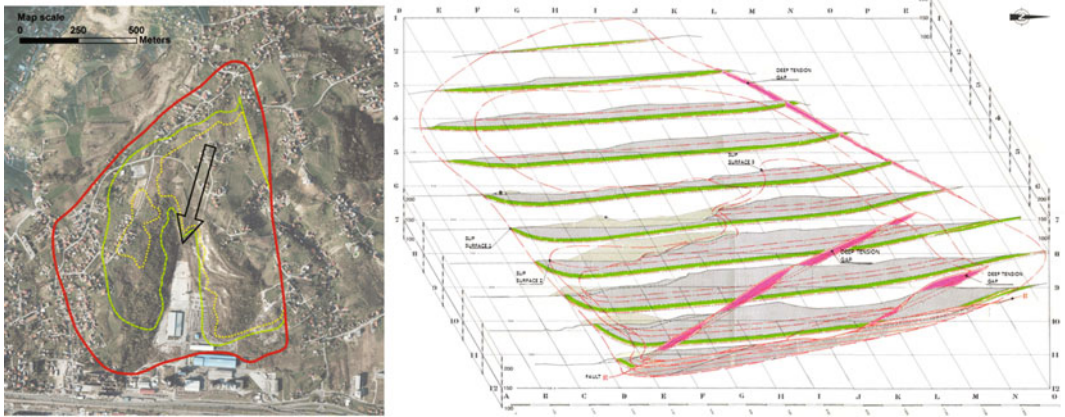


Fig. 1 Engineering geological model according to Ortolan (1996). *Left* landslide contours of the Kostanjek landslide (*red line* the deepest sliding surface landslide contour; *green line* the intermediate sliding surface

landslide contour; *yellow line* the superficial sliding surface landslide contour). *Right* 3D engineering geological model of the Kostanjek landslide

Geotechnical properties of the materials in the landslide body were determined from laboratory test of the undisturbed soil samples taken from the boreholes in the Lower Panonian, Upper Panonian and Sarmatian deposits, especially from the varved Sarmatian deposits (i.e. thinly laminated alteration of carbonate and clayey layers) in which the deepest sliding plane was developed (Stanić and Nonveiller 1996). The following laboratory tests were carried out: grain size distribution and soil classification, unconfined soil strength, shear strength in drained slow tests in triaxial tests and in the direct shear tests, and the residual shear strength in a ring shear apparatus. The results of these tests are shown in Table 1.

The results of shear strength tests, which were verified in the stability analyses show that under the given geometric setting and hydrogeological conditions, the residual shear strength defined by the parameters $c_r = 0$, $\phi = 9^\circ$, brings the slide to a stable condition with a factor of safety FoS = 1.0.

Stability Analysis According to Stanić and Nonveiller (1996)

The stability analyses of the Kostanjek landslide were presented by Mihalinc and Stanić (1991), Stanić and Nonveiller (1996) and Stanić and

Nonveiller (1995). For the given landslide model they have presented a 3D solution for the analysis of slope slides. The sliding body is divided into elements, each of which is defined by representative cross-section (Fig. 2). The resisting and active forces, and the 2D safety factors are computed for all cross-sections, and they form, along with the width of the elements, the necessary data for the computation of the 3D safety factor.

The 2D analyses were carried out by the Spencer's method (Spencer 1967), using the software SSTAB1 which was modified to enable the computation of the input data for the 3D analysis (Stanić and Nonveiller 1996). The data required for the compatibility check and 3D effects (transversal inclination and width of element, computational length of section, shear strength parameters on the vertical contacts, average depth of groundwater on the slip surface) are added to the input data for selected cross-sections (2D FoS, resisting forces, active forces, weight of the elements) (Stanić and Nonveiller 1996). The results of the computation obtained for the geometry of the marl excavation in quarry in 1988 are shown on Fig. 2.

According to Stanić and Nonveiller (1996), the differences between the maximum and minimum 2D safety factors are caused by much higher pore pressures on the right part of the slide

Table 1 Physical and mechanical soil properties (Stanić and Nonveiller 1996)

Parameter	Pannonian		Sarmatian	
	Clayey-limely marl	Thin clay layers	Varved layers	Laminated silty marl
WL (%)	33.5–81.5	77.5–94.5	54.9–143.0	40.0–105.5
WP (%)	14.1–41.6	30.0–42.2	31.5–126.7	13.8–62.9
IP (%)	19.5–27.5	43.1–54.8	16.3–28.3	17.3–42.6
AC class	–	CI/CH	MH	CI/CH
ρ (g/cm ³)	1.75	2.15	1.22–1.59	1.39–2.18
ρ_s (g/cm ³)	2.60	2.83	2.32–2.50	2.36–2.78
ρ_d (g/cm ³)	1.25	1.80	0.71–1.09	0.82–1.78
Φ_d (°)	27.5–35	–	23–28	23–28
c_d (kPa)	0–40	–	6–40	6–40
Φ_r (°)	–	7–8	8–20	8–20
c_r (kPa)	–	0	0	0
q_u (kPa)	500–5000	–	–	–

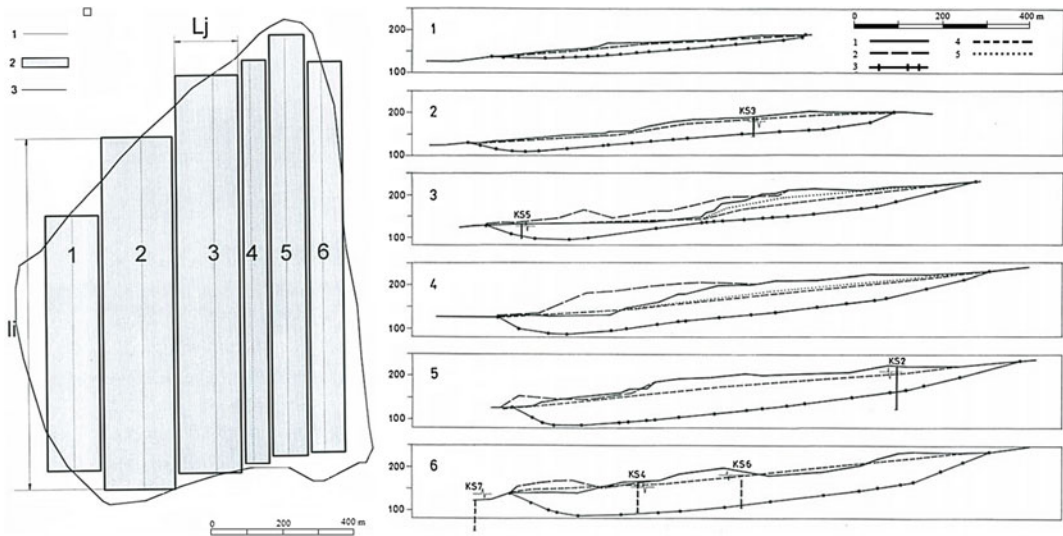


Fig. 2 Stability computation of the Kostanjek slide according to Stanić and Nonveiller (1996). *Left* plan view of analyzed landslide and elements used in the analysis (1 computational cross-sections; 2 elements; 3 landslide

contour). *Right* cross-sections used in the computation (1 ground surface in 1988; 2 ground surface in 1963; 3 deep slide surface; 4 groundwater level in 1963; 5 groundwater level in 1988)

and a deficit of mass at the toe in the central part. The stability analyses for slope geometry from 1963 gave the safety factor of 1.17, which confirmed that the start of slide was caused by excavation in quarry.

Stanić and Nonveiller (1996) concluded that possible causes for the landslide activation may

be extremely high pore pressures and/or the dynamic effects caused by the excavation of marl by mass blasting. The critical acceleration which brings the computed safety factor to FoS = 1 amounts to $a_{cri} = 0.014$ g, which corresponds to the order of magnitude of the acceleration caused by mass blasting.

3 Stability Analysis Using LS-RAPID Software

About LS-RAPID Software

The Integrated Landslide Simulation Model (LS-RAPID) is simulation software that has been developed to assess the initiation and motion of landslides triggered by earthquakes, rainfalls or the combined effects of rainfalls and earthquakes (Sassa 2010). The software has following characteristics (Sassa 2010):

- It is the first simulation model to reproduce the initiation process and the run out process from stable state until deposition within the same model.
- It is the simulation model based on the key parameter, shear resistance at the steady state with physical meaning, which can be measured or estimated from experiments.
- Landslide can be triggered by seismic loading either using real seismic record or simple cyclic waves under a certain pore water pressure (pore pressure ratio) within LS-RAPID.
- The model can simulate the entrainment of unstable deposits along the run out path, which increases landslide volume and hazard area.
- The model can reproduce “Progressive failure phenomenon”. This phenomenon manifests

when weak zones subjected by higher pore pressure will firstly fail and the failure area will expand around the initial failure zone, then finally a whole landslide mass will start to move.

- The basic equation of LS-RAPID is established on the assumption in which all potential energy is consumed as the frictional energy at the sliding surface. However, the landslide mass may lose kinetic energy during collision of sub-masses within a landslide mass, momentum transfer to engulfed materials and the movement passing over vertical gaps/falls, horizontal bent or other not-smooth ground surface. The model incorporates a non-frictional energy loss function only for a specific mesh and a specific time step by the threshold values of extraordinary velocity or/and thickness.

The basic concept of LS-RAPID simulation model is presented on Fig. 3. A vertical imaginary column is considered within a moving landslide mass. The forces acting on the column are the following: (1) self-weight of column (W), (2) seismic forces (vertical seismic force F_v , horizontal x–y direction seismic forces F_x and F_y), (3) lateral pressure acting on the side column walls (P), (4) shear resistance acting on the bottom (R), (5) normal stress acting on the bottom (N), (6) pore pressure acting on the bottom (U).

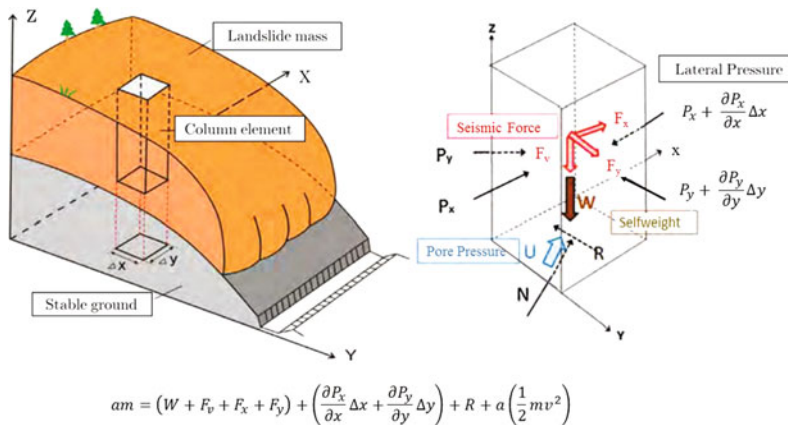


Fig. 3 Basic principles of LS-RAPID (Sassa et al. 2010)

The landslide mass (m) will be accelerated by the acceleration (a) given by the sum of the following forces: driving forces (self weight + seismic forces) + lateral pressure ratio + shear resistance + non-frictional energy consumption in a column (Sassa et al. 2010). Described LS-RAPID software is used for stability analyses of the Kostanjek landslide.

Input Data for Analysis

The Kostanjek landslide is a complex landslide with a deficit of a mass in the middle part of the landslide body and with slip surface inclined to the south-southeast. As it is aforementioned, slip surface reaches maximum depth of the 90 m in the southeastern part of the landslide body. Topography input data were created by combining Digital Elevation Model (DEM) data 5×5 m resolution and geodetic survey data with 1×1 m resolution. For creating the slip surface position, the structural-tectonic map presented by Ortolan (1996) was used.

The same slip surface topography data were used in stability analysis presented by Stanić and Nonveiller (1995, 1996). The topography of ground surface and slip surface is presented on Fig. 4a. Slope stability analyses were also conducted for ellipsoidal slip surface, shown on Fig. 4b. The biggest difference between this two sliding surface models is on the eastern part of the sliding body.

Ellipsoidal slip surface was used to check how the different shape of the sliding body affect the results of slope stability within LS-RAPID software.

Parameters used for these two analyses (case A and case B) were the same and they were determined from undrained test of samples in ring shear apparatus. The test was performed on sample taken from artificial outcrop, i.e. abandoned mining cut placed in the central part of landslide body, assumed as a position of the deepest slip surface at the depth of around 65 m

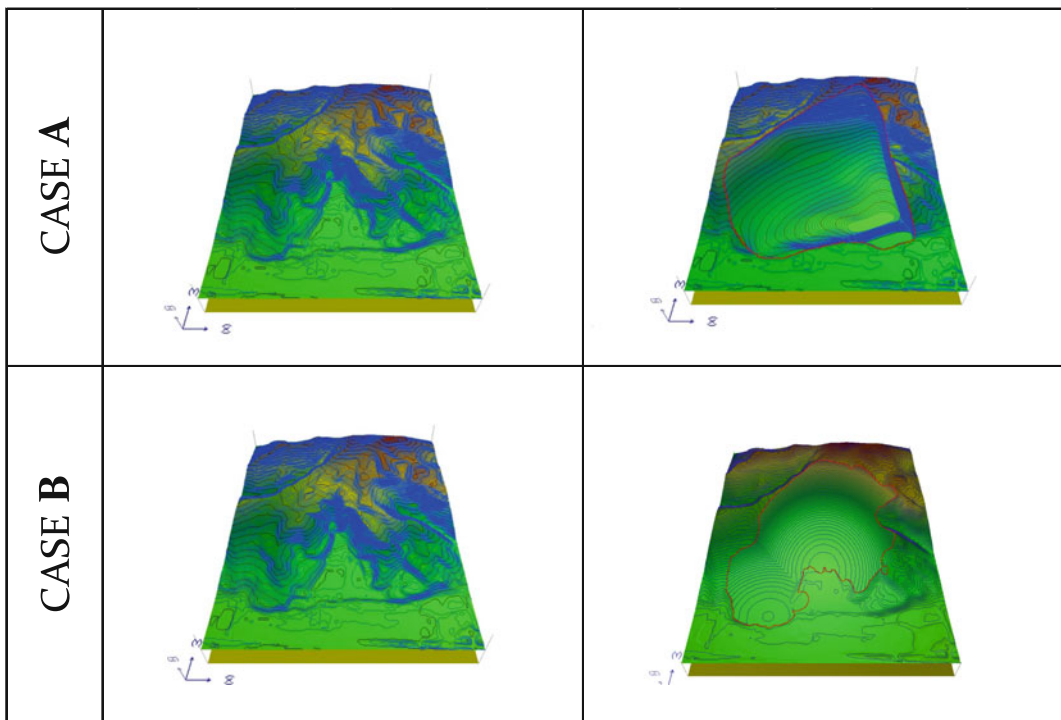


Fig. 4 Topography and sliding surface for Case A (Ortolan's model) and Case B (ellipsoidal sliding surface)

(Oštrić et al. 2012a, b). Soil parameters used for these analyses are already presented in Table 2.

For the both analyses, two different landslide triggering factors were examined. In the cases IA and IB the triggering factor was pore water pressure and in the cases IIA and IIB the triggering factors were pore water pressure and dynamic loading. In the cases IA and IB pore pressure ratio (r_u) was set as a fluctuating value and it was increased from 0.0 to 0.8. For the dynamic loading the real earthquake loadings were used with maximum acceleration of $a_{max} = 0.344 \text{ cm/s}^2$. Results of the analyses are presented on the Fig. 5.

The blue zones represent soil columns stable or with moving velocity less than 0.04 m/s. Red zones show columns with velocity values greater than 0.04 m/s.

4 Results

According to the results of the analysis, the eastern and central parts of the landslide are more unstable than the western part of the landslide. This corresponds to the results of the historical

slope stability analysis from 1995 and 1996 performed by Stanić and Nonveiller.

The eastern part of the deepest slip surface according to Ortolan (1996) is inclined steeply to the surface which seems unrealistic. This element cause the significant difference in the analyses results obtained using the Ortolan's model and ellipsoidal slip surface. It should be necessary to carry out additional field investigations to verify this part and overall geometry of the slip surface(s).

The earthquake with maximal acceleration of 0.344 cm/s^2 will cause movements of overall defined landslide body.

The velocities analyzed by LS-RAPID are much higher than measured in the field. It could be caused by the fact that the LS-RAPID software was primarily developed for rapid motion landslide analyses and the motions of the Kostanjek landslide are very slow to slow.

The soil strength parameters used in the analyses are based on the ring shear test results on the samples taken from the ground surface. Before the next phase of analyses, it should be necessary to conduct testing on the samples taken from appropriate depths which correspond to the slip surface position.

Table 2 Soil parameters used for stability analysis using

Soil parameters	Value	Unit
Lateral pressure ratio (k)	0.6	–
Friction angle inside landslide mass (Φ_i)	18.3	°
Friction angle during motion (Φ_m)	18.3	°
Steady state shear resistance (τ_{ss})	150	kPa
Pore pressure generation rate (B_{ss})	0.95	–
Peak friction angle at sliding surface (Φ_p)	29.5	°
Peak cohesion at sliding surface (c_p)	0.1	kPa
Total unit weight of the mass (γ_t)	20	kN/m ³
Unit weight of water (γ_w)	9.81	kN/m ³
Cohesion inside mass (c_i)	0.1	kPa
Cohesion at sliding surface during motion (c_m)	0.1	kPa
Shear displacement at the start of strength reduction	25	mm

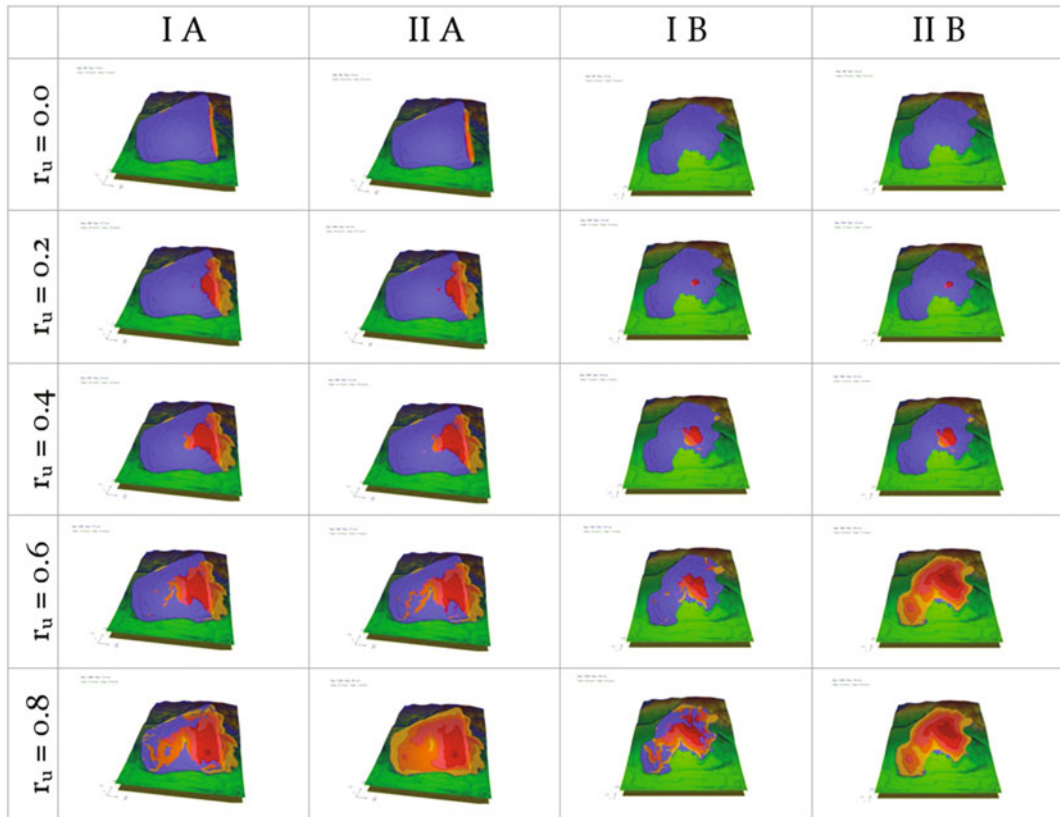


Fig. 5 Results of the analysis for two different cases: Case A (Ortolan's model) and Case B (ellipsoidal sliding surface)

Acknowledgements Equipment and software used in the study was obtained with financial support from the SATREPS [Science and Technology Research Partnership for Sustainable Development] program, financed by the Japan Science and Technology Agency and Japan International Cooperation Agency through the Project Risk Identification and Land-Use Planning for Disaster Mitigation of Landslides and Floods in Croatia. This support is gratefully acknowledged. This work is an expanded version of the paper published and presented on the 1st Regional Symposium of Landslides in the Adriatic-Balkan Region and the 3rd Workshop of the Croatian-Japanese Project "Risk Identification and Land-Use Planning for Disaster Mitigation of Landslides and Floods in Croatia" in Zagreb in March 2103.

References

- Mihalinec Z, Stanić B (1991) Procedure of 3D slope stability. *Građevinar* 43:441–447 (In Croatian)
- Ortolan Ž (1996) Development of 3D engineering geological model of deep landslide with multiple sliding surfaces (example of the Kostanjek landslide) PhD thesis. Faculty of Mining, Geology and Petroleum Engineering, University of Zagreb, Zagreb (in Croatian)
- Ortolan Ž, Pleško J (1992) Repeated photogrammetric measurements at shaping geotechnical models of multi-layer landslides. *Rudarsko Geološko Naftni Zbornik* 4:51–58

- Oštrić M, Ljutić K, Krkač M, Setaiwan H, He B, Sassa K (2012a) Undrained Ring Shear Test Performed on Samples from Kostanjek and Grohovo Landslide. In: Proceeding of the 10th anniversary of ICL, January 2012, Kyoto, Japan
- Oštrić M, Ljutić K, Krkač M, Sassa K, He B, Takara K, Yamashiki Y (2012b) Portable ring shear apparatus and its application on Croatian landslides. *Disaster Prevent Res Inst Annu B* 55:57–65
- Sassa K (2010) Integrated landslide simulation model LS-RAPID operation manual. Godai Kaihatsu Corporation, ICL
- Sassa K, Nagai O, Solidum R, Yamazaki Y, Ohta H (2010) An integrated model simulating the initiation and motion of earthquake and rain induced rapid landslides and its application to the 2006 Leyte landslide. *Landslides* 7:219–236
- Spencer E (1967) A method of analysis of the stability of embankments assuming parallel inter-slice forces. *Geotechnique* 17(1):11–26
- Stanić B, Nonveiller E (1995) Large scale landslide in Kostanjek area. *Gradevinar* 47(4):201–209 (In Croatian)
- Stanić B, Nonveiller E (1996) The Kostanjek landslide in Zagreb. *Eng Geol* 42:269–283

TXT-tool 3.081-1.2 Simulation of Landslide Induced Tsunami (LS-Tsunami) Based on the Landslide Motion Predicted by LS-RAPID

Khang Dang, Kyoji Sassa, Hideaki Yanagisawa
and Bin He

Abstract

By combining landslide dynamics research and tsunami research, we present an integrated series of numerical models quantitatively simulating the complete evolution of a landslide-induced tsunami. The integrated model simulating the landslide initiation and motion uses measured landslide dynamic parameters from a high-stress undrained dynamic-loading ring shear apparatus. It provides the numerical data of a landslide mass entering and moving under water to the tsunami simulation model as the trigger of tsunami. The series of landslide and tsunami simulation models were applied to the 1792 Unzen-Mayuyama megaslide and the ensuing tsunami disaster, which is the largest landslide disaster, the largest volcanic disaster and the largest landslide-induced tsunami disaster to have occurred in Japan. Both the 1792 megaslide and the tsunami portions of the disaster are well documented, making this an excellent test of the reliability and precision of the new simulation model. The simulated tsunami heights at the coasts well match the historical tsunami heights recorded by “Tsunami-Dome-Ishi” (a stone showing the tsunami reaching point) and memorial stone pillars.

Keywords

Unzen-Mayuyama landslide · Landslide-induced tsunami
Undrained ring shear test · Computer simulation

K. Dang · K. Sassa (✉)
International Consortium on Landslides, 138-1,
Tanaka Asukaicho, Sakyo-Ku, Kyoto 606-8226,
Japan
e-mail: sassa@iclhq.org

K. Dang
VNU University of Science, Hanoi, Vietnam

H. Yanagisawa
Department of Regional Design, Faculty of Liberal
Arts, Tohoku Gakuin University, Sendai, Japan

B. He
State Key Laboratory of Lake Science and
Environment, Nanjing Institute of Geography and
Limnology, Chinese Academy of Science, Nanjing,
China
e-mail: hebin@niglas.ac.cn

Contents

1 Introduction	112
2 Basic Principle of the Landslide-Induced Tsunami Model	112
3 Two Sets of Equations to Simulate Landslide Motion and Tsunami Motion	114
4 Application of the Model to Two Hypothetical Simple Coastal Landslides	116
5 Application of the Model to the Unzen-Mayuyama Landslide and Its Resulting Tsunami Wave	119
6 Conclusion	128
References.....	129

1 Introduction

A new 3-D landslide dynamics model (LS-RAPID) has been developed integrating the initiation and motion of landslides based on measured landslide dynamic parameters (Sassa et al. 2010). We have decided to use the landslide motion simulated by LS-RAPID as the trigger of tsunami. The tsunami simulation model used in this study is a well established and widely used model (IOC, 1997). We assumed that horizontal forces between landslide mass and water can be neglected, and tsunami is triggered only by upheaved water mass on the submarine ground due to a moving landslide mass. This assumption is the same with Baba et al. (2012), Abe et al. (2008) and Satake (2001). The tsunami simulation code using the landslide motion data from LS-RAPID was developed (LS-Tsunami) for this study.

The objective of this paper is to define the precision of the series of landslide-induced tsunami models (LS-RAPID + LS-Tsunami). The 1792 Unzen-Mayuyama landslide-and-tsunami disaster was selected as the test case to examine the precision. Both the initial landslide, the landslide displacement, and the tsunami disaster were well investigated and documented. This

landslide (volume $3.4 \times 10^8 \text{ m}^3$; maximum depth 400 m) killed 10,139 persons directly by the displaced landslide mass and also by the triggered tsunami wave in the Shimabara Peninsula. The landslide-induced tsunami crossed the Ariake Sea and killed 4653 people in Kumamoto Prefecture on the opposite bank, 343 people on Amakusa Island and 18 people in other areas (Usami 1996). Sassa et al. investigated the Unzen Mayuyama landslide by measuring the appropriate dynamic parameters for two samples taken from the site using a newly developed high-stress undrained ring-shear apparatus (up to 3 MPa in normal stress and pore pressure). The LS-RAPID simulation using these parameters successfully reproduced the motion of the 1792 Unzen-Mayuyama megaslide in Japan (Sassa et al. 2014a, b). Those measured landslide dynamics parameter are used in this study.

2 Basic Principle of the Landslide-Induced Tsunami Model

The basic principle of the landslide-induced tsunami model used in this study is illustrated in Fig. 1. The left part of Fig. 1 is same as the principle of the integrated landslide simulation model (LS-RAPID) of Sassa et al. (2010). The only difference here is that the landslide mass is located beneath a water surface. The right part of Fig. 1 illustrates the elevated water mass (which causes a tsunami wave) by the upward displacement of the interface between the landslide and the water due to the movement of the landslide mass over the sea floor.

When the landslide mass enters or travels across the sea floor, the elevation of the submarine ground surface (which is the interface of landslide mass and submarine water) will be increased. The submarine ground surface elevated by the landslide mass will raise the water

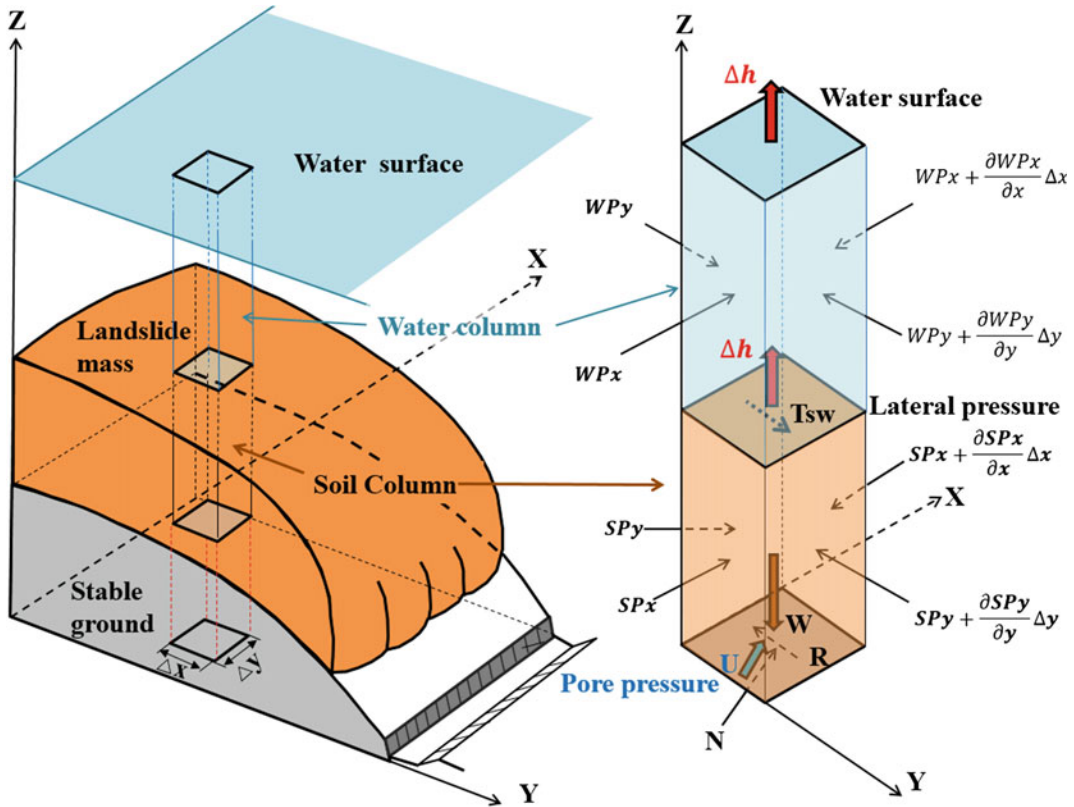


Fig. 1 Basic principle of the landslide-induced tsunami simulation model

mass above the landslide-water interface by an amount, Δh , in a unit time, Δt . The shear resistance (τ_{sw}) between soil and water at this interface should be much smaller than the shear resistance within the soil. Hence, this resistance, τ_{sw} was ignored in the simulation. The effective stress acting on the surface between the bottom of the soil column and the top of the sea floor was regarded as being unaffected by the increase in water height for the following two reasons: (1) the surficial deposit on the sea floor is unconsolidated, and hence is expected to be permeable enough to transmit the water-pressure change due to water height change to the bottom of the soil column above the sea floor; and (2) the soil column of the moving mass is both unconsolidated and water saturated, hence the transmission of water-pressure change from the top of soil column to the bottom of the soil column is fast (elastic wave velocity of water is around 1.5 km/s) and can be regarded as instantaneous.

When a landslide mass enters into water, the buoyant force by water will act on the soil mass. Namely the unit weight of soil mass (γ_t) on land will change to the buoyant unit weight of soil mass, the difference between γ_t and γ_w (unit weight of sea water) under water. In the case of partial submersion, the buoyant force by water will act only on the part of soil mass below the water surface. No tangential force between soil and water is considered because the tangential force by water will be negligible compared to the shear resistance mobilized in the shear surface of large-scale landslides.

There are many parameters to regulate landslide motion on land (Sassa et al. 2010, 2014a, b) and submarine landslide motion (Sassa et al. 2012). The values of such landslide dynamics parameters were mostly measured by the undrained ring shear testing on the samples taken from the landslide source area and its moving area. The parameters used in tsunami simulation

(LS-Tsunami) are the unit weight of sea water and Manning's roughness coefficient for basal resistance between water and ground.

3 Two Sets of Equations to Simulate Landslide Motion and Tsunami Motion

The calculation part of the landslide-induced tsunami model contains the following two steps.

The first step: simulation of landslide mass by the integrated landslide simulation model "LS-RAPID" on land and on the sea floor. The equations of the first step are (1)–(4), which are the same as in LS-RAPID (Sassa et al. 2010).

The second step: simulation of the tsunami by LS-Tsunami. The equations of the second step are (5)–(8), which is an established tsunami simulation model (IOC 1997).

The concept of LS-RAPID is that the acceleration (a) of the soil mass (m_s) is induced by the sum of forces of the self-weight of soil mass, the seismic force acting on the soil column, the shear force acting on the bottom of soil column, and lateral pressure acting on the sides of the soil column (Eq. 1).

The concept of the landslide-induced tsunami simulation (LS-Tsunami) is that the acceleration (a) of the water mass (m_w) is induced by the sum of forces of the lateral pressure acting on the sides of the water column and the Manning's basal shear resistance due to roughness of the ground (Eq. 5). Both sets of equations are shown from (1) to (8) below.

Basic Equations for Motion of Landslide (LS-RAPID)

$$am_s = (W + F_v + F_x + F_y) + \left(\frac{\partial P_x}{\partial x} \Delta x + \frac{\partial P_y}{\partial y} \Delta y \right) R \quad (1)$$

where

a Acceleration of a soil column,
 m_s : landslide mass in a column;
 W Self-weight of column,

F_v, F_x, F_y Three components of seismic forces;

$\frac{\partial P_x}{\partial x} \Delta x, \frac{\partial P_y}{\partial y} \Delta y$ Lateral pressure acting on the side walls of the column in the x and y directions;

R Shear resistance acting on the base of the column.

Expressing Eq. (1) in x, y directions, Eqs. (2) and (3) are obtained. Assuming the total mass of landslide does not change during motion, Eq. (4) is obtained.

$$\begin{aligned} & \frac{\partial M}{\partial t} + \frac{\partial}{\partial x}(u_0 M) + \frac{\partial}{\partial y}(v_0 M) \\ &= gh \left\{ \frac{\tan \alpha}{q+1} (1 + Kv) + Kx \cos^2 \alpha \right\} - (1 + Kv) kgh \frac{\partial h}{\partial x} \\ & \quad - \frac{g}{(q+1)^{1/2}} \cdot \frac{u_0}{(u_0^2 + v_0^2 + w_0^2)^{1/2}} \{ h_c (q+1) \\ & \quad + (1 - r_u) h \tan \phi_a \} \end{aligned} \quad (2)$$

$$\begin{aligned} & \frac{\partial N}{\partial t} + \frac{\partial}{\partial x}(u_0 N) + \frac{\partial}{\partial y}(v_0 N) \\ &= gh \left\{ \frac{\tan \beta}{q+1} (1 + Kv) + Ky \cos^2 \beta \right\} \\ & \quad - (1 + Kv) kgh \frac{\partial h}{\partial y} - \frac{g}{(q+1)^{1/2}} \cdot \\ & \quad \frac{v_0}{(u_0^2 + v_0^2 + w_0^2)^{1/2}} \{ h_c (q+1) + (1 - r_u) h \tan \phi_a \} \end{aligned} \quad (3)$$

$$\frac{\partial h}{\partial t} + \frac{\partial M}{\partial x} + \frac{\partial N}{\partial y} = 0 \quad (4)$$

where

h Height of soil column within a mesh;
 u_0, v_0 Velocity of a soil column to X and Y directions, respectively (velocity distribution in Z direction is neglected, and assumed to be a constant);

M, N Discharge of soil per unit width in X and Y directions respectively ($M = u_0 h, N = v_0 h$);

g Acceleration due to gravity;

α, β

	Angles of the ground surface to X–Z plain and Y–Z plain, respectively;
k	Lateral pressure ratio (ratio of lateral pressure and vertical pressure);
$\tan \phi_a$	Apparent friction coefficient mobilized at the sliding surface of landslide;
hc	Cohesion c expressed in the unit of height ($c = \rho g hc$, ρ : density of soil);
r_u	Pore pressure ratio (u/σ);
Kv, Kx, Ky	Seismic coefficients to the vertical, x and y directions;

$$q = \tan^2 \alpha + \tan^2 \beta$$

$$w_0 = -(u_0 \tan \alpha + v_0 \tan \beta)$$

Basic Equations for Motion of Water (LS-Tsunami)

$$am_w = \frac{\partial P_x}{\partial x} \Delta x + \frac{\partial P_y}{\partial y} \Delta y + R(\text{Manning}) \quad (5)$$

where

a	Acceleration of a water column;
m_w	Water mass in a column;
R(Manning)	Manning's basal resistance between water and ground;
$\frac{\partial P_x}{\partial x} \Delta x, \frac{\partial P_y}{\partial y} \Delta y$	Lateral pressure acting on the side wall of column in x and y directions.

Equation (5) is expressed by Eqs. (6), (7) and (8).

$$\frac{\partial M}{\partial t} + \frac{\partial}{\partial x}(u_0 M) + \frac{\partial}{\partial y}(v_0 M) = -gh \frac{\partial \eta}{\partial x} - \frac{\tau_x}{\rho} \quad (6)$$

$$\frac{\partial N}{\partial t} + \frac{\partial}{\partial x}(u_0 N) + \frac{\partial}{\partial y}(v_0 N) = -gh \frac{\partial \eta}{\partial y} - \frac{\tau_y}{\rho} \quad (7)$$

$$\frac{\partial h}{\partial t} + \frac{\partial M}{\partial x} + \frac{\partial N}{\partial y} = 0 \quad (8)$$

where

h	Height of water column within a mesh;
η	Elevation of water surface above sea level datum;
u_0, v_0	Velocity of a water column in X and Y directions, respectively (velocity distribution in Z direction is neglected, and assumed to be a constant);
M, N	Discharge of water per unit width in X and Y directions respectively ($M = u_0 h, N = v_0 h$);
g	Acceleration due to gravity.

Manning's basal resistance R(Manning) is expressed as below:

$$\text{X-component} : \frac{\tau_x}{\rho} = \frac{gn^2}{h^{7/3}} M \sqrt{M^2 + N^2}$$

$$\text{Y-component} : \frac{\tau_y}{\rho} = \frac{gn^2}{h^{7/3}} N \sqrt{M^2 + N^2}$$

ρ	Density of sea water;
n	Manning's roughness coefficient.

Visual Presentation of the Simulation Results by LS-RAPID and LS-Tsunami

Figure 2 shows the three steps of the series of landslide-induced tsunami simulation. The first step is landslide motion simulation by LS-RAPID. The second step is the tsunami simulation by LS-Tsunami using the calculated landslide motion data. The third step is visual presentation stage without calculation. The landslide and tsunami motions are visually

presented without calculation by a viewing code “LS-Motion” with different speed (time span of each image), color, balls/contours/three dimensional view/two dimensional view, photos, and video. The visual presentation of landslide hazard assessment and tsunami hazard assessment is important for risk management.

- Case A: Maximum depth = 100 m. Maximum length = 500 m, Maximum width = 300 m, Volume = $5.8 \times 10^6 \text{ m}^3$
- Case B: Maximum depth = 313 m. Maximum length = 1230 m, Maximum width = 1000 m, Volume = $170 \times 10^6 \text{ m}^3$.

4 Application of the Model to Two Hypothetical Simple Coastal Landslides

The new landslide-induced tsunami simulation was initially applied to two hypothetical landslides (A and B) on an imaginary slope.

The top of the slope was flat, the slope angle was 35° , and the bottom of the slope was a flat sea bed. The peak friction angle (ϕ_p) was 42° and the friction angle during motion (ϕ_m) was 40° . The heads of both landslides are at the top of the slope, and the toes of both landslide are at the water surface. The distance between the left end and the coast is 2000 m, and the distance from the coast to the bottom of the figure is 100,000 m in Figs. 3 and 4.

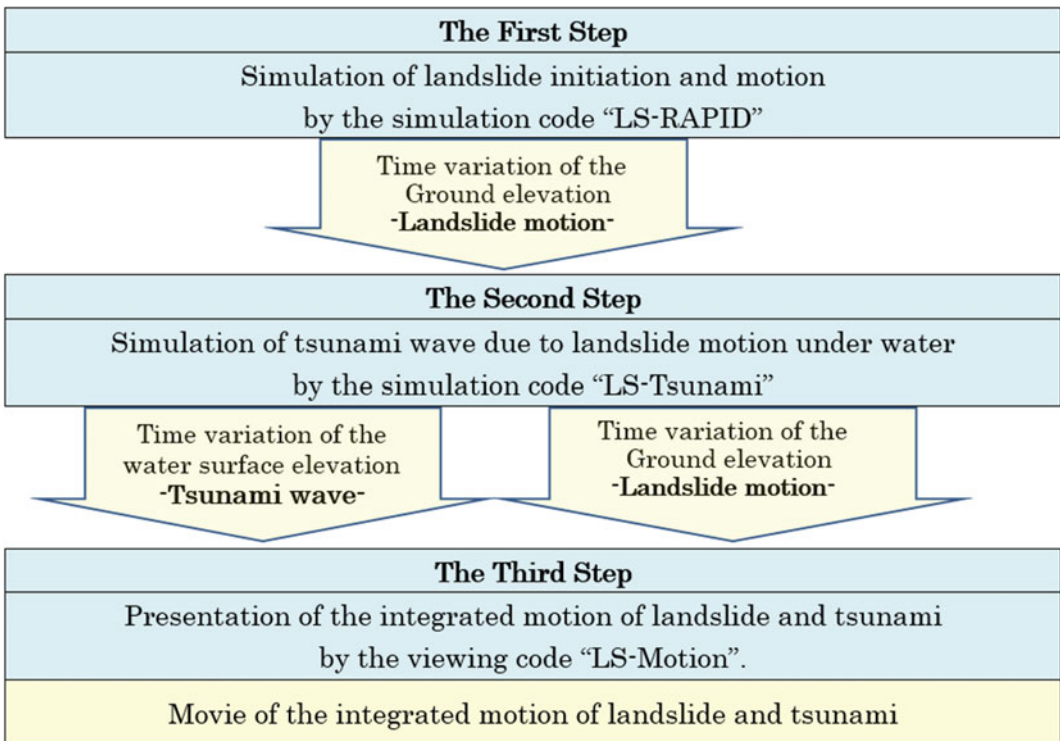


Fig. 2 Three steps of the landslide-induced-tsunami simulation

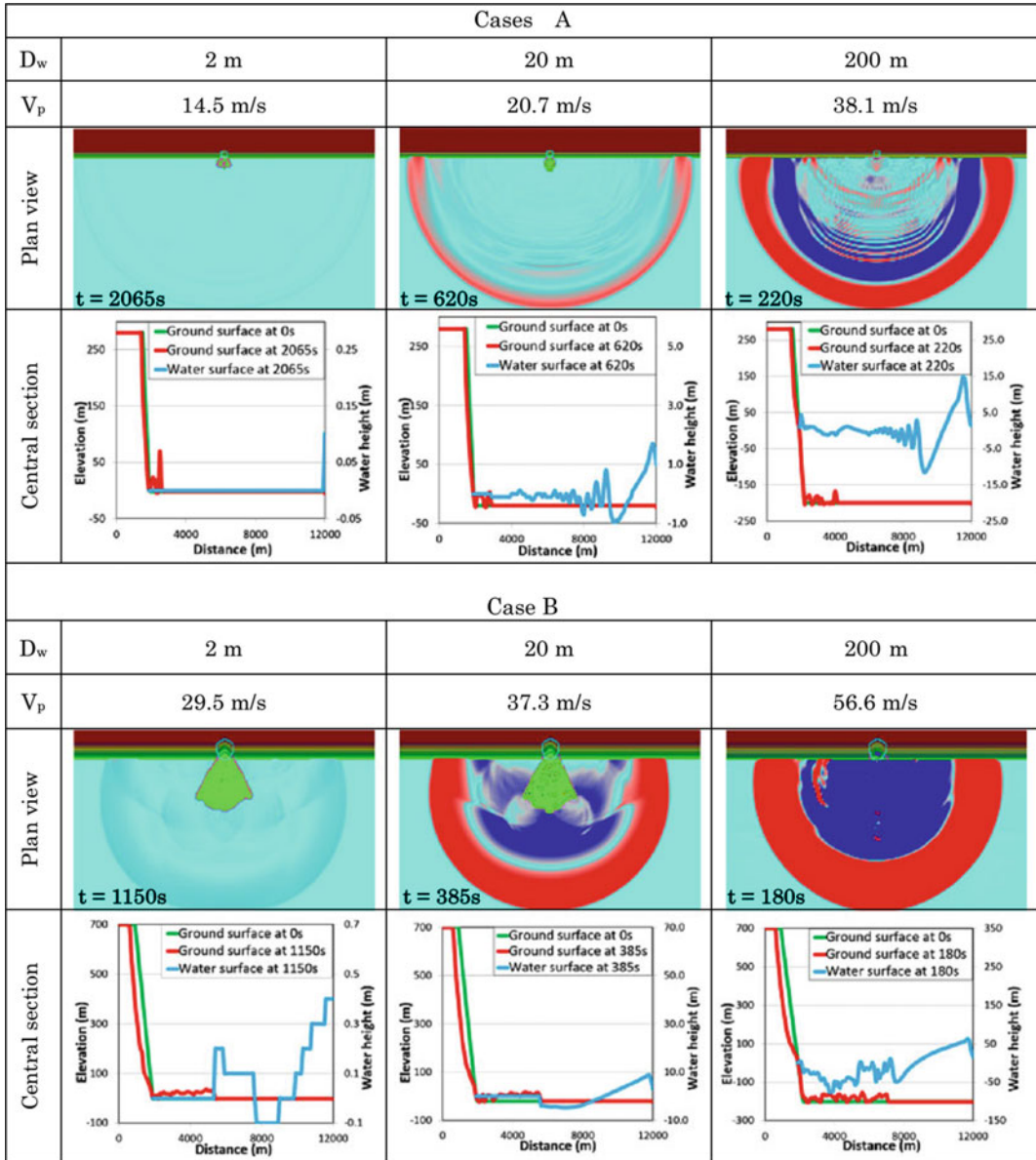


Fig. 3 Tsunami and landslide profiles when the tsunami front reached at 12,000 m

Definition of the maximum landslide velocity and the maximum tsunami height in Tables 1 and 2 are as follows.

- The *maximum landslide velocity* is the maximum velocity within the landslide mass when the front of the landslide mass reaches the flat sea/lake floor. Landslide velocity is one of indexes of triggering of tsunami as well as the landslide depth and the water depth.
- The *maximum tsunami height* is the maximum height in the tsunami profile (in Figs. 3

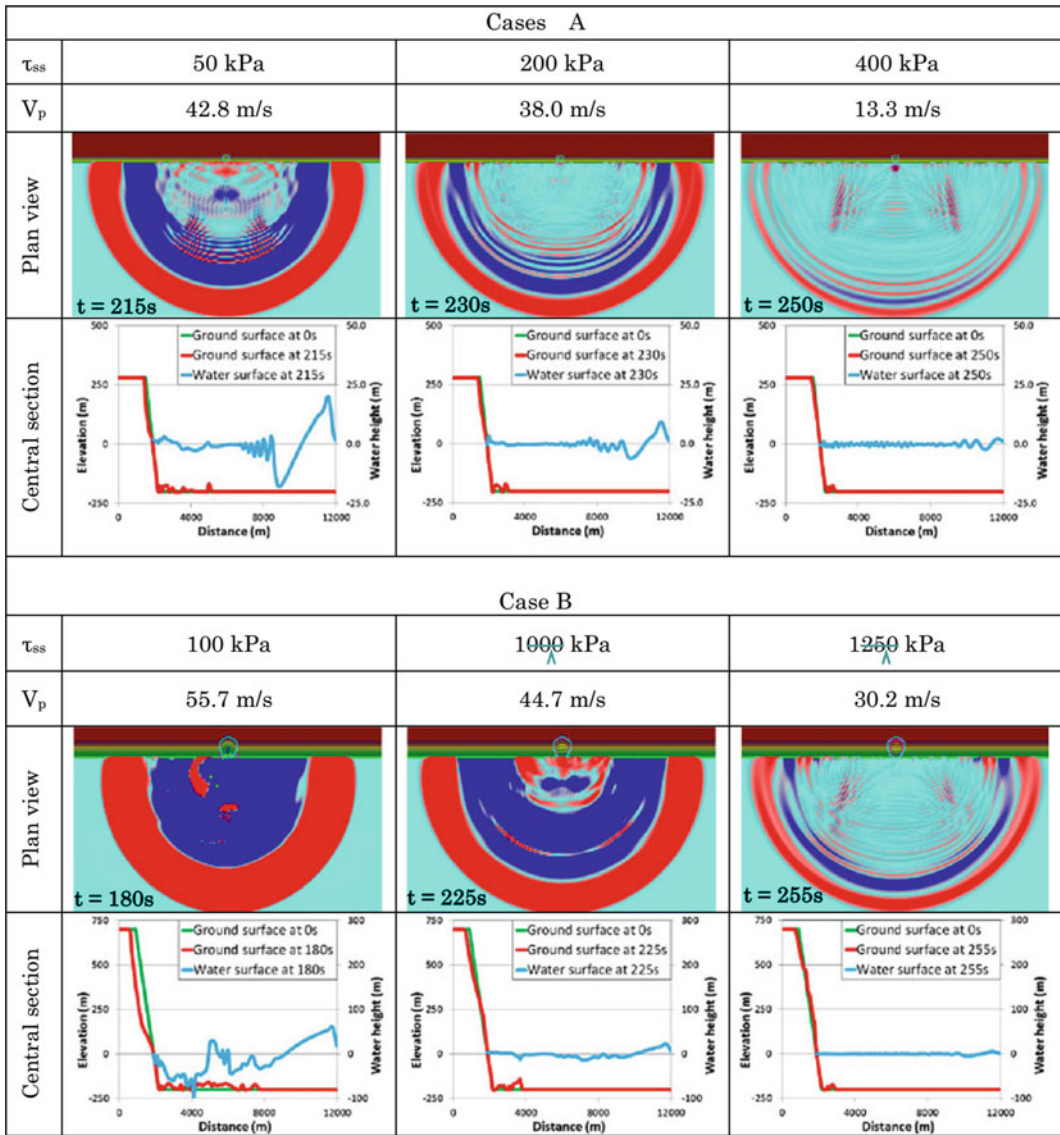


Fig. 4 Tsunami and landslide profiles when the tsunami front reached at 12,000 m

Table 1 Relation between water depth and tsunami behavior (steady state shear resistance = 80 kPa)

Landslide volume	Depth of water (m)	Maximum landslide velocity (m/s)	Tsunami traveling time (s) to 10 km from the coast	Maximum tsunami height (m) in Fig. 3
A: $5.8 \times 10^6 \text{ m}^3$	2	14.5	2,065	0.1
	20	20.7	620	1.7
	200	38.1	220	14.7
B: $170 \times 10^6 \text{ m}^3$	2	29.5	1,150	0.4
	20	37.3	385	8.7
	200	56.6	180	62.0

Table 2 Relation between the steady state shear resistance and tsunami behavior (depth of water is 200 m)

Landslide volume (m ³)	Steady state shear resistance (kPa)	Maximum landslide velocity (m/s)	Tsunami traveling time (s) to 10 km from the coast	Maximum tsunami height (m) in Fig. 4
A: 5.8 × 10 ⁶	50	42.8	215	20.0
	200	38.0	230	9.2
	400	13.3	250	2.2
B: 170 × 10 ⁶	100	55.7	180	62.0
	1000	44.7	225	23.4
	1250	30.2	255	5.9

and 4) when the front of tsunami reaches 10 km from the coast. It is an index of tsunami effect over a sea/lake.

The motion of tsunami is calculated at each 0.05 s, but the profiles in Figs. 3 and 4 and 2 D views in Fig. 8 are outputted and saved as the figures at each 5 s.

Figure 3 and Table 1 shows the relation between the water depth and the tsunami behavior at a constant steady state shear resistance (80 kPa), and different water depths (2, 20, 200 m).

The maximum tsunami heights are from 0.1 to 62.0 m. It increased with the depth of water and the landslide volume. As the depth of water increases, the maximum landslide velocity increases because the longer acceleration will increase landslide velocity on the longer steep slope below sea level. The larger volume of water in the deeper water depth is upheaved by the moving landslide mass and causes the greater tsunami height.

Figure 4 and Table 2 shows the relation between the steady state shear strength and the tsunami behavior at a constant water depth (200 m), and different steady state shear resistance. As the steady state shear resistance increases, the maximum velocity decreases, and also the maximum tsunami height decreases. The relationships between the maximum tsunami height and the tsunami traveling time is inversely proportional in Table 1. However, the effect of steady state shear resistance and the maximum landslide velocity on the tsunami traveling time is limited at the same water depth (Table 2).

5 Application of the Model to the Unzen-Mayuyama Landslide and Its Resulting Tsunami Wave

The 1792 Unzen-Mayuyama Landslide and Its Analysis

The series of landslide-induced tsunami simulation LS-RAPID + LS-Tsunami + LS-Motion was applied to the 1792 Unzen-Mayuyama landslide-and-tsunami disaster. Figure 5 presents a Google view of the landslide. The displaced landslide mass created many islands in the Ariake Sea. Most of them disappeared by sea erosion after the event. But some landslide mounds still exist as islands. Figure 6 presents the section of this landslide (Sassa et al. 2014a, b, modified from the Unzen Restoration Office of the Ministry of Land, Infrastructure, and Transport (MLIT) of Japan, 2002 and 2003). The Unzen-Mayuyama mountain consists of volcanic lava rock and unconsolidated eruption products (sand and debris). Two samples (S1 and S2) were taken from the site for testing to obtain the landslide dynamic parameters by the undrained dynamic-loading ring-shear apparatus (Sassa et al. 2014a, b). The sliding surface of the landslide should be formed within a sandy layer rather than in a layer consisting of strong intact lava rocks and boulders. Hence, sample S1 was taken from a sandy layer exposed along a torrent gully in the source area of the landslide. The original soil layer (a black dotted soil layer in

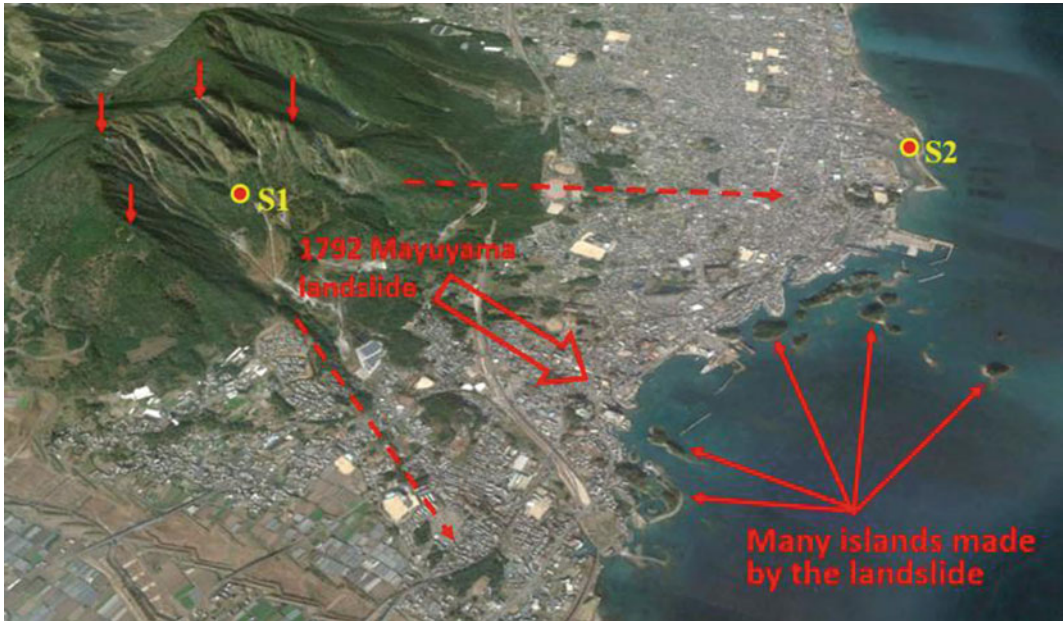


Fig. 5 1792 Unzen-Mayuyama landslide. The overview of the landslide. The headscarp is indicated by *vertical red arrows*, the direction of the landslide motion is shown by a *thick red arrow* in the center and *two dotted lines* in the sides

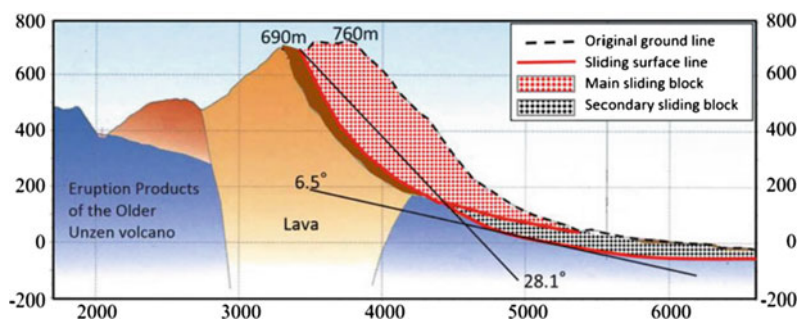
Fig. 6) was displaced or covered by the moved landslide mass and the original soil layer could not be found at the site. Hence, a sample S2 representing this soil layer was taken from the coastal area outside of the landslide moving area.

The necessary landslide dynamics parameters were measured and estimated by a series of undrained ring shear tests; drained speed-control test, undrained monotonic shear-stress loading test, pore pressure control test to simulate landslide initiation by pore pressure increasing, undrained cyclic-loading test, and undrained pore pressure and seismic-loading test simulating the

earthquake-induced landslide in the Mayuyama landslide (Sassa et al. 2014a, b).

The landslide is known to have been triggered by a nearby earthquake (of estimated magnitude, $M = 6.4 \pm 0.2$, Usami 1996). The amount of damage to houses caused by the earthquake suggests that the seismic acceleration was 400 cm/s^2 or greater (Unzen Restoration Office 2002, 2003). There is no seismic wave record from this earthquake which predates recording seismometers. So we used a recent seismic record (MYG004 that of the 2008 Iwate Miyagi-earthquake, $M = 7.2$, which triggered the 67 million m^3 Aratozawa landslide, maximum

Fig. 6 Section of the 1792 Unzen-Mayuyama landslide and its interpretation



acceleration was 739 cm/s^2 (Sassa et al. 2014a, b) for the seismic shear stress loading in the undrained ring shear test. The test result showed that the necessary maximum acceleration to initiate this landslide was 216 cm/s^2 . It means that the smaller earthquake can produce this landslide. Then, 0.7 times and 0.5 times of the acceleration of MYG004 (507 and 370 cm/s^2) were input to LS-RAPID. Both cases gave the very similar result of landslide motion. We used 0.5 times of MYG004 (Maximum acceleration of 370 cm/s^2) was given as the triggering factor to LS-RAPID. The landslide dynamics parameters used in this simulation are shown in Table 3.

Simulation of the Unzen-Mayuyama Landslide by LS-RAPID

The simulation area for the landslide-induced tsunami including the Ariake Sea and Kumamoto Prefecture on the opposite bank is $59 \text{ km} \times 37.4 \text{ km}$. It is much wider than the simulation area for the Mayuyama landslide ($12 \text{ km} \times 8 \text{ km}$). Due to the computer capacity and the time for one simulation, the mesh size was increased from 50 m (used in the previous study of 2014, Sassa et al. 2014a, b) to 100 m in this landslide-induced tsunami study. The results from the landslide simulation are shown in Fig. 7.

LS-RAPID has two presentation modes showing the moving landslide mass. One mode is color balls with different sizes and different color intensities for the landslide depth which was used for the Leyte landslide simulation in Fig. 12 of Sassa et al. (2010). This makes it easier to visualize the landslide motion. However, it does not show the real ground surface of the landslide during motion. Another mode is either a three-dimensional or a two-dimensional view of the moving landslide. The three-dimensional view is suitable to visually show the motion. However, the two dimensional-view is good for the precise location as a map. 4 Figures of Fig. 7 show a two-dimensional view of the landslide motion from the initiation to the termination. The initial landslide mass before

motion is delineated by a blue line and the moving landslide mass is delineated by a red line. The figure shows that the landslide mass moved into the Ariake Sea, and tops of moving landslide masses appeared above the sea and stopped its motion partly filling the Shimabara port. After the 1792 Unzen-Mayuyama landslide event, coastal erosion changed the topography of this port because most of displaced landslide masses were weak to coastal erosion. But some strong parts are still left as islands in the sea as seen in Fig. 5.

Simulation of the Landslide-Induced Tsunami by LS-Tsunami

The yellow color line is the coastal line before the landslides. The red line is the border of displaced landslide mass. The left-top figure ($t = 0 \text{ s}$) presents the location of the initial landslide mass, the right-top figure ($t = 35 \text{ s}$) presents the instant when the landslide moving mass reached the coast. The left-bottom figure ($t = 100 \text{ s}$) shows the moving landslide mass in the Ariake Sea. Parts of moving landslide blocks (gray color parts) are found above the sea. The right-bottom figure ($t = 226 \text{ s}$) presents the state when the landslide motion was terminated.

The landslide motion was firstly calculated by LS-RAPID as Fig. 7. The data set of calculated landslide motion at each 0.1 s was saved, and used as input to LS-Tsunami as the tsunami trigger. Additional parameters input in the LS-Tsunami is the unit weight of sea water and the Manning's roughness coefficient for basal resistance in the sea. The Manning's roughness coefficient is not testing value, but an empirical value used for analysis of water movement such as tsunamis and floods. Tsunami motion generated by the landslide motion was calculated by LS-Tsunami. The result of simulated tsunami height at each mesh and at each 0.05 s was saved. These data sets were then used as input to LS-Motion. The tsunami simulation is shown in whatever preferred mode, color, and speed by LS-Motion. Figure 8 is an example from

Table 3 Parameters used in computer simulation of Unzen-Mayuyama landslide-and-tsunami disaster

Parameters used in simulation	Value	Source
<i>Parameters of soils in the source area (deeper area)</i>		
Steady state shear resistance (τ_{ss})	120 kPa	Test data
Lateral pressure ratio ($k = \sigma_h/\sigma_v$)	0.7–0.8	Estimation (see text)
Friction angle at peak (ϕ_p)	42.0°	Test data
Cohesion at peak (c)	10 kPa	Assuming small
Friction angle during motion (ϕ_m)	40.0°	Test data
Shear displacement at the start of strength reduction (D_L)	6 mm	Test data
Shear displacement at the start of steady state (D_U)	90 mm	Test data
Pore pressure generation rate (B_{ss})	0.7–0.9	estimated
Total unit weight of the mass (γ_t)	19.5 kN/m ³	From the test
Unit weight of sea water (γ_w)	10.1 kN/m ³	Average sea water density (1.026 kg/m ³)
<i>Parameters of soils in the moving area (shallower area)</i>		
Steady state shear resistance (τ_{ss})	30–80 kPa	Test data
Lateral pressure ratio ($k = \sigma_h/\sigma_v$)	0.8–0.9	Estimated
Friction angle at peak (ϕ_p)	40.0°	Test data
Cohesion at peak (c)	10 kPa	Assuming small
Friction angle during motion (ϕ_m)	40.0°	Test data
Shear displacement at the start of strength reduction (D_L)	6 mm	Test data
Shear displacement at the end of strength reduction (D_U)	90 mm	Test data
Pore pressure generation rate (B_{ss})	0.7–0.9	Estimated
Total unit weight of the mass (γ_t)	19.5 kN/m ³	From the test
<i>Triggering factor</i>		
Excess pore pressure ratio in the fractured zone (r_u)	0.21	Assumption
0.5 times of the 2008 Iwate-Miyagi earthquake	Max: 370 cm/s ²	Wave form of the Ground motion record at MYG004
<i>Parameters of the function for non-frictional energy consumption</i>		
Coefficient for non-frictional energy consumption	1.0	See Sassa et al. 2010
Threshold value of velocity	100 m/s	A few times greater than maximum reported speed
Threshold value of soil height	400 m	Maximum depth of the initial source area
<i>Other factors</i>		
Steady state shear resistance under sea	10 kPa	Data (Sassa et al. 2004)
Unit weight of sea water	10.1 kN/m ³	Average sea water density
Manning's roughness coefficient	0.025	Under water and vacant lots (MLIT Guideline 2012)

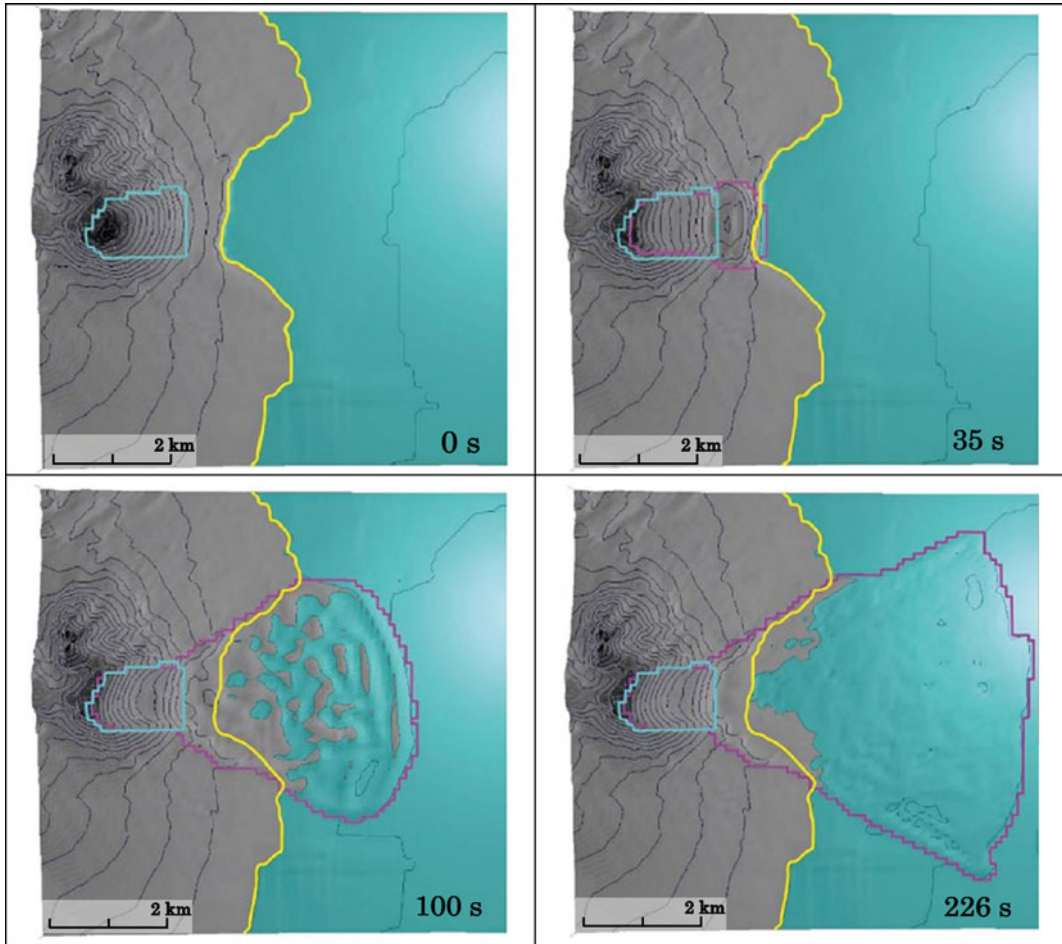


Fig. 7 Landslide motion simulated by the landslide simulation code “LS-RAPID”

LS-Motion. The explanation/interpretation of the behavior of landslide and tsunami at each figure of Fig. 8 is directly written in the caption.

The tsunami disaster investigated by the Unzen Restoration office (2002, 2003) is shown in Fig. 9. The residents in the community erected the Tsunami-Dome-Ishi (tsunami stopping stones) at the highest points where the tsunami reached. Tsunami-Dome-Ishi are found in Kyodomari, in Umedo and in Ohtao along the coast of Kumamoto Prefecture, which were carefully investigated by Tsuji and Hino (1993). People in the Shimabara Peninsula built stone pillars in memory of the tsunami disasters. Tsuji and Murakami (1997) investigated Tsunami heights in the Shimabara Peninsula. Figure 9 was made

using those investigation, the historical data as well as stone pillars.

The original file of Fig. 9 is a Japanese printed figure. It can not be changed. English explanation is written in the figure caption 8 by adding A-I within Fig. 9. *Shimabara-Taihen, Higo-Meiwaku*. in A is a lesson from this historically largest landslide and volcanic disaster. We should not neglect disasters in the opposite bank. Adverse effects may reach the opposite bank.

Five sites (3 sites from the Kumamoto coast and 2 sites from Shimabara coast) with clearer evidences were selected to compare the results simulated by the LS-Tsunami based on LS-RAPID to the tsunami heights by historical records in both coasts. The maximum tsunami

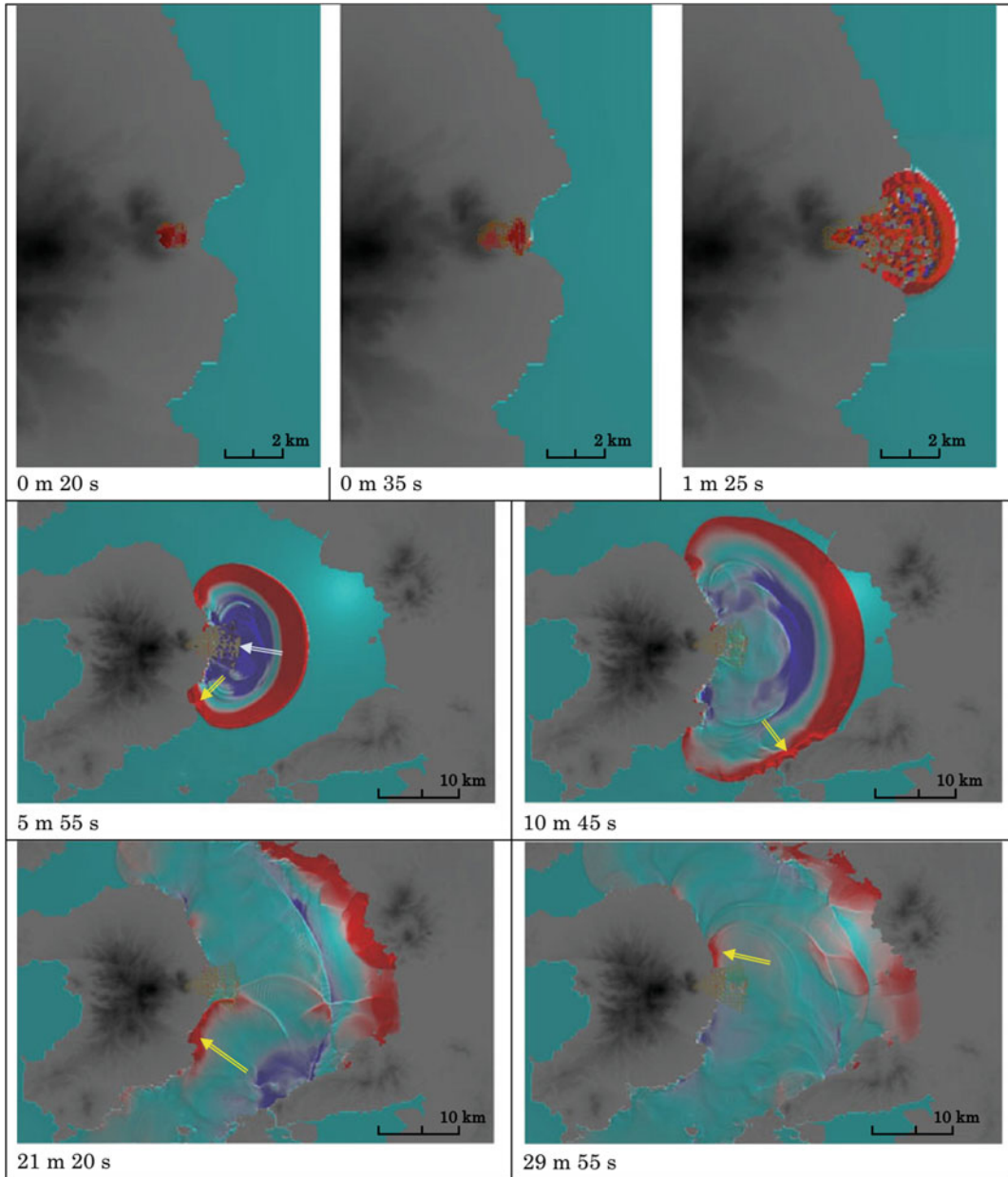


Fig. 8 Simulation result of Landslide-induced-tsunami wave using the simulation code “LS-Tsunami” and “LS-Motion”. The *first figure on the top* shows when the initial landslide started to move at 0 min 20 s. The *second figure on the top* at 35 s shows the landslide mass reached the coastal line and triggering the tsunami wave. The *third figure on the top* at 1 min 25 s shows the landslide mass entering into the sea and triggering the tsunami wave. The *left figure* (5 min 55 s) in the center shows the expanding tsunami wave into the Ariake Sea, and the top parts of moving landslide blocks (dark brown color dots) are seen above sea level as shown by a white color arrow. The yellow color arrow shows the attack of tsunami wave to Futsu town. The

right figure in the center presents when the tsunami wave reached Kumamoto Prefecture on the opposite bank. The *left figure* (21 min 20 s) on the bottom shows that the tsunami wave was returned from the opposite bank to attack the southern part of Shimabara peninsula (around Futsu town) again as shown in the yellow arrow. Around 3500 persons were killed in the southern part of Shimabara peninsula by the Tsunami (Fig. 9). The *right figure on the bottom* at 29 min 55 s shows another returned wave attacking the northern side of Mayuyama landslide area. In this figure, the bright red color presents the wave more than 5 m above sea level and the dark blue color presents the wave less than 5 m below sea level



Fig. 9 Records of disaster by the Unzen landslide-and-tsunami disaster (by Unzen Restoration Office 2003)

heights at each 0.05 s for each mesh were plotted on the map and the contour map was made to visualize the tsunami wave (Fig. 10). Locations of these five sites are shown in this figure. The simulated tsunami wave reached more than 5 km inland on the Kumamoto coast.

Comparison was conducted between:

1. Tsunami heights estimated from the simulation (LS-RAPID and LS-Tsunami) based on the values of landslide dynamics parameters measured and estimated by the undrained ring shear testing on the samples taken from the site.
2. Tsunami heights reported by the Unzen Restoration office (2002, 2003) based on the

records including Tsuji and Hino (1993) and Tsuji and Murakami (1997) in the Shimabara and Kumamoto areas. Tsunami heights in the sea were not recorded. But the landslide depth under the sea was investigated and reported by the office.

Manning’s roughness coefficient

The simulated tsunami heights are affected by the value of Manning’s roughness coefficient. The coefficient was reported to be between 0.010 and 0.060 m^{1/3} s as empirical values in the cases of water channels with different materials (Linsley and Franzini 1979). The coefficient used for Tsunami simulation were reported between 0.01 and 0.08 m^{1/3} s by many reports and guidelines

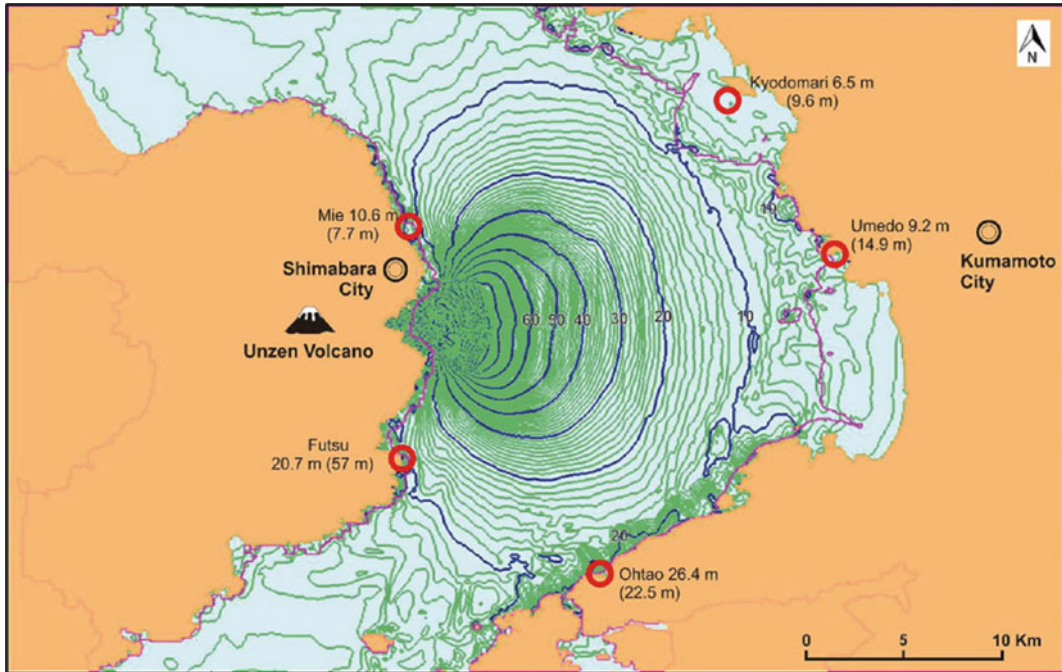


Fig. 10 Contour of the maximum tsunami height at each mesh with the tsunami height records in the Kumamoto side coast and in the Shimabara side coast. The coastline is shown in red where the tsunami wave moved up to the land

such as MLIT 2012, Fraser et al. 2014, Imamura 2009, Tinti and Tonini 2013. $0.03\text{--}0.08\text{ m}^{1/3}\text{ s}$ are used for forests and buildings areas. The most commonly used value of Manning's coefficient for tsunami simulation is $0.025\text{ m}^{1/3}\text{ s}$ (MLIT 2012; Tinti and Tonini 2013; Imamura 2009). The purpose of this research is not examination of the value of Manning's roughness coefficient, but the examination of the reliability of the new landslide-induced tsunami simulation. Then, we used the most commonly used value of $0.025\text{ m}^{1/3}\text{ s}$ for Figs. 8 and 10 of this paper.

Total number of death is 15,153 persons. The size of circles is proportional to the number of human fatalities in the area. The legend for the number of deaths is show in the right-top corner. A: Disasters around Ariake sea and monuments by the *Shimabara-Taihen*, *Higo-Meiwaku*. "Catastrophe" in Shimabara area and "Annoyance" or "adversely affected" in Higo (Kumamoto) region. B: The numbers of deaths are shown in the circles (the largest is 500 persons) C: The greatest deaths are Shimabara town

around the castle (5251 persons). D: The second largest deaths are the southern part of Shimabara Peninsula (around 3500 persons) E, F, G: Tsunami-Dome-Ishi (A stone showing the tsunami reaching point) was set to record the tsunami by the community in Kyodomari (E), Umedo (F) and Otao (G) of the Higo (Kumamoto) Han area. The tsunami-Dome-Ishi in Kyodomari was moved for the construction of a road, but its former location is marked on the road retaining wall (by the regional education committee). The Tsunami-Dome-Ishi is limited in Higo (Kumamoto) Han area. These tsunami records are reliable. H, I: Stone pillars for memorial service for deaths by Tsunami in Futsu (H) and Mie (I) in Shimabara Han area.

Manning's basal resistance is caused by the roughness of the ground surface during relative movement of water on the ground. When water depth is greater, the effect of basal resistance for the movement of tsunami will be decreased and the value will be smaller. The deposits in the deeper sea is usually finer, then the roughness is

decreased. Fraser et al (2014) used $0.013 \text{ m}^{1/3} \text{ s}$ for ocean and rivers. Ariake Sea which is the major part of Tsunami propagation in this area is 10–50 m deep. It is deeper than pond, river and shallow sea near coast. Therefore, we examined the case of 0.02 and $0.015 \text{ m}^{1/3} \text{ s}$ in addition to $0.025 \text{ m}^{1/3} \text{ s}$ in Table 4.

Comparison of Tsunami Heights Between Historical Records and Simulation Results

Table 4 presented the reported and simulated tsunami heights at 5 sites along the Kumamoto and the Shimabara coasts. Differences between the computer simulation and the historical records for the 5 specific points are less than 5.7 m for Manning's coefficient $0.025 \text{ m}^{1/3} \text{ s}$, 4.6 m for Manning's coefficient $0.020 \text{ m}^{1/3} \text{ s}$, and 5.2 m for Manning's coefficient $0.015 \text{ m}^{1/3} \text{ s}$ except the case at Futsu.

Futsu is a special case where the first direct tsunami wave from the source of tsunami hit the cliff of the Futsu terrace, and probably amplified due to the gulf-shaped coast line. The tsunami wave flowed up to the Terrace (Tsuji and Murakami 1997). The Tsunami wave attacking Futsu is seen at 5 m 55 s in Fig. 8 and the return wave also attacked Futsu from the different direction at 21 m 20 s in Fig. 8. Many people were killed in this area. The simulation of LS-Tsunami used 100 m mesh data. It can not include the effect of local amplification of tsunami height due to the sharp topography in this part of the coast.

LS-Tsunami uses the average elevation for each 100 m mesh. The elevation of Tsunami-Dome-Ishi on the slope is not always

close to the average height of calculated mesh. In the case of 15–20° slope, 25 m (1/4 of one mesh) difference in horizontal distance cause 6.7–9.1 m elevation difference. The maximum 5.7 m difference in Table 4 is within the elevation difference on the slope. Considering these conditions, the estimated area of tsunami and the tsunami heights along the coast by LS-Tsunami match with the historical record (Fig. 10 and Table 4). It can be understood that the result of this trial test on the Unzen-Mayuyama landslide-and-tsunami disaster presented a reasonable extent of reliability and a meaningful extent of precision within the variation of Manning's coefficient and the resolution of ground elevation. Carefully examining the value difference in different Manning's coefficient, the effect of the coefficient is greater in the long travel distance of tsunami and gives closer tsunami heights in Kyodomari and Umedo.

Comparison of the Maximum Heights of the Landslide and the Maximum Heights of Tsunami Along the Central Section

The upper figure of Fig. 11 presents the maximum landslide moving height and the maximum tsunami height calculated by LS-RAPID and LS-Tsunami at each time step (0.1 s for landslide, and 0.05 s for tsunami wave) at each mesh along the central line of landslide. The ground surface before the landslide and the ground surface after the deposition of the landslide were investigated by Inoue 1999 and MLIT 2002 and 2003. The lower figure of Fig. 11 presents the central section of ground surface before and after the landslide. The landslide travel distance

Table 4 Comparison of Tsunami heights between the simulation result and the historical record

Location		Tsunami heights from tsunami-Dome-Ishi and memorial stone pillars (m)	Tsunami heights by LS-tsunami Manning's coefficient = $0.025 \text{ m}^{1/3} \text{ s}$ (m)	Tsunami heights by LS-tsunami Manning's coefficient = $0.020 \text{ m}^{1/3} \text{ s}$ (m)	Tsunami heights by LS-tsunami Manning's coefficient = $0.015 \text{ m}^{1/3} \text{ s}$ (m)
Kumamoto coast	Kyodomari	9.6	6.5	7.7	9.7
	Umedo	14.9	9.2	11.2	13.2
	Ohtao	22.5	26.4	27.1	27.7
Shimabara coast	Futsu	57	20.7	21.0	21.3
	Mie	7.7	10.6	10.9	11.0

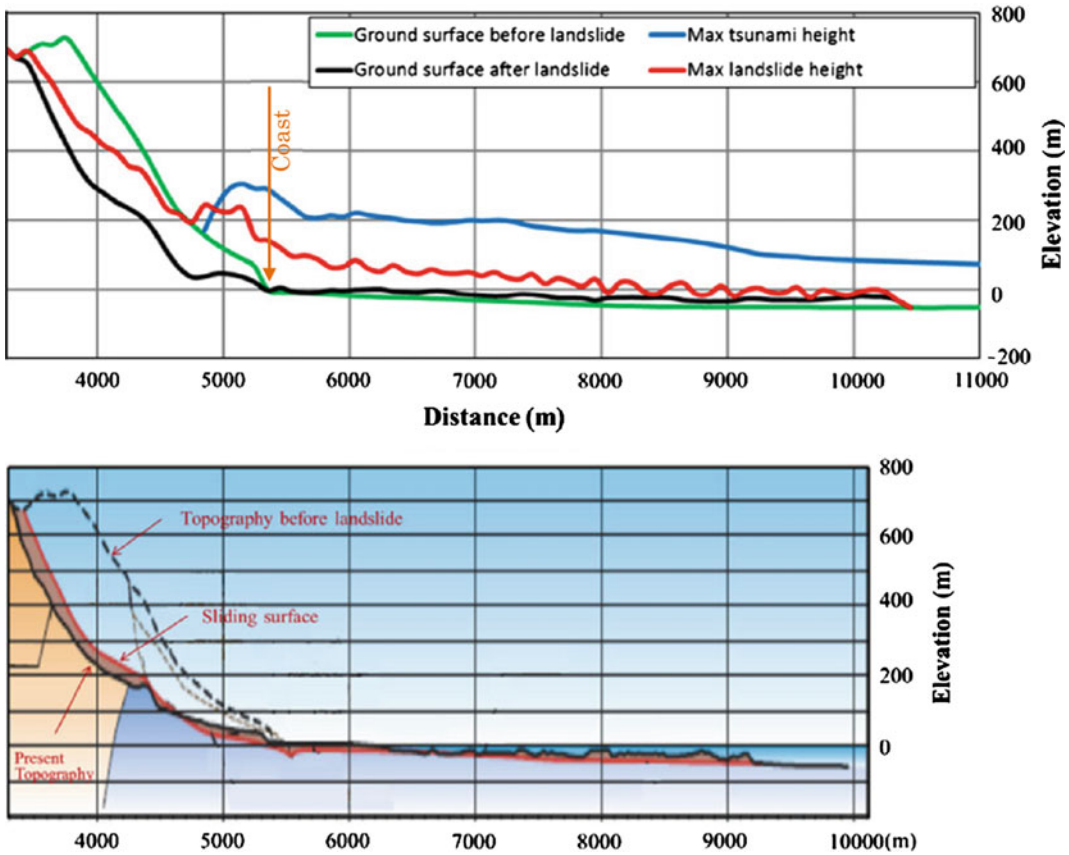


Fig. 11 The simulated maximum heights of tsunami wave and the landslide mass (*top*) and the central section of landslide reported by MLIT (*bottom*)

estimated by LS-RAPID is a little longer than the real one. However, the horizontal distance from the headscarp to the landslide toe is around 10,000 m in both cases. The highest landslide mass above the original ground surface near the coast is 127 m at the time resolution of 0.1 s. The highest tsunami height near the coast is 70 m higher than the surface of the moving landslide mass at the time resolution of 0.05 s.

The landslide dynamics research group and the tsunami research group cooperated to develop the landslide-induced tsunami model. Based on the joint research, the tsunami research group earlier developed a soil and water double layer model and applied it to the 1792 Unzen-Mayuyama landslide-induced tsunami (Yanagisawa et al. 2014). The model calculates movement of two layers: a water layer and a soil

layer, with simultaneous interaction of the two layers. While the proposed model fully separated the motion of landslide and the motion of tsunami. The landslide motion was given to the tsunami simulation as the trigger only. The tsunami simulation model is a well established and widely used one (IOC 1997). This study could not have been completed without the close cooperation between hydraulics researchers and landslide researchers.

6 Conclusion

Hazard assessment technology for landslide-induced tsunami is one of the frontiers in Landslide Science. A tsunami wave is induced by the landslide mass entering into and moving

under the water. The reliable estimation of landslide motion is the most important as the trigger of the landslide-induced tsunami hazard. The integrated model simulating the initiation and the motion of landslide (LS-RAPID) and the measurement of the landslide dynamics parameters by the undrained dynamic-loading ring-shear apparatus enabled estimation of the landslide motion as the trigger of a tsunami wave. The concept of tsunami simulation (LS-Tsunami) is simple: a water mass is elevated by a landslide mass moving on the sea floor. The increased water height causes a tsunami wave. Possible shear resistance between the landslide mass and water due to viscosity is neglected because it is much smaller than the shear resistance mobilized along the shear surface within soils. The tsunami simulation model is a well established model (IOC 1997). The parameters used related to water were only the unit weight of sea water and the Manning's roughness coefficient without other uncertain parameters. This new landslide-induced tsunami model could provide a simulation result well matching the tsunami heights in the Unzen Mayuyama landslide-and-tsunami disaster. This result presented an evidence of reliability and precision of this new landslide-induced tsunami model in this well documented and historically largest landslide-induced tsunami in Japan. Further application to other cases of landslide-induced tsunami can define the reliability and precision of this new model from different aspects.

References

- Abe I, Goto K, Imamura F, Shimizu K (2008) Numerical simulation of the tsunami generated by the 2007 Noto Hanto Earthquake and implications for unusual tidal surges observed in Toyama Bay. *Earth Planets Space* 60:133–138
- Baba T, Matsumoto H, Kashiwase K, Hyakudome T, Kaneda Y, Sano M (2012) Microbathymetric evidence for the effect of submarine mass movement on tsunami generation during the 2009 Suruga bay earthquake, Japan. In: Yamada et al (eds) Submarine mass movements and their consequences. *Advances in natural and technological hazards research* 31. Springer, Berlin, pp 485–494
- Fraser SA, Power WL, Wang X, Wallace LM, Mueller C, Johnston DM (2014) Tsunami inundation in Napier, New Zealand, due to local earthquake sources. *Nat Hazard* 70:415–445
- Imamura F (2009) Tsunami modeling: calculating inundation and hazard maps. In: Bernard EN, Robinson AR (eds) *THE SEA tsunamis*. Harvard University Press, London, pp 321–332
- Inoue K (1999) Shimabara-Shigatsusaku Earthquake and topographic changes by Shimabara catastrophe. *J Jpn Soc Eros Control Eng* 52(4):45–54 (in Japanese)
- Intergovernmental Oceanographic Commission (IOC) (1997) Numerical method of tsunami simulation with the leap-frog scheme. IUGG/IOC Time Project IOC Manuals and Guides, No. 3, UNESCO
- Linsley RK, Franzini JB (1979) *Water resource engineering*, 3rd edn. McGraw-Hill, New York
- Ministry of Land, Infrastructure, Transport and Tourism (MLIT), Water and Disaster Management Bureau, Coastal management office (2012) Guideline for the assessment for Tsunami inundation area. Ver.1.00, http://www.mlit.go.jp/river/shishin_guideline/bousai/saigai/tsunami/shinsui_settei_ver100.pdf
- Sassa K, Fukuoka H, Wang G, Ishikawa N (2004) Undrained dynamic-loading ring-shear apparatus and its application to landslide dynamics. *Landslides* 1(1):7–19
- Sassa K, Nagai O, Solidum R, Yamazaki Y, Ohta H (2010) An integrated model simulating the initiation and motion of earthquake and rain induced rapid landslides and its application to the 2006 Leyte landslide. *Landslides* 7(3):219–236
- Sassa K, He B, Miyagi T, Strasser M, Konagai K, Ostric M, Setiawan H, Takara K, Nagai O, Yamashiki Y, Tutumi S (2012) A hypothesis of the Senoumi submarine megaslide in Suruga Bay in Japan-based on the undrained dynamic-loading ring shear tests and computer simulation. *Landslides* 9(4):439–455
- Sassa K, Dang K, He B, Takara K, Inoue K, Nagai O (2014a) A new high-stress undrained ring-shear apparatus and its application to the 1792 Unzen-Mayuyama megaslide in Japan. *Landslides* 11(5):827–842
- Sassa K, Bin H, Dang K, Nagai O, Takara K (2014b) Plenary: progress in landslide dynamics. *Landslide Sci Saf Geoenviron* 1:37–67
- Satake K (2001) Tsunami modeling from submarine landslides. In: *Proceedings of the international tsunami symposium*, pp 665–674
- Tinti S, Tonini R (2013) The UBO-TSUFSD tsunami inundation model: validation and application to a tsunami case study focused on the city of Catania, Italy. *Nat Hazards Earth Syst Sci* 13:1795–1816
- Tsuji Y, Hino T (1993) Damage and Inundation height of the 1792 Shimabara landslide tsunami along the coast

- of Kumamoto Prefecture. *Bull Earthq Res Inst Univ Tokyo* 68:91–176 (in Japanese)
- Tsuji Y, Murakami Y (1997): Inundation height of the 1792 Mayuyama landslide tsunami in the Shimabara Peninsula side. In: *Historical earthquake, No. 13, Soc. of historical earthquake studies*, pp 135–197
- Unzen Restoration Office of the Ministry of Land, Infrastructure and Transport of Japan (2002) *The Catastrophe in Shimabara—1791–92 eruption of Unzen–Fugendake and the sector collapse of Mayu-Yama*. An English leaflet
- Unzen Restoration Office of the Ministry of Land, Infrastructure and Transport of Japan (2003) *The Catastrophe in Shimabara—1791–92 eruption of Unzen–Fugendake and the sector collapse of Mayu-Yama*. A Japanese leaflet
- Usami T (1996) *Materials for comprehensive list of destructive earthquakes in Japan*. University of Tokyo Press, Tokyo (in Japanese)
- Yanagisawa H, Aoki A, Sassa K, Inoue K (2014) Numerical simulation of 1792 Ariake-Kai Tsunami using Landslide-Tsunami model. *J Jpn Soc Civil Eng Ser. B2 (Coast Eng)* 70(2):151–155 (in Japanese)

TXT-tool 3.081-1.3

A Hypothesis of the Senoumi Submarine Megaslide in Suruga Bay in Japan—Based on the Undrained Dynamic-Loading Ring Shear Tests and Computer Simulation

Hendy Setiawan, Kyoji Sassa and Bin He

Abstract

The Senoumi (stone flower sea), which is located in the Suruga Bay, has a distinctive bathymetric feature and a concave shape with the dimension approximately 30 km in width and 20 in length. The shape of Senoumi was believed as results of the intense tectonic activity in the plate border, the submarine slides and flows from the Oi River of Shizuoka Prefecture. This paper presents the study of Senoumi area as a submarine mega-slide by analyzing the shear behaviors of three samples through ring shear tests. One sample was drilled from the submarine floor by the Integrated Ocean Drilling Program (IODP), while two samples were taken from Omaezaki Hill near Senoumi area. The measured parameters from the ring shear tests then used as an input in the integrated model of landslide simulation (LS-RAPID) for the initiation and motion of earthquake-induced rapid landslide of Senoumi. We used the strong motion record of the 2011 Tohoku Earthquake at the observation point of MYG004 in Miyagi Prefecture. The results of this study indicated the importance of further investigation for the risk of large-scale submarine megaslide that may occur in the Senoumi area, including tsunami and the enlargement of submarine landslide into the adjacent coastal area particularly due to the mega earthquake in the Nankai Trough in the future.

Keywords

Submarine landslide · Undrained ring shear test · Integrated Ocean Drilling Program (IODP) · Computer simulation
Earthquake-induced landslide

H. Setiawan
Disaster Prevention Research Institute, Kyoto
University, Uji 611-0011, Japan
e-mail: hendy@flood.dpri.kyoto-u.ac.jp

K. Sassa (✉)
International Consortium on Landslides,
138-1 Tanaka Asukaicho, Sakyo-ku, Kyoto
606-8226, Japan
e-mail: sassa@iclhq.org

B. He
State Key Laboratory of Lake Science and
Environment, Nanjing Institute of Geography and
Limnology, Chinese Academy of Science, 73 East
Beijing Road, Nanjing 210008, People's Republic of
China
e-mail: hebin@niglas.ac.cn

Contents

1	Introduction	132
2	Senoumi Area in the Suruga Bay	132
3	A Transportable Undrained-Loading Ring Shear Apparatus ICL-1	135
4	Specimens from Investigated Areas	135
4.1	Submarine Deposits in the Nankai Trough.....	136
4.2	Neogene Deposits in the Omaezaki Hill.....	136
5	Undrained Cyclic Loading Ring-Shear Tests	137
5.1	Undrained Cyclic Loading Tests.....	137
6	Undrained Seismic Loading Ring-Shear Tests	139
7	The Integrated Simulation of Initiation Process and Post-Failure Motion (LS-RAPID)	140
8	Simulation Result for Senoumi Area	144
9	Conclusion	145
	References.....	147

1 Introduction

Comparing to the aerial landslides, study and investigation of the submarine landslides are carried out in lesser extent, possibly due to its complicated factors and difficulties. However, report of the worldwide submarine landslides has been presented (Locat and Lee 2008) and particular submarine landslide that caused tsunami in the past has been traced in Scandinavia area (Bondevik et al. 2005). In Japan, a submarine landslide triggered by the earthquake (Mw 6.4) occurred in 2009 near Suruga Bay. This landslide has caused tsunami, as investigated by the Japan Agency for Marine-Earth Science and Technology (JAMSTEC) and has been reported by Baba et al. (2011). By the 2011 Tohoku earthquake which triggered tsunami, attention to the Nankai Trough tectonic activities in the centre coast of Japan has been arise. Based on the submarine landslides that appeared in the Nankai Trough due to the 2011 Tohoku earthquake (Cochonat et al. 2002; Strasser et al. 2011), the investigation and detailed study of Senoumi area in Suruga Bay is important to be carried out, particularly for the possibility of submarine landslide that might be triggered by mega earthquake of the Nankai Trough in the future.

2 Senoumi Area in the Suruga Bay

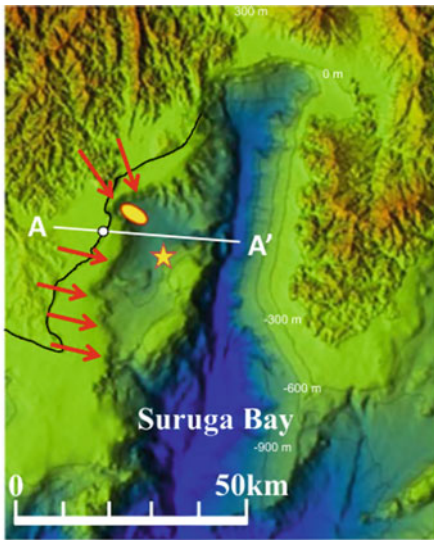
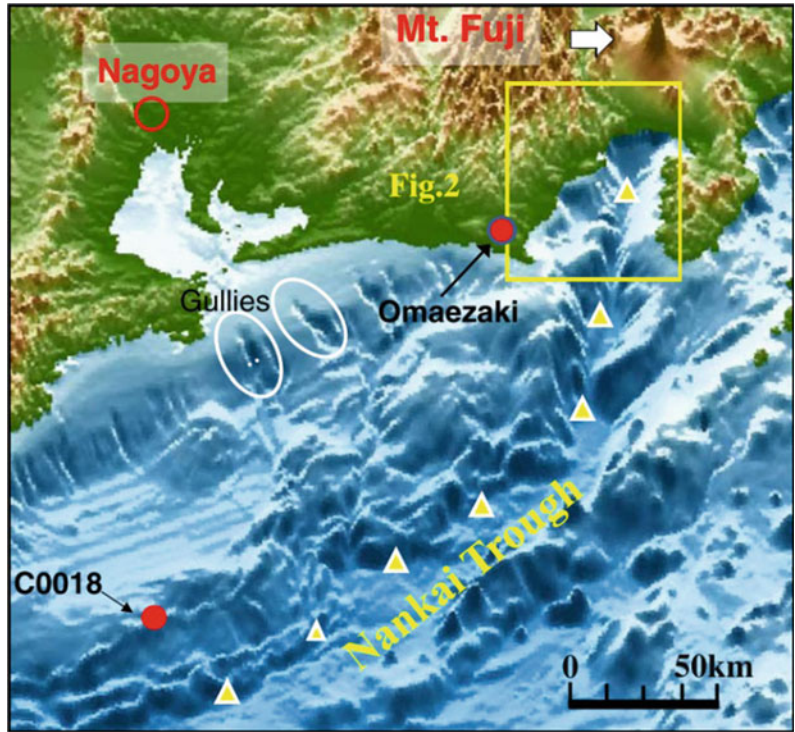
The Senoumi area located in the Suruga Bay near Shizuoka Prefecture, and tectonically situated on the edge of the Nankai Trough (Fig. 1). The Nankai Trough recognized as the plate boundary where the Philippine Sea Plate met the continental plate under SW Japan (Ando 1975). Several submarine slope deformation features were found along the sea floor between Kii Peninsula and Izu Peninsula, where Senoumi feature is of main concern due to its location that adjacent to Yaizu city (dense population with the existed Shinkansen route).




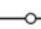
The hypothesis of megaslide is shown by looking at the distinctive shape of Senoumi, where the head scarps were formed (red arrows in Fig. 2).

The slopes ranged from 8° to 12° when we took cross section of A–A' across the gully of Senoumi. Since the exit of Suruga Trough is narrow, a large strength reduction of mass might occur in the Senoumi feature (when the submarine landslide takes place). In addition, tectonic activities between the Eurasian plate, Philippines plate and the Itoigawa-Shizuoka local tectonic line might be the other influential factors. We believed that the shear bands in Senoumi area may develop along the section where the Itoigawa and Shizuoka tectonic lines are met (Fig. 3). The geological condition of Senoumi area is mainly structured by Neogene layers, covered the area of Omaezaki Hill, Izu Peninsula and eastern side of Itoigawa-Shizuoka tectonic line. The submarine sea floors are dominantly composed by silt. By this condition, we assumed the Neogene soils of the Senoumi area are the cumulative results of transported deposits from the Oi River, including the volcanic ash.

A small submarine landslide triggered by the Mw 6.4 earthquake in 2009 (Baba et al. 2011) is an entry point to consider the effect of tsunami caused by large submarine landslide triggered by huge earthquake in the Senoumi area. Such great event may occur in the future and will definitely influence the head scarp instability and

Fig. 1 Location of the Senoumi area (yellow square). Red circles are the sampling points



-  Possible border of head scarp of landslide
-  Epicenter of 2009 Suruga bay earthquake
-  Submarine landslide induced by the earthquake which caused a small scale Tsunami
-  Coast line

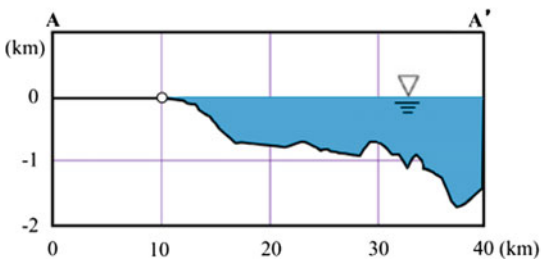
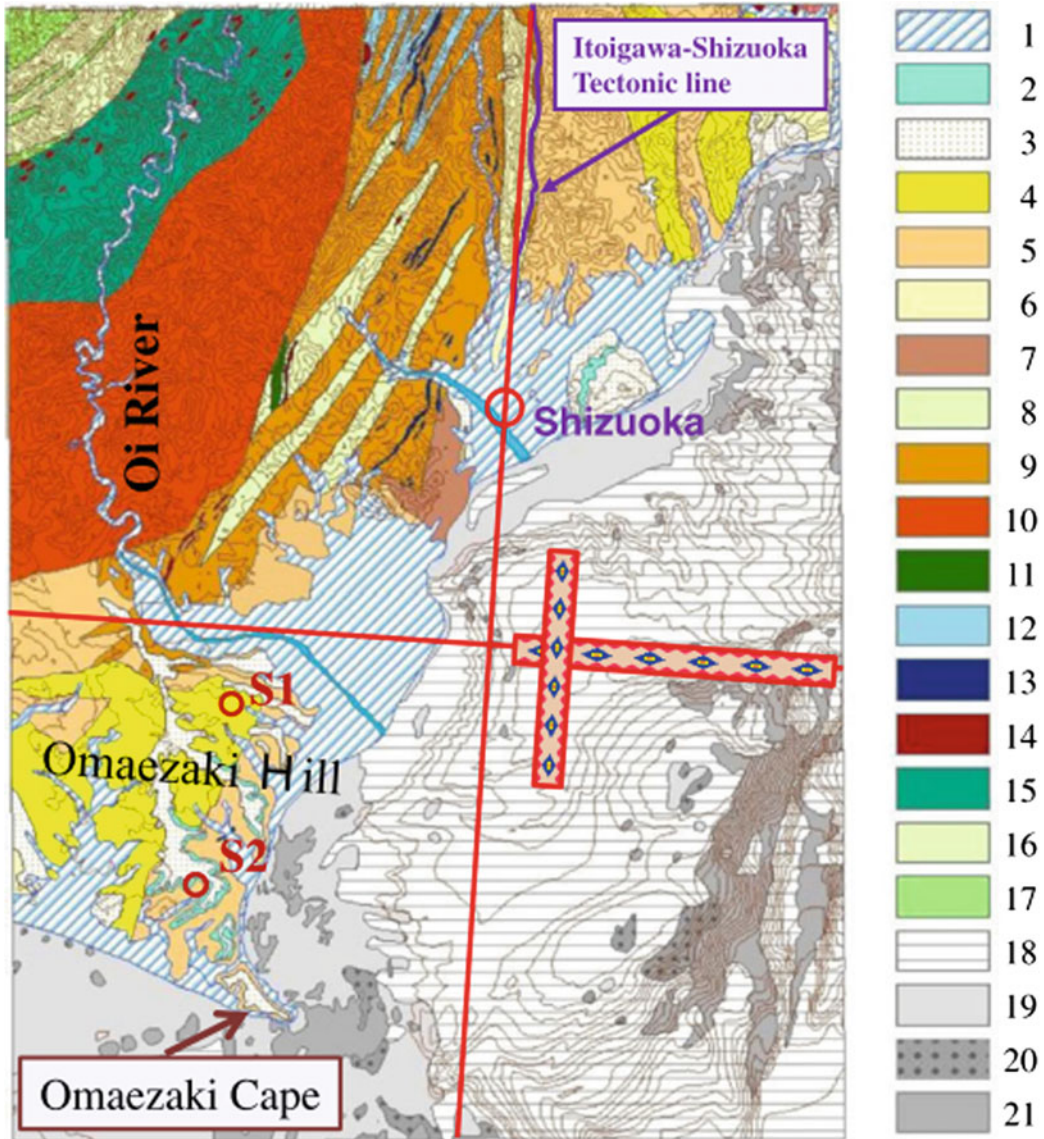


Fig. 2 Bathymetric feature of the Senoumi-stone flower area



1: Holocene (Alluvial deposit); 2: Pleistocene silty deposits; 3: Pleistocene terrace gravels; 4: Pliocene (Kakegawa groups); 5: Upper Miocene (Sagara groups); 6: Lower Miocene; 7: Paleogene alkali basalt; 8: Oligocene; 9: Eocene to Oligocene; 10: Eocene; 11: Diabase; 12: Turbidity & Shale; 13: Limestone; 14: Green stone & Red chert; 15: Latest Cretaceous - Paleogene; 16: Late Cretaceous (Sandstone-rich alternation); 17: Late Cretaceous (Mudstone-rich alternation); 18: Silt; 19: Sand; 20: Gravel; 21: Rock.

Fig. 3 Geological map in the Senoumi area and the possibility of shear bands developed due to the extension meeting of the Itoigawa-Shizuoka tectonic line

retrogressive enlargement of pre-existing submarine landslides in the Senoumi area.

The developed shear bands in the Senoumi area that we described here act as a medium when the submarine landslide takes place. Those shear bands convey the excess pore water pressure from the upper elevation (Fig. 4). The continental shelf in Fig. 4 formed as the extension of the in situ Neogene soil layer which was produced from the land or transported deposits from the Oi River.

3 A Transportable Undrained-Loading Ring Shear Apparatus ICL-1

The undrained dynamic-loading ring shear apparatus was developed mainly to simulate the shear surface of landslide and in the same time to observe the pore pressure generation within the large shear displacement as well as the post-failure motion behaviour of the samples (Sassa et al. 2004). The load cells and a displacement sensor in the ring shear apparatus are employed to monitor the excess pore water pressure, mobilized shear displacement and shear resistance of the samples during failure and subsequent post-failure motion. The stresses in the field which are represented in the shear box are shown in Fig. 5.

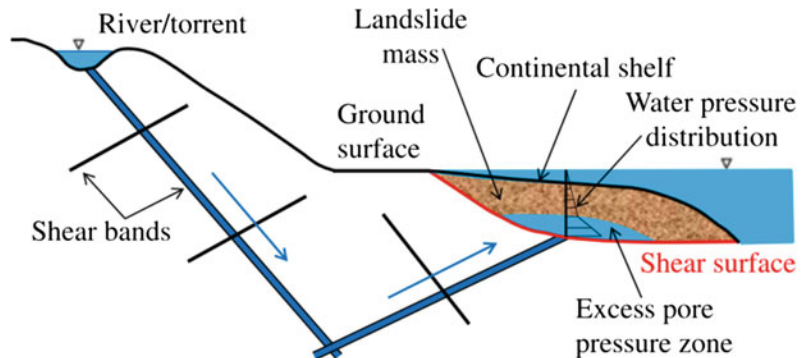
Due to gravity, the normal stress acting on the slope is $\sigma_o = m.g.\cos \theta$, and the static shear stress is $\tau_o = m.g.\sin \theta$. Thus, the initial stress point is $I(\sigma_o, \tau_o)$ as shown in Fig. 7b. When the

slope experienced the earthquake with seismic stress ($m.a$), the stress point of I will be shifted either by the change of total stress path (TSP) or the effective stress path (ESP). During the seismic loading, the excess pore water pressure is generated and the ESP is shifted to the failure line. Shear failure of the samples occur when the ESP reaches the failure line, that indicated as the landslide occurrence in the field. The newest version of ring shear apparatus, called the ICL-1 was used for the Senoumi submarine landslide. The ICL-1 has a compact dimension and transportable, which was developed by Sassa as a part of Science and Technology Research Partnership for Sustainable Developments (SATREPS) program between the Government of Japan and Croatia. Not like the previous DPRI versions of ring shear apparatus, the normal stress loading system of the ICL-1 was changed into central axis based without loading frame. Moreover, the capacity of ICL-1 is upgraded up to 1000 kPa for the normal stress and pore pressure measurement in undrained condition.

4 Specimens from Investigated Areas

For the Senoumi landslide, we examined two cases: (1) the sliding surface which is a transported deposit of volcanic ash, Neogene silty-sand or Neogene silt; (2) the sliding surface from the in situ layer of silty-sand or silt. We assumed there is no difference of shear strength parameters in those two cases, neither consolidated deposits nor

Fig. 4 Shear bands as the medium for the excess pore water pressure in continental shelf



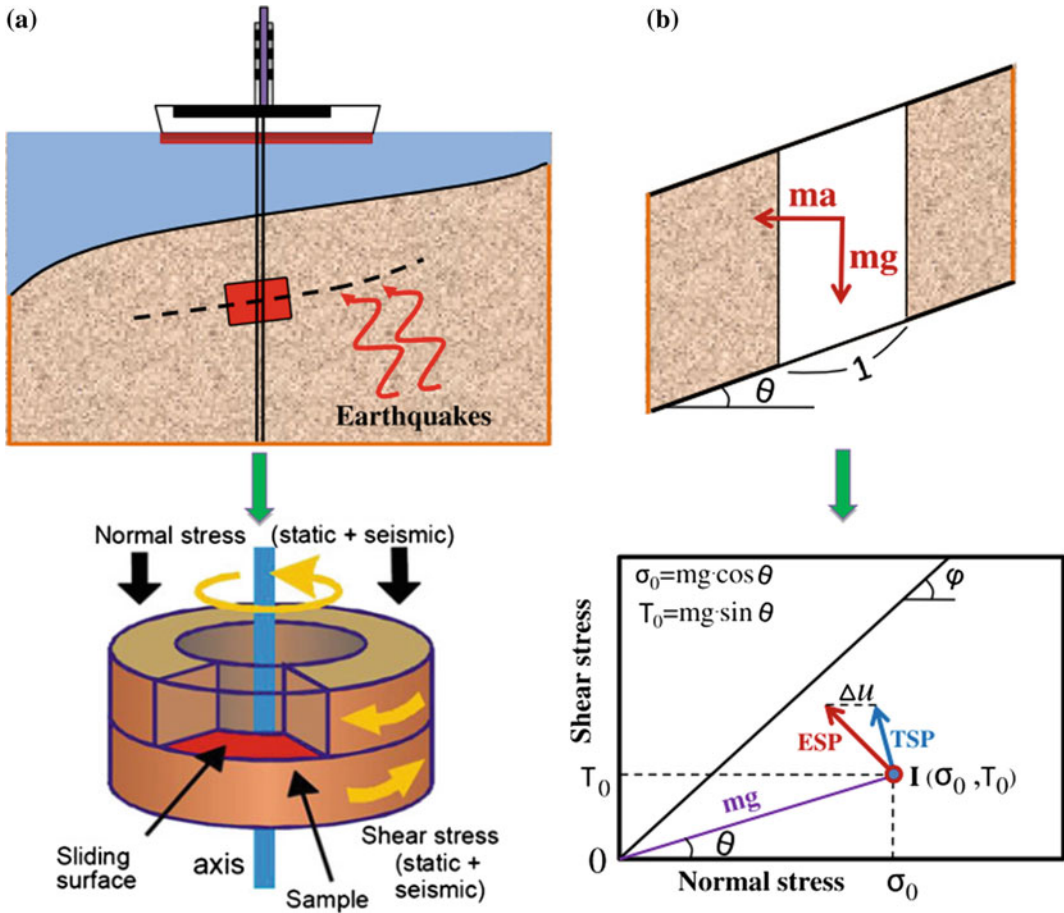


Fig. 5 Stresses concept for landslide simulation through ring shear apparatus

disturbed in situ layer, since the location of sliding surface should be very deep around more than hundreds of meters. Thus, we took samples from drilling submarine deposit in the Nankai Trough and aerial deposit in the Omaezaki Hill.

4.1 Submarine Deposits in the Nankai Trough

The Integrated Ocean Drilling (IODP) has investigated and cored a Pleistocene to Holocene layers of slope basin on the accretionary wedge of Nankai Trough, southwest offshore of Japan (Strasser et al. 2012). This Expedition 333 has brought the core samples of sea bed of more than 300 m of deep, particularly at Site C0018. We

detached the volcanic ash specimens from the bore log to be tested for the Senoumi submarine landslide study. Based on the IODP drilling core, this volcanic ash was located about 188–189 m under the sea bed in the Nankai Trough.

4.2 Neogene Deposits in the Omaezaki Hill

Based on the geological map shown in Fig. 3, the Neogene sediments are also found in the Omaezaki Hill adjacent to the Senoumi area. Landslides involving the Neogene sediments were reported previously for the case of the 2004 Mid-Niigata Prefecture Earthquake (Sato et al. 2005; Sassa et al. 2005). The results implied that

the Neogene sand experienced a large shear strength reduction and contributed to the earthquake-induced rapid moving landslide. By this reference, we took samples of Neogene silty-sand (S1) and silt (S2) from the Omaezaki Hill where the locations are shown in Fig. 3.

The grain size distributions of all samples are plotted in Fig. 6. It shows that Omaezaki silt is poorly graded compared to other two samples.

5 Undrained Cyclic Loading Ring-Shear Tests

Test Procedure

The sample depth of volcanic ash which was taken under the sea bed at Site C0018 of IODP Expedition 333 is about 189 m. The unit weight of sea water was 10.1 kN/m^3 and the total unit weight of submarine soil layer was 18.6 kN/m^3 (Expedition 333 Scientists 2012), which resulted into the effective unit weight of soils under the sea water as 8.5 kN/m^3 . Thus, the normal stress of 1000 kPa as the maximum capacity of the ICL-1 represents the depth of 117 m., not close enough to the depth of submarine sample that we took. However, we decided to apply 1000 kPa normal stress in this study.

Based on Fig. 2, the slopes angle (θ) of Senoumi area is between 8° and 12° . We applied the initial shear stress (τ_o) of 160 kPa within the normal stress (σ_o) of 1000 kPa ($\theta = \tan^{-1}(\tau_o/\sigma_o)$, where $\theta = 9.09^\circ$ is obtained). The tested samples were saturated in advance by de-aired water and

kept in a vacuum cell for one night. Then, the fully saturated samples were inserted into the shear box which already filled by de-aired water. After this step, we circulate again the shear box using the de-aired water. These procedures were carried out to obtain the B_D value ($B_D = \Delta u/\Delta\sigma$) as the saturation parameter in the ring shear tests. We obtained the B_D value higher than 0.95 for all tested samples. Subsequently, the normal stress was applied up to 1000 kPa and shear stress up to 160 kPa under drained condition. Those two stresses condition is given to create the initial stress state of the samples (normally consolidation state).

5.1 Undrained Cyclic Loading Tests

The cyclic loading tests were carried out under undrained condition with the frequency of 0.1 Hz for all three samples (IODP volcanic ash, Neogene silty-sand and silt). The cyclic test consists of the cyclic increment of shear stress up to 400 kPa, cyclic constant to monitor the pore pressure generation and cyclic decrement when the shear resistance of sample reached steady state condition. Those loading steps in the cyclic test were decided to cover all processes of the sample since failure, then pore pressure generation, post failure shear strength reduction and up to steady state condition. The undrained condition during cyclic loading test (and later on the seismic loading test) was applied because the generated pore pressure might be very quick to dissipate if the drained condition takes place. Thus, we kept the normal stress in a constant value and only shear stress was loaded through automatic servo-control system. The cyclic loading tests results are shown in Fig. 7.

From the test results, we obtained several findings as follows:

- The largest shear strength reduction and highest pore water pressure during cyclic loading was found in the IODP volcanic sand. The steady state shear resistance recorded is 72 kPa, as a result of progressive shear

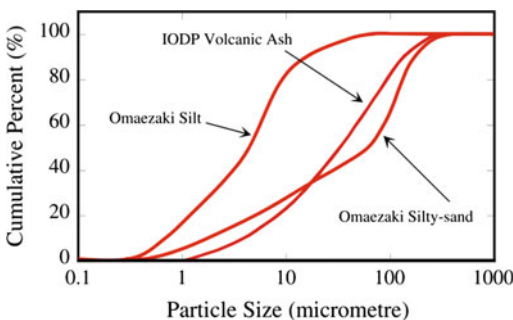


Fig. 6 Grain size distribution of three samples for the Senoumi submarine landslide

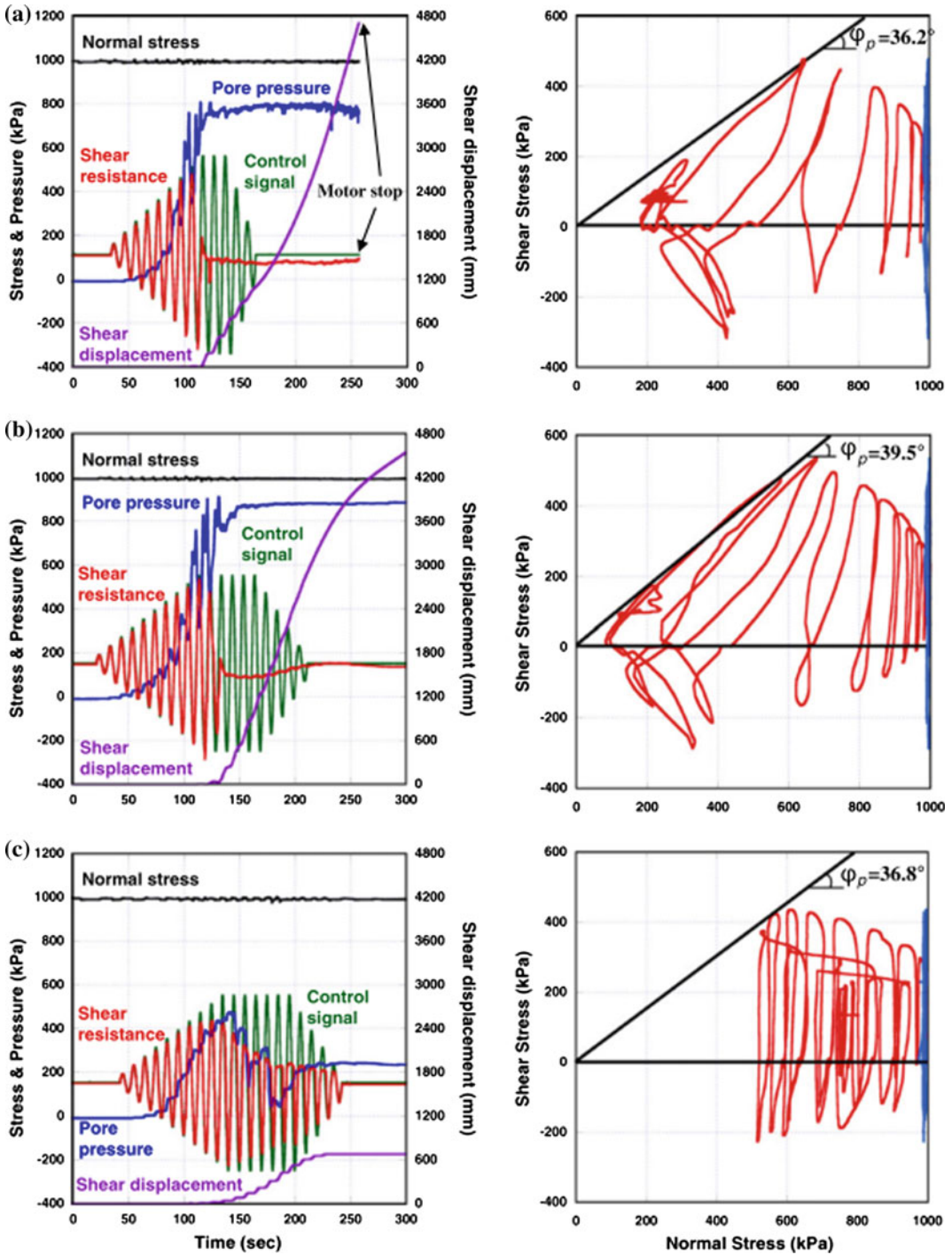


Fig. 7 The undrained cyclic loading tests of **a** IODP volcanic ash, **b** Omaezaki Neogene silty-sand, **c** Omaezaki Neogene silt

displacement. The peak friction angle reached 36.2° and the pore pressure ratio was 0.80.

- A slight difference of shear behaviour was found in the Neogene silty-sand. Although high pore water pressure was generated, the shear displacement was accelerated only during cyclic loading and showed slowing down tendency when the cyclic loading was stopped. The shear stress at the final stage of loading was similar to the initial stage of 160 kPa. No difference between stress and shear resistance causing no further acceleration at the final stage. However, the peak friction angle reached 39.5° , the highest value compared to the other samples.
- In Neogene silt, the pore water pressure generation during cyclic loading was small and peak friction angle was 36.8° . The shear displacement was appeared but stopped at around 600 mm when the cyclic loading had finished.

2011, 2012). In regard with the possibility of submarine landslides that might be triggered by such mega-earthquake, we used the 2011 Tohoku earthquake wave to examine the samples of volcanic ash and Neogene silty-sand from Senoumi area. The seismic record at station MYG004 of Tsukidate in Miyagi Prefecture was used, particularly of the NS component which has two main shocks (long duration shaking). According to the cyclic test results (Fig. 7), the sample fails within 400 kPa of the additional shear stress. Meanwhile the acceleration in NS wave of MYG004 is 2699 gal. We decided to apply the seismic wave of NS component only 0.3 times of the real wave. The cyclic loading test that already described formerly was conducted within the loading frequency of 0.1 Hz. Since the capacity of servo-shear control motor of the ICL-1 is limited, the undrained seismic loading for the Senoumi case was carried out in 30 times longer of the time period. This time scale could reproduce the shear stress similar to the real recorded wave form even though in a lower frequency loading.

6 Undrained Seismic Loading Ring-Shear Tests

A similar mega-earthquake like the 2011 Tohoku earthquake is indicated to occur around the Nankai Trough in the future (Cabinet Office

The results of undrained seismic loading are shown in Fig. 8, for the volcanic ash sample (left figure) and Omaezaki Neogene silty-sand sample (right figure). From the results, we observed that the high pore-water pressure was rapidly increased in the volcanic ash sample during the

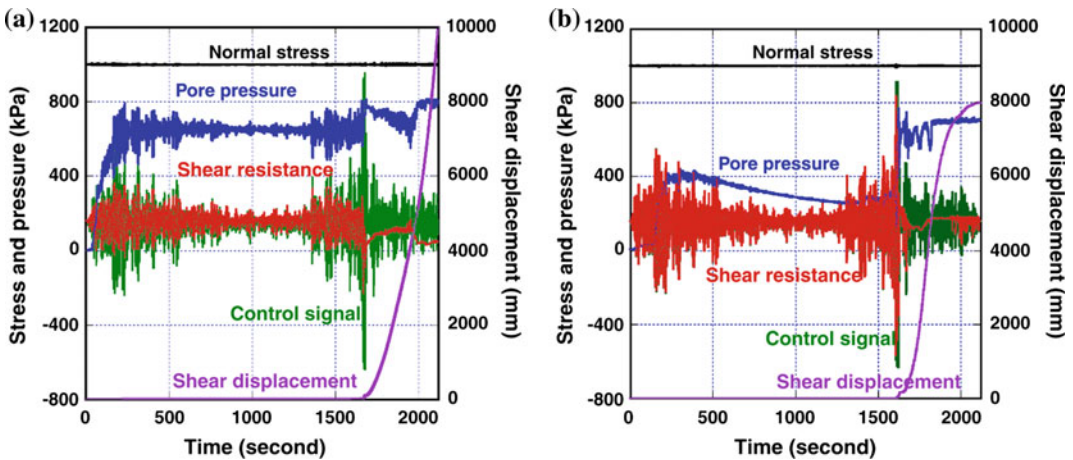


Fig. 8 The undrained seismic loading test results using the 2011 Tohoku earthquake. **a** The volcanic ash, **b** Neogene silty-sand

first main shock. While it also generated in the Neogene silty-sand sample though in a smaller value. During the second main shock, the shear displacement in volcanic ash was produced rapidly and was accelerated even the seismic wave has decreased. Different characteristic we found in Neogene silty-sand, where the shear displacement was rapidly produced during the second main shock but slowing down at the end of seismic wave. Based on the cyclic test results, the peak friction angle was found higher in the Neogene silty-sand (39.5°) than the volcanic ash (36.2°). The results indicated that the behaviour of both samples during seismic loading tests has in line characteristic with the cyclic loading tests. Within the normal stress of 1000 kPa and initial shear stress of 160 kPa (means slope angle is 9.09°), the volcanic ash might produce a rapid landslide. For the same slope and initial stress condition, the MYG004 seismic loading given to Neogene silty-sand sample would not generate a rapid landslide unless the slope angle is greater than 9.09° .

7 The Integrated Simulation of Initiation Process and Post-Failure Motion (LS-RAPID)

The LS-RAPID is the integrated landslide simulation model that aims to model the whole process of landslide from stable state, failure stage, post-failure shear strength reduction, landslide motion and mass deposit stage. This model was applied for the mitigation of earthquake and rainfall induced rapid landslide in the Philippines (Sassa et al. 2010). Fundamental concept of the LS-RAPID is described through vertical imaginary column of a landslide mass on the stable ground (Fig. 9). The forces and pressures that are acting on the column are consists of (1) self-weight of column, indicated as W , (2) normal stress acting on the bottom of column, N , which is act as a reaction from the stable ground to the self-weight of column, (3) lateral pressure acting on the side walls, P , (4) vertical seismic force, F_v , (5) horizontal seismic forces, F_x and F_y , (6) shear resistance acting on the bottom, R , and (7) pore water pressure acting from the bottom, U .

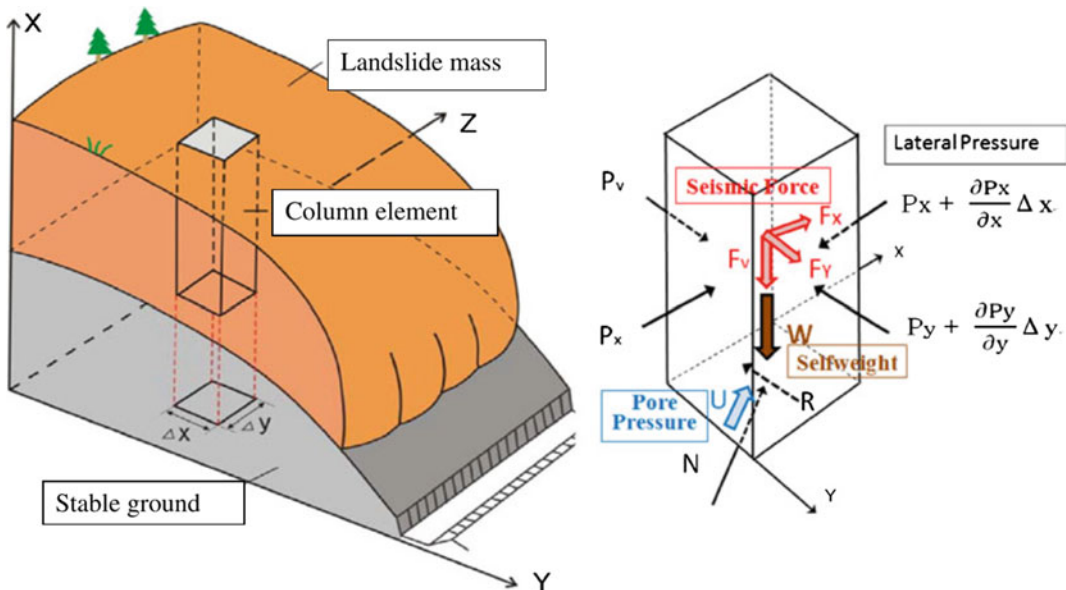


Fig. 9 Concept of the LS-RAPID landslide simulation

Based on the forces components on imaginary column described above, the landslide mass (m) will be accelerated by an acceleration (a) given by the total of all forces: driving force (self-weight and seismic forces) + lateral pressure from the walls + shear resistance from the ground, as stated in the equation below,

$$a.m = (W + F_v + F_x + F_y) + \left(\frac{\partial P_x}{\partial x} \Delta x + \frac{\partial P_y}{\partial y} \Delta y \right) + R \quad (1)$$

The R includes the effects of N and U in Fig. 9 on upward direction of the slope before the motion takes place and on downward direction when the landslide mass is moved. All calculated stresses and displacements are projected on the horizontal plane while the slope angles on each columns of landslide mass are varied depend on the topography condition. The ratio between horizontal stress (σ_h) and vertical stress (σ_v) is referred to as the lateral pressure ratio (k). In case of liquid body, k equals to 0, and $k = 1$ when the body is completely rigid. In this paper, the landslide simulation is carried out by combining the effects of pore water pressure and seismic loading.

The shear strength reduction of landslide mass from the pre-failure state to the steady-state motion is presented in the LS-RAPID. Process of landslide simulation in the LS-RAPID covers the following stages:

- i. The initial state, stable condition when the friction coefficient at peak ($\tan \phi_p$) works in a soil layer (slope).
- ii. Failure state, the condition when the soil fails due to the intense/prolonged rainfall, groundwater level rapidly rise and or seismic loading. The peak shear resistance appears during the failure state.
- iii. Transient state, the transition phase from failure to steady state. In this phase, the shear strength reduction in progress of shear displacement takes place.

- iv. The steady state, when there is no further strength reduction in the moving landslide mass.

The shear stress and displacement relationship of the undrained cyclic tests results are shown in Fig. 10. The red line shows the shear behaviour of samples from pre-failure state to a steady state. The shear strength reduction together with shear displacement will start from DL (point of failure) to DU (end of strength reduction). The apparent friction coefficient ($\tan \phi_{a(ss)}$) will produced under steady-state condition after DU.

The most necessary parameters to be consider in the LS-RAPID landslide simulation are the steady-state shear resistance (σ_{ss}), the lateral pressure ratio ($k = \sigma_h/\sigma_v$) and the critical shear displacement during failure (DL) and right before steady-state condition (DU). Former research conducted by Sassa et al. (2004) for the 2003 Minamata landslide debris flow in Japan has shown that the excess pore pressure will be generated by the undrained dynamic loading of landslide mass. This finding shall be similar with the case of Senoumi as submarine megaslides where the mass is under the sea water and fully saturated. Thus, the steady-state shear resistance of soil layer where the excess pore pressure exists must be very small. We assumed that the steady-state shear resistance is of about 10 kPa along the bottom of the subjected submarine landslide in the Senoumi area. Most of the soil parameters that were used in the LS-RAPID simulation are shown in Table 1.

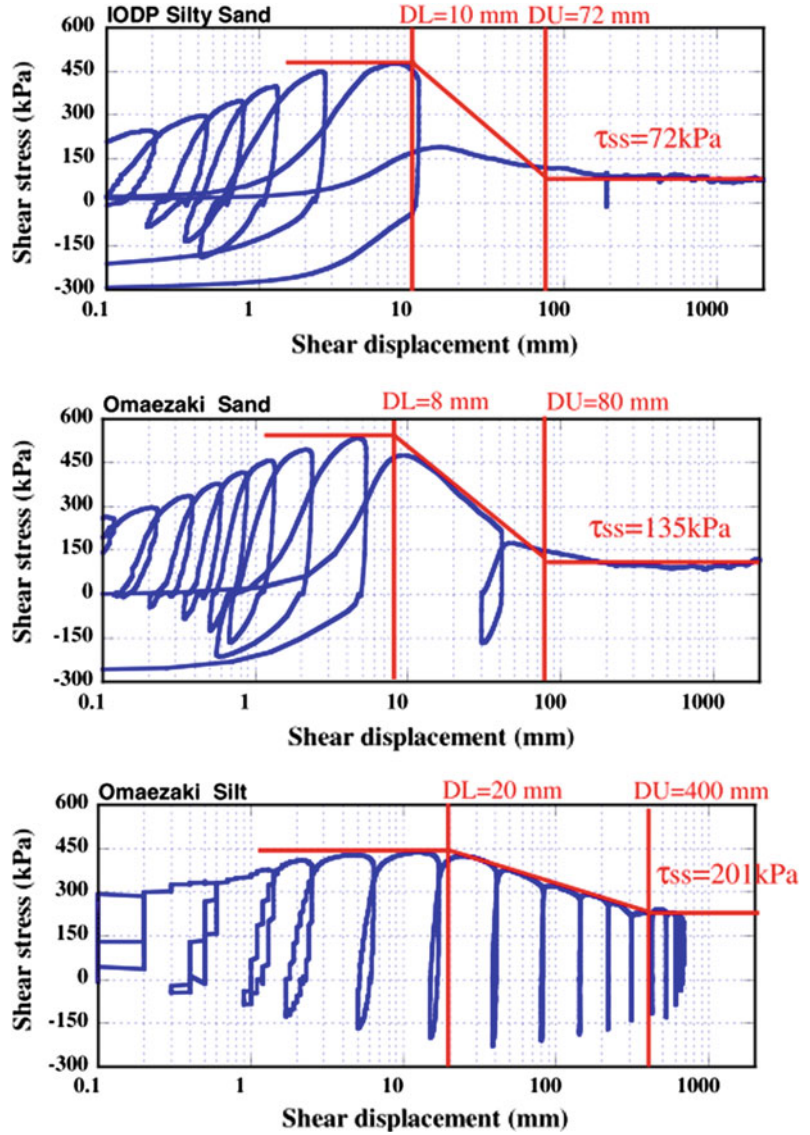
The constant speed shearing tests with the changing of normal stress in drained condition were carried out to obtain the friction angle during motion (ϕ_m) (Sassa et al. 2005). The lateral pressure ratio was estimated using the Jaky's equation as follows,

$$k = 1 - \sin \phi_{ia} \quad (2)$$

here,

$$\tan \phi_{ia} = (c + (\sigma - u) / \tan \phi_i / \sigma) \quad (3)$$

Fig. 10 Shear stress and displacement relationship for observing the DL and DU



where, $\tan \phi_{ia}$ is the apparent friction coefficient within the landslide mass and $\tan \phi_i$ is the effective friction within the landslide mass. The value of c is considered to be zero, while ϕ_i is approached by the friction angle during motion (ϕ_m). The pore pressure generation rate (B_{ss}) indicated the saturation condition of the soil layer. The B_{ss} equals to 0 if the layer condition is on dry state, and equals to 1 if completely saturated. Since under the sea, we used the $B_{ss} =$

0.99 for the submarine sand layer for the whole modelled area.

During the motion, landslide mass may lose its kinetic energy through collision, horizontal bends and or momentum transfer to the eroded materials. Concerning to this phenomenon, an energy loss function is applied for a specific mesh and time step using the threshold values of extraordinary velocity and thickness (as described in Sassa et al. 2010). This function

Table 1 Soil parameters used in the LS-RAPID simulation for Senoumi area

Parameters	Value	Source
Total unit weight of the mass (γ_t)	18.6 kN/m ³	Data from the IODP-333
Unit weight of sea water (γ_w)	10.1 kN/m ³	Average sea water density (1026 kg/m ³)
<i>Acceleration of the 2011 Tohoku earthquake:</i>		
1.0 times	2699 gal	Wave form of the ground motion record at MYG004
0.7 times	1889 gal	
0.3 times	809 gal	
Excess pore pressure ratio in the fractured zone (r_u)	0.3	Assumption
<i>Shear strength parameters of the IODP volcanic ash</i>		
Steady-state shear resistance (τ_{ss}) in the source area	72 kPa	Test data
Lateral pressure ratio ($k = \sigma_h/\sigma_v$)	0.85	Estimation from test data
Friction angle at peak (ϕ_p)	36.2°	Test data
Friction angle during motion (ϕ_m)	34.5°	Test data
Shear displacement at the start of strength reduction (D_L)	10 mm	Test data
Shear displacement at the end of strength reduction (D_U)	72 mm	Test data
<i>Shear strength parameters of the Omaezaki Neogene silty-sand</i>		
Steady-state shear resistance (τ_{ss}) in the source area	135 kPa	Test data
Lateral pressure ratio ($k = \sigma_h/\sigma_v$)	0.90	Estimation from test data
Friction angle at peak (ϕ_p)	39.5°	Test data
Friction angle during motion (ϕ_m)	35.8°	Test data
Shear displacement at the start of strength reduction (D_L)	8 mm	Test data
Shear displacement at the end of strength reduction (D_U)	100 mm	Test data
<i>Shear strength parameters of the Omaezaki Neogene silt</i>		
Steady-state shear resistance (τ_{ss}) in the source area	201 kPa	Test data
Lateral pressure ratio ($k = \sigma_h/\sigma_v$)	0.70	Estimation from test data
Friction angle at peak (ϕ_p)	36.8°	Test data
Friction angle during motion (ϕ_m)	23.5°	Test data
Shear displacement at the start of strength reduction (D_L)	20 mm	Test data
Shear displacement at the end of strength reduction (D_U)	400 mm	Test data
<i>Other parameters</i>		
Steady-state shear resistance of the surface deposit in the Suruga through mobilized by undrained loading	10 kPa	Estimated from undrained loading ring shear test (Sassa et al. 2004)
Pore pressure generation rate (B_{ss})	0.99	Full saturation of all soil mass under the sea
<i>Parameters for the function for non-frictional energy consumption</i>		
Energy loss coefficient of the function (α)	1.0	Sassa et al. (2010)
Threshold value of velocity	200 m/s	Impossible velocity
Threshold value of soil height	2000 m	2.5 times the initial maximum depth

represented mainly as the loss of kinetic energy. The function of non-frictional energy consumption in a column of landslide mass at a mesh is represented as the loss of kinetic energy, which is stated as,

$$\alpha \left(\frac{1}{2} m \cdot v^2 \right)$$

where m is the soil mass within a column at the mesh, v is the velocity at the mesh and α is a coefficient for non-frictional energy consumption (a constant with dimension of reciprocal length). This velocity-dependent energy loss is only performed at the specific mesh and times when the soil height exceeds the threshold value (2000 m) and the velocity is greater than 200 m/s. The energy loss coefficient, $\alpha = 1$ (Sassa et al. 2010).

8 Simulation Result for Senoumi Area

In the LS-RAPID simulation for the Senoumi area submarine landslide, we inserted all three wave components (EW, NS and UD) of the 2011 Tohoku earthquake acceleration wave record which was obtained from MYG004 station. The amplitude of acceleration was given in three cases, namely 0.3, 0.4, 0.7 and 1.0 times the real wave record for all soil samples. Another triggering factor, the excess pore pressure ratio (r_u) of 0.3 was applied in the simulation. The layout of LS-RAPID simulation results which is performed for the IODP volcanic ash is presented in Fig. 11.

Blue dots represents the stable soil columns with moving velocity of less than 0.5 m/s while red dots shows unstable soil columns with

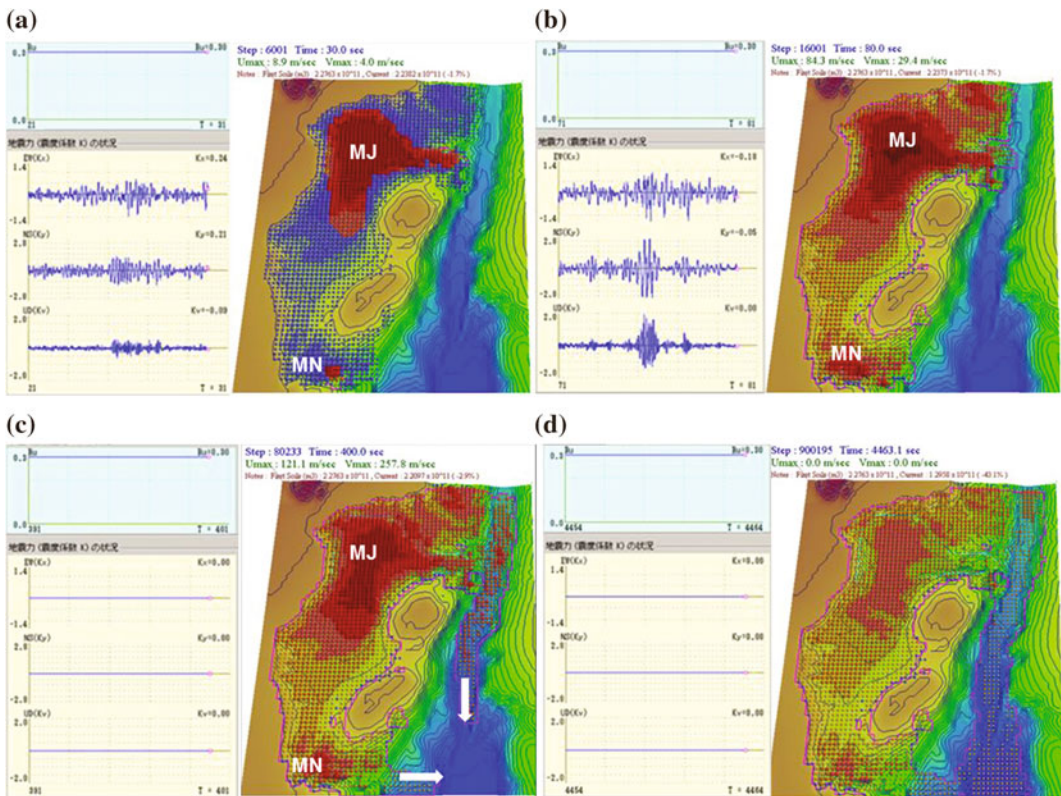


Fig. 11 Landslide simulation result for the IODP volcanic ash using 1.0 times of the Tohoku earthquake record

moving velocity of higher than 0.5 m/s. After the first shock (Fig. 11a), failure occurred on the major landslide block (MJ) which is produced the excess pore pressure (red dots) as well as minor landslide block (MN). Soon after the second shock (Fig. 11b), all soil columns in the simulation area were subjected to slide with the velocity of more than 0.5 m/s. Finally after the seismic wave finished, all landslide masses has moved downward to a narrow channel of the Suruga Trough and the simulation was stopped. Table 2 shows simulation results of the LS-RAPID for all samples in three cases of seismic wave.

Landslides were occurred in all samples when the seismic wave is given in 0.4, 0.7 and 1.0 times of the MYG004. In the 0.3xMYG004, no landslide appeared in Omaezaki Neogene silt, only minor landslide block (MN) moved in Omaezaki Neogene silty-sand soil while landslide occurred completely in IODP volcanic ash. Figure 12a presents the x section (EW) and the y section (NS) of Senoumi submarine landslide area.

Landslide of the IODP volcanic ash with the 0.3xMYG004, Neogene silty-sand with the 0.4xMYG004 and Neogene silt with the 0.4xMYG004 are sequentially presented in Fig. 12b–d. In the IODP volcanic ash, landslide was triggered within depth of 400 m. Shallower landslides were appeared in the samples of Neogene silty-sand and Neogene silt. In the resultant of all seismic wave acceleration components, the 400 m deep large-scale landslide may occur if sliding surface formed in the volcanic ash layer.

9 Conclusion

The observation of pore pressure generation as well as shear strength reduction in the progress of shear displacement during seismic loading and the post-failure motion behaviour is very important to understand the dynamics of earthquake-induced submarine landslides, such may occur in the Senoumi area of Suruga Bay. We successfully tested the cored sample of volcanic ash taken from the depth of 189 m below the sea bed using a transportable undrained dynamic loading ring shear apparatus of ICL-1. The results are compared with the samples of Neogene silty-sand and silt from Omaezaki hill that is located adjacent to the Suruga Bay. Several parameters obtained from the ring shear tests were then used as an input for the LS-RAPID computer simulation. We assumed that the excess pore water pressure may contribute to the submarine landslide zone of Senoumi area. The IODP volcanic ash sample experienced accelerated motion in 9.09° of gentle slope during shear stress of 0.3 times NS component of MYG004 seismic wave record (equals to 810 gal at peak). In addition, the computer simulation for volcanic ash produced 400 m deep landslide when the 0.3xMYG004 of seismic acceleration in all three wave components is given. Different results were appeared for the Neogene silty-sand and silt samples. The Neogene silty-sand experienced shear displacement up to 8 m during seismic loading but stopped soon at the end of loading. The landslide was occurred in the Neogene silty-sand by the 0.4xMYG004 even though the thickness is not so significant compared to the volcanic ash. Finally, very limited landslide was appeared in the Neogene

Table 2 Simulation results of the LS-RAPID for Senoumi submarine landslide (red texts are described visually in Fig. 12)

Samples	0.3xMYG004	0.4xMYG004	0.7xMYG004	1.0xMYG004
IODP volcanic ash	Landslide	Landslide	Landslide	Landslide
Omaezaki Neogene silty-sand	No (only MN)	Landslide	Landslide	Landslide
Omaezaki Neogene silt	No	Landslide	Landslide	Landslide

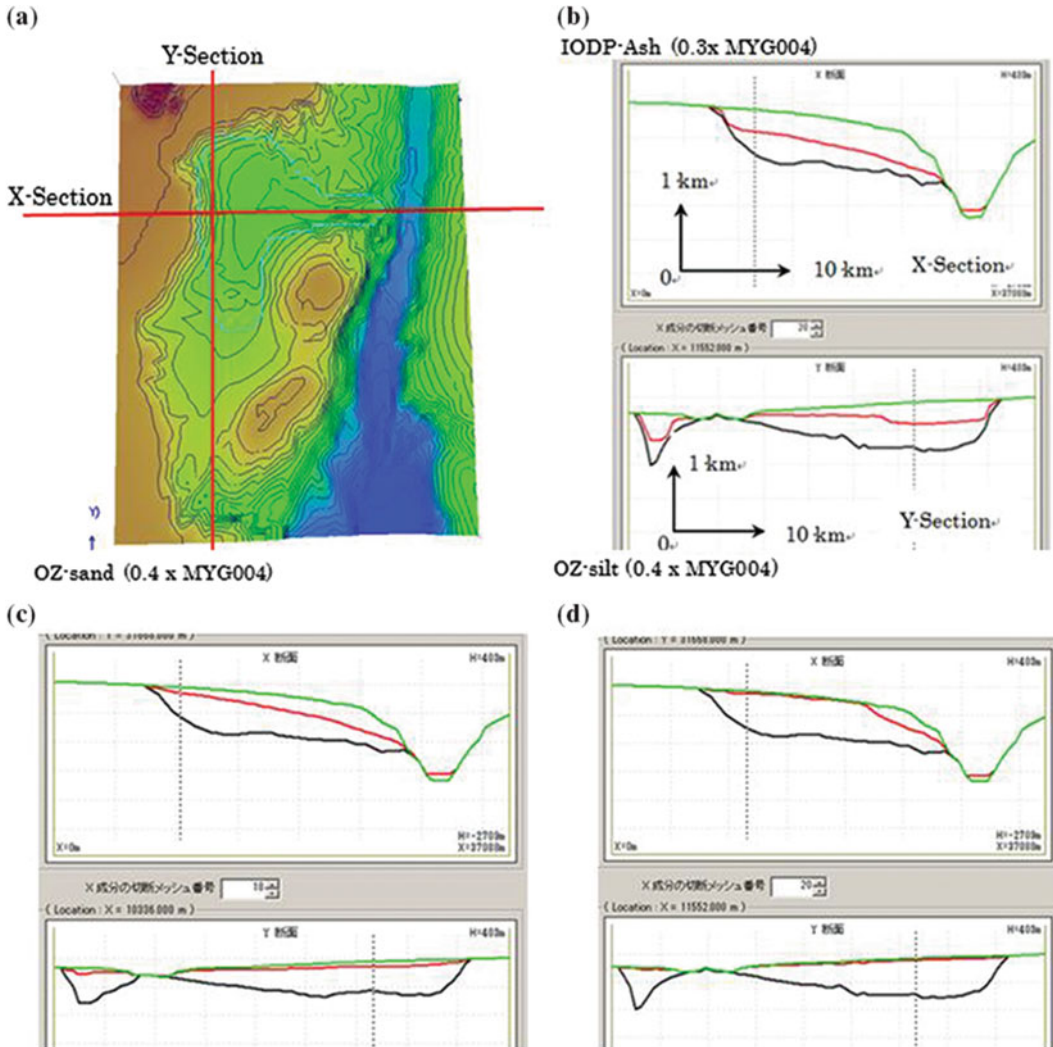


Fig. 12 Senoumi landslides cross-section for all samples triggered by different intensities of the 2011 Tohoku earthquake

silt for the seismic acceleration of 0.3xMYG004. This study implied that there is a possibility to occur a large-scale submarine megaslide in Senoumi area due to the mega earthquake of Nankai Trough in the future. Since the location of Senoumi area is near to the coastal area with dense population, further investigation of the risks and impacts that may arise is necessary to be carried out.

Acknowledgements We acknowledge the SATREPS of the Government of Japan and two projects of the International Programme on Landslides (IPL-157 and

IPL-161). Thanks go to R. Urgeles of the Institut de Ciències del Mar, Spain for information on marine landslides and T. Furumura of the Center for Integrated Disaster Information Research, the University of Tokyo for information on earthquake shaking. The authors thank to Y. Kaneda and M. Yasunaga as well as the ship and personnel of the Drilling Vessel Chikyu of the Japan Agency for Marine-Earth Science and Technology for their kind cooperation. The support from Croatian young researchers of Rijeka University during experiments is highly acknowledged. This research used data and samples provided by the Integrated Ocean Drilling Program (IODP) and the Geological Survey of Japan.

References

- Ando M (1975) Source mechanisms and tectonic significance of historical earthquakes along the Nankai Trough, Japan. *Tectonophysics* 27:119–140
- Baba T, Matsumoto H, Kashiwase K, Hyakudome T, Kaneda Y, Sano M (2011) Micro-bathymetric evidence for the effect of submarine mass movement on tsunami generation during the 2009 Suruga bay earthquake, Japan. In: Yamada et al (eds) *Submarine mass movements and their consequences*, vol 31. *Advances in natural and technological hazard research*. Springer, New York, pp 485–494
- Bondevik S, Mangerud J, Dawson S, Dawson A, Lohne P (2005) Evidence for three North Sea tsunamis at the Shetland Islands between 8000 and 1500 years ago. *Quat Sci Rev* 24:1757–1775
- Cabinet Office of the Government of Japan (Committee on Megaquake Model in Nankai Trough) (2011) Intermediate report of the study team for the Mega-quake model in Nankai trough. http://www.bousai.go.jp/jishin/chubou/nankai_trough/chukan_matome.pdf
- Cabinet Office of the Government of Japan (Committee on Megaquake Model in Nankai Trough) (2012) The tsunami-fault model in the 2011 off the Pacific coast of 2011 Tohoku earthquake, reference no. 1 of the 12th meeting of Megaquake model in Nankai Trough. http://www.bousai.go.jp/jishin/chubou/nankai_trough/12/sub_1.pdf
- Cochoonat P, Cadet J, Lallemand S, Mazzotti S, Nouze H, Fouchet C, Foucher J (2002) Slope instabilities and gravity processes in fluid mitigation and tectonically active environment in the eastern Nankai accretionary wedge (KAIKO-Tokai' 96 cruise). *Mar Geol* 187:193–202
- Expedition 333 Scientists (2012) Site C0018. In: Henry P, Kanamatsu T, Moe K, The Expedition 333 Scientists (eds) *Proceedings IODP, 333. Integrated Ocean Drilling Program Management International, Inc.*, Tokyo. doi:10.2204/iodp.proc.333.103.201
- Locat J, Lee H (2008) Submarine mass movement and their consequences: an overview. In: Sassa K, Canuti P (eds) *Landslides—disaster risk reduction*. Springer, New York, pp 115–142
- Sassa K, Fukuoka H, Wang G, Ishikawa N (2004) Undrained dynamic-loading ring-shear apparatus and its application to landslide dynamics. *Landslides* 1–1:7–19
- Sassa K, Fukuoka H, Wang F, Wang G (2005) Dynamic properties of earthquake-induced large-scale rapid landslides within past landslide mass. *Landslides* 2–2:125–134
- Sassa K, Nagai O, Solidum R, Yamazaki Y, Ohta H (2010) An integrated model simulating the initiation and motion of earthquake and rain induced rapid landslides and its application to the 2006 Leyte landslide. *Landslides* 7–3:219–236
- Sato H, Sekiguchi T, Kojiro R, Suzuki Y, Iida M (2005) Overlying landslides distribution on the earthquake source, geological and topographical data: the Mid Niigata prefecture earthquake in 2004. *Landslides* 2–2:143–152
- Strasser M, Moore G, Kimura G, Kopf A, Underwurd M, Guo J, Scream E (2011) Slumping and mass transport deposition in the Nankai fore arc: evidence from IODP drilling and 3-D reflection seismic data. *Geochem Geophys Geosyst* 12:Q0AD13. doi:10.1029/2010GC003431
- Strasser M, Henry P, Kanamatsu T, Thu M, Moore G (2012) Scientific drilling of mass-transport deposits in the Nankai accretionary wedge: first result of from IODP Expedition 333. In: Yamada et al (eds) *Submarine mass movements and their consequences*, vol 31. *Advances in natural and technological hazards research*. Springer, New York, pp 671–681

TXT-tool 3.081-1.4 Initiation Mechanism of Rapid and Long Run-Out Landslide and Simulation of Hiroshima Landslide Disasters Using the Integrated Simulation Model (LS-RAPID)

Loi Doan Huy, Kyoji Sassa, Hiroshi Fukuoka, Yuji Sato,
Kaoru Takara, Hendy Setiawan, Tien Pham
and Khang Dang

Abstract

On August 20, 2014 many landslides and debris flows occurred in Hiroshima city during the heavy rainfall. Ring shear apparatus (ICL-1) was used to simulate the failure of soils, the formation of sliding surfaces and the steady-state motion of Hiroshima landslide disasters. Samples were taken from source area in Midorii and Yagi district. The ring shear tests on Midorii and Yagi samples were carried out under the normal stress of 50 and 100 kPa that assumed the landslide depth from 4 to 8 m. The triggering factor such as pore-water pressure was calculated by using the Slope-Infiltration-Distributed Equilibrium (SLIDE) model that developed by Liao et al. (Landslides 7:317–324, 2010, Environ Earth Sci 55:1697–1705, 2012). The rainfall record monitored at the Miiri JMA station for each 10 min from 8:30 PM on August 19, 2014 was used to calculate pore-water pressure and landslide occurred when pore-water pressure reached 15.2 kPa. All test results were input to an integrated simulation model (LS-RAPID) as dynamic parameter of landslide. The combination of landslide ring shear simulator and integrated landslide simulation model provides a new tool for landslide assessment. The hazard area and time of

L.D. Huy (✉)
Institute of Transport Science and Technology,
Hanoi, Vietnam
e-mail: doanhuyloidkt@gmail.com

K. Sassa · K. Dang
International Consortium on Landslides, 138-1,
Tanaka Asukaicho, Sakyo-ku, Kyoto 606-8226,
Japan

H. Fukuoka
Research Institute for Natural Hazards and Disaster
Recovery, Niigata University, Niigata, Japan

Y. Sato
Godai Kaihatsu Corporation, Kanazawa, Japan

K. Takara
Disaster Prevention Research Institute, Kyoto
University, Kyoto, Japan

H. Setiawan · T. Pham
Graduate School of Engineering, Kyoto University,
Kyoto, Japan

K. Dang
VNU University of Science, Hanoi, Vietnam

occurrence in Hiroshima disaster were estimated by LS-RAPID. The estimated hazard area is similar with landslide moving area reported by Geospatial Information Authority of Japan (GSI). This research will contribute to understanding the mechanism of landslide and debris flow during heavy rainfall as a basic knowledge for disaster prevention.

Keywords

Hiroshima landslide · SLIDE model · Undrained ring shear apparatus
Integrated simulation model · Rainfall

Contents

1	Introduction	150
2	Geological Setting and Sampling	150
3	Landslide Ring-Shear Simulator	150
4	Test Result	156
4.1	Undrained Monotonic Test.....	156
4.2	Undrained Dynamic Loading Test.....	156
4.3	Pore-Water Pressure Control Test.....	159
5	Application of LS-RAPID and SLIDE Model to the 2014 Hiroshima Landslide	160
5.1	Integrated Simulation Model (LS-RAPID).....	160
5.2	SLIDE Model.....	160
5.3	Application of LS-RAPID Model to the 2014 Hiroshima Landslide.....	161
6	Conclusion	166
	References.....	168

in Hiroshima disasters. This process can be reproduced using undrained dynamic loading test of ring shear apparatus.

The most catastrophic landslides and debris flows occurred in Midorii and Yagi area of Hiroshima city which were studied in detail in this research. Figure 1 presents the landslides and debris flows in Midorii and Yagi community. Like the 1999 Hiroshima landslide disasters, the 2014 landslides took place in heavily weathered granitic sand “masa” on sliding surface, resulting in landslide-induced debris flow (Fukuoka et al. 2014). Most of them were shallow (0.5–2.0 m deep) (Fig. 2).

1 Introduction

Many debris flows and landslides took place in Hiroshima city in the early morning of 20 August, 2014. This disaster claimed 74 dead, 255 houses damaged and 4562 houses were affected (MLIT-Ministry of Land, Infrastructure, Transport and Tourism). The cumulative rainfall from 20:30 PM of 19 August until 04:30 AM of 20 August reached 248 mm at Miiri rain gauge station in Hiroshima. This is main reason caused the Hiroshima disasters.

Landslide occurred in head scarp and it rode on the debris deposits. The debris deposits were sheared and moved together with the landslide mass. Landslide triggered debris flow plays a key role on the occurrence and motion of debris flows

2 Geological Setting and Sampling

Two samples were taken in the source head as shown in Fig. 3 and sent to International Consortium Landslide (ICL) laboratory in Kyoto University. Both samples were tested to study characteristic of soil in the source and represent the initiation and motion of Hiroshima landslides (Figs. 4, 5, 6).

3 Landslide Ring-Shear Simulator

Ring shear apparatus was designed initially to investigate the residual shear resistance along the sliding surface at large shear displacement in landslides because it provides unlimited shear



Fig. 1 Landslides in Yagi and Midorii community (Photo by PASCO)

displacement (Sassa et al. 2004). The ring shear test was introduced by Hvorslev (1939) and improved by Bishop (1971), Bromhead (1979), Savage and Sayed (1984), Sassa (1984), Hungr and Morgenstern (1984), Tika (1989), and Garga and Sendano (2002).

Ring shear apparatus is suitable for simulation of sliding surface. In the sliding surface, size and shape of soil grains are changed because of their crush or breaking. Those changes lead to volume and pore-water pressure change in the shear zone. The extent of change is different for different soils such as volcanic or sedimentary, angular or round, hard or soft minerals. It is difficult to infer a reliable general principle for all case of concern.

The basic concept of ring shear apparatus is illustrated in Fig. 7a. Samples are taken from landslide area and set into the shear box. All stresses acting on the potential sliding surface; normal and shear stresses due to gravity, seismic stress due to seismic shaking as well as generated pore pressures, can be reproduced in the shear box. When stresses are high enough to trigger sample failure, a shear surface will develop

within the shear box, and the rotary lower half of the shear box will start turning. During the shearing process, ring shear apparatus measures excess pore water pressure, shear resistance mobilized and shear displacement.

Figure 8 illustrates the case where initial stress + pore water pressure reach failure line (red line). In the rainy season, ground water table/pore-water pressure increases due to rainfall infiltration. The initial point (I) moves toward to the failure line, shear failure will occur at the stress at failure (shown as red circle along the failure line).

Debris flows can develop during heavy rainfall but in most cases, they are mobilized from landslides (Sassa 1998; Iverson et al. 1997). When the initial landslide mass rides on the torrent bed deposits, an undrained loading process may generate a high pore-water pressure within torrent deposits and this helps incorporate those deposits into moving mass (Sassa 2004).

Figure 9a illustrates the model for undrained loading of saturated deposits by a displaced mass. Landslide takes place at the head scarp and the displaced soil mass slide down the slope (step

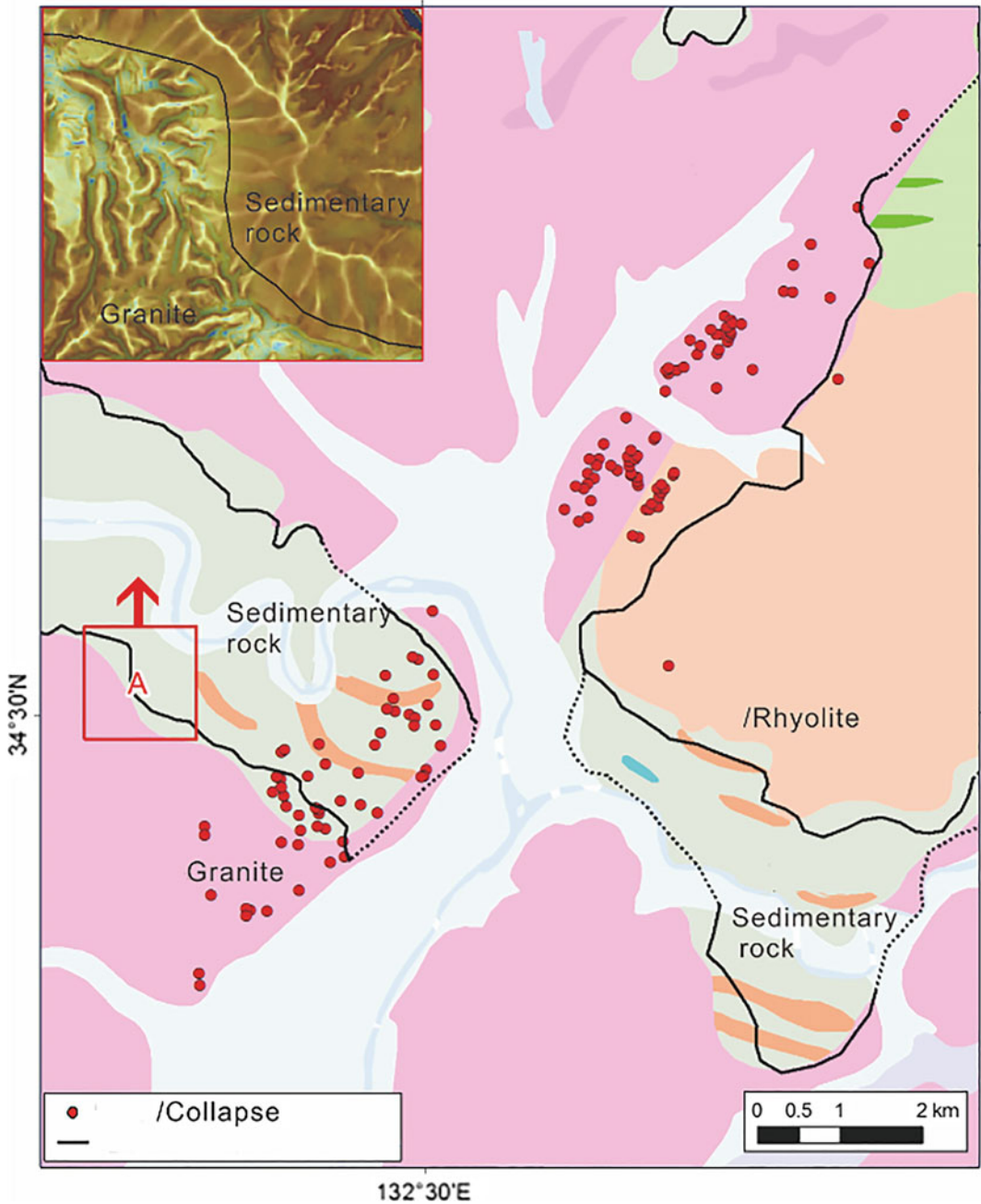


Fig. 2 Geological map and landslide distribution (Matsushi 2014)

I) and then ride onto debris deposit at the toe of the slope (step II). The debris deposits were sheared and moved together with displaced soil mass (step III). In the initial state [step (I)], it is

assumed that applied stress on the torrent debris deposits was self weight of the column of the debris deposit, W and is expressed by the point "A". If no excess pore pressure gene is generated

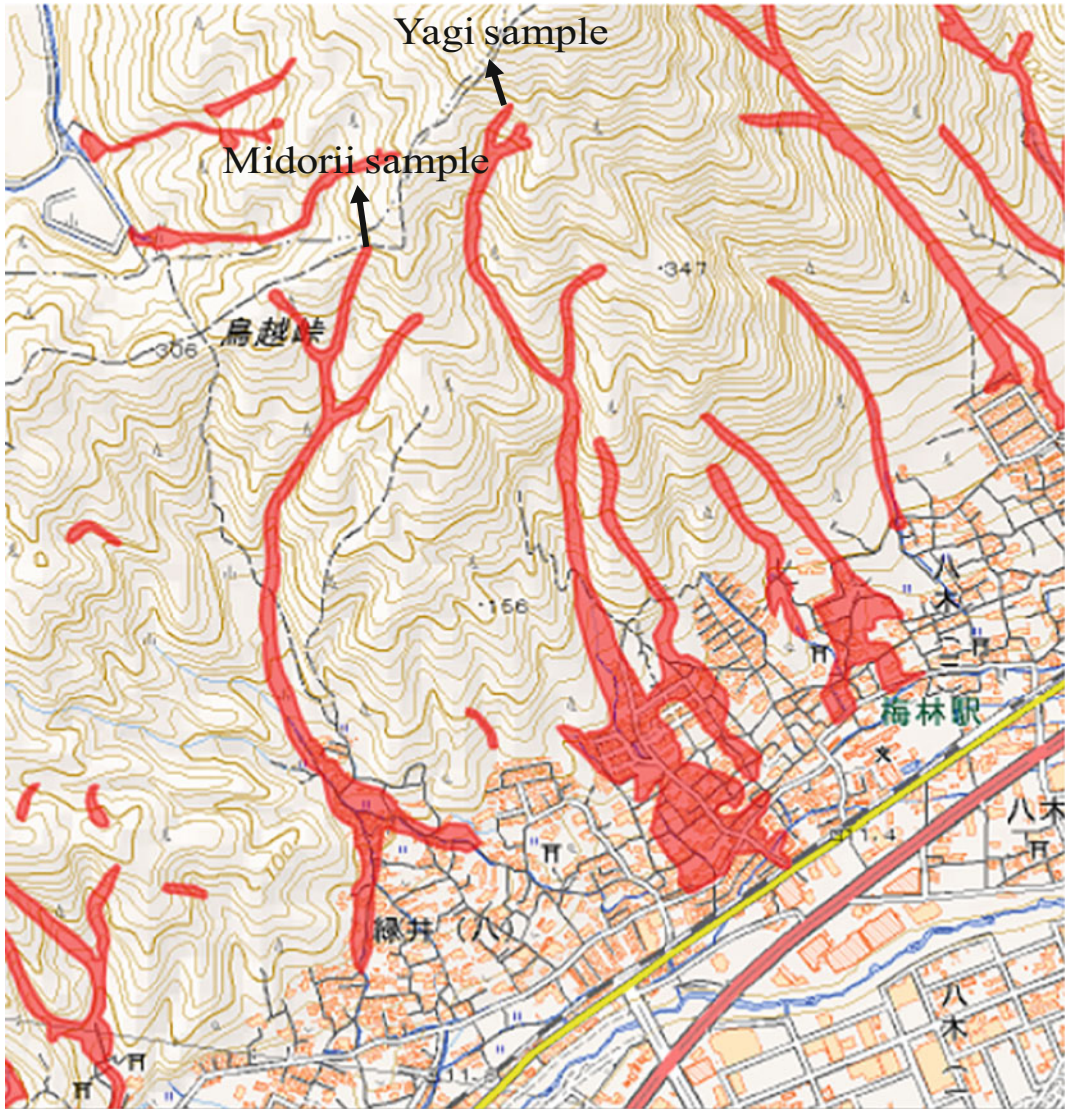


Fig. 3 Landslide hazard area reported by the Geospatial Information Authority of Japan (GSI) from air photo interpretation and the locations of sampling sites

during the step (II), the initial point moves to point (C) by plus static stress (ΔW) to the initial stress. When sliding mass ride on the debris deposits with a certain velocity, it caused a dynamic stress (F_d). Here, assume the applied stress as the sum of static stress (ΔW) and dynamic stress (F_d). So, by adding applied stress to the initial stress, total stress move to point (B) as is expressed the stress path in the field.

However, stress path reaches the failure line, it moves along the failure line as seen in Fig. 10b. Sassa et al. (1997) proposed that the dynamic force (F_d) is calculated by using the static stress and the dynamic coefficient (K_d). The dynamic normal and shear stress are calculated by using the angle thrust between the slope and the debris bed (α):



Fig. 4 Photos of landslide and sampling in Yagi (Left) and Midorii (Right) area

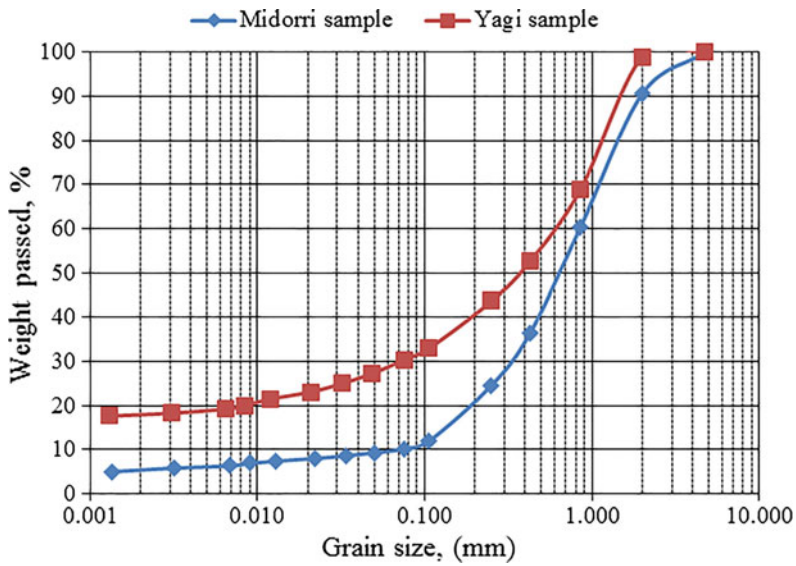


Fig. 5 Grain size distribution on Yagi and Midorii sample

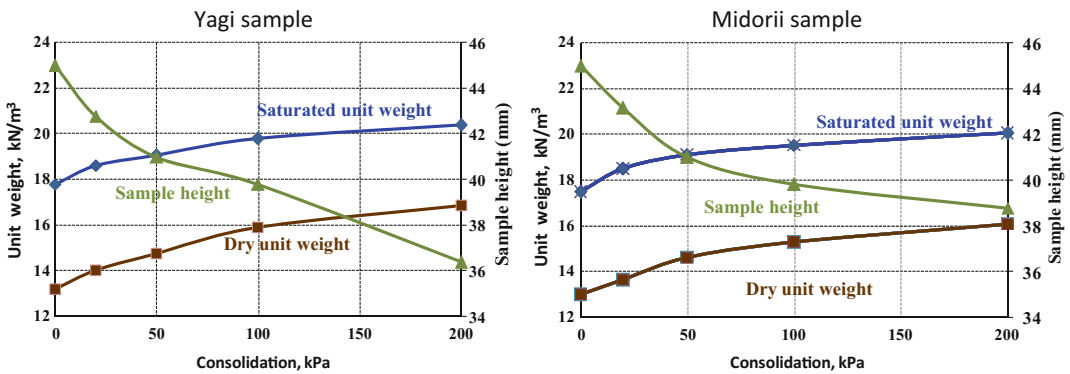


Fig. 6 Dry and Saturated unit weight of Yagi and Midorii samples at different consolidation pressure

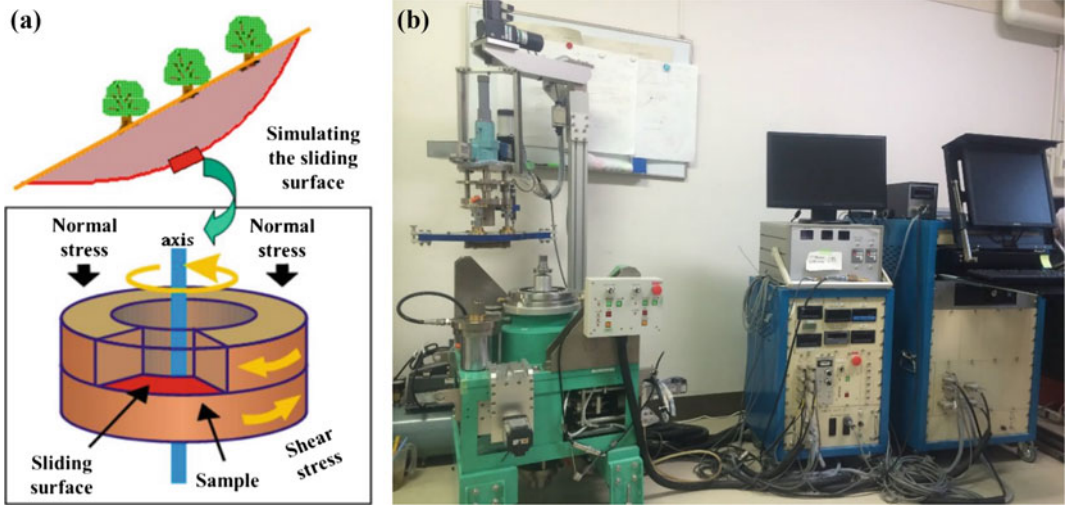


Fig. 7 Concept of the ring-shear landslide simulator (a) and General view of the portable ring shear apparatus, ICL-1 (b)

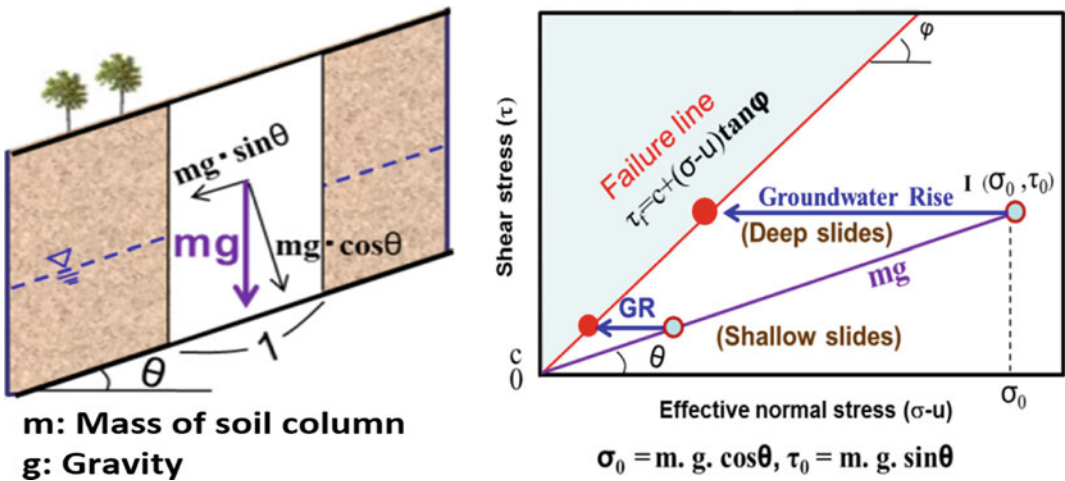


Fig. 8 Stresses acting on a potential sliding surface in a slope (Left), Stresses reproduced in the ring shear landslide simulator (Right)

$$\tau_d = Fd \cos \alpha, \quad \sigma_d = Fd \sin \alpha, \quad Fd = Kd\Delta W$$

Figure 9b presents two stress paths: the total stress path (ABC) and the effective stress path (AD). The effective stress path will deviate from the total normal stress because the excess pore-water pressure is generated during the loading and shearing process.

When the displacement mass moves from the steep slope to a gentle slope, the angle α is great, but when it moves along the torrent, the angle α is zero and the dynamic stress is zero (as shown in Fig. 10). A ring shear test was conducted to reproduce the motion debris flow when landslide mass moves along a torrent. The test result will present in the next section.

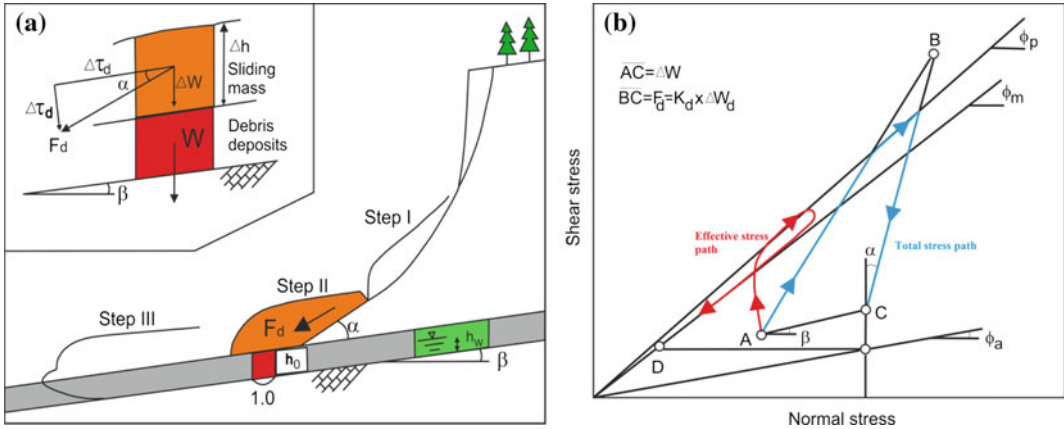


Fig. 9 Model for undrained loading of saturated deposits by a displaced mass (Sassa et al., 2004). **a** Illustration of the landslide triggered debris flow. **b** Stress path of debris deposit during loading. W represents the self-weight of the column of the debris deposit; ΔW the increment of the static stress due to self-weight of the sliding mass; α the

angle thrust between the slope and the debris bed; K_d dynamic coefficient ($F_d/\Delta W$); F_d dynamic stress; Δh : the thickness of sliding mass; h_0 : the thickness of torrent deposit and ϕ_p , ϕ_m , ϕ_a the peak, residual, and apparent friction angles, respectively

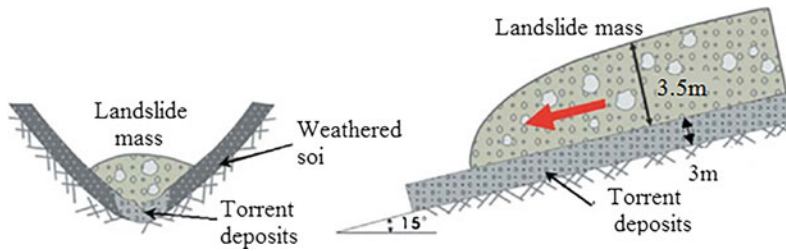


Fig. 10 Illustration of moving landslide mass along a torrent (Sassa et al. 2004)

4 Test Result

4.1 Undrained Monotonic Test

Undrained monotonic shear stress controlled tests were conducted under three different normal stresses. For each test, normal stress was increased to 50, 100 and 50 kPa (over consolidation = 2: normal stress was increased from 0 to 100 kPa and decreased to 50 kPa) with a rate of $\Delta\sigma = 0.5$ kPa/s in the drained condition. This corresponds to the landslide initiation in the field (Fig. 11).

Combined stress path graph on Midorii and Yagi sample were shown in Fig. 12. Combined shear displacement and shear resistance on

Midorii and Yagi sample were shown in Fig. 13. Three tests overlapped along the failure line during motion at 41.20 (Midorii) and 37.50 (Yagi). Shear displacement at start of strength reduction was 3.5–8 mm (Midorii) and 7–10 mm (Yagi). Shear displacement at start of steady state was 80–300 mm (Midorii) and 200–300 mm (Yagi). All test results was used to simulate the initiation and motion of Hiroshima landslides using the LS-RAPID.

4.2 Undrained Dynamic Loading Test

To examine the model in Figs. 9 and 10 for Hiroshima landslides, Midorii sample was used to simulate landslide triggered debris flow. The

Fig. 11 Combined stress path graph on Midorii (a) and Yagi (b) sample

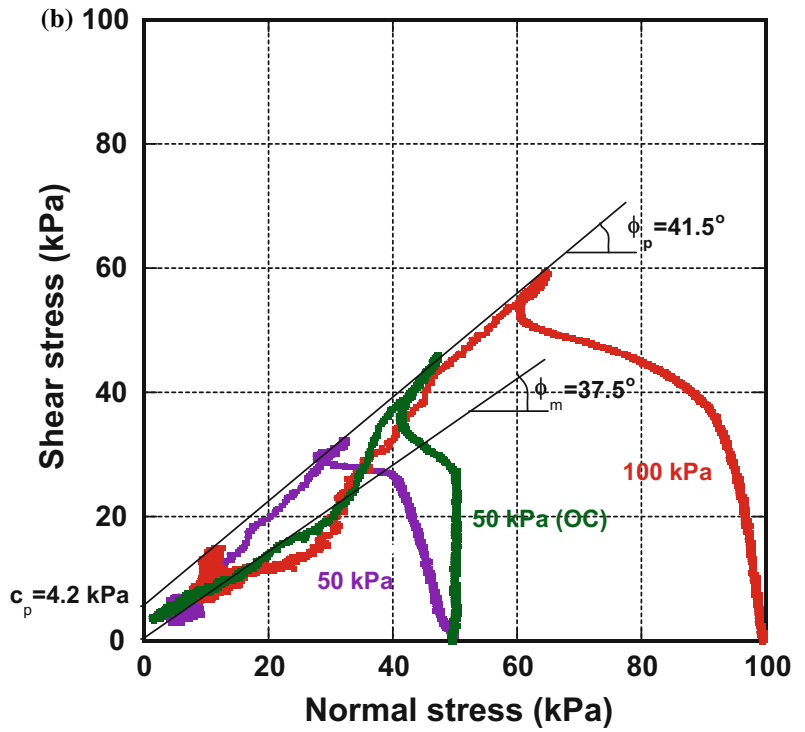
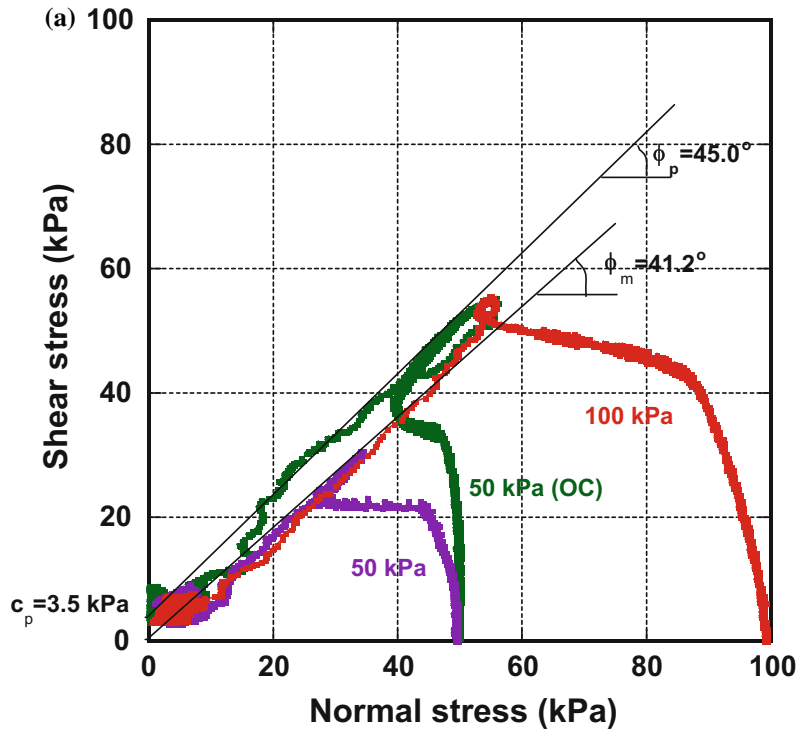
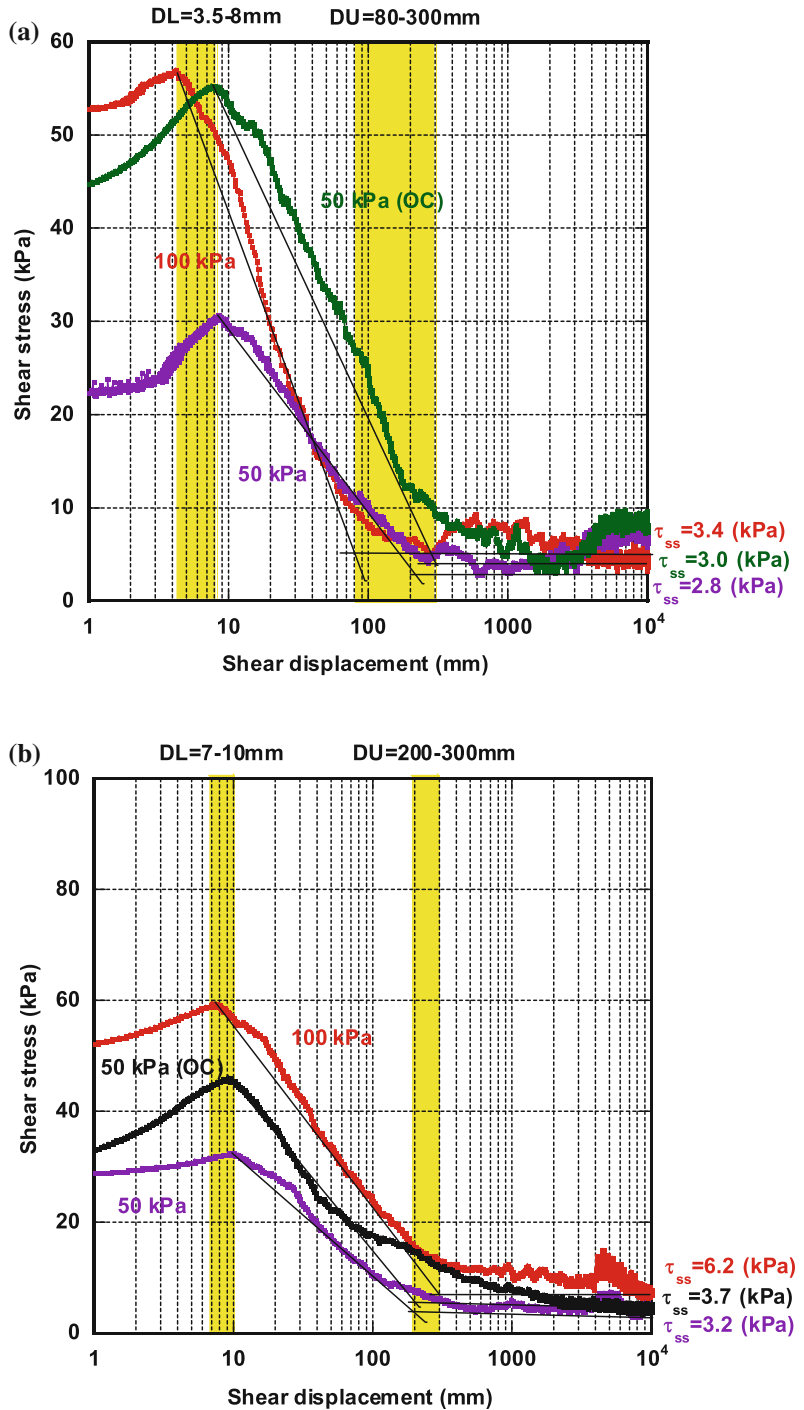


Fig. 12 Shear displacement and shear resistance path graph on Midorii (a) and Yagi (b) sample



test parameters were: $\Delta h = 3.5$ m, $h_0 = 3$ m, $\beta = 150$, $\alpha = 0^\circ$. The unit weight of Midorii sample was $\gamma = 20$ kN/m.

The initial stress due to W_o were $\sigma_o = 56$ kPa, $\tau_o = 15$ kPa, the increase of static loading due to ΔW of displaced mass were $\Delta\sigma_o = 66$ kPa, $\Delta\tau_o = 20$ kPa, and the

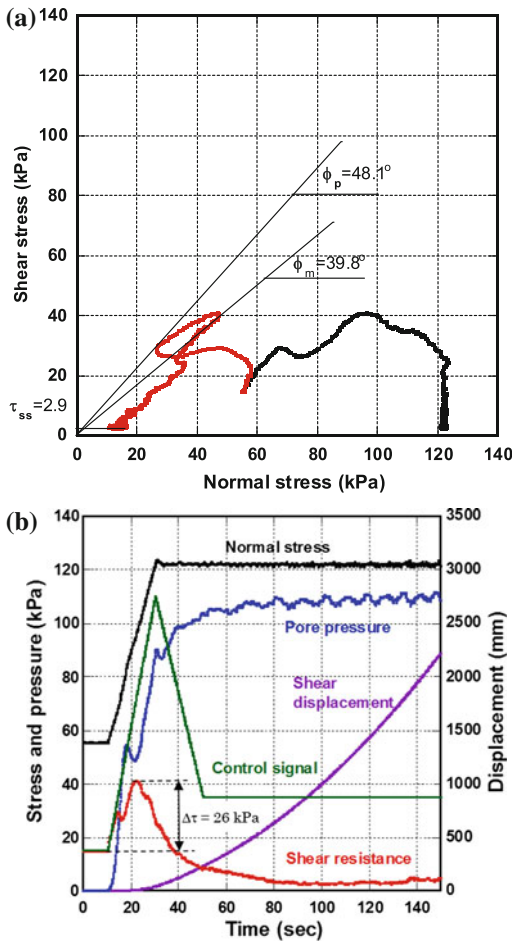


Fig. 13 Stress path (a) and time series data (b) of undrained dynamic loading test on Midorii sample

dynamic stresses caused by displaced mass were assumed to be $\sigma_d = 0$ kPa, $\tau_d = 75$ kPa. The slide mass moves quickly, so the test was carried out under the undrained condition. The test result was shown in Fig. 13. When shear stress increases only 26 kPa, the torrent deposits will shear and move together with the original slide mass. The peak friction angle was 48.1° and the motion friction angle was 39.8° . The steady state shear resistance reached 2.9 kPa and the apparent friction angle at the steady state was 1.4° . Therefore, rapid motion could continue in a torrent bed steeper than 1.4° .

4.3 Pore-Water Pressure Control Test

Hiroshima landslides were triggered by heavy rainfall that can be simulated using ring shear apparatus. Firstly, the sample was saturated ($B_d = 0.99$), then consolidated to 50 kPa normal stress and 15 kPa shear stress in a drained condition. This preparatory stage was to reproduce the initial stress in the slope, and is shown as a black line in Fig. 14a.

In order to simulate the pore-pressure induced landslide process, the pore-water pressure was gradually increased at a rate of $\Delta u = 0.02$ kPa/s up to 30 kPa, however, landslide did not occur.

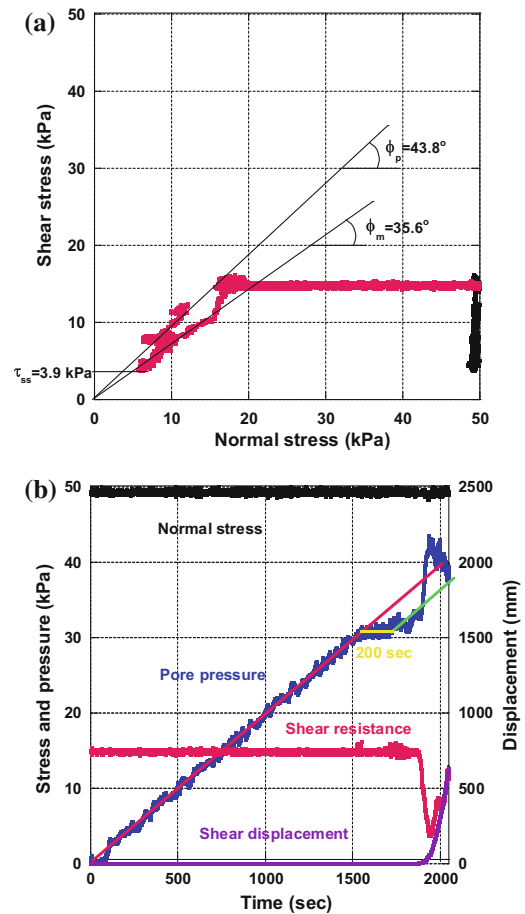


Fig. 14 Stress path (a) and time series data (b) of pore water pressure test on Yagi sample

After 200 s, pore-water pressure was increased to 40 kPa at the same rate. Failure occurred at a pore-water pressure of 32 kPa. The peak friction angle was 43.8° and the motion friction angle was 35.6°. The steady state shear resistance reached 3.9 kPa.

5 Application of LS-RAPID and SLIDE Model to the 2014 Hiroshima Landslide

5.1 Integrated Simulation Model (LS-RAPID)

LS-RAPID is a new integrated computer model that can be simulated the initiation and motion of a landslide using soil parameter obtained from ring shear apparatus. This simulation model LS-RAPID was developed from the geotechnical model for the motion of landslides (Sassa 1988) and its improved simulation model and new knowledge obtained from a new dynamic loading ring shear apparatus (Sassa et al. 2004). The basic concept of LS-RAPID is illustrated in

Fig. 15. The detail information of LS-RAPID was described in TXT-tool 3.081-1.2.

5.2 SLIDE Model

Landslide often occurs in the rainy season. To simulate the landslides caused by rainfall, pore-water pressure needs to be calculated. Based on the research of Montarasio and Valentino (2008) and Liao et al. (2010), the SLIDE model can be calculated pore water pressure from rainfall intensity (Fig. 16).

According to Liao et al. (2010) pore pressure rise (ΔU) is expressed by equation:

$$\Delta U = m \cdot H \cdot \gamma_n \cdot \cos^2 \beta$$

And, changes in the ratio of groundwater layer to the soil layer pressure (m) is calculated by equation

$$\begin{cases} m_1 = 0 \\ O_t = K_r \cdot \sin \beta \cdot m_t \cdot H \cdot \cos \beta \cdot \Delta t \\ \Delta m_t = \frac{(I_t - O_t)}{n \cdot H \cdot (1 - S_r)} \\ m_{t+1} = m_t + \Delta m_t \end{cases}$$

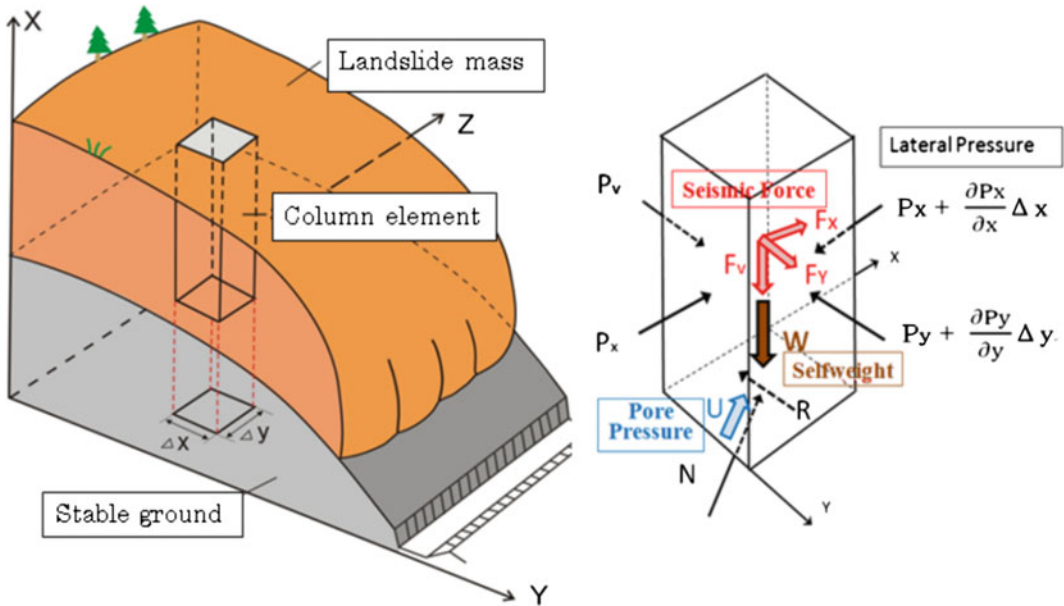
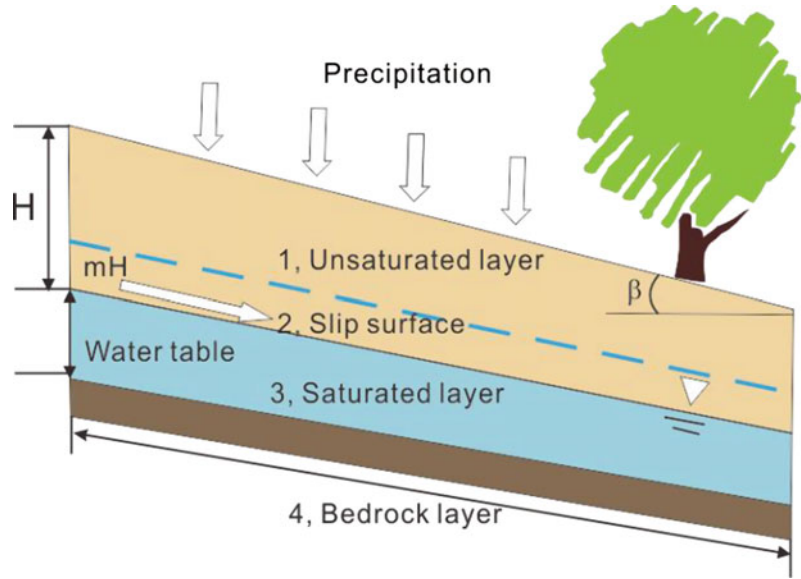


Fig. 15 Concept of landslide simulation model (Sassa et al. 2010)

Fig. 16 Schematic illustrating the water infiltration the infinite slope (from Liao et al. 2010)



where t is time, Δt is time interval, m_1 is initial value of m , and mt is calculated at each time-step. O_t represents the water outlet of a finite portion of a slope of finite length L . It is rainfall intensity, and Kt is the significance of a global drainage capability due to both the intrinsic soil permeability and the presence of numerous preferential down-flow ways, H is Landslide depth, n is Porosity; β is Slope angle; S_r is degree of saturation.

Figure 17 presents the result with rainfall data from Miiri station. From this result, Hiroshima landslide occurred when pore-water pressure increased up to 15 kPa. The maximum pore-water pressure is 21.5 kPa. The total unit weight of nearly saturated of the soil layer is 18.5 kN/m³, $H = 4$ m, and $\beta = 30^\circ$. Excess pore-water pressure ratio was expressed as:

$$r_u = u/\sigma$$

The excess pore-water pressure ratio when landslide occurred was calculated approximately as $r_u = 15/(4 \times 18.5 \times \cos^2 30) = 0.27$.

The maximum of excess pore-water ratio as: $r_u = 21.5/(4 \times 18.5 \times \cos^2 30) = 0.39$.

5.3 Application of LS-RAPID Model to the 2014 Hiroshima Landslide

Triggering factor

The 2014 Hiroshima landslides were triggered by heavy rainfall in Hiroshima. This was calculated by using the SLIDE model.

Landslide dynamics parameters

The parameters used in the computer simulation are listed in Table 1.

1. Steady-state shear resistance: 3.2 in the landslide source in Yagi area and 3.0 kPa in Midorii area based on the undrained monotonic stress control test results at normal stress of 50 kPa; 2.9 in landslide moving area (debris flow area) based on undrained dynamic loading test)
2. Friction angle during motion: 41.2° and 37.5° from the combined undrained monotonic stress control tests on Midorii and Yagi samples.

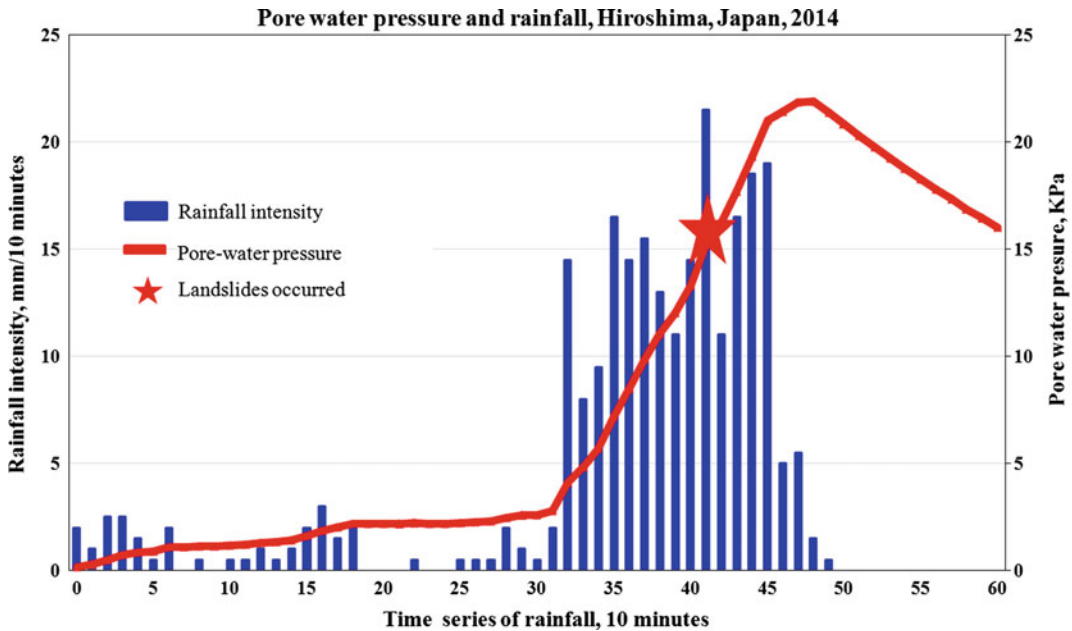


Fig. 17 Pore pressure calculation by the SLIDE model (Liao et al. 2010) from the rainfall record monitored at the Miiri JMA station for each 10 min from 8:30 PM on 19 August 2014

3. Peak friction angle: 46.5° in Yagi area and 45.0° in Midorii area based on control series of tests.
 4. Critical shear displacements for start of strength reduction (DL): 5 and 8 mm for Midorii and Yagi area from the shear resistance and shear displacement relationship for Midorii and Yagi sample.
 5. Critical shear displacements for start of steady state (DU): 200 mm for both Yagi and Midorii area from the shear resistance and shear displacement relationship for Midorii and Yagi sample.
 6. Pore-pressure generation rate Bss: 0.2–0.95 (assumed).
 7. Lateral pressure ratio k: 0.7–0.9 (assumed).
 8. Unit weight of soils: 18 kN/m³, estimated from consolidation of sample and saturated and dry unit weight of Yagi and Midorii sample.
- At 3 h 21 m 04 s, landslides occurred in the top of Yagi district (Yagi-1)
 At 3 h 21 m 53 s, Yagi-1 and Yagi-2 flowed together to residential areas.
 At 3 h 23 m 03 s, the displacement mass reached residential areas in Yagi district.
 At 3 h 44 m 22 s, failure occurred in the central of Midorii (Midorii-2).
 At 3 h 54 m 45 s, failure occurred in the other part of Midorii district (Midorii-3).
 At 4 h 01 m 25 s, two landslides in Midorii district (Midorii- 2, -3) flowed into the residential area.
 At 4 h 13 m 50 s, Midorii-3 and Yagi-3 started to move.
 At 4 h 15 m 29 s, the landslide mass stopped moving
 Landslide development process in Yagi-1 and Yagi-2 are shown in Fig. 19.

The simulation results are presented in Fig. 18:

Red colour balls represent the moving mass, while blue balls represent the stable mass (Fig. 19).

At 3 h 18 m 00 s, the pore-water pressure reached 15.2 kPa, landslide started in Yagi-1.

At 3 h 21 m 21 s, Yagi-1 reached to the toe of Yagi-2 and the toe of Yagi-2 failed. This process was very interesting because landslide occurred from toe to top of Yagi-2.

Table 1 Parameters used in LS-RAPID simulation

Parameters	Value	Source
<i>Parameters of soils in the Yagi area</i>		
Steady state shear resistance (τ_{ss} , kPa)	3.2/2.9	Test data
Lateral pressure ratio ($k = \sigma_h/\sigma_v$)	0.5–0.95	Estimation
Friction angle at peak (ϕ_p , degree)	44.0	Test data
Cohesion at peak (c , kPa)	0.5–1.0	Test data
Friction angle during motion (ϕ_m , degree)	37.5	Test data
Shear displacement at the start of strength reduction (DL, mm)	5	Test data
Shear displacement at the start of steady state (DU, mm)	200	Test data
Pore pressure generation rate (Bss)	0.2–0.95	Estimated
Total unit weight of the mass (γ_t , kN/m ³)	18	Test data
Specific gravity (G_s , g/cm ³)	2.64	Test data
Porosity (n)	0.44	Test data
Degree of saturation (S_r , %)	0.82	Estimated
Permeability (K_t , m/s)	0.001	Estimated
<i>Parameters of soils in the Midorii area</i>		
Steady state shear resistance (τ_{ss} , kPa)	3.0	Test data
Lateral pressure ratio ($k = \sigma_h/\sigma_v$)	0.2–0.95	Estimation
Friction angle at peak (ϕ_p , %)	36.0–44.0	Test data
Cohesion at peak (c , kPa)	0.5–1.0	Test data
Friction angle during motion (ϕ_m , degree)	37.5	Test data
Shear displacement at the start of strength reduction (DL, mm)	5	Test data
Shear displacement at the start of steady state (DU, mm)	200	Test data
Pore pressure generation rate (Bss)	0.2–0.95	Estimated
Total unit weight of the mass (γ_t , kN/m ³)	18	Test data
Specific gravity (G_s , g/cm ³)	2.68	Test data
Porosity (n)	0.44	Test data
Degree of saturation (S_r , %)	0.82	Estimated
Permeability (K_t , m/s)	0.001	Estimated
<i>Triggering factor</i>		
Excess pore pressure ratio in the fractured zone (r_u)	0.03–0.4	Calculated from SLIDE model
<i>Other parameters</i>		
Slope angle (θ , degree)	30	Investigated
Landslide depth (H, m)	4	Investigated
Unit weight of water (γ_w , N/m ³)	9.8	Normal value
Rainfall intensity (I_t , mm/10 min)	0–21.5	Monitoring

At 3 h 21 m 25 s, The whole Yagi-2 moved.

At 3 h 21 m 37 s, he combined mass of Yagi-1 and Yagi-2 flowed down to residential areas.

3D view of landslide deposits by LS-RAPID, LP data analysis (Air-borne Laser Profiler: LIDAR) and Air photo interpretation by GSI

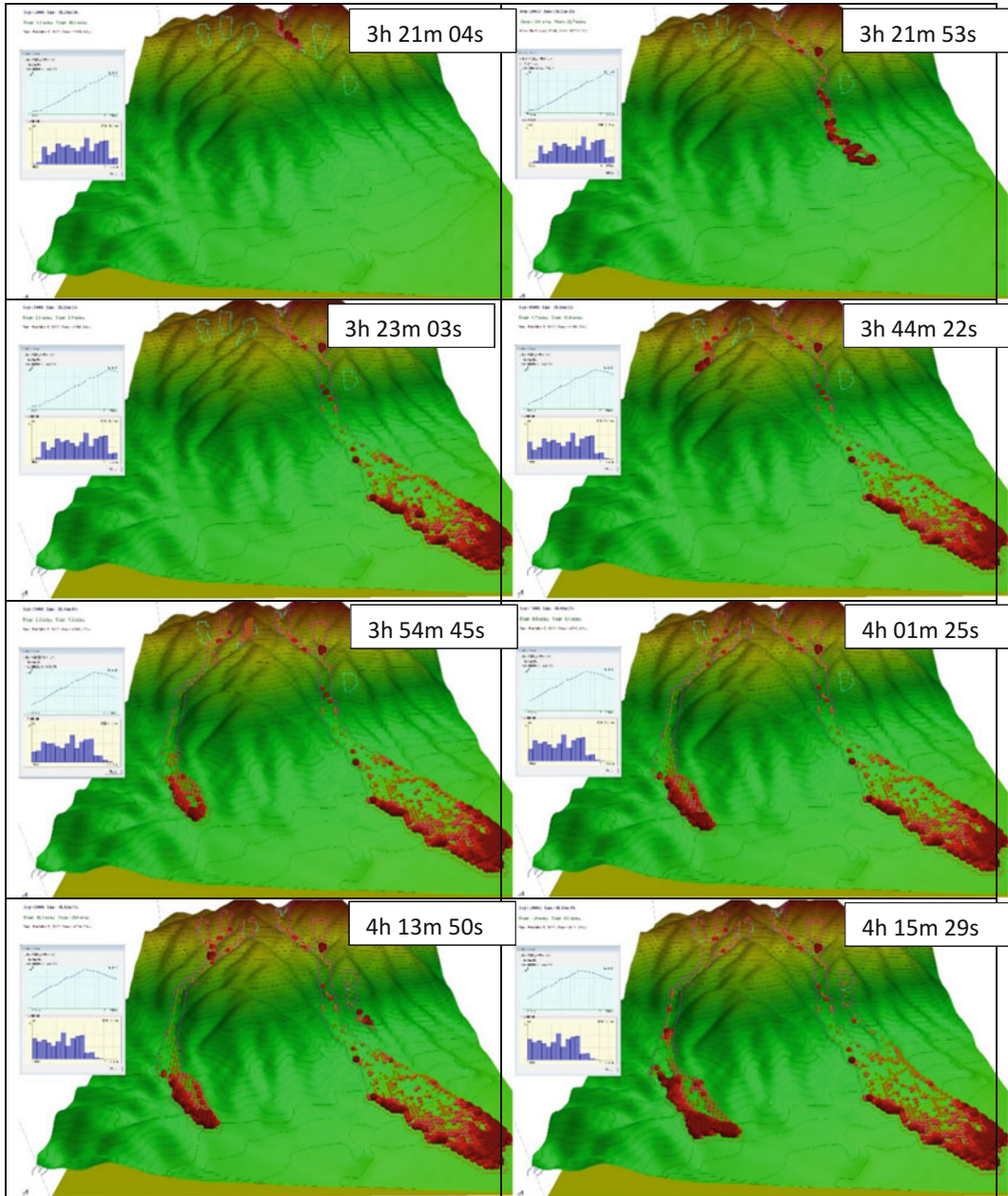


Fig. 18 Simulation result of Hiroshima landslide using LS-RAPID

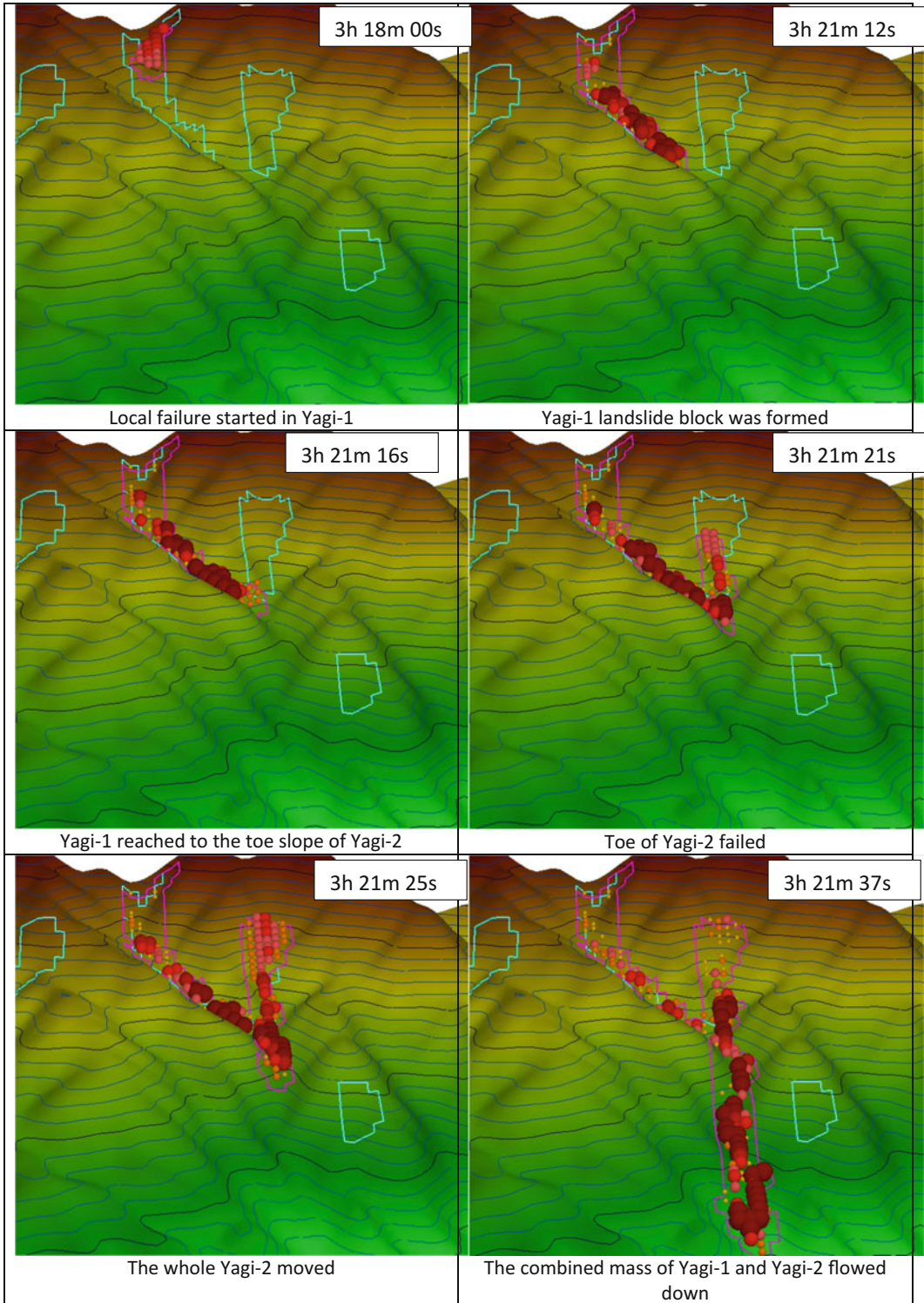


Fig. 19 Landslide development process in Yagi-1 and Yagi-2 using LS-RAPID

were used to evaluate the LS-RAPID results (Fig. 20). The simulation results indicated a landslide hazard that were similar to those determined by the LP data and air photo interpretation

6 Conclusion

Landslide and debris flow have caused great disaster as Hiroshima case. The main objectives of this research are to study the initiation mechanism and motion behavior of the Hiroshima landslides triggered by heavy rainfall through laboratory testing using ring shear apparatus (ICL-1) and using an integrated simulation model (LS-RAPID) and the SLIDE model. This research gives an interpretation of landslide triggered debris flows and examines the influence of rainfall to triggers the landslide and debris flow.

From the ring shear test results and the Hiroshima landslide simulation using LS-RAPID, the conclusions can be described as follows:

1. The main factor of Hiroshima landslides is heavy rainfall in a short time. The maximum hourly precipitation was 101 mm at Mirii station.
2. Many landslides occurred in the weathered granites following heavy rains resulting in great numbers of casualties that have been recorded in Hiroshima region such as landslides in 1999 and 2014.
3. Landslide triggered debris flow plays a key role on the occurrence and motion of Hiroshima landslide disaster. This process can be reproduced using undrained dynamic loading test with ring shear apparatus. This results indicated only small increment of shear stress (26 kPa) due to the impact of displacement soil mass could result in debris flow with the generation of high pore-water pressure.
4. The most important parameter for landslide motion was steady state shear resistance. Because, the steady state shear resistance was very low (2.9–3.2 kPa at normal stress is 50 kPa), Hiroshima landslide and debris flow could travel several kilometres from their source, causing great number of casualties and properties.
5. The SLIDE model is simple model to calculate pore-water pressure from rainfall intensity that could be accepted for shallow landslide and debris flow.
6. In Hiroshima landslide, key parameters in landslide dynamic involve the steady state shear resistance (τ_{ss}), the critical shear displacement (DL, DU) and triggering factor of pore-water pressure were input into the integrated computer simulation model (LS-RAPID). The simulation results can present the initiation as a local failure in Midorii and Yagi; and then present the motion of landslide mass and the distribution of deposit area.
7. The LS-RAPID results indicated the landslides area that was similar to those determined by LP data analysis and Air photo interpretation by GSI. In addition, the time of landslide occurrence is closed with actual occurrence that was reported by Hiroshima city office.
8. Landslides in Yagi district occurred when pore-water pressure reached 15.2 kPa and landslides in Midorii occurred when pore-water pressure reached 16.2 kPa. Slope failure began from Yagi-1 at 3h18m00s and rainfall still continued that caused landslides in Yagi-2,3 and Midorii-1,2,3.

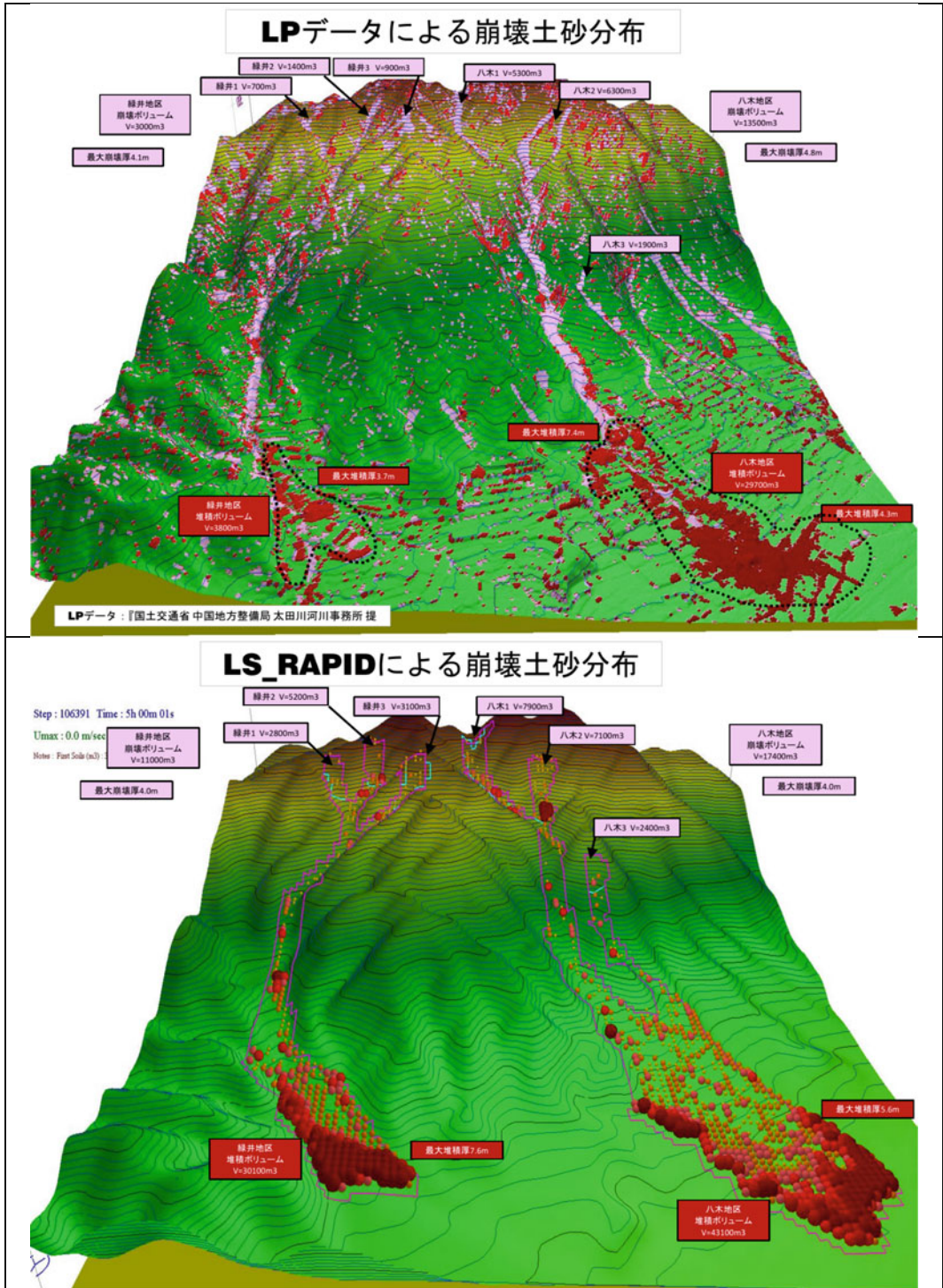


Fig. 20 Landslide soil distribution by the comparison between the LP-Data (Air-borne Laser Profiler: LIDAR) provided by MLIT and LS-RAPID simulation

References

- Jovančević S, Nagai O, Sassa K, Arbanas Z (2014) Deterministic landslide susceptibility analyses using LS-Rapid software. In: The first regional symposium on landslides in Adrian-Balkan Region, pp 73–77
- Liao Z, Hong Y, Wang J, Fukuoka H, Sassa K, Karnawati D, Fathani F (2010) Prototyping an experimental early warning system for rainfall-induced landslides in Indonesia using satellite remote sensing and geospatial datasets. *Landslides* 7(3):317–324
- Liao Z, Hong Y, Kirschbaum D, Liu C (2012) Assessment of shallow landslides from Hurricane Mitch in central America using a physically based model. *Environ Earth Sci* 55:1697–1705
- Montarasio L, Valentino R (2008) A model for triggering mechanisms of shallow landslides. *Nat Hazards Earth Sci* 8:1149–1159
- Sassa K, Fukuoka H, Scarascia-Mugnozza G (1996) Earthquake-induced-landslides: distribution, motion and mechanism. Special issue of soils and foundation, *Jpn Geotech Soc*, 53–64
- Sassa K, Fukuoka H, Wang G, Ishikawa N (2004) Undrained dynamic-loading ring-shear apparatus and its application to landslide dynamics. *Landslides* 1(1):7–19
- Sassa K, Nagai O, Solidum R, Yamazaki Y, Ohta H (2010) An integrated model simulating the initiation and motion of earthquake and rain induced rapid landslides and its application to the 2006 Leyte landslide. *Landslides* 7(3):219–236
- Sassa K, Nagai O, He B, Gradiski K (2013) PDF-tool 3.081-1.2 manual for the LS-RAPID software. ICL landslide teaching tools, p 363, 43 p (pdf) in the attached CD
- Sassa K, Dang K, He B, Takara K, Inoue K, Nagai O (2014a) Development of a new high-stress undrained ring shear apparatus and its application to the 1792 Unzen-Mayuyama megaslide in Japan. *Landslide* 11(5):827–842
- Sassa K, He B, Dang K, Nagai O, Takara K (2014b) Plenary: progress in landslide dynamics. In: Sassa K, Canuti P, Yin Y (eds) *Landslide science for a safer geoenvironment*, vol 1, pp 37–67

TXT-tool 3.385-1.2

Deterministic Landslide Susceptibility Analyses Using LS-Rapid Software

Sanja Dugonjić Jovančević, Osamu Nagai, Kyoji Sassa
and Željko Arbanas

Abstract

This paper presents the landslide susceptibility analyses on flysch slopes in Istra, Croatia, performed using deterministic three dimensional analyses in LS-Rapid software. The area of investigation is in the Pazin Paleogene Flysch Basin in the northeastern part of the Istrian Peninsula. Using deterministic approach in landslide hazard and risk analysis includes gathering of fundamental data about geometry, soil strength parameters, cover thickness and groundwater level, as well as the application of numerical models in safety factor calculation. LS-Rapid uses 3D models for simulation of progressive failure phenomena, developed to assess the sliding initiation and activation of landslides triggered by earthquake, rainfall or their combination. Detail distribution of pore pressures or the groundwater level inside the slope is taken into account through the pore pressure ratio r_u , which gradually increases until the failure appears in a certain part of the slope. If this approach is applied on the wider area, in which it is possible to define the relative position of the sliding surface, it is possible to obtain the values of the critical pore pressure ratio that causes conditions in which failures occur in specific parts of the investigation area. Connecting the critical pore pressure ratio with distribution of rainfall it is possible to obtain the landslide susceptibility and landslide hazard. The model was validated through the interpretation of stereopairs and engineering geological mapping, and the results have shown that landslides inside the zones in the model that were characterized as highly susceptible, occurred in the nearest of farthest past.

S. Dugonjić Jovančević (✉) · Ž. Arbanas
Department of Geotechnics, Faculty of Civil
Engineering, University of Rijeka, Radmile
Matejčić, No. 3, 51000 Rijeka, Croatia
e-mail: sanja.dugonjic.jovancevic@uniri.hr

Ž. Arbanas
e-mail: zeljko.arbanas@uniri.hr

O. Nagai · K. Sassa
International Consortium on Landslides, Kyoto
University Uji-Campus, Kyoto, Japan
e-mail: evrwell@gmail.com

K. Sassa
e-mail: sassa@iclhq.org

Keywords

Landslide susceptibility · Deterministic analyses · LS-Rapid
Triggering factor · Pore pressure ratio

Contents

1	Introduction	170
2	Deterministic Approach in Landslide Hazard and Risk Analyses	171
3	Application of LS-Rapid Software on the Investigation Area in Istria, Croatia	172
3.1	Theoretical Background of LS-Rapid Software	172
3.2	General Features of the Analysed Area Around City of Buzet	172
3.3	Characteristics of the Performed LS-Rapid Model.....	173
4	Results of the Performed Analyses	176
5	Conclusion	178
	References	178

1 Introduction

There are no significant analyses in the area of landslide susceptibility and landslide hazard assessment in Croatia at regional scale, although they can be significant in land use management. Landslide susceptibility zonation and hazard mapping of the investigation areas were some of the key objectives within the Working Group 3 inside the Japanese-Croatian Project “Risk Identification and Land-Use Planning for Disaster Mitigation of Landslides and Floods in Croatia”. Landslide susceptibility is function of the present slope stability (expressed through the safety factor), together with the existence and activity of triggering factors which cause an increase in active forces or reduction in strength and, consequently, landslide activation.

Deterministic approach, using LS-Rapid software has been applied on the flysch area in Istria, Croatia. This area is in the Pazin Paleogene Flysch Basin in the north-eastern part of the Istrian Peninsula which stretches from Trieste

Bay in the west to the Učka Mountain in the east (Fig. 1). This area is formed of flysch units and, because of their grey colour, is called Grey Istria. Types of landslides that generally occurred in the area are rotational and translational type landslides, as well as rock falls and debris flows.

According to the well-known and widely applied principle “The past and the present are keys to the future” (Varnes 1984; Carrara et al. 1995), it is assumed that new landslide occurrences on the flysch slopes will appear in morphological, geological, hydrogeological and geotechnical conditions that are similar to the conditions of recent landslide occurrences (Dugonjić et al. 2008; Dugonjić Jovančević and Arbanas 2012).

From the previous investigations performed in the flysch area of Grey Istria, conditions that predispose future landslides on flysch slopes can be listed as follows: (1) geological conditions in which the clayey superficial deposit is present over the flysch bedrock on a slope with suitable inclination and kinematic conditions for sliding; (2) conditions that allow the admission of a corresponding amount of water from higher parts of the slope; (3) conditions in which the inclination of the almost-impermeable flysch bedrock retaining the groundwater at the location or in the direction where the groundwater flows is close to the slope inclination; and (4) conditions in which the slope is exposed to a sufficiently long, continuous period of rainfall with corresponding infiltration. The fourth condition is the main triggering factor for the activation of landslides on the flysch slopes of Grey Istria, and is important to landslide susceptibility and hazards assessment as well as mitigation measures and risk management (Dugonjić Jovančević and Arbanas 2012). Influence of the relief can be seen

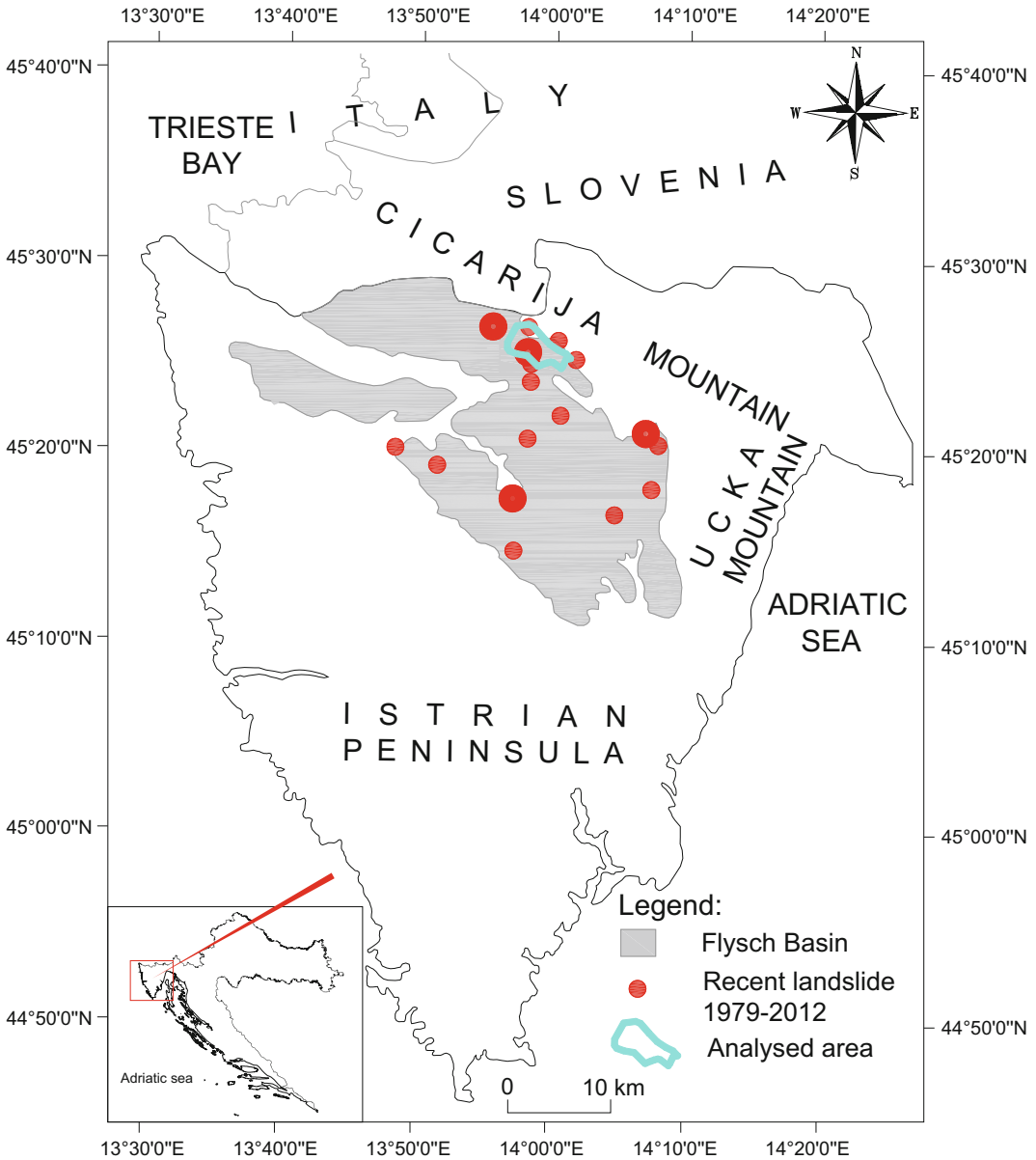


Fig. 1 Simplified map of the Istrian Peninsula with the position of the area around the City of Buzet analysed in LS-Rapid software

in the Čićarija and Učka Mountain area (1401 m a.s.l.), where due to the higher elevations, the precipitation values are high (mean annual precipitation up to 2000 mm). Therefore, landslides in grey Istria are usually caused by heavy rainfall and/or human activity while others factors, such as snow melting and earthquakes, cannot be considered significant.

2 Deterministic Approach in Landslide Hazard and Risk Analyses

The use of deterministic models in landslide hazard analyses has not been the pretention to calculate in an absolute and precise way the safety

factor at each site in the terrain. The high spatial variability of geotechnical parameters is serious limitation of this model. The final stage in deterministic landslide hazard zonation consists of the calculation of failure probability maps to convert factor of safety maps into failure probability maps.

Using deterministic approach in landslide hazard and risk analysis includes gathering of fundamental data about geometry, soil strength parameters, cover thickness and groundwater level, as well as the application of numerical models in safety factor calculation. Such an approach is often used in geotechnical engineering in slope stability analysis for common engineering problems. Most common is the one-dimensional deterministic model, and one of the mostly used methods inside its framework is stability analysis of infinite slope. Accuracy and reliability of safety factor calculation in each model are defined by the level of field investigations at the location, accuracy of the input data and understanding of the stress history. Detailed study of the whole area can give relatively accurate input parameters for the model, but is hard and demanding work. In some cases, heterogeneous areas are simplified and the gained input parameters are extrapolated to a wider area than the investigated location. These are basic limitations of the deterministic model.

Use of Geographic Information System (GIS) can facilitate deterministic as well as probabilistic geotechnical approach, as part of landslide hazard assessment methodology. However, high accuracy in data preview inside GIS cannot replace high impropriety in the assessment of the failure probability which is result of the wrong selection of the geotechnical model or inappropriate failure mechanism. Two dimensional and three dimensional deterministic analyses currently cannot be performed inside GIS, yet the data are being exported in some external software for 2D and 3D slope stability analyses and then restored in GIS as a results preview tool. That is applicable on a very small investigation area with huge amount of available information, where the data conversion between software presents the highest challenge.

3 Application of LS-Rapid Software on the Investigation Area in Istria, Croatia

3.1 Theoretical Background of LS-Rapid Software

LS-Rapid software uses three dimensional models for simulation of the progressive failure phenomena, developed to assess the sliding initiation and activation of landslides triggered by earthquake, rainfall or their combination. LS-Rapid aims to combine the process of landslide initiation and process of sliding mass movement (dynamic analysis), including the process of the sliding mass volume enlargement on the sliding path (Sassa et al. 2010). This model is based on the key parameter—shear resistance in the steady state which can be measured or established by soil laboratory testing. The software offers the recommended values for the input parameters in case when no detail data of the investigation area are available. The basic concept of simulation is based on the analysis of the forces acting on a vertical column inside the moving mass (Fig. 2).

Increase in pore pressure during the rainfall affects the development of the sliding surface and initiation of the landslide. In similar way it is possible to use LS-Rapid in seismic analyses to establish landslide susceptibility and landslide hazard caused by earthquake motions.

3.2 General Features of the Analysed Area Around City of Buzet

Landslides in Grey Istria usually occur on the contact of the bedrock and colluvial soil deposit. This layer is product of soil formed in various mechanical processes of bedrock weathering. The instabilities are usually caused by heavy rainfall and/or human activity that significantly change the slope geometry and/or assists in leading and retaining surface water in the sliding zone (Arbanas et al. 2007).

The geological fabric of Istria today is a result of repeated tectonic deformations from the Cretaceous in addition to the intensive processes of

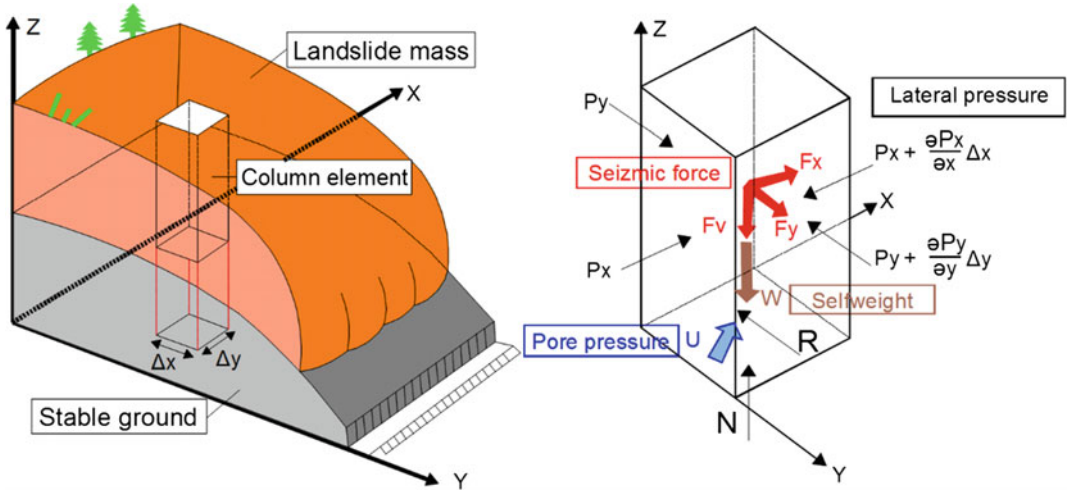


Fig. 2 Column element inside the moving landslide mass (Sassa et al. 2010)

erosion and accumulation. Sediments have nearly subhorizontal layers, except for the contacts with the Čićarija Mountain range in the northeast and the Učka Mountain in the east, where the flysch rock mass was significantly deformed during tectonic activities (Dugonjić Jovančević and Arbanas 2012).

In a typical situation, the flysch bedrock is covered by quaternary deposits, except the isolated areas where the erosion is more expressed. This is particularly evident on the southwestern margin of the Čićarija Mountain, at the foot of the cliffs, where the coarse-grained fragments have mixed with the silty clay materials from the flysch rock mass weathering zone (Arbanas et al. 2006). Two zones of different hydraulic conductivity can be recognized in the geological profile: the clayey and silty superficial deposit with low hydraulic conductivity and the fresh rock mass in the flysch bedrock, which can be considered to be completely impermeable. Systems of vertical fissures and joints in marls and sandstones allow easy infiltration and flow of groundwater from the upper part of the slope. Deeper, slightly weathered and fresh siltstone layers act as watertight zones, causing the draining of groundwater along the fissure-joint system running down the slope. After long rainy periods, the joint system cannot completely drain the infiltrated water, resulting in the rise of the groundwater level in the vertical joints

and a subsequent increase in pore pressures (Arbanas et al. 2010; Dugonjić Jovančević and Arbanas 2012).

Geological profiles of the studied landslides mainly consist of flysch bedrock (of Paleogene age) covered by a clayey colluvium and/or residual soil. It appears that nearly all of the studied landslides were caused by a longer rainy period and water infiltration, which caused a rise in the groundwater level, a pore water pressure increase and a decrease in strength on the slip surface from total to effective values.

3.3 Characteristics of the Performed LS-Rapid Model

The three dimensional deterministic landslide susceptibility analysis, performed in LS-Rapid model, is based on the input parameters of the slope geometry, cover thickness, sliding surface position, and soil parameters. The depth of the potential failure surface and the groundwater table, the two main factors in landslide hazard zonation, are very difficult to map in the field. They were determined from the existing data collected during the investigation works performed for remedial work designs of few landslides in the area and extrapolated on the wider area.

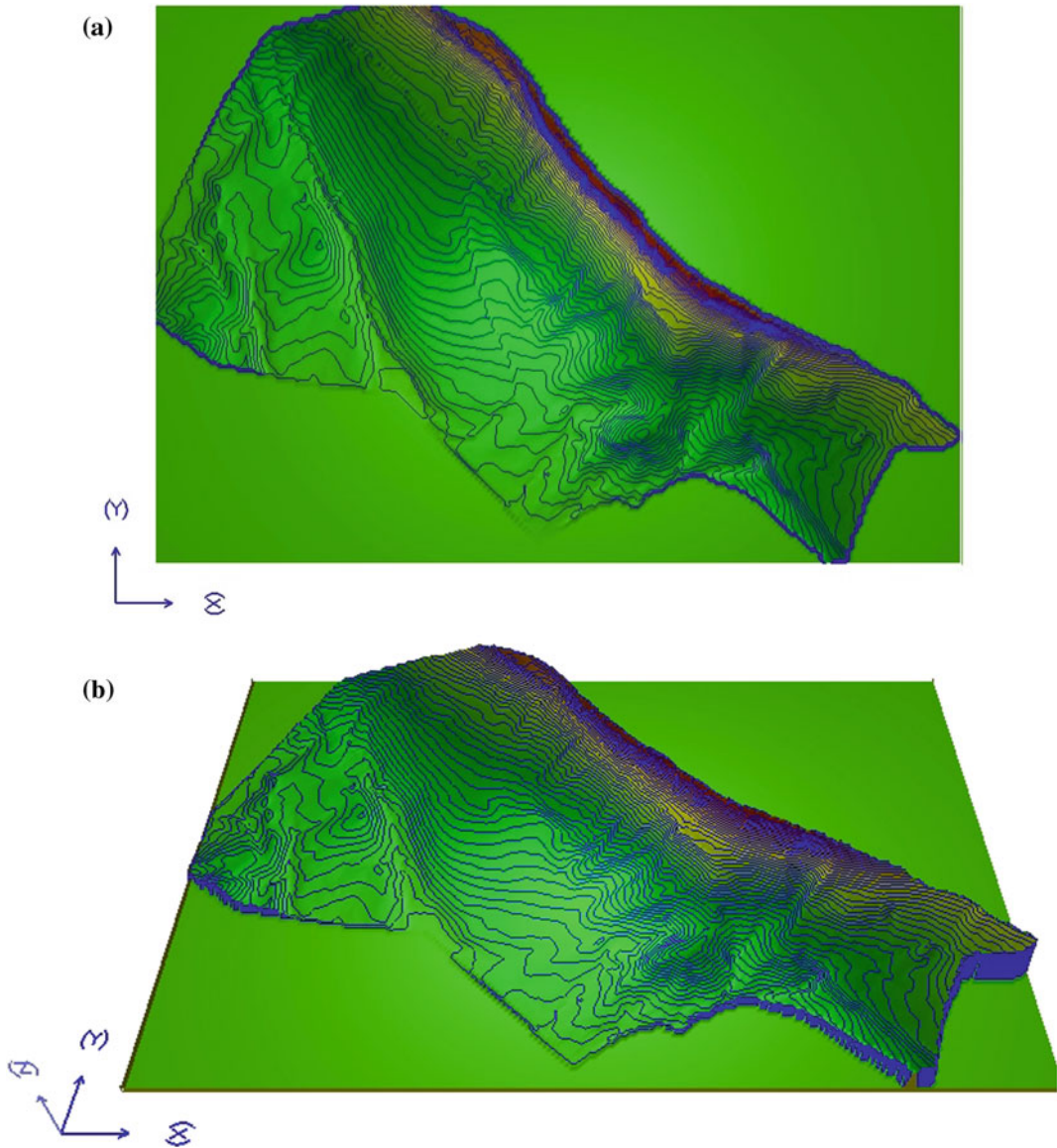


Fig. 3 Simulation model of Buzet area in LS-Rapid software (contours 10 m): **a** 2D view; **b** 3D view

The effect of earthquake on slope stability was not taken into account in this analysis since the area is not seismically active. Other triggering factors, such as snow melting and climate change were also not significant for this area. The main triggering factor of the past and present landslides in the area is rainfall. Rainfall is hydrological trigger which can be defined as decrease in shear strength on the potential sliding surface due to the increase in pore water pressure as result of rainfall infiltration and

percolation (Terlien 1996, 1998). Rainfall is more evident and instantaneous than other natural processes which act gradually and trough decades, as for example erosion. Daily amount of rainfall is an instant trigger while the antecedent rainfall involves the progressive weakening of materials. Combination of both factors gives the triggering threshold for landslides.

In the simulation model of the Buzet area (Fig. 3) soil strength parameters from the

performed 2D back stability analyses and some laboratory testing from the similar flysch locations were used. For the parameters with no investigation background, recommended values (Sassa et al. 2010) were used (Table 1).

Performed model covers the matrix 205×143 in x and y direction. The height of 50 m above the sea level has been given to the area outside the analysed polygon, because the model demands the rectangular mesh. Due to this reason all instability processes occurring on the polygon edges can be considered unreal and cannot be taken into account.

Some geological units (Fig. 4) inside the area (limestone and sandstones) have no cover thickness. There are no results of the stability analyses in these areas, because the possibility of sliding is negligible. Based on the former investigation works the average cover thickness is 10 m. According to the performed back stability analyses on landslides in the flysch area of

Gray Istria, the unit weight of mass is $\gamma = 20 \text{ kN/m}^3$, cohesion inside the mass $c_i = 3 \text{ kPa}$ and the cohesion at sliding surface during motion $c_m = 5 \text{ kPa}$. The friction angles are given also based on the back analyses.

Other parameters used values from the similar materials or recommended values (Table 1). Pore water pressure generation and the apparent friction angle are affected by the degree of saturation. Parameter of pore-pressure generation B_{ss} is defined in the undrained ring shear test ($B_{ss} = 1.0$ at full saturation, $B_{ss} = 0.0$ at dry state). The apparent friction angle $\varphi_a = \varphi_m$ in the dry state, φ_a is the lowest at full saturation and in between at partial saturation (Sassa et al. 2010). The rate of excess pore-pressure generation used in this analysis is $B_{ss} = 0.5$, and lateral pressure ratio is $k = 0.35$.

The pore pressure ratio r_u increases from 0.0 to 0.6 in the time period that is corresponding to 30 days. Pore pressure ratio is calculated as

Table 1 Values for soil parameters in LS-Rapid model: (*) after Sassa et al. (2010)

Item	Lower case (*)	Upper case (*)	Probable case (*)	Value used in the model
Friction angle during motion at sliding surface (φ_m) and coefficient ($\tan \varphi_m$)	25° ($\tan \varphi_m = 0.466$)	35° ($\tan \varphi_m = 0.700$)	30° ($\tan \varphi_m = 0.577$)	25°
Peak friction angle at sliding surface (φ_p) and coefficient ($\tan \varphi_p$)	33° ($\tan \varphi_p = 0.649$)	38° ($\tan \varphi_p = 0.781$)	35° ($\tan \varphi_p = 0.700$)	32°
Friction angle inside landslide mass (φ_i) and coefficient ($\tan \varphi_i$)	20° ($\tan \varphi_i = 0.364$)	30° ($\tan \varphi_i = 0.577$)	25° ($\tan \varphi_i = 0.466$)	28°
Steady state shear resistance at sliding surface (τ_{ss}) (kPa)	5	50	20	60
Cohesion inside mass (C_i) (kPa)	0.1	0.5	0.2	3
Cohesion at sliding surface during motion (C_m) (kPa)	0.1	0.5	0.2	5
Peak cohesion at sliding surface (C_p) (kPa)	2	200	10–100	10

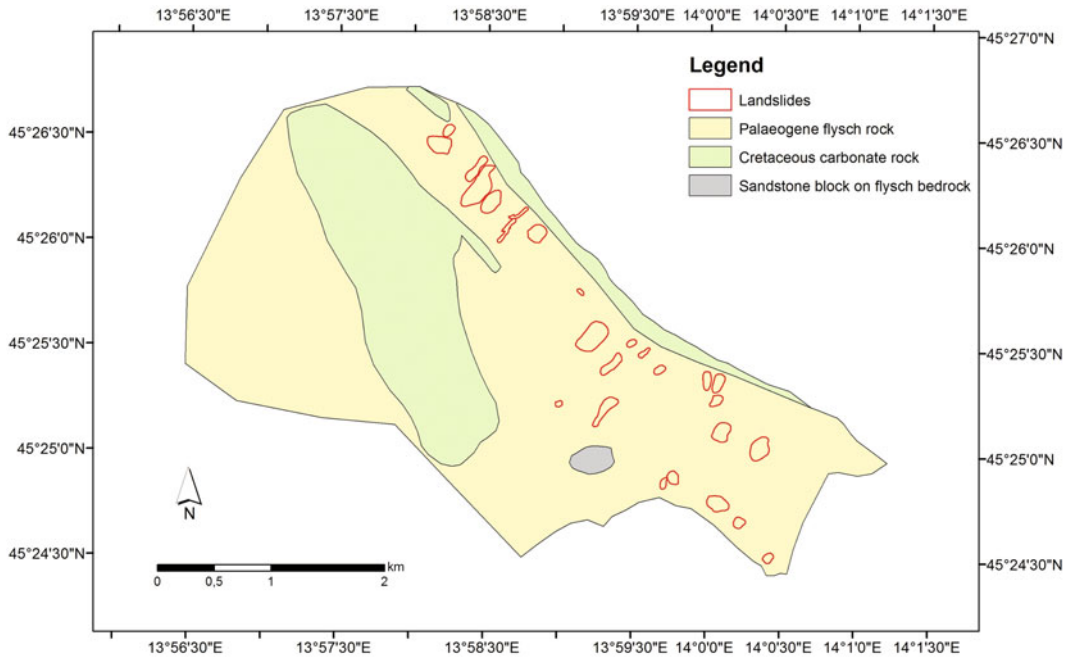


Fig. 4 Simplified lithological map of the analysed area

relation between pore pressure and the geostatic stress at specific depth. Value $r_u = 0.6$ is reached when complete superficial deposit is saturated and the groundwater level reaches the ground surface. The results have been set to calculate stability every 24 h inside 1-month period.

4 Results of the Performed Analyses

The gradual increase of the r_u and its influence on the 3D stability analyses are shown in Fig. 5. From the results of the analyses it can be seen that the r_u reaches the full value of 0.6 within the period of 9 days, after what its value remains constant. The stable areas are shown in blue colour, while the unstable, orange areas increase progressively due to the pore pressure increase and afterwards, when it remains constant ($r_u = 0.6$).

According to the deterministic model in LS-Rapid it can be concluded that critical area for the landslide appearance is the fault zone (Fig. 6) in the north-eastern part of the analysed area. Part of the terrain northeast from this critical zone is formed in the limestone rock mass of the Ćićarija Mountain range, where very steep, often vertical slope angles prevail, so the sliding in these zones can be excluded. Southwest from the critical zone considerably gentle slopes formed in flysch rock mass proceed. Sliding in these areas is occasional, but exists, what is also visible in the model.

Deterministic model performed in LS-Rapid provided the critical area for landslide occurrence which corresponds to the real conditions. Validation of the model was carried out by interpretation of stereopairs and engineering geological mapping (Fig. 6).

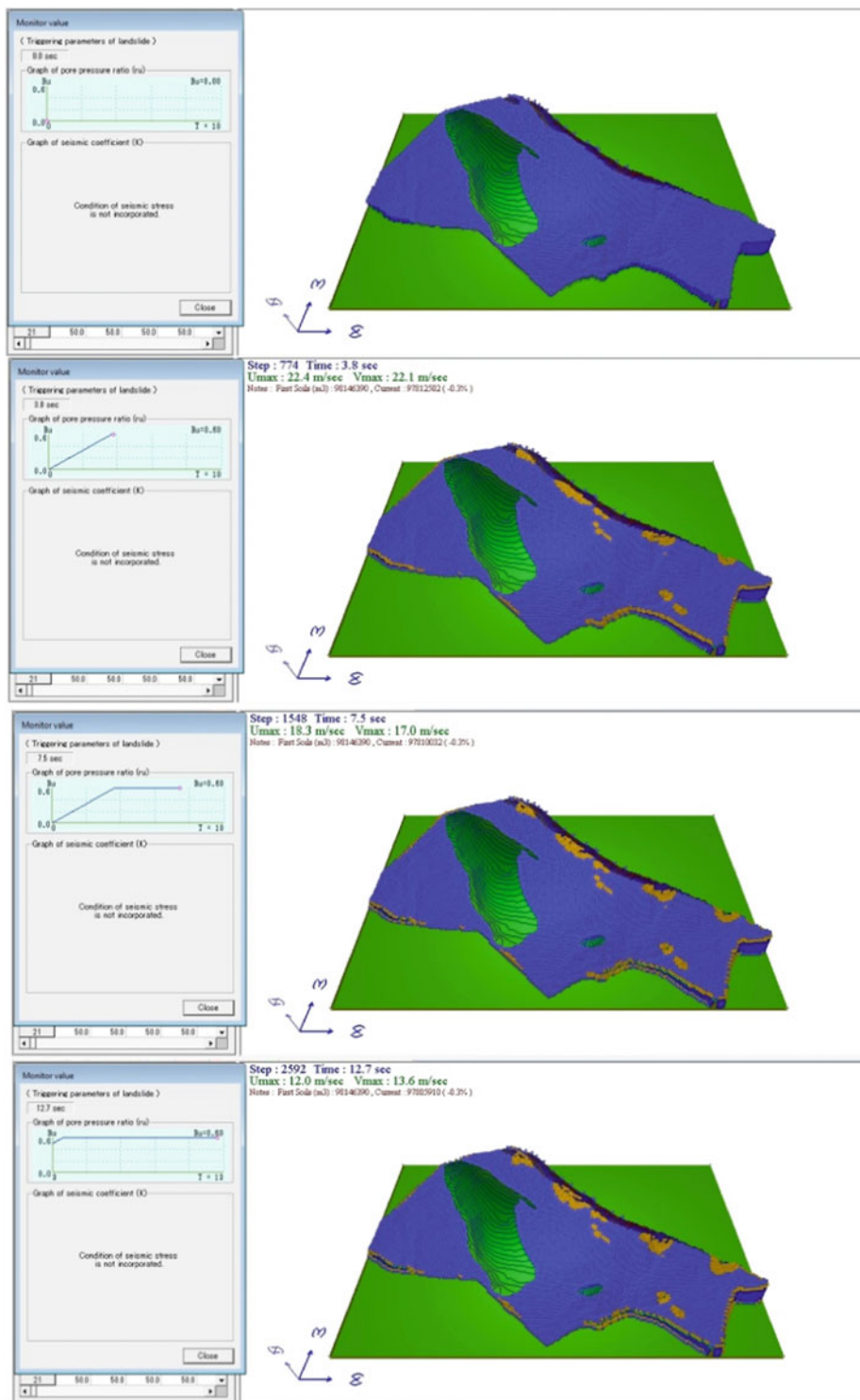


Fig. 5 Gradual increase of the pore pressure ratio (r_u) from value 0.0 to value 0.6 and its influence on the stability shown in LS-Rapid simulation model for landslide susceptibility in the Buzet area: *blue*-stable areas, *orange*-unstable areas

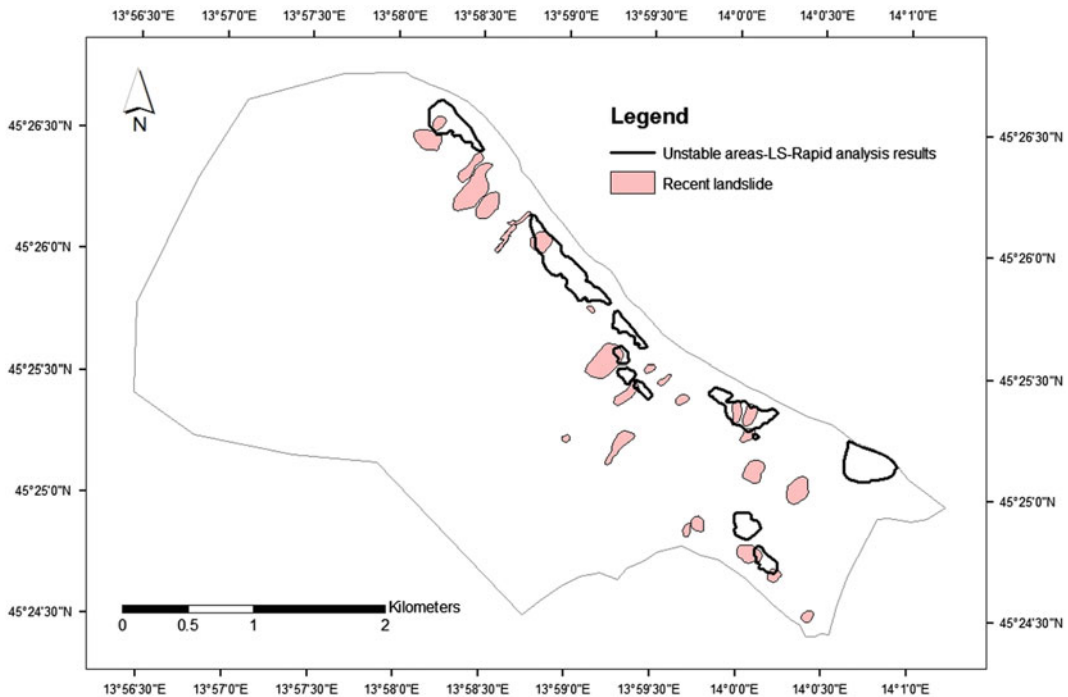


Fig. 6 Comparison of the deterministic analysis results and the recent landslides position in the analysed area around the City of Buzet

5 Conclusion

Validation of the performed deterministic analysis has shown that landslides which occurred in the nearest of farthest past, are inside the zones that are highly susceptible to sliding according to the LS-Rapid regional stability analysis. In other words, it can be concluded that results of the performed analyses confirmed that LS-Rapid, except for the detailed analysis of slope stability at one specific location, can also be used for the landslide susceptibility and hazard assessment in the wider area. The regional analysis unlike the analysis of one specific landslide location is less precise and more indicative, but the results have shown that LS-Rapid can be used as a powerful tool in deterministic analyses in landslide prediction, susceptibility and landslide hazard assessment.

Acknowledgements Equipment used in the study was obtained with financial support from the SATREPS [Science and Technology Research Partnership for

Sustainable Development] program, financed by the Japan Science and Technology Agency and Japan International Cooperation Agency through the Project Risk Identification and Land-Use Planning for Disaster Mitigation of Landslides and Floods in Croatia. This support is gratefully acknowledged. This work is an expanded version of the paper published and presented on the 1st Regional Symposium of Landslides in the Adriatic-Balkan Region and the 3rd Workshop of the Croatian-Japanese Project "Risk Identification and Land-Use Planning for Disaster Mitigation of Landslides and Floods in Croatia".

References

- Arbanas Ž, Benac Č, Jurak V (2006) Causes of debris flow formation in flysch area of North Istria, Croatia. In: Lorenzini G, Brebbia CA, Emmanouloudis DE (eds) Monitoring, simulation, prevention and remediation of dense and debris flows. WIT transaction on ecology and the environment, vol 90. WIT Press, Ashurst, pp 283–292
- Arbanas Ž, Grošić M, Goršić D, Griparić B (2007) Landslides remedial works on small roads of Istria. In: Raus B (ed) Proceedings of the 4th Croatian roads congress. Croatian Road Society-Via Vita, Zagreb, p 38

- Arbanas Ž, Mihalić S, Grošić M, Dugonjić S, Vivoda M (2010) Brus Landslide, translational block sliding in flysch rock mass. In: Rock mechanics in civil and environmental engineering. Proceedings of the European rock mechanics symposium. CRC Press, Balkema, pp 635–638
- Carrara A, Cardinali M, Guzzetti F, Reichenbach P (1995) GIS technology in mapping landslide hazard. In: Carrara A, Guzzetti F (eds) Geographical information systems in assessing natural hazards. Kluwer Academic Publishers, Dordrecht, pp 135–175
- Dugonjić S, Arbanas Ž, Benac Č (2008) Assessment of landslide hazard on flysch slopes. In: Proceedings of 5th Slovenian geotechnical symposium and 9. Šuklje's day, 12–14 June 2008, Nova Gorica, Slovenia, pp 263–272
- Dugonjić Jovančević S, Arbanas Ž (2012) Recent landslides on the Istrian Peninsula, Croatia. *Nat Hazards* 62(3):1323–1338
- Sassa K, Nagai O, Solidum R, Yamazaki Y, Ohta H (2010) An integrated model simulating the initiation and motion of earthquake and rain induced rapid landslides and its application to the 2006 Leyte landslide. *Landslides* 7(3):219–236
- Terlien MTJ (1996) Modelling spatial and temporal variations in rainfall-triggered landslides. ITC Publication, No. 32, Enschede, Netherlands, p 50
- Terlien MTJ (1998) The determination of statistical and deterministic hydrological landslide-triggering thresholds. *Environ Geol* 35(2–3):124–130
- Varnes DJ (1984) Landslide hazard zonation: a review of principles and practice, natural hazards, vol 3. UNESCO, Paris

TXT-tool 3.886-1.1

Debris2D Tutorial

Ko-Fei Liu and Ying-Hsin Wu

Abstract

The introduction of the Debris-2D program for two-dimensional debris flow simulation is presented. Debris-2D is one of the most used models in Taiwan, and it has been verified as a practical tool for debris flow assessment. The introduction focuses on the theoretical background, computational algorithm, program input and output data, and applications review. In the fundamental theory, debris flow is treated as a non-Newtonian fluid with a yield stress. For simulations, the input data includes initial mass distributions of debris flow and yield stress. Debris-2D can simulate and output flow depth, flow velocity, impact force, and affected area of time variation with high spatial and arbitrary temporal resolution. Some simulation results of real cases in Taiwan are described. These results show that Debris-2D is a practical and effective program for debris flow assessment.

Keywords

Debris-2D · Debris flow · Numerical simulation · Assessment

Contents

1	Introduction	182	2.2	Computational Algorithm	183
2	Introduction to the Debris-2D Program	182	2.3	Program Input	183
2.1	Theoretical Background	182	2.4	Program Output	184
			3	Application Reviews of Case Study	185
			3.1	ShenMu Village, Central Taiwan	185
			3.2	Xinfa Village, Southwest Taiwan	187
			3.3	Daniao Tribe, Southeast Taiwan	187
			4	Summary	188
				References	188

K.-F. Liu (✉)
Department of Civil Engineering, National Taiwan
University, Taipei 10617, Taiwan, Republic of
China
e-mail: kfliu@ntu.edu.tw

Y.-H. Wu
Disaster Research Prevention Institute, Kyoto
University, Gokasho, Uji, Kyoto 611-0011, Japan
e-mail: wu.ahsin@gmail.com

1 Introduction

In Taiwan, debris flows are frequent phenomena in mountain areas during typhoons and heavy rainfall. They usually cause a lot of casualties and severe damage to human property and infrastructure. To mitigate the threat of debris flow hazards, one should establish countermeasures, including control engineering works or evacuation maps for residents. To obtain reference information for debris flow mitigation and risk assessment, numerical simulations of debris flows are widely conducted in Taiwan. Debris-2D is one of the most used simulation programs.

Debris-2D is a two-dimensional debris flow simulation model. This program was developed and first appeared in 2006. Liu and Huang (2006) used this program to simulate the debris flow hazard in Nantou County, Taiwan. When compared with the field measurements, the simulated result had less than a 5% error in affected area, as well as in the final height of deposition. From then on, Debris-2D has been widely applied to the assessment of debris flow hazards for several local governments in Taiwan, including Taipei City, New Taipei City, Taitung County, etc. In addition, Debris-2D has also been successfully promoted for assessing debris flow hazards in other countries, including South Korea, India, and Brazil. Liu and Wu (2010) assessed a debris flow event in Inje, in northeast South Korea, in 2006, and the simulation results of flow depth and affected area also agreed very well with the field investigation. There are also several successful predictions by Debris-2D. For example, in 2006, Debris-2D was applied to the assessment of the affected area of debris flow in the village of Daniao tribe, in southeast Taiwan. The simulation results agreed very well with the real event, which occurred in 2009 (Tsai et al. 2011). Debris-2D can also be used as a reference tool for vulnerability risk assessment (Liu and Li 2007; Tsai et al. 2011) and mitigation design evaluation (Liu et al. 2009).

In what follows we introduce many aspects of the Debris-2D program briefly, including,

theoretical background, computational algorithm, program input and output. The simulation results of some real cases are then shown to demonstrate and verify the practicability of the Debris-2D program.

2 Introduction to the Debris-2D Program

2.1 Theoretical Background

The fundamental theory used in the program is based on non-Newtonian fluid mechanics, which treats a debris flow as a continuum. The governing equations involve conservation of mass and momentum with shallow water assumption. The coordinate system is the Cartesian one with the average bed elevation as the x-axis. The constitutive relation used is the one proposed by Julien and Lan (1991) in a three-dimensional generalization form as:

$$\tau_{ij} = \left(\frac{\tau_0}{\varepsilon_{II}} + \mu_d + \mu_c \varepsilon_{II} \right) \varepsilon_{ij}, \quad \text{for } \tau_{II} \geq \tau_0, \quad (1)$$

$$\varepsilon_{II} = 0, \quad \text{for } \tau_{II} < \tau_0, \quad (2)$$

where $\varepsilon_{II} = \left(\frac{1}{2} \varepsilon_{ij} \varepsilon_{ij} \right)^{1/2}$, $\tau_{II} = \left(\frac{1}{2} \tau_{ij} \tau_{ij} \right)^{1/2}$, and $\varepsilon_{ij} = \frac{1}{2} \left(\frac{\partial u_i}{\partial x_j} + \frac{\partial u_j}{\partial x_i} \right)$.

In Eqs. (1) and (2), τ_0 is yield stress; ε_{ij} is strain-rate tensor; μ_d is dynamic viscosity; μ_c is turbulent-dispersive coefficient. Equation (1) represents the constitutive relation in the shear layer where the shear stress is greater than yield stress. Equation (2) is for the plug layer, that the shear stress is less than yield stress.

From the field data analysis, Liu and Huang (2006) found that the shear layer thickness is less than 10% of the total flow depth. The shear layer can thus be ignored to the leading order. After depth-averaging method and simplification, the resulting equation for mass conservation is

$$\frac{\partial H}{\partial t} + \frac{\partial(uH)}{\partial x} + \frac{\partial(vH)}{\partial y} = 0, \quad (3)$$

and the equations of momentum conservation in x- and y-directions are

$$\begin{aligned} \frac{\partial(uH)}{\partial t} + \frac{\partial(u^2H)}{\partial x} + \frac{\partial(uvH)}{\partial y} = -gH \cos \theta \frac{\partial B}{\partial x} \\ - gH \cos \theta \frac{\partial H}{\partial x} + gH \sin \theta - \frac{1}{\rho} \frac{\tau_0 u}{\sqrt{u^2 + v^2}}, \end{aligned} \quad (4)$$

and

$$\begin{aligned} \frac{\partial(vH)}{\partial t} + \frac{\partial(uvH)}{\partial x} + \frac{\partial(v^2H)}{\partial y} \\ = -gH \cos \theta \frac{\partial B}{\partial y} - gH \cos \theta \frac{\partial H}{\partial y} \\ - \frac{1}{\rho} \frac{\tau_0 v}{\sqrt{u^2 + v^2}}, \end{aligned} \quad (5)$$

where H denotes flow depth; B denotes fixed bed topography; u and v are the depth-averaged velocities in x - and y -directions respectively, and they are functions of spatial variables x , y and temporal variable t ; $\tan \theta$ is the bottom bed slope; ρ is debris-flow density, which is assumed to be constant; g is the gravitational acceleration. The effects of bottom erosion and deposition process are not considered in this version, but they will be involved in the future release.

Using a nonlinear treatment, Debris-2D can derive the initiation criterion for any originally stationary debris pile. The initiation condition reads

$$\begin{aligned} \left(\frac{\partial B}{\partial x} + \frac{\partial H}{\partial x} - \tan \theta \right)^2 \\ + \left(\frac{\partial B}{\partial y} + \frac{\partial H}{\partial y} \right)^2 > \left(\frac{\tau_0}{\rho g \cos \theta H} \right)^2. \end{aligned} \quad (6)$$

The derivative of B and H represent pressure effect and $\tan \theta$ denotes the gravitational effect. The right hand side is the resistance from yield stress. As in Eq. (6), the debris flow can move only if pressure and gravitational effects exceed the yield stress effects.

2.2 Computational Algorithm

Finite difference method is applied to discretize the governing equations, i.e., Eqs. (3)–(5). In space, the 1st-order Upwind method is applied to

discretize convective term and the 2nd-order central difference method is used for the remaining terms. The explicit 3rd-order Adams-Bashforth method is used for time advancing.

To start the computation, Debris-2D use Eq. (6) to determine where debris flow can be initialized. At a given location, if Eq. (6) is not satisfied, the mass stays stationary with a zero velocity and an unchanged flow depth. During computation, if the maximum velocity in the whole computation domain is less than the numerical error, the computation terminates automatically.

2.3 Program Input

2.3.1 Mass Volume and Distribution

For the simulation, the mass distribution of the debris flow is one of the most important inputs. Different from the concept of discharge hydrograph used in flood routing, Debris-2D simulates the motion and spread of the debris flow over the topography.

The triggering locations and volumes of dry debris can be determined and measured by field survey or other techniques. With the dry debris volumes, we estimate the total mass volume V of debris flow using the concept of equilibrium volume concentration. From Takahashi (1981) the formula of solid volume concentration C_v (%) of a flowing debris flow can be expressed as

$$C_v = \frac{\rho_w \tan \theta}{(\sigma - \rho_w)(\tan \varphi - \tan \theta)}, \quad (7)$$

where ρ_w is water density; σ is the density of dry debris (around 2.65 g/cm³); φ is internal friction angle (about 37°); θ is average bottom slope angle in the field. The maximum value of C_v cannot exceed 0.603 (Liu and Huang, 2006). Then, the debris flow mass volume V can be obtained by dividing the dry debris volume V_d with the equilibrium volume concentration C_v (%), i.e., $V = V_d/C_v$.

2.3.2 Determination of Yield Stress

Yield stress is the only material parameter for input. It represents the effect of basal shear stress

of a flowing debris flow. To determine a reasonable value of yield stress, one could carry out the calibration using the method proposed in Liu and Huang (2006) with the material collected in the field.

2.3.3 Program Graphical User Interface for Input

Table 1 illustrates the five categories for input. The first category is data of topography, which is digital elevation model (DEM for short). Two or more DEM files can be inputted for interpolation. The grids in DEM files for input should be rectangular. The second one is a simulation range. This range should also be rectangular. Thirdly, information on the mass source (e.g., location, volume and distribution type) is also needed. Then, the fourth category is the rheological parameter of the debris flow, i.e., the yield stress. The final category is simulation parameters, required for output, such as output time interval, setups of specified output locations and so on.

Including the datum and parameters, massive data pre-processing is needed in order to run Debris-2D. So we developed a graphic user interface (GUI for abbreviation) in the Windows® operating system for a user to follow the steps to input all required data and parameters, to make pre-processing in the simulation easier and more efficient. A sample user interface is showed in Fig. 1. Once data is provided by the user, the GUI program will start to process all the inputs, and connect them with the simulation program.

Without knowing anything about Debris-2D itself, users can still use the GUI program to run a simulation. This was proven during cooperation with Korean researchers (Liu and Wu 2010). Besides, no calibration is needed to use Debris-2D, and all parameters for input must be determined according to guidelines.

To help users understand how to use Debris-2D, the program tutorial is given in the appendix. In the tutorial, there are four parts in the introduction, including the program system requirements, a model framework overview, operation procedures, and a GUI model manual. Developed using the Microsoft®.NET framework, the Debris-2D GUI program (also called WinDebris2D, or WD2 for short, see Fig. 1 for a screenshot) can only be run in the Microsoft® Windows operating system with .NET framework library. Any geographic information system (GIS) program is recommended for processing the input or output data (e.g., DEM, output demonstration).

2.4 Program Output

Debris-2D can output temporal variations of flow depth and depth-averaged velocities in the whole domain. It also can calculate impact force (Liu et al. 1997) at any specified location, and can output the final affected area and the maximum flow depth and velocities at varying times. The output time interval can be arbitrary. With the

Table 1 All inputs for Debris-2D program

Steps	Description	Inputs
1	Topography	Input DEM file for interpolation to generate grids, two or more DEM files are also available
2	Simulation range	Typing or circling by mouse from the screen to set the simulation range
3	Mass information	<ul style="list-style-type: none"> • Select the type of depositions • Input mass locations and volumes
4	Material parameter	Input the yield stress of mass
5	Ouput setup	<ul style="list-style-type: none"> • Set the time interval of output • Set the locations of specified output • Set if output the final deposition and velocity or flow depth distribution or not after the end of simulation

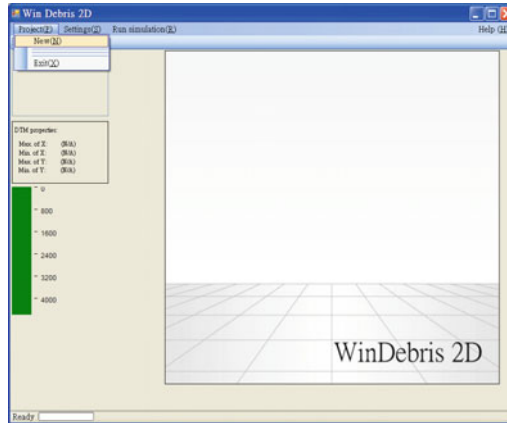


Fig. 1 A screenshot of the Debris-2D graphical user interface (GUI) program (also called WinDebris2D, or WD2 for short)

simulated output, one can use geographic information system software for mapping and demonstration. Figures 2, 3 and 4 show illustrations of simulation output for real case studies. The appendix also includes an illustrative animation of the simulation output (filename: 1-3-1_Debris2D_video.mp4).

3 Application Reviews of Case Study

To demonstrate the application of Debris-2D to the assessment of debris flow hazards, we show simulation results for three case studies of real hazards, all of which occurred in Taiwan.

3.1 ShenMu Village, Central Taiwan

This case was the first application of Debris-2D to the assessment of debris flows. Shenmu Village is located in Nantou County, central Taiwan. Hazardous debris flows occurred on July 31, 1996, during Typhoon Herb. The river length is about 5 km and the average bottom slope is about 11.5° . The topographic contour map is shown in Fig. 2a. The total volume of the debris

flow deposit is about $560,000 \text{ m}^3$. The value of yield stress is set to be 1150 Pa, based on the calibration of the method proposed in Liu and Huang (2006). The initial mass was located within the ellipse (marked B) in Fig. 2a. The simulated final deposition profile is plotted in Fig. 2b. The solid red lines denote the deposition boundary measured in the field after the disaster. The simulated range is very close to the measured one. The only difference is at $x = 2300$. There a tributary joined the main river (top right corner of Fig. 2b) and this stopped the debris flow from flowing into the tributary area at the time of the disaster. However, as no inflow was assigned from the merging boundary, the modeled debris flow flowed into and deposited material in the lower part of tributary. Except in the region near the junction of tributaries, the maximum error for boundary of final deposition area is only 20 m. In addition, Fig. 2c shows a comparison between the simulated (pink solid line) and measured (black diamonds) depths of final deposition along the cross-section marked A in Fig. 2a. The results show that the simulated depth coincides well with the measured one, with a maximum difference of less than one meter (Liu and Huang 2006). The simulation results show that Debris-2D simulated the affected area and flow depth of the debris flow.

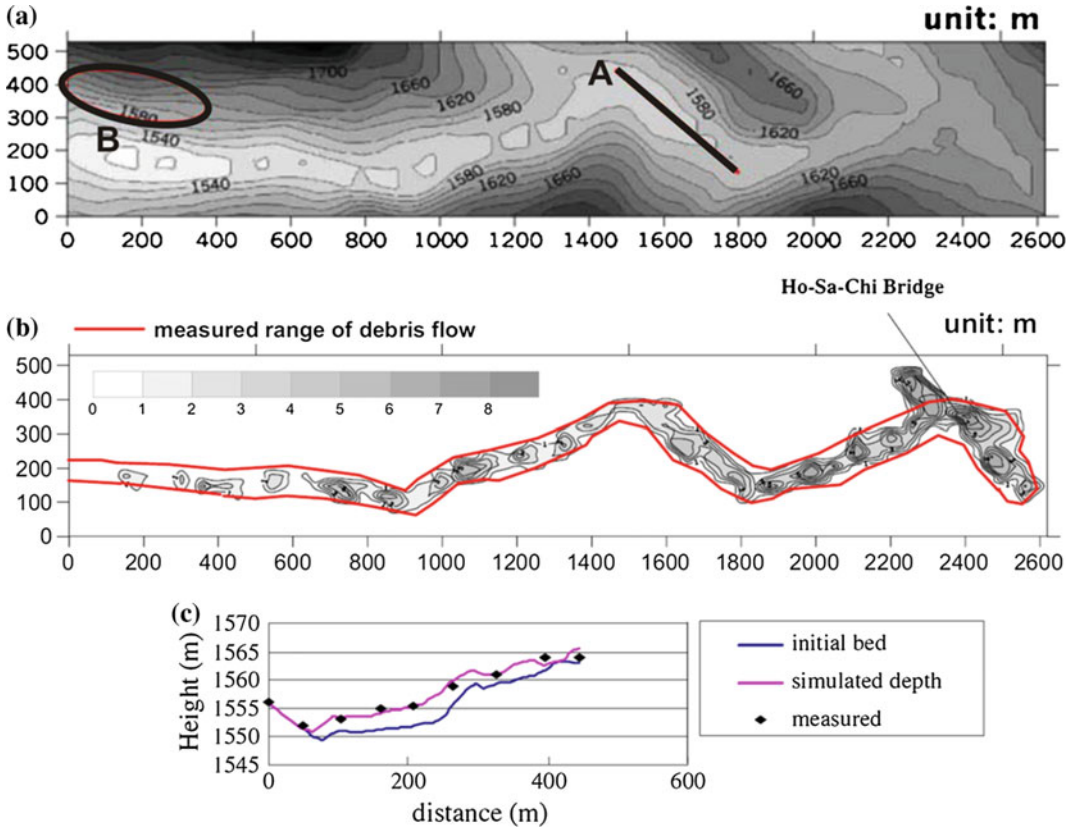


Fig. 2 Simulation results for the case of Shenmu village: **a** topographic contour map of simulation range. Initial mass is located at the elliptical range marked by B. The straight line (marked by A) is the cross-section where the numerical result is compared with measured final

deposition depth, see chart **c**; **b** comparison of simulated and measured boundaries of the debris flow; **c** comparison of simulated (pink solid line) and measured (black diamonds) depths; the blue solid line is bed elevation before the disaster (Liu and Huang 2006)

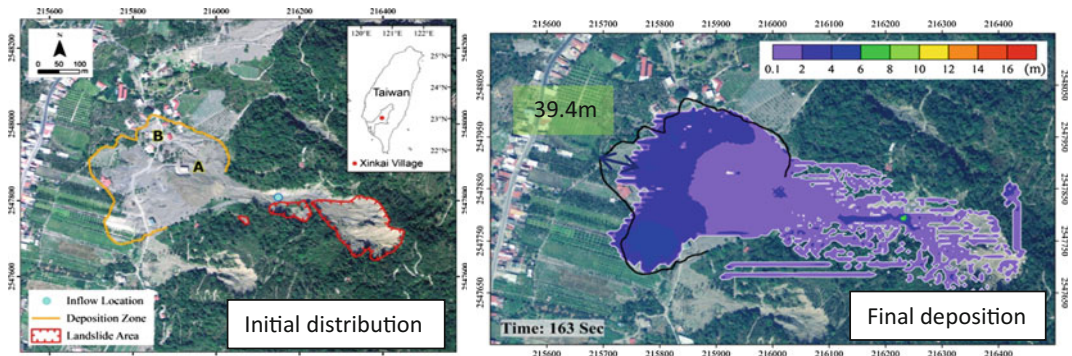


Fig. 3 Simulation result of the case of Xinfu village. Black line shows the front of debris flow deposition. Left figure shows the three initial mass distributions in red.

Right figure shows the simulated final deposition which fits the black line with error less than 15% (Wu et al. 2013)



Fig. 4 Simulation results for a debris flow at Daniao Village. The region marked in red is the affected area triggered by Typhoon Morakot (measured in 2009), and the region bounded by a white line is the simulation result

(assessed in 2006). At the location marked by a red triangle, the simulated final depth (i.e., 13.06 m) is very close to the in situ deposition depth (i.e., about 13 m) estimated by the locals (Tsai et al. 2011)

3.2 Xinfa Village, Southwest Taiwan

On August 5–10 in 2009, Typhoon Morakot hit Taiwan and brought world record heavy rainfall. The maximum cumulative rainfall in five days approached about 2900 mm. There were severe floods, countless landslides, and disastrous debris flows associated with Typhoon Morakot. During the typhoon, a debris flow, triggered by a landslide occurred in Xinfa Village, in southwest Taiwan, and killed five people, buried six houses, and destroyed about 15 ha of agriculture area. According to field measurements and surveys after the disaster, the total debris flow volume was about 215,600 m³, and there were three landslides triggering the debris flows upstream. Figure 3 illustrates the initial mass distribution for the simulation and the final simulated affected area for this case. There are three initial mass distributions with assumed uniform depths. The simulated affected area fits the deposition range in the aerial photo with an error of less than 15%. In addition, the flow depth prediction also agrees very well with the in situ conditions (Wu et al. 2013).

3.3 Daniao Tribe, Southeast Taiwan

This case is one of the successful predictions of a debris flow using Debris-2D. The potential debris flow torrent near the village of the Daniao Tribe in Taitung County, southeast Taiwan is called DF097. The watershed area of DF097 is approximately 0.86 km². The average bottom slope of creek is about 13°. The solids in the mixture were composed of slate, mudstone and weathered gravel, which are all easily movable under external forces.

In 2006, as a reference for debris flow control engineering in DF097, the debris flow hazard was assessed using Debris-2D. According to field investigations, loose deposits were distributed over several locations on the upstream hillside and riverbed. The total volume of the deposits was about 20,000 m³. However, for a heavy rainfall event, more mass can be added. Based on the results of hydrological analysis and the formula for equilibrium volume concentration, i.e., Eq. (7), the total debris flow volume for the design capacity of an extreme event was 500,000 m³ (Tsai et al. 2011). The value of yield

stress of debris flow was 250 dyne/cm^2 based on measurements in the field. The simulated final deposition area is the region bounded by a white line in Fig. 4. The simulation result showed that the debris flow invaded and deposited over a part of the tribe area. In 2007, on the basis of this assessment, two drainage ditches were built on both sides of Daniao tribe village and a series of check dams were also constructed along the creek of DF097.

In 2009, during Typhoon Morakot, the heavy rainfall induced landslides in the upstream reaches of DF097 and formed a debris flow that invaded the village of the Daniao Tribe. From a field survey after the disaster, the total debris flow volume exceeded $500,000 \text{ m}^3$. Figure 4 also shows an aerial photograph the affected area, bounded by a red line, after the disaster. In Fig. 4, we see that the front of the simulated distribution differed from the front in the real event. The main reason for this difference is the construction of debris flow control structures. The simulation, in 2006, used the topography data without the countermeasures, so the simulated debris flow flowed and deposited over the tribe area. However, in the real event in 2009, a part of the debris flow spread along the drainage ditches without invading the tribe village. The control engineering did protect the village from damage by the debris flow. According to estimates by local witnesses, the depth of in situ deposit at the observed location (marked by a red triangle in Fig. 4) was between 12 m and 13 m. The simulated depth at the same location was 13.06 m, and it agreed very well with the in situ conditions. The results from this case show that Debris-2D could reflect characteristics of the motion of debris flows. Also, Debris-2D was validated to be a practical reference tool for engineering design.

From the above three simulation results, we find that Debris-2D is validated as a practical and reliable debris flow simulation program.

4 Summary

A brief introduction to the Debris-2D program is presented in this chapter, including the theoretical background, computational algorithms, program input and output, and application reviews based on three case studies. In the fundamental theory, debris flow is treated as a non-Newtonian fluid with a yield stress. For computational efficiency, the fundamental theory is simplified to leading order with a truncation error less than 10%. However, so far the effects of bottom erosion and deposition are not considered in the program, but they will be involved in the future release.

Using Debris-2D for simulation, the input for mass sources is the initial debris flow distributions based on field surveys or other physical assumptions. The output of Debris-2D includes the flow depth, flow velocities in x - and y -directions, impact force at any specified location, and affected area of time variation with a high spatial and arbitrary temporal resolution. A GUI program was also developed for users to run Debris-2D more efficiently and correctly. Based on the results of case studies, Debris-2D can simulate and reflect the characteristics of debris flow phenomena, and it has been verified as a practical tool for engineering design.

References

- Julien PY, Lan Y (1991) Rheology of hyperconcentrations. *J Hydr Eng ASCE* 117(3):346–353
- Liu KF, Lee FC, Tsai SP (1997) The flow field and impact force on a debris dam. In: *Proceedings of the first international conference on debris-flow hazards mitigation: mechanics, prediction, and assessment*, pp 737–746
- Liu KF, Huang MC (2006) Numerical simulation of debris flow with application on hazard area mapping. *Comput Geosci* 10:221–240
- Liu KF, Li HC (2007) The assessment of debris flow emergency measures. *J City Plann* 34(1):57–73 (in Chinese)

- Liu KF, Li HC, Hsu YC (2009) Debris flow hazard defense magnitude assessment with numerical simulation. *Nat Hazards* 49(1):137–161
- Liu KF, Wu YH (2010) The assessment of debris flow hazard in Korea using Debris-2D. In: *Interpraevent 2010 international symposium in Pacific Rim, Taiwan*
- Wu YH, Liu KF, Chen YC (2013) Comparison between FLO-2D and Debris-2D on the application of assessment of granular debris flow hazards with case study. *J Mt Sci*. doi:[10.1007/s11629-013-2511-1](https://doi.org/10.1007/s11629-013-2511-1)
- Takahashi T (1981) Debris flow. *Ann Rev Fluid Mech* 13:57–77
- Tsai MP, Hsu YC, Li HC, Shu HM, Liu KF (2011) Applications of simulation technique on debris flow hazard zone delineation: a case study in Daniao tribe, Eastern Taiwan. *Nat Hazard Earth Syst* 11:3053–3062

TXT-tool 3.081-1.5

Manual for the LS-RAPID Software

Kyoji Sassa, Hendy Setiawan, Bin He, Karolina Gradiški
and Khang Dang

Abstract

This paper highlights the LS RAPID software that has ability to simulate the initiation and motion of landslides. Fundamental equations and concepts in the LS RAPID model are briefly explained. Step by step procedure of the use of this software are presented, which started from setting of the topography, creating the possible sliding surface using the ellipsoidal parameter, delineation of the unstable mass, soil and water parameters input, triggering factors for the inducement of landslides, the conditions for calculation, running the landslide simulation and up to the output settings after the simulation. Several cases of landslides which were analyzed by LS RAPID are described further in the PDF Tool: Manual for the LS-RAPID software.

Keywords

LS-RAPID · Topography · Sliding surface · Seismic wave
Pore pressure · Lateral pressure · Steady state shear resistance

K. Sassa (✉) · K. Dang
International Consortium on Landslides, 138-1,
Tanaka Asukaicho, Sakyo-Ku, Kyoto 606-8226,
Japan
e-mail: sassa@iclhq.org

H. Setiawan
Disaster Prevention Research Institute, Kyoto
University, Uji 611-0011, Japan
e-mail: hendy@flood.dpri.kyoto-u.ac.jp

B. He
Chinese Academy of Science, 73 East Beijing Road,
Nanjing 210008, People's Republic of China

e-mail: hebin@niglas.ac.cn

K. Gradiški
Faculty of Mining, Geology and Petroleum
Engineering, University of Zagreb, Pierottijeva 6,
10000 Zagreb, Croatia
e-mail: karolina.gradiski@rgn.hr

K. Dang
VNU University of Science, Hanoi, Vietnam

Contents

- 1 Introduction to LS-RAPID Software.....** 192
- 2 Setting of the Topography** 194
 - 2.1 Initial Setting of the Topography 194
 - 2.2 Relationship Between the Tabs and Options .. 194
 - 2.3 Editing the Topography Control Point..... 196
 - 2.4 Converting the Control Point Data into the Mesh Data 197
 - 2.5 Editing the Topography Mesh Data..... 197
 - 2.6 Creating the Possible Sliding Surface Using the Ellipsoidal Parameter 197
 - 2.7 Filling and Excavating the Current Topography to Estimate Pre-failure Topography 201
 - 2.8 Delineation the Unstable Mass (Source and Moving Area)..... 205
- 3 Parameters and Conditions for Simulation..** 206
 - 3.1 Setting the Soil Parameters..... 206
 - 3.2 Conditions for Calculation..... 207
 - 3.3 Registration of Seismic Waveform..... 210
 - 3.4 Setting the Time Step and Other Conditions.. 211
 - 3.5 Output Settings for the Landslide Simulation. 213
- 4 Run the Simulation.....** 214
- 5 Other Commands in the LS-RAPID** 215
- 6 Conclusion** 224
- References 224

1 Introduction to LS-RAPID Software

An integrated landslide simulation model, called LS-RAPID, is a computer simulation code that integrating the initiation and motion of landslides which are triggered by earthquakes, rain-fall or both. The LS RAPID aims to integrate the initiation process (stability analysis) by pore pressure increase and seismic loading, and the moving process (dynamic analysis) including the process of volume enlargement by entraining the unstable deposits within the travelling course. In short, the concept of LS RAPID brings the whole processes of landslide from stable state, failure, post-failure strength reduction, motion up to deposit stage (Sassa et al. 2012). Landslide simulation model in the LS RAPID could express the behaviour changes of soil masses when the triggering factors are initiated.

A concept of the LS RAPID model is established by considering vertical imaginary column with the acting forces within a moving landslide mass (Fig. 1). These forces are the self-weight of column (W), vertical seismic force (F_v), horizontal x–y direction seismic forces (F_x and F_y), lateral pressure acting on the side walls (P), shear

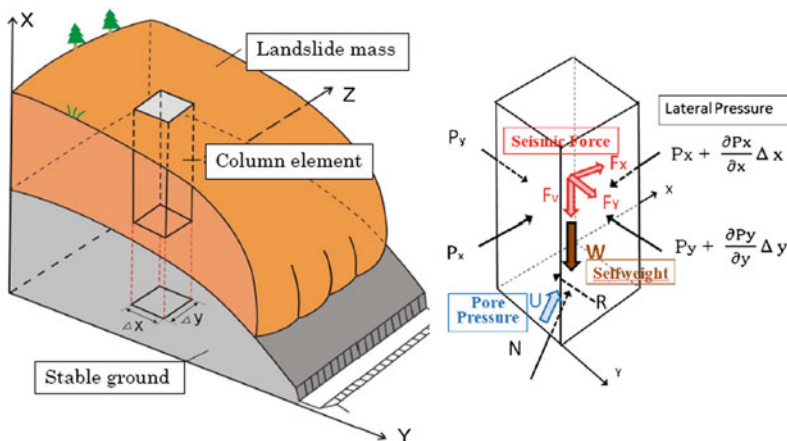


Fig. 1 A column element within a moving landslide mass, as concept of the LS-RAPID model

resistance acting on the bottom (R), the normal stress acting on the bottom (N) given from the stable ground as a reaction of normal component of the self-weight, and the pore pressure acting on the bottom (U).

The landslide mass (m) will be accelerated by acceleration (a), with the total forces as the sum of driving force (self-weight and seismic force), lateral pressure and shear resistance, denoted as:

$$a \cdot m = (W + F_v + F_x + F_y) + \left(\frac{\partial P_x}{\partial x} \Delta x + \frac{\partial P_y}{\partial y} \Delta y \right) + R \quad (1)$$

where R includes the effects of forces of N and U that works in the upward direction of the maximum slope line before motion and in the opposite direction of landslide movement during motion. All stresses and displacements are projected and calculated into the horizontal plane (Sassa 1988).

Equation (1) can be expressed into x and y directions (Sassa et al. 2010), with the assumption that the sum of landslide mass that flow into a column (M , N) is the same with the change or increase of height of the soil column, as follows: (Table 1)

$$\begin{aligned} \frac{\partial M}{\partial t} + \frac{\partial}{\partial x}(u_o M) + \frac{\partial}{\partial y}(v_o M) \\ = gh \left\{ \frac{\tan \alpha}{q+1} (1 + Kv) + Kx \cos^2 \alpha \right\} \\ - (1 + Kv) kgh \frac{\partial h}{\partial x} - \frac{g}{(q+1)^{1/2}} \\ \cdot \frac{u_o}{(u_o^2 + v_o^2 + w_o^2)^{1/2}} \{ h_c (q+1) + (1 - r_u) h \tan \phi_a \} \end{aligned} \quad (2)$$

$$\begin{aligned} \frac{\partial N}{\partial t} + \frac{\partial}{\partial x}(u_o N) + \frac{\partial}{\partial y}(v_o N) \\ = gh \left\{ \frac{\tan \beta}{q+1} (1 + Kv) + Ky \cos^2 \beta \right\} \\ - (1 + Kv) kgh \frac{\partial h}{\partial y} - \frac{g}{(q+1)^{1/2}} \\ \cdot \frac{v_o}{(u_o^2 + v_o^2 + w_o^2)^{1/2}} \{ h_c (q+1) + (1 - r_u) h \tan \phi_a \} \end{aligned} \quad (3)$$

$$\frac{\partial h}{\partial t} + \frac{\partial M}{\partial x} + \frac{\partial N}{\partial y} = 0 \quad (4)$$

Equations (2), (3) and (4) above were established for both processes of landslide initiation and motion. The value of ϕ_a , h_c , r_u varies in three states: (i) pre-failure state before shear

Table 1 Remarks of the LS RAPID model equations

Symbol/remarks	Description
h	Height of soil column within a mesh (depth of the moving mass)
g	Gravity (acceleration)
α , β	Angles of the ground surface to x-z plain and y-z plain
u_o , v_o , w_o	Velocity of a soil column to x, y, z directions (velocity distribution in z direction is neglected, regarded to be a constant)
M, N	Discharge of soil per unit width in x, y directions, respectively ($M = u_o h$, $N = v_o h$)
k	Lateral pressure ratio (ratio of lateral pressure and vertical pressure)
$\tan \phi_a$	Apparent friction coefficient mobilized at the sliding surface of landslide
h_c	Cohesion c expressed in the unit of height ($c = \rho g h_c$, ρ : density of soil)
q	$\tan^2 \alpha + \tan^2 \beta$
w_o	$-(u_o \tan \alpha + v_o \tan \beta)$
Kv, Kx, Ky	Seismic coefficients to the vertical, x and y directions
r_u	Pore pressure ratio (u/σ)

displacement at failure (start of strength reduction), (ii) transient state between pre-failure state and steady state, and (iii) steady state after the end of strength reduction. The lateral pressure ratio (k) in Eqs. (2) and (3) is expressed by using the Jakey's equation (Sassa 1988) as follows,

$$k = 1 - \sin \phi_{ia}$$

$$\tan \phi_{ia} = \frac{(c + (\sigma - u) \tan \phi_i)}{\sigma} \quad (5)$$

where $\tan \phi_{ia}$ is the apparent friction coefficient within the landslide mass and $\tan \phi_i$ is the effective friction within the landslide mass which is not always the same with the effective friction during motion on the sliding surface (ϕ_m). The value of $k = 1.0$ when the sample is in the liquefied state ($\sigma = u$ and $c = 0$), and $k = 0$ when in the rigid state. The apparent friction coefficient ($\tan \phi_{a(ss)}$) can be obtained by knowing the steady state shear resistance (τ_{ss}) and the total normal stress (σ) from ring shear tests. In further, detail explanation of conceptual model and other parameters of the LS-RAPID software can be found in Sassa (1988) and Sassa et al. (2010, 2012).

Flowchart of the landslide simulation using the LS-RAPID software is shown in Fig. 2. Setting the topography, control point for the sliding surface and configure the triggering factors, soil and water parameters are necessary within the LS-RAPID.

2 Setting of the Topography

2.1 Initial Setting of the Topography

Landslide simulation using the LS-RAPID is started by creating a new document with the initial settings to generate and view the topography data. We choose the option of [Setting of Calculation Area and Input-data Type] from [Edit] toolbar or directly choose [Simulation Area Setting] icon in the toolbar, then layout in Fig. 3 as shown below.



The 'Axial Setting of Calculation Area' indicates the range for X and Y direction of the calculation area for the mesh. The maximum

coordinate values are automatically computed by the number of mesh, pitch and minimum coordinate values that we entered. The range is between -999999.999 up to $+999999.99$ (m). The 'Mesh Setting of Calculation Area' indicates the number of mesh and pitch in both X and Y direction of the mesh in the calculation area. 'Pitch' means the interval of X and Y coordinates. The number of mesh ranged between 2 and 9999, and the pitch between 0.001 and 999999.99 (m). The maximum numbers of control points ranged between 0 and 999999.

The Input-data Types can be selected: (a) Slope surface elevation and sliding surface elevation; (b) Slope surface elevation and sliding mass thickness; or (c) Sliding surface elevation and sliding mass thickness. After setting all the numbers above, the following windows (Fig. 4) will appear after pressing "OK".

2.2 Relationship Between the Tabs and Options

The Control Point and the Mesh Data topography are shown on each tab of "Slope Surface Elevation", "Sliding Surface Elevation" and "Sliding Mass Thickness". The following options can be edited for each tab:

- *Display of unstable mass* the thickness of the unstable mass is displayed by the globe if in "Slope Surface" or "Sliding Surface" mode.
- *Creation of sliding surface* the sliding surface can be created by setting the ellipsoidal body or by filling/excavation.
- *Editing the selected area* by clicking the button  or , when ON is chosen, we can create the any-shape area by using left click and pressing the keys [Ctrl] + [Shift].
- *Set for all* first we input the value of elevation in the blank box beside the button of "set for all". Then we can choose the objective area. Finally, we click the button of "set for all". As a result, the same values of elevation will be set for all the meshes we selected (this

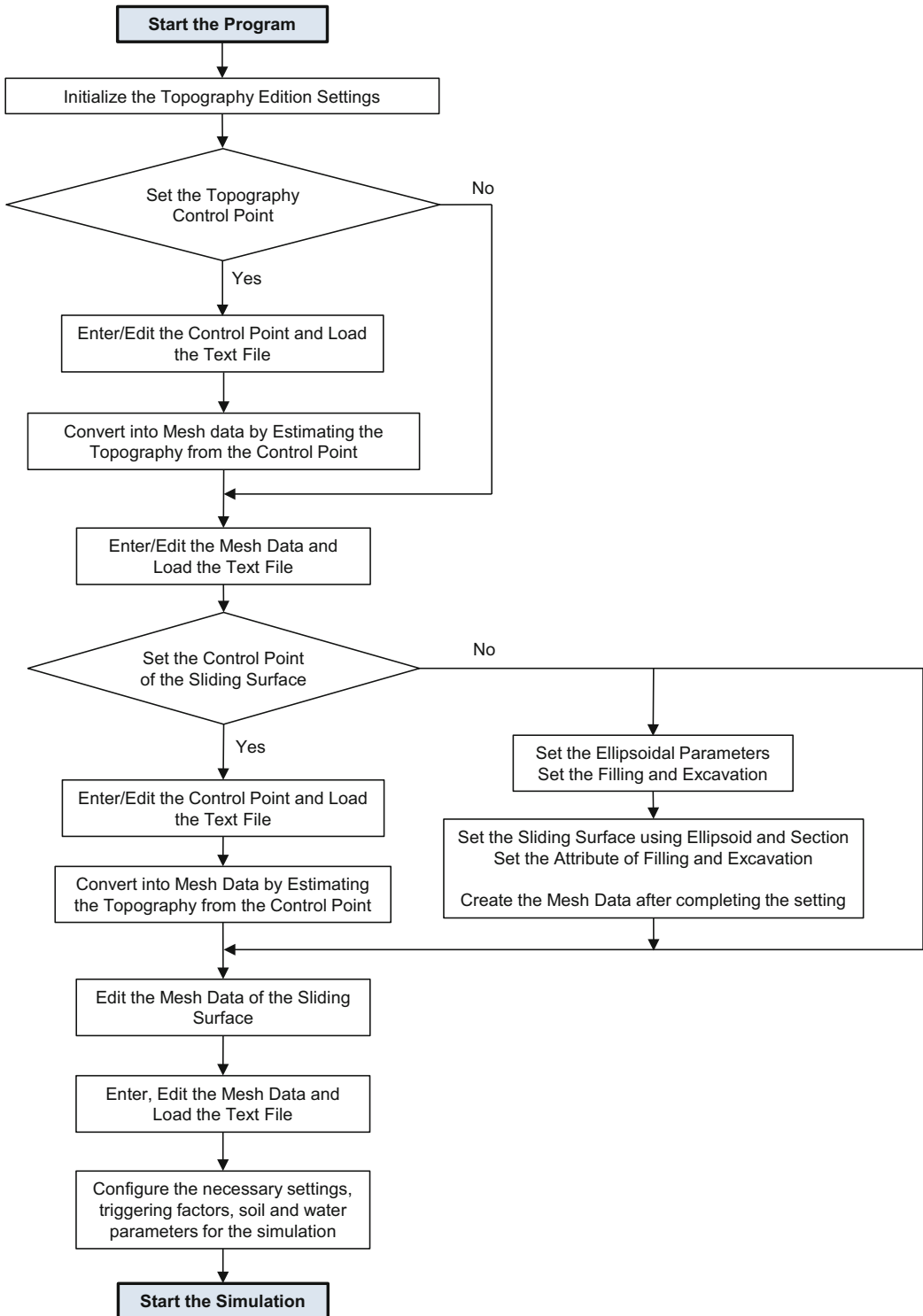
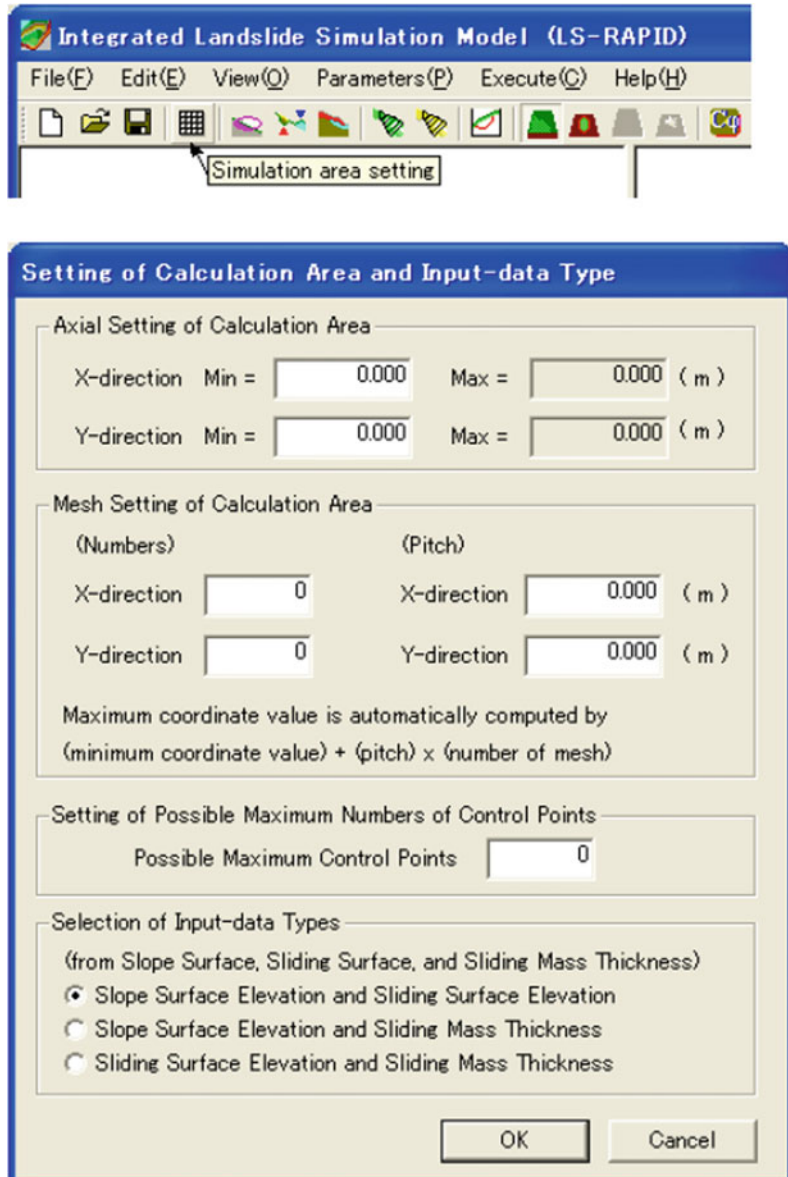


Fig. 2 Simulation flowchart of the LS RAPID

Fig. 3 Layout to set the calculation area and input data type



method can save the time if we want to input the same elevation values in the meshes).

command means “Back an Area Point”, and the second command means “Delete All Area Point”.

If we use the “Edition of the selected area” button clicked as ON, we can input the same value for any-shape area we have created. If we click the “Edition of the selected area” button to choose any-shape area, Fig. 5 can be as an example. If we right-click the windows of 3D-View, the pop-up menu will appear. The first

2.3 Editing the Topography Control Point

The Control Point can be edited manually by selecting the tab and choosing the “Control Point” button. If we already have a text file for

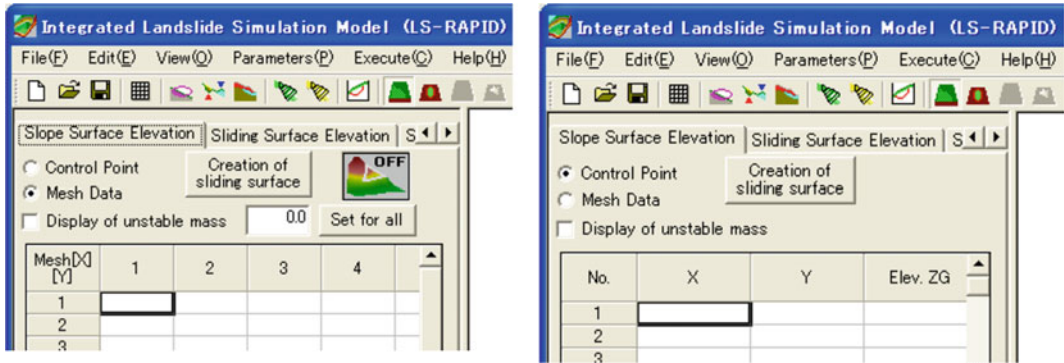


Fig. 4 Layout options for mesh data (left) and control point (right)

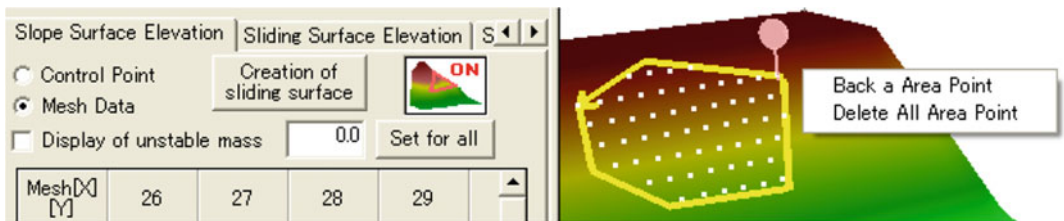


Fig. 5 Layout of the any-shape of selected area

the Control Point data, we can select [Load Text Data File] from [File] menu, and then select [Load/Read (Slope Surface Elevation, or Sliding Surface Elevation, or Sliding Mass Thickness) Control Point] to load the appropriate file. Data in the text file should be separated by a space, tab or comma (CSV) to load correctly. After editing, the following window will appear (Fig. 6).

2.4 Converting the Control Point Data into the Mesh Data

We can convert the Control Point data that already obtained into Mesh data, by clicking [Menu], then [Edit], and then [Convert/Transfer Control Point to Mesh Data]. The image of the mesh topography with the reflected Control Point data will appear if the process is successful. If necessary, we still can edit the Control Point after creating the Mesh Data and return back to this section.

2.5 Editing the Topography Mesh Data

The Mesh Data can be edited manually by selecting the tab and choosing the “Mesh Data” button to start editing the mesh values. If we already have a text file for the Mesh data, we can select [Load Text Data File] from [File] menu, and then select [Load/Read (Mesh Data of Slope Surface/Ground Elevation, or Mesh Data of Sliding Surface Elevation, or Mesh Data of Sliding Mass Thickness)] to choose the appropriate file. After selecting and editing the mesh data, the following window will appear (Fig. 7).

2.6 Creating the Possible Sliding Surface Using the Ellipsoidal Parameter

The possible Sliding Surface can be built using the ellipsoidal parameter, after creating the Mesh

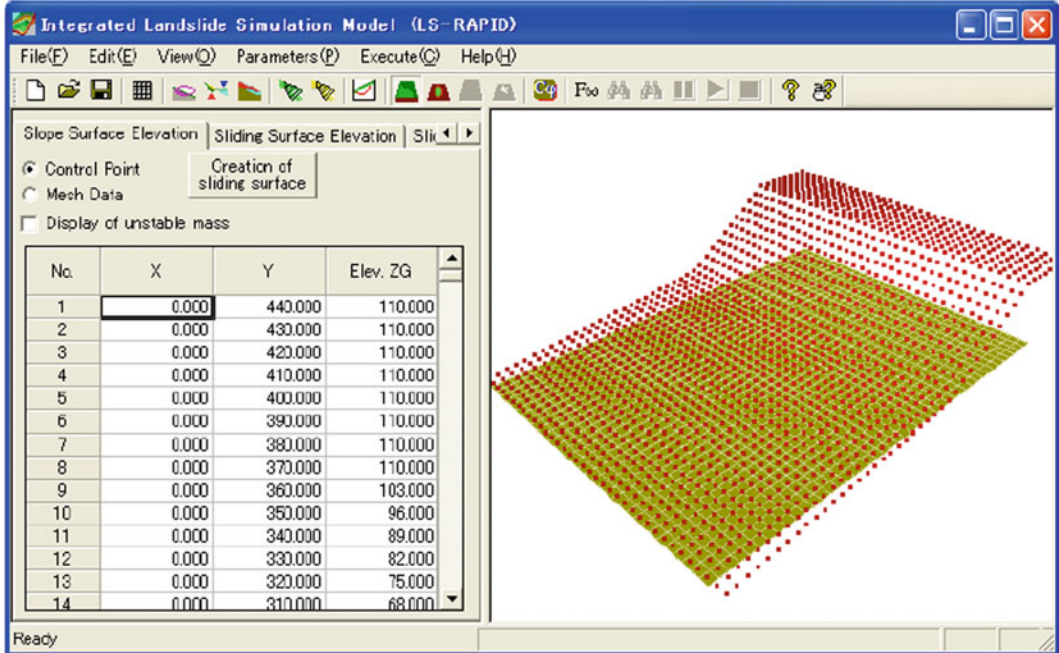


Fig. 6 Layout window after editing the topography control point

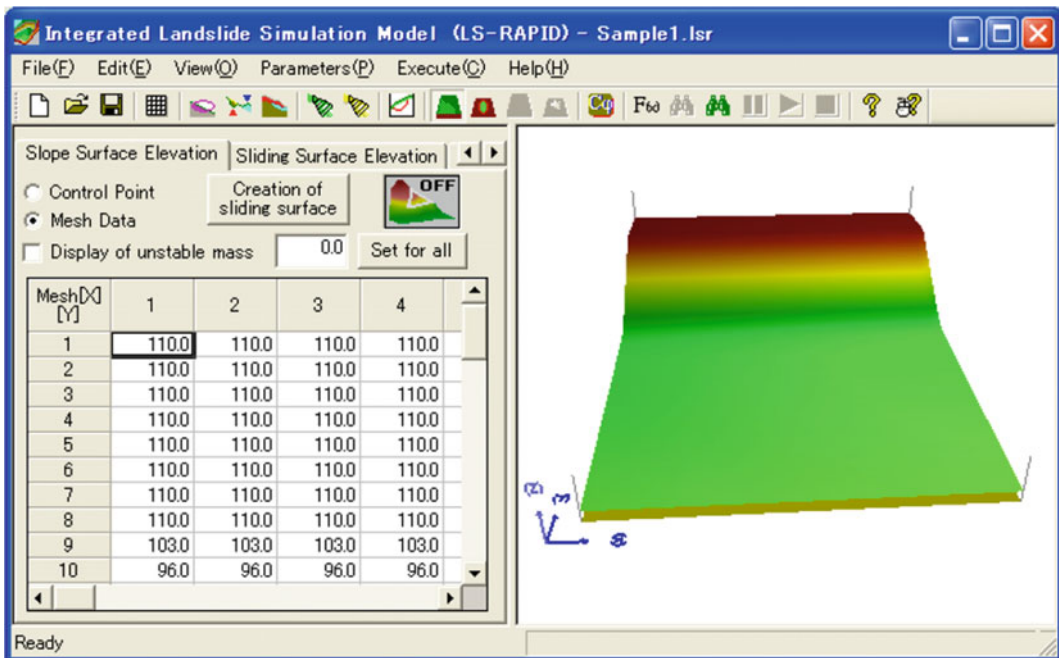


Fig. 7 Layout window after editing topography mesh data

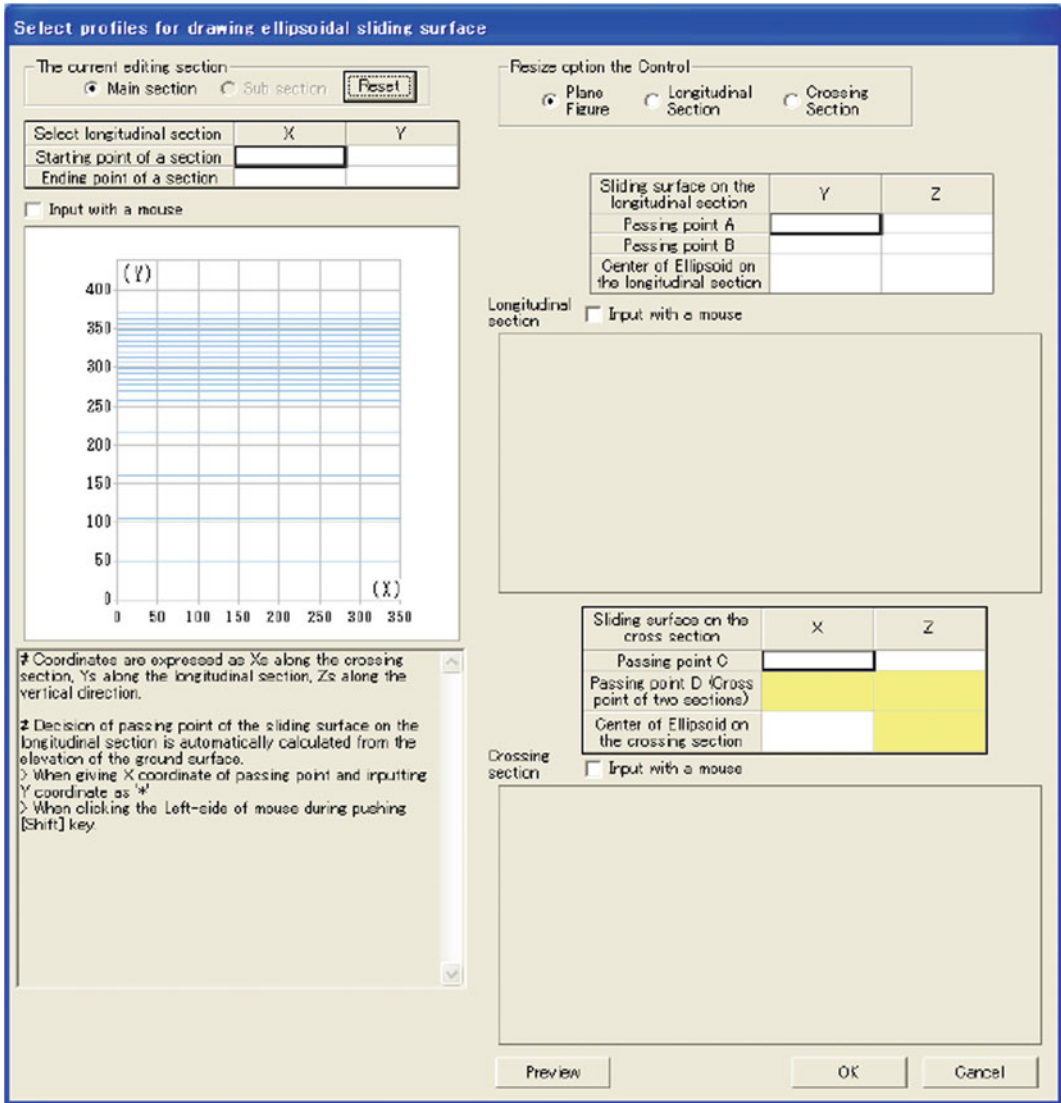
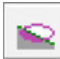


Fig. 8 Initial dialog box for ellipsoidal sliding surface setting

data of the slope surface. We select [Ellipsoid Sliding Surface setting] from the [Edit] menu, or can select icon  as 'Ellipsoid Sliding Surface setting', or using [Creating of sliding surface] on the tab of Slope Surface Elevation' and choose [Create sliding surface with section profile of Ellipsoid] for a new landslide.

The initial view after we select [Ellipsoid Sliding Surface setting] is shown in Fig. 8. We can create an ellipsoidal sliding surface by setting the

longitudinal section of the landslide on the left side of the dialog box. The corresponding longitudinal section will appear on the right side once after we enter the starting and ending points (Fig. 9). We can also input the points using the mouse.

The passing points of sliding surface and the center point of ellipsoid then can be set on the longitudinal section. By setting the passing points, the cross section which passes through the center of the passing points will appear (Fig. 10).

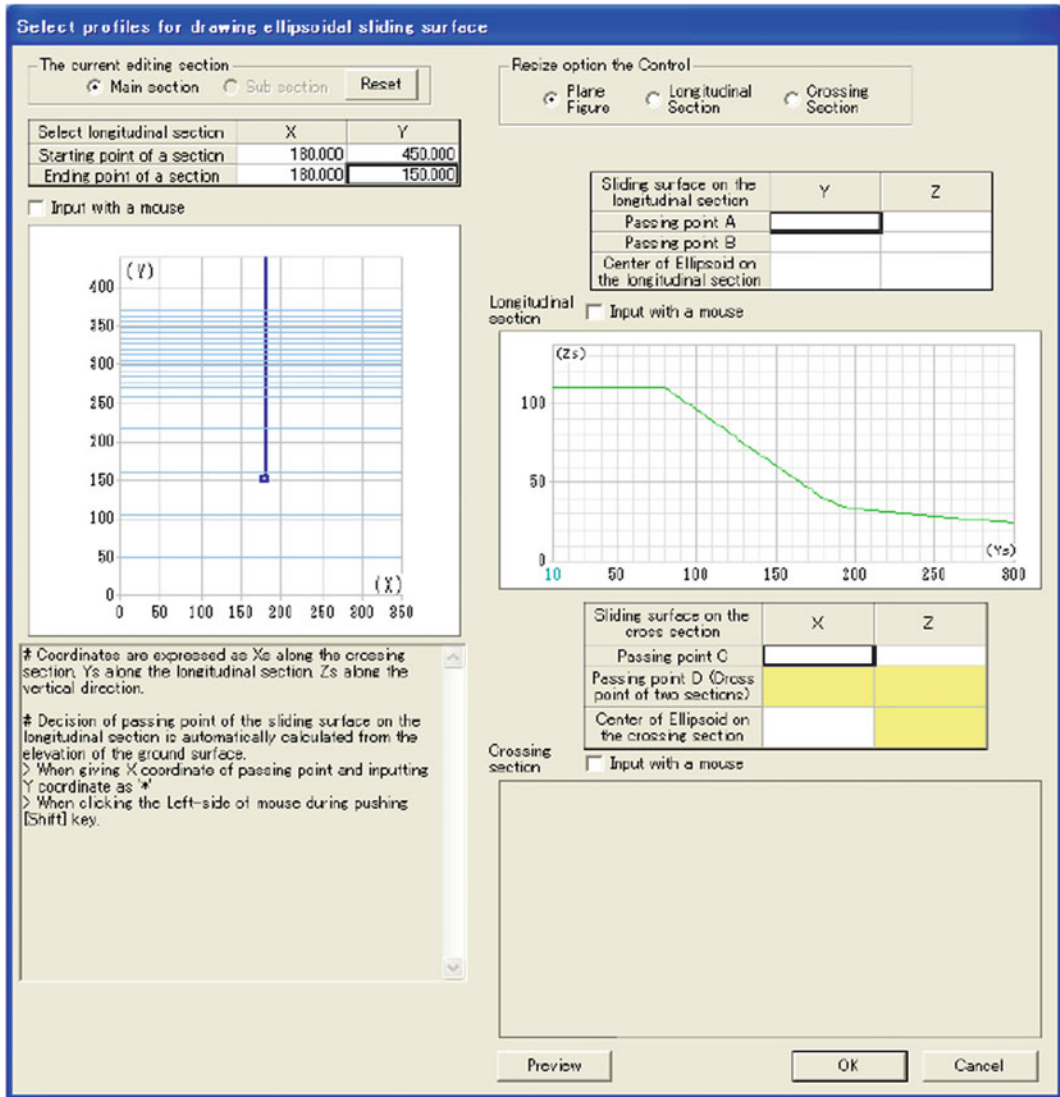


Fig. 9 Dialog box after inserting points to create the longitudinal section

The left part of the screen will display the position information. The ellipsoid will be displayed on the longitudinal section when we enter the center point of the ellipsoid. Crossing points between the cross section and the ellipsoid will appear. If the ellipsoid is not seen after entering its center point, we can adjust the location of the center point and the passing points. We can also input the passing points and the center point using the mouse. Similar to the longitudinal section, the passing points and the center point of

the ellipsoid can be set on the cross section. We can set the crossing point between the sliding surface, the slope and the x-coordinate of the center point of the ellipsoid (Fig. 11). The cross point of the two sections and the elevation of the center of ellipsoid are already determined on the cross section.

If there is a subsection, the ellipsoidal subsection can be created using similar steps as described above. Commands in the dialog box in Fig. 11 are explained in Table 2. The appropriate

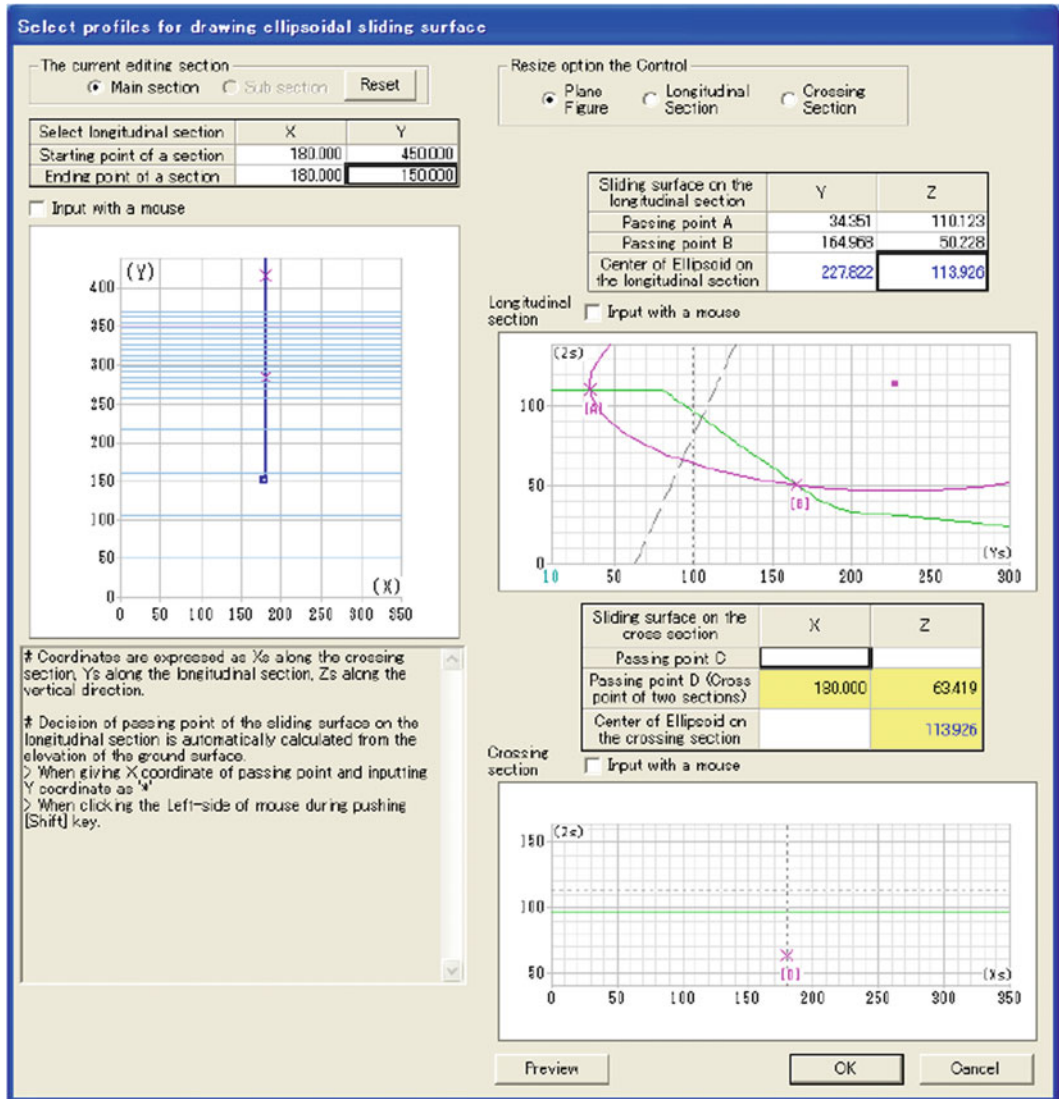


Fig. 10 Dialog box showing the passing points and the center point of ellipsoid on the longitudinal section

ellipsoid will appear after the ellipsoid on the longitudinal and cross sections were created. The region for the ellipsoid on the longitudinal section and the 3D view can be seen in the screen, while the characteristics of the ellipsoid will appear in the dialog box (Fig. 12).

The coordinates in this model are expressed as X's along the cross section, Y's along the longitudinal section and Z's along the vertical direction. The X and Y coordinates on the longitudinal and the crossing sections represent the

distances from the starting point of the sections and the Z coordinate represents the elevation.

2.7 Filling and Excavating the Current Topography to Estimate Pre-failure Topography

Once the mesh data of the slope surface is provided, the sliding surface and the original

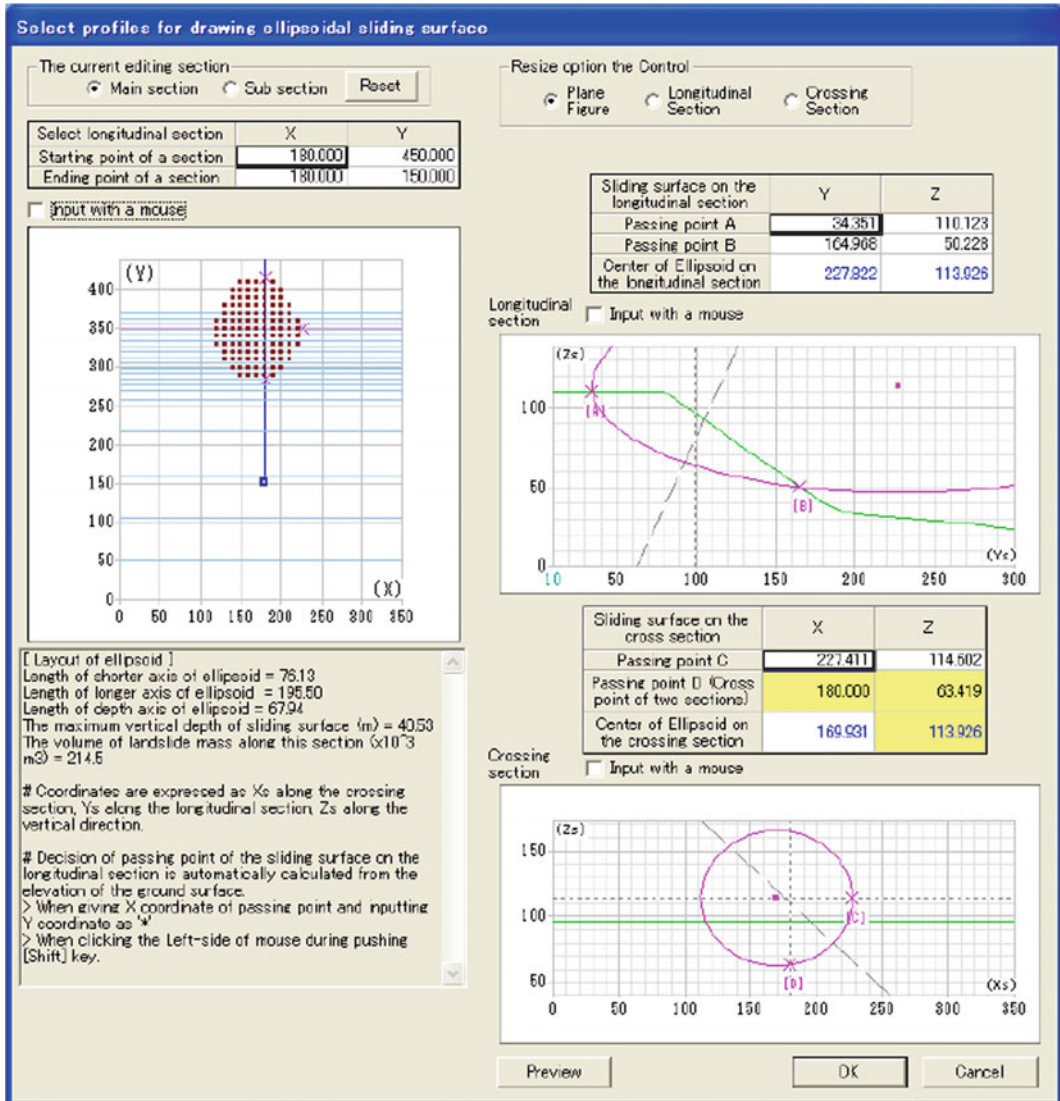



Fig. 11 Dialog box showing the passing points and the center point of ellipsoid on the longitudinal section (upper-right) and crossing section (lower-right)

topography before the landslide gets triggered can be created by filling and excavating the current slope surface. To set the filling and excavation, select [Recover (Source area/Deposition area)] from the [Edit] menu, or click directly the icon  as 'Recovery (Source area/Deposition area)' from the toolbar, or click the button [Creation of sliding surface] then method to create sliding surface by clicking

the [Create sliding surface with recovery setting] option. The following dialog box will appear (Fig. 13) with the command explanations are given in Table 3.

If we select the checkbox "Input with a mouse", and click the contour map, the cursor on the mesh chart will move. The delineated area will be updated by clicking the map while holding down the "Shift" key (created through undo of setting, recovery of source area by filling

Table 2 Remarks of the dialog box for ellipsoidal sliding surface setting

Commands	Description
The current editing section	To create sliding surface, by clicking “Main section” if there is only one sliding surface or “Sub section” if there is a subsection sliding surface
Select longitudinal section	Set the landslide longitudinal section to create an ellipsoidal sliding surface. The corresponding image will appear after the starting point and the ending point of the longitudinal section are entered
Resize option the control	The size of view windows can be changed (○ plane figure, ○ longitudinal section, or ○ crossing section) when we change the size of the dialogue
Sliding surface (longitudinal section): Passing points A, B, center of Ellipsoid Sliding surface (cross section): Passing points C, D, center of ellipsoid	On the longitudinal section, set the passing points A and B which the sliding ellipsoid passes through and the center of the ellipsoid. The crossing section which passes through the center of passing points will be displayed after setting the passing points. Once the ellipsoid is created, the matched coordinates will appear on the crossing section. Passing points data can be entered by clicking the points using mouse For the crossing section, the passing points C and D are set which the ellipsoid passes through, and the center point of the ellipsoid (point D may be determined depends on the longitudinal section) After entering the X-coordinate of the sliding surface passing point, input the Y-coordinate as “*” or by left-clicking while holding down the [Shift] key; the elevation of the slope surface corresponding X-coordinate will be automatically calculated

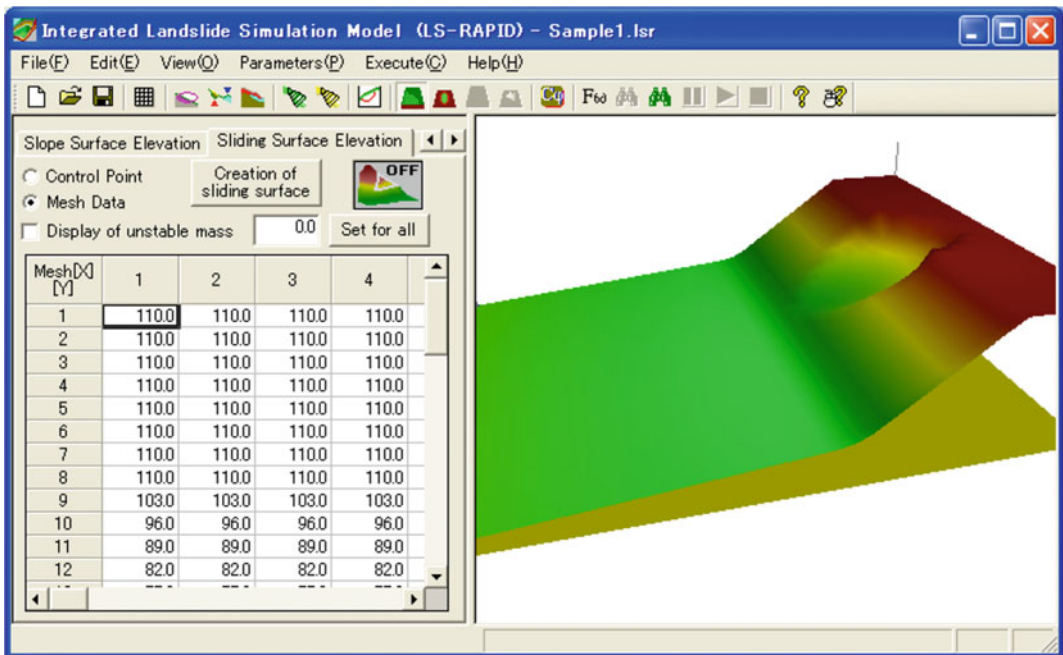


Fig. 12 Layout window after creating possible sliding surface through ellipsoidal parameter

or recovery of deposition area by excavation). We can also update the delineated area by clicking on a cell in the mesh chart.

Click [OK (Reflect topographical recovery)] after finishing all the settings, the following final confirmation message will appear:

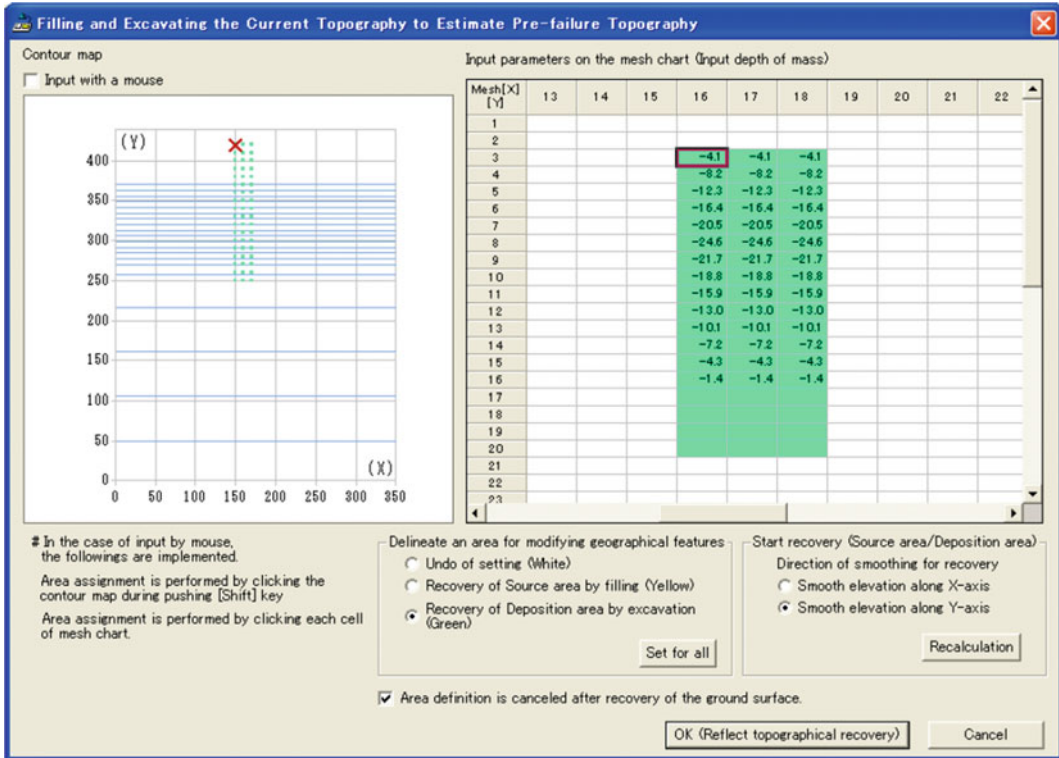
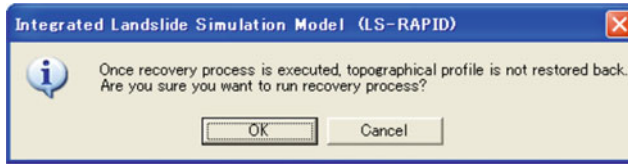


Fig. 13 Dialog box setting the filling and the excavation (recover)

Table 3 Remarks of the dialog box for filling and excavation setting

Commands	Description
Delineate an area for modifying geographical features <input type="radio"/> Undo or setting [white] <input type="radio"/> Recovery of source area by filling [yellow] <input type="radio"/> Recovery of deposition area by excavation [green] [Set for all] button	The filling and excavation attributes can be specified for each mesh data of the current geographical feature. After selecting the mesh, the area will be updated by the selected attribute through clicking the [Set for all] button
Start recovery (source area/deposition area) Direction of smoothing for recovery <input type="radio"/> Smooth elevation along X-axis <input type="radio"/> Smooth elevation along Y-axis [Recalculation] button	After deciding on the attribute, by clicking the [Recalculation] button, the value of fluctuations from the current elevation of the geographical features will be calculated and appear on the mesh chart If we change the direction of smoothing recovery, the re-calculation may start automatically The depth of mass can be entered and the input data will be valid by re-calculate

Note The re-calculation will not start if only changing the attribute of the area

The recovery process based on settings will be executed by clicking the [OK] button, while the [Cancel] button will bring back to the settings dialog box.

After running the recovery process, the slope surface of the current settings will become the sliding surface. The source area created by filling will become a new slope surface. If only processing the recovery of deposition area by excavation, the elevations of the sliding surface and the slope surface will be the same. In this case, the range of the original slope surface will be deleted. The calculation of filling and excavation for an example elevation distribution is shown in Fig. 14.

If we select the entire section as the deposition area by excavation, the red dotted line will show the standard elevation line for excavation. If a mesh elevation value exceeds the standard line, the deposition area will be excavated up to the elevation of the standard line (Fig. 14a). Nothing will be done for the area below the standard line. If we select the entire section as the source area by filling, the blue dotted line will indicate the standard elevation line for filling. Thus, if a mesh

elevation value falls below the standard line, the source area will be filled up to the elevation of the standard line (Fig. 14b). Nothing will be done for the area above the standard line. The geographical feature before filling will be a new sliding surface, while a new slope surface resulted from the geographical feature after filling.

2.8 Delineation the Unstable Mass (Source and Moving Area)


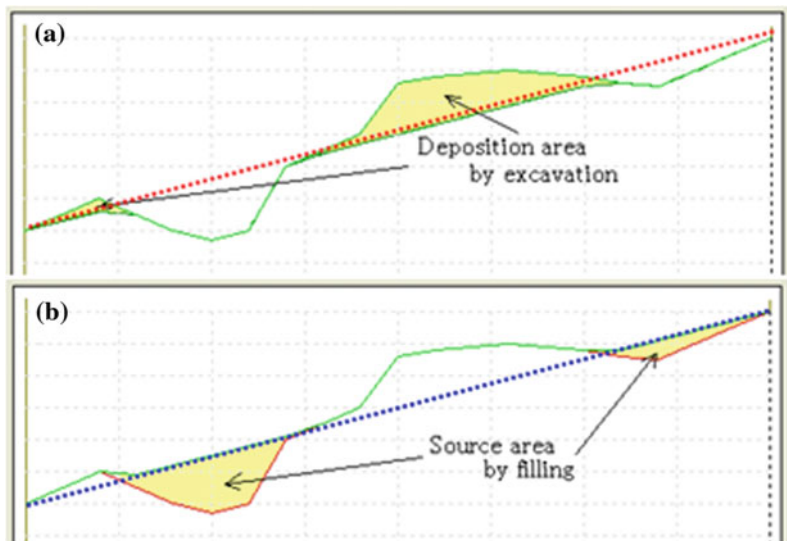
The distribution of the unstable mass height can be seen after we create the geographical features of both the slope surface and the sliding surface. In the distribution, delineation of elements can be specified such as “landslide source area” and “volume enlargement area”. The delineation of unstable mass can be set by selecting [Delineation of unstable mass] in the [Edit] menu, or directly click the icon  as ‘Delineation of unstable mass’ from the toolbar. Then, the dialog box will be displayed, as shown in Fig. 15, with the commands explained in Table 4.

Fig. 14 Calculation of **a** the excavation, and **b** the filling



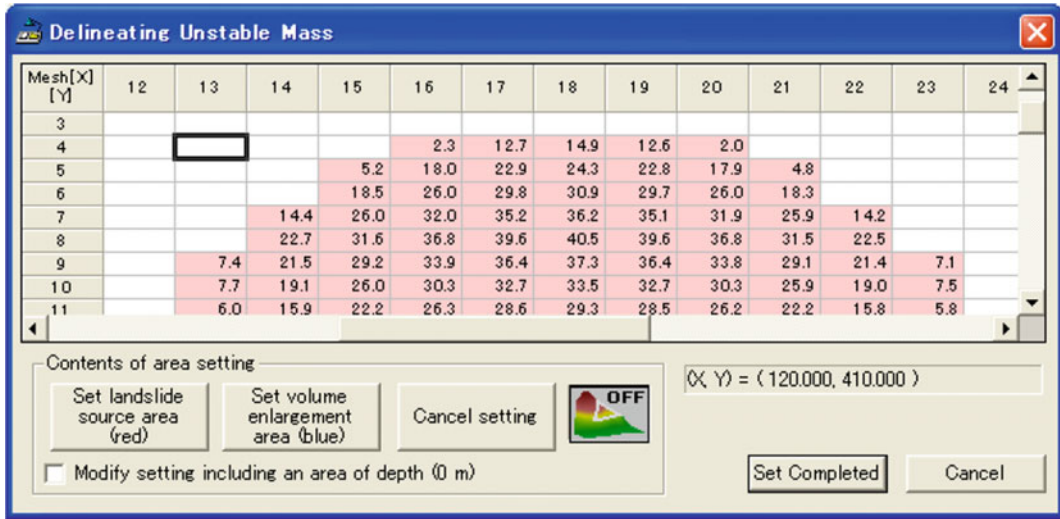



Fig. 15 Dialog box for delineating the unstable mass

Table 4 Remarks of the dialog box for delineating the unstable mass

Commands	Description
Set landslide source area (red) Set volume enlargement area (blue)	Setting up the selected range on the height distribution mesh of the delineation of unstable mass to either “landslide source area” or “volume enlargement area”
Cancel setting	The selected range on the height distribution mesh of the delineation of unstable mass will be cancelled by clicking this button
Editing the selected area	By clicking the button below, ON or OFF can be chosen  When ON is chosen, we can create the any-shape area by using left click and pushing the keys of [Ctrl]+[Shift]
Modify setting including an area of depth (0 m)	If we select this checkbox, we can set an area which does not contribute to the depth of the unstable mass (this area cannot specify by default)

Note This area setting is effective for performing “Initiation + Motion + Expansion Simulation”

After finishing the setting, we click [Set completed] to close the dialog box. When the process is completed, we can see the mass distribution in the elevation edit area (Fig. 16).

3 Parameters and Conditions for Simulation

3.1 Setting the Soil Parameters

After creating the mesh data representing the geographical features of the slope surface and the

sliding surface, the configuration of necessary parameter settings for the simulation is needed. There are two sets of soil parameters. One is the parameters for the whole area and the other is the parameter for each mesh. For the whole area, we select the [Setting the soil parameters] from the [Parameters] menu, then choose [Input for the whole area]. The dialog box in Fig. 17 below will appear. The unit weight of mass (γ_t , kN/m^3) and cohesion inside mass (C_i , kPa with the range of 0.1–0.5 kPa) are set for all the geographical features. Cohesion at sliding surface during motion (C_m , kPa with the range of 0.1–0.5 kPa)

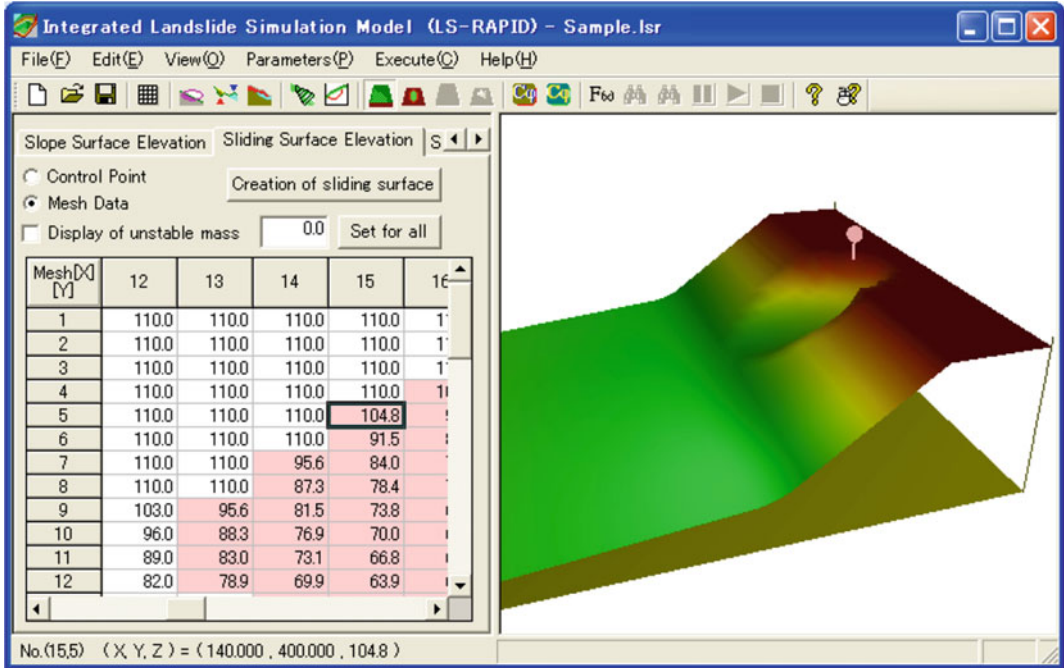


Fig. 16 Layout window after creating delineation of the unstable mass

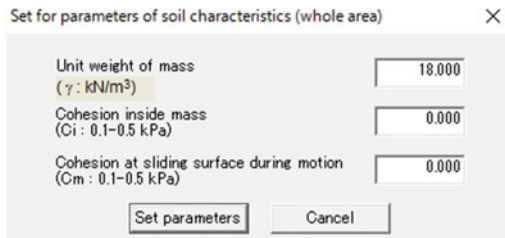



Fig. 17 Dialog box of setting soil parameters for whole area

is also set for all the geographical features. The range of Ci and Cm in the dialog box represents typical values.

To set the soil parameters for each mesh, we select [Setting the soil parameters] from the [Parameters] menu, then choose [Input for each mesh], or by directly clicking the icon  as “parameter (each mesh)” from the toolbar. The dialog box in Fig. 18 below will appear.

An asterisk mark “*” in the Edit column indicates the current parameter being edited. The ‘normal value’ column represents the typical

values of each soil parameters. The data can be entered in the columns and rows that indicate mesh [X] and [Y]. If we press the keys [Ctrl] +[Shift] and left click in the 3D-View window, the corresponding mesh cell in red colour will be viewed in the window for mesh editing. Table 5 shows remarks on each command in the dialog box of setting soil parameters for each mesh, while Table 6 presents the seven parameters that can be set for different grid points. Symbol “○” in Table 6 represents the required items, “Δ” represents the required item for considering the strength reduction for the “Initiation + Motion + Expansion Simulation”.

3.2 Conditions for Calculation

In the LS-RAPID, various pattern of landslide simulation can be set in the dialog box by selecting [Conditions for calculation] from the [Parameters] menu (Fig. 19). The simulation type can be performed either ○ Motion simulation, ○ Full mode simulation (Initiation + Motion + Expansion), or

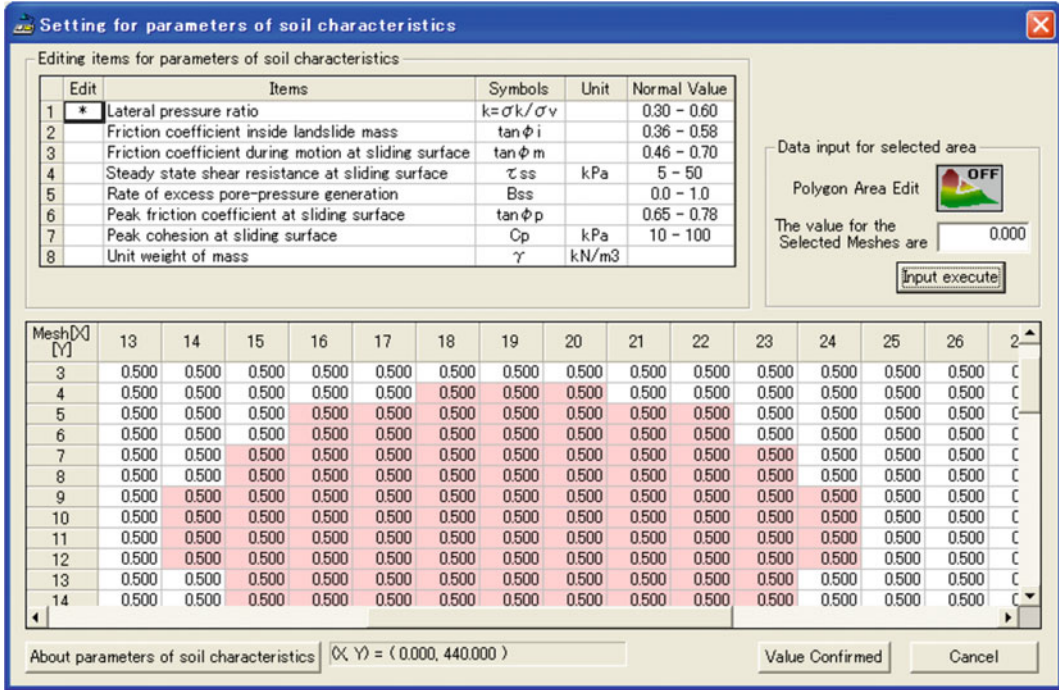



Fig. 18 Dialog box of setting soil parameters for each mesh

Table 5 Remarks of the dialog box for setting soil parameters on each mesh

Commands	Description
Editing items for parameters of soil characteristics	Set the parameters for different grid points
Data input for selected area	By clicking the button below, ON or OFF can be chosen  When ON is chosen, we can create the any-shape area by using left click and pressing the keys [Ctrl]+[Shift] The value for the Selected Meshes can be entered, and then click [Input execute]. As a result, the same values will be set for all meshes that we selected
About parameters of soil characteristics	Opens the description dialog box about the parameters of the soil characteristics

○ Pore pressure ratio. The soil mass under water will be considered as buoyancy if ○ Pore pressure ratio is chosen. To conduct a simulation of marine landslide, the ○ Pore pressure ratio type can be chosen.

The parameters of condition for strength reduction in the dialog box can be explained as follows. In the (Initiation + Motion + Expansion) simulation mode, the simulation will reduce the friction coefficient and the cohesion from

their peak values to the normal motion time values within the source area in the determined distribution of the unstable mass (reducing from “ $\tan \phi_p$ ” to “ $\tan \phi_m$ ” and from “ C_p ” to “ C_m ”). For the ‘source area (by travel length)’, when the travel length becomes DL (mm), reduction will be started. Once the travel length reaches DU (mm), the reduction will be completed and then normal motion simulation will start. For the ‘except source area (by depth of mass)’, when the

Table 6 Parameters that set for different grid points

Items	Symbol (Unit)	Remarks
Lateral pressure ratio	K	○
Friction coefficient inside landslide mass	$\tan \varphi_i$	○
Friction coefficient during motion at sliding surface	$\tan \varphi_m$	○
Steady state shear resistance at sliding surface	τ_{ss} (kPa)	○
Rate of excess pore-pressure generation	B _{ss}	○
Peak friction coefficient at sliding surface	$\tan \varphi_p$	Δ
Peak cohesion at sliding surface	C _p (kPa)	Δ
Unit weight of mass	γ (kN/m ³)	○

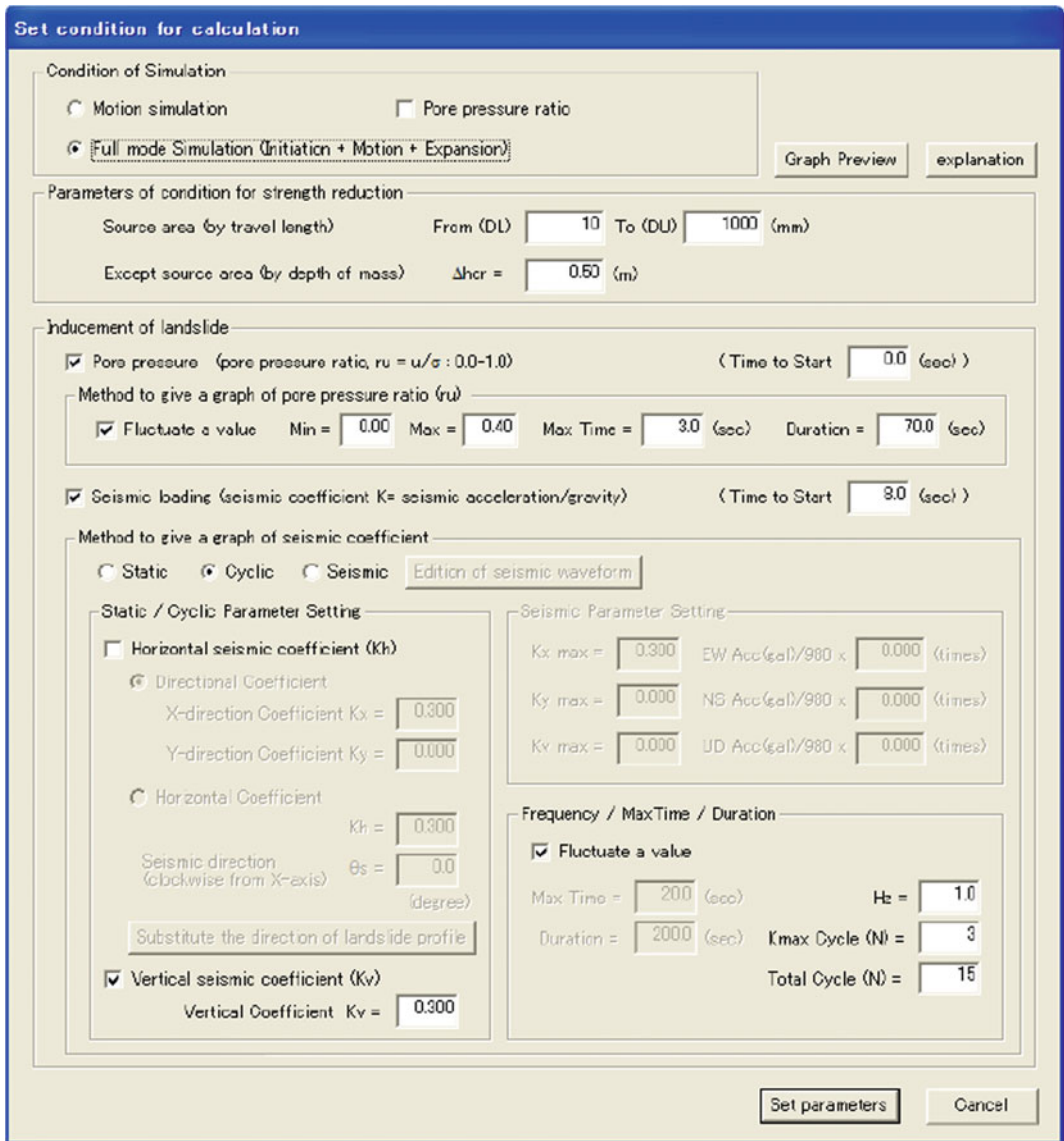


Fig. 19 Dialog box setting the condition for calculation

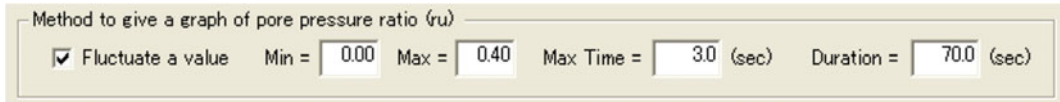


Fig. 20 Dialog box to set the pore pressure for simulation

depth of mass reaches Δh_{cr} (m), the reduction will be completed and the normal motion simulation will start.

The graph preview button in the dialog box shows the graph of the determined pore pressure ratio (r_u) and the force of seismic loading. The explanation button presents the explanation of the initiation simulation. In the “Initiation + Motion + Expansion” option, pore pressure and the seismic loading can be set at the induction of landslide. The starting time of the induction of the landslide can also be determined. The pore pressure ratio ($r_u = u/\sigma$) ranged between 0.0 up to 1.0. An inducement of the landslide can be set through a constant pore pressure or a fluctuating pore pressure over time. Example of the fluctuating pore pressure setting can be seen in Fig. 20. Setting in the dialog box means that the pore pressure ratio will go up from $r_u = 0.0$ at the beginning of the simulation to $r_u = 0.4$ in three seconds and remain fixed for seventy seconds.

The seismic loading force can be set as a constant seismic load or a fluctuating seismic load over time, for an inducement of the landslide. The seismic coefficient (K) is the ratio of seismic acceleration over the gravity. We can choose one of the following seismic operation methods: Static, Cyclic or Seismic. The seismic coefficient (K) varies linearly in the static method. While in the cyclic method, the K varies as a sine wave while the value of the amplitude changes linearly. In the seismic method, the K varies based on the actual seismic wave form data. The example of settings for static method and cyclic method are shown in Fig. 21, while for the seismic method is presented in Fig. 22.

The above static setting will cause the seismic coefficient to go up from $K = 0$ at the beginning

of the simulation to K_{max} in four seconds and it will remain fixed for thirty seconds. The cyclic setting presents the amplitude of the seismic coefficient to go up from $K = 0$ at the beginning of the simulation to K_{max} in three seconds ($=6/2$ Hz) and it will remain fixed for fifteen seconds ($=30/2$ Hz). For the seismic setting (Fig. 21), the seismic coefficient becomes $K_{max} = 0.15$ based on the edited seismic waveform. The value of “ K_{max} ” can be for the seismic coefficient in the X-direction, Y-direction, and Vertical direction. The button [Substitute the direction of landslide profile] in Figs. 21 and 22 means if we created the sliding surface (in the main section) from an ellipsoid, the direction of the land sliding longitudinal section will be set as the seismic direction.

3.3 Registration of Seismic Waveform

In the landslide simulation using LS-RAPID, we can set the seismic waveform based on the model seismic waveform or on the actual observation data. The seismic method with an actual seismic wave data can be selected by clicking the [Edition of seismic waveform] button in the “Condition of calculation” dialog box, or by selecting [Registration of seismic waveform] from the [Parameters] menu. Then, three observational cases of seismic waveform can be registered in the dialog box (Fig. 23).

In the actual landslide simulation, one of these cases should be selected to start the calculation. We can enter a name for the data-set in the top box and enter the values of the observation times and the acceleration K (unit: Gal) in the appropriate columns. The observation time should be entered in chronological order. EW means the seismic

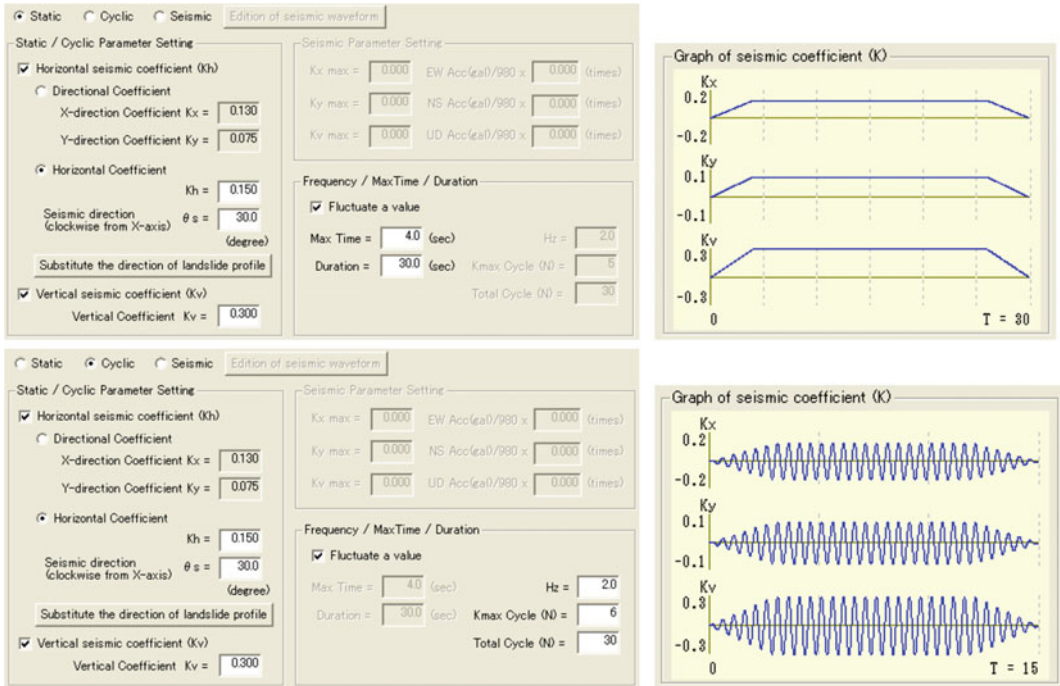


Fig. 21 Dialog box settings for static method (top) and cyclic method (down)

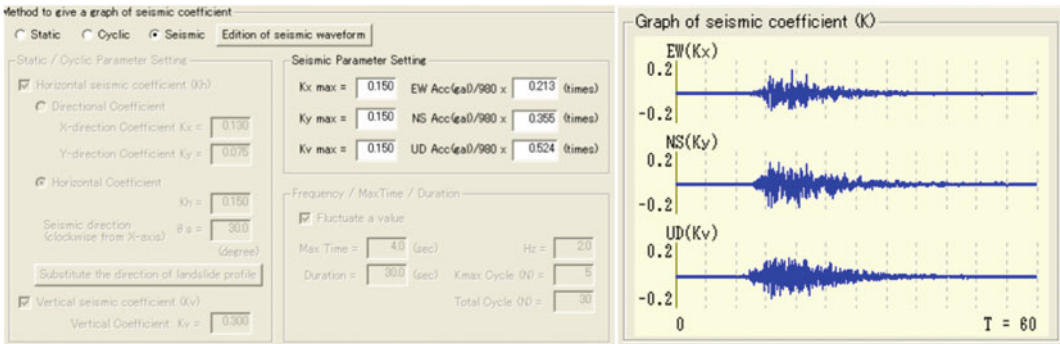


Fig. 22 Dialog box settings for seismic method

coefficient in X-direction and NS means in Y-direction. In order to perform the simulation using seismic type of the waveform, we need to select “Full mode Simulation (Initiation + Motion + Expansion)” from the [Conditions for Simulation] of the [Parameters] menu, and select “Seismic loading” for the induction of landslide.

3.4 Setting the Time Step and Other Conditions

The motion process degree can be adjusted by using a specified time step by selecting [Set time step] from the [Parameters] menu (Fig. 24) with command remarks are shown in Table 7.

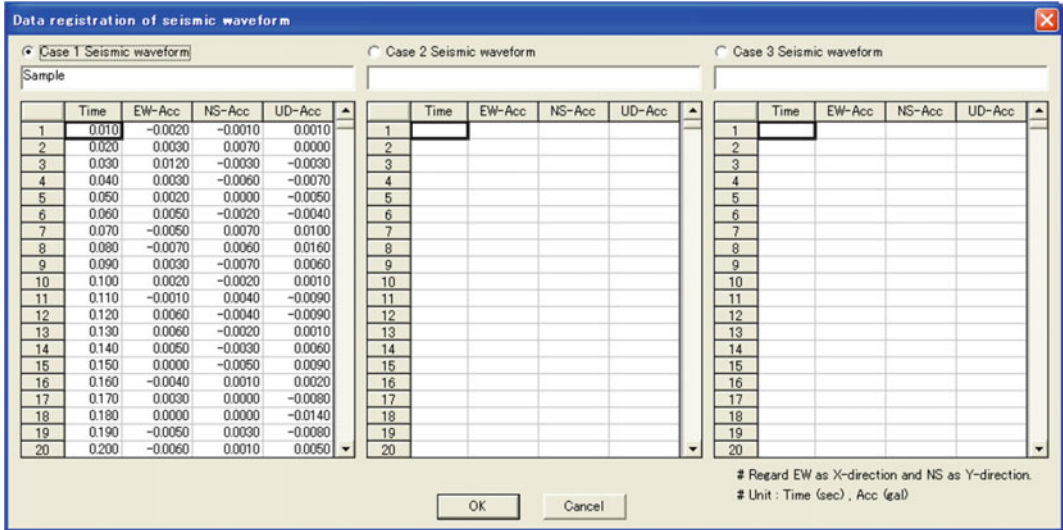


Fig. 23 Dialog box for data registration of seismic waveform

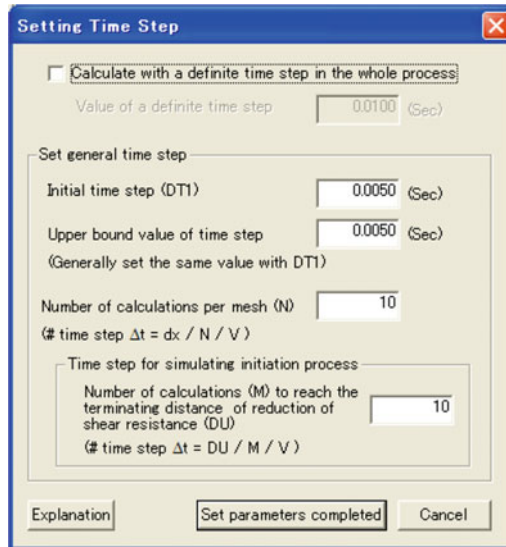


Fig. 24 Dialog box for setting the time step

Table 7 Remarks for setting the time step

Commands	Description
Calculate with a definite time step in the whole process	The simulation time step will remain constant as the simulation proceeds
Initial time step (<i>DTI</i>)	Set the time step for the first step of the simulation
Upper bound value of time step	If the next time step calculated from the average maximal velocity of $v = \sqrt{u_{max}^2 + v_{max}^2}$ is more than the entered value, set the next time step to the value entered here
Number of calculations per mesh (<i>N</i>)	To set the number of calculations by mesh <i>N</i> where the next time step is defined by $dx(= mesh\ pitch)/N/v$
Number of calculations (<i>M</i>) to reach the terminating distance of reduction of shear resistance (<i>DU</i>)	To set the number of calculations <i>M</i> to define the time step by $DU/M/v$ in the parameters of the initial simulation. After reaching the terminating distance of reduction of shear resistance, the simulation proceeds with the time step of the motion simulation

Other conditions that might be needed for landslide simulation are provided by selecting [Set other conditions] from the [Parameters] menu (Fig. 25; Table 8).

3.5 Output Settings for the Landslide Simulation

The output settings for the landslide simulation can be carried out by selecting [Set calculation

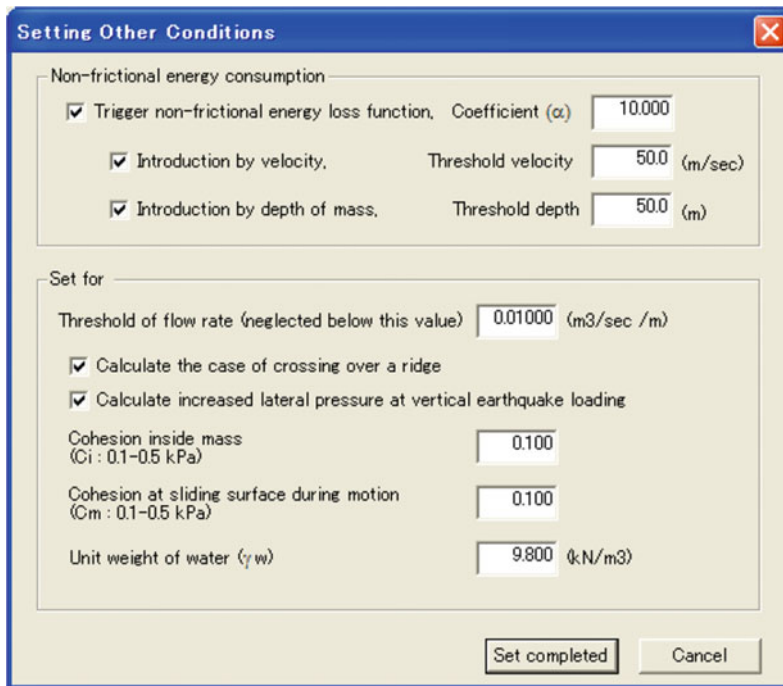


Fig. 25 Dialog box for setting other conditions in the simulation

Table 8 Remarks for setting the other conditions in LS-RAPID

Commands	Description
Trigger non-frictional energy loss function	The non-frictional energy consumption ($= \alpha \cdot 1/2 \cdot m \cdot v^2$) will be considered in the simulation
Coefficient α	The coefficient for the simulation when triggering the non-frictional energy loss function
Introduction by velocity Introduction by depth of mass	The non-frictional energy consumption ($= \alpha \cdot 1/2 \cdot m \cdot v^2$) will be considered, corresponding to the mesh which reaches the specified velocity (and or depth of mass)
Threshold of flow rate (neglected below this value)	Threshold of flow rate is the minimum amount the soil is moving in the calculated mesh within the unit time (in m^3/s). In the case of landslide, the “mm” unit landslide is thinner than water; therefore, the landslide cannot usually flow. Thus, if the flow rate goes below threshold, the mesh does not accept the flow. The value depends on the size of the landslides, but $\sim 0.01 m^3/s$ can be used as the first approximation for usual landslides
Calculate the case of crossing over a ridge	When the landslide mass travels down a curved torrent, most of the mass travels along the torrent. However, there is a case in which the upper part of the landslide mass, if it is higher than the ridge, will goes over the ridge. The effect can be included in the simulation by selecting this option (There is no harm in leaving the checkbox selected whether there is a case of crossing over the ridge or not)
Calculate increased lateral pressure at vertical earthquake loading	Three seismic stress factors are considered in the simulation. When the vertical stress is increased, the lateral stress should be increased accordingly to the lateral pressure coefficient (the ratio between the vertical pressure and the lateral pressure). The effect is facilitated by choosing this option (the checkbox should be selected under normal conditions)
Cohesion inside mass (C_i , kPa)	Set the cohesion inside mass for all the geographical features (typical values between 0.1 and 0.5 kPa)
Cohesion at sliding surface during motion (C_m , kPa)	Set the cohesion at sliding surface during motion for all the geographical features (typical values between 0.1 and 0.5 kPa)
Unit weight of water (γ_w , kN/m^3)	Set the unit weight of water

output] from the [Execute] menu (Fig. 26; Table 9).

In order to be displayed properly in the 3D view, the comments field should be filled by half-width alphanumeric characters. If the mass soil is flowing out of the border limit despite the settings in the field, the following example in the comments field will appear: “First Soils: 45110000, Current: 44829105 (−0.6%)”.

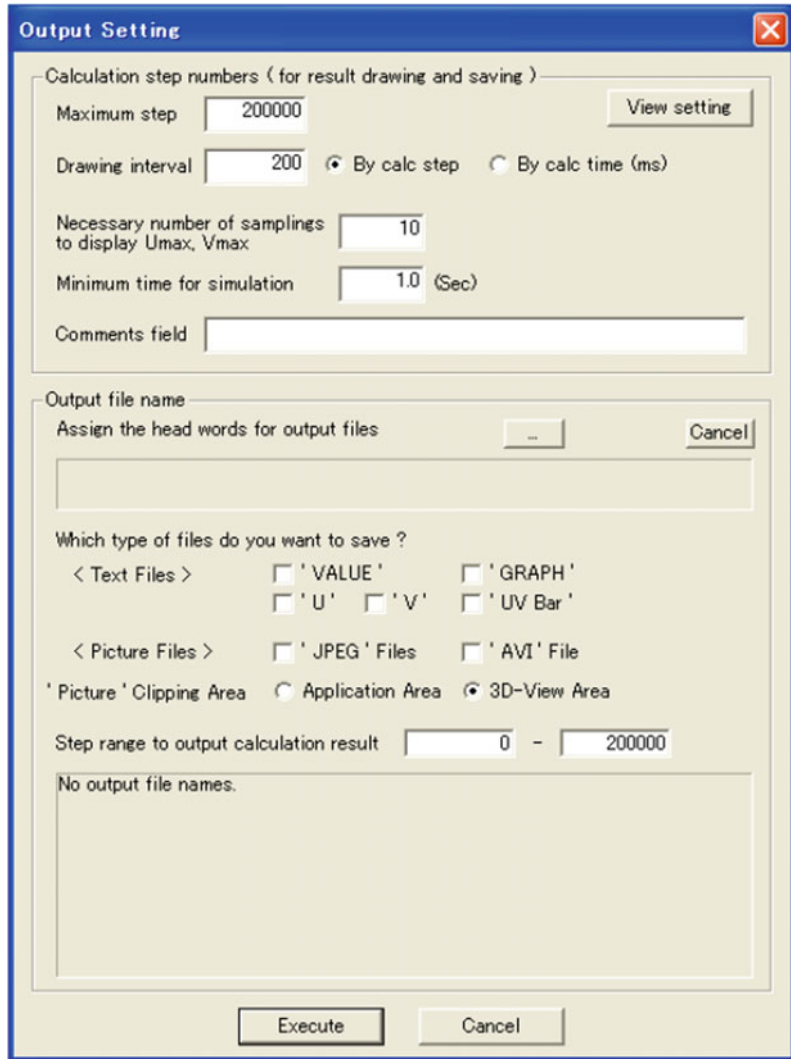
Different output files for the intermediate results during the simulation are shown below (Table 10). The range of the output screen for

JPEG and AVI files can either be the 3D view area or the application area. If the ‘Application Area’ as the output range is not able properly to give an output screen, then the ‘3D-View Area’ can be selected.

4 Run the Simulation

The simulation of LS-RAPID can be started by selecting [Start Simulation] from the [Execute] menu, or clicking the icon as “Start Simulation”

Fig. 26 Dialog box for the output settings of landslide simulation



from the toolbar. The simulation will begin. Figure 27 shows an example screens captured during simulation.

The following commands (Table 11) can be run during the simulation. Both the “Calculation monitoring” and “Given triggering factors” commands can also be called from the [View] menu by selecting [Display of calculation values].

5 Other Commands in the LS-RAPID

There are several other commands in the LS-RAPID that are not yet described in the above sections. Tables 12 and 13 below presents commands in the [File] and [View] menu.

If we choose [Setting of the View Point of Topography] from the [View] menu, the

Table 9 Remarks for the output settings

Commands	Description
Calculation step numbers (for result drawing and saving)	Set the number of the calculation steps
Maximum step	Set the maximum step
Drawing interval <ul style="list-style-type: none"> • By calc step • By calc time (ms) 	Set the time interval for updating the geographical features during the simulation. The intermediate simulation results will be saved in the output files at the end of each time interval
Necessary number of samplings to display Umax, Vmax	The number of samples of the velocity per mesh in order to display the X and Y components of the maximal velocity during the simulation (the displayed velocity values for each mesh are the average over the samples)
Minimum time for simulation	The simulation will be finished when all the solid features are stopped. But if the minimum time is set, the simulation will run until the end of the entered time, even if all the solids have stopped
Comments field	Enter any comments that necessary to be displayed during the simulation
Output file name	Select the folder for the output data
Types of files	The corresponding data files will be saved in the output folder by checking the checkboxes
Step range to output calculation result	The data will be outputted within the specified time range by entering the step range (if we enter "0", the output will start from the beginning to the end of the simulation)

Table 10 Different output files of the simulation

Output files	Types	Description
Text file	'VALUE'	The value of the depth for the unstable mass per mesh
	'GRAPH'	Symbol representation of the depth for the unstable mass per mesh.
	'U', 'V', 'UV Bar'	The flow velocity per mesh (U: X-direction, V: Y-direction, UV Bar: the average value)
Picture file	'JPEG'	Output the calculation results as a still image in JPEG format once the screen is updated
	'AVI'	Create a video using the images of the updated screens in AVI format

parameters for viewing topography can be defined in the dialog box below (Fig. 28). We can set the value of View Point (X, Y, Z), Zoom Ratio and Rotation Angle (X, Y, Z) in "Degree" units. The preferable viewpoints can be registered in the View Point History and for the next

simulation can be recalled by just clicking the registered viewpoint and then click "Adoption".

Setting of the topography, including lines, mesh, contour or colours, can be done through the [Setting of Topography View] from the [View] menu (Fig. 29; Table 14).

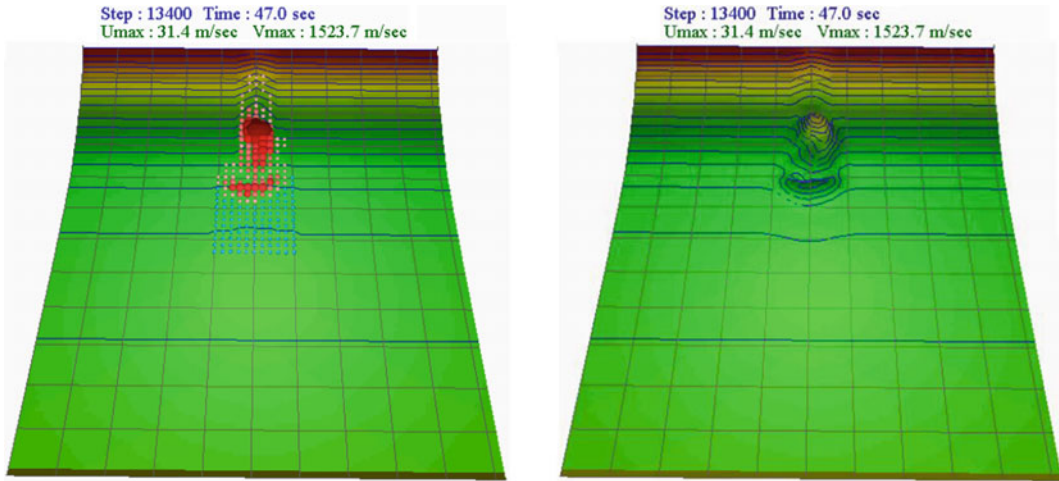


Fig. 27 Example of the simulation: an illustration of the ellipsoid (*left*) and an illustration of the mass thickness expanded three times (*right*)

Table 11 Commands during the simulation






Commands	Description
 Calculation monitoring	Opening dialog box to show the mass thickness and the values of different components of the velocity
 Given triggering factors	Opening dialog box to show the pore pressure and seismic loading
 Pause	Pauses the simulation temporarily
 Restart	Restarts the simulation which has been paused temporarily
 Stop	Forces the simulation to stop

Figure 30 and Table 15 shows the dialog box of the “Setting for Topography Color” menu that used to set the topography view as necessary.

In the [View Cross or Longitudinal Section] from the [View] menu, the cross sections parallel to the X and Y axis can be viewed as shown in the dialog box below (Fig. 31). In the default condition, green color means slope surface, red color means sliding surface and pink color means the section of the slope surface after simulation. The order of the section display will be reversed by selecting the “Locate Y-Section Above” checkbox in the dialog box. The color and thick of the cross sections can be defined through

the dialogue of “Information of sections” in the “Information” button (Fig. 32).

The section layout can be set through the [Output of arbitrary section profile] from the [View] menu (Fig. 33; Table 16).

The option of [Set the system environmental parameters] in the [Parameters] menu is used for the basic settings of the LS-RAPID model (Fig. 34). The introduction window of LS-RAPID will appear when it is started if “Skip the opening title” option is not checked. “3D-View is not moved with a mouse during Simulation Calculation” can be checked in case of the topography suddenly starts to move. If we

Table 12 Commands in the File menu

Menu item	Description
New	Creates a new data file for the landslide simulation system
Open	Opens a data file
Save	Saves the data file
Save as	Saves the document as a different file. Choose the new file name and location for the document
Write to a text data	Export the entered numerical values (control point, mesh data, parameters of soil characteristics) to a text data file <input type="radio"/> All data: all values will be exported to a text file. The location of the exported file need to be specified as the same way for the simulation output file under the “assign the head words for output files” in the “output setting” dialog box <input type="radio"/> Specific data: have to select the value to be exported from the list that will show up, then select the location of the exported file and save it
Save image by JPEG	Saves the image currently displayed in the 3D view as a
Close of file	Close the editing file
Exit of application	Exit

Table 13 Commands in the View menu

Menu item	Description
Setting the view point of topography	Update the viewpoint by setting the angle of rotation for each axis. The viewpoint of the screen can be updated by using the mouse
Reset geographical viewpoint	Reset the topography viewpoint to the default setting
Reset geographical feature	Reset the topography data that has been previously calculated
Setting of topography view	Set how the topography will be illustrated
Setting of topography color	Setting of the topography color and contour
Current figure	Select the topography options below that would like to display: <input type="radio"/> Slope surface, sliding surface (default) <input type="radio"/> Thickness of sliding mass <input type="radio"/> The last view of calculation <input type="radio"/> Sliding mass thickness distribution
View cross or longitudinal section	View the cross section at the selected (mesh-grid) location, both displayed in cross and longitudinal sections
Output of arbitrary section profile	Set the output section arbitrarily, includes the section coordinates
Display of calculation values	Display the value of each mesh data during the simulation. In “Landslide inducement parameter”, the values indicate the pore pressure and the seismic loading for the initial simulation

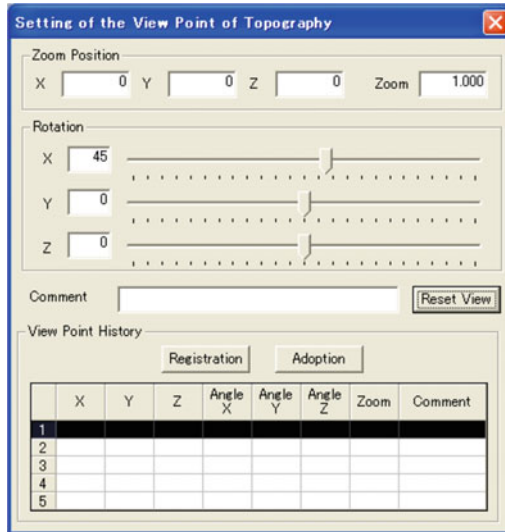


Fig. 28 Dialog box for view point setting of the topography

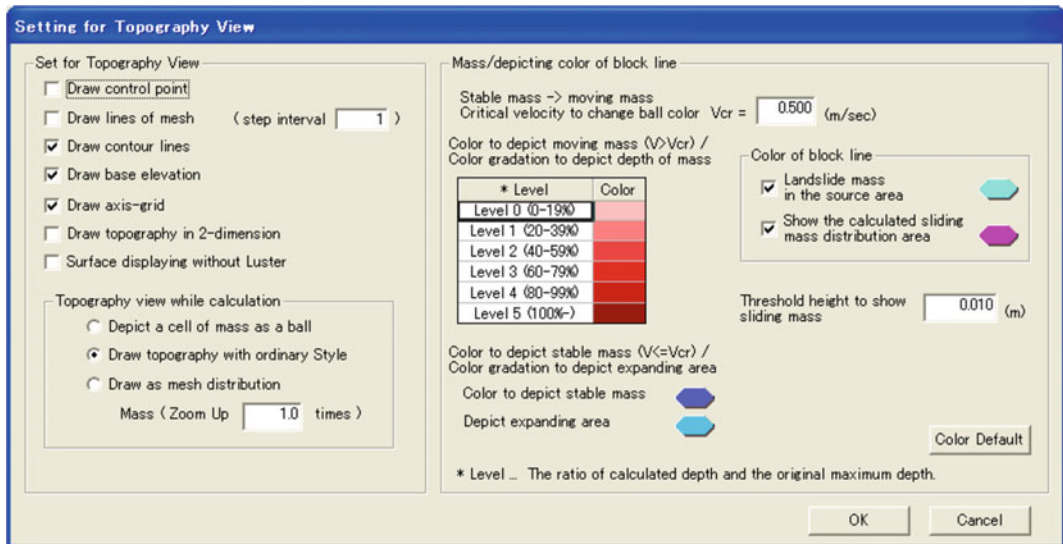


Fig. 29 Dialog box for setting of topography view

Table 14 Commands in setting of topography view

Menu Item	Description
<i>Set for topography view</i>	
Draw control point	The control point will be displayed if there is any
Draw lines of mesh	The grid lines will be displayed and the step interval can be specified
Draw contour lines	The contour lines will be displayed and the interval can be specified
Draw base elevation	Draw the base elevation
Draw axis-grid	Draw an axis of coordinates
Draw topography in 2-dimension	Draw the topography in two dimensions
Surface displaying without Luster	Check this item if the topography does not show up in the 3D view (this setting is usually unnecessary)
Topography view while calculation	To display topography change during calculation/simulation: <ul style="list-style-type: none"> • Depict a cell of mass as a ball • Draw topography with ordinary style • Draw as a mesh distribution
Mass zoom up	Customizing the zoom level of the mass when displaying the topography with the option either “Draw topography with ordinary style” or “Draw as mesh distribution”
<i>Mass/depicting color of block line</i>	
Critical velocity to change ball color, $V_{cr} =$	Set the critical velocity (V_{cr}) at which the stable mass changes to a moving mass
Threshold height to show sliding mass	Display a mass depth greater than the specified value as “sliding mass”
Color gradation to depict depth of mass/color gradation to depict expanding area	Set the color gradient to depict the depth of the mass when describing the moving mass and the stable mass by an ellipsoid or a mesh The “Level” means the ratio of calculated depth and the original maximum depth The color of mass can be depicted by double clicking the “Color” palette or hexagon and change the color
Color of block line	Displays the block line for showing the simulated sliding mass distribution area and for the landslide mass in the source area of the motion simulation

select this option, nothing will happen when we click or drag the mouse during the simulation.

In the dialogue of the “Calculation Result”, we can choose whether the value of 0.0 in third option in Fig. 34 will be displayed or not. Generally, it will not be displayed when we start the

LS-RAPID. When we check this option, value “0.0” will be displayed in “Calculation Result”.

The [Help] menu displays the help for the software. The [Explanations of LS-RAPID] in the [Menu] menu describes the concepts in the LS-RAPID simulator: The apparent friction

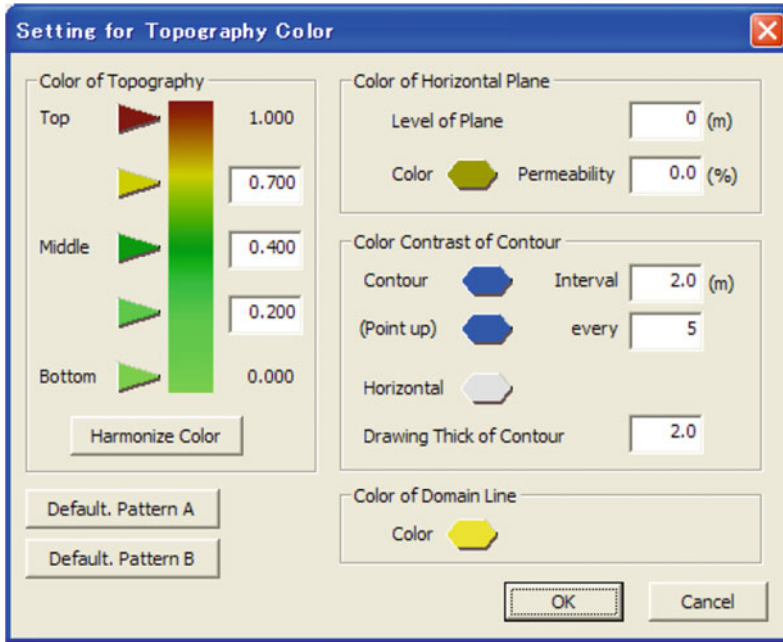


Fig. 30 Dialog box for topography color setting

Table 15 Commands in setting for topography color

Menu item	Description
Color of topography	The color can be set according to the elevation of topography by clicking the triangle on the left side of color palette. The elevation ratio (0.0–1.0) can be entered on the right side according to the specified color
Harmonize color	To adjust the color between the ranges
Color of horizontal plane	To set the color/level/permeability for some topographic surface. The water surface can be defined here when running the submarine landslide simulation
Color contrast of contour	To set the interval, color, thickness and horizontal option of the contour lines when depict the contours
Color of domain line	Set the color for the selected objective area
Default color (pattern A, B)	Set the color using the default patterns. Pattern A is mainly used for subaerial landslides, and pattern B is mainly used for submarine landslides

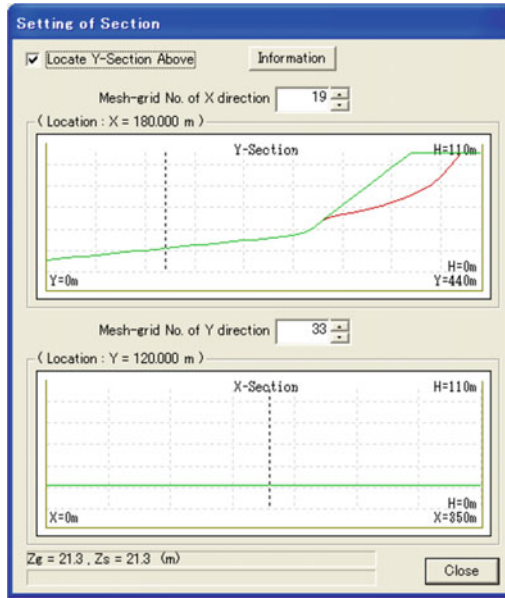


Fig. 31 Dialogue box for viewing the cross or longitudinal section

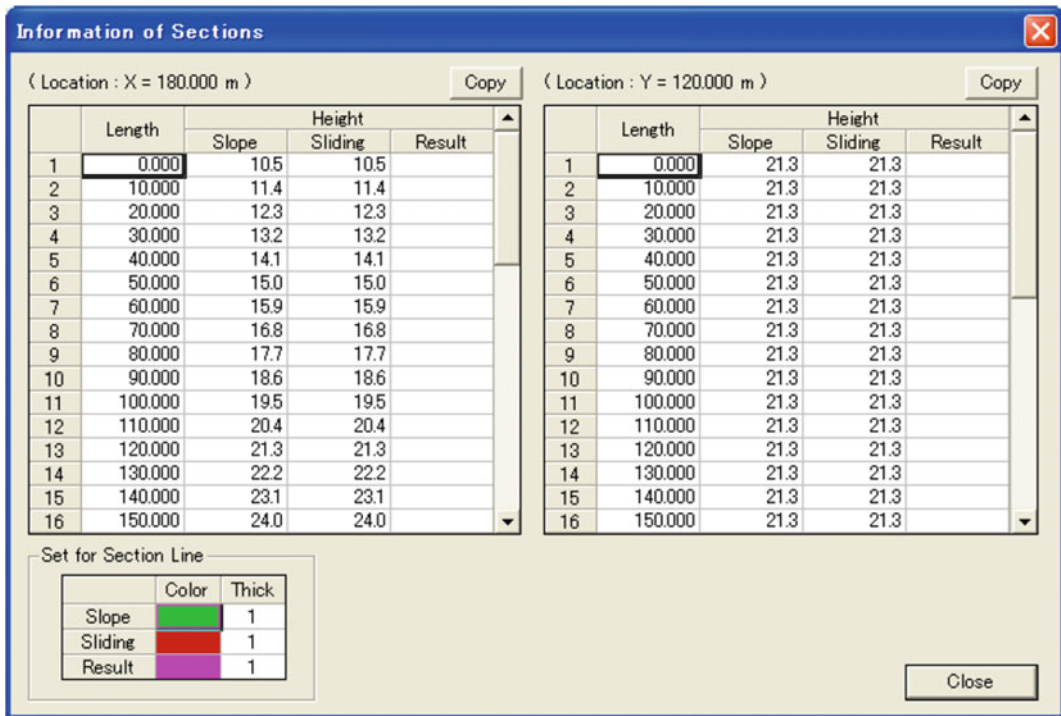


Fig. 32 Information of sections

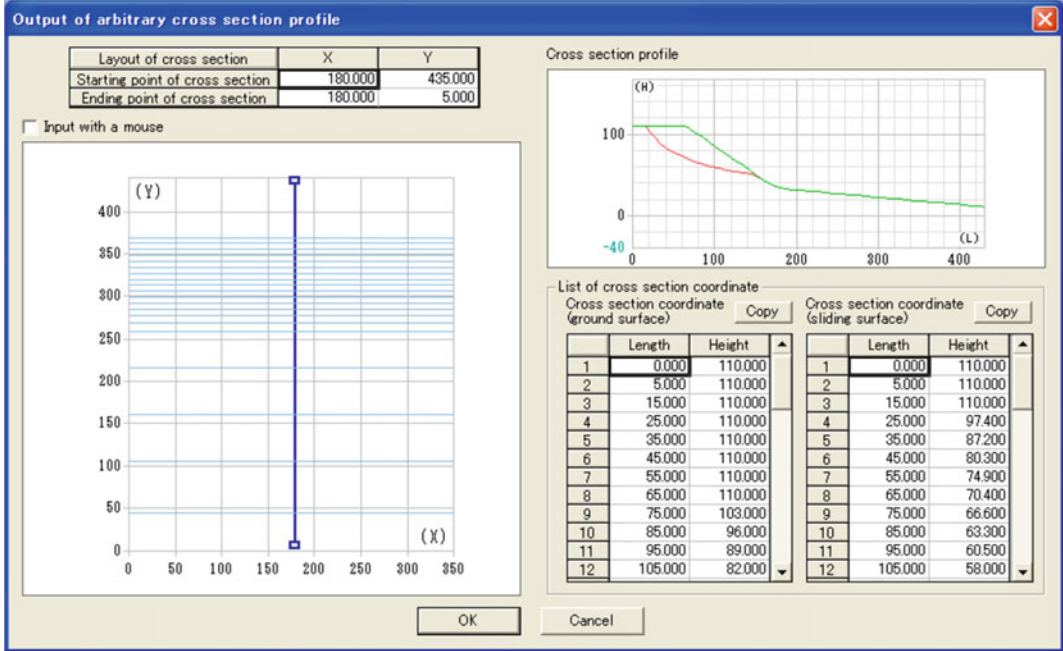
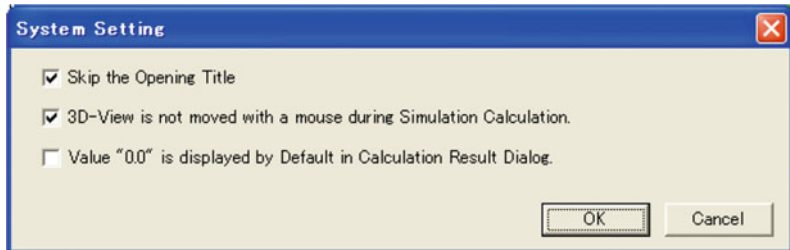


Fig. 33 Output of arbitrary cross section profile

Table 16 Commands in setting for arbitrary cross section profile

Menu item	Description
Layout of cross section	Enter the starting and the ending points of the cross section to be displayed. Points can be selected using mouse
Cross section profile	Displays the cross section profile based on the specified values of the section coordinates
List of cross section coordinate	Displays the coordinate values of the cross sections of the slope surface and the sliding surface corresponding to the above cross section profile

Fig. 34 System setting in the LS-RAPID



coefficient on the sliding surface; the initiation model of the landslide; and the expansion model of the landslide. The [Control Guide] explains

how to move the screen using a mouse. Finally, the [Version Information] displays the version of the LS-RAPID software.

6 Conclusion

The development of LS-RAPID software is aimed to simulate the whole process of landslides from the initiation, motion, volume enlargement and travelling materials up to the deposited area. Triggering factors from the earthquake and rainfall (manifested as pore pressure ratio) were able to produce within the simulation as the inducement of landslides. The LS RAPID model can be used both for aerial landslide and submarine landslides. As an integrated model, the use of LS RAPID is more satisfied by conducting the ring shear tests in advance, to obtain critical parameters for landslide simulation, such as steady state shear resistance, apparent friction angle and shear displacement at the beginning of soil failure and at the end of soil shear strength reduction. Several cases of landslides (in Japan,

Croatia and the Philippines) which were analysed by LS RAPID are described further in the PDF Tool: Manual for the LS-RAPID software.

References

- Sassa K, He B, Miyagi T, Strasser M, Konagai K, Oštrić M, Setiawan H, Takara K, Nagai O, Yamashiki Y, Tutumi S (2012) A hypothesis of the Senoumi submarine megaslide in Suruga Bay in Japan: based on the undrained dynamic-loading ring shear tests and computer simulation. *Landslides* 9–4:439–455
- Sassa K, Nagai O, Solidum R, Yamazaki Y, Ohta H (2010) An integrated model simulating the initiation and motion of earthquake and rain induced rapid landslides and its application to the 2006 Leyte landslide. *Landslides* 7–3:219–236
- Sassa K (1988) Geotechnical model for the motion of landslides. In: *Proceedings of the 5th international symposium on landslides*, Landslides, Balkema, Rotterdam, vol 1, pp 37–56

TXT-tool 3.034-2.1

A Debris Flow Regional Fast Hazard Assessment Toolbox

Francesco Bregoli, Vicente Medina and Allen Bateman

Abstract

The rapid development of GIS techniques permits the regional scale assessment for natural hazards. In this work different declared as GNU/GPL open source codes for debris flow hazard assessment have been developed for risk management and educational purposes. The toolbox here presented manages the large amount of regional spatially distributed geographic information and includes: shallow landslide susceptibility assessment tools; an in-channel debris flow triggering mechanism evaluation tool; and the stochastic debris flow propagation tool “DebrisDice”. The tools are presented as executables in order to enhance the usability. Input/output are in ASCII grid format.

Keywords

Debris flow · Shallow landslide · Physical models · GIS
Regional hazard assessment

F. Bregoli (✉)
Catalan Institute for Water Research (ICRA), Emili
Grahit 101, 17003 Gerona, Spain
e-mail: f.bregoli@un-ihe.org;
francescobrieg@gmail.com

F. Bregoli · V. Medina · A. Bateman
Sediment Transport Research Group (GITS),
Department of Hydraulic, Marine, and
Environmental Engineering, Universitat Politècnica
de Catalunya—BarcelonaTech (UPC), UPC Campus
Nord, C/Jordi Girona 31, Building D1, Office 210,
08034 Barcelona, Spain
e-mail: vicente.medina@gits.ws

A. Bateman
e-mail: allen.bateman@upc.edu

Present address:

F. Bregoli
Water Science and Engineering Department, IHE
Delft Institute for Water Education, Westvest 7, 2611
AX Delft, 3015 2601 DA Delft, The Netherlands

Contents

1 Introduction	226
2 Physical Background	226
2.1 Susceptibility Models.....	227
2.2 Propagation Model.....	229
3 Data Requirement and Operational Details ...	231
4 Applications	232
5 Conclusion	233
References.....	234

1 Introduction

Debris flow (DF) is one of the main hazards in mountain areas. Steep slopes and high rainfall intensities are, among others, the key conditions for the triggering of the process. The recurrence of this kind of events is low. Hence in most cases there is not available information regarding previous occurrences. Deposition fans are the flattest areas in mountainous morphology and therefore the most appealing for urban developments. Public concern about DF events is poor, although a large portion of urban areas are under risk. To address this issue, susceptibility analysis should be performed in large areas, at regional scale, finding locations for potential DF events prescribing further detailed studies. The aim of the toolbox presented here is to provide fast assessment tools for the risk management authorities and stakeholders.

A DF can be triggered by means of different processes e.g.: increasing of pore pressure due to heavy rainfall; sediment entrainment; earthquake; volcanic eruptions; soil burnt; soil liquefaction (Coussot and Meunier 1996). Here two of the most recurring triggering mechanisms of DF are selected: shallow landslides triggered by water infiltration and basal entrainment of sediments. The propagation is usually simulated with complex 1D or 2D numerical models which necessitate detailed and generally not easily available inputs. In this study we have selected a simplified flow routing algorithm with low requirements in terms of data input.

In the spatial planning GIS tools are the optimum choice for information management. In

particular those tools have already been employed in terrain morphology and stability (e.g. Carrara et al. 1991; Tarboton 1997; Montgomery and Dietrich 1994; Pack et al. 2005; Rigon et al. 2006). Probably the most extended GIS software is the ESRI ArcGIS, but being proprietary software the distribution is limited. The range of open source GIS is wide and includes, among others, QGIS, GRASS GIS, Open Jump, GeoTools or gvSIG. In the present work SEXTANTE open source GIS JAVA library (Olaya 2008) is selected as a starting point. It provides the framework to develop and implement all the proposed algorithms except the DF propagation tool, which is implemented in FORTRAN due to the higher computational request. In order to reduce the complexity of the programming and to enhance the portability to other software, all raster data input and output are provided in ESRI ASCII grid format.

First the physics of the models is described, later the implementation details and data requirement of the toolbox are explained and finally the selected models are applied in a test case within the Eastern Catalonian Pyrenees (Spain).

2 Physical Background

A DF is initiated generally on a steep slope and propagated with high velocity on steep gullies. The flow can travel for kilometres on those gullies, incorporating or not basal material. It finally deposits on an alluvial fan. The total solid volume involved can vary from 10^2 to 10^6 m³. The behaviour of DF is complex, involving a biphasic fluid (solid and liquid), thus the simplified assumption of monophasic viscous fluid implies the knowledge of the rheology of the mixture. The initiation of DF depends mainly on rainfall input (Iverson 1997) and is locally influenced by the spatial variation of terrain morphology and soil availability. Thus spatially detailed data are necessary to correctly reproduce the event. The aim of this framework is to assess DF with a fast

and simple toolbox, so simplified methods are taken into account.

2.1 Susceptibility Models

The models dealing with the triggering of a landslide or a debris flow are known as “*susceptibility models*”, assessing the disposition to the instability of a slope or a volume of soil. Here are selected two specific triggering behaviours: shallow landslides and basal entrainment. The two behaviours often coexist in the real world. However they are here handled separately.

2.1.1 Shallow Landslide Initiation

Debris flows can be triggered during intense rainfall when high pore pressure is produced inside a loose sediment layer, reducing the ratio between resisting stresses and acting stresses. When the latter exceeds the former, a landslide, likely to be propagated as a DF, can be initiated. In case of shallow landslides, having a very small thickness when compared to the length and width of the slide, the behavior is described by the common Mohr–Coulomb failure approach to the infinite slope stability (Bromhead 1992).

Two different models are here adapted for the study of the initiation of DF. The first one, the *Steady State Infinite Slope Method* (SSISM), couples a Mohr–Coulomb failure mechanism with a steady state lateral flow. It takes into account the cumulated area and the local slope (as TOPMODEL, Beven and Kirkby 1979). The ratio between the water table depth h and the thickness of the soil layer z may be derived, for a given topographic element of the domain having b as width and a as upslope cumulative drainage area, by the following equation (Montgomery and Dietrich 1994):

$$\frac{h}{z} = \frac{I a}{K z b \sin \alpha \cos \alpha} \quad (1)$$

where K is the soil hydraulic conductivity, α is the slope, I the net rainfall rate after subtracting the potential evapotranspiration. Using the classical approach of Skempton and DeLory (1957)

for the stability of a completely saturated shallow soil layer, the factor of safety (FS) may be then computed as follows:

$$FS = \frac{c' + z\gamma_w \cos^2 \alpha \tan \varphi}{z\gamma_s \sin \alpha \cos \alpha} - \frac{\gamma_w \tan \varphi}{\gamma_s \tan \alpha} \left(\frac{h}{z} \right) \quad (2)$$

where γ_s is the specific weight of saturated soil, γ_w is the specific weight of water, c' is the soil cohesion and φ is the soil internal friction angle.

Coupling Eqs. (1) and (2) at limit equilibrium condition ($FS = 1$), the critical rainfall rate I_c , for a selected return period, may be evaluated as follow:

$$I_c = \left(\frac{\tan \alpha}{\tan \varphi} \frac{c'}{\gamma_w \sin \alpha \cos \alpha} + \frac{\gamma_s}{\gamma_w} z \left(1 - \frac{\tan \alpha}{\tan \varphi} \right) \right) K \frac{b}{a} \sin \alpha \cos \alpha \quad (3)$$

I_c is calculated for each element of the domain, or, in practice, for every cell of the digital elevation model (DEM) of the selected area of study.

To determine the probability in terms of return period of an event, a statistical analysis on rainfall extreme values must be performed for large durations of events (Bregoli et al. 2015). A large duration is considered because the mechanism of lateral flow evolves to reach the steady state condition in a relative long time.

The second initiation model, the *Transient Vertical Infinite Slope Method* (TVISM), couples a Mohr–Coulomb failure mechanism to a vertical flow model (Green and Ampt 1911). It is also known as transient piston flow of wetting front model (Iverson 2000; Crosta and Frattini 2003). Iverson (2000) gives the following analysis of the time scale of the infiltration process: the quasi-steady (same of SSISM) groundwater response in time is in the range from 10^0 days to 10^2 years being proportional to a/D_0 , where D_0 is the reference diffusivity of the soil; the transient groundwater response in time is in the range from 10^0 min to 10^0 years being proportional to z^2/D_0 . The time scale of the studied processes seems to be more congruent with the latter. This explains the

interest in introducing a model of vertical infiltration. The infinite slope stability analysis is coupled to the vertical flow mechanism. This method is valid for initial condition of partial saturated soil. First of all the critical water table depth h_c is calculated thanks to the Eq. (2) for $FS = 1$. Then the infiltrated volume (F), the infiltration rate (f) and time (t_c) of Green and Ampt theory are calculated respectively in Eqs. (4), (5) and (6).

$$F = z_f \Delta\theta \quad (4)$$

$$f = \frac{dF}{dt} = K \left(1 + \frac{\Delta\theta}{F} \psi_f \right) \quad (5)$$

$$Kt_c = F - \psi_f \Delta\theta \ln \left(1 + \frac{F}{\Delta\theta \psi_f} \right) \quad (6)$$

where z_f is the water table depth, $\Delta\theta = (\theta_s - \theta_i)$ where θ_s is the saturated soil moisture content and θ_i the initial soil moisture content and ψ_f the suction (negative). Generally $\theta_i = 0.0$ for initial dry condition and $\theta_s = 0.4$ as a maximum value. Assuming that $h = h_c = z_f$ at critical condition, the Eqs. (4), (5) and (6) are solved with known values at critical condition. Expecting a short time of response, the total daily critical rainfall volume P_d can be back calculated using the infiltration rate f and the time t_c in the IDF curves. The return period of events is estimated through the *Generalized Extreme Value* (GEV) analysis (Jenkinson 1955) as in Bregoli et al. (2015).

In both the selected approaches, rainfall is spatially distributed and represented by a constant-in-time value of intensity. Temporal and spatial rainfall uniformities are assumed, as they are one of the most important simplifications of the model (Montgomery and Dietrich 1994; Pack et al. 1998). The rainfall intensity is intrinsically related to duration; and the duration strongly influences the landslides' trigger (Iverson 2000). Further details of the two presented shallow landslide initiation methods are presented in Bregoli et al. (2015) where they are also tested on a database of DF events.

2.1.2 Basal Entrainment

The basal entrainment of solids is a process that may occur in-channel where available sediments are incorporated in the flow. For relatively mild channel slope only an "ordinary" fluvial bed load transport is possible. In this case the solid concentration is generally lower than 20%. For relatively high slopes and in case of sediment availability, the solid transport can change the behavior to DF (Takahashi 1991; Coussot and Meunier 1996). Using the Takahashi's approach (Takahashi 1991), the shear stress mobilized by hydrodynamic flow (with a certain water depth h_w and solid concentration C) over a saturated soil layer of thickness z , is given by the following equation:

$$\tau_m = [(zC_b + h_w C)(\rho_s - \rho_w) + (z + h_w)\rho]g \cos \alpha \sin \alpha \quad (7)$$

where C_b is the concentration of the soil bed layer. The shear strength at the same depth z is given by the follow:

$$\tau = (zC + h_w C)(\rho_s - \rho_w) \cos^2 \alpha \tan \varphi \quad (8)$$

Balancing the mobilized shear stress and the shear strength, the erosion depth h_s can be obtained as:

$$h_s = \frac{\tan \alpha - C\Delta(\tan \varphi - \tan \alpha)}{C_b\Delta(\tan \varphi - \tan \alpha) - \tan \alpha} h_w \quad (9)$$

It can be proved that at limits conditions, when the flow concentration C tends to a limit concentration C_∞ , h_s tends to 0. Thus the C_∞ limit value is given by the relation:

$$C_\infty = \frac{\tan \alpha}{(\rho_s - \rho_w)(\tan \varphi - \tan \alpha)} \quad (10)$$

The tool *In-Channel-Debris-Program* (InCDP) calculates this limit value. If $C_\infty > 0.2$ an initiation is considered.

2.2 Propagation Model

DebrisDice is a stochastic model for propagation of debris flow based on terrain morphology and thus on DEM. This method permits to achieve qualitative results in terms of flooded areas and flow velocity but not a quantitative hazard in terms of flow energy as in Rickenmann (2005). However the tool is really useful for its compromise between computational time and quality of results. With the correct calibration, results are similar to more complex models (e.g.: 1D or 2D models). The stochastic model consists in a flow routing algorithm incorporated into a random walk to generate trajectories of debris flow. Gamma (1999) and Hürlimann et al. (2008) combined a *D8* flow routing algorithm (O'Callaghan and Mark 1984) with *Montecarlo* and random walk theory. The method was successfully applied in the European Alps and the Spanish Pyrenees catchments.

The model used here is a modification of the previous one with the incorporation of local flow velocity computation and two different stopping mechanisms. One of the key improvements in the model is the possibility of counter slope flow: a small probability of flooding is assigned to cells with higher elevation than the focused one. This idea follows the fluid behaviour were the inertial forces allow counter slope movements. Starting from initiation points evaluated with the susceptibility models or field data (when available), that procedure permits to obtain a flow path of propagation for each point, and subsequently n_{iter} flow trajectories are calculated. Finally the probability to invade a cell P_{xy} , is computed for each cell of the DEM using the following equation

$$P_{xy} = \frac{n_{affect}}{n_{iter}} \quad (11)$$

where n_{affect} is the number of DF trajectories that pass through a cell. The output of this method is a map containing information on the probability of each cell of the DEM to be affected by a future

DF. The result depends strongly on the DEM resolution and on the number of iterations. In practice the optimum n_{iter} is the one that, even for higher value of n_{iter} , the result does not change. Gamma (1999) and Hürlimann et al. (2008) recommend setting $n_{iter} = 10^4$, but values of 10^2 should be enough for large areas of study.

Two flow stopping methods are here used. *DebrisDice* provides separate results for each of the stopping method. The first stopping mechanism of the routing is assessed by the relationship between the reach angle and the total debris flow volume as follow (Corominas 1996):

$$\tan \beta = H/L_{max} = 0.97V^{-0.105} \quad (12)$$

where β is the reach angle, H is the gradient between the centre of mass of landslide and fan, L_{max} is the travel distance and V is the total volume of mobilized sediment in m^3 . This volume may be estimated through the initiation model introduced above. The computation of flow velocity is achieved applying the Voellmy's Fluid Flow Rheology for Granular Debris Flow (Voellmy 1955):

$$\frac{1}{2} \frac{dv^2}{dl} = g(\sin \alpha - \mu_m \cos \alpha) - \frac{v^2}{k} \quad (13)$$

where v is velocity of the mixture, l is the flow path line, μ_m is the sliding friction coefficient, k is the turbulence coefficient, also called "mass to drag ratio". μ_m and k should be defined by back-analysis, but typical values can be settled. When the velocity is zero, the flow stops (second stopping method). Additionally to the two stopping methods, a minimum angle slope angle to stop the flow can be settled manually within the *DebrisDice* master file (see Table 1).

It is important to note that this methodology is valid only in a natural environment, where anthropogenic modification on streams is low: presence of dams or retention dams, as well as channelized streams can imply an important drawback. Further details of this method are presented in Hürlimann et al. (2008).

Table 1 Input and output of the presented tools

Program		Filename	Type	Description	Unit
SSISM	Input	topo.asc	Raster ESRI ASCII	DEM	(m)
		cohesion.asc	Raster ESRI ASCII	Soil cohesion	(Pa)
		phi.asc	Raster ESRI ASCII	Soil internal friction angle	(rad.)
		thick.asc	Raster ESRI ASCII	Soil thickness	(m)
		k.asc	Raster ESRI ASCII	Hydraulic conductivity	(mm/day) or same that rain.asc
		rain.asc	Raster ESRI ASCII	Rain intensity for a selected return period	(mm/day) or same that k.asc
		input.txt	Master text file	Saturated density of soil	(kg/m ³)
	Output	fillsinks.asc	Raster ESRI ASCII	DEM with filled depressions	(m)
		slope.asc	Raster ESRI ASCII	Local slope	(rad.)
		acc.asc	Raster ESRI ASCII	Accumulation grid <i>a/b</i>	(m)
		h_z.asc	Raster ESRI ASCII	Saturation degree <i>h/z</i>	–
		FS.asc	Raster ESRI ASCII	Safety factor (main result)	–
		TVISM	Input	topo.asc	Raster ESRI ASCII
cohesion.asc	Raster ESRI ASCII			Soil cohesion	(Pa)
phi.asc	Raster ESRI ASCII			Soil internal friction angle	(rad.)
thick.asc	Raster ESRI ASCII			Soil thickness	(m)
k.asc	Raster ESRI ASCII			Hydraulic conductivity	(mm/day)
porosity.asc	Raster ESRI ASCII			Porosity, usually 40% for dry soil	(%)
suction.asc	Raster ESRI ASCII			Suction	(–cm)
input.txt	Master text file			Parameters of GEV	Various
Output	fillsinks.asc			Raster ESRI ASCII	DEM with filled depressions
	slope.asc		Raster ESRI ASCII	Local slope	(rad.)
	f.asc		Raster ESRI ASCII	GA infiltrated rate	(mm/day)
	rain_vol.asc		Raster ESRI ASCII	GA infiltrated rain volume	(m)
	h.asc		Raster ESRI ASCII	Critical water table depth from slope stability	(m)
	D.asc		Raster ESRI ASCII	GA infiltration duration	(s)
	Pd.asc		Raster ESRI ASCII	Critical cumulated rainfall from IDF curve	(mm)
	probability.asc		Raster ESRI ASCII	Critical return period (main result)	(years)

(continued)

Table 1 (continued)

Program		Filename	Type	Description	Unit
InCDP	Input	topo.asc	Raster ESRI ASCII	DEM	(m)
		input.txt	Master text file	Parameters as unique values	Various
	Output	fillsinks.asc	Raster ESRI ASCII	DEM with filled depressions	(m)
		acc.asc	Raster ESRI ASCII	Accumulation grid a/b	(m)
		meanslope.asc	Raster ESRI ASCII	Mean slope along channels	(rad.)
		concentration.asc	Raster ESRI ASCII	Limit concentration, $C?$	–
DebrisDice	Input	topo.dat	Raster ESRI ASCII	DEM	(m)
		ini.dat	Binary raster ESRI ASCII	Initiation grid (binary)	–
		input.dat	Master text file	Parameters	Various
		Niter	Parameter	Number of iterations (in input.dat)	–
		Alpha	Parameter	Reach angle (in input.dat)	(rad.)
		Beta	Parameter	Min. slope angle to stop the flow (in input.dat)	(rad.)
		Mu	Parameter	Coulomb dynamic friction factor (in input.dat)	–
		K	Parameter	Mass to drag ratio (in input.dat)	(m)
	Output	maxpend.dat	Raster ESRI ASCII	“Steepest” flow path	–
		control.dat	Raster ESRI ASCII	Depressions in topography and “stop-cells”	–
		result_angle.dat	Raster ESRI ASCII	Norm. probability of flow invasion (reach angle)	–
		result_vel.dat	Raster ESRI ASCII	Norm. probability of flow invasion (eq. of Voellmy)	–
		velocity.dat	Raster ESRI ASCII	Velocity of flow (eq. of Voellmy)	(m/s)

3 Data Requirement and Operational Details

An analysis of slope stability at large scale deals with the spatial variability of parameters. The values can strongly vary in a given small area. Unique physical and mechanical properties of soil can be fixed in the study area, as well as different values for every homogeneous region. It is important to point out that the correct procedure to distinguish between regions with different

physical–mechanical characteristics is based on soil maps. Nowadays such maps are sometimes available at local scale but not usually available at regional scale. A common way to define soil properties is to extrapolate them from geological and land coverage maps that are more ordinary. Homogeneous regions can be reclassified as portion of territories with the same geology formation and/or the same land coverage feature. To define properly physical–mechanical soil properties of a given homogeneous region, laboratory tests should be carried out. This tests concern the

evaluation of soil parameters as for instance cohesion, internal friction angle or hydraulic conductivity. However the lab tests are not always feasible when dealing with a wide territory. When that condition occurs, expert criteria help in the task of assigning soil parameter values at homogenous portion of territory. However, this approach is a rather delicate task and should be carried out by a geologist or engineer, familiar with the geological, geomorphological and soil geotechnical characteristics of the study area.

The data exchange formats of information are in ESRI ASCII grid. Resolution and extension of dataset input has to be the same for each raster used and it has to be congruent with the resolution of the DEM. Nowadays, local authorities provide more and more free, high resolution DEMs. These models have a grid sizes equal or smaller than 10×10 m. Usually, for a regional survey, a study area of the order of 10^2 km² is common. As a reference, if the raster resolution of an area of 10^2 km² is 5×5 m, the resulting DEM is of the order of 10^2 MB and the minimum hardware requirement to use this volume of data in the present framework is a workstation of 8 GB of RAM.

The inputs and outputs details of each program are presented in Table 1.

4 Applications

A 1st order small catchment of the Boi Valley (Eastern Pyrenees, Spain) is selected to show an example of application of some of the mentioned tools. More details on data input and on all the models results are provided in the supporting materials. The selected catchment has an area of 3.1 km², a maximum elevation of 2532 m a.s.l and a minimum elevation of 1132 m a.s.l. The outlet is located in the town of Erill la Vall which has been developed on the depositional fan. The catchment has been recognized as prone to DF events (Bregoli et al. 2015; Chevalier et al. 2013) and presents a deep and active scar located on a glacial quaternary deposit (Fig. 1).

The available DEM has a resolution of 5×5 m. Geotechnical parameters have been defined following Bregoli et al. (2015). Landslide susceptibility for a return period of event of 10 years is here calculated using TVISM, giving an estimated total mobilized volume of

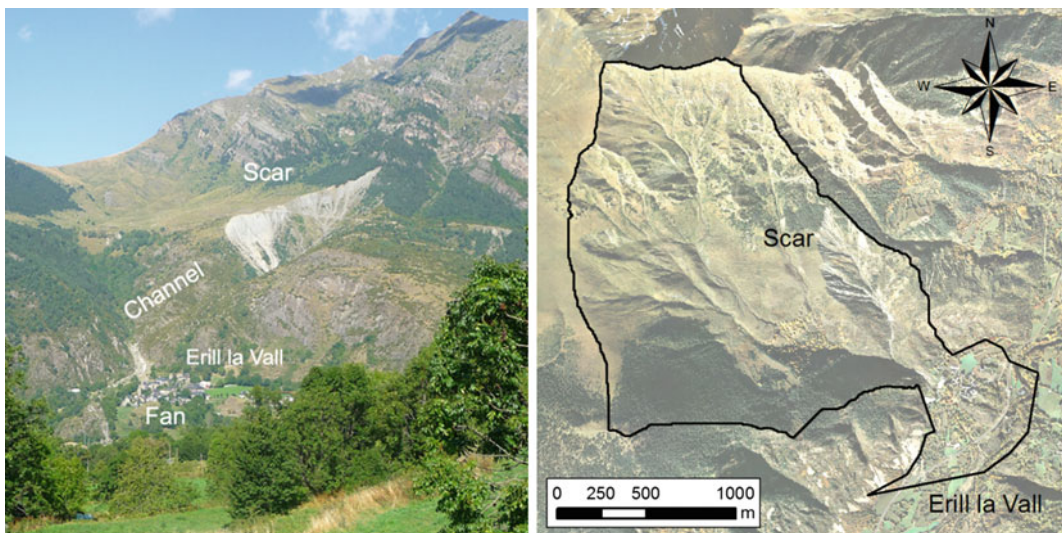


Fig. 1 Example of erosional activity in the Boi Valley (Eastern Pyrenees) where a scar located on an ancient glacial deposit favored a debris flow in Erill la Vall. It is shown an oblique photo taken in 2011 (*left*) and an aerial photo (ICC 2011) where the 1st order basin object of this application is marked (*right*)

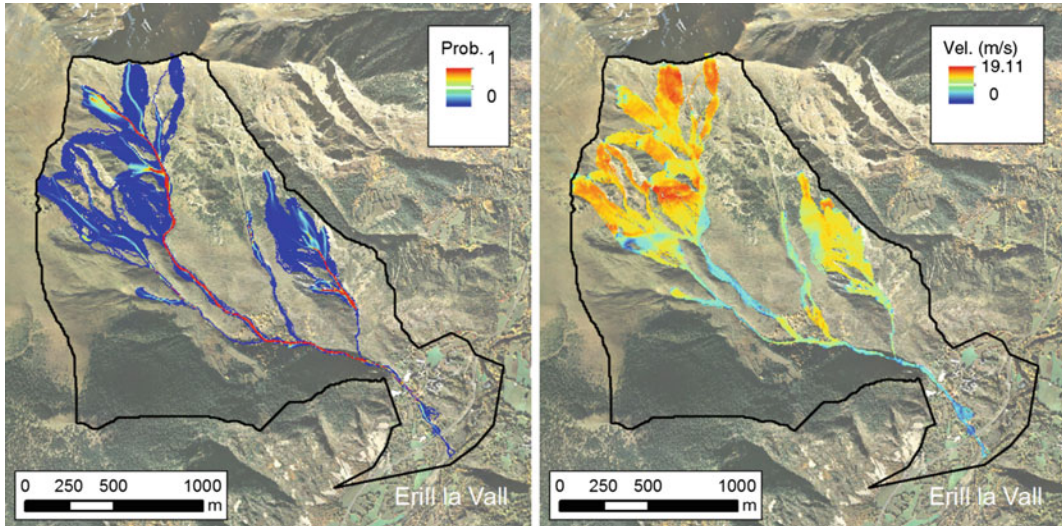


Fig. 2 Results of DF propagation by means of normalized probability of flow invasion following the range angle stopping method (*left*) and velocity calculated by the Voellmy rheology equation (*right*)

$12 \times 10^3 \text{ m}^3$. Successively the susceptible areas are propagated through the DEM using *DebrisDice* run with $n_{iter} = 10^4$, $\beta = 0.35 \text{ rad.}$, $\mu_m = 0.1$ and $k = 50$. β is evaluated by Eq. (12) by means of the mobilized volume. The parameters μ_m and k should be defined by back analysis as suggested by Hürlimann et al. (2008). Normalized probability of flow invasion by means of reach angle stopping method is presented in Fig. 2(left). Velocity of the flow calculated by means of Eq. (13) in m/s is presented in Fig. 2 (right).

5 Conclusion

A toolbox has been defined in order to delineate zones prone to be affected by debris flows in a simplified and relatively quick fashion. The toolbox is formed by four programs based on physical background and working at regional scale, being able to handle wide areas of territory. Algorithms are based on known and tested methodologies. The toolbox consists in three algorithms, developed in JAVA, used to assess the susceptibility of debris flow initiation, by means of shallow landslides and basal entrainment of bed material. The fourth program

(*DebrisDice*), developed in FORTRAN, evaluates the debris flow propagation in term of probability and velocity. The toolbox partially takes advantage of all the basic GIS algorithms included in the open source SEXTANTE library. In the presented applications the well portable ESRI ASCII grid format is selected as input/output of the algorithms. For a given domain firstly the cells prone to be mobilized are identified (susceptibility task), secondly the cells are propagated with the *DebrisDice* program. The latter tool is able to assess cell-by-cell the flooded areas in term of probability and velocity of the flow. This method is extremely easy to use, requiring only the DEM and few calibrated parameters, settled by regional back analysis. As a practical example, the algorithms have been applied in a selected small catchment on the Eastern Pyrenees (Spain).

Acknowledgements The study was financially supported by European Community, through the project IMPRINTS (Agreement: FP7-ENV-2008-1-226555) and the projects “DEBRIS FLOW” and “DEBRISTART” (Agreement CGL2009-13039 and CGL2011-23300) of the Spanish Ministry of Education. The authors want to acknowledge the collaboration of Guillaume Chevalier and Marcel Hürlimann of the Technical University of Catalonia (Barcelona, Spain) and Maria Nicolina Papa and Fabio Ciervo of the Università degli Studi di Salerno (Italy).

References

- Beven KJ, Kirkby MJ (1979) A physically based, variable contributing area model of basin hydrology/un modèle à base physique de zone d'appel variable de l'hydrologie du bassin versant. *Hydrol Sci Bull* 24(1): 43–69
- Bregoli F, Medina V, Chevalier G, Hürlimann M, Bateman A (2015) Debris-flow susceptibility assessment at regional scale: validation on an alpine environment. *Landslides* 12(3):437–454
- Bromhead EN (1992) *The stability of slopes*. Blackie Academic and Professional, London
- Carrara A, Cardinali M, Detti R, Guzzetti F, Pasqui V, Reichenbach P (1991) GIS techniques and statistical models in evaluating landslide hazard. *Earth Surf Proc Land* 16(5):427–445
- Chevalier G, Medina V, Hürlimann M, Bateman A (2013) Debris-flow susceptibility analysis using fluvio-morphological parameters and data mining: application to the Central-Eastern Pyrenees. *Nat Hazards* 67:213–238
- Corominas J (1996) The angle of reach as a mobility index for small and large landslides. *Can Geotech J* 33(2):260–271
- Coussot P, Meunier M (1996) Recognition, classification and mechanical description of debris flows. *Earth-Sci Rev* 40:209–227
- Crosta G, Frattini P (2003) Distributed modelling of shallow landslides triggered by intense rainfall. *Nat Hazards Earth Syst Sci* 3(1/2):81–93
- Gamma P (1999) *dfwalk—Ein Murgang—Simulationsprogramm zur Gefahrenzonierung*. Ph.D. thesis, University of Berne
- Green WH, Ampt G (1911) Studies of soil physics, part 1. The flow of air and water through soils. *J Agric Sci* 4:1–24
- Hürlimann M, Rickenmann D, Medina V, Bateman A (2008) Evaluation of approaches to calculate debris-flow parameters for hazard assessment. *Eng Geol* 102(3–4):152–163
- Iverson R (1997) The physics of debris flows. *Rev Geophys* 35:245–296
- Iverson RM (2000) Landslide triggering by rain infiltration. *Water Resour Res* 36(7):1897–1910
- Jenkinson A (1955) The frequency distribution of the annual maximum (or minimum) values of meteorological elements. *Q J R Meteorol Soc* 81:58–171
- Montgomery D, Dietrich W (1994) A physically-based model for the topographic control on shallow landsliding. *Water Resour Res* 30(4):1153–1171
- O'Callaghan JF, Mark DM (1984) The extraction of drainage networks from digital elevation data. *Comput Vis Graph Image Process* 28(3):323–344
- Olaya V (2008) Sextante, a free platform for geospatial analysis. *OSGeo J* 6:32–39
- Pack R, Tarboton D, Goodwin C (1998) The SINMAP approach to terrain stability mapping. In: 8th congress of the international association of engineering geology, Vancouver, BC, Canada, pp 21–25
- Pack RT, Tarboton DG, Goodwin CN, Prasad A (2005) SINMAP 2. A stability index approach to terrain stability hazard mapping. In: Technical description and users guide for version 2.0. Utah State University
- Rickenmann D (2005) *Runout prediction methods. Debris-flow hazards and related phenomena*, Springer Praxis Books. Springer, Berlin, pp 305–324
- Rigon R, Ghesla E, Tiso C, Cozzini A (2006) *The HORTON machine: a system for DEM analysis. The reference manual*. Università di Trento. Dipartimento di Ingegneria Civile e Ambientale, Trento. e-book
- Skempton A, DeLory F (1957) Stability of natural slopes in London clay. *Proc Int Conf Soil Mech Found Eng* 4(2):378–381
- Takahashi T (1991) *Debris flow*. Balkema, Rotterdam
- Tarboton DG (1997) A new method for the determination of flow directions and upslope areas in grid digital elevation models. *Water Resour Res* 33(2):309–319
- Voellmy A (1955) Über die zerstörungskraft von lawinen. *Schweizerische Bauzeitung* 73:212–285

TXT-tool 3.386-1.1

Two-Dimensional Debris-Flow Modelling and Topographic Data

Jošt Sodnik and Matjaž Mikoš

Abstract

Two-dimensional (2-D) debris-flow mathematical modeling is a useful and widely used tool when assessing debris-flow hazard. A high accuracy for 2-D model input parameters is essential for obtaining acceptable simulation results, especially for potential debris flows without a recent history of activity. The numerical grid in the debris-flow transport area is usually generated from available topographic data. In Slovenia, DEM5 and DEM12.5 are publicly available data. However, the morphological accuracy of those datasets is questionable because of their development methods and their low resolution. A better solution is using LiDAR-derived data with their higher resolution and a lot of options for further improvements using different methods and algorithms. 2-D debris-flow simulation results using LiDAR data, compared to less accurate DEMs, are more accurate and more useful for debris-flow hazard mapping. The modelled debris-flow depths and velocities are more accurate and better follow field conditions. Although using high-resolution topographic data results in much longer computational time, this shouldn't be a problem for potential debris flows. For debris-flow endangered and populated torrential fans, modelling of the influence of built structures on flow is important. With adequate numerical modelling of such structures the obtained simulation results are more meaningful, with better expressed

J. Sodnik (✉)
Tempos d.o.o., Cesta v Kleče 16, 1000 Ljubljana,
Slovenia
e-mail: jost.sodnik@gmail.com

J. Sodnik · M. Mikoš
Faculty of Civil and Geodetic Engineering,
University of Ljubljana, Jamova C. 2, 1000
Ljubljana, Slovenia
e-mail: matjaz.mikos@fgg.uni-lj.si

local flow conditions. Comparisons using publicly available topographic data sets also show that higher resolution (DEM5 vs. DEM12.5) doesn't always mean better morphologic accuracy.

Keywords

Debris flows · Digital elevation model · Hazard assessment
LiDAR · Mathematical modeling · Topographical data

Contents

1 Introduction	236
2 The Flo-2D Mathematical Model	236
3 Topographic Data	238
4 Results and Discussion	239
4.1 The Koroška Bela Case (DEM5, DEM12.5-LiDAR-Derived DEMs).....	239
4.2 The Trebiža Torrent Case (DEM5 and DEM12.5).....	242
4.3 The Hrenovec Torrent Case (DEM5).....	243
4.4 Discussion.....	245
5 Conclusions	250
References.....	250

1 Introduction

Different topographic data can be used for two-dimensional debris-flow mathematical modelling. Digital Terrain Model (DTM) data is widely applicable, with a good price/performance ratio. Classical terrestrial surveys are not suitable for large areas due to high costs. Therefore, remote sensing data sets have become a first choice in preparing topographic data for modelling different natural processes and assessing their hazard. But the question of topographic data quality and reliability/trustworthiness of simulation results exists, since topographic data is used for generating the computational numerical grid of the 2-D debris-flow mathematical models. We input various topographic data with different resolutions (and precision) in a widely-used 2-D

mathematical model (i.e., Flo-2D) to test the quality and the influence of the topographic data on final simulation results. The LiDAR-derived data has shown a lot of advantages, but also some disadvantages, as presented in this tool.

Besides precision of the applied DTM data in debris-flow simulations, built structures on inhabited torrential fans play an important role in simulations. We tested two options for incorporating built structures (residential houses) into 2-D debris flow modelling, and we present these results in this tool. Built structures are the main reason, why we need trustworthy debris-flow simulation results in order to assess debris-flow hazard and risk in areas endangered by potential debris flows that were active in the past, but for which no accurate historical documents exist for a proper 2-D debris-flow model validation.

2 The Flo-2D Mathematical Model

Flo-2D (O'Brien 2011) is a mathematical tool that is widely and efficiently used for two-dimensional mathematical modelling of water movement and of fast flowing slope mass wasting processes, including debris flows. In the USA this model is a software tool recommended by the Environmental Protection Agency (EPA) for analysis of natural hazards and it has found wide application in many countries over the world. Modelling is

based on physical laws of the flow and is useful under different geographical conditions. The specialties of each single treated problem are taken into account by selecting different model coefficients and, of course, by the input of local topographic data. For the description of the area geometry under investigation, the Flo-2D model uses a numeric grid made out of quadratic cells of the selected size. Computational grid-cell size is user-defined. After definition of the grid-cell size, the model uses interpolation methods to define the height of each cell, based on the applied DEM. Water flow, and in particular debris flow, modeling depends on the form of the computational model as well as on the roughness of each computing cell (energy dissipation). A very important role when modelling debris-flow movement is also given to rheological parameters of a water-debris mixture that are described in more detail in a continuation of this tool. The basic model equations in all directions (shown here are only equations for the x -direction) are the continuity equation:

$$\frac{\partial h}{\partial t} + \frac{\partial h V_x}{\partial x} = i \quad (1)$$

and the dynamic equation:

$$S_{fx} = S_{0x} - \frac{\partial h}{\partial x} - \frac{V_x \partial V_x}{\partial x} - \frac{V_x \partial V_x}{g \partial x} - \frac{1 \partial V_x}{g \partial t} \quad (2)$$

where h is flow depth [m], V_x is depth-averaged flow-velocity component in the x -direction [m/s], S_{fx} is slope of energy line or simply the total friction slope [-], and S_{0x} is the channel (relief) slope [-]. Part of the equations also include pressure gradient i [-] and local flow accelerations.

The dynamic equation is used to compute the depth-averaged flow velocity in each computing cell separately for the eight directions (similar to the way directions in the sky are defined; a similar procedure named the D8 algorithm is used for modelling rock falls on slopes; e.g., Petje et al. 2005). The velocity in each direction is computed as a one-dimensional quantity not

dependent on the other velocities. The stability of the computing numerical scheme is assured by selecting a correspondingly short computing step as a function of the selected computing cell size.

Debris flows are non-homogenous (anisotropic) and non-Newtonian fluids (Balmforth and Craster 2001). Their movement is dependent on the rheological properties of the mixture, relief, surface slope and surface roughness. The debris flow mixture is composed of water and debris of different sizes; the debris flow movement is thus actually a multi-phase flow that might also have wood constituents (bushes, trees, stumps, branches). The quantity of material with respect to material concentration determines the specific gravity, shear strength and mixture viscosity. The material concentration in the mixture is expressed by the volumetric concentration C_v that is itself expressed by a ratio of the debris volume to the total volume of the water–debris mixture. This concentration is of importance for further treatment of debris flow movement, since this data helps to determine the debris flow magnitude. Also the manner of flow is dependent on the concentration of the water–debris mixture. That is why, apart from the volumetric concentration, the following data also are needed for modelling a debris flow:

- the resistance parameter for laminar flow,
- specific weight,
- yield stress, and
- viscosity.

The resistance parameter for laminar flow K [-] expresses the surface roughness, over which the debris flow moves. This parameter is important for phases when the flow is laminar or in a transient regime, but is less important for strict turbulent flows. The value of the resistance parameter K goes from 24 for smooth prismatic channels all the way up to 50,000 for rough and geometrically more complicated cases. For modelling of debris flows, its calibrated value is set to 2285 (O'Brien 2011). For turbulent flow, resistance is presented with n_d being the turbulent dispersive n of the Manning roughness

coefficient, which is user-defined for each computational grid-cell. The depth-integrated dissipative friction slope (S_f) is shown in following equation:

$$S_f = \frac{\tau_c}{\gamma_m h} + \frac{K \mu_N u}{8 \gamma_m h^2} + \frac{n_d^2 u^2}{h^{4/3}} \quad (3)$$

where γ_m is specific debris flow weight, h the flow depth, u the mean flow velocity, K the resistance parameter for laminar flow and n_d the turbulent dispersive n of Manning (Cesca and D'Agostino 2008).

Debris specific weight γ_m [N/m³] is an important parameter for determining the mixture specific weight, which depends on the debris specific weight and the volumetric concentration C_v of the debris in the mixture. The mixture's flow characteristics on the slope strongly depend on the specific weight of the mixture. When modelling the debris flow on the Koroška Bela inhabited torrential fan, we used the specific weight of 27 kN/m³.

Yield stress depends on the volumetric concentration C_v of the debris in the mixture. We should determine two coefficients, namely α and β , because the yield stress is determined from the equation of the following form:

$$\tau_y = \alpha e^{\beta C_v} \quad [\text{dyn/cm}^2 = 10^{-5} \text{N/cm}^2] \quad (4)$$

The viscosity of the mixture depends on the volumetric concentration C_v of the debris in the mixture. Also here we should determine two coefficients, namely α and β , because the viscosity is determined from the equation of the following form:

$$\eta = \alpha e^{\beta C_v} \quad [\text{P} = \text{g/cm}^{-1}/\text{s}^{-1} = 10^{-1} \text{Pa s}] \quad (5)$$

3 Topographic Data

The Digital Elevation Model (DEM) is basically recorded as raster layers in 2.5D, with one attribute of elevation. The 3-D DEM production requires much more complex structure and

modelling, especially when using very detailed laser scanning-based (LiDAR) data. In our case the solution of the problem requires only 2.5D DEMs that are realised as raster data sets where each square cell contains an elevation value.

Quality of the DEMs has been considerably increased during the last years and consequently more advanced applications based on DEM-analysis are used, e.g., for enhancing morphometric analysis of floods or debris flows (Podobnikar 2008). The quality of any spatial analyses that is based on a DEM depends greatly on its geometrical and, especially, on its morphological accuracy. However, due to its complexity, the primary challenge is to produce a high quality DEM according to well defined nominal grounds (data model), ideally without errors and in an appropriate resolution. Many acquisition methods, especially contemporary ones through LiDAR or radar interferometry, are relatively fast and can offer quality data sources.

Four DEMs were applied in our study: DEM12.5, DEM5, DEM0.5, and DEM5 derived from DEM0.5 (Table 1). The first two are the property of Surveying and Mapping Authority of the Republic of Slovenia (public available data) and the second two of the local Flycom Company.

The DEM12.5 was produced based on appropriately fused various existing data sources, which were of different quality, in which their best properties were exposed (Podobnikar 2005, 2010). The final DEM is overall of better quality than any other used data source. The method of weighted sum of sources with morphologic enhancement includes iterative repeated processes where the experiences and evaluations of the procedures and results acquired from previous steps provide better starting-points for each of the subsequent steps. Such iterative processes takes more time, however it was rationally finished within two loops. The principal steps for such DEM production are:

- mosaicking selected data sources to produce a principal DEM,
- weighted sum of secondary data sources,
- (geo)morphologic enhancement, and

Table 1 Characteristics of the DEMs used in the Koroška Bela case

Name (produced)	Accuracy (RMSE)	Production method
DEM12.5 (2001–2005)	3.8 m	Fusion of existing geodetic datasets of different type/quality
DEM5 (2006–2007)	3.5 m	Resampling of DEM12.5 + stereo photogrammetry and local adjusting with CAD-tools
DEM0.5 (2009–2010)	5–10 cm (in channels gross errors >1 m)	Datasets of 12 blocks (leaves and snow); different approaches to filtering and interpolation
DEM5 from DEM0.5 (2010)	5–10 cm (in channels gross errors >1 m)	Resampling of DEM0.5

RMSE root means square error

- reference point consideration in the modelling.

Different aspects of quality were continuously monitored through the process. The final product was an optimised DEM that considered different properties of landform, geometrical and morphological accuracy, and a wide range of users and applications. The DEM is more-or-less universal for the requirements of many different users.

The DEM5 was produced by simply resampling the DEM12.5, and with further improving of geometrical accuracy on the areas where the previously RMSE was considerably significant (Podobnikar 2008). Aerial photographs and principles of stereo photogrammetry were applied. The areas with significant RMSE were locally adjusted with CAD-tools. The final DEM5 is geometrically of higher quality than the DEM12.5, but quite inhomogeneous, with low morphological accuracy. This DEM is unfortunately not very useful for geomorphometric spatial analysis, i.e., for debris flow modelling.

The DEM0.5 was captured as a fullwave point cloud in two different periods, where some snow in the high mountains and leaves on most trees in the lower elevations occurred. The point density was inhomogeneous, from 1 to 10 points/m². The vertical angle of scanning was 0° to ±30° with laser scanner Litemapper LM 5600 (alias Riegl LMS-Q560). Orthophotos with a resolution of 0.5 m were acquired together with the scanning. The final DEM of 0.5 m resolution was produced with Terrasolid software. The result is

not perfect. One problem was reconstruction of the surface of the bare ground in areas with leaf canopies, buildings and especially in the areas of streams. The main problems for our debris flow simulation are the areas of steams and their surroundings—at some places there are combinations of trees and bushes, and the buildings are located along the streams. Less important, but obvious errors occur due to the rough mountain landscape. The produced DEM0.5 needs further improvement, in which more advanced filtering and a possible combination and fusion of the other data sources will be implemented. Additional model for the debris flow simulation will be produced—a digital surface model (DSM), as a combination of the DEM and buildings, in which the required level of detail (LOD), according CityGML standard, is 0.

All DEMs were resampled to resolution of 5 and 12.5 m using two interpolation approaches. In the case of interpolation to a lower resolution, a bilinear interpolation was applied, and in the case of interpolation to a higher resolution, a spline interpolation with filtering was applied.

4 Results and Discussion

4.1 The Koroška Bela Case (DEM5, DEM12.5-LiDAR-Derived DEMs)

In this study we used publicly available DEM5, DEM12.5 and LiDAR-derived DEM0.5 and DEM5 (re-sampled DEM0.5) (LiDAR).

The debris-flow event scenario is defined using the inflow hydrograph on the peak of the fan. We used a 15-min potential event scenario with a $250 \text{ m}^3/\text{s}$ peak discharge + debris = $431 \text{ m}^3/\text{s}$. The total magnitude of the event was $155,500 \text{ m}^3$ (water + debris). The volumetric concentration was 0.42, the critical shear stress 20 Pa and the Bingham viscosity 10 Pa s. The defined control parameters of the model were: the surface detention 0.03, the percent change in flow depth 0.2 and the dynamic wave stability coefficient 5. The following Manning roughness coefficients were used: n_g (forest) = $0.16 \text{ sm}^{-1/3}$, n_g (meadow) = $0.033 \text{ sm}^{-1/3}$, n_g (channel) = $0.13 \text{ sm}^{-1/3}$ and n_g (buildings) = $0.2 \text{ sm}^{-1/3}$. Buildings are represented by higher n_g roughness values, since the objective of the research was to research the influence of topographic data on modelling results.

Figure 1 shows the lack of morphologic accuracy of DEM5. Even with lower resolution of data, the model with DEM12.5 (Fig. 2) is more correct. In the upper part of the fan in Fig. 1

debris flow overbanks and depths are practically the same all over the fan (no concentration of the flow in the channel). The width of the channel in that part is 5–7 m. In Fig. 2 the channel is made wider than in nature due to the DEM resolution 12.5 m, but is morphologically more correct, since the torrential channel is better expressed. Comparison between Figs. 1 and 2 shows that despite its poor resolution, the DEM12.5 is more useful for preliminary hazard assessment because the flow is more concentrated in the channel. DEM5 underestimates the channel, which leads to an increase in the assessed hazard outside the channel. The answer for a better quality of DEM12.5 lies in the different creation processes of DEM12.5 and classic DEM5.

LiDAR-derived DEMs (Figs. 3 and 4) produce much more accurate topographic data for the fan. Both models (DEM5 and DEM0.5) are morphologically more correct than the other two models (public DEM5 and DEM12.5). The main difference is in the topography of the torrential

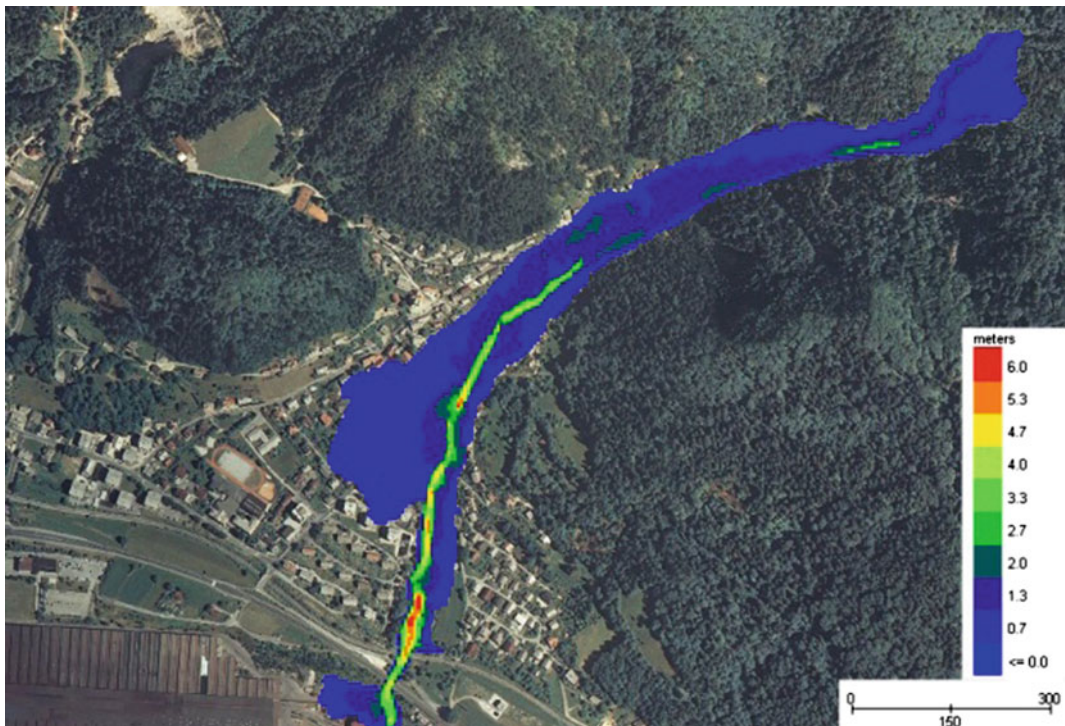


Fig. 1 Maximum flow depths using public DEM5

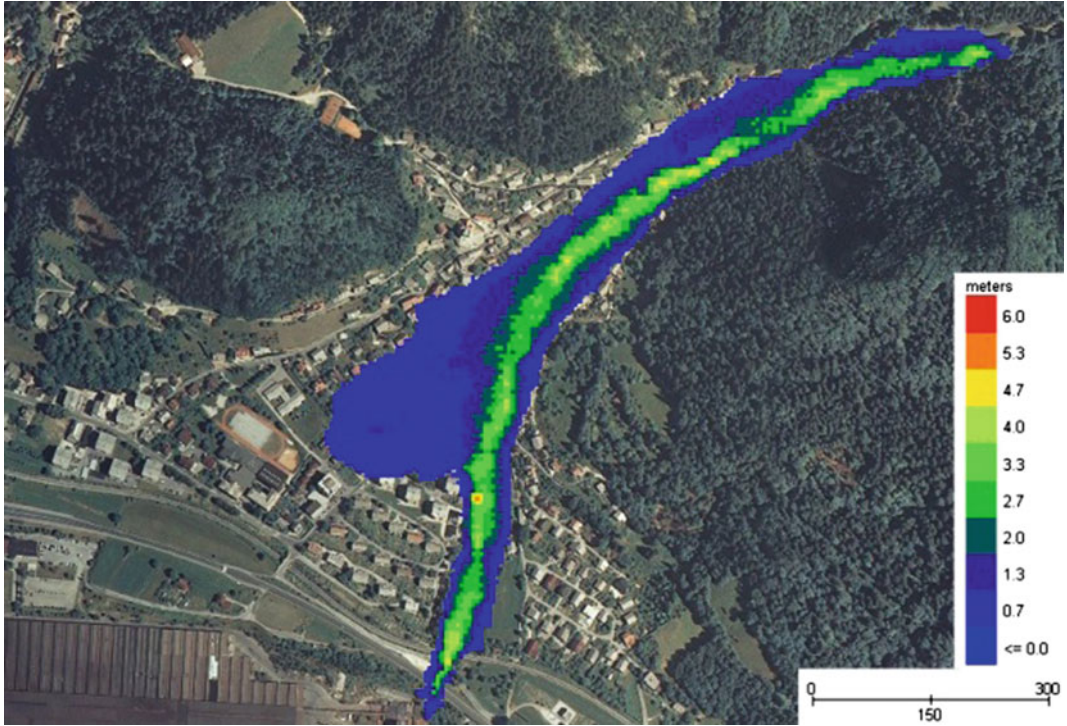


Fig. 2 Maximum flow depths using public DEM12.5

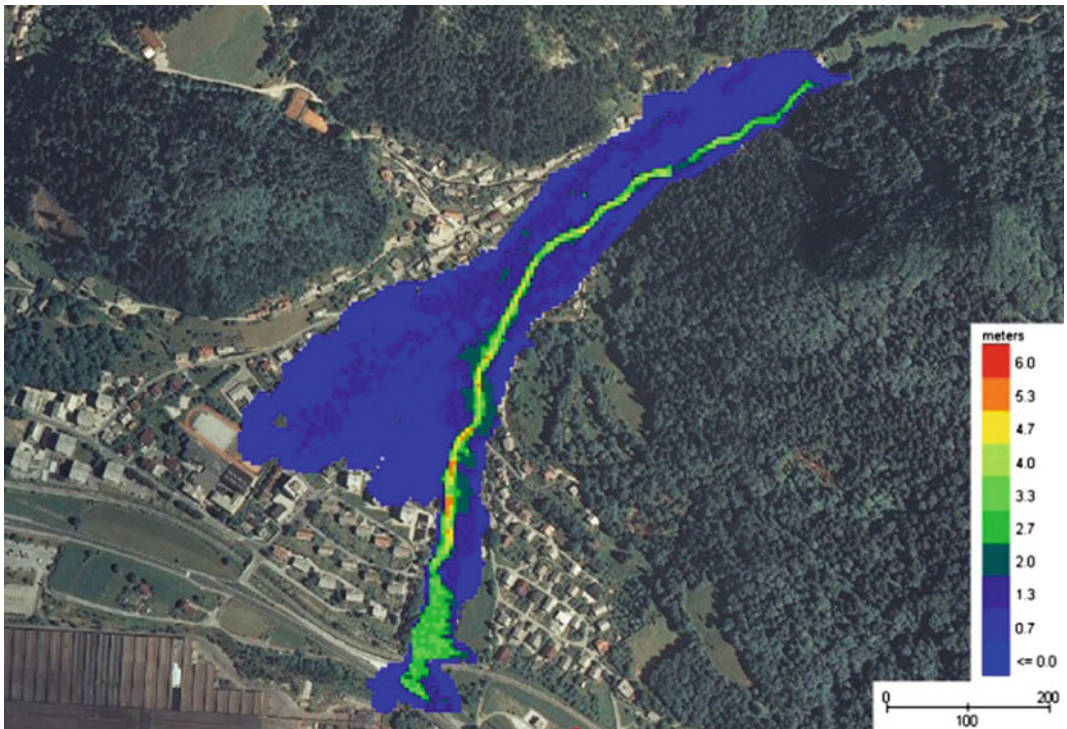


Fig. 3 Maximum flow depths using Lidar DEM0.5

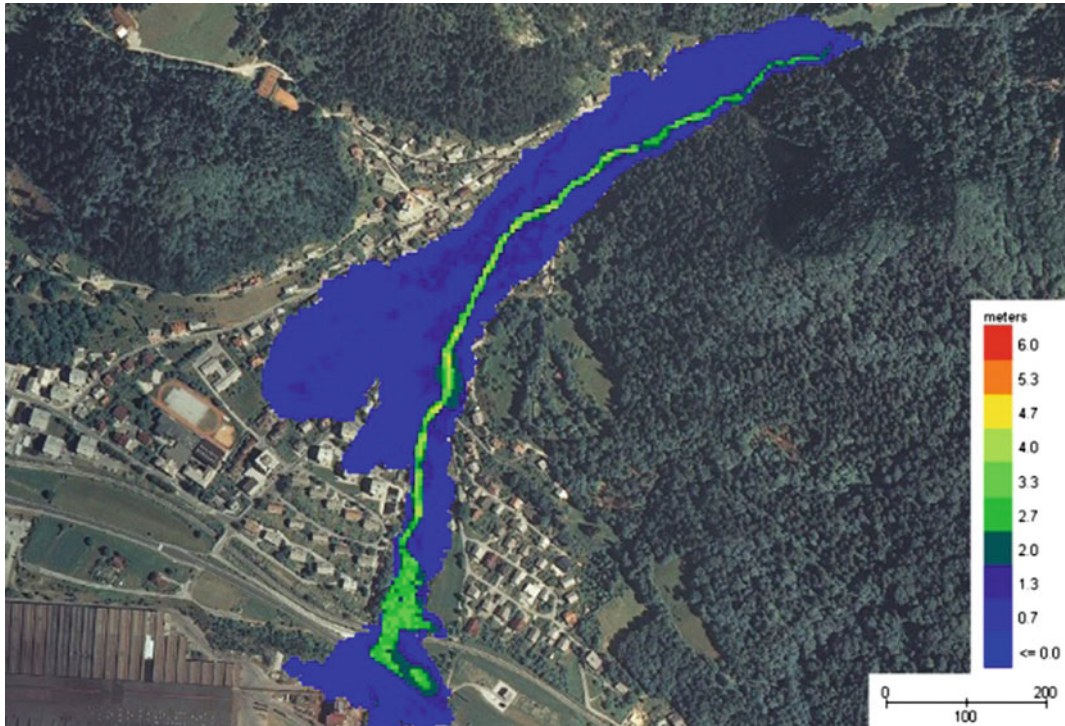


Fig. 4 Maximum flow depths using DEM5 (re-sampled LiDAR)

channel. With LiDAR-derived data the channel is better expressed and the larger part of the debris flow travels in the channel. Flow depths on the fan are more heterogeneous because the surface is more agitated due to more precise data. Variations in the flow depths lead to more accurate hazard mapping.

Inter-comparison between the models with LiDAR-derived DEMs (Figs. 3 and 4) shows that the main difference is the modelled flow depths in the inundation areas outside of the channel. The model with DEM0.5 (grid cell height interpolation integrated in a Flo-2D) indicates bigger differences in flow depths in the inundation area when compared to LiDAR-derived DEM5 (bilinear interpolation), which leads to more precise hazard mapping. With higher resolution DEM data, local conditions of the flow are better represented. More detailed results from the study on the Koroška Bela torrential fan can be found in Sodnik et al. (2012, 2013a,b).

4.2 The Trebiža Torrent Case (DEM5 and DEM12.5)

For Trebiža torrent we used the public DEM 5 and public DEM12.5. Since for a potential debris flow event in the test region we do not have precise material rheological data from past (recent) debris-flow events, we used parameter values gathered when calibrating the Flo-2D model for other recent debris flows in Slovenia (Stože above Log pod Mangartom in 2000 and Koseč above Kobarid in 2002) (Četina et al. 2006; Mikoš et al. 2006). Therefore, we used a critical shear stress of 20 Pa, a Bingham viscosity of 10 Pa s for $C_v = 0.42$. In this case, structures are modelled as blocked or dry cells.

Using DEM5 the flow “jumps” out of the channel close to the torrential apex (presumably due to a road bridge that was interpreted in DEM 5 as terrain) and runs down the inclined fan through the inhabited area that is lower than the Trebiža torrential channel (Fig. 5). The problem

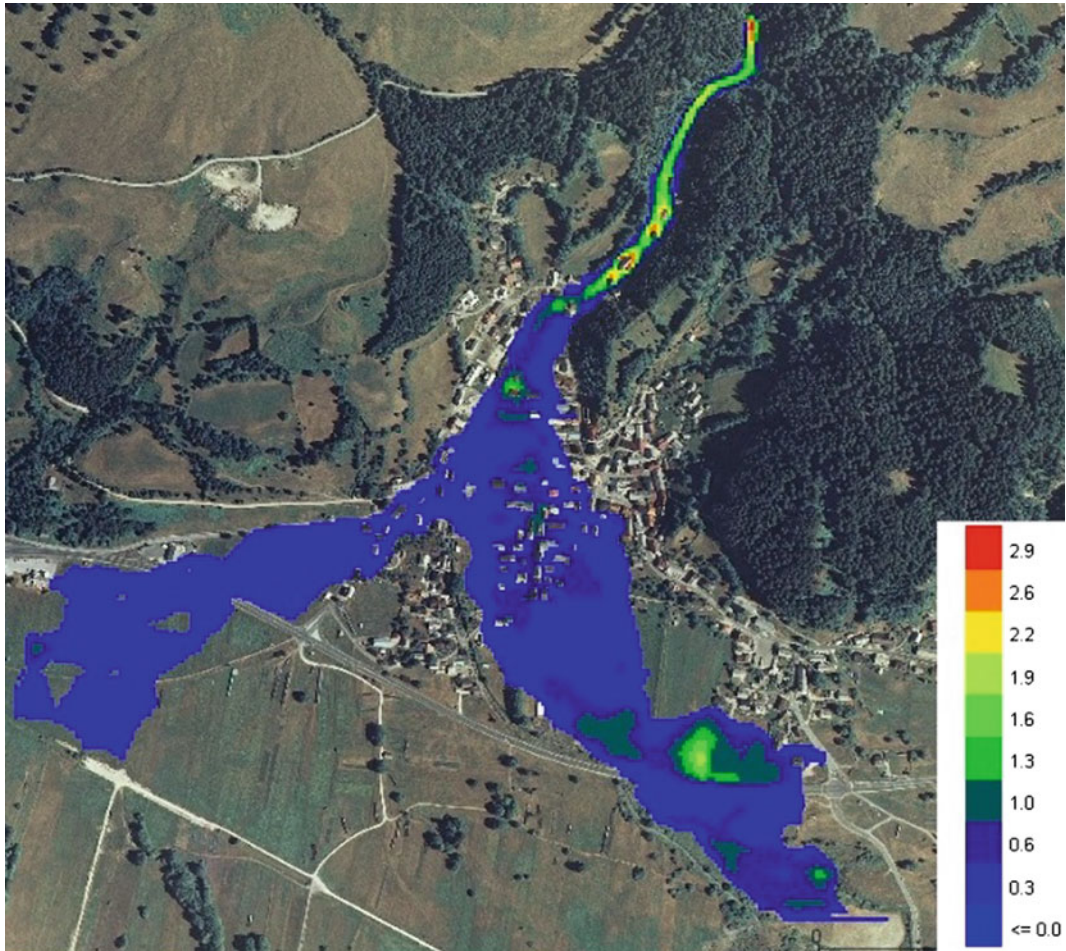


Fig. 5 Maximum flow depths using DEM5

with the grid generated from DEM 5 in the case of the Trebiža torrential fan is a clear example how problematic DEM 5 may be due to its limited capability to reproduce channel features for steep torrential channels on fans. Because the torrential channel in the upper part of its course on the fan is poorly reproduced, the debris flow reach out of the channel and start inundating the fan.

On the other hand, model with DEM 12.5 yields much more physically realistic results (Fig. 6), since it was produced by combining different existing data using an innovative

approach and applying high quality assurance standards.

More detailed results from the study on the Trebiža torrential fan can be found in Sodnik et al. (2009, 2010).

4.3 The Hrenovec Torrent Case (DEM5)

Flo-2D model was also applied using public DEM5 on the Hrenovec torrent above the Kropa village (W. Slovenia) to assess a potential

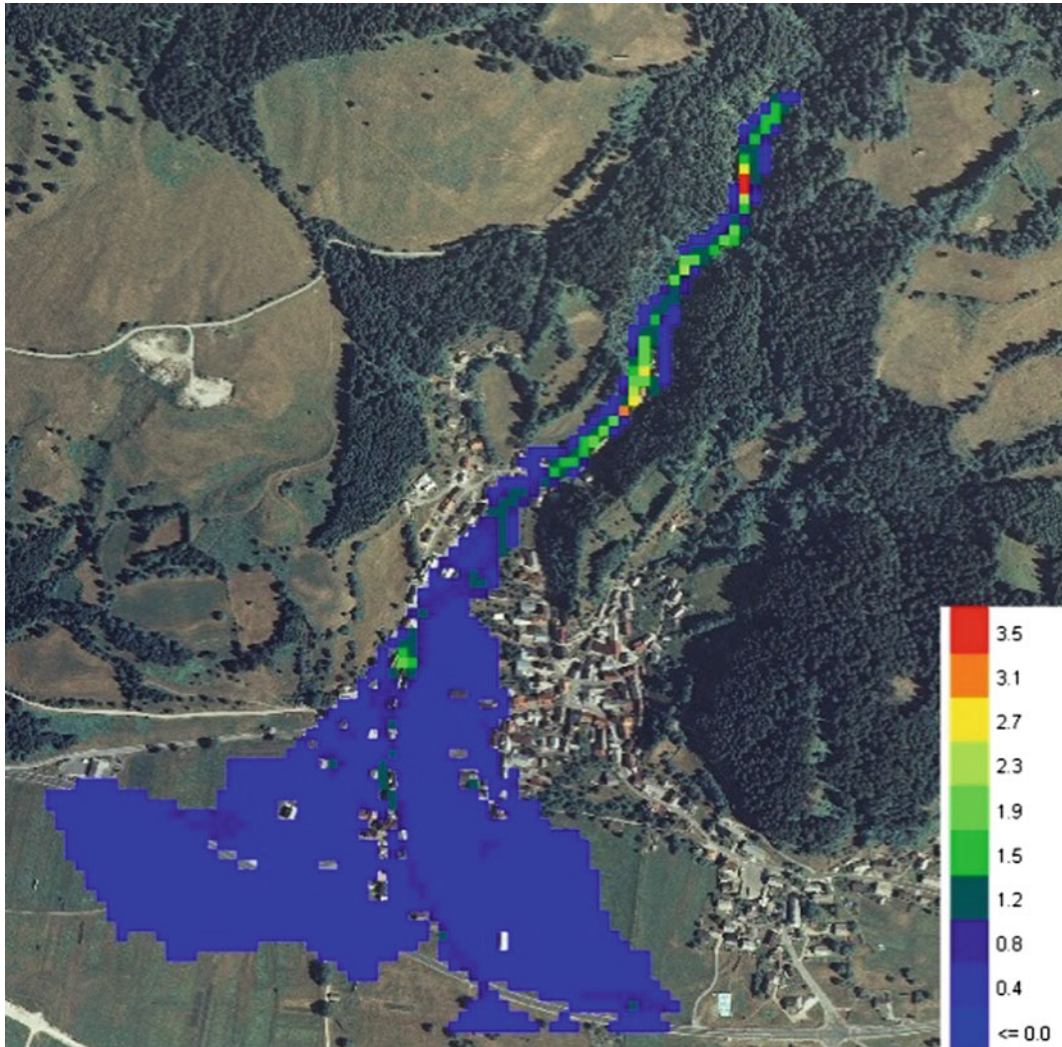


Fig. 6 Maximum flow depths using DEM12.5

debris-flow hazard. Two scenarios were taken into account, a 100-year return period event and an event with the same precipitation and discharge as a September 2007 flash flood (Rusjan et al. 2009) (Figs. 7 and 8; Table 2).

Figure 9 shows the results of the 100-year return period simulation, and Fig. 10 shows how public DEM5 underestimates the torrential channel in some reaches. With regard to these uncertainties of DEM 5, more refined



Fig. 7 Consequences of September 2007 flash flood in the centre of the Kropa village

topographic representation is needed in some field cases when modeling torrential flows or debris flows. Again we can see that high resolution does not necessary ensure more precise results in the mathematical modeling. More detailed results from study on the Hrenovec torrent can be found in Sodnik and Mikoš (2010).

4.4 Discussion

Study results show that topographical data is very important to get reliable and accurate results when applying a mathematical model for debris flow simulation. Quality of topographical data can make a significant change in modelling



Fig. 8 Debris flow deposition in the watershed of the Hrenovec torrent

Table 2 The main characteristics of the two scenarios for the Hrenovec torrent case

Parameter	100-year return period	September 2007 event
Peak discharge (m ³ /s)	21.09	39.82
Magnitude (m ³)	32,633	60,375
Volumetric concentration	0.5	0.5

results such as inundation area, flow depths and local flow conditions. In the Slovenia case, higher resolution data does not necessary mean a higher quality of modelling results. Morphological accuracy is the most important and it mostly depends on the procedure and interpolation

methods it has been created with (Sodnik et al. 2013b). The advantage of LiDAR-derived data is higher accuracy of the results and more reliable hazard assessment, but a downside of the more precise data is bigger sizes of model files, slower work, and much longer computational times.

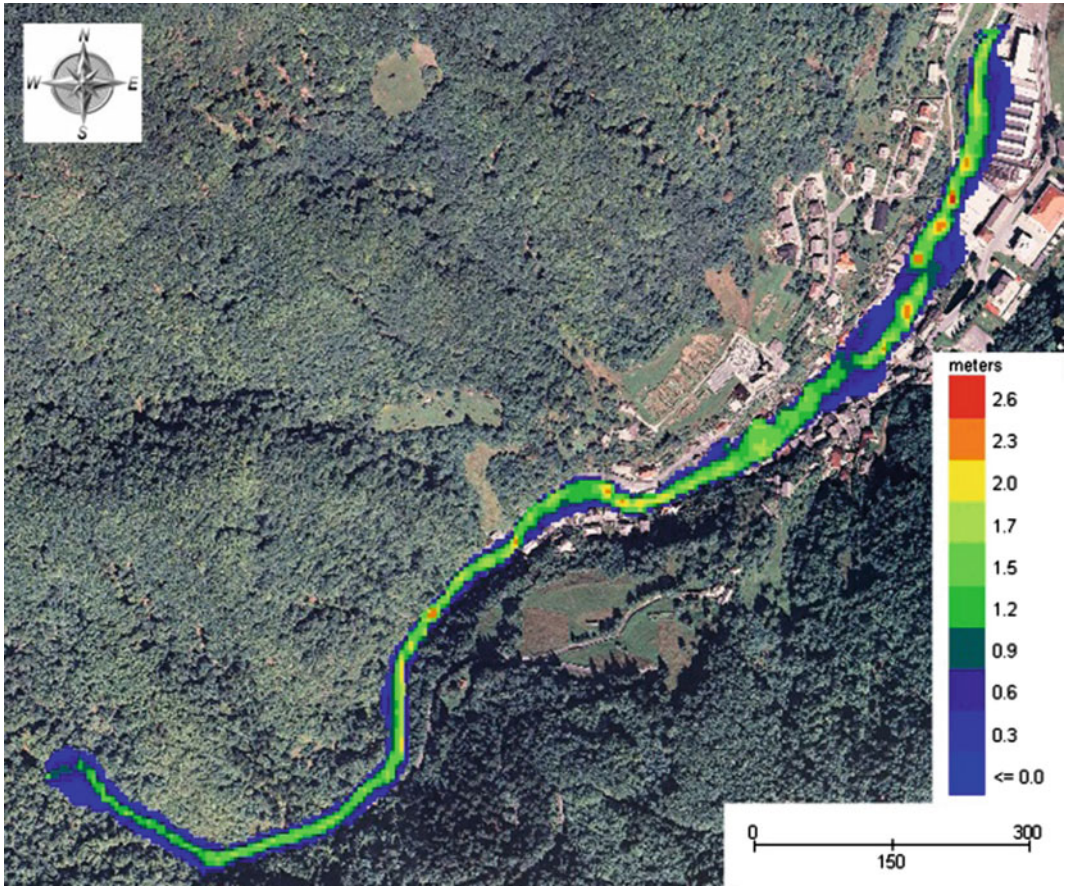


Fig. 9 Maximum flow depths using DEM5

Another question concerning model geometry is how to model built structures (residential buildings—houses, etc.) on the computational grid. One option is to use a higher Manning ruggedness coefficient for the area with structures,

a second one is to use dry or blocked cells. Using aerial photos, we recognized objects on the fan and defined blocked cells for the buildings, using the function “area reduction factor” of the Flo-2D model. Buildings are represented by higher

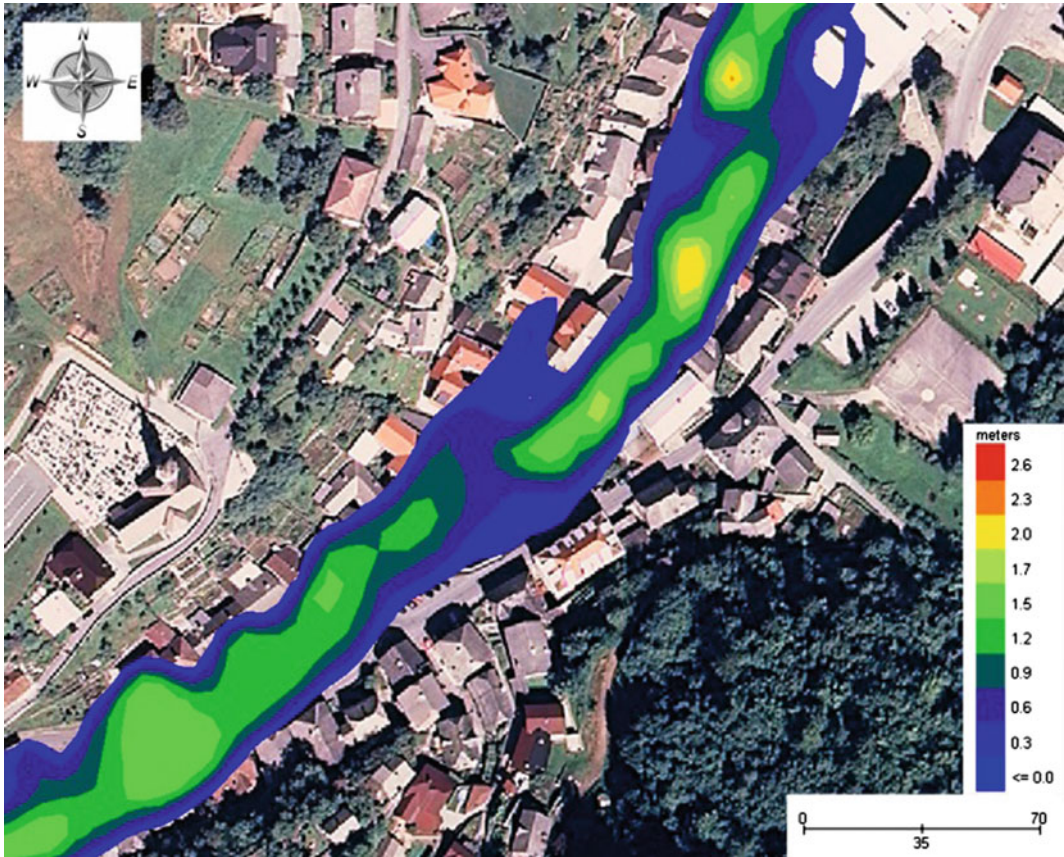


Fig. 10 Poorly expressed channel with DEM5

roughness values (n_g (buildings) = $0.2 \text{ sm}^{-1/3}$) or buildings are represented by blocked (dry) grid cells (for the area around dry cells we used n_g (building area) = $0.035 \text{ sm}^{-1/3}$). This two possibilities yield different simulation results, as shown in Figs. 11 and 12.

The option with dry cells shows higher local velocities (between buildings), which are more useful when assessing hazard and impact forces on structures. More about options for integrating built structures into 2-D debris-flow modelling can be found in Sodnik et al. (2012).



Fig. 11 Structures as higher n_g values



Fig. 12 Structures as blocked cells

5 Conclusions

Several studies have shown that the quality (morphological accuracy) of a DEM used for computational grid generation to perform a 2-D debris-flow mathematical simulation is very important. Higher DEM resolution does not always bring higher trustworthiness of debris-flow simulation results. The morphologic accuracy of a DEM can bring more precise results in terms of a debris-flow channel position, higher resolution data bring more realistic dimensions of the channel. A DEM12.5 cannot realistically represent, e.g., a 6–8 m wide torrential channel. A step forward for producing DEMs is LiDAR-derived data with higher resolutions. The interpolation method of the LiDAR point cloud is especially important when producing a DEM for end users. Different interpolation methods can bring varied results when a DEM is applied in a mathematical model, such as a 2-D model for a debris flow (Sodnik et al. 2013b). In 2015, LiDAR data became publicly available in Slovenia for the whole country. The usefulness and accuracy of these high resolution data for mathematical modelling of debris flows still need to be tested and reported.

References

- Balmforth NJ, Craster RV (2001) Geophysical aspects of non-Newtonian fluid mechanics. In: Balmforth NJ, Provenzal A (eds) *Geomorphological fluid mechanics*, Lecture notes in physics, vol 582. Springer, Berlin, pp 34–51. doi:10.1007/3-540-45670-8_2
- Cesca M, d'Agostino V (2008) Comparison between Flo-2D and RAMMS in debris flow modelling: a case study in the Dolomites. In: De Wrachien D, Brebbia CA, Lenzi MA (eds) *International conference on monitoring, simulation, prevention and remediation of dense and debris flow II*. WIT Press, Southampton, pp 197–206
- Četina M, Rajar R, Hojnik T, Zakrajšek M, Krzyk M, Mikoš M (2006) Case study: numerical simulations of debris flow below Stože, Slovenia. *J Hydraul Eng* 132(2):121–130. doi:10.1061/(ASCE)0733-9429(2006)132:2(121)
- Mikoš M, Fazarinc R, Majes B, Rajar R, Žagar D, Krzyk M, Hojnik T, Četina M (2006) Numerical simulation of debris flows triggered from the Strug rock fall source area, W Slovenia. *Nat Hazards Earth Syst Sci* 6:261–270
- O'Brien J (2011) FLO-2D reference manual, version 2009. <http://www.flo-2d.com/wp-content/uploads/FLO-2D-Reference-Manual-2009.pdf>. Accessed 6 June 2011
- Petje U, Ribičič M, Mikoš M (2005) Computer simulation of stone falls and rockfalls = Računalniško simuliranje skalnih odlomov in podorov. *Acta geographica Slovenica* 45(2):93–120. <https://ojs.zrc-sazu.si/ags/article/download/1234/1003> Accessed 31 July 2017
- Podobnikar T (2005) Production of integrated digital terrain model from multiple datasets of different quality. *Int J Geogr Inf Sci* 19:69–89
- Podobnikar T (2008) High-quality data for enhancement of the terrain model of Slovenia. *Geodetski Vestnik* 52(4):834–853
- Podobnikar T (2010) DEM production/updating based on environmental variables modeling and conflation of data sources. *J Civ Eng Arch* 4(11):33–44
- Rusjan S, Kobold M, Mikoš M (2009) Characteristics of the extreme rainfall event and consequent flash floods in W Slovenia in September 2007. *Nat Hazards Earth Syst Sci* 9:947–956. doi:10.5194/nhess-9-947-2009
- Sodnik J, Petje U, Mikoš M (2009) Terrain topography and debris flow modelling. *Geodetski Vestnik* 53(2):305–318
- Sodnik J, Mikoš M (2010) Modeling of a debris flow from the Hrenovec torrential watershed above the village of Kropa. *Acta Geogr Slovenica* 50(1):59–84
- Sodnik J, Petje U, Četina M, Mikoš M (2010) On how terrain topography and rheological properties influence modeling of the debris flow run-out distances—case study of the Sava Dolinka Valley, NW Slovenia, *Interpraevent 2010*, Conference proceedings, 283–292
- Sodnik J, Podobnikar T, Mikoš M (2012) Using Lidar data for debris flow modelling. *Interpraevent 2012*, Conference proceedings, 573–583. http://www.interpraevent.at/palm-cms/upload_files/Publikationen/Tagungsbeitraege/2012_1_573.pdf
- Sodnik J, Podobnikar T, Petje U, Mikoš M (2013a) Topographic data and numerical debris flow modeling. In: Margottini C, Canuti P, Sassa K (eds) *Land-slide Science and Practice*, Vol. 1. Springer, Berlin & Heidelberg, pp. 573–578
- Sodnik J, Vrečko A, Podobnikar T, Mikoš M (2013b) Digital terrain models and mathematical modelling of debris flows. *Geodetski Vestnik* 56(4):826–837

TXT-tool 3.886-1.2 Simulation for the Debris Flow and Sediment Transport in a Large-Scale Watershed

Ying-Hsin Wu, Ko-Fei Liu, Yi-Chin Chen, Yu-Jia Chiu
and Shang-Shu Shih

Abstract

We highlight a methodology of simulation of large-scale watershed mass transport, including landslide, debris flow, and sediment transport. A case study of Tsengwen reservoir watershed under the extreme rainfall triggered by typhoon Morakot is demonstrated. This approach starts with volume-area relation with landslide inventory method to predict temporal and regional landslide volume production and distribution. Then, debris flow model, Debris-2D, is applied to simulate the mass transport from hillslope to fluvial channel. Finally, a sediment transport model, NETSTARS, is used for hydraulic and sediment routing in river and reservoir. Near the water intake at the reservoir dam, the simulated sediment concentration is in good agreement with the measured one. The proposed approach gives good prediction and should help the management of reservoir operation and disaster prevention.

Keywords

Regional-scale simulation · Watershed · Mass movement
Landslide · Debris-2D · Sediment transport

Contents

1 Introduction	252	6.2 Prediction of Shallow Landslide Volume and Location	257
2 Overview of Methodology	252	6.3 Simulation of Debris-Flow Transport	258
3 Shallow Landslide Model	252	6.4 Simulation of Sediment Transport	259
4 Debris Flow Simulation	254	6.5 Result and Analysis	260
5 Sediment Transport Simulation	256	7 Discussion and Conclusion	260
6 Case Study—Tsengwen Watershed Reservoir 257		References	261
6.1 Brief Introduction to Target Area.....	257		

Y.-H. Wu
Disaster Prevention Research Institute, Kyoto
University, Gokasho, Uji, Kyoto 611-0011, Japan
e-mail: wu.ahsin@gmail.com

K.-F. Liu (✉)
Department of Civil Engineering, National Taiwan
University, Taipei 10617, Taiwan
e-mail: kfliu@ntu.edu.tw

Y.-C. Chen
Department of Geography, National Changhwa
University of Education, Changhua 50007, Taiwan

Y.-J. Chiu · S.-S. Shih
Hydrotech Research Institute, National Taiwan
University, Taipei 10617, Taiwan

1 Introduction

Landslide, debris flow, and sediment transport are usually combined to be a complete sediment transport phenomenon in mountainous area. This chain of mass transport presents multi-hazard potential to threat human lives, properties and water resource infrastructures. Requiring a comprehensive approach to evaluate this mass transport process is a critical issue for disaster mitigation and water resources management.

In the past decades, many models have proposed for simulation of landslides, debris flows, sediment transport process individually. For landslide, researchers have used empirical or physical models to evaluate the landslide susceptibility (e.g., Guzzetti et al. 2005; Reichenbach et al. 2005; Gabet and Mudd 2006; Chen et al. 2006; Chang and Chiang 2009) and mobilization (Iverson et al. 1997). To estimate landslide volume, the volume-area relation using statistical approach gave reasonable predictions (e.g., Guzzetti et al. 2009; Klar et al. 2011; Parker et al. 2011; Chen et al. 2012). For debris flow simulation, several numerical models, e.g., FLO-2D (2006), RAMMS (2012), George and Iverson (2014), and Debris-2D (Liu and Huang 2006; Liu and Wu 2013), have been widely used in debris flow assessment (e.g., O'Brien et al. 1993; Tsai et al. 2011; Hussin et al. 2012; Wu et al. 2013). Particularly, Wu et al. (2013) found that Debris-2D can simulate the granular debris flow triggered by landslide very well. As for sediment transport assessment, various hydraulic models had been developed for hydraulic and sediment routing, such as HEC-RAS (2010), NETSTARS (e.g., Lee et al. 1997; Lee and Hsieh 2003; Shih et al. 2008), and CCHE2D (e.g., Rathburn and Wohl 2001; Huang et al. 2006). The main difficulty is to connect models above to achieve accurate simulation of mass movement phenomena from hillslopes, creeks, to a downstream river in a large-scale watershed.

In this study, to simulate watershed mass transport from hillslope to downstream river, we

highlight an integrated approach by combining landslide volume model, Debris-2D and NETSTARS. This approach has been verified to be reliable (Liu et al. 2013). For demonstration, we present a case study of Tsengwen reservoir watershed, southwest Taiwan, under extreme rainfall triggered by typhoon Morakot. In the following we introduce our approach part by part, and then present the result of case study.

2 Overview of Methodology

This integrated approach can be separated into three parts: (a) shallow landslide model; (b) debris flow simulation, and (c) river sediment routing. The first step is to develop a landslide model for volume estimation by using a landslide volume-area relation calibrated by landslide inventories. Then, using a calibrated empirical formula with cumulative rainfall, the model can predict temporal distribution and volume production of landslides. Second, the output of landslide model is used as initial condition and temporal input for debris flow simulation. A watershed-scale simulation for transport of landslide mass is then performed using Debris-2D. Finally, the simulation output from Debris-2D at tributary junction is used as sedimentary boundary condition input for NETSTARS to perform hydraulic and sediment routing in fluvial channels and reservoir. The detailed descriptions for each model are given in the follows.

3 Shallow Landslide Model

To estimate landslide volume and temporal distribution, statistical and empirical methods are applied in our shallow landslide model. We collect long term event-based inventory data covered landslides triggered by typhoon events and heavy rainfalls to develop empirical relations between landslide volume and accumulated rainfall. Since most of events are shallow landslides, we assume that all occurred landslides are

shallow ones in our simulation. To obtain each landslide area in the inventory, landslide scars are mapped manually by comparing the Formosa-2 and SPOT-4 satellite images taken before and after each event. Then, with many datasets of landslide area and volume, a volume-area relation is calibrated as below:

$$V_L = \alpha(A_L)^\gamma, \quad (1)$$

where V_L (unit: m^3) is landslide volume; A_L (m^2) is landslide area; α and γ are calibrated parameters.

For demonstration of case study, Chen et al. (2012) found that event-based landslide volume in the Tsengwen Reservoir watershed was highly correlated with corresponding cumulative rainfall. Hence, to link landslide volume with rainfall in a sub-watershed, the empirical equation proposed by Uchihugi (1971) is used as follows:

$$V_L = KA(P - P_0)^r, \quad (2)$$

where A (m^2) is area of watershed; P (mm) is cumulative rainfall, P_0 (mm) is a critical rainfall threshold for landslide occurrence (Central Geological Survey 2011) and K and r are parameters calibrated by the long term inventory data. Except the cumulative rainfall, all parameters above are calibrated at sub-watershed level and are different for each sub-watershed. Figure 1 illustrates an example of the relation between event-based landslide volume and cumulative rainfall. A different interpretation for this curve is used. For a single landslide, this curve can represent an increase of volume in time for increased accumulative rainfall at each landslide. So at each landslide location, mass will accumulate due to a given time series of cumulative rainfall. Then, the process from accumulation to mobilization is simulated by using Debris-2D, which will be introduced in the next section. For each landslide, when the produced volume is small, it can stay in the original location due to yield stress effect in Debris-2D model. Then, the mass will slide down only if the accumulated mass is large enough.

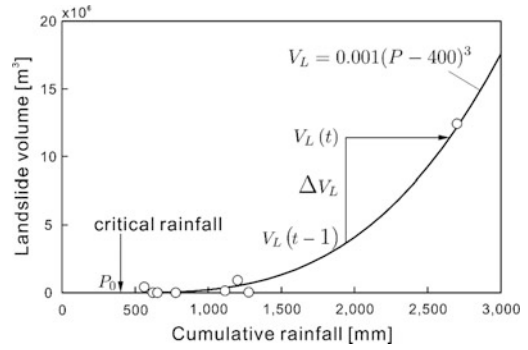


Fig. 1 Illustration of the relation between landslide volume V_L and cumulative rainfall P using Uchihugi (1971) empirical equation (Eq. 2) for the W3 sub-watershed which is located in the upstream of the Tsengwen reservoir watershed (see Fig. 2). P_0 is the critical rainfall (Central Geological Survey 2011) for landslide occurrence. The hollow dots denote the eight landslide events occurred in W3 sub-watershed since 2001. All parameters in Eq. 2 for all sub-watershed are listed in Table 1

With the above interpretation, a hydrograph of landslide volume production can be calculated by Eq. 2. Volume production from a landslide within a specified time interval can be evaluated as below:

$$\Delta V_L = V_L(t) - V_L(t-1). \quad (3)$$

Equation 3 denotes the volume production within a time interval in a sub-watershed. The distribution of this produced volume is also critical for a precise simulation. For determination of landslide occurrence timing and location, we refer to landslide inventory of the Tsengwen reservoir watershed (see Fig. 2). Malamud et al. (2004) shows that landslide tends to occur at where it occurred in the past. Also, in the literatures, shallow landslides usually occur before the peak of rainfall (Godt et al. 2006; Yu et al. 2006), and large ones usually occur after the rainfall peak (Lollino et al. 2006; Tsou et al. 2011). According to these evidences, we assume that old landslide sites tend to be reactivated, and small landslides occurred prior to large ones.

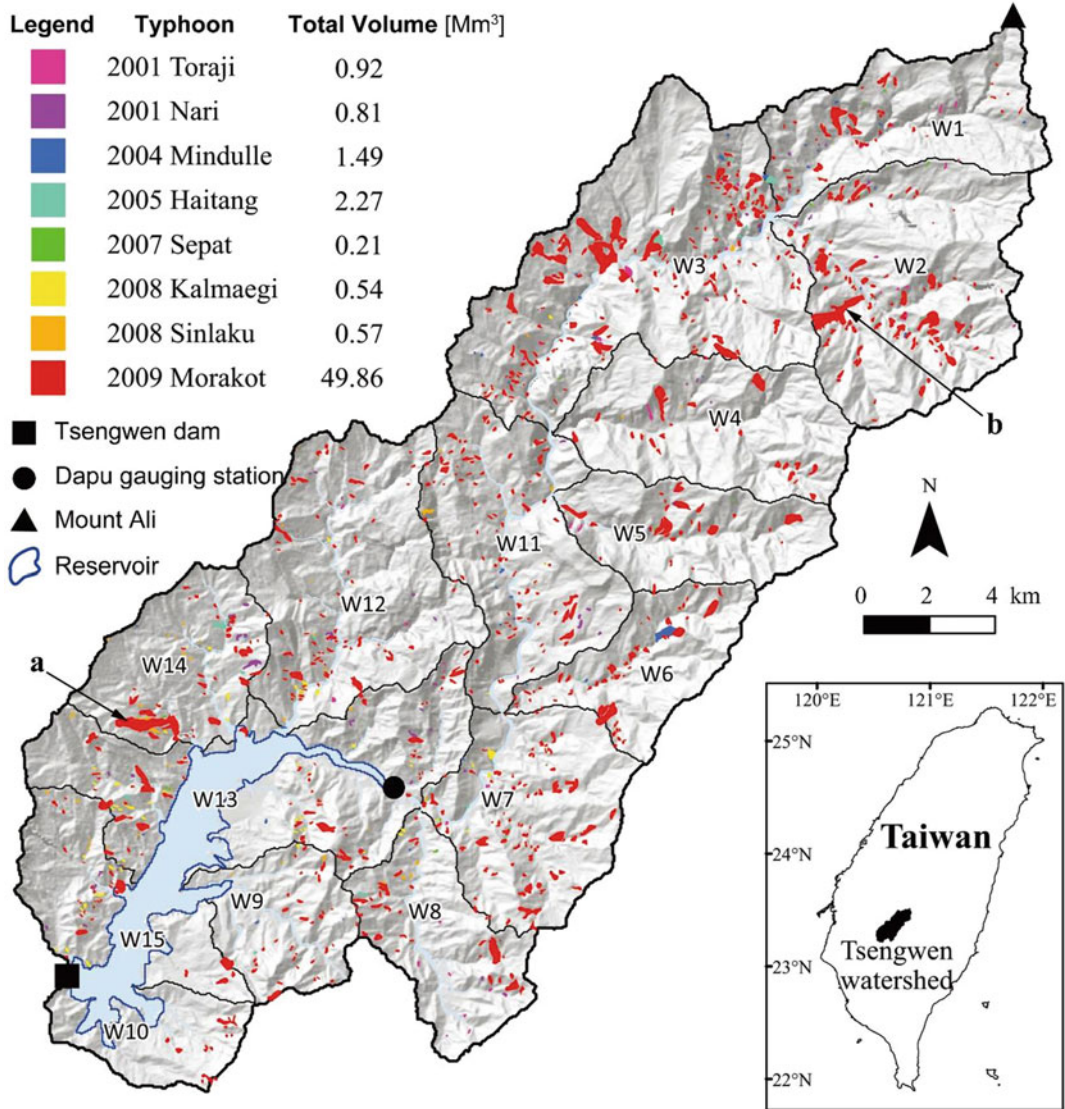


Fig. 2 The distribution of all landslide locations for all sub-watersheds in the Tsengwen reservoir watershed. Data are collected from 8 different typhoon events. The

landslide locations *a* and *b* caused the corresponding peaks *a* and *b* in Fig. 3 (Liu et al. 2013)

4 Debris Flow Simulation

Being mixed with water from rainfall or overland flow, landslide material on slopland forms debris flow and transports downstream into the

fluvial channel. In this study, this process is simulated using Debris-2D model (Liu and Huang 2006; Liu and Wu 2013; Liu et al. 2014; Wu and Liu 2014). The fundamental theory of Debris-2D is based on the mass and momentum conservation with shallow water assumption and

depth-averaging method. The adopted constitutive relation between shear stress and strain rate is proposed by Julien and Lan (1991). The governing equations are all in the conservative form and Cartesian coordinates. The mass conservation equation is

$$\frac{\partial H}{\partial t} + \frac{\partial(uH)}{\partial x} + \frac{\partial(vH)}{\partial y} = 0, \quad (4)$$

and the (x, y) -momentum conservation equations are

$$\begin{aligned} \frac{\partial(uH)}{\partial t} + \frac{\partial(u^2H)}{\partial x} + \frac{\partial(uvH)}{\partial y} \\ = -gH \cos \theta \frac{\partial(B+H)}{\partial x} + gH \sin \theta \\ - \frac{1}{\rho} \frac{\tau_0 u}{\sqrt{u^2 + v^2}}, \end{aligned} \quad (5)$$

$$\begin{aligned} \frac{\partial(vH)}{\partial t} + \frac{\partial(uvH)}{\partial x} + \frac{\partial(v^2H)}{\partial y} \\ = -gH \cos \theta \frac{\partial(B+H)}{\partial y} - \frac{1}{\rho} \frac{\tau_0 v}{\sqrt{u^2 + v^2}}, \end{aligned} \quad (6)$$

where $H = H(x, y, t)$ is debris flow depth (m); $B = B(x, y)$ is bed topography (m) which assumed to be fixed; u and v are depth-averaged velocities (m/s) in (x, y) -direction respectively, and they are functions of spatial variables x, y and temporal variable t ; $\tan \theta$ is the average bottom bed slope; ρ is debris flow density (kg/m^3), which is assumed to be constant; g is the gravitational acceleration (m^2/s); τ_0 is yield stress (Pa), which represents the material property of debris flow. The yield stress is the only one material parameter for simulation, and it can be obtained using rheological tests (e.g., Liu and Huang 2006; Wu and Liu 2015).

The erosion effect is very common in mountainous region. There are places that bed erosion and deposition creates large variation for bed topography (e.g., Dhital 2003; Haas et al. 2004). Debris-2D can be used with bottom erosion effect in most cases. But, in the case study in the present

work, we shall use fixed bed condition. The reason is explained in the following. Fixed bed assumption only applies, strictly speaking, to rock bottom or erosion depth much less than the flow depth. In our study, the only topography data available is that measured after disaster, which means nothing can be eroded from the topography if we want to simulate the past event. The data used in calibrating the landslide prediction model needs the volume production of each landslide. However, any field investigation will give the total volume at downstream without distinguishing material between bed erosion and real slides. This means the landslide prediction model has already taken the erosion amount into account. Then it is incorrect to calculate the erosion effect again during debris flow simulation. So in the present study, fixed bed topography is used to go along with the landslide prediction model. The amount of erosion is considered redistributed at upstream landslide location.

In Debris-2D, an initiation condition for any originally stationary debris pile is

$$\left(\frac{\partial B}{\partial x} + \frac{\partial H}{\partial x} - \tan \theta \right)^2 + \left(\frac{\partial B}{\partial y} + \frac{\partial H}{\partial y} \right)^2 > \left(\frac{\tau_0}{\rho g \cos \theta H} \right)^2. \quad (7)$$

Equation 7 means that a debris flow can mobilize only if sum of pressure and gravitational effects (i.e., two terms on the left-hand side) exceeds yield stress effect (i.e., the right-hand side of Eq. 7).

For Debris-2D simulation, the main input is debris flow mass volume distribution. This is the most important advantage to connect with our shallow landslide model, which predicts landslide spatial distribution and volume. The output of shallow landslide model includes dry debris volume V_d and initial mass distribution. For Debris-2D model, the simulation input of mass volume V is evaluated by dividing V_d by the equilibrium volume concentration C_v (%) of debris flow (Takahashi 1981) as follows:

$$C_v = \frac{\rho_w \tan \theta}{(\sigma - \rho_w)(\tan \phi - \tan \theta)}, \quad (8)$$

where ρ_w is water density; σ is the density of dry debris (around 2.65 g/cm^3); ϕ is internal friction angle (about 37°); θ is average bottom slope angle in the field. Using Eq. 8 the density of debris flow is determined using $\sigma C_v + \rho_w(1 - C_v)$. With total debris flow volume V , distribution obtained by our landslide model, and yield stress measured using rheological tests or estimation, we can simulate the transport process of all landslide volumes.

From simulated results of Debris-2D, we can obtain the locations and sediment inflow hydrographs for creeks. Then, these inputs in space and time are used for sediment routing as side inflows in creeks.

5 Sediment Transport Simulation

To model sediment transport process in creeks and reservoir, we use a quasi-two-dimensional numerical model, called Network Sediment Transport Model for Alluvial River Simulation or NETSTARS as an abbreviation (Lee et al. 1997). In NETSTAR, the flow in channel can be divided into several stream tubes that all physical properties will be averaged over each stream tube cross-section. For unsteady hydraulic routing, the one-dimensional Saint Venant equations (Chow et al. 1988) are used. As x -coordinate represents transverse direction along the stream tube, the continuity equation reads

$$\frac{\partial A_s}{\partial t} + \frac{\partial Q}{\partial x} = 0, \quad (9)$$

and the momentum equation reads

$$\frac{\partial Q}{\partial t} + \frac{\partial}{\partial x} \left(\alpha_m \frac{Q^2}{A_s} \right) + gA_s \frac{\partial \eta}{\partial x} + gA_s S_f - \frac{Q}{A_s} q = 0, \quad (10)$$

where A_s is channel cross-sectional area as a function of streamwise direction x ; Q is flow discharge; q is lateral inflow or outflow discharge per unit stream length; α_m is momentum correction coefficient; η is water surface elevation as a function of x and t ; $S_f = Q|Q|/K_c^2$ is friction slope, where $K_c = (A/n)R^{2/3}$ denotes channel conveyance, and n and R are roughness coefficient for Manning formula and hydraulic radius respectively. Based on the result of hydraulic routing, flow condition in the channel can be obtained and is applied as the input of sediment routing.

For sediment routing, NETSTARS considers equilibrium and non-equilibrium flow conditions. If flow condition is equilibrium, the total transport capacity of sediment load Q_s is expressed by the total load equations as below:

$$\frac{\partial Q_s}{\partial x} + (1 - p_s) \frac{\partial A_{dt}}{\partial t} = 0, \quad (11)$$

where A_{dt} is amount of sediment deposition/scouring per unit length of stream tube; p_s is sedimentary deposit porosity for riverbed, and $(1 - p_s)$ stands for volumetric sediment concentration. Equation 11 is also referred to as the famous one-dimensional Exner equation (Julien 2002). On the other hand, for non-equilibrium flow condition, the separate treatment method includes three equations, which are the sediment continuity, sediment concentration convection-diffusion equation and bed load equation. The Rouse number is used to separate suspended and bed load. Particle with Rouse number >5 is treated as bed load, but suspended load if Rouse number ≤ 5 . The sediment continuity equation is

$$\frac{\partial Q_b}{\partial x} + (1 - p_s) \frac{\partial A_{dt}}{\partial t} + \frac{\partial}{\partial x} \sum_{k=1}^N (q_t C_k) = 0, \quad (12)$$

where Q_b and q_t are bed load transport rate and flow discharge in stream tube respectively; C_k is depth-averaged concentration of suspended sediment of size class k (Holly and Rahuel 1990),

and it can be obtained using the convection-diffusion equations as follows:

$$\begin{aligned} & \frac{\partial(C_k A_r)}{\partial t} + \frac{\partial}{\partial x}(q_r C_k) \\ &= \frac{\partial}{\partial x} \left(A_r k_x \frac{\partial C_k}{\partial x} \right) + S_k \\ &+ \left(h k_z \frac{\partial C_k}{\partial z} \right)_r, \end{aligned} \quad (13)$$

where k_x and k_z are longitudinal and transverse dispersion coefficients; A_r is stream tube cross sectional area; h is flow depth; S_k is a source term of suspended sediment of size fraction k , and stands for effects of sediment resuspension and deposition. Therefore, the evolution of channel bed can also be assessed during the simulation.

For simulation, NETSTARS requires two categories of input, including (1) topography and channel cross-section data, and (2) boundary conditions at the upstream and downstream boundaries. For hydraulic routing, a discharge hydrograph and a rating curve are needed at the upstream and downstream boundaries, respectively. For sediment routing, both the inflow suspended-load concentration and bed-load discharge are required at the upstream boundary. The zero concentration gradient is imposed at the downstream end to begin with. The simulation result from Debris-2D is used as lateral mass input for NETSTARS simulation.

6 Case Study—Tsengwen Watershed Reservoir

6.1 Brief Introduction to Target Area

Tsengwen reservoir watershed, with total drainage area of 480 km², is located in southwest Taiwan, as is shown in Fig. 2. Elevation ranges from 126 m near the Tsengwen dam (solid black square in Fig. 2) to 2610 m at the upstream boundary, which is Mount Ali (black triangular in Fig. 2). There are 15 sub-watersheds. Lithological setting in these watersheds is dominated by sandstones and shale with weak rock strength of 10–64 MPa (Taiwan Central Geological

Survey 2012). Annual accumulative precipitation in the Tsengwen reservoir watershed is about 2800 mm (Water Resources Agency 2008). Up to 90% of annual accumulative precipitation occurs in the flood season (from May to September), and the main source is typhoons. Heavy rainfall from typhoons usually caused numerous landslides and debris flows on hill-slopes in this watershed, and these abundant sediments were transported into Tsengwen reservoir to affect drinking water quality and reservoir operation.

Between August 5 and 10 in 2009, typhoon Morakot set a new rainfall record for a single typhoon event in Taiwan. The rainfall hydrograph is plotted in Fig. 3a. Particularly, the cumulative rainfall reached 3059 mm at Mount Ali weather station, which is located in the northeast Tsengwen watershed (black triangular in Fig. 2). This extreme rainfall induced large number of landslides and produced a great quantity of sediments, which equaled to the total amount accumulated in the past 19.5 years in the Tsengwen reservoir watershed (Water Resources Agency 2011).

In this study, the watershed topography is obtained after typhoon Morakot. With the deposit soil samples in the field, we used the method proposed by Liu and Huang (2006) to obtain a representative yield stress in the laboratory. The obtained value of yield stress is about 1000 Pa and is used for all sub-watersheds in the debris flow simulation.

6.2 Prediction of Shallow Landslide Volume and Location

The landslide volumes triggered by the past eight typhoon events range from $0.21 \pm 0.09 \times 10^6$ to $49.86 \pm 6.36 \times 10^6$ m³ (Chen et al. 2012). Figure 2 illustrates landslide area distributions and total volumes triggered by the eight typhoons. Particularly, typhoon Morakot triggered the largest landslide volume, accounting for 88% of the total accumulated volume. The volume-area relation for the Tsengwen watershed is

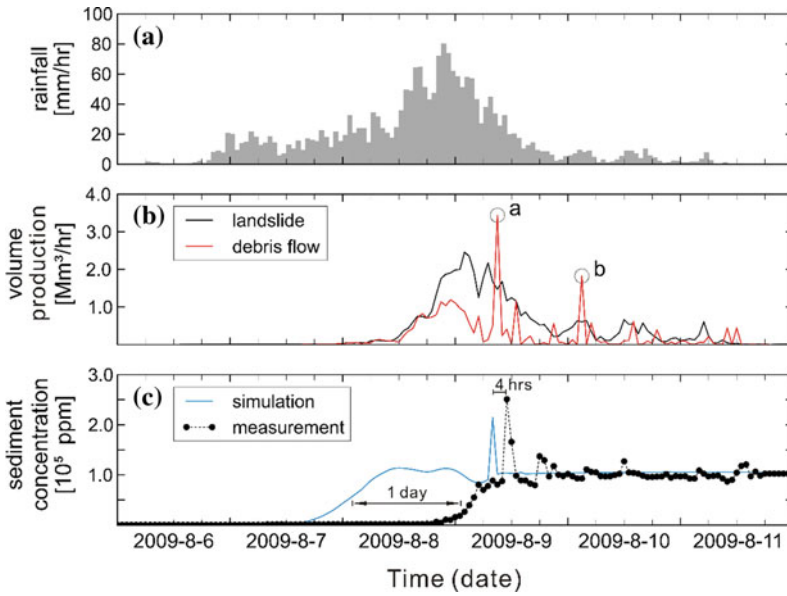


Fig. 3 Hydrographs: **a** rainfall event of typhoon Morakot; **b** total volume production of simulated landslide (black line) and total debris flow inflow into river (blue line). The peaks *a* and *b* come from the landslides occurred at the locations marked *a* and *b* in Fig. 2

respectively; **c** comparison of simulated and measured sediment concentration. The data of sediment was recorded at Tsengwen reservoir dam (see black square in Fig. 2) (Liu et al. 2013)

$$V_L = 0.202(A_L)^{1.268}, \quad (14)$$

with the coefficient of determination $R^2 = 0.78$ (Chen et al. 2012).

Table 1 summarizes landslide volumes and all parameters for Eq. 2 for the 15 sub-watersheds in the Tsengwen reservoir watershed. The root-mean-square-error (RSME) ranges from 1.87×10^4 to 4.65×10^5 m³. The percentage error (PE) is between 17 and 53% for predicted volumes. The exponent r of Eq. 2 ranges from 2.4 to 3.0, and this implies that a small increase in rainfall can result in large increase of landslide volume production. From the predicted results, the total landslide volume for the case of typhoon Morakot is 49,075,413 m³, and the temporal variation for sum of landslide volume production from all sub-watersheds is plotted in Fig. 3b. This total production results in debris flows in many locations, and the temporal production at each location is inputted as sources for debris flow simulation using Debris-2D.

6.3 Simulation of Debris-Flow Transport

The mass of debris flow into the fluvial channels is considered as the lateral sediment inflow discharge. From the simulation result, the total volume of debris flow from all tributaries into the main river is plotted in Fig. 3b. This total discharge is the sum of all inflows from many different locations. There are two peaks of sediment inflow discharge in Fig. 3b. The first peak *a* with volume discharge 2.46 Mm³ per hour comes from the landslide located at point *a* in W14 sub-watershed (Fig. 2). The second peak *b* is from the landslide occurred at point *b* in W2 sub-watershed (Fig. 2).

Table 1 also summarizes the simulated sediment inflow to the main river from each sub-watershed. It shows that total volume of sediment inflow from debris flows is about 16,618,171 m³. So only 33.9% of the total landslide volume flowed into river through debris flows. The simulated ratio is very close to the

Table 1 All parameters for Uchihugi relation (Eq. 2) and field measured landslide volumes and simulated lateral inflow to channel from debris flow simulation in the 15 sub-watersheds in the Tsengwen reservoir watershed

Watershed ID	A	P_0	KA	r	RMSE	PE	Landslide volume (m ³)	Channel inflow volume (m ³)
W1	28.2	156	0.001	2.7	1.26×10^5	43	1,970,125	668,087
W2	45.8	156	0.001	2.9	4.65×10^5	41	8,384,991	3,605,216
W3	64.6	400	0.001	3.0	3.30×10^5	19	12,428,657	2,950,378
W4	31.3	400	0.001	2.8	7.81×10^4	25	2,186,534	474,199
W5	22.3	400	0.007	2.6	8.00×10^4	23	2,497,126	549,704
W6	19.3	159	0.015	2.5	1.95×10^5	43	2,545,912	853,018
W7	31.8	159	0.003	2.8	2.17×10^5	53	3,078,364	1,211,712
W8	22.5	159	0.005	2.7	9.20×10^4	34	1,953,766	369,982
W9	17.5	120	0.011	2.4	2.39×10^4	30	585,776	155,834
W10	14.7	120	0.004	2.5	1.87×10^4	37	403,793	86,137
W11	36.7	400	0.012	2.5	6.06×10^4	25	1,685,969	918,750
W12	45.0	400	0.008	2.6	4.09×10^4	17	1,636,836	700,049
W13	21.5	805	0.140	2.4	7.26×10^4	17	2,986,346	1,214,953
W14	23.2	175	0.002	2.9	1.47×10^5	19	5,264,517	2,136,202
W15	24.7	120	0.006	2.6	3.66×10^4	18	1,466,701	723,947
Total							49,075,413	16,618,171

A is watershed area (km²); P_0 is the critical rainfall (mm) for each sub-watershed (Taiwan Central Geological Survey 2011); KA and r are parameters in Eq. 2. For volume prediction, RMSE denotes root-mean-square-error (m³), and PE is percentage of error (%). The ratio of total channel inflow volume to total predicted landslide volume is 33.9%

averaged ratio 33.3% published officially by Morakot Post-Disaster Reconstruction Council (2012). This has verified the capability of simulating mass movement from hillslopes to rivers using our approach.

6.4 Simulation of Sediment Transport

Since no data of channel cross sections before the disaster are available, the 240 cross sections, extracted by fluvial topography measured by LiDAR in 1 m resolution after the disaster, were used as inputs for NETSTARS simulation. This means the bed topography is the result after erosion, and the fixed-bed assumption is also used for sediment routing.

Besides, without real measurement of water/sediment inflow data at the upstream

boundary, the water inflow discharge hydrograph at the upstream boundary was calculated by using area ratio method from transferring the downstream measured discharge hydrograph recorded at Tsengwen reservoir dam (solid square in Fig. 2). For the sediment rating curve at upstream boundary, we used the data of suspended sediment concentration measured at downstream Dapu gauging station (black circle in Fig. 2). Figure 4 illustrates the sediment yield Q_s (ton/day) as a function of river discharge Q (cm), and the rating curve equation is as follows:

$$Q_s = 0.6833Q^{1.9118}, \quad (15)$$

where the coefficient of determination $R^2 = 0.9421$. Equation 15 is used as the sediment inflow discharge at the upstream boundary.

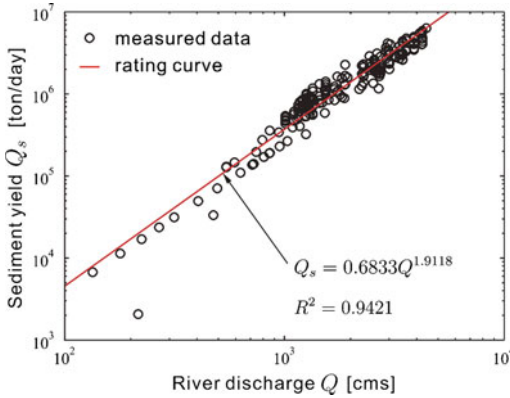


Fig. 4 Sediment yield Q_s (ton/day) as a function of river discharge Q (cm). The rating curve is expressed as Eq. 15, with the coefficient of determination $R^2 = 0.9421$. The sediment data was measured at Dapu gauging station (at black circle in Fig. 2)

6.5 Result and Analysis

From the simulation result (see Fig. 3c), when the cumulative rainfall exceeded the critical rainfall (from 05:00 AM to 12:00 PM on Aug. 7), landslides started to occur and produced mass at many locations in all sub-watersheds. The highest peak of sediment and debris flow discharges happened at the same time, i.e., 8:00 AM on Aug. 9. This peak comes from the landslide located at point a in Fig. 2 in W14 sub-watershed.

For verification of our approach, we used the sediment concentration measured at the reservoir dam during typhoon Morakot. Comparison of the simulated (blue line) and measured sediment discharges at the Tsengwen dam (black circles) is shown in Fig. 3c. The peak value of the simulated sediment discharge (i.e., 6.5×10^6 ton/h) is very close to the measured one (6.8×10^6 ton/h), which was measured at the reservoir dam at 11:00 AM on Aug. 9. However, the simulation result shows that the starting time of concentration increase was one day ahead of the measured data. This is due to the assumed water discharge hydrograph at the upstream boundary. In our simulation, the input discharge was determined by the measured one at the downstream Tsengwen dam with area ratio method. So the upstream

hydrograph started too early. Therefore, the input hydrograph causes the advance of initialization time in the simulation. However, those peak concentrations are results from sediment brought into river by debris flow; it does not depend on upstream sediment hydrograph. But the speed of transportation of this peak concentration does depend on the upstream water hydrograph, so the time difference between simulated peak and measured peak is only 4 h and is much closer to measured one.

Although the starting time of concentration increase from simulation is different from the measured one, the temporal variation of the concentration is similar. So if input discharge hydrograph is reasonably determined by using other rainfall-runoff models, e.g., HEC-HMS (2010), it is convinced to obtain a more accurate simulated result.

7 Discussion and Conclusion

We introduced an integrated approach for simulation of mass transport simulation including landslide, debris flow and sediment transport in a large-scale watershed. In our approach, the shallow landslide model is used to obtain the temporal and spatial distribution of landslides on hillslopes. Then, with the output of landslide model, Debris-2D is utilized to simulate mass transport process from hillslopes to tributaries in every sub-watershed. Then, the output of debris flow simulation is served as the input of lateral mass into the fluvial channel for sediment routing. Finally, NETSTARS is applied to obtain the time-varying sediment transport concentration in the fluvial channel and reservoir.

The application on a real case in Tsengwen reservoir watershed during typhoon Morakot was demonstrated for verification. The simulation result shows that our approach can accurately predict the process of mass movement from hillslopes to the main river as well as the peak value of sediment concentration. However, the simulated peak concentration occurrence time was earlier than the real measured data. This was due to the early start of the assumed upstream

input of water/sediment discharge. It is suggested that a rainfall-runoff model (e.g., HEC-HMS, Artificial neural network model) can be utilized to provide more correct estimation of hydrographs at the upstream boundary, then to help our approach predict more accurate temporal variation of sediment concentration. Although early arrival of the peak is not precise, but this result can still be used as warning mechanism where early arrival gives more time for preparation. Also, this approach can also provide the temporal variation of sediment concentration in fluvial channel and reservoir as a guide line for reservoir operation. In summary, the integrated approach proposed for mass transport simulation in a large-scale watershed is a promising tool for disaster reduction and water resources management.

Acknowledgements The authors would like to thank Water Resource Agency, Ministry of Economic Affairs of Taiwan for financially supporting this research and many valuable hydrological data.

References

- Central Geological Survey (2011) Survey of hydrological and geological influences on slope stability. Ministry of Economic Affairs, Taiwan (in Chinese)
- Central Geological Survey (2012) Surveys of characteristic of engineering rock masses on hillslopes (in Chinese).s http://envgeo.moeacgs.gov.tw/moeapaper/rock/rock_main.htm. Accessed 15 Jan 2013
- Chang KT, Chiang SH (2009) An integrated model for predicting rainfall-induced landslides. *Geomorphology* 105(3–4):366–373
- Chen H, Dadson S, Chi YG (2006) Recent rainfall-induced landslides and debris flow in northern Taiwan. *Geomorphology* 77:112–125
- Chen YC, Chang KT, Chiu YJ, Lau SM, Lee HY (2012) Quantifying rainfall controls on catchment-scale landslide erosion in Taiwan. *Earth Surf Proc Land*. doi:10.1002/esp.3284
- Chow VT, Maidment DR, Mays LW (1988) *Applied hydrology*. McGraw-Hill, Singapore, pp 272–282
- Dhital MR (2003) Causes and consequences of the 1993 debris flows and landslides in the Kulekhani watershed, central Nepal. In: Rickenmann D, Chen C (eds) *Debris-flow hazards and mitigation: mechanics, prediction, and assessment*, vol 2. Millpress, Rotterdam, pp 931–942
- FLO-2D (2006) *FLO-2D User's manual* (version 2006.01), FLO-2D Software, Inc., Arizona
- Gabet EJ, Mudd SM (2006) The mobilization of debris flows from shallow landslides. *Geomorphology* 74:207–218
- George DL, Iverson RM (2014) A depth-averaged debris-flow model that includes the effects of evolving dilatancy. II. Numerical predictions and experimental tests. *Proc R Soc A* 470:20130820
- Godt JW, Baum RL, Chleborad AF (2006) *Rainfall characteristics for shallow landsliding in Seattle, Washington, USA*. *Earth Surf Proc Land* 31:97–110
- Guzzetti F, Reichenbach P, Cardinali M, Galli M, Ardizzone F (2005) Probabilistic landslide hazard assessment at the basin scale. *Geomorphology* 72(1–4):272–299
- Guzzetti F, Ardizzone F, Cardinali M, Rossi M, Valigi D (2009) Landslide volumes and landslide mobilization rates in Umbria, central Italy. *Earth Planet Sci Lett* 279(3–4):222–229
- Haas F, Heckmann T, Wichmann V, Becht M (2004) Change of fluvial sediment transport rates after a high magnitude debris flow event in a drainage basin in the northern Limestone Alps., Germany. In: Golosov et al (eds) *Sediment transfer through the fluvial system*. IAHS Press, Wallingford, pp 34–43
- HEC-HMS (2010) *Hydrological engineering center-hydrological modeling system, user's manual* (version 3.4). US Army Corps of Engineers
- HEC-RAS (2010) *Hydrological engineering center-river analysis system, user's manual* (version 4.1). US Army Corps of Engineers
- Holly FM, Rahuel JL (1990) New numerical/physical framework for mobile-bed modeling, Part I: numerical and physical principles. *J Hydraul Res* 28(4): 401–416
- Huang SL, Jia YF, Wang SS (2006) Numerical modeling of suspended sediment transport in channel bends. *J Hydrodyn* 18(4):411–417
- Hussin HY, Quan Kuna B, van Westen CJ, Christen M, Malet JP, van Asch TW (2012) Parameterization of a numerical 2-D debris flow model with entrainment: a case study of the Faucon catchment, Southern French Alps. *Nat Hazard Earth Syst* 12:3075–3090
- Iverson RM, Reid ME, LaHusen RG (1997) Debris-flow mobilization from landslide. *Annu Rev Earth Planet Sci* 25:85–138
- Julien PY (2002) *River mechanics*. Cambridge University Press, Cambridge
- Julien PY, Lan Y (1991) Rheology of hyperconcentration. *J Hydraul Eng ASCE* 117(3):346–353
- Klar A, Aharonov E, Kalderon-Asael B, Katz O (2011) Analytical and observational relations between landslide volume and surface area. *J Geophys Res* 116 (F2):F02001

- Lee HY, Hsieh HM (2003) Numerical simulations of scour and deposition in a channel network. *Int J Sediment Res* 18(1):32–49
- Lee HY, Hsieh HM, Yang JC, Yang CT (1997) Quasi-two-dimensional simulation of scour and deposition in alluvial channels. *J Hydraul Eng ASCE* 123(7):600–609
- Liu KF, Huang MC (2006) Numerical simulation of debris flow with application on hazard area mapping. *Comput Geosci* 10:221–240
- Liu KF, Wu HF (2013) Introduction to Debris-2D—a debris flow simulation program. In: Sassa K (eds) *ICL landslide teaching tools*, ICL Press, pp 238–246
- Liu KF, Wu YH, Chen YC, Chiu YJ, Shih SS (2013) Large-scale simulation of watershed mass transport—a case study of Tsengwen reservoir watershed, southwest Taiwan. *Nat Hazards* 67(2):855–867
- Liu KF, Wei SC, Wu YH (2014) The Influence of accumulated precipitation on debris flow hazard area. In: Sassa K (eds) *Landslide science for a safer geo-environment*, vol 3, Springer, pp 45–50
- Lollino G, Arattano M, Allasia P, Giordan D (2006) Time response of a landslide to meteorological events. *Nat Hazard Earth Syst* 6:179–184
- Malamud BD, Turcotte DL, Guzzetti F, Reichenbach P (2004) Landslide inventories and their statistical properties. *Earth Surf Proc Land* 29(6):687–711
- Morakot Post-Disaster Reconstruction Council, Executive Yuan, Taiwan (2012) (in Chinese). <http://88flood.www.gov.tw/eng/> Accessed 15 Jan 2013
- O'Brien JS, Julien PY, Fullerton WT (1993) Two-dimensional water flood and mudflow simulation. *J Hydraul Eng ASCE* 119(2):244–260
- Parker RN, Densmore AL, Rosser NJ, de Michele M, Li Y, Hunag R, Whadcoat S, Petley DN (2011) Mass wasting triggered by the 2008 Wenchuan earthquake is greater than orogenic growth. *Nat Geosci* 4(7):449–452
- RAMMS (2012) User manual v1.4 debris flow. SLF/WSL
- Rathburn SL, Wohl EE (2001) One-dimensional sediment transport modeling of pool recovery along a mountain channel after a reservoir sediment release. *Regul River* 17(3):251–273
- Reichenbach P, Cardinali M, Galli M, Ardizzone F (2005) Probabilistic landslide hazard assessment at the basin scale. *Geomorphology* 72(1):272–299
- Shih SS, Lee HY, Chen CC (2008) Model-based evaluations of spur dikes for fish habitat and improvement: a case study of endemic species *Varichorhinus barbatulus* (Cyprinidae) and *Hemimyzon formosanum* (Homalopteridae) in Lanyang river, Taiwan. *Ecol Eng* 34:127–136
- Takahashi T (1981) Debris flow. *Annu Rev Fluid Mech* 13:57–77
- Tsai MP, Hsu YC, Li HC, Shu HM, Liu KF (2011) Applications of simulation technique on debris flow hazard zone delineation: a case study in Daniao tribe, Eastern Taiwan. *Nat Hazard Earth Syst* 11:3053–3062
- Tsou CY, Feng ZY, Chigira M (2011) Catastrophic landslide induced by typhoon Morakot, Shiaolin, Taiwan. *Geomorphology* 127(3):166–178
- Uchihugi T (1971) Landslides due to one continual rainfall. *JSECE* 23(4):79 (in Japanese)
- Water Resources Agency (2008) *Hydrological yearbook of Taiwan, Republic of China, Part I—rainfall*. Ministry of Economic Affairs, Taiwan (in Chinese)
- Water Resources Agency (2011) *Tsengwen reservoir sedimentation measurements*. Ministry of Economic Affairs, Taiwan (in Chinese)
- Wu YH, Liu KF (2014) The influence of countermeasure on debris flow hazards with numerical simulation. In: Sassa K (eds) *Landslide science for a safer geo-environment*, vol 1, Springer, pp 473–478
- Wu YH, Liu KF (2015) Formulas for calibration of rheological parameters of Bingham fluid in Couette rheometer. *ASME J Fluids Eng* 137(4):041202
- Wu YH, Liu KF, Chen YC (2013) Comparison between FLO-2D and Debris-2D on application of assessment of granular debris flow hazard with case study. *J Mt Sci* 10(2):293–304
- Yu FC, Chen TC, Lin ML, Chen CY, Yu WH (2006) Landslides and rainfall characteristics analysis in Taipei City during the Typhoon Nari event. *Nat Hazards* 37:153–167

TXT-tool 3.385-1.3

Landslide Occurrence Prediction in the Rječina River Valley as a Base for an Early Warning System

Martina Vivoda Prodan, Sanja Dugonjić Jovančević
and Željko Arbanas

Abstract

This paper presents deterministic 3D stability analyses using LS-Rapid software applied to the wider area of the Grohovo landslide on the north-eastern slope of the Rječina River Valley near the city of Rijeka, Croatia. Results of these analyses, in combination with results of existing monitoring data, are necessary for predicting future landslide behavior as a base for establishing an early warning system at the Grohovo landslide.

Keywords

Landslide · Early warning system · Stability analyses

Contents

1 Introduction	263	5.1 Parameters Used for the Computer Simulation	268
2 Early Warning System	265	5.2 Results of the Computer Simulation	268
3 Deterministic 3D Stability Analyses	265	6 Conclusion	272
4 Soil Testing	266	References.....	274
4.1 Testing Apparatus.....	266		
4.2 Samples, Testing Conditions and Results.....	266		
5 The Integrated Model of Landslide Simulation for the North-Eastern Slope of the Rječina River Valley	267		

1 Introduction

The Grohovo landslide is a reactivated complex landslide in the outskirts of the city of Rijeka, Croatia. Several historical episodes of landslide movements and their consequences demonstrate the need for landslide forecasting and an early warning system in order to reduce the landslide risk and to protect human lives.

The part of the Rječina River Valley between the Valići Lake and the Pašac Bridge (Fig. 1) is the most unstable part of the wider area of the city of Rijeka, with the highest landslide hazard and possible sliding risk (Benac et al. 2006).

M. Vivoda Prodan (✉) · S. Dugonjić Jovančević ·
Ž. Arbanas

Faculty of Civil Engineering, University of Rijeka,
Radmile Matejčić 3, 51000 Rijeka, Croatia
e-mail: martina.vivoda@gradri.uniri.hr

S. Dugonjić Jovančević
e-mail: sanja.dugonjic@gradri.uniri.hr

Ž. Arbanas
e-mail: zeljko.arbanas@gradri.uniri.hr



Fig. 1 Investigated area of the Rječina River Valley. *Photo* Ž. Arbanas

Numerous historical descriptions, figures and maps describing landslides were found in the Croatian State Archive in Rijeka (Fig. 2). The

last large reactivation of the Grohovo landslide occurred on 5th December 1996 after a long rainy period in autumn and early winter. At the

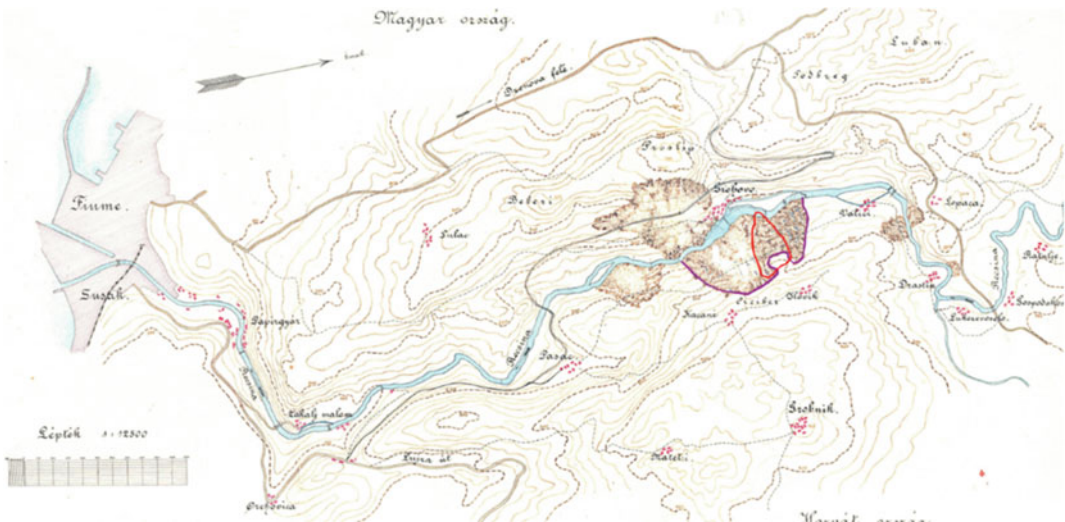


Fig. 2 Topographic map of the Rječina River Valley from 1894 showing landslides that occurred until 1894 (Anon 2011) (*purple line* contours landslide from the 19th

century and *red line* presents area of recent Grohovo landslide from 1996)

same location as a landslide from the 19th century, on the north-eastern slope of the Rječina River Valley. A significantly smaller volume of sliding mass was reactivated in this recent landslide in relation to a volume affected by older sliding.

As part of the research activities in the Croatian–Japanese Bilateral Project ‘Risk Identification and Land-Use Planning for Disaster Mitigation of Landslides and Floods in Croatia’, a comprehensive integrated real-time monitoring system was installed at the Grohovo landslide. It consists of geodetic and geotechnical monitoring. Geodetic monitoring includes geodetic surveys with a robotic total station and a GPS network for displacement measurements. Geotechnical monitoring consists of pore pressure gauges, inclinometers and wire extensometers (Arbanas et al. 2011a). The monitoring system enables real-time transmission of the data to the control centre and presentation to the public. This real-time transmission will aid in establishing an early warning system for landslide hazard when the measured values exceed defined limits (Mihalić and Arbanas 2013). The deterministic 3D stability analyses of the wider zone of the north-eastern slope of the Rječina River Valley were carried out as a base for an early warning system defining and establishment (Arbanas et al. 2011b).

2 Early Warning System

According to Thiebes (2012), an early warning is broadly defined as timely advice before a potentially hazardous phenomenon occurs. An efficient early warning system comprises identification and estimation of hazardous processes, communication of warnings and adapted reaction of local population. Moreover, early warning systems have to be embedded into local communities to ensure effectiveness of the entire system (Thiebes 2012).

An early warning system in the Rječina River Valley should be established based on prediction of movements and the appearance of instabilities in the zones where the monitoring equipment is

installed. Prediction of possible movements was carried out on the basis of the results of 2D or 3D landslide stability analyses of wider landslide areas in combination with the results of existing monitoring data. Critical limit values (thresholds) were defined to indicate new sliding appearances and to issue the alarm. Critical limit value determination was based on the monitoring results and accuracy of installed monitoring equipment.

3 Deterministic 3D Stability Analyses

Landslide modelling is, along with experimental subsoil exploration and experience—driven safety assessment, one of the main tasks of slope stability analysis practice (Janbu 1996). Models are applied to analyse current stability status and to predict slope behaviour under certain conditions such as rainfall events or scenarios for environmental change. The intent of deterministic models usage in landslide hazard analyses is not to define the safety factor in an absolute and precise way at each point in the analysed area. The high spatial variability of geotechnical parameters is a serious limitation of deterministic models. The final stage in deterministic landslide hazard zonation consists of failure probability calculation and conversion of the factor of safety maps into failure probability maps.

The deterministic 3D landslide stability analyses of the most unstable part of the Rječina River Valley (Fig. 1) enable indications of possible sliding zones under unfavourable groundwater conditions. The deterministic 3D stability analyses were carried out using landslide simulation model software LS-Rapid (Sassa et al. 2010). LS-Rapid software could integrate the initiation of the landslide process triggered by rainfalls and/or earthquakes and the development of sliding due to strength reduction and the entrainment of deposits in the runout path. Stability analyses are based on strength parameters obtained from laboratory tests on soil samples taken from the slip zones.

4 Soil Testing

Soil testing was conducted on representative samples in a portable ring shear apparatus ICL-1 designed for testing the residual shear resistance mobilized along the sliding surface at large shear displacements under static and/or dynamic local conditions (Oštrić et al. 2012). The results of the ring shear tests are necessary to calculate input data for analyses of the development and propagation of the sliding mass in LS-Rapid software.

4.1 Testing Apparatus

No other laboratory apparatus than the ring shear apparatus has so far been able to provide an integrated simulation of the natural landslide process. A ring shear apparatus has two important purposes: it can be used as the basic soil test to obtain soil strength parameters and as a landslide simulation test.

The developed portable ring shear apparatus, ICL-1 (Fig. 3), was developed in 2010, as an activity of a Croatian–Japanese bilateral project ‘Risk identification and land-use planning for disaster mitigation of landslides and floods in Croatia’, SATREPS (Science and Technology

Research Partnership for Sustainable Development) project financed by Japan International Cooperation Agency (JICA) and Japan Agency for Science and Technology (JST) and donated to Croatian research group in 2012. Compared to similar existing apparatuses, the new apparatus is smaller in its dimensions but with higher performances; it can maintain an undrained condition up to 1.0 MPa of pore water pressure and normal stress, which makes it suitable for investigations of large-scale and deep-seated landslides with high values of normal stresses applied to the slip surface.

4.2 Samples, Testing Conditions and Results

The soil samples from the Grohovo landslide were taken from the flysch outcrop in the central part of the landslide body. A speed control test was conducted under a constant shear speed of 0.002 cm/s in undrained conditions (Fig. 4). The sample was sheared until the shear displacement reached 1.0 m and steady-state conditions were obtained. As a results of this test, the basic parameters values (peak, mobilized and apparent friction angle, also cohesion) as well as



Fig. 3 Portable ring shear apparatus, ICL-1. *Photo* M. Vivoda Prodan

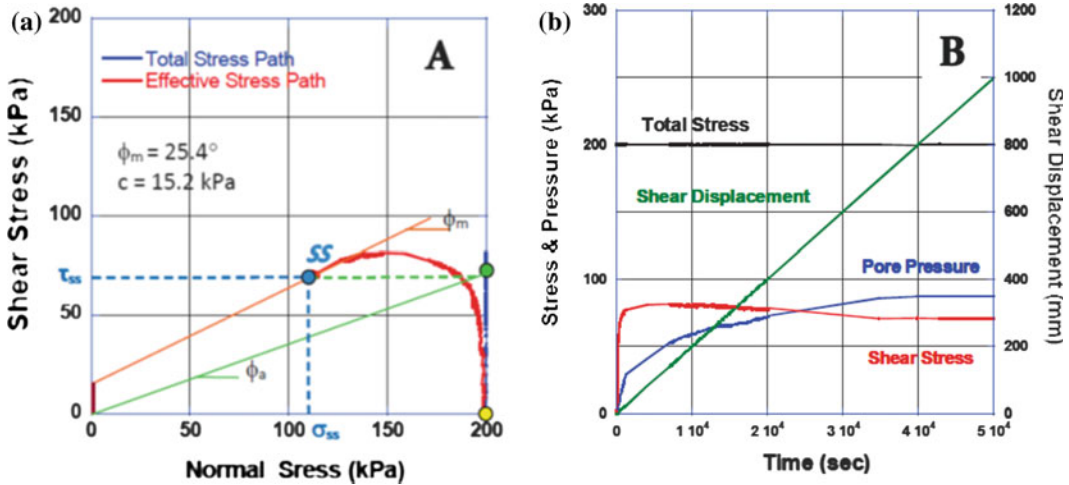


Fig. 4 Undrained speed control test on saturated clayey sample from the Grohovo landslide: **a** stress path; **b** time series data for stress, pressure and shear displacement (Oštrić et al. 2012)

steady-state normal and shear stress of the soil sample were obtained. The straight line fitting the stress path gave values of the friction angle as $\varphi_m = 25.4^\circ$, cohesion as $c = 15.2$ kPa and apparent friction angle $\varphi_a = 20.4^\circ$ (Oštrić et al. 2012).

5 The Integrated Model of Landslide Simulation for the North-Eastern Slope of the Rječina River Valley

The LS-Rapid software is the first landslide simulation model able to integrate the whole process of stable state, failure, post-failure strength reduction, motion and deposition of sliding mass (Sassa et al. 2010). In the simulation, the friction angle and cohesion will be reduced from their peak values to the normal motion time values within the source area in the determined distribution of the unstable mass (reducing from $\tan \phi_p$ to $\tan \phi_m$ and from c_p to c_m). The strength reduction will start when the travel length will become equal to the shear displacement at the start of strength reduction

(DL, mm). The strength reduction will be completed and the normal motion simulation will start when the travel length will reach the value of shear displacement at the end of strength reduction (DU, mm).

The topography of the Rječina River Valley (Fig. 5a) was determined using original DEM data. The limestone rock mass is situated at the top of the slopes, while the siliciclastic rocks and flysch are situated on the lower slopes and the bottom of the valley. Depth of the sliding mass varies from 3 to 10 m over the flysch bedrock and from 0.0 to 0.5 m over the limestone rock mass (Fig. 5b). This assumption is based on knowledge that the existing slip surface is positioned at the contact between superficial slope deposits and flysch bedrock (Benac et al. 2005).

The long-term rainfalls and consequent rise in ground water level were the main triggering factor for the existing landslide occurrences in the Rječina River Valley. This ground water level rise in the model was expressed by excess of the pore pressure ratio until the value of $r_u = 0.60$, which corresponds to the ground water level being equal to terrain surface (Fig. 6). The time period of ground water level rise in the

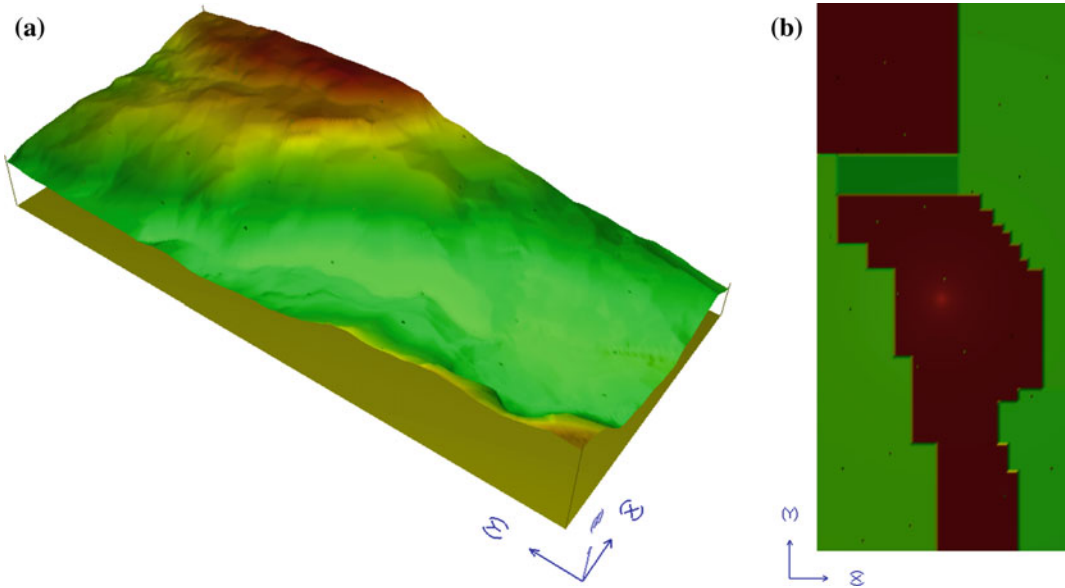


Fig. 5 Computer simulation area: **a** slope surface 3D model before the landslide event; **b** superficial deposits thickness distribution

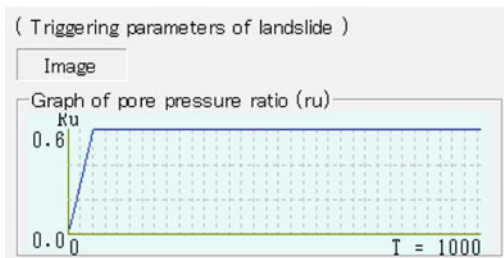


Fig. 6 Triggering factor of landslides in the Rječina River Valley (rise of pore pressure ratio, r_u from 0.0 to 0.6 value in 60 s)

model was set up as 60 s and one second in the model corresponded to one day in real time.

5.1 Parameters Used for the Computer Simulation

Important parameters for the integrated landslide computer simulation are the steady state shear resistance (τ_{ss}), the lateral pressure ratio ($k = \sigma_h / \sigma_v$) and the critical shear displacements (DL, DU). Most of the soil parameters used in

conducted computer simulation (Table 1) were determined from the undrained speed controlling shear test (Oštrić et al. 2012) and some of them from older laboratory testing results (Benac et al. 2005).

5.2 Results of the Computer Simulation

Excess of pore pressures significantly influence the shear strength reduction and appearance of sliding events on the north eastern slope of the Rječina River Valley. The simulation results are shown on Fig. 7a–e. The blue colored areas represent the stable areas or areas with movement velocity less than 0.1 m/s. The orange and red colored zones represent areas where the sliding occurred (Fig. 7a–e—left). Sliding mass distribution area is marked with a magenta line on Fig. 7a–e—right, and also contour lines at intervals of 5 m are presented. Figure 7b represents the state of the slope soon after the start of pore pressure rising and strength reduction. The sliding in simulation was started at the top of the slope in the upper part of the existing Grohovo

Table 1 Soil parameters used in the computer simulation

Soil parameters	Value	Source
Total unit weight of the mass (γ_t)	20 kN/m ³	Benac et al. (2005)
Steady state shear resistance in the source area (τ_{ss})	65 kPa	Test data, Oštrić et al. (2012)
Lateral pressure ratio ($k = \sigma_h/\sigma_v$)	0.7	Estimation from the test data
Friction angle inside landslide mass (ϕ_i)	33°	Benac et al. (2005)
Friction angle during motion (ϕ_m)	26°	Test data, Oštrić et al. (2012)
Peak friction angle at sliding surface (ϕ_p)	34°	Benac et al. (2005)
Peak cohesion at slip surface (c_p)	7.5 kPa	Benac et al. (2005)
Shear displacement at the start of strength reduction (DL)	30 mm	Test data, Oštrić et al. (2012)
Shear displacement at the end of strength reduction (DU)	1000 mm	Test data, Oštrić et al. (2012)
Pore pressure generation rate (B_{ss})	0.7	Estimation
Cohesion inside mass (c_i)	0 kPa	Benac et al. (2005)
Cohesion at sliding surface during motion (c_m)	0 kPa	Benac et al. (2005)
Excess pore pressure (r_u)	0.0–0.6	Assumption

landslide. Figure 7b–d show development of new sliding as the pore pressure ratio rises. A new landslide above the Valiči Lake appears in the correspondent time of 23 days and a pore pressure ratio of $r_u = 0.23$ (Fig. 7c). Figure 7d shows landslide appearances at the end of the pore pressure rising after 60 days from the process initiation. Landslide movements were continued at the constant ground water level and the process landslide movements were terminated after 100 days of simulation (Fig. 7e).

The location of the longitudinal and crossing sections through the investigated area after motion are shown on Fig. 8a. The pink color represents the surface of landslide mass after motion and filling of the Rječina River channel is visible (Fig. 8b).

The results of the conducted simulation very clearly suggest that new slides, caused by future unfavorable hydrogeological conditions, can

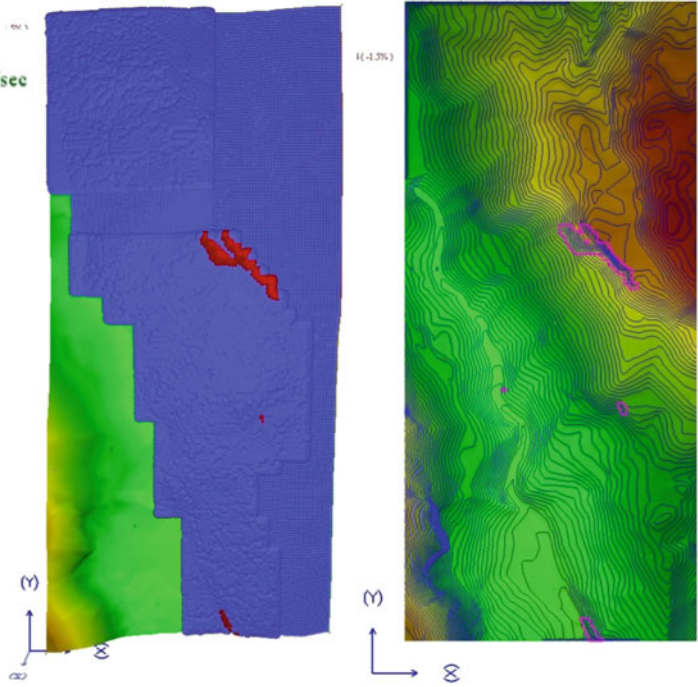
occur in the area of the existing landslide. The zone affected by sliding shown in Fig. 7c is very similar to the area of the existing landslide (Fig. 9). The new slides could also be expected at some other locations in the slope as shown in Fig. 7d. Some of these predictions are confirmed by scars and small slides northwest of the existing landslide that occurred during the winter and spring 2013. The most interesting and dangerous prediction is the possibility of landslide occurrence on the slope above Valiči Lake (Fig. 7c–e). This landslide could have very serious consequences, such as filling the lake with a landslide deposit and possible impulse wave generation. This possibility should be seriously analyzed as an important potential hazardous event.

The results of the conducted deterministic slope stability analyses using LS-Rapid software clearly show the critical areas for future landslide occurrences in unfavorable hydrogeological

Fig. 7 a Landslide simulation results for the north-eastern slope of the Rječina River Valley area at beginning of pore pressure rising and strength reduction with forming of the Grohovo landslide (*left—blue balls for stable area, red balls for unstable area; right—magenta line for sliding mass distribution area*), Landslide simulation results for the north-eastern slope of the Rječina River Valley area: **b** r_u rising to 0.10 with local failure; **c** r_u rising to 0.23 with landslide above the Valiči

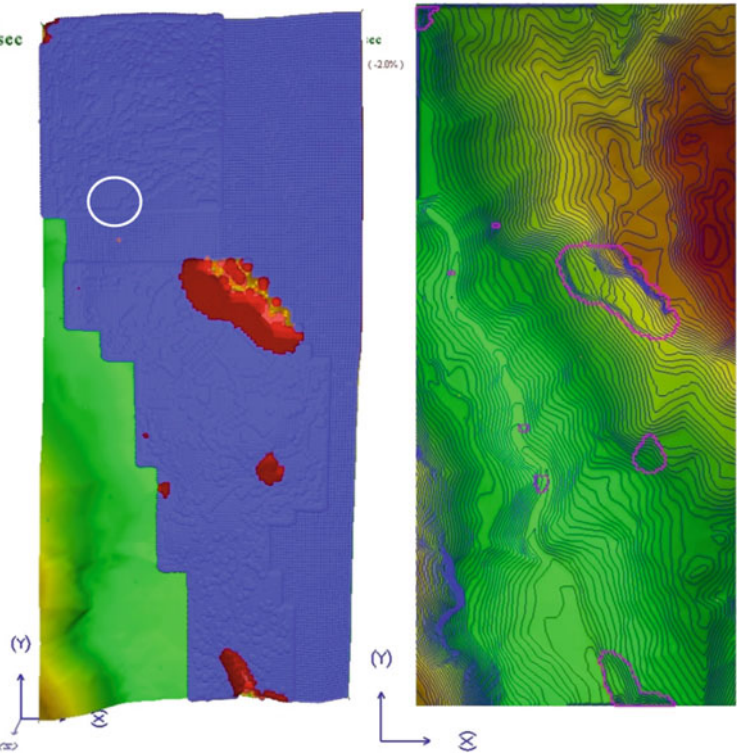
Lake (*left—blue balls for stable area, red balls for unstable area; right—magenta line for sliding mass distribution area*), Landslide simulation results for the north-eastern slope of the Rječina River Valley area: **d** end of pore pressure rise at $r_u = 0.60$; **e** landslide areas at the end of the movements (*left—blue balls for stable area, red balls for unstable area; right—magenta line for sliding mass distribution area*)

Step : 100 Time : 0.5 sec
Umax : 0.9 m/sec Vmax : 0.9 m/sec



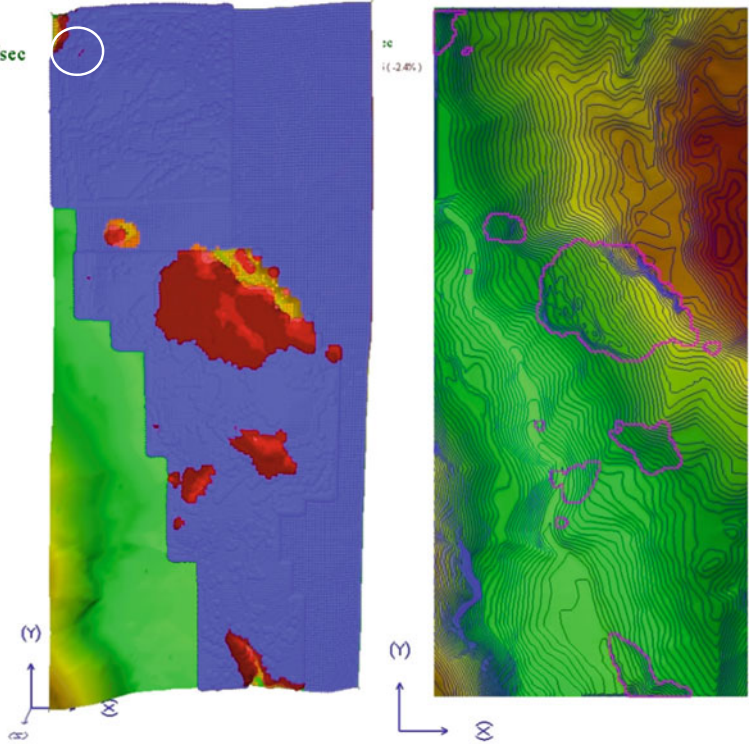
(a) $r_u=0$ $t=12$ h

Step : 2500 Time : 10.3 sec
Umax : 102.5 m/sec Vmax : 18.8 m/sec



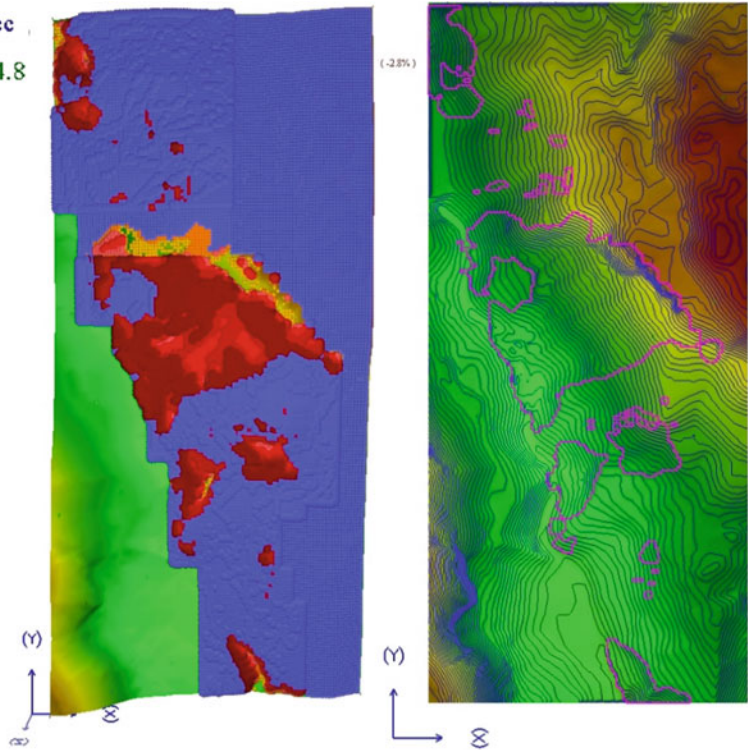
(b) $r_u=0.10$ $t=10.3$ days

Step : 5900 Time : 23.5 sec
Umax : 30.1 m/sec Vmax : 20.3 m/sec



(c) $r_u=0.23$ $t=23.5$ days

Step : 12700 Time : 57.2 sec
Umax : 3.4 m/sec Vmax : 4.8



(d) $r_u=0.57$ $t=57.2$ days

Fig. 7 (continued)

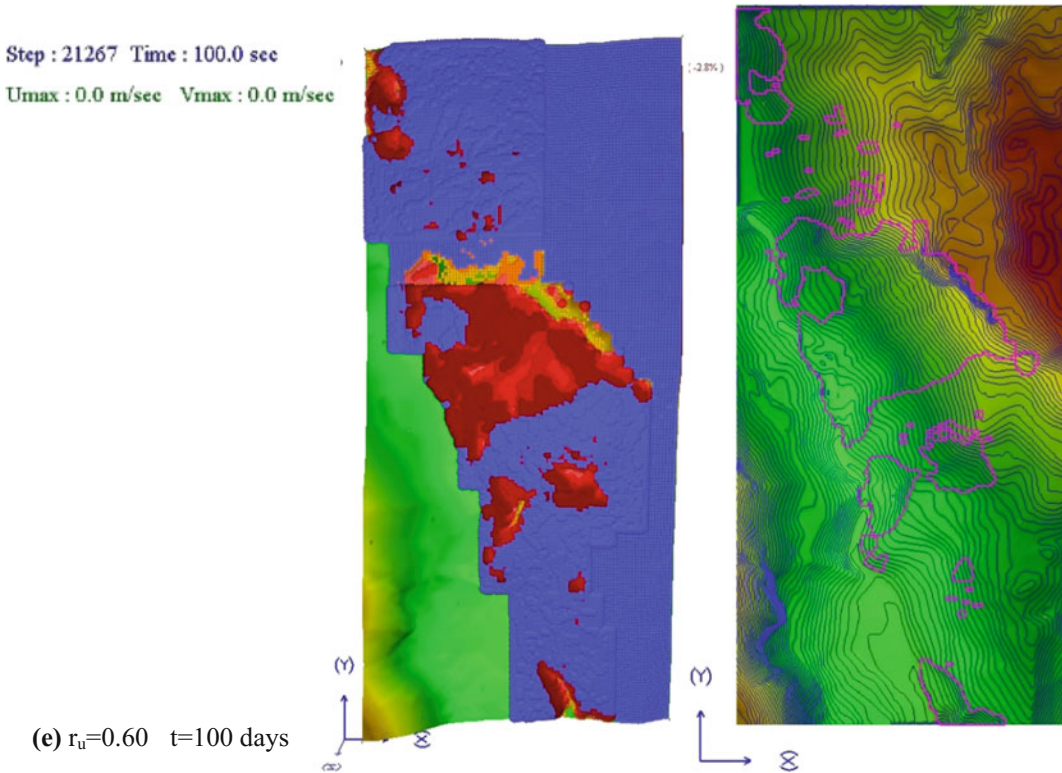


Fig. 7 (continued)

conditions. The predicted landslide occurrences are validated by existing landslide occurrences or scars that suggest the start of instability processes. So, the results of the conducted analyses can be used for landslide prediction and susceptibility maps, and, if it is possible to connect rainfalls and infiltration with the time component of occurrences, as landslide hazard maps in the Rječina River Valley.

6 Conclusion

The Grohovo landslide is a reactivated complex landslide in the Rječina River Valley in the outskirts of the city of Rijeka, Croatia. The part of the Rječina River Valley between the Valići Lake and the Pašac Bridge is the most unstable part of the Rječina River Valley, with the highest

landslide hazard and correspondent sliding risk. All these facts point to a need for landslide behavior forecasting and an early warning system in order to reduce related hazard and risk and to protect human lives.

The deterministic 3D stability analyses were carried out using landslide simulation model software LS-Rapid, which can integrate the initiation of the landslide process triggered by rainfalls and/or earthquakes and the development of sliding due to strength reduction and the entrainment of deposits in the runout path. Stability analyses are based on strength parameters obtained from laboratory tests on soil samples taken from slip surface zones. The results of the conducted deterministic 3D slope stability analyses using LS-Rapid software clearly show the critical areas for future landslide occurrence in unfavorable hydrogeological conditions and they

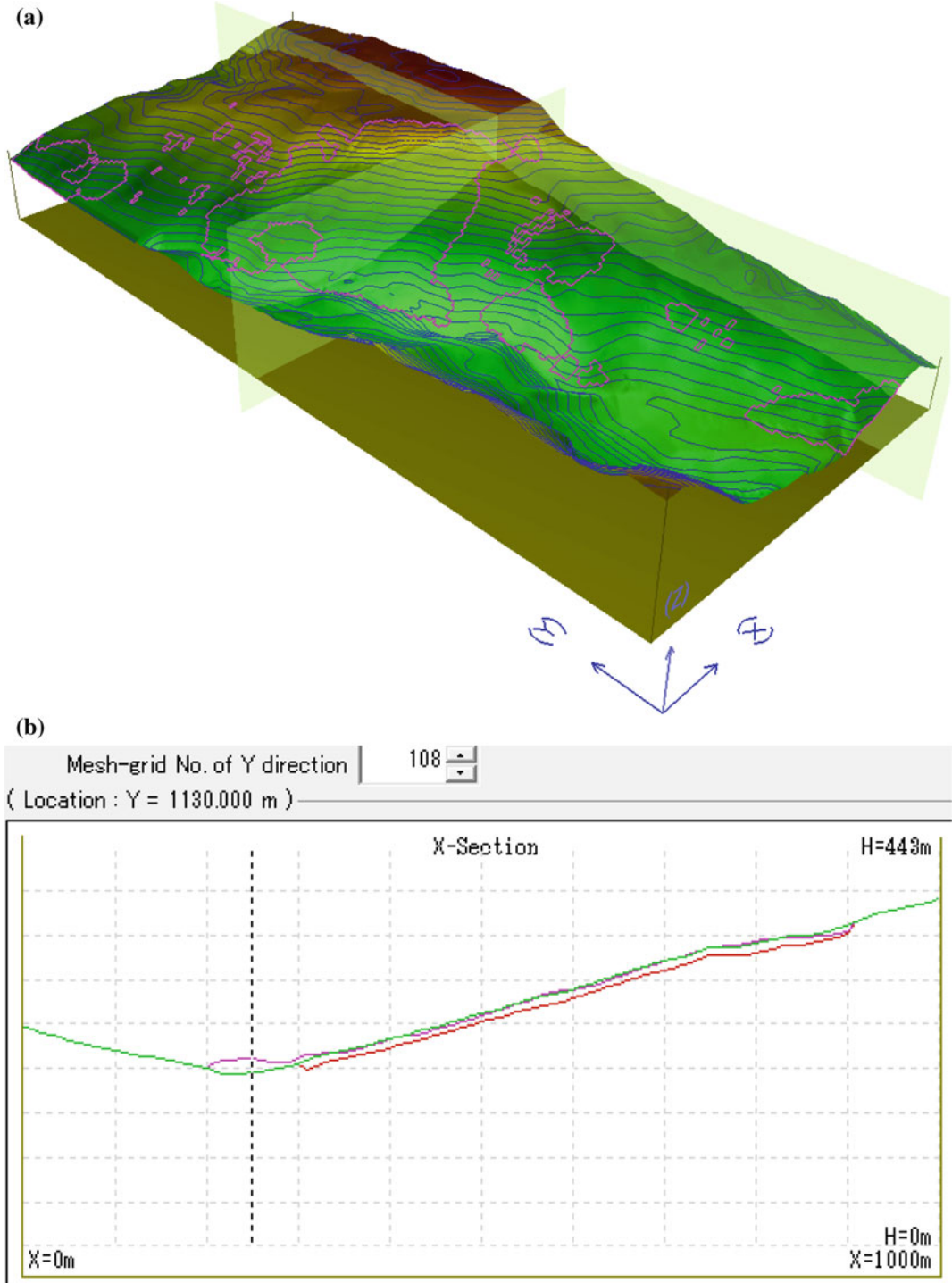


Fig. 8 a Location of the longitudinal and cross section through the investigated Rječina River Valley; b view of the cross section (the green color is the original ground surface, the red color presents the sliding surface in the source area and the pink color represents the surface of landslide mass after motion)

Fig. 9 View of the Grohovo landslide from the opposite side of the valley. *Photo* M. Vivoda Prodan



can be used as landslide prediction, susceptibility and hazard maps in the Rječina River Valley.

The most important indicators for the alarm decision should be measured values, such as displacements and pore pressures, on installed monitoring equipment at the moment when measured values reach proposed critical values.

Acknowledgements Equipment used in the study was obtained with financial support from the SATREPS [Science and Technology Research Partnership for Sustainable Development] program, financed by the Japan Science and Technology Agency and Japan International Cooperation Agency through the Project Risk Identification and Land-Use Planning for Disaster Mitigation of Landslides and Floods in Croatia. This support is gratefully acknowledged. This work is an expanded version of the paper published and presented on the 1st Regional Symposium of Landslides in the Adriatic-Balkan Region and the 3rd Workshop of the Croatian-Japanese Project “Risk Identification and Land-Use Planning for Disaster Mitigation of Landslides and Floods in Croatia”.

References

- Anon (2011) City of Rijeka. Technical department (1840–1918). State archive in Rijeka (unpublished documents, in Hungarian)
- Arbanas Ž, Benac Č, Dugonjić S (2011a) Dynamic and prediction of future behavior of the Grohovo landslide. In: Proceedings of the 1st workshop of the project ‘risk identification and land-use planning for disaster mitigation of landslides and floods in Croatia’. Dubrovnik
- Arbanas Ž, Vivoda M, Jagodnik V, Dugonjić Jovančević S, Ljutić K (2011b) Consideration of early warning system on the Grohovo landslide. In: Proceedings of the 2nd workshop of the project ‘risk identification and land-use planning for disaster mitigation of landslides and floods in Croatia’, Rijeka, pp 51–54
- Benac Č, Arbanas Ž, Jurak V, Oštrić M, Ožanić N (2005) Complex landslide in the Rječina River Valley (Croatia): origin and sliding mechanism. *Bull Eng Geol Env* 64(4):361–371
- Benac Č, Jurak V, Oštrić M (2006) Qualitative assessment of geohazard in the Rječina Valley, Croatia. In:

- Proceedings of the 10th IAEG international congress: IAEG engineering geology for tomorrow's cities (658). The Geological Society of London, pp 1–7
- Janbu N (1996) Slope stability evaluations in engineering practice. In: Proceedings 7th international symposium on landslides. Trondheim, Norway, pp 17–34
- Mihalić S, Arbanas Ž (2013) The Croatian-Japanese joint research project on landslides: activities and public benefits. In: Sassa K, Rouhban B, Briceño S, McSaveney M, He B (eds) Landslides: global risk preparedness. Springer, Heidelberg, pp 333–349
- Oštrić M, Ljutić K, Krkač M, Setiawan H, He B, Sassa K (2012) Undrained ring shear tests performed on samples from Kostanjek and Grohovo landslide. In: Sassa K, Takara K, He B (eds) Proceedings of the IPL symposium, Kyoto, pp 47–52
- Sassa K, Nagai O, Solidum R, Yamazaki Y, Ohta H (2010) An integrated model simulating the initiation and motion of earthquake and rain induced rapid landslides and its application to the 2006 Leyte landslide. *Landslides* 7(3):219–236
- Thiebes B (2012) Landslide analysis and early warning systems. PhD thesis. The University of Vienna, Austria, Heidelberg

TXT-tool 3.001-1.1

Physical Modelling of Rain-Induced Landslides

Binod Tiwari and Beena Ajmera

Abstract

Stability of a slope depends on many factors including geotechnical properties of soil, slope inclination and other slope geometry, position of water table, as well as external factors such as amount of rainfall and infiltration velocity, magnitude and frequency of ground shaking, etc. As the field condition is non-homogenous and is hard to simulate, sensitivity analysis is generally performed on laboratory based models to evaluate rainfall induced slope failure. These models are helpful in evaluating seepage velocity and reduction in suction with intensity and duration of rainfall and deformation of slope with rainfall. This tool explains on how the simple laboratory based models are developed to evaluate the effect of rainfall intensity and duration on the stability and deformation of slopes.

Keywords

Intensity and duration of rainfall · Seepage velocity · Wetting front Suction · Deformation · Tensiometer · Slope stability

Contents

1 Introduction	277	6 Conclusion	284
2 Experimental Set Up	278	References	284
3 Analysis of Experimental Result	281		
4 Example of the Experimental Modeling and Data Analysis	282		
5 Limitation and Expansion of the Modeling Techniques	284		

1 Introduction

Although landslides and earthquakes are considered to be two major natural triggers of landslides, rainfall induced landslides are much more frequent and common compared to the earthquake induced landslides. Moreover, the annual losses due to rainfall induced landslides are significantly high compared to the landslides triggered by other factors. While dealing with rainfall induced landslides, specifically for the

B. Tiwari (✉) · B. Ajmera
Department of Civil and Environmental Engineering,
California State University, Fullerton, 800 N State
College Blvd., Fullerton, CA, USA
e-mail: btiwari@fullerton.edu

B. Ajmera
e-mail: bajmera@fullerton.edu

slope stability and deformation analysis, it is important to evaluate the rate of infiltration of rainwater into the ground due to a specific intensity and duration of rainfall. Soil slopes generally possess high factors of safety when they are partially saturated. That is mainly due to the available apparent cohesion in the partially saturated soil due to suction. When the suction induced cohesion ceases due to the saturation of soil, the factor of safety of slope reduces significantly and may trigger a landslide if the value of factor of safety decreases to lower than unity. The rate of infiltration of the rainwater, which is generally calculated based on the velocity of movement of wetting front, depends on many factors including hydraulic conductivity of soil, soil density, degree of saturation of soil, initial suction, and slope inclination. Therefore, performance of sensitivity analysis to evaluate the major contributing factor on rate of infiltration of rainwater helps in understanding the effect of certain rainstorm on the stability of slopes. Results of several experimental as well as numerical modelling are available in literature that provide information on how the intensity and duration of rainfall affect slope stability in different types of soils (Tiwari et al. 2013, 2014a, b, c, 2015; Phommachanh et al. 2014; Hearn et al. 2014; Tran 2016; Tiwari and Lewis 2014a, b; Tiwari and Caballero 2015, 2014; Tiwari and Lewis 2012). In this tool, we explain how laboratory based models are developed to evaluate the stability and deformation of laboratory scale slopes and pertinent procedures to calculate stability factors as well as deformation of slope due to rainfall induced infiltration and loss of strength.

2 Experimental Set Up

Preparation of laboratory based rainfall induced slope models depends on available materials and scale of the experiments. In this tool, we will present an example of such slopes. First, soil container, preferably made of Plexiglas, is assembled tightly. Attention should be paid to

make sure that there is no leakage from the side of the container. Depending on whether the drainage is allowed or not, sufficient holes should be provided to ensure continuous drainage of seepage water during rainfall. Gravels and compacted at the base of the container to prepare the drainage layer (Fig. 1). At the base of gravel layer, perforated pipes are laid to collect the infiltration and run-off water at the base of the container and drain them out. Several layers of geo-textiles are placed on the gravel layer to separate the model soil from the drainage layer and act as a filter layer. Then, soil slope is prepared at desired density, moisture content and inclination. For this purpose, the lift, i.e. thickness of each layer, is fixed first and amount of soil and water required to compact the soil at the target density and moisture content is calculated. The calculated amount of soil and water is thoroughly mixed and placed into the container and compacted appropriately using mechanical or pneumatic compactor until the entire soil mass is used (Fig. 2). This procedure is used until the completion of final slope to the desired geometry. It is important to mark the position of the slope at the inside of the Plexiglas wall to ensure the accuracy of designed geometry. It is important to leave sufficient width of the slope both on the top and bottom of the slope so that the soil can freely deform or slide.

After the completion of compacted soil slope, tensiometers are installed at desired locations (Fig. 3). Tensiometers measure the real-time suction values at desired locations and also verify whether the externally observed wetting front movement matches well with the suction data observed inside the soil slope. This will help to verify uniform movement of the wetting front inside the slope during a rainfall event. It is recommended to set up tensiometers at same height at multiple locations on top, middle and bottom of the slope so that the spatial variation of suction can be observed throughout the slope. Prior to installation of tensiometers, the ceramic discs of the tensiometers should be saturated and all tensiometers should be calibrated to zero pore water pressure. Then, using a hand drill, holes



Fig. 1 Drainage layer for the collection of seepage water



Fig. 2 Completed compacted slope model

of the appropriate size are drilled inside the slope at pre-defined locations to install the tensiometers. Once the tensiometers are set up and the data acquisition system is set up through the cables connected to the tensiometers, the same soil is compacted back to the remaining space of the drilled holes. To prevent the rainwater from traveling faster than at the other locations due to potential low density of the backfilled soil, the top of the tensiometers are sealed with bentonite slurry (Fig. 3).

To measure the deformation of slope at different locations during a rainfall event, straight copper wires are inserted in the slope at multiple locations, spread throughout the slope (Fig. 3). Those copper wires are painted with black and white stripes for visual observation of the slope deformation, if it is obvious. The deformation of these copper wires at different depths at the end of the model experiment provides information on the deformation inside the slope.

Once the instrumentation is completed, a rain simulation system is placed on the slope at a defined height (Fig. 4). An example of such rainfall simulation device is a series of sprinkler heads set at specific spacing and connected with pipes. Amount of rainfall in those sprinkler heads

can be controlled by adjusting the opening of the sprinkler heads.

After the completion of the model set up, the slope is subjected to a target intensity of rainfall through the tap water connected through the pipe and connection hose. Movement of wetting front is recorded in a regular interval (typically in a 15 min interval) in all four outside walls of the Plexiglas container. The amount of runoff water is collected in a regular interval (typically in every 15–30 min) and the weight/volume of the run-off water is recorded to estimate the amount of infiltration water. At the end of the complete saturation of the slope, deformation of the copper wires and moisture content of the soil at different depths are measured. Based on these measurements, spatial distribution of the amount of deformation at different depths and the degrees of saturation of soil at different locations are calculated. The slope deformation data helps in identifying the critical sliding plane.

In addition to preparation of the experimental models, it is important to conduct appropriate laboratory tests to prepare a grain size distribution curve of the soil material and measure the specific gravity, saturated hydraulic conductivity, Atterberg limits, maximum dry density and optimum moisture content of the soil samples,

Fig. 3 Installation of tensiometers and copper wires on the slope

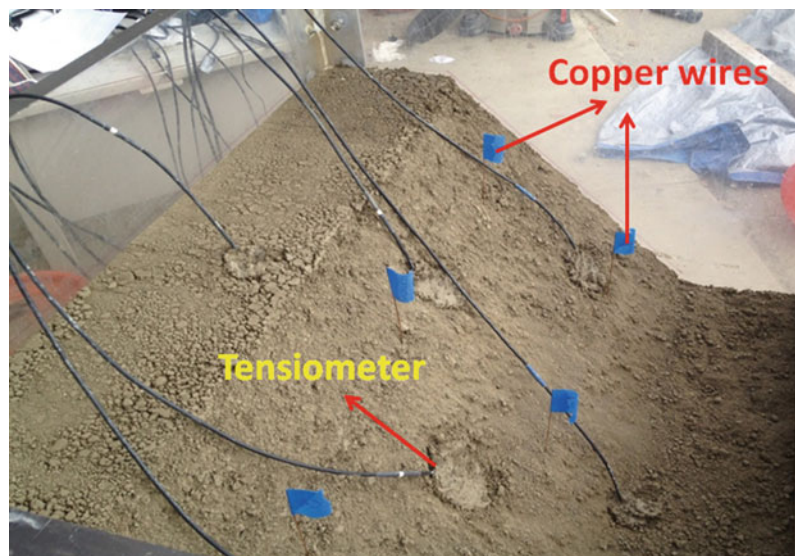


Fig. 4 Setting up of rain simulator system on top of the slope



drained shear strength parameters and stiffness for saturated and unsaturated soil samples.

3 Analysis of Experimental Result

At the completion of the model experiments, various analyses are performed. These analyses include—(a) seepage velocity, (b) variation of suction with time, (c) spatial distribution of deformation (d) time-wise variation of run-off, (e) variation of seepage velocity on top, middle and bottom of the slope, (f) calculation of slope deformation with time using an automated computer program, (g) calculation of factor of safety of the slope using an automated computer program, and (h) calculation of variation of seepage velocity and factor of safety of slope with density of slope and intensity and duration of rainfall as well as slope inclination using the analysed data from different intensity and duration of rainfalls as well as density and inclination of slope models.

Seepage velocity is calculated by measuring the depth of wetting front at different time periods. The depth of wetting front is verified with the suction data obtained with the tensiometers,

especially by checking the time required for the tensiometer recorded suction value at specific location to become zero. Spatial distribution of deformation is obtained by dissecting the soil, carefully releasing the copper wires and measuring the depth-wise deformation of the copper wires. Timewise variation of runoff is measured by dividing the total volume of water at specific time with the surface area of the slope and the time interval. Using the contours of wetting front, seepage velocities at different locations on the slopes are calculated. This data is useful to calculate the variation in seepage velocity on slopes due to the density and inclination of slope. Geometry of the slopes and geotechnical properties of soil can be put into various commercially available software or any custom-developed computer programs. Transient and steady-state seepage analysis can be performed on those slopes for applied intensity and duration of rainfall and the software computed values are calibrated through the laboratory experiment based values. Once the seepage velocity is calibrated, the seepage analysis results are coupled with a deformation analysis module as well as limit equilibrium based slope stability analysis modules. These computer based tools can be

used to generate any intensity and duration of rainfall and any density and inclination of slopes for parametric study and sensitivity analysis.

4 Example of the Experimental Modeling and Data Analysis

Soil samples were collected from a housing development site in Southern California and compacted at a slope inclination of 40° in the Plexiglas container at different void ratios, instrumented as mentioned earlier, and subjected to different rainfall intensities, as summarized in Table 1. Movement of wetting front, variation in suction, and deformation were recorded with time. Presented in Figs. 5 and 6 are the recorded wetting front and tensiometer data at different periods for Model 2. T1 through T8 in Fig. 5 are the locations of the tensiometers. Deformations obtained from the copper wires are also recorded separately. Seepage velocities were calculated by dividing the distance travelled by the wetting

front at specific location with the corresponding time. In the tensiometer data, seepage velocity is calculated by dividing the vertical distance from the top to the slope at a particular location to the tensiometer location with the time required for the suction to reduce to 0 kPa. The seepage velocities measured with the movement of the wetting front and the suction records matched well and are within an accuracy of 98%.

Using the data obtained from the experimental modeling, variation in seepage velocity with density of compaction and rainfall intensity were calculated as presented in Fig. 7. As can be observed in Fig. 7, positive correlations were developed between the seepage velocity and intensity of rainfall as well as the slope density. In Fig. 7, the data point with “?” was obtained solely through numerical analysis. The data obtained from this modeling matched well with the results obtained from the SEEP/W based analysis. The seepage information was coupled with deformation analysis using the SIGMA/W analysis and the deformation obtained from the copper-wire

Table 1 Geometric properties of the experimental models

Model no.	1	2	3	4	5
Void ratio	0.89	1.00	1.20	1.20	0.89
Rainfall intensity (cm/h)	1.68	1.68	1.68	3.60	3.60

Fig. 5 Advancement of wetting front with time

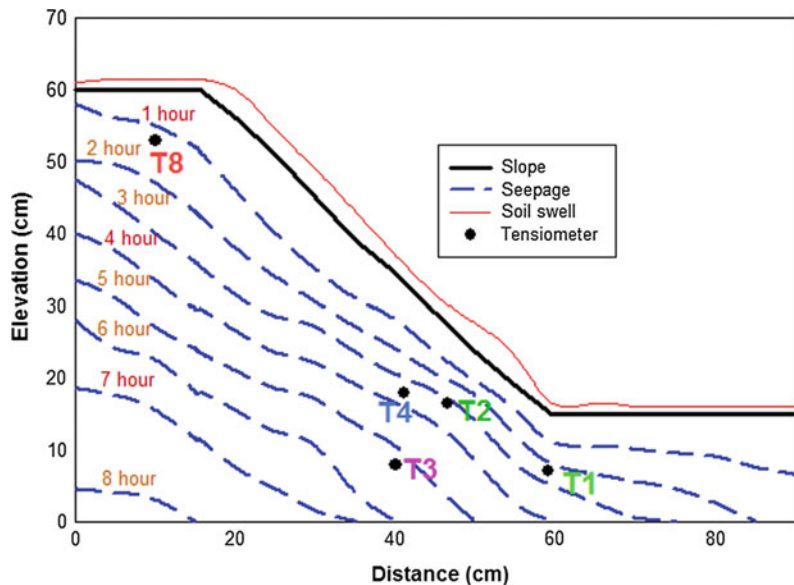


Fig. 6 Variation of suction with time, recorded with the tensiometers

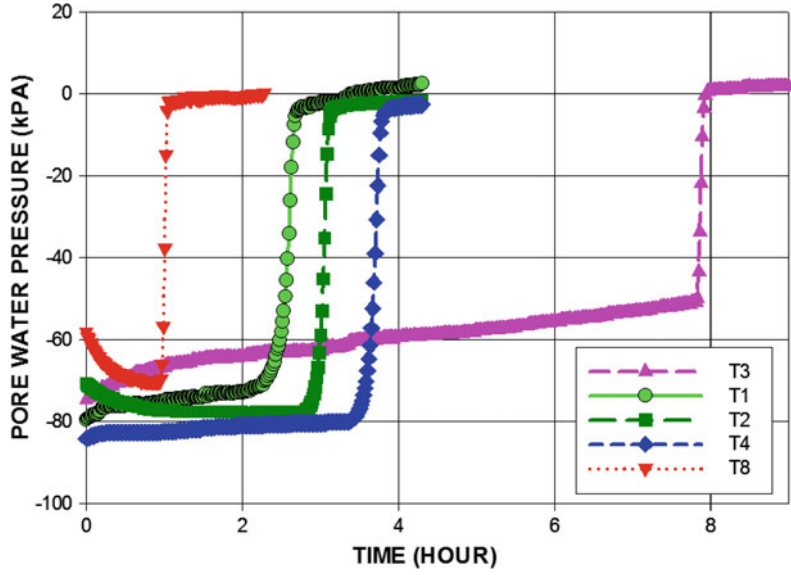


Fig. 7 Variation in seepage velocity with the density of slope and rainfall intensity

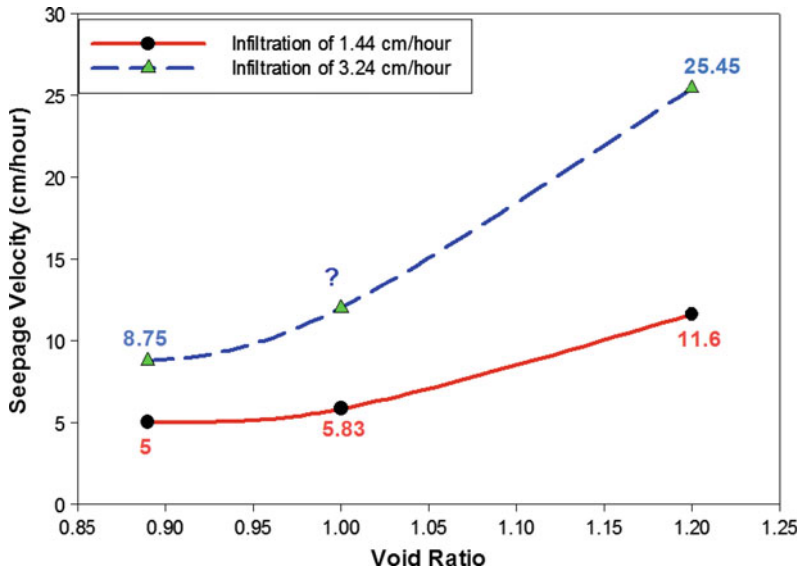
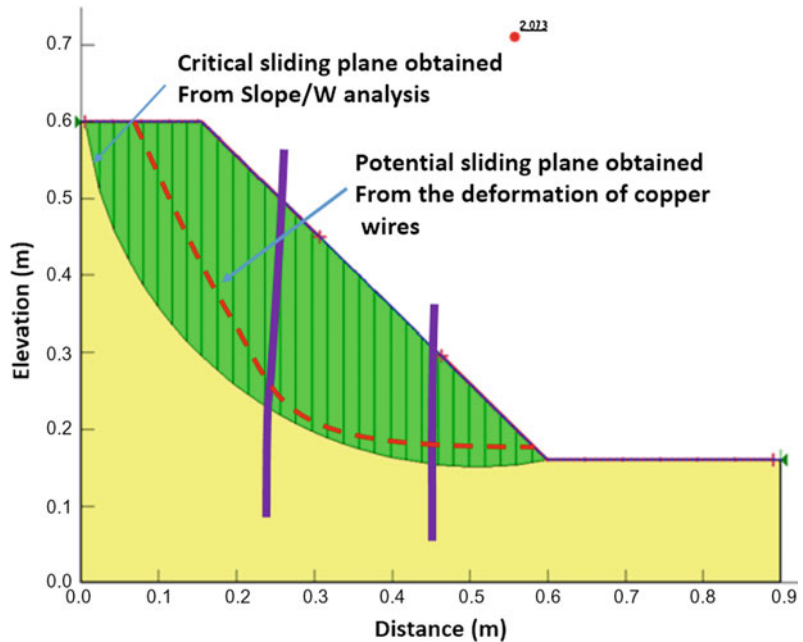


Fig. 8 Comparison of critical sliding planes obtained with the copper-wires and from deformation analysis using SIGMA/W



measurement matched well with the numerical analysis results (Fig. 8). For details of study results obtained for the above mentioned slopes and other slope inclinations, please refer to Tran (2016).

5 Limitation and Expansion of the Modeling Techniques

Like any other experimental laboratory based models, such modelling also have their limitations. A few of these limitations include—(a) Scale of the experimental model compared to actual slope is too small, (b) the surface roughness in the actual slope varies significantly with the one used in the experimental models, and (c) the intensity and duration of rainfall and the actual amount of run off may differ significantly. Therefore, the study results should be used with caution in practice.

6 Conclusion

To conduct sensitivity analysis for the effect of rainfall, slope inclination, and slope density to trigger landslides, experimental models can be

developed in a lab with relatively cheaper investment. Various parametric relations can be developed to estimate the seepage velocity with slope inclination, rainfall intensity and slope density, separately or by combining these parameters. The seepage velocity obtained from these correlations can be used to perform slope stability analysis and evaluate the risk to slope due to any expected rainfall event.

Acknowledgements The authors would like to thank IRA funding # 361 at CSU Fullerton for providing financial support to conduct the experiments. Moreover, the authors would like to acknowledge their graduate students Duc Tran, Santiago Caballero, and Adam Lewis and undergraduate students John Stapleton and Yuliana Carrillo.

References

- Heark D, Tiwari B, Ahmad S, Stapleton J (2014) Effect of rainfall in matric suction and seepage in clay slopes. In: Proceedings of the 12th international symposium on geo-disaster reduction, 1, pp 65–73 (awarded: Third Best Student Presentation)
- Phommachanh V, Matsuo N, Inegawa K, Kawai K, Iizuka A, Tiwari B (2014) Application of soil/water/air coupled F.E. code to predict seepage and deformation on sandy slopes. In: UNSAT 2014,

- unsaturated soils—research and application, Sydney, Australia
- Tiwari B, Caballero S (2015) Experimental model of rainfall induced slope failure in compacted clays. *Geotech Spec Publ* 256:1217–1226
- Tiwari B, Caballero S (2014) Experimental model of rainfall induced slope failure in compacted clays. In: *Proceedings of the 12th international symposium on geo-disaster reduction*, 1, pp 199–207 (awarded: Best Student Presentation)
- Tiwari B, Lewis A (2012) Experimental modeling of rainfall and seismic activities as landslide triggers. *Geotech Spec Publ* 225:471–478
- Tiwari B, Lewis A (2014a) Experimental modeling of rainfall and seismic activities as landslide triggers. In: *Proceedings of the 12th international symposium on geo-disaster reduction*, 1, pp 229–239
- Tiwari B, Lewis A (2014b) Experimental modeling of seepage on sandy slope. *Landslide Sci Safer Geo Environ* 2:109–116
- Tiwari B, Caballero S, Zalzali W (2014a) Experimental modeling for the effect of rainfall and earthquake on slope stability of engineered fill. *Landslide Sci Safer Geo Environ* 2:101–108
- Tiwari B, Kawai K, Viradeth P (2014b) Experimental and numerical studies on the effect of rainfall on triggering shallow landslide. *Landslide Sci Safer Geo Environ* 2:123–128
- Tiwari B, Kawai K, Viradeth P (2014c) Numerical modelling of deformation for partially saturated slopes subjected to rainfall. *Landslide Sci Safer Geo Environ* 2:281–286
- Tiwari B, Lewis A, Ferrar E (2013) Experimental simulation of rainfall and seismic effects to trigger slope failures. *Geotech Spec Publ* 231(1):448–451
- Tiwari B, Tran D, Ajmera B, Carrillo Y, Stapleton J, Khan M, Mohiuddin S (2015) Effect of slope steepness, void ratio and intensity of rainfall on seepage velocity and stability of slopes. In: *Proceedings of the geotechnical and structural engineering congress 2016*
- Tran D (2016) Effect of rainfall and seismic activities on compacted clay slopes having different void ratios and inclinations. MSc. Thesis, California State University, Fullerton

TXT-tool 3.001-1.2 Physical Modelling of Earthquake-Induced Landslides

Beena Ajmera and Binod Tiwari

Abstract

Earthquakes can be disastrous events causing loss of lives, damage to and destruction of infrastructure, economic losses, and can lead to other disasters such as tsunamis and fires. Moreover, they can serve as a triggering factor for hundreds to thousands of landslides in the region affecting by ground shaking. Asides from the ground shaking intensity resulting from an earthquake, several other factors including slope inclination, density of the slope material, antecedent and intensity and duration of post-earthquake rainfall can also influence the stability of a slope. As it is difficult to simulate field conditions and expected ground shaking, laboratory based models can assist in performing sensitivity analyses to understand the effect of various factors in triggering earthquake-induced landslides. In this tool, procedures for the development of simple laboratory models to perform such sensitivity analyses are described.

Keywords

Earthquake induced landslides • Suction • Deformation • Tensiometers
Accelerometers • Shake table • Slope stability • Post-earthquake rainfall

B. Ajmera (✉)
Department of Civil and Environmental Engineering,
California State University, Fullerton, 800 N. State
College Blvd., E-318, Fullerton, CA 92831, USA
e-mail: bajmera@fullerton.edu

B. Tiwari
Department of Civil and Environmental Engineering,
California State University, Fullerton, 800 N. State
College Blvd., E-419, Fullerton, CA 92831, USA
e-mail: btiwari@fullerton.edu

Contents

1	Introduction	288
2	Experimental Set-Up	288
3	Analysis of Experimental Results	292
4	Example of Experimental Modelling and Data Analysis for Slope Subjected to Earthquake Loading	292
5	Limitations of Modelling Techniques	294
6	Conclusions	295
	References	295

1 Introduction

Several thousands of landslides have been triggered by earthquakes around the world. For example, over 3400 landslides triggered by the 2011 Tohoku Earthquake (Wartman et al. 2013) and thousands of landslides triggered by the 2015 Gorkha Earthquake in Nepal (Tiwari et al. 2016a, b) were identified. These landslides can cause significant amount of economic losses, loss of lives and damage to infrastructure. Other than the ground shaking induced by an earthquake, there are a number of other factors that influence the stability of slopes following an earthquake. Specifically, factors such as the slope inclination, density of the slope material, antecedent rainfall and intensity and duration of post-earthquake rainfall influence the stability of the slope. Sensitivity analyses can help to evaluate the effect of these factors and ground shaking intensity on the stability of slopes. The literature contains the results of many experimental and numerical modelling analyses for different types of soils as well as analyses of coseismic landslides triggered by different earthquakes in recent history (Wartman et al. 2013; Tiwari et al. 2016a, b; Khazai and Sitar 2004; Gorum et al. 2011; Bommer and Rodriguez 2002; Woli 2015). In this tool, procedures for developing laboratory based models to evaluate the stability of slopes subjected to different ground shaking intensities for various controlling factors are provided.

2 Experimental Set-Up

The materials available, scale of the experiment and capacity of the shake table used for the testing will govern the preparation of the laboratory based earthquake induced slope models. A container, which will contain the modelled slope, should be assembled and secured on top of a shake table. It is preferred that this container be constructed from Plexiglas to allow for visibility into the container to the model slope during the

experimental proceedings. The sides and base of the container should be properly sealed to ensure that there are no leaks. If the model is being prepared to examine the influence of antecedent or post-earthquake rainfall on the stability of slopes or if drainage will be allowed during any phase of the testing, sufficient holes should be included to allow for continuous and adequate drainage. In this tool, the process of preparing a model slope to examine the influence of post-earthquake rainfall on the stability of the slope is described.

Once the Plexiglas container is securely fastened to the shake table, install perforated pipes at the base of the container to collect the infiltrated and runoff water during the rainfall events (Fig. 1a). A drainage layer consisting of compacted gravels and/or sands, as shown in Fig. 1b, is then prepared on top of the perforated pipes. The gravel layer is, then, covered with several layers of geotextiles, which act as a filter separating the soil used for the model from the drainage layer. Next, the soil slope is constructed to the desired geometry, density and moisture content. In the example presented here, the lift thickness, or the thickness of each layer of soil, was held constant and the amount of dry soil necessary for the desired density was calculated. The amount of water required to obtain the target moisture content was then computed and thoroughly mixed with the dry soil. This mixture was, then, compacted to the appropriate height using mechanical and/or pneumatic compactors until the desired slope geometry was constructed. To assist in the compaction process and to allow for the greater control and accuracy in the slope model, it is useful to draw the slope geometry and lift thickness on the Plexiglass wall. A picture of a constructed model is available in Fig. 2. When preparing the model, sufficient widths should be provided at the head and toe of the slope to allow the slope to freely deform and/or slide.

Once the desired slope geometry is constructed, the model slope is instrumented with

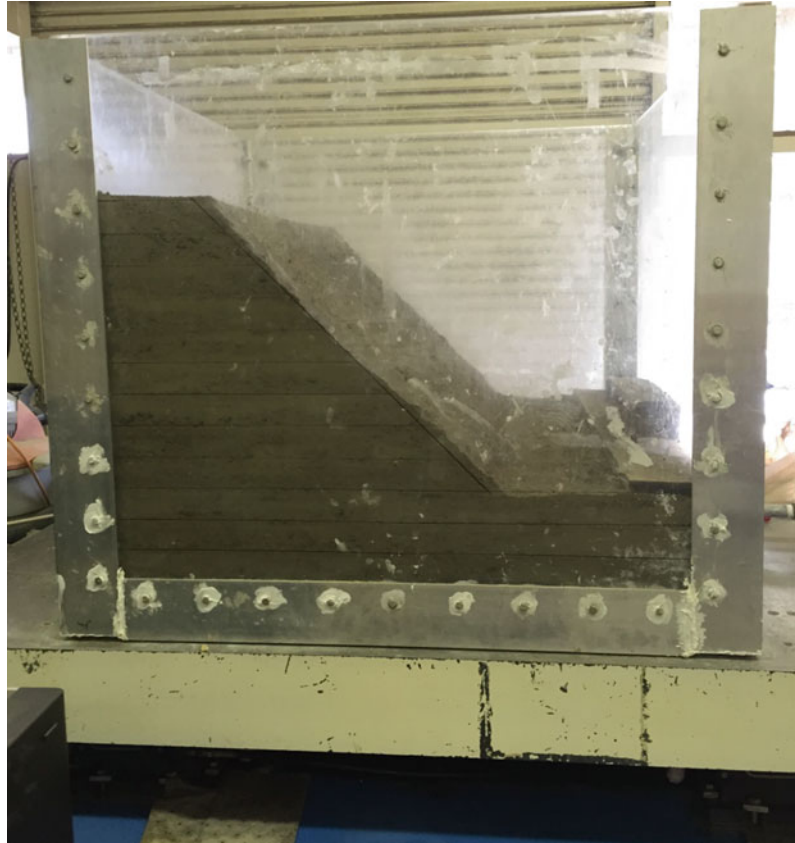


Fig. 1 **a** Perforated pipe installed at the base of the Plexiglass container and **b** gravel layer compacted above the perforated pipe to serve as a drainage layer during the model test

accelerometers, tensiometers, and copper wires, as shown in Fig. 3. The accelerometers will measure real-time accelerations experienced by the soil mass at the desired locations. Accelerometers should be installed to accomplish this task. Tensiometers are used to obtain real-time suction values at the desired locations. These results are used to verify the wetting front movements observed externally during the rainfall events. Accelerometers and tensiometers should be installed at the same height at multiple locations at the head and toe of the slope as well as along the middle of the slope. Doing so will allow an understanding of the spatial variation of the accelerations and suction throughout the model slope. The ceramic discs of the tensiometers should be saturated and used to calibrate the tensiometers to a zero pore water pressure reading prior to the installation of the devices into the slope. A hand drill can be used to

drill holes of the appropriate sizes to the desired depths for the tensiometers and accelerometers. After the installation of the accelerometers and tensiometers, a data acquisition system is set-up through cables connected to the instruments. The soil that was removed by the hand drill is then compacted back to fill the remaining space of the drilled holes. A bentonite slurry is, then, used to seal the holes for the tensiometers at the ground surface in order to prevent the rainwater from travelling faster through the potentially lower density backfilled soil than the rest of the slope. The copper wires will be used to determine the deformation of the slope at different locations. Straight copper wires are installed through the slope at multiple locations, as illustrated in Fig. 3. Black and white stripes were painted on the copper wires to easily visualize the deformation of the slope. Information about the deformation along the length of the copper wire

Fig. 2 Completed compacted slope model secured on shake table



can be determined from the deformation observed in the copper wires.

After all of the instrumentation has been completed, the soil model is ready for testing. The testing procedures can be customized based on the factors that are being studied. For example, in order to study the influence of antecedent rainfall on the stability of slope, the soil model should be subjected to rainfall using a rain simulator system and then subjected to seismic shaking using the shake table. If the influence of post-earthquake rainfall is of concern, then the soil model should be subjected to seismic loading using the shake table followed by rainfall using a rain simulator system. A rain simulator system can be constructed using sprinkler heads connected with pipes at the desired spacing. Figure 4 shows the rain simulator system used in the example presented in this tool, which consisted of 16 sprinkler heads connected with PVC

pipings. The intensity of the rainfall could be controlled by adjusting the opening of the sprinkler heads. After the desired testing is completed, the copper wires should be carefully excavated from the soil model and used to determine the amount of deformation experienced by the slope during the testing procedures. This deformation data will be useful in determining the critical sliding plane if the slope did not experience a slide.

The soils used in the experimental model preparation should also be used to conduct the appropriate laboratory tests to obtain a better understanding of the properties of the soil. These laboratory testing are performed to determine the grain size distribution curve, specific gravity, maximum dry density and optimum moisture content, drained and undrained shear strength parameters and stiffness of the soil used in the model for specific conditions.

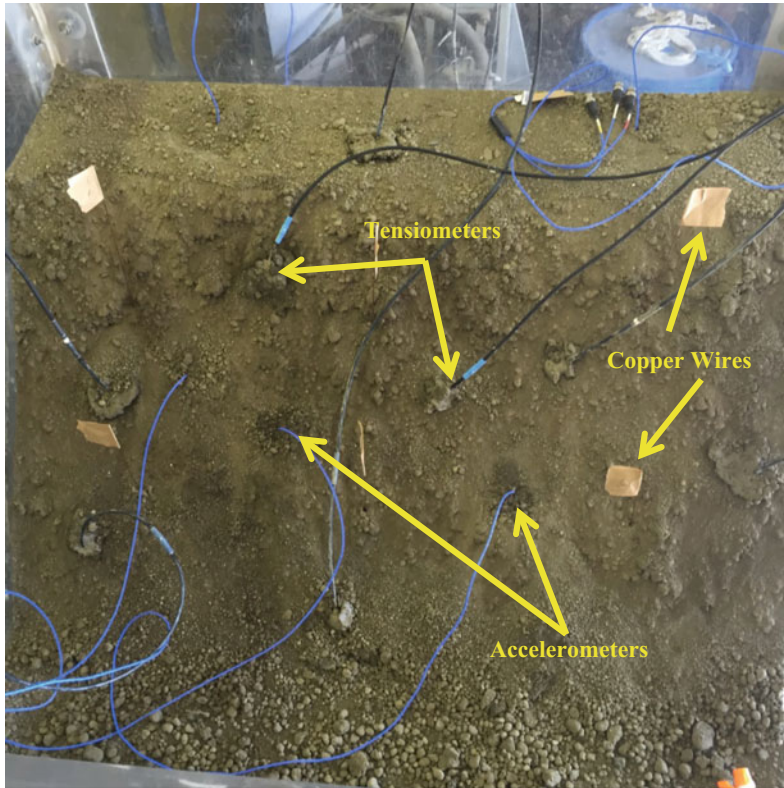


Fig. 3 Instrumentation of model slope with accelerometers (*blue wires*), tensiometers (*black wires*) and copper wires (*beige flags*)



Fig. 4 Example of rain simulator system consisting of 16 sprinkler heads with adjustable nozzles connected with PVC piping to the desired spacing

3 Analysis of Experimental Results

A number of analyses should be performed using the results obtained from the experimental modelling. Specifically, the analyses should be used to determine the spatial variation of the ground motion parameters and deformation in the model, to calculate the deformation and factor of safety of the slope using automated computer program, and/or to compute the factor of safety of the slope using automated computer programs. If rainfall was applied to the slope to examine the influence of either antecedent rainfall or post-earthquake rainfall on the stability of the slope, the analyses should also attempt to gain an understanding of the seepage velocity of the infiltrating rainwater and the variation of suction with time. The results from slope models with different geometries, densities, and shaking intensities may be used to analyse the influence of these parameters on the stability and deformation of slopes subjected to earthquake loading. In addition, slope geometries, geotechnical properties of the soils and shaking intensities may be inputted into commercially available software to perform parametric studies and sensitivity analyses for various parameters. The results from the software may be calibrated

based on the results obtained from the experimental models prepared in a manner similar to that described in this tool. GeoStudio Quake/W is one of the available software packages available that can be used to examine the stability and deformation characteristics of slopes subjected to earthquake loading. This program can also be coupled with other packages within the GeoStudio suite to perform seepage and deformation analyses for steady-state and transient ground water conditions.

4 Example of Experimental Modelling and Data Analysis for Slope Subjected to Earthquake Loading

Using soil collected from a housing development site in Mission Viejo, California, an experimental model slope was constructed using the procedure described in the previous sections. The slope model (Fig. 5) was prepared to have a slope inclination of 40° and compacted so that the initial void ratio the slope material was 1.2. Accelerometers, tensiometers and copper wires were installed at various locations as shown in

Fig. 5 Slope geometry before and after earthquake loading, lines representing the location of the observed wetting front at various times during the post-earthquake rainfall event and the corresponding swelling of the soil model as well as locations of the tensiometers used in the experimental model prepared

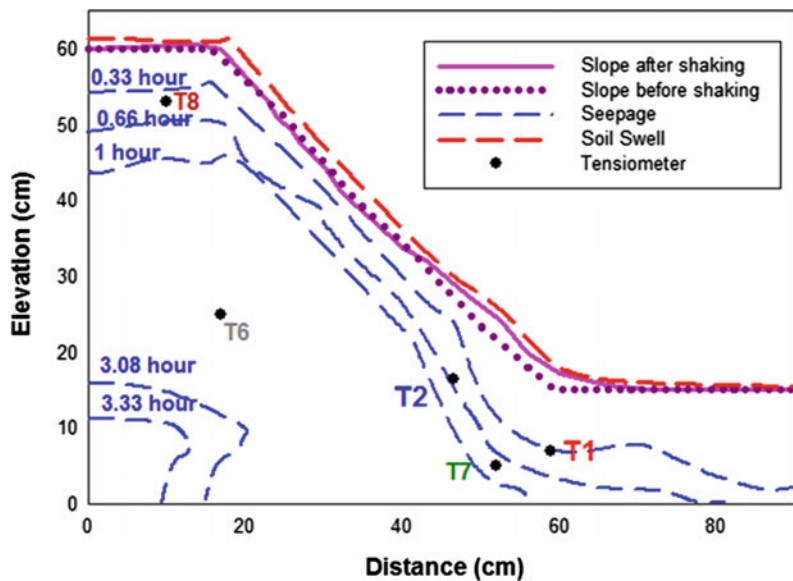


Fig. 3. A series of sinusoidal waves with various amplitudes and frequencies were used to apply the earthquake loading to the slope using the shake table. The applied acceleration time history is presented in Fig. 6. The model was subjected to rainfall with an intensity of 3.6 cm/h following the earthquake loading until complete saturation of the slope was observed. Although the results of the observed wetting front are presented in Fig. 5, the focus of this document will be results obtained from the earthquake loading. Copper

wires were used to determine the deformation in the slope.

Copper wires were also installed at various locations within the slope. After the completion of the experiment, the wires were carefully excavated from the slope and the measured deformations were used to determine a potential sliding surface for the model slope. The observed deformations in the slope as well as the hypothesized critical sliding surface are presented in Fig. 7. The slope geometry and soil

Fig. 6 Applied acceleration time history

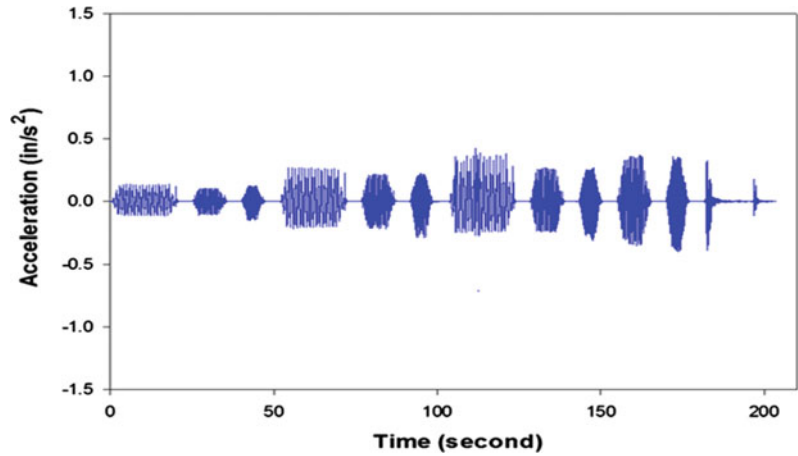
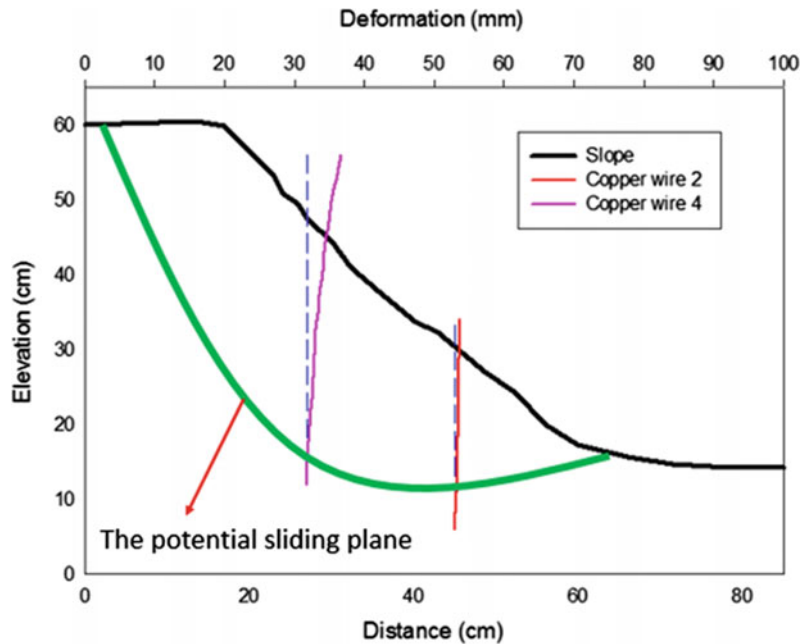


Fig. 7 Deformation along two of the copper wires installed in the slope and location of a hypothetical potential sliding surface for the slope geometry



properties were then inputted into GeoStudio Quake/W and Sigma/W and used to determine the factor of safety and deformation in the model slope. Figure 8 contains a comparison of the potential sliding surface predicted from the numerical analysis to that obtained based on the deformations in the copper wires. It is clear from this figure that the results agree well. Similarly, the variation in the factor of safety of the experimental slope with the application of the seismic accelerations were computed using GeoStudio Slope/W. The obtained results are presented in Fig. 9. Detailed discussions about the results are available in Tran (2016).

5 Limitations of Modelling Techniques

Study results should be used with caution since as with any experimental laboratory based models, the modelling has several limitations. Specifically, there are a number of limitations with the modelling described in this tool such as the scale of the experimental model is much smaller than the dimensions of an actual slope, the homogeneity obtained in the laboratory based models is significantly greater than what could be expected in actual slopes, there are substantial variations in the surface roughness of the actual

Fig. 8 Comparison of critical sliding planes obtained based on the deformations in the copper wires during the experimental modeling to that obtained from GeoStudio Sigma/W analyses

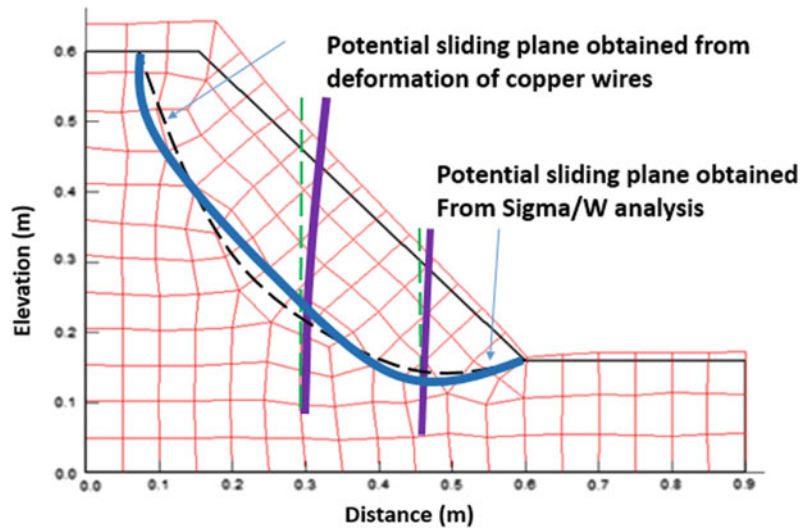
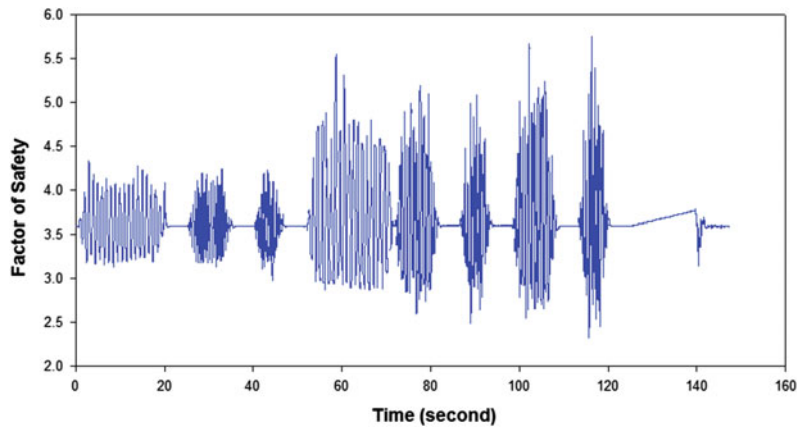


Fig. 9 Variation in the factor of safety of the experimental model slope based on GeoStudio Sigma/W analyses during the earthquake loading



slopes versus the experimental models and the intensity and duration of the earthquake loading will vary significantly. Moreover, conducting experiments on a laminar container will provide a free field shaking, as opposed to the rigid container used in the experiments presented above.

6 Conclusions

Experimental models prepared in the laboratory can be used to effectively and inexpensively perform sensitivity analyses to understand the influence of slope geometry, soil properties, and seismic shaking intensity and duration on the stability and deformation of slopes subjected to earthquake loading. The results obtained may be used to calibrate numerical models that can be used to determine the factor of safety and deformation of slopes subjected to earthquakes. In addition, the influence of various factors such as the antecedent and/or post-earthquake rainfall may also be studied with the use of experimental slope models. The details of preparing such models, analysing the data obtained and the results of an example model were provided in this tool.

Acknowledgements The authors would like to acknowledge the financial support provided by IRA Grant #3361 from California State University, Fullerton to conduct the experiments presented above. In addition, the authors would like to acknowledge their graduate students Duc Tran, Santiago Caballero and Hari Woli for conducting the experimental work.

References

- Bommer JJ, Rodriguez CE (2002) Earthquake-induced landslides in Central America. *Eng Geol* 63(3–4):189–220
- Gorum T, Fan X, van Westen CJ, Huang RQ, Xu Q, Tang C, Wang G (2011) Distribution pattern of earthquake-induced landslides by the 12 May 2008 Wenchuan earthquake. *Geomorphology* 133(3–4):152–167
- Khazai B, Sitar N (2004) Evaluation of factors controlling earthquake-induced landslides caused by Chi-Chi earthquake and comparison with the Northridge and Loma Prieta events. *Eng Geol* 71(1–2):79–95
- Tiwari B, Ajmera B, Dhital S (2016) Photographic database and geospatial analyses of co-seismic landslides triggered by the main shock and aftershocks of the 2015 Gorkha earthquake. Report submitted to the Department of Civil and Environmental Engineering, California State University, Fullerton
- Tiwari B, Tran D, Ajmera B, Woli H, Stapleton J (2016) Effect of pre and post earthquake rainfall events on deformation and stability of slopes. In: Proceedings of geotechnical and structural engineering congress
- Tran D (2016) Effect of rainfall and seismic activities on compacted clay slopes having different void ratios and inclinations. Masters thesis submitted to the Department of Civil and Environmental Engineering, California State University, Fullerton
- Wartman J, Dunham L, Tiwari B, Pradel D (2013) Landslides in Eastern Honshu induced by the 2011 off the Pacific Coast of Tohoku Earthquake. *Bull Seismol Soc Am* 103(2B):1503–1521
- Woli H (2015) Effect of post-earthquake rainfall on slope stability. Masters thesis submitted to Department of Civil and Environmental Engineering, California State University, Fullerton

TXT-tool 3.044-1.1

The Runout of Chalk Cliff Collapses— Case Studies and Physical Model Experiments

Elisabeth T. Bowman and W. Andy Take

Abstract

Chalk exposures in coastal cliff faces extend from Yorkshire to Devon in England and from Boulonnais to Normandy in France. The failure of chalk cliffs is a long-recognised hazard along parts of these coastlines, however variation in the chalk's lithology, stratigraphy and physical properties coupled with changing topographic relief, means that the nature of the hazard is variable. This tool is concerned with cliff failures that may lead to chalk flow resulting in catastrophic flow slide or rock avalanche-like behaviour. We discuss the nature of chalk flows and how they relate to other types of flow-like avalanches. Recently published and unpublished work is used to unify simple mechanical index properties between the French and English coastal chalks. Some well-documented studies are then re-examined, using these results to show how runout is controlled by chalk porosity. Finally, a series of physical model tests are described in which some of the controls on runout of the chalk are examined.

Keywords

Chalk · Sturzstrom · Landslide · Cliff · Physical model · Case study

Contents

1 Introduction	298	4.1 Incidence	301
2 Occurrence and Geometry	298	4.2 Sturzstrom-Like Behaviour	301
3 Case Studies	299	4.3 Moisture State	302
4 Mechanisms	301	4.4 Chalk Cliff Strength and Porosity Characteristics	303
		4.5 Spreading Efficiency and Energy Ratio	303
		5 Physical Modelling	305
		5.1 Methodology	305
		5.2 Materials.....	306
		5.3 Test Series.....	307
		5.4 Coriolis Effect	307
		5.5 Breakage.....	309
		6 Discussion	310
		6.1 Scaling.....	310
		6.2 Dynamic Fragmentation.....	311

E.T. Bowman (✉)
Department of Civil and Structural Engineering,
University of Sheffield, Mappin St, Sheffield, UK
e-mail: e.bowman@sheffield.ac.uk

W.A. Take
Department of Civil and Environmental Engineering,
Queens University, Kingston, ON, Canada
e-mail: andy.take@civil.queensu.ca

7 Conclusions.....	312
References.....	313

1 Introduction

Chalk exposures in coastal cliff faces on either side of the English Channel extend from Yorkshire to Devon in England and from Boulonnais to Normandy in France. Two sections of cliff on the English side (approximately 40 km in East Sussex and 40 km in Kent) and sections of the cliffs in France from Upper Normandy to Picardy—known as the Pays de Caux (approximately 120 km) as well as three zones in the Boulonnais—Cap d’Alpreche, Cap Gris-Nez, Cap Blanc-Nez, are known for their hazardous chalk cliff collapses. Occurring in areas popular for tourism, the hazard consists of the spontaneous and somewhat stochastic nature of the removal of the head scarp at the cliff top, where walking paths and other infrastructure are typically located, and runout onto what may be a beach platform or transport corridor below. In some localities large chalk falls are known to develop into chalk “flows” (Hutchinson 2002), which are considered particularly hazardous due to their long runout at the cliff base. Hutchinson (1988, 2002) defines chalk flows as being part of a wider family of flow slides in which the collapse of a metastable near-saturated soil or rock leads through undrained loading to the generation of high excess pore pressures and high temporary mobility. Following Hutchinson (1988), Cruden and Varnes (1996) considered chalk flows to be a form of debris flow.

As noted by Hutchinson (1988), there is a strong resemblance of long runout chalk flows to large rock avalanches (with volumes typically exceeding one million cubic meters), albeit in weaker material, at a smaller scale, and with simpler geometry. Recent work has added support to the hypothesis that dynamic fragmentation of rock is responsible for the extraordinary spreading of large rock avalanches (Bowman et al. 2012; De Blasio and Crosta 2013; Davies and McSaveney 2009). The objective of this tool is to place closer constraints on the distal reach of

chalk falls and flows. In doing so we examine field case studies reported in the literature and note the relative importance of potential energy input and chalk strength on their behaviour. To investigate potential rock avalanche-like behaviour as generated by the process of dynamic fragmentation in chalk falls we further perform physical modelling to better understand the processes in question, which are controlled by strength, input energy, and geometry.

2 Occurrence and Geometry

Chalk cliff collapses are of frequent occurrence—an average of ten falls per year of volumes greater than 1000 m³ in Pays de Caux was reported between 1998 and 2001 by Duperré et al. (2004), and on average one very large fall (volume greater than 50,000 m³) per year occurs on each of the English and French sides.

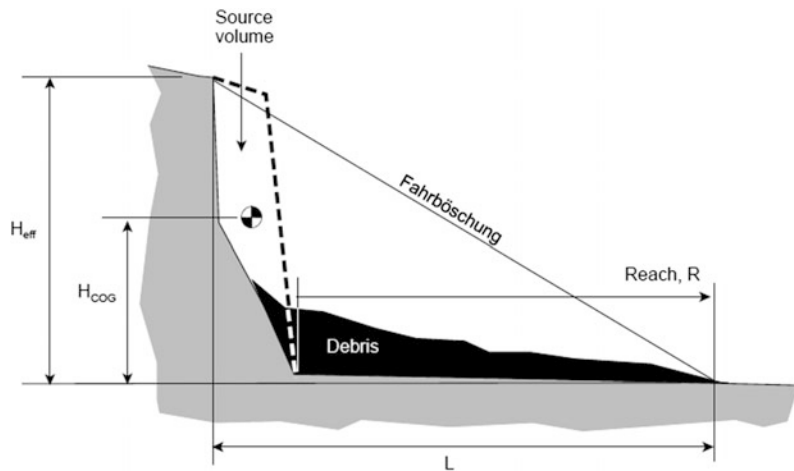
One recent very large volume fall, determined by the authors as approximately 52,000 m³ via photogrammetric methods, occurred along the Kentish coastline on 9th March 2012 at Fan Bay (Ledwith and Cohen 2012). Figure 1 shows a photograph of the Fan Bay fall taken by the authors from the cliff top on 20th March 2012. The geometric definitions used in this paper to quantify the distal reach of falls are presented in Fig. 2. These include effective cliff height H_{eff} (note that on occasion, this may be less than the actual cliff height where a cliff collapse event involves only the lower portion of the cliff), the centre of gravity of the failing cliff, H_{COG} (taken to be $\frac{1}{2} H_{\text{eff}}$ in the analyses herein), runout length L , runout spread R , and Fahrböschung angle which is $\tan^{-1}(H/L)$ (e.g. Corominas 1996; Hsu 1978).

As the figure shows, due to the steepness of the cliff, which typically ranges from 60° to 90° to the vertical, the dimensions R and L are often close, so that some case studies in the literature only report the one of these values. Here, for the analysis of case study data, R is assumed to be approximately equal to L where only one value is given. Deposit volume V is generally taken from reportedly measured or estimated values. Where a scar volume has been reported

Fig. 1 Chalk cliff collapse at Fan Bay, March 9th, 2012



Fig. 2 Definition of morphological parameters to describe reach of cliff landslide debris



rather than a deposit volume, a bulking factor of 1.4 has been assumed for chalk, following Hutchinson (2002).

3 Case Studies

Figure 3 includes field cases presented from various sources. Fourteen cases are taken from Hutchinson (2002), based on very large historic collapses in England and France and Germany.

A further 50 are taken from Duperret et al. (2004) based on a project which regularly mapped cliff failures between 1998 and 2001 along the coastline of Pays de Caux from Upper Normandy to Picardy in northern France. Two further case studies in England are taken from Williams et al. (2004) and Mortimore et al. (2004a) and two recent large falls that occurred along the Kentish coastline on 1st January 2011 at St Margaret’s Bay (Mitchell 2011) and 9th March 2012 at Fan Bay (Ledwith and Cohen 2012) are also

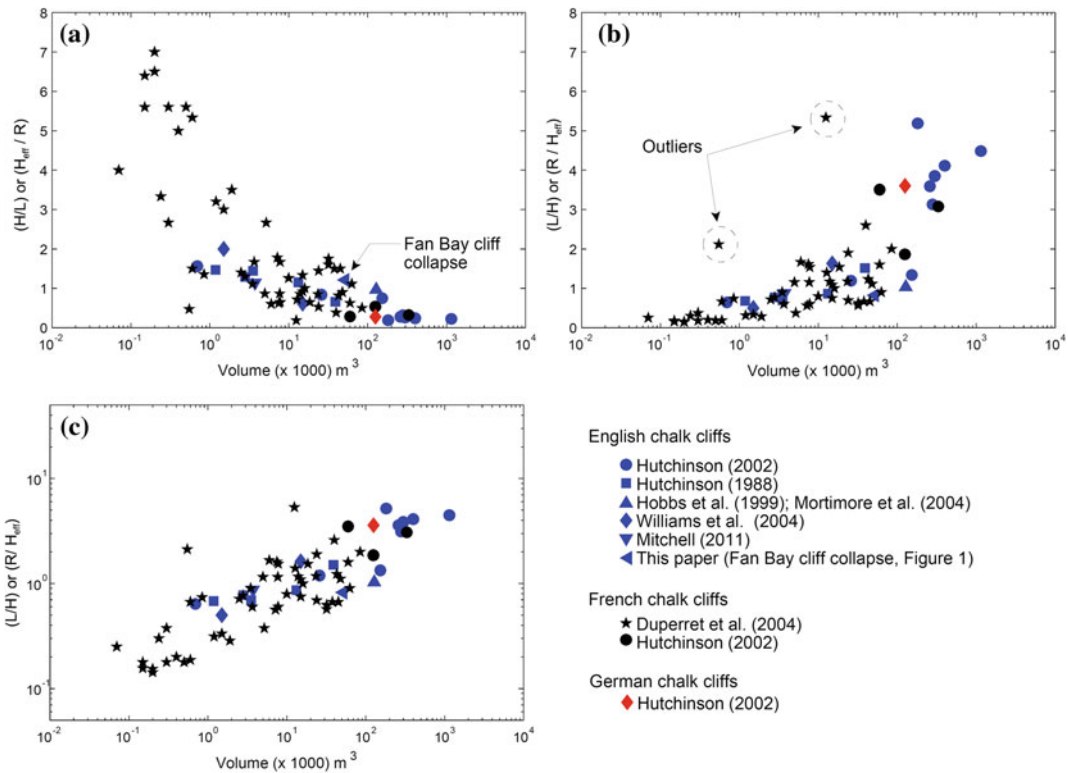


Fig. 3 Distal extent of chalk cliff landslide debris expressed as relationship between **a** H/L and logarithm of volume, **b** L/H and logarithm of volume, and **c** logarithm of L/H and logarithm of volume

included. In total, 68 cases are therefore considered here, of which 53 are greater in volume than 1000 m³.

Previously Hutchinson (1988) and Hutchinson (2002) have shown that the trend of reducing H/L with increasing debris volume, as seen in large rock avalanches or sturzstroms, is also seen in chalk cliff collapses. However, the threshold at which such flow behaviour begins (defined by Hutchinson (2002) as $L/H > 1.3$ or $H/L < \sim 0.8$), is at a much lower volume (approximately 10⁴ m³) than for rock avalanches (approximately 10⁶ m³—Davies and McSaveney 1999). Additionally, Williams et al. (2004) have noted the sturzstrom-like behaviour of “The Great Fall” in chalk of 1914 at Went Hill in Sussex, England and further point out that there appears to be no evidence of excessive moisture that would have been needed to generate an excess pore pressure induced wet flow.

Figure 3a presents the data from Hutchinson (2002), Duperret et al. (2004), Williams et al. (2004), Mortimore et al. (2004a), Ledwith and Cohen (2012) and Mitchell (2011), on graphs of H/L against the logarithm of debris volume. For the chalk falls there is a clear continuum of behaviour from less than 1000 m³, from which H/L gradually decreases with increasing volume. There is no abrupt change with volume which might indicate a sudden change of mechanism of travel and emplacement—suggesting that whatever mechanisms act to increase runout gradually come into play as the volume increases. Figure 3a appears to show a relatively poorly constrained problem at smaller volumes, which becomes better constrained at larger volumes. Figure 3b represents the same data on a plot of L/H against log debris volume. In contrast to Fig. 3a, this plot appears to show that as the volume increases, the data to be less well

constrained than at smaller problems. Coupled with the increasing magnitude of the hazard with volume, the data indicates a large degree of uncertainty on absolute runout for a given fall height—suggestive of a higher risk with event volume. It should be noted however, that both Fig. 3a, b draw the viewer to a particular viewpoint as a result of the scales used. In terms of mechanics, a more objective representation of the data is to plot both axes as logarithms as shown in Fig. 3c. From this plot, it may be seen that the data lie within a band that is close to parallel. Hence, while the problem scale still clearly influences the hazard in terms of absolute size, the data plotted this way highlights the continuum of behaviour from small to large scale.

As an aid to mechanical understanding, there is still a problem in presenting data as shown in Fig. 3, since while volume may vary over three orders of magnitude, the fall height is generally limited to between 20 and 150 m (i.e. the cliff height). As a result, the plot mixes apparent volumetric effects due to a limited H value with actual changes in cliff collapse “efficiency” at generally larger scale. We suggest that a better measure of spreading efficiency is the normalised spread—i.e. the ratio of the fall spread R from the base of the cliff to the cube root of the fall volume V (Bowman et al. 2012; Davies and McSaveney 1999), rather than H/L . This separates the variable H —which influences the potential energy of the event—from the volumetric data. This is further discussed later in the paper.

4 Mechanisms

4.1 Incidence

Hutchinson (2002) examined the seasonal incidence of extremely large historic chalk falls in NW Europe and found that they predominantly occurred during the wetter and cooler months, with none recorded between June and August. This was later confirmed by Mortimore et al. (2004a) in their study focusing on the East

Sussex coastline. For the Pays de Caux region which was regularly surveyed in detail over four years, however, Duperret et al. (2004) found a broader distribution of small to large sized chalk falls, with collapses occurring at all times of the year—particularly during drier-than-average, as well as wetter-than-average periods. It was suggested that cycles of wetting and drying may weaken the chalk, as supported by tests subsequently carried out by Duperret et al. (2005). Hence it appears that while the most hazardous falls occur from September through May, the increased presence of water alone does not account for their incidence.

4.2 Sturzstrom-Like Behaviour

Hutchinson (2002) noted that flowslides only occurred in relatively high porosity chalks and the occurrence was greater the higher the porosity. He suggested the greater retention of moisture and lower strength of more porous chalk to be responsible for this—resulting in saturated undrained flow sliding due to pore volume collapse upon debris impact. This hypothesis appears reasonable if it can be assumed that the chalk is in a sufficient state of saturation and if the excess pore pressures generated during collapse can be maintained during motion (Leddra and Jones 1990). Upon examination of field cases, Hutchinson (2002) found no particular evidence for undrained loading of the shore platform where these might be hard jointed chalk, gravel beach or chalk talus—although he did not preclude the possibility.

In this paper we investigate an alternative hypothesis that appears equally valid—that the mechanism of emplacement of flow-type chalk cliff collapses is similar to that of much larger scale sturzstroms or rock avalanches. There are a number of ways in which chalk cliff collapses resemble large-scale rock avalanches: the ratio H/L decreases with event volume (Scheidegger 1973); intact rock blocks fragment into much smaller pieces (Davies and McSaveney 1999); the stratigraphy is preserved with the base of the

chalk cliff appearing at the distal ends of the deposits (Hsu 1978); clouds of dust are observed during events suggestive of material that is not fully saturated throughout (Cruden and Hungr 1986) and the mass dilates or bulks during motion, increasing in volume by 20–30% in rock avalanches compared to 20–40% for chalk cliff collapses (Duperret et al. 2002; Hutchinson 2002). One point in which chalk collapses are different from rock avalanches is that larger blocks tend to be more prevalent at the distal edge of deposits in chalk falls (Duperret et al. 2002; Hutchinson 2002), whereas the distal end of rock avalanches tend to be more pulverised and fragmented (Locat et al. 2006).

4.3 Moisture State

There is clearly a major role played by water in the incidence of chalk falls. Water serves to increase the unit weight of the chalk by around 30% for saturated high porosity chalk compared with the dry state, and to weaken it. Water ingress into joints can cause a weakening of contacts and may generate hydrostatic pressures within them (Duperret et al. 2004; Mortimore et al. 2004a), while generalised softening of the

chalk may also occur. Unconfined compression tests by Matthews and Clayton (1993) on a range of saturated and dry English chalks have shown that saturated chalk, on average, is approximately two times weaker than dry chalk at the same dry density. The UCS of French coastal chalk (Duperret et al. 2005) is also shown to approximately halve upon saturation. However, Duperret et al. (2005) also report that the dry UCS value of French coastal chalks are generally lower than that of English chalks for a given porosity, even when comparing the same stratigraphic unit. They also found that a relatively low moisture content (~5%) was needed to reduce the UCS significantly to become close to the value for a saturated chalk.

More recent saturated UCS tests on soft English chalks taken from southerly locations have been reported as part of a study by Katsaros (2008). Katsaros (2008) conducted tests on saturated Seaford chalk from the Tarring Neville quarry in East Sussex and also reports unpublished UCS tests conducted by Soil Mechanics Ltd (2001) on saturated Lewes, New Pit and Holywell chalks from Kent. These data are plotted in Fig. 4 along with the data from saturated on French coastal chalks conducted by Duperret et al. (2005). Data from French chalks

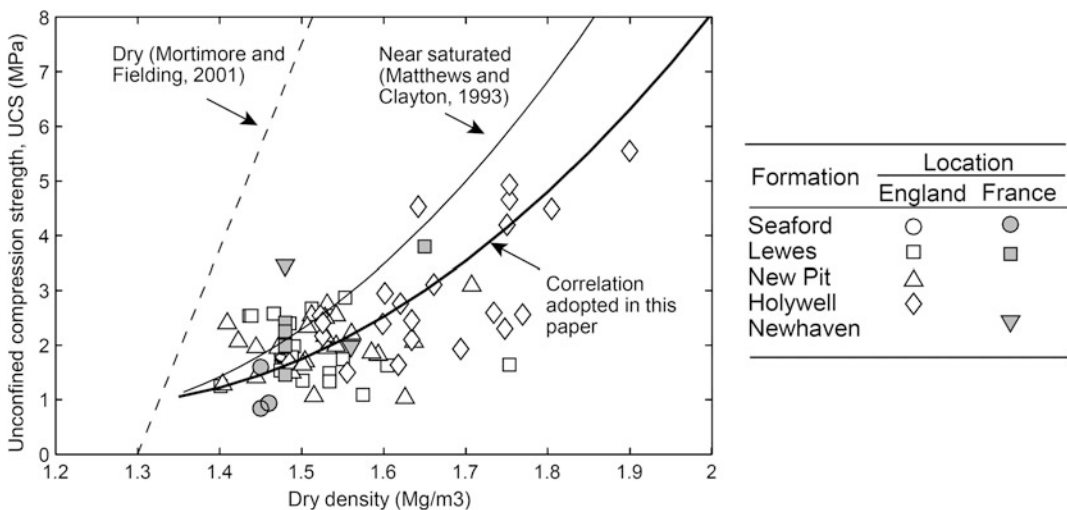


Fig. 4 Correlation between unconfined compression strength and dry density. Source for English chalk data: Seaford (Katsaros 2008); Lewes, New Pit, and Holywell (Soil Mechanics, 2001). Source for French chalk data: Duperret et al. (2005)

are shown with closed symbols, while English UCS data are shown by open symbols. Trend-lines from Matthews and Clayton (1993), as published by Lord et al. (2002)—and Mortimore and Fielding (1990) are also given for comparison.

There are several points of note regarding the degree of scatter and the grouping of data. The saturated UCS data show much greater scatter than indicated previously in Matthews and Clayton (1993) and the results on average lie below their trend-line, particularly for the most porous chalks. The scatter is perhaps not surprising. While it is not clear what is the degree of anisotropy in the English and French chalks, (Talesnicka et al. 2001) showed that for a low density anisotropic chalk, the strength measured was approximately 50% higher when loaded parallel to its bedding compared to being loaded perpendicular to it. In addition it is also not always clear from the literature (Matthews and Clayton 1993; Mortimore et al. 2004b) whether a dry UCS test on chalk was carried out under “air-dry” (Carter and Mallard 1974) or “oven-dried” (Duperret et al. 2005) conditions. It has been found that a small degree of moisture being present (as little as 1%) can reduce the strength of chalk appreciably in comparison with fully dry chalk (Talesnicka and Shehadeh 2006). Finally, cycles of moisture and the presence of salts can also result in changes in measured saturated UCS as the chemical bonding between chalk particles is disrupted (Duperret et al. 2005).

With regard to the grouping of data in Fig. 4, for the very soft chalks examined here, there is no clear difference between different chalk formations (Seaford, Newhaven, Lewes) in the relationship between density and strength as characterised by UCS. It also appears that the saturated UCS values are similar for the French and English chalks, despite the dry UCS values apparently being higher for the English chalks.

Therefore a revised trend-line, relating saturated UCS to dry density that is common to both French and English coastal chalks located either side of the English Channel, is plotted through this data (denoted “correlation adopted in this paper”), as shown. This trend-line is used later to relate

recorded porosity or dry density to approximate strength for the reported case studies (Fig. 4).

4.4 Chalk Cliff Strength and Porosity Characteristics

Average porosity or dry density values for the cliff collapses considered have been obtained, where possible, from measurements taken at or near the site in question, as found in the literature. That is, the dry density data quoted for many of the different case studies is derived directly from chalk cliff collapse literature: Hutchinson et al. (1980), Hutchinson (2002), Mortimore et al. (2004) and Duperret et al. (2005) as well as general literature on the chalk. References include: Duperret et al. (2004), Lautridou et al. (1986), LIFE_97_ENV/UK/000510 (2000), Mortimore et al. (1990), Rat and Schaeffner (1983), Hénaff et al. (2002), Hobbs et al. (1999), Hutchinson (1988), Mitchell (2011) and Williams et al. (2004). In a few cases, where no data were readily found in the literature for the site, data were obtained by reference to the chalk stratigraphy and nearby density values in the same chalk unit. Further information can be found in Bowman and Take (2015).

Using the mean trend determined between saturated UCS and dry density for the coastal Channel chalk, a single mean UCS value of the chalk involved in each cliff collapse case study has been obtained. In all cases it is assumed that the chalk is in a near-saturated (or otherwise weakened) state, which, given that the presence of moisture plays a major role in generating cliff failures, appears to be a valid assumption.

4.5 Spreading Efficiency and Energy Ratio

To assess the influence of energy on the spreading behaviour of the cliff collapse, a measure of the relative input to output energy is required. In order to account for this, in their investigation of the influence of rock strength upon fragmentation in rock avalanches, Locat

et al. (2006) normalised the potential energy of an avalanche per unit volume with respect to the point load strength for the rock ($\rho g H / \sigma$) where ρ is bulk density of the rock, g is gravity and σ is point load strength. In this paper we use this concept—by normalising the potential energy per unit volume calculated for a particular event by the average unconfined compressive strength (UCS) estimated for the chalk cliff. We use UCS rather than point load strength because there is far more data given in terms of UCS for chalk. Clearly however, any trends should be comparable given that UCS and point load are correlated (Mortimore et al. 2004b). In the paper, since H/L is more commonly plotted, we use both the H/L framework and the normalised spread framework to re-examine the field cases considered.

The geometry of cliff collapses and estimated strength data compiled from the literature enable the data plotted in Fig. 3 to be replotted in Fig. 5 using the concepts of spreading efficiency ($R/V^{1/3}$) versus cliff height, H , or energy ratio ($\rho g H_{COG} / UCS$). Note that reasonably precise locations are given in only 64 cases of the total of 68 (see Bowman and Take 2015), so four cases are omitted in Fig. 5.

Figure 5 shows the spreading efficiency to correlate better with the energy ratio than simply the cliff height. A line drawn above the data appears to delineate an upper bound on the

expected runout that applies to the data irrespective of cliff provenance or volume. Two data points from Duperret et al. (2004) lie above this line, both recorded at St Marguerite sur Mer (North) during Winter-Spring 2001 [denoted Chalk falls numbers 22 and 37 in Duperret et al. (2004)]. In a review of the specific details relating to these cases, it is not clear why these particular field events are outliers—however they are distinctly anomalous. The rest of the data lies below this line. Most usefully for hazard assessment, it can be seen that for a given energy ratio (a function of the initial conditions of the cliff from whence the fall originates, which can be determined a priori in the field), an upper bound on collapse runout may therefore be found for a given volume. It may also be seen that the lower bound is approximately a factor of two below the upper bound—below this line represents a zone which is virtually guaranteed to be overrun by any collapse recorded.

The scatter in the data may be due to a number of factors. Clearly there will be errors due to uncertainties in the estimated volumes and runout (particularly for older, anecdotal assessments) and the estimated porosity or strength of the chalk. However, there may also be scatter due to geometric effects (intact block geometry, back scarp geometry, initiating collapse mechanism) and degree of saturation and therefore strength. These are likely to have an impact on the

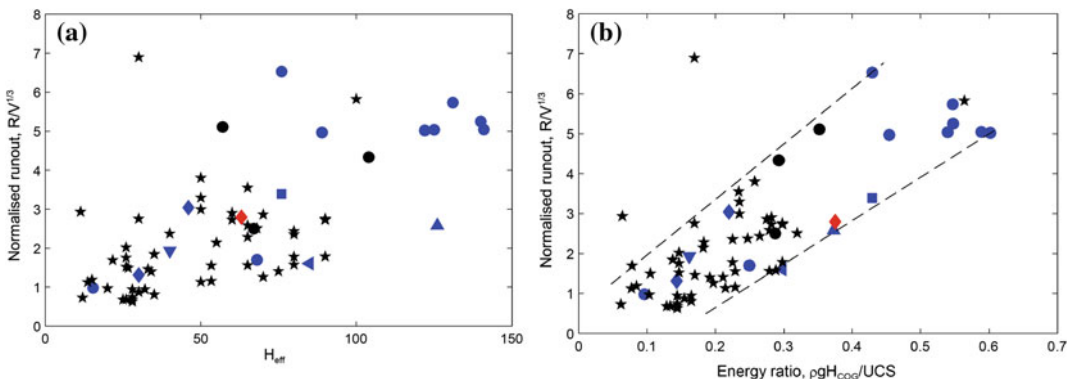


Fig. 5 Relationship between normalised runout of chalk debris and **a** effective cliff height and **b** energy ratio

potential runout for a given event. Physical modelling was used to investigate these influences, as discussed below.

5 Physical Modelling

Physical modelling was carried out to see whether flowside-like or sturzstom-like behaviour could be achieved using Seaford chalk [a weak chalk typically involved in flowsliding—e.g. Hutchinson (2002)] using scarp geometries similar to chalk cliffs. The purpose of the physical models was also to investigate the degree of scatter that may occur in runout due to differences in source geometry, slope and saturation. The aim was to understand better the relationship between runout and the variables that affect it.

5.1 Methodology

The physical model experiments were carried out at enhanced-g level by use of a geotechnical centrifuge at the University of Cambridge. The configuration of the tests was similar to that described in Bowman et al. (2012), in which coal was used as an analogue material to rock. In a similar approach to Bowman et al. (2012), the centrifuge was used to provide a greater energy input to the modelled collapses than could be achieved at 1 g. In addition, the use of impact loading at the base of the model cliff ensured a high strain rate load was applied to the mass to produce particle breakage. This is of particular importance in this study as the fracture and fragmentation of the source rock volume via high strain rate loading, albeit under more complex geometric conditions in a field scale event, will have a direct influence on the distal reach of the landslide debris (Fig. 6).

General centrifuge scaling principles are discussed in Taylor (1984) and Garnier et al. (2007), while Table 1 gives a summary of the scaling principles relevant to this study. In summary, the stress in a $1/N$ scaled model may be increased to prototype stress level by applying N times the Earth's gravity to a model via centrifugal

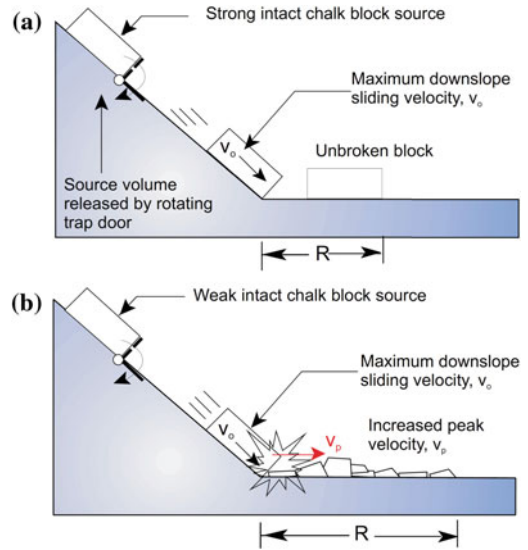


Fig. 6 Physical models of fragmentation and chalk cliff collapse runout

acceleration. For a gravity acceleration increased by N times and a model scale reduced by N times, the moving elements within the model will develop a velocity with a unity scale-factor, while the potential energy will scale with the cube of N . While chalk cliffs generally fail over their full height (e.g. Figs. 1 and 2), as shown in Fig. 6 the arrangement of the physical model test had the chalk material dropping down a slope before impacting the base. As discussed above, the reason for this arrangement is that a greater potential energy input and loading strain rate could be imparted to the chalk blocks at the chosen nominal centrifuge g-level, N of 50 g (limited so as not to cause damage to a high speed camera mounted in the centrifuge to record the tests) and a relatively small quantity of material could be used in the tests.

The test set up consisted of chalk blocks held in a regular arrangement in a release box at the head of a slope of either 60° or 70° . These slopes were chosen as typical of back scarp geometries seen in chalk cliff collapses. Before each test, the centre of gravity of the chalk was recorded (note that the 60° slope case had the release box at a slightly lower height than for the 70° slope) as well as the mass of the different blocks and their

Table 1 Summary of centrifuge scaling rules

Parameter	Prototype (field)	Model (centrifuge)
Gravity acceleration	g	Ng
Stress	σ	σ
Linear geometry	x	x/N
Velocity	v	v
Acceleration	a	a/N
Time (inertial)	t	t/N
Energy	E	E/N^3

pre-release arrangement. After centrifuge spin up to the desired g -level, a trapdoor at the base of the box was opened via a pneumatic switch to release the chalk blocks downslope. The release of the blocks also triggered a high speed camera placed above the runout zone to record the motion of debris and breakage upon impact at the base of the slope (see Fig. 7).

5.2 Materials

The experimental model tests were conducted using chalk blocks obtained from a quarry at Tarring Neville, Sussex, in the Seaford chalk formation. For the “as supplied” (i.e. bagged) state in which the chalk arrived, a moisture content of 2.7% was found for one sample taken.

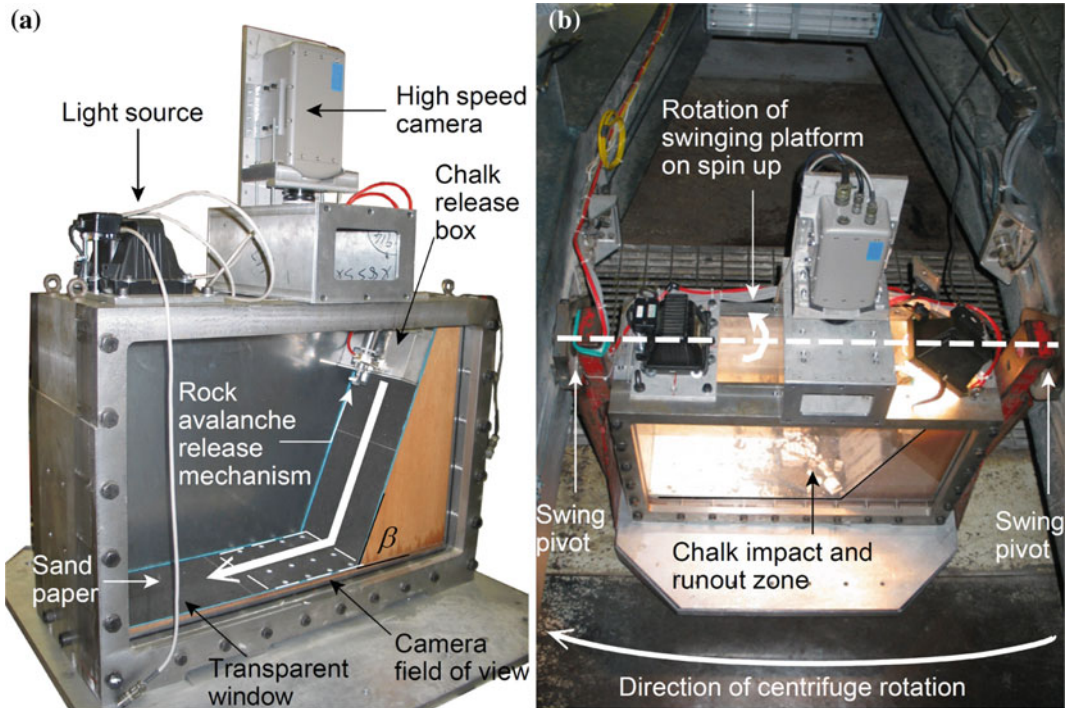


Fig. 7 a Geometry of physical model, and b installation of testing apparatus on the centrifuge showing direction of centrifuge motion. Modified after Bowman et al. (2012)

The dry density of the chalk was found to be 1.61 Mg/m^3 . According to the relationship developed for saturated chalk in Fig. 4, the saturated UCS will be approximately 2.7 MPa for this dry density. It is not known precisely what influence a lower degree of saturation will have on this chalk, however it has been shown that for high porosity chalks in general, the addition of only 2–5% moisture can reduce the UCS by 40–60% (Duperret et al. 2005; Talesnicka and Shehadeh 2006). Based on this, a single saturated strength is used for all of the test analyses.

5.3 Test Series

A total of 9 model tests were carried out, termed C9 through to C17 (Table 2). The block arrangements within the release box for each test are shown in Fig. 8. One test had different block configurations on the right and left hand-side of the plane strain box, resulting in correspondingly different behaviour on each side. This test, C9, is therefore treated as two separate plane-strain tests for analysis and is split into C9a and C9b. One further test, C16, was carried out with a single chalk block on the right-hand side and a coal block of similar dimensions and arrangement on left-hand side. Only the chalk block behaviour is considered in this paper.

Four tests, C9, C10, C11 and C13, were carried out under an “as-supplied” condition of cut and bagged samples. Five tests, C12 and C14, C15, C16 and C17, were carried out after blocks were soaked in water for 1–2 h to achieve a near saturated condition (moisture content between 19.7 and 24.7% corresponding to saturation ratio, S_r , between 0.79 and 0.99). The influence of this is reflected in the bulk density for these tests being higher than for the unsoaked tests, which were all assumed to have a bulk density based on a 2.7% moisture content. It is notable that after completion of the soaked-chalk tests, “putty” chalk was found at the base of the deposits upon excavation, as also found in field cliff collapse events (Hutchinson 2002).

5.4 Coriolis Effect

As discussed in detail in Bowman et al. (2012), for a particle moving at relatively high speed within the rotational reference frame of a geotechnical centrifuge, an additional (apparent) Coriolis acceleration (or deceleration) will be applied to the particle (Steedman and Zeng 1995). Account must be made of this Coriolis contribution to the particle’s motion, relative to the measurement frame, in order to model how far the debris would have travelled in its absence. This can be achieved if the velocity of the particle is

Table 2 Centrifuge test arrangements

Test	Slope (°)	Dry or wet	Initiating block dimensions L up × W across × H normal to slope (mm)	Model volume ($\text{m}^3 \times 10^{-4}$)	H (mm)	H_{eff} (mm)
C9a	60	D	2 of $95 \times 105 \times 22$	6.84	409	366
C9b	60	D	1 of $95 \times 91 \times 40$	5.54	409	366
C10	70	D	8 of $22 \times 92 \times 38$	4.63	470	423
C11	70	D	5 of $102 \times 35 \times 38$	8.15	470	423
C13	70	D	1 of $96 \times 110 \times 36$	8.81	470	423
C12	70	W	1 of $95 \times 103 \times 39$	5.26	470	423
C14	70	W	5 of $102 \times 93 \times 15$	4.69	470	423
C15	70	W	2 of $47 \times 92 \times 40$; 4 of $22 \times 92 \times 40$	9.26	470	423
C16	70	W	2 of $93 \times 95 \times 39$	8.62	470	423
C17	70	W	7 of $15 \times 104 \times 52$	4.62	470	423

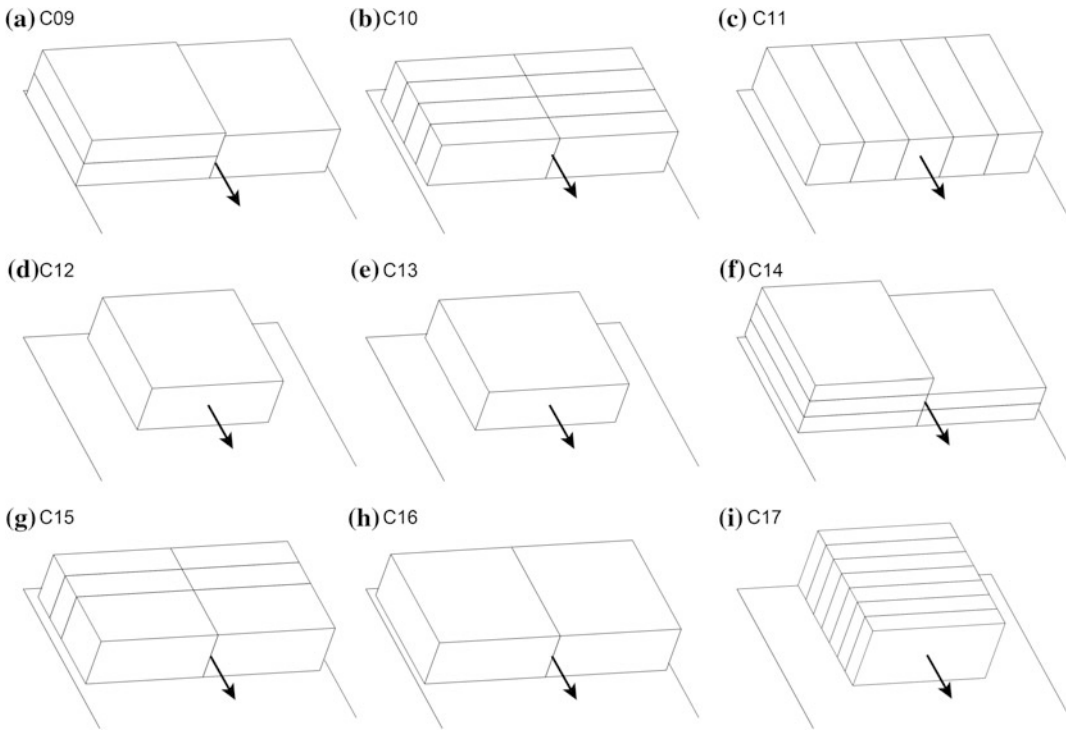


Fig. 8 Experimental source block geometry

known, its radius and the acceleration field. Accordingly, for these tests, displacement versus time information from the high speed camera was used to determine the Coriolis acceleration experienced at the front of the spreading debris.

Hence the front velocity was tracked at every point in the test, enabling the contribution of Coriolis to be mathematically removed to give a runout displacement with no Coriolis acting. This data is given in Table 3, in which L_c and R_c

Table 3 Centrifuge test results

Test	Model ^a volume ($m^3 \times 10^{-4}$)	H_{eff} (mm)	L_c (mm)	R_c (mm)	L_{nc} (mm)	R_{nc} (mm)	$\rho g H_{eff} / UCS$	Hardin's B_R
C9a	6.84	366	346	160	326	140	0.108	0.192
C9b	5.54	366	256	70	251	65	0.108	0.089
C10	4.63	423	342	205	313	176	0.125	0.155
C11	8.15	423	292	155	286	149	0.125	0.126
C13	8.81	423	322	185	301	164	0.125	0.195
C12	5.26	423	332	195	308	171	0.152	0.162
C14	4.69	423	317	180	285	148	0.155	0.125
C15	9.26	423	377	240	350	213	0.154	0.177
C16	8.62	423	197	60	192	55	0.149	0.055
C17	4.62	423	302	165	285	148	0.154	0.164

^aNote that prototype volume can be determined as model volume multiplied by N^3 (50^3 in these tests, see Table 1)

denote runout length and spread with Coriolis included, while L_{nc} and R_{nc} denote runout length and spread with Coriolis contribution removed.

5.5 Breakage

After each test, fragments from the experiments were collected by hand or by vacuum and sand-trap and separated into particle size ranges. Results were combined to produce particle size

distributions by mass. From those found before and after each test, a relative breakage parameter, B_R (Hardin 1985) was determined (Table 3). The parameter B_R is a measure of the clast size reduction ratio, and has been found to correlate well to normalised runout for sturzstroms and physically modelled rock avalanches (Bowman et al. 2012).

Figure 9 shows the progression of the front of a typical test, C10, arriving at the base of the cliff as taken in plan view via the high speed camera.

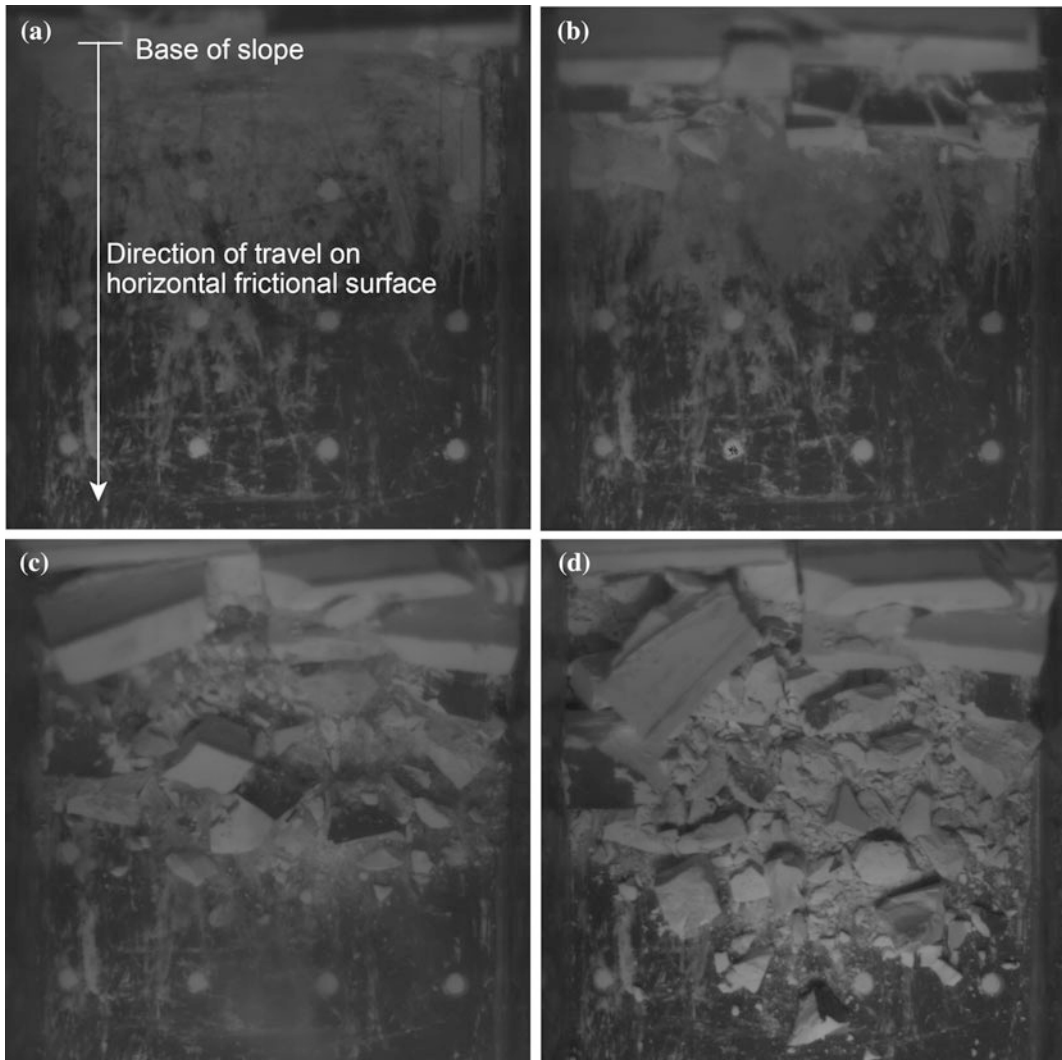


Fig. 9 Selected frames from high speed camera footage of landslide runout test C10 illustrating **a** the arrival of the blocks at the base of the slope, **b** impact and clast breakage, **c** spreading of fragmented debris, and **d** flow arrest

Key stages of (a) the arrival of the chalk blocks at the base of the cliff, (b) impact and clast breakage, (c) spreading and (d) flow arrest are indicated with time. The source volume, originally consisting of eight 22 mm (length upslope) 92 mm (width across slope) × 38 mm (height) blocks has experienced considerable fragmentation into a debris field of a wide range of smaller particle sizes (note: for scale, the horizontal field of view of the high speed camera is 200 mm in width).

6 Discussion

6.1 Scaling

Figure 10 shows the field data previously plotted in Figs. 3 and 5 along with the physical model

experimental data. For the experimental data, the plot symbols differentiate between tests conducted at 60° and 70° and between saturated and unsaturated cases. The volume of the physical model experiments is scaled up from model to prototype scale by a factor of N^3 as linear geometry is scaled as N (Table 1). In Fig. 10a–c, in which the ratio of fall height to runout is plotted against volume, it is notable that the physical model data do not compare well with the field cases—plotting well below the field data in terms of volume, and offset above the field data in the case of (a) or below the field data in the case of (b) and (c). This might appear to suggest that the centrifuge experiments scale inappropriately for the problem considered. However if one plots the data as normalised spread against energy ratio, as in Fig. 10d, it is evident that the data lie closely within the upper and lower bounds defined by the field cases (see Fig. 5). It

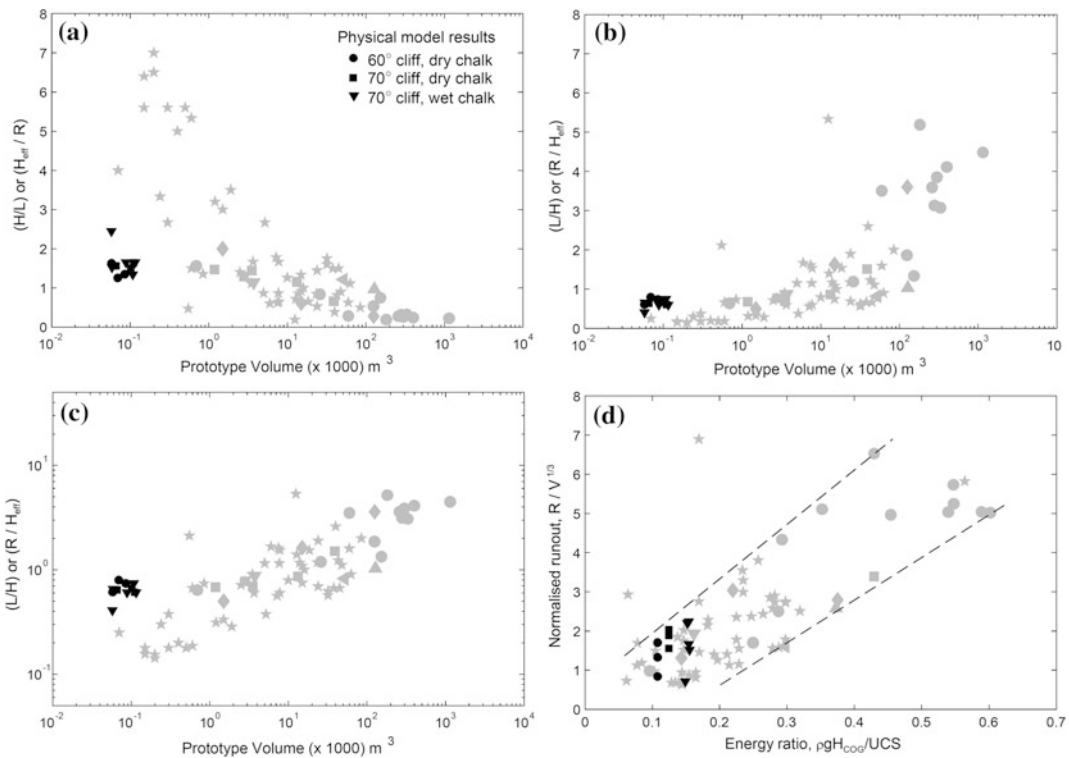


Fig. 10 Comparison of distal reach of chalk landslide debris observed in physical model experiments to database of field case studies expressed using correlations based on landslide volume and energy ratio

therefore seems promising to considering the behaviour of chalk cliff collapse via dimensionless energy and spread.

Regarding Fig. 10d, the degree of scatter of experimental data appears to be similar to that of the field data. The tests conducted at 70° plot with a higher energy ratio than those conducted at 60° because the fall height is greater for these tests. Saturated tests also plot with a higher energy ratio because the bulk density is greater. However, a higher degree of saturation does not necessarily result in greater runout, as might be expected if elevated pore pressures were a factor in reducing the effective stress and therefore flow resistance for the tests. Instead the runout may be governed by the alternative mechanism of dynamic fragmentation.

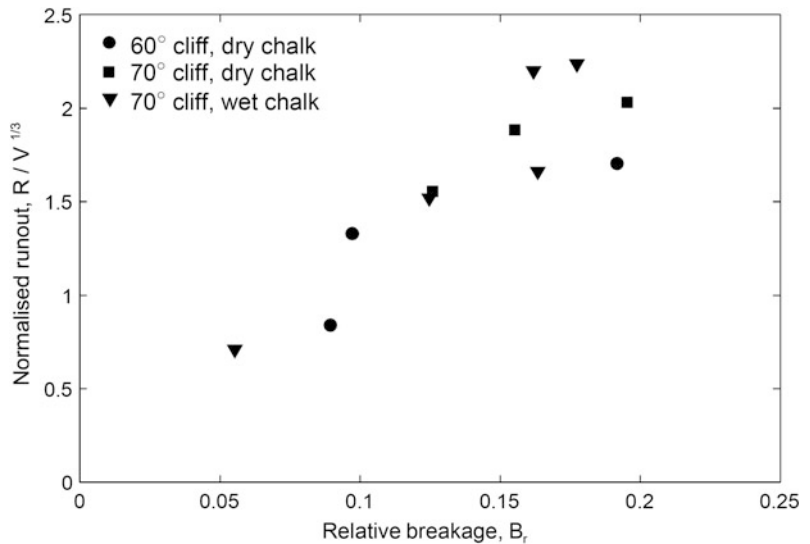
For the experimental data, while individual blocks were not tested for UCS, the chalk blocks all were cut from the same larger block of chalk, so it is not expected that the porosity varied greatly. On the other hand, the data presented in Fig. 4 show that while the porosity and UCS of chalk are related, there is a reasonable degree of scatter around the mean trend. The scatter of both

case study and experimental data plotted in Fig. 10, appears to reflect the relative crudeness of the UCS-porosity relationship.

6.2 Dynamic Fragmentation

In order to determine the influence of clast fragmentation on the extent of debris spread, the experimental data are plotted in Fig. 11 as normalised runout against Hardin’s relative breakage parameter B_R (Hardin 1985). For clarity, only data corrected for Coriolis are plotted. The figure shows a clear relationship between the parameter B_R , a measure of the clast size reduction ratio, and normalised runout (assuming a linear relationship, correlation coefficient $R = 0.88$). An interrogation of the data (i.e. a comparison of runout values listed in Table 3 with source block geometry in Fig. 8) does not reveal any particular influence of block arrangement or saturation on the runout or breakage behaviour, although there is a tendency for the 70° slope cases (with one notable exception) to produce the greatest runout. This may be

Fig. 11 Observed increase in normalised runout with increased fragmentation, as quantified using the concept of relative breakage



attributable to the slightly higher energy input due to the higher release of blocks and reduction in friction on the steeper slope.

7 Conclusions

To understand the behaviour of chalk cliff collapses, it is better to plot spreading efficiency $R/V^{1/3}$ against energy ratio $\rho gH/UCS$ rather than H/L against the volume of the event. Using this method constrains the expected maximum reach and least reach that the debris will travel, as well as establishing an expected mean response. In the absence of directly obtained data, the energy ratio may be obtained for chalk from a correlation of saturated UCS with average porosity of the cliff in question.

We performed physical model tests to investigate the influence of intact block geometry, saturation, and topography on chalk cliff collapse runout. The experimental results reinforce the use of the energy ratio concept and suggest that increased moisture may be more important as a trigger of cliff collapse in chalk than as an influence on the resulting runout.

The qualitative and quantitative behaviour of chalk collapse field events and the strong relationship between relative breakage B_R and spreading efficiency in the experimental results, shows that chalk collapses behave rather like rock avalanches in terms of propagation and emplacement mechanisms. The differences are that the chalk is relatively weak in comparison to most rock types, the fall height much smaller and the geometry of the runout path generally much simpler and shorter. This final point may indicate reasons for the one qualitative difference between rock avalanche and chalk flow deposits—that the degree of fragmentation is greater at the distal ends of rock avalanches, while the reverse appears to occur for chalk collapses. The short drop and near-horizontal travel path of chalk cliff collapses may preclude on-going fragmentation at the base of the chalk with distance. Indeed, high speed camera footage of the experiments shows the base of the chalk generally shooting

outward once impacting with the base, ahead of the collapsing debris above it. The result is that it is not continuously loaded once the initial impact has occurred, which would lead to further fragmentation—resulting in relatively large chalk blocks at the distal end of the collapse.

Note that physical model tests only modelled the post failure behaviour of the cliff—i.e. it was assumed that the collapsing element had already detached itself from the rest of the cliff. In addition, a greater initial (scaled) fall height than is generally observed at field scale was used in the tests to generate particle breakage at the cliff base. While this single-impact loading may not be entirely realistic, it enabled high strain rates to be generated within the mass, which were necessary to produce dynamic fragmentation of the chalk, leading to greater runout via generation of high particle velocities upon fragmentation, a process that undoubtedly occurs within field scale events under more complex geometric conditions. It should be noted that the relatively close packing of blocks in their initial configuration will also have assisted in the transfer of momentum between the blocks [as observed by (Manzella and Labiouse 2009)] and their fragmenting components during runout—which would be expected to lead to greater spreading efficiency than otherwise.

Physical model tests exhibited the same range of scatter in terms of normalised distal reach as found in field case histories, although the degree of fragmentation correlated very well with the normalised runout. Block geometry may play a role in the dynamic fragmentation of the collapsing mass, leading to greater or lesser runout as observed in the experiments, however there was no clear trend observable in the data for these tests. Further work may serve to elucidate this influence. Future centrifuge tests carried out at higher g -level and with larger masses may also enable more realistic and complex scenarios to be investigated and further examination of these mechanisms.

Acknowledgements Experimental work for this project was funded by the Royal Academy of Engineering, UK, via a postdoctoral research fellowship award. The authors

wish to thank Dr Kevin Stone of the University of Brighton for providing chalk samples for the experiments and would like to express their gratitude to the technicians at the Schofield Centre, University of Cambridge.

References

- Bowman ET, Take WA, Rait KL, Hann C (2012) Physical models of rock avalanche spreading behaviour with dynamic fragmentation. *Can Geotech J* 49(4):460–476
- Bowman, Take (2015) The runout of chalk cliff collapses in England and France—Case studies and physical model experiments landslides. 12(2):225–239
- Carter PG, Mallard DJ (1974) A study of the strength, compressibility, and density trends within the chalk of South East England. *Q J Eng Geol Hydrogeol* 7:43–55. doi:10.1144/GSL.QJEG.1974.007.01.03
- Corominas J (1996) Angle of reach as a mobility index for small and large landslides. *Can Geotech J* 33:260–271
- Cruden DM, Hungr O (1986) The debris of the Frank Slide and theories of rockslide—avalanche mobility. *Can J Earth Sci* 23:425–432
- Cruden DM, Varnes DJ (1996) Landslide types and processes. In: Turner AK, Shuster RL (eds) *Landslides: investigation and mitigation*, vol Special Report 247. Transportation Research Board, Washington DC, pp 36–75
- Davies TR, McSaveney MJ (1999) Runout of dry granular avalanches. *Can Geotech J* 36:313–320
- Davies TRH, McSaveney MJ (2009) The role of dynamic rock fragmentation in reducing frictional resistance to large landslides. *Eng Geol* 109:67–79
- De Blasio FV, Crosta GB (2013) Simple physical model for the fragmentation of rock avalanches. *Acta Mech* (August). doi:10.1007/s00707-013-0942-y
- Duperret A, Genter A, Mortimore RN, Delacourt B, De Pomerai MR (2002) Coastal rock cliff erosion by collapse at Puys, France: the role of impervious marl seams within chalk of NW Europe. *J Coast Res* 18(1):52–61
- Duperret A, Genter A, Martinez A, Mortimore RN (2004) Coastal chalk cliff instability in NW France: role of lithology, fracture pattern and rainfall. In: Mortimore RN, Duperret A (eds) *Coastal chalk cliff instability*, vol 20. Engineering Geology Special Publications, Geological Society of London, London, pp 33–55
- Duperret A, Taibi S, Mortimore RN, Daigneault M (2005) Effect of groundwater and sea weathering cycles on the strength of chalk rock from unstable coastal cliffs of NW France. *Eng Geol* 78:321–343
- Garnier J, Gaudin C, Springman SM, Culligan PJ, Goodings DJ, Konig D, Kutter BL, Phillips R, Randolph MF, Thorel L (2007) Catalogue of scaling laws and similitude questions in geotechnical centrifuge modelling. *Int J Phys Model Geotech* 7(3):1–23
- Hardin BO (1985) Crushing of soil particles. *J Geotech Eng* 111(10):1177–1191
- Hénaff A, Lageat Y, Costa S, Plessis E (2002) Le recul des falaises crayeuses du Pays de Caux: détermination des processus d'érosion et quantification des rythmes d'évolution. *Géomorpho Relief Processus Environ* 2:107–118
- Hobbs PRN, Flint RC, Balson PS, Entwisle DC, Forster A (1999) Slope stability assessment of the cliff behind the Beachy Head lighthouse. BGS technical report
- Hsu KJ (1978) Albert Heim: observations on landslides and relevance to modern interpretations. In: Voight B (ed) *Rockslides and avalanches 1. Natural phenomena*, vol 1. Elsevier, New York, pp 71–93
- Hutchinson JN (1988) General report: morphological and geotechnical parameters of landslides in relation to geology and hydrogeology. In: Paper presented at the 5th international symposium on landslides, Lausanne, pp 3–35
- Hutchinson JN (2002) Chalk flows from the coastal cliffs of northwest Europe. In: Evans SG, DeGraff JV (eds) *Catastrophic landslides: effects, occurrence, and mechanisms*, vol 15. Reviews in engineering geology. Geological Society of America, Boulder, Colorado, pp 257–302
- Hutchinson JN, Bromhead EN, Lupini JF (1980) Additional observations on the Folkesone Warren landslides. *Q J Eng Geol Hydrogeol* 13:1–31
- Katsaros KI (2008) The long-term stress-strain behaviour of chalk. PhD thesis, University of Brighton, Brighton
- Lautridou JP, Letavernier G, Linde K, Etlicher B, Ozouf JC (1986) Porosity and frost susceptibility of flints and chalk: laboratory experiments, comparison of 'glacial' and 'periglacial' surface texture of flint materials, and field investigations. In: Paper presented at the The Scientific Study of Flint and Chert, Brighton Polytechnic, 10–15 Apr 1983
- Leddra MJ, Jones ME (1990) Steady-state flow during undrained loading of chalk. In: Paper presented at the international chalk symposium, Brighton, 4–7 Sept 1989
- Ledwith M, Cohen T (2012) The crumbling cliffs of Dover: now France is even further away as thousands of tons of chalk crash into sea after frost and drought. Daily mail <http://www.dailymail.co.uk/news/article-2114912/White-Cliffs-Dover-Thousands-tons-chalk-crash-sea-large-section-collapses.html>. Accessed 30 July 2012
- LIFE_97_ENV/UK/000510 (2000) Geotechnical study area G16, Criel-sur-Mer, Seine Maritime, France. EU project: coastal change, climate and instability, vol 2
- Locat P, Couture R, Leroueil S, Locat J, Jaboyedoff M (2006) Fragmentation energy in rock avalanches. *Can Geotech J* 43:830–851
- Lord JA, Clayton CRI, Mortimore RN (2002) Engineering in chalk. CIRIA report, vol C574. Construction Industry Research and Information Association, London
- Manzella I, Labiouse V (2009) Flow experiments with gravel and blocks at small scale to investigate

- parameters and mechanisms involved in rock avalanches. *Eng Geol* 109(1–2):146–158
- Matthews MC, Clayton CRI (1993) Influence of intact porosity on the engineering properties of a weak rock. In: Paper presented at the geotechnical engineering of hard soils—soft rocks, Athens, 20–23 Sept 1993
- Mitchell G (2011) Large section of White Cliffs near Dover crashes into sea. Demotix. <http://cdn3.demotix.com/news/548741/large-section-white-cliffs-near-dover-crashes-sea>. Accessed 30 July 2012
- Mortimore RN, Fielding PM (1990) The relationship between texture, density and strength of chalk. In: Paper presented at the international chalk symposium, Brighton, pp 109–132
- Mortimore RN, Pomerol B, Foord R (1990) Engineering stratigraphy and palaeogeography for the chalk in the Anglo-Paris basin. In: Paper presented at the international symposium on chalk, Brighton, pp 47–62
- Mortimore RN, Lawrence J, Pope D, Duperret A, Genter A (2004a) Coastal cliff geohazards in weak rock: the UK chalk cliffs of Sussex. In: Mortimore RN, Duperret A (eds) Coastal chalk cliff instability, vol 20. Engineering Geology Special Publications, Geological Society of London, London, pp 3–31
- Mortimore RN, Stone KJ, Lawrence J, Duperret A (2004b) Chalk physical properties and cliff instability. In: Mortimore RN, Duperret A (eds) Coastal chalk cliff instability, vol 20. Engineering Geology Special Publications, Geological Society of London, London, pp 75–88
- Rat M, Schaeffner M (1983) Classification des craies et conditions de réutilisation en remblai. *Bulletin de Liaison des Laboratoires des Ponts et Chaussées* 123 (2770):65–74
- Scheidegger AE (1973) On the prediction of reach and velocity of catastrophic landslides. *Rock Mech* 5 (4):231–236
- Soil Mechanics Ltd (2001) Laboratory testing and records of additional borehole RC9599. Rail link engineering and Eurolink JV, channel tunnel rail link-medway crossing and north downs tunnel (unpublished), vol 3. Report No. 108230/3
- Steedman RS (1995) Dynamics. In: Taylor RN (ed) Geotechnical centrifuge technology. Blackie Academic & Professional, London
- Talesnicka M, Shehadeh S (2006) The effect of water content on the mechanical response of a high-porosity chalk. *Int J Rock Mech Min Sci*. doi:10.1016/j.ijrmms.2006.07.016
- Talesnicka ML, Hatzorb YH, Tsesarsky M (2001) The elastic deformability and strength of a high porosity, anisotropic chalk. *Int J Rock Mech Min Sci* 38:543–555
- Taylor RN (ed) (1984) Geotechnical centrifuge technology. Blackie Academic & Professional, London
- Williams RBG, Robinson DA, Dornbusch U, Foote YLM, Moses CA, Saddleton PR (2004) A Sturzstrom-like cliff fall on the chalk coast of Sussex, UK. In: Mortimore RN, Duperret A (eds) Coastal chalk cliff instability, vol 20. Engineering Geology Special Publication, Geological Society of London, London, pp 89–97

TXT-tool 3.007-1.1

Mechanical-Mathematical Modeling and Monitoring for Landslide Processes

Valentina Svalova

Abstract

Mechanical-mathematical model of high viscous fluid was used for modeling of the matter movement on landslide slopes. Equation of continuity and approximated Navier–Stokes equation for slow motions in a thin layer of the matter were used. The results of modelling give possibility to define the place of highest velocity on landslide surface, that could be the best place for monitoring post failure position. The proposed model can be used for comparison of calculated and measured velocities of the matter and gives possibility to investigate some fundamental aspects of the matter movement on landslide slope.

Keywords

Landslides · Modelling · Monitoring

Contents

1 Introduction.....	315
2 Mechanical-Mathematical Model.....	316
3 Conclusion.....	318
References.....	318

1 Introduction

Landslides process is one of the most widespread and dangerous processes in the urbanized territories. The landslide process activation took place in Moscow in past few years. Such com-

pllicated situation demands development of new investigations of landslide prone zones.

One of the methods of studying the landslide processes is Mechanical-mathematical modelling of gravitational movement of the matter on landslide slope. At different stages of the process development the landslide movement can be described by various mechanical and rheological models. At the stage of formation of cracks, losses of stability, break of blocks of the models of the elastic medium and model of destruction are applied. During slow movement of soil on the slope the model of high viscous incompressible fluid can be used. Such model allows to calculate velocities of movement in the layer of the matter and to compare them with results of velocity monitoring. Boundary conditions of the problem

V. Svalova (✉)
Sergeev Institute of Environmental Geoscience RAS,
Ulansky per., 13, PB 145, Moscow 101000, Russia
e-mail: inter@geoenv.ru

also depend on concrete situation. So, the condition of sticking is used on the bottom border of the layer in case of slow movement. The condition of sliding or more complex boundary condition is possible on the bottom border, if the process of debris flow, underwater landslide or snow avalanche is considered. The choice of adequate model of the process and statement of initial and boundary conditions are the special mechanical problems.

Our approach is close to works of Fathani and Nakamura (2005), Lang and Nakamura (1998), Nakamura and Fathani (2002), Nakamura et al. (1989), Suzuki (2001), Tsurugaya (2001).

2 Mechanical-Mathematical Model

Let's consider movement of landslide masses on the slope as movement of high viscous incompressible fluid described by equation of Navier-Stokes and continuity:

$$\frac{d\vec{v}}{dt} = \vec{F} - \frac{1}{\rho} \text{grad}p + \frac{\mu}{\rho} \Delta \vec{v}$$

$$\text{div } \vec{v} = 0$$

\vec{v} —vector of velocity, F —force of gravity, p —pressure, ρ —density, μ —viscosity, t —time.

Such a model can be successfully used for the lithosphere movements simulation (Svalova 1975) and for soil movements on the slope (Fathani and Nakamura 2005). The problem is to estimate effective viscosity for real matter. It can be done by comparison of calculated and measured velocities of the matter movements.

Let the characteristic horizontal scale of a body of landslide L considerably surpasses its thickness h . We shall count also a landslide extended enough in the plan that allows to consider three-dimensional model as two-dimensional one for sections of landslide bodies. Following works (Svalova 1975, 1992, 1993; Svalova and Sharkov 1992) and applying the method of decomposition on small parameter,

it is possible to get the equation of continuity and an approximated equation of the Navier–Stokes in dimensionless form for slow motions in a thin layer:

$$\begin{cases} \frac{\partial P}{\partial X} = \alpha \mu \frac{\partial^2 U}{\partial Z^2} \\ \frac{\partial P}{\partial Z} = -\rho \\ \frac{\partial U}{\partial X} + \frac{\partial W}{\partial Z} = 0 \\ \alpha = \frac{F}{R \left(\frac{h}{L}\right)^3} \\ R = \frac{u_0 L \rho_0}{\mu_0} \\ F = \frac{u_0^2}{gL} \end{cases}$$

P is dimensionless pressure, U , W —dimensionless velocities, F —Frude number, R —Reynolds number, ρ —density, μ —viscosity, ρ_0 , μ_0 , u_0 —scales of density, viscosity and velocity.

Then it is possible to get the velocities and pressure in the layer:

$$P = \rho(\zeta^* - Z)$$

$$U = U_0 + \frac{\rho}{2\alpha\mu} \frac{\partial \zeta^*}{\partial X} \left[(\zeta^* - Z)^2 - (\zeta^* - \zeta_0)^2 \right]$$

$$W = W_0 + \frac{\partial U_0}{\partial X} (\zeta_0 - Z) + \frac{\rho}{\alpha\mu} \frac{\partial^2 \zeta^*}{\partial X^2} \left[\frac{1}{6}(\zeta^* - Z)^3 + \frac{1}{3}(\zeta^* - \zeta_0)^3 - \frac{1}{2}(\zeta^* - Z)(\zeta^* - \zeta_0)^2 \right] + \frac{\rho}{2\alpha\mu} \left(\frac{\partial \zeta^*}{\partial X} \right)^2 (Z - \zeta_0)^2 + \frac{\rho}{\alpha\mu} \frac{\partial \zeta^*}{\partial X} \frac{\partial \zeta_0}{\partial X} \zeta_0 (\zeta^* - \zeta_0)$$

ζ_0 the bottom border of the layer,
 ζ^* the top border.

Let on the bottom border the condition of sticking is satisfied:

$$U_0 = W_0 = 0$$

The discharge of matter along the layer is:

$$Q = \int_{\zeta_0}^{\zeta^*} Udz = -\frac{\rho}{3\alpha\mu} \frac{\partial \zeta^*}{\partial X} (\zeta^* - \zeta_0)^3$$

Since $Q = \text{const}$ along the X , then:

$$\frac{\partial Q}{\partial X} = 0$$

$$\frac{\partial^2 \zeta^*}{\partial X^2} (\zeta^* - \zeta_0)^3 + \frac{9\alpha\mu Q}{\rho} \left[\frac{3\alpha\mu Q}{\rho} + (\zeta^* - \zeta_0)^3 \frac{\partial \zeta_0}{\partial X} \right] = 0$$

The condition of convexity of upper boundary is:

$$\frac{\partial^2 \zeta^*}{\partial X^2} < 0 \Rightarrow \frac{3\alpha\mu Q}{\rho} > -(\zeta^* - \zeta_0)^3 \frac{\partial \zeta_0}{\partial X}$$

This condition enables to analyze the form of the surface of moving matter (Fig. 1).

Structure of clinoforms (convex) can arise, if:

1. Q is large, that is flux is high
2. μ is large. It means that matter spreads bad and can support big angle
3. ρ is small. It means that matter has large specific volume and is friable
4. $\text{grad } \zeta_0$ is small, that is angle of lower boundary is small
5. $(\zeta^* - \zeta_0)$ is small, that is thickness of sedimentary layer is small. Under fixed Q it means that velocity of flux is high and

formation of clinoforms and even overturning of rocks are possible.

All these conditions seem to be natural enough for explanation of formation of structures such as inflows and clinoforms of sedimentary cover that validates the model.

It is important to define the place of maximal velocity on the slope. An optimum place for location of monitoring post is the point of maximal speeds of movement of landslide masses.

Let's consider the massif of sedimentary rocks with the top border ζ^* representing landslide slope. The bottom border ζ_0 is compatible with an axis X . The maximum of horizontal speed U is reached on the top border ζ^* of the massif according to condition:

$$\frac{\partial U}{\partial Z} = -\frac{\rho}{\alpha\mu} \frac{\partial \zeta^*}{\partial X} (\zeta^* - Z) = 0 \Rightarrow Z = \zeta^*$$

Point of the maximal horizontal speed on the surface ζ^* can be found from condition of equality to zero of the first derivative:

$$\frac{\partial U^*}{\partial X} = 0, \text{ where } U^* = -\frac{\rho}{2\alpha\mu} \frac{\partial \zeta^*}{\partial X} (\zeta^*)^2$$

From here it is easy to receive the condition:

$$\frac{\partial^2 \zeta^*}{\partial X^2} \zeta^* + 2 \left(\frac{\partial \zeta^*}{\partial X} \right)^2 = 0 \tag{1}$$

It is necessary to stress, that $\zeta^*(X)$ is known function—the surface of landslide slope. And the

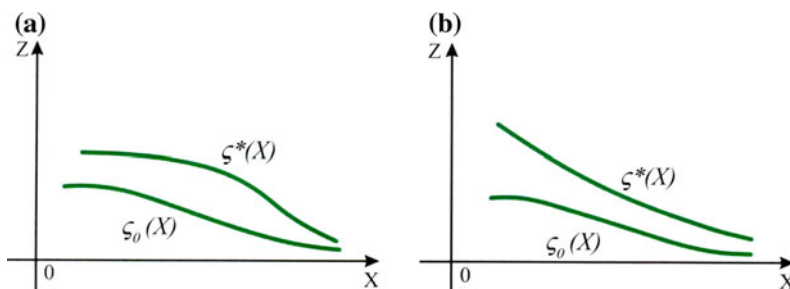


Fig. 1 Sketches of dimensionless landslide surface. Various possible forms of landslide ground surfaces: **a** convex, **b** concave

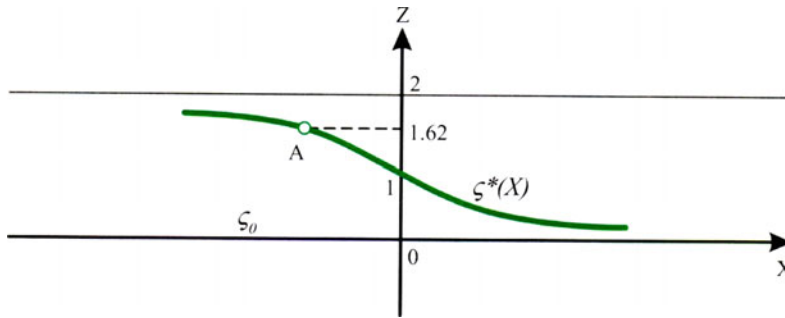


Fig. 2 Sketch of dimensionless slope surface. Point A is the point of maximal horizontal speed of movement of masses on the ground surface of the slope

received condition allows to find a point on a slope where speed of movement is maximal.

Let's consider for illustration of the received decision the surface of landslide as (Fig. 2):

$$\zeta^*(X) = -thX + 1$$

It reflexes roughly the form of landslide surface.

Then the condition (1) gives:

$$th^2X - thX - 1 = 0$$

Whence we receive $thX = \frac{1-\sqrt{5}}{2}$ and

$$\zeta^* = \frac{1 + \sqrt{5}}{2} \approx 1.62$$

Such position of the point of the maximal horizontal speed seems to be real, and more exact data on the structure of landslide and its surface will enable to define such point on a concrete slope. The point of maximum speed on a slope defines the place of possible failure of a landslide in case of achievement of limiting pressure in mass of rocks.

There could be several points of local maximum speed on a slope, that characterizes an opportunity of failure of a landslide on each terrace of a slope.

The places of minimum speed can be used for building constructions and oil-gas pipelines.

Model velocities of matter can be compared with real velocities that gives possibility to define the real mechanical parameters of media.

3 Conclusion

Mechanical-mathematical model of high viscous fluid is elaborated for simulation of matter movement on landslide slopes. The results of modelling give possibility to define the place of highest velocity on landslide surface, which could be the best place for monitoring post failure position. Model can be used for comparison of calculated and measured velocities and estimation of effective viscosity of real matter that is subject of future research. The results of modelling give possibility to investigate some fundamental aspects of landslide matter movement.

References

- Fathani TF, Nakamura H (2005) Numerical analysis of the movement distance and velocity of landslides. In: Proceedings of the international conference on landslides, Vancouver, Canada, p 10
- Lang YH, Nakamura H (1998) Characteristics of slip surface of loess landslides and their hazard area prediction. *J Jpn Landslide Soc* 35(1):9–18
- Nakamura H, Fathani TF (2002) Hazard area prediction for landslide debris. In: Proceedings of the tenth

- international conference and fieldtrip on landslide, Krakow, pp 129–142
- Nakamura H, Tsunaki R, Ishihama S (1989) Simulation model for debris movement of landslides. In: Proceedings of the Japan–China symposium on landslides and Debris Flows, Niigata, Tokyo, pp 81–86
- Suzuki K (2001) Estimation of the travel distance of landslide debris in granite area. Master thesis at Tokyo University of Agriculture and Technology, Tokyo, pp 32–47
- Svalova VB (1975) The models of the lithosphere movements. Ph.D. thesis at Moscow State University, p 130
- Svalova VB (1992) Mechanical-mathematical models of the formation and evolution of sedimentary basins. *Sci.de la Terre Ser Inf Nancy* 31:201–208
- Svalova VB (1993) Mechanical-mathematical simulation of geological structures evolution. *Geoinformatics* 4 (3):153–160
- Svalova VB, Sharkov EV (1992) Mantle diapirs and surface depression in back-arc areas: a rheological model. *Ofiolity* 17(1):165–170
- Tsurugaya K (2001) Study of the occurrence and flow mechanism of the large-scale landslides caused by an earthquake. Master thesis at Tokyo University of Agriculture and Technology, Tokyo, pp 80–108

TXT-tool 3.081-1.6

Manual for the Undrained Dynamic-Loading Ring-Shear Apparatus

Hendy Setiawan, Kyoji Sassa, Khang Dang, Maja Ostric,
Kaoru Takara and Martina Vivoda

Abstract

The development of the ring shear device was upgraded since 2010, particularly for the loading system. Previous version of the ring shear apparatus of DPRI series has a long loading frame consists of pillars and beam for the normal stress system. Recently, loading piston through the single central axis was applied for the normal stress in the newest version of ring shear apparatus. There are two version of this new apparatus, called the ICL-1 and the ICL-2. The ICL-1 version was developed since 2010 as a part of SATREPS project for 'Risk identification and land-use planning for disaster mitigation of landslides and floods in Croatia.' Meanwhile, the development of the ICL-2 was carried out since 2012 as a part of SATREPS project between Japan and Vietnam for 'Development of landslide risk assessment technology along transportation arteries in Vietnam'. As for practical purpose, both version of the undrained dynamic-loading ring-shear apparatus were designed in a small dimensions (compare with DPRI series) but with high performances. Thus, shallow landslide as well as deep landslide can be simulated geotechnically using this apparatus. In this paper, the structure, control and loading system of the apparatus are described in detail. The testing procedures and data analysis of ring shear tests are also explained.

H. Setiawan (✉) · K. Takara
Disaster Prevention Research Institute, Kyoto
University, Uji 611-0011, Japan
e-mail: hendy@flood.dpri.kyoto-u.ac.jp

K. Takara
e-mail: takara.kaoru.7v@kyoto-u.ac.jp

K. Sassa · K. Dang
International Consortium on Landslides, 138-1,
Tanaka Asukaicho, Sakyo-Ku, Kyoto 606-8226,
Japan
e-mail: sassa@iclhq.org

K. Dang
VNU University of Science, Hanoi, Vietnam
e-mail: khangdq@gmail.com

M. Ostric
Croatian Waters, Rijeka, Croatia
e-mail: ostric.maja@gmail.com

M. Vivoda
Faculty of Civil Engineering, University of Rijeka,
Rijeka, Croatia
e-mail: martina.vivoda@uniri.hr

Keywords

Ring shear apparatus ICL series • Loading system • Undrained cyclic test
Monotonic stress control test • Seismic test • Pore pressure control test

Contents

1	Introduction	322
2	Concept of the Ring Shear Apparatus	323
3	Structure and Control System	327
3.1	Monitoring System.....	330
3.2	Loading System.....	331
4	Testing Procedure	334
4.1	Sample Preparation.....	334
4.2	Gap Adjustment and Shear Box Saturation....	334
4.3	Checking of the Degree of Saturation.....	335
4.4	Sample Consolidation.....	335
5	Shearing	335
5.1	Speed Control Test.....	335
5.2	Stress Control Test.....	335
6	Sample Removal and Cleaning	338
7	Data Analysis	339
7.1	Speed Control Results.....	342
7.2	Cyclic Test Results.....	342
7.3	Seismic Test Result.....	344
7.4	Pore Pressure Control Test Results.....	345
8	Conclusion	347
	Appendices	347
	References	350

1 Introduction

Historically, the ring shear device was firstly introduced by Hvorslev in 1939, where samples in a predefined plane at the interface of upper and lower confining rings was sheared. This concept then used and improved by several researchers such as Bishop et al. (1971), Bromhead (1979), Savage and Sayed (1984), Hungr and Morgenstern (1984), Sassa (1984), Tika (1989) and Garga and Infante Sedano (2002). The ring shear apparatus that was developed by Bishop and his colleagues in 1971 is widely adopted. Bishop's ring shear apparatus was aimed to study the post peak shear resistance and shear displacement, particularly for the case of clayey soils in slow landslides. Seven designs of the ring shear apparatus had been developed by Sassa and his colleagues since 1984 in the Disaster Prevention

Research Institute (DPRI) of Kyoto University (Sassa et al. 2004). The high speed ring shear apparatus DPRI-1 used a conventional shear-speed control motor although it cannot produce cyclic shear-stress loading. The seismic loading was successfully reproduced by using DPRI-3 as the first dynamic-loading ring-shear apparatus (Sassa 1996). Afterwards, the following versions of DPRI series (up to DPRI-7) has enable to conduct monotonic test as well as dynamic loading test in undrained conditions.

The project called 'Risk identification and land-use planning for disaster mitigation of landslides and floods in Croatia' was launched in 2009 by SATREPS (Science and Technology Research Partnership for Sustainable Development) Program between the Government of Japan and Croatia. This project was initiated as a part of the cooperation program of UNESCO, Kyoto University and ICL-UNITWIN (International Consortium on Landslides—University Twinning and Networking Programme of UNESCO) and identified as the IPL-161 by the International Consortium on Landslides. One part of this project is aim to produce the ring shear apparatus that enable to simulate the landslide initiation and motion and to investigate the residual shear resistance along sliding surface at a large shear displacement. The apparatus called ICL-1 (ICL stands for International Consortium on Landslides) was developed for this project (Oštrić et al. 2012b). After development, the ICL-1 was donated in 2012 to the University of Rijeka in Croatia. Another SATREPS project was launched in 2012, called 'Development of landslide risk assessment technology along transportation arteries in Vietnam', conducting between the Government of Japan and Vietnam. The apparatus called ICL-2 was developed as a part of this project. After several tests and improvement system, this apparatus was donated

to the Institute of Transport Science and Technology (ITST) of the Ministry of Transport, Vietnam in 2015.

Although has similar structure, control and monitoring system, both ICL-1 and ICL-2 have different in maximum undrained capacity and the maximum shear speed. This paper describes the detailed features and testing procedures of both apparatus as the undrained dynamic-loading ring-shear apparatus. In addition, this paper aims as an updated manual from the previous internal use manual of the Portable Ring Shear Apparatus ICL-1 (Oštrić et al. 2012a, c; Oštrić 2013).

2 Concept of the Ring Shear Apparatus

The main purposes of the DPRI series of ring shear apparatus is to simulate all the entire processes of landslide mechanism from the shear failure of soil sample, post-failure motion in the form of shear displacement, pore pressure generation in undrained condition and mobilized shear resistance up to the steady state condition. All these processes were resulted from static loading as a manifestation of rainfall or dynamic loading as an earthquake. The ICL version of ring shear apparatus has similar function with the DPRI series, but has smaller dimensions and higher performances. The ICL undrained dynamic loading ring shear apparatus was developed inexpensively, transportable with a standard electricity supply that can be used anywhere. The ICL-1 could perform normal stress up to 1 MPa, while the ICL-2 stands for normal stress up to 3 MPa. The observation of pore-water pressure generation in the ICL-1 was reached of 1 MPa, with 3 MPa for the ICL-2, all in undrained condition. Within these capacities, the apparatus is suitable to investigate either shallow landslides or large deep-seated landslides. Structure of the undrained dynamic-loading ring-shear apparatus has separable parts that can be easily transported and re-assembled in laboratory (Fig. 1):

- *Instrument box*, consists of the upper shear box (inner and outer), lower (rotatable) shear box which is integrated with three servo motors for normal stress, shear stress and gap control, vertical displacement sensor, shear displacement sensors, gap sensor, load cells for normal stress and shear resistance, and pore-water pressure transducers.
- *Main control unit as control and monitoring box*, consists of servo amplifier to give the feedback signal loading from servo motor of the instrument box to the control box and vice versa.
- *Computer system*, with monitor for setting the test, controlling the apparatus and recording data measurement. Recently, the data acquisition and control is provided through software version 6.0.5823.29888 for portable ring shear apparatus ICL-1 and version 6.0.5850.32247 for ICL-2 (it all updated gradually in line with the improvement system of the apparatus).
- *De-aired system*, which provides the de-aired water to supply to the ring shear box during saturation process, and the vacuum tank to prepare the samples that immersed with de-aired water before placing to the ring shear box (in a moist placement method).
- *Pore pressure supply system*, consists of gear box with servo motor for pore pressure control test (Fig. 2). The servo motor is connected to the servo amplifier in the main control unit.

The landslide simulation concept using the undrained dynamic-loading ring shear apparatus is illustrated in Fig. 3 where the samples are taken from the susceptible sliding surface or landslide mass. The samples then poured into the installed shear box of the apparatus. The normal stress and shear stress loading due to gravity, cyclic stress, seismic loading, and or pore pressure can be applied within samples inside the shear box.

Fundamentally, the stresses conditions in the slope are well represented in the ring shear apparatus (Fig. 4). By considering a soil column

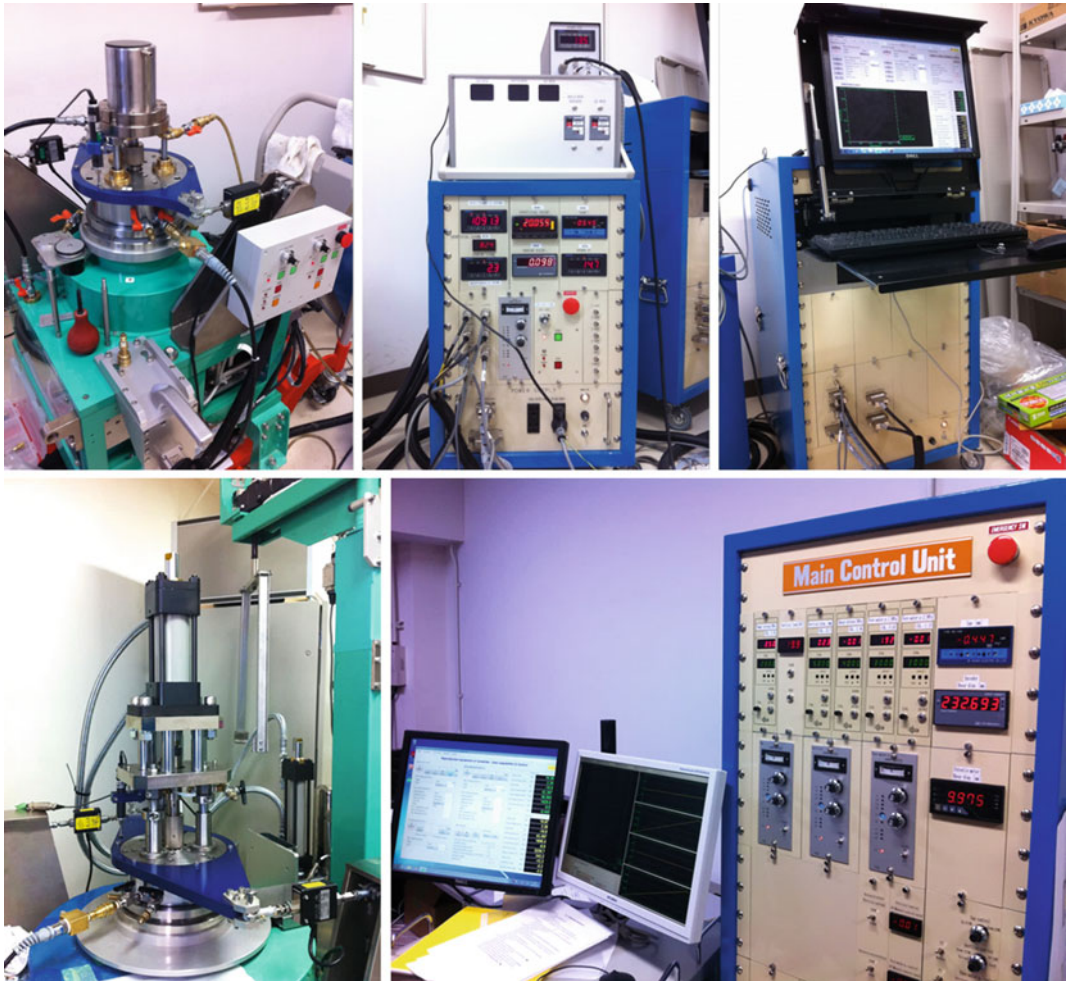


Fig. 1 Overview of the undrained dynamic loading ring shear apparatus, the ICL-1 (top) and ICL-2 (bottom), both shows the ring shear box unit, main control unit and

computer system. Recently, normal stress system in the ICL-1 is changed similarly to the ICL-2

per unit width along the slope, the vertical stress acting on the slope is the soil mass (m) multiplied by the gravity (g). Due to gravity, the normal stress is denoted as $\sigma_0 = m \cdot g \cdot \cos \theta$ and the shear stress is $\tau_0 = m \cdot g \cdot \sin \theta$, where θ is the slope inclination.

The initial stress point in the slope before rain or earthquake is I (σ_0, τ_0) (Fig. 4). When the earthquake with acceleration (a) occurs, the seismic force of $m \cdot a$ is applied. During the seismic loading, the stress path is represented either as the total stress path (TSP) where the pore pressure is not generated, or as the effective stress path

(ESP) considering the effect of pore pressure generation. If the shear stress is loaded parallel to the slope inclination then the direction of TSP is vertical. However, due to pore pressure generation, the effective stress path will shift to the failure line. This path indicates the landslide initiation in the field. In the ring shear apparatus, when the samples fails due to loading, a shear surface generates inside samples in the interface between upper loaded shear box and lower rotated shear box. The shear failure development following post-failure motion has resulted excess pore-water pressure, mobilized shear resistance

Fig. 2 The de-aired system (left) and pore pressure supply system (right)

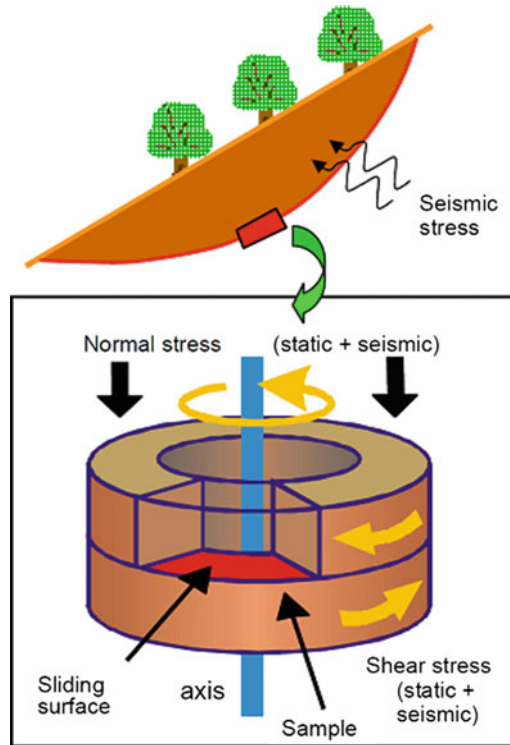
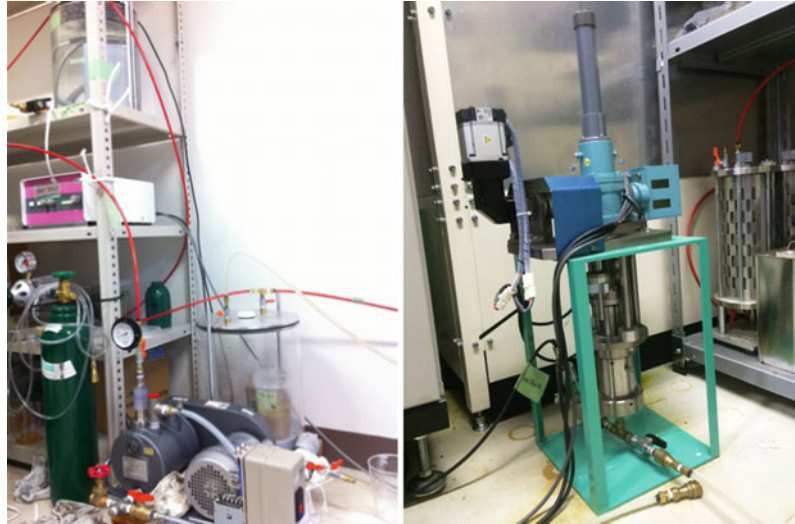


Fig. 3 Design concept of the undrained dynamic loading ring shear apparatus

and large shear displacement, which are observed by sensors and recorded in control box. The typical graph for these test results is shown in Fig. 5.

Pore pressure generation occurs in the process of grain crushing or particle breakage of soil samples in the saturated condition within shear

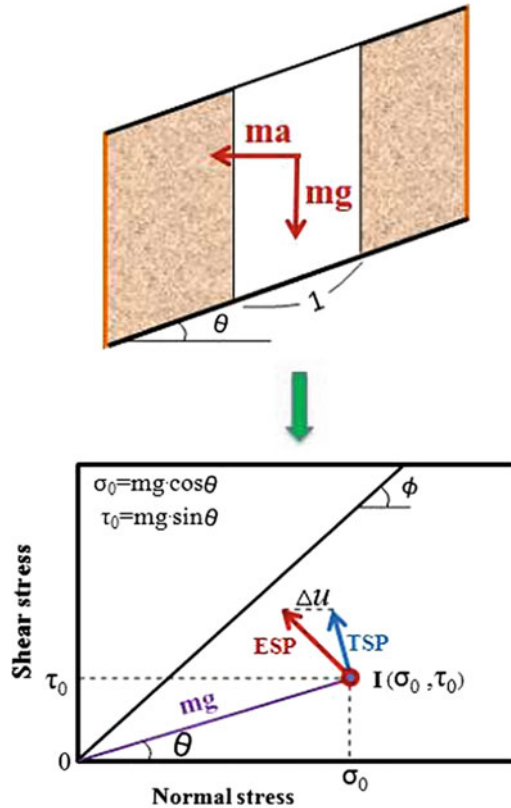


Fig. 4 Stress conditions in slope and in the ring shear apparatus

displacement and volume reduction. In that process, the stress path continues move down along the failure line during motion and reach to a steady state (SS in Fig. 5) with the mobilized friction angle of ϕ_m . The steady state shear resistance will reached when there is no further

grain crushing, no pore pressure change while the volume and shear resistance are constant.

In the steady state condition, following equation is used:

$$\tau_{ss} = \sigma_{ss} \cdot \tan \phi_m = \sigma_o \cdot \tan \phi_{a(ss)}$$

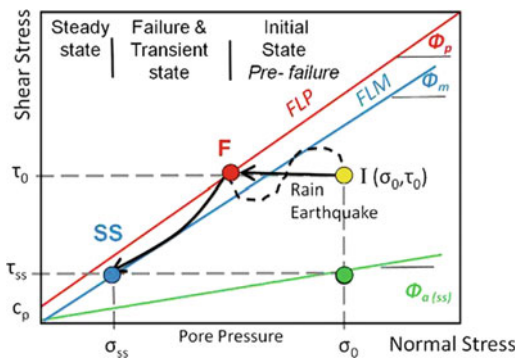


Fig. 5 Typical graph of the effective stress path resulted from undrained ring shear apparatus

where τ_{ss} , σ_{ss} and $\phi_{a(ss)}$ are the shear stress, normal stress and apparent friction coefficient at the steady state condition. The apparent steady-state friction coefficient then expressed as the ratio of steady-state shear resistance (τ_{ss}) and the normal stress that acting on the sliding surface (σ_o) which corresponds to the total normal stress due to the soil weight at the site (σ).

$$\tan \phi_{a(ss)} = \tau_{ss} / \sigma$$

3 Structure and Control System

As designed for practical purpose, the undrained dynamic-loading ring shear apparatus ICL versions has smaller dimensions compared with previous ring shear apparatus DPRI versions (Table 1). For example, the portable ring shear apparatus ICL-1 (in Croatian project) has dimension of 500 × 500 mm, height of 950 mm (Fig. 1) and maximum weight of 100 kg that can produce a high normal stress and pore pressure measurement of up to 1000 kPa in undrained condition, with maximum velocity of shearing reached 5.4 cm/s. In the ICL-2, the structure has enlarged due to the larger capacity in normal stress (3000 kPa) and shear velocity (50 cm/s) though the loading principal is similar to the ICL-1. Instead of using a large and tall loading frame which consumes a lot of space like in the DPRI versions, the normal stress in ICL versions

are loaded by pulling the central axis within the apparatus (Fig. 6). A 200-W servo-motor is used for normal stress loading and a 400-W servo-motor for shear stress. This servo-motor capacity can be fulfilled by using a 100–200-V single-phase electrical supply to accommodate the maximum shear velocity of 5.4 cm/s (ICL-1) and 50 cm/s (ICL-2).

The most important part of the ring shear apparatus is the annular undrained shear box. Figure 7 shows the design of shear box with enlarged diagram of the left half of the cross section, including the water-pressure measurement system. Soil sample is placed inside between the upper inner and outer ring shear box, restrained up to the lower ring shear box, forming the annulus or ‘doughnut’ like shape. Then soil sample is loaded through annular loading plate which connected to the oil piston. The inner shear box of the ICL-1 has diameter of 100 mm and the outer shear box is of 140 mm, resulting the shear area approximately of 75.36 cm². The ICL-2 has 100 mm of inner shear box and 142 mm of outer shear box, with the shear area of 79.79 cm². The lower height of the shear box (h_1) consists of porous metal part and rubber edge, with the depth can be adjusted around 163, 133 or 103 mm depends on the number of porous metals which are placed on the bottom. The upper part of the shear box has height (h_2) which depends on the sample-volume change during consolidation (explained in “Appendix 3”).

Table 1 Features of the undrained dynamic loading ring shear apparatus ICL versions

Specification	Unit	ICL-1	ICL-2
<i>Shear box</i>			
– Inner diameter	cm	10.0	10.0
– Outer diameter	cm	14.0	14.2
Maximum height of sample	cm	5.2	5.2
Ratio of maximum height/width	–	2.60	2.48
Shear area of sample	cm ²	75.36	79.79
Maximum shear speed	cm/s	5.4	50
Maximum normal stress	kPa	1000	3000
Maximum pore-water pressure	kPa	1000	3000
Resolution of gap control system	mm	0.001	0.001
Maximum data acquisition rate	Per second	1000	1000
Maximum frequency of loading	Hz	20	20

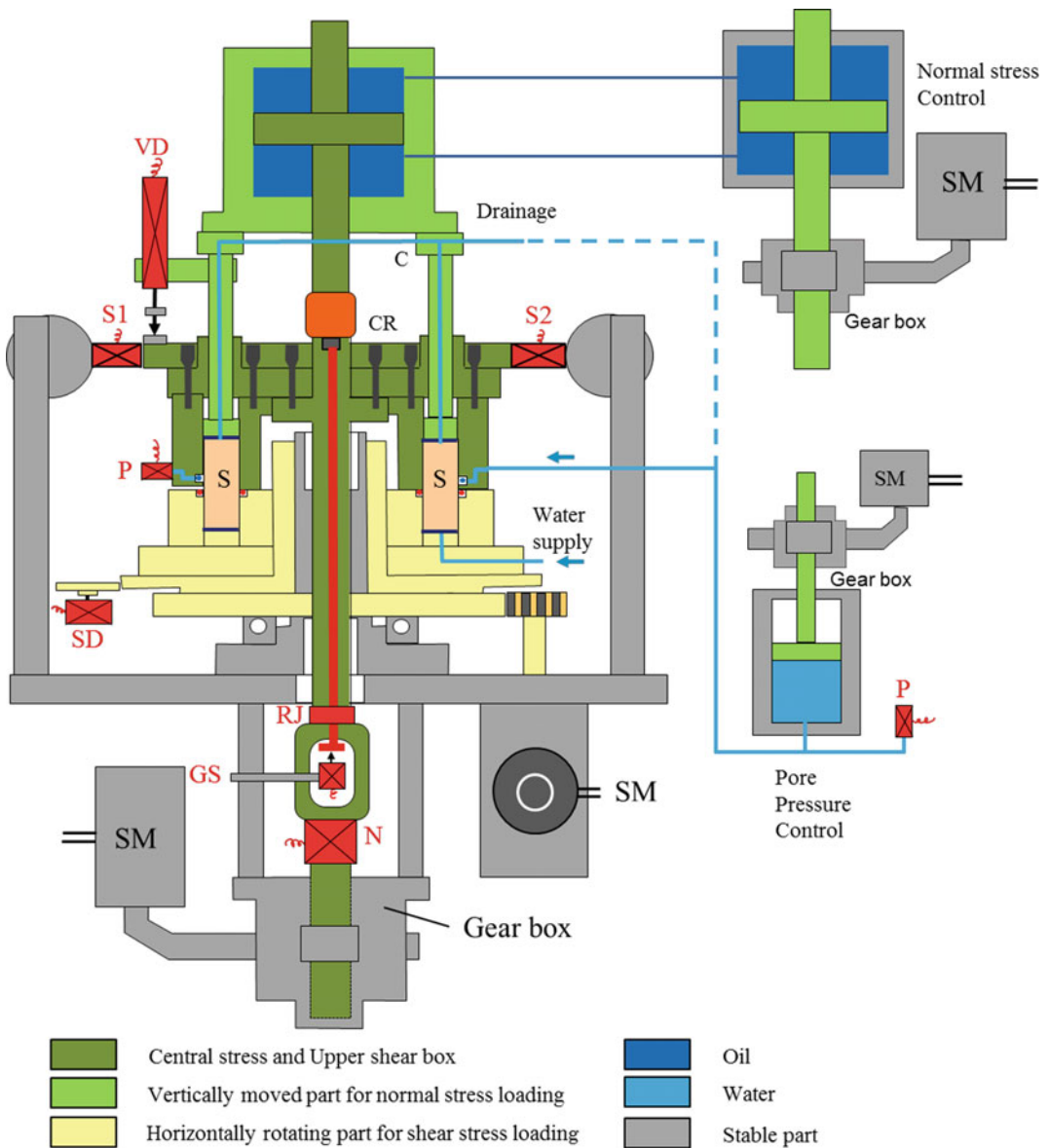


Fig. 6 Mechanical structure (central section of the main body) of the undrained ring shear apparatus: *S* sample, *CR* connection ring, *N* load cell for normal stress, *C* connection, *GS* gap sensor, *S1* and *S2* load cells for shear

resistance, *VD* vertical displacement, *P* pore pressure transducer, *SD* shear displacement, *RJ* rotary joint, *SM* servo motor. The ICL-1 and ICL-2 has the same structure

The minimum sample height after consolidation should be around 33–40 mm, where 20 mm is above the rubber edge. The sample height after loading or consolidation is also depends on the characteristic of the samples itself. For example, the Kostanjek marls sample (landslide in Croatia) has experienced almost 50% decreasing height

during consolidation, while only 20% found in sand samples. The loading plate cannot reach and apply the normal stress if the sample placement is not thick enough (an over-ride protection initiates when the O rings of the loading plate reaches a particular depth inside the shear box). Eight segments of a porous metal filter disks are fixed

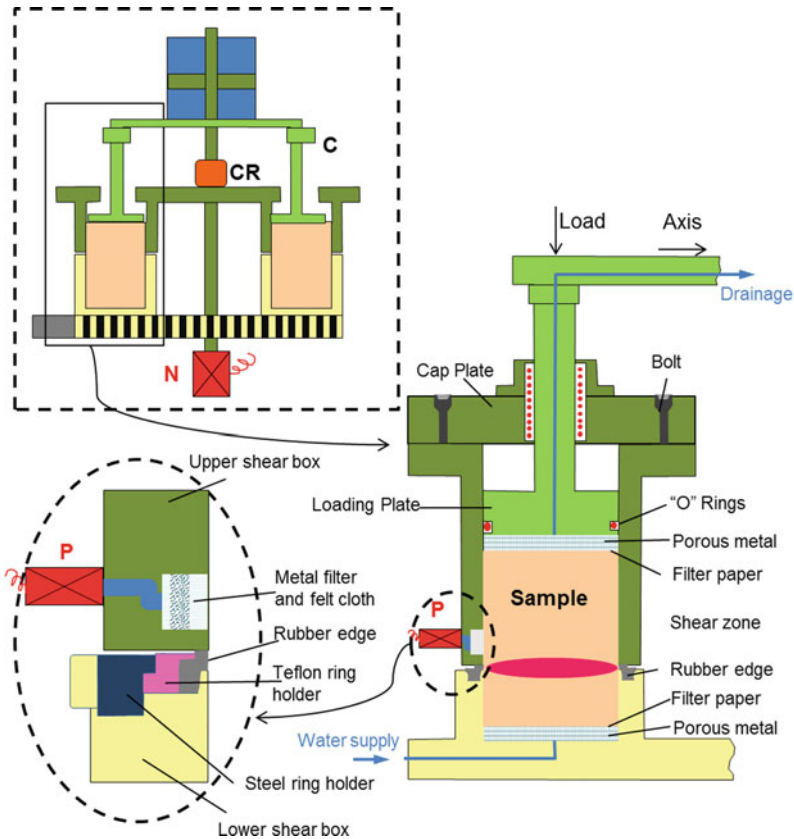


Fig. 7 Detail cross section of the shear box and a close-up diagram of the edges (*S* sample, *CR* connection ring, *N* load cell for normal stress, *C* connection, *P* pore pressure transducer)

on the base of the lower part of the shear box (between inner and outer rings) and another eight segments on the lower loading plate (LP) which face to the soil samples (Fig. 7). This porous metal filter disks are placed to allow water drains out from the shear box through upper and lower valves that opened during consolidation and drained loading conditions. Conversely, during undrained loading condition, all drainage valves are closed. Filter papers are placed between porous metal filter disks and samples to avoid fine soil particles drains out with water. In addition, eight small strips (blades) are attached on the loading plate and on the base of the shear box to prevent slippage of the samples inside the shear box.

Preventing water leakage through the gap or interface between the upper and lower shear box during consolidation as well as shear loading is

the most difficult part in conducting landslide simulation using the ring shear apparatus. To overcome such problem, the rubber edges are placed at the lower pair of the rotary rings of the shear box. In the DPRI series, rubber edges are glued to the lower pair of rings. While in the ICL versions, two rubber edges are placed and hold by Teflon rings at the lower pair of the rotary rings, while Teflon rings are fixed by steel ring holder (Fig. 7). When the rubber edges are ruined or damaged, it can be quickly replaced with new pair. Two types of rubber edges that can be installed in the ICL versions (for different loading purpose) are 2 mm wide with a hardness index of 90 and 3 mm wide with a hardness index of 65. After installed, the rubber edges are coated with Teflon spray, while bottom of the upper shear boxes that will touch the rubber edge during loading are daubed by vacuum silicon

grease. A very smooth surface of the silicon grease on the rubber edges and equal height of both outer and inner rings are extremely important.

An initial contact force is applied to make a contact pressure between the upper pair of ring shear boxes and the rubber edges on the lower part of the shear box. The contact force remained constant during the tests and maintained by a gap control system. The contact force may range from 0 to 1.5 kN, and higher contact force of about 1.5–2.0 kN is needed when a vacuum is being applied in the tests. Water inside the ring shear box then can be restrained from leakage with the help from the O-rings on the upper loading plate and the rubber edges system on the two confining rings of the lower rotary shear box.

Two pore pressure transducers (PPT1 and PPT2) are connected to the valves placed on the gutter to monitor the pore water pressure. The gutter (4 × 4 mm) is placed circumferentially on the inner wall of the upper outer ring shear box. This gutter is covered by filters and located about 3 mm above the established shear surface. A filter of felted cloth is placed between two metal filters in the gutter to prevent the outside filter clogging with clay particles. In the DPRI series, two annular metal filters with pore sizes (from inside) of 40 and 100 μm were placed in the annular gutter. Since the outer filters of 100 μm were often clogged by fine soil particles, the removable filters are introduced in the ICL versions. By unscrewing the gutter, the metal filters are enabled to remove to be cleaned or changed. Pore size of the metal filters can be chosen based on the tested soil material. For instance, metal filters in the ICL-1 were used both of 40 μm for the Grohovo samples (landslide in Croatia). However, changing the metal filters may influence permeability and dissipation time of the pore pressure.

A smaller pore pressure transducer (PPT1) is connected on the side valve of the upper outer part of the shear box which closes above the gutter. While a larger pore pressure transducer (PPT2) is connected to the valve on the gutter level. Locations of the valves and pore pressure

transducers are shown on the Photographs in “Appendix 1”.

3.1 Monitoring System

In the ICL versions, all sensors for vertical displacement (VD), shear displacement (SD), pore-pressure (P) and gap sensor (GS) are placed in the instrument box together with load cells for normal stress (N) and shear stress (S1 and S2). The instrument box connected to the monitoring box which displaying the sensor values which are real values measured directly on the sample in the shear box. The monitoring box is connected to the control box showing the test values. Test values shown in the control box are not the same as sensor values. Explanations of sensor and test values are given in “Appendix 2”.

During normal loading, the loading plate (LP) is pushed by the vertical load cylinder (VLC). The vertical load is measured by the normal load cell (N). The measured vertical load is the sum of the loads on the rubber edge, friction between the sample and the sides of the upper shear box and the weight of the upper part of the shear box (SB-Up). The normal stress acting on the shear surface is monitored by the load cell N by maintaining the verticality of the upper shear box.

The shear load acting on the shear surface is monitored by the pair of shear-load cells (S1 and S2 on Fig. 6) by maintaining the upper shear box horizontal. The shear resistance is calculated from the measured loads on the shear-load cells that keep the upper half of shear box from rotating against the loaded shear stress. The test value of the shear stress in the output file is the sum of the shear resistance mobilized during shearing and the rubber-edge friction.

The horizontal shear displacement (D_s , in mm) is monitored by a rotary shear displacement transducer (SD). The displacement in the center of the shear surface, $(r_1 + r_2)/2 = 6$ cm, is used as the shear displacement. The sensor records a maximum displacement of 94 mm (one

revolution of the lower shear box) before resetting back to zero, but the number of revolution are monitored by a counter. The maximum displacement is possible to limit through apparatus control settings.

The vertical displacement (D_v in mm) of the sample (during consolidation) is measured by a linear vertical displacement transducer (VD) which monitoring also the displacement of the loading plate (LP). This sensor is installed on the vertical load cylinder (VLC) and attached on the upper of loading plate. The vertical displacement sensor must be protected to avoid damage due to shearing and rotation. The maximum vertical displacement that can be measured is 25 mm. Manual measurements of sample height can be made during testing besides the recorded values of vertical displacement stored in the output file. Calculation of the sample height is given in the “Appendix 3”.

Computer in the control box is provided to store the data of normal stress (σ), shear stress (τ), pore pressure (u), sample height variation (D_v) and shear displacement (D_s). The ring shear apparatus is controlled by computer with data acquisition software in the control box. The output data file contains both sensors and test values also test conditions and settings. The output file is used as the input data for further analysis.

3.2 Loading System

Loading system for static and normal stresses are generated by an oil piston that controlled by a servo-motor (200 W) (Fig. 8). An electric control signal is supplied by personal computer to the normal stress servo-amplifier. The servo-motor provides a certain pressure to the oil piston corresponding to the control signal from the servo-amplifier. The feedback signal of the monitored total normal load on the potential shear surface is supplied to the servo-amplifier.

A servo-motor with capacity of 400 W generates the static and cyclic shear stresses (Fig. 8).

Similar with normal stress, the shear stress servo-amplifier receives an electric control signal that is supplied by a personal computer. The feedback signal of the monitored shear load on the shear surface is supplied to the servo-amplifier. A servo-control motor can apply the shear stress for different purpose such as shear-stress control, speed control or displacement control tests.

During setting of the shear boxes, an initial contact force between the upper pair of ring shear boxes and the rubber edges which attached to the lower rings is necessary to avoid sample and water leakage. This process is applied by lowering the gap-control oil piston to a specific value. The gap value is maintained constant automatically during the test by a third servo-motor using the feedback signal obtained from the high-precision gap sensor (GS). This third servo-motor has function to control the gap between the upper shear box and the lower shear box. Through an oil piston, the contact pressure of the rubber edge against the edge of shear box is maintained by servo-motor to be greater than the generated pore pressure within the shear box. With oil loading piston, servo-motor and gap sensor, the system in the ICL versions is provided to prevent water and sample leakage during rapid shearing.

3.2.1 Normal Stress

The vertical load is generated by an oil piston controlled by a servo-motor. The servo-motor drives the Vertical Load Cylinder (VLC) which pushes the Loading Plate (LP). The sample is loaded by the Loading Plate (LP) and the vertical load is measured by the Normal Load cell (N). The normal stress on the shear surface is equal to the measured vertical load divided by shear surface area:

$$\sigma_n = F_v/A = F_v/0.007536 = F_v \cdot 132.69$$

for the ICL-1, and

$$\sigma_n = F_v \cdot 125.33, \text{ for the ICL-2}$$

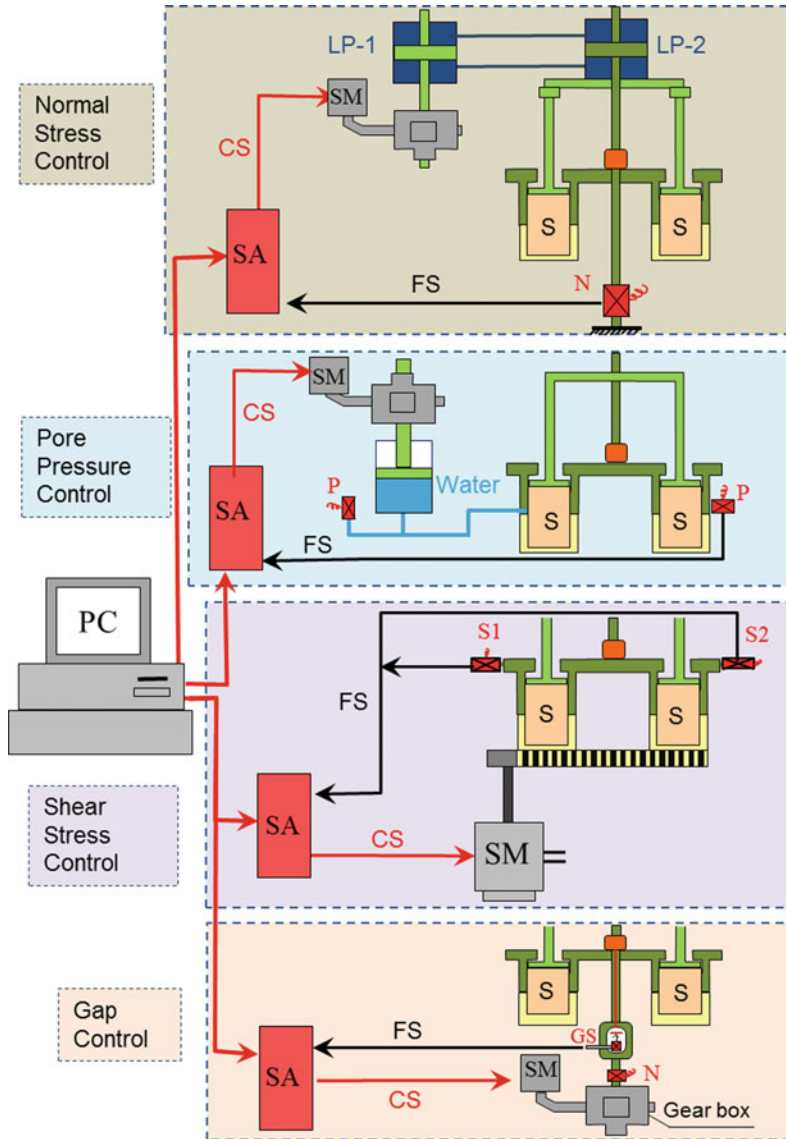


Fig. 8 Electronic control system of the ring shear apparatus ICL versions (*S* sample, *CR* connection ring, *N* load cell for normal stress, *S1*, *S2* load cell for shear resistance, *GS* gap sensor, *PC* computer, *SG* signal generator, *FS* feedback signal, *CS* control signal, *SM* servo motor, *LP* loading piston, *SA* servo amplifier)

where,

- σ_n is normal stress (kPa),
- F_v is vertical load (kN),
- A is shear surface area (m^2) which is assumed to be planar.

The maximum normal stress that the portable ring shear apparatus ICL-1 can measure is calculated from the capacity of the normal stress cell of 10 kN.

$$\begin{aligned} \sigma_{max} &= F_v \cdot 132.69 = 10 \cdot 132.69 \\ &= 1,326.90 \text{ kPa} = 1.33 \text{ MPa} \end{aligned}$$

The ring dimensions are shown in Fig. 8 with remarks below:

load (F_s) by a constant $K = 0.46$. This constant is obtained from equation below:

Inner-ring radius	$r_1 = 5 \text{ cm} = 0.05 \text{ m}$
Outer-ring radius	$r_2 = 7 \text{ cm} = 0.07 \text{ m}$ (0.071 m for the ICL-2)
Shear surface area	$A = (r_2^2 - r_1^2)\pi$

The distance between shear load cells (S1, S2) and the axis of the shear box, $R = 21 \text{ cm} = 0.21 \text{ m}$. The normal stress (σ_n) as a sensor value is obtained and shown in the monitor. The test value (σ_n^*) is different and calculated by multiplying the sensor value of normal stress by a correction factor (α).

$$\sigma_n^* = \alpha \cdot \sigma_n$$

Correction factor of the rubber edge (α) depends on soil properties, and varies between 0.8 (for fully water) and 1.0 (for rock) (Fig. 9) (Oštrić et al. 2012a).

$$F_s \times R = \int_{r_1}^{r_2} 2\pi\tau_t r^2 dr$$

$$= 2\pi\tau_t \frac{1}{3}(r_2^3 - r_1^3) = \frac{2}{3}\pi(r_2^3 - r_1^3) \times \tau_t$$

where,

- F_s is the shear load (N)
- τ_t is the shear stress total test value (kPa)
- r_2 is the outer ring radius (m)
- r_1 is the inner ring radius (m)
- R is the distance between the shear load cells (S1, S2) and the axis of the shear box.

3.2.2 Shear Resistance

The shear stress (τ_t) in the output file means the test value and calculated by multiplying the shear

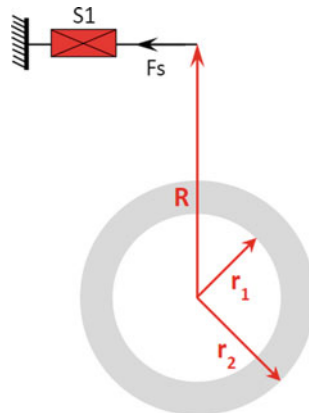


Fig. 9 Dimensions of the shear box

$$\begin{aligned}
 F_S(N) \times 0.21(\text{m}) &= \frac{2}{3} \pi (0.07^3 - 0.05^3) \times \tau_t \\
 &= 0.000457(\text{m}^3) \times \tau_t(1000 \text{ kPa}) \\
 \tau_t &= \frac{3R \cdot F_S}{2\pi(r_2^3 - r_1^3)} = 0.46 \cdot F_S
 \end{aligned}$$

The maximum shear stress that the portable ring shear apparatus ICL-1 can measure is calculated from the capacity of shear cells (S1 and S2) of 1 kN.

$$\begin{aligned}
 \tau_{\max} &= 0.462 \times 2 \times F_S \\
 &= 0.462 \times 2 \times 1000 = 920 \text{ kPa}
 \end{aligned}$$

The shear load is monitored by the two shear load cells (S1 and S2) with capacity each of 1 kN. The obtained test value of shear stress (τ_t) is the sum of mobilized shear resistance of the soil during shearing (τ) and the rubber edge friction (τ_r). To obtain the correct value of shear resistance, the rubber edge friction value is subtracted from the shear stress data in the output file.

$$\tau = \tau_t - \tau_r = (0.46 \times F_S) - \tau_r$$

where,

- τ is the shear resistance (kPa)
- τ_t is the test value of shear stress (kPa)
- τ_r is the rubber edge friction (kPa)

4 Testing Procedure

Soil samples that are used for ring shear tests can be dry or fully saturated. Different procedures are used for fully saturated samples. The procedures are described in the following sections.

4.1 Sample Preparation

In order to obtain full saturation condition, careful preparation is necessary conducted for the soil samples. The soil samples is crushed by rubber hammer and placed into a bottle/box

together with the de-aired water to avoid too much air entrainment. The usual ratio for de-aired water and soil sample is 300 ml and 500 ml. Bottle filled with samples and de-aired water then put into the vacuum water tank. In this process, bubbles of air will come out from the samples. The sample then leaves in the vacuum until bubbles of air stop coming out and the sample settles (it takes about one to two days). After settled, release slowly the vacuum from the water tank and take the bottle with prepared sample. For fine-grained samples, the preparation takes about 3 days, while 2 days is necessary for coarse-grained samples. In the case of Croatian landslides (Grohovo and Kostanjek landslides), fully saturated samples were successfully prepared by this procedure and the circulation of de-aired water through the shear box was shortening to one hour.

4.2 Gap Adjustment and Shear Box Saturation

The initial contact pressure (0.8 to 1.5 kN) between the upper pair of ring shear boxes and the rubber edges is applied by lowering the gap-control oil piston to a specific gap value. The gap value is necessary to keep in a constant to maintain undrained condition during the test and to prevent sample and water leakage during rapid shearing. Therefore, water leakage and rubber edge friction tests (using water only) are very important to carry out before sample setting and sample test.

After the upper ring shear box is attached to the rubber edge and lower rings and the gap is fixed, the empty shear box is filled first with CO₂ and followed by de-aired water. This preliminary step is necessary to prevent any entrapped air in the shear box especially in the gutter of the box. The heavier-than-air CO₂ is very slowly flowed into the shear box through the lower drainage line and discharged from the upper drainage line to displace the air (Fig. 6). After filling the shear box with CO₂, the de-aired water then inserted in the shear box with the same way as the CO₂.

4.3 Checking of the Degree of Saturation

The sample can be slowly inserted into the shear box after CO₂ and de-aired water processes. Filter papers must be placed on the bottom of the shear box before placing the sample and on the top of the sample to prevent sample seep out and clogged into the porous metal filter disks. Then, the contact of the loading plate should be made by applying a vertical load. Following the contact load, circulation of the de-aired water is carried out by gravity or suction if it is necessary. During circulation, de-aired water is supplied through the lower drainage line and discharged to the upper drainage line until all air bubbles are expelled out. After fully saturated (either in preparation phase or during the water circulation), the degree of saturation is checked by using the B_D value which is a pore pressure parameter related to the degree of saturation in the direct-shear state, and is stated as:

$$B_D = \Delta u / \Delta \sigma$$

where,

Δu is an increment of pore pressure, and
 $\Delta \sigma$ is an increment of normal stress.

The B_D values varies depend on the correction factor that is set in the application software. For fully saturated samples, B_D should be greater than 0.95.

4.4 Sample Consolidation

The initial stress state of the soil by gravity is applied after checking the degree of saturation. The sample should be normally consolidated under these pre-determined normal and shear stresses, depending on the sample depth and the slope angle. After consolidation in drained conditions has been completed, shearing can start as explained in the following chapter.

5 Shearing

The soil sample can be sheared optionally in fully drained, partially drained or undrained conditions. Drainage condition is conducted by keeping the upper valve open, while undrained condition is applied when all drainage valves are closed. The shear stress is applied by a servo-control motor under one or three optional controls: shear-stress control, shear-rate (speed) control or shear displacement control (Fig. 10). The use of speed-control test or the stress-control test depends on the purpose of the test. A speed-control test is usually used to obtain soil parameters, and stress-control test is used for simulating a landslide.

5.1 Speed Control Test

The normal and shear stresses at the steady state to get the mobilized and peak friction angles can be obtained through undrained speed control test. To observe pore pressure generation in a slow rate, a slow shear speed should be applied for fine grained materials that have a low permeability. Shear speed test can be conducted in cm/s and held constant during the test. ‘Slope’ is the time that will be taken to achieve certain constant shear speed (Fig. 11).

5.2 Stress Control Test

The stress control test is applied for landslide simulation because earthquake shaking or groundwater fluctuation as the triggering factors are associated with the stress changes within the slope. Stress control test can be conducted in static-monotonic load, dynamic-cyclic load or seismic load.

Monotonic stress is used in the process of consolidation by applying normal stress using static control mode. The initial stress conditions have to be defined before applying dynamic loading (either cyclic or seismic), namely σ_0 and

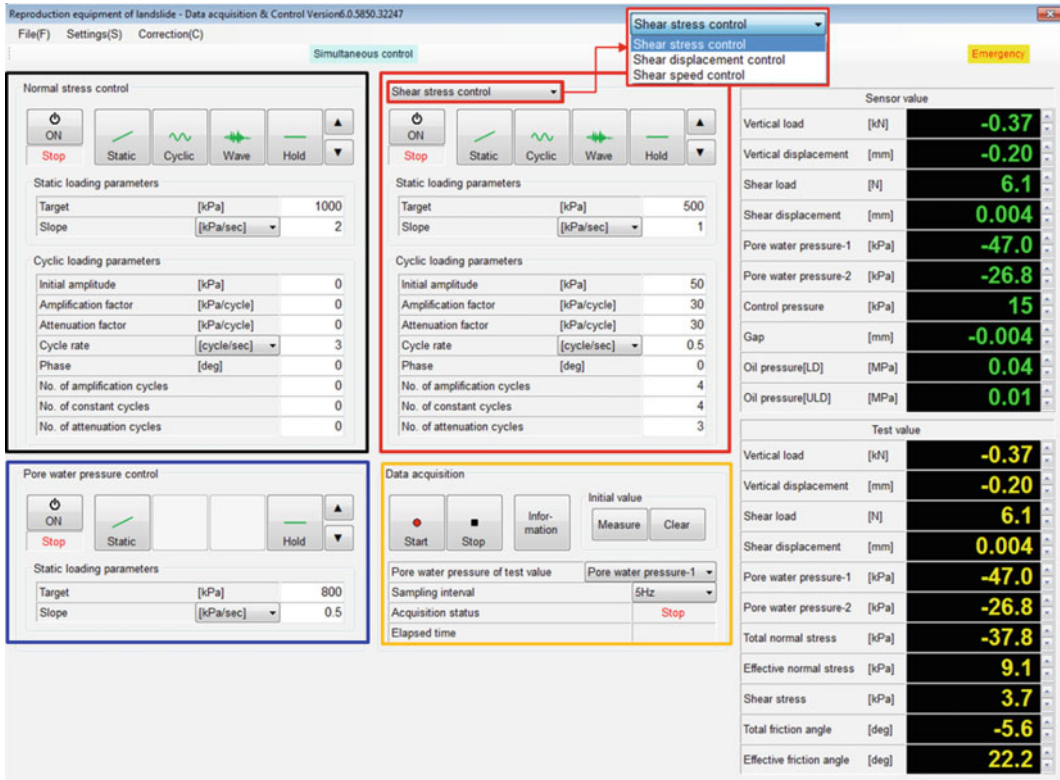


Fig. 10 Print screen of the ring shear apparatus software showing normal stress control (in black frame), shear stress control with different control modes: stress, speed

or displacement (red frame), pore water pressure control (blue frame) and data acquisition (orange frame)

τ_0 . For example $\sigma_0 = 1000$ kPa and $\tau_0 = 500$ kPa (Fig. 12). The initial normal stress represents the total of consolidation of soil sample within a certain depth, while the initial shear stress applies based on the slope angle of soil sample. Both normal and shear stresses are applied in static mode and under drained conditions. A ‘slope’ in the static-loading parameters refers to the rate of loading in kPa/s. A low rate of loading is applied for fine-grained materials with low permeability and slow pore pressure generation. While for coarse-grained materials, faster loading rate value is more preferable. Loading rate of less than 1 kPa/s (slow loading) is used for marls and clays, and a ‘slope’ greater than 1 kPa/s (fast loading) is applied for sands.

The dynamic-cyclic loading is applied after consolidation, in undrained conditions. However, the cyclic loading can be applied in partly drained or fully drained conditions. Cyclic shear

stress is conducted in a form of a sine wave in which the amplitude, period and number of cycles can be defined by cyclic loading parameters (Figs. 13 and 14).

In previous versions of the ring shear apparatus, the sine wave was defined only by an amplification factor which was terminated suddenly. The control of the cyclic load in the ICL versions of the ring shear apparatus can vary the amplification of the sine wave allowing the cyclic shear stress to be optionally increased, kept constant or decreased by independent factors (Fig. 14).

The selected cycle rate will depend on the soil properties. For fine-grained materials, slow loading in cycle/hour is preferable, while for coarse-grained materials a faster rate can be selected (cycle/min or cycle/s). The maximum cyclic shear load that can be applied is calculated from equation below:

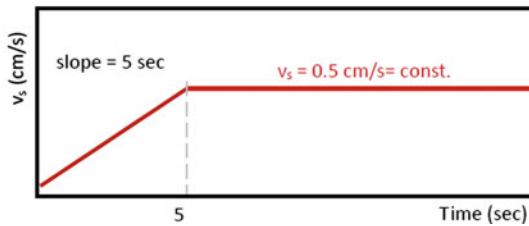
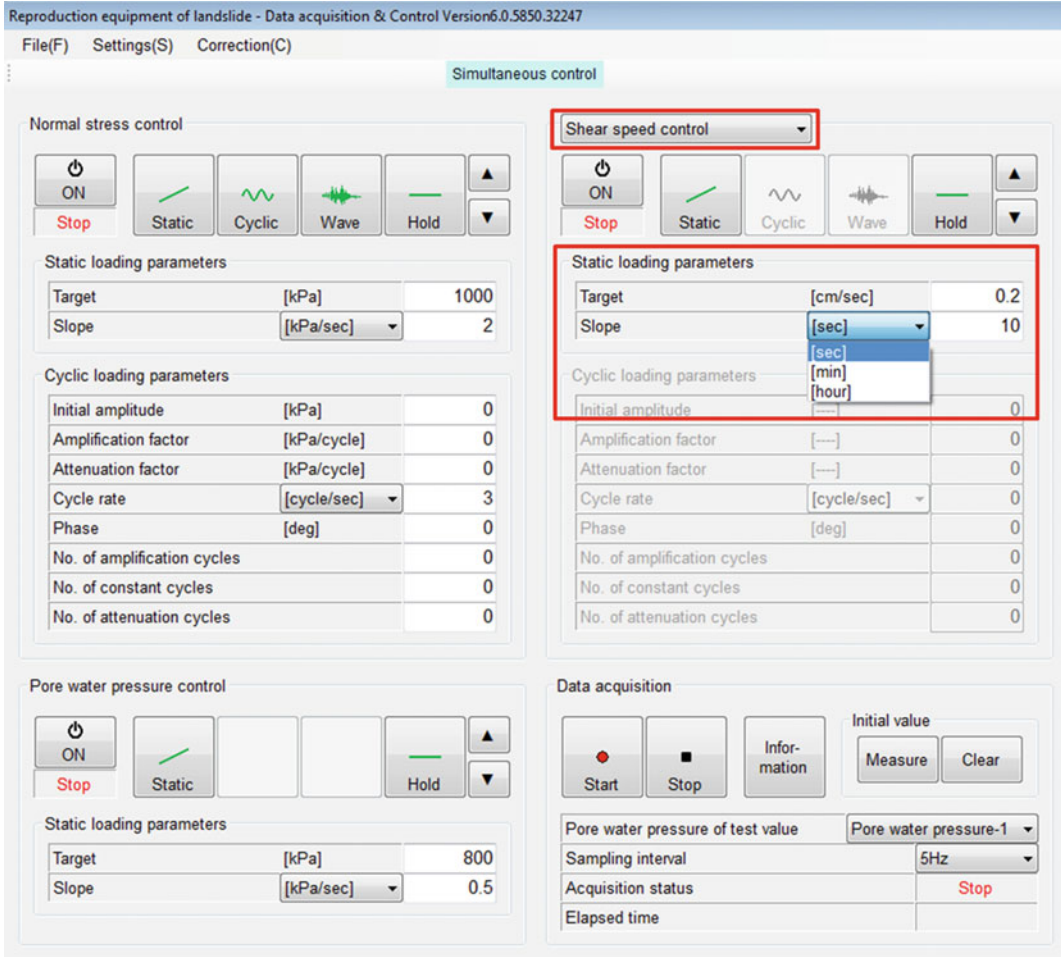


Fig. 11 Speed-control mode and functions in the software application with the graph explaining the slope to reach constant shear speed

$$\tau_{max} = \tau_0 + N_{am} \cdot \Delta\tau_{am}$$

where,

- τ_{max} is the maximum applied shear stress,
- τ_0 is the initial shear stress,
- N_{am} is the number of amplification cycles,
- $\Delta\tau_{am}$ is the amplification increment.

Rapid stress changes like earthquakes in the field can be simulated using the ICL versions through rapid loading with a high-speed data acquisition (Figs. 15 and 16). A simulated seismic wave can be reproduced with data-acquisition rate of up to 50 Hz.

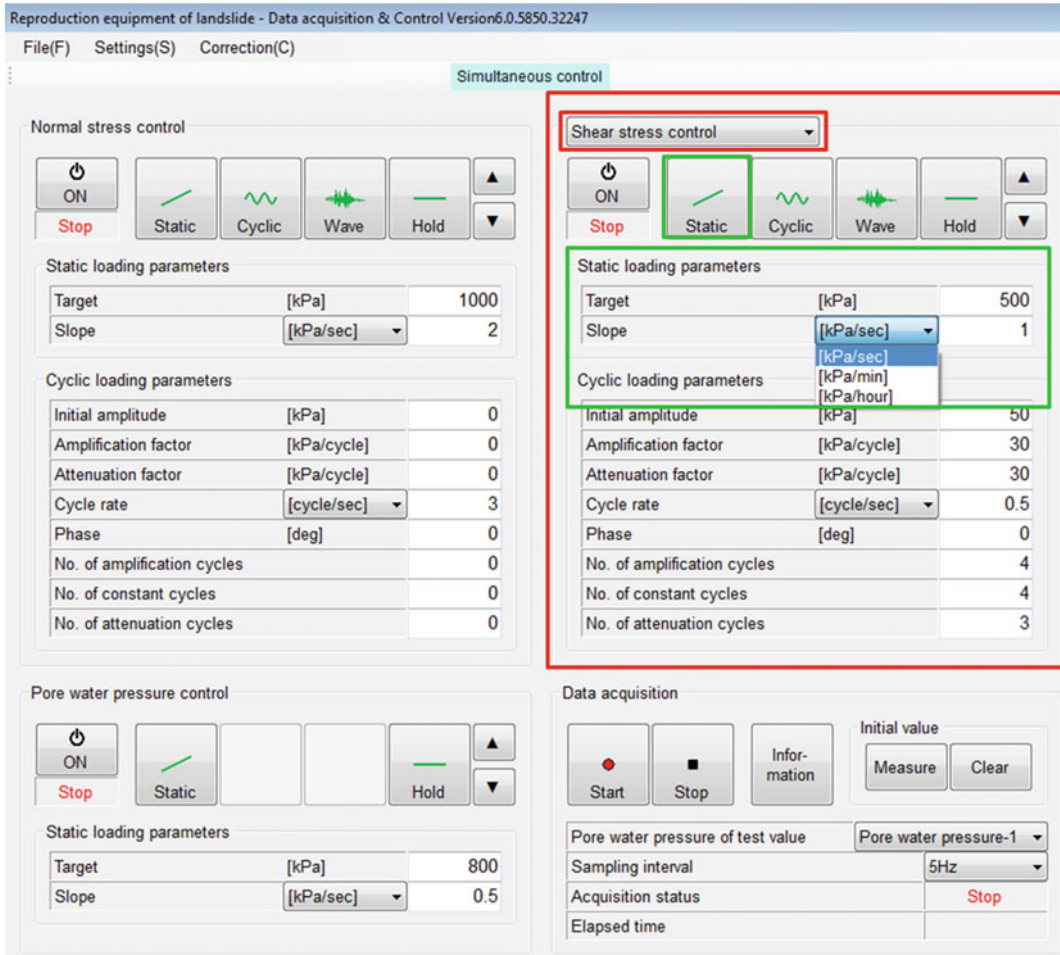


Fig. 12 Shear stress control mode in the software application (red frame) and static loading parameters (green frame)

The seismic waves real records are include high frequency waves with high accelerations (up to 2699 gal at peak for the 2011 Tohoku earthquake). The shear stress control servo motor (400 W) in the portable apparatus ICL-1 cannot reproduce the high frequency of loading and acceleration. Because of its limitations, scale factor and output intervals are used to modify the real seismic record. In the example of the Tohoku earthquake, 30% of the normal stress component of the real wave (2699 gal × scale factor 0.3 = 810 gal), and 30 times longer of time scale interval were used (Fig. 17).

6 Sample Removal and Cleaning

After conducting test series, it is important to de-install carefully all parts of the apparatus and then clean them neatly to prevent damage. Cleaning process is a must particularly for the upper-outer part of the shear box and its gutter which can be filled with fine-grained material from the test samples. All parts of the ring shear apparatus can be cleaned using water, brush, vacuum cleaner and acetone (Fig. 18). The rubber edge needs to be carefully cleaned by using

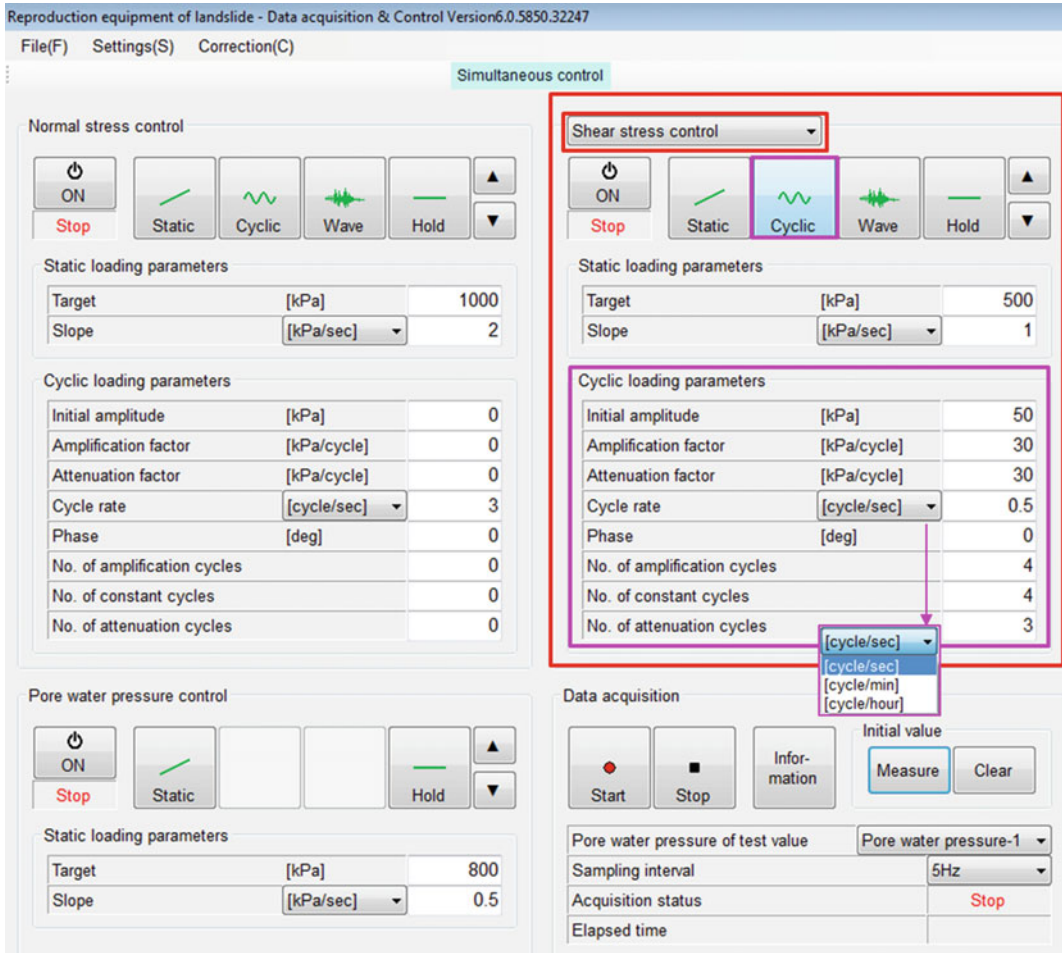


Fig. 13 Shear stress control mode in the software application (red frame) with the cyclic loading parameters (magenta frame) for cyclic loading

acetone to remove all of the Teflon spray and Silicon grease that used in the test. After cleaning, the upper-outer part of the shear box and the loading plate are immersed with water in the washbasin (Fig. 19). Special attention must be given to the gutter as the most important part in pore pressure measurement, as well as metal filters in the loading plate and on the base of the shear box (Fig. 20).

The O-ring gutter is necessary to clean periodically by carefully removed from the gutter which is also cleaned as well. The O-ring gutter should be cleaned with acetone with the help of tweezers or a pincette. If some fine material or sand remains adhering to an O-ring or gutter, it

can cause leakage of water and sample. Moreover, fine particles can possibly enter to the space between lower rings, Teflon ring and rubber edges due to the use of vacuum or during pore pressure control test. Thus, the inner and outer of lower rings should also be dismantled and cleaned periodically.

7 Data Analysis

All measured data from ring shear tests are controlled and recorded by the software application of Portable ring shear apparatus—Data acquisition and control—Version 6.0.5823.29888

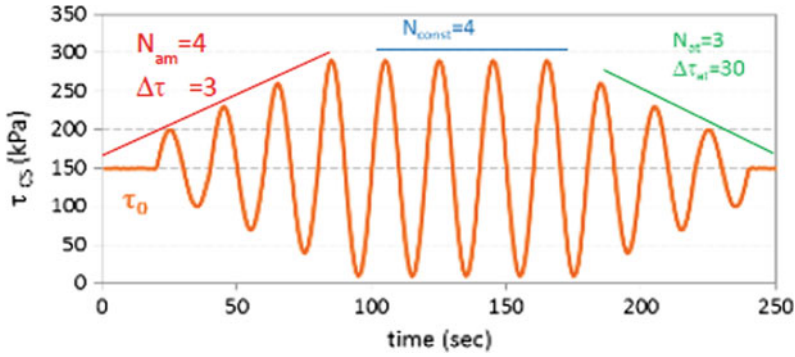


Fig. 14 Diagram of time and shear stress applied for cyclic loading

Reproduction equipment of landslide - Data acquisition & Control Version 6.0.5850.32247

File(F) Settings(S) Correction(C)

Simultaneous control

Normal stress control

ON [Static] [Cyclic] [Wave] [Hold] [▲] [▼]

Static loading parameters

Target	[kPa]	1000
Slope	[kPa/sec]	2

Cyclic loading parameters

Initial amplitude	[kPa]	0
Amplification factor	[kPa/cycle]	0
Attenuation factor	[kPa/cycle]	0
Cycle rate	[cycle/sec]	3
Phase	[deg]	0
No. of amplification cycles		0
No. of constant cycles		0
No. of attenuation cycles		0

Shear stress control

ON [Static] [Cyclic] [Wave] [Hold] [▲] [▼]

Static loading parameters

Target	[kPa]	500
Slope	[kPa/sec]	1

Cyclic loading parameters

Initial amplitude	[kPa]	50
Amplification factor	[kPa/cycle]	30
Attenuation factor	[kPa/cycle]	30
Cycle rate	[cycle/sec]	0.5
Phase	[deg]	0
No. of amplification cycles		4
No. of constant cycles		4
No. of attenuation cycles		3

Pore water pressure control

ON [Static] [Hold] [▲] [▼]

Static loading parameters

Target	[kPa]	800
Slope	[kPa/sec]	0.5

Data acquisition

Start [Stop] [Information] [Initial value: Measure] [Clear]

Pore water pressure of test value: Pore water pressure-1

Sampling interval: 5Hz

Acquisition status: Stop

Elapsed time:

Fig. 15 Stress control mode in the software application (red frame) and seismic mode (magenta frame) with parameters for input of seismic wave data

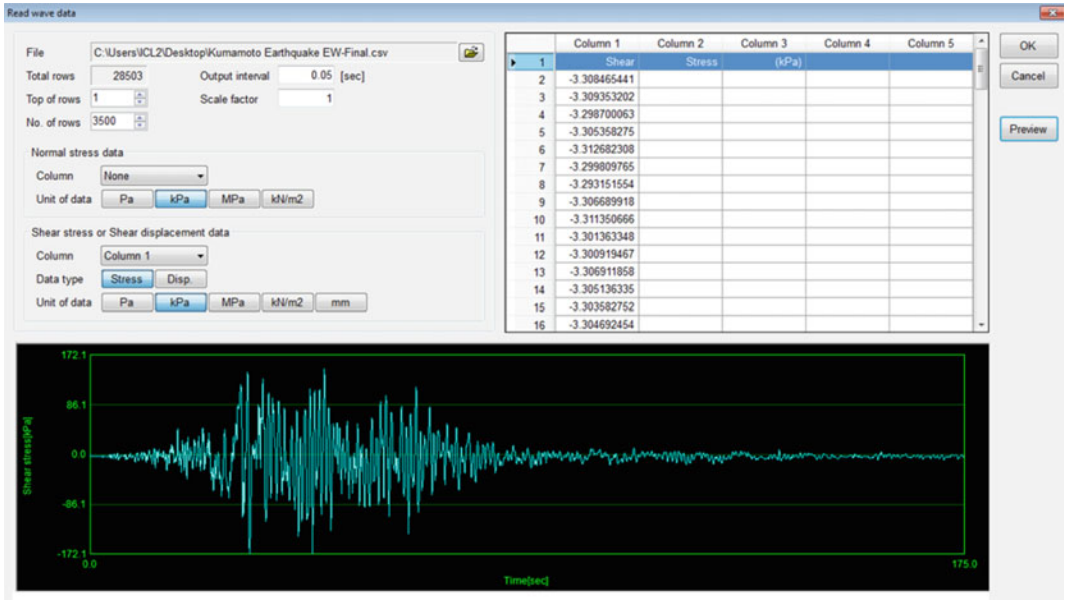


Fig. 16 The parameters for input of wave data in the software application

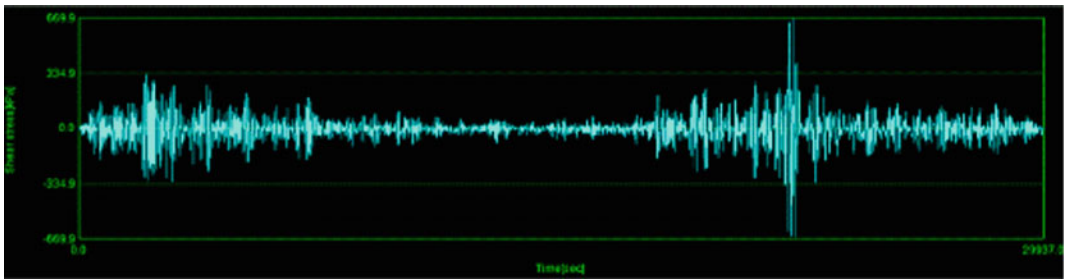


Fig. 17 Preview of an imported seismic wave of the 2011 Tohoku earthquake



Fig. 18 Cleaning metal filters and blades on the base of the shear box with water and brush with vacuum cleaner



Fig. 19 The upper-outer ring shear box immersed in water after test and cleaning (*left*), and the loading plate where the O-ring can be removed and cleaned (*right*)

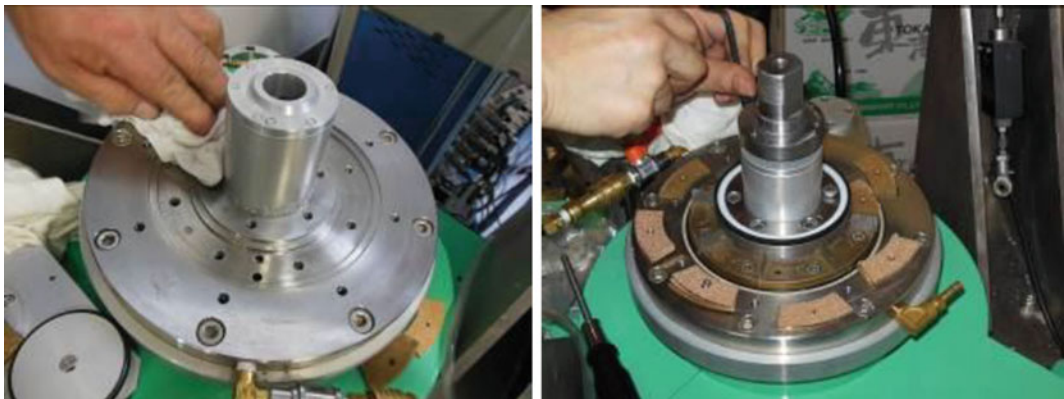


Fig. 20 Cleaning process for the lower rings, rubber edges and porous metal filter disks

(ICL-1) and Version 6.0.5850.32247 (ICL-2) that installed in the control box. Both sensor and test values are produced as the output file in the control box. However, only the test values are used in the data analysis. Data from the control box are then prepared in the Excel and visualized using the KaleidaGraph software. Subtraction of the rubber edge friction from the shear data test in the output file is important to get the correct shear stress values.

7.1 Speed Control Results

Figure 21 shows the results of speed control test on a saturated sand sample. The graph denotes the effective stress path (ESP) and the total stress

path (TSP). The peak friction angle ($\phi_p = 39.8^\circ$) and mobilized friction angle at failure ($\phi_m = 38^\circ$) are obtained in this speed control test.

7.2 Cyclic Test Results

The stress path of the cyclic test results is shown in Fig. 22, where the blue path denotes as the total stress path and the red line shows the effective stress path. The mobilized friction angle at failure (ϕ_m) reached 43° . The times-series data from undrained cyclic test is shown in Fig. 23. The green line indicates the shear-stress control signal which was applied to the stress-control servo-motor, while the red line is the shear resistance mobilized on the sliding surface. The blue

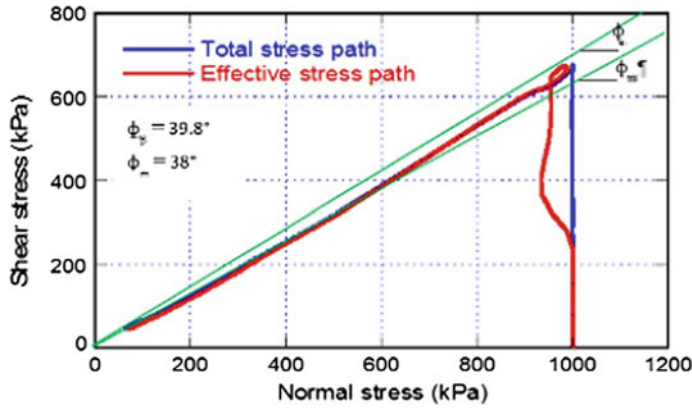


Fig. 21 Total stress path (TSP) and effective stress path (ESP) of speed control test on a saturated sand sample

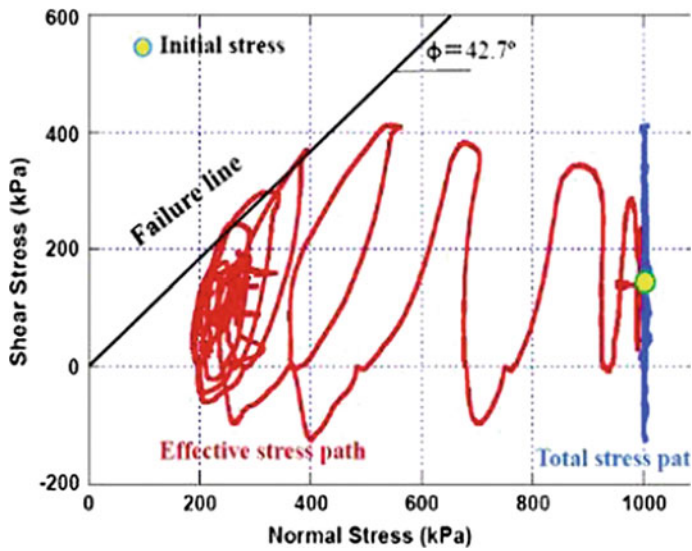


Fig. 22 Stress path of the undrained cyclic loading test on a saturated sand sample

line indicates pore water pressure and the purple line is the shear displacement. During the cyclic loading, pore pressure was generated which triggers soil failure. Further increase of pore-water pressure then appeared in the progress of shear displacement, with resulting shear strength reduction. In this stage, the accelerated motion was produced. A steady state condition was reached when there is no further pore pressure generation and residual shear resistance remaining constant. This phenomenon has been termed as ‘sliding-surface liquefaction’ (Sassa 1996).

In the initial condition, the control signal for shear stress and the mobilized shear resistance are in the same level. When soil failure occurs, these two lines are differing. The control signal increases in accordance with the defined cyclic loading, while the shear resistance decreases until steady-state shear resistance is reached. The excess stress over shear resistance accelerates the shear displacement. Even after cyclic shear stress loading has stopped, the motion continues to accelerate due to the mobilized steady state shear stress that is smaller than the initial stress

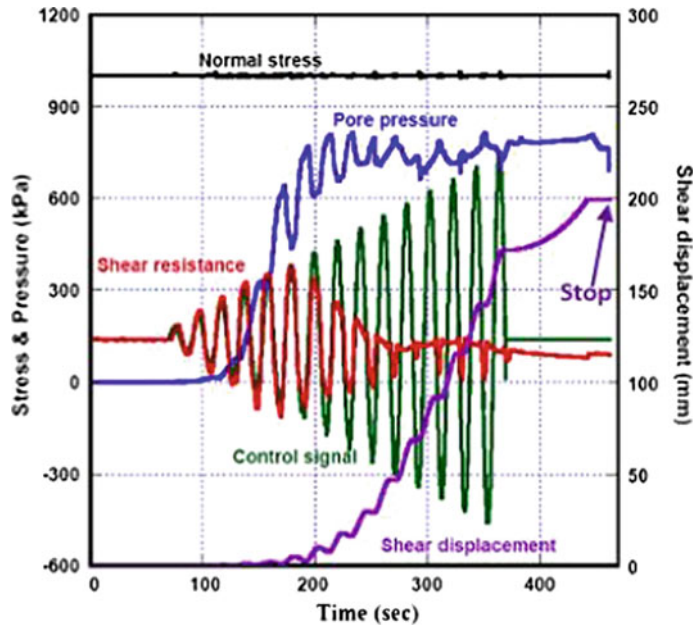


Fig. 23 Time series data of the undrained cyclic loading test showing stresses, control signal, pore pressure and shear displacement

corresponding to the stress due to gravity. It is implied that a landslide which represents in this soil material was triggered by an additional shear stress increment that continue to move and accelerate after the end of the additional shear stress from earthquakes or cyclic shear stress.

7.3 Seismic Test Result

The example for seismic test in the ring shear apparatus that described here is to examine the possibility of a large submarine landslide triggered by a great Tohoku earthquake which might cause tsunami. The purpose of this drained dynamic-loading test was to reproduce the stresses experienced by a gently dipping volcanoclastic sand layer about 200 m depth below sea level. The 2011 Tohoku earthquake record at monitoring site MYG004 is used with peak ground acceleration of 2699 gal. However due to the apparatus capacity, the test was conducted with lower stress values and longer time scale interval than the original seismic data.

Figure 24 shows the stress path of the undrained dynamic-loading ring-shear test on the sample using seismic shear stress of the 2011 Tohoku earthquake wave. Total stress path is shown in the blue line, while the red line indicates the effective stress path. Pore pressure was generated during the seismic loading and the stress path reached the failure line of $\phi_m = 35.4^\circ$.

The time-series data from seismic test is shown in Fig. 25. The loading period was given in 2250 s, about 30 times of the 75 s of the real main shocks. The monitored normal stress is shown in black line and control signal for the shear stress is shown in green line. The red line indicates the mobilized shear resistance which varied proportionally to the control signal. The difference between control signal of shear stress and the mobilized shear resistance became large after soil failure, which accelerates the mass motion. The shear displacement rapidly increased after failure in the second shock, with very high pore pressure generation. The mobilized shear resistance at the steady

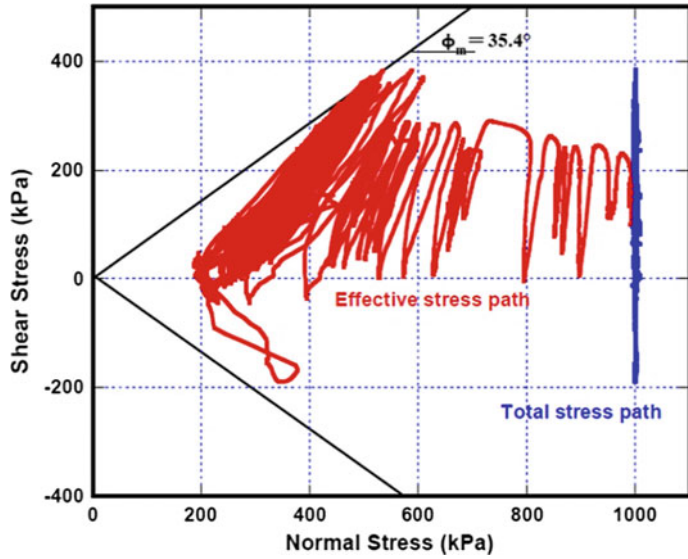


Fig. 24 Stress path of the undrained seismic loading test on saturated volcanoclastic sand

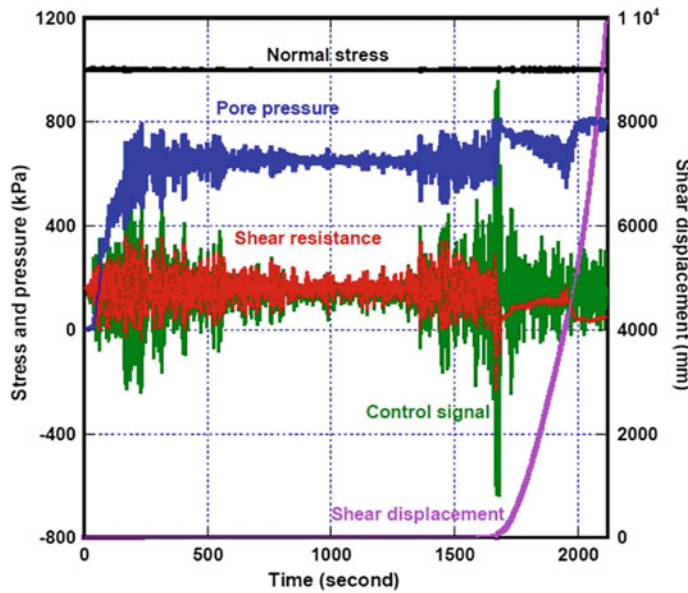


Fig. 25 The time series of undrained seismic loading test, showing stresses, control signal, pore pressure and shear displacement

state condition reached 48 kPa, which was smaller than the initial shear condition due to gravity (160 kPa). With that difference, the shear displacement continued to move and accelerate.

7.4 Pore Pressure Control Test Results

The ring-shear apparatus ICL versions can geotechnically simulate landslide triggered by a

heavy rainfall. The initial stresses on the sliding surface are first applied and then pore pressure is gradually increased, simulating the groundwater level rise during rainfall. The groundwater level rise may not be rapid in natural slopes, thus, the undrained loading condition was not used. To simulate drained groundwater condition, water pressure is gradually increased to the shear box through the lower drainage valve. In this step, water pressure is controlled (with system shown in Fig. 2) but the water is free to move through the upper drainage valve (Fig. 6). Thus, the sample is subjected to natural drained condition. If pore water pressure is generated during loading in the shear zone, it can be dissipated naturally through the upper drainage valve. The pore pressure control test result in naturally drained condition is presented in Fig. 26.

The stress path suddenly drops into lower value after reach the failure line. Thereafter, shear resistance slightly recovers to a certain value. The rapid drop of shear resistance is interpreted as follows: when shear failure occurs, volume reduction takes place due to grain crushing and consequent collapse of the soil structure that cause rapid excess pore-pressure generation. However, the excess pore pressure is not monitored by pore-pressure transducer because the upper drainage valve remains open and the transducer is not located at the shear zone. Therefore, the stress path deviated from the failure line and dropped vertically.

Although pore pressure in the shear zone is dissipated through the upper drainage valve, some excess pore pressure remained as a result of the combined effect of pore pressure generation and pore fluid flowing out from the shear zone. In the

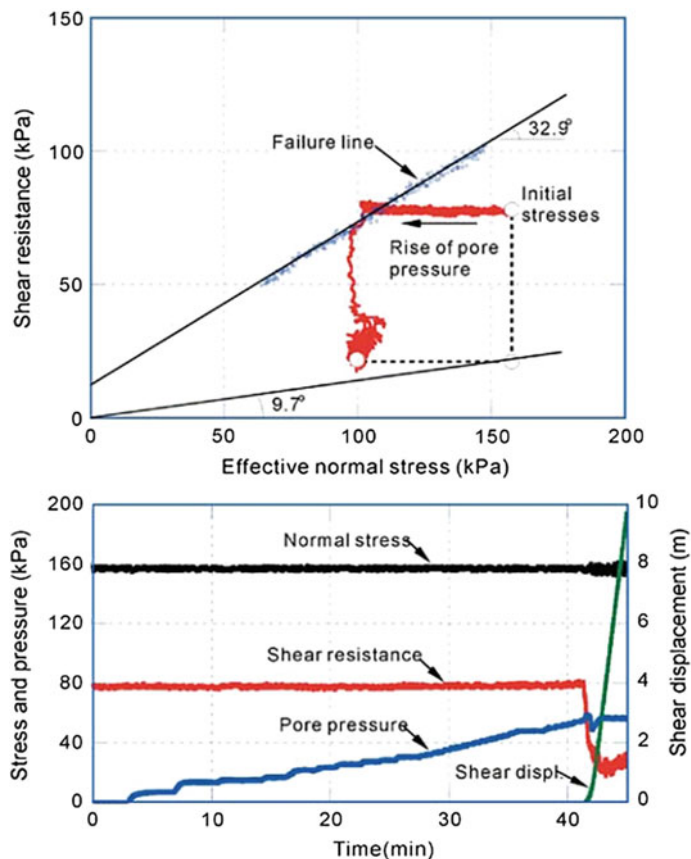


Fig. 26 Pore pressure control test in naturally drained condition: **a** stress path, **b** time-series data for normal stress, shear resistance, pore pressure and shear displacement (as taken from Sassa et al. 2004)

immediate post-failure condition, the speed of pore pressure generation decreases while pore pressure dissipation is maintained. Therefore, shear resistance recovers and settles to a certain value. The apparent friction angle (ϕ_a) of 9.7° is obtained.

The test in Fig. 26 called pore pressure control test in naturally drained condition, because the generated excess pore pressure is naturally drained from the shear zone to the upper drainage valve. After naturally drained test, the sample was consolidated again by dissipating the generated pore pressure and following by applying slow shearing. After failure, the normal stress was decreased slowly to maintain drained condition, continuing slow movement without generating any pore water pressure. This test determined the failure line during motion as indicated by the blue line in Fig. 26a. The friction angle during motion (ϕ_m) is 32.9° . These test results implies that the sample can experience high excess pore-pressure generation due to post-failure shearing and mobilize low apparent friction angle (ϕ_a) of 9.7° .

8 Conclusion

The development of undrained dynamic-loading ring-shear apparatus ICL versions are part of the project of the International Consortium on

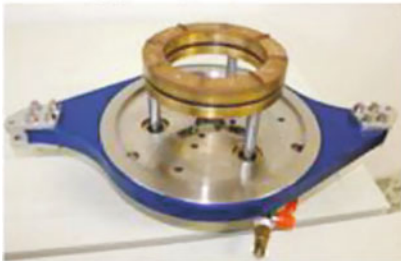
Landslides between Japan and Croatia (ICL-1), as well as Japan and Vietnam (ICL-2). The ICL versions are used to geotechnically simulate the landslide initiation and motion as well as to observe pore pressure generation and residual shear resistance along sliding surface within a large shear displacement. As for new and upgrading tools from the previous version, the loading system for normal stress is applied by using the central axis that pulled within the apparatus. Therefore, the use of ICL versions is not required a lot of space and can be transportable to other laboratory. With the rubber edge on the interface of rotatable and fixed shear box, and also pore pressure transducer within the upper outer shear box, the undrained stress control tests are possible to be carried out.

Appendices

Appendix 1: Parts and Valves of the Ring Shear Apparatus

A shear box, B normal stress loading piston, C shear stress sensors, D loading plate, E hanging

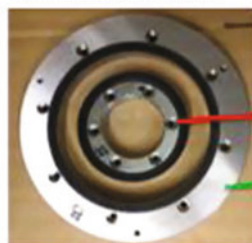
Loading plate (LP)



Upper shear box



Lower shear box



Inner ring

Outer ring



lift frame, *F* pore pressure transducer, *G* valve to pore pressure control system, *H* valve for water drainage, *I* valve for de-aired water supply.

Appendix 2: Sensor and Test Values in the Main Control Unit

Sensor value	
Vertical load [kN]	-0.37
Vertical displacement [mm]	-0.20
Shear load [N]	6.1
Shear displacement [mm]	0.004
Pore water pressure-1 [kPa]	-47.0
Pore water pressure-2 [kPa]	-26.8
Control pressure [kPa]	15
Gap [mm]	-0.004
Oil pressure[LD] [MPa]	0.04
Oil pressure[ULD] [MPa]	0.01

<i>F_v</i> (kN)
<i>D_v</i> (mm)
<i>F_s</i> (kN)
<i>D_s</i> (mm)
<i>u₁</i> (kPa)
<i>u₂</i> (kPa)

Test value	
Vertical load [kN]	-0.37
Vertical displacement [mm]	-0.20
Shear load [N]	6.1
Shear displacement [mm]	0.004
Pore water pressure-1 [kPa]	-47.0
Pore water pressure-2 [kPa]	-26.8
Total normal stress [kPa]	-37.8
Effective normal stress [kPa]	9.1
Shear stress [kPa]	3.7
Total friction angle [deg]	-5.6
Effective friction angle [deg]	22.2

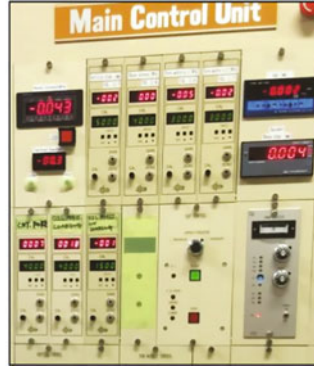
<i>F_v</i> (kN)
<i>D_v</i> (mm)
<i>F_s</i> (kN)
<i>D_s</i> (mm)
<i>u₁</i> (kPa)
<i>u₂</i> (kPa)
σ (kPa)
σ' (kPa)
τ (kPa)

Print screen of the ring shear apparatus software application (ICL-2 Data acquisition and control Version 6.0.5850.32247)

Appendix 3: Sample Height Calculation (Example for the ICL-1)

Sensor values displayed on the main control unit of ICI-1 (left) and ICI-2 (right)

The height of the lower part of the shear box (h_1) consists of the metal part and rubber edge. It



- Sensor Values are the real values measured directly with the sensors or the load cells in the instrument box. They are displayed on the Monitoring Box.
- Test Values (each with ‘*’ mark) are the data acquisition resulted from the calculation of sensor values with correction factor of each sensor in the apparatus.
- τ_t is Test value of the shear stress and its represents the sum of the real shear resistance and the rubber edge friction. Both sensor and test values are in the output file.

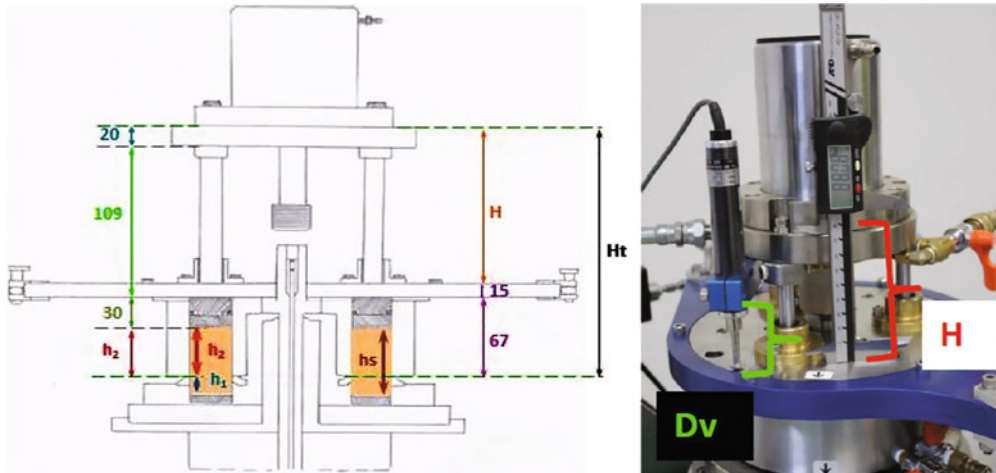
depends on the number of porous metals and rubber edge height which is decreases during use.

$$\begin{aligned}
 h_1 &= 12.3 + 4 = 16.3 \text{ mm} && \text{1 ring of porous metal plates} \\
 h_1 &= 9.3 + 4 = 13.3 \text{ mm} && \text{2 rings of porous metal plates} \\
 h_1 &= 6.3 + 4 = 10.3 \text{ mm} && \text{3 rings of porous metal plates}
 \end{aligned}$$

The sample height in the upper part of the shear box (h_2) depends on the volume change during consolidation, due to the soil type and the testing conditions. It must be measured in each test, before and after consolidation.

Value	Elapsed time	Sensor value								
		Vertical load	Vertical displacement	Shear load	Shear displacement	Pore pressure 1	Pore pressure 2	Gap	SV [Vertical]	SV [Shear]
Unit	[s]	[kN]	[mm]	[N]	[mm]	[kPa]	[kPa]	[mm]	[kPa]	[kPa]
Symbol	t	Fv	Dv	Fs	Ds	u1	u2			

Value	Test value										
	*Vertical load	*Vertical displacement	*Shear load	*Shear displacement	*Pore pressure 1	*Pore pressure 2	*Total normal stress	*Effective normal stress	*Shear stress	*Total friction angle	*Effective friction angle
Unit	[kN]	[mm]	[N]	[mm]	[kPa]	[kPa]	[kPa]	[kPa]	[kPa]	[°]	[°]
Symbol	Fv	Dv	Fs	Ds	u1	u2	σ	σ'	τ_t		



The total sample height, $h_s = h_1 + h_2$

(left side)

(right side)

$$H_t = h_2 + 30 + 109 + 20 = h_2 + 159$$

$$H_t = 67 + 15 + H = 82 + H$$

$$h_2 + 159.05 = 82 + H$$

$$h_2 = H - 77.05$$

$$h_s = h_1 + h_2 = h_1 + H - 77.05$$

H —The height which is measured manually (before and after consolidation) and checked against the vertical displacement, D_v .

References

- Bishop AW, Green GE, Garga VK, Andersen A, Brown JD (1971) A new ring shear apparatus and its application to the measurement of residual strength. *Géotechnique* 21(1):273–328
- Bromhead EN (1979) A simple ring shear apparatus. *Ground Eng* 12(5):40–44
- Garga V, Infante Sedano JA (2002) Steady state strength of sands in a constant volume ring shear apparatus. *Geotech Test J* 25(4):414–421
- Hungry O, Morgenstern NR (1984) High velocity ring shear tests on sand. *Géotechnique* 34(3):415–421
- Oštrić M (2013) Development of portable undrained ring shear apparatus and its application. Doctoral thesis, Graduate School of Engineering, Kyoto University
- Oštrić M, Vivoda M, Ljutić K (2012a) Manual of the portable ring-shear apparatus ICL-1. International Consortium on Landslides, Kyoto (for internal use)
- Oštrić M, Ljutić K, Krkač M, Setiawan H, He B, Sassa K (2012b) Undrained ring shear tests performed on samples from Kostanjek and Grohovo landslide. In: Sassa K, Takara K, He B (eds) *Proceedings of the IPL symposium, Kyoto*, pp 47–52
- Oštrić M, Ljutić K, Krkač M, Sassa K, He B, Takara K, Yamashiki Y (2012c) Portable ring shear apparatus and its application on Croatian landslides. *Annals of Disas*, pp 57–65 (Prev. Res. Inst., Kyoto Univ., No. 55B)
- Sassa K (1984) The mechanism starting liquefied landslides and debris flows. In: *Proceedings of 4th international symposium on landslides, Toronto, June*, pp 349–354
- Sassa K (1996) Prediction of earthquake induced landslides. In: *Proceedings of 7th international symposium on landslides. A.A. Balkema, Trondheim, 17–21 June*, pp 115–132
- Sassa K, Fukuoka H, Wang G, Ishikawa N (2004) Undrained dynamic-loading ring-shear apparatus and its application to landslide dynamics. *Landslides* 1–1:7–19
- Savage SB, Sayed M (1984) Stresses developed in dry cohesionless granular materials sheared in an annular shear cell. *J Fluid Mech* 142:391–430
- Tika TM (1989) The effect of rate of shear on the residual strength of soil. PhD thesis, University of London (Imperial College of Science and Technology)

TXT-tool 3.081-1.7

Undrained Dynamic-Loading Ring-Shear Apparatus and Its Application to Landslide Dynamics

Hendy Setiawan, Kyoji Sassa, Hiroshi Fukuoka,
Gonghui Wang and Naohide Ishikawa

Abstract

Landslides are the mass of rock, debris and or earth that moves down a slope by gravity. Study on landslide dynamics, including the dynamic of loading and excess pore-pressure generation and dissipation, is necessary to understand the initiation and motion of rapid landslides. This paper presents the development of ring shear apparatus that can facilitate the simulation of landslides, particularly for the formation of shear zone and followed by long and rapid shear displacement. A series of different types of ring shear apparatus (i.e. DPRI-3, 4, 5, 6 and 7) were developed by Prof. K. Sassa and his colleagues at the Disaster Prevention Research Institute (DPRI) of Kyoto University. The application of this apparatus to study the earthquake-induced landslides and landslide-triggered debris flow in Japan are explained in this paper. In addition, the tests using a transparent shear box of the DPRI-7 for visual observation of the shear zone during rapid shearing are also described.

Keywords

Ring-shear test · Landslide dynamics · Earthquake-induced landslides
Landslide-triggered debris flows · Undrained loading

H. Setiawan (✉) · G. Wang · N. Ishikawa
Disaster Prevention Research Institute,
Kyoto University, Uji 611-0011, Japan
e-mail: hendy@flood.dpri.kyoto-u.ac.jp

G. Wang
e-mail: wanggh@landslide.dpri.kyoto-u.ac.jp

K. Sassa
International Consortium on Landslides,
138-1, Tanaka Asukaicho, Sakyo-ku,
Kyoto 606-8226, Japan
e-mail: sassa@iclhq.org

H. Fukuoka
Research Institute for Natural Hazards
and Disaster Recovery, Niigata University,
Niigata 950-2181, Japan
e-mail: fukuoka@cc.niigata-u.ac.jp

Contents

1 Introduction	352
2 Structure and Control System of Ring Shear Apparatus	354
2.1 Water Leakage Prevention.....	355
2.2 Monitoring of Pore-Pressure Generation.....	356
3 Testing Procedure	357
3.1 Sample Setting and Saturation Process.....	357
3.2 Sample Consolidation, Loading and Monitoring of Shearing.....	358
4 Geotechnical Simulation of Earthquake-Induced Landslides	358
5 Landslide-Triggered Debris Flow	361
6 The DPRI-7 Ring Shear Apparatus with a Transparent Shear Box	364
7 Conclusion	366
References.....	368

1 Introduction

The ring-shear apparatus was designed initially to study and investigate the residual shear resistance of soils which mobilized along the sliding surface of landslides. The apparatus enables to observe large shear displacement of the soil specimens. The ring-shear apparatus that was developed by scientists and engineers at the Imperial College of Science and Technology (United Kingdom) and the Norwegian Geotechnical Institutes is widely adopted (Bishop et al. 1971). The ring-shear apparatus of the Bishop type has ability to measure the friction between soil sample and sidewalls of the upper shear box. This advantage is important to ensure the accurate measurement of the total normal stress acting on the soil specimen during the tests.

Features of previous series of ring shear apparatus which were developed by scientists and researchers are shown in Table 1. The ring shear apparatus by Hungr and Morgenstern (1984) and Tika (1989) were the improvement of previous apparatus which was introduced by Hvorslev (1939) using the separated upper and lower confining rings to shear the samples. However these series are unable to perform the undrained and cyclic control tests. Garga and Sendano (2002) used their version of ring shear apparatus with one sample box that is loaded and

sheared by the upper loading platen. In this version, the shearing takes place between the upper loading platen, bottom of the shear box and the soil sample. The first DPRI version of high-speed ring-shear apparatus was developed by Sassa (1984) using a conventional shear-speed control motor but still could not produce the cyclic shear-stress loading. The dynamic-loading ring shear apparatus that has ability to give the seismic loading was found in the DPRI-3. In this version, a torque-control motor and a servo-control system are applied for the feed-back signal from a load cell that measured the torque (Sassa 1994, 1996). After that, several series of dynamic-loading ring shear apparatus have been developed with different features (DPRI-4, DPRI-5, DPRI-6 and DPRI-7).

The main purpose of the DPRI versions of ring-shear apparatus is to simulate quantitatively all process of soil sample failure of the slope or suspected landslides, from the initial static and dynamic loading condition, in the form of shear failure, with measurement of pore-pressure generation, possible liquefaction, shear strength reduction in progress of large shear displacement, up to steady-state shear condition. The working of the DPRI versions of undrained-dynamic loading ring-shear apparatus has similar concept with the ring-shear apparatus developed by Bishop et al. (1971) (Fig. 1). The ring-shear apparatus by Bishop et al. (1971) emphasizing the post-peak interval of the shear resistance and displacement curve with residual strength developed in the case of slow clayey-landslides. Meanwhile, the current undrained ring shear apparatus which was developed by Sassa is purposed to geotechnically simulate the shear zone formation of high-speed landslides and post-failure mobility as well as mobilized shear resistance and shear displacement within generated pore-water pressure.

According to the features of the ring shear apparatus which are described in Table 1, landslides simulation were carried out by considering several conditions as follows:

Table 1 Features of previous ring shear apparatus, compared with the DPRI-7

Author(s)	Bishop et al. (1971)	Hungr and Morgenstern (1984)	Tika (1989)	Garga and Sendano (2002)	Sassa DPRI-3 (1992)	Sassa DPRI-4 (1996)	Sassa DPRI-5 (1997)	Sassa DPRI-6 (1997)	Sassa DPRI-7 (this paper)
<i>Shear box</i>									
Inner diameter (cm)	10.16	22.0	10.16	9.2	21.0	21.0	12.0	25.0	27.0
Outer diameter (cm)	15.24	30.0	15.24	13.3	31.0	29.0	18.0	35.0	35.0
Max. height of sample (cm)	1.9	2.0	1.9	2.0	9.0	9.5	11.5	15.0	11.5
Ratio of max. height/width	0.75	0.5	0.75	0.98	1.8	2.38	3.83	3.0	2.88
Shear area (cm ²)	101.34	326.73	101.34	72.45	408.41	314.16	141.37	471.24	389.56
Max. normal stress (kPa)	980	200	980	660	500	3,000	2,000	3,000	500
Max. shear speed (cm/s)	–	100	9.33	–	30.0	18.0	10.0	224.0	300
Cyclic torque control (max. frequency)	No	No	No	No	Yes (0.5 Hz)	Yes (5 Hz)	Yes (5 Hz)	Yes (5 Hz)	Yes (5 Hz)
Undrained testing and pore pressure monitoring	No	No	No	No	Yes	Yes	Yes	Yes	Yes
Max. data acquisition rate (readings/s)	–	–	10	–	12	200	200	200	1000

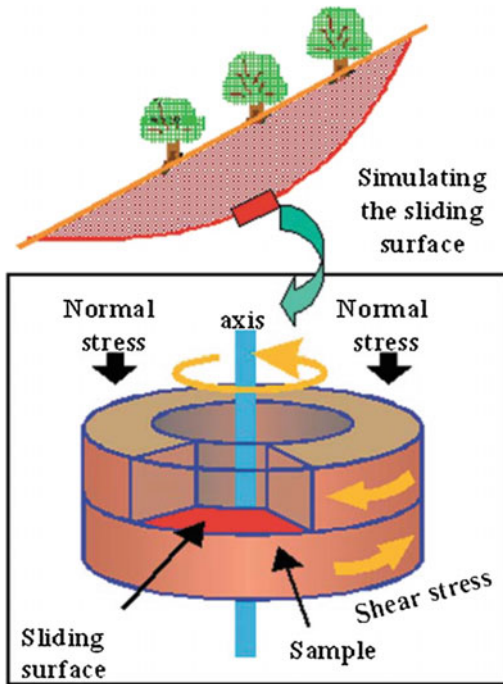


Fig. 1 Fundamental concept of the ring-shear apparatus

- a. The stress torque control is used to give the shearing process for soil samples. This system is applied because the triggering factors of landslides such as rainfalls, groundwater fluctuation and earthquake are related with the changes of stress within the slope. In addition, the residual friction angle of the soil samples could be obtained from shearing through the speed-controlled test.
- b. Rapid landslide simulation can be carried out using the DPRI-3 with the maximum shear speed of 33 cm/s, while the newest version DPRI-7 can produce shear speed up to 300 cm/s.
- c. The rubber edge is pressed to the bottom of an upper shear boxes to prevent the water leakage in undrained condition. The contact pressure then applied through servo-oil piston and gap sensor with precision of 1/1000 mm.
- d. Monitoring of pore pressure is carried out through pore pressure gauge that is connected to the circumferential filtered gutter (4 × 4 mm) located inside the upper outer ring shear box.
- e. A seismic wave form with the frequency of 5 Hz and a high-speed data acquisition rate from 12 readings/s (DPRI-3) to 1000 readings/s (DPRI-7) are provided to conduct the rapid earthquake loading in the apparatus.
- f. The shear zone of soil specimens is produced within the interface between the fixed upper shear box and the rotatable part of ring shear apparatus.
- g. The cyclic shear-displacement control tests, shear-speed control tests and torque-control tests are possible to conduct using the DPRI-4 and DPRI-7.

2 Structure and Control System of Ring Shear Apparatus

Figure 2 shows the undrained-dynamic loading ring-shear apparatus of DPRI-6, the largest type of the DPRI versions with total height up to 5.1 m. The DPRI-6 consists of main apparatus (including the shear boxes and loading system), computerized control and monitoring system. The apparatus was installed at the DPRI laboratory with the sample box level placed about 1 m above the floor and the lower parts of mechanical structure are located in a pit. There are four computers used in the DPRI-6 with different purposes. First computer is for the test (signal) control when the monotonic/cyclic or seismic loading takes place. The second computer is to monitor the transducers responses, to record the data and draws the effective-stress path visually. The third computer is used for monitoring the system functions by providing the safeguard alarm. When the apparatus and mechanical structure works incorrectly, the alarm goes on and the test will stopped automatically. The test procedures and data analysis will be memorized through the fourth computer.

The soil sample is loaded by a loading plate which supported from an oil piston (OP). The normal stress given to the sample is measured by an upper load cell (N1), while the total friction between loaded sample and the sidewall of the upper rings is measured by a lower load cell

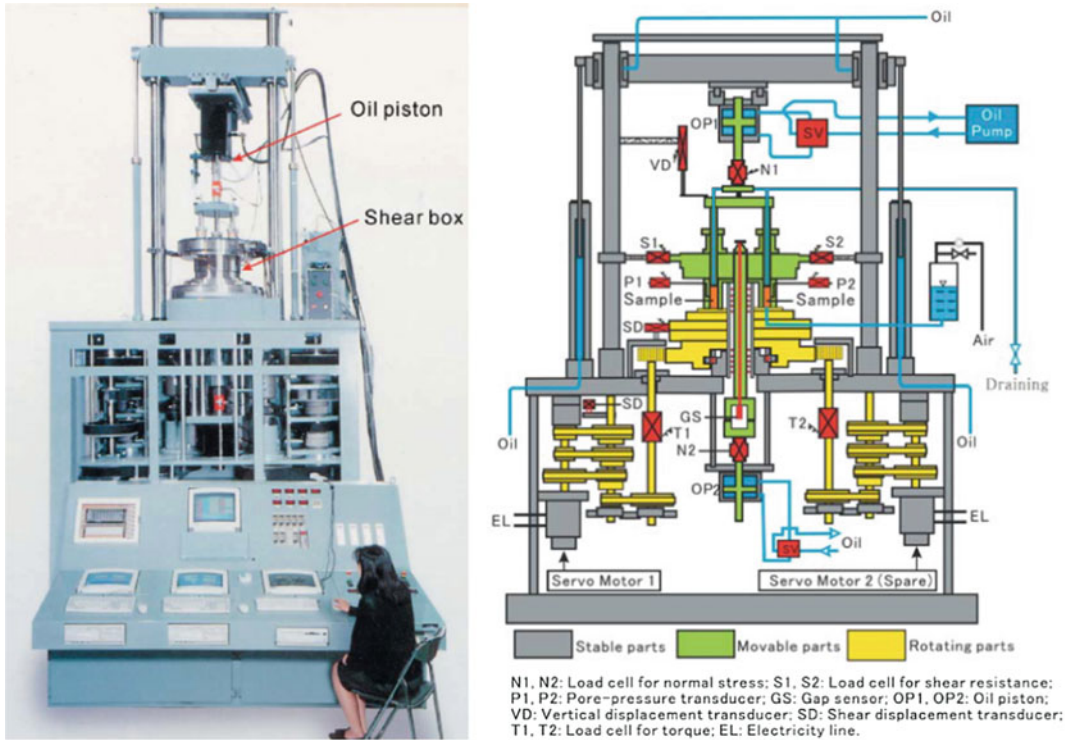


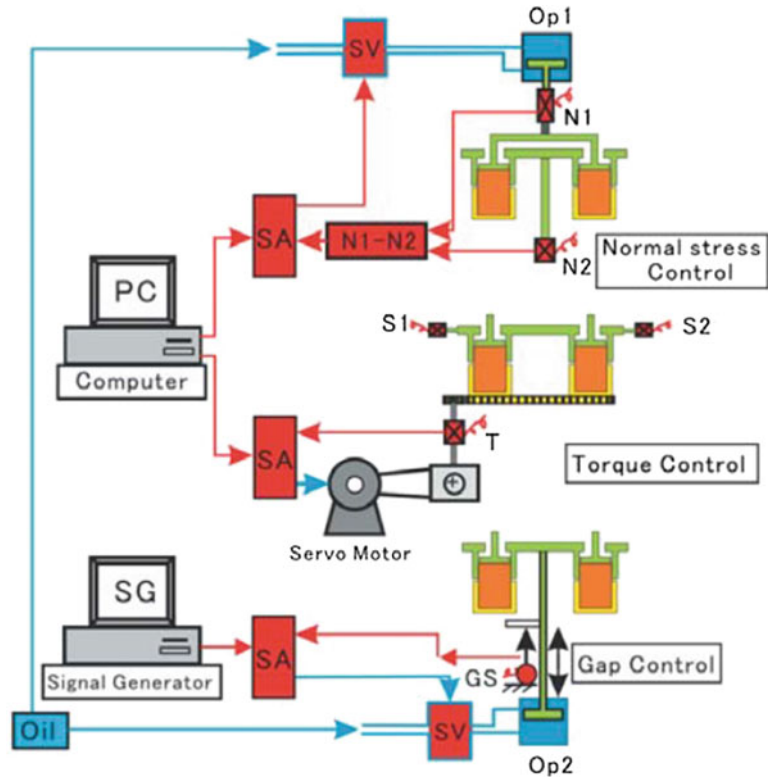
Fig. 2 The undrained dynamic-loading ring-shear apparatus of DPRI-6 and its mechanical structure

(N2). Thus, the difference in values of N1 and N2, resulting the actual normal stress which is acting on the shear surface of the sample. The actual normal stress as a feedback signal is sent to a servo-amplifier, that makes the normal stress acting on the shear surface is automatically same and controlled by a signal from the computer (Fig. 3). A torque-controlled servo-motor is provided to give the shear stress which is then measured by a torque transducer (T1 or T2). The feedback signal of applied shear stress from torque transducer is then controlled by a servo-amplifier and a servo-motor where the value is kept the same as pre-determined from the computer. The two load cells (S1 and S2) are installed on the upper shear box (green colour in Fig. 2) to measure the shear resistance acting on the shear surface when the lower shear box (yellow colour in Fig. 2) is rotated.

2.1 Water Leakage Prevention

The structure of undrained shear box of the ring-shear apparatus is shown in Fig. 4. The most important but difficult task of the test by means of ring-shear apparatus is the water leakage that might appear through the gap between the upper and the lower shear box during high-speed shearing (33–300 cm/s). The water leakage prevention efforts were carried out through several tests in the development of DPRI-3 (Shoaei and Sassa 1994) by attaching various types and shapes of rubber edges on the upper rings of rotatable parts of the apparatus. Eventually, a stair-shaped rubber ring with the rubber hardness index of 45° JIS (Fig. 4) was used. On the DPRI-7, the outer confining rings of the shear box were made of the transparent acrylic which is deformable under the increasing temperature

Fig. 3 Electronic control system of the DPRI-5, DPRI-6 and DPRI-7



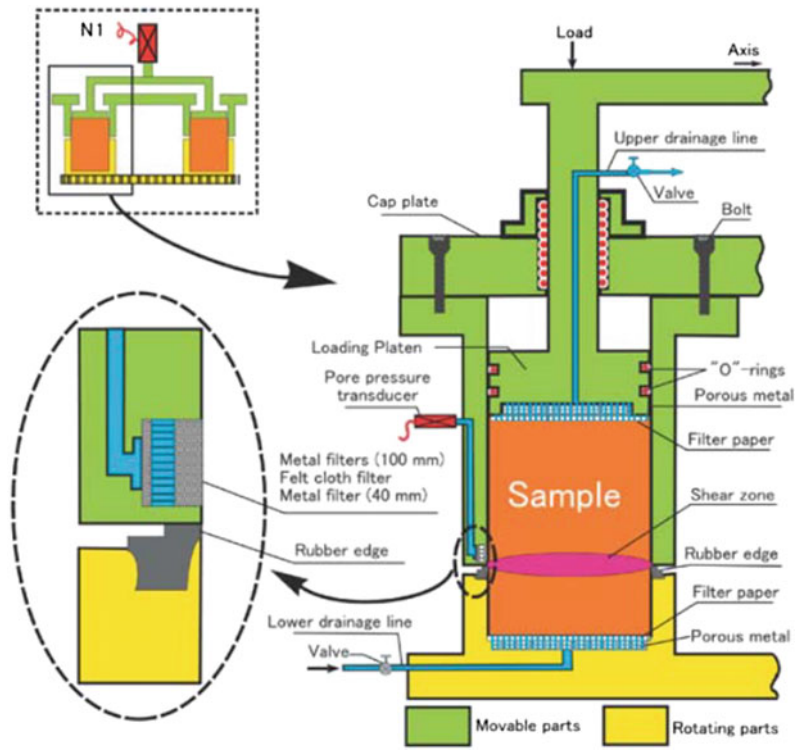
N1, N2: Load cell for normal stress; T: Load cell for torque; S1, S2: Load cell for shear resistance; GS: Gap sensor; OP: Oil piston; SV: Serve-oil valve; SA: Servo amplifier.

during shearing process. The rubber edges were sprayed with a friction coat of Teflon (polytetrafluoroethylene) and daubed with a vacuum silicon grease in advance before doing the tests. A certain value of contact pressure is given to the upper pair of rings and the rubber edges, called the gap value, through the gap control oil piston (OP2 in Fig. 3). To achieve the undrained condition during the tests, the gap value should be higher than the generated pore pressure and maintained almost constantly and using the feed-back signal obtained from a gap sensor (GS) with a precision of 1/1000 mm.

2.2 Monitoring of Pore-Pressure Generation

The attempts to provide an effective and strong pore-pressure monitoring system were carried out initially by using the needle that connected to a pore-pressure transducer (Sassa 1996). However, the results were quite unsatisfied since the needle was broken during the shearing and the pore-pressure was not perfectly measured. To produce the pore-pressure value measurement effectively and more durable, the pore pressure transducer installation was then improved by

Fig. 4 Close-up of a half section of the shear box showing the rubber edge and the connected pore pressure transducer to the circumferential filtered gutter



connecting to a circumferential gutter of the inner wall of the outer ring shear box (Fig. 4). The gutter is located about 2 mm above the shear surface of the sample which is covered by two metal filters and filter cloth. This system is more effective to ensure the monitoring of pore-pressure generation and to keep the sensitivity of the pore-pressure transducers during rapid shearing process.

3 Testing Procedure

3.1 Sample Setting and Saturation Process

According to Ishihara (1993), the soil samples could be prepared through moist placement or dry deposition method. To perform a very loose sample, the moist placement method was used. The dry deposition method was carried out by pouring the oven-dried sample into the shear box in layers without tamped to achieve a normally consolidation state. Tamping the placed soil

samples in the ring shear box may create an over-consolidation state before the loading process of the apparatus. The saturation process of soil samples which was already placed inside the shear box was conducted by inserting the CO₂ and following by the de-aired water circulation from the lower drainage valve to the upper drainage valve sequentially. This process was applied in a very slow rate and a small water head. Sassa (1988) introduced the B_D value as the pore pressure parameter to check the degree of saturation in the direct-shear state, defined as

$$B_D = \Delta u / \Delta \sigma$$

where Δu is the increment of pore pressure and $\Delta \sigma$ is the increment of normal stress. Initially, the sample was consolidated in drained condition under the normal stress of 49 kPa then the drainage valve was closed. Hereafter, the normal stress was increased at the same rate and the increment of pore pressure was measured. The undrained ring shear tests were performed within the $B_D \geq 0.95$.

3.2 Sample Consolidation, Loading and Monitoring of Shearing

In most cases of landslides simulation, the samples taken from the sites were normally consolidated before the tests. But in some cases, over-consolidation samples were reproduced for the dense soil layer condition. To produce the initial stress state which is similar to the real conditions on the field, the initial shear stress and normal stress were given to the samples in accordance with the weight of soil mass and slope condition. Testing of the soil samples by means of the ring shear apparatus could be carried out in the drained or undrained conditions, depends on the purposes of loading. For example, the simulation of landslides triggered by the earthquake or pore-pressure increase should be conducted in undrained condition to observe the excess pore pressure that may contribute to the soil failure. However, the drained tests are possible to do by opening the upper drainage valve during shearing process. Other tests such as shear displacement control tests or cyclic shearing with constant shear displacement amplitude may possible to conduct using the ring shear apparatus.

The two load cells (S1 and S2 in Fig. 2) were provided to measure the change of mobilized shear resistance. To get the correct mobilized shear resistance from the tests, the monitored shear resistance was subtracted from the rubber-edge friction. This friction was appeared as a result of gap pressure for the prevention of water leakage in undrained condition, though a smaller rubber edge friction is preferable. An example of shear resistance caused by the rubber edge friction is shown in Fig. 5. For practical purposes, a constant friction could be used when the shear displacement reached more than 0.1 mm and the fluctuation difference is in the order of ± 1 kPa. Before doing the tests using soil samples, it is important to conduct the rubber edge friction tests to find the best minimum gap pressure where the water leakage do not occur. Further detail explanation can be found in Sassa et al. (2003a, b).

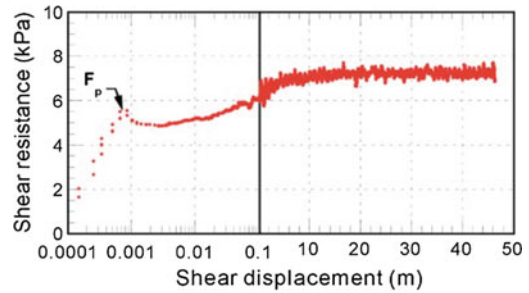


Fig. 5 Shear resistance produced from the rubber edge friction test

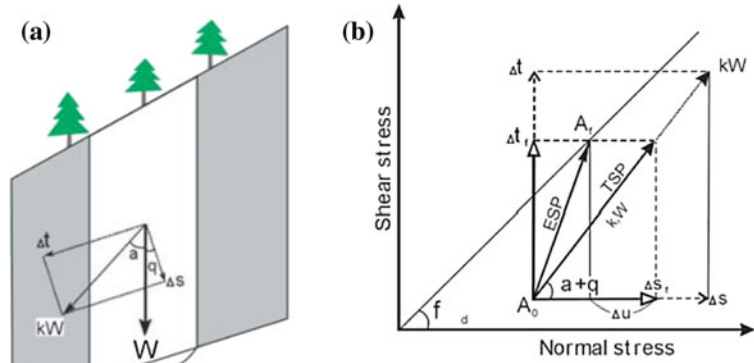
4 Geotechnical Simulation of Earthquake-Induced Landslides

The stress conditions acting within a slope consists of self-weight of the soil (W) and the dynamic stress ($k \cdot W$) (Fig. 6a). When we expressed those stress conditions in the graph of the ring-shear tests results, the total stress path (TSP) and the effective stress path (ESP) are formed due to dynamic stress loading (Fig. 6b). Not like the TSP that determined automatically, the ESP is developed depends on the generated excess pore-pressure during loading, soil failure and motion after failure. Since the direction of the seismic stress is dynamically changed in the real condition, the loading angle (α) and the seismic coefficient (k) are the functions of time.

The earthquake-induced Nikawa landslide was investigated, as a part of the M101-APERITIF (Areal Prediction of Earthquake and Rainfall Induced Rapid and Long-traveling Flow Phenomena) Project of the International Consortium on Landslides in 2002. This project was launched by the Special Coordinating Fund for Science and Technology of the Ministry of Education, Culture, Sports, Science and Technology (MEXT) of Japan.

The Nikawa landslide was triggered by the 1995 Hyogo-Ken Nanbu earthquake where about 34 people were found dead. The investigation of Nikawa landslide is very important to determine

Fig. 6 Stress conditions in a slope (a) and in the ring-shear apparatus (b)



TSP: Total Stress Path; ESP: Effective Stress Path

whether the slope could experience a retrogressive rapid landslide if similar earthquake occurs. Geological layers of the Nikawa slope are consists of granite, gravel layer, granitic-sandy soils and some fills as shown in Fig. 7. The low permeability silts were found within the gravel layer. The granitic sand and silty gravel soils were taken to be tested using the ring-shear apparatus (Sassa 2002; Sassa et al. 2003a, b).

The seismic wave record from the Japan railway Takarazuka station was used for the seismic tests. The synthesis method of the seismic waves was adopted from the attenuation laws for horizontal peak acceleration (Fukushima and Tanaka 1990) and the vertical peak acceleration (Ambraseys and Bommer 1991). The amplification was estimated about 1.4 times when the seismic waves are transferred from hard rock layer to weak soil layer (Fukushima and Tanaka 1990). The ring shear tests for the granitic sand layer and the silty gravel layer were conducted in the normally consolidation, then

followed by seismic loadings (Fig. 8) in undrained condition. The tests results of the granitic sand layer in the form of time series and stress path are shown in Fig. 9.

The B_D value was 0.99 and the initial dry density reached 15.2 kN/m^3 . The failure was occurred for the granitic sand layer because the mobilized shear resistance was less than the shear stress. The pore-pressure was rapidly increased during the main shock and the shear displacement was accelerated in the post-failure stage (Fig. 9b). The starting point of the total stress path (TSP) corresponds to the potential sliding surface at a depth of 26 m with a slope of 26° . The starting point difference of the effective stress path (ESP) (Fig. 9c) expresses the groundwater level of 16 m above the sliding surface. The ESP was soon decreased to a very low steady-state stress after reaching the failure line, and the mobilized apparent friction angle was reached about 3.5° . These results implied that the similar earthquake of the 1995

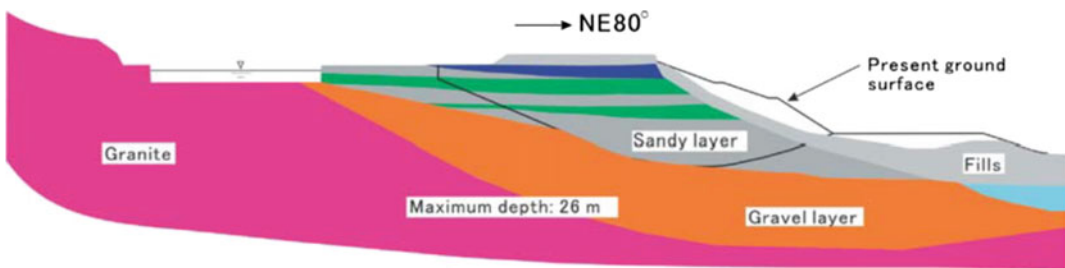


Fig. 7 Cross section of the Nikawa slope

Fig. 8 Seismic loadings applied for the granitic sand layer and the silty gravel layer of the Nikawa landslide

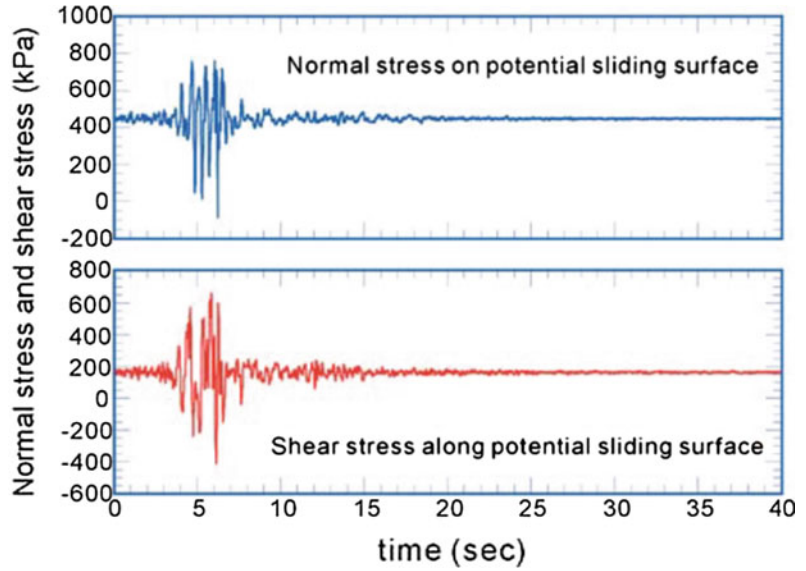
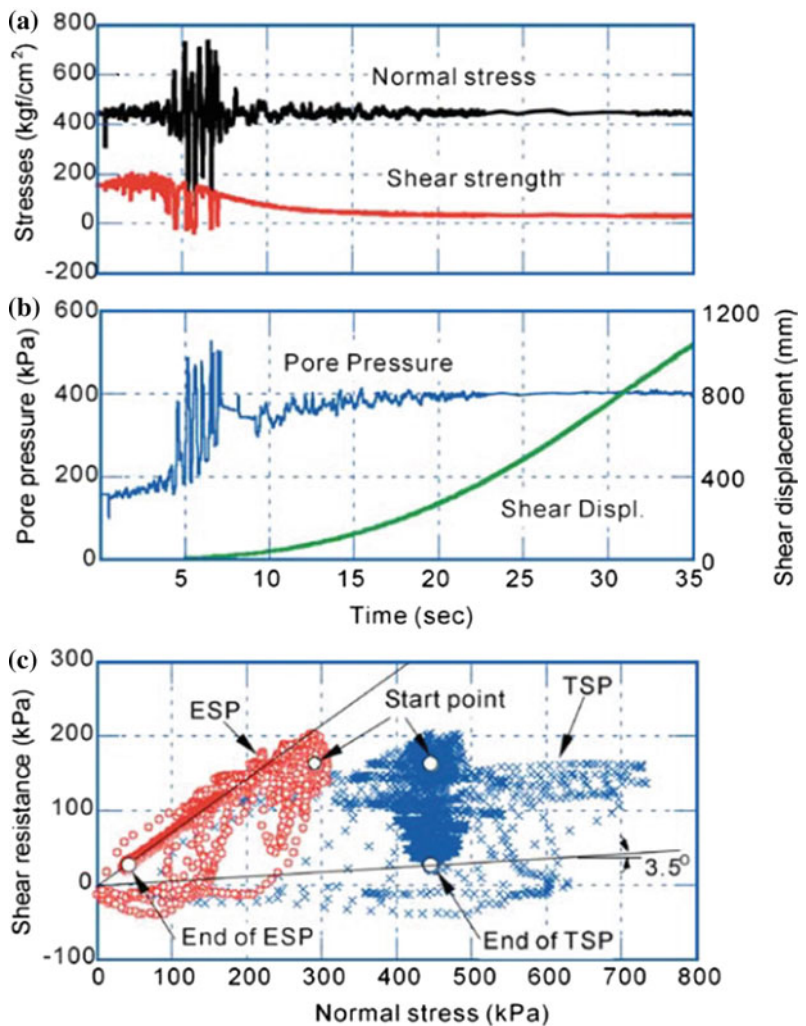


Fig. 9 Undrained cyclic tests on saturated granitic sand layer, **a** time series data for normal stress and shear stress, **b** time series data for pore-water pressure and shear displacement, **c** total and effective stress paths



Hyogo-Ken Nanbu earthquake that might occur in the future could trigger a rapid landslide under the undrained condition. Even though the granitic sand layer has high permeability and the pore pressure dissipation may take place during the earthquake, but the excess pore-pressure generation is still of the main concern. Thus, as reported in Sassa et al. (2003a, b), the mitigation effort by lowering the groundwater level in the slope to prevent landslides during the earthquake was proposed.

5 Landslide-Triggered Debris Flow

Landslide-triggered debris flow was occurred on 20 July 2003 in Minamata City, Kumamoto Prefecture, Kyushu Island, Japan. Landslide in Minamata that located in an andesitic weathered lava mountain slope was triggered by a heavy rainstorm with the total rainfall of 314 mm and the maximum rainfall rate of 91 mm/h. The landslide was transformed into a debris flow that killing 15 people and destroying 15 houses (Fig. 10).

The source of landslide was found at the top of mountain slope, and was flown down along



Fig. 10 Aerial view of the 2003 Minamata debris flow

the torrent. Through this process, the weathered material along the torrent and channel slopes was entrained, causing the enlargement of debris volume. The cross section of Minamata landslide-triggered debris flow is shown in Fig. 11. The inclination of slope failure at the source was estimated about 26.5° with the depth of 10–12 m. Samples were taken from two locations, the weathered andesitic lava (Sample A in Fig. 11) which is located near the head scarp, and the tuff breccia (Sample B) on the flank side of the torrent.

The DPRI-5 ring-shear apparatus was used to simulate the initiation of the Minamata landslide. By considering the slope condition of the landslide source, the initial stresses were reproduced. Further, the rise of groundwater level during rainfall was simulated by increasing the pore pressure of samples at a slow rate while the upper drainage valve was opened, corresponding the natural drained condition in the field. The test result is shown in Fig. 12. The effective stress path was dropped into a lower shear resistance after reached the failure line. In this result, the grain crushing was contributed to the volume reduction and the excess pore pressure generation. Due to the drained condition, the high pore pressure generation in the shear zone was dissipated through the upper drainage valve. However, the failure was occurred due the excess pore pressure that exists within the shear zone. In the post-failure stage, the pore pressure generation was decelerated in the progress of rapid shear displacement (Fig. 12b). The apparent friction angle was about 9.7° . After the naturally drained test, all generated pore pressure was dissipated and again the consolidation process took place. The slow shearing was conducted in a drained condition up to the failure line then the normal stress was decreased slowly. In this test, the failure line path was confirmed through the friction angle during motion of 32.9° . The tests results implied that the excess pore pressure generation was occurred in the andesitic lava deposit which slides rapidly to the torrent. When the landslide mass reached the torrent with a slope of 17° , it was transformed into a debris flow and moved rapidly to a downstream.

Fig. 11 Cross section showing the initial condition of the Minamata landslide

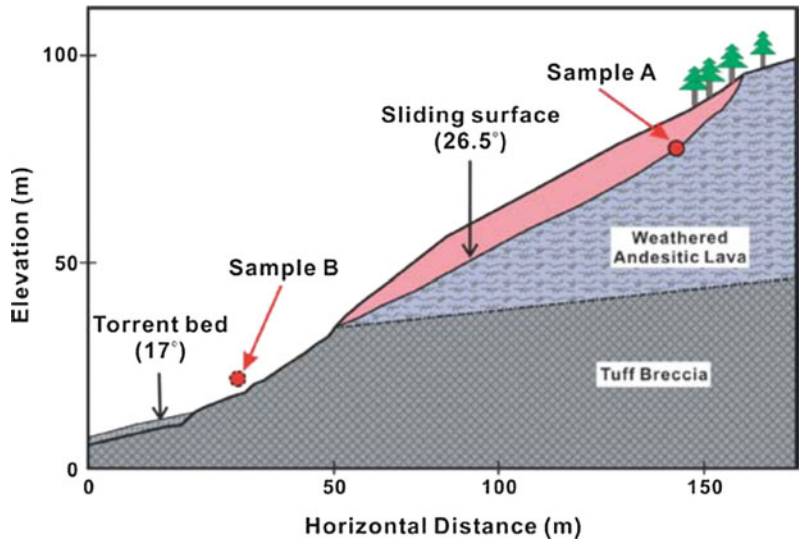
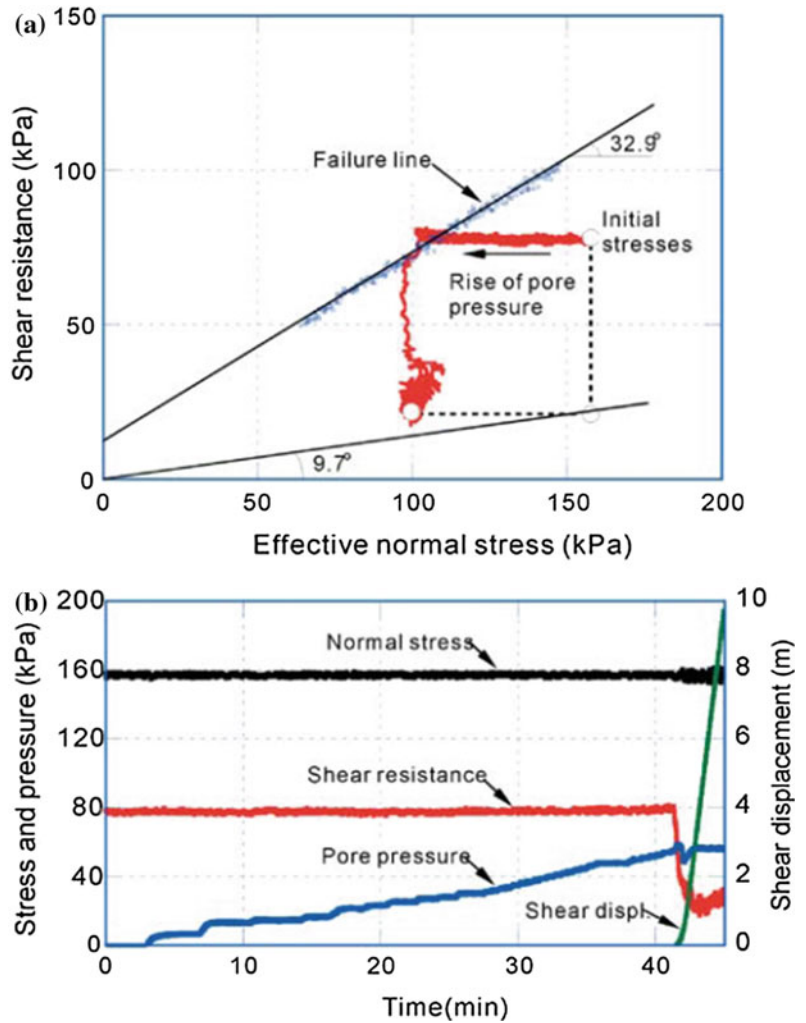


Fig. 12 Tests results of the Minamata landslide ($B_D = 0.86$), **a** stress path, **b** time series



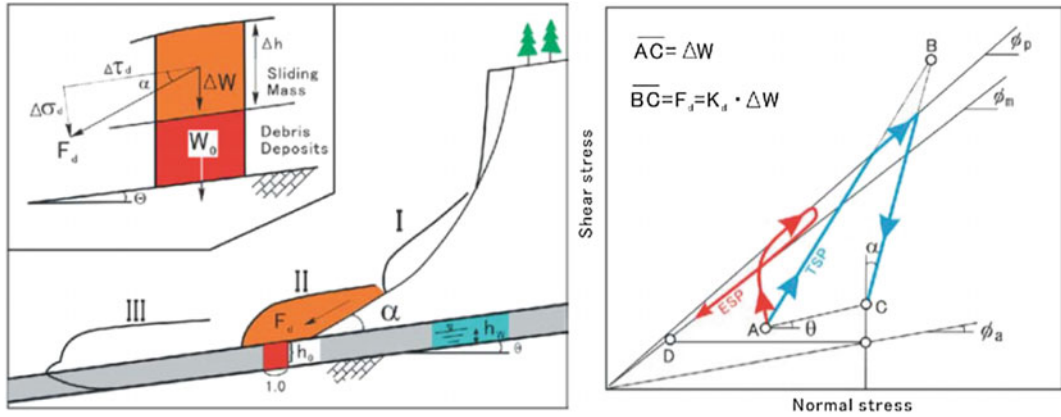


Fig. 13 Model of the landslide triggered debris flow (Sassa et al. 1997) (left); stress path of the torrent deposit during loading (right)

Sassa et al. (1997) introduced a model of landslide triggered debris flow, where the pre-existing torrent deposit was loaded by the moving landslide mass (Fig. 13). The landslide mass moves down a slope (I), then met the torrent deposit at the foot of the slope (II). In this stage, the torrent deposit was loaded by the landslide mass. The torrent deposit was sheared by the undrained loading of the landslide mass, if the surface water stream or subsurface flow was existed and the deposit was in a saturated condition. The entrained torrent deposit then moved downstream together with the sliding mass (III) in the form of a debris flow.

The self-weight (W_0) was worked in the torrent deposit during the landslide mass moves down a slope (I). But when the sliding mass reaches to the torrent deposit (II) with a certain velocity, the applied stress on the deposit was the sum of the static stress, including ΔW (due to the weight of the sliding mass) and the dynamic (impact) stress, F_d in the direction of sliding mass motion. The stress path in Fig. 13 describes the stress condition on the bottom of deposit. Point A means the initial stress condition of the torrent deposit (when slide mass moves in the position I) and the total stress path shifts to point C due to the additional static stress (ΔW) without excess pore pressure generation. The total stress path moves to point B if there is a dynamic stress (F_d) works on the torrent deposit, which is the obvious case found in the field. After failure, the

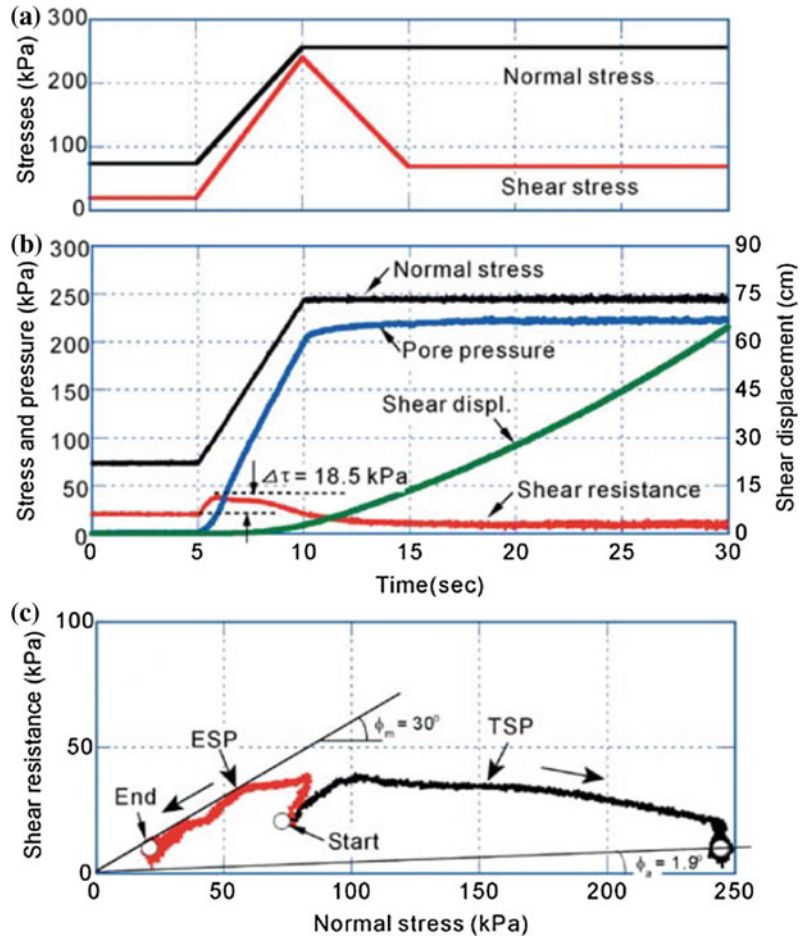
stress path then moves along the failure line. The stress path moves back to point C if the dynamic stress reduces to zero, indicating the total stresses are equal to W_0 and ΔW .

The dynamic shear stress and normal stress acting on the torrent deposit are formulated as:

$$F_d \cos \alpha = \tau_d, \quad F_d \sin \alpha = \sigma_d$$

where α is the angle at the collision between sliding mass and the torrent deposit, F_d is the dynamic stress, and the dynamic coefficient is stated as $k_d = (F_d/\Delta W)$. In the case where the excess pore pressure was generated due to the loading and shearing after failure, the effective stress path will shift from point A to D (red line in Fig. 13). The angle α works when the landslide mass moves from a steep slope to the torrent and becomes zero when the sliding mass travels together with entrained deposit within the torrent. The tests were conducted to simulate the sliding mass movement into the torrent deposits, with assumptions that the depth of sliding mass was approximately of 10 m, the depth of torrent deposits was 2–4 m with the gradient of about 15° and the dynamic coefficient was 0.9. Two samples, andesitic lava and tuff breccia, were tested by rapid loading using the ring shear apparatus in undrained condition. The tests results are shown in Fig. 14 for the tuff breccia and Fig. 15 for the weathered andesitic lava.

Fig. 14 Tests results of the undrained loading tests for the tuff breccia deposits ($B_D = 0.89$)



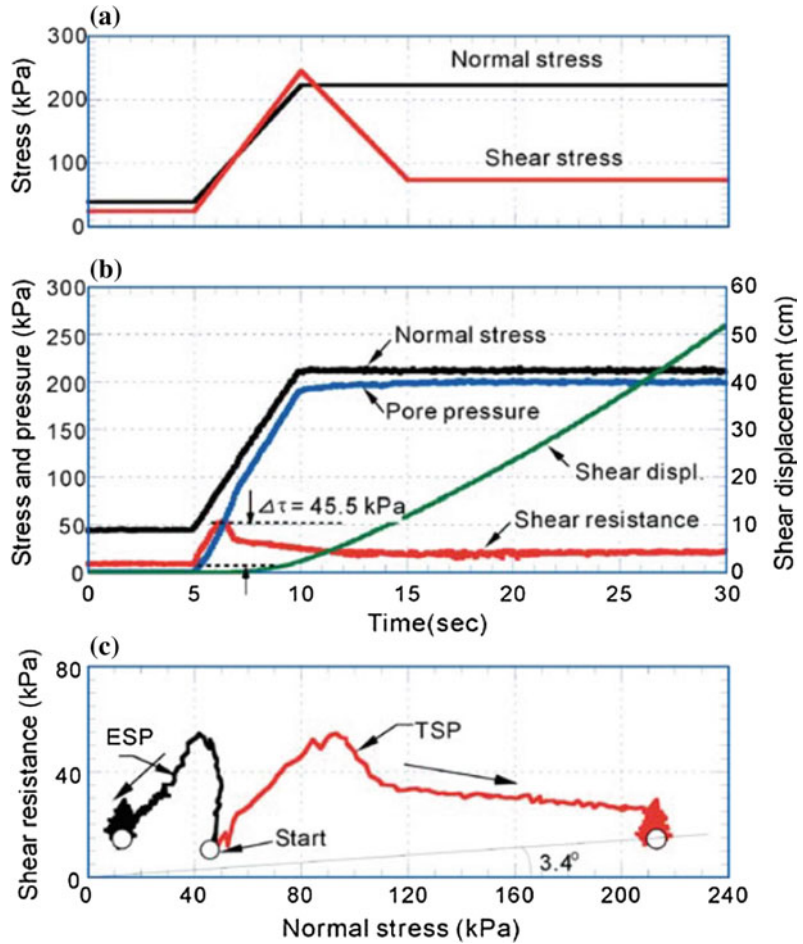
In the tuff breccia, shear failure within undrained rapid loading was occurred in the additional shear stress of 18.5 kPa (Fig. 14b) with a very small apparent friction angle (ϕ_a) of 1.9° (Fig. 14c). Meanwhile, the additional shear stress for the andesitic lava was 45.5 kPa (Fig. 15b) and the mobilized apparent friction angle of 3.4° produced in the steady state (Fig. 15c). Both samples were experienced the excess pore pressure during undrained rapid shear loading. These results implied that the saturated deposits were entrained by the sliding mass. The use of ring shear apparatus is very

effective to study the mechanism of landslide mass entrained the torrent deposit which then transformed into a debris flow.

6 The DPRI-7 Ring Shear Apparatus with a Transparent Shear Box

The DPRI-7 ring shear apparatus with a transparent shear box was developed with the maximum shear speed of 300 cm/s (Fig. 16). This version aims to observe the formation of shear zone during the landslide initiation and

Fig. 15 Tests results of the undrained loading tests for the weathered andesitic lava ($B_D = 0.97$)



post-failure motion. The structure is similar with the DPRI-5 and DPRI-6. The outer ring shear box was made by a transparent acrylic where 1.5 mm thickness of stainless steel plate was attached on the bottom of the upper ring (to be touched by rubber edge during shearing). The gutter and metal filters for the pore-pressure measurement were installed in the inner ring of the upper shear box.

The sample of silica sand, with the mean diameter (D_{50}) of 3.00 mm and the coefficient of uniformity (U_c) of 1.3, was used for the undrained shear test using the DPRI-7. The sample was saturated and loaded with the normal stress of

200 kPa in normally consolidation state. The low B_D value was achieved only 0.66 due to a high bulk modulus of the sample within large grain size. The shearing was conducted through undrained speed controlled test by increasing the velocity up to 200 cm/s within 5 s. The shearing was stopped after 30 m of shear displacement. The test results are shown in Fig. 17. The negative pore-water pressure was appeared at the beginning of shearing when the peak shear resistance produced (Fig. 17a). Slight increment of the normal stress was occurred due to dilation phenomena in a relatively dense sample. The pore-water pressure then increased significantly



Fig. 16 View of the ring-shear apparatus DPRI-7 with a transparent shear box

at the same time when the shear resistance decreased during failure. The steady state was reached when the shear displacement reached 30 m and no further increase of the pore-water pressure. The stress path shown in Fig. 17c implied that the sample had a sliding-surface liquefaction (described also in Sassa 1996, 2000).

Observation of the shear zone development in a transparent ring shear box of the DPRI-7 is shown in Fig. 18. From the middle of shearing (Fig. 18b), the shear zone was developed and became wider when the large shear displacement takes place (Fig. 18c). The murky pore water within the shear zone was resulted due to the progressive grain crushing. Those grain crushing makes the fine particles floated in the shear zone during shearing and settled down to the bottom of shear box after the test finished. The grain size distribution was compared between the original sample and the tested sample from the lower half

of the shear box (Fig. 19). With all these results, the DPRI-7 with a transparent shear box has shown that the grain crushing and sliding surface liquefaction were took place in undrained shearing of the apparatus, as explained in Sassa (1996) and Sassa et al. (1996).

7 Conclusion

The series of undrained ring shear apparatus developed by Professor Sassa and his colleagues at the DPRI of Kyoto University were presented in this paper. The rubber edge and gap controlling system were introduced to prevent the water leakage during shearing in undrained condition. The assessment of Nikawa landslide was carried out through ring shear tests for the samples of granitic sand and silty gravel. The results showed that a rapid landslide might be triggered by a similar earthquake of the 1995 Hyogo-Ken Nanbu event. Simulation using the DPRI-5 ring shear apparatus for landslide-triggered debris flow in the Minamata City was also described. The groundwater level increase up to a failure state was expressed by the drained pore pressure control test. Moreover, the entrainment process of the torrent deposit and weathered surface soils along the torrent by the moving sliding mass was carried out through the undrained loading test. This is the main process when the Minamata landslide was transformed into a debris flow with the volume enlargement. The results gave us information that the shear failure was achieved in a small increment of shear stress while the pore pressure was highly generated. In addition, observation of the shear zone development and grain crushing process during shearing were conducted using the DPRI-7 with a transparent shear box. The shear zone of the silica sand sample was established during shearing, and was enlarged in the progress of large shear displacement. By these results, we could clarify that the DPRI-7 was an effective tool to study the flow behaviour of saturated granular material during the failure state.

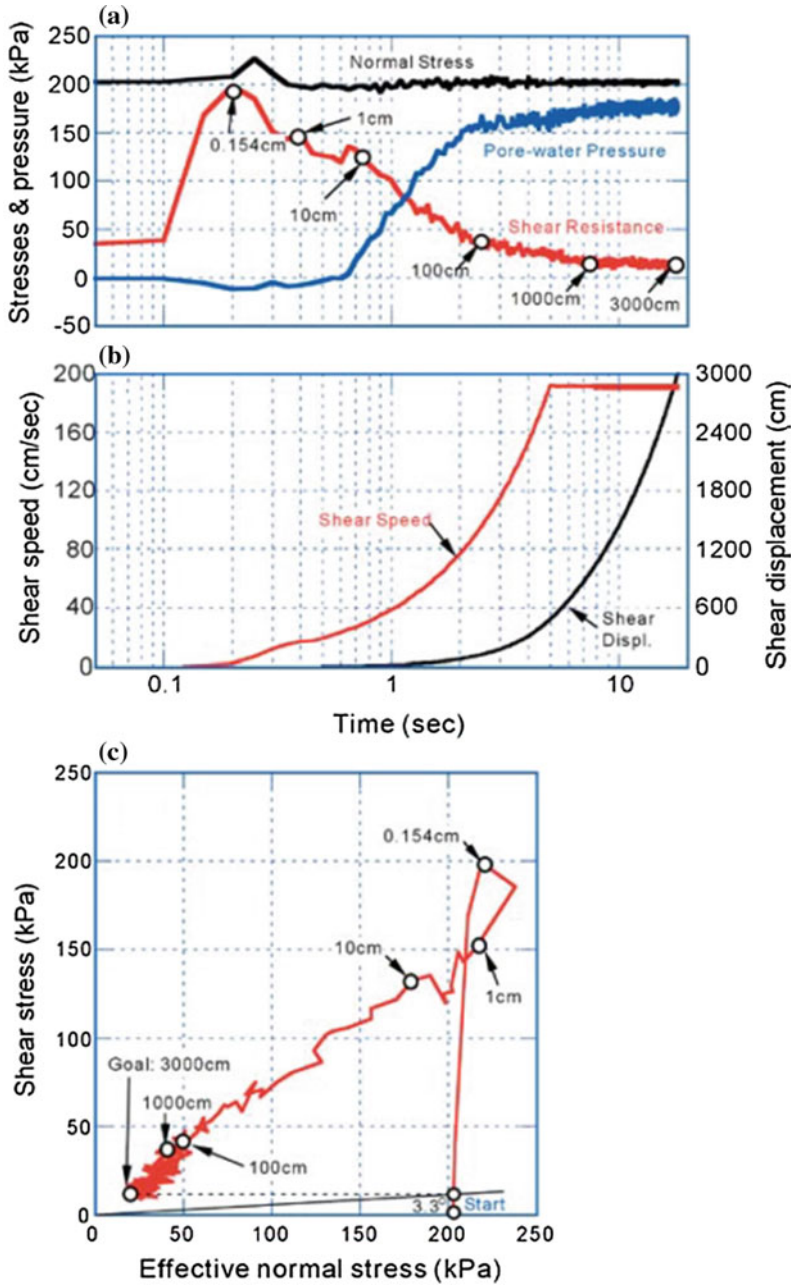


Fig. 17 The undrained high-speed shearing (2.0 m/s) for the silica sand

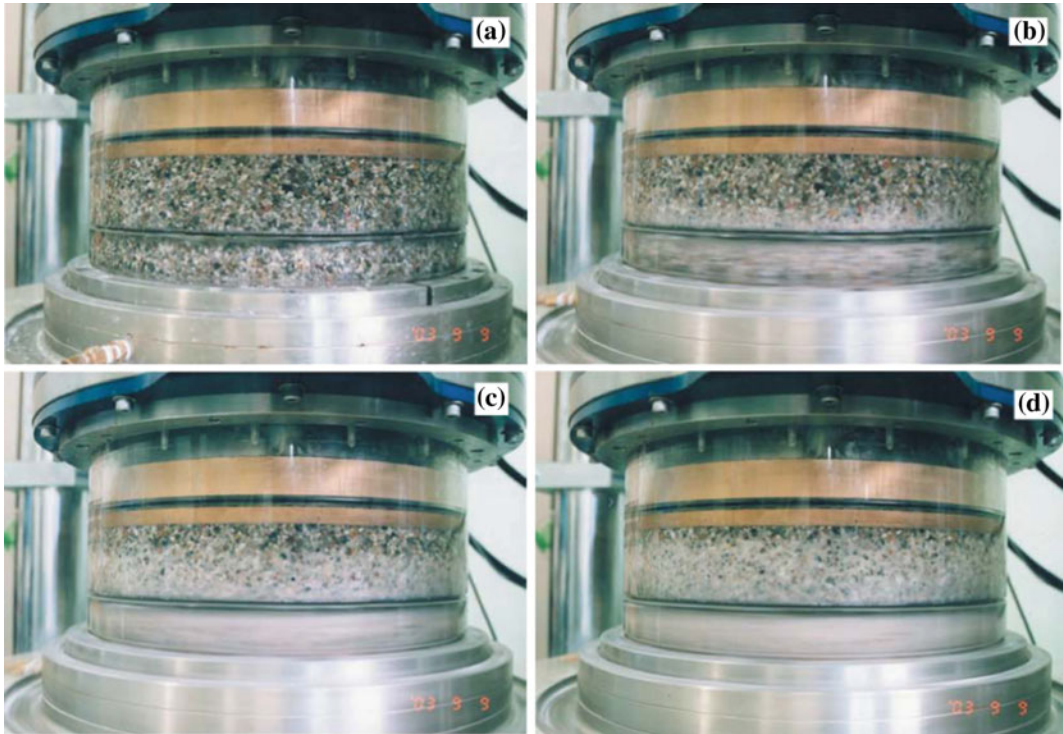


Fig. 18 Shear zone evolution and the grain crushing process **a** before the undrained shearing, **b** at the middle of shearing, **c** shearing process with large shear-displacement, **d** before the shearing termination

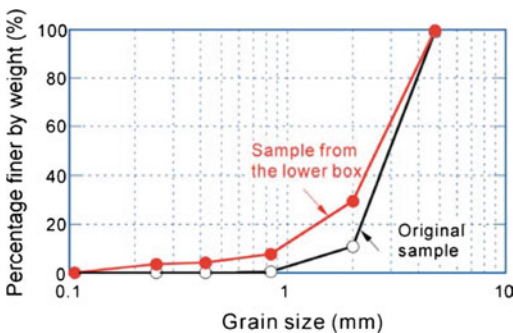


Fig. 19 Grain size distribution of the samples after undrained shearing compared with the original samples before the test

Acknowledgements We acknowledge the support of Scientific-Grant-in-Aid (No.03556021) of the Ministry of Education, Science, Culture and Sport of Japan in 1992 for the development of DPRI-3 (Sassa 1994), as well as DPRI-5 and DPRI-6 for the mitigation purpose of the Hyogo-Ken Nanbu earthquake. The help from Dr. Zieaoddin Shoaie and Dr. Fawu Wang for the system improvement and testing procedures are highly appreciated. The DPRI-7 was developed with support from APERIF Project, funded by

Ministry of Education, Culture, Sports, Science and Technology of Japan (MEXT). The project was approved by the International Consortium on Landslides (ICL) as the IPL M-101 APERITIF Project. Many thanks go to all colleagues of the Research Centre on Landslides of the DPRI, Kyoto University for their cooperation.

References

Ambraseys NN, Bommer JJ (1991) The attenuation of ground accelerations in Europe. *Earthq Eng Struct Dyn* 20:1179–1202

Bishop AW, Green GE, Garga VK, Andersen A, Brown JD (1971) A new ring-shear apparatus and its application to the measurement of residual strength. *Geotechnique* 21(1):273–328

Fukushima Y, Tanaka T (1990) A new attenuation relation for peak horizontal acceleration of strong earthquake ground motion in Japan. *Bull Seismol Soc Am* 80(4):757–783

Garga VK, Sendano JI (2002) Steady state strength of sands in a constant volume ring-shear apparatus. *Geotech Test J* 25(4):414–421

Hung O, Morgenstern NR (1984) High-velocity ring-shear tests on sand. *Geotechnique* 34(3):415–421

- Hvorslev MJ (1939) Torsion shear tests and their place in the determination of the shearing resistance of soils. *Proc Am Soc Test Mater* 39:999–1022
- Ishihara K (1993) Liquefaction and flow failure during earthquakes. *Geotechnique* 43(3):349–451
- Sassa K (1984) The mechanism starting liquefied landslides and debris flows. In: *Proceedings of 4th international symposium on landslides*, Toronto, June, vol 2, pp 349–354
- Sassa K (1988) Geotechnical model for the motion of landslides. In: *Special lecture of 5th international symposium on landslides*, “landslides”, 10–15 July, vol 1, pp 37–55
- Sassa K (1992) Access to the dynamics of landslides during earthquakes by a new cyclic loading high-speed ring-shear apparatus (keynote paper). In: Balkema AA (ed) *6th International Symposium on Landslides*, “Landslides”, vol 3. Christchurch, 10–14 February, pp 1919–1937
- Sassa K (1994) Development of a new cyclic loading ring-shear apparatus to study earthquake-induced-landslides. Report of grain-in-aid for development scientific research by the Ministry of Education, Science and Culture, Japan (Project No. 03556021)
- Sassa K (1996) Prediction of earthquake induced landslides. In: *Proceedings of 7th international symposium on landslides*, vol 1. A.A. Balkema, Trondheim, pp 115–132 (17–21 June)
- Sassa K (1997) A new intelligent-type dynamic-loading ring-shear apparatus. *Landslide News* 10:33
- Sassa K (2000) Mechanism of flows in granular soils. In: *Proceedings of GeoEng2000*, Melbourne, vol 1, pp 1671–1702
- Sassa K (2002) Study on the mechanism of earthquake and rainfall induced rapid flow phenomena—disasters and their mitigation in large-scale cities. In: *Proceedings of the symposium on aerial prediction of earthquake and rainfall induced flow phenomena (APERIF)*, “New century of urban area landslide disaster mitigation,” Tokyo, 31 Aug–1 Sept 2002, pp 7–33 (in Japanese)
- Sassa K, Fukuoka H, Scarascia-Mugnozza G, Evans S (1996) Earthquake-induced landslides: distribution, motion and mechanisms. Soils and foundations, special issue for the Great Hanshin earthquake disaster, pp 53–64
- Sassa K, Fukuoka H, Wang FW (1997) Mechanism and risk assessment of landslide-triggered-debris flows: lesson from the 1996.12.6 Otari debris flow disaster, Nagano, Japan. In: Cruden DM, Fell R (eds) *Landslide risk assessment*, proceedings of the international workshop on landslide risk assessment, Honolulu, pp 347–356 (19–21 Feb)
- Sassa K, Wang G, Fukuoka H (2003a) Assessment of earthquake-induced catastrophic landslides in urban areas and their prevention planning. In: *Proceedings of international conference on slope engineering*, Dec 2003, vol 1. The University of Hong Kong, pp 26–49
- Sassa K, Wang G, Fukuoka H (2003b) Performing undrained shear tests on saturated sands in a new intelligent type of ring-shear apparatus. *Geotech Test J* 26(3):257–265
- Shoaei Z, Sassa K (1994) Basic study on the shear behavior of landslides during earthquakes—excess pore pressure in the undrained cyclic loading ring-shear tests. *Bull Disaster Prevent Res Inst Kyoto Univ* 44(1):1–43
- Tika TM (1989) The effect of rate of shear on the residual strength of soil. PhD thesis, University of London (Imperial College of Science and Technology)

TXT-tool 3.081-1.8

A New High-Stress Undrained Ring-Shear Apparatus and Its Application to the 1792 Unzen–Mayuyama Megaslide in Japan

Khang Dang, Kyoji Sassa, Bin He, Kaoru Takara,
Kimio Inoue and Osamu Nagai

Abstract

Sassa and others in the International Consortium on Landslides (ICL) have developed a new series of undrained ring-shear apparatus (ICL-1 and ICL-2) for two projects of the International Programme on Landslides (IPL-161 and IPL-175). Both projects are supported by the Science and Technology Research Partnership for Sustainable Development Program (SATREPS) of Japan. ICL-1 was developed to create a compact and transportable apparatus for practical use in Croatia; one set was donated to Croatia in 2012. ICL-2 was developed in 2012–2013 to simulate the initiation and motion of megaslides of more than 100 m in thickness. The successful undrained capacity of ICL-2 is 3 MPa. This apparatus was used to simulate possible conditions for the initiation and motion of the 1792 Unzen–Mayuyama megaslide (volume, $3.4 \times 10^8 \text{ m}^3$; maximum depth, 400 m) triggered by an earthquake. The megaslide and resulting tsunami killed about 15,000 people. Samples were taken from the source area (for initiation) and the moving area (for motion). The hazard area was estimated by the integrated landslide simulation model LS-RAPID, using parameters obtained with the ICL-2 undrained ring-shear apparatus.

K. Dang (✉) · K. Sassa · O. Nagai
International Consortium on Landslides, Kyoto,
Japan
e-mail: khang@iclhq.org

K. Sassa
VNU University of Science, Hanoi, Vietnam

B. He
CAS Key Laboratory of Watershed Geographic
Sciences, Nanjing Institute of Geography and
Limnology, Chinese Academy of Sciences (CAS),
Nanjing, China

K. Takara
Disaster Prevention Research Institute, Kyoto
University, Kyoto, Japan

K. Inoue
Sabo Frontier Foundation, Tokyo, Japan

Keywords

Landslide • Undrained ring-shear apparatus • Unzen • Mayuyama

Contents

1	Introduction	372
2	Development of a New High-Stress Dynamic-Loading Undrained Ring-Shear Apparatus (ICL-2)	372
2.1	Apparatus Configuration.....	372
2.2	Basic Tests of the ICL-2.....	373
3	Application of the ICL-2 Apparatus to the 1792 Unzen–Mayuyama Megaslide	380
3.1	Ring-Shear Tests to Simulate Initiation of the Unzen–Mayuyama Landslide.....	381
3.2	Pore-Water Pressure Controlled Test.....	381
3.3	Undrained Cyclic Loading Test.....	382
3.4	Seismic-Loading Test.....	383
3.5	Ring-Shear Tests to Simulate the Motion of the Unzen–Mayuyama Landslide.....	384
4	Application of the Integrated Computer Simulation Model (LS-RAPID) to the Mayuyama Landslide	386
4.1	Triggering Factors.....	386
4.2	Unit Weight of Soils in the Unzen Volcano.....	387
4.3	Landslide Dynamics Parameters.....	387
5	Conclusion	390
	References.....	391

1 Introduction

The greatest landslide disaster in the history of Japan is the 1792 Unzen–Mayuyama megaslide (Nakada et al. 1992, 1999). Its volume was $3.4 \times 10^8 \text{ m}^3$ and the maximum depth was 400 m; around 15,000 people were killed by the landslide and its resulting tsunami (Unzen Restoration Office of the Ministry of Land, Infrastructure and Transport of Japan 2002, 2003). The objective of this research is to develop a reliable hazard assessment technology for such megaslides based on measurements of the dynamic parameters of samples taken from the landslide source area and the travel area, and an integrated numerical simulation of the initiation and motion using those parameters. The newly developed ICL-2 high stress ring-shear apparatus, its initial test results and its application

to the 1792 Unzen–Mayuyama landslide are reported in this paper.

2 Development of a New High-Stress Dynamic-Loading Undrained Ring-Shear Apparatus (ICL-2)

2.1 Apparatus Configuration

A general view of the ICL-2 ring-shear apparatus is shown in Fig. 1. A computer with dual monitors (① ② in Fig. 1) provides automated control for a variety of predetermined tests (such as monotonic loading tests, cyclic loading tests, seismic loading tests using the real seismic records, pore-pressure control tests and various combinations of these). This computer displays signals from sensors for shear stress/torques, normal stress/vertical load, pore pressure, effective pressure, mobilized friction angle, shear displacement and vertical displacement as time-series data plots and as stress-path data plots. Servo-control systems drive the shear motor and gap control motor, oil servo-valves for the normal-stress control and pore-pressure control. The servo-control systems and amplifiers for data monitoring are included in the amplifier box (③ of Fig. 1). The main apparatus, including the shear box, loading piston, and shear- and gap-control motors, is shown in ④ (Fig. 1). Other components (⑤, ⑥ and ⑦ in Fig. 1) are a power supply, oil pump and the pore-pressure loading unit.

The photograph and three diagrams of Fig. 2 show (a) a general view of the apparatus; (b) the apparatus cross-section; (c) close-up detail of the soil-filled upper and lower shear boxes equipped with pore-water pressure sensors, also the detailed structure of the rubber-edge sealing to maintain undrained condition; and (d) the



Fig. 1 General View of ICL-2. From left to right: (1) monitor for signals to control experiments and to control recording, (2) monitor for the stress path and time series

data, (3) amplifier box, (4) main apparatus, (5) power supply box, (6) oil pump inside the cover, and (7) pore pressure control unit

signal-flow chart for the servo device controlling normal stress, pore-water pressure, shear stress and the gap between upper and lower shear boxes, respectively.

2.2 Basic Tests of the ICL-2

To examine the rubber-edge friction and the performance of the newly developed high-stress dynamic-loading ring-shear apparatus during drained speed-controlled and undrained monotonic stress-controlled tests, a series of basic tests were conducted using a sample taken from a megaslide, the Unzen–Mayuyama landslide.

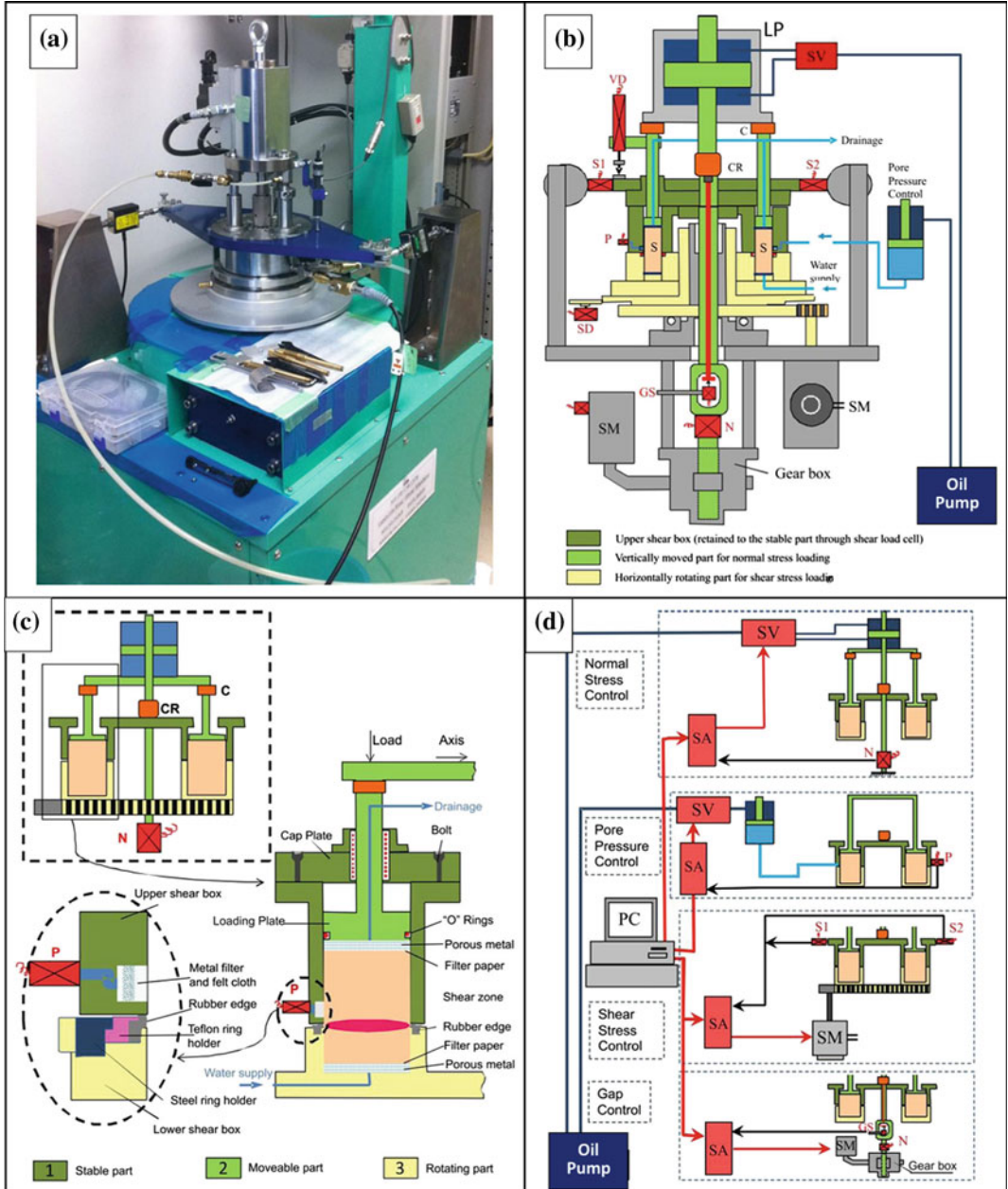
2.2.1 Rubber-Edge Friction

The shear stress mobilized on the sliding surface is equal to the measured value of the shear load cell (S1 + S2) minus the rubber-edge friction. When a normal stress is loaded on the sample in the shear box, a lateral pressure acts on the

rubber edge, as shown in the two lower figures of Fig. 2c. The rubber edge is compressed by the lateral pressure, but due to an arch action of the rigid stainless steel shear box, less pressure will act on the soft rubber edge. The lateral pressure ratio (k is the ratio of lateral pressure to vertical pressure) is approximately expressed by the Jakey’s equation (Sassa 1988) as $k = 1 - \sin \phi$. When $\phi = 30^\circ$, $k = 0.5$.

We initially believed that the lateral pressure would be approximately 1/2 to 1/3 of the normal stress. We therefore chose to fill the shear box with water and consecutively loaded normal stresses of 0.5, 1.0 and 1.5 MPa and sheared water in a speed-controlled test.

Figure 3 presents the measured shear resistance of the rubber edge at 0.5, 1.0, and 1.5 MPa. The 1.5 MPa test result was unstable, whereas 1.0 and 0.5 MPa tests were stable. Both the 1.0 and 0.5 MPa tests indicated a rubber edge friction of 20–25 kPa; however, the value varied with shear displacement. The most important



◀ **Fig. 2** Configuration of ICL-2. **a** Photo of the shear box and loading piston. **b** Outline of the mechanical structure. **c** Mechanical structure for shear box and the close-up view of the undrained gap. **d** Servo-control system. The mechanical configuration of the apparatus is shown in panel (b). The parts of the apparatus are coded with different colors in the figure as follows: *gray* (lower part), stable part; *yellow* (lower shear box and rotating table), rotates horizontally for shearing; *dark green* (upper shear box and loading cap), rotates horizontally and moves vertically. This part is horizontally restrained by a pair of load cells (S1 and S2) which monitor shear stress and vertically restrained by the load cell which monitors

normal stress (N). Each load cell is very slightly extended or compressed as required to measure forces. *Light green* (central axis to connect to the loading piston), can move vertically to adjust the gap between the upper and lower shear boxes. The *light green colored* part is fixed to the *dark green part* after the sample has been set until the conclusion of testing. *Light gray* (top, loading piston), the piston rod (*light green*) connects to the stable part (*gray*) through the load cell for normal stress (N). When oil pressure is supplied to the lower chamber (*blue*) of the loading piston, a tensile stress acts through the central axis (*light green*), to pull the housing of the loading piston (*light gray*) down on the sample, thus loading the normal stress

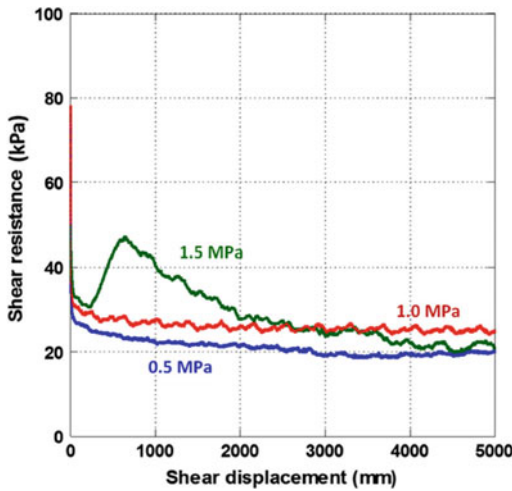


Fig. 3 Relationship between rubber-edge friction and shear displacement. Shear box is filled with water. Shear speed: 10 mm/s. Loaded normal stress on water: 0.5, 1.0 and 1.5 Mpa

value is the steady-state resistance after a large shear displacement. It was found to be 20 kPa at 0.5 MPa, and 25 kPa at 1.0 MPa. The precision of the shear load cell and normal stress load cell are 0.01–0.03% of the full scale. The precision of the pore-pressure sensors is 0.14–0.15%. The precision of the rubber-edge frictional resistance (± 2.5) will be 0.08% of the full scale (3 MPa) of the load cell for normal and shear stresses.

When conducting tests at lower normal stresses, the load cells can be replaced by those of lower capacities.

2.2.2 Sample From the 1792 Unzen–Mayuyama Landslide

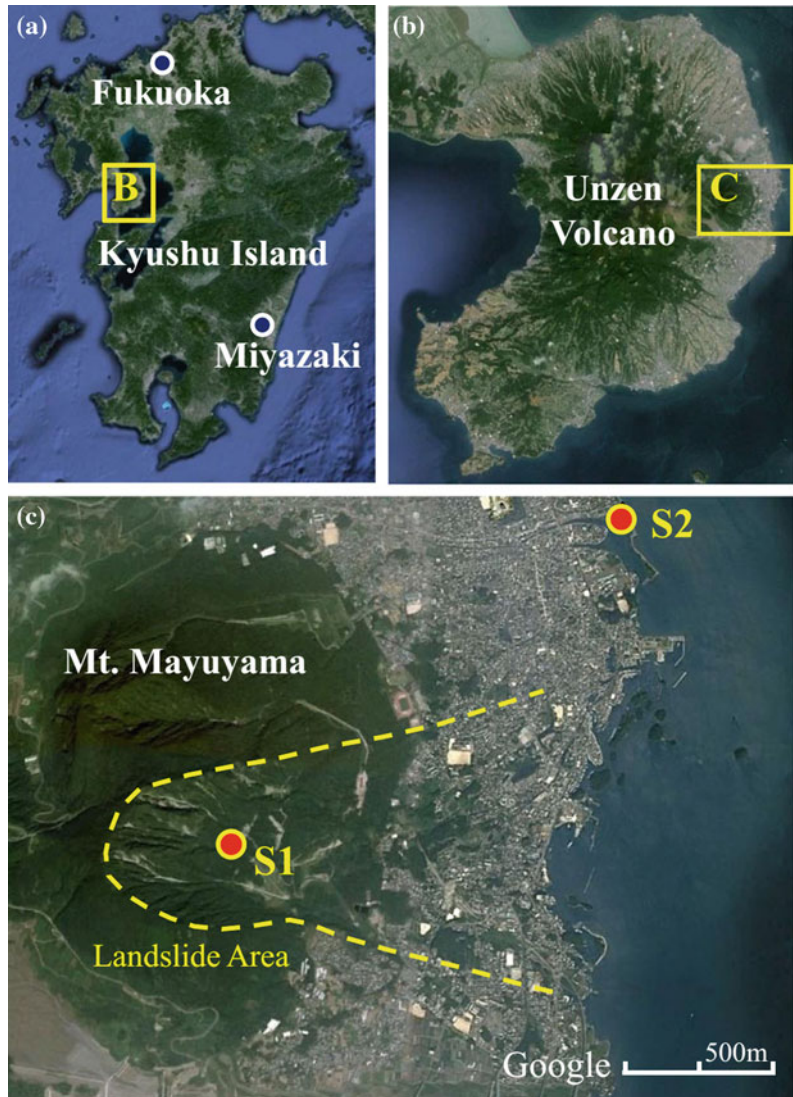
For initial tests of ICL-2, we chose samples from the 1792 Unzen–Mayuyama landslide in Shimabara City, Kyushu Island, Japan. Mayuyama is a dome of the Unzen Volcano. The location of sampling is shown in Fig. 4. Sample S1 was taken from a sand layer exposed along a torrent gully in the source area of the landslide. Sample 2 was taken from the coastal area outside the landslide area to represent the soil overridden by the landslide.

The mountain consists of volcanic lava rock and unconsolidated eruption products (debris and sands). The sliding surface of the landslide probably formed within a sandy layer rather than in the strong intact lava rocks and boulders. We took samples from a sandy zone exposed along a torrent gully side slope in the source area. A series of tests to examine the capability and performance of the ICL-2 apparatus were conducted on sample S1 from this megaslide.

2.2.3 Drained Speed-Control Test

A drained test is the best way to measure the friction angle of a sample and also to check the apparatus without any effect of pore water pressure. A drained speed-controlled test was conducted as a basic test. First, the sample was fully saturated to $B_D = 0.97$, consolidated to close to 3 MPa and then sheared at 0.2 cm/s in the drained condition. After the shear surface had

Fig. 4 The sampling locations in the Unzen Mayuyama area (image from Google Earth)



reached peak shear resistance, the drained normal stress was reduced to zero at a rate of $\Delta\sigma = 5$ kPa/s to obtain the drained stress path and friction angle of the sample (Fig. 5). The peak friction angle for S1 was 39.1° , and the friction angle during motion was 35.9° . The stress path and the friction angles appeared to be reasonable for the nature of the sample. The right graph in Fig. 5 is the time-series data for total normal stress, shear resistance and pore pressure.

Pore pressure remained zero throughout the test, since the test was under a drained condition. This drained, speed-controlled test result

indicated that each of the ICL-2 servo-control system for normal-stress loading and unloading, the monitoring system, and the undrained capability of the apparatus could successfully function even under the very high normal stress of 3 MPa.

2.2.4 Undrained Monotonic Stress-Control Tests

The ring-shear test able to simulate the landslide phenomena is a stress-controlled test which can provide appropriate shear stresses under rainfall, earthquake or undrained loading in the moving

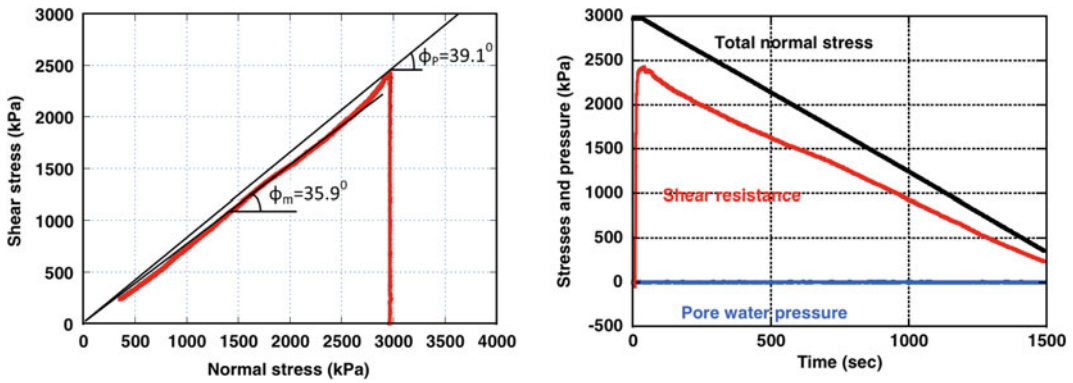


Fig. 5 Drained speed-control normal-stress-reducing test on Sample 1. $B_D = 0.97$, velocity = 0.2 cm/s. After reaching the peak, the normal stress was reduced at a rate of $\Delta\sigma = 5$ kPa/s

landslide mass. Undrained monotonic shear-stress controlled tests were conducted under four different normal stresses as tests of undrained capability, stress-control capability and precision of stress and pore-pressure monitoring.

For each test, normal stress was first loaded in the drained condition to close to the planned normal stress (0.3–3.0 MPa). The shear box was then changed to the undrained condition, and shear stress was loaded gradually at a rate of $\Delta\tau = 1\text{--}5$ kPa/s. When the effective stress path reached the failure line, it began to decrease due to pore-pressure generation (the mechanism for this is sliding-surface liquefaction as explained in “Sliding-surface liquefaction” section) along the failure line until the steady-state shear resistance was reached. Shearing was continued in each test until there was 3 m or more of shear displacement.

The stress paths and time-series data for each test are shown in Fig. 6a–d. The stress path at a normal stress of 375 kPa (Fig. 6a) reached the failure line (39.8°) showing dilative behavior and then decreased along the failure line until it reached a steady-state shear resistance of 37 kPa. Negative pore-pressure was measured just before failure. After failure, the pore pressure increased during shear displacement. This is a typical sliding-surface liquefaction behavior for a dense material: dilation of the sample near failure caused negative pore pressure, and grain crushing occurred in the shear zone. The resulting

volume reduction, together with the accumulating post-failure shear displacement, generated positive pore pressure, even in the dense material (Fig. 8).

Shear behavior at 1030 kPa (Fig. 6b) normal stress was similar, but there was no negative pore pressure, although a zero pore pressure was measured just before failure. The steady-state shear resistance was 45 kPa, slightly higher than in the test at 375 kPa. The friction angle of the peak failure line was 41.2° , which also was slightly higher than at 375 kPa.

Shear behavior at 1970 kPa (Fig. 6c) normal stress was contractive. Pore-water pressure was generated during shearing before failure. The steady-state shear resistance was 80 kPa. Shear behavior at a normal stress of 2900 kPa, close to 3 MPa (Fig. 6d) presented a more contractive stress path and reached a failure line of 40.3° , then went down the line to a steady-state shear resistance of 120 kPa. The stress paths and time-series data of these four undrained monotonic stress-controlled tests showed no aberrations, and did not conflict with previous ring-shear tests such as those reported by Sassa et al. (2004, 2010) and others. All stress paths are plotted in the same figure in Fig. 7. As shown, the four tests overlapped along the failure line during motion at 39.8° .

The undrained test results for four different normal stresses, ranging from 375 to 2900 kPa, are plotted in Fig. 7. All stress

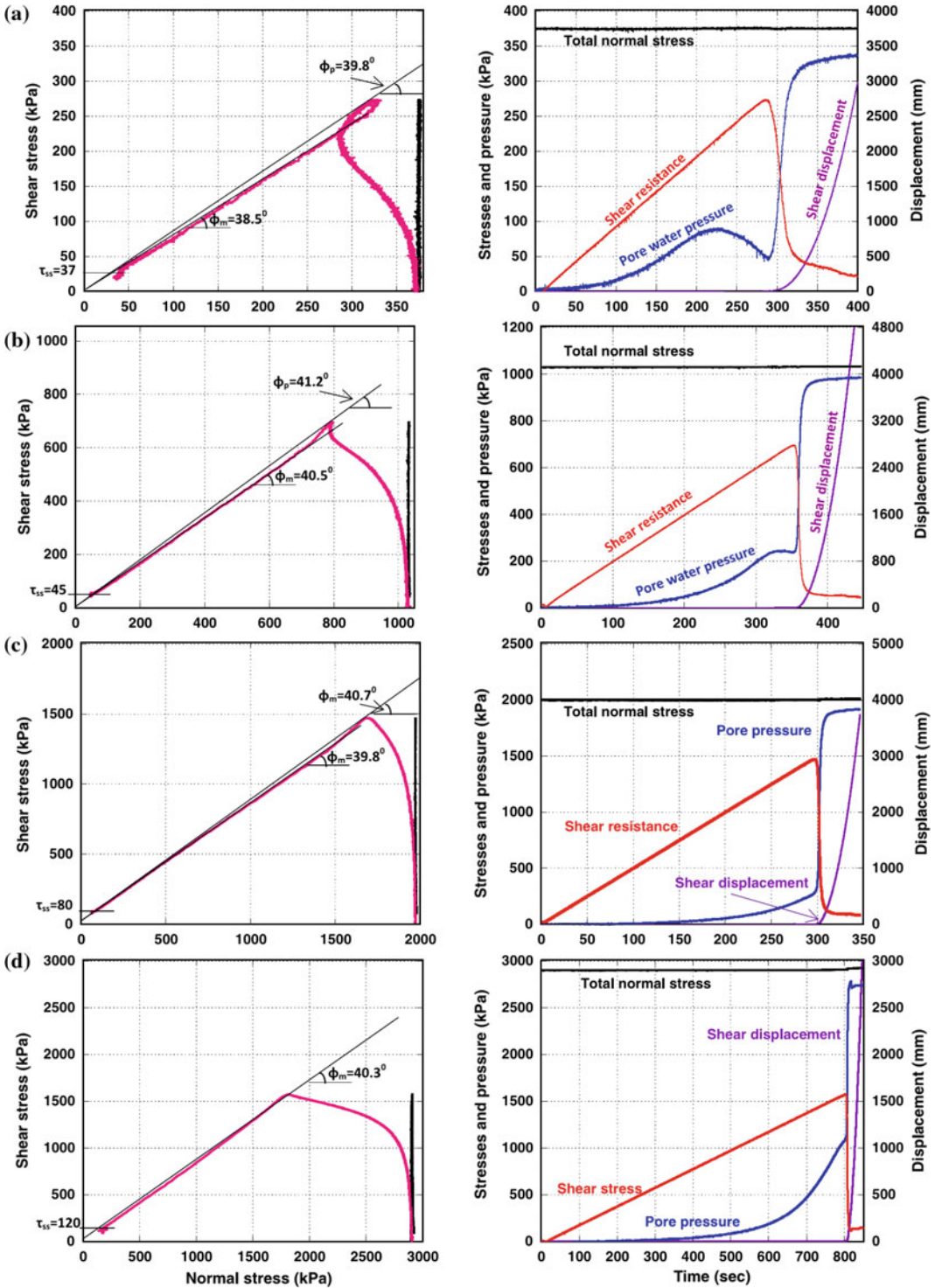


Fig. 6 Undrained monotonic stress control tests at different normal stresses. Sample: S1 from Unzen–Mayuyama.
a Normal stress = 375 kPa, $B_D = 0.93$, $\Delta\tau/s = 1$ kPa/s.

b Normal stress = 1030 kPa, $B_D = 0.95$, $\Delta\tau/s = 2$ kPa/s.
c Normal stress = 1970 kPa, $B_D = 0.95$, $\Delta\tau/s = 5$ kPa/s.
d Normal stress = 2900 kPa, $B_D = 0.96$, $\Delta\tau/s = 2$ kPa/s

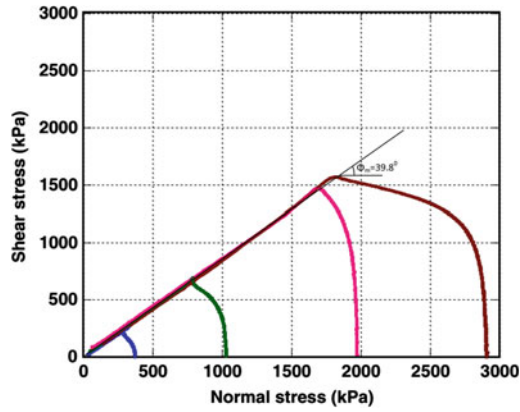
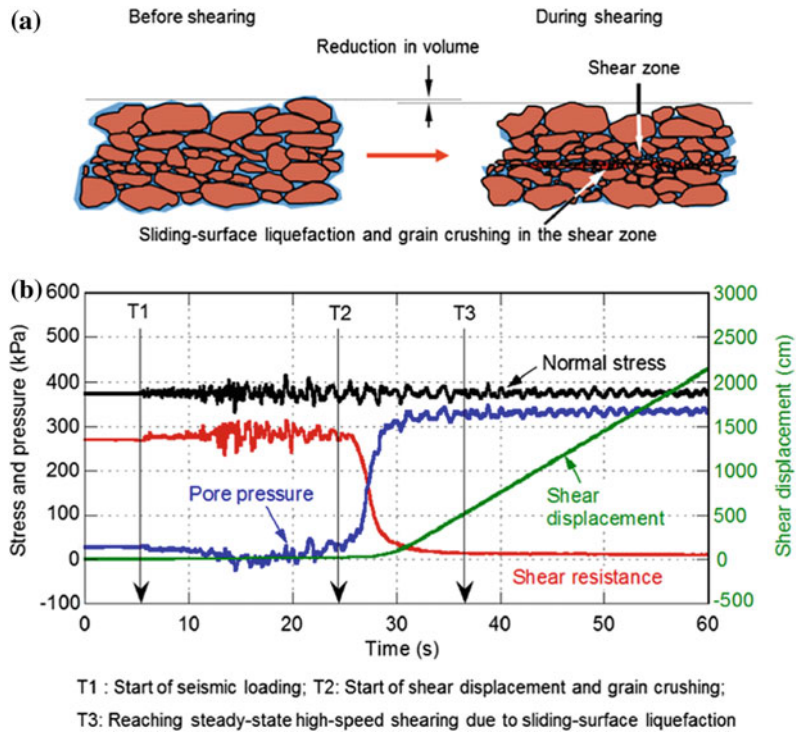


Fig. 7 Combined undrained monotonic control test on Sample S1 ($B_D = 0.93-0.96$)

Fig. 8 Illustration of the sliding surface liquefaction and a typical test result. Example for volcanic debris from the 2006 Leyte landslide (Sassa et al. 2010)



paths had the same friction angle (39.8°) during motion. All tests showed sliding-surface liquefaction, that is, high pore-water pressure generated during the postfailure shear displacement. The values of steady-state shear

resistance range from 37 to 120 kPa. The test at higher normal stress shows the higher steady-state shear resistance, although the difference is smaller than the difference in loaded normal stresses (Fig. 6).

3 Application of the ICL-2 Apparatus to the 1792 Unzen–Mayuyama Megaslide

The 1792 Unzen–Mayuyama megaslide is both the largest landslide disaster and the largest volcanic disaster in Japan. This landslide killed 15,153 people including 10,139 in the Shimabara area. The other people were killed on the opposite coast by a landslide-induced tsunami wave: 4653 in Kumamoto Prefecture, 343 on Amakusa Island and 18 people in other areas (Usami 1996). The landslide is illustrated on the cover of

a leaflet published by the Unzen Restoration Office of the Ministry of Land, Infrastructure and Transport of Japan (2003), based on a topographic survey. This illustration is reproduced here (Fig. 9).

Figure 10 is a cross-section of the Unzen–Mayuyama megaslide. The estimated ground surface before the landslide is based on the paintings of Unzen–Mayuyama from the top of Shimabara castle and other locations from the Unzen Restoration Office of the Ministry of Land, Infrastructure and Transport of Japan (2002) referring to Inoue (1999, 2000). The

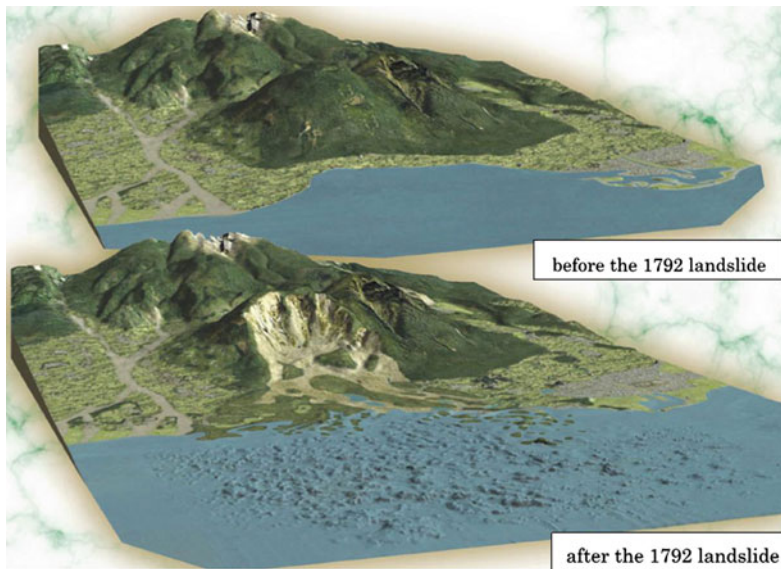


Fig. 9 The 1792 Unzen Mayuyama landslide (estimation before and after the landslide) (Unzen Restoration Office of the Ministry of Land, Infrastructure and Transport of Japan 2003)

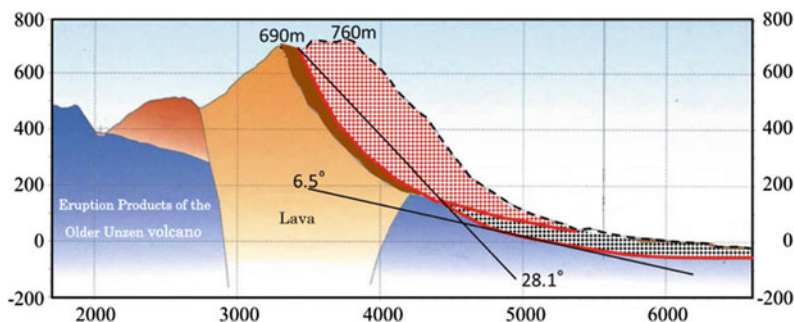


Fig. 10 Section of Mayuyama landslide and its interpretation. Modified from the Unzen Restoration Office of the Ministry of Land, Infrastructure and Transport of Japan (2002)

bedrock surface in the source area on the upper slope is drawn from the current topography and the bedrock surface in the lower area is estimated from drilling (Fig. 10). The authors suggest that there were two original landslide blocks (shown in Fig. 10 as blocks with red dots and black dots) and two possible sliding surfaces in the section. The lower block was assumed to have moved because of the undrained loading of the displaced landslide mass (red dots). The average slope angle of the sliding surface in the upper slope was 28.1° , and the average slope angle of the lower slope was around 6.5° .

3.1 Ring-Shear Tests to Simulate Initiation of the Unzen–Mayuyama Landslide

A series of earthquakes struck the Shimabara area in April 1792. The largest earthquake hit the area on 21 May 1792. The magnitude of this nearby earthquake is estimated to have been $M = 6.4 \pm 0.2$ (Usami 1996).

Usami estimated that the seismic intensity at Shimabara was at least V and possibly VI. The Unzen Restoration Office, however, estimates that the seismic intensity which triggered the Unzen–Mayuyama landslide was VII, because more than 30% of the houses were destroyed in the Shimabara area. Exact seismic accelerations may never be known, but probably were around 400 cm/s^2 or greater.

The Japanese seismic intensities (Usami 1996) are as follows:

- V: $80\text{--}250 \text{ cm/s}^2$ (where walls and fences are cracked, and Japanese gravestones fall down)
- VI: $250\text{--}400 \text{ cm/s}^2$ (where less than 30% of Japanese wooden houses are destroyed)
- VII: More than 400 cm/s^2 (where more than 30% of the houses are destroyed, landslides are triggered and surface fault rupture is seen).

The estimate of an acceleration of more than 400 cm/s^2 by the Restoration Office is probably correct, as it is based on a detailed study of house damage.

There are no seismic records of the 1792 earthquake so we chose to use a record from a recent earthquake. The 2008 Iwate–Miyagi Nairiku Earthquake ($M = 7.2$) triggered the Aratozawa landslide (67 million m^3) in Miyagi Prefecture. The maximum recorded acceleration was 739.9 cm/s^2 at MYG004 (National Research Institute for Earth Science and Disaster, Prevention [NIED]). We have used the Iwate–Miyagi earthquake wave form recorded in Miyagi Prefecture (MYG004) for the ring-shear simulation test and also in the computer simulation for 1792 Unzen–Mayuyama landslide.

We performed three tests on the sample (S1) taken from the source area of Unzen–Mayuyama (Fig. 5) to investigate the initiation of the landslide block in the upper slope (block with red dots in Fig. 10) using the ICL-2 apparatus.

3.2 Pore-Water Pressure Controlled Test

The first basic test for this landslide (Fig. 11) was to trigger landslide failure by increasing only the pore-water pressure.

Firstly, the sample was saturated (B_D value, 0.98), then consolidated to 3.0 MPa normal stress and 1.5 MPa shear stress in a drained condition. This preparatory stage was to reproduce the initial stress in the slope, and is shown as a black line in Fig. 11.

This initial stress corresponded to a slope of $\arctan(1.5/3.0) = 26.5^\circ$. This is a similar slope to the landslide block in Fig. 10. Then, in order to simulate the pore-pressure-induced landslide process, the pore-water pressure was gradually increased at a rate of $\Delta\sigma = 5 \text{ kPa/s}$. Failure occurred at a pore-water pressure of 1.2 MPa (a pore water pressure ratio $r_u = 1.2/3.0 = 0.4$). The friction angle at failure was 39.4° .

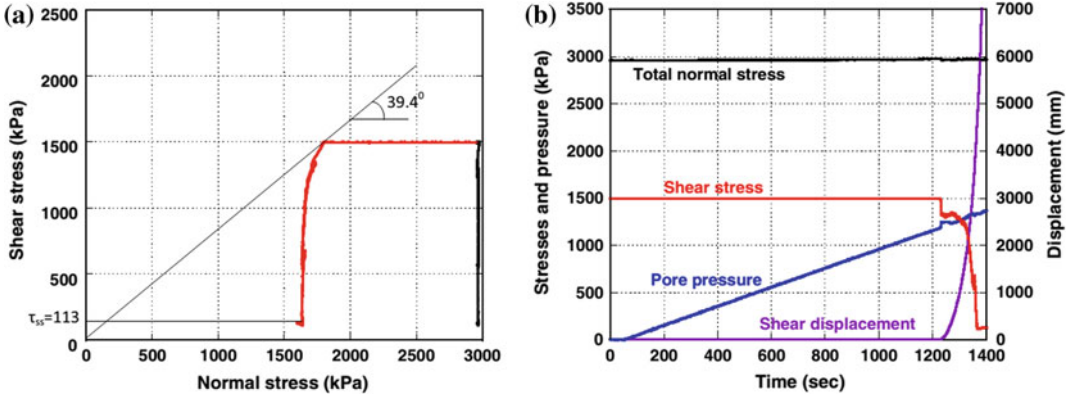


Fig. 11 Pore pressure control test on Sample 1. Sample: S1 from Mayuyama source area. $B_D = 0.98$

3.3 Undrained Cyclic Loading Test

The second basic test (Fig. 12) was an undrained cyclic loading test on the saturated Sample S1. Initially, the saturated sample was consolidated at 2.0 MPa normal stress, then a 1.2-MPa shear stress was loaded in the drained state to create the initial stress state. The slope angle for this combination of normal and shear stresses corresponded to $\arctan(1.2/2.0)$, i.e., 31.0° . The shear box was then switched to the undrained state for the undrained cyclic loading test. We applied the control signal for the computer as follows: an initial cycle of shear stress increment of ± 300 kPa was to be loaded as a sine curve, in

which the second, third and fourth cycles of shear stress were to be loaded as increasing ± 300 kPa in each step. (Normal stress was 2 MPa. It was expected that the soil would fail before the loading of the fourth cycle when the total shear stress would be 2.4 MPa.)

Thereafter, three cycles would be kept constant before the cyclic shear stress was reduced to zero. This computer signal was sent to the servo-amplifier for shear stress, while the control signal for normal stress was held constant. The pore-water pressure generation during the test, mobilized shear resistance, and shear displacement were each monitored continuously during the test. The stress path and the time-series data

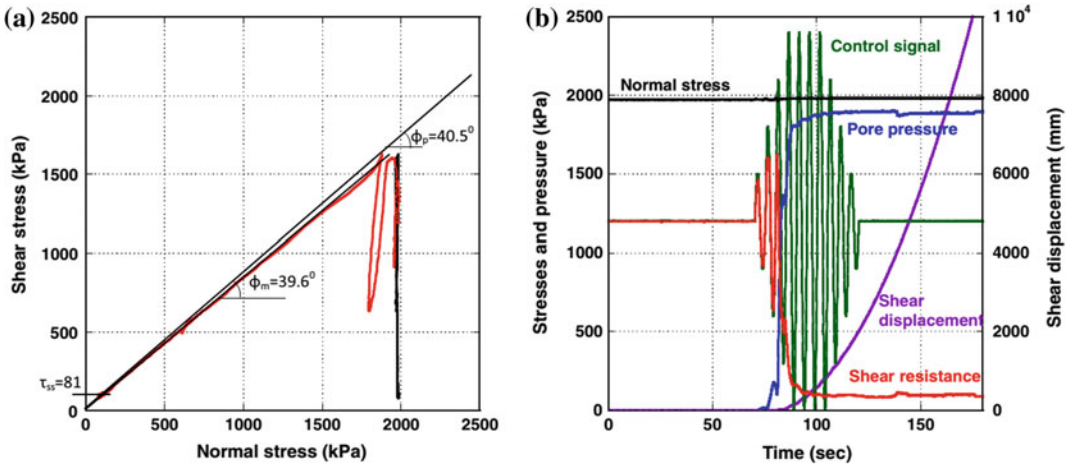


Fig. 12 Undrained cyclic loading test on Sample 1. $B_D = 0.98$, cycle rate: 0.2 cycle/s, shear stress step: 300 kPa

for this test are shown in Fig. 12. The shear stress reached the failure line during the second shear–stress cycle and shear stress decreased after the peak of the third cycle due to generation of high pore-water pressure. This phenomenon is what we have called sliding surface liquefaction. Then, the rate of shear displacement (the purple line in Fig. 12) accelerated and displacement reached to more than 10 m. The peak friction angle was 40.5° , and the friction angle during motion was 39.6° . The steady-state shear resistance was 81 kPa.

3.4 Seismic-Loading Test

The third test (Fig. 13) was a seismic-loading ring-shear test to simulate the landslide initiation of the Mayuyama landslide by the combined effect of pore-water pressure and earthquake shaking.

Initially, the sample (S1) was saturated ($B_D = 0.94$) and consolidated to 3 MPa in normal stress and 1.5 MPa in shear stress (the corresponding slope angle was $\arctan(1.5/3.0) = 26.6^\circ$). Then pore water pressure was increased up to 800 kPa, (a pore water pressure ratio $r_u = 800/3,000 = 0.27$) as the initial slope condition. An exact value remains unknown, but it must have been smaller than 0.4. A preparatory test (Fig. 11) showed that $r_u = 1.2/3.0 = 0.4$ was a critical pore-water pressure which could cause a

landslide without an earthquake. The earthquake which triggered the 1792 Unzen–Mayuyama landslide was estimated to be magnitude $M = 6.4 \pm 0.2$, with a seismic intensity of VII during the earthquake; in the Japanese standard, this corresponds to a seismic acceleration of more than 400 cm/s^2 , as explained above.

The maximum recorded seismic acceleration in the 2008 Iwate–Miyagi earthquake was 739.9 cm/s^2 , which caused the Aratozawa landslide. We loaded the N–S component of the 2008 Iwate–Miyagi earthquake record (maximum acceleration is 739.9 cm/s^2) MYG004 as the additional shear stress. For precise pore-pressure monitoring, as well as to maintain servo-stress control, a five times slower rate was used in applying the recorded seismic acceleration. The test result is shown in Fig. 13.

The green line indicates the control signal. The maximum value is 2469 kPa ($1500 + 969 \text{ kPa}$) and the minimum value is 369 kPa ($1500 - 1131$). The loaded acceleration (a) is calculated from the ratio of seismic acceleration and gravitational acceleration: $a/g = 969/1500$ or $a/g = 1131/1500$, because $ma = 969 \text{ kPa}$ and $mg = 1500 \text{ kPa}$, expressing the landslide mass at unit area asm . The acceleration corresponds to $+633$ and -739 cm/s^2 . Therefore, the control signal for shear stress sent to the ring-shear apparatus exactly corresponded to the monitored acceleration record.

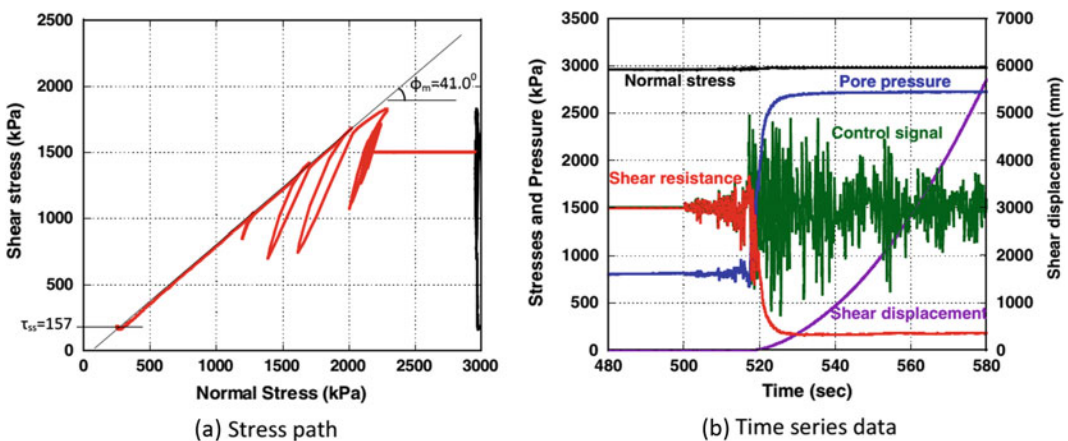


Fig. 13 Undrained pore water pressure and seismic loading test. Sample: S1 from Mayuyama source area. $B_D = 0.94$

As Fig. 13 shows, failure occurred around 1825 kPa, namely, $a/g = (1825 - 1500)/1500 = 0.22$; the necessary acceleration to failure was 216 cm/s^2 . This test result suggested that a lesser earthquake shaking (of around $216/633 = 0.34$) than occurred in the Iwate–Miyagi earthquake could have caused failure under a slope condition with a pore-pressure ratio of 0.27. The steady-state shear strength was 157 kPa.

3.5 Ring-Shear Tests to Simulate the Motion of the Unzen–Mayuyama Landslide

We collected two samples during the Unzen–Mayuyama field investigation. One sample (S1) was taken from the current ground in the source area (red dot zone of Fig. 10) of the Unzen–Mayuyama landslide to study the initiation of the landslide. In order to investigate the motion of the landslide, we took another sample (S2) from a location close to the landslide area, but not covered by the landslide source area mass, i.e., from exposed ground along the coast. We assumed that S2 could represent soils in the lower slope and deposits along the coast (black dot zone of Fig. 10).

We first carried out a basic undrained monotonic speed-control test on S2 (Fig. 14). The peak shear strength appeared below the failure line. The friction angle during motion was 40.4° , and steady-state shear resistance was 100 kPa. The friction angle and the steady-state shear resistance were similar to S1 (40.3° and 120 kPa). Thus, both samples were very similar in their undrained shearing behavior, even though they were sampled from different points.

When a landslide mass on the upper slope moves, it applies undrained loading to the soil mass on the lower slope and initiates motion of the lower slope in addition to the motion from the upper slope. A study of a landslide-induced debris flow, where the landslide mass in the slope moved onto and mobilized a torrent deposit, was reported by Sassa et al. (2004), although the stress level is much different.

ICL-2 was used to simulate undrained loading on the black-dot layer in the lower slope (Fig. 10) using the displaced mass from the upper slope (red-dot block). Figure 15 presents the test result of an undrained dynamic loading test simulating this scenario. Firstly, the initial normal stress and the initial shear stress ($\sigma_0 = 1000 \text{ kPa}$, $\tau_0 = 150 \text{ kPa}$, corresponding to an 8.5° slope) were loaded in the drained condition to reproduce the initial stress state at the bottom of the

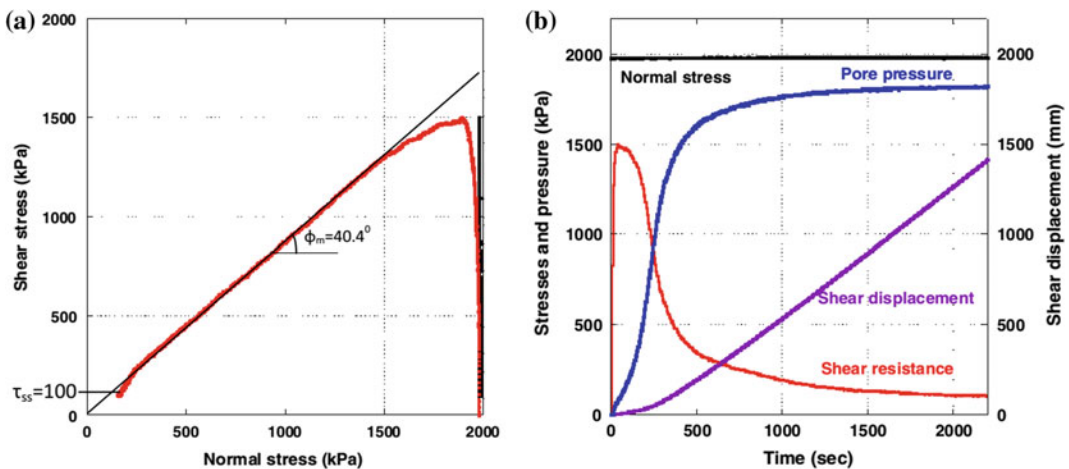


Fig. 14 Undrained speed-control test on Sample 2. $B_D = 0.95$, shear velocity = 0.1 m/s

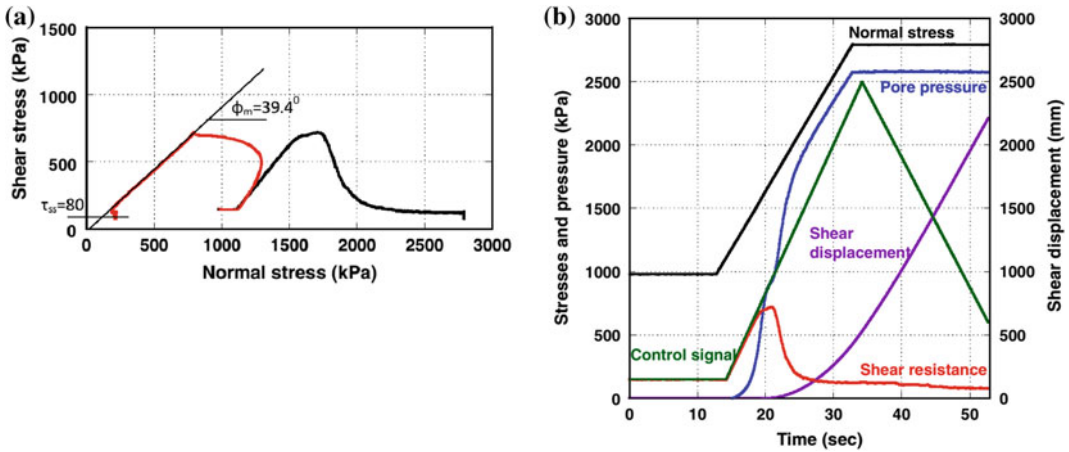


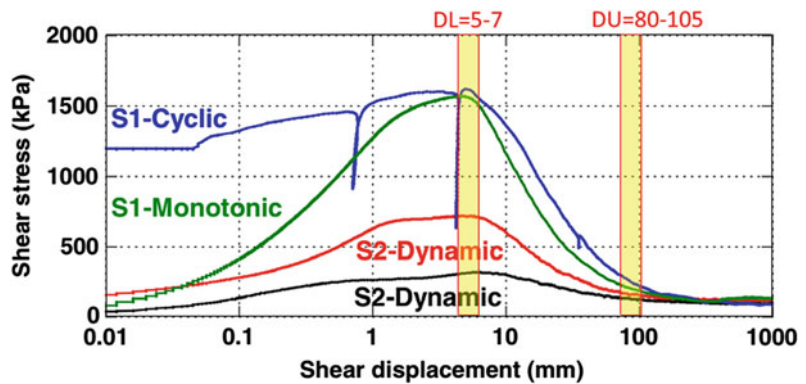
Fig. 15 Undrained dynamic loading test on Sample 2. $B_D = 0.97$, initial stresses ($\sigma_0 = 1000$ kPa, $\tau_0 = 150$ kPa)

black-dot layer. The normal stress was increased to 2790 kPa (which is close to the 3 MPa capacity of the apparatus) as the undrained load, although a 400-m-deep initial landslide will result in a greater normal stress. If the lower slope mass can resist the undrained load from the upper slope without raised pore water pressure, it may resist around 2374 kPa ($2790 \times \tan(40.4^\circ)$) in this dynamic loading. However, as seen in Fig. 15, a high pore water pressure was generated in the undrained loading. The sample failed at 720 kPa and its steady-state stress was 80 kPa. The landslide mass from the upper slope should scrape off

a layer of the lower slope and move together as a combined greater mass toward the sea. This scenario was proven to be possible by this landslide simulation test using ICL-2.

The integrated model simulating the initiation and the motion of landslides (LS-RAPID; Sassa et al. 2010) uses the shear displacement at peak strength (D_L) and the shear displacement for the initiation of steady-state shear resistance (D_U). The shear stress and the shear displacement curves for the tests conducted for S1 and S2 are shown in Fig. 16. The figure presents $D_L = 5\text{--}7$ mm, $D_U = 80\text{--}105$ mm.

Fig. 16 Shear resistance and shear displacement by different mode of shearing



4 Application of the Integrated Computer Simulation Model (LS-RAPID) to the Mayuyama Landslide

4.1 Triggering Factors

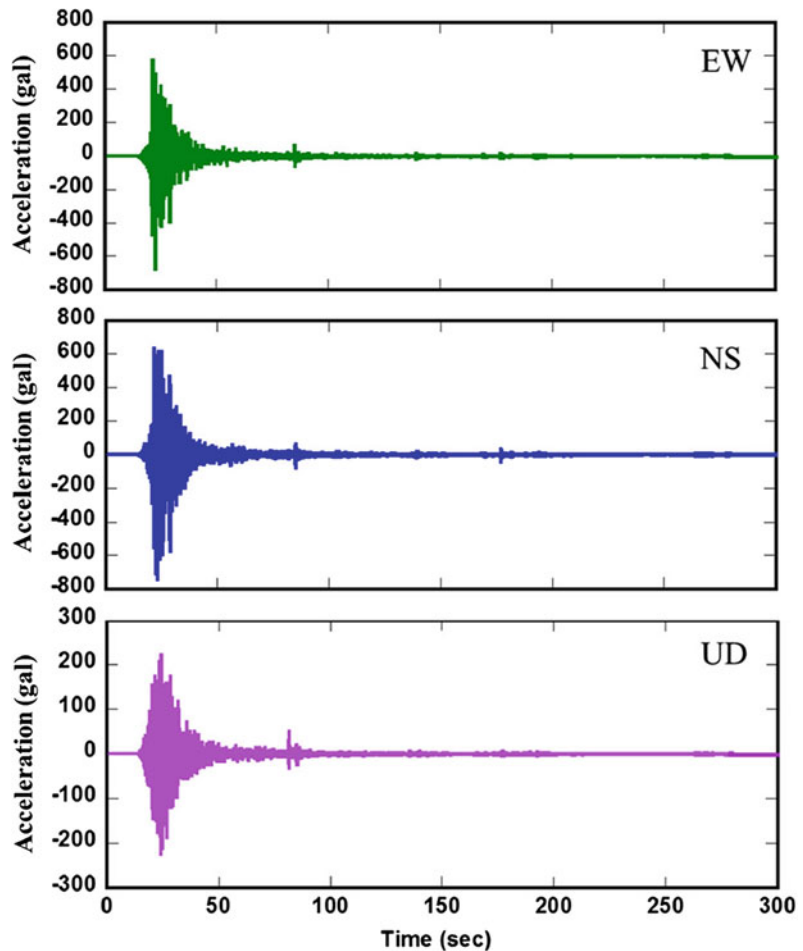
The 1792 Unzen–Mayuyama landslide was triggered by a nearby earthquake of seismic intensity VII (a seismic acceleration of more than 400 cm/s^2) in Shimabara. Since we did not have its earthquake record, we used the 2008 Iwate–Miyagi earthquake record (MYG004) which triggered the Aratozawa landslides (Fig. 17). The maximum acceleration was 739 cm/s^2 for the S component, but we applied sets of smaller accelerations, namely,

0.7 times (507 cm/s^2) and 0.5 times (370 cm/s^2) the MYG004 record, because the result of the seismic-loading ring-shear test (Fig. 13) showed that the necessary acceleration to failure was 216 cm/s^2 . Both sets of simulated earthquake shaking caused similar landslide motion, although the moving shape was slightly different. Then, 0.5 times the 2008 Iwate–Miyagi earthquake record was adopted as the triggering seismic parameter.

We assigned a pore-water pressure before the earthquake of $r_u = 0.21$ because:

- (1) The pore water pressure control ring-shear test result (Fig. 11) indicated that $r_u = 0.4$ would trigger the landslide without an earthquake.

Fig. 17 2008 Iwate–Miyagi earthquake record (MYG004). From K-net of National Research Institute for Earth Science and Disaster Prevention (NIED)



- (2) The seismic loading ring-shear test (Fig. 13) indicated that a pore-pressure ratio ($r_u = 0.27$) and a seismic acceleration of $+216 \text{ cm/s}^2$ would cause failure.

4.2 Unit Weight of Soils in the Unzen Volcano

The unit weight of soils in the Unzen volcano was not measured. To estimate it, we consolidated sample (S1) in the ring-shear apparatus in a saturated condition. The consolidation stress, sample height, dry unit weight and saturated unit weight are shown in Fig. 18. The saturated unit weight reached 21 kN/m^3 at 3 MPa, but the dry unit weight was 19 kN/m^3 at 3 MPa. Smaller values would have occurred in shallower areas. We assumed a single value for the entire area: 19.5 kN/m^3 .

4.3 Landslide Dynamics Parameters

The parameters used in the computer simulation are listed in Table 1.

1. Steady-state shear resistance: 120 kPa in the landslide source area (deep soil layer), and 40–80 kPa in the landslide moving area

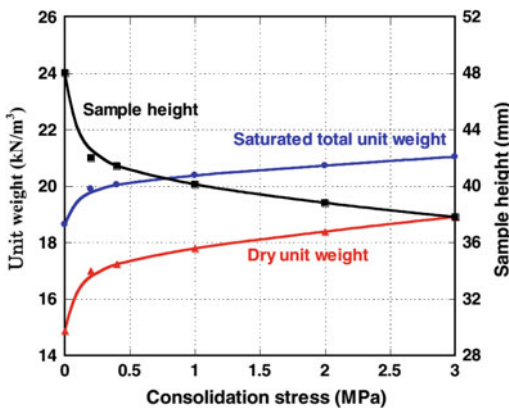


Fig. 18 Consolidation of sample and saturated unit weight. Sample S1 was consolidated in the ring-shear apparatus

- (shallower soil layer), based on the undrained monotonic stress control test results (Fig. 6).
2. Friction angle during motion: 40.0° from the combined undrained monotonic stress control tests on sample S1 (Fig. 7).
3. Peak friction angle: 42.0° . The maximum was 41.2° in control series of tests (Fig. 6). However, the value in undisturbed field conditions can be greater.
4. Critical shear displacements for start of strength reduction (D_L) and the start of steady state (D_U): 6 and 90 mm from the shear resistance and shear displacement relationship for S1 and S2 (Fig. 16).
5. Pore-pressure generation rate B_{ss} was 0.7–0.9 in the source area, and 0.99 under the sea (completely saturated). Outside of the landslide, a value was 0.2 was assumed (unsaturated).
6. Lateral pressure ratio k : 0.7–0.9. We assumed the ratio to be 0.9 in the coastal area and under the sea. Outside of the landslide, it was 0.4 (unsaturated).
7. Unit weight of soils: 19.5 kN/m^3 , estimated from consolidation of sample and saturated and dry unit weight of sample S1 (Fig. 18).
8. Pore-pressure ratio before earthquake: 0.21 (assumed).
9. Seismic loading: 0.5 times that of the three components of the Miyagi–Iwate earthquake (maximum acceleration of 370 cm/s^2).
10. Coefficient for non-friction energy consumption: 1.0 (the same value used for the 2006 Leyte landslide; Sassa et al. 2010).

The simulation results are presented in Fig. 19.

Red color balls represent the moving mass, while blue balls represent the stable mass.

At 11 s, the pore-water pressure reached 0.21 and the earthquake started, but no motion occurred.

At 17 s, the main shock of earthquake struck the area and failure occurred within the slope. Failure began from the middle of the slope.

At 26 s, the earthquake has almost terminated. The whole landslide mass was formed during the earthquake shaking.

Table 1 Parameters used in computer simulation of Unzen–Mayuyama landslide

Parameters used in simulation	Value	Source
<i>Parameters of soils in the source area (deeper area)</i>		
Steady state shear resistance (τ_{ss})	120 kPa	Test data
Lateral Pressure ratio [$k = \sigma_h/\sigma_v$]	0.7–0.8	Estimation (see text)
Friction angle at peak (ϕ_p)	42.0°	Test data
Cohesion at peak (c)	10 kPa	Assuming small
Friction angle during motion (ϕ_m)	40.0°	Test data
Shear displacement at the start of strength reduction (D_L)	6 mm	Test data
Shear displacement at the start of steady state (D_U)	90 mm	Test data
Pore pressure generation rate (B_{SS})*	0.7–0.9	Estimated
Total unit weight of the mass (γ_t)	19.5 kN/m ³	From the test
<i>Parameters of soils in the moving area (shallower area)</i>		
Steady state shear resistance (τ_{ss})	30–80 kPa	Test data
Lateral Pressure ratio ($k = \sigma_h/\sigma_v$)	0.8–0.9	Estimated
Friction angle at peak (ϕ_p)	40.0°	Test data
Cohesion at peak (c)	10 kPa	Assuming small
Friction angle during motion (ϕ_m)	40.0°	Test data
Shear displacement at the start of strength reduction (D_L)	6 mm	Test data
Shear displacement at the end of strength reduction (D_U)	90 mm	Test data
Pore pressure generation rate (B_{ss})	0.7–0.9	Estimated
Total unit weight of the mass (γ_t)	19.5 kN/m ³	From the test
<i>Triggering factor</i>		
Excess pore pressure ratio in the fractured zone (r_u)	0.21	Assumption
0.5 times of the 2008 Iwate-Miyagi earthquake	Max: 370 cm/s ²	Wave form of the Ground motion record at MYG004
<i>Parameters of the function for non-frictional energy consumption</i>		
Coefficient for non-frictional energy consumption	1.0	Data (Sassa et al. 2010)
Threshold value of velocity	100 m/s	A few times greater than maximum reported speed
Threshold value of soil height	400 m	Maximum depth of the initial source area
<i>Other factors</i>		
Steady state shear resistance under sea	10 kPa	Data (Sassa et al. 2004)
Unit weight of sea water	10.1 kN/m ³	Average sea water density

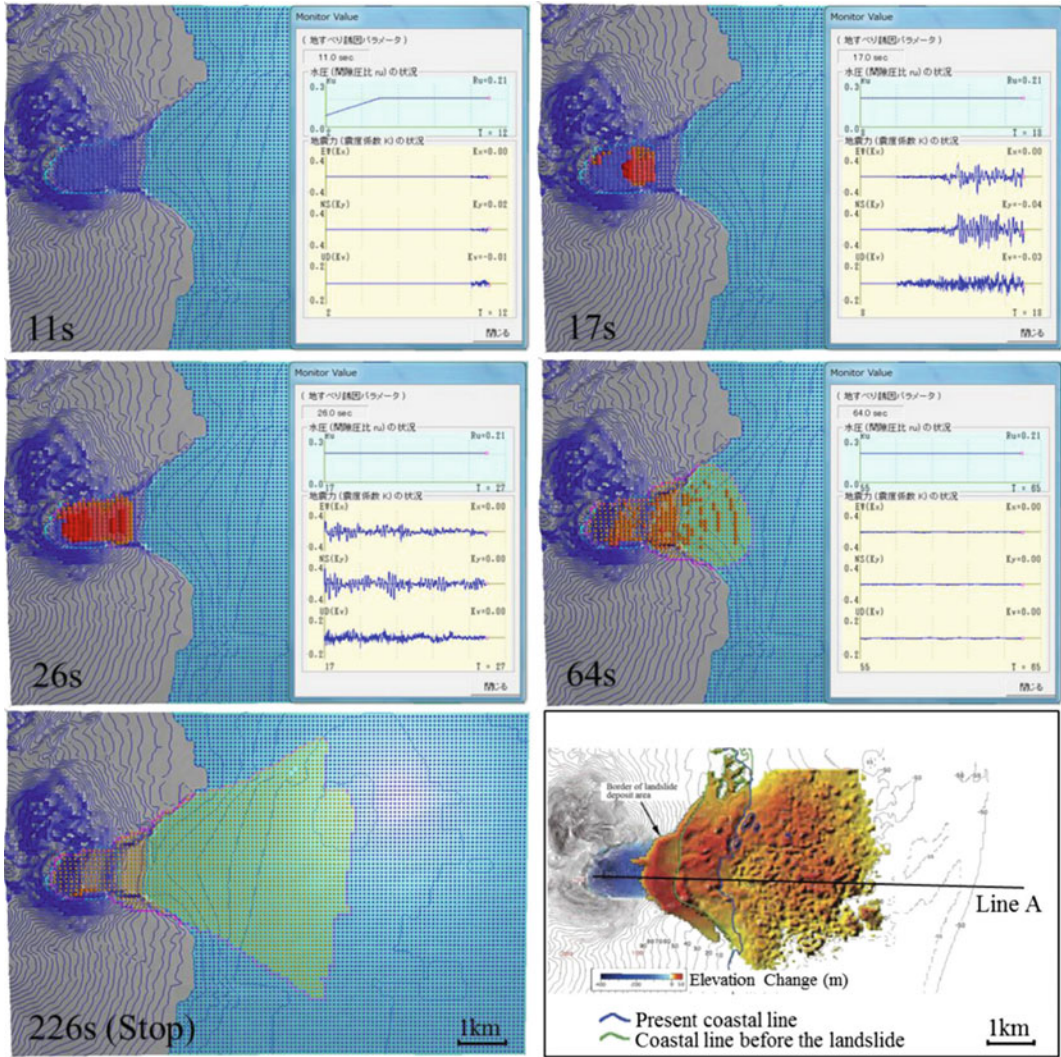


Fig. 19 Simulation result of 1792 Unzen–Mayuyama landslide

At 64 s, the landslide mass continued to move after the earthquake ended and entered into the sea

At 226 s, the landslide mass stopped moving and was deposited.

In Fig. 20, the simulated deposition area was compared with the map made by the Unzen Restoration Office of the Ministry of Land, Infrastructure and Transport of Japan (2002) based on topographic survey. To compare both

landslide motions, the section of line A in the right-bottom figure and the E–W section (almost the same as line A) of the computer simulation were compared. Both movements were very similar. The travel distances from the head scarp of the initial landslide to the toe of the displaced landslide mass were also very close—around 6 km (the travel distance in the computer simulation is 6.6 km, while the distance based on field investigation of the deposits is 5.9 km).

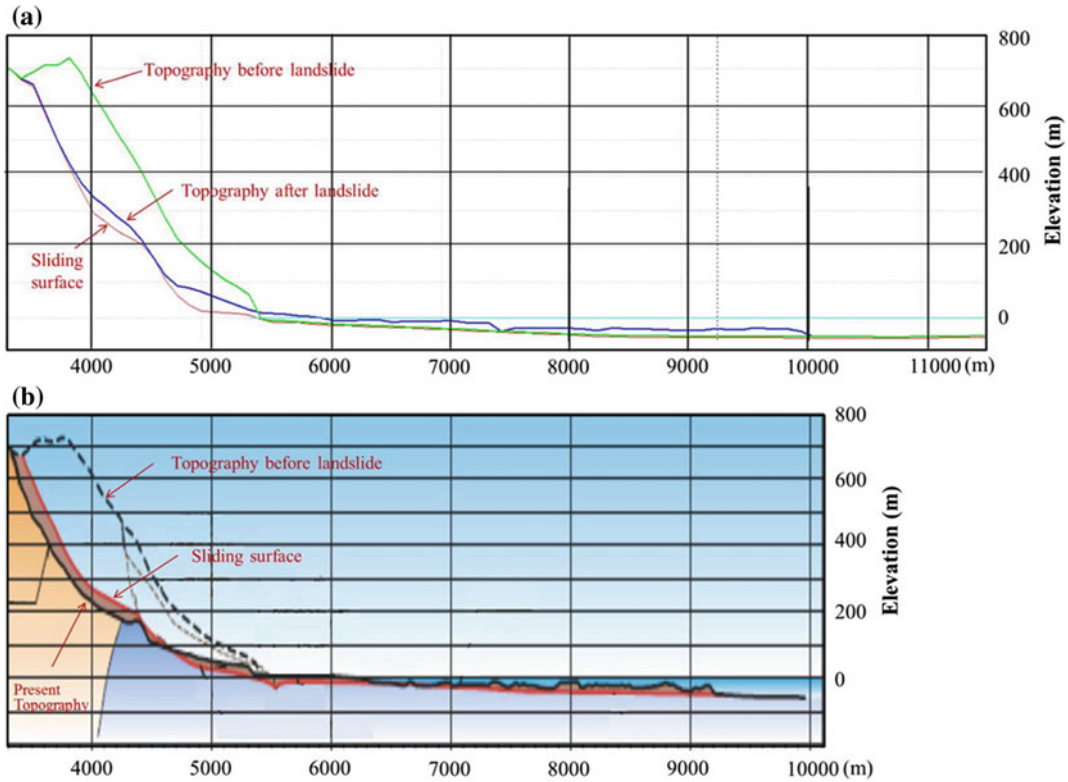


Fig. 20 Comparison of the central sections between simulation result (*upper*) and topographic survey (*lower*)

5 Conclusion

Megaslides deeper than 100 m have caused great disasters. Sassa and others developed a series of undrained ring-shear testing apparatus (from DPRI-3 to DPRI-7) to geotechnically simulate the failure of soils, the formation of sliding surfaces and the steady-state motion of landslides within the apparatus. However, the undrained capacity was limited to several hundred kPa. In order to investigate megaslides, which are deeper than 100 m, test pressures of more than 1 MPa are needed.

With support from the Science and Technology Research Partnership for Sustainable Development Program (SATREPS) of Japan, Sassa and ICL members in 2012–2013 developed a new high-stress undrained ring-shear apparatus, with a maximum undrained capacity of 3 MPa. Developments also include improved

performance, and easier handling and maintenance (particularly for outside of Japan). For the first application of ICL-2, we performed a series of tests using a sample taken from the 1792 Unzen–Mayuyama landslide, the greatest landslide disaster in Japan. This landslide disaster is well documented, but the landslide dynamics had hitherto not been studied. The major results from applying ICL-2 to this landslide are summarized:

1. Undrained tests were successful up to 3 MPa in the monotonic speed-control test, monotonic stress-control test, pore-pressure control test, cyclic-shear-stress loading test and seismic-shear stress loading test using the real earthquake records.
2. Undrained monotonic loading tests were conducted for the same sample under different normal stresses ranging from 300 kPa to 3 MPa. The friction angle during motion remained almost constant (around 39.8°)

throughout. The undrained steady-state shear resistance from 37 to 120 kPa was proportional to the loaded normal stress across the entire tested range.

3. The pore-pressure control test for simulating the source area of the landslide suggested that a pore-pressure ratio of 0.4 could have caused the landslide without an earthquake. The seismic-shear-stress loading test under a pore-pressure ratio of 0.27 indicated that the landslide could be initiated by a seismic acceleration of 216 cm/s^2 .
4. We input a pore-pressure ratio $r_u = 0.21$ and 0.5 times the seismic acceleration of the 2008 Iwate Miyagi earthquake record (MYG004), (maximum acceleration = 370 cm/s^2) into the integrated landslide simulation model (LSRAPID) as triggering factors. Soil parameters estimated from the undrained ring-shear tests were also input into the model. The simulation results indicated a landslide hazard area and its central section that were similar to those determined by the Unzen Restoration Office of the Ministry of Land, Infrastructure and Transport of Japan (2002, 2003) based on a topographic survey.
5. This first application of the new ICL-2 high-stress undrained dynamic loading ring-shear apparatus to the 1792 Unzen–Mayuyama landslide showed that the apparatus and the integrated computer simulation (LS-RAPID) using the measured parameters were effective tools for understanding the initiation and motion mechanisms of mega-slides and their hazard assessment.

References

- Philippines occurred on 17 February 2006. In: Proceedings of the international conference on management of landslide hazard in the Asia-Pacific Region (Satellite symposium on the first world landslide forum), pp 434–443
- Inoue K (1999) Shimabara-Shigatusaku earthquake and topographic changes by Shimabara catastrophe. *J Jpn Soc Erosion Control Eng* 52(4):45–54
- Inoue K (2000) Shimabara–Shigatusaku earthquake and topographic change by Shimabara Catastrophe in 1792. *Geographical Reports of Tokyo Metropolitan University*, No. 35, pp 59–69
- Nakada S, Suzuki H, Furuya T (1992) Volcanic hazard at Unzen, Japan. *Int News Landslide News* 6:2–6
- Nakada S, Suzuki H, Furuya T (1999) Volcanic hazard at Unzen, Japan. In: Sassa K (ed) *Landslides of the world*. Kyoto University Press, Kyoto, pp 311–316
- Sassa K (1988) Geotechnical model for the motion of landslides. In: *Proceedings of the 5th international symposium on landslides, "landslides"*. Balkema, Rotterdam, vol 1, pp 37–56
- Sassa K, Fukuoka H, Wang G, Ishikawa N (2004) Undrained dynamic-loading ring-shear apparatus and its application to landslide dynamics. *Landslides* 1 (1):7–19
- Sassa K, Nagai O, Solidum R, Yamazaki Y, Ohta H (2010) An integrated model simulating the initiation and motion of earthquake and rain induced rapid landslides and its application to the 2006 Leyte landslide. *Landslides* 7(3):219–236
- Unzen Restoration Office of the Ministry of Land, Infrastructure and Transport of Japan (2002) *The Catastrophe in Shimabara—1791–92 eruption of Unzen–Fugendake and the sector collapse of Mayu-Yama*. An English leaflet (23 p)
- Unzen Restoration Office of the Ministry of Land, Infrastructure and Transport of Japan (2003) *The Catastrophe in Shimabara—1791–92 eruption of Unzen–Fugendake and the sector collapse of Mayu-Yama*. A Japanese leaflet (44 p)
- Usami T (1996) *Materials for comprehensive list of destructive earthquakes in Japan*. University of Tokyo Press, Tokyo

TXT-tool 3.001-1.3

Laboratory Measurement of Fully Softened Shear Strength and Its Application for Landslide Analysis

Binod Tiwari and Beena Ajmera

Abstract

Fully softened shear strength is equivalent to the peak shear strength of remolded soil specimens. Fully softened shear strength is important when evaluating the stability of first time slides and compacted fills. It is generally measured using various soil testing methods such as direct shear, direct simple shear, triaxial or ring shear tests. However, as the direct shear test devices are readily available in many geotechnical engineering laboratories, it is recommended to use this device to measure the fully softened shear strength. Generally, the fully softened shear envelopes are curved, starting from origin. Therefore, using constant volume direct simple shear devices are recommended to obtain the fully softened shear envelopes in order to accurately capture this curvature. This tool explains the importance of fully softened shear strength for slope stability analysis, methods used to measure the fully softened shear strengths in laboratory, and available correlations to estimate the fully softened shear strength with index properties.

Keywords

Fully softened shear strength • Direct shear test • Slope stability
Plasticity index • Liquid limit

B. Tiwari (✉)
Department of Civil and Environmental Engineering,
California State University, Fullerton, 800 N. State
College Blvd., E-419, Fullerton, CA 92831, USA
e-mail: btiwari@fullerton.edu

B. Ajmera
Department of Civil and Environmental Engineering,
California State University, Fullerton, 800 N. State
College Blvd., E-318, Fullerton, CA 92831, USA
e-mail: bajmera@fullerton.edu

Contents

1 Introduction	394
2 Measurement of the Fully Softened Shear Strength	394
3 Available Relationships for the Fully Softened Shear Strength	396
4 Application of Fully Softened Shear Strength for Slope Stability Analysis	400
5 Concluding Remarks	401
References	401

1 Introduction

The peak shear strength of soil is the maximum strength of the soil in the in situ condition and will depend on a number of parameters including the geotechnical properties as well as the stress history of the soil. The peak shear strength of the soil that has been reconstituted at a moisture content greater than or equal to the liquid limit of the soil is known as the fully softened shear strength (Skempton 1977, 1985) and has also been referred to as the critical state shear strength or the intrinsic shear strength by Burland (1990). The effects of the previous stress history are not observed in a soil mass that is in the fully softened shear strength condition. The minimum shear strength of soil after large displacements perpendicular to the application of the normal stress is referred to as the residual shear strength. This strength is achieved with increasing shear displacements after the fully softened shear strength and is obtained as particles reorient to their preferred orientations.

Terzaghi (1936) first pointed out that the strength mobilized in excavations in stiff fissured clays was significantly lower than the strength measured from laboratory tests. This reduced strength was attributed to the weakened state of the clay as rainwater entered the fissures in these clays. Based on failures in a number of slopes in the United Kingdom, Skempton (1964) observed that the peak strength developed along the entire sliding surface in clays with no fissures or joints, but was less than the peak strength for failures in clays which were heavily fissured or jointed. Mesri and Shahein (2003) and Morgenstern (1977) concluded that the fully softened shear strength should be used in conducting stability analysis of first time slides.

2 Measurement of the Fully Softened Shear Strength

Typically, the fully softened shear strength has been measured using either the direct shear or the triaxial devices (Gibson 1953; Bishop et al.

1965; Skempton 1977, 1985; Cancelli 1981; Stark and Eid 1997; Stark et al. 2005; Bhattarai et al. 2006; Wright et al. 2007; Tiwari and Ajmera 2011; Duncan et al. 2011). The simple shear (Bhattarai et al. 2006; Tiwari and Ajmera 2014) and ring shear devices (Stark and Eid 1997; Stark et al. 2005) have also been recently used to measure the fully softened shear strength. However, caution should be provided when using the ring shear device to measure fully softened shear strength as there is unequal strain distribution and potential for progressive failure within the shearing plane. In this document, the procedures to measure the fully softened shear strength of clays using the direct shear and simple shear devices, which are more appropriate methods, are described. The procedures to determine the fully softened shear strength using a torsional ring shear device are described in the *ASTM Standard Test Method for Torsional Ring Shear Test to Determine Drained Fully Softened Shear Strength and Nonlinear Shear Envelope of Cohesive Soils (Using Normally Consolidated Specimen) for Slopes with No Preexisting Shear Surfaces* (ASTM 7608-10 2010). Castellanos (2014) provides detailed procedures for obtaining the fully softened shear strength using the triaxial device.

The sample preparation procedures for the direct shear and simple shear apparatus are essentially the same. First, the soil mass is reconstituted to have an initial moisture content greater than or equal to its liquid limit (in other words, an initial liquidity index equal to at least unity) based on the recommendations of Burland (1990). The sample is, then, allowed to hydrate for at least 24 h during which time special attention should be paid to ensure moisture is not lost from the specimen. Following the hydration period, the sample is mixed using a batch mixer to create a slurry. Next, the slurry is transferred to a vinyl bag used for cake decoration in order to maintain uniformity. The cake decoration bag is used to gently squeeze the slurry uniformly into the direct shear box. For the simple shear test, the sample is gently squeezed into a rubber membrane confined by a stack of Teflon[®] rings.

The assembled samples are transferred to the direct shear or simple shear devices, where a series of incremental consolidation pressures will be applied.

To prevent extrusion of the slurry from the direct shear box or from the membrane of the simple shear assembly, a series of incremental pressures are used to consolidate the specimen. Typically, the consolidation pressures are doubled in each increment, corresponding to an increment ratio of one. Real-time observations of the logarithm of time versus displacement graphs are recommended to be used to determine the completion of the primary consolidation under any consolidation pressure prior to proceeding to the next consolidation pressure. Once the completion of the primary consolidation at the desired (final) consolidation pressure has been determined, the sample will be advanced to the shearing stage. For the direct shear test, the maximum shearing rate can be computed using the consolidation characteristics and the displacement required to cause shear failure using the procedure outlined in the *ASTM Standard Test Method for Direct Shear Test of Soils under Consolidated Drained Conditions* (ASTM D3080-11 2011). A simple and general condition to calculate the shearing rate is by considering the time required for 100% consolidation at 0.5–1 mm of shear displacement. In *ASTM Standard Test Method for Consolidated Undrained Direct Simple Shear Testing of Cohesive Soils* (ASTM D6528-07), it is recommended that a shearing rate of 5% per hour be used. The shearing stage should be continued until the peak shear strength is measured. In the simple shear device, the shearing stage should be continued until the recorded shear force has dropped by at least 20% of the maximum recorded value or for a maximum shear strain of 20%. The sample may be disassembled after the shearing stage is completed in the direct shear device. However, ASTM D6528-07 recommends that the simple

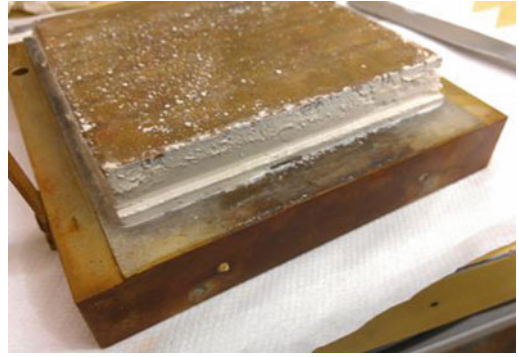


Fig. 1 Soil sample at the completion of DS test

shear specimen be allowed to swell for the smaller of the time required for 95% consolidation or one hour. Presented in Figs. 1 and 2 are the soil samples obtained at the completion of direct shear and direct simple shear tests, respectively. Typical stress-strain curves obtained for the fully softened shear strength using the direct shear and direct simple shear devices are presented in Figs. 3 and 4, respectively. Using the shear envelopes, such as the ones presented in Figs. 5 (direct shear test) and 6 (simple shear test), fully softened shear strengths are measured. Typical fully softened friction angles for some pure minerals such as montmorillonite, kaolinite, and quartz are 8°, 22°, and 31°, respectively (Tiwari and Ajmera 2011).

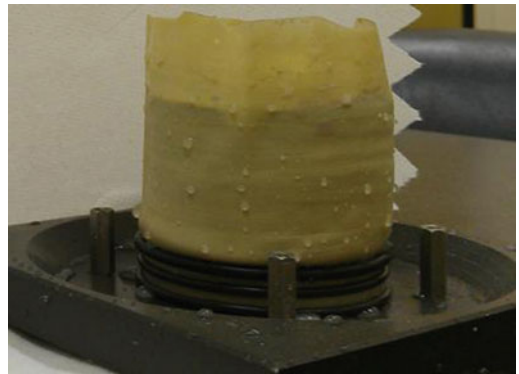


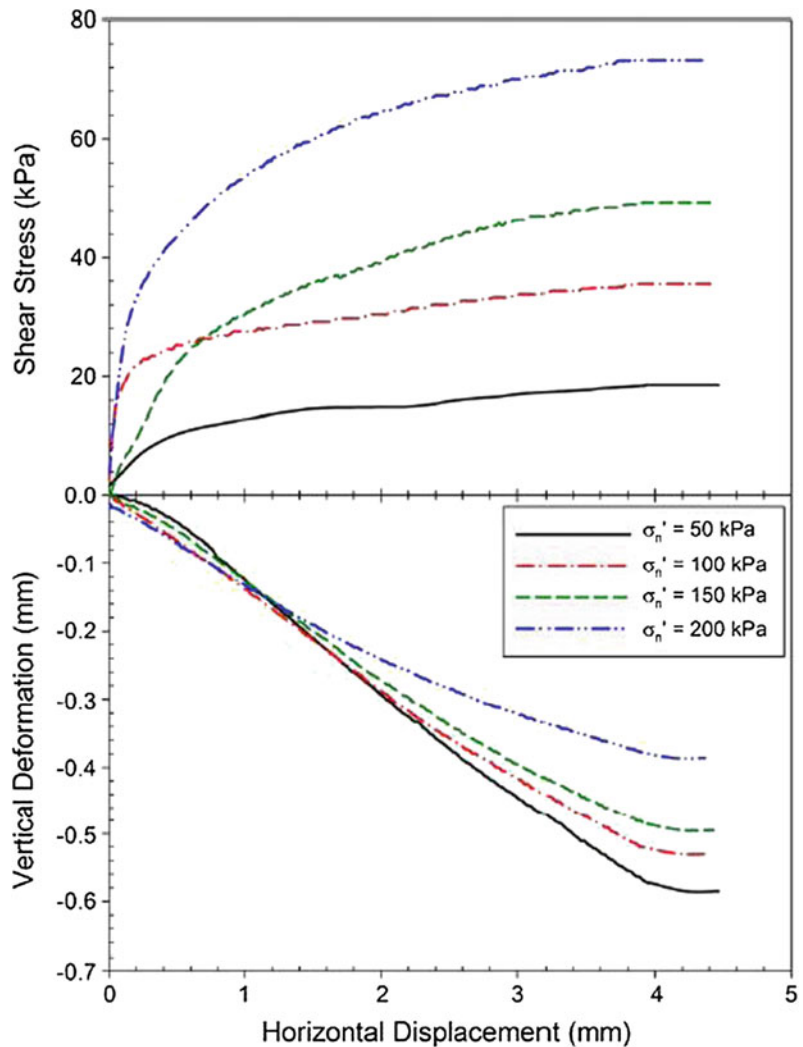
Fig. 2 Soil sample at the completion of SS test

3 Available Relationships for the Fully Softened Shear Strength

In the absence of laboratory test results or to confirm the laboratory test results, fully softened shear strength can be obtained using various correlations. The literature contains several correlations between the fully softened shear strength and the index properties of the soil mass. One such correlation is the relationship, first proposed by Stark and Eid (1997), is to

determine the secant fully softened friction angle based on the liquid limit and clay fraction of the soil mass. This relationship was later updated by Stark et al. (2005) and again, by Stark and Hussain (2013). The latest of the suggested relationships is presented in Fig. 7, which is obtained from the results of torsional ring shear tests on ball-milled samples. According to Stark et al. (2005) and Stark and Hussain (2013), these results have been increased by 2.5° in order to match the results expected from soils under tri-axial compression conditions. Therefore, extreme

Fig. 3 Typical stress-strain behavior observed in a direct shear test (Tiwari and Ajmera 2011)



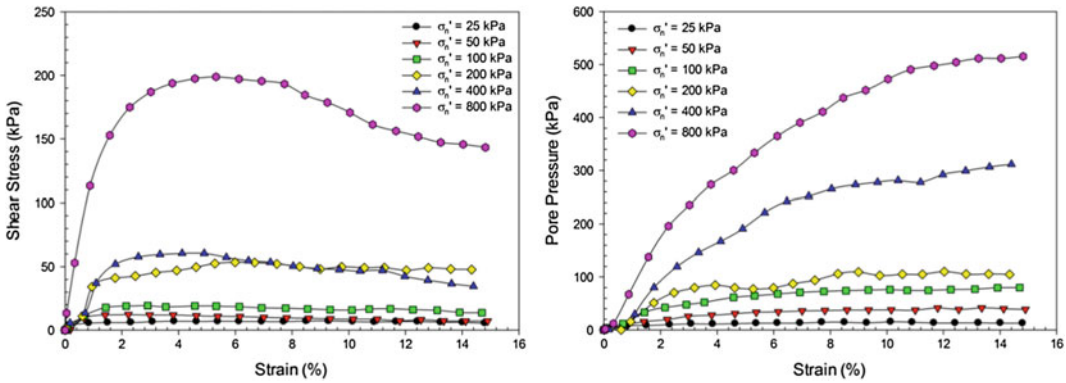
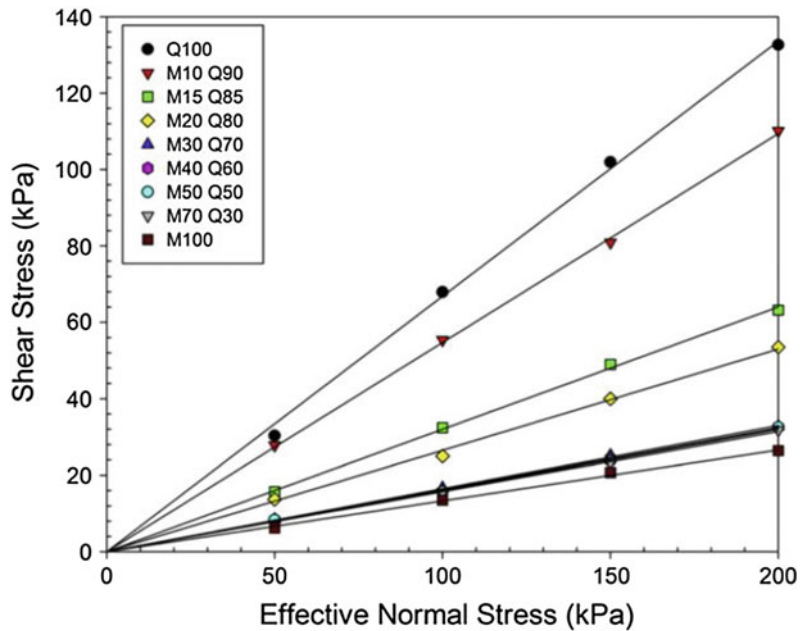


Fig. 4 Typical stress-strain behavior and pore pressure response observed in a simple shear test (Tiwari and Ajmera 2014)

Fig. 5 Failure envelopes obtained from direct shear tests on montmorillonite-quartz mixtures (Tiwari and Ajmera 2014)



caution should be paid while using Stark et al. (2005) and Stark and Hussain (2013)’s correlation. In addition, Stark and Hussain (2013) present three sets of equations for the curves presented in Fig. 7, which depend on the clay-fraction of the soil mass.

Tiwari and Ajmera (2011) used the direct shear device to obtain the fully softened shear strength of thirty-six different mixtures prepared in the laboratory as mixtures of montmorillonite, kaolinite, and quartz. Sample results of these

experiments are provided in Figs. 3, 4, 5 and 6. They systematically evaluated the influence of the mineralogical composition on the fully softened shear strength finding that as the proportion of montmorillonite and kaolinite in the samples increased, the measured average fully softened friction angle decreased. The relationships they obtained between the fully softened friction angle and the clay content, liquid limit and plasticity index are presented in Figs. 8, 9 and 10, respectively. These figures show that the fully

Fig. 6 Typical failure envelope obtained from simple shear test (Tiwari and Ajmera 2014)

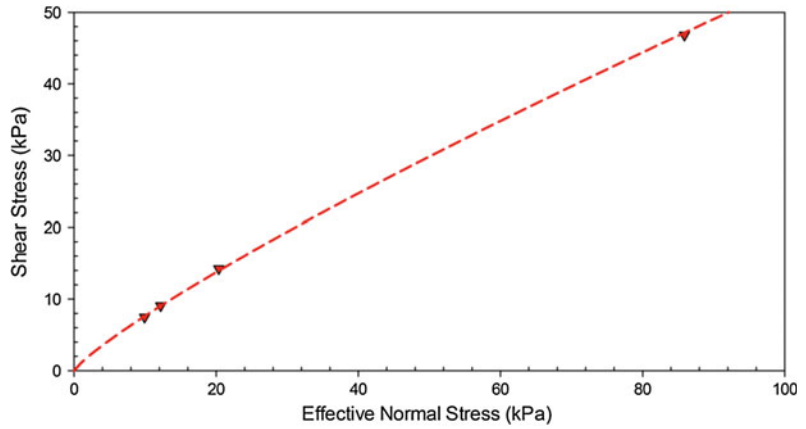
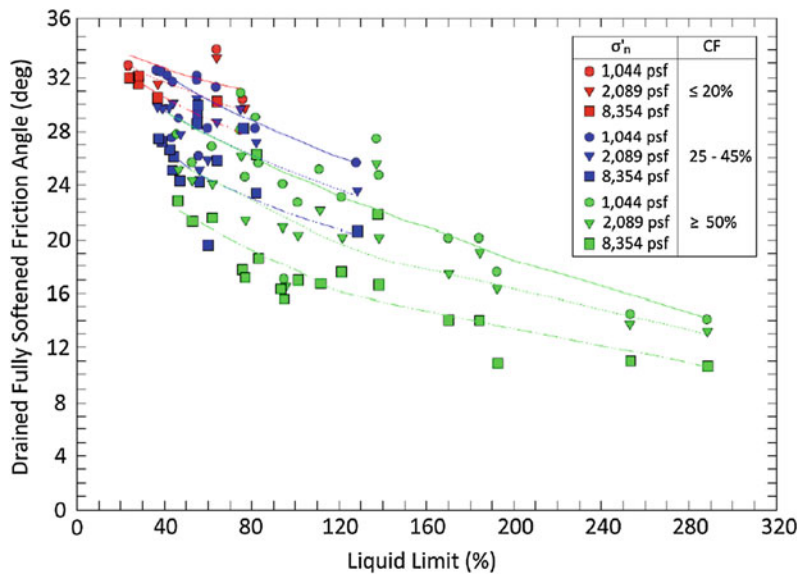


Fig. 7 Latest version of the relationship presented in Stark and Hussain (2013), first suggested by Stark and Eid (1997) and later updated by Stark et al. (2005) (Stark and Hussain 2013)



softened friction angle decreases with an increase in the clay content, liquid limit and the plasticity index. They also demonstrate the dependence of the fully softened shear strength on the mineralogical composition of the soil mass. Tiwari and Ajmera (2011) used the relationships to estimate the fully softened friction angle for 82 natural samples and found that the estimates were within 15% of the measured values for the majority of the soils. Moreover, Tiwari and Ajmera (2011) provided the relationship between fully softened shear strength, residual shear strength, and index properties, as presented in Figs. 11 and 12. This relationship can be used to estimate residual

shear strength of soil with the fully softened shear strength. Measuring residual shear strength of soil is expensive as the ring shear device is not readily available in all geotechnical engineering laboratories. Therefore, the correlation proposed in Figs. 11 and 12 are very useful to estimate residual shear strength as well. Please note that correlation between fully softened shear strength and liquid limit as well as plasticity index provides negligible scatter compared to those presented by Stark et al. (2005) and Stark and Hussain (2013) and can provide better estimates even though the mineralogical composition is unknown. It is important to note that the

Fig. 8 Relationship proposed by Tiwari and Ajmera (2011) between the fully softened friction angle and clay content (Tiwari and Ajmera 2011)

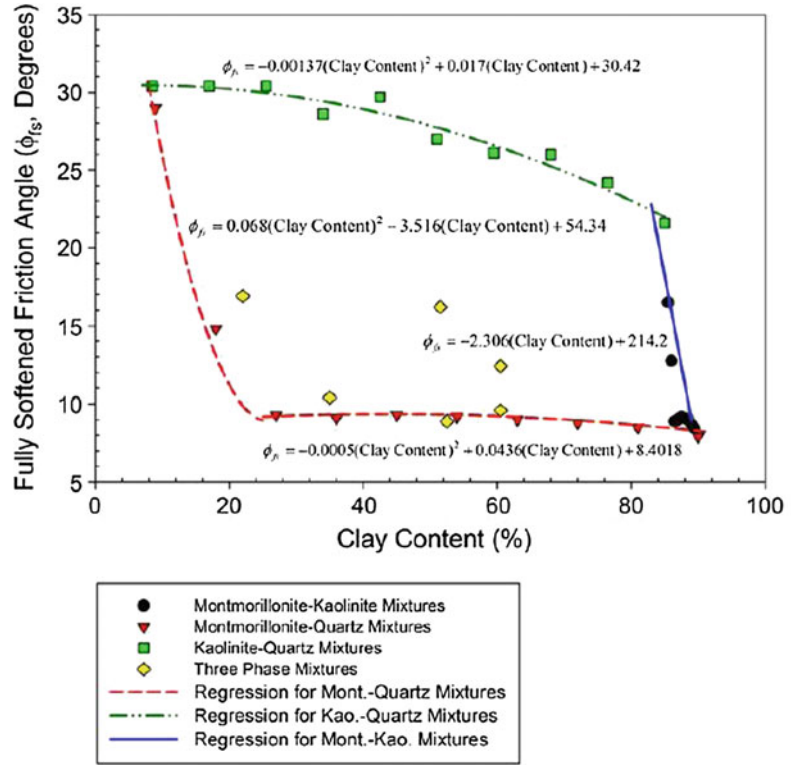
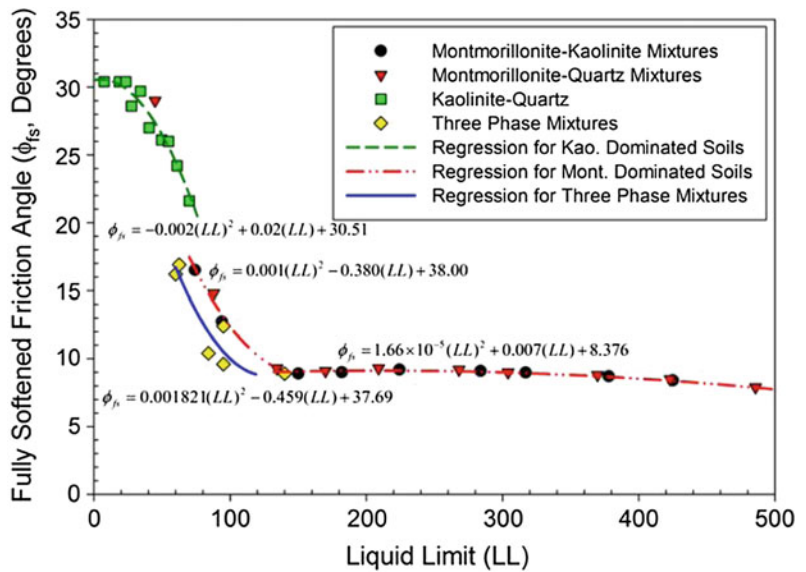


Fig. 9 Relationship proposed by Tiwari and Ajmera (2011) between the fully softened friction angle and the liquid limit (Tiwari and Ajmera 2011)



curvature of shear envelopes are prominent when the effective normal stress is lower than 50 kPa and the plasticity index of the soil sample is

significantly high. In such cases, shear envelopes obtained from the simple shear devices can be beneficially used.

Fig. 10 Relationship proposed by Tiwari and Ajmera (2011) between the fully softened friction angle and the plasticity index (Tiwari and Ajmera 2011)

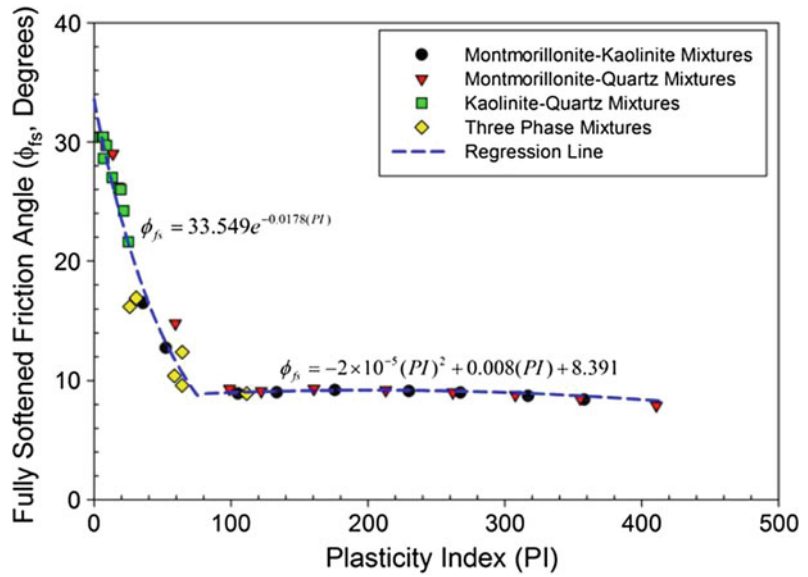
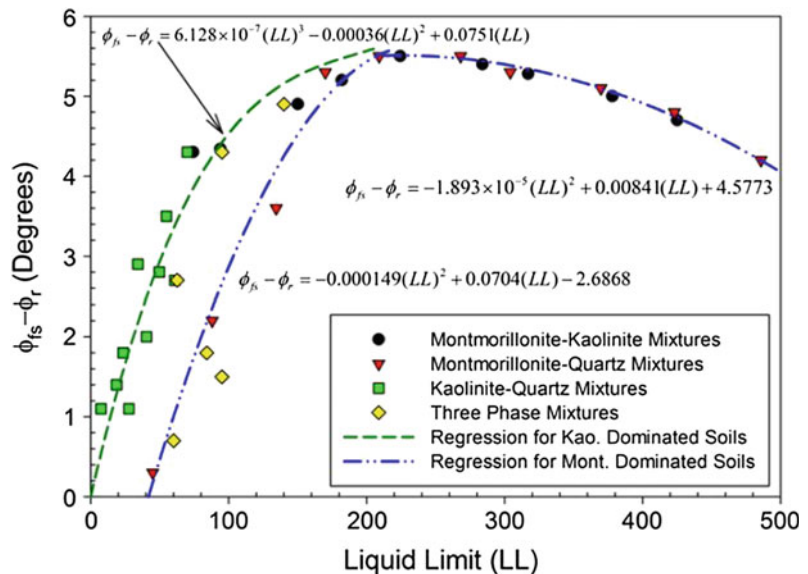


Fig. 11 Relationship proposed by Tiwari and Ajmera (2011) between the fully softened and residual shear strengths and the liquid limit (Tiwari and Ajmera 2011)

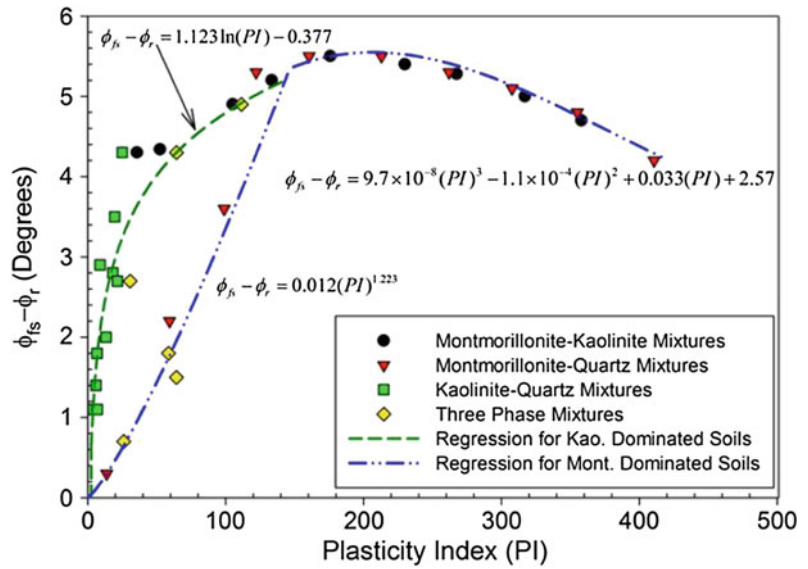


4 Application of Fully Softened Shear Strength for Slope Stability Analysis

Fully softened shear strength is an intrinsic property of a soil. Like the residual shear strength, it mainly depends on the mineral composition of soil and plasticity characteristics. The fully softened shear strength is used in general

application of slope stability such as the design of compacted fill, excavation of slopes and stability of dams. As cohesion is negligible, if not zero, in the case of slope to be analyzed with the fully softened shear strength, it is highly recommended that it be measured with the use of direct shear or direct simple shear device. Comparison of the laboratory obtained fully softened shear strength with the correlations proposed by Tiwari and Ajmera (2011) or Stark and Hussain

Fig. 12 Relationship proposed by Tiwari and Ajmera (2011) between the fully softened and residual shear strengths and the plasticity index (Tiwari and Ajmera 2011)



(2013) can provide cross check on the laboratory obtained shear strengths. If curvature of failure envelope is prominent, it is important to obtain the fully softened shear strength for the low effective normal stress range. It is recommended to use constant volume direct simple shear device in such cases to measure the drained fully softened shear strength.

5 Concluding Remarks

Fully softened shear strength is used when stability analyses of slopes are performed for first time slides or a conservative value of shear strength of soil is to be used for the analysis. In general, fully softened shear envelopes are curved and start from the origin, and thus, the fully softened friction angles depend on the effective normal stress for lower normal stress ranges, typically lower than 100 kPa. The curvature of failure envelope depends on the type of clay mineralogy and activity of soil. If the effective normal stress of concern is higher than 50 kPa, fully softened shear strength, which is the peak shear strength of remolded soil, can be measured with the traditional direct shear device.

However, using the constant volume direct simple shear device is recommended to measure the fully softened shear strength as it can measure the pore water pressure and corresponding value of effective normal stress for undrained shearing mode. In the absence of the laboratory measured shear strength or for confirmation of the laboratory measured shear strength, it is recommended to use the correlation available in practice. The correlations such as the ones proposed by Tiwari and Ajmera (2011) can be helpful to obtain the residual shear strength of soil as well based on the available fully softened shear strength and plasticity characteristics of soil.

Acknowledgements The authors would like to acknowledge the support of California State University Fullerton through intramural grant to conduct laboratory experiments pertinent to this research.

References

ASTM D3080-11 (2011) Standard test method for direct shear test of soils under consolidated drained conditions. ASTM International
 ASTM D7608-10 (2010) Standard test method for torsional ring shear test to determine drained fully softened shear strength and nonlinear strength

- envelope of cohesive soils (using normally consolidated specimen) for slopes with no preexisting shear surfaces. ASTM International
- Bhattarai P, Marui H, Tiwari B, Watanabe N, Aoyama K (2006) Influence of weathering on physical and mechanical properties of mudstone. In: Proceedings of the international symposium on disaster mitigation of debris flows, slope failures and landslides, pp 467–479
- Bishop AW, Webb DL, Lewin PI (1965) Undisturbed samples of london clay from the ashford common shaft: strength-effective stress relationships. *Géotechnique* 15(1):1–31
- Burland JB (1990) On the compressibility and shear strength of natural clays. *Géotechnique* 40(3):329–378
- Cancelli A (1981) Evolution of slopes in over-consolidated clays. In: Proceedings of the 10th international conference on soil mechanics and foundations engineering, vol 3, pp 377–380
- Castellanos BA (2014) Use and measurement of fully softened shear strength. Ph.D. dissertation, Virginia Polytechnic Institute and State University
- Duncan JM, Brandon T, VandenBerge D (2011) Report of the workshop on shear strength for stability of slopes in highly plastic clays. Center for geotechnical practice and research report. Virginia Polytechnic Institute and State University
- Gibson RE (1953) Experimental determination of the true cohesion and true angle of internal friction in clays. In: Proceedings of the 3rd international conference in soil mechanics, vol 1, pp 126–130
- Mesri G, Shahein M (2003) Residual shear strength mobilized in first-time slope failures. *J Geotech Geoenviron Eng* 129(1):12–31
- Morgenstern N (1977) Slopes and excavations in heavily over-consolidated clays. In: Proceedings of the 9th international conference on soil mechanics and foundation engineering, vol 2, pp 567–581
- Skempton AW (1964) Long-term stability of clay slopes. *Géotechnique* 14(2):77–102
- Skempton AW (1977) Slope stability of cuttings in Brown London clay. In: Proceedings of the 9th international conference on soil mechanics and foundation engineering, vol 3, pp 261–270
- Skempton AW (1985) Residual strength of clays in landslides, folded strata and the laboratory. *Géotechnique* 35(1):3–18
- Stark TD, Eid HT (1997) Slope stability analysis in stiff fissured clays. *J Geotech Geoenviron Eng* 123(4):335–343
- Stark TD, Choi H, McCone S (2005) Drained shear strength parameters for analysis of landslides. *J Geotech Geoenviron Eng* 131(5):575–588
- Stark TD, Hussain M (2013) Drained shear strength correlations for slope stability analyses. *J Geotech Geoenviron Eng* 139(6):853–862
- Terzaghi K (1936) Stability of slopes of natural clay. In: Proceedings of the 1st international conference on soil mechanics and foundation engineering, vol 1, pp 161–165
- Tiwari B, Ajmera B (2011) A new correlation relating the shear strength of reconstituted soil to the proportions of clay minerals and plasticity characteristics. *Appl Clay Sci* 53(1):48–57
- Tiwari B, Ajmera B (2014) Curvature of failure envelopes for normally consolidated clays. *Landslide Sci Saf Geoenviron* 2:123–128
- Wright SG, Zornberg JG, Aguetant JE (2007) The fully softened shear strength of high plasticity clays. Center for Transportation Research, University of Texas at Austin

TXT-tool 3.081-1.9

Dynamic Properties of Earthquake-Induced Large-Scale Rapid Landslides Within Past Landslide Masses

Pham Van Tien and Kyoji Sassa

Abstract

On October 23, 2004, an earthquake with a magnitude of 6.8 struck the central region of Niigata Prefecture. Several hundreds of earthquake-triggered landslides brought great damages to important public infrastructures and human lives. Among them, two large-scale rapid landslides, namely Higashi Takezawa and Terano landslides occurred within past landslide masses and blocked the river flows posing significant secondary risks to the society situated both downstream and upstream of the damped river site by dam failure. The paper seeks to examine triggering factors and interpret movement mechanisms of two landslides through ring shear tests on samples taken at landslide sites during a detailed field investigation. In order to reproduce exactly the landslide occurrences, real earthquake wave loading test and cyclic loading tests were performed on these samples. The test results revealed that those sand samples from both landslides are easily susceptible to sliding surface liquefaction phenomenon with very low final apparent friction angles, while the silt sample from Terano landslide did not show liquefaction behavior, indicating that the sliding surfaces of these rapid landslides must have been formed within the sand layer in the past landslide masses.

Keywords

Higashi Takezawa and Terano landslides · Dynamic properties
Ring shear apparatus · Earthquakes · Sliding surface liquefaction

Contents

1 Introduction	404
2 The Higashi Takezawa Landslide	404
3 The Terano Landslide	406
4 Ring Shear Apparatus and Testing Procedure	406
5 The Results of Dynamics Tests	407
5.1 Real Earthquake Wave Loading Test for the Higashi Takezawa Sand (H2).....	407
5.2 Cyclic Loading Test for the Higashi Takezawa Sand (H2).....	408

P. Van Tien (✉)
Graduate School of Engineering, Disaster Prevention
Research Institute, Kyoto University, Kyoto, Japan
e-mail: phamtiengtvt@gmail.com

K. Sassa
International Consortium on Landslides, Kyoto,
Japan
e-mail: sassa@iclhq.org

5.3 Cyclic Loading Tests for the Sand (T1) and Silt (T2) of the Terano Landslide	408
6 Interpretations and Discussions	409
7 Conclusions	411
References	412

1 Introduction

The 2004 Mid-Niigata Prefecture earthquake triggered 362 landslides wider than 50 m, and 12 large-scale landslides of more than one million cubic meters, and the total amount of sediment generated was estimated to be about 100 million m^3 (Ministry of Land, Infrastructure and Transport 2004). Most of the landslides were reactivated from past large-scale landslide masses. Landslide dams were formed in 45 locations by this earthquake. In this paper, two major landslides, namely the Higashi Takezawa landslide and the Terano landslide which formed landslide dams higher than 25 m, were investigated to study dynamic properties and initiation and motion mechanism of large-scale rapid landslides (Fig. 1).

2 The Higashi Takezawa Landslide

The Higashi Takezawa landslide dam was the largest one that was formed by a rapid mass movement approximately 100 m. A part of landslide mass spread across the road, moved upward along the slope of opposite bank of the Imokawa River and damaged an elementary

school (Fig. 2a). The site investigation result showed that the head scarp of this landslide was very straight and a part of the sliding plane placed on a gently-dipping (around 20°) stiff silt (stone) layer which was relatively impermeable as shown in Fig. 3. The sand layer over this stiff silt layer was soft. It was probably a part of previously moved landslide mass. After 3 days of the disaster occurrence, the topography and the central cross-section of the landslides were mapped based on the combination of field observations and an airborne laser scanning survey, which present an interpretation of landslide process.

As can be seen in Fig. 2b, the initial slope angle was 14.6° between P1 and P2 at the top of the river bank, and 17.5° between P1 and P3 along the river. The mobilized average apparent friction angle drawing by the mobilized energy line between P1 and P4 (highest point) was 7.5° . The difference between the energy line from P1 to P4 and the centre of gravity suggests a slower landslide than the Higashi Takezawa landslide. The sequence of landslide movement could be followed by two scenarios: (1) Block B was firstly liquefied, then the Block A started to move due to loss of support in its toe, (2) Block A initially started to move due to combining factors of seismic loading and static shear stress due to its self-weight. Then, the movement of Block A gave an undrained loading to Block B below and made the block B started to move together.

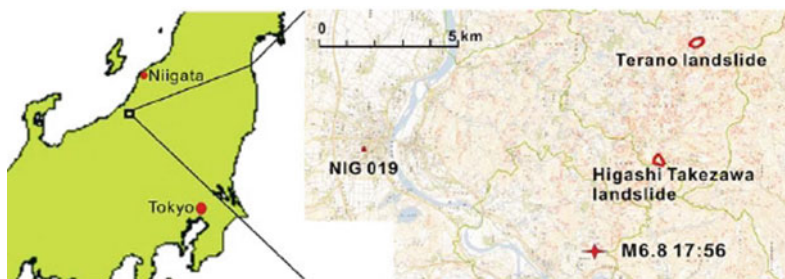


Fig. 1 Site map of the Higashi Takezawa landslide and Terano landslide with the epicenter and the seismograph gauge NIG019 of K-NET

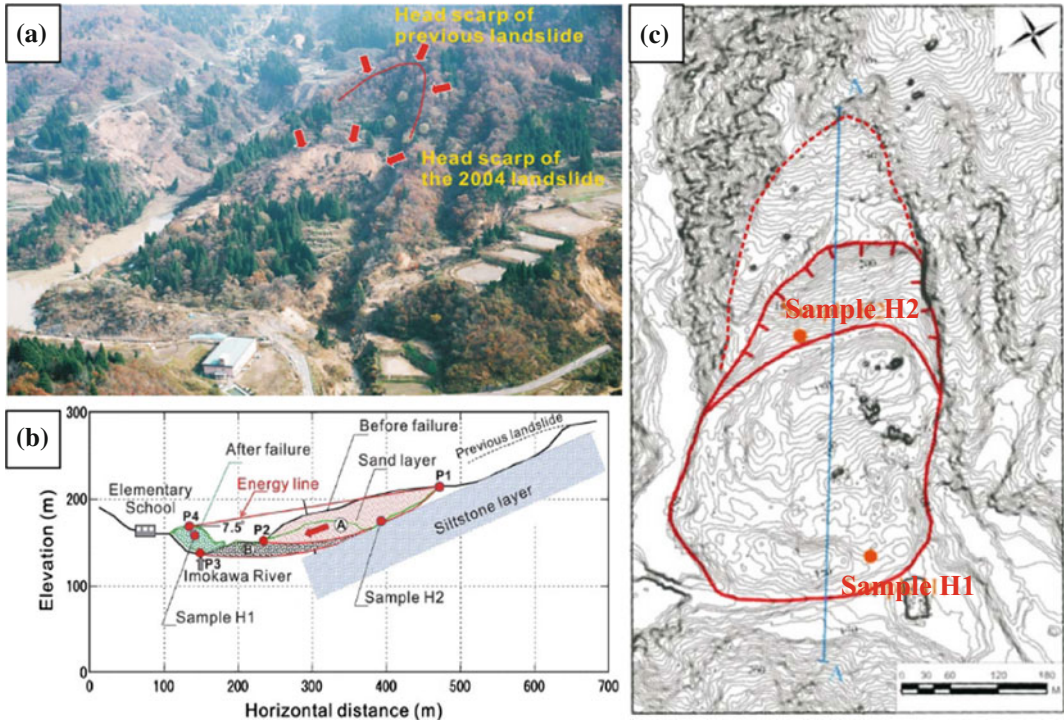


Fig. 2 Overview of Higashi Takezawa landslide (a), a longitudinal section (b) and a plan of the landslide (c) (Sassa et al. 2005)

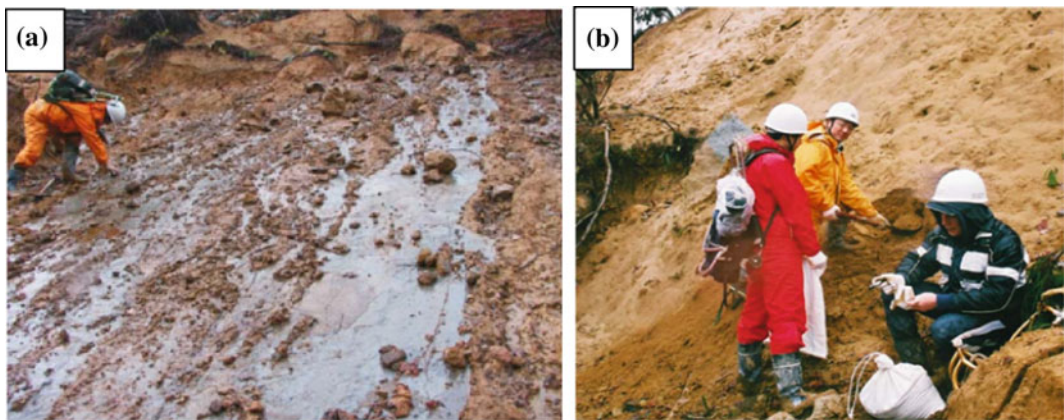


Fig. 3 Stiff silt layer outcropped in the headscarp (a) and soil sampling from the sand layer behind the sliding surface and over the stiff silt layer (b) (Sassa et al. 2005)

Taking account into Fig. 2c, Block B could be loaded almost exclusively by seismic loading due to its flat position while Block A was loaded by shear stress due to self-weight and seismic loading in both. Since pore pressure generation

on the shear surface in crushable sands is greatly affected by shear displacement (Wafid et al. 2004; Sassa et al. 2004a), the shear zone of Block A should be subjected to greater shear displacement and generate greater pore pressure

compared to Block B under the same shear stress conditions. Additionally, the depth of Block B (around 13 m above the river bed) is much smaller than Block A (around 40 m), thus shaking or shearing under a greater overburden pressure could facilitate grain crushing and resulting pore pressure generation as a major triggering mechanism of the landslide. Therefore, it could be concluded that Block A moved firstly due to strong seismic shaking plus the static shear stress due to self-weight of the around 40 m thick soil layer. Therefore, dynamic loading ring shear tests were conducted to simulate the initial movement of Block A.

As the results of site investigation and the examination mentioned, the landslide triggered by the earthquake possibly in the sand layer or/and silt layer. The most important question to answer for understanding the mechanism of Higashi Takezawa landslide is on which material layer sliding surface has formed on the outcropped head scarp by weathered top part of the lower silt layer or the bottom of upper sand layer. This concern will be solved in the paper based on the dynamic loading tests afterward. For studying landslide dynamic, a sample (H2) was taken from this sand layer behind the current sliding surface (Figs. 2b, c and 3b).

3 The Terano Landslide

The Terano landslide also formed a landslide dam 4.5 km north of the Higashi Takezawa landslide in the Tertiary mudstone landslide-prone area (Fig. 1). An overview, longitudinal section, a plan and sampling locations of the landslide are depicted in Fig. 4. This landslide occurred on a gentle slope of sand layer and/or a silty sand or silt layer in which nearly a half of the layer of sliding surface (10 m deep) submerged under the groundwater (Fig. 4a). Similarly, the position of sliding surface formed at the bottom of the sand layer or at the top of the siltstone was the main concern of this landslide.

The slope of the ground surface is 17.5° at an average from the toe of the slope at the Imokawa River (P3) to the top of head scarp (P1) in

Fig. 4b. Sand samples (T1) at the toe of the landslide mass seem to be similar to the samples of H1 and H2 of the Higashi-Takezawa landslide. In contrast to the Higashi Takezawa landslide, the silt sample (T2) taken from the head scarp is well weathered and soft due to the landslide motion and well oxidized as which was suggested by its brown color. While the siltstone outcropped in the head scarp in the Higashi Takezawa landslide is very stiff and in the stable layer below the landslide mass and probably always saturated suggested by its gray color of deoxidization. The grain size distributions of samples T2 is much finer than that of samples T1 and H2 (Fig. 5). The total density of soil layer was assumed to be 18.0 kN/m^3 in this research.

4 Ring Shear Apparatus and Testing Procedure

A version DPRI-5 of ring shear apparatus was applied to investigate the dynamic properties of two earthquake-induced rapid landslides by using dynamic (seismic and cyclic) loading. Model DPRI-5 is one of five dynamic-loading ring-shear apparatuses (DPRI-3,4,5,6,7) developed in DPRI, Kyoto University (Sassa et al. 2003, 2004b). The size of sample box in donuts shape is 120 mm in inside diameter and 180 mm in outside diameter, the maximum shear speed in the centre of a sample is 10 cm/s, the maximum frequency of cyclic loading is 5 Hz, and the maximum rate of data recording is 200 readings/s.

The testing procedure was as follows; (1) dry samples was firstly built into the shear box and then saturated by replacing pore air by CO_2 gas and replacing CO_2 by de-aired water later. The degree of saturation was checked indirectly by measuring the pore pressure parameter ($\text{BD} = u/\Delta\sigma$) (Sassa 1988). In this study, undrained tests were usually carried out with $\text{BD} \geq 0.98$. (2) Next, the initial shear stress at sliding surface before landslide was reproduced by loading 230 kPa of shear stress under drained conditions. (3) Finally, the samples were sheared under undrained dynamic loading conditions by closing the drainage valve.

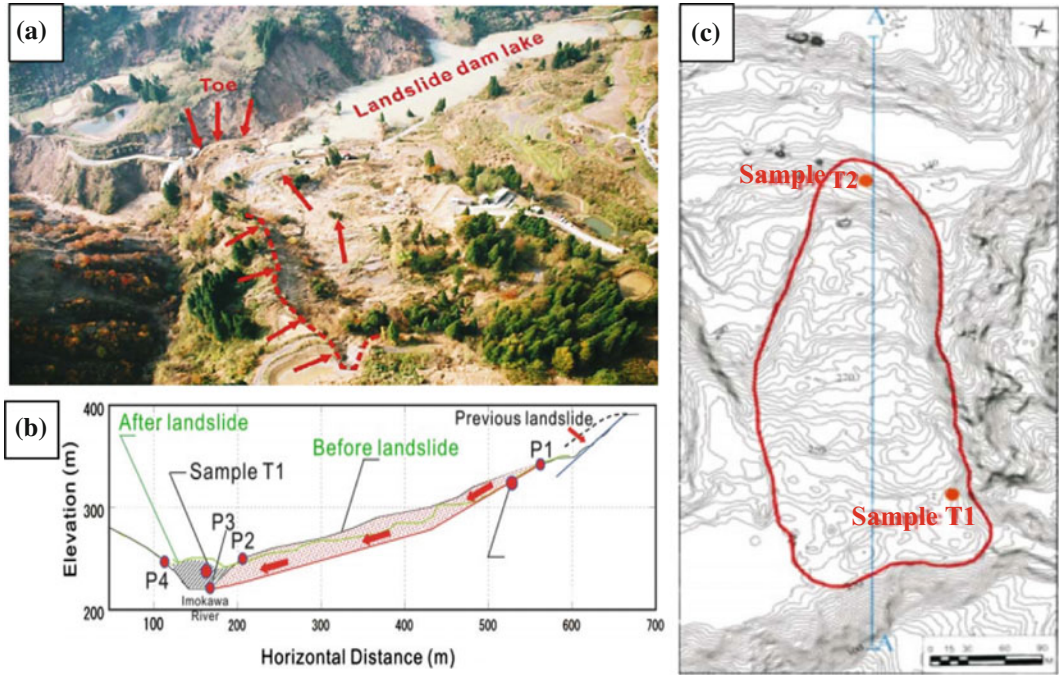


Fig. 4 Overview of Terano landslide (a), a longitudinal section (b) and a plan of the landslide (c) (Sassa et al. 2005)

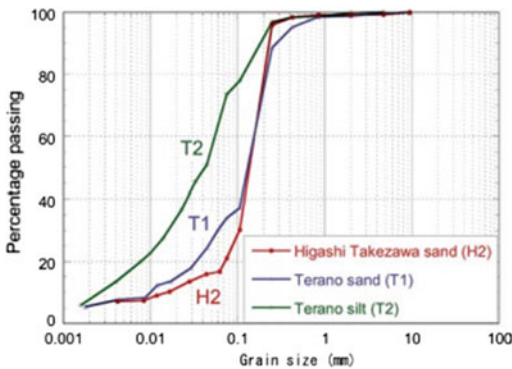


Fig. 5 Grain size distribution of three samples

5 The Results of Dynamics Tests

5.1 Real Earthquake Wave Loading Test for the Higashi Takezawa Sand (H2)

Seismic-loading ring shear test is conducted to simulate the initiation and motion of earthquake-triggered Higashi-Takezawa landslide. The

seismic loadings were calculated by using the nearest seismic record of the Mid-Niigata earthquake (Fig. 6). The nearest monitoring site to the Higashi Takezawa landslide is the observation station of NIG019 in K-NET of the National Research Institute for Earth Science and Disaster Prevention (NIED) at Ojiya, around 10 km west of the Higashi Takezawa landslide, and WNW 7 km from the epicenter of the main shock.

The test results are shown in Fig. 7a, graph of time series data and Fig. 7b, the stress path of the seismic loading test. In which normal stress and shear stress are denoted by the green color line and the red color line, respectively. The monitored pore pressure in the blue color increased during seismic loading and also in the progress of shear displacement and reached a level very close to the normal stress path. Therefore, shear resistance at steady state is very low as shown in the red effective stress path in Fig. 7b. The mobilized apparent friction angle defined as the ratio of mobilized steady state shear resistance and initial normal stress is only 2.5° at the steady state. The sample is subjected to the sliding

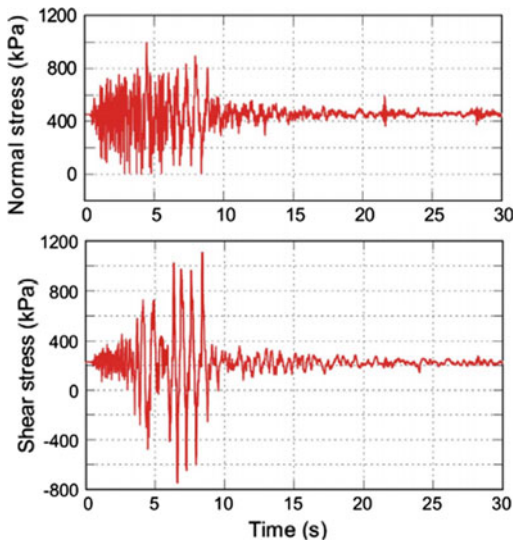


Fig. 6 Stresses working on the sliding surface of Higashi-Takezawa landslide monitored at the site NIG019 in the Mid-Niigata earthquake

surface liquefaction (Sassa 1996, 2000; Sassa et al. 2004a) due to grain crushing along the shear zone resulting in volume reduction and excess pore pressure generation at large shear displacement.

Since the effective friction angle mobilized in the post failure process is not so clear in Fig. 7b, another test with shear speed control mode was performed under drainage condition. In this test, the sample was sheared under the speed control condition at 0.2 mm/s. Normal stress was reduced at the unloading rate of 0.5 kPa/s after reaching the peak shear resistance. The failure line mobilized in the post failure process (residual state) gave 36.9° for the friction angle (Fig. 8a).

5.2 Cyclic Loading Test for the Higashi Takezawa Sand (H2)

The undrained cyclic loading test firstly was performed on the sample H2 in the same sample setting and test condition. The main differences were the loading stress, frequency, and waveform. During this test, initial normal stress was

kept constant while shear stress with the waveform of sine curve at 1 Hz frequency was applied. To ensure the failure, the shear stress was increased step by step until 15 cycles. The test result for the Higashi Takezawa sand is presented in Fig. 9. Sliding surface liquefaction behavior was observed under cyclic loadings at large shear displacement as excess pore pressure generated and grain crushing occurred in the shear zone. The mobilized apparent friction angle at the steady state is 3.3°, almost the same level with that obtained in the seismic loading test. In this test, the friction angle at peak is 36.9° (Fig. 9b).

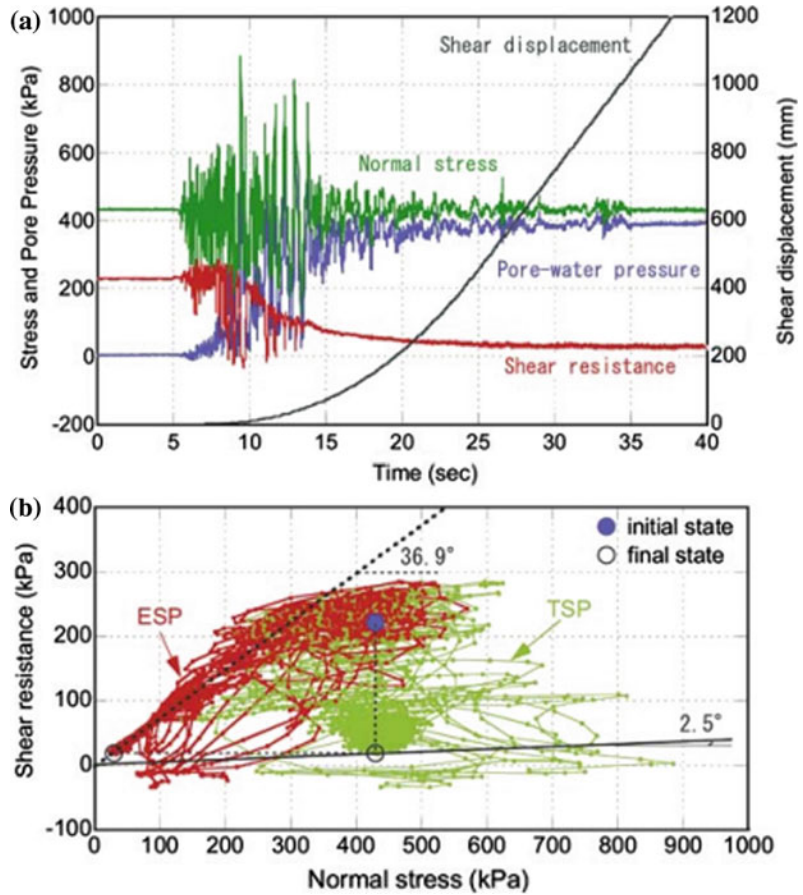
5.3 Cyclic Loading Tests for the Sand (T1) and Silt (T2) of the Terano Landslide

A series of cyclic loading tests was conducted on samples T1 and T2 of Terano landslide in order to compare its dynamic properties with dynamic parameters of the sand H2 of the Higashi Takezawa landslide. For all tests for Terano T1 sand and T2 silt, saturated samples were firstly consolidated at 250 kPa of normal stress and about 100 kPa of shear stress as the initial stress condition of the slope. Then, the cyclic loading control with a shear stress of sine curve of 1 Hz loading frequency was applied while normal stress was kept constant, and. The shear stress was increased step by step until 15 cycles.

The test results for the Terano sand (T1) are shown in Fig. 10. As can be seen, the Terano sand is clearly subjected to sliding surface liquefaction after failure. The mobilized apparent friction angle at the steady state is 3.8°, slightly greater than H2 (2.5° in Fig. 7b, and 3.3° in Fig. 9b). The mobilized effective friction angle that is estimated from the stress path after the peak is 35.7°, about 1° less than the 36.9° for the Higashi Takezawa sand. This may be due to the fact that the Terano sand is slightly finer than the Higashi Takezawa sand as found in Fig. 5. However, the both sand samples are generally similar.

The results of cyclic loading test on the Terano silt (T2) is shown in Fig. 11. The dynamic

Fig. 7 Undrained seismic loading test to simulate the Higashi-Takezawa landslide (BD = 0.98). **a** Time series data, and **b** stress path



properties of the Terano silt are quite different to the sands. In this regard, the sliding surface liquefaction and its resulting rapid landslide motion were not produced in this test. Shear displacement was increased only during the cyclic loading, precisely say, only in the time span when the loaded stress reached or exceeded the peak shear strength. It was the repeated movements of stop and move, and the shear movement stopped at the same time with the final cycle of loading. High pore pressure was probably not generated or at least not monitored as seen in Fig. 11a.

To obtain the effective friction angle in the residual state or the post failure condition, the silt sample was sheared at a constant shear speed of 0.05 mm/s by using the shear-speed-controlled method, while the normal stress from was increased from 50 kPa to more than 250 kPa at a loading speed of 0.1 kPa/s in the drained

condition. The residual friction angle is 23.9° for the friction angle (Fig. 8b). The friction angle is 13° less than the Higashi Takezawa sand, and around 12° less than the Terano sand. The silts and sands display quite different shear characteristics.

6 Interpretations and Discussions

During site investigation a stiff silt (stone) layer outcropped above the sand layer in the head scarp of the Higashi Takezawa and Dainichisan landslides (Sassa 2005) were observed. Therefore, a key concern that whether the sliding surface is formed on the top weathered part of silt or on the bottom of sand layer is of great importance for understanding the triggering mechanisms of these landslides. The weathered

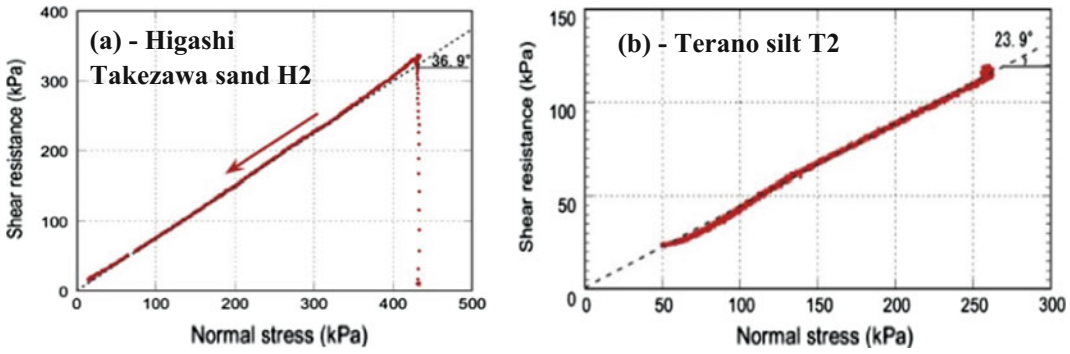


Fig. 8 Stress path (a) and the residual state of friction angle (b) monitored in the drained shear speed control test on landslide samples

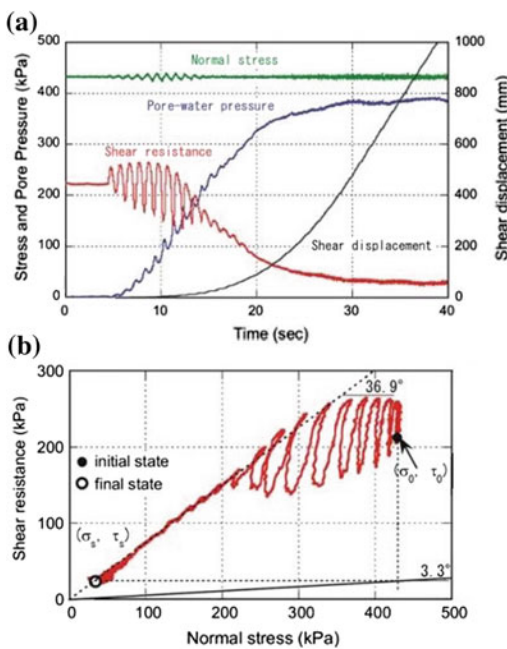


Fig. 9 Undrained cyclic loading test of the Higashi Takezawa sand (H2) (BD = 0.98). **a** Time series data, and **b** stress path

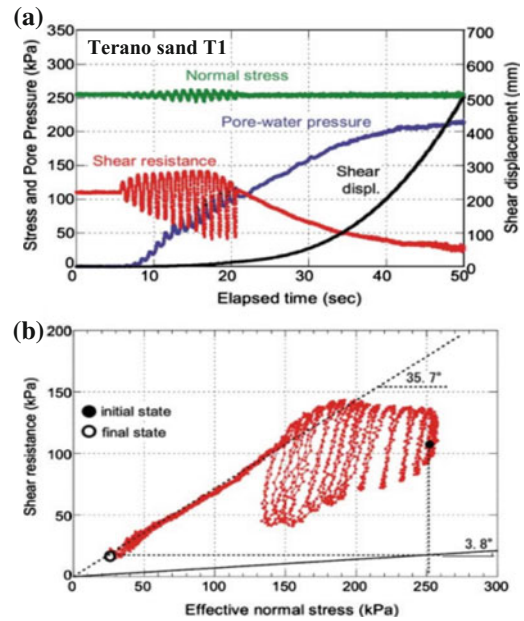


Fig. 10 Undrained cyclic loading test on the Terano sand (T1) (BD = 0.98). **a** Time series data, and **b** stress path

part of silt layer could not be found on the site, probably it is very thin. However, a sample of weathered silt (T2) was taken in the Terano landslide. The effective friction angle of this sample is 12–13° less than the sand. It means a landslide should occur in the silt layer when rain or melting snow is the triggering factor of landslides. This area is known as a Tertiary mudstone landslide area. Many landslides cover this area

(Shimizu et al. 2004 or NIED Web page for landslide map). The area of Niigata Prefecture is known as a heavy snow area and snow melt is the usual main source of water supply for the ground.

Slow and limited shear displacement is the common form of movement of landslides here. In the case of water supply due to snow melting or long rain, it is certain that silt is much weaker

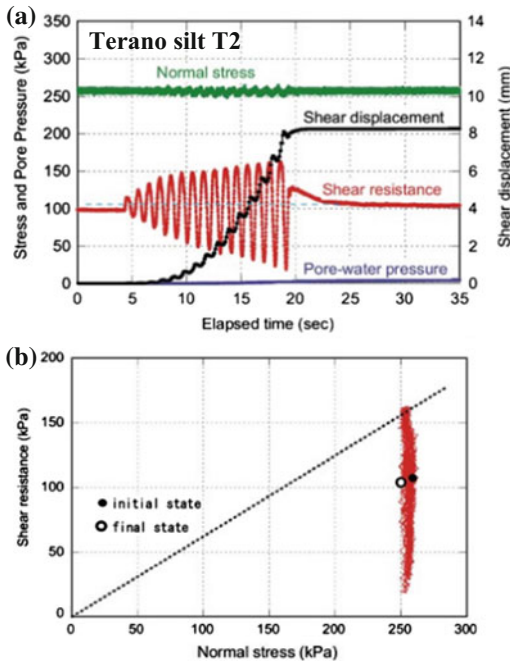


Fig. 11 Undrained cyclic loading test on the Terano silt (T2) (BD = 0.98). **a** Time series data, and **b** stress path

than the sand. Therefore, previous landslides probably occurred at the sliding surface of the silt layer, most likely in the weathered part of silt just below the sand layer. In contrast, the silt is strong against the earthquake, while sand is weak against earthquake loading. Sand grains are much easy to crush and susceptible for volume reduction. Therefore, earthquake-induced landslides should form its sliding surface within the sand. The dynamic loading ring shear tests indicate that the most likely scenario to cause the Higashi Takezawa and the Terano landslides were one in which the sliding surface liquefaction phenomenon occurred within the sand layer under a high overburden pressure.

7 Conclusions

This research presented the characteristics of landslides triggered by the 2004 Mid-Niigata earthquake through the field investigation and

interpreted the dynamic properties of the landslides by ring shear tests. Both targeted landslides were initiated within the landslide mass of the previous landslides in which the mobilized apparent friction angles are 7.1° and 12.7° in the Higashi Takezawa landslide and in the Terano landslide, respectively. The cyclic loading ring shear tests on sands from the Higashi Takezawa landslide and the Terano landslide proved that both sand samples can be subjected to sliding surface liquefaction phenomenon at shear zone under 20–40 m overburden pressure. Whereas the silt sample taken from the Terano landslide seems not to be liquefied under cyclic loading due to less generated pore pressure and only limited shear displacement. Even when the shear stress reached or exceeded the failure line, the movement stopped at the end of cyclic loading. On the contrary, the effective friction angle of silt is 23.9° , smaller than those of sands (36.9° and 35.7°). Therefore, landslide movement due to snow melting or rainfalls should have its sliding surface in the silt layer. It is estimated from these test results that previous landslides in both areas probably slid in the silt layer; however the rapid landslides triggered by the 2004 Mid-Niigata earthquake formed their sliding surface within the sand layer. Additionally, the reproduction of Higashi Takezawa landslide with a dynamic loading ring shear test using the monitored seismic record in Ojiya (NIG019) on the sand collected from the head scarp of the landslide resulted in the initiation of a rapid landslide in addition to the observation of the sliding surface liquefaction.

Acknowledgements This research was conducted as a part of Theme 2: Landslide Investigation of the 2004 Mid-Niigata prefecture earthquake disaster investigation by MEXT (Ministry of Education, Culture, Sports, Science and Technology, Japan) Special Coordinating Fund for Science and Technology. The authors acknowledge its special coordinating fund to conduct this investigation and thank all members of this investigation team for discussion. We are grateful for Dr. Gen Furuya and other post-doctoral students and graduate students of the Research Centre on Landslides, Disaster Prevention Research Institute of Kyoto University for cooperation in the field investigation and sampling.

References

- Ministry of Land, Infrastructure and Transport (2004) Quick report for Landslides triggered by 2004 Niigata-Chuetsu earthquake. <http://www.mlit.go.jp/kisha/kisha04/05/0511012.html>
- Sassa K (1988) Geotechnical Model for the motion of landslides. In: Special lecture of 5th international symposium on landslides, Toronto, June, vol 2, pp 349–354
- Sassa K (1996) Prediction of earthquake induced landslides. In: Special lecture for 7th international symposium on landslides. “landslides”, vol 1. Balkema Co. Ltd., pp 115–132
- Sassa K (2000) Mechanism of flows in granular soils. Invited paper. In: Proceedings of the GeoEng2000, Melbourne 1, pp 1671–1702
- Sassa K (2005) Landslide disasters in the 2004 Mid-Niigata earthquake in Japan. *Landslides* 2(2) (in press)
- Sassa K, Wang G, Fukuoka H, Wang W, Ochiai T, Sugiyama M, Sekiguchi T (2004a) Landslide risk evaluation and hazard zoning for rapid and long-travel landslide in urban development areas. *Landslides* 1 (3):221–235
- Sassa K, Fukuoka H, Wang G, Ishikawa H (2004b) Undrained dynamic-loading ring-shear apparatus and its application to landslide dynamics. *N Landslides* 1 (1):9–17
- Sassa K, Fukuoka H, Wang F, Wang G (2005) Dynamic properties of earthquake-induced large-scale rapid landslides within past landslide masses. *Landslides* 2:125–134
- Sassa K, Wang G, Fukuoka H (2003) Performing undrained shear tests on saturated sands in a new intelligent type of ring shear apparatus. *Geotech Test J ASTM* 26(3):257–265
- Shimizu F, Oyagi N, Miyagi T, Inoguchi T (2004) Landslide topography Map, vol 17 (Nagaoka & Takada), 1/50,000 and 1/25,000
- Wafid M, Sassa K, Fukuoka H, Wang G (2004) Evolution of shear-zone structure in undrained ring shear tests. *Landslides* 1(2):101–112
- National Research Institute for Earth Science and Disaster Prevention (NIED): Web of K-Net <http://www.k-net.bosai.go.jp/k-net/data/>
- National Research Institute for Earth Science and Disaster Prevention. Web for Landslide map: http://lsweb1.ess.bosai.go.jp/jisuberi/jisuberimini/jisuberi_top.html

TXT-tool 3.001-1.4

Using Excel Tools for Slope Stability Analysis

Beena Ajmera and Binod Tiwari

Abstract

Each year landslides around the world are responsible for the loss of hundreds of lives, damage to infrastructure, billions of dollars in economic loss and have an impact on the environment. An understanding of the stability of slopes is crucial to reduce the impact of landslides and there are several available methods and computer programs to do so. However, the development of simple spreadsheets to evaluate the stability of slopes can be beneficial in reducing the cost of purchasing commercially available programs and the learning component associated with these programs. This teaching tools outlines the procedures to develop Excel Spreadsheets for four commonly used slope stability analysis methods. Specifically, step-by-step procedures to determine the factor of safety using the Ordinary Method of Slices, Bishop's Simplified Method, Simplified Janbu Method and the Lowe and Karafiath Method are provided.

Keywords

Slope stability · Excel tools · Ordinary method of slices
Bishop's simplified method · Janbu simplified method · Lowe's method

B. Ajmera
Department of Civil and Environmental Engineering,
California State University Fullerton, 800 N. State
College Blvd., E-318, Fullerton, CA 92831, USA
e-mail: bajmera@fullerton.edu

B. Tiwari (✉)
Department of Civil and Environmental Engineering,
California State University Fullerton, 800 N. State
College Blvd., E-419, Fullerton, CA 92831, USA
e-mail: btiwari@fullerton.edu

Contents

1	Introduction	414
2	Available Methods and Software for Conducting Slope Stability Analysis	414
3	Spreadsheet for Ordinary Method of Slices	414
4	Spreadsheet for Bishop's Simplified Method	417
5	Spreadsheet for Lowe and Karafiath and Simplified Janbu Methods	418

6 Conclusions	420
References	420

1 Introduction

Landslides are widespread hazards occurring worldwide as a result of a variety of natural and manmade causes. Each year they cause billions of dollars of property damage, the loss of life and infrastructures. Thus, it is crucial to understand the stability of the slope and design preventive measures accordingly. The stability of the slope is usually expressed as the ratio of resisting forces to driving forces in terms of a quantity known as the factor of safety (FS). There are many available methods to determine the factor of safety of a slope. These methods vary in the complexity of the formulations from very simple to computational intensive numerical calculations. While some of the available techniques can be easily programmed into spreadsheets, several software programs are commercially available to conduct slope stability analysis. This teaching tool will first briefly summarize the commonly methods for determining the factor of safety of slope and a list of commercially available software programs to preform analysis using these methods will be provided. However, the focus will be on the development and use of Excel spreadsheets for four methods.

2 Available Methods and Software for Conducting Slope Stability Analysis

The literature contains a number of limit equilibrium methods for determining the stability of slopes. As the focus of this teaching tool is in the development of simple spreadsheets for conducting slope stability analysis, the details of each of these methods are not provided within this document. However, Table 1 briefly summarizes these methods, the assumptions made, the equilibrium conditions satisfied, the

unknowns in each method and some of the situations where the method is commonly used. A number of software programs have been developed that incorporate the methods described in Table 1 to evaluate the stability of slopes. Some such programs are *RocScience Slide 6.0* and *GeoStudio Slope/W*. The remainder of this tool will focus on the development of simple spreadsheets using Microsoft Excel to conduct slope stability analysis using the Ordinary Method of Slices, Bishop's Simplified Method, Simplified Janbu and Lowe and Karafaith procedures.

3 Spreadsheet for Ordinary Method of Slices

Figure 1 shows a screenshot of an Excel Spreadsheet developed to use the Ordinary Method of Slices (Fellenius 1936) to evaluate the factor of safety of the slope. In Row 1, the input parameters for the slope are presented. Specifically, n is the number of slices, γ is the unit weight of the slope material, γ_w is the unit weight of water, c is the cohesion and ϕ is the friction angle of the material at the sliding surface. Beginning from Row 2, the details of the contents of each of the columns are provided next. Column A is simply a count of the number of slices beginning at one and extending to the desired number of slices. Column B represents the x-coordinate of the left hand side of the corresponding slice. For example, the value in Cell B5 is the x-coordinate corresponding to the left edge of Slice 3. Columns C, D, and E represent the y-coordinate of the sliding surface (y_s), ground water table (y_w) and ground surface (y_g) at the corresponding x-coordinate in Column B. The information in the rows and columns described are required in order to perform the remainder of the computations necessary in order to determine the factor of safety.

The width of each slice is computed in Column F as the difference the x-coordinates for the left and right hand side of each slice. For

Table 1 Summary of some common limit equilibrium slope stability analysis methods

Procedure	Assumptions	Equilibrium	Unknowns	Uses
Infinite slope (Taylor 1948)	Infinite extent of sloe with a slip surface parallel to the slope face	Forces perpendicular and parallel to slope	Factor of safety, normal force on base	Homogenous cohesionless slopes and slopes were stratigraphy restricts surface to shallow depths and parallel to slope face; very accurate where applicable
Swedish circle (Fellenius 1922; Skempton 1948)	Circular slip surface; friction angle is equal to zero	Moments about center	Factor of safety	Slopes where $\varphi = 0$; relatively thick zones of weaker materials where the slip surface is approximately circular
Ordinary method of slices (Fellenius 1936)	Circular slip surface; neglects forces on the slice sides	Moments about center	Factor of safety	Nonhomogeneous slopes and c - φ soils where slip surface can be approximated by a circle; very convenient for hand calculations; inaccurate for effective stress analysis with high pore water pressures
Bishop simplified method (Bishop 1955)	Circular slip surface; horizontal forces on the slice sides of the slices	Moments about center; forces in the vertical direction	Factor of safety; normal force on bases	Nonhomogeneous slopes and c - φ soils where slip surface can be approximated by a circle; more accurate than OMS especially for analyses with high pore water pressures; calculation feasible by hand or spreadsheet
Lowe and Karafiath (1959) method	Slice side forces are inclined at the average slope of the ground and sliding surfaces	Forces in the vertical and horizontal directions	Factor of safety; normal force on bases; interslice forces	Virtually all slope geometries and soil profiles; less accurate than complete equilibrium procedures; results are sensitive to assumed inclinations for interslice force
Spencer (1967) method	Parallel interslice forces; normal force is acting at the center of the slice base	Moments about any point; forces in the horizontal and vertical direction	Factor of safety; interslice force inclination; normal force on bases; interslice forces; location of side forces	Accurate procedure; virtually all slope geometries and soil profiles; simplest complete equilibrium procedure
Morgenstern and Price (1967) method	Interslice shear force and normal force are related; normal force is acting at the center of the slice base	Moments about any point; forces in the horizontal and vertical direction	Factor of safety; interslice force inclination and location; normal force on bases; horizontal interslice forces	Accurate procedure; virtually all slope geometries and soil profiles; rigorous; well-established complete equilibrium procedure

#	A	B	C	D	E	F	G	H	I	J	K	L	M	N	O	P	Q	R	S	T	U
1	n =	73			γ =	18.66	γ _w =	9.81	c =	0	φ =	28.63									
2	Slice No.	x	y ₁	y _w	y ₂	b	h ₁	h _w	h _{s,ave}	h _{w,ave}	W	α	u	W cos α	W sin α	l	U	W cos α · U			
3	1	0.00	710.00	706.00	710.00		0.00	0.00													
4	2	4.00	709.00	706.00	710.00	4.00	1.00	0.00	0.50	0.00	37.32	-14.04	0.00	36.21	-9.05	4.12	0.00	36.21			
5	3	6.90	710.46	708.00	712.00	2.90	1.54	0.00	1.27	0.00	68.71	26.73	0.00	61.37	30.91	3.25	0.00	61.37			
6	4	9.60	711.42	710.00	714.00	2.70	2.58	0.00	2.06	0.00	103.69	19.63	0.00	97.66	34.83	2.87	0.00	97.66			
7	5	13.70	712.89	712.00	716.00	4.10	3.11	0.00	2.85	0.00	217.71	19.63	0.00	205.06	73.12	4.35	0.00	205.06			
8	6	22.51	716.03	714.00	718.00	8.81	1.97	0.00	2.54	0.00	418.18	19.63	0.00	393.89	140.46	9.35	0.00	393.89			
9	7	27.98	717.98	716.00	720.00	5.47	2.02	0.00	2.00	0.00	203.90	19.63	0.00	192.05	68.49	5.81	0.00	192.05			
10	8	33.84	720.07	718.00	722.00	5.86	1.93	0.00	1.98	0.00	216.23	19.63	0.00	203.67	72.63	6.22	0.00	203.67			
11	9	42.82	723.00	720.00	724.00	8.98	1.00	0.00	1.47	0.00	245.71	18.09	0.00	233.57	76.28	9.45	0.00	233.57			
12	10	48.22	725.00	722.00	726.00	5.40	1.00	0.00	1.00	0.00	100.76	20.32	0.00	94.49	35.00	5.76	0.00	94.49			
13	11	56.72	727.00	724.00	728.00	8.50	1.00	0.00	1.00	0.00	158.61	13.24	0.00	154.39	36.33	8.73	0.00	154.39			
14	12	61.45	729.00	726.00	730.00	4.73	1.00	0.00	1.00	0.00	88.26	22.92	0.00	81.29	34.37	5.14	0.00	81.29			
15	13	64.82	731.00	728.00	732.00	3.37	1.00	0.00	1.00	0.00	62.88	30.69	0.00	54.08	32.09	3.92	0.00	54.08			
16	14	66.89	731.85	730.00	734.00	2.07	2.15	0.00	1.57	0.00	60.78	22.39	0.00	56.19	23.16	2.24	0.00	56.19			
17	15	75.08	734.77	732.00	736.00	8.19	1.23	0.00	1.69	0.00	257.78	19.63	0.00	242.80	86.58	8.70	0.00	242.80			
18	16	78.14	735.86	734.00	738.00	3.06	2.14	0.00	1.68	0.00	95.98	19.63	0.00	90.40	32.24	3.25	0.00	90.40			
19	17	81.03	736.90	736.00	740.00	2.89	3.10	0.00	2.62	0.00	141.29	19.63	0.00	133.08	47.46	3.07	0.00	133.08			
20	18	84.89	738.27	738.00	742.00	3.86	3.73	0.00	3.42	0.00	246.08	19.63	0.00	231.78	82.65	4.10	0.00	231.78			
21	19	88.39	739.52	740.00	744.00	3.50	4.48	0.00	4.10	0.24	268.04	19.63	2.36	252.47	90.03	3.72	8.75	243.72			
22	20	90.00	740.09	742.00	746.00	1.61	5.91	1.91	5.19	1.19	156.01	19.63	11.70	146.95	52.40	1.71	20.01	126.94			
23	21	92.71	741.06	744.00	748.00	2.71	6.94	2.94	6.42	2.42	324.79	19.63	23.77	305.92	109.09	2.88	68.38	237.54			
24	22	97.97	742.94	746.00	750.00	5.26	7.06	3.06	7.00	3.00	687.23	19.63	29.45	647.31	230.83	5.58	164.45	482.86			
25	23	101.01	744.02	746.00	752.00	3.04	7.98	1.98	7.52	2.52	426.69	19.63	24.74	401.90	143.32	3.23	79.85	322.05			
26	24	104.99	745.44	748.00	754.00	3.98	8.56	2.56	8.27	2.27	614.20	19.63	22.27	578.52	206.90	4.23	94.10	484.41			

Results	
Σ[W sin α]	9058.62
Σ[W cos α · U]	19434.57
Σl	244.63
FS	1.17

Fig. 1 Screenshot of excel spreadsheet for ordinary method of slices

example, the formula in Cell F5 would be “=B5-B4”. Column G contains the height of the soil mass above the sliding surface (h_s) and is computed for the i -th slice using:

$$h_{s,i} = y_{g,i} - y_{s,i}$$

Thus, the Cell G5 contains the formula “=E5-C5”. Similarly, Column H represents the height of the water column (h_w) above the sliding surface. This value is found for the i -th slice using:

$$h_{w,i} = y_{w,i} - y_{s,i}$$

when the ground water table is above the sliding surface. If the ground water table is below the sliding surface, this value should be equal to zero. This is established using an IF command in Excel, which converts the negative values to zero. The Cell H5 would contain the formula “=IF(D5-C5 < 0,0,D5-C5)”. As the values in Columns G and H represent the values of h_s and h_w on the left hand side of the i th slice, the average values of h_s and h_w in each slice, denoted $h_{s,ave}$ and $h_{w,ave}$ are calculated in Columns I and J, respectively. Specifically, the formulas in Cells I5 and J5 are “=AVERAGE(G4:G5)” and “=AVERAGE(H4:H5)”, respectively.

Column K contains the weight of the slice (W), which is determined for the i th slice using the following equation:

$$W_i = \gamma b_i h_{s,ave,i}$$

As the unit weight is considered to be a constant across all of the material above the sliding surface, this cell is fixed. Thus, the formula in Cell K5 is “F5 * I5 * \$F\$1”. The inclination of the base of the slice, α , is determined using the difference between the y -coordinates of the left and right hand side of the slice and the width of the slice and compiled in Column L. The formula in Cell L5 is “=DEGREES(ATAN((C5-C4)/F5))”. Column M contains the pore water pressure (u) acting at the base of the slice, which is determined for the i -th slice from:

$$u_i = \gamma_w h_{w,ave,i}$$

This corresponds to the formula “=\$H\$1 * J5” in Cell M5. Columns N and O resolve the weight into its normal ($W \cos \alpha$) and tangential ($W \sin \alpha$) components, respectively, relative to the base of the slice. Thus, the formulas in Cells N5 and O5 are “=K5 * COS(RADIANS(L5))” and “=K5 * SIN(RADIANS(L5))”, respectively. The length

(L) of the sliding surface for the *i*th slice is computed using:

$$L_i = \frac{b_i}{\cos \alpha_i}$$

This value is calculated in Column P, with the formula in Cell P5 being “=F5/COS(RADIANS(L5))”. The weight of water (U) in Column Q are computed for the *i*-th slice from:

$$U_i = u_i L_i$$

This would imply that Cell Q5 contains the formula “=M5 * P5”. Finally, Column R contains the sum of the normal forces on the base of the slice ($W \cos \alpha - U$). Thus, Cell R5 contains the formula “=N5-Q5”.

To compute the factor of safety using the Ordinary Method of Slices, the sum of the values in Columns O, R, and P are determined in Cells U4, U5, and U6, respectively. The factor of safety (FS) is then:

$$FS = \frac{c \sum L + \sum (W \cos \alpha - U) \tan \phi}{\sum W \sin \alpha}$$

Therefore, the formula in Cell U7 is “=(J1 * U6) + (U5 * TAN(RADIANS(L1)))/U4”.

4 Spreadsheet for Bishop’s Simplified Method

Presented in Fig. 2 is a screenshot of an Excel Spreadsheet for Bishop’s Simplified Method (Bishop 1955). The information and computations presented in Row 1 and Columns A through Q are the same as those presented above in Sect. 3 for the Ordinary Method of Slices. Column R contains the difference in the weight of the slice and the weight of water. This would correspond to the formula “=K5-Q5” in Cell R5. Column S contains the values of m_{α} , which is computed for the *i*-th slice using:

$$m_{\alpha,i} = \cos \alpha_i + \frac{\tan \phi \sin \alpha_i}{FS}$$

Note that in order to solve for the value of m_{α} , the value of the factor of safety must be known. Thus, Bishop’s Simplified Method becomes an iterative process, which can still be solved using the spreadsheet, but with the creation of a cell containing a trial value for the factor of safety. In the example shown in Fig. 2, this corresponds to Cell W7. Therefore, the formula for m_{α} entered in Cell S5 is “=(COS(RADIANS(L5))) + ((TAN(RADIANS(\$L\$1)) * SIN(RADIANS(L5)))/\$W\$7)”.

1	A	B	C	D	E	F	G	H	I	J	K	L	M	N	O	P	Q	R	S	T	U	V	W	
2	Slice No.	x	Y ₁	Y ₂	Y ₃	b	h ₁	h ₂	h ₃	h ₄	W	α	u	W cos α	W sin α	L	U	W-U	m _α	Numerator				
3	1	0.00	710.00	706.00	710.00	0.00	0.00	0.00	0.00	0.00	0.00	0.00	0.00	0.00	0.00	0.00	0.00	0.00	0.00	0.00	0.00	0.00	0.00	0.00
4	2	4.00	709.00	706.00	710.00	4.00	1.00	0.00	0.50	0.00	37.32	-14.04	0.00	36.21	-9.05	4.12	0.00	37.32	0.86	23.83				
5	3	8.90	710.46	708.00	712.00	2.90	1.54	0.00	1.27	0.00	68.71	-26.73	0.00	61.37	-30.91	3.25	0.00	68.71	1.11	33.89				
6	4	9.60	711.42	710.00	714.00	2.10	2.58	0.00	2.06	0.00	103.69	-19.63	0.00	97.66	-34.83	2.87	0.00	103.69	1.10	51.39				
7	5	13.70	712.89	712.00	716.00	4.10	3.11	0.00	2.85	0.00	217.71	-19.63	0.00	205.06	-73.12	4.35	0.00	217.71	1.10	107.91				
8	6	22.51	716.03	714.00	718.00	8.81	1.97	0.00	2.54	0.00	418.18	-19.63	0.00	393.89	-140.46	9.35	0.00	418.18	1.10	207.28				
9	7	27.98	717.98	716.00	720.00	5.47	2.02	0.00	2.00	0.00	203.90	-19.63	0.00	192.05	-68.49	5.81	0.00	203.90	1.10	101.07				
10	8	33.84	720.07	718.00	722.00	5.86	1.93	0.00	1.98	0.00	216.23	-19.63	0.00	203.67	-72.63	6.22	0.00	216.23	1.10	107.18				
11	9	42.82	723.00	720.00	724.00	8.98	1.00	0.00	1.47	0.00	245.71	-18.09	0.00	233.57	-76.28	9.45	0.00	245.71	1.10	122.16				
12	10	48.22	725.00	722.00	726.00	5.40	1.00	0.00	1.00	0.00	100.76	-20.32	0.00	94.49	-35.00	5.76	0.00	100.76	1.10	49.89				
13	11	56.72	727.00	724.00	728.00	8.50	1.00	0.00	1.00	0.00	158.61	-13.24	0.00	154.39	-36.33	8.73	0.00	158.61	1.08	80.01				
14	12	61.45	729.00	726.00	730.00	4.73	1.00	0.00	1.00	0.00	88.26	-22.92	0.00	81.29	-34.37	5.14	0.00	88.26	1.11	43.57				
15	13	64.82	731.00	728.00	732.00	3.37	1.00	0.00	1.00	0.00	62.88	-30.69	0.00	54.08	-32.09	3.92	0.00	62.88	1.10	31.14				
16	14	66.89	731.85	730.00	734.00	2.07	2.15	0.00	1.37	0.00	60.78	-22.39	0.00	56.19	-23.16	2.24	0.00	60.78	1.11	30.01				
17	15	75.08	734.77	732.00	736.00	8.19	1.23	0.00	1.69	0.00	257.78	-19.63	0.00	242.80	-66.58	8.70	0.00	257.78	1.10	127.77				
18	16	78.14	735.86	734.00	738.00	3.06	2.14	0.00	1.68	0.00	95.98	-19.63	0.00	90.40	-32.24	3.25	0.00	95.98	1.10	47.57				
19	17	81.03	736.90	736.00	740.00	2.89	3.10	0.00	2.62	0.00	141.29	-19.63	0.00	133.08	-47.46	3.07	0.00	141.29	1.10	70.03				
20	18	84.89	738.27	738.00	742.00	3.86	3.73	0.00	3.42	0.00	246.08	-19.63	0.00	231.78	-82.65	4.10	0.00	246.08	1.10	121.97				
21	19	88.39	739.52	740.00	744.00	3.50	4.48	0.00	4.10	0.24	268.04	-19.63	2.36	252.47	-90.03	3.72	8.75	259.29	1.10	128.52				
22	20	90.00	740.09	742.00	746.00	1.61	5.91	1.91	5.19	1.19	156.01	-19.63	11.70	146.95	-52.40	1.71	20.01	136.01	1.10	67.41				
23	21	92.71	741.06	744.00	748.00	2.71	6.94	2.94	6.42	2.42	324.79	-19.63	23.77	305.92	-109.09	2.88	66.38	236.41	1.10	127.09				
24	22	97.97	742.94	746.00	750.00	5.26	7.06	3.06	7.00	3.00	687.23	-19.63	29.45	647.31	-230.83	5.58	184.45	522.79	1.10	259.13				
25	23	101.01	744.02	746.00	752.00	3.04	7.98	1.98	7.52	2.52	426.69	-19.63	24.74	401.90	-143.32	3.23	79.85	346.84	1.10	171.92				
26	24	104.99	745.44	748.00	754.00	3.98	8.56	2.56	8.27	2.27	614.20	-19.63	22.27	578.52	-206.30	4.23	94.10	520.10	1.10	257.79				
27	25	108.71	746.77	750.00	756.00	3.72	9.23	3.23	8.90	2.90	617.61	-19.63	28.42	581.73	-207.44	3.95	112.25	505.35	1.10	250.49				
28	26	110.62	747.45	751.00	758.00	1.91	10.55	3.55	9.89	3.39	352.61	-19.63	33.29	332.12	-118.44	2.03	67.51	285.10	1.10	141.32				
29	27	112.38	748.07	751.00	760.00	1.76	11.99	2.99	11.24	3.24	369.11	-19.63	31.78	347.67	-123.98	1.87	59.37	309.74	1.10	153.52				
30	28	114.89	749.66	753.00	762.00	4.17	13.34	3.34	13.12	3.12	1007.08	-19.63	39.73	947.87	-239.32	1.73	146.14	868.74	1.10	433.26				

Fig. 2 Screenshot of excel spreadsheet for Bishop’s simplified method

Column T contains the value of the numerator for the equation for the factor of safety for Bishop’s Simplified Method, which is computed as shown in the following equation:

$$FS = \frac{\sum (cL + (W - U) \tan \phi) \frac{1}{m_x}}{\sum W \sin \alpha}$$

The formula in Cell T5 is, then, “=(((\$J\$1 * F5) + R5 * TAN(RADIANS(\$L\$1)))/S5”.

Cells W4, W5 and W6 contain the sum of the values in Columns O, P, and T, respectively. Using this information, the factor of safety is calculated in Cell W8 as “=W6/W4”. To determine the factor of safety, the value of the trial factor of safety is W7 should be changed until it is equal to the value of the calculated factor of safety in Cell W8.

5 Spreadsheet for Lowe and Karafiath and Simplified Janbu Methods

A simple spreadsheet can also be developed to determine the stability of slopes using the Lowe and Karafiath (1959) and Simplified Janbu Methods (Janbu et al. 1956). The formulas required to do so will be outlined in this section of this teaching tool. A screenshot of an Excel Spreadsheet created for the Lowe and Karafiath

Method is provided in Fig. 3. The formulas and contents of Row 1 and Columns A through L and N through R are the same as that described previously for the Ordinary Method of Slices in Sect. 3. The contents and formulas in Column S were described in Sect. 4. The remaining columns and the calculation for the factor of safety are presented in this section.

In the Lowe and Karafiath Method, the inclination of the interslice forces is assumed to be at the average inclination of the ground surface and the sliding surface. To determine this inclination, Column M contains the inclination of the ground surface (α_g), which is computed by considering the difference in the y-coordinates of the ground surface at the left and right hand side of the slice and the thickness of the slice. Specifically, the formula in Cell M5 is “=DEGREES(ATAN((E5–E4)/F5))”. Thus, the inclination of the interslice force at the left hand side of the ith slice is computed using:

$$\theta_i = \frac{\alpha_i + \alpha_{g,i}}{2}$$

This translates to the formula “=AVERAGE(L5: M5)” in Cell T5. In the Simplified Janbu Method, the interslice force is assumed to be horizontal; that is, the angle of inclination from the horizontal (θ) is equal to zero. This is inputted into Column T instead of the computation presented above. The magnitude of the

Fig. 3 Screenshot of excel spreadsheet for Lowe and Karafiath method

interslice force at the left side of ith slice (Z_{i+1}) will be calculated using: $(L4-T3))) * (TAN(RADIANS(L1)))/Z4) + (J1 * Q4/Z4)".$

$$Z_{i+1} = \frac{F_v \sin \alpha + F_H \cos \alpha + Z_i \cos(\alpha - \theta) - [F_v \cos \alpha - F_H \sin \alpha + U + Z_i \sin(\alpha - \theta)] \frac{\tan(\phi)}{FS} + \frac{cL}{FS}}{\cos(\alpha - \theta_{i+1}) + \frac{\sin(\alpha - \theta_{i+1}) \tan \phi}{FS}}$$

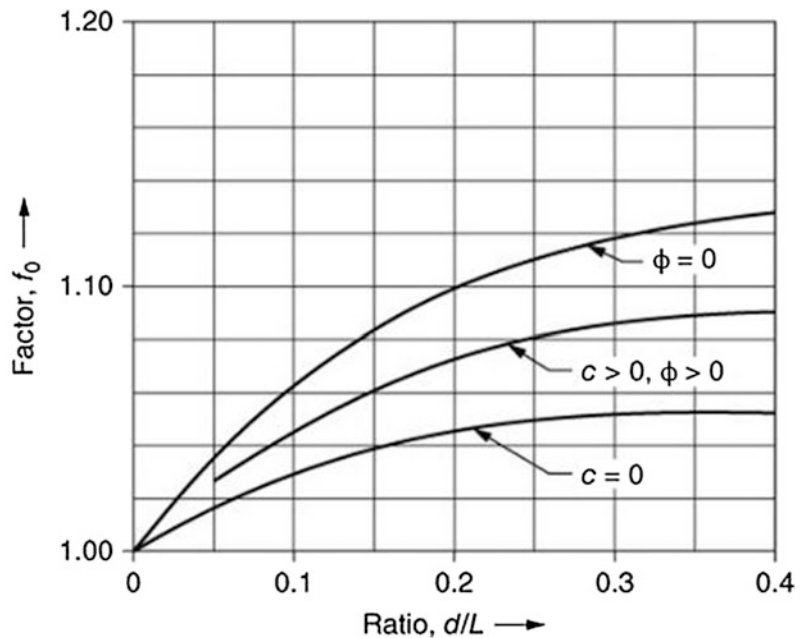
where, F_v is the sum of all known forces in the vertical direction including the weight of the slice and F_H is the sum of all known forces in the horizontal direction. When there are no surface loads, no seismic forces and no forces from reinforcement, F_v will be equal to $-W$ and F_H will be equal to zero. In the example in Fig. 3, it was assumed that there are no surface loads, no seismic forces and no forces from reinforcement. Columns U and V represent the numerator ($Z_{i,NUM}$) and denominator ($Z_{i,DEM}$), of the equation given above. Thus, the formula in Cell U5 is “=(P4) + (W3 * COS(RADIANS(L4-T3))) - (((O4 + R4 + W3 * SIN(RADIANS

Similarly, the formula in Cell V5 is “=(COS(RADIANS(L4-T4))) + ((SIN(RADIANS(L4-T4)) * TAN(RADIANS(\$L\$1)))/\$Z\$4).

The magnitude of the interslice force is, then, calculated in Column W. The formula in Cell W5 is “=U5/V5”.

To determine the factor of safety using the Lowe and Karafiath Method and the Simplified Janbu Method, the value of the factor of safety (FS_o) in Cell Z4 is changed until the value of Z_i for the last slice is equal to zero or within a tolerance range close to zero. As the Simplified Janbu method always yielded factors of safety values that are lower than those from more

Fig. 4 Correction factors for simplified Janbu method as summarized by Duncan et al. (2014)



rigorous procedures, Janbu (1973) proposed a series of factors to increase the factor of safety. These factors, presented in Fig. 4, are dependent on the ratio of the maximum depth and the length of the sliding surface. From Fig. 4, the corresponding value of the factor (f_o) is, then, used to compute the factor of safety (FS) using:

$$FS = f_o FS_o$$

The geometry and parameters from the slope used as an example in this document were inputted in *RocScience Slide 6.0*. The factors of safety for each method were determined using this program and compared to the results obtained from the spreadsheets developed. It was found that the results for the factors of safety obtained from these sample spreadsheets were within 10% of the results obtained from the software.

6 Conclusions

Understanding the stability of slopes is critical in order to prevent the loss of lives and damage to infrastructure. There are a number of available methods to determine the stability of slopes. The methods consider different conditions of equilibrium and directions of interslice forces and vary in simplicity from simple to very complex. Moreover, while there are several software programs available to compute the factor of safety of slopes, these programs need to be purchased and require user familiarity with the available functions in order to operate. It is, therefore, beneficial to use simple spreadsheets to gain an understanding of the stability of slope. This

teaching tool outlined the procedures to develop such spreadsheets for four commonly used slope stability analysis methods, namely, the Ordinary Method of Slices, Bishop's Simplified Method, Simplified Janbu Method and the Lowe and Karafiath Method.

References

- Bishop AW (1955) The use of slip circle in the stability analysis of earth slopes. *Géotechnique* 5(1):7–17
- Duncan JM, Wright SG, Brandon TL (2014) *Soil strength and slope stability*. Wiley, New Jersey, p 2
- Fellenius W (1922) *Staten Jarnjvagens Geotekniska Commission*. Stockholm, Sweden
- Fellenius W (1936) Calculation of the stability of earth dams. In: *Transactions of the 2nd congress on large dams, international commission on large dams of the world power conference, vol 4*, pp 445–462
- Janbu N (1973) *Slope stability computations. Embankment-dam engineering-Casagrande*. Wiley, New York, pp 47–86
- Janbu N, Bjerrum L, Kjærnsli B (1956) *Veiledning ved Løsnig av Fundamenteringsoppgaver (Soil mechanics applied to some engineering problems) vol 16*. Norwegian Geotechnical Institute
- Lowe J, Karafiath L (1959) Stability of earth dams upon drawdown. In: *Proceedings of first pan American conference on soil mechanics and foundation engineering, vol 2*, pp 537–552
- Morgenstern NR, Price VE (1967) A numerical method for solving the equations of stability of general slip surfaces. *Comput J* 9(4):388–393
- Skempton AW (1948) The $\phi = 0$ analysis of stability and its theoretical basis. In: *Proceedings of the second international conference on soil mechanics and foundation engineering, vol 1*, pp 72–78
- Spencer E (1967) A method of analysis of the stability of embankments assuming parallel inter-slice forces. *Géotechnique* 17(1):11–26
- Taylor DW (1948) *Fundamentals of soil mechanics*. Wiley, New York

TXT-tool 3.034-1.1

A Textural Classification of Argillaceous Rocks and Their Durability

Jordi Corominas, Joan Martinez-Bofill and Albert Soler

Abstract

Argillaceous rocks can display a wide range of durability behavior after excavation and in cut slopes. This Text-Tool describes a new classification of argillaceous rocks based on their textural characteristics, highlighting the importance of properly classifying this type of rocks in order to predict the cut slope deterioration rates. Three main components of the classification scheme are the clastic framework, the fine-grained matrix, and the cementing agent. Unlike other schemes, the unlithified argillaceous sediments are included as well. The names proposed for the rocks broadly follow the existing nomenclature used in petrographic classifications. The durability of some argillaceous rock types has been assessed by taking into account a set of degradation features of the excavated slopes. It has been observed that the ratios of these textural components exert a strong control on the long-term durability of slopes.

J. Corominas (✉) · J. Martinez-Bofill
Department of Civil and Environmental Engineering,
Universitat Politècnica de Catalunya BarcelonaTech,
Jordi Girona 1-3, 08034 Barcelona, Spain
e-mail: jordi.corominas@upc.edu

J. Martinez-Bofill
e-mail: joan.martinez-bofill@upc.edu;
martinezbofill@geomar.cat

J. Martinez-Bofill
GEOMAR Enginyeria del Terreny, SLP. Valencia 1
subsòl Local 12, 08015 Barcelona, Spain

A. Soler
Grup de Mineralogia Aplicada i Geoquímica de
Fluids, Departament de Mineralogia, Petrologia i
Geologia Aplicada, Facultat de Geologia,
Universitat de Barcelona (UB), Martí Franquès, s/n,
Barcelona, Spain
e-mail: albertsolergil@ub.edu

Keywords

Argillaceous rock · Durability · Slope deterioration · Classification

Contents

1	Introduction	422
2	Characterization of the Durability of Argillaceous Rocks	423
3	A Classification Scheme for Argillaceous Rocks	423
4	Quantifying the Constituents of the Argillaceous	425
5	Performance of the Classification Scheme of the Argillaceous Rocks	426
5.1	Field Characterization of the Cut Slopes.....	427
5.2	Petrographic and Mineralogical Characterization.....	427
5.3	Characterization of the Durability.....	427
5.4	Analysis of the Influence of Textural Composition in Durability.....	429
6	Conclusion	431
	References.....	432

1 Introduction

Argillaceous rocks are frequent in the nature, and form around two-thirds of the stratigraphic column (Blatt 1982) and about one third of all rocks exposed at the earth surface (Franklin 1983). Although strictly speaking an argillaceous rock is a rock made of clay, in its practical usage, it has a broader meaning and it is equivalent to terms such as lutite or mudrock, and encompasses many fine-grained sedimentary detrital rocks such as argillite, claystone, siltstone, mudstone, shale, clay shale, or marl (Potter et al. 2005), whose predominant constituent are silt and/or clay-sized particles, coming from preexisting rocks. Thus, the mineralogy of the argillaceous rocks is controlled by the source of the sediment and the conditions of the depositional environment. Typical clastic components are quartz, feldspar, and phyllosilicates such as mica, chlorite, illite, and other clay minerals, and they may contain significant amounts of chemically precipitated cement such as calcium carbonate, silica, iron oxide, among others. During diagenesis, compaction and cementation transform sediment into a rock. This is an ongoing

process involving the progressive reduction of void space and the crystallization of authigenic minerals that results in an increase in strength and decrease in compressibility and permeability. This process is summarized by Czerewko and Cripps (2006).

Argillaceous rocks display a contrasting behavior in construction works. Blasting is often required to excavate these rocks, but the newly excavated slope surfaces may experience physical weathering and disintegrate in a short span of time. The shallow, progressive, physical, and chemical alteration of rock material and its subsequent detachment and removal or redistribution by transport agents is defined as deterioration (Nicholson 2004). Listric joints may develop parallel to the slope face being a main source of instability. The exposed rock surface may experience swelling and breakdown facilitating the erosion and compromising the appropriate performance of the remedial and/or stabilization measures (Fig. 1a). When interbedded layers of limestone, sandstone, or conglomerate are present, disaggregation of the argillaceous rock results in overhangs, which may produce topples and failures, especially if vertical joints parallel to the slope face exist (Fig. 1b). However, the described behavior cannot be generalized, and some road cuts in argillaceous rocks may remain virtually unweathered without signs of degradation for years. Although surface deterioration of cuts is perceived as minor slope instability process, it affects the safety of the users (highways, high-speed railways ...) and generates costly maintenance works (Martinez-Bofill et al. 2004).

This contrasting behavior has attracted the interest of engineers involved in the design, construction, and maintenance of embankments, road cuts, and tunnels. In fact, most the maintenance cost is due to the inability to accurately identify and classify these rocks and anticipate their behavior.

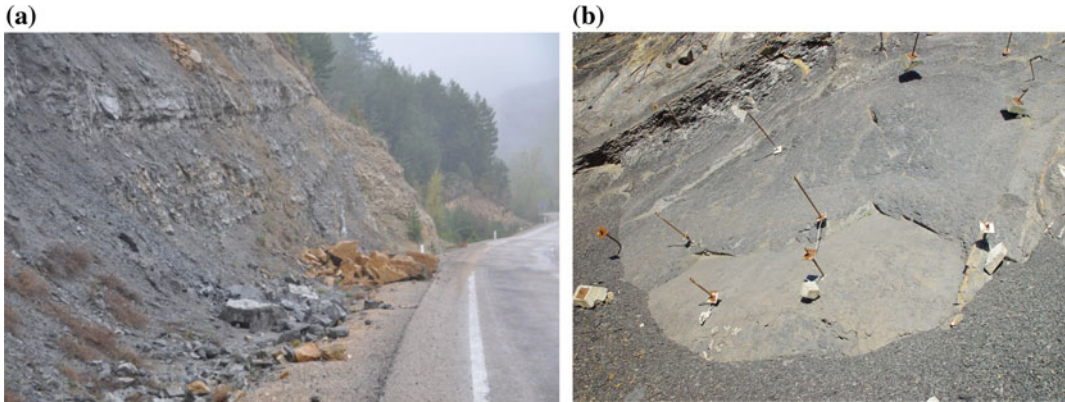


Fig. 1 *Left a* Differential weathering along a road at Cantavieja, Teruel Spain. Spalling and disaggregation of the mudstones have generated overhangs in the sandstone layers which eventually fail. *Right b* Cut slope surface

deterioration at Ormaiztegi, Spain. The argillaceous rock decomposes around the bolt thus preventing its proper operation

2 Characterization of the Durability of Argillaceous Rocks

The successful construction and performance of engineering works in argillaceous rocks depends on correctly anticipating the long-term behavior of these particular materials. Many attempts have been made to classify and characterize the argillaceous rocks in order to predict their behavior. Despite all this work, standard rock tests have found to be unsuitable to properly characterize the long-term behavior for most of argillaceous rocks and its durability (Czerewko and Cripps 2006; Nickmann et al. 2006, 2010). The reason is that routine geomechanical tests are oriented to determine rock strength or the capability to withstand loads but they are not primarily focused to assess the susceptibility of the rock to weaken upon exposure and disintegrate along time. In other words, they are not designed to assess the durability.

Different tests have been proposed to assess rock durability. The most widely used are the slake durability test (SDT) (Franklin and Chandra 1972) and the jar test (Wood and Deo 1975) which aim at determining the effects of alternate drying and wetting on the durability of soil and rock. Although these tests may be useful for assessing the short-term performance of certain argillaceous rocks, the extensive experience on their performance indicates that their results are

far from yielding fully satisfactory results in the characterization of the long-term durability of argillaceous rocks (Nickmann et al. 2006). This is attributed to the fact that durability is not dependent on a single property but on combination of parameters such as the porosity, compressive strength (expression of the bond strength of the matrix), grain size distribution, texture (grain or matrix supported), mineralogical constituent, degree of cementation, and stress history (Santi 1998; Czerewko and Cripps 2006; Nickmann et al. 2006; Martinez-Bofill 2011).

The mineralogy (Grainger 1984), particularly expansive clays (Dick and Shakoor 1992, 1997) and the cementation (Shakoor and Brock 1987), are widely accepted as important factors controlling the deterioration of the rock cuts. Consequently, it might be possible to establish a relationship between the mineralogical constituent, the cement content, and the durability of the argillaceous rocks.

3 A Classification Scheme for Argillaceous Rocks

Mineralogical content and cementation have been identified as key factors that control the long-term behavior of the weak rocks after their exposure.

We present here a new classification scheme of the argillaceous rocks, which is based on the rock texture and accounts specifically for the bonding constituent (Corominas et al. 2015). This classification does not attempt to replace the existing and widely accepted terms. It also does not intend to change the established proportions of the constituents of the argillaceous rocks and soils. The nomenclature consists of root names which combine information on grain size (grain framework, matrix) and the amount of cementing agent. To classify a sample, one needs to

determine the content of clastic framework (sand size), matrix, and cement.

The proposed scheme (Fig. 2) is based on a ternary plot in which the vertices are sand-size content (between 0.032 and 2 mm), mud-size content (<0.032 mm), and cement (calcium carbonate). The boundary of 0.032 mm is the one proposed by Dott (1964), Hallsworth and Knox (1999), and USGS (2004). It is also found as a practical boundary for visually identifying individual grains using a petrographical microscope. Smaller-sized grains often appear overlapped in

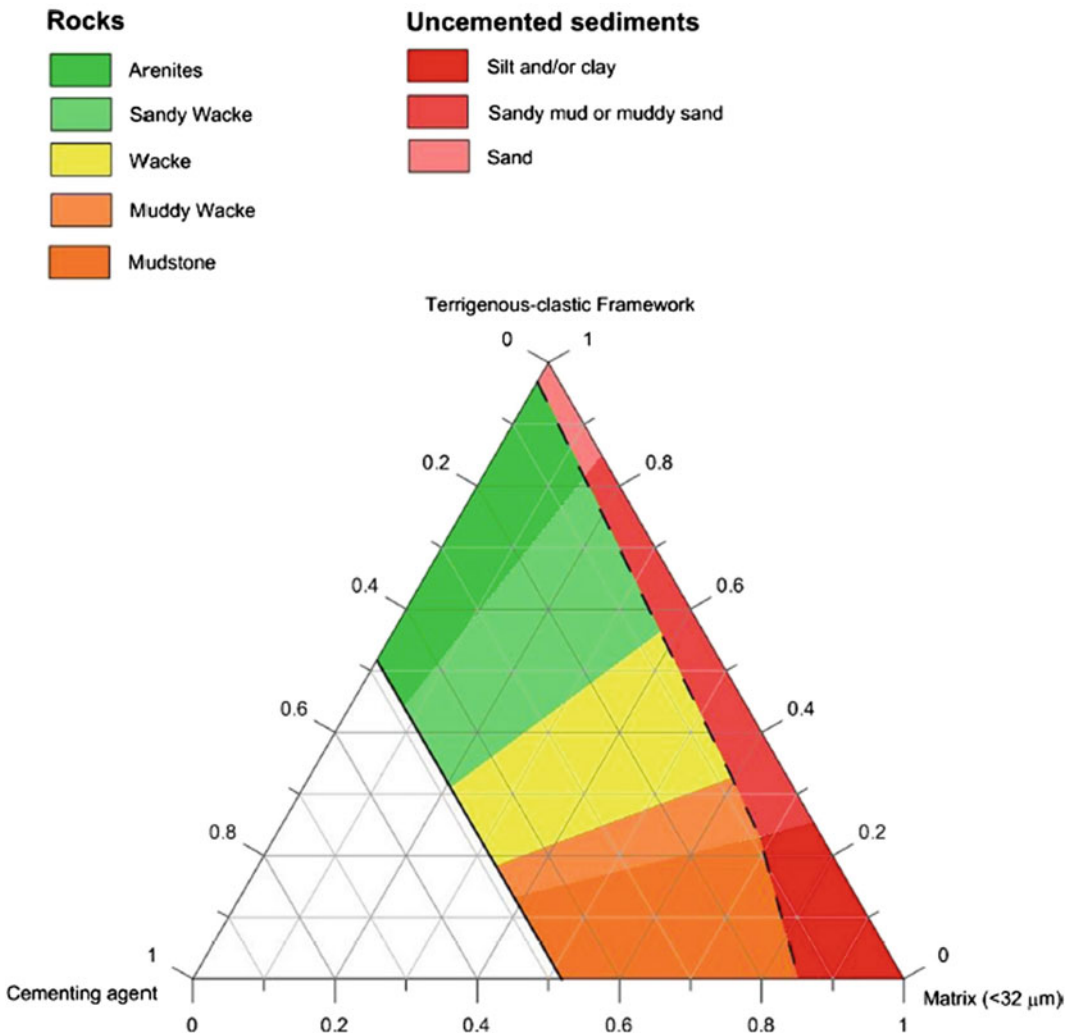


Fig. 2 Proposed textural classification of the argillaceous rocks (Corominas et al. 2015)

thin sections and may be subjected to misinterpretations. A detailed explanation about how boundaries and names were selected can be found at Corominas et al. (2015).

The scheme includes the boundary proposed by Dott (1964) between arenites, mudstones, and wackes. Usually, most of wackes are classified as shales or mudstones in the field. No distinction has been made on whether the grain framework is mostly siliciclastic, carbonate, or other.

The term mud and mudstone is given to sediments and rocks containing at least 75% of fine-grained constituent. Mixtures of mud with sand with the former ranging between 75 and 15% are named wackes. The predominance of fine components (up to 65%) or sandy components (up to 60%) qualifies wackes as muddy wacke or sandy wacke, respectively.

Cement is the textural constituent of the proposed classification not considered in other classification schemes. Cement is a fundamental rock constituent that determines the strength and makes the difference between soils and rocks. Cement is usually calcium carbonate (calcite) or calcium magnesium carbonate (dolomite). However, cementing agents of a different composition (i.e., silica, iron oxide) may also be present.

The proposed classification (Fig. 2) establishes the boundary between sediments and rocks ranging between 4 and 15% of cement content. At the other extreme of the plot, a 48% of cementing agent content has been taken to define the boundary between detrital rocks and chemical sedimentary rocks. In chemical sedimentary rocks, the cementing agent can be found not only as a post-sedimentary phase, but also having been formed during the sedimentation.

4 Quantifying the Constituents of the Argillaceous

Determining the components of the proposed classification scheme is not straightforward, because they cannot be mechanically separated. The composition of terrigenous clastic constituents can be determined reliably with the petrographic microscope and by X-ray diffraction.

Fine matrix has a size smaller than 32 μm and may be identified in the microscope as well. However, the distinction between matrix and cement can be only achieved if the cement crystals are bigger than 32 μm (i.e., sparite in carbonate cemented rocks). Smaller crystals (microsparite and micrite) are unresolvable for quantitative analysis with the petrographic microscope, and the cement cannot be distinguished from the matrix. In order to overcome this uncertainty and determine the composition of the argillaceous rocks, the following procedure (Fig. 3 left) developed for rocks containing carbonate cement is proposed (Martinez-Bofill 2011). This procedure may be adapted for the quantification of the components of the argillaceous rocks indurated with other cementing agents (i.e. silica, iron oxides):

- First, the terrigenous clastic framework, the matrix content, and sparite cement ($>32 \mu\text{m}$) are determined in the optical microscope on thin sections of rock samples, provided with a point counter. Mineral constituents are obtained by counting each mineral occurrence along a series of traverse line across the thin section (Fig. 3 right). All clasts are identified and counted using the polarizing microscope. The terrigenous framework is mostly composed of siliciclastic constituents although it may contain clasts of calcium carbonate composition (i.e., limestone fragments, bioclasts). The terrigenous framework is then divided between carbonate clasts (limestone fragments, bioclasts) and the rests (mostly quartz, feldspars, and lithic fragments). We recommend to carry out between 1000 and 2000 counts per each analyzed thin section. The petrographical microscope allows to identify textures (homogeneous and heterogeneous) as well as grain size, grain distribution and any textural features that can't be observed with XRD and other mineralogical techniques.
- The total amount of carbonate content of the sample is determined with the Bernard calcimeter method (ASTM D4373). The total carbonate content includes both carbonate clasts and carbonate cement. By subtracting the amount of carbonate clasts from the total

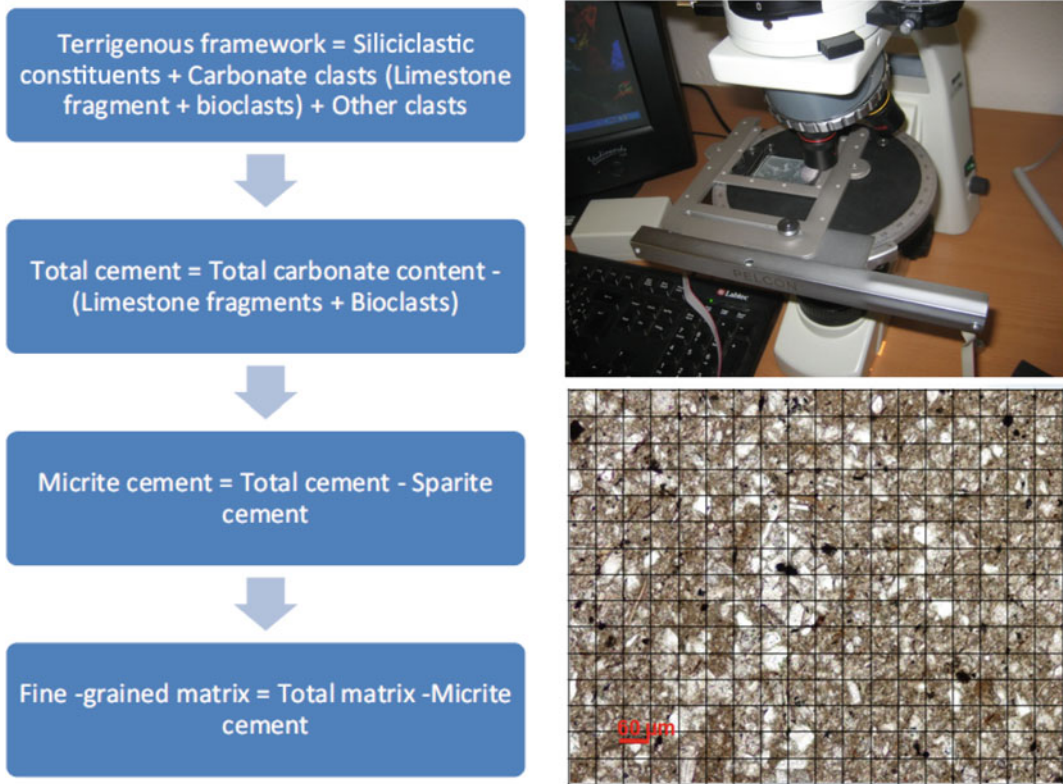


Fig. 3 *Left* procedure for determining the textural components of the argillaceous rocks. *Right* determination of the clastic framework, matrix and cement bigger than 32 µm in the petrographic microscope

carbonate, the total amount of cement is obtained. The latter is composed of sparite carbonate crystals (>32 µm) and microsparite and micrite (<32 µm) which are included within the matrix. The micrite content which is unresolvable with the petrographic microscope is obtained by subtracting the sparite content from the total cement.

- The fine-grained matrix contains all constituents smaller than 32 µm including the micritic cementing agent. The amount of silt and clay (mud) constituents is obtained by subtracting the microsparite and micrite content from the total amount of matrix.

We have checked the results obtained with the X-ray powder diffraction (XRD) technique, which is a common and rapid analytical technique used for mineral identification. It yields the mineralogical composition of the whole rock.

This is especially useful for determining the fine grained minerals that compose the matrix and cannot be identified by using the microscope. The amount of minerals can be determined by the semiquantitative Rietveld analysis of X-ray powder diffraction, (Young 1993). The Rietveld XRD accurately determines and quantifies the mineral species present in the rock although no information is provided on whether these minerals are part of the terrigenous framework or of the fine-grained matrix.

5 Performance of the Classification Scheme of the Argillaceous Rocks

The aim of this classification is to provide a concise and systematic method for designating various types of rocks, and also enable to derive durability properties.

The potential of this classification in predicting the durability of the argillaceous rocks was assessed by analyzing the mid/long-term behavior (between 2 and 30 years) of cut slopes excavated in different argillaceous rock formations of Catalonia and Basque Country in Spain.

The analysis consisted of confronting the qualitative description of the deterioration features of the cuts (accounting for the time elapsed since its excavation) with both the slake durability index (SDI) and the textural composition of intact rock samples collected in the cuts. The samples cover a wide range of argillaceous rock compositions, and were obtained taking into account the following factors: (i) presence of either marine or continental formations; (ii) lithological variety such as mudstones, marls, and shales, in order to assess the influence of the mineralogical and textural components; (iii) absence or a low degree of structural deformation of the layers and, whenever possible, the absence of expandable clays to avoid the inclusion of factors that may generate additional scattering in the assessment of the durability of the materials.

5.1 Field Characterization of the Cut Slopes

The cut slopes were first grouped based on their deterioration stage, which are defined using the following descriptors (Martinez-Bofill et al. 2004) (Fig. 4):

5.2 Petrographic and Mineralogical Characterization

The petrographic and mineralogical characterization was performed following the procedure described at Sect. 4. As mentioned above, the procedure to quantify the textural components has some uncertainty due to the assumptions made for the quantification of the cementing agent. It is noticeable that despite most of the samples have been classified in the field as mudstones and shales, only a few of them fulfil the requirement of having more than 75% of fine-grained constituents.

The main textural feature that can be identified at first sight during the microscope observation or even at nude eyesight in the counterlight is the homogeneity. Samples may be homogeneous or heterogeneous (Martinez-Bofill et al. 2008): homogeneous textures are characterized by a regular and uniform grain-size and matrix distribution, without remarkable disturbing signs (Fig. 5a). Conversely, heterogeneous textures show a pattern of different types of textures and grain size distribution (Fig. 5b).

The most distinctive features that classify homogeneous textures are grain size distribution that can be coarse (sandy) or fine (muddy), or presence of fine matrix between coarse clasts (wacky). Fine-grained matrix can be bonded either by micrite or sparite crystals or both. Matrix may also be indurated but not cemented, composed by silt and clay without carbonate cement. The heterogeneous textures are characterized by the presence of clusters of either coarse grains or fine grained matrix.

5.3 Characterization of the Durability

All the samples were tested using a standard slaking test to characterize their durability. The procedure followed was the slake durability test (Franklin and Chandra 1972, ASTM D4644) up to five cycles.

Samples extracted from cut slopes classified as deterioration stages 1 and 2 have homogeneous coarse and sandy wacke texture and yield slake durability indexes (SDI) higher than 90% for the two-cycle test. These samples correspond to wackestones, with a high content of sandy grains and, commonly, a grain-supported texture and carbonate bonding. Conversely, samples displaying two-cycle SDI smaller than 60% were obtained from cut slopes with deterioration stages 4 or 5. These samples correspond to rocks with both homogeneous and heterogeneous muddy textures (Martinez-Bofill et al. 2008).

However, results show that no unique SDI range of values can be assigned to a specific deterioration stage. Despite the fact that several classification schemes consider those rocks




	<p>Stage 1: Intact cut slope. Blast holes are fully visible. Intact or virtually intact excavated slope surface. The slope is stable and only sporadic rockfalls occur More than 20 years after its excavation..</p>
	<p>Stage 2: Slightly weathered slope surface. Fissures and spheroidal exfoliation cracks may appear after some years. It is an overall stable slope. Local (small size) rockfalls occur associated to scattered listric joints. Blast holes are observable for most of the length. The original profile of the excavated slope is kept in average. Unweathered rock chips of a few centimeters in length may accumulate at the bottom of the slope</p>
	<p>Stage 3: Weathered slope surface. The excavated surface loses the rocky appearance with time. Spalling and disintegration of the rock surface takes place in less than 10 years. Blast holes are poorly preserved. Frequent small size slides and falls occur through listric joints (curved) generated after the excavation. Debris starts accumulating at the slope foot. The accumulated material decomposed up to sand size and rarely to smaller sizes. Generally stable but receding slope.</p>

Fig. 4 Deterioration features observed in selected excavated slopes. The period of time during which these deterioration features are generated reduces from stages 1 to 5



	<p>Stage 4: Heavily weathered slope surface. Six years after its excavation, intense slaking of the rock surface is observed and tendency to form regolith. Continuous slaking and falling of chunks prevent the slope from rock falls. Weathered rock surface (regolith) may reach depths up to several decimeters. Original rock structure cannot be recognized at the slope face. Blast holes have virtually disappeared. Erosion and gulying often appear at the slope surface. Fallen debris easily decomposes to silt-clay size fragments. Receding slope profile. Steep slopes tend to be unstable.</p>
	<p>Stage 5: Slope composed of poorly indurated silt and clay. Steep slopes are unstable with frequent rotational failures. Gulying develops even with low slope angles.</p>

Fig. 4 (continued)

displaying two-cycle SDI over 80% as durable rocks (Franklin and Dusseault 1989; Sadisun et al. 2005; Santi 2006), in our study area high SDI values do not guarantee the presence of intact slopes on the mid/long term. High values (>90%) of the SDI may also be found in cuts with deterioration stages 1–4, indicating that in the study area, the SDI is unable to adequately predict whether any particular slope will evolve towards deterioration stages 3 and 4 or it will remain unweathered. The lack of sensitivity of the two-cycle SDT to the rock durability (here, to the cut slope behavior) has been observed by several researchers (Taylor 1988; Moon and

Beattie 1995; Gökçeoglu et al. 2000; Erguler and Shakoor 2009).

5.4 Analysis of the Influence of Textural Composition in Durability

The cut slope degradation stages have been contrasted against the textural composition of the exposed argillaceous rocks. The results have been split considering homogeneous and heterogeneous rock textures (Fig. 6a, b).

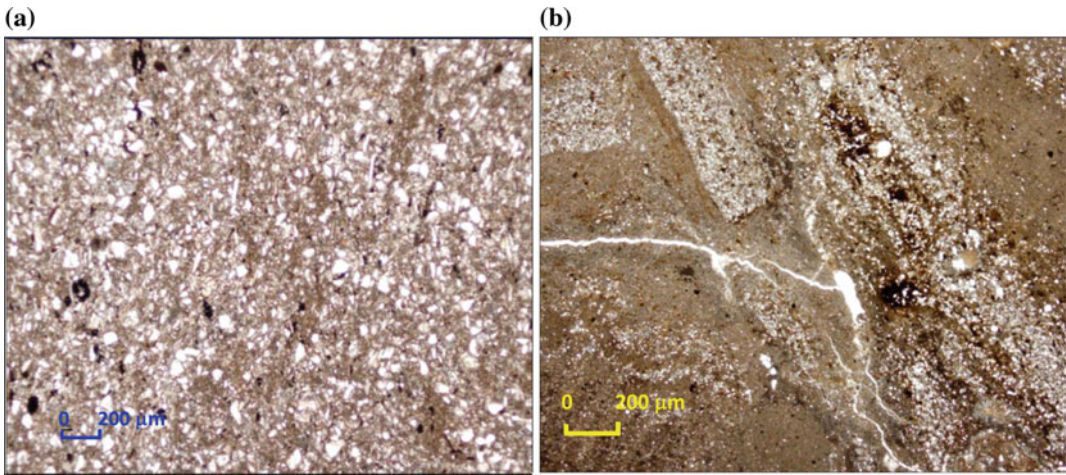


Fig. 5 *Left a* homogeneous texture in thin section: wacky texture, composed of sand sized quartz grains with fine-grained cemented matrix. *Right b* heterogeneous texture in thin section: heterogeneous muddy predominant

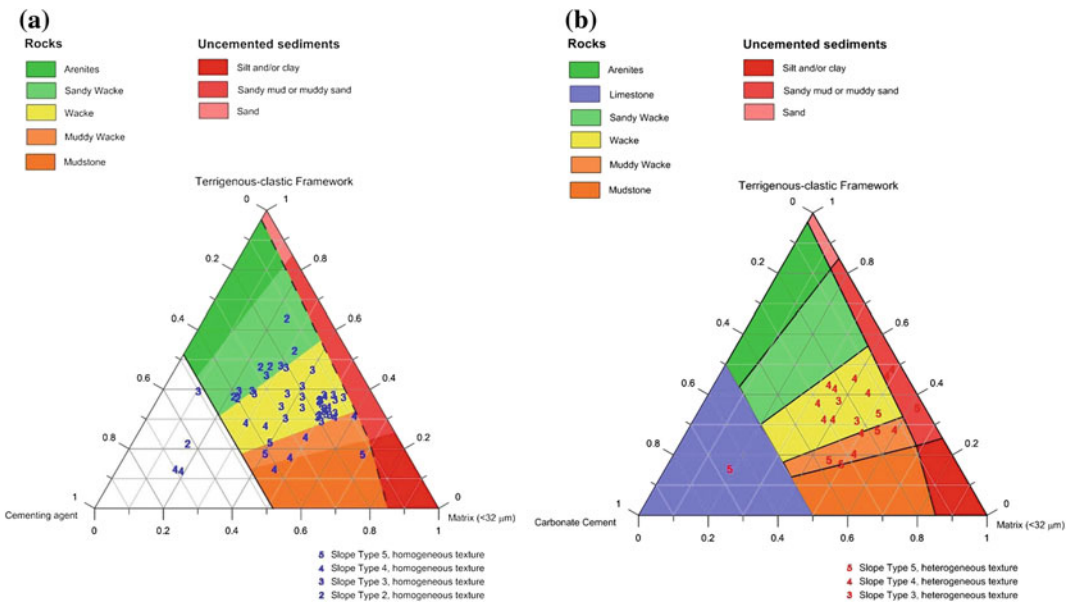


Fig. 6 Distribution of the samples showing homogeneous textures (*left, a*) compared to samples with heterogeneous texture (*right, b*) from the analyzed cut

slopes and their relation to the slope deterioration stages plotted on the classification scheme proposed in this paper

5.4.1 Slopes in Homogeneous Argillaceous Rocks

Slopes excavated in sandy wackes consistently show few deterioration features while the slopes excavated in mudstones and muddy wackes deteriorate easily and are highly erodible and

show instability features. In that respect, the response of the texturally homogeneous argillaceous rocks (Fig. 6a) shows a contrasting response and has a reasonable correspondence with the deterioration stage of the excavated slopes.

5.4.2 Slopes in Heterogeneous Argillaceous Rocks

The texturally heterogeneous slopes (Fig. 6b) are more degradable than the homogeneous ones. It is suggestive that heterogeneity, and particularly the uneven distribution of the grain, favors on one hand the existence of preferential flow paths (highly connected porosity or permeability) which allows the penetration of the weathering agents into the rock and on the other hand the cementing agents are unable for accessing the fine-grained clusters.

The results obtained so far, show that the proposed classification scheme is capable to explain the mid-long term road cut evolution: However, there exist additional factors that can influence the actual performance. Therefore, for the use of this classification scheme and for the interpretation of the results, the following factors should be taken into account:

- The proposed classification is based on the behaviour of rocks with absence or a low degree of tectonic deformation and with a low content of expansive clays. These factors may generate additional scattering in the assessment of the durability of the materials.
- Furthermore, other well-known factors affecting rock durability such as the connected porosity or the presence of soluble minerals have not been considered in the scheme either.
- The excavation process disturbs the rock mass by releasing confinement and causing expansive recovery and cracks (Gerber and Scheidegger 1969; Nichols 1980). This makes the rock more susceptible to the environmental conditions particularly to moisture and temperature changes.
- The relationship between cement content and durability is complex. The results show that the increase in content of the calcium carbonate cement in the different types of wackestones does not result in a significant reduction of the deterioration of the excavated slope face. Instead, the analysis of the textural diagrams suggests that the clastic framework and the fine-grained matrix ratio is what

control the efficiency of the bonding and consequently, the durability of the argillaceous rocks.

In summary, further work is still needed on the role of factors not considered in the classification scheme and on how to integrate them. Despite of this, texturally homogeneous argillaceous rocks have shown a satisfactory correspondence with the long-term performance of the excavated slopes.

6 Conclusion

This Text-Tool describes a new classification of argillaceous rocks based on their textures. This highlights the importance of properly classifying this type of rocks in order to explain the mid-long term deterioration behaviour of the cut slopes. Although the texture and the mineralogical composition of the argillaceous rocks are well-known factors controlling their durability (i.e., Gökçeoglu et al. 2000; Sadisun et al. 2005), the textural-based classification scheme presented here provides a quantitative measure of the texture and unlike other classification schemes, the cementing agent has been included. Three components form the basis for the classification: the clastic framework, the fine-grained matrix, and the cement content.

To implement this classification, quantitative petrographical and mineralogical analysis is required to determine the textural components, by using an optical microscope and supported with semi-quantitative Rietveld mineralogical analysis based on X-ray powder diffraction. This procedure might appear time-consuming and expensive for the durability analyses of the rock. However, this drawback is not more restrictive than other mechanical analysis (i.e., UCS, triaxial tests) routinely performed in engineering projects.

The analysis of the behavior of the argillaceous rocks in different excavated slopes in Spain shows that road cuts in sandy wackes consistently show minor deterioration features while the slopes excavated in muddy wackes and mudstones deteriorate more rapidly, are highly

erodible, and produce frequent falls. Texturally homogeneous sandy wackes, wackes, and muddy wackes are mostly associated with slope deterioration stages 2, 3, and 4–5, respectively.

The relationship between the cement content and the durability of the rock is complex. Results suggest that the ratio between the clastic framework and the fine-grained matrix exerts a strong control on the durability of the argillaceous rock. The increase of cementing agent beyond a certain amount does not result in an improvement of the durability.

Argillaceous rocks showing heterogeneous textures are less durable. We interpret that heterogeneity favors the existence of preferential flow paths where the weathering agents can penetrate more easily and the presence of fine-grained clusters where the cementing agents are less effective.

The proposed classification scheme provides a first order estimate of the mid-long term behavior of argillaceous rock cuts but there are still shortcomings that need to be overcome with future research. There are a variety of factors that are not considered as the presence of either expansive or soluble minerals, the stress history of the rock, the effect of textural heterogeneity, among others. The influence on durability of the different types of cementing agents (calcite, silica, iron oxide, etc.) also has to be addressed in future investigations.

In the study area, the proposed classification scheme performs more satisfactorily than the two-cycle SDT in assessing the potential of the slopes to deterioration. Rock samples having two-cycle SDT values higher than 90% are associated to cuts showing a wide range of deterioration stages (from stage 2 to 4).

References

- Blatt H (1982) *Sedimentary petrology*. WH Freeman and Company, San Francisco
- Corominas J, Martínez-Bofill J, Soler A (2015) A textural classification of argillaceous rocks and their durability. *Landslides* 12(4):669–687
- Czerewko MA, Cripps JC (2006) The implication of diagenetic history and weathering on the engineering behaviour of mudrocks. In: 10th IAEG international congress: engineering geology for tomorrow's cities. Paper number 118. <http://www.iaeg.info/iaeg2006/start.htm>
- Dick JC, Shakoor A (1992) Lithological controls of mudrock durability. *Quat J Eng Geol* 25:31–46
- Dick JC, Shakoor A (1997) Predicting the durability of mudrocks from geological characteristics of mudrocks: In: Santi P, Shakoor A (eds) *Association of environmental and engineering geologists*. Special Publication No. 9, pp 89–105
- Dott RH (1964) Wackstone, graywacke and matrix—what approach to immature sandstone classification? *Num* 34:625–632
- Erguler ZA, Shakoor A (2009) Quantification of fragment size distribution of clay-bearing rocks after slake durability testing. *Environ Eng Geosci* 15:81–89
- Franklin JA (1983) Report RR29 research and development branch research. Toronto, Ministry of Transportation and, Evaluation of shales for construction projects: an Ontario shale rating system
- Franklin JA, Chandra R (1972) The slake durability test. *Int J Rock Mech Mining Sci Geomech Abstracts* 9:325–328
- Franklin JA, Dusseault MB (1989) *Rock engineering*. McGraw Hill Inc, New York, p 600
- Gerber E, Scheidegger AE (1969) Stress-induced weathering of rock masses. *Eclogae Geol Helv* 62:401–416
- Gökçeoglu C, Ulusay R, Sönmez H (2000) Factors affecting the durability of selected weak and clay-bearing rocks from Turkey, with particular emphasis on the influence of the number of drying and wetting cycles. *Eng Geol* 57:215–237
- Grainger P (1984) The influence of clay mineralogy and diagenesis of Upper Carboniferous shales on soil formation in parts of Devon. *J Soil Sci* 35:599–606
- Hallsworth CR, Knox RWO'B (1999) BGS rock classification scheme, vol 3. Classification of sediments and sedimentary rocks. British Geological Survey. Research report number rr 99–03. Nottingham UK, 44 pp
- Martínez-Bofill J (2011) *Alterabilidad de limolitas, arcil-litas y margas. Aplicación a la estabilidad de desmontes y excavaciones*. PhD thesis. Universitat Politècnica de Catalunya, 427 pp
- Martínez-Bofill J, Corominas J, Soler A (2004) Behaviour of the weak rock cutslopes and their characterization using the results of the slake durability test. In: *Lecture notes in earth sciences*, 104. Engineering geology for infrastructure planning in Europe, pp 405–413
- Martínez-Bofill J, Corominas J, Soler A (2008) Analysis of the relationship between durability and petrological characteristics of weak rocks. *Euroengeo*. In: *Proceedings of the II European conference of international association for engineering geology*, Madrid
- Moon VG, Beattie AG (1995) Textural and microstructural influences on the durability of Waikato coal measures mudrocks. *Q J Eng Geol* 28:303–312
- Nichols TC (1980) Rebound its nature and effect on engineering works. *Q J Eng Geol* 13:133–152

- Nicholson DT (2004) Hazard assessment for progressive, weathering-related breakdown of excavated rock-slopes. *Q J Eng Geol Hydrogeol* 37:327–346
- Nickmann M, Spaun G, Thuro K (2006) Engineering geological classification of weak rocks. In: 10th congress of the international association of engineering geology and the environment, paper number 492, Nottingham
- Nickmann M, Sailer S, Ljubescic J, Thuro K (2010) Engineering geological investigations into the border between hard and weak rocks. In: Williams L et al (eds) *Geologically active*. Taylor & Francis Group, London, pp 2265–2272
- Potter PE, Maynard JB, Depetris PJ (2005) Mud and mudstones. Springer, Berlin, p 308
- Sadisun IA, Shimada H, Ichinose M, Matsui K (2005) Study on the physical disintegration characteristics of Subang claystone subjected to a modified slaking index test. *Geotech Geol Eng* 23:199–218
- Santi P (1998) Improving jar slake, slake index, and slake durability tests for shales. *Environ Eng Geosci* 4:385–396
- Santi P (2006) Field methods for characterizing weak rocks for engineering. *Environ Eng Geosci* 12:1–11
- Shakoor A, Brock D (1987) Relationship between fissility, composition and engineering properties of selected shales from northeast Ohio. *Bull Assoc Eng Geol* 24:363–379
- Taylor RK (1988) Coal measures mudrocks: composition, classification and weathering processes. *Q J Eng Geol Hydrogeol* 21:85–99
- U.S. Geological Survey (USGS), North American Geologic-Map Data Model Science Language Technical Team (2004) Report on progress to develop a North American science-language standard for digital geologic-map databases; Appendix C1—sedimentary materials: science language for their classification, description, and interpretation in digital geologic-map databases; version 1.0 (12/18/2004). In: Soller DR (ed) *Digital mapping techniques'04—workshop proceedings*: U.S. Geological Survey open-file report 2004–1451, 595 p. Appendix C1 accessed at http://pubs.usgs.gov/of/2004/1451/sltt/appendixC/appendixC_pdf.zip
- Wood LE, Deo P (1975) A suggested system for classifying shale materials form embankments. *Bull Assoc Eng Geol* 12:39–55
- Young RA (1993) *International union crystallography. The Rietveld method*. Oxford University Press, New York

TXT-tool 3.039-1.1

Landslide-Related WPS Services

Ivan Marchesini, Massimiliano Alvioli and Mauro Rossi

Abstract

Researchers have developed and implemented software tools for a number of geospatial algorithms to support the analysis of the slope movements at different spatial scales. Frequently, these tools are implemented using Open Source software and are based on specific combinations of software libraries, programming languages and operating systems. This often limits the portability of these tools and hampers their sharing with a large community of potential users. To overcome these limitations, some researchers have started to make available their software tools through the Web Processing Service standard. This work introduces the reader to the WPS usage and explains how to take advantage of some existing WPS processes dealing with landslide size probability, bedding attitude estimation, morpho-structural domain definition, slope-units delineation.

Keywords

WPS · Standard · Landslide · Geospatial · Slope-units · Software

Contents

1	Introduction	435	7	Morpho-Structural Domain Definition	440
2	WPS	436	8	Slope-Units Delineation	441
3	WPS Clients	438	9	Conclusions	442
4	Landslide-Related WPS	440		References	442
5	Landslide Size Probability Distribution	440			
6	Bedding Attitude Estimation	440			

1 Introduction

Geospatial information plays a crucial role in the landslide mapping, and hazard and risk management. As a matter of fact, a large number of different kinds of landslide-related maps (susceptibility maps, inventory maps, hazard maps, etc.) are published by means of web mapping sites and maps services. These maps are most

I. Marchesini (✉) · M. Alvioli · M. Rossi
Research Institute for Geo-Hydrological Protection,
Via Madonna Alta 126, 06128 Perugia, Italy
e-mail: Ivan.Marchesini@irpi.cnr.it

M. Alvioli
e-mail: Massimiliano.Alvioli@irpi.cnr.it

M. Rossi
e-mail: Mauro.Rossi@irpi.cnr.it

commonly obtained through complex procedures implemented using different programming languages and software. The software is not always available to scientists, students, public administrators, or to general public. The implemented procedures are occasionally described in scientific articles, or technical reports. However, incompatibility and portability problems, the dependence on additional external libraries and the incomplete understanding of software limit an extensive use of these resources. We describe, using specific examples, how to overcome some of these limitations using the Web Processing Service (WPS) standard, which is a specific OGC (Open Geospatial Consortium) standard designed to facilitate the publication of geospatial processes.

This document is organized as follow: Sect. 2 introduces the reader to the basic knowledge of the WPS standard, Sect. 3 briefly describes a WPS client (software), Sects. 4, 5, 6, 7 and 8 describe some experimental landslide-related WPS processes developed by our institute.

2 WPS

Among the OGC Web Services (<http://www.opengeospatial.org/>), WPS is a specific standard for the design of interfaces to facilitate the publication of geospatial processes.

The WPS standard can be used to publish on-line geospatial processes (algorithms developed in different research environments).

Researchers or professionals can use these processes (i) connecting to a WPS server, (ii) uploading their data through service-specific forms and (iii) collecting the results provided by the software, which is run on the server side.

With reference to Fig. 1, we define:

- WPS service: the server side service interface,
- WPS process: a geospatial algorithm exposed by the WPS service,
- WPS request: a request sent to a WPS service or to a WPS process,
- WPS client: a software able to make WPS requests.

The WPS service is identified through a web URL.

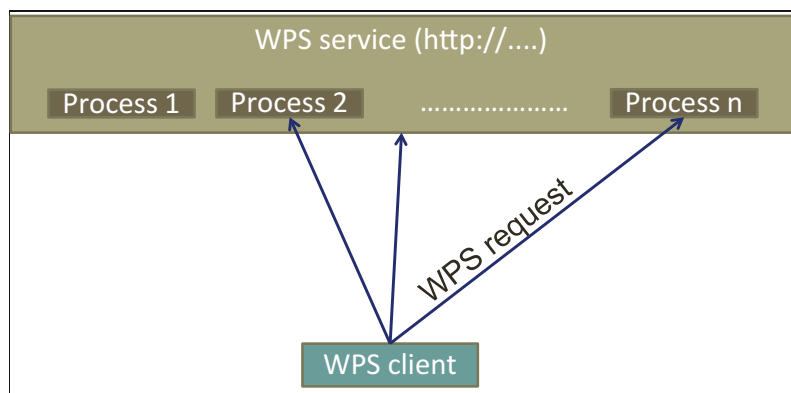
More than one WPS processes can be provided by a single WPS service.

A WPS client can do more WPS requests to more WPS processes provided by a WPS service. In this short paper we will not focus on the implementation of the WPS services and processes but only on the WPS clients side, describing the requests that they can do.

In general, the WPS standard defines how the process interface must be exposed by the server. It also defines how a client can request the execution of a process and how the output is handled.

A WPS service can manage three kinds of requests:

Fig. 1 Schema describing a generic WPS



- GetCapabilities, allows a client to get a document that describes the abilities of the server
- DescribeProcess, give back a description of a particular process provided by the server
- Execute, starts the particular process.

In the following we describe the basic application of these requests.

Taking as a reference one of the WPS services (the URL is <http://alpha.irpi.cnr.it/cgi-bin/pywps.cgi>) implemented by IRPI, the next string describes an example of a “GetCapabilities” request.

<http://alpha.irpi.cnr.it/cgi-bin/pywps.cgi?service=WPS&Request=GetCapabilities>

The request is performed using the *http GET method* (see http://www.w3schools.com/tags/ref_httpmethods.asp).

The first part of the string (left to the question mark “?”) is the address of the WPS service. The second part of the string contains the parameters of the request. They are separated by the ampersand “&” and expressed as KVP (Key Value Pair).

Since a server can provide different kinds of web services, the first parameter (“service”) clarifies that the request is addressed to the WPS service. The second parameter is the type of

request: in this case a GetCapabilities request, i.e. the string is asking the WPS service to list its capabilities.

Figure 2 shows an extract of the XML document returned by the WPS service.

The document lists the service metadata (e.g. the version of the service) and other information, as the names (“identifiers”) of the exposed processes.

The next string is an example of a “DescribeProcess” request.

<http://alpha.irpi.cnr.it/cgi-bin/pywps.cgi?service=WPS&Request=describeprocess&identifier=areaStat&version=1.0.0>

The “version” of the WPS service and the “identifier” of the process are mandatory parameters. They can be obtained from the aforementioned “GetCapabilities” XML document. In this example the version is “1.0.0” and the identifier of the process is “areaStat”.

Figure 3 shows part of the XML document that is returned by the WPS server when a DescribeProcess request is made.

The XML document contains the process metadata and a description of the input and output parameters that a user must provide to the process.

```
<?xml:namespace xmlns:xlink="http://www.w3.org/1999/xlink" xmlns:wps="http://www.opengis.net/wps/1.0.0" xmlns:ows="http://www.opengis.net/ows/1.1"
xmlns:xsi="http://www.w3.org/2001/XMLSchema-instance" service="WPS" version="1.0.0" xml:lang="en-CA"
xsi:schemaLocation="http://www.opengis.net/wps/1.0.0 http://schemas.opengis.net/wps/1.0.0/wpsGetCapabilities_response.xsd" updateSequence="1">
  <ows:ServiceIdentification>
    <ows:Title>PyWPS Server</ows:Title>
  </ows:ServiceIdentification>
  <ows:Abstract>
    See http://pywps.wald.intevation.org and http://www.openeospatial.org/standards/wps
  </ows:Abstract>
  <ows:Keywords>
    <ows:Keyword>GRASS</ows:Keyword>
    <ows:Keyword>GIS</ows:Keyword>
    <ows:Keyword>WPS</ows:Keyword>
  </ows:Keywords>
  <ows:ServiceType>WPS</ows:ServiceType>
  <ows:ServiceTypeVersion>1.0.0</ows:ServiceTypeVersion>
  <ows:Fees>None</ows:Fees>
  <ows:AccessConstraints>none</ows:AccessConstraints>
  </ows:ServiceIdentification>
  <ows:ServiceProvider>
    <ows:ProviderName>CNR IRPI Perugia</ows:ProviderName>
    <ows:ProviderSite xlink:href="http://geomorphology.irpi.cnr.it"/>
  </ows:ServiceProvider>
  <ows:ServiceContact>
    <ows:IndividualName>Ivan Marchesini</ows:IndividualName>
    <ows:PositionName>Technologist</ows:PositionName>
  </ows:ServiceContact>
  <ows:ContactInfo>
    <ows:Address>
      <ows:DeliveryPoint>Via della Madonna Alta 126</ows:DeliveryPoint>
      <ows:City>Perugia</ows:City>
      <ows:PostalCode>06128</ows:PostalCode>
      <ows:Country>it</ows:Country>
      <ows:ElectronicMailAddress>ivan.marchesini@irpi.cnr.it</ows:ElectronicMailAddress>
    </ows:Address>
    <ows:OnlineResource xlink:href="http://geomorphology.irpi.cnr.it"/>
    <ows:HoursOfService>0:00-24:00</ows:HoursOfService>
    <ows:ContactInstructions>none</ows:ContactInstructions>
  </ows:ContactInfo>
</?xml:namespace>
```

Fig. 2 Answer, of the WPS server, to a GetCapabilities request

```

<wps:ProcessDescriptions xmlns:wps="http://www.opengis.net/wps/1.0.0" xmlns:ows="http://www.opengis.net/ows/1.1"
xmlns:xlink="http://www.w3.org/1999/xlink" xmlns:xsi="http://www.w3.org/2001/XMLSchema-instance" xsi:schemaLocation="http://www.opengis.net/wps/1.0.0
http://schemas.opengis.net/wps/1.0.0/wpsDescribeProcess.xsd" service="WPS" version="1.0.0" xml:lang="en-CA">
  <ProcessDescription wps:processVersion="1.0" storeSupported="true" statusSupported="true">
    <ows:Identifier>areaStat</ows:Identifier>
    <ows:Title>Landslides area distribution statistics</ows:Title>
    <ows:Abstract>
      ----- Creates landslides area distribution statistics starting from one attribute field ----- Using the WPS QGIS plugin any type of
      vector layers can be used. Otherwise a GML layer must be provided. Help for QGIS (and other clients) users. The user must choose a layer already
      loaded into the QGIS canvas from the dropdown list [data]. The user must also fill a form [DB , default value='AREA'] to indicate the name of the
      attribute data field containing landslide area size informations. The user can also pass, to the process, his name and e-mail address. Storing
      these last two informations we can contact you for a possible scientific collaboration. The remaining parameters values usually should not be
      changed. At the end of the process, the QGIS user, must control the 'detail' tab to obtain the output file from the indicated web address. -----
      -- Help for other users. Use next parameters for a test: HTTP GET request: request=execute service=WPS version=1.0.0 Identifier=areaStat
      datainputs=[data=http://ackmena.irpi.cnr.it/test.gml;DB=AREA] Please cite: ---> Rossi et al. 2012. A tool for the estimation of the distribution
      of landslide area in R. Geophysical Research Abstracts, Vol. 14, EGU2012-9438-1, 2012. -----
    </ows:Abstract>
    <DataInputs>
      <Input minOccurs="1" maxOccurs="1">
        <ows:Identifier>EMAIL-ADDRESS</ows:Identifier>
        <ows:Title>Researcher_email</ows:Title>
        <LiteralData>
          <ows:DataType ows:reference="http://www.w3.org/TR/xmlschema-2/#string">string</ows:DataType>
          <ows:AnyValue/>
          <DefaultValue/>
        </LiteralData>
      </Input>
      <Input minOccurs="0" maxOccurs="1">
        <ows:Identifier>DB</ows:Identifier>
        <ows:Title>Field containing values to analyse</ows:Title>
        <LiteralData>

```

Fig. 3 Answer, of the WPS server, to a DescribeProcess request

In the following string an example of an “Execute” request is shown.

```

http://alpha.irpi.cnr.it/cgi-bin/pywps.cgi?re-
quest=execute&service=WPS&ver-
sion=1.0.0&identifier=areaStat&dataInputs=[-
data=http://ackmena.irpi.cnr.it/test.gml;
DB=AREA]

```

The “dataInputs” parameter is used to define the inputs of the process. Inputs are enclosed inside square brackets and consist of the URL to a geospatial layer (in this case the URL to a geospatial layer in.gml format—see http://www.gdal.org/drv_gml.html) and a literal value (in this case the string “AREA” is assigned to the variable “DB”).

The process waits for the full download of the.gml layer before starting the execution.

The input type of the WPS processes can be “complex” (vector or raster geospatial layers) and “literal” (strings and numbers).

The outputs provided by the WPS processes can be (i) vector or raster geospatial layers, (ii) strings, (iii) documents.

As an example, a process can provide a landslide susceptibility map (vector or raster), a list of probability values (strings) or a PDF file (document).

Layers and documents can be returned directly to the client or can be stored on the server for a deferred download.

3 WPS Clients

A few WPS clients have been developed to facilitate the end users in the exploitation of the WPS services exposed by the existing WPS servers.

In the following sections the WPS client plugin implemented in QGIS is described.

Quantum GIS (www.qgis.org) is an Open Source GIS and it provides a specific WPS client plugin that can be installed both using the integrated “Plugins” menu and directly downloading the compressed file available online (<http://geolabs.fr/plugins.xml>).

When started, the WPS client allows the user to define the URL of the WPS service (Fig. 4). Then the user can connect to the service, and a list of the available processes is displayed (the result of a “GetCapabilities” request). Once a single process is selected a form is shown (the result of a “DescribeProcess” request, see Fig. 5) where the input parameters must be filled in. The last step is the “Execute” request, which includes the dispatching of the input data (literal or

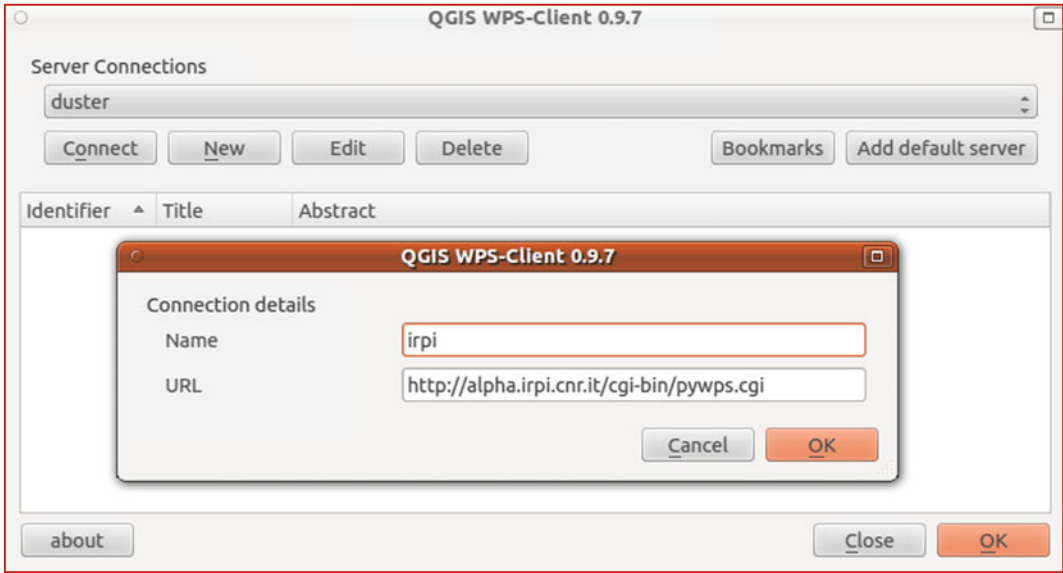


Fig. 4 The definition of the URL of the WPS service

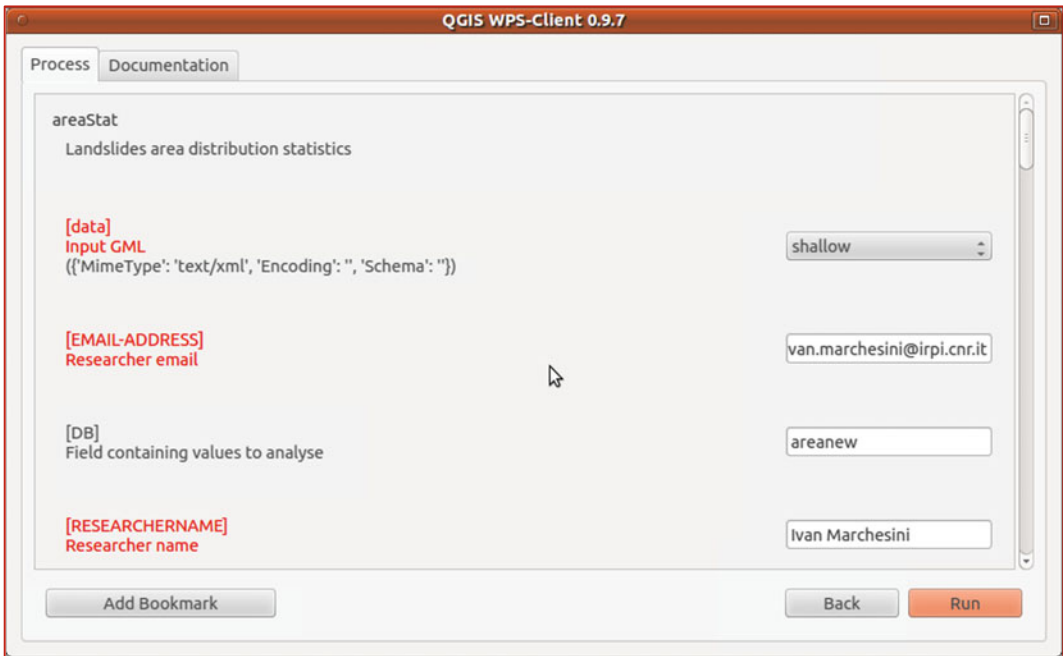


Fig. 5 Filling-in the form of a specific process

complex) to the server that hosts the WPS processes. Depending on the type of process and the size of the input data, the output can be returned rapidly (from seconds to minutes), or an e-mail can be sent to the user when the process is terminated, incorporating information on how to get the results.

4 Landslide-Related WPS

The IRPI CNR institute provides some experimental landslide-related WPS processes (tools) dealing with landslide size probability distribution, bedding attitude estimation, morpho-structural domain definition, slope-units delineation.

In the following, a quick description of the aims of the four processes is given.

5 Landslide Size Probability Distribution

Given a landslide inventory map, this WPS service calculates an estimate of the probability density and the frequency density of landslide areas (Rossi et al. 2012).

The tool implements parametric and non-parametric statistical approaches, including Histogram Density Estimation (HDE), Kernel Density Estimation (KDE), and Maximum Likelihood Estimation (MLE). Such information can be used, as an example, to evaluate the inventory completeness and/or to estimate landslide hazard (Guzzetti et al. 2005).

The process returns a PDF document containing the parameters of the statistical distributions of landslide size and charts. In Fig. 6 we show an example of one of the charts produced by the WPS.

6 Bedding Attitude Estimation

This WPS process produces a map of points describing the local bedding attitude, i.e. the dip direction and inclination of geologic strata

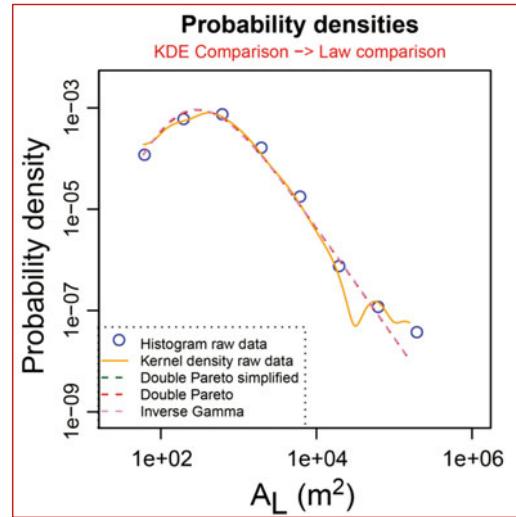


Fig. 6 An example of the output of the landslide size probability WPS tool

(Marchesini et al. 2013), based on the morphometric analysis of their intersection with the land surface. User must provide a Digital Elevation Model (DEM) and a map of the “bedding traces” (BT). BT are lines representing the geometrical intersection between strata and terrain, and are derived mainly through visual interpretation of aerial photographs and field mapping by geologists and geomorphologists.

Figure 7 shows an example of the output map loaded in the QGIS interface. Points represent the bedding attitudes location, and the points attributes (the table shown in the figure) describes the dip direction, inclination and the corresponding uncertainties.

7 Morpho-Structural Domain Definition

This WPS tool implements a procedure to derive maps of the geometric relationship between bedding planes and local terrain (morpho-structural settings, Santangelo et al. 2015), based on the interpolation of bedding attitudes data. The output aids geological field mapping (Barchi et al. 1991), and can be used as an input terrain variable to determine landslide

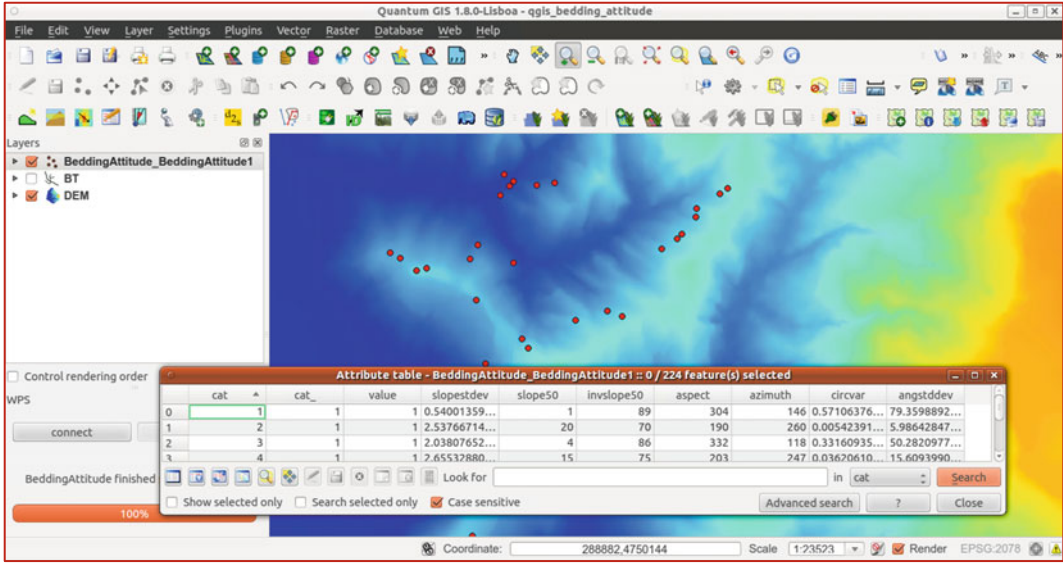


Fig. 7 An example of the output of the bedding attitude estimation process

susceptibility (Carrara et al. 1991). A DEM and a map of the bedding attitudes (potentially derived using the WPS tool described in the previous section) are the two mandatory inputs.

Figure 8 shows an example of the morpho-structural settings map produced by the tool.

8 Slope-Units Delineation

This WPs service produces a partition of a territory into slope-units exploiting a digital representation of the terrain (Alvioli et al. 2014).

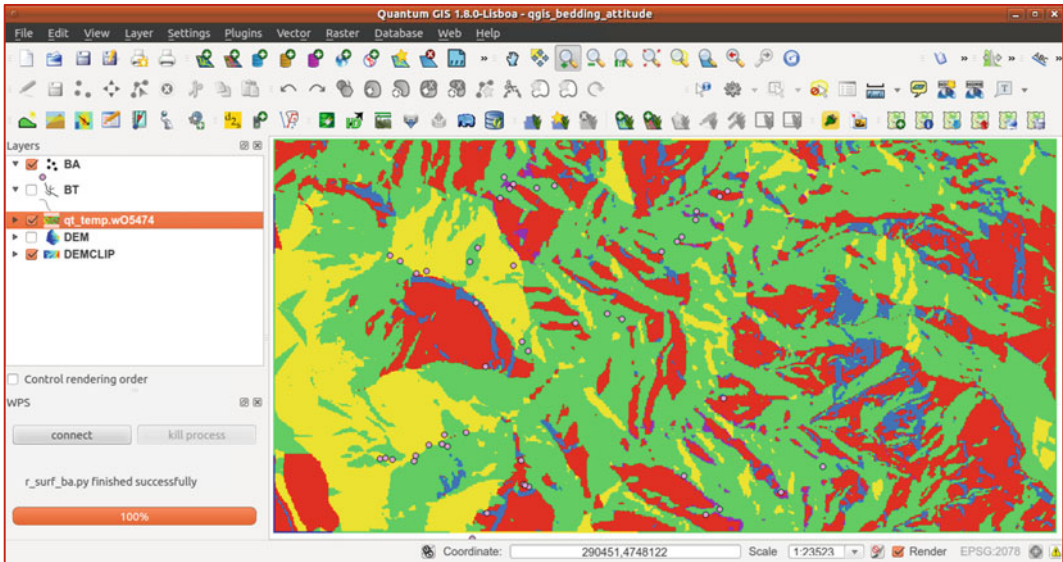


Fig. 8 Example of the output of the morpho-structural domain definition process. Different colours define the morpho-structural settings: yellow anaclinal slopes, green

orthoclinal slopes, blue cataclinal overdip slopes, purple cataclinal underdip slopes, red cataclinal dip slopes (Santangelo et al. 2015)

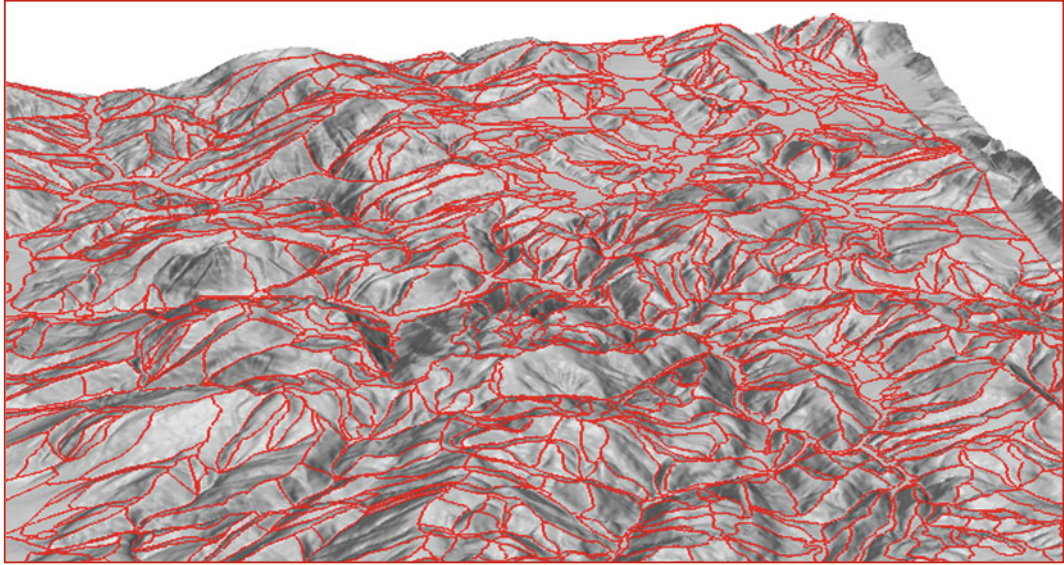


Fig. 9 Example of the output of the slope-units WPS process. The slope-unit map (*red*) produced by the process is draped on a three-dimensional representation of the DEM

Slope-units are hydrological terrain subdivisions bounded by drainage and divide lines.

The slope-unit size is controlled by user-defined parameters, including the minimum half-basin surface area, and the maximum aspect circular variance. The terrain subdivision obtained by the tool can be used to model landslide susceptibility or hazard (Guzzetti et al. 2005) and possibly for other geomorphological analyses.

Figure 9 shows a three-dimensional visualization of a slope-units map superimposed on the original DEM used to derive it.

9 Conclusions

Geospatial algorithms aimed to support landslides studies are frequently developed by researchers with the only purpose of solving well-defined problems. Scarce consideration is given to the portability of the codes and this often hampers their potential adoption by a large number of users. Exploiting the WPS standard interface, it is possible to share tools for landslide

and geomorphological analysis and modelling. Among all the possible advantages, the publication of a WPS processes guarantees the users to have always the last implemented software version, without need to update the software installed on their computers.

Open Source and proprietary software clients can be exploited to implement and to use the WPS processes. In particular, we have shown how the QGIS WPS Plugin can be used to take advantage of the landslide-related WPS processes published by IRPI CNR.

References

- Alvioli M, Marchesini I, Fiorucci F, Ardizzone F, Rossi M, Reichenbach P, Guzzetti F (2014) Automatic delineation of geomorphological slope units. In: EGU general assembly conference abstracts, vol 16, p 12697
- Barchi M, Guzzetti F, Federico C (1991) Reconstructing thrust geometry by map analysis techniques: three examples from the Central Apennines (Italy). *Boll Soc Geol Italiana* 110:833–841
- Carrara A, Cardinali M, Detti R, Guzzetti F, Pasqui V, Reichenbach P (1991) GIS Techniques and statistical

- models in evaluating landslide hazard. *Earth Surf Process Landform* 16:427–445
- Guzzetti F, Reichenbach P, Cardinali M, Galli M, Ardizzone F (2005) Probabilistic landslide hazard assessment at the basin scale. *Geomorphology* 72:272–299. doi:[10.1016/j.geomorph.2005.06.002](https://doi.org/10.1016/j.geomorph.2005.06.002)
- Marchesini I, Santangelo M, Fiorucci F, Cardinali M, Rossi M, Guzzetti F (2013) A GIS method for obtaining geologic bedding attitude. *Landslide science and practice*. Springer, Berlin, pp 243–247
- Rossi M, Cardinali M, Fiorucci F, Marchesini I, Mondini AC, Santangelo M, Ghosh S, Riguer DEL, Lahousse T, Chang KT, Guzzetti F (2012) A tool for the estimation of the distribution of landslide area in R. *Geophysical research abstracts*, vol 14, EGU2012-9438-1, 2012 EGU General Assembly 2012
- Santangelo M, Marchesini I, Cardinali M, Fiorucci F, Rossi M, Bucci F, Guzzetti F (2015) A method for the assessment of the influence of bedding on landslide abundance and types. *Landslides* 12(2):295–309

Part IV
Risk Management and Country
Practices

TXT-tool 4.084-1.1

Soil Slope Stability Analysis

Do Minh Duc

Abstract

Analysis of soil slope stability by the limit equilibrium method is presented. First, fundamental concepts of the method are described. Geotechnical parameters of soils for stability analysis are then discussed. Infinite slope stability is assessed with SINMAP in a GIS-based environment. Then a method of slope stability analyses is presented using the software SLOPE/W. Rainfall-induced slope instability is analyzed with the support of SEEP/W software, which can export pore-water pressure distributions in different rainfall into the analysis of SLOPE/W. Charts for rapid assessment of infinite slope stability are also introduced.

Keywords

Slope stability · Limit equilibrium · Factor of safety
SINMAP · GEOSLOPE

Contents

1	Introduction	447	4	Infinite Slope Stability Analysis with SINMAP	452
2	Limit Equilibrium Method	448	5	Slope-Stability Analysis with GEOSLOPE	453
3	Soil Parameters for Analysis of Slope Stability	449	5.1	Routine of Analysis	453
3.1	Post-slope Failures Along an Existing Slip Surface.....	449	5.2	Analysis of Rainfall-Induced Landslides	455
3.2	New Slope Failures.....	451	6	Infinite-Slope Stability Analysis Using Charts	458
3.3	Sandy Soils.....	451		References	466
3.4	Unsaturated Soils.....	452			

D.M. Duc (✉)

VNU University of Science, Vietnam National University, Hanoi (VNU), 334 Nguyen Trai, Thanh Xuan, Hanoi, Vietnam
e-mail: ducdm@vnu.edu.vn

D.M. Duc

International Consortium on Landslides, Gokasho, Uji, Kyoto 611-0011, Japan

1 Introduction

This topic is common in geotechnical engineering and can be found in many textbooks. To avoid duplication, the main goal of this TXT-tool is to provide basic information and tools for engineers and practitioners to perform slope-stability

analysis. It is also intended to be a reference for lecturing at undergraduate and graduate levels on landslide study. The paper is organized in 3 parts, including basic knowledge, simple tools for preliminary assessment of slope stability, and detail analysis with computer-aided software.

2 Limit Equilibrium Method

The most widely applied analytical technique for slope stability analysis is the limit equilibrium method, whereby force and/or moment equilibrium are examined as if the forces are static and the landslide is not moving. The analysis requires shear-strength parameters of soils, but not stress-strain behavior. The typical result of this analysis is a factor of safety (Fs).

The steps in calculating a limit-equilibrium solution are as follows:

1. Draw an arbitrary collapse mechanism of slip surfaces; this may consist of any combination of straight lines or curves.
2. Calculate the static equilibrium of the components by resolving forces or moments and hence calculate the strength mobilized in the soil or the external forces.
3. Examine the static equilibrium.

The fundamental shortcoming of limit-equilibrium methods is that they only satisfy equations of statics. Strain and displacement compatibility are not considered. However, this limitation can be overcome by using finite-element computed stresses inside a conventional limit-equilibrium framework (Krahn 2003). With computer-aided programs using the finite-element method, stresses are calculated and then both the total shear resistance and the total mobilized shear stress on a slip surface can be computed and used to determine the factor of safety.

The requirements for slope-stability analysis include the following steps of data collection and evaluation: Site investigation (geometry, geological and hydrological conditions);

geotechnical properties of soils; and modes of potential failure.

The geometry of the slip surfaces must form a mechanism that will allow collapse to occur, but the surfaces may be any shape so they need not meet all of the requirements of compatibility. The overall conditions of equilibrium of forces on blocks within the mechanism must be satisfied, but the local states of stress within the blocks are not investigated. Although there is no formal proof that the limit equilibrium method leads to correct solutions, experience has shown that the method usually gives solutions that agree quite well with observations of the collapse of real structures and the method is firmly established among the techniques of geotechnical engineering (Atkinson 2007).

$$F_s = \frac{\text{resisting forces}}{\text{sliding forces}} = \frac{\text{shear strength of soils}}{\text{shear stress required for equilibrium}}$$

We consider a circular slip surface as an example which is based on the limit-equilibrium method. Assume there is a slope with height H , slope angle $1:m$ (Fig. 1). To analyze its stability, the method of slices can be performed as following steps:

- Draw a potential slip surface across the slope;
- Divide the sliding mass into a set of slices with parallel sides.

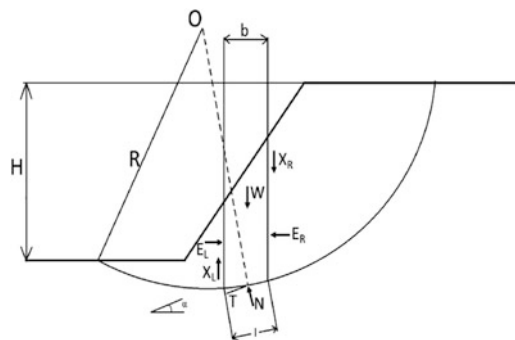


Fig. 1 Circular slip surface

Assume that the slip surface is an arc of a circle with center “O” and radius “R”, failure only develops along the slip surface and the soil mass fails as a Mohr-Coulomb material. When we change the position of the center “O” and the value of radius “R”, different slip surfaces will be formed and then different factors of safety (Fs) will be obtained. The most dangerous slip surface is the surface with the smallest Fs. Theoretically, the slope is stable if the minimum value of $F_s \geq 1$.

Fs is determined by dividing the circle into “n” slices which have the same width, “b”. The default number of slices at about 30 is acceptable in most cases. Then, the detailed forces on each slide will include slice weight (W), slice base normal force on the bottom of each slice (N), the mobilized shear strength (T), and horizontal (EL, ER) and vertical (XL, XR) interslice forces (Fig. 1). Depending on the horizontal, vertical force equilibrium and moment equilibrium, the number of equations available is shown in Table 1. Therefore, the solution becomes statically indeterminate because of the imbalance between unknowns and equations (2n – 2). Normally, the slice base normal force is recommended to be perpendicular and located at the midpoint of the bottom of slice so that the number of unknowns decreases to (n – 2).

This problem can be solved by adding assumptions. Then, these assumptions will be associated with force and moment equilibrium equations to determine Fs. Several methods have been proposed as shown in Tables 2 and 3.

For example, the usual method is assumed to ignore horizontal (EL, ER) and vertical (XL, XR) interslice forces. Thus, Fs can be determined by the following equation:

$$F_s = \frac{\sum_{i=1}^n (c_i l_i + W_i \cos \alpha_i \text{tg } \phi_i)}{\sum_{i=1}^n W_i \sin \alpha_i}$$

where i presents the ith slice, Wi is slice weight, ci, φi: cohesion and internal friction angle of soil at the bottom of slice, li is the length of the arc of the circle, αi is the angle between the tangent of the slip surface and a horizontal plane at midpoint.

3 Soil Parameters for Analysis of Slope Stability

3.1 Post-slope Failures Along an Existing Slip Surface

This failure only happens in a soil mass after some movement, which can be several meters. In

Table 1 The number of equations and unknown in the method of slices

Condition	Equations
Moment equilibrium for each slice	n
Force equilibrium in two direction (for each slice)	2n
Mohr–Coulomb relationship between shear strength and normal effective stress	n
Total number of equation	4n
Unknowns	Variable
Factor of safety	1
Normal force at base of each slice, N'	n
Location of normal force, N'	n
Shear force at base of each slice, Sm	n
Interslice forces, Z	n – 1
Inclination of interslice force, θ	n – 1
Location of interslice force (line of thrust)	n – 1
Total number of unknowns	6n – 2

Table 2 Characteristics of commonly used methods of limit equilibrium analysis (Duncan 1996)

Method	Limitation, assumption, and equilibrium conditions satisfied
Ordinary method of slices (Fellenius 1927)	Factors of safety low—very inaccurate for flat slopes with high pore pressures; only for circular slip surfaces; assumes that normal force on the base of each slice is $W \cos \alpha$; one equation (moment equilibrium of entire mass), one unknown (factor of safety)
Bishop’s modified method (Bishop 1955)	Accurate method; only for circular slip surface; satisfies vertical equilibrium and overall moment equilibrium; assumes side forces on slices are horizontal; $N + 1$ equations and unknowns
Janbu’s simplified method (Janbu 1968)	Force equilibrium method; applicable to any shape of slip surface; assumes side forces are horizontal (same for all slices); factors of safety are usually considerably lower than calculated using methods that satisfy all conditions of equilibrium; $2N$ equations and unknowns
Lowe and Karafiath’s method (Lowe and Karafiath 1960)	Generally most accurate of the force equilibrium methods; applicable to any shape of slip surface; assumes side force inclinations are average of slope surface and slip surface (varying from slice to slice); satisfied vertical and horizontal force equilibrium; $2N$ equations and unknowns
Janbu’s generalized procedure of slices (Janbu 1968)	Satisfies all conditions of equilibrium; applicable to any shape of slip surface; assumes that inclinations of side forces are the same for every slice; side force inclination is calculated in the process of solution so that all conditions of equilibrium are satisfied; accurate method; $3N$ equations and unknowns
Sarma’s method (Sarma 1973)	Satisfies all conditions of equilibrium; applicable to any shape of slip surface; assumes that magnitudes of vertical side forces follow prescribed patterns; calculates horizontal acceleration for barely stable equilibrium; by pre-factoring strength and iterating to find the value of the pre-factor that results in zero horizontal acceleration for barely stable equilibrium, the value of the conventional factor of safety can be determined; $3N$ equations, $3N$ unknowns

Table 3 Static condition satisfied and interslice forces in various methods

Method	Moment equilibrium	Horizontal force equilibrium	Interslice normal (E)	Interslice shear (X)	Inclination of X/E resultant
Ordinary of Fellenius	Yes	No	No	No	No force
Bishop’s simplified	Yes	No	Yes	No	Horizontal
Janbu’s simplified	No	Yes	Yes	No	Horizontal
Spencer	Yes	Yes	Yes	Yes	Constant
Morgenstern-Price	Yes	Yes	Yes	Yes	Variable
Corps of Engineering #1	No	Yes	Yes	Yes	Inclination of a line from crest to toe
Corps of Engineering #2	No	Yes	Yes	Yes	Slice top ground surface inclination
Lowe-Karafiath	No	Yes	Yes	Yes	Average of ground surface slope and slice base inclination

Table 4 Definition of slope stability index SI classes

Condition	Class	Predicted state	Parameter range	Possible influence of factors not modeled
SI > 1.5	1	Stable slope zone	Range cannot model instability	Significant destabilizing factors are required for instability
1.5 > SI > 1.25	2	Moderately stable zone	Range cannot model instability	Moderate destabilizing factors are required for instability
1.25 > SI > 1.0	3	Quasi-stable slope zone	Range cannot model instability	Minor destabilizing factors could lead to instability
1.0 > SI > 0.5	4	Lower threshold slope zone	Pessimistic half of range required for instability	Destabilizing factors are not required for instability
0.5 > SI > 0.0	5	Upper threshold slope zone	Optimistic half of range required for stability	Stabilizing factors may be responsible for stability
0.0 > SI	6	Defended slope zone	Range cannot model stability	Stabilizing factors are required for stability

calculating, we have to use the following parameters of residual resistance:

$$\begin{aligned} \text{Undrained condition : } & \tau = c_{ur} \\ \text{Drained condition : } & \tau' = \sigma_n' \text{tg}\phi_r' \end{aligned}$$

3.2 New Slope Failures

A new slip surface will occur when the strength of a soil mass is at peak strength. The selection of parameters can only be carried out after carefully examining historical stress and forecasting a drained condition.

Normal consolidated soils

This kind of soil includes normal consolidated state and slightly over-consolidated soils.

In the undrained condition, the peak strength will be smaller than the critical strength, so we use: $\tau = c_u$.

In the drained condition, we must use the critical strength: $\tau' = \sigma_n' \text{tg}\phi_c'$

Overconsolidated soil

This kind of soil is dryer (or denser) than other soils at critical state so that in the case of small deformations, the peak strength is higher than the critical strength. This case is

complicated, and so we have to be very careful when forecasting the deformation.

- Small deformation (based on peak strength):
- + Undrained condition: $\tau = c_u$
- + Drained condition: $\tau' = \sigma_n' \text{tg}\phi_f' + c'$
- Based on critical strength:
- + Undrained condition: $\tau = c_u$
- + Drained condition: $\tau' = \sigma_n' \text{tg}\phi_f' + c'$

With overconsolidated clay with a large amount of deformation, the decrease in strength after reaching peak value must be considered. In this case, it is recommended to use the following parameters:

$$\tau = c_u \text{ and } \tau = \sigma_n' \text{tg}\phi_r'$$

3.3 Sandy Soils

- Denser than critical state:

$$\tau = \text{tg}\phi_f' \text{ (peak strength)}$$

- Looser than critical state:

$$\tau = \text{tg}\phi_c'$$

3.4 Unsaturated Soils

Shear-strength equation of unsaturated soil can be expressed:

$$\tau = c' + (\sigma - u_a) \text{tg } \phi' + (u_a - u_w) \text{tg } \phi^b$$

(Fredlund and Rahardjo 1993) where: ϕ' , c' – effective internal friction angle and effective cohesion

u_a , u_w —pore air pressure and pore water pressure

$(\sigma - u_a)$ —effective normal stress (variable of the first stress state)

$(u_a - u_w)$ —suction ratio (variable of the second stress state)

ϕ^b —soil property that reflects influence of suction ($u_w - u_a$) on strength.

The parameters of ϕ' , c' are determined by unsaturated soil experiments. ϕ^b is obtained by triaxial tests or direct shear tests with tensiometers. In slope stability analysis of soils, ϕ^b can be chosen by $1/2\phi'$ for safety. Other research identifies the approximate arithmetical relationship between ϕ^b and ϕ' (Vanapalli et al. 1996; Tekinsoy et al. 2004). Vanapalli et al. (1996) proposed the formula:

$$\tan \phi^b = \left(\frac{S - S_r}{100 - S_r} \right) \tan \phi'$$

S , S_r —current and residual degree of saturation (%), ϕ' —effective angle of friction.

4 Infinite Slope Stability Analysis with SINMAP

SINMAP (Stability Index Mapping) software was developed by Utah State University as a tool for automatic calculation of infinite slope stability (Fig. 2). SINMAP 2.0 had been integrated onto ArcGIS® and applied in many regions of the world for landslide study. It is a tool for calculation of slope stability in ArcGIS®. The input data are landslide points, digital elevation model and hydrological and soil and rock mechanical properties (Fig. 3). It is not a conventional slope

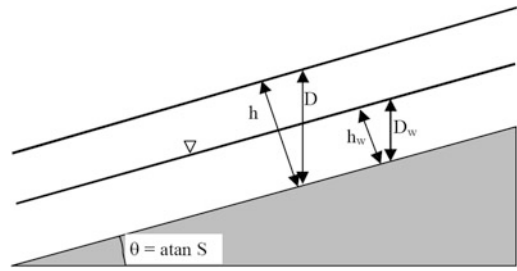


Fig. 2 Infinite slope stability model schematic

stability analysis. But it is useful tool to assess stability at a large scale and provides preliminary results for geotechnical engineering analysis.

The SINMAP slope stability model uses surface soil moisture under hydrological balance condition. A digital elevation model (DEM) is used to determine necessary input data (slope and catchment information). They can be adjusted (quantitatively) based on soil mechanical properties, vegetation or geological data.

SINMAP was firstly intended for terrain stability mapping practice in British Columbia. Table 1 gives an example of how broad stability classes may be defined in terms of the stability index (SI). The selection of breakpoints (1.5, 1.25, 1.0, 0.5, 0.0) is subjective, requiring judgement and interpretation in terms of the class definitions.

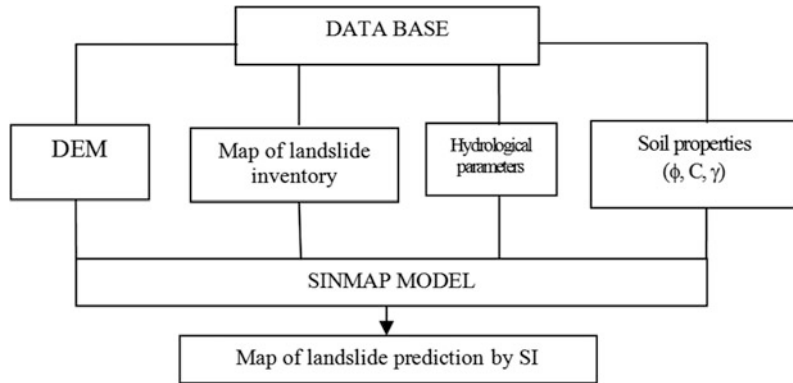
SINMAP uses the formula for the factor of safety (Fs) for the infinite slope stability model (ratio of stabilizing to destabilizing forces) developed by Hammond et al. (1992) and Montgomery and Dietrich 1994. Based on the above assumptions and through mathematical manipulations (see detail in the user’s manual—Pack et al. 1999), the Fs is expressed as:

$$Fs = \frac{C + \cos \theta \left[1 - \min \left(\frac{R}{T} \frac{a}{\sin \theta}, 1 \right) r \right] \tan \phi}{\sin \theta}$$

where:

$C = (C_r + C_s)/(h\rho_s g)$ the combined cohesion made dimensionless relative to the perpendicular soil thickness; θ is slope angle; a is specific catchment area; $h = D \cos \theta$ soil thickness, perpendicular to the slope, and $r = \rho_w/\rho_s$ is the water to soil density ratio; the ratio R/T has units of (m^{-1}), quantifies the relative wetness in terms

Fig. 3 Necessary data for landslide prediction mapping



of assumed steady state recharge relative to the soil’s capacity for lateral drainage of water.

The variables “a” and θ are the specific catchment area and slope respectively and are derived from the topography. C is the dimensionless cohesion of the soil and tree roots combined, $\tan \phi$ is the soil friction angle, r is the water/soil density ratio, and R/T is the water recharge divided by the soil transmissivity. These last four parameters are manually input into the model. We treat the density ratio r as essentially constant (with a value of 0.5) but allow uncertainty in the other three quantities through the specification of lower and upper bounds. Formally these bounds define uniform probability distributions over which these quantities are assumed to vary at random. We denote R/T = x, $\tan \phi = t$, and the uniform distributions with lower and upper bounds as (Pack et al. 2005):

$$C \sim U(C_1, C_2); x \sim U(x_1, x_2); t \sim U(t_1, t_2)$$

The smallest C and t, (i.e. C_1 and t_1) together with the largest x (i.e. x_2) defines the worst case (most conservative) scenario under this assumed uncertainty (variability) in the parameters. Areas where under this worst case scenario FS is greater than 1 are in terms of this model, unconditionally stable and therefore FS is defined as:

$$SI = F_{S_{\min}} = \frac{C_1 + \cos \theta [1 - \min(x_2 \frac{a}{\sin \theta}, 1)] r}{\sin \theta} t_1$$

For areas where the minimum factor of safety is less than 1, there is a possibility (probability)

of failure (Table 4). This is a spatial probability due to the uncertainty (spatial variability) in C, $\tan \phi$ and T. This probability does have a temporal element in that R characterizes a wetness that may vary with time. Therefore the uncertainty in x combines both spatial and temporal probabilities. In these regions (with $F_{S_{\min}} < 1$) then $SI = \text{Prob}(F_s > 1)$ over the distributions of C, x, and t. The best case scenario is when $C = C_2$, $x = x_1$, and $t = t_2$, which leads to:

$$F_{S_{\max}} = \frac{C_2 + \cos \theta [1 - \min(x_1 \frac{a}{\sin \theta}, 1)] r}{\sin \theta} t_2$$

In the case that $F_{S_{\max}} < 1$, then $SI = \text{Prob}(F_s > 1) = 0$.

Regions with $SI > 1$ ($F_{S_{\min}} > 1$), $0 < SI < 1$ and $SI = 0$ ($F_{S_{\max}} < 1$) are illustrated in Fig. 4 in a space defined in terms of slope ($\tan \theta$) and specific catchment area.

As an example, results of slope stability analysis using SINMAP are shown in Fig. 5.

5 Slope-Stability Analysis with GEOSLOPE

5.1 Routine of Analysis

Soil slope stability can be assessed by using SLOPE/W—a module of GeoStudio software package (the former name was GEOSLOPE), which is a product of the GeoSlope International Ltd. The Student Edition series was released in 2002 providing 13 different examples of using

Fig. 4 Stability Index defined in area-slope space

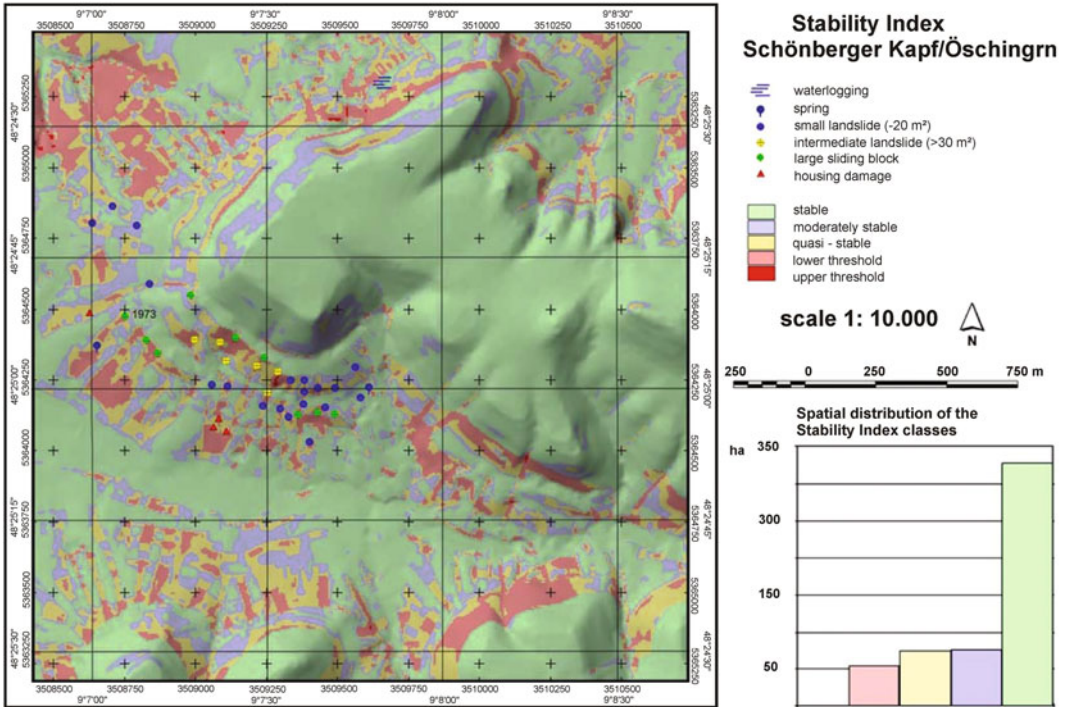
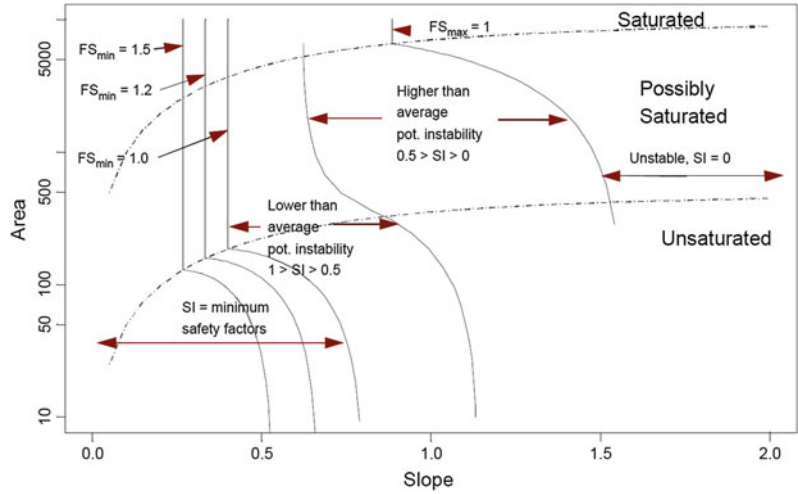


Fig. 5 A stability index map (SINMAP) (Terhorst and Kreja 2009)

SLOPE/W (GeoSlope, International Ltd. 2002a, b). Readers who have not been familiar with this software are highly recommended to read the student edition workbook. It can be retrieved at

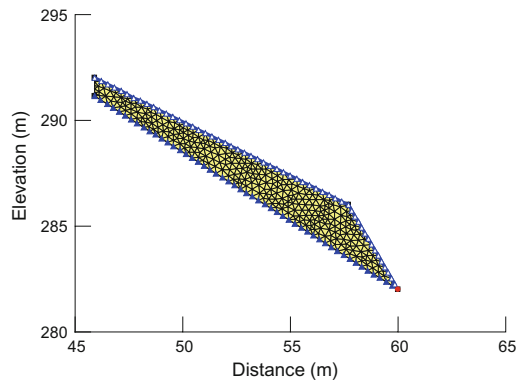
<http://www.geoslope.com>. As a summary, relevant steps are outlined in Table 5. The illustrations were carried out by using GeoStudio, 2004 (GeoSlope, International Ltd. 2004a, b).

Table 5 Conventional steps to perform slope stability analysis in SLOPE/W

Step	Activity
Defining problem	<p><i>Convention</i></p> <ul style="list-style-type: none"> – Set the scale and grid spacing (grid can also be turned off) – Sketch problem (geometry) of the analysis – Specifying analysis methods (ordinary, simplified Bishop and Janbu are defaults, one more can be included such as Morgenstern-Price, Spencer, GLE, Corps of Engineers # 1, 2 and Lowe–Karafiath) – Specifying analysis options on pore water pressure – Specifying controlling options (probabilistic analysis, slip surface option, tension crack, direction of movement) – Defining soil properties (in KeyIn menu). SLOPE/W provides a wide range of different materials such as Mohr–Coulomb, undrained, anisotropic strength, no strength and bedrock, etc. – Drawing lines and assigning soil types to lines – Drawing piezometric lines – Drawing slip surfaces: radius, grid, etc. (depending on how option slip surface is set in last activity) – Viewing preferences to change graphical display of the problem – Sketch axes – Adding label to soils, project title – Saving the problem <p><i>Advanced</i></p> <ul style="list-style-type: none"> – Setting rigorous method of analysis – Probabilistic analysis – Tension crack settings – Auto locate mode of slip surface – Integration with results of other modules (i.e. SIGMA/W, SEEP/W, QUAKE/W)
Verifying problem	<ul style="list-style-type: none"> – Choose verify from Tools menu – Getting the report of verification (if error reported, normally it should be fixed by reviewing the step of defining problem)
Solving problem	<ul style="list-style-type: none"> – Start solving – Quit solving
Displaying results	<ul style="list-style-type: none"> – Plotting critical or any analyzed slip surfaces with corresponding Fs – Contour plot of Fs – Displaying slice information – Plotting graphs of computed results – Import picture, copy and export graphical results – Printing

5.2 Analysis of Rainfall-Induced Landslides

When water gets into a slope, it increases pore water pressure (PWP) and reduces the slope's stability. The seepage is a transient process and is analyzed by SEEP/W software using the finite element method (Fig. 6). Pore water pressure distributions in different scenarios of rainfall can be analyzed by SEEP/W software and then exported to SLOPE/W for slope stability analysis.

**Fig. 6** FEM mesh and boundary condition

Soil properties: Besides the conventional soil properties, some advanced parameters of unsaturated soils have to be taken into account. First, the “volumetric water content function” must be set up (Fig. 7). It is data from soil testing of the soil-water characteristic curve (SWCC) or it can be indirectly estimated from other properties of soils, e.g. grain sizes and/or Atterberg limits (Aubertin et al. 2004). Then hydraulic conductivity (k) of soil is calculated from the saturated hydraulic conductivity and SWCC (Fig. 8).

There are 3 options for “k” estimation which are Fredlund and Xing (1994), Green and Corey (1971) and Van Genuchten (1980).

The initial negative PWP (i.e. maximum negative pressure head in “Initial Water Table”) can be set based on soil-water characteristic curve and natural moisture content of soils.

Boundary condition: Bedrock is set as an impermeable boundary. The slope surface is set as unit discharge condition with a value as the rate of rainfall. The boundary is also set as

Fig. 7 Defining volumetric water content function of soil in SEEP/W

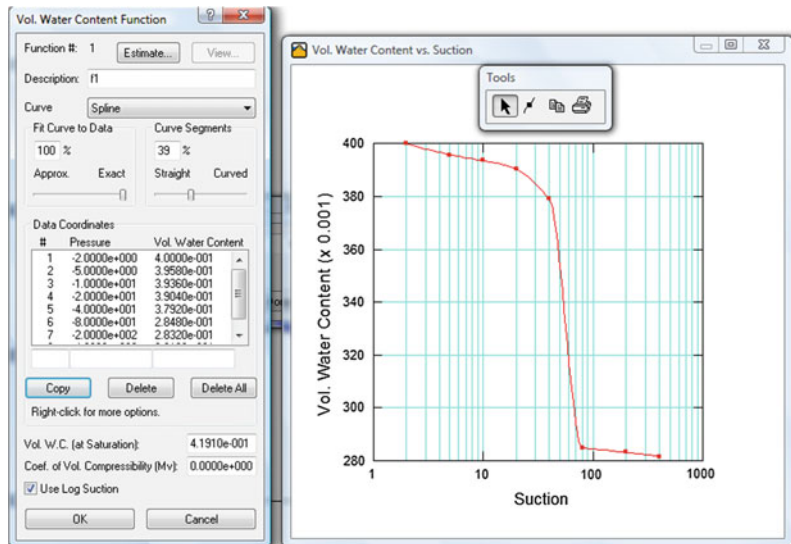
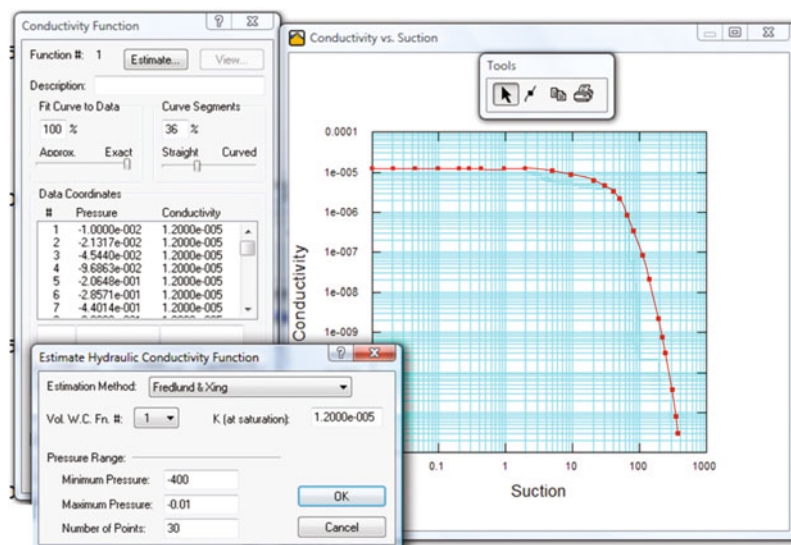


Fig. 8 Estimation of soil hydraulic conductivity in SEEP/W



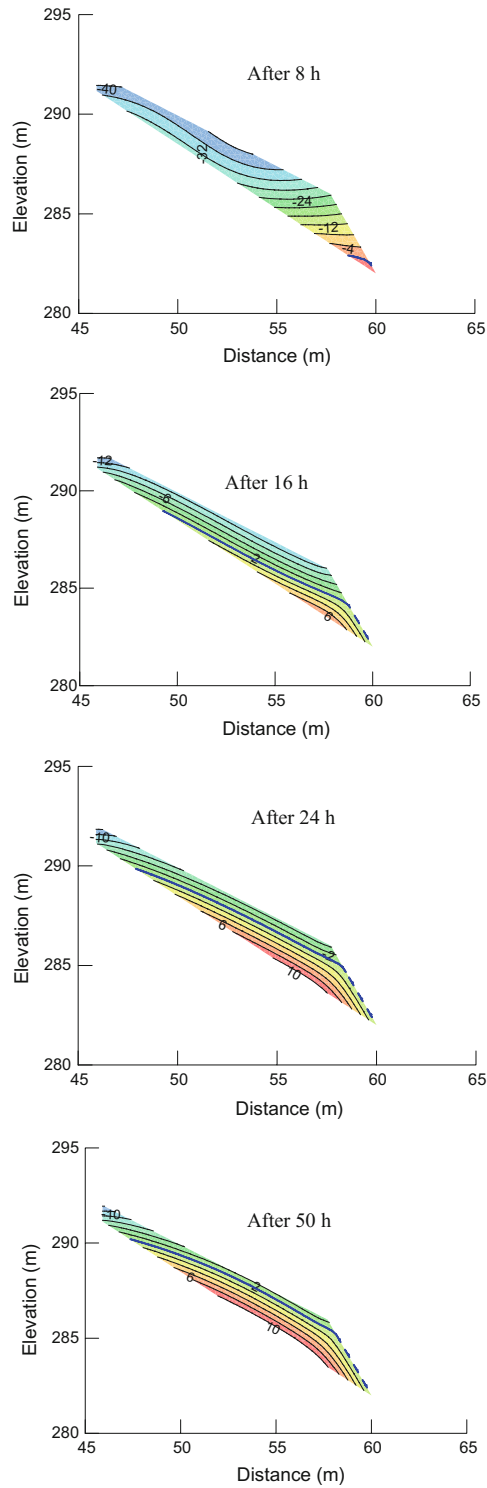


Fig. 9 PWP versus elapsed time of rain

Table 6 Geotechnical properties of residual soils

Properties	Value
Wet density (KN/m ³)	17.8
Void ratio	0.759
Effective angle of friction (°)	23.5
Effective cohesions (KPa)	8
Saturated coefficient of hydraulic conductivity (m/s)	1.2×10^{-5}
ϕ_b (°)	14.3

potential seepage face review to avoid surface water pond on the slope. The upper and lower parts of the slope are set as no flow boundary conditions. One point at the toe of the slope is set as a constant head to ensure convergence of the numerical calculation. The analysis type is set as “Transient” in “*Analysis settings*” (Fig. 9).

An example analysis of slope stability is shown in Fig. 6, for a slope subjected to rainfall intensity of 3.75 mm/h. Properties of its soil are shown in Table 6. Results of PWP distributions and Fs after different time periods are shown in Figs. 10 and 11, respectively.

6 Infinite-Slope Stability Analysis Using Charts

Another practical method to analyze infinite-slope stability was introduced by Duncan (1996). This method quantitatively analyzes the effect of soil saturation on the stability of those slopes where potential for translational sliding exists. The analysis assumes the slip surfaces are long compared to their depth, and it ignores the driving force at the upper end of the sliding mass and the resisting force at the lower end (Fig. 11). The method requires a procedure with three steps:

1. Determination of the factor of safety (Fs) using the following equation:

$$F_s = A(\tan \phi' / \tan \alpha) + B(c' / \gamma / H)$$

where H is the depth of soil measured vertically from the slope surface to the surface of sliding; ϕ' are the effective strength parameters; α is the slope angle; and γ is soil density.

2. Determination of parameters A and B from the following equations:

$$A = 1 - (r_u / \cos^2 \alpha)$$

$$B = 1 / (\sin \alpha \cdot \cos \alpha)$$

where parameter A accounts for the pore pressure acting normal to the sliding surface and parameter B accounts for the shear resistance along the sliding surface.

3. Determination of r_u , the pore pressure ratio, is as follows:

$$r_u = (X/T)(\gamma_w / \gamma)(\cos^2 \alpha)$$

where X is the thickness of the soil mantle that is saturated, T is the total thickness of the residual soil mantle, γ_w and γ are the water and soil densities, respectively.

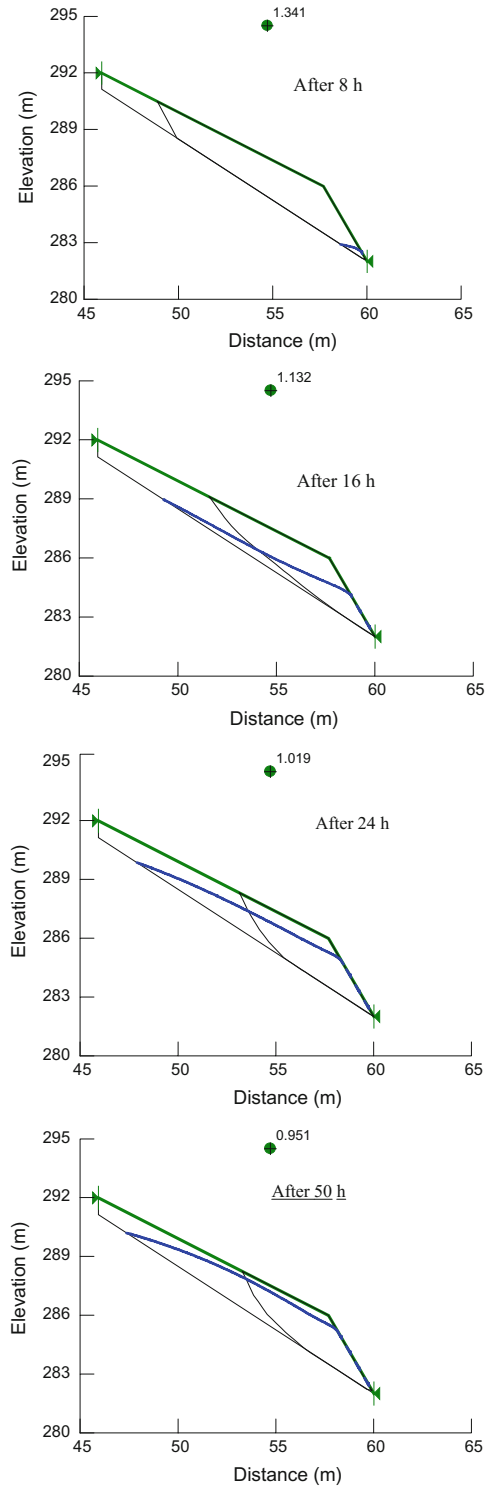
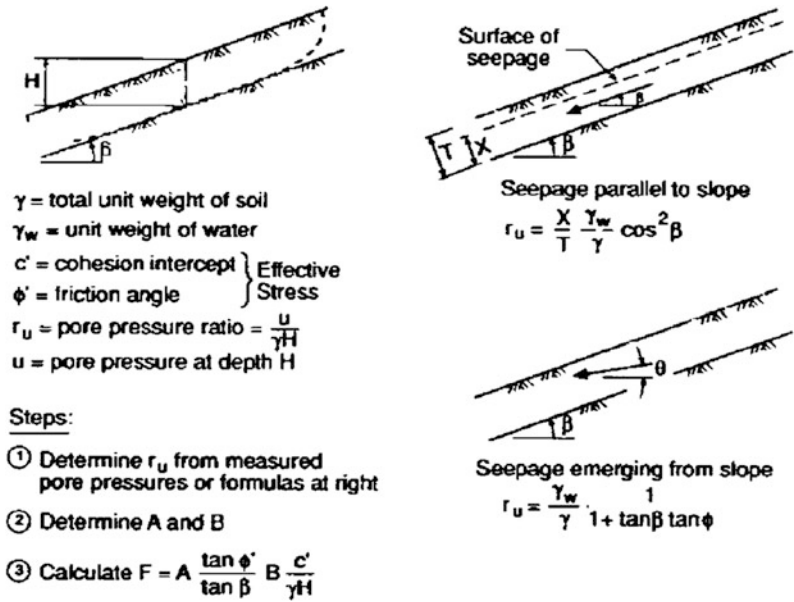


Fig. 10 Factors of safety versus rainy time (slip surface is set to “Auto Locate” mode)

Fig. 11 Illustration of infinite-slope-analysis method (taken from Duncan 1996)



References

- Atkinson J (2007) The soil mechanics and foundations. Taylor & Francis, Routledge
- Aubertin M, Mbonimpa M, Bussiere B, Chapuis RP (2004) A model to predict the water retention curve from basic geotechnical properties. *Can Geotech J* 40:1104–1122
- Bishop AW (1955) The use of the slip circle in the stability analysis of slopes. *Géotechnique* 5(1):7–17
- Duncan MJ (1996) Soil slope stability analysis. Landslides: investigations and mitigation. Special Report, vol 247, Chapter 13. Transportation Research Board, National Research Council, Washington, pp 337–371
- Fellenius W (1927) Erdstatische Berechnungen mit Reibung und Kohäsion. Ernst, Berlin
- Fredlund DG, Rahardjo H (1993) Soil mechanics for unsaturated soils. Wiley, New York
- Fredlund DG, Xing A (1994) Equations for the soil–water characteristic curve. *Can Geotech J* 31:521–532
- GeoSlope, International Ltd. (2002a) Chapter 3 SLOPE/W tutorials
- GeoSlope, International Ltd. (2002b) SLOPE/W student edition workbook
- GeoSlope, International Ltd. (2004a) Stability modeling with SLOPE/W—an engineering methodology
- GeoSlope, International Ltd. (2004b) Seepage modeling with SEEP/W—an engineering methodology
- Green RE, Corey JC (1971) Calculation of hydraulic conductivity: a further evaluation of some predictive methods. *Soil Sci Soc Am Proc* 35:3–8
- Hammond C, Hall D, Miller S, Swetik P (1992) Level I Stability Analysis (LISA) Documentation for Version 2.0. General Technical Report INT-285, USDA Forest Service Intermountain Research Station
- Krahn J (2003) The 2001 R.M. Hardy lecture: the limits of limit equilibrium analyses. *Can Geotech J* 40:643–660
- Janbu N (1968) Slope stability computations. Institutt for Geoteknikk og Fundamenteringslære, Norges Tekniske Høgskole. Soils Mechanics and Foundation Engineering, the Technical University of Norway
- Lowe J, Karafiath L (1960) Stability of earth dams upon drawdown. Proceedings of the first PanAmerican conference on soil mechanics and foundation engineering. Mexican Society of Soil Mechanics, Mexico D.F., pp 537–552
- Montgomery DR, Dietrich WE (1994) A physically based model for the topographic control on shallow landsliding. *Water Resour Res* 30(4):1153–1171
- Pack RT, Tarboton DG, Goodwin CN (1999) SINMAP - A Stability Index Approach to Terrain Stability Hazard Mapping, User's Manual. Produced in ArcView Avenue and C++ for Forest Renewal B.C. under Research Contract No: PA97537-ORE
- Pack RT, Tarboton DG, Goodwin CN, Prasad A (2005) SINMAP 2. A stability index approach to terrain stability hazard mapping. Technical description and users guide for version 2.0. Utah State University
- Sarma SK (1973) Stability analysis of embankments and slopes. *Géotechnique* 23(3):423–433
- Tekinsoy MA, Kayadelen C, Keskin MS, Soylemez M (2004) An equation for predicting shear strength envelope with respect to matric suction. *Comput Geotech* 31(2004):589–593
- Terhorst B, Kreja R (2009) Slope stability modelling with SINMAP in a settlement area of the Swabian Alb. *Landslides* 2009(6):309–319
- Vanapalli SK, Fredlund DG, Pufahl DE, Clifton AW (1996) Model for prediction of shear strength with respect to matric suction. *Can Geotech J* 33:379–392
- Van Genuchten MT (1980) A closed-form equation for predicting the hydraulic conductivity of unsaturated soils. *Soil Sci Soc Am J* 44:892–898

TXT-tool 1.081-2.4

Risk Evaluation Using the Analytic Hierarchy Process (AHP)— Introduction to the Process Concept

Eisaku Hamasaki and Toyohiko Miyagi

Abstract

In this paper, risk evaluation of Landslide using the Analytic Hierarchy Process (AHP) is introduced. AHP, which was established by Thomas L. Saaty in 1971, is decision-making method based on a pair comparison. Since its proposal by Saaty, the of evaluation standard the AHP method has been as an extremely technique in many evaluation method. However, in order to make decision using by ordinary AHP, it needs paired comparison with not only criteria but also alternatives. Therefore, we propose that to apply the AHP of an absolute evaluation method to risk evaluation in this paper. Here, first of all, the basic AHP of a relative method is described using ordinary simple example. Next, the main characteristics of the relative and absolute methods are summarized. Then we describe how to adopt AHP method to risk evaluation system using the example data to estimate of people's ages. Moreover, Japanese inspection sheet for landslide risk evaluation system which use their aerial photography using absolute method of AHP is explained. Last we will consider a framework for converting implicit knowledge into explicit knowledge through these AHP algorithm.

Keywords

AHP · Risk evaluation · Absolute evaluation method
Micro-topography

E. Hamasaki (✉)
Advantech Co. Ltd, Aobaku, Sendai, Japan
e-mail: hamasaki@adovantech.co.jp

T. Miyagi
Faculty of Arts, Department of Regional
Management, Tohoku-Gakuin University, 2-1-1,
Tenjinsawa, Izumi, Sendai 981-3193, Japan
e-mail: miyagi@mail.tohoku-gakuin.ac.jp

Contents

1	Basics of the Analytic Hierarchy Process	462
1.1	About the Analytic Hierarchy Process.....	462
1.2	Simple Example of the Analytic Hierarchy Process Method	463
1.3	Instructions for the Most Commonly Used Analytic Hierarchy Process Method: Relative Comparison.....	463
2	Concept of the Absolute Evaluation Method in the Analytic Hierarchy Process	464
2.1	Problems with Relative Comparisons in the Analytic Hierarchy Process.....	464
2.2	The Absolute Evaluation Method	466
2.3	Reasons for Applying the Absolute Evaluation Method to Landslide Risk Evaluation When Using Aerial Photographs	466
2.4	Converting Implicit Knowledge into Explicit Knowledge.....	466
3	Creating Evaluation Criteria	467
3.1	General Categories.....	467
3.2	Categories of Evaluation Criteria and Weighting	468
3.3	Definition of Landslide Topography and Occurrence Risk, and Scope/Perspective of Interpretation	470
3.4	The Analytic Hierarchy Process Method.....	471
4	Conclusion	474
	References	474

1 Basics of the Analytic Hierarchy Process

1.1 About the Analytic Hierarchy Process

When purchasing expensive items, such as cars or houses, we become very cautious and deeply indecisive about various criteria. Given that there are multiple judgment criteria (for example, when buying a house: the price, distance from a train station, space, natural environment, convenience etc.) leading to a decision. It would be easier to make a decision if the buyer's criteria are simple and clear. If they are ambiguous, a buyer will become very indecisive, and later will often regret their decision. When a decision is not personal, but rather an important matter that needs to be made by a company or group (for example, where to locate the company offices), an objective

and rational judgment process (judgment basis) leading to a decision, is strongly required.

In order to resolve such problems, Dr. T.L. Saaty, University of Pittsburgh, proposed the Analytic Hierarchy Process (Saaty 1980). This method's greatest merit is that it "clearly quantifies ambiguous judgment criteria." Put another way, it "determines the relative influence among items of judgment criteria."

Specifically, this method ascertains the problem using a hierarchy for each element: Level 1, Goal; Level 2, Evaluation Criteria; and Level 3, Alternatives. A weight is assigned to each element by performing paired comparisons with other elements on the same level. The comprehensive score derived from this assists decision-making. In essence, when one must select the best choice from a number of candidates, this method enables one to make rational decisions using paired comparison, while taking intuition and hunches into account.

The main characteristics of this method are as follows: (1) Since each element is evaluated on subjective criteria, elements that express conflicting concepts or differing measurement scales can be compared; (2) use of paired comparison simplifies evaluation, enabling importance throughout to be ascertained cumulatively; (3) as it is a quantitative method, it can be quantitatively compared with other plans (4) it enables confirmation of the influence a given element exerts on the whole, and the consistency of the judgment.

The method is extremely simple, requiring only the key ideas of "paired comparisons" and their "weighting" (usually calculated by geometric mean). Using Excel, an experienced user can determine the best selection plan (called an "alternative" in the Analytic Hierarchy Process) in an hour.

There are many famous applications of Analytic Hierarchy Process. For example, in the 1996–1997 hostage crisis at the Japanese Ambassador's residence in Peru, Dr. Saaty used it to help Peruvian officials consider what action the government should take. In Japan in 1996, the Council for Relocation of the Diet and Other Organizations used the method to select the Tochigi/Fukushima and Gifu/Aichi regions from among 10 candidate regions.

1.2 Simple Example of the Analytic Hierarchy Process Method

The example we will use is “buying a new car.” Our objective is to visualize this as a hierarchical chart (Fig. 1).

Here, we will examine the evaluation criteria of “comfort,” “price,” and “style.”

There are four types of car: Car A, Car B, Car C, and Car D. The plans to be compared are generally called the “alternative plans,” but they can also be called “comparison plans.”

1.3 Instructions for the Most Commonly Used Analytic Hierarchy Process Method: Relative Comparison

In this example, we consider a buyer looking for a new car. The buyer values comfort, but is not very concerned with style.

1. First, make paired comparisons of the evaluation criteria, “comfort,” “price,” and “style.” The paired comparisons are rearranged as a matrix, as shown in Table 1. Same items are written as “Same = 1.”

- (a) Looking at the table from the side, if “comfort” is 3 times more important than “price,” it will be assigned a “3.”
- (b) If we look at the items along the diagonal lines, and compare “price” with “comfort,” we see that the numbers from (1) are reversed: 1/3.

- (c) As shown in Table 1, the degrees of comparison are 3, 5, and 7 (or conversely, 1/3, 1/5 and 1/7). Sometimes, these are even numbers (2, 4, 6), but generally odd numbers are used.
- (d) When all comparisons on the 3 × 3 matrix have been completed, the geometric mean* is calculated for each item. E.g., Comfort = (1 × 3 × 5) 1/3 = 2.466
- (e) After each geometric mean has been found, the total sum is recalculated to equal 100. This becomes the weight for the evaluation criteria. Here we will refer to it as “weight a.”

2. Next we perform paired comparisons for each of the cars under consideration (alternatives) with respect to “comfort,” “price,” and “style.” Finding “weight b” for each alternative within the conceptualization and evaluation items, is the same as in (1)–(5). However, in the overall evaluation, the true weight is weight a multiplied by weight b (a*b on Table 2).
3. When all weights have been found, the evaluation criteria weights for all cars (alternatives) are totaled.

As a result, evaluation scores (Analytic Hierarchy Process scores) are found for each alternative. Specifically, in the below list, since Car A has the highest evaluation score, it was selected. In general, the weights are adjusted so that they add up to 100 points when the evaluation scores are totaled.

Car A: Comfort (28.0) + Price (3.2) + Style (4.4) = 35.6

Table 1 Analytic hierarchy process method paired-comparison table

	Comfort	Price	Style	Geometric mean	Weight a
Comfort	1	3	5	2.466	64
Price	1/3	1	3	1.000	26
Style	1/5	1/3	1	0.405	10
				3.872	100

Geometric mean (Gm)

$$Gm = \left(\prod_{i=1}^n X_i \right)^{1/n}$$

Degrees of the paired comparisons:

- 1 Both of the items are equally important
- 3 The item in the row is slightly more important than the item in the column (or conversely, 1/3)
- 5 The item in the row is more important than the item in the column (or conversely, 1/5)
- 7 The item in the row is considerable more important than the item in the column (or conversely, 1/7).

Table 2 Values used in the relative car comparison example

Comfort	Car A	Car B	Car C	Car D	Geometric mean	Weight b	a*b
Car A	1	2	3	3	2.060	0.44	28.0
Car B	1/2	1	3	3	1.456	0.31	19.8
Car C	1/3	1/3	1	2	0.687	0.15	9.3
Car D	1/3	1/3	1/2	1	0.485	0.10	6.6
					4.688	Sum = 63.7	
Price	Car A	Car B	Car C	Car D	Geometric mean	Weight b	a*b
Car A	1	1	1/3	1/3	0.577	0.13	3.2
Car B	1	1	1/2	1/3	0.639	0.14	3.6
Car C	3	2	1	1/2	1.316	0.29	7.4
Car D	3	3	2	1	2.060	0.45	11.6
					4.592	sum = 25.8	
Style	Car A	Car B	Car C	Car D	Geometric mean	Weight b	a * b
Car A	1	1	3	7	2.141	0.42	4.4
Car B	1	1	3	5	1.968	0.39	4.0
Car C	1/3	1/3	1	1	0.577	0.11	1.2
Car D	1/7	1/5	1	1	0.411	0.08	0.8
					5.097	Sum = 10.5	
						Sum*(all) =100.0	

Car B: Comfort (19.8) + Price (3.6) + Style (4.0) = 27.4
 Car C: Comfort (9.3) + Price (7.4) + Style (1.2) = 17.9 (18.0)
 Car D: Comfort (6.6) + Price (11.6) + Style (0.8) = 19.0

- Step 1: Determine weights on evaluation axis by paired comparison of each element in it.
- Step 2: Create a paired-comparison matrix of alternatives from which the final selection will be made, and determine a weight for each evaluation element.
- Step 3: Estimate weights for each alternative on the evaluation axis, and find the best one in terms of the various alternatives' weights (evaluation scores).

There are two drawbacks to this relative comparison method.

- (1) There is no problem when the number of alternatives is small, but when it is large, this method is cumbersome.
- (2) Once determined, if alternative items are added, all paired comparisons must be performed again; in rare cases, the initial ranking of the weights of alternatives may even reverse.

2 Concept of the Absolute Evaluation Method in the Analytic Hierarchy Process

2.1 Problems with Relative Comparisons in the Analytic Hierarchy Process

The relative comparison method often used in the Analytic Hierarchy Process has the following three steps.

For example, suppose one has structured a system for looking for the best candidate among hundreds of apartments. Performing paired comparisons on each of the countless apartments is not the best system. However, if a system were designed so that the final judgment was not affected even if conditions under consideration in the paired comparisons were added or subtracted, this would be a more usable system.

To overcome this shortcoming, Saaty proposed an Analytic Hierarchy Process “absolute evaluation method.” This model is effective when structuring diagnostic systems for judging many objects.

2.2 The Absolute Evaluation Method

In the absolute evaluation method, the weights found through paired comparisons of the evaluation criteria are implemented as common scale values. Essentially, the calculation of weights through paired comparisons on the evaluation axis in Step 1 is performed in a manner similar to the relative comparison method, but in Steps 2 and 3, paired comparisons of the alternatives are not performed. Instead, a scale is structured to judge the approximate rank of importance of each item on the evaluation axis.

Let us return to the problem of selecting a car from the previous section. The weights found through paired comparison on the evaluation axis are the same. That is, as evaluation axes, Comfort has a maximum score of 64 points, Price, a maximum of 26, and Style, a maximum of 10. When considering absolute evaluations of

qualitative elements such as Comfort and Style, it is important to create specific standards for the evaluation axis, such as best (1) and worst (0), that are intuitive.

In other words, when evaluating Car A, it is necessary to consider weights while comparing the standard values on its evaluation axis. For example, in comparatively evaluating Car A, the buyer would have specific ideas, such as “Model 1 is the best (1.0), Model 2 the worst (0), while Model 3 is average (0.5).” So it would be impossible to infer that if Car A was better than Model 3, but worse than Model 1, it would score 0.75. Next, “Price” seems like something that can be expressed quantitatively. For example, the buyer can assign it an approximate weight by setting a score of 1.0 for cars less than one million yen, 0.5 for cars 3 million yen and over, and approaching 0 for cars over ten million yen.

The results of the absolute evaluation method applied to the car-purchasing problem are shown in Table 3.

The scale is such that positive factors such as high quality, inexpensiveness, etc. are scored as 1.0, while negative factors, such as poor quality, expensiveness etc. are rated as 0.0. The position that each evaluation should assume is compared to the criteria scale and assigned a numeric value from 0.0 to 1.0.

The results are consistent with those from the initial relative comparison method, with the order unaltered, and Car A is indicated as the best alternative. Thus, if the evaluation scale (standard) for absolute evaluation can be clarified, this method produces similar weights and evaluations to those obtained using the relative comparison method.

Table 3 Comparison of weights according to absolute comparison table and gross comparison

Evaluation criteria	Weight a	1	0.5	0	Car A		Car B		Car C		Car D	
Comfort	64	Good	Average	Bad	0.7	44.8	0.5	32.0	0.3	19.2	0.2	12.8
Price	26	In expensive	Average	Expensive	0.1	2.6	0.2	5.2	0.5	13.0	1.0	26.0
Style	10	Good	Average	Bad	1.0	10.0	0.8	8.0	0.5	5.0	0.3	3.0
		Absolute evaluation method			1	57.4	2	45.2	4	37.2	3	41.8
		Relative comparison method			1	35.6	2	27.4	4	17.9	3	19.0

2.3 Reasons for Applying the Absolute Evaluation Method to Landslide Risk Evaluation When Using Aerial Photographs

The main goal of applying the method in risk-evaluation system structures when using aerial photographs is to convert the implicit knowledge possessed by the landslide engineers into explicit knowledge. In other words, by expressing judgments (“dangerous,” “safe” etc.) that rely on experience and intuition as a numeric risk score, a common evaluation axis can be created. It will be accepted by more people since it will be objective. Also, if the resulting “explicit knowledge” is set down in a textbook, and if risk points and the order of risk weights are organized, it will create a cornerstone, enabling students just starting their study of landslide engineering to easily draw upon the knowledge of their predecessors.

This is not possible with methods other than Analytic Hierarchy Process. The method is deemed particularly well-suited for the following three reasons.

1. In constructing the landslide risk evaluation method, it is difficult to obtain with standable load and uniform analysis data. In other words, in the field where landslides have actually occurred, it is very rare to obtain all of the items—quantity, topography, and geology—of the elements used in making judgments.
2. Even if a number of experienced landslide engineers are brought together, each has a

different level of experience, making normal statistical methods (such as surveys) difficult. Each engineer’s field or area of landslide expertise will be slightly different, making it hard to decide on an evaluation axis using normal methods.

3. Brainstorming among experienced engineers is critical to determining evaluation items and evaluation axes. For this, “quality control,” at which the Analytic Hierarchy Process method excels, is better than “regular statistical analysis.”

2.4 Converting Implicit Knowledge into Explicit Knowledge

Here we will consider a framework for converting implicit knowledge into explicit knowledge. Consider the relationship between a person’s face and their age. Generally, people can intuitively judge the ages of others within their population group—for instance whether they are in their 30s–40s, or around 20.

Moreover, as shown in Fig. 2, people can, mostly correctly, arrange many people in order of age by comparing their faces and sorting them. In particular, in cases where there are only subtle differences between the people, careful guesses must be made, while doing paired comparisons of the faces.

This is precisely the essence of Analytic Hierarchy Process. That is, if the intuitive judgment criteria we use to determine a person’s age can be clarified, hierarchized, and a weighted evaluation A trial evaluation of the five people in Fig. 1 based

Fig. 1 A hierarchy chart for a new car purchase

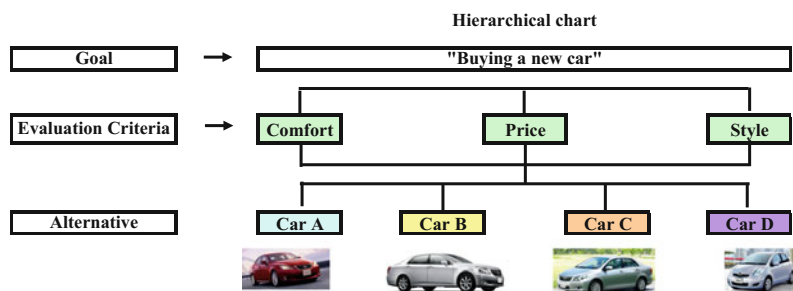


Table 4 Analytic hierarchy process relative comparison method for evaluating criteria for judging age from faces between five people, A–D

Apparent age	Number of wrinkles	Extent of sagging	Amount of hair	Texture and gloss of skin	Geometric mean	Weight
Number of wrinkles	1	2	3	7	2.55	49
Extent of sagging	1/2	1	2	5	1.50	29
Amount of hair	1/3	1/2	1	2	0.76	15
Texture and gloss of skin	1/7	1/5	1/2	1	0.35	7
					5.15	100

Table 5 AHP evaluation performed by absolute comparisons between five people, A–D

	Weight	Evaluation axis			A		B		C		D		E	
		1	0.5	0	a	a*w	b	b*w	c	c*w	d	d*w	e	e*w
Number of wrinkles	49	Many	Average	None	0.8	39.6	0.3	14.8	0.1	4.9	1.0	49.5	0.5	24.7
Extent of sagging	29	Much	Average	None	0.7	20.3	0.4	11.6	0.1	2.9	1.0	29.1	0.6	17.4
Amount of hair	15	None	Average	Thick	0.5	7.4	0.3	4.4	0.1	1.5	0.7	10.3	0.3	4.4
Texture and gloss of skin	7	Rough	Average	Smooth	0.2	1.3	0.6	4.0	0.2	1.3	0.3	2.0	0.5	3.4
Evaluation on absolute scale					Sum	67	Sum	31	Sum	11	Sum	89	Sum	47

on these criteria was performed. The results, shown in Table 4, generally indicate the appropriate ages. This is the essence of the Analytic Hierarchy Process method made, this evaluation method will lead to “explicit knowledge.”

In Table 5, paired comparisons using Analytic Hierarchy Process were made along the evaluation axes of “Number of wrinkles,” “Extent of sagging,” “Amount of hair,” and “Texture and Gloss of skin.” To the right of the table, weights derived from the table are shown. A standard is prepared for each.

3 Creating Evaluation Criteria

3.1 General Categories

Persons experienced in landslides in Japan (Tohoku) compiled their previous experience with

landslides in the Tohoku region, then created a hierarchy of evaluation criteria for interpretation based on this experience. As a result of brainstorming the engineers judged that three general classifications are important, as shown in Figs. 3 and 4: “(α) landslide body micro-topography,” “(β) landslide body boundary,” and “(γ) topography surrounding the landslide body”.

- α. Landslide body micro-topography (index related to movement characteristics) Various kinds of micro-topography, mainly distributed within the region of the landslide body, suggesting movement characteristics, and their spatial placement.
- β. Landslide body boundary (index related to time elapsed) Extent of dissection, due to subsequent non-landslide processes, i.e. constant topographical fluctuations, of

Fig. 2 Estimating age through faces between five people, A–D

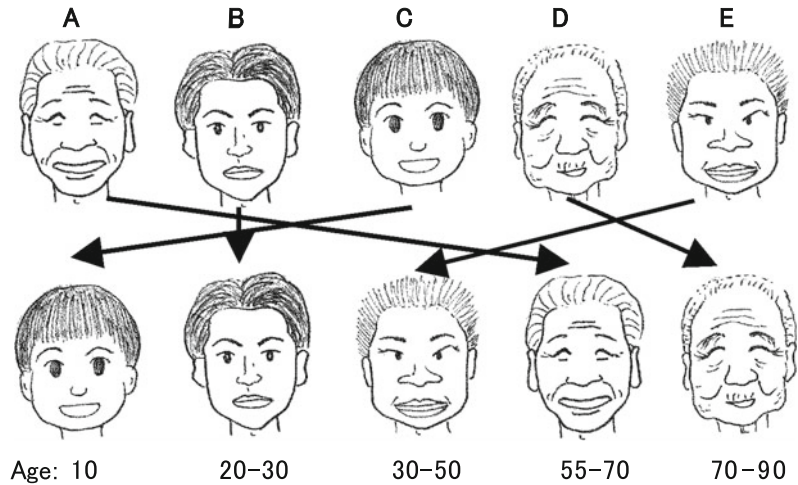
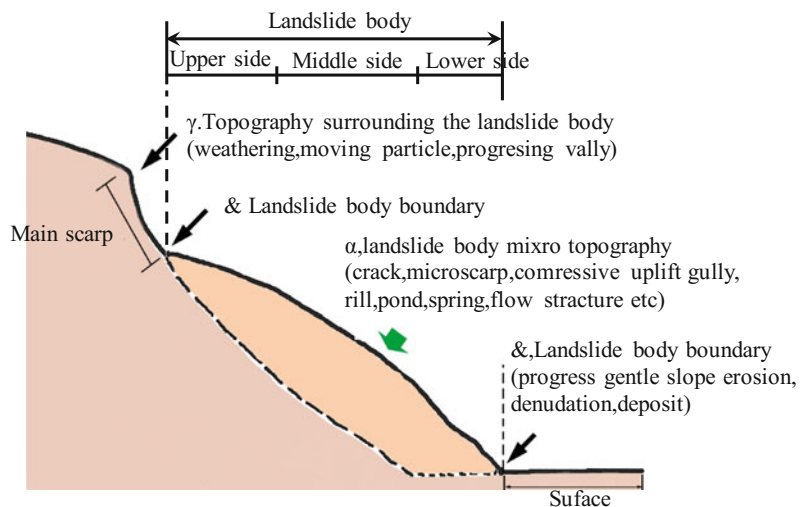


Fig. 3 Diagram of interpretation items (Miyagi et al. 2004)



displacement traces remaining around the landslide circumference.

γ. Topography surrounding the landslide body (index related to the topographic area). Factors impacting stability of the landslide body’s displacement. Here, topographical area refers to the topographical location where the landslide is occurring.

3.2 Categories of Evaluation Criteria and Weighting

Japan’s National Research Institute for Earth Science and Disaster Prevention (the former

National Research Center for Disaster Prevention) has conducted large-scale aerial photography projects which have been published since 1982 as topographic landslide maps with a scale of 1:50,000 (Fig. 5). In addition, the Tohoku research group of the Japan Landslide Society has developed a risk assessment system based on aerial photography maps (Hamasaki et al. 2003; Miyagi et al. 2004; Yagi and Higaki 2009, Hamasaki 2013).

A large number of landslide experts participated in the building of this model. Based on the experience points of each expert, the AHP has been applied to stratify the conditions of the evaluated micro topography and its surrounding

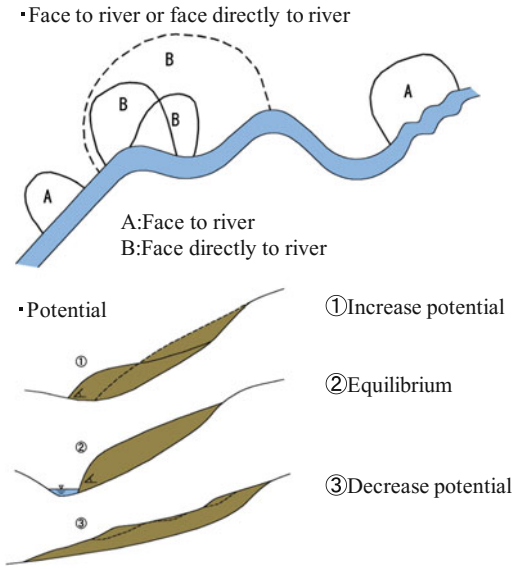


Fig. 4 Landslide topography and surrounding environment written by Mr. Tsurumi (Miyagi et al. 2004)

areas. Building on these procedures, evaluations of the weight of the decision standards have been discussed. In principle, this approach applies the AHP absolute evaluation method: scored decision standards are integrated into a data sheet while a risk assessment is conducted through the inclusion of level checks for each decision element. That is, established standards for each evaluation item are stratified with declining scores from left to right. As such, this system allows for decisions through ‘paired comparisons’ thus avoiding deviation in decision on each item of a respective slope ground. After the completion of this AHP risk assessment model, our model region investigated has witnessed several cases of landslide through earthquakes and thaw, as well as rainfall. Most of these landslides occurred in areas considered to be high risk under the AHP assessment system, thus proving the model’s validity.

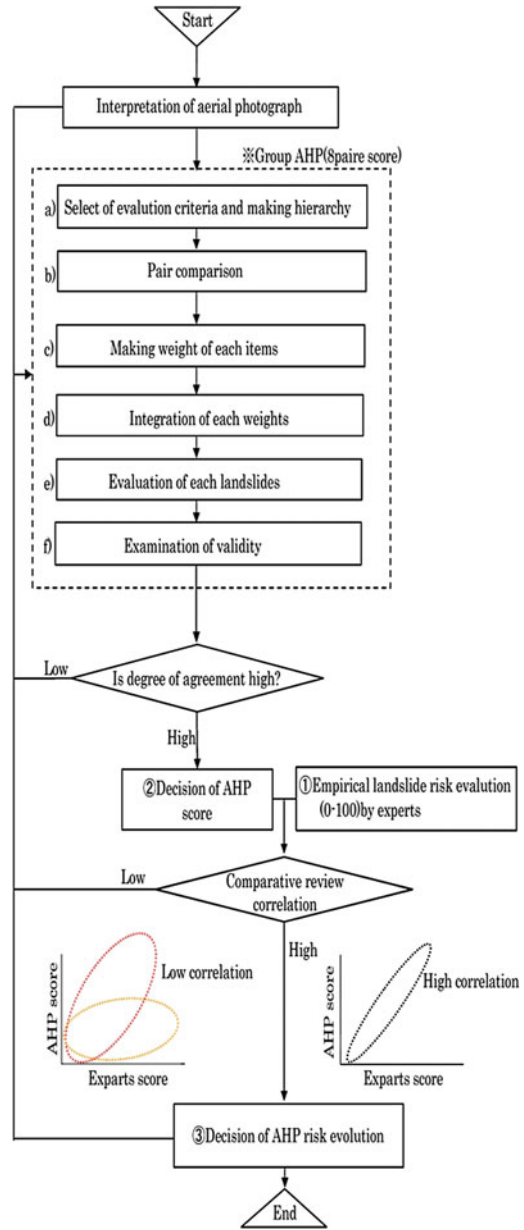


Fig. 5 Flow chart showing the determination process for the analytic hierarchy process score weights in Tohoku district, Japan (Miyagi et al. 2004)

3.3 Definition of Landslide Topography and Occurrence Risk, and Scope/Perspective of Interpretation

1. Definition of landslide topography

Landslide activity forms a characteristic “landslide topography” that can be distinguished from other topographical units. In other words, “landslide topography” is the topographical structure of the main scarp and landslide body formed by the landslide.

Consequently, the “landslide topography” used here for risk assessment is the most exterior part within the region topographically distinguishable from the surrounding slope as a result of past landslide displacement (including all micro-topography formed as a result of displacement).

Although bedrock fluctuations, such as bedrock creep, are sometimes mentioned among phenomena that lead to landslides, they are basically beyond the scope of the risk assessment considered here (Fig. 6).

2. Definition of occurrence risk

This refers to the probability of occurrence of the next landslide phenomena (including repeated displacements) somewhere within the “landslide topography” as defined in (1) above. The unit of risk evaluation is the entire “landslide

topography,” regardless of the location where the phenomenon occurs. However, this limit does not apply when the unstable portion is small in area, and the phenomenon is disconnected from the overall landslide failure chain. Also, the occurrence of landslides due to human impact, such as artificial land modification, is a major geological factor, but is beyond the scope of this evaluation. Here, “occurrence risk” refers only to likelihood of occurrence, and is not an evaluation of scale of occurrence or impact on surroundings at the time of movement.

In cases where the entire “landslide topography” is evaluated using a partial, unstable region within it, the interpretation figure will clearly indicate said region; the presence or absence of other such regions, and its position and relative relationship with regard to the entire earthquake topography will also be noted in the “Landslide causes, other” section of the chart.

The items below are given for background information. The majority of landslides that occur in Japan are due to repeated displacement of past landslides.

Causes (or contributing factors) of landslide occurrences that formed the current topography may include sudden events, such as earthquakes. However, in keeping with the goals of risk evaluation (determining the likelihood of the next displacement) described here, contributing factors such as earthquakes and rainfall will not be included in our considerations/evaluation.

3. Scope of interpretation and positioning of items within landslide topography

The scope of interpretation is essentially the “landslide topography” as defined in (1) above, its internal micro-topography, and its surrounding environment. Bedrock creep will also be considered, but basically only for reference; it should be recognized that landslide risk assessment is a difficult matter. We will attempt to use the Analytic Hierarchy Process to rank and score each item, but in aerial photo interpretation, it is rare for there to be just one category in each item category; in most cases, there will be many. In

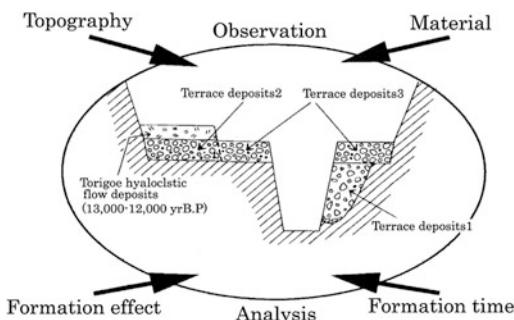


Fig. 6 Relationship of four elements controlling the topography of a river terrace

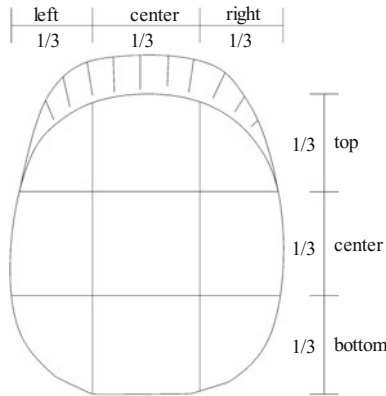


Fig. 7 Grid for defining positions within a landslide

terms of making judgments on safety, it is advisable to focus on instability checks, even in the middle of the category. In order to show the micro-topography that is subject to interpretation, the position of the landslide interior is defined in Fig. 7. The length and width of the landslide have been divided into thirds—right, center, left; top, center, bottom. Positions in the description will follow this pattern.

4. Perspectives on interpretation

- (1) Natural slopes are subject to continuous, constant topographical fluctuations, caused by processes such as weathering, erosion, and sedimentation.
- (2) Landslides occur intermittently and suddenly. Actual landslide topography is structured by a combination of landslide-prone topography and the above-mentioned topography. These two topographical phenomena are rigorously distinguished in photographic interpretation.
- (3) The risk of landslide occurrence is high for newer and more recently active landslides, as repeated activity occurs easily. The scope of the above two topographical phenomena are compared, and the amount of elapsed time since landslide activity is sought.

- (4) The landslide body degrades with repeated activity, leading to increased viscosity of soil, and a higher tendency toward repeated activity. Part of the micro-topography that structures the landslide body displays physical properties of the landslide body.
- (5) For locations where no landslide is occurring, evaluations cannot be performed for initial landslides, nor for landslide topographies where the main scarp and landslide body have been mostly lost.

In topographical approaches to risk evaluation, (2), (3) and (4) above are performed via photographic interpretation.

3.4 The Analytic Hierarchy Process Method

1. Abstracting and classifying evaluation criteria within the Analytic Hierarchy Process

The working group should brainstorm to abstract evaluation criteria related to landslide risk, and classify them as shown in Fig. 5. First, separate base-line items for “landslide risk evaluation” into three general levels.

General categories are: (α) “landslide body micro-topography” as an index related to movement characteristics, (β) “landslide body boundary” as an index related to time elapsed, (γ) “topography surrounding the landslide body” as an index related to the topographic area.

Further subdivide each of these into six intermediate elements: (a) mode of movement, (b) landslide body micro-topography, (c) head boundary, (d) toe boundary, (e) tip of landslide body tip, (f) potential.

Create categories (minor elements) for the intermediate elements that will be the check indexes of the actual chart, and use the Analytic Hierarchy Process method to make paired comparisons for each of the major elements, intermediate elements, and minor elements. For practical purposes, the categories shown in Fig. 8

are arranged by intermediate items so that risk level increases from bottom to top.

These items were organized from left to right when the chart was created, to facilitate understanding of topography formation mechanisms. Incidentally, this structure permits the position of checks for categories to be placed between categories. In other words, in Fig. 8, if item F was determined to be between “talus” and “large scale talus,” a check could be placed between the two.

However, when it is clear that multiple categories exist, the contribution of the one with the most weight is given priority.

2. Paired comparisons, determining and integrating weights

First, each person in the working group implements Analytic Hierarchy Process evaluations. The results are used as a springboard for creating the group’s Analytic Hierarchy Process weights.

Here, we have set the Analytic Hierarchy Process paired comparison values as follows.

- 1: Both elements are about equally important.
- 3: Previous element is slightly more important than following one.
- 5: Previous element is slightly more important than following one.
- 7: Previous element is much more important than following one
- (Other: 2, 4, 6, and 8 are interpolative values).

There are many references on calculating weight for each item in Analytic Hierarchy Process paired comparisons, but when finding the final weight for each category, we used the formula:

Final weight of minor element category = general AHP weight \times intermediate AHP weight \times minor AHP weight.

Among the coefficients obtained from integrating the weights, when checking the highest categories in the intermediate items a-f, compensating coefficients are added so that the total will be 100.

On the chart, the total of these check scores are termed the Analytic Hierarchy Process scores (total of model weight coefficients). In other words:

$$\text{AHP score} = \alpha \cdot \sum X(A \sim I)$$

Here α is the compensating coefficient

3. Paired comparison and weight determination methods

The specific steps for determining weight are as follows.

- (1) Paired comparison of “general categories” related to risk estimation.

At this stage, 3×3 paired comparisons are made, based on:

- I. Landslide body micro topography;
- II. Landslide body boundary; and
- III. Landslide body and surrounding environment.

For example, a matrix is shown below for paired comparisons assuming that “landslide body micro-topography is three times more important to risk evaluation than landslide body boundary.” In the Analytic Hierarchy Process method, paired comparisons are performed in the same way for all elements, then geometric means are found for the horizontals of the matrix, and these ratios are converted into weights (Fig. 8).

4. Final inspection sheet for Landslide risk evaluation using AHP in Croatia

The Croatian working group carried out interpretation and made charts to build a consensus on risk evaluation methods. As a result, they were able to create a road map for a rational, objective quantification method. Moreover, when this method was applied to landslides occurring in the Tohoku region, it was shown to be largely suitable.

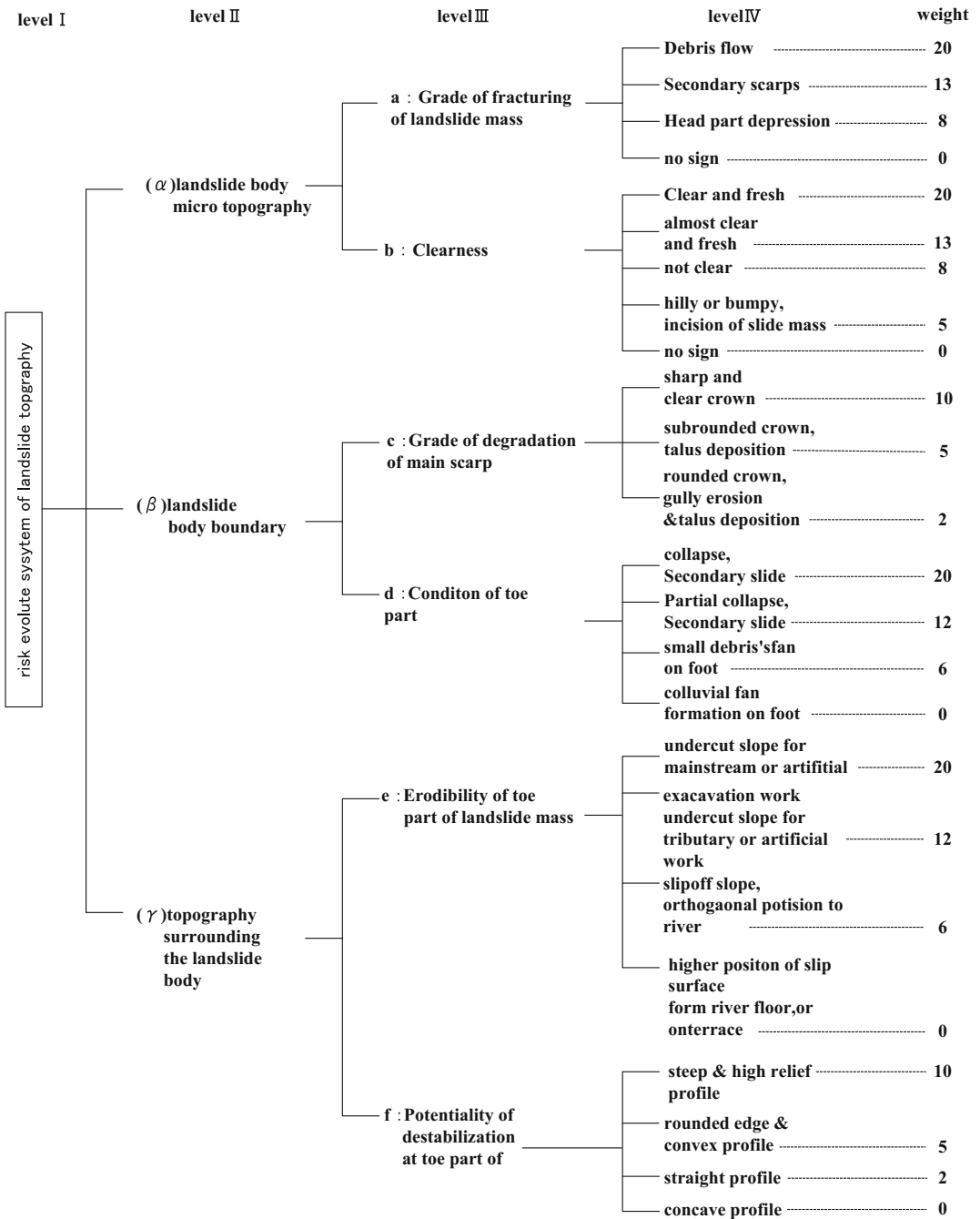


Fig. 8 Risk evaluation criteria for landslide topography

		Check list for risk evaluation of landslide				AHP score
Level II	Level III	Indicative signs of instability				sum
		High			Low	
A	a	20 Debris flow Mudflow, earth flow	13 Secondary scarp Secondary multi slump, mudflow	8 Head part depression Minor scarp crack, pressure ridge	0 no sign	
	b	20 Clear and fresh Closely-spaced scarps & linear depression	13 almost clear and fresh a series of scarps & linear depression	8 not clear rounded scarps & burried depressions	5...0 hilly or bumpy, incision of slide mass	
B	c	10 sharp and clear crown	5 subrounded crown, talus deposition	2 rounded crown, gully erosion & talus deposition		
	d	20 collapse, Secondary slide	12 Partial collapse, Secondary slide	6 gullies small debris' fan on foot	0 colluvial fan formation on foot	
C	e	20 undercut slope for mainstream or artificial excavation work	12 undercut slope for tributary or artificial work	6 slipoff slope, orthogonal position to river	2 terrace higher position of slip surface from river floor, or on terrace	
	f	10 steep & high relief profile	5 rounded edge & convex profile	2 straight profile	0 concave profile	

Fig. 9 Inspection Sheet for Risk evaluation of landslide topography using AHP method

During the Croatian disaster relief project, Profs. Miyagi, Yagi, and Hamasaki utilized their experience to rigorously narrow down the number of items and implemented weighted evaluations. To evaluate risk, this system uses an aggregate Analytic Hierarchy Process result, in which 100 is the highest score, and 0 the lowest. In other words, the Analytic Hierarchy Process score is the risk evaluation score for that point in time (Fig. 9).

assessment system, as well as on the necessary conditions of using the AHP method. Furthermore, as a teaching tool we have elaborated on the process of transforming ‘tacit knowledge’ into ‘explicit knowledge’. Here, we applied the example of guessing ‘a person’s face and age’ to illustrate the utility of the AHP method. In conclusion, the AHP method has achieved tutorial application.

4 Conclusion

Here, we have explained on the conventional methods in the form of the ‘AHP relative evaluation method’ and the ‘AHP absolute evaluation method’ and elaborated on the possibility of applying the approach to a slope

References

Hamasaki E, Hirai T, Miyagi T (2003) Evaluation of the probability of landslide occurrence by AHP based on the Results of Aerial-photo Interpretation. In: Conference proceedings of the 42nd annual meeting of Japan Landslide Society, 19–22 August 2003, Japan. pp 227–230
 Hamasaki E (2013) Structure of the AHP method, and landslide risk evaluation system based on it, Daichi ga

- ugoku. Tohoku branch of Japan Association for Slope Disaster Management, Japan, pp 20–48
- Miyagi T, Prasada GB, Tanavud C, Potichan A, Hamasaki E (2004) Landslide risk evaluation and mapping—manual of landslide topography and risk management, Report of the National Research Institute for Earth Science and Disaster Prevention No. 66, pp 75–137
- Saaty TL (1980) The analytic hierarchy process. McGraw-Hill Book Company, New York, p 265p
- Yagi H, Higaki D (2009) Methodological study on landslide hazard assessment by interpretation of aerial photographs combined with AHP in the middle course area of Agano River, Central Japan. *Jpn Landslide Soc* 45(5):356–366

TXT-tool 4.039-3.1 Terrestrial Laser Scanner and Geomechanical Surveys for the Rapid Evaluation of Rock Fall Susceptibility Scenarios

Giovanni Gigli, Stefano Morelli, Simone Fornera
and Nicola Casagli

Abstract

This paper is aimed at presenting a semiautomatic procedure that, coupled with conventional methods, can be useful for a prompt definition of rock fall susceptibility scenarios with civil protection purposes. Due to its landscape morphology (steep slopes and narrow valley), regional seismicity, and rock mass characteristics, the Nera Valley (Valnerina, Umbria Region, Italy) is highly prone to rock falls. In order to cover a wide range of features and investigate the main advantages and drawbacks of the proposed approach, data collection was carried out in three different slopes by means of terrestrial laser scanning (TLS) and geomechanical surveys. Detailed three-dimensional (3D) terrain models were reconstructed to obtain the geometry of the most unstable blocks, to define the position of the main rock fall source areas, and to precisely distinguish the outcropping materials and the position of the elements at risk for reliable runout analyses. Consequently, the proposed approach can positively support proper maintenance and land management programs both in ordinary and in emergency circumstances.

G. Gigli (✉) · S. Morelli · S. Fornera · N. Casagli
Department of Earth Sciences, University of Firenze,
via G. La Pira n.4, I-20121 Florence, Italy
e-mail: giovanni.gigli@unifi.it

S. Morelli
e-mail: stefano.morelli@unifi.it

S. Fornera
e-mail: sformera@gmail.com

N. Casagli
e-mail: nicola.casagli@unifi.it

Keywords

Rock mass · Landslide · Kinematic analysis · DiAna · Valnerina

Contents

1 Introduction	478
2 Investigated Area	479
3 Data Collection	480
3.1 Laser Scanning Survey.....	480
3.2 Traditional Geomechanical Survey.....	480
4 TLS Data Processing	481
4.1 Analysis of Rock Mass Discontinuities.....	481
4.2 Estimation of Block Volumes.....	482
4.3 3D Surface Creation.....	483
5 Susceptibility Scenarios	484
5.1 Kinematic Analysis.....	484
5.2 Rock Fall Simulations.....	485
6 Discussion and Conclusions	486
References.....	489

1 Introduction

Rock falls are common fast-moving slope failures from steep rock faces or cliffs that can affect long stretches of road infrastructures and other communication routes, villages, isolated dwellings, and other anthropic goods. Due to their hard unpredictability and high velocities, these events can cause casualties, even where the mobilized mass is very small (less than 1 m³) (Hungri et al. 1999).

Rock fall risk is usually analyzed through performing two-dimensional (2D) (Azzoni et al. 1995; Pfeiffer and Bowen 1989; Piteau and Clayton 1976; Rocscience 2005) or three-dimensional (3D) (Agliardi and Crosta 2003; Descouedres and Zimmermann 1987; Dorren and Seijmonsbergen 2003; Guzzetti et al. 2002; Lan et al. 2007) simulations, with the aim of evaluating runout distances, velocities (and associated kinetic energy), and bounce heights of falling blocks. Rock fall trajectory is controlled by local topography, the source area location, the mechanical properties of outcropping materials (Ritchie 1963), and falling rocks properties such as their shape and mass (Giani 1992). However, these parameters are often difficult to evaluate and the most common approach is based on probabilistic analyses by statistically varying the input parameters that are

characterized by the highest uncertainties (Azzoni et al. 1995; Giani et al. 2004; Hoek 2000).

The proposed methodology aims at objectively, rapidly, and accurately defining the detailed topography of the slopes, the accurate 3D position of the objects of interest (such as element at risk, existing protective measures, etc.), block shape and dimension, and the main rock fall source areas (through a 3D kinematic analysis). Several researchers have already dealt with some of these topics either from photogrammetric or LIDAR data (Abellan et al. 2006, 2010; Armesto et al. 2009; Bauer et al. 2006; Ferrero and Umili 2011; Ferrero et al. 2009, 2011; Lato and Vöge 2012; Mikos et al. 2005; Rosser et al. 2005; Strouth and Eberhardt 2005; Wickens and Barton 1971). The proposed approach is presented in Fig. 1. It is composed of two main steps: in situ data collection and data processing (scenario definition). During the first phase, a Terrestrial Laser Scanning (TLS) campaign was performed together with a traditional geomechanical survey in order to create integrated high-resolution 3D models with the following objectives: to calculate the spatial geometry of blocks involved in rock falls, to perform kinematic analyses of the main

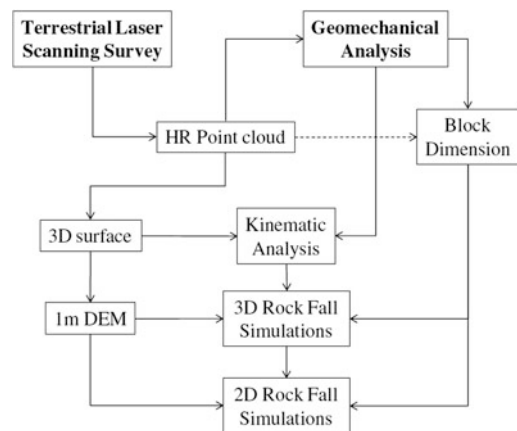


Fig. 1 Logic scheme of the proposed procedure: the geometric input parameters are all obtained through TLS data processing

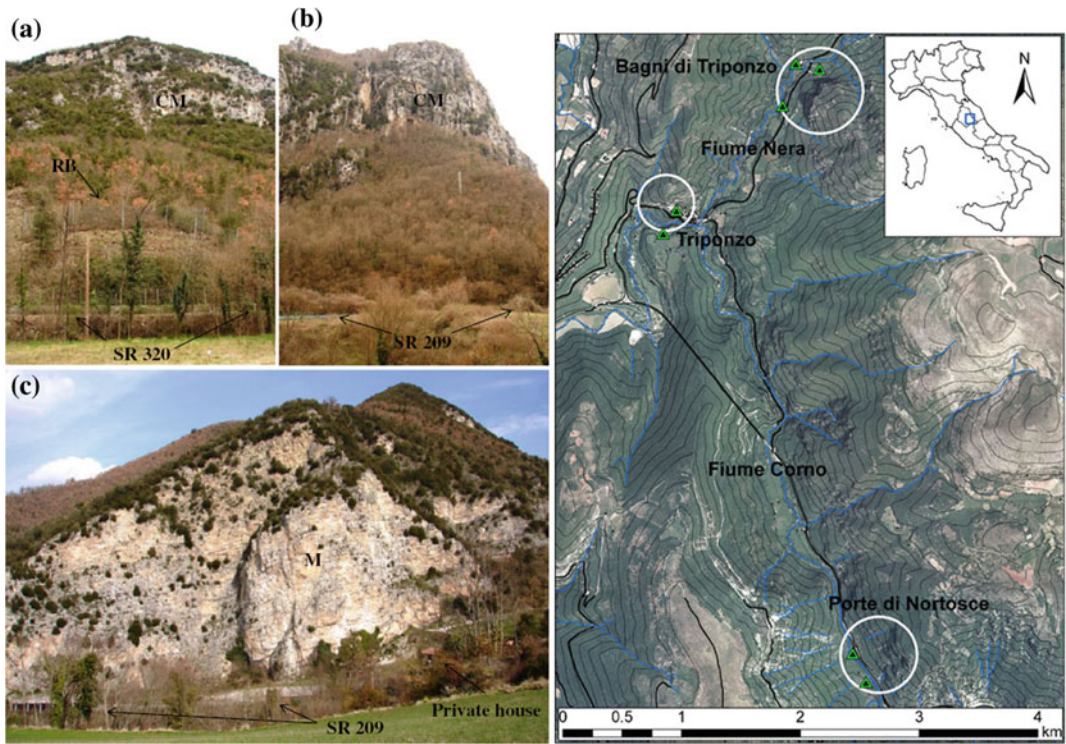


Fig. 2 (Left) Comprehensive location map of the investigated sites (white circles), triangles indicate TLS observation points; (right) detailed view of the investigated rock outcrops: **a** Ponte di Nortosce, **b** Bagni di

Triponzo, and **c** Triponzo. The main elements at risk, the location of rock fall barriers (RB), and the symbols of the outcropping geological formations are also reported: CM Calcare Massiccio, M Maiolica

mechanisms of instability, and to reconstruct the trajectories followed by the blocks and their associated energy. The proposed procedure has been applied on three different test sites in order to be representative of the entire investigated area. These are located in the central sector of Valnerina (Umbria Region, Italy) (Fig. 2), where the Calcare Massiccio (massive limestone) and the Maiolica (micritic limestone) Formations outcrop.

2 Investigated Area

Valnerina is a narrow valley formed by the evolutionary dynamics of the Nera River. This valley is delimited by rugged mountains, which are characterized by high rock fall risk because of its rough morphology, local seismic activity, and heterogeneous rock mass fracturing. Rock falls

abound near the Triponzo village; in September and October 1997, a seismic sequence affected the investigated area (Amato et al. 1998; Carro et al. 2003; Marzorati et al. 2002) and many rock fall events seriously damaged the main roads in the valley floor and the village itself (Guzzetti et al. 2004, 2009). All these features make the Valnerina a suitable place where the proposed procedure for the quick and complete definition of susceptibility scenarios associated with rock mass instability can be tested.

Three different rock slopes were analyzed (Fig. 2): the Calcare Massiccio outcrops located at Ponte di Nortosce (Fig. 2a) and Bagni di Triponzo (Fig. 2b) and the Maiolica subvertical rock wall close to the Triponzo village (Fig. 2c). Almost everywhere, the rock outcrops are characterized by steep slopes, vertical walls, and ledges.

In this area the overall stratigraphy is typical of the Umbria-Marche region: the lower part (lower

Lias) consists of massive limestones of the carbonate platform (Calcare Massiccio) and the upper part is composed of stratified or thinly laminated formations, mainly marly and cherty limestones, deposited in a pelagic environment from the middle Lias to the Oligocene (Barchi et al. 1993). The local landforms are closely related to the nature of the rock varieties and to the structural setting (Guzzetti et al. 2004). In areas where limestones are characterized by high mechanical strength outcrop (e.g., Maiolica and Calcare Massiccio), the soil thickness is reduced or absent, the slopes are very steep (ranging from 40° to 90°), and rock falls are the most common instability mechanisms. Most of the landslide slip surfaces are located in areas dominated by calcareous marly lithology, where the slopes are less steep even though the gradients are high (25° – 40°). Here, the clayey elements constitute impermeable barriers for the groundwater flow, so that the mechanical weakness, in conjunction with the permeability limits at structurally oriented surfaces, is a key factor in influencing the location and the type of landslides (Barchi et al. 1993).

3 Data Collection

Thanks to its high accuracy, resolution, and quick data collection, the TLS technique is widely used in rock fall studies (Abellan et al. 2006; Fanti et al. 2012; Gigli et al. 2012; Jaboyedoff et al. 2012; Lan et al. 2010; Lato et al. 2009, 2012; Tapete et al. 2012). The selected case study is an excellent application for exploiting the advantages of TLS, since it was impossible to directly reach the rock outcrops, with the exception of the lowest limit of the rock face close to the Triponzo village. In this site, the main rock mass geomechanical properties were also collected using traditional survey methods in order to validate the results derived from the TLS elaborations.

3.1 Laser Scanning Survey

The laser scanning investigation was performed by means of a long range 3D Terrestrial Laser

Imaging Sensor (RIEGL LMS-Z420i device), with an accuracy of 0.01 m (one σ at 50-m range under RIEGL test conditions). The laser scanning output is an array of points, called a point cloud, which is a set of vertices defined in a 3D coordinate system (x, y, z), able to reconstruct a highly detailed 3D environment. With the aim of experimenting a rapid application of the proposed approach, TLS surveys were carried out from easily reachable points that, in Valnerina, are located along the main roads only (Fig. 2). The objective of the TLS campaign was to build 3D surface models of the whole slopes to be investigated (for the kinematic analyses and rock fall simulations) and to reconstruct the geomechanical features of the rock masses (for the identification of the main rock fall source areas and the evaluation of the shape and volume of falling blocks). To accomplish this dual objective, either raw point clouds or derived surfaces have been employed. For this reason, the angular resolution for each scan position has been selected by choosing the best arrangement between the number of points (to avoid large and too heavy datasets) and the distance between contiguous points on the rock slopes, which must be related to the minimum dimension of the features to be extracted (i.e., discontinuity surfaces, anthropic structures, and Digital Elevation Model resolution). Due to the roughness of the slopes and to the scan position constraints, with the aim of limiting the shadow areas as much as possible, each slope has been investigated from different observation points. Seven scan positions have been performed to cover all the investigated sites, and more than 70 million points were collected. The resulting point clouds were subsequently aligned and georeferenced by using a geodetic GPS antenna to determine the accurate position of a number of scanned tie points (Morelli et al. 2012).

3.2 Traditional Geomechanical Survey

The traditional quantitative description of discontinuities was executed using analytical methods proposed by the International Society for

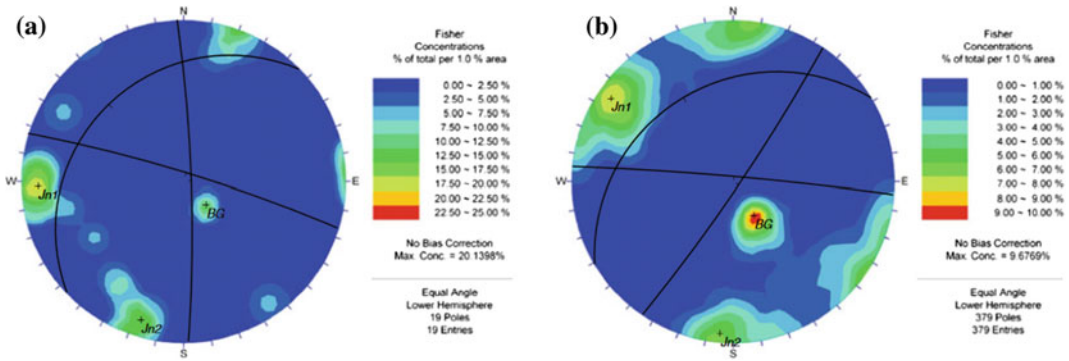


Fig. 3 Stereographic projection of concentration lines of discontinuity poles and modal planes of discontinuity sets: **a** from traditional geomechanical survey and **b** extracted from TLS data through the semiautomatic procedure

Table 1 Discontinuity set orientation and standard deviation from field survey and TLS data processing at Triponzo site

	Field survey			Semiautomatic extraction		
	α (°)	β (°)	σ (°)	α (°)	β (°)	σ (°)
JN1	087	82	6.6	124	85	16.3
JN2	021	85	8.4	005	7	14.1
BG	318	23	11.0	329	28	12.9

Rock Mechanics (1978) which is a scanline survey. This survey was carried out for validation purposes on the sole easily accessible rock mass exposure, located close to the Triponzo village (Fig. 2c). Discontinuity orientation data were represented in stereographic projection (lower hemisphere) for the recognition of the main sets (Fig. 3a). The resulting modal plane orientation and standard deviation of each set are reported in Table 1.

4 TLS Data Processing

4.1 Analysis of Rock Mass Discontinuities

An important limitation of traditional geomechanical surveys often consists in the difficulty to reach the rock walls. Another common problem, is the intrinsic danger of the site when dealing with active landslides. The laser scanning technique, on the other hand, allows to remotely, quickly, and accurately measure all the main geometric characteristics of a rock mass. To perform this task, the raw point clouds were

employed (Fig. 1). This choice was supported by the need of keeping the maximum spatial resolution, so that even the smallest features could be detected. In this case, the presence of vegetation was not a problem. In fact, the TLS acquisition was scheduled in order to correct geometrically irregular portions of the point clouds, which can be associated to vegetation. If the 3D model is correctly georeferenced, by estimating the best-fitting plane of a point cloud subset (associated to a discontinuity surface), it is possible to directly determine its dip and dip direction. This manual procedure was applied to the rock slopes where the Calcare Massiccio formation outcrops (Ponte di Nortosce, in Fig. 2a and Bagni di Triponzo in Fig. 2b) (Fig. 4a). Here, the rock mass is characterized by very poor and irregular fracturing, and the point to point spacing is too high (due to the distance of up to 500 m from the scan positions) for the application of a semiautomatic procedure, as described afterwards. A semiautomatic extraction procedure was also tested on a portion of the point cloud representing the rock mass next to the Triponzo village.

Rock faces with rugged shape can be investigated by inspecting the discontinuity surfaces

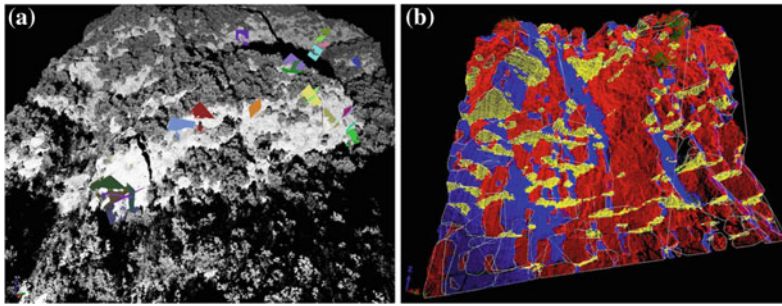


Fig. 4 Extraction of discontinuity orientation from TLS data: a manual selection and best-fitting plane calculation at Ponte di Nortosce and b semiautomatic extraction at Triponzo. *Red* discontinuity set Jn1, *blue* Jn2, *yellow* BG

exposed on the slope. Such 3D approach requires the extraction from the point cloud of clusters of points belonging to the same discontinuity plane; subsequently, a spatial analysis for the quantitative description of discontinuities within the rock mass has to be performed. The adopted approach consists of a MATLAB tool, which is explained in Gigli and Casagli (2011a). It is based on the definition of least-squares fitting planes on clusters of points extracted by moving a sampling cube on the point cloud; the cube size is based on TLS data resolution and on the dimension of the features to be investigated. If the associated standard deviation is below a defined threshold, the cluster is considered valid. By applying geometric criteria, it is possible to join all the clusters lying on the same surface; in this way, discontinuity planes can be reconstructed, and rock mass geometrical properties are calculated.

The advantage of using this procedure lies in its capability to investigate all the geomechanical parameters that do not require direct access to the rock mass. The output International Society for Rock Mechanics (1978) parameters are: orientation, number of sets, spacing/frequency (and derived RQD), persistence, block size, and scale-dependent roughness. The latter parameter can be measured if high resolution data (i.e., centimetric point–point distance) are available on large discontinuity surfaces (Gigli and Casagli 2011b). Compared to the manual recognition of discontinuities, this methodology allows the identification of a larger number of surfaces, according to an objective choice criterion. A total number of 379 discontinuities were extracted

from the investigated portion of the point cloud (Fig. 4b), and their dip and dip direction values were then represented in a stereographic projection (Fig. 3b). Again, three main discontinuity sets are evident, the modal orientations and standard deviation of which are reported in Table 1.

4.2 Estimation of Block Volumes

Block volume is a fundamental parameter for performing reliable rock fall simulations (Fig. 1), as it directly influences the kinetic energy expected along the trajectory. Moreover, block predisposition to move with a rolling behaviour and high runout distance strongly depends on its shape and dimension (Evans and Hungr 1993; Giani et al. 2004). Within the proposed approach (Fig. 1), the information about the block volumes were acquired by TLS data and compared with field observations and bibliographic sources (Table 2).

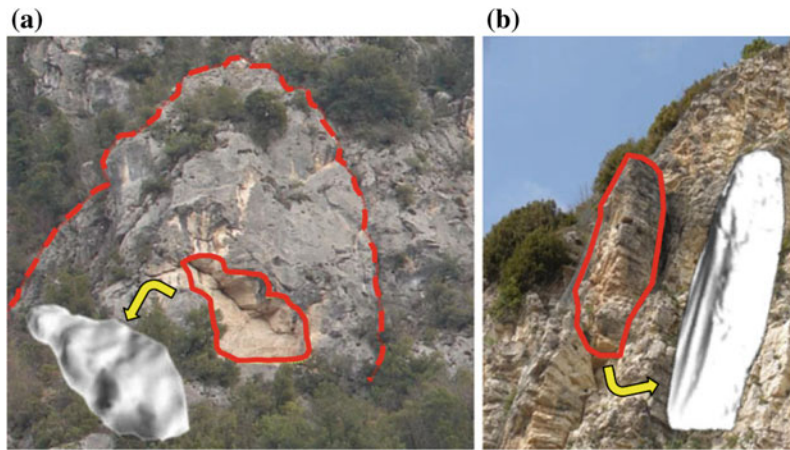
As regards the Triponzo site, complete geomechanical geometric data were extracted through the semiautomatic procedure described above and validated with field data. Thus, it has been possible to calculate mean and maximum block size based on the number of sets and their true spacing (Palmstrom 2005). The resulting mean size was 0.27 m^3 , corresponding to a mass of approximately 750 kg; therefore, according also to field evidences, a precautionary mass of 1000 kg was considered for the rock fall simulations at this site (Table 2). By analyzing the high resolution point

Table 2 Comparison of block dimension (in m³) for each investigated lithology, extracted from the field surveys, the literature, and TLS data processing, and the one employed in the rock fall simulations

	Field surveys from geomechanical data (Palmstrom 2005)	Inventory (max)	Inventory (mean)	Antonini et al. (2002)	TLS from geomechanical data (Palmstrom 2005)	Measured mean ^a	Employed in simulations
Calcare Massiccio	/	3.9	1.2	4.6	/	2.8	5
Maiolica	0.21	0.32	0.13	/	0.27	/	0.35

^aOnly two block volumes calculated from TLS data

Fig. 5 Reconstruction of the shape and size of unstable blocks from the TLS data: **a** Ponte di Nortosce and **b** Triponzo



cloud, the volume of a large block about to topple was also reconstructed at Triponzo (Fig. 5b). Here, the rock mass is broken down into columnar elements because of the local discontinuity sets pertaining to the Maiolica formation. Due to the block position and to the extreme verticality of the slope, direct surveys were not possible and consequently, accurate measurements were performed only by means of the TLS data. The calculated volume was 136 m³, with an estimated mass of about 379 t. The block is covered with rock fall protection wire net. just to keep boulders of limited size. A large unstable mass delimited by persistent discontinuities was identified from TLS data at Ponte di Nortosce (dashed line in Fig. 5a); within the same outcrop, a recent mass detachment was also present (continuous line in Fig. 5a). These blocks were virtually reconstructed and their calculated volumes were 1024 m³ and 15 m³, respectively, representing masses of about 2660 t and 39 t. A quick in situ inventory of fallen blocks revealed a

maximum block size of 3–4 m³ (Table 2). This difference is mainly ascribable to the breakage of the blocks whenever they impact on the ground during the movement on the slope.

Two detached block volumes were also measured by analyzing TLS point clouds (Table 2). The block sizes found by the surveys agree with those sampled by Antonini et al. (2002) along an abandoned stretch of the S.S. 320 road. In their study, the average size of the limestone blocks pertaining to the Calcare Massiccio Formation is 4.6 m³. For these reasons, a volume of 5 m³ was considered for the rock fall simulations both in Bagni di Triponzo and in Ponte di Nortosce (Table 2).

4.3 3D Surface Creation

The extraction of high-resolution surface models was necessary for performing the kinematic analyses and rock fall simulations (Fig. 1). To

achieve this, it was necessary to filter the point clouds acquired with the TLS because of the presence of vegetation on the slopes (Fig. 2). Because of the shape of the slopes, and of the need to keep the procedure as rapid and objective as possible, a 2.5 D raster algorithm was chosen to eliminate nonground points, since it was actually able to eliminate the vegetation and, at the same time, to maintain an accurate level of detail. The method involves the projection of the point cloud perpendicularly to a planar raster surface (1-m cell size) and the selection, for each cell, of the point nearest to the plane; identified points are then triangulated to generate a surface. For each scan position, the orientation of the best-fitting plane of the slope 3D model was considered as base reference, so as to keep overhanging sectors.

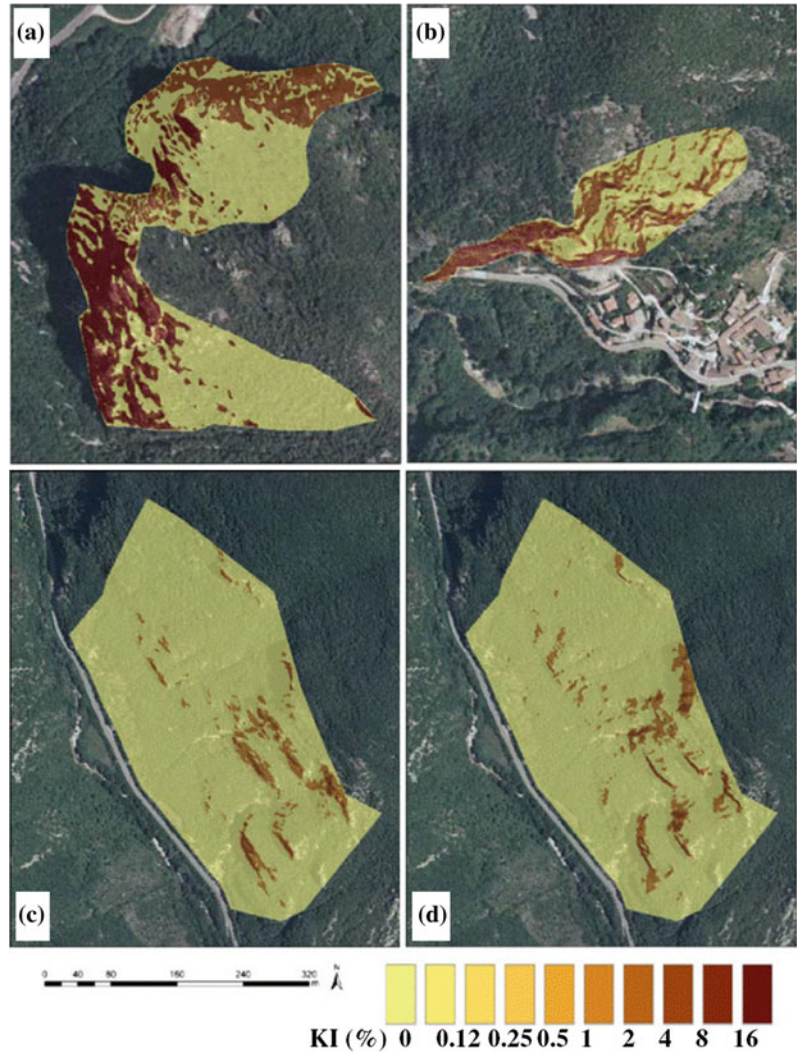
However, as regards the scans performed at Ponte di Nortosce (Fig. 2a) and at Bagni di Triponzo (Fig. 2b), data integration was necessary because of the presence of some shadow areas. For this reason, a second point cloud obtained from an existing 1:10,000 Regional Technical Map (CTR) was employed. Then the point cloud resulting from the CTR map was exported to AutoCAD® and aligned, by rototranslation, to the one obtained with the TLS survey. Once the point clouds were filtered and aligned, 3D slope surfaces were created through point triangulation. To remove possible spikes due to incomplete vegetation removal and to improve uniformity, a smoothing procedure was also applied. The three surfaces have the same resolution (1 m), and even the subvertical walls are properly and realistically reconstructed, thus allowing performance of reliable kinematic analyses and rock fall simulations. Finally, for 3D and 2D rock fall simulations, a DEM (1-m resolution) (Fig. 1) was created for each slope in a Geographical Information System (GIS) environment, and the position of roads, tunnels, and housing was extracted from the TLS products and overlapped to the terrain models.

5 Susceptibility Scenarios

5.1 Kinematic Analysis

For the definition of the main rock fall source areas, a spatial kinematic analysis was performed by using discontinuity orientation data semiautomatically and manually extracted from the point cloud and the 3D surface models obtained from the TLS data. This kind of analysis is able to establish if and where a particular instability mechanism is kinematically feasible, given the slope geometry and the discontinuity orientation (Goodman and Bray 1976; Hoek and Bray 1981; Hudson and Harrison 1997; Matheson 1989). The main instability mechanisms investigated with this approach are: plane failure, wedge failure, block toppling, and flexural toppling. Casagli and Pini (1993) introduced a kinematic hazard index for each instability mechanism. These values are calculated by counting poles and discontinuities falling in critical areas of the stereographic projection. A spatial kinematic analysis (Fig. 1) was performed on each unit triangle of the 3D surface models by employing a new Visual Basic software called Rock Slope Stability (RSS) proposed by Lombardi (2007) and developed specifically for true 3D kinematic analyses. This tool overcomes many limitations of the traditional approaches, as it is possible to employ true 3D surfaces, and the kinematic conditions leading to the investigated instability mechanisms have been extended to overhanging slopes. The kinematic analysis results are illustrated in Fig. 6. All the investigated sites show quite high probability of occurrence of kinematic instability mechanisms (max kinematic index up to 20%), mainly located in the steepest sectors of the slopes. The latter correspond to the main source areas, where blocks were seeded from in rock fall simulations. The prevailing instability mechanism is toppling, associated to planar failure (at Ponte di Nortosce and Triponzo) and wedge failure (at Bagni di Triponzo and Triponzo).

Fig. 6 Results from the kinematic analysis for Bagni di Triponzo (a), Triponzo (b) and Ponte di Nortosce (c, d) sites. This mosaic shows the highest kinematic indexes (KI) which correspond to a higher probability that the investigated instability mechanism will take place: planar failure (c), and flexural toppling (a, b, d)



5.2 Rock Fall Simulations

2D and 3D rock fall simulations were performed (Fig. 1). 3D modeling was used in order to evaluate at large scale the influence of the slope morphology on the block trajectories, while 2D analyses allowed us to perform a larger number of simulations (statistically more significant) on the most critical profiles identified with the 3D approach.

Both methods apply lumped mass logic: each single block is represented by a simple point with its mass concentrated at the center, and its trajectory is analyzed considering the physical laws

governing the sequence of different types of motion (free fall, bouncing, rolling, and sliding) (Giani 1992).

Input data for rock fall simulations can be classified as geometric parameters (topography, identification of seed points, limits of outcropping materials, location of element at risk or points of interest, block shape, and volume) or mechanical parameters (normal and tangential coefficient of restitution and friction angle).

All geometric data can be retrieved through the analysis of TLS point clouds. The extraction of high resolution DEMs, block volumes, and rock fall source areas for the investigated cases

have already been described in the previous sections. In addition, an accurate location of the limits of the outcropping materials and the location of other elements of interest was possible thanks to the coupled observation of the point clouds and the oriented optical images acquired during the TLS survey.

As regards the remaining parameters, an inventory of fallen blocks has been carried out at all the investigated sites by integrating field observation and TLS data (black points in Fig. 7); the mechanical properties were calibrated by performing a 3D back analysis to obtain the best agreement between the distribution of the blocks found in situ and the one derived from the simulations. The resulting values and associated standard deviation employed in the simulations are summarized in Table 3. 3D simulations were performed by using the Rock fall Analyst software (Lan et al. 2007), which directly works in GIS environment. The employed reference surface was the 1-m DEM obtained from the TLS data, and blocks were seeded from the areas associated to kinematic indexes higher than 10. The resulting rock fall paths are presented in Fig. 7.

In order to obtain a more accurate assessment of susceptibility scenarios, 2D rock fall simulations were also performed by using the RocFall software (Rocscience 2005).

The analysis was carried out along three profiles for each rock slope analyzed, according to the criticalities from the 3D approach (Fig. 7), and the same input parameters of 3D simulations were employed. For each profile, 10,000 rock falls were simulated, since the larger the number of simulations, the more statistically significant the results will be (Fig. 8a–c). Fundamental output parameters (such as the horizontal location of rock end points, the kinetic energy, and the bounce height) were, thus, determined according to the progression along the profile or in correspondence of sensitive elements (rock fall barriers, roads, and buildings).

6 Discussion and Conclusions

The objective of this work was to experiment and evaluate the advantages and drawbacks of a procedure for the complete definition of susceptibility scenarios associated to rock falls using

Fig. 7 3D rock fall simulation results: **a** Triponzo, **b** Ponte di Nortosce, and **c** Bagni di Triponzo. The position of fallen blocks extracted from TLS and field surveys (black points) and those found during the validation inventory (white points) are also reported. The white lines indicate the traces of the profiles employed in the 2D analyses

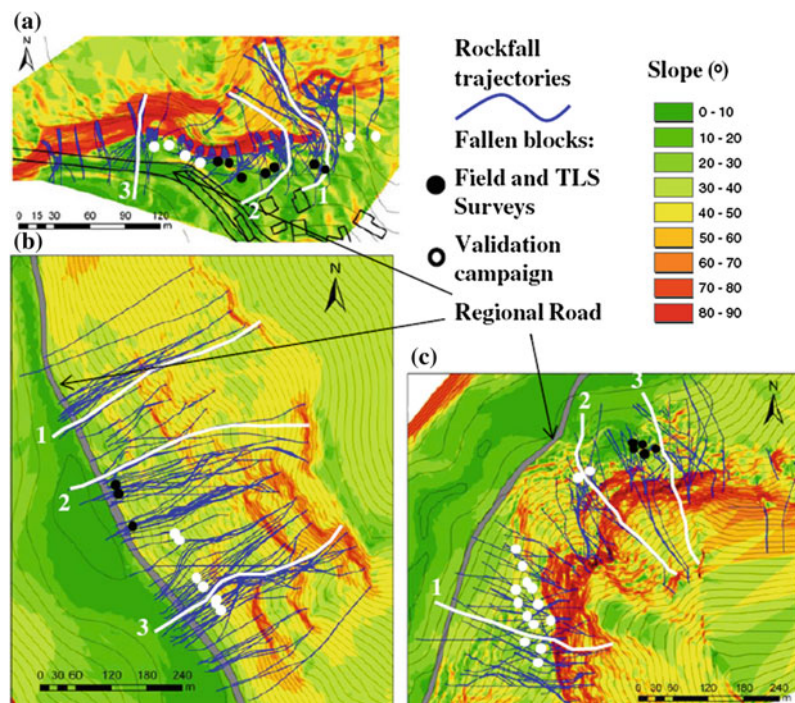


Table 3 Mechanical parameters retrieved through back analysis, employed in the rock fall simulations

Material type	Rn mean	σ	Rt mean	σ	friction mean	σ
Bare rock	0.6	0.05	0.8	0.05	30	2
Vegetated rack	0.5	0.05	0.6	0.05	30	4
Soil	0.3	0.05	0.5	0.05	30	2
Vegetated soil	0.3	0.05	0.4	0.05	30	4

Rn normal coefficient of restitution, *Rt* tangential coefficient of restitution, *friction* friction angle, σ standard deviation

primarily the TLS technique. The methodology has been applied in three test sites located in Valnerina (Umbria Region, Italy). Due to its sharp morphology, the investigated area is characterized by steep slopes and deep valleys, and as a consequence, the risk of rock falls is particularly high, especially along the roads and in the villages next to the slopes. Furthermore, this predisposition is exacerbated by the intense seismic activity of the entire area. The main advantages and drawbacks of the proposed approach are here discussed, keeping in mind its original purposes (rapidity, objectivity, high resolution, and reliability). The main obstacle for the complete compliance of the quickness requirement was the occurrence, within TLS data, of shadow areas, which required a filling procedure in order to get complete spatial information. Moreover, even though these sectors were limited in number and extension, their filling caused a lack of accuracy and resolution homogeneity within the 3D surface models; consequently, the results of kinematic and runout analyses in these areas should be considered with care. For a complete and precise rock fall analysis, an accurate reconstruction of the main characteristics of the rock mass is required. In this work, three different approaches for geomechanical analyses were considered and compared: traditional in situ survey and manual and semiautomatic extraction of the most important geometric characteristics of the rock mass from the high resolution point clouds.

The application of the semiautomatic procedure can give a contribution to improve the safety level (since it is not necessary to physically reach dangerous areas), the spatial resolution, the quickness, and the objectivity of the whole approach. In order to accurately locate

the discontinuity sets of a rock mass, it is necessary to have the largest number of measures and a good sampling methodology. The semiautomatic procedure, through its analysis algorithm, allows acquisition of a huge amount of data with an objective criterion and investigation of major portions of the rock mass. The application of the presented semiautomatic approach, however, does not always provide satisfying results, such as in the case of rock masses characterized by prevailing discontinuity traces (Gigli and Casagli 2011a; Kemeny and Post 2003; Ferrero and Umili 2011) by very irregular (Lato et al. 2012) or poor fracturing, or if the spatial resolution of the point cloud is too low (usually due to the high distance of the object of interest from the scan position). Moreover, the TLS line of sight acquisition may result in wide shadow areas and significant bias if data are acquired from a single scan position (Lato et al. 2010). Thus, representative block dimensions can be semiautomatically calculated only if specific conditions take place (rock mass characterized by well-developed discontinuity surfaces and point cloud resolution high enough to appreciate geometric features); otherwise, additional integrative data processing is necessary. This is a very important point that should be kept in mind when exporting the procedure to other sites, since block size is a key parameter for the forecasting of the kinetic energy in correspondence of the elements at risk, and its quick and reliable definition is fundamental for correct rock fall analyses. The kinematic analysis allowed quick and objective definition of the main rock fall source areas. These results were also confirmed by field observations that show evidences of occurrence of the predicted instability mechanisms (Fig. 5).

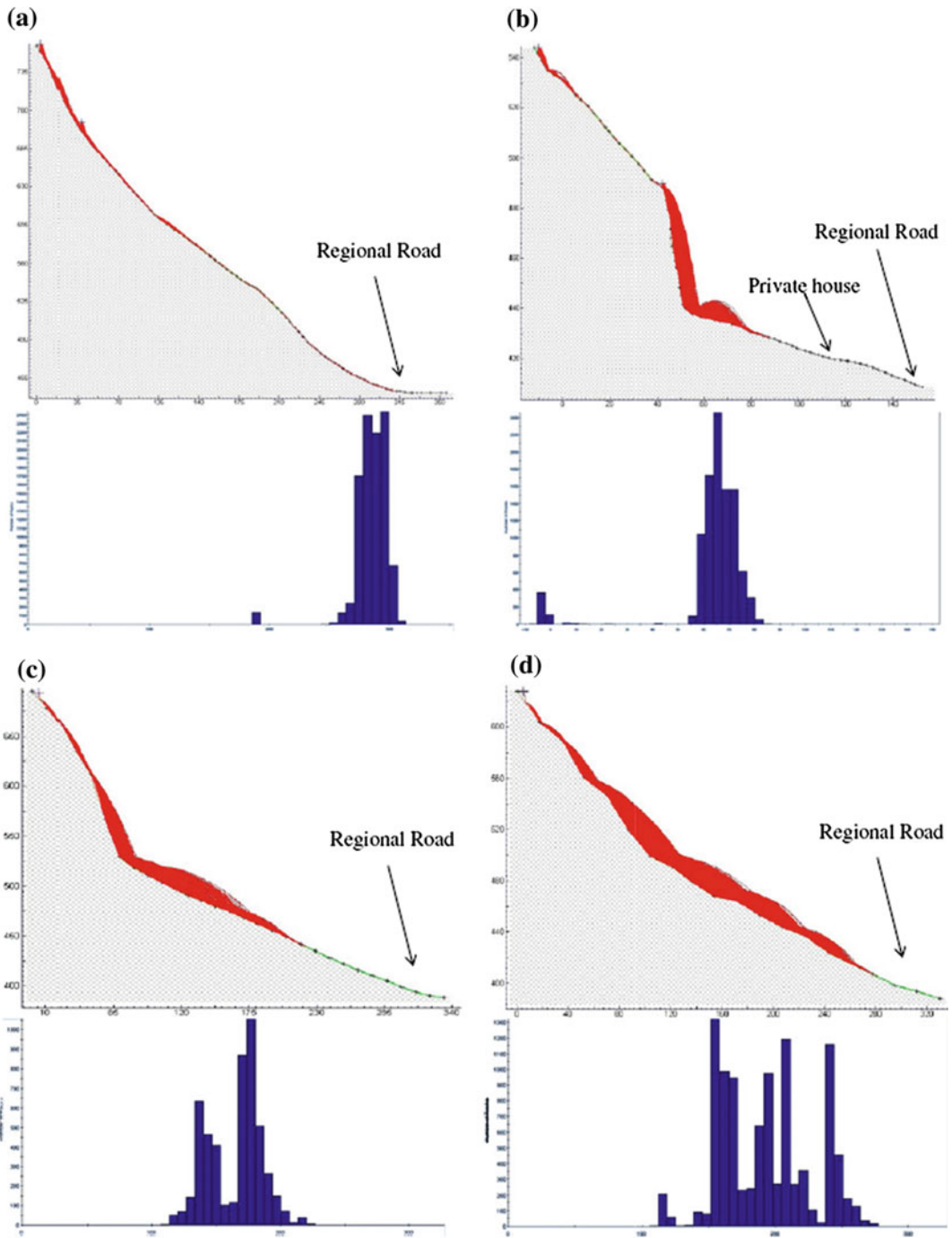


Fig. 8 2D rock fall trajectories and location of end points: **a** profile 3 (Fig. 7) at Ponte di Nortosce, **b** profile 2 (Fig. 7) at Triponzo, **c** profile 1 (Fig. 7) at Bagni di

Triponzo, and **d** profile 1 at Bagni di Triponzo extracted from a topographic map 1:10,000

The geometric inputs of rock fall analyses are, therefore, completely defined; however, to improve simulation reliability, a back analysis for the calibration of the coefficients of restitution and friction angle of the outcropping materials is strongly suggested. This is usually done by performing an inventory of fallen block and carrying out a parametric analysis with the aim of obtaining the best agreement between the in situ block distribution and the simulated one. The high-resolution point clouds acquired by the TLS can be useful also for this purpose, allowing for accurate estimation of both the position and dimension of fallen blocks.

The results of rock fall analyses at Ponte di Nortosce show that the regional road appears to be heavily rock fall prone, since 88% of simulations reach the roadway, stopping, in some cases, in the fields beyond it. The associated maximum bounce height and kinetic energy are about 1.5 m and 210 kJ, respectively. At Bagni di Triponzo, the blocks reach the roadway only in exceptional cases (1%). Almost all the simulations stop at the base of the rock slope, where the vegetation is denser. Figure 8 shows the importance of employing a realistic topographic base for reliable rock fall analyses. A comparison between 2D simulations performed on profiles extracted from high-resolution TLS data (Fig. 8c) and from a regional technical map (scale 1:10,000) (Fig. 8d) is presented. Low-resolution topographic maps usually strongly underestimate slope steepness, especially in subvertical areas (thus, overestimating it at their base). At Triponzo, due to the high steepness of the slope, the horizontal component of block velocity is low, resulting in a higher energy dissipation and, consequently, in moderate runout distances. The road network and the buildings closest to the rock wall are, therefore, marginally affected by the rock falls, with the exception of the western portion of the regional road, where a rock fall gallery was built to reduce the risk.

A validation inventory has been carried out after the application of the whole procedure (white points in Fig. 7). The results show a good agreement with 3D (Fig. 7) and 2D (Fig. 8) simulations as regards Ponte di Nortosce (where

blocks are retained by a recent rock fall barrier) and Triponzo, while some discrepancies between true and simulated block distributions can be observed in the southwestern of the Bagni di Triponzo site, where probably the restitution coefficient were overestimated due to the presence of thick vegetation (Fig. 2b).

Acknowledgements This work was carried out within a research contract between the Department of Civil and Environmental Engineering of the University of Perugia and the Department of Earth Sciences, University of Firenze. The authors are also thankful to Prof. Hengxing Lan for his kind authorization to employ the Rockfall Analyst software for 3D simulations.

References

- Abellan A, Vilaplana JM, Martinez J (2006) Application of a long-range terrestrial laser scanner to a detailed rockfall study at Vall de Nuria (Eastern Pyrenees, Spain). *Eng Geol* 88(3):136–148
- Abellan A, Vilaplana JM, Calvet J, Blanchard J (2010) Detection and spatial prediction of rockfalls by means of terrestrial laser scanning modelling. *Geomorphology* 119:162–171
- Agliardi F, Crosta GB (2003) High resolution three-dimensional numerical modelling of rockfalls. *Int J Rock Mech Min Sci* 40:455–471
- Amato A, Azzara R, Chiarabba C, Cimini GB, Cocco M, Di Bona M, Margheriti L, Mazza S, Mele F, Selvaggi G, Basili A, Boschi E, Courboulex F, Deschamps A, Gaffet S, Bittarelli G, Chiaraluce L, Piccinini D, Ripepe M (1998) The 1997 Umbria–Marche, Italy, earthquake sequence: a first look at the main shocks and aftershocks. *Geophys Res Lett* 25:2861–2864
- Antonini G, Ardizzone F, Cardinali M, Galli M, Guzzetti F, Reichenbach P (2002) Surface deposits and landslide inventory map of the area affected by the 1997 Umbria–Marche earthquakes. *Boll Soc Geol Ital* 121:843–853
- Armesto J, Ordóñez C, Alejano L, Arias P (2009) Terrestrial laser scanning used to determine the geometry of a granite boulder for stability analysis purposes. *Geomorphology* 106:271–277
- Azzoni A, La Barbera G, Zaninetti A (1995) Analysis and prediction of rockfalls using a mathematical model. *Int J Rock Mech Min Sci Geomech Abstr* 32:709–724
- Barchi M, Cardinali M, Guzzetti F, Lemmi M (1993) Relazioni fra movimenti di versante e fenomeni tettonici nell'area del M. Coscerno—M. di Civitella, Valnerina (Umbria). *Boll Soc Geol Ital* 112:83–111 (in Italian)
- Bauer A, Paar G, Kaltenböck A (2006) Mass movement monitoring using terrestrial laser scanner for rockfall management. In: van Oosterom P, Zlatanova S,

- Fendel EM (eds) *Geo-information for disaster management*. Springer, Berlin, pp 393–406
- Carro M, De Amicis M, Luzi L, Marzorati S (2003) The application of predictive modeling techniques to landslides induced by earthquakes: the case study of the 26 September 1997 Umbria-Marche earthquake (Italy). *Eng Geol* 69:139–159
- Casagli N, Pini G (1993) Analisi cinematica della stabilità di versanti naturali e fronti di scavo in roccia. *Geol Appl Idrogeol* 28:223–232 (in Italian)
- Descouedres F, Zimmermann TH (1987) Three-dimensional dynamic calculation of rockfalls. In: *Proceedings of the sixth international congress of rock mechanics*, Montreal, Canada, pp 337–342
- Dorren LKA, Seijmonsbergen AC (2003) Comparison of three GIS-based models for predicting rockfall runout zones at a regional scale. *Geomorphology* 56:49–64
- Evans SG, Hungr O (1993) The assessment of rockfall hazard at the base of talus slopes. *Can Geotech J* 30:620–636
- Fanti R, Gigli G, Lombardi L, Tapete D, Canuti P (2012) Terrestrial laser scanning for rockfall stability analysis in the cultural heritage site of Pitigliano (Italy). *Landslides*. doi:10.1007/s10346-012-0329-5
- Ferrero AM, Umili G (2011) Comparison of methods for estimating fracture size and intensity applied to Aiguille Marbrée (Mont Blanc). *Int J Rock Mech Min Sci* 48(8):1262–1270
- Ferrero AM, Forlani G, Roncella R, Voyat HI (2009) Advanced geosstructural survey methods applied to rock mass characterization. *Rock Mech Rock Eng* 42:631–665
- Ferrero AM, Migliazza M, Roncella R, Rabbi E (2011) Rock slopes risk assessment based on advanced geosstructural survey techniques. *Landslides* 8:221–231
- Giani GP (1992) *Rock slope stability analysis*. Balkema, Rotterdam
- Giani GP, Giacomini A, Migliazza M, Segalini A (2004) Experimental and theoretical studies to improve rock fall analysis and protection work design. *Rock Mech Rock Eng* 37:369–389
- Gigli G, Casagli N (2011a) Semi-automatic extraction of rock mass structural data from high resolution LIDAR point clouds. *Int J Rock Mech Min Sci* 48:187–198
- Gigli G, Casagli N (2011b) Extraction of rock mass structural data from high resolution laser scanning products. In: *Proceedings of 2nd world landslide forum*, Rome, 3–7 October, 2011
- Gigli G, Frodella W, Mugnai F, Tapete D, Cigna F, Fanti R, Intrieri E, Lombardi L (2012) Instability mechanisms affecting cultural heritage sites in the Maltese Archipelago. *Nat Hazards Earth Syst Sci* 12:1883–1903. doi:10.5194/nhess-12-1883-2012
- Goodman RE, Bray JW (1976) Toppling of rock slopes. In: *ASCE specialty conference on rock engineering for foundations and slopes*, Boulder Colorado, vol 2, pp 201–234
- Guzzetti F, Crosta GB, Detti R, Agliardi F (2002) STONE: a computer program for the three-dimensional simulation of rock-falls. *Comput Geosci* 28:1079–1093
- Guzzetti F, Reichenbach P, Ghigi S (2004) Rockfall hazard and risk assessment along a transportation corridor in the Nera Valley, Central Italy. *Environ Manag* 34:191–208
- Guzzetti F, Esposito E, Balducci V, Porfido S, Cardinali M, Violante C, Fiorucci F, Sacchi M, Ardizzone F, Mondini A, Reichenbach P, Rossi M (2009) Central Italy seismic sequence-induced landsliding: 1997–1998 Umbria-Marche and 2008–2009 l’Aquila cases. In: *The next generation of research on earthquake-induced landslides: an international conference in commemoration of 10th anniversary of the Chi-Chi earthquake*, pp 52–60
- Hoek E (2000) *Practical rock engineering*. www.rocksience.com
- Hoek E, Bray JW (1981) *Rock slope engineering*. Revised third edition, Institute of Mining and Metallurgy, London
- Hudson JA, Harrison JP (1997) *Engineering rock mechanics*. Pergamon Press, Oxford, p 444
- Hungr O, Evans SG, Hazzard J (1999) Magnitude and frequency of rock falls and rock slides along the main transportation corridors of southwestern British Columbia. *Can Geotech J* 36:224–238
- International Society for Rock Mechanics (ISRM)—Commission on The Standardization of Laboratory and Field Test (1978) Suggested methods for the quantitative description of discontinuities in rock masses. *Int J Rock Mech Min Sci Geomech Abstr* 15:319–368
- Jaboyedoff M, Oppikofer T, Abellán A, Derron M, Loye A, Metzger R, Pedrazzini A (2012) Use of LIDAR in landslide investigations: a review. *Nat Hazards* 61:5–28
- Kemeny J, Post R (2003) Estimating three-dimensional rock discontinuity orientation from digital images of fracture traces. *Comput Geosci* 29:65–77
- Lan H, Martin CD, Lim CH (2007) RockFall analyst: a GIS extension for three-dimensional and spatially distributed rockfall hazard modeling. *Comput Geosci* 33:262–279
- Lan H, Martin CD, Zhou C, Lim CH (2010) Rockfall hazard analysis using LiDAR and spatial modeling. *Geomorphology* 118:213–223
- Lato M, Vöge M (2012) Automated mapping of rock discontinuities in 3D lidar and photogrammetry models. *Int J Rock Mech Min Sci* 54:150–158
- Lato M, Hutchinson J, Diederichs M, Ball D, Harrap R (2009) Engineering monitoring of rockfall hazards along transportation corridors: using mobile terrestrial LiDAR. *Nat Hazards Earth Syst Sci* 9:935–946
- Lato M, Diederichs M, Hutchinson DJ (2010) Bias correction for static LiDAR scanning of rock outcrops

- for structural characterization. *Rock Mech Rock Eng* 43(5):615–628
- Lato MJ, Diederichs MS, Hutchinson DJ (2012) Evaluating roadside rockmasses for rockfall hazards using LiDAR data: optimizing data collection and processing protocols. *Nat Hazards* 60:831–864
- Lombardi L (2007) Nuove tecnologie di rilevamento e di analisi di dati geomeccanici per la valutazione della sicurezza. Ph.D. Thesis, Università degli studi di Firenze (in Italian)
- Marzorati S, Luzi L, De Amicis M (2002) Rock falls induced by earthquakes: a statistical approach. *Soil Dyn Earthq Eng* 22:565–577
- Matheson GD (1989) The collection and use of field discontinuity data in rock slope design. *Q J Eng Geol* 22:19–30
- Mikos M, Vidmar A, Brilly M (2005) Using a laser measurement system for monitoring morphological changes on the Strug rock fall, Slovenia. *Nat Hazard Earth Syst Sci* 5:143–153
- Morelli S, Segoni S, Manzo G, Ermini L, Catani F (2012) Urban planning, flood risk and public policy: the case of the Arno River, Firenze, Italy. *Appl Geogr* 34:205–218
- Palmstrom A (2005) Measurement of correlations between block size and rock quality designation (RQD). *Tunn Undergr Space Technol* 20:362–377
- Pfeiffer TJ, Bowen T (1989) Computer simulation of rockfalls. *Bull Assoc Eng Geol* 26:135–146
- Piteau DR, Clayton R (1976) Computer rockfall model. In: Proceedings of the meeting on rockfall dynamics and protective works effectiveness, Bergamo, Italy, ISMES Publication No. 90, pp 123–125
- Ritchie AM (1963) Evaluation of rockfall and its control. *Highw Res Rec* 17:13–28
- Rocscience (2005) RocFall software for risk analysis of falling rocks on steep slopes. Ver. 4.0. User's Guide
- Rosser NJ, Dunning SA, Lim M, Petley DN (2005) Terrestrial laser scanning for monitoring the process of hard rock coastal cliff erosion. *Q J Eng Geol Hydrogeol* 38:363–375
- Strouth A, Eberhardt E (2005) The use of LiDAR to overcome rock slope hazard data collection challenges at Afternoon Creek, Washington. In: 41st US symposium on rock mechanics, Golden, Colorado. American Rock Mechanics Association
- Tapete D, Gigli G, Mugnai F, Vannocci P, Pecchioni E, Morelli S, Fanti R, Casagli N (2012) Correlation between erosion patterns and rockfall hazard susceptibility in hilltop fortifications by terrestrial laser scanning and diagnostic investigations. In: IEEE international geoscience and remote sensing symposium. Remote sensing for a dynamic earth. Munich, Germany, 22–27 July 2012, pp 4809–4812. ISBN 978-1-4673-1159-5
- Wickens EH, Barton NR (1971) The application of photogrammetry to the stability of excavated rock slopes. *Photogram Rec* 7(37):46–54

TXT-tool 4.039-3.2

How to Assess Landslide Activity and Intensity with Persistent Scatterer Interferometry (PSI): The PSI-Based Matrix Approach

Francesca Cigna, Silvia Bianchini and Nicola Casagli

Abstract

This paper provides a step-by-step analysis and discussion of the ‘PSI-based matrix approach’, a methodology that exploits ground deformation velocities derived through Persistent Scatterer Interferometry (PSI) for the assessment of the state of activity and intensity of extremely to very slow landslides. Two matrices based on historical and recent PSI data are designed respectively for landslides already mapped in preexisting inventories and for newly identified phenomena. A unique intensity scale is proposed applicable to both cases. An example application in the 14 km² area of Verbicaro in Northern Calabria (Italy) is presented. For this sample site, PSI data derived from SAR (Synthetic Aperture Radar) images acquired by ERS1/2 and RADARSAT1/2 satellites in the period 1992–2011 are employed. Ground velocities measured along the satellite Line Of Sight (LOS) are projected along the maximum slope directions to derive more reliable deformation rates. An activity threshold of ± 5 mm/year is determined by applying the average projected velocity of local slopes to the PSI data precision. The intensity threshold between extremely and very slow phenomena (16 mm/year) is reduced by $\sim 20\%$ to account for temporal and spatial averages, being applied to attribute representative velocities to each landslide. The methodology allows assessing the state of activity and the intensity for 13 of the 24 landslides pre-mapped in the 2007 inventory and for two newly identified phenomena. Results, as well as the major factors influencing the approach, are shown and discussed. Pending issues of the proposed methodology are critically tackled and include the lack of PSI data within the landslide boundaries, temporal coverage of the available estimates, need of field checks, and operative procedures to set the activity and intensity thresholds.

F. Cigna (✉)
British Geological Survey (BGS), Natural
Environment Research Council (NERC),
Environmental Science Centre, Nicker Hill,
Keyworth, Nottingham NG12 5GG, UK
e-mail: francesca.cigna@asi.it

S. Bianchini · N. Casagli
Italian Space Agency, Via del Politecnico s.n.c.,
00133 Rome, Italy
e-mail: silvia.bianchini@unifi.it
N. Casagli
e-mail: nicola.casagli@unifi.it

Keywords

Landslides · Persistent scatterer interferometry · State of activity
Intensity · SAR interferometry · PSI-based matrix

Contents

1 Introduction	494
2 The PSI-Based Matrix Approach: State of the Art	494
3 Definitions and Applicability	497
4 Implementation of the Activity Matrices and Intensity Scale	498
4.1 Activity Matrix for Pre-mapped Landslides....	499
4.2 Activity Matrix for Newly Detected Landslides	500
4.3 Intensity Scale.....	501
5 Sample Site: Verbicaro (Calabria)	501
5.1 Input Data and Preparatory Phase	501
5.2 Implementation.....	504
5.3 Results.....	505
6 Discussion and Pending Issues	506
7 Conclusions	507
References.....	508

1 Introduction

Systematic investigation and characterization of landslides at a regional scale is an essential requirement for risk assessment and for consequent planning of proper hazard-reduction resources and actions. Inventory maps of landslide processes deal with the detection of ground mass movements and provide spatial distribution and parameters of each landslide (e.g., extension, typology, and state of activity).

Landslide inventories are usually based on conventional geomorphologic studies, which rely on intensive field surveys and on time-consuming manual interpretation of aerial and satellite optical images.

Remote sensing technologies can considerably reduce technical problems of difficult access and related economic efforts of field campaigns thanks to their high precision, wide area coverage, non-invasiveness, and cost-efficiency. Persistent Scatterer Interferometry (PSI) is a

multi-temporal interferometric technique which analyzes long temporal series of satellite SAR (Synthetic Aperture Radar) data, and provides annual velocities and time series of ground deformation on dense grids of point-wise targets, the so-called PS or Persistent Scatterers (Ferretti et al. 2001). PS analysis has recently been demonstrated to be a valuable and useful tool for detecting surface displacements with millimetre precision, and has been successfully used for identification and mapping of slow-moving landslide phenomena and for evaluation of their state of activity and intensity, at regional and local scales (e.g., Farina et al. 2006; Notti et al. 2010; Righini et al. 2012). In this paper we present an innovative approach for updating and improving landslide inventories by means of PSI analysis, using radar images acquired by satellites ERS1/2 in 1992–2001 and RADARSAT-1 in 2003–2011 of the test area of Verbicaro, located in Northern Calabria (South Italy) and extensively affected by landslide hazards.

2 The PSI-Based Matrix Approach: State of the Art

The ‘PSI-based matrix approach’ is an innovative method for assessing (or updating) a landslide’s state of activity and intensity, which exploits PSI-derived multi-temporal estimates of ground deformation as indicators of activity and magnitude of landslide processes. This methodology was initially conceived within the Earth Sciences Department of the University of Firenze, and applied to several test sites in the framework of national and international projects, such as ESA SLAM (Service for LAndslide Monitoring), Terrafirma and PREVIEW (Farina et al. 2006) and in several scientific works

(Bianchini et al. 2012; Righini et al. 2012; Frangioni et al. 2015).

The operational methodology of “PSI-based matrix” integrates qualitative (state of activity) and quantitative information (intensity) of the phenomenon. Activity matrices and intensity scales are, respectively, 2D and 1D grids defined in terms of PS average annual velocity.

Firstly, a representative ground displacement velocity value is determined for each landslide, through the analysis of available PS data. These representative values, in terms of Line Of Sight (LOS) deformation velocity (mm/year), are referred to the coverage time of satellite acquisitions; for each landslide the values are determined by calculating the average velocity of all the PS included within its boundary. Then, the representative ground motion rates of each landslide are compared to some displacement thresholds (e.g., ± 2 mm/year in the LOS direction, away or towards the satellite), whose values depend on the characteristics of each application (landslide main typology, InSAR data, measurement accuracy, distance from reference point, etc.), to distinguish ‘moving’ from ‘not moving’ phenomena. Finally, the state of activity and intensity are assigned

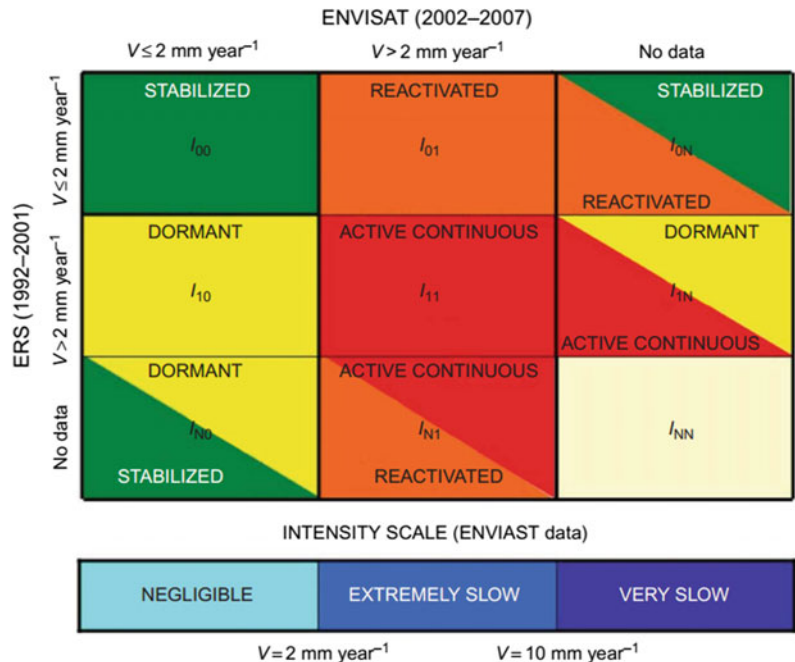
through the use of one matrix and one scale (for activity and for intensity evaluations, respectively), which are defined in terms of velocity and acquisition time and consist of cell grids with different velocity combinations, whose inputs are past or present PS velocities or/and information coming from pre-existing inventories.

The first attempt at creating an activity matrix was by Righini et al. (2012) and makes use of an activity cell-grid, whose inputs are InSAR measurements of past (ERS 1/2) and present (ENVISAT) displacement. Representative ground motion values of each landslide are compared to the velocity threshold of 2 mm/year, and finally, by means of the matrix, the state of activity is determined (Fig. 1). The threshold of 2 mm/year is precautionary, chosen as the minimum value exceeding the precision of the PSI technique, as found also within other studies (Meisina et al. 2008; Frangioni et al. 2015).

The intensity scale is defined in terms of mean yearly velocity and consists of three different classes: ‘negligible’, ‘extremely slow’ and ‘very slow’ (Cruden and Varnes 1996).

The second version of the activity matrix has been implemented by Bianchini et al. (2012).

Fig. 1 First attempt at an activity matrix and intensity scale, based on Righini et al. (2012)



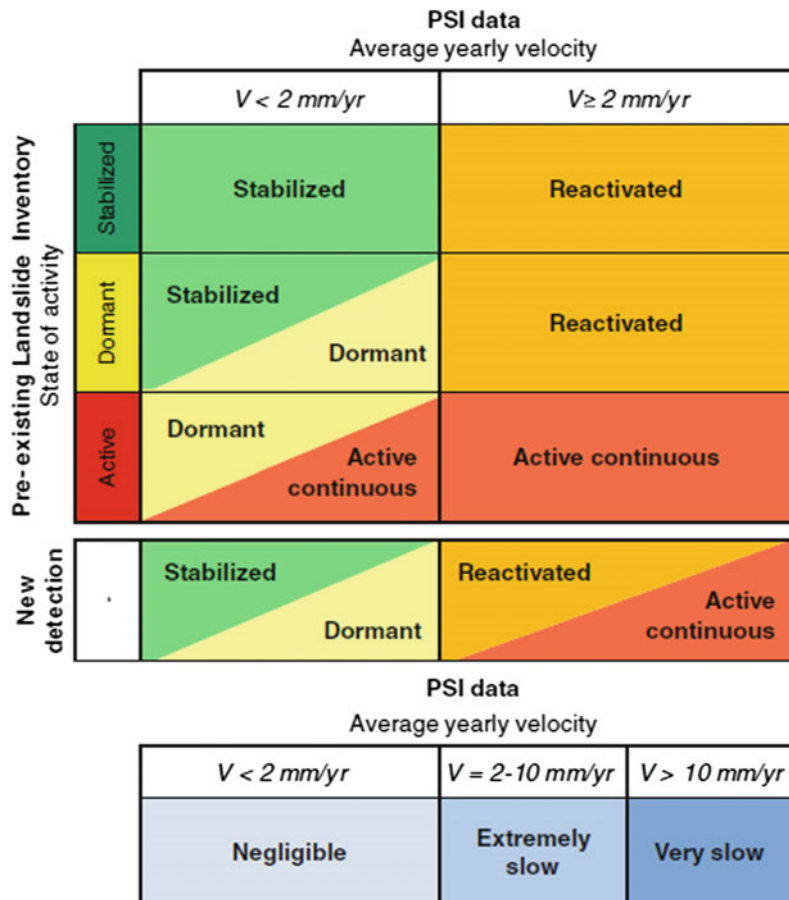
While previous studies (Righini et al. 2012) used PSI measures derived from two different satellites providing interferometric data for two distinct time intervals, e.g., historical ERS and recent ENVISAT measurements, this development of the activity matrix is based on the information coming from the pre-existing inventory map and PS average yearly velocity extracted from a single PSI dataset (Fig. 2). Thus, this matrix can be used when interferometric data are available for only a single period of acquisition (e.g., ENVISAT data). In order to determine the state of activity of each phenomenon, the representative landslide velocity is first compared to the velocity threshold. The result is eventually combined with the landslide information extracted from the pre-existing inventory (i.e., state of activity referred to the

time of updating of the pre-existing inventory) and the state of activity of each phenomenon is evaluated.

Subsequently, the matrix-based procedure for the evaluation of landslide activity has been enhanced by Bianchini et al. (2013) and Cigna et al. (2013). In particular, Cigna et al. (2013) standardized the method for a generic case study, as well as improved it through consideration of the whole range of input data availabilities and combinations.

In this improved version, which is explained below and applied to the Verbicaro sample site, the evaluation of activity and intensity is computed by analyzing separately present and historical PS data for each landslide, and by calculating the average velocity of the PS identified within its boundary.

Fig. 2 Second version of the activity matrix as implemented by Cigna et al. (2010) and Bianchini et al. (2012)



3 Definitions and Applicability

When preparing or updating a landslide inventory map, once the spatial distribution of landslides is mapped, then the state of activity and intensity of the phenomena can be evaluated.

The classification of the activity of landslides proposed in the Multilingual Landslide Glossary (WP/WLI 1993) includes the following states: (i) “active”, for a landslide that is currently moving; (ii) “suspended”, for a landslide that has moved within the last 12 months (i.e., last seasonal cycle), but is not active at present; (iii) “Reactivated”, for a phenomenon that is now active, after being inactive; (iv) “inactive”, for a landslide that has not moved within the last 12 months. Inactive landslides can be divided into four more states: “Dormant” (an inactive landslide that can be reactivated by its original causes or other causes), “Abandoned” (an inactive landslide that is no longer affected by its original triggering causes), “Stabilized” (an inactive landslide that has been protected from its original triggering causes by remedial measures, naturally or artificially) and “relict” (an inactive landslide that developed under climatic or geomorphological conditions considerably different from those at present, i.e., a “paleo-landslide”).

The ‘PSI-based matrix approach’ uses a simplified version of the official classification of the states of activity defined in the multilingual landslide glossary (WP/WLI 1993), distinguishing the following four classes of activity:

- ‘Stabilized’ (S), not affected by their original causes anymore;
- ‘Dormant’ (D), potentially being reactivated;
- ‘Active’ (A), currently moving;
- ‘Reactivated’ (R), moving after being inactive.

The first two classes are included in the inactive one, comprising all phenomena which did not move in the last 12 months. The stabilized class includes both artificially stabilized phenomena (artificially protected from their causes through remedial measures) and naturally stabilized ones, i.e., abandoned (no longer

affected by their original causes) and relict landslides (developed under different climatic and geomorphologic conditions from the current ones). Suspended landslides (moved in the last 12 months but not moving at present) are incorporated into the active class.

The “intensity” of a landslide is a difficult parameter to evaluate, since many features must be accounted for. Hungr (1997) defines the intensity as the destructiveness of a landslide, in terms of energy, volume, area, depth, movement velocity or total displacement, etc. Intensity expresses the geometrical and mechanical severity of a landslide, associated with its destructive power (Einstein 1988). The intensity depends upon kinetic energy, mass and/or velocity (Hungr 1997). At basin scale, the intensity is not easily measurable, due to the lack of detailed information on volume and expected velocity for a large number of landslides (Catani et al. 2005). Usually, the landslide intensity assessment, also adopted by the IUGS/WGL (1995), refers to range scales based on possible consequent damages (Cruden and Varnes 1996).

In this context, the landslide intensity can be assessed by PSI data in terms of movement velocity (Righini et al. 2012). Thus, the PSI-based matrix approach considers the landslide potential to cause damage in terms of movement velocity, exploiting the velocity classification of Cruden and Varnes (1996). Due to the main intrinsic characteristic of PSI-derived estimates, the methodology is currently applicable just to the classes of Extremely Slow (ES) and Very Slow (VS) movements (Velocity < 16 mm/year and 16 mm/year ≤ Velocity < 1.6 m/year, respectively).

This limits the applicability of the PSI-based methodology in terms of landslide typology, restricting its range to the analysis of phenomena with very slow dynamics, such as deep-seated gravitational slope deformations, creep, and, just partially, roto-translational slides, flows, and complex landslides, as long as their velocities do not exceed the above-mentioned rates. It is worthwhile to highlight that the landslide-induced displacements that are

detectable through PSI techniques mainly concern post-failure residual deformation and landslide reactivations involving naturally degraded slopes and pre-existing shear surfaces, since they usually evolve with very low velocities (few tens of centimetres per year) with respect to first-time activations and generally persist over long time periods, i.e., several years.

In order to increase the reliability of the representative velocity evaluations, a minimum number of targets (about 20–30 PS/km², or at least three to five radar targets per phenomenon) should be considered, because data retrieved on single targets may not be indicative of a real landslide process but are more likely due to single instable structures, e.g., building settlement (Meisina et al. 2008; Notti et al. 2010).

In order to overcome limitations and underestimates due to the acquisition geometry of the satellite systems, LOS velocities can be re-projected along the local steepest slope, assuming this movement as the most probable direction of movement and assuming pure translational mechanisms (Cascini et al. 2010).

4 Implementation of the Activity Matrices and Intensity Scale

The application of the PSI-based matrix method follows a preliminary evaluation of spatial distribution and boundaries of landslide phenomena within an area of interest. Once this preparatory phase is completed, usually through conventional geomorphologic approaches, photo-interpretation and even the support from PSI data (e.g., Bianchini et al. 2012; Righini et al. 2012), the PSI-based matrix approach starts with the estimation of landslide representative velocities.

Assuming the availability of both past and recent PSI-derived data, two (or more) different time spans can be considered for the analysis: the historical and present intervals, whose respective temporal coverages can be defined as $[D_{H1}-D_{H2}]$ and $[D_{P1}-D_{P2}]$. The historical and present representative velocities of each landslide, named V_H and V_P , are evaluated separately through the

analysis of the available PSI data in the $[D_{H1}-D_{H2}]$ and $[D_{P1}-D_{P2}]$ periods, respectively.

Once the representative velocities of each landslide have been evaluated, PSI-based activity matrices and intensity scales are exploited to identify its state of activity and intensity. Firstly, two or more deformation thresholds have to be preliminarily fixed to discriminate moving/stable phenomena as well as different states of activity and intensities:

- V_{ACT} , distinguishing moving from non-moving areas;
- V_{INT} , discriminating extremely from very slow landslides.

These values are strictly dependent on the case studies at hand and are empirically determined taking into account both the typology of deformation processes affecting the investigated area and the specific characteristics of the available PSI data, e.g., landslide geometry, LOS direction, measurement precision, and relativity of PSI estimates with respect to the reference point. Examples of V_{ACT} velocity thresholds exploited for recent landslide studies at the regional scale range between ± 1.5 and ± 4.0 mm/year, referred to LOS data (Bianchini et al. 2012; Cascini et al. 2010; Farina et al. 2006; Righini et al. 2012), whereas an example of intensity threshold distinguishing extremely slow from very slow phenomena, V_{INT} , is ± 10 mm/year (Bianchini et al. 2012; Righini et al. 2012).

The representative velocities (V_P and V_H) are compared with the activity and intensity thresholds (i.e., ± 2 and ± 10 mm/year), and the state of activity and intensity of landslides are assigned through two activity matrices and an intensity scale (Fig. 3). The first one is used for already pre-mapped phenomena and it is based on the information coming from the pre-existing inventory map (reference data: D_{INV}) and present PS measures ($D_{P1}-D_{P2}$). The second one is used for newly mapped phenomena and it is based only on the exploitation of historical $[D_{H1}-D_{H2}]$ and present $[D_{P1}-D_{P2}]$ PSI data. The third column of this

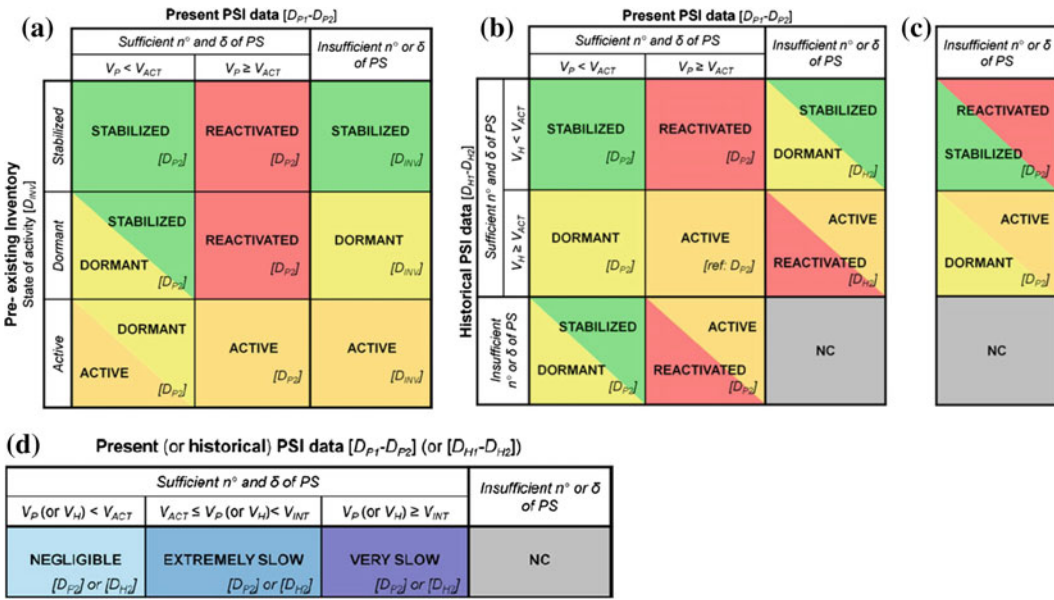


Fig. 3 Landslide activity matrices and intensity scale according to Cigna et al. (2013): **a** activity matrix to be used for already pre-mapped phenomena; it is based on

matrix (Fig. 3b) may be substituted with (Fig. 3c) to refer all the assessments to the past date $[D_{P2}]$. The reference year of the classified activity is pointed out in every cell-grid of the matrices.

4.1 Activity Matrix for Pre-mapped Landslides

This matrix combines past time-referenced activity information included in pre-existing inventories with more recent PSI-derived estimates of ground displacements (Fig. 3a). Input parameters of such a matrix thereby consist of:

- Time-referenced state of activity from a pre-existing inventory, defined at date D_{INV} ;
- Representative velocity V_P , defined in the interval $[D_{P1}-D_{P2}]$, subsequent to D_{INV} .

The nine different combinations that constitute this first typology of the activity matrix, and their outcomes in terms of updated activities and respective temporal references, can be summarized as follows:

the information coming from the pre-existing inventory map and present PS measures; **b**, **c** activity matrix to be used for newly mapped phenomena; **d** intensity scale

1. Stabilized $[D_{INV}]$ landslides, whose V_P is:
 - (a) Lower than $V_{ACT} \rightarrow$ Stabilized $[D_{P2}]$
 - (b) Higher than (or equal to) $V_{ACT} \rightarrow$ Reactivated $[D_{P2}]$
 - (c) Not assessable \rightarrow Stabilized $[D_{INV}]$
2. Dormant $[D_{INV}]$ landslides, whose V_P is:
 - (a) Lower than $V_{ACT} \rightarrow$ Stabilized/Dormant $[D_{P2}]$
 - (b) Higher than (or equal to) $V_{ACT} \rightarrow$ Reactivated $[D_{P2}]$
 - (c) Not assessable \rightarrow Dormant $[D_{INV}]$
3. Active $[D_{INV}]$ landslides, whose V_P is:
 - (a) Lower than $V_{ACT} \rightarrow$ Dormant/Active $[D_{P2}]$
 - (b) Higher than (or equal to) $V_{ACT} \rightarrow$ Active $[D_{P2}]$
 - (c) Not assessable \rightarrow Active $[D_{INV}]$

The ambiguous (double) classification in the lowermost-left cells of the activity matrix for

pre-mapped phenomena reflects the ‘conservative’ or ‘cautionary’ approach the activity matrices are based on. Even if PSI data register low movement rates, the state of activity recorded in the pre-existing inventory is not lowered (i.e., from dormant to stabilized, or from active to dormant), unless field evidence and in situ monitoring data confirm an actual lowering of activity (e.g., pre-mapped dormant and active landslides showing recent PSI-derived velocity lower than V_{ACT}).

The temporal coverage of PSI data influences the final time reference of the updated inventory; this will correspond to the last acquisition of the PSI monitoring interval. Thus, for those phenomena whose updating is performed by using PSI estimates, the reference will be $[D_{P2}]$; for instance, the employment of RADARSAT1 [2003–2009] data produces an updated inventory referenced to 2009. On the other hand, landslides with total absence or insufficiency of PSI-based deformation velocities (i.e., not assessable V_P) will retain the time reference of the inventory from which they belong to, i.e., $[D_{INV}]$.

4.2 Activity Matrix for Newly Detected Landslides

For newly detected landslides or for pre-mapped phenomena lacking in past evaluation of activity, an activity matrix combining historical and recent deformation PSI data can be used. In this case, the input parameters of the matrix are the historical representative velocity V_H , defined in the interval $[D_{H1}-D_{H2}]$ and present representative velocity V_P , defined in the $[D_{P1}-D_{P2}]$, subsequent to $[D_{H1}-D_{H2}]$.

The nine different combinations constituting this second type of activity matrix, and their respective outcomes, can be summarized as follows:

1. Landslides whose V_H is lower than the threshold V_{ACT} and whose V_P is:

(a) Lower than $V_{ACT} \rightarrow$ Stabilized $[D_{P2}]$

(b) Higher than (or equal to) $V_{ACT} \rightarrow$ Reactivated $[D_{P2}]$

(c) Not assessable \rightarrow Stabilized/Dormant $[D_{H2}]$

2. Landslides whose V_H is higher than (or equal to) V_{ACT} and whose V_P is:

(a) Lower than $V_{ACT} \rightarrow$ Dormant $[D_{P2}]$

(b) Higher than (or equal to) $V_{ACT} \rightarrow$ Active $[D_{P2}]$

(c) Not assessable \rightarrow Active/Reactivated $[D_{H2}]$

3. Landslides with not assessable V_H and whose V_P is:

(a) Lower than $V_{ACT} \rightarrow$ Stabilized/Dormant $[D_{P2}]$

(b) Higher than (or equal to) $V_{ACT} \rightarrow$ Active/Reactivated $[D_{P2}]$

(c) Not assessable \rightarrow not classified (NC)

As well as the first typology of matrices, the temporal coverage of PSI data also influences the time reference of the evaluations for newly detected phenomena. For those phenomena whose updating is performed by using historical estimates, the reference will be $[D_{H2}]$, while for present data it will be $[D_{P2}]$.

An alternative for the matrix in Fig. 3b is the substitution of its third column with the modified version which is shown in Fig. 3c and corresponds to the typology of matrix used by Righini et al. (2012). In this case, when the present PSI data are insufficient within the landslide boundary, but the information on the historical landslide velocity is available, the following conditions are modified as follows:

1(c) V_H lower than $V_{ACT} \rightarrow$ Stabilized/Reactivated $[D_{P2}]$

2(c) V_H higher than (or equal to) $V_{ACT} \rightarrow$ Dormant/Active $[D_{P2}]$.

The difference with the original matrix in Fig. 3b consists in the reference time of the

assessment, which is $[D_{P2}]$ and the uncertainty is between the two states of activity, with V_H information but no V_P information.

Further double names of cells in Fig. 3b, c are still resolvable only through field validation and reflect the uncertainty in the assessment of the state of activity. For new detections, despite the availability of recent deformation measurements, the lack of sufficient present or historical PS ground displacements prevents discernment between stabilized and dormant, or between active and reactivated phenomena (i.e., the two lowermost and two left cells in the matrix).

4.3 Intensity Scale

The landslide intensity is evaluated by comparing the PSI-derived landslide velocity with the intensity threshold, V_{INT} , which discriminates between extremely and very slow velocities (Fig. 3d). The only input parameter for the employment of this scale is the representative velocity of each landslide, in the present (or historical) interval, i.e., V_P (or V_H). The four different combinations of the intensity scale, and their outcomes in terms of intensities and respective temporal references, can therefore be summarized as follows:

1. V_P (or V_H) is lower than $V_{ACT} \rightarrow$ Negligible $[D_{P2}]$ (or $[D_{H2}]$)
2. V_P (or V_H) is higher than (or equal to) V_{ACT} but lower than $V_{INT} \rightarrow$ Extremely Slow $[D_{P2}]$ (or $[D_{H2}]$)
3. V_P (or V_H) is higher than (or equal to) $V_{INT} \rightarrow$ Very Slow $[D_{P2}]$ (or $[D_{H2}]$)
4. Neither V_P nor V_H are assessable \rightarrow Not Classified (NC).

As for the activity matrices, the coverage of PSI data influences the time reference of the intensity evaluation, which will correspond to the last acquisition of the PSI monitoring interval, i.e., $[D_{P2}]$ or $[D_{H2}]$. Total absence or insufficiency of PSI data force the analyzed phenomenon to be attributed to the NC class.

5 Sample Site: Verbicaro (Calabria)

A small area in the province of Cosenza, in the northern sector of Calabria Region, was chosen as an example for the application of the PSI-based matrix approach: a sector extending $\sim 14 \text{ km}^2$ and located within the municipality of Verbicaro. This choice was driven by the geomorphologic characteristics of this area and its variety in terms of landslide activity and intensity, as well as availability of PSI data for the different phenomena affecting its urban and suburban infrastructures.

The geological setting of Verbicaro is characterized by tectono-stratigraphic units piled up and locally dislocated by normal faults. Basal Hercynian crystalline and metamorphic units are overlaid by Mesozoic and Tertiary sedimentary rocks, and finally covered by Upper Neogene and Quaternary sediments (Amodio Morelli et al. 1976).

5.1 Input Data and Preparatory Phase

The pre-existing inventory available for the sample area is the Italian Landslide Inventory (Inventario Fenomeni Franosi in Italia, IFFI) produced by the Italian Institute for Environmental Protection and Research in 2007, set as D_{INV} . This inventory map was created on a reference scale of 1:10,000 by means of aerial photo-interpretation, field campaigns, and local databases. Inside this inventory, three different states of activity are distinguished, i.e., active (including active, reactivated, and suspended), dormant, and stabilized (including artificially and naturally stabilized).

Within the sample area, a total of 24 landslides are mapped in the pre-existing inventory of IFFI. For the sake of simplicity and to identify them easily, we have assigned these unstable areas a short code, going from L1 to L24 (Fig. 4). Most of the identified phenomena are classified as rotational/translational slides (i.e., L6 to L13, and L16 to L21) and complex

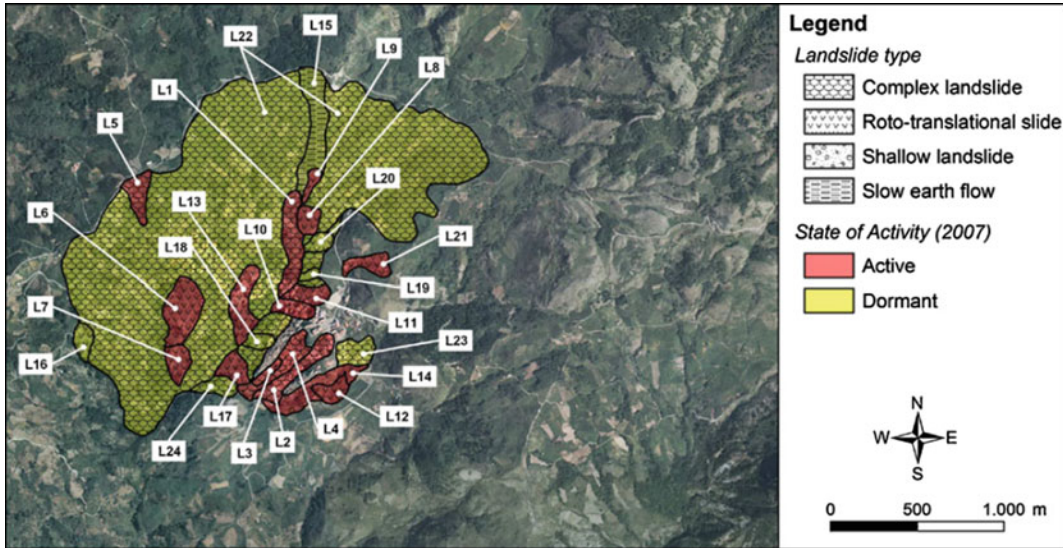


Fig. 4 Preexisting landslide mapping in the area of Verbicaro, overlapped on a color orthophoto acquired in 2000

movements (i.e., L1 to L5, and L22 to L24), and involve mainly low-grade metamorphic rocks and occasionally well-stratified limestones. A dormant complex landslide, L22, constitutes the larger phenomenon affecting the area, with an area of $\sim 2.1 \text{ km}^2$. It involves the whole north-western sector of the village of Verbicaro and is partially overlaid by smaller-scale active slides and complex landslides (e.g., L5 to L7) as well as a flow-like phenomenon characterized by a N to S motion direction (L15) and, to the S, a complex landslide (L1) whose foot reaches the village downstream. The larger portion of Verbicaro village is affected by phenomena moving towards the W and SW, mainly complex (L2 to L4) and rotational/translational slides (e.g., L10, L11, L17, and L18). The latter overlay a dormant complex landslide (L24) involving the whole left bank of the incision where L1 flows. Despite the limited extent of these phenomena, generally less than 0.07 km^2 , they represent a major risk to the local population and urban structures, since their main bodies involve the whole portion of the village located on the W and SW-facing slopes.

PSI data employed in this work were:

- ERS1/2 stack consisting of 78 scenes in descending mode, processed through

PSInSARTM technique (Ferretti et al. 2001), spanning the interval 17/05/1992–20/12/2000, look angle 23.4° , and directional cosines: 0.38972 (E), -0.07976 (N), 0.91747 (Z)

- RADARSAT1 Standard Beam S3 stack consisting of 80 scenes in descending mode, processed through PSP-DIFSAR technique (Costantini et al. 2000), spanning the interval 19/03/2003–17/01/2010, look angle 34.5° , and directional cosines: 0.55423851 (E), -0.11857239 (N), 0.82386907 (Z)
- RADARSAT2 Standard Beam S3 stack consisting of 33 scenes in descending mode, processed through PSP-DIFSAR technique (Costantini et al. 2000), spanning the interval 10/01/2009–06/04/2011, look angle 33.9° , and directional cosines: 0.54939554 (E), -0.09516750 (N) and 0.83012510 (Z).

D_{H1} and D_{H2} were thereby set to 1992 and 2000, while D_{P1} and D_{P2} corresponded to 2003 and 2010 for the RADARSAT1 stack, and 2009 and 2011 for the RADARSAT2 stack. Although the use of both ascending and descending data stacks is generally suggested to implement the approach, for Verbicaro, only data stacks with descending acquisition geometry were used

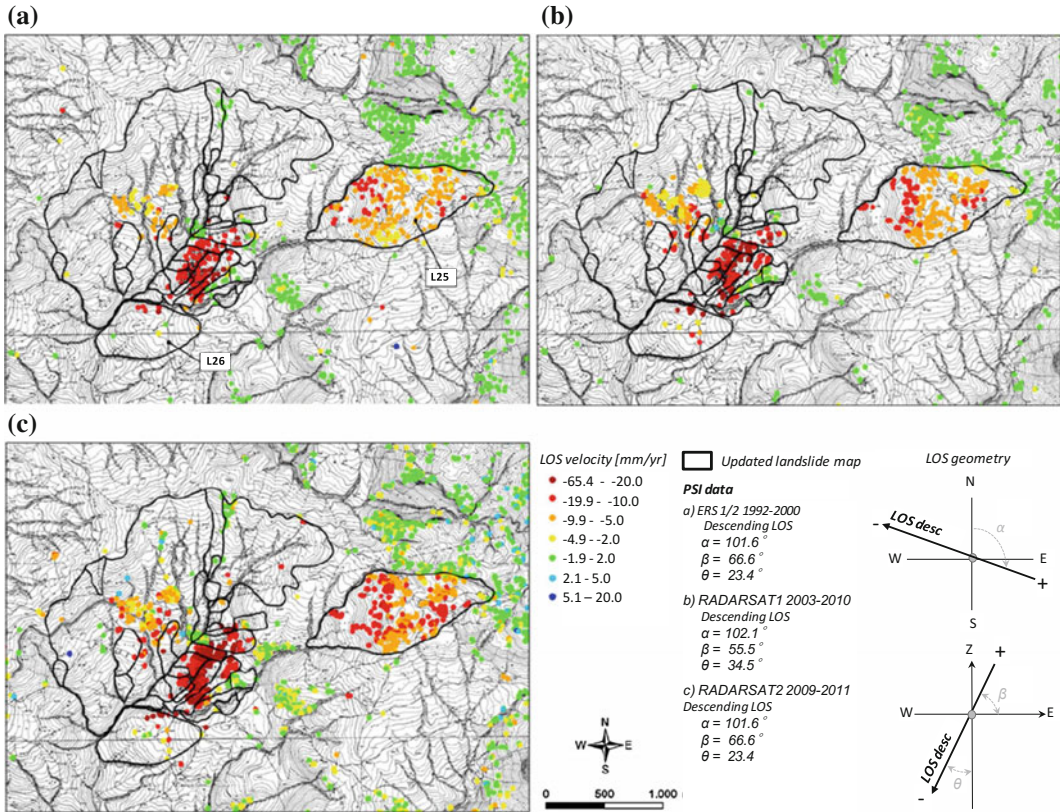


Fig. 5 Updated landslide inventory and PSI-derived deformation in the area of Verbicaro, overlapped on a 1:10,000 topographic map, **a** ERS1/2 descending data in

1992–2001, **b** descending RADARSAT1 data in 2003–2010, **c** RADARSAT2 descending data in 2009–2011

(Fig. 5). This is due to the local morphology of the area, which is predominantly oriented in the SW, W, and NW directions and consequently should be suitably analyzed with PSI descending data.

PS velocities showed higher spatial variability for the RADARSAT2 stack in the whole area of Verbicaro (Fig. 5). This reflects the lower number of scenes used to perform the PSP processing, the short temporal interval (only 2 years) and significant orbital and atmospheric errors, and the consequent lower precision in the estimated velocities. Standard deviations of RADARSAT2 targets ranged between 1.1 and 4.1 mm/year, unlike the lower values recorded for the other two stacks, i.e., 0.6–1.0 mm/year for Radarsat1 and 0.4–0.8 mm/year for ERS1/2.

The pre-existing inventory was firstly updated and improved by combining a monoscopic photo interpretation of the aerial orthophotos, DTM and derived thematic layers with the radar interpretation of PSI-derived ground motion data in 1992–2000 (ERS1/2 descending) and 2003–2011 (RADARSAT1 and RADARSAT2 descending). The methodology allowed us to update the boundaries of pre-mapped phenomena and to identify new landslides. For eight pre-mapped landslides, we applied modifications to their boundaries. Furthermore, two additional phenomena, L25 and L26, were also detected by exploiting the information gathered from optical and radar data (Fig. 6).

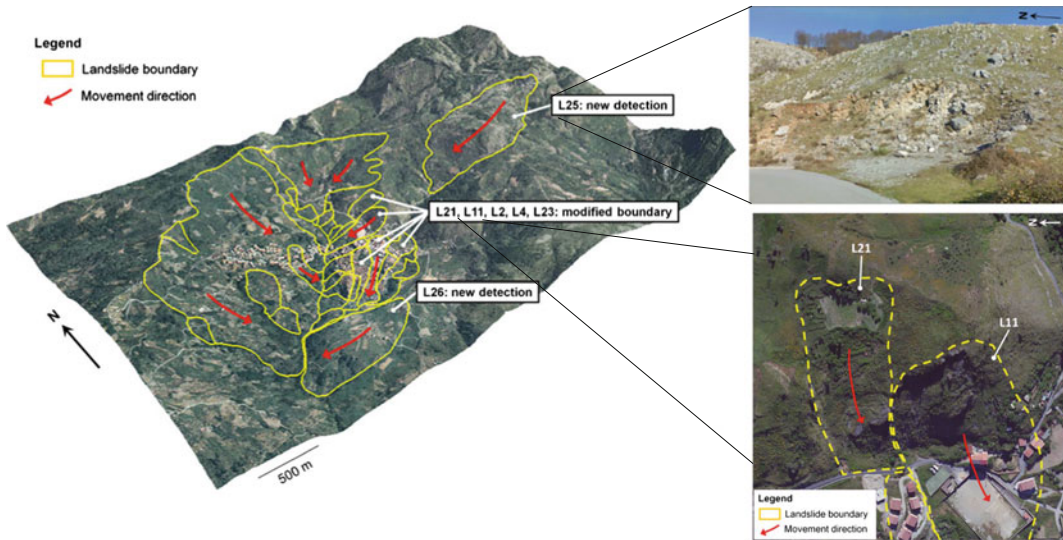


Fig. 6 3D view of the updated landslide mapping in the Verbicaro village, captured from SW at a $\sim 45^\circ$ angle. Heights of the DEM are amplified by a factor of 1.3.

Direction of landslide movements and main modifications to the preexisting inventory are also shown

5.2 Implementation

The representative velocities of the 26 landslides (L1 to L26) in the historical ($V_{H,LOS}$) and present ($V_{P,LOS}$) intervals were evaluated as the average yearly velocity of the available ERS1/2 and RADARSAT1/2 PS data included within each landslide area. For both historical and recent PSI data, the calculation of the representative velocities was performed only for those unstable areas where a sufficient number of PS data was retrieved (at least 4 PS within the landslide boundary).

Using a simplified geomorphologic scheme, we assumed the motions affecting the area to be purely translational mechanisms; thus, we converted LOS deformation data in the descending mode (V_{LOS}) to the most probable direction of displacement, i.e., the steepest slope direction (V_{SLOPE}). This conversion was performed through the use of local topography (aspect and slope data with 20 m cellsize) and the satellite directional cosines, in accordance with Cascini et al. (2010) and Notti et al. (2014).

To implement the matrix approach, we used the ERS1/2-based velocity estimate as the

historical representative velocity ($V_{H,SLOPE}$), while, for the present velocity ($V_{P,SLOPE}$), the highest between $V_{RSAT1,SLOPE}$ and $V_{RSAT2,SLOPE}$ and the respective reference year [D_{P2}] (i.e., 2010 or 2011) was selected.

The V_{ACT} to be applied to the SLOPE-projected velocities was set as ± 5 mm/year. This is because the usual threshold of ± 2 mm/year used for LOS values, based on standard deviations and technique precision of PSI, was incremented by a value of 2.5 (increase of 150%). This value corresponds to the average re-projection factor of 2.5 used to convert LOS to SLOPE estimates, for all the landslides mapped in Verbicaro.

V_{INT} of ± 13 mm/year was selected to discriminate extremely slow from very slow phenomena; the official threshold of 16 mm/year (Cruden and Varnes 1996) was precautionarily reduced by $\sim 20\%$ to account not only for the difference between peak values and temporally averaged velocities (PSI-derived estimates are averages over long observation periods) but also for the spatial averaging that was performed to assess the representative velocity of each analyzed phenomenon.

The application of identical thresholds for both ERS1/2 and RADARSAT1/2 data do not represent a major source of errors in the present application, since LOS velocities of all the PSI stacks were preliminarily projected along the slope directions and so cannot be considered influenced by the slightly different orientations of the LOS.

5.3 Results

Active complex landslides, L1 and L4, and roto-translational slides, L10, L11, L13, L14, and L21, showed a sufficient number of both historical and present PS data within their boundaries (Fig. 7). According to the activity matrix shown in Fig. 3a, specifically devoted to pre-mapped phenomena, only the present representative

velocities were considered for the application of the PSI-based matrix approach. All these landslides revealed $V_{P,SLOPE}$ exceeding the activity threshold of ± 5 mm/year and were thereby reattributed to the state of active (A), with a new reference year of 2011 (L1 to L4, L21) or 2010 (L11, L13, L14)—depending on the Radarsat stack showing the highest rates.

Similar to these landslides, L22 to L24, previously classified as dormant complex landslides, were updated using the matrix of Fig. 3a. In particular, while for L22 and L24, the $V_{P,SLOPE}$ exceeded the activity threshold and thus they were classified as reactivated (R), for L23 we observed a representative velocity lower than the threshold, suggesting the stabilization of this phenomenon. However, following the conservative principle of not lowering the activity before confirming the actual lowering through on-site

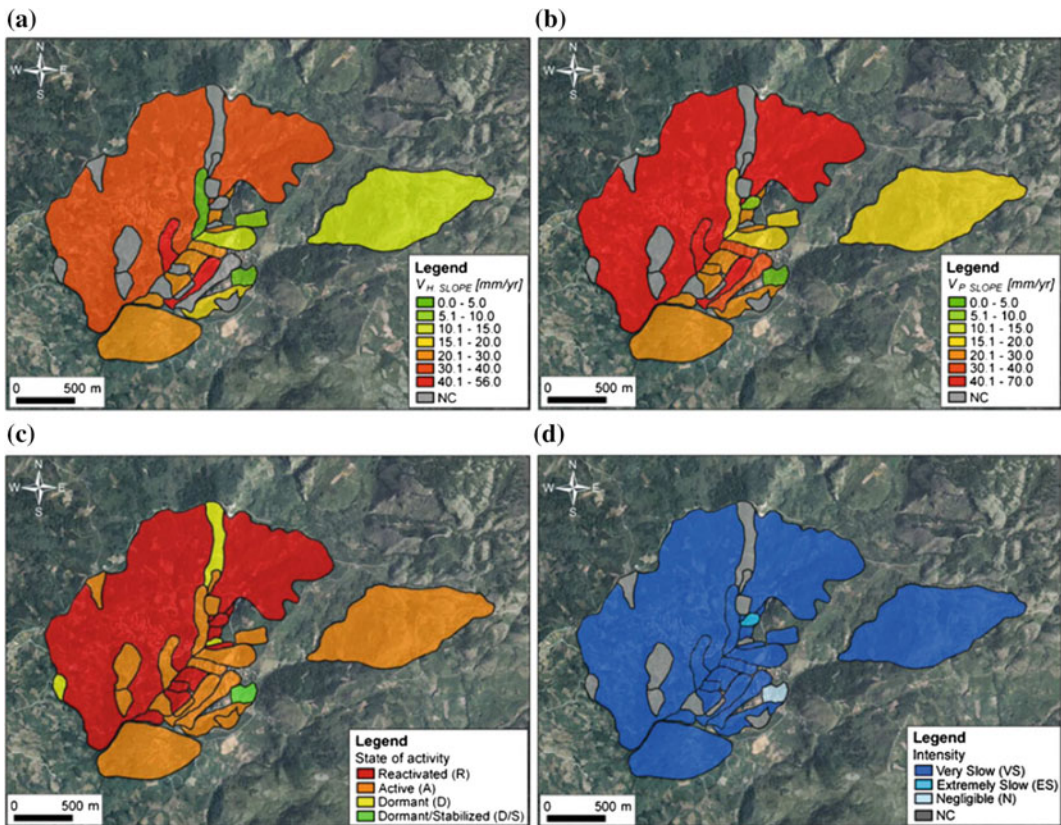


Fig. 7 Historical (a) and present (b) representative velocities, and states of activity (c) and intensity (d) of landslides mapped in Verbicaro, overlaid on a color orthophoto

validation, we attributed to L23 the ambiguous state of dormant/stabilized (D/S). As for the assessment of the intensity of these pre-mapped phenomena, all were classified as very slow (VS), since their $V_{P,SLOPE}$ were all higher than the intensity threshold of ± 13 mm/year (Fig. 7 d), with the exception of L23, which was classified as negligible (N), since its velocity $V_{P,SLOPE}$ was only a few millimeters per year.

Complex landslide L2, active in 2007, and roto-translational slides L18 and L20, dormant in 2007, showed situations that typically occur when one or more stacks of PSI data are not available or insufficiently distributed within the landslide boundaries. For L2 and L20, PSI-derived estimates of ground deformation were only available for the present scenario (i.e., RADARSAT1/2 stacks). For L2, the active (A) state was confirmed and the very slow intensity (VS) was attributed, given that its $V_{P,SLOPE}$ exceeded both the V_{ACT} and the V_{INT} . On the other hand, for L20, the state of activity was updated to reactivated (R) and the intensity to extremely slow (ES) in 2011, as its $V_{P,SLOPE}$ was between V_{ACT} and V_{INT} (Fig. 7). For the pre-mapped landslides L3, L5 to L9, L12, L15 to L17, and L19, partial lack or total absence of PSI data was observed within the respective boundaries and thereby the employment of the matrix and scale of Fig. 3a, d caused these phenomena neither to be updated in terms of state of activity (their reference year was left as 2007) nor to be attributed an intensity (Fig. 7c, d).

Summing up, for 13 of the 24 pre-mapped landslides, the activity was updated to 2011 or 2010 and the intensity was also assessed with same reference year; on the other hand, for the remaining 11 phenomena, the activity recorded in the IFFI inventory was left unchanged and no evaluation of the intensity was performed due to the absence or insufficiency of PS data within the boundaries of these landslides (NC). A total of 4 reactivated (R), 16 active (A), three dormant (D), and one dormant/stabilized (D/S) phenomena were finally identified. Considering the intensity, the 13 updated landslides were distributed as follows: 11 very slow (VS), one extremely slow (ES), and one negligible (N).

The two newly identified phenomena, L25 and L26, were covered by PSI data in all the available stacks, i.e., ERS1/2, RADARSAT1, and RADARSAT2. Both these unstable areas showed historical and present velocities exceeding the activity threshold of ± 5 mm/year and the intensity threshold of ± 13 mm/year. L25 average motions in the slope direction were 12.8 and 16.0 mm/year in 1992–2000 and 2009–2011 respectively, while L26 showed slightly higher rates, i.e., 20.8 and 24.5 mm/year in 1992–2000 and 2003–2010. These phenomena were thereby attributed the state of active (A) and the intensity of very slow (VS); L25 had a new reference year of 2011 and L26 a year of 2010 (Fig. 7). Given the areal extent of L25 and the variable morphology of this unstable area, the use of a unique representative velocity for the whole phenomenon is inappropriate. Further studies could be focused on a segmentation of the unstable area into subsectors of homogeneous morphology for which velocities for specific sectors might be calculated.

6 Discussion and Pending Issues

Major influencing factors of the PSI-based matrix approach are the lack of PS within the landslide boundary, the temporal coverage of PSI data, the choice of activity and intensity thresholds, and the need for field validation. The total lack or insufficiency of targets within the landslide boundaries induce uncertainties in the activity and intensity evaluations, or even prevent the analyzed phenomena from being classified and/or updated (e.g., landslides L5 to L9 in Verbicaro). A combination of local topography and LOS orientation may cause significant underestimation of land motions, or even hamper the identification of PS within the observed scene. The re-projection of LOS velocities along the local steepest slope allowed us to avoid limitations due to the different acquisition geometries. The geometrical visibility of an area can be detected according to already developed criteria, i.e., Notti et al. (2010), or Cascini et al. (2010).

It is worthwhile to highlight that rapid movements cannot be detected by SAR data because of aliasing effects due to ambiguity problems. Maximum measurable velocities depend on the employed SAR wavelengths and satellite revisiting times, e.g., 15 cm/year for ERS data and 20 cm/yr for RADARSAT data.

Depending on the temporal coverage of PSI-derived deformation data, the matrix approach may modify the temporal scale for the evaluation of the states of activity, changing the time interval for discriminating different states from a single cycle of seasons (i.e., 12 months; WP/WLI 1993) to two or more years (e.g., 2 years, using 2009–2011 Radarsat 2 data for the analysis of recent deformation velocities in Verbicaro). The lengthening of the reference time interval makes the evaluation of the activity more precautionary, since the behaviour of each landslide is analyzed within a wider time frame with respect to the 12-month-based observation range proposed by the WP/WLI in 1993. Furthermore, when the interval spanned by the available PSI-derived data may temporally overlap with the date of completion of the pre-existing inventory, the PSI velocities do not represent just the deformational scenario subsequent to the time reference of the inventory itself, but they rather include some contributions from the scenario antecedent to this reference.

The choice of activity and intensity thresholds is a key point for the PSI-based matrix analysis and needs to be performed taking into account the typology of observed deformation processes (e.g., geometry and expected velocity), the characteristics of available PSI data (i.e., V_{LOS} or V_{SLOPE}). Usually, V_{INT} is precautionarily assumed to be lower than the official velocity threshold discriminating extremely from very slow landslides (i.e., 16 mm/year; Cruden and Varnes 1996), since PSI rates are average velocities both in space and time. The V_{ACT} threshold is usually chosen as the minimum value exceeding the precision of the PSI technique, i.e., a few millimeters per year (e.g., Righini et al. 2012). It is worth to highlight that the use of significantly low activity thresholds reduces the probability of discarding movements

that are potentially critical, guaranteeing that even the slower motions are detected and classified. However, it causes some gravitational movements, such erosion or downhill creep, to be included in the updated inventory maps.

Finally, the PSI-based matrix approach, as any landslide study supported by remote sensing data, should always be validated through field checks and surveys in order to confirm, or even improve, all the information and evaluations performed through satellite radar interpretation. The need of field checks is also necessary for those ambiguous classifications of the states of activity included in the activity matrices (e.g., what happened for landslide L23 in Verbicaro), for which on-site inspections are required to confirm an actual lowering of the landslide activity.

7 Conclusions

We presented the definition, procedures, discussion, and one example of application of the ‘PSI-based matrix’ approach used to assess or update the state of activity and intensity of extremely to very slow landslide processes. For the sample site of Verbicaro, we exploited 1992–2011 PSI data, and the methodology allowed the assessment of the state of activity and the intensity for 13 of the 24 pre-mapped phenomena and also for two newly identified phenomena, L25 and L26, with the year 2011 or 2010 as temporal reference of these estimations. The application for the test area of Verbicaro brought to light the major influencing factors of the PSI-based matrix approach, such as the lack of PS data within the landslide boundaries, the temporal coverage of the available data, and the need for field checks and validation, as well as the operative procedures to choose the activity and intensity thresholds.

Acknowledgements This work was carried out within the SAFER (Services and Applications For Emergency Response) project, funded by the European Commission within the 7th Framework Programme under the Global Monitoring for Environment and Security initiative, with Grant Agreement no. 218802.

References

- Amodio Morelli L, Bonardi G, Colonna V, Dietrich D, Giunta G, Ippolito F et al (1976) L'arco Calabro-Peloritano nell'orogene Appenninico-Maghrebide. *Mem Soc Geol Ital* 17:1–60
- Bianchini S, Cigna F, Righini G, Proietti C, Casagli N (2012) Landslide hotspot mapping by means of persistent scatterer interferometry. *Environ Earth Sci* 67:1155–1172
- Bianchini S, Cigna F, Casagli N (2013) Improving landslide inventories with multi-temporal measures of ground displacements retrieved through Persistent Scatterer Interferometry. In: *Proceedings of the second world landslide forum, Rome (Italy)*, vol 3, pp 7–13
- Cascini L, Fornaro G, Peduto D (2010) Advanced low and full resolution DInSAR map generation for slow-moving landslide analysis at different scales. *Eng Geol* 112:29–42
- Catani F, Casagli N, Ermini L, Righini G, Menduni G (2005) Landslide hazard and risk mapping at catchment scale in the Arno River basin. *Landslides* 2(4):329–342
- Cigna F, Bianchini S, Casagli N (2013) How to assess landslide activity and intensity with persistent scatterer interferometry (PSI): the PSI-based matrix approach. *Landslides* 3(10):267–283
- Cigna F, Bianchini S, Righini G, Proietti C, Casagli N (2010). Updating landslide inventory maps in mountain areas by means of Persistent Scatterer Interferometry (PSI) and photo-interpretation: Central Calabria (Italy) case study. In: Malet JP, Glade T, Casagli N (eds) *Mountain risks: bringing science to society* (572 pp). CERG Editions, Strasbourg, France, pp 3–9
- Costantini M, Iodice A, Magnapane L, Pietranera L (2000) Monitoring terrain movements by means of sparse SAR differential interferometric measurements. In: *Proceedings of IGARSS 2000, 20th IEEE international geoscience and remote sensing symposium, Honolulu, Hawaii, USA, 24–28 July 2000*, pp 3225–3227
- Cruden DM, Varnes DJ (1996) Landslide types and processes. In: Turner AK, Schuster RL (eds) *Landslides: investigation and mitigation*, Sp. Rep. 247, Transportation Research Board, National Research Council. National Academy, Washington DC, pp 36–75
- Einstein HH (1988) Landslide risk assessment procedure. In: *Special Lecture, Proceedings of 5th international symposium on landslides*. Lausanne, Switzerland, Rotterdam, Balkema, vol 2, pp 1075–1090
- Farina P, Colombo D, Fumagalli A, Marks F, Moretti S (2006) Permanent scatterers for landslide investigations: outcomes from the ESA-SLAM project. *Eng Geol* 88:200–217
- Ferretti A, Prati C, Rocca F (2001) Permanent scatterers in SAR interferometry. *IEEE Trans Geosci Remote Sens* 39(1):8–20
- Frangioni S, Bianchini S, Moretti S (2015) Landslide inventory updating by means of persistent scatterer interferometry (PSI): the Setta basin (Italy) case study. *Geomat Nat Hazards Risk* 6(5-7):419–438
- Hungr O (1997) Some methods of landslide intensity mapping. In: Cruden D, Fell R (eds) *Landslide risk assessment. Proceedings of the international workshop on landslide risk assessment, Honolulu, USA, 19–21 Feb 1997*. Balkema, Rotterdam, pp 215–226
- IUGS/WGL-International Union of Geological Sciences Working Group on Landslides (1995) A suggested method for describing the rate of movement of a landslide. *IAEG Bull* 52(75–78):1933–1939
- Meisina C, Zucca F, Notti D, Colombo A, Cucchi A, Savio G, Giannico C, Bianchi M (2008) Geological interpretation of PSInSAR data at regional scale. *Sensors* 8(11):7469–7492
- Notti D, Davalillo JC, Herrera G, Mora O (2010) Assessment of the performance of X-band satellite radar data for landslide mapping and monitoring: Upper Tena Valley case study. *Nat Hazards Earth Syst Sci* 10:1865–1875
- Notti D, Herrera G, Bianchini S, Meisina C, García-Davalillo JC, Zucca F (2014) A methodology for improving landslide PSI data analysis. *Int J Remote Sens* 35(6):2186–2214
- Righini G, Pancioli V, Casagli N (2012) Updating landslide inventory maps using persistent scatterer interferometry (PSI). *Int J Remote Sens* 33(7):2068–2096. doi:10.1080/01431161.2011.605087
- WP/WLI—Working Party on World Landslide Inventory (1993) *Multilingual glossary for landslides*. The Canadian Geotechnical Society, BiTech, Richmond BC

TXT-tool 4.034-1.1

Quantitative Rockfall Risk Assessment for Roadways and Railways

Olga Mavrouli and Jordi Corominas

Abstract

This tool presents a methodology for quantifying the rockfall risk and the consequences for vehicles circulating on roadways and railways. We present a complete and comprehensive methodology for risk assessment, using various risk descriptors, with an emphasis on the quantification of the exposure of the vehicles and the consequences from rockfall hits, in function of the rockfall frequency and magnitude. Indications on the calculation of the repair costs for damaged roadways and railways and for the indirect loss, due to their temporary closure, are also given. This methodology is useful for end-users involved in the risk management and the design of protection measures.

Keywords

Rockfalls • Risk assessment • Roadways • Railways • Vehicles

Contents

1	Introduction	510	3.2	Probability that a Rockfall Occupies Partially or Totally One or Two Lanes of the Roadway, P(S:A)	514
2	Rockfall Consequences and Risk Descriptors	510	3.3	Probability that a Moving Vehicle Passes by the Affected Section at the Moment of the Rockfall, P(T:S).....	515
3	Risk Assessment for Rockfall Impacts on Vehicles	511	3.4	Vulnerability, V_i	515
3.1	Rockfall Frequency, f_a	513	3.5	Rockfall Scenarios	516
			4	Repair Costs for Damaged Transportation Corridors	516
			5	Indirect Loss Due to Closure of Transportation Corridors	517
			6	Example	517
				References	518

O. Mavrouli (✉) · J. Corominas
Division of Geotechnical Engineering and
Geosciences, Department of Civil and
Environmental Engineering, Universitat Politècnica
de Catalunya, 08034 Barcelona, Spain
e-mail: olga-christina.mavrouli@upc.edu

J. Corominas
e-mail: jordi.corominas@upc.edu

1 Introduction

Rockfalls occur in mountain environments, coastal cliffs and cuts. Rockfalls are frequent rock instabilities that affect transportation corridors such as roadways and railways and result in the damage of vehicles and the injury of their passengers. Administrative authorities and professionals working on the protection of roadway and railway networks, are often required to consider such loss and to evaluate its potential and extent in order to prepare a rockfall management plan. Besides, the prioritization of stabilization and/or protection measures as well as the drawing of emergency preparedness plans in case of transportation corridor interruption, it requires the assessment of the rockfall risk.

Several approaches of risk analysis at site-specific and local scale for transportation routes are found in the literature (Budetta 2004; Ferlisi et al. 2012; Corominas et al. 2014). However, only few examples of rockfall risk tools, taking into account local scale data for the hazard and the consequences have been presented so far. Here, we present a tool for the quantification of the rockfall risk in roadways and highways. It can be applied at site-specific, local and regional scale. The risk calculation integrates the local data for the rockfall hazard as well as for the transportation corridors. Moreover, users can easily automatize it (e.g. using Microsoft Excel).

Risk can be defined as a measure of the probability and severity of an adverse effect to health, property or the environment (Fell et al. 2005). It is estimated as the product of probability (or frequency) of the potentially damaging event and its consequences, as given by Eq. 1:

$$R = H \times E \times (V \times C) \quad (1)$$

where

- H hazard term expressed by frequency/probability of a potentially damaging event (rockfall) of a given magnitude
- E the element or set of elements at risk (property, persons) exposed to the hazardous event

- V vulnerability of the exposed element(s)
- C cost of the exposed element(s)

The quantitative rockfall risk analysis entails the evaluation of Eq. 1 and of its components in quantitative terms, using numerical scales or ranges of values to express the probability of an expected level of loss, as opposed to the qualitative methods that employ nominal ranks. The quantitative rockfall risk analysis has been gaining ground over the qualitative one for overcoming the use of ambiguous terms and for yielding reproducible, standardized and comparable results among distant locations and regions. It provides a potential tool for taking coherent criteria-based decisions and for assessing objectively their efficacy.

In this chapter, it is described how Eq. 1 can be applied for the quantification of the rockfall risk in transportation corridors, using different risk descriptors (Sect. 2) for: vehicle damage (Sect. 3), roadways and railways repair costs (Sect. 4), and indirect costs resulting from the roadways/railway temporary closure (Sect. 5).

2 Rockfall Consequences and Risk Descriptors

Rockfalls affect transportation corridors in diverse ways. Different risk descriptors are required to express the type and extent of the consequences, depending on the affected elements, the objective of the risk assessment and the work scale. Descriptors consist of parameters or combinations of parameters that provide information on the terms of Eq. 1. This tool treats the following types of consequences, which are classified into two main groups (Corominas and Mavrouli 2013, 2014):

- (a) Direct consequences: (i) physical damage of vehicles and (ii) destruction of roadways/highways resulting from a rockfall impact.
- (b) Indirect consequences: traffic detours resulting from the blockage of transportation corridors and the disruption of activities.

Here, the risk descriptors for expressing the risk deriving from the physical damage of vehicles (a-i) include:

- the expected annual number of the impacted vehicles;
- the expected annual repair cost of vehicles in the road/rail section;
- the return period for 1 vehicle being completely destroyed;
- the return period of 1 vehicle being impacted.

As an example of the difference in the use of these descriptors, the annual number of the impacted vehicles and the expected annual repair cost of vehicles are often solicited by administrative authorities in order to manage the rockfall risk, whereas the return period for 1 vehicle being impacted or completely destroyed, is mostly useful for insurance companies.

Additional risk descriptors can be delivered as frequency-consequence or probability-consequence pairs for given scenarios. This output is essential for evaluating whether the risk is acceptable/tolerable, after comparison with pre-established thresholds (Finlay and Fell 1997).

The destruction of roadways/highways (a-ii) is quantified in terms of the average annual cost for repair. It is taken into account that depending on the rockfall magnitude, damage may vary from small fissures on the pavement to total collapse.

Last, we show how indirect causes (b) can be assessed considering the excess expenses arising from obligatory traffic detours via alternative routes in case of route blockage. Vehicle circulating costs and lost work-hours are integrated.

3 Risk Assessment for Rockfall Impacts on Vehicles

Figure 1 shows the risk generated by the rockfalls on a rocky cliff, threatening a road. The assessment of the risk deriving from damage due

to rockfall impact(s) on vehicle(s) is made by the adaptation of the Eq. 2 and the assessment of its terms. The risk equation in quantitative terms can be expressed as (modified from Dai et al. 2002; Fell et al. 2005):

$$R = \sum_{M_i} R(A) = f_a \times P(S:A) \times P(T:S) \times V_i \quad (2)$$

where:

$R(A)$	annual risk for every class of rockfall
f_a	annual frequency of a rockfall of a given class (non cumulative)
$P(S:A)$	conditional probability that a rockfall occupies partially or totally one or two lanes of the roadway
$P(T:S)$	conditional probability that a moving vehicle passes by the affected section at the moment of the rockfall
V_i	vulnerability of the vehicle for the magnitude M_i
M_i	magnitude range corresponding to the rockfall class.

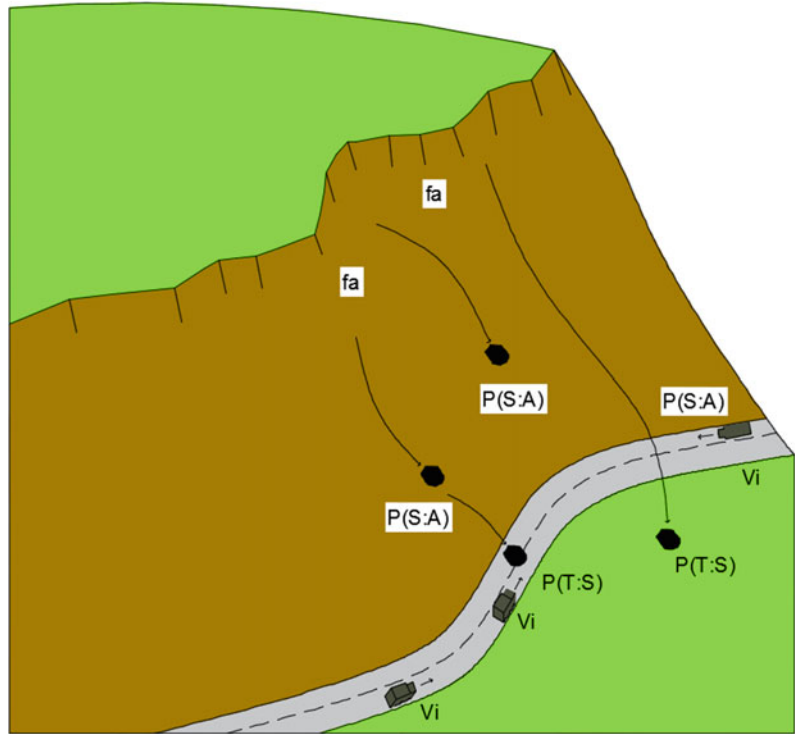
In link with Eq. 1, the rockfall hazard is expressed by two terms in the risk equation: the frequency, f_a and the conditional probability that a rockfall occupies partially or totally one or two lanes of the roadway, $P(S:A)$. The conditional probability that a moving vehicle passes by the affected section at the moment of the failure $P(T:S)$ expresses the exposure and the term V_i the vulnerability.

Diverse risk descriptors are evaluated by Eqs. 3–6, as adaptations of Eq. 2, introducing additionally, in some cases, the cost C of a vehicle (p.e. in €):

Expected annual number of the impacted vehicles, N :

$$N = \sum_{M_i} N(A) = f_a \times P(S:A) \times P(T:S) \quad (3)$$

Fig. 1 Schematic representation of the rockfall risk components of Eq. 1



Expected annual repair cost of vehicles in the road/rail section, R:

$$RC = \sum_{Mi} RC(A) = f_a \times P(S:A) \times P(T:S) \times V \times C \quad (4)$$

Return period of 1 vehicle being impacted (in years), T_{imp} :

$$T_{imp} = 1 / \sum_{Mi} N(A) = 1 / [f_a \times P(S:A) \times P(T:S)] \quad (5)$$

Return period for 1 vehicle being completely destroyed (in years):

$$T_{des} = 1 / \sum_{Mi} R(A) = 1 / [f_a \times P(S:A) \times P(T:S) \times V] \quad (6)$$

The approaches for the risk analysis vary depending on whether it refers to a single object (i.e. road cutting), a linear feature (i.e. road/rail

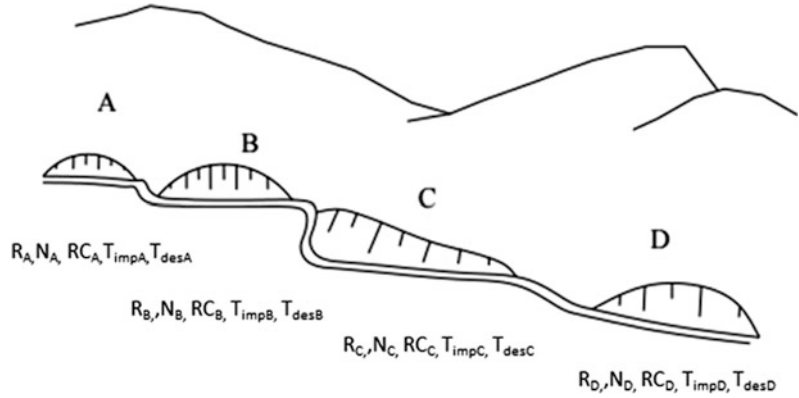
section) or an area (i.e. an entire municipality). Local and regional governments in charge of land-use planning and urban development are mostly interested in the spatial (areal) analysis, the outputs of which usually provide data on the spatial distribution of the risk and can be presented as maps.

The risk descriptors of Eqs. 2–6, calculated partially for single objects can be summed up to provide the risk for linear sections and in their turn for an entire transportation network. An example is presented in Fig. 2. It shows a mountain road, crossing four road cuts (A to D). The risk descriptors are obtained in function of the separate section risks (marked with the index of each section) using the afore-mentioned expressions.

Total annual risk, R_T :

$$R_T = \sum_{Mi} R(A)_A + \sum_{Mi} R(A)_B + \sum_{Mi} R(A)_C + \sum_{Mi} R(A)_D \quad (7)$$

Fig. 2 Road cuts and risk descriptors for each section



Total expected annual number of the impacted vehicles, N_T :

$$N_T = N_A + N_B + N_C + N_D \quad (8)$$

Expected annual repair cost of vehicles in the road/rail section, RC_T :

$$RC_T = RC_A + RC_B + RC_C + RC_D \quad (9)$$

Return period of 1 vehicle being impacted (in years), T_{Timp} :

$$T_{Timp} = 1/N_T \quad (10)$$

Return period for 1 vehicle being completely destroyed (in years), T_{Tdes} :

$$T_{Tdes} = 1/R_T \quad (11)$$

The coverage and the scale of work as well as the amount of available data affect substantially the resolution of the analysis and the calculation of the risk components. In the following sections specific instructions are given for it.

3.1 Rockfall Frequency, f_a

For the calculation of the frequency, f_a , which usually expresses the average number of events per years, rockfall inventories are required. The most reliable sources of data come from rockfall records from maintenance units of roads and railways, park services or civil protection (Bunce

et al. 1997; Hungr et al. 1999; Guzzetti et al. 2003). However, some of these inventories have some limitations. Mainly, they cover a short time-span and often deal with rockfall events of a minimum size. Ground impact features and damages to vegetation located in the rockfall paths are an alternative to prepare a series of rockfall events (Schnewly and Stoffel 2008; Corominas and Moya 2010). In some few cases, rockfall inventories may be completed by dating the features of the ancient deposits and silent witnesses.

Roberds (2005) has made a critical distinction for the evaluation of f_a : the occurrence of the rockfall may be determined either at the source or at the potentially affected area, in this case the roadway/highway. To address this, two different approaches can be followed: (a) assess the failure frequency of each slope and propagation separately, and assess in this way the frequency of the blocks reaching the road. In this case, a magnitude-frequency relation is required at each slope or land unit and, afterwards, the estimation of the run-out distance for each landslide magnitude (Corominas and Moya 2008; Algiardi et al. 2009); (b) assess the frequency directly on a roadway/railway based on statistics of past rockfall impacts (Bunce et al. 1997; Hungr et al. 1999; Dussage-Peisser et al. 2002). The latter is the most common, as data are usually inventoried for those rockfalls reaching the road/rail.

Small and even mid-sized events produce accumulation of boulders that are often indistinguishable among them and, as a consequence,

some censoring takes place in the series. The censoring effect may be eliminated with a careful selection of the volume ranges and determination of the frequency of each of them. As a simple example, the frequency of small-sized events may be established based on the data gathered in the technical reports covering a time span of several tens of years. The frequency of mid-sized events might be established based on the historical data and high-resolution absolute dating techniques, such as dendrochronology.

Parameters relevant to triggering factors, such as earthquake shaking, are often used in hazard analyses, in order to investigate their correlation with rockfalls, and to establish thresholds for the failure initiation. The correlation of rockfalls with rainfall events is very weak thus the collection of rainfall data is usually a secondary priority for the quantification of rockfall hazard and risk.

Magnitude-frequency relations are fundamental for performing quantitative rockfall risk analysis. Magnitude expresses the rockfall volume. The observed magnitude-frequency distribution of rockfalls in different regions can be represented by statistical distribution laws. The most accepted is the power law (Hungry et al. 1999; Dussauge-Peisser et al. 2002; Guzzetti et al. 2003), which takes the following form (Eq. 12):

$$f_a(V) = \lambda V^{-b} \quad (12)$$

where:

$f_a(V)$ annual frequency of rockfall events of a given volume V
 V rockfall volume
 λ, b constants

The conceptual relationship between rockfall magnitude and frequency is shown in Fig. 3 (Corominas and Moya 2008). Typically, the power law relation is valid for a defined range of rockfall volumes. Malamud et al. (2004) and Picarelli et al. (2005) suggested the extrapolation of power-law magnitude-frequency relations, for a preliminary assessment of the largest events. Instead, a truncation of the afore-mentioned distributions has been suggested by other

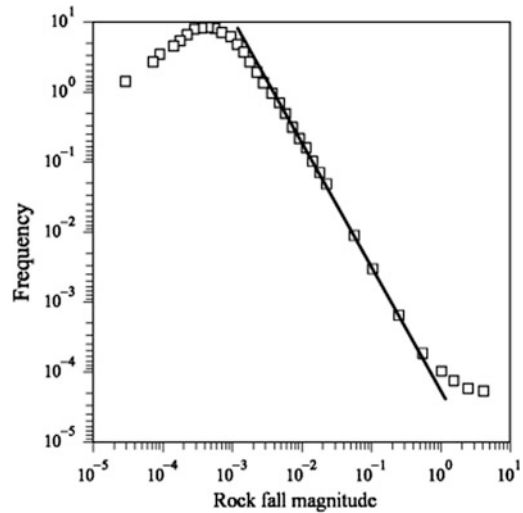


Fig. 3 Typical plot of the magnitude-frequency relation observed in landslide inventories (Corominas and Moya 2008)

researchers (Ruiz-Carulla et al. 2015; Turcotte et al. 2002), which suggests that this extrapolation should be performed with caution.

The expected rockfall volumes should be ranked into different classes, as for example: 0.05–0.5, 0.5–5, 5–50, 50–500, 500–5000, >5000 (m^3). These classes should be established according to local inventory data, considering that different classes lead to different levels of damage.

3.2 Probability that a Rockfall Occupies Partially or Totally One or Two Lanes of the Roadway, $P(S:A)$

The probability that a rock block path affects the whole width of the roadway, $P(S:A)$ is evaluated judgmentally in function of the magnitude of the event; while small rockfalls occupy only very small parts of the road (and usually stop close to the verge of the roadway), larger rockfalls occupy its whole width. Some indicative values are given in Table 1. For wide roads, it might be considered that it varies according to the lane direction (lanes right next to the slope and lanes of the opposite direction).

Table 1 Indicative rockfall classes for a local road and values of P(S:A)

Rockfall class (m ³)	P(S:A)
0.05–0.5	0.4
0.5–5	0.6
5–50	0.8
50–500	1
500–5000	1
>5000	1

3.3 Probability that a Moving Vehicle Passes by the Affected Section at the Moment of the Rockfall, P(T:S)

The probability that a moving vehicle passes by the affected section at the moment of the rockfall is spatial and temporal. Diverse approaches exist for its calculation, depending on whether they integrate the length of the vehicle (car, truck or train) and/or the affected road/rail length by the rockfall (Nicolet et al. 2015).

The most common methods take into consideration the length of the vehicle, as in Eq. 13. This is strongly suggested for railways, where the train length is substantial.

$$P(T:S) = \frac{N_v \times L_v}{24 \times \frac{1000}{V_v}} \tag{13}$$

where:

- N_v circulation intensity (number of vehicles/day)
- V_v velocity (average value) (km/h)
- L_v vehicle length (average value) (m)

For rockfalls with a length significantly larger than the circulating vehicles, the affected road/rail length can be instead taken into account. This approach is less often, as in most cases rockfalls affecting small sections are the most common. Equation 14 represents the probability

of the geometric centre of a moving vehicle being located in the section covered by the event.

$$P(T:S) = \frac{N_v \times L_r}{24 \times \frac{1000}{V_v}} \tag{14}$$

where:

- N_v circulation intensity (number of vehicles/day)
- V_v velocity (average value) (km/h)
- L_r road/rail length affected by the rockfall (m)

With this approach, P(T:S) contemplates that several cars may be hit in an affected section simultaneously. In fact, it expresses the expected number of the affected cars instead of a probability (Nicolet et al. 2015).

Information relative to the daily traffic needed for this evaluation may be found from public services for the administration of highways.

3.4 Vulnerability, V_i

For moving vehicles at roadways and railways, the kinetic energy during the impact is up to 1.4 times higher than for the stationary vehicles or impacts with the pavement, due to the velocity of the vehicle (Bunce et al. 1997). To define a relevant kinetic energy threshold, it can be considered that any rock with kinetic energy sufficient to damage the pavement could damage a vehicle

and injure or kill its passengers. In that case, the vulnerability V_i would be 1.

To evaluate the risk for passengers, V_i should refer to the people instead of vehicles. For simplicity reasons, it is often conservatively assumed that every hit may lead to a fatality, thus the vulnerability of persons is $V_i = 1$ (Roberds 2005). However, real events indicate that slight injuries instead of fatalities are also possible. The vulnerability of persons due to rockfalls is a function of the magnitude of the event. In the case of a person being inside a vehicle, the protective role of the car/train shell in addition to the fact that only a part of the space inside the car is occupied by people, should be co-evaluated. Considering the difficulty in quantifying the latter, the vulnerability of the person might then, in a misuse of language, be replaced by the reduced vulnerability of the system of both the car and the person. Wong et al. (1997) have proposed a value of 0.3 for people inside the vehicles. If the vehicle is buried/crashed this value raises again to 1.

3.5 Rockfall Scenarios

Three scenario-based risk descriptors are assessed here, in terms of probability of occurrence. These are:

Scenario A: The annual probability of one or more vehicles being hit, as given by Eq. 15 (Bunce et al. 1997).

$$P1 = \sum_{M_i} P(S1) = \sum_{M_i} 1 - (1 - P(T:S))^{f_a} \quad (15)$$

where:

$P(S1)$ Probability of scenario A for every class of rockfall M_i .

$P(T:S)$ Probability that a vehicle is found on the roadway/section that is affected by the rockfall given by Eq. 12.

f_a Annual frequency of a rockfall of magnitude M_i (non-cumulative).

Scenario B: The probability of a vehicle being hit on a one-way trip, as given by Eq. 16.

$$P2 = \sum_{M_i} P(S2) = \sum_{M_i} 1 - (1 - P(T:S))^{f_v} \quad (16)$$

The Eq. 16 is similar to the Eq. 15 with two adaptations: (i) the annual frequency f_a is replaced by the f_v which is the rockfall (non-cumulative) frequency that corresponds to the duration of one trip through the dangerous area, as given by Eq. [17], and (ii) the probability $P(T:S)$ is evaluated by Eq. 18.

$$f_v = \frac{f_a \times \frac{L_c(\text{km})}{V_v \left(\frac{\text{km}}{\text{h}} \right)}}{365 \text{ days} \times 24 \text{ h}} \quad (17)$$

$$P(T:S) = \frac{L_v}{L_c} \quad (18)$$

where:

L_v vehicle length (average value) (m)

L_c road/rail section length (m)

Scenario C: The annual probability of a vehicle being hit on a daily two-way trip, given by Eq. 1.

$$P3 = \sum_{M_i} P(S3) = 2 \times 365 \times \sum_{M_i} 1 - (1 - P(T:S))^{f_v} \quad (19)$$

$P(T:S)$ and f_v are the same with scenario B.

4 Repair Costs for Damaged Transportation Corridors

The repair costs for damaged transportation corridors depend on the frequency of the events and their magnitude, which determines the extent of the damage. Repair costs should be established for different rockfall magnitude classes, depending on the type of roadway (i.e. local,

regional or national) and railway. They can be assessed by Eq. 20.

$$RC = \sum_{Mi} f_a \times C \tag{20}$$

where

- f_a annual frequency of a rockfall of a given class (non cumulative)
- C repair cost for the affected roadway/railway.

The repair costs for a network are obtained by aggregation for all partial sections.

5 Indirect Loss Due to Closure of Transportation Corridors

Traffic detours due to rockfalls in a roadway occur due to temporary traffic interruption at the affected sections. The indirect loss is calculated here as the additional costs that result from the use of alternative paths (if any). This includes increased fuel costs in function of the distance difference, lost working-time costs for the commuters and toll difference costs. The expression to assess them is (Eq. 21):

$$\begin{aligned} \text{Daily loss} = & \Delta \text{Distance} \times \text{Fuel costs} \\ & + \Delta \text{Time} \times \text{Number of workers} \\ & \times \text{Working cost} \\ & + \Delta \text{Toll cost} \end{aligned} \tag{21}$$

6 Example

A5 is a mountainous road connecting a village with a city. In the past 10 years, rockfalls reaching the road have been inventoried in two sections of the roadway (1 km each). For the section K50–K1050: 15 rockfalls of 1 m³ and 1 rockfall of 7 m³ and for the section K1200–K2200: 11 rockfalls of 1 m³ and 3 rockfalls of 5 m³.

The average daily traffic density is $N_V = 3000$, the average vehicle length is $L_V = 6$ m, the average speed is $v = 50$ km/hr and the average vehicle cost is $C = 30000$ €. Consider for vehicles $V_i = 1$, for all rockfall classes. Calculate the risk related to vehicle(s) being hit by a rockfall using the proposed descriptors.

If the repair cost for roadway damage is 1500 € for rockfalls up to 5 m³, and 4000 € for rockfalls of 5–50 m³, calculate the expected average annual repair cost.

- Frequency assessment, f_a
 Section K50–K1050: 15/10 = 1.5 rockfalls of 1 m³ and 1/10 = 0.1 rockfalls of 7 m³ per year
 Section K1200–K2200: 11/10 = 1.1 rockfalls of 1 m³ and 3/10 = 0.3 rockfalls of 5 m³ per year
- Calculation of risk descriptors

Section	Rockfall volume (m ³)	f_a	P(S:A) from Table 1	P(T:S) from Eq. 13	V	R from Eq. 2	N from Eq. 3	RC from Eq. 4	T_{imp} from Eq. 5	T_{dest} from Eq. 6
K50–K1050	1	1.5	0.6	0.015	1	0.0147	0.0147	441	68	68
	7	0.1	0.8	0.015	1					
K1200–K2200	1	1.1	0.6	0.015	1	0.0135	0.0135	405	74	74
	5	0.3	0.8	0.015	1					

For A5:

Total annual risk from Eq. 7: $R_T = 0.0282$

Total expected annual number of the impacted vehicles (Eq. 9): $N_T = 0.0282$

Expected annual repair cost of vehicles in the road/rail section (Eq. 10): $RC_T = 846 \text{ €}$

Return period of 1 vehicle being impacted (in years) (Eq. 11): $T_{imp} = 35$

Return period for 1 vehicle being completely destroyed (in years) (Eq. 12): $T_{Tdest} = 35$

• Scenarios

Section	Rockfall volume (m ³)	f _a	f _v from Eq. 17	P(T:S) from Eq. 13
K50–K1050	1	1.5	3.42E–06	0.015
	7	0.1	2.28E–07	0.015
K1200–K2200	1	1.1	2.51E–06	0.015
	5	0.3	6.8E–07	0.015

Section	P(T:S) from Eq. 18	P(S1) from Eq. 15	P(S2) from Eq. 16	P(S3) from Eq. 19
K50–K1050	0.006	0.0224	2.06E–08	1.50E–05
	0.006	0.0015	1.37E–09	1.00E–06
K1200–K2200	0.006	0.016	1.51E–08	1.10E–05
	0.006	0.0045	4.12E–09	3.01E–06

Annual probability of one or more vehicles being hit, P1 (sum): 0.0449

Probability of a vehicle being hit on a one-way trip, P2 (sum): 4.12E–08

Annual probability of a vehicle being hit on a daily two-way trip P3 (sum): 3.01E–05

• Average annual repair cost for damage of the roadway

Section	Rockfall volume (m ³)	f _a	C (€)	RC from Eq. 20
K50–K1050	1	1.5	1500	2250
	7	0.1	4000	400
K1200–K2200	1	1.1	1500	1650
	5	0.3	4000	1200

For A5:

Total annual repair cost (sum): 5500 €

Acknowledgements This work was realized with the support of the project RockRisk funded by the Spanish Ministry of Economy and Competitiveness (BIA2013-42582-P).

References

Algiardi F, Crosta GB, Frattini P (2009) Integrating rockfall risk assessment and countermeasure design by 3D modeling techniques. *Nat Hazards Earth Syst Sci* 9:1059–1073

Budetta P (2004) Assessment of rockfall risk along roads. *Nat Hazards Earth Syst Sci* 4(1):71–81

Bunce CM, Cruden DM, Morgenstem NR (1997) Assessment of the hazard from rockfall on a highway. *Can Geotech J* 34:344–356

Corominas J, Mavrouli O (2013) Rockfall quantitative risk assessment. In: Lambert S, Nicot F (eds) *Rockfall engineering*. Wiley, Hoboken

Corominas J, Mavrouli O (2014) Quantitative rockfall risk assessment in the roadways of Gipuzkoa, AEG XII Congress, vol 2, Torino, 15–19 Sept 2014, pp 1813–1813

Corominas J, Moya J (2008) Assessing landslide frequency: a review. *Eng Geol* 102:193–213

Corominas J, Moya J (2010) Contribution of dendrochronology to the determination of magnitude–frequency relationships for landslides. *Geomorphology* 124(3):137–149

Corominas J, Van WC, Frattini P, Cascini L, Malet JP, Fotopoulou S, Ptilakis K (2014) Recommendations for the quantitative analysis of landslide risk. *Bull Eng Geol Env* 73(2):209–263

Dai FC, Lee CF, Ngai YY (2002) Landslide risk assessment and management: an overview. *Eng Geol* 64:65–87

Dussauge-Peisser C, Helmstetter A, Grasso JR, Hantz D, Desvarreux P, Jeannin M, Giraud A (2002) Probabilistic approach to rock fall hazard assessment: potential of historical data analysis. *Nat Hazards Earth Syst Sci* 2(1/2):15–26

Fell R, Ho KK, Lacasse S, Leroi E (2005) A framework for landslide risk assessment and management. In: *Landslide risk management*, pp 3–25

Ferlisi S, Cascini L, Corominas J, Matano F (2012) Rockfall risk assessment to persons travelling in vehicles along a road: the case study of the Amalfi coastal road (southern Italy). *Nat Hazards* 62(2): 691–721

Finlay PJ, Fell R (1997) Landslides: risk perception and acceptance. *Can Geotech J* 34(2):169–188

Guzzetti F, Reichenbach P, Wieczorek GF (2003) Rockfall hazard and risk assessment in the Yosemite

- Valley, California, USA. *Nat Hazards Earth Syst Sci* 3:491–503
- Hungr O, Evans SG, Hazzard J (1999) Magnitude and frequency of rockfalls and rock slides along the main transportation corridors of southwestern British Columbia". *Can Geotech J* 36:224–238
- Malamud BD, Turcotte DL, Guzzetti F, Reichenbach P (2004) Landslide inventories and their statistical properties. *Earth Surf Proc Land* 29(6):687–711
- Nicolet P, Jaboyedoff M, Cloutier C, Crosta GB, Lévy S (2015) Brief Communication: On direct impact probability of landslides on vehicles. *Hazards Earth Syst Sci* 16:995–1004
- Picarelli L, Oboni F, Evans SG, Mostyn G, Fell R (2005) Hazard characterization and quantification. In: *Landslide risk management*, pp 27–62
- Roberds W (2005) Estimating temporal and spatial variability and vulnerability. In: Hungr O, Fell R, Couture R, Eberhardt EI (eds) *Landslide risk management*. Taylor and Francis, London, pp 129–157
- Ruiz-Carulla R, Corominas J, Mavrouli O (2015) A methodology to obtain the block size distribution of fragmental rockfall deposits. *Landslides* 12(4):815–825
- Schnewly DM, Stoffel (2008) Spatial analysis of rockfall activity, bounce heights and geomorphic changes over the last 50 years—a case study using dendrogeomorphology. *Geomorphology* 102:522–531
- Turcotte DL, Malamud BD, Guzzetti F, Reichenbach P (2002) Self-organization, the cascade model, and natural hazards. *Proc Natl Acad Sci* 99(suppl 1):2530–2537
- Wong HN, Ho KKS, Chan YC (1997) Assessment of consequence of landslides. In: Cruden DM, Fell R (eds) *Landslide risk assessment—proceedings of the international workshop on landslide risk assessment*, Honolulu, Balkema, Rotterdam, pp 111–149

TXT-tool 4.084-1.2

Landslide Vulnerability Assessment: A Case Study of Backan Town, Northeast Vietnam

Do Minh Duc, Mai Trong Nhuan, Tran Dang Quy
and Tran Manh Lieu

Abstract

Intensive excavation of slopes for land use and infrastructure development has taken place in Backan town. Consequently, landslides are very frequent in rainstorms, threatening the safety of residents at home and on roads. In the 132 km² area of Backan town, significant landslide hazards are distributed in distinct strips, zones and points as a result of geological setting, weathering crust, soil and rock properties, topography and excavation for development. This study assesses the relative risk from landslides in Backan town to residents and transportation infrastructure. Vulnerable elements and resilience factors are investigated by field survey and questionnaires. The analyses of natural and social conditions in the GIS platform of Arc-GIS[®] enable a zonation of relative risk from landslide of residents and transportation infrastructure at 4 levels: low; medium; high and very high.

Keywords

Landslide · Vulnerability · Resilience · Field survey · Arc-GIS

Contents

1 Introduction	522	2.4 Geology.....	523
2 Summary of Natural and Social Conditions ..	522	2.5 Socio-economic Characteristics.....	524
2.1 Climatic Characteristics	522	3 Materials and Methods	524
2.2 Topography and Geomorphology	523	3.1 Vulnerability Assessment Method.....	525
2.3 Vegetation Cover	523	3.2 Vulnerability Mapping.....	526
		4 Results and Discussion	526
		4.1 Hazard Levels of Landslide	526
		4.2 Human Vulnerability to Landslide.....	528
		4.3 Transportation Vulnerability.....	533
		5 Concluding Remarks	536
		References	536

D.M. Duc (✉) · M.T. Nhuan · T.D. Quy · T.M. Lieu
VNU University of Science, Vietnam National
University, Hanoi (VNU), 334 Nguyen Trai, Thanh
Xuan, Hanoi, Vietnam
e-mail: ducdm@vnu.edu.vn

D.M. Duc
International Consortium on Landslides, Gokasho,
Uji, Kyoto 611-0011, Japan

1 Introduction

Bac Kan is a mountainous province in northeast Vietnam (Fig. 1). It is in the northeast folding region, along the Paleozoic folded belt. The territory of Bac Kan province is located primarily in the East margin of the Lo Gam structural zone, bordering with the Song Hien zone through the deep-seated fault along highway No. 3. The study area is the entire Bac Kan town with an area of 13,195 km² and a population of 29,277 people. The study area includes 4 wards (Duc Xuan, Song Cau, Minh Khai, and Phung Chi Kien) and 4 communes (Xuat Hoa, Nong Thuong, Duong Quang, and Huyen Tung) of Bac Kan Town, Bac Kan Province, northern Vietnam.

Due to complex geological structure, and especially to neo-tectonic activity, variable and complex topographical characteristics have been created in Bac Kan province, leading to the formation of gravity landslides. This study focuses

on assessing the vulnerability to landslide in Bac Kan Town of people and transportation infrastructure.

2 Summary of Natural and Social Conditions

2.1 Climatic Characteristics

Rainfall in Bac Kan Town is higher than average rainfall of Vietnam. Annual average rainfall is 1400–1600 mm; about 70–80% of the total in rainy season (Bien et al. 2000) (Fig. 2). The intense rainfall is an important cause of landslides in the study area.

Humidity in the study area varies between months, reaching the highest value in July (87–90%) and the lowest value in February (75–80%) (Bien et al. 2000). High humidity favours moisture retention in weathering layers,

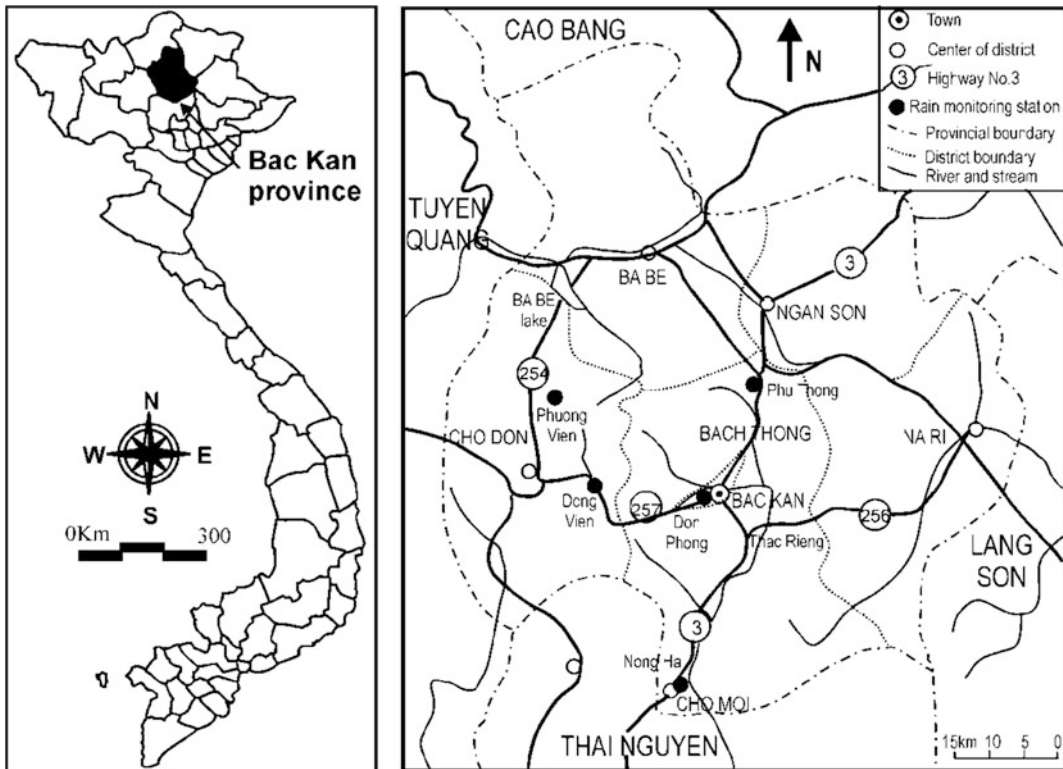


Fig. 1 Location of study area

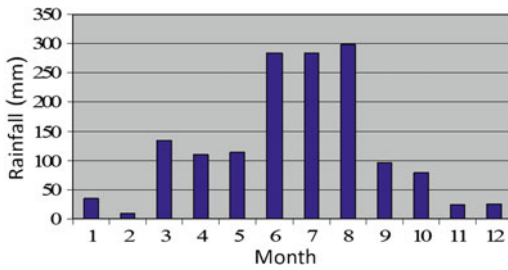


Fig. 2 Annual rainfall of Backan town (mm)

decreasing soil adhesion; thereby enhancing landslides in the study area. Annual average temperature is 21–22 °C, reaching the highest value in July (26–27 °C) and the lowest value in January (13–14 °C) (Bien et al. 2000).

2.2 Topography and Geomorphology

Backan Town is a valley on both sides of Cau River, surrounded by hills and mountains. Average mountain height in the study area is 150–200 m with the highest mountain tops at 728 m in Nam Dat (Xuat Hoa commune), and 746 m in Khau Lang mountain (Duong Quang commune).

In general, there are 3 main topographical types in Backan Town: limestone topography: mainly occurs in Xuat Hoa commune; land/soil hill topography: is found in most communes/wards with average height of 150–160 m; valley topography: occurs mainly in wards with relatively flat topography.

Backan Town is located at the junction of Cau River and two main tributaries (Dong Phong and Nam Cai). The study area has a relatively high drainage density. The total length of Cau River is approximately 35 km with an average discharge of 150 m³/s in the rainy season and 10–12 m³/s in the dry season.

2.3 Vegetation Cover

The study area is characterized by high vegetation coverage, of which a majority is from reforestation in the last 10 years. There are

various kinds of vegetation, including ironwood, teakwood, pine, small bamboo, brushwood and creeper and cultivated crops (manioc, tea, rice, corn, and pea). High vegetation coverage plays a large role in stabilizing the weathering crust; thereby reducing landslides in the study area.

2.4 Geology

Geologic formations in the study area mainly include metamorphic and sedimentary rocks of Phu Ngu formation (O-Spn) and Mia Le formation (D₁m). The Phu Ngu formation is exposed in a large area in the west, southwest, and center of Backan Town. The lower layer consists of shale, sandstone and siltstone varying within 1100–1200 m thick. The upper layer consists of black shale, siliceous silt, and limestone of 300 m thick. The Mia Le formation is exposed in the east and southeast of Backan Town. The lower layer occurs in the southeast, consisting of black shale, limestone, and silicic 400–500 m thick. The upper layer occurs mainly in the northeast, consisting of black limestone, sandstone, siltstone, shale, and black shale and is 500 m thick.

Weathering crust (regolith): There is only one kind of inadequate weathering cross-section in Backan Town. The weathering crust structure is characterized by clearly vertical zonation as follows:

Soil layer: is the uppermost layer which varies about 0.2–0.5 m thick, mainly consisting of yellow-brown and black-brown sand and silt and partly consisting of humus, plants, and tree roots.

Speckled/spotted clay layer: there are two secondary layers. The upper layer varies within 3–5 m thick which mainly consists of red-brown, yellow-brown, and spotted white-brown silt-clay-sand. The lower layer varies within 5–7 m thick which mainly consists of yellow-brown, white-brown, and spotted brown silt-clay-sand and reflects traces of bedrock.

Semi-weathering bedrock layer: varies within 8–10 m thick which mainly consists of bedrock formation such as broken shale, sericite, lime-shale, sand-gritstone, and claystone.

Mechanical property of soil: the results of 80 soil samples (30 primitive state samples) show that mechanical property of soil in Backan Town is significantly changed. Internal friction angle varies within 210–30.30 with the calculated first limit status of 23.50. The effective adhesive force varies from 4.2 to 23.6 kPa with the calculated value is 6.8 kPa (Duc and Son 2008).

2.5 Socio-economic Characteristics

The average population density in 2003 was 240 people/km², mainly concentrated in a few wards (i.e., Duc Xuan, Minh Khai, and Song Cau) (Table 1). In the study area, the highest and lowest populated wards/communes are Duc Xuan (7157 people) and Xuat Hoa (2592 people), respectively. The highest and lowest population density areas belong to Minh Khai ward (2767 people/km²) and Xuat Hoa commune (59 people/km²), respectively. The main ethnic groups living in the study area are Tay, Kinh, H'Mong, and Dao.

Agriculture: Crop productivity, crop yields, and cultivated area have been increased. In 2010, rice and maize areas were 720.7 and 288 ha, respectively, which were 100 and 39.6 ha higher than those in 2006. The total cereal production was 4387 tons, which increased 986 tons than that in 2006. Pig and poultry products have shifted from the traditional household model to farm livestock development, semi-industrial and industrial farming.

Industry and handicraft: There are some production and processing facilities in the study

area, such as Backan fruit—vegetable processing and a beverage factory, Chien Thang clothing joint stock company, small and medium production and processing facilities of forest products, large assembling manufactures, Backan cement factory, and Backan mineral company.

Forestry: Between 2000 and 2005, the area of protective and productive forest decreased. Especially in 2005, approximately 65,000 ha of productive forest decreased. Special-use forest areas tended to decrease between 2000 and 2004; however, the reverse tendency was observed from 2004 to 2005. In 2010, 477 ha of forestation were planted, reaching forest coverage of 55.6%.

Transportation: Most major roads in the area are paved; paths are concreted to help households move easily.

Public health: There is one provincial general hospital, one regional clinic, one nursing home, and 8 medical clinics in the study area. The number of hospital beds in Backan province is higher than the national average; however, facilities are limited. In 2003, the ratios of doctors and physicians–technicians per 1000 population reached 4.05 and 1.74, respectively.

3 Materials and Methods

Landslides have caused frequent and widespread damage to populations and the built environment over many areas (Dai et al. 2002; Galli and Guzzetti 2007). The literature on landslide hazard assessment is extensive; however, studies of the vulnerability to landslides, including methods

Table 1 Population and population density

Ward/commune	Population (people)	Density (persons/km ²)
Backan Town	31,607	240
Duc Xuan	7157	1549
Song Cau	6078	1407
Minh Khai	3874	2767
Phung Chi Kien	3134	866
Huyen Tung	3481	127
Xuat Hoa	2592	59

Source Land use planning of Backan Town, 2010

to determine vulnerability and examples of damage assessments, are far less abundant (Galli and Guzzetti 2007). Current research on landslides mainly focuses on landslide zonation and modeling (Kaynia et al. 2008). Studies of vulnerability to landslides have considered different priorities such as the built environment, human life, and local economy (Bell and Glade 2004; Galli and Guzzetti 2007; Glade 2003; Gomes 2003). Guinau et al. (2005) proposed a method for landslide susceptibility assessment in developing countries with a case study of northwest Nicaragua, Central America after Hurricane Mitch. Susceptibility of structures (slope, lithology, soil thickness, soil texture, land use) was evaluated. Msilimba and Holmes (2005) proposed a landslide hazard assessment and vulnerability appraisal procedure. The authors proposed criteria to determine vulnerability scores, including slope, disturbance of land surface, vegetation, % sand, hydraulic conductivity (cm/h), porosity index, plasticity index, and bulk density (g/cm^3). A conceptual framework for quantitative estimation of physical vulnerability to landslides was proposed (Uzielli et al. 2008) and was applied to vulnerability assessment from landslides at a village of Lichtenstein, Germany (Kaynia et al. 2008). However, studies on quantitative assessment of vulnerability of communities subjected to landslides are still limited.

In Backan town, to date, there has been no assessment of vulnerability in general or for landslides in particular. Research related to landslides in the study area have focused only on basic studies and hazard level. For examples, study and assessment of landslides for planning and transportation system development in the Cau River basin, Backan province (Duc 2010); relationships between geological structure and landslides on either sides of Cau River, Backan Province (Me and Toat 2002); effects of natural conditions and human activities on landslide in Backan Town (Duc and Son 2008).

A survey in Backan Town for vulnerability assessment was carried out between February 18 and 22, 2011. In this survey, data on natural conditions (e.g., geology, geomorphology, hydrology, and climate) and socio-economic

characteristics were investigated to determine vulnerability objects and the resilience of natural–social system. Interviews were held at the same time to obtain the following information:

- Population and buildings: population distribution, sex, occupation, education level, infrastructure;
- Economic development activities: agriculture, industry, services, transportation, socio-economic growth rate;
- Culture and art: communal house, pagoda, cultural palace, park;
- Natural-environment protection, hazard prevention, national park, reserve;
- Hazards and natural resources.

Approximately 400 household questionnaires for vulnerability assessment were returned.

3.1 Vulnerability Assessment Method

The vulnerability assessment for landslides method applied in this study was derived from the methods and criteria for coastal zone vulnerability assessment (CVIs) of the U.S.A. (Elizabeth et al. 2005), environmental vulnerability (EVI) of SOPAC (Kaly et al. 2005), the process of vulnerability assessment of NOAA (1999), Cutter (1996), Cutter et al. (2000), vulnerability assessment of landslide of Uzielli (2008), and the assessment by Mai Trong Nhuan et al. (2005, 2011).

Vulnerability assessment was carried out in a GIS-based environment using ArcGIS[®] software. The whole area was divided into pixels of 10×10 m each. Then vulnerability to landslides of each “point” (pixel) was estimated by the formula:

$$V(x_i y_j) = f \left[aH(x_i y_j), bP(x_i y_j), cC(x_i y_j) \right]$$

$V(x_i y_j)$ is Vulnerability to landslide; $H(x_i y_j)$ is Hazard level of landslide; $P(x_i y_j)$ is density of the vulnerable element; $C(x_i y_j)$ is Resilience capacity of natural–social systems; x_i, y_j are Geographical co-ordinates of the pixel; a, b, c are weights of relevant factors.

The evaluation criteria are determined by paired comparison matrix method of Saaty (2003). The calculation process consists of three steps: (1) set paired comparison matrix; (2) calculation of these criteria, (3) stability rate assessment (CR) of the weights. If $CR \leq 0$ (stability accepted), weights are calculated.

Vulnerability to landslide is assessed through the following steps:

- Step 1: Landslide hazard mapping;
- Step 2: Analyzing and assessing the vulnerable elements;
- Step 3: Analyzing and assessing the factors of resilience capacity;
- Step 4: Zonation of the vulnerable element density;
- Step 5: Zonation of the resilience capacity of natural–social systems;
- Step 6: Calculating and zoning the vulnerability to landslide.

Vulnerability assessment of landslide in the present study includes: human and transportation systems directly and intensively affected by landslide.

Human vulnerability to landslide is assessed based on 3 components: (1) hazard level of landslide; (2) density of vulnerable elements with a focus on affected people; and (3) human resilience capacity.

Age and sex should be taken into account because elderly people and infants are more vulnerable to hazards than other people, and Women are more vulnerable to hazards than Men. Education and income are also taken into account (Table 2). Support from local government includes level 1: yes and level 2: no. House types are categorized into four levels: Temporary houses (made of wood and/or soils), semi-permanent houses (made of a thin layer of bricks), concrete one-storey, and concrete multistorey houses.

Transportation vulnerability to landslide with a focus on bridges, roads, and cut slopes is assessed based on 3 components: (1) density of vulnerable transportation infrastructure; (2) resilience capacity (natural and economic conditions restricting/limiting the ability of solving

problems related to landslide and road repair); and (3) hazard level of landslide. Vulnerability of transportation infrastructure is assessed using the following criteria: road types, transportation density (calculated by length of road per pixel in an area of 10,000 m²), and number of bridges (Table 2).

Transportation resilience capacity is assessed based on factors that restrict road repairing capacity: topographical elevation and slope angle, river and stream system, and population density (Table 3). Population density is used to calculate transport demand (human and goods), areas of low population density will have lower priority for making roads. Higher altitudes and steeper slope angles are considered to restrict the capacity of road repair.

River and stream system: this is considered as hydrological channels. Landslides occur commonly on banks of rivers and streams during heavy rain. Therefore, the higher the density of rivers and streams is, the greater is the probability of landslides.

3.2 Vulnerability Mapping

The spatial distribution of various vulnerability levels is shown by vulnerability maps which are the results of mapping vulnerability process. GIS software is the main tool for mapping vulnerability. In vulnerability assessment, spatial analysis and data processing are the most important factors for mapping vulnerability levels. Based on weighted results from Analytic Hierarchy Process (Saaty 2003) and map algebra, maps of human and transportation vulnerability to landslides were established (Figs. 3 and 4).

4 Results and Discussion

4.1 Hazard Levels of Landslide

Map of landslide hazard is established based on the following factors: (1) altitude, (2) slope angle, (3) slope aspect, (4) petrography, (5) geomorphology, (6) dip angle of bedrocks,

Table 2 Categorizing affecting factor to transportation vulnerability to landslides

Level	Road type	Number of bridges	m/pixel	Person/km ²
1	Path/track	0	0–1.20	0–16
2	Pathway: >3 m wide	2	1.20–3.60	17–37
3	Asphalt road, village scale, 6 m wide	4	3.60–6.00	38–62
4	Asphalt road, district scale, 6–8 m wide	6	6.00–8.39	63–91
5	Asphalt road, 8–10 m wide	8	8.39–10.91	92–123
6	Cut slopes	10	10.91–13.43	124–160
7	Asphalt road, province scale, 15 m wide	12	13.43–15.95	161–205
8	Two lane in the center, 30 m wide	14	15.95–18.71	206–265
9		16	18.71–22.18	266–345
10		19	22.18–30.70	346–480

Table 3 Categorizing affecting factor to transportation resilience

Level	Altitude (m)	Slope angle (°)	River and stream density (m/pixel)	Population density (person/km ²)
1	0–119	0–3	0–1.38	0–16
2	119–138	3–5	1.38–4.27	17–37
3	138–151	5–8	4.27–7.16	38–62
4	151–164	8–10	7.16–9.93	63–91
5	164–177	10–15	9.93–12.69	92–123
6	177–190	15–20	12.69–15.46	124–160
7	190–205	20–25	15.46–18.35	161–205
8	205–225	25–30	18.35–21.50	206–265
9	225–250	30–50	21.50–25.51	266–345
10	250–316	50–75	25.51–32.17	346–480

(7) engineering geology, (8) lineament density, (9) weathering crust, (10) faults, and (11) land use. Each factor is considered as one layer. The higher the weighted value of each layer is, the higher the risk of landslides. The role of each factor is assessed, in which landslides are likely to occur in areas with the following characteristics: Geology (black shalestone and silicic layer of the Phu Ngu formation), geomorphology (integrated denudation surface), cut (excavated) slope, weathering crust mainly constituted by residual soils, land use (bare hills, annual cultivation land, and rice field), altitude: 150–177 m,

slope angle and aspect, lineament density (31.46–50.02 km/km²). Hazard levels of landslide are then mapped, in which the study area can be divided into 4 areas (Fig. 5)

Zone I (low hazard level): occurs mainly surrounding the Cau River. This zone is characterized by low occurrence of landslides (3 sites out of a total of 250 landslides recorded).

Zone II (moderate hazard level): scattered occurrences, mainly in Duc Xuan ward, Duong Quang and Huyen Tung communes.

Zone III (high hazard level): mainly occurs in Song Cau, Phung Chi Kien wards, and Duong

Fig. 3 Flow chart of assessment of human vulnerability to landslides

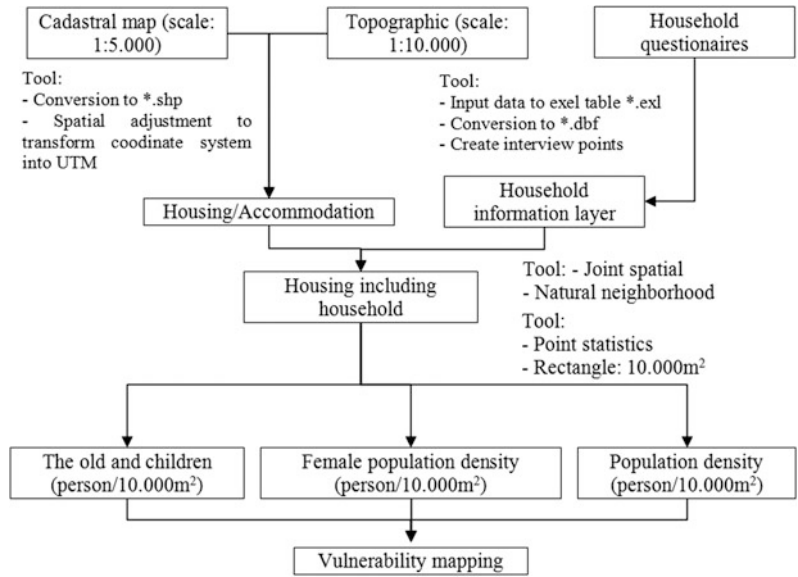
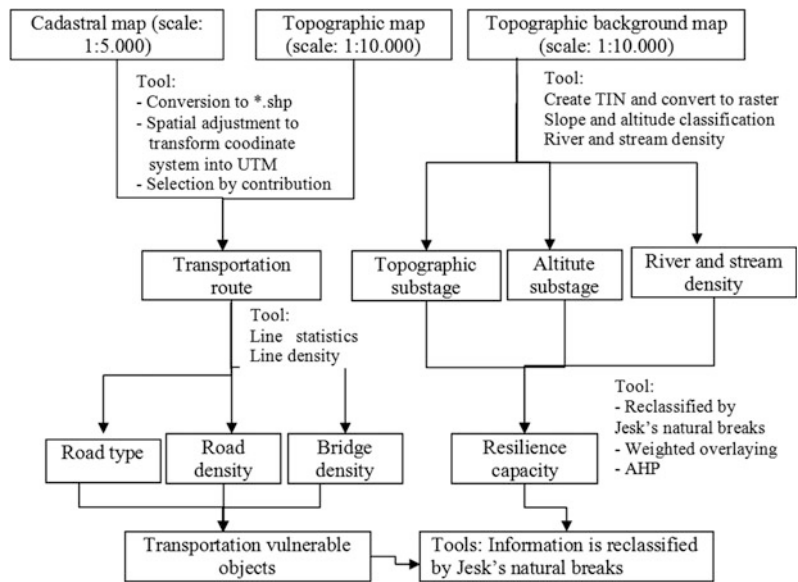


Fig. 4 Flow chart of assessment of transportation vulnerability to landslide



Quang, Huyen Tung communes. Of the total 250 landslides, 77 sites were recorded in this zone.

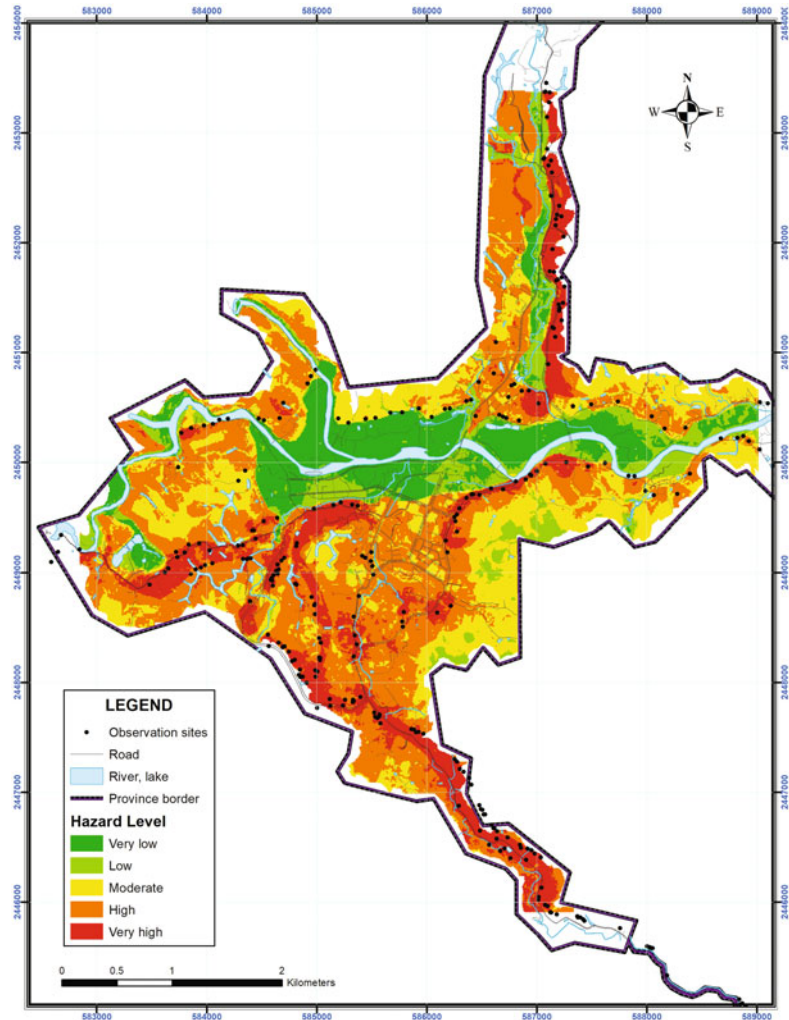
Zone IV (very high hazard level): mainly occurs along the 3B and 257 highways. This zone is characterized by a high potential for landslides. Of the total of 250 landslide sites in the study area, 150 sites were recorded in this zone.

4.2 Human Vulnerability to Landslide

4.2.1 Density of Landslide-Vulnerable People

On the basis of field survey, interview, data collection and processing, density maps of female and number of population affected by landslide (Fig. 6) and vulnerable human (Fig. 7)

Fig. 5 Hazard levels of landslide in the centre part of Backan town



are established. The figure shows that the study area is divided into 4 areas with different density values as follows:

Zone I (low density of vulnerability): mainly occurs in Duong Quang, Huyen Tung, Nong Thuong, and Xuat Hoa communes. This zone is characterized by long distance to roads, few facilities, leading to low density of people in general, and, children women and the elderly in particular.

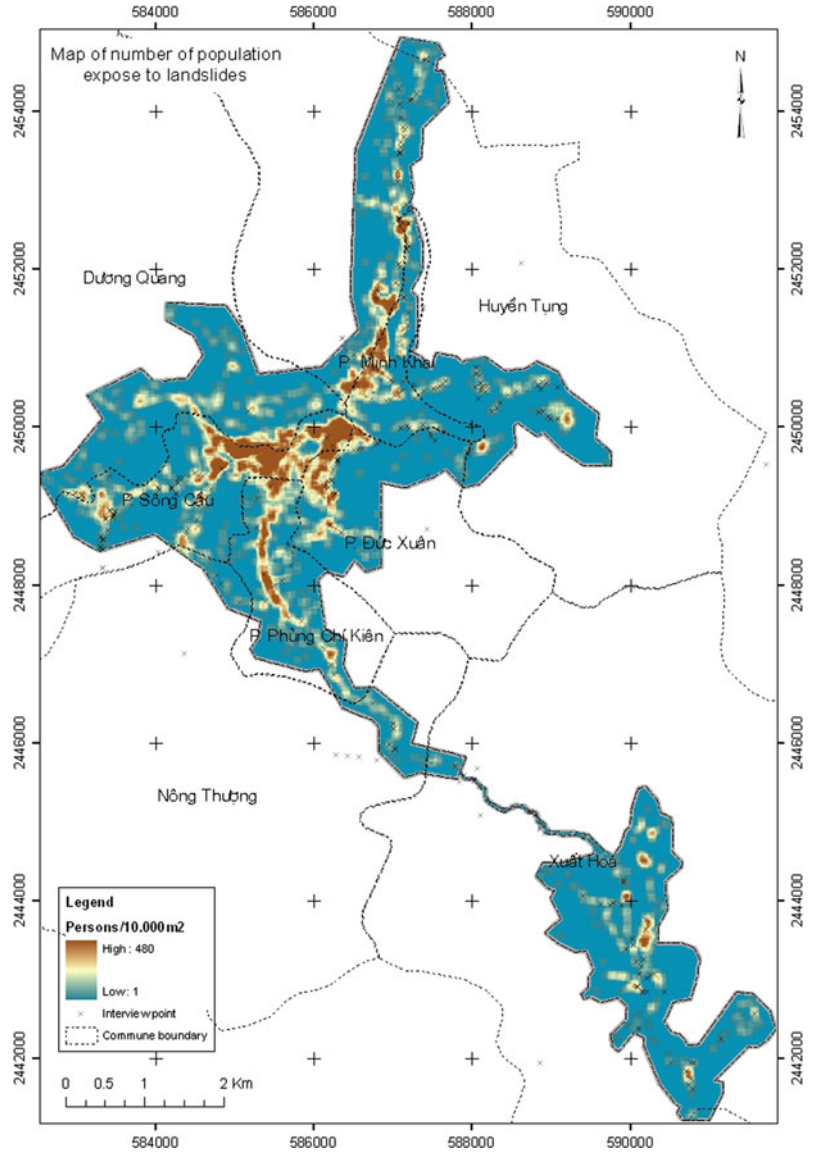
Zone II (medium density of vulnerability): occupies a narrower area than zone I. This zone

has a scattered distribution and a medium density of population.

Zone III (high density of vulnerability): occurs mainly in Phung Chi Kien ward, and Nong Thuong and Xuat Hoa communes. This zone is characterized by relatively dense population and a high ratio of ethnic people.

Zone IV (very high density of vulnerability): occurs mainly in the center of Backan Town (Minh Khai, Song Cau, Duc Xuan, and Phung Chi Kien wards) and along major transport routes due to the

Fig. 6 Density of population affected by landslides (people/10,000 m²)



high density of people. The highest density of women is found in the east of Song Cau ward.

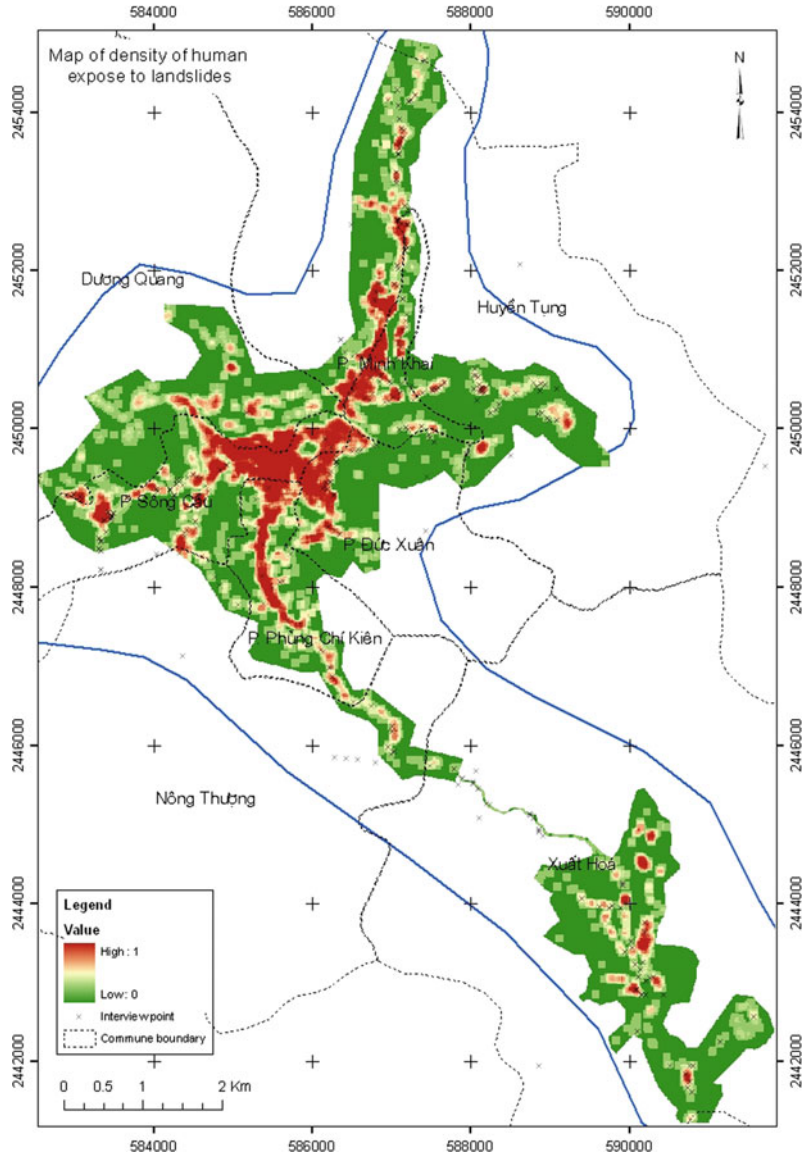
4.2.2 Human Resilience Capacity to Landslide

The resilience capacity of people to landslides is assessed from the following information: house types, supportive policies of local government, education level, number of people of working age, and income. Households living in concrete

buildings, high education levels and receiving support from local government will be likely to respond to landslides better than others. A map of human resilience capacity to landslides is shown in Fig. 8.

Zones I–II—areas with low and medium resilience capacity: these occupy a large portion of the study area, including Dương Quang, Huyện Tùng communes, southwest of Song Cau ward, Minh Khai, Phùng Chí Kiên and Xuât Hoà

Fig. 7 Vulnerability levels of local people to landslides

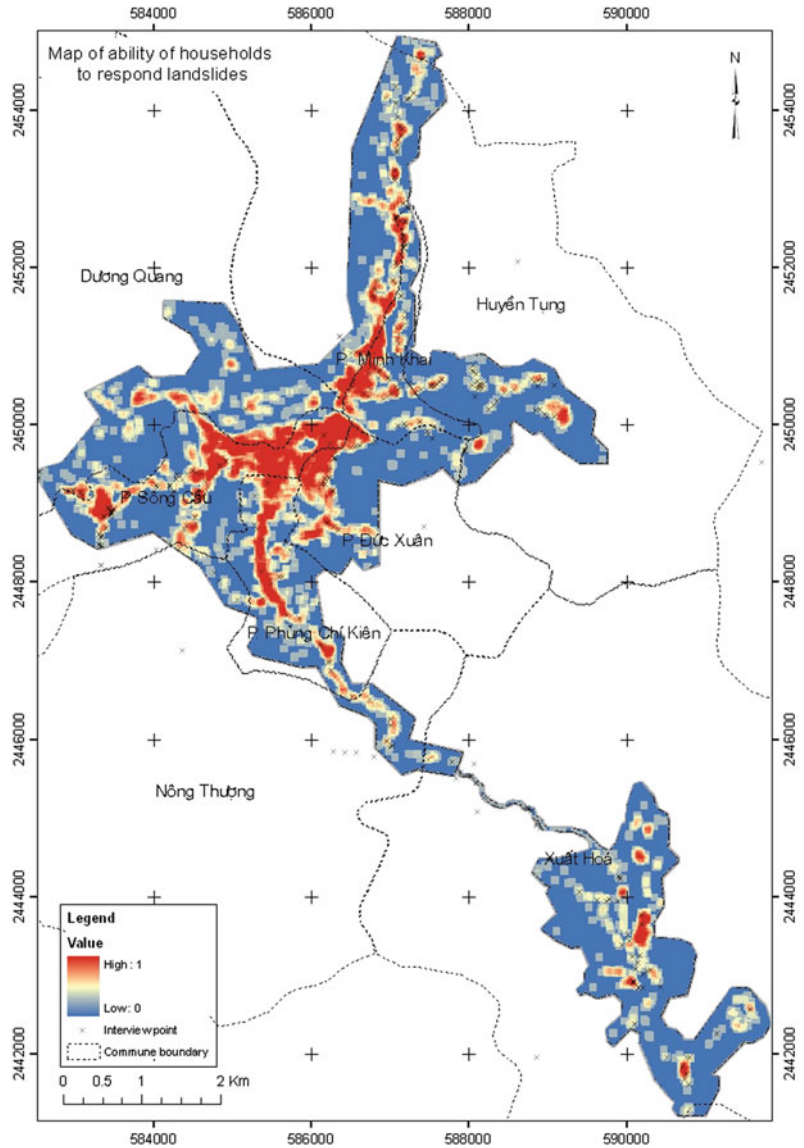


wards. These zones are far from main roads, have low population density, temporary houses, lack of coordination of local government, relatively low education levels, and few works to mitigate landslides.

Zones III–IV (relatively high and high resilience capacity): These occupy smaller areas than zones I–II, including the southeast of Song Cau ward, northwest of Duc Xuan ward, and along the

main roads of Minh Khai and Phung Chi Kien wards, and scattered in Xuat Hoa, Duong Quang, and Huyen Tung communes. These areas are in the center of Backan Town; therefore, the infrastructure system is relatively well developed. The living standard of people is relatively high. There is a majority of concrete houses. These areas also have local-government offices. These factors lead to high capacity for landslide resilience.

Fig. 8 Human resilience capacity to landslides



4.2.3 Vulnerability Assessment of People to Landslides

In assessing the human vulnerability to landslide, the study area was divided into 4 zones with different levels of vulnerability (Fig. 9).

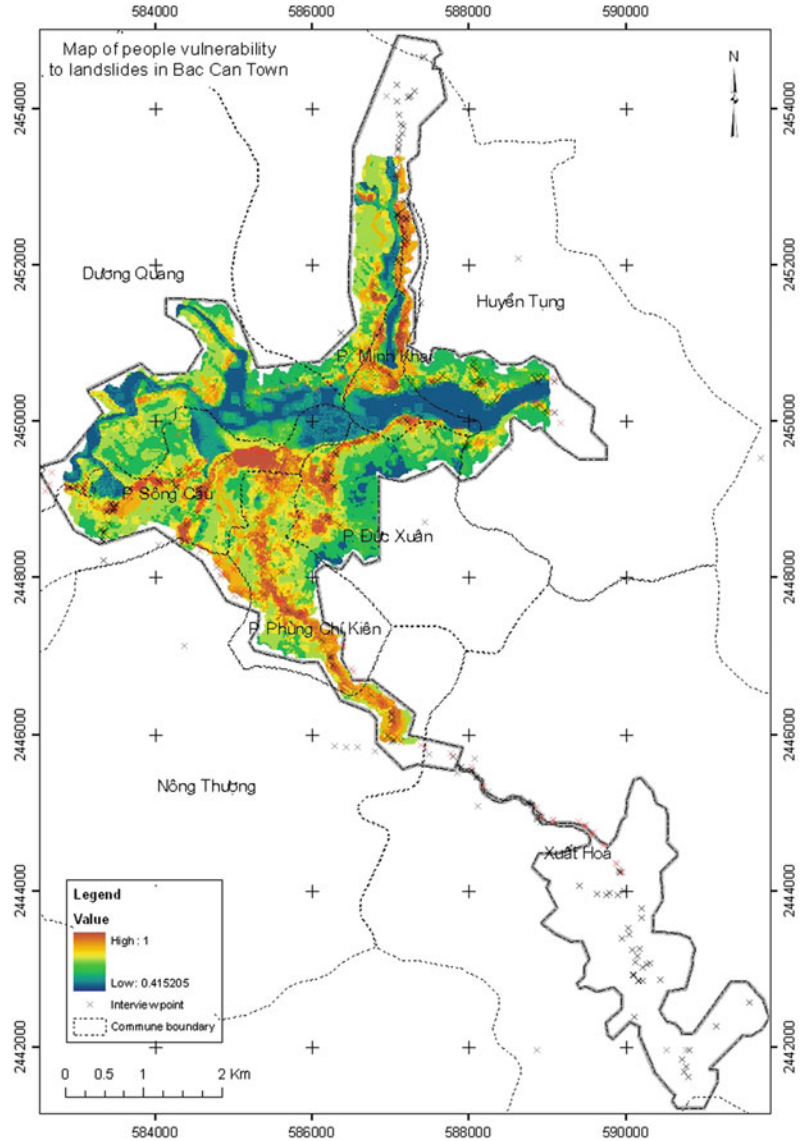
Zone I (low human vulnerability): occupies a small area, distributing in the center of Backan Town (area of intersection between four center wards). High living standard, good awareness, support from local government, and good

infrastructure help to increase the human resilience, and therefore, to decrease the human vulnerability to landslide in this zone.

Zone II (medium human vulnerability): occupies a larger area than zone I, but occurs around zone I, such as: Duc Xuan ward, Huyen Tung and Duong Quang communes.

Zone III (relatively high human vulnerability): covers a large area in the north, mainly in Song Cau and Phung Chi Kien wards. This zone is has

Fig. 9 Human vulnerability to landslide in the central part of Backan town



many poor households, relatively low education level, and the local people have low awareness of hazard adaptation and protection.

Zone IV (high human vulnerability): mainly occurs along roads, and near excavated slopes. The local people have low awareness of landslide risks.

4.3 Transportation Vulnerability

In order to assess transportation vulnerability to landslides, transportation density and resilience

were assessed. Backan Town has recently built new roads and upgraded old road systems. Many roads in the town are paved and concreted, some inter-communal roads have been concreted. However, there are still many paths in the study area. Moreover, the mountainous terrain causes many problems for infrastructure, including roads and bridges. The density maps of vulnerable transportation were calculated using length and investment values and the number of bridges. The following trends were found:

Density of vulnerable transportation calculated by length and investment values: a high density is found along the road system, especially along the 3B and 257 highways. The highest value is in the areas where the administrative offices of Backan Town are located.

Density of vulnerable bridges: there is a high density at the intersections between river/stream systems and roads. The highest value was found in Xuat Hoa commune.

4.3.1 Transportation Resilience Capacity to Landslides

The transportation resilience capacity is calculated based on the factors restricting/limiting the ability to repair roads, including topographic substage, slope substage, and stream and river systems. Therefore, areas with high transportation resilience capacity to landslides are areas of with few restriction factors. The map is established and the study area can be divided into the following zones (Fig. 10).

Fig. 10 Limitation of human resilience to transportation

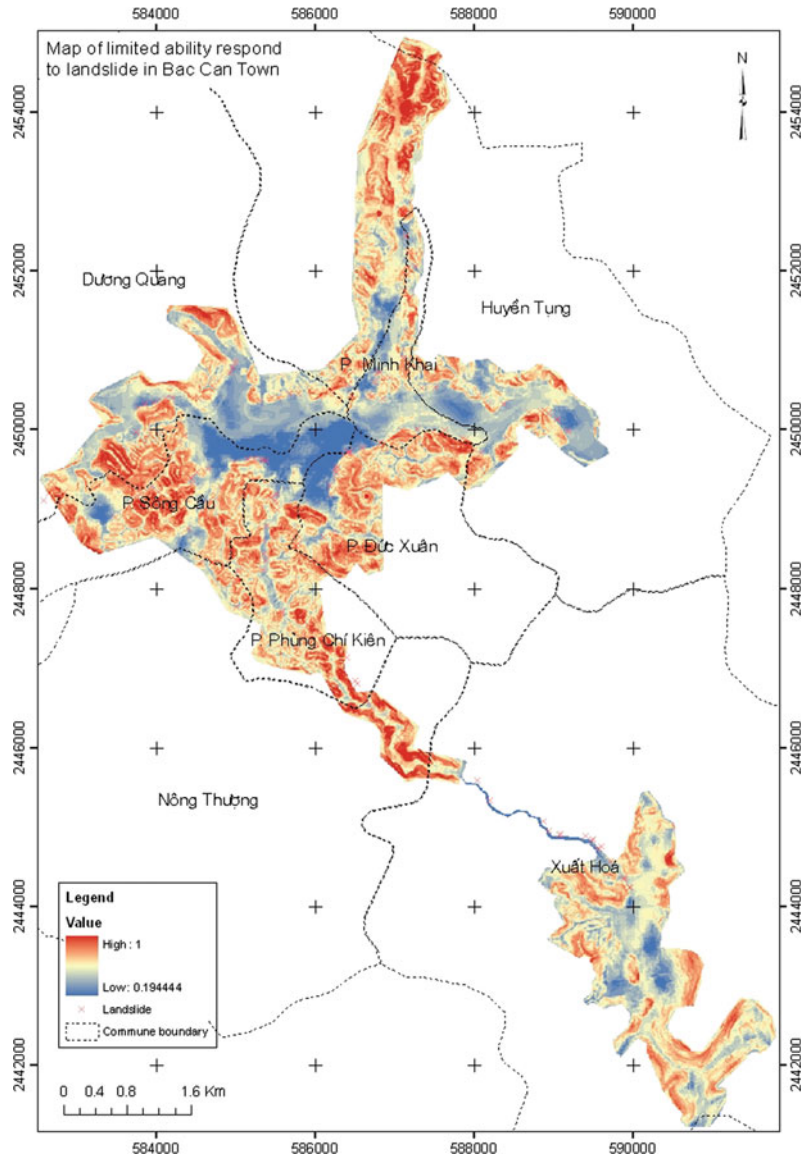
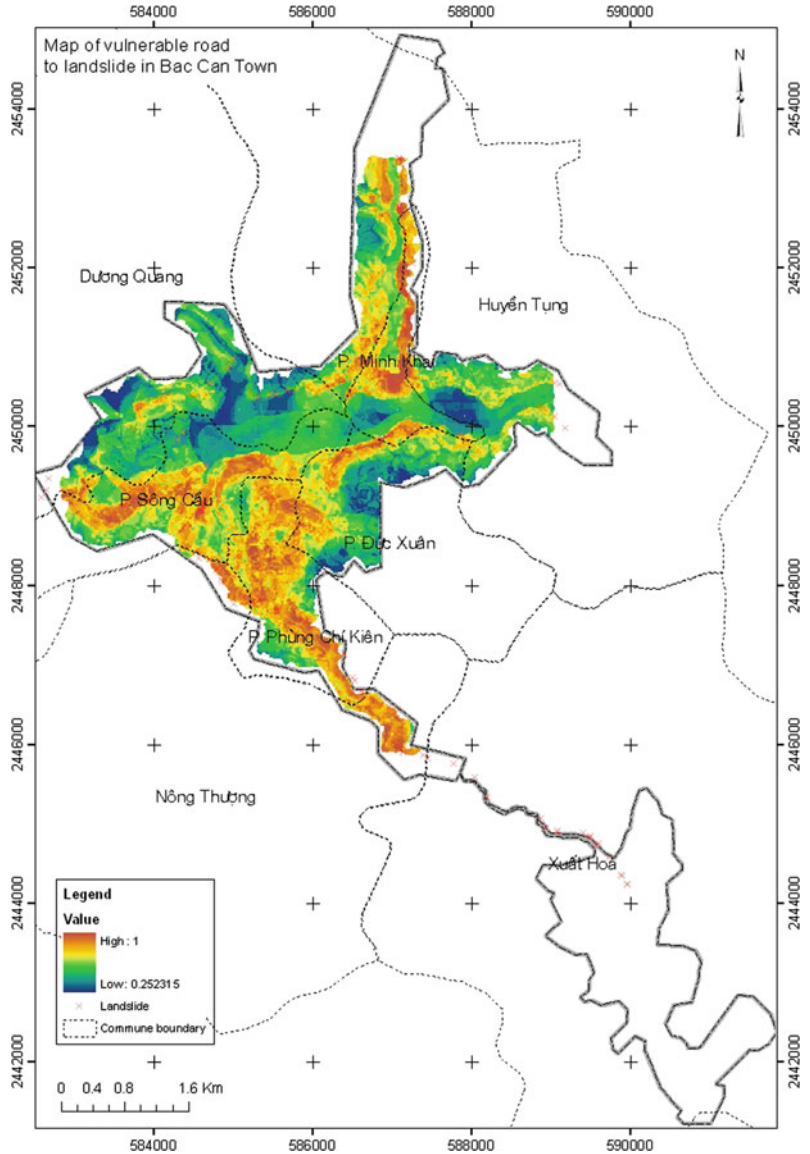


Fig. 11 Assessment of transportation vulnerability to landslides



Zone I—Areas with low transportation resilience capacity to landslides: Occurs scattered through the study area, mainly in Nong Thung commune, Phung Chi Kien ward, the west of Huyen Tung commune and the center of Song Cau ward. This zone is characterized by high topography and slope subgrade.

Zone II—Areas with medium transportation resilience capacity to landslides: covers a large area and distributes mainly in Xuat Hoa and Duong Quang communes, Duc Xuan and Phung Chi Kien wards.

Zone III—Areas with relatively high transportation resilience capacity to landslide: occurs mainly in Duong Quang commune, and the southeast of Huyen Tung commune. This zone is characterized by relatively low topography and slope subgrade and relatively high density of river and stream systems.

Zone IV—Areas with high transportation resilience capacity to landslide: covers a small area and mainly occurs in the east of Song Cau ward and northwest of Duc Xuan ward.

4.3.2 Vulnerability Assessment of Transportation System to Landslides

This vulnerability assessment map is based on 3 components maps using weighted overlying methods, in which, the study area is divided into 4 zones as follows (Fig. 11).

Zone I—Areas with low transportation vulnerability: covers a small area in Duong Quang, Huyen Tung communes, Duc Xuan ward, and in the north of Song Cau ward.

Zone II—Areas with medium transportation vulnerability: covers more area than zone I, occurring mainly in Xuong Quang and Huyen Tung communes, and Duc Xuan ward.

Zone III—Areas with relatively high transportation vulnerability: covers a relatively large area of Backan Town, occurs mainly along main roads, such as in Minh Khai ward, in the south of Song Cau ward, Duc Xuan anh Phung Chi Kien wards.

Zone IV—Areas with high transportation vulnerability: occurs along Highway 3 at areas such as Minh Khai, Duc Xuan, and Song Cau wards. In this zone, infrastructure in general and transportation in particular is well developed. However, the steep slopes in many areas pose a high landslide risk.

5 Concluding Remarks

In the present study, human vulnerability to landslide is assessed based on 3 components: (1) hazard level of landslide; (2) density of vulnerable elements with a focus on affected people; and (3) human resilience capacity. Vulnerability level is assessed based on age, sex, and population density.

Transportation vulnerability to landslides with a focus on bridge, road, and cut slopes is assessed based on 3 components: (1) density of vulnerable transportation infrastructure; (2) resilience capacity (natural and economic conditions restricting/limiting the ability to solve problems related to landslides and road repair); and (3) landslide hazard level.

A field survey with well-designed questionnaires helped to collect needed data for the vulnerability mapping. ArcGIS® is a suitable tool to manage the data and perform vulnerability mapping. The study area is divided into 4 zones with different levels of vulnerability to landslides—low, medium, high and very high.

The vulnerability assessment based planning of land use and transportation should be established for sustainable development.

References

- Bien MT et al (2000) Geography of Backan Province. Backan Department of Science, Technology and Environment (in Vietnamese)
- Bell R, Glade T (2004) Quantitative risk analysis for landslide—examples from Bildudalur, NW-Iceland. *Nat Hazards Earth Syst Sci* 4:117–131
- Cutter SL (1996) Vulnerability to environmental hazards. *Prog Hum Geogr* 20:529–539
- Cutter SL, Mitchell JT, Scott MS (2000) Revealing the vulnerability of people and places: a case study of Georgetown County, South Carolina. *Ann Assoc Am Geogr* 90(4):713–737
- Dai FC, Lee CF, Ngai YY (2002) Landslide risk assessment and management: an overview. *Eng Geol* 64:65–87
- Duc DM (2010) Study and assessment of landslides for planning and transportation system development in Cau River basin, Backan Province. Project Report QG.08.16, Hanoi University of Science
- Duc DM, Son NH (2008) Affects of natural condition and human activities on landslides in Backan Town. *Geotech J* 1:22–30
- Elizabeth AP, Thieler ER, Williams SJ (2005) Coastal vulnerability assessment of point Reyes National Seashore to sea-level rise. Open-File Report 2005-1059. U.S. Geological Survey, Coastal and Marine Geology Program
- Galli M, Guzzetti F (2007) Landslide vulnerability criteria: a case study from Umbria, Central Italy. *Environ Manag* 40:649–664
- Glade T (2003) Vulnerability assessment in landslide risk analysis. *Erde* 134:121–138
- Gomes J (2003) Landslide susceptibility and risk maps of Regua (Douro basin, NE Portugal). In: *Proceeding of the IAG and IGU-C12 regional conference “geomorphic hazards; towards the prevention of disasters”*, Mexico City, Mexico
- Guinau M, Pallas R, Vilaplana JM (2005) A feasible methodology for landslide susceptibility assessment in developing countries: a case-study of NW Nicaragua after Hurricane Mitch. *Eng Geol* 80:316–327

- Kaly UL, Pratt C, Mitchell J (2005) The environmental vulnerability index (EVI) 2004. SOPAC Technical Report 384
- Kaynia AM, Papathoma-Köhleb M, Neuhäuser B, Ratzinger K, Wenzel H, Medina-Cetina Z (2008) Probabilistic assessment of vulnerability to landslide: application to the village of Lichtenstein, Baden-Württemberg, Germany. *Eng Geol* 101:33–48
- Me LT, Toat DD (2002) Relationship between geological structure and landslide surround Song Cau riverside of Backan Province. In: *Proceeding of the 15th conference*, Hanoi University of Mining and Geology
- Msilimba GG, Holmes PJ (2005) A landslide hazard assessment and vulnerability appraisal procedure: Vunguvungu/Banga catchment, Northern Malawi. *Nat Hazards* 34:199–216
- Nhuan MT, Tien DM, Hue NTH, Tue NT, Quy TD, Ha NTH (2005) Vulnerability assessment of Phan Thiet-Ho Tram Coastal zone for sustainable development. *VNU J Sci Earth Sci* 21(4):6–16
- Nhuan MT, Ha NTH, Quy TD, Hue NTH, Hien LTT (2011) Integrated vulnerability assessment of natural resources and environment for sustainable development of Vietnam coastal zone. *VNU J Sci Earth Sci* 27 (1S):114–124
- NOAA (1999) Community vulnerability assessment tool. CD-ROM, NOAA Coastal Services Center
- Saaty T (2003) Decision aiding: decision-making with the AHP: why is the principal eigenvector necessary? *Eur J Oper Res* 145:6
- Uzielli M, Nadim F, Lacasse S, Kaynia AM (2008) A conceptual framework for quantitative estimation of physical vulnerability to landslides. *Eng Geol* 102:251–256

TXT-tool 4.086-1.1

Landslide Investigations in the Northwest Section of the Lesser Khingan Range in China Using Combined HDR and GPR Methods

Zhaoguang Hu, Wei Shan and Hua Jiang

Abstract

In the northwest section of the Lesser Khingan Range located in the high-latitude permafrost region of northeast China, landslides occur frequently due to permafrost melting and atmospheric precipitation. High-density resistivity (HDR) and ground penetrating radar (GPR) methods are based on soil resistivity values and characteristics of radar-wave reflection, respectively. The combination of these methods together with geological drilling can be used to determine the stratigraphic distribution of this region, which will allow precise determination of the exact location of the sliding surface of the landslide. Field test results show that the resistivity values and radar reflectivity characteristics of the soil in the landslide mass are largely different from the soil outside the landslide mass. The apparent resistivity values exhibit abrupt layering at the position of the sliding surface in the landslide mass, and the apparent resistivity value decreased suddenly. In addition, the radar wave shows strong reflection at the position of the sliding surface where the amplitude of the radar wave exhibits a sudden increase. Drilling results indicate that at the location of the sliding surface of the landslide mass in the study area, the soil has high water content, which is entirely consistent with the GPR and HDR results. Thus, in practice, sudden changes in the apparent resistivity values and abnormal radar-wave reflection can be used as a basis for determining the locations of sliding surfaces of landslide masses in this region.

Keywords

Landslide · Drilling · High-density resistivity (HDR)
Ground penetrating radar (GPR) · Sliding surface

Z. Hu · W. Shan (✉) · H. Jiang
Institute of Cold Regions Science and Engineering,
Northeast Forestry University, Harbin 150040, China
e-mail: shanwei456@163.com

Z. Hu
e-mail: huzhaoguang008@163.com
H. Jiang
e-mail: jianghua3433@163.com

Contents

1 Introduction.....	540
2 Study Area.....	540
3 Methods.....	543
4 Results, Analysis, and Discussion.....	545
Reference.....	553

1 Introduction

In recent decades, geophysical investigations for assessing stratigraphic distribution have become a common tool in geological research. In situ geophysical techniques are able to measure physical parameters directly or indirectly linked with the lithological, hydrological and geotechnical characteristics of the terrains related to the movement. These techniques, less invasive than direct ground-based techniques (i.e. drilling, inclinometer, laboratory tests, etc.), provide information integrated on a greater volume of the soil thus overcoming the point-scale feature of classic geotechnical measurements. Among the in situ geophysical techniques, The High Density Resistivity method (HDR) and Ground Penetrating Radar method (GPR) have been increasingly applied for landslide investigation.

HDR is based on the measure of the electrical resistivity and can provide 2D and 3D images of its distribution in the subsoil. It is one of the standard methods of the geophysical prospecting for solution of shallow geological problems. Current applications of HDR focus on landslide recognition and permafrost detection while investigations on debris thickness in arctic and alpine environments are comparatively sparse. GPR is based on the measure of reflection of radar waves in the subsoil, which mainly focus on the fields of exploration of natural resources, hydrogeology, engineering purposes and archaeological investigation.

HDR and GPR are useful to determine some characteristics of landslides such as main body, geometry, surface of rupture and it has been used in landslide investigations since late 1970s. However, the applicability of the various

geophysical methods, including regional limitations and reliability, for stratum thickness estimation and sliding surface location of landslide in high latitude permafrost regions in northeast China has not been addressed in detail. Applications of geophysical prospecting on landslide in cold regions were rare in Lesser Khingan Range of China.

Using Landslide K178 + 530 in the landslide area as an example, in this paper we present a combination of traditional methods (drilling and mapping) and geophysical techniques (HDR and GPR) on landslide in Lesser Khingan Range of northeast China, being applied to gain knowledge about the thickness and internal structure of the landslide that occur frequently due to permafrost melting and atmospheric precipitation, endeavouring to ascertain the applicability of HDR and GPR on the regional type of landslide.

2 Study Area

The Bei'an-Heihe Highway is located in the northwest section of the Lesser Khingan Range of northeast China, between east longitude 127°17'31"–127°21'24" and north latitude 49°30'57"–49°41'50" (Fig. 1). This area is situated on the southern fringe of China's high-latitude permafrost region and has typical periglacial landforms. The discontinuous permafrost in this region belongs to residual paleoglacial deposition and is currently in degradation. Hence, the geological conditions are extremely unstable (Shan et al. 2015). In 2010, the survey conducted in the project of widening the Bei'an-Heihe road and constructing the Bei'an-Heihe Highway also showed that, in the K177 + 400–K179 + 200 section, within 10 m of the left of the roadbed there were four landslides with the surface area of over 2000 m², as illustrated in Fig. 1 (four landslides are located in A, B, C and D position, respectively. C shows Landslide K178 + 530). Figure 1 shows the geologic and geomorphic map of the landside road area of the study area plotted from the field survey conducted in June 2010.

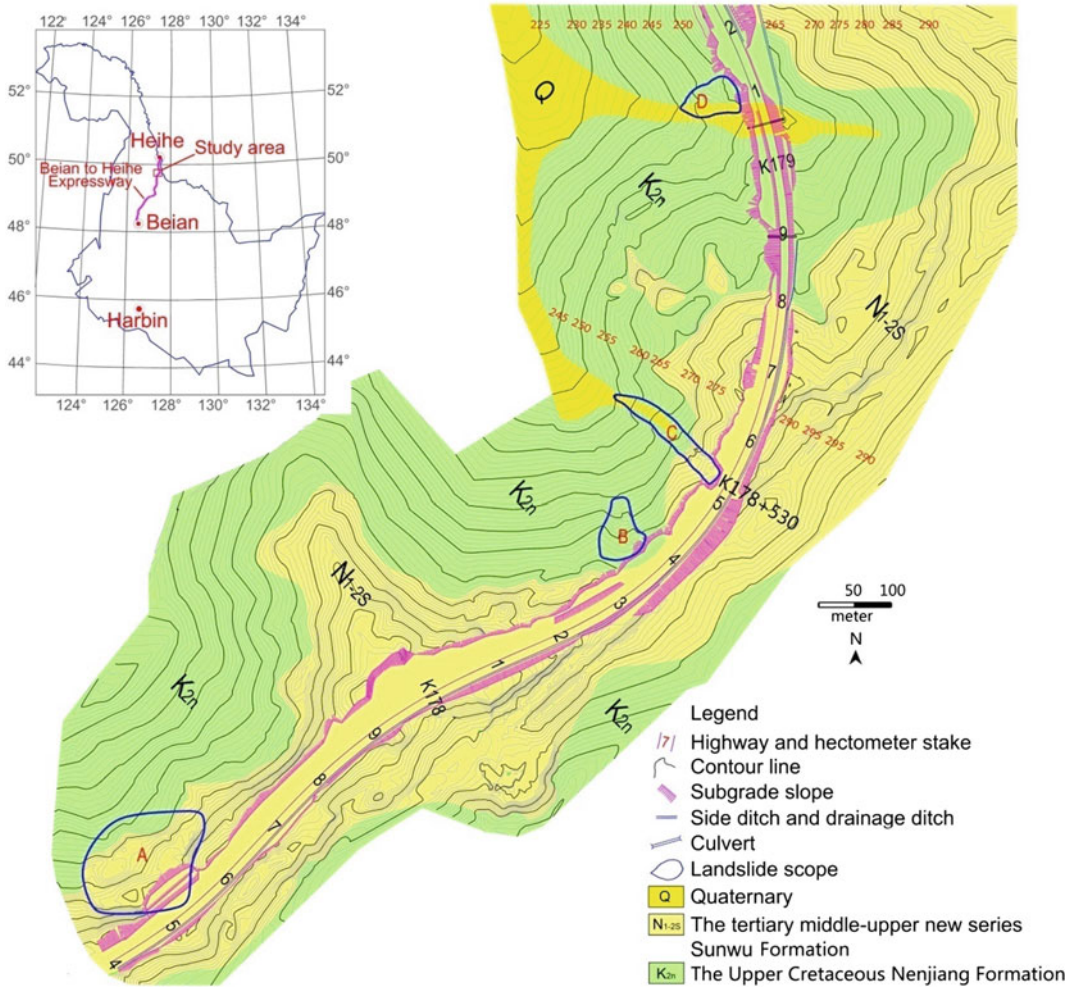


Fig. 1 Geologic and geomorphic map of the field area (in June 2010)

The geological structure of the study area belongs to the Khingan-Haixi fold belt. From the bottom up, the stratigraphy is composed by Cretaceous mudstone, Tertiary pebbly sandstone, silty mudstone, and powdery sandstone. From the late Tertiary to the early Quaternary, the Lesser Khingan Range experienced block uplift. Due to long-term erosion and leveling, loose sediments on the summit and the slope of the hills have gradually thinned, and the thickness of the current residual layer is generally only 1–2 m. The loose deposits accumulate mainly in the basin and valley areas between mountains, with a thickness of about 10 m. The soil is

mainly composed of clayey silt, mild clay, and gravelly sand, and the surface is covered with a relatively thick layer of grass peat and turf. The surface vegetation is that of grassland and woodland, and there are inverted trees in the woodlands.

The Landslide K178 + 530 on the Bei'an--Heihe Highway is located at the widened embankment on the left side of the road, as shown in Fig. 2. The roadbed soil and the surface soil slide together along the valley, and the farthest slip is 200 m away from the road. The landslide mass has a flat tongue shape, is 20–30 m wide, and covers an area of

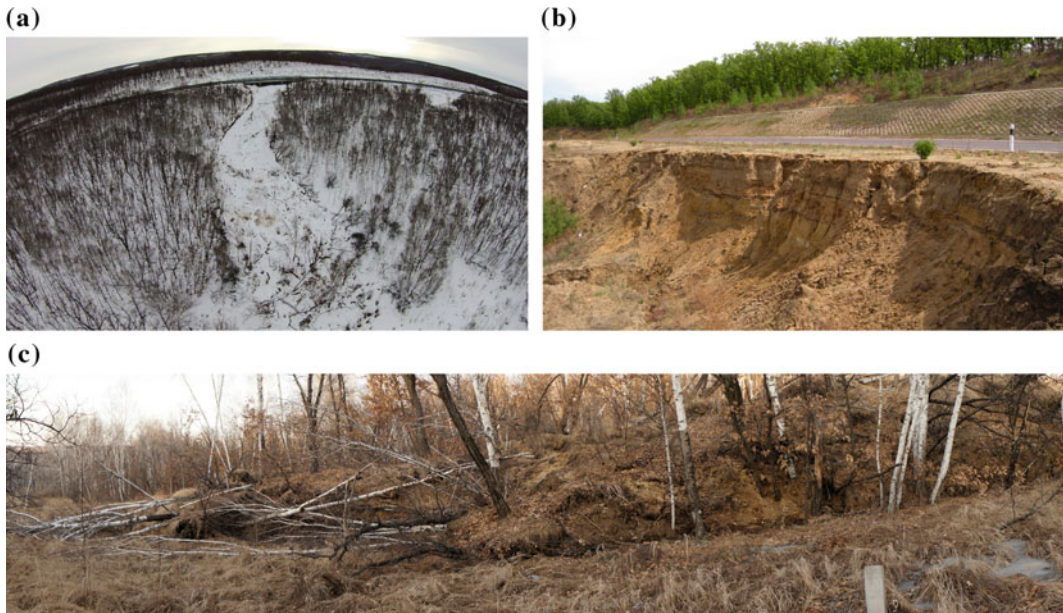


Fig. 2 Landslide scene photos: **a** panoramic view of landslide (in November 2014); **b** the trailing edge of landslide (in June 2010); **c** the leading edge of landslide (in October 2013)

approximately 6000 m². The distance between the leading and trailing edges is 200 m. The height of the leading edge is 254 m, and that of the trailing edge is 285 m. The leading edge of the landslide pushes the soil on the original ground surface and slides forward together with it. The trailing edge of the landslide has an arc-shaped dislocation, which is located inside the range of the widened embankment.

Four engineering geological boreholes were drilled into K178 + 530 section for prospecting purposes. The depths of the boreholes range from 14 to 26 m, and the borehole distribution is shown in Fig. 3. The drilling revealed that the soil distribution along the profile from top to bottom is: Quaternary loose soils, Tertiary pebbly sandstones, siltstones, and Cretaceous mudstones. The geological profile is illustrated in Fig. 5.

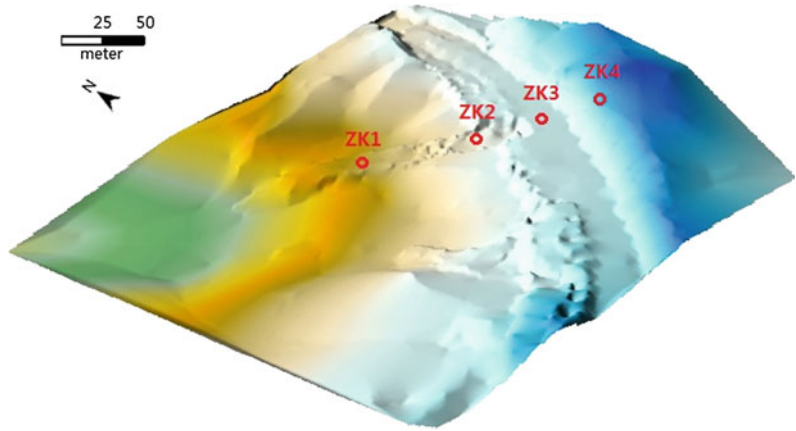
Embankment: yellow, mainly composed of loosely mixed Tertiary pebbly sandstones, Cretaceous mudstones and sandy mudstones; the soil is loose when dry, plastic when saturated with water. **Clay:** yellow, soft and plastic, of high strength and toughness when dry. The upstream

region of the landslide mass has a depth distribution of 1.5–3.8 m. The downstream region of the landslide mass has a depth distribution of 0–6.7 m, and there is more than one sandwiched grit layer; the thickness of a single layer is approximately 1–10 cm, which greatly enhances the water seepage capacity of the soil.

Tertiary pebbly sandstones: distributed in the embankment at a depth of 2.0–3.4 m and the upstream region of the landslide mass at a depth of 3.8–4.5 m, all weathered, composed mainly of feldspar stone and mineral sands, well-graded, high permeability. **Fully weathered siltstones:** yellow, distributed in the upstream region of the landslide mass at a depth of 4.5–9.7 m, sandy, of bedding structure and poor water seepage capacity.

Fully weathered mudstone: yellow or gray-green, pelite, of layered structure, easy to soften with water, of poor water seepage capacity. **Strongly weathered mudstones:** dark gray, pelite, of layered structure, weakly cemented rock. **Moderately weathered mudstones:** brown, black and gray, pelite, layered structure.

Fig. 3 Drilling borehole layout on Landslide K178 + 530 and the geomorphological map of the landslide area (using SURFER software to draw the geomorphological map based on GPS terrain data in June 2010)



3 Methods

In this paper we present combination geophysical techniques of HDR and GPR on the landslide K178 + 530 on the Bei'an-Heihe Highway in Lesser Khingan Range of northeast China. The survey lines were established, as shown in Fig. 4.

HDR Method

The instrument used in this study was the WGMD-9 Super HDR system produced by the Chongqing Benteng Digital Control Technical Institute (Chongqing, China). In this system, the WDA-1 super digital direct current electric device is used as the measurement and control host, and with the optional WDZJ-4 multi-channel electrode converter, centralized high-density cables and electrodes, centralized two-dimensional HDR measurements can be achieved. The inversion of the obtained apparent resistivity data sets was performed using the software RES2DINV. This software package produces a two-dimensional subsurface model from the apparent resistivity pseudosection. Data were acquired by a Wenner configuration. The method is based on the smoothness-constrained least squares inversion of pseudo-section data. In this algorithm, the subsurface is divided into rectangular blocks of constant resistivity. Then the resistivity of each block is evaluated by minimizing the difference between observed and

calculated pseudo-sections using an iterative scheme. The smoothness-constraint leads the algorithm to yield a solution with smooth resistivity changes. The calculated pseudo-sections can be obtained by either finite-difference or finite-element methods. In this case, the finite element scheme was employed due to the topographical changes in the field.

The smoothness-constraint least squares method was used in the inversion model. Essentially, this method is used to constantly adjust the model resistivity through model correction to reduce the difference between the calculated apparent resistivity and the measured resistivity, and to describe the degree of fit between the two using the mean square error. The smoothness-constraint least squares method, which has been widely applied, has a number of advantages, such as adaptability to different types of data and models, relatively small influence of noise on the inversion data, high sensitivity to deep units, rapid inversion, and a small number of iterations. In tests using the HDR method, the spacing between unit electrodes was 3.0 m, and the maximum exploration depth of the survey lines was 30 m.

On the road section of Landslide K178 + 530, a total of three HDR survey lines, i.e., I-I', II-II' and III-III', were established, as shown in Fig. 4. The measuring date is September 3, 2012.

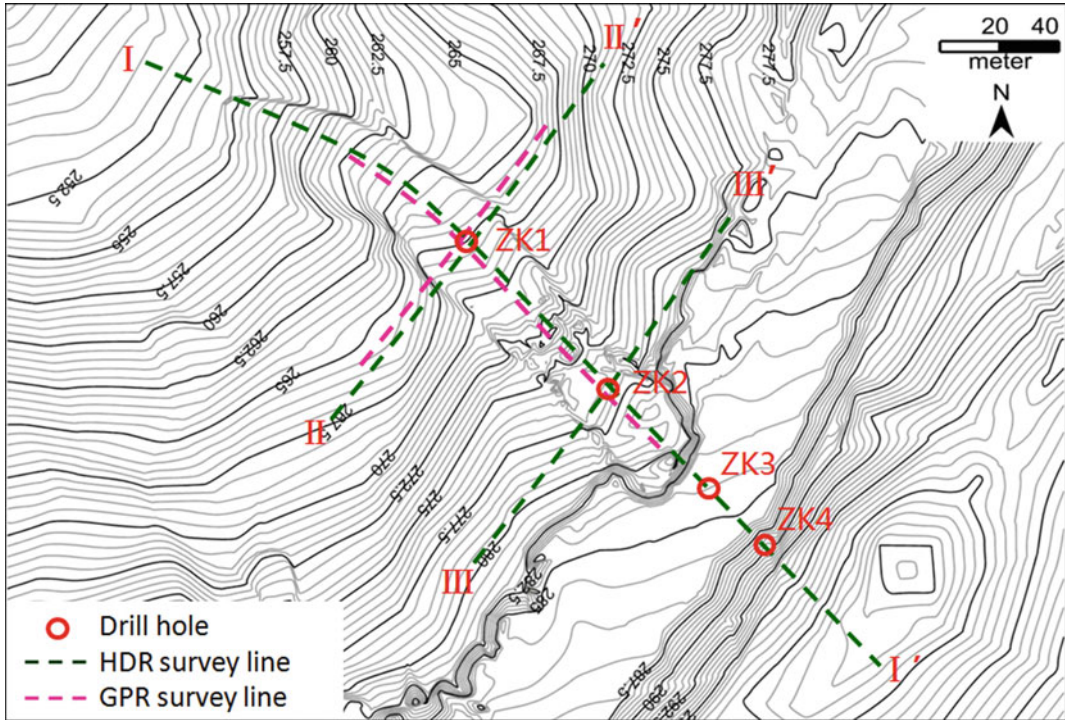


Fig. 4 The layout of the geophysical prospecting survey lines on Landslide K178 + 530. *I* HDR survey lines: on the road section of Landslide K178 + 530, a total of three HDR survey lines, i.e., *I-I'*, *II-II'* and *III-III'*, were established. Line *I-I'* ran along the sliding direction of the landslide mass and passed through its center. The starting point of the survey line was located 40 m away from the leading edge of the landslide mass, and the line sequentially passed through the drilling boreholes ZK1, ZK2, ZK3 and ZK4. The total length of this survey line was 357 m (horizontal distance of 300 m). Line *II-II'* was perpendicular to the sliding direction of the landslide mass, 110 m away from the trailing edge, with point ZK1 serving as the midpoint, electrodes numbered 1–60 were

arranged in order from left to right, the total length of this survey line was 177 m. Line *III-III'* was perpendicular to the sliding direction of the landslide mass, 50 m away from the trailing edge, with point ZK2 serving as the midpoint, electrodes numbered 1–60 were arranged in order from left to right, the total length of this survey line was 177 m. The measuring date is September 3, 2012. 2 GPR survey lines: two survey lines were set up, of which the positions coincided with those of the HDR survey lines, but the start and end points were different, the GPR survey lines lengths were shorter than HDR survey lines. The lengths of the two survey lines (*I-I'* and *II-II'*) were 150 and 118 m, respectively. The measuring date is October 1, 2013

GPR Method

The GPR instrument used was the RIS-K2 FastWave Ground Penetrating Radar produced by IDS Corporation (Italy). The radar antenna was a low-frequency 40-MHz unshielded dual antenna. The detection time window was set to 600 ns, the sampling rate to 1024, the data acquisition track pitch is 0.05 m. Two GPR survey lines were set up, as shown in Fig. 4, of which the positions coincided with those of the HDR survey lines, but the start and end points were different. The

lengths of the two survey lines (*I-I'* and *II-II'*) were 150 and 118 m, respectively. The measuring date is October 1, 2013. GPR raw data were processed applying the REFLEXW software from Sandmeier Scientific Software (Karlsruhe, Germany). Coordinates for each trace were calculated at equal distances. The surface signal reflection was set to time zero. Low frequency parts and noise in the spectrum were filtered applying a dewow and bandpass filter. In a next step temporally consistent signals were

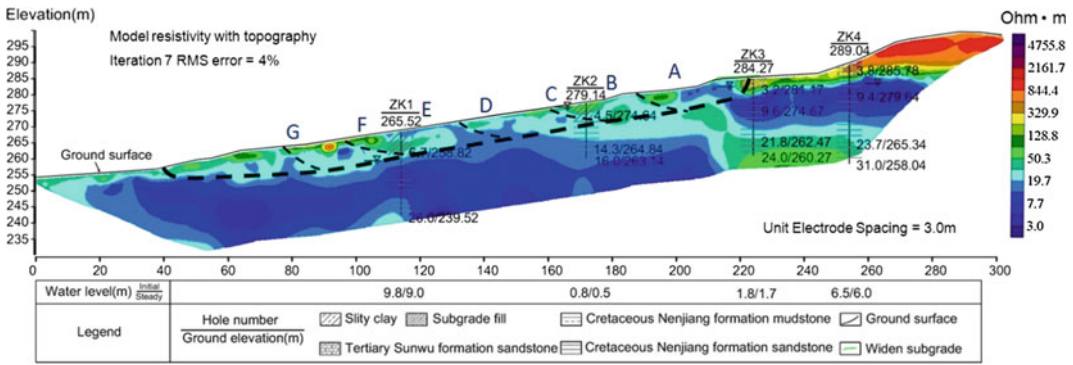


Fig. 5 The drilling results compared with electrical resistivity profile of the survey line I-I'. Geological drilling date is in June 2010, HDR detection date is on September 3, 2012. The thick black dashed line show the

position of the major sliding surface, the thin black dashed lines show the secondary sliding surfaces (see text for discussion)

eliminated utilising a background removal, and topographical correction were applied. The picks were exported with the attribute of the two-way travel time, the velocity of propagation of the wave in this case appears to be about 0.10 m/ns.

4 Results, Analysis, and Discussion

HDR

Survey line I-I'

The measured apparent electrical resistivity profile of line I-I' obtained on September 3, 2012 is shown in Fig. 5. As can be seen from the image, the soil resistivity values of the landslide mass exhibited distinct layering. To better analyze how soil resistivity changes with depth, the software RES2DINV can be used to extract the resistivity curve value of any point on the survey line. Figure 6 illustrates the soil resistivity versus depth curves at boreholes ZK1 and ZK2. Taken together with the drilling result, changes in the characteristics of soil resistivity are analyzed as in Figs. 6 and 7.

The borehole ZK1 is 115 m away from the starting point of the HDR survey line. At a depth of 0–2.1 m, the soil is silty clay and rather loose, containing approximately 15% grass roots and other organic matters. The resistivity value

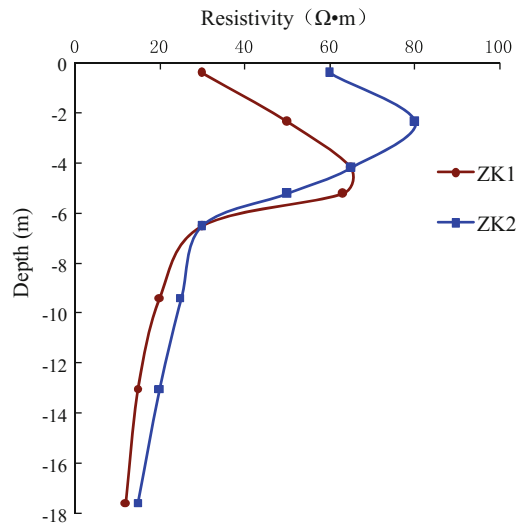


Fig. 6 The electrical resistivity curves at positions ZK1 and ZK2

ranges from 25 to 45 Ω m. At a depth of 2.1–6.7 m, the soil is silty clay, and there are local weathered sand layers. The resistivity value ranges from 45 to 65 Ω m. At a depth of 6.7–8.0 m, the soil is yellow mudstone. The permeability coefficient is small, and it is difficult for the water to infiltrate downward, forming a watertight layer, water easily gathered here. The resistivity value is relatively low, i.e., 20–30 Ω m. At a depth of 8.0–26 m, the soil is gray mudstone, close to or below the water table. The resistivity value is relatively low, i.e.,

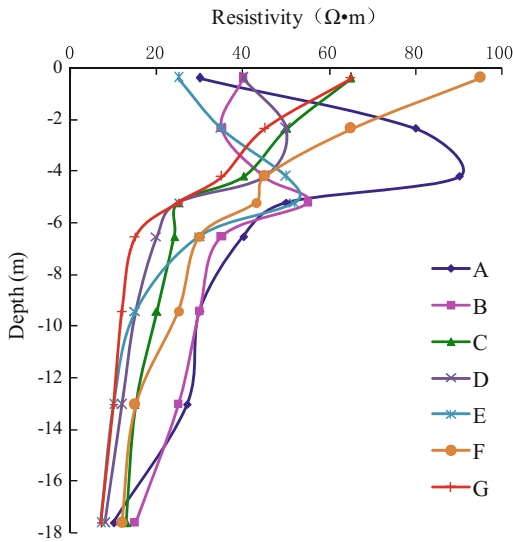


Fig. 7 The electrical resistivity curves at different points on the survey line I-I'

10–25 Ω m. As shown in the curve, silty clay contacts mudstone at a depth of 6.7 m, and resistivity exhibits apparent layering, the resistivity value decreased suddenly.

The borehole ZK2 is 175 m away from the starting point of the survey line. At a depth of 0–4.5 m, the soil is rather loose. The resistivity values range from 45 to 80 Ω m. The resistivity of the surface embankment soil dominated by silty clay (depth 0–3.8 m) ranges from 60 to 80 Ω m, and that of gravelly sand (depth 3.8–4.5 m) ranges from 45 to 60 Ω m. At a depth of 4.5–9.7 m, the soil is siltstone and composed of rather small particles. The permeability is poor, forming a watertight layer, water easily gathered here. The resistivity value ranges from 25 to 35 Ω m. At a depth of 9.7–14.6 m, the soil is sandstone, and the resistivity value ranges from 15 to 25 Ω m. As evident in the curve, gravelly sand contacts the siltstone at a depth of 4.5 m, and there is apparent resistivity layering, the resistivity value decreased suddenly.

To better understand the changes in the soil resistivity at different positions of line I-I', the software RES2DINV was used to extract the soil resistivity curves at points A, B, C, D, E, F and G on the survey line (Fig. 5). The horizontal distances from A, B, C, D, E, F and G to the starting

point of line I-I' are 80, 100, 120, 140, 160, 180 and 200 m, respectively. The obtained soil resistivity curves are shown in Fig. 7. At position A, the soil resistivity value decreased abruptly at a depth of 4.5 m. In other words, the soil resistivity values exhibited abrupt stratification at this depth. It can thus be determined that the sliding surface is located at a depth of 4.5 m. Similarly, the depths of the sliding surface at points B, C, D, E, F and G on line I-I' were determined to be 5, 4.7, 5.5, 6.5, 6, and 5.5 m, respectively.

The above HDR profiles and resistivity curves show that the soil resistivity values above and below the sliding surface of the landslide mass are clearly different and exhibit an abrupt stratification. According to this typical characteristic of the sliding surface, the positions of the major sliding surfaces along line I-I' were deduced, as shown by the thick black dashed line in Fig. 5. The type of sliding type for this landslide was propelled sliding, and the sliding power originated from the trailing edge of the landslide. The slip rate of the trailing edge was the greatest, followed by the middle part of the landslide; the minimum slip rate occurred at the leading edge. As a result, secondary sliding occurred in the landslide mass. Combining the changes in the soil resistivity values of different positions in the landslide mass and drilling exploration, the secondary sliding surface was obtained, as shown by the thin black dashed line in Fig. 5.

Survey line II-II'

The measured apparent electrical resistivity profile of survey line II-II' is shown in Fig. 8, and the soil resistivity curves of points C, D ZK1, E and F along line II-II' are shown in Fig. 9a. The distances from C, D ZK1, E and F to the starting point of the survey line are 80, 85, 90, 95 and 100 m, respectively. Based on Figs. 8 and 9a, we can know the changes in the soil resistivity values, there are apparent resistivity layering at the depths of the sliding surfaces, the resistivity value decreased suddenly. According to this characteristic of the sliding surface, the

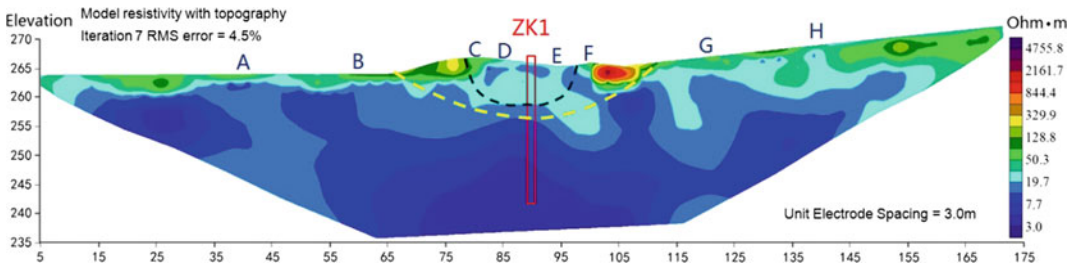


Fig. 8 The electrical resistivity profile of the survey line II-II'. HDR detection date is on September 3, 2012. The black dashed line in this figure shows the current sliding

surface. The yellow dashed line shows the position of the sliding surface for the paleo-landslide

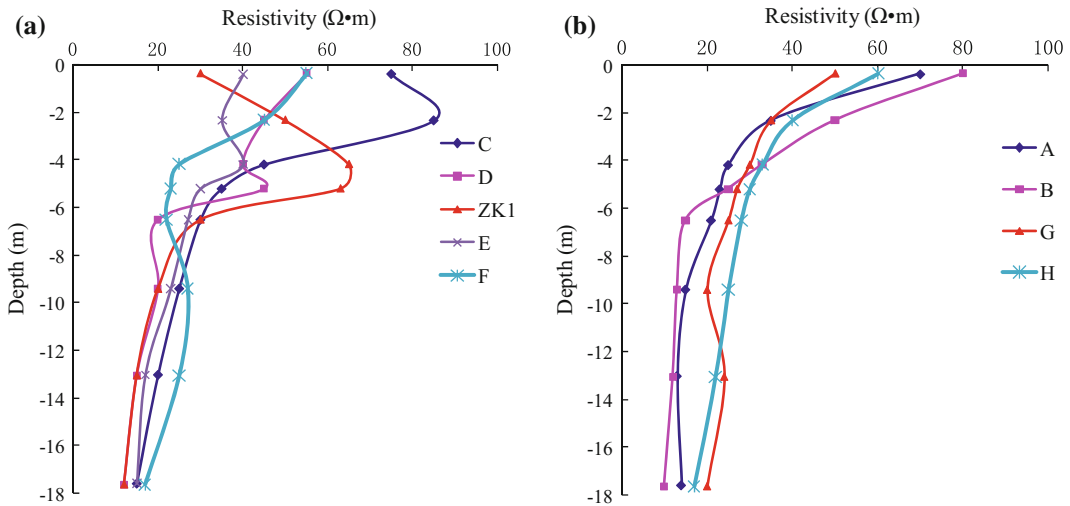


Fig. 9 The electrical resistivity curves at different points on the survey line II-II' (points C, D, ZK1, E and F are all on the landslide mass, points A, B, G and H are all outside the landslide mass)

positions of the sliding surfaces along line II-II' were deduced, as shown by the black dotted line in Fig. 8. Based on the changes in the soil resistivity values, it can be inferred that the depths of the sliding surfaces at positions C, D, ZK1, E and F on line II-II' were 4, 6, 6.5, 5.5 and 3.5 m, respectively. Figure 9b shows the soil resistivity curves of positions A, B, G and H (all outside the landslide mass) on the survey line II-II'. The distances from A, B, G and H to the starting point of the survey line were 40, 60, 110 and 130 m, respectively. As can be seen in Fig. 9b, the soil resistivity values of the stable

soil body outside the landslide only showed stratification in the surface loose layer. As depth increased, the resistivity basically exhibited a monotonic decline, and there was no abrupt stratification.

This landslide belongs to a recurring old landslide that slipped again. The black dashed line in Fig. 8 shows the current sliding surface. According to the site geological survey, combined with characteristics of resistivity changes, the position of the sliding surface for the paleo-landslide can be inferred, as shown by the yellow dashed line in Fig. 8.

GPR

Survey line I–I'

The profile determined by the GPR survey line I–I' is illustrated in Fig. 10 (due to the constraints under field conditions, this GPR survey line can only be used to measure this long section). Using layer picking option (phase follower) in the REFLEXW software can search continuous reflector, as shown in Fig. 10 (the thick red dashed line). The intensity of the radar-wave reflection was significantly different from that of the surrounding medium. The signal of the reflected-wave is strong and shows distinctive horizon characteristics, presenting a low-frequency high-amplitude sync-phase axis, which can be inferred as the sliding surface. The continuity of the sliding surfaces is good, basically reflecting the depth range of the landslide mass development.

Using REFLEXW radar data processing software, the radar waves amplitude values of all the data acquisition track points in the profile at different depths can be extracted. In order to better understand the changes in the intensity of

the reflected radar waves, the radar-wave amplitude curves at positions A, B, ZK2, C, D, E, ZK1, F and G (as shown in Fig. 10) on the survey line I–I' were plotted, as shown in Fig. 11. A higher radar-wave amplitude value indicates a greater intensity of the reflected radar wave. As can be seen from Fig. 11, because the surface soil body is rather loose in this area, most curves showed relatively large amplitudes in the depth range of 0–2.5 m. In position A, at a depth of 4.5 m, the radar-wave amplitude increased substantially, exhibiting an abrupt change. According to characteristic differences in the radar-wave reflection in different types of soil bodies, it can be inferred that the soil moisture content was relatively high in this position, and thus the position of the sliding surface of the landslide mass can be deduced. Similarly, in positions B, ZK2, C, D, E, ZK1, F and G on line I–I', an abrupt increase in radar-wave amplitudes occurred at depths of 4.7, 4.7, 5.5, 5.5, 6.7, 6.5, 5.6 and 5 m, respectively, and the position of the sliding surface can be inferred. This is very close to the position of the sliding surface as denoted by thick the red line in Fig. 10.

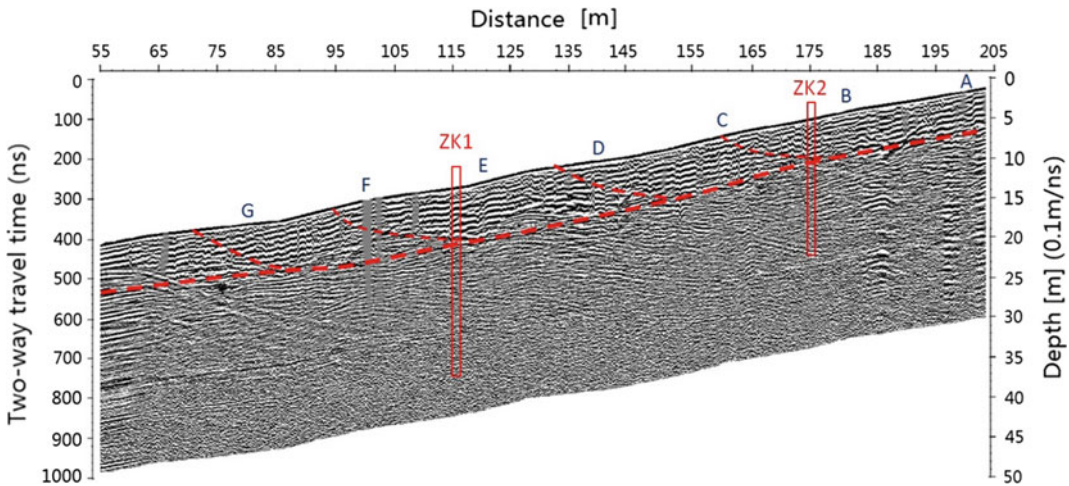


Fig. 10 The GPR profile of the survey line I–I'. The radar antenna was a low-frequency 40-MHz unshielded dual antenna, the measuring date is October 1, 2013. The

thick red dashed line show the position of the major sliding surface, *the thin red dashed lines* show the secondary sliding surfaces (see text for discussion)

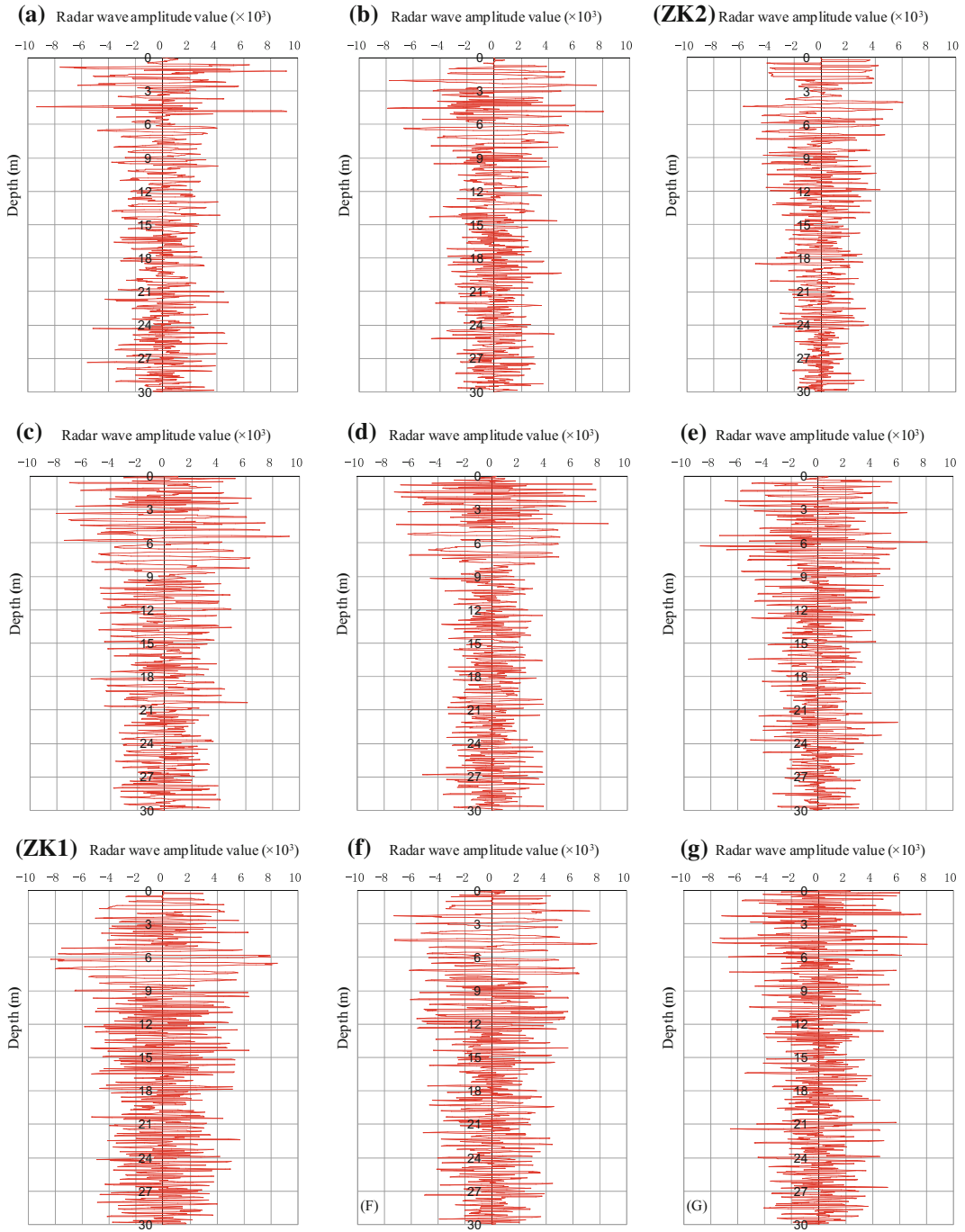


Fig. 11 The radar-wave amplitude curves on the survey line *I-I'*. Positions A, B, ZK2, C, D, E, ZK1, F and G are all on the survey line *I-I'* (as shown in Fig. 10)

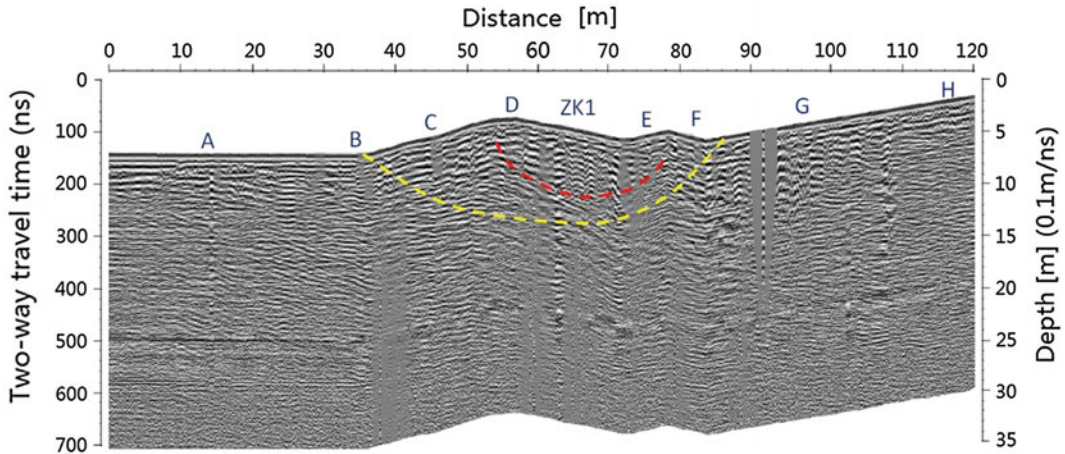


Fig. 12 The GPR profile of the survey line II-II'. GPR detection date is on October 1, 2013. The red dashed line shows the current sliding surface. The yellow dashed line

shows the position of the sliding surface for the paleo-landslide

Survey line II-II'

The measured GPR profile of the survey line II-II' is illustrated in Fig. 12. The red dotted line on the profile is the low-frequency high-amplitude sync-phase axis, and is deduced to be the sliding surface of this profile. This reflects the depth range of the landslide mass development.

Using REFLEXW radar data processing software, we can obtain the radar-wave amplitude curves at positions A, B, C, D, ZK1, E, F, G and H (as shown in Fig. 12) on the survey line II-II', as shown in Fig. 13. As can be seen from Fig. 13, because the surface soil body is rather loose in this area, most curves showed relatively large amplitudes in the depth range of 0–2.5 m. D, ZK1 and E are all on the landslide mass, in positions D, ZK1 and E, a sudden and substantial increase in the radar-wave amplitude occurred at depths of 3.5, 6.5 and 3.2 m, respectively, exhibiting abrupt changes. According to characteristic differences in radar-wave reflection in different types of soil bodies, it can be inferred that the soil moisture content in this position is relatively high, and thus the position of the sliding surface of the landslide mass can be inferred. The deduced position of the sliding

surface is about the same as that denoted by the red dashed line in Fig. 12. Positions A, B, G and H were all located outside of the landslide mass. Except in the surface layer, i.e., in the depth range of 0–2.5 m, there were abrupt changes in the radar-wave amplitudes; at deeper depths, no abrupt changes were observed in the radar-wave amplitude curves.

As shown in Fig. 13, in positions C, D, ZK1, E and F, the amplitude values showed substantial increases at depths of 6, 9.5, 9, 7 and 3.5 m, respectively, exhibiting abrupt changes. These positions can be used to deduce the position of the sliding surface of the paleo-landslide, as denoted by the yellow dashed lines in Fig. 12. Meanwhile, the magnitude of the abrupt change in the radar-wave amplitudes at the position of the sliding surface of the paleo-landslide was smaller than that at the position of the current sliding surface.

The GPR results show that the moisture content of soils at the sliding surface of the landslide mass is relatively high. The drilling data also show that the moisture content of the sliding surface of the landslide mass in the study area is very high, which is completely consistent with the results obtained from the GPR profile and the HDR profile.

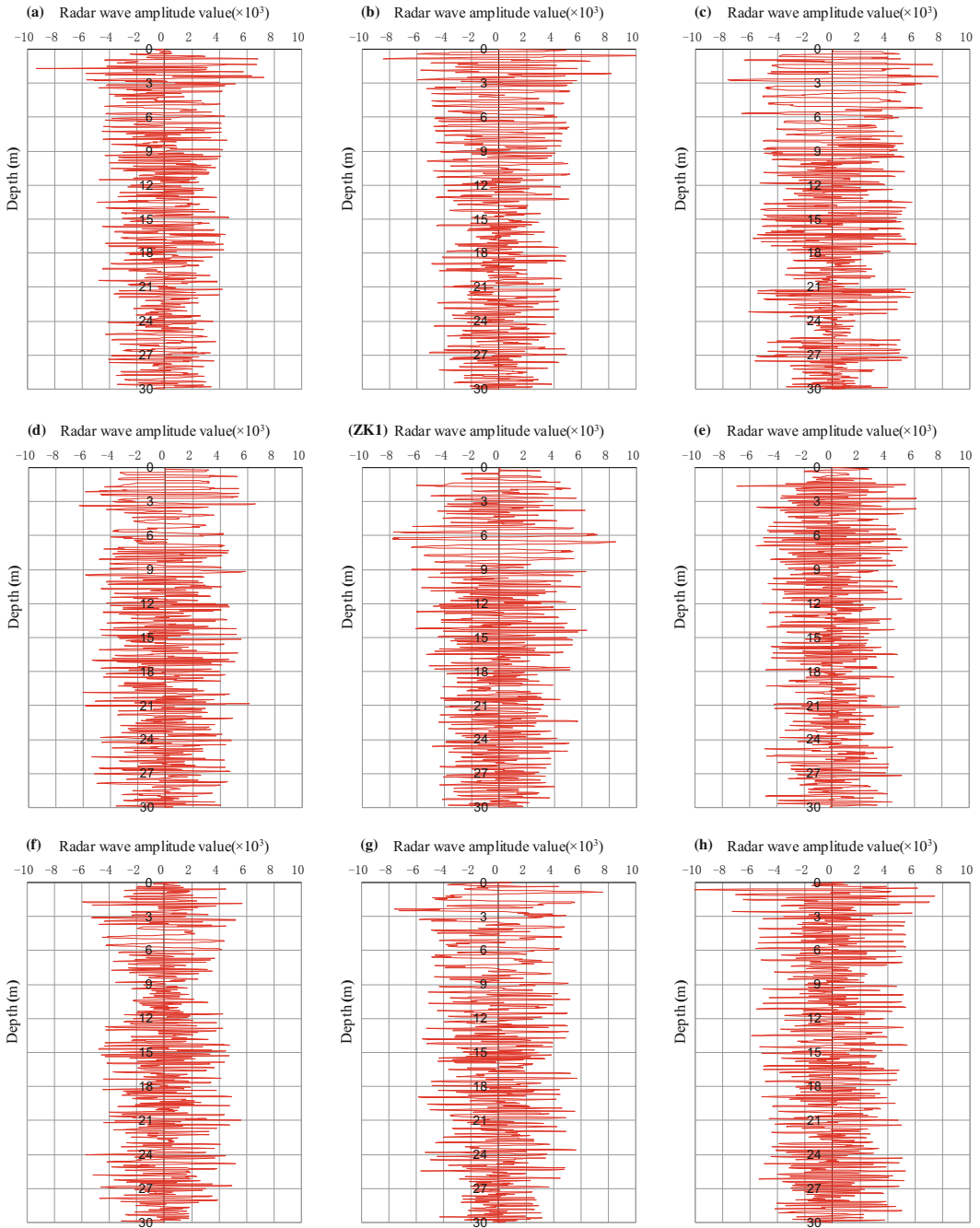


Fig. 13 The radar-wave amplitude curves on the survey line II-II'. Positions A, B, C, D, ZK1, E, F, G and H are all on the survey line II-II' (as shown in Fig. 12)

Analysis of the Mechanism Underlying Landslide Development

In May 2010, a geological survey of the study area revealed that there is permafrost in the shady slopes on the two sides of the landslides in this area. Permafrost was found by drilling on the profile of the survey line III–III', as shown in Fig. 14 for permafrost soil sample photos. In addition, the HDR method was used on June 2, 2010 for prospecting on the profile of the survey line III–III', based on soil resistivity characteristics, we can infer the permafrost layer range on the profile of the survey line III–III', the measured apparent electrical resistivity profile of survey line III–III' obtained in June 2, 2010 is shown in Fig. 15 (as shown by the black dotted line).

Due to permafrost melting and concentrated summer rainfall, the landslide mass started to slip

at the end of July 2010, and the landslide was formed. Site surveys and borehole drilling data demonstrate that Landslide K178 + 530 is a shallow creeping consequent landslide in the permafrost region. Water seepage generated from permafrost melting together with water infiltration generated from concentrated summer precipitation increases the local moisture content of the hillside soil. This is the main reason for landslide formation in the northwest section of the Lesser Khingan Range in China. Instability may easily occur in the rainy season and the spring melting season. The relatively large number of bulging cracks on the landslide mass makes it easy for water to accumulate and infiltrate downward. The highly permeable surface soil, the gravel and sand layer, and the silty clay containing a weathered sand interlayer provide a convenient channel for water infiltration. The mudstone and siltstone layers below have small

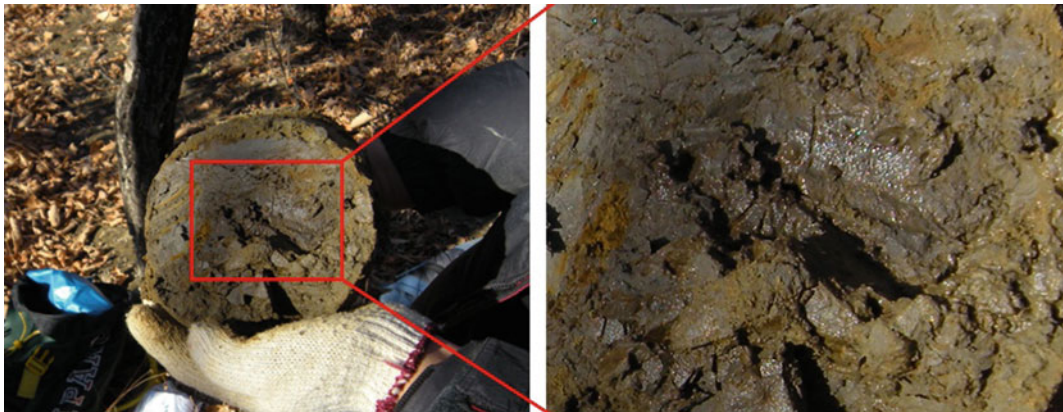


Fig. 14 The photo of high temperature permafrost. Sampling location is in the survey line III–III', at 40 m position on the X axis, the drilling time is in May 2010

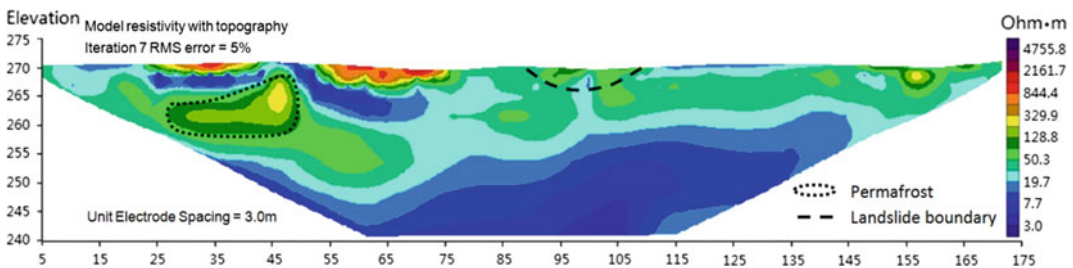


Fig. 15 The electrical resistivity profile of the survey line III–III' (2010-6-2)

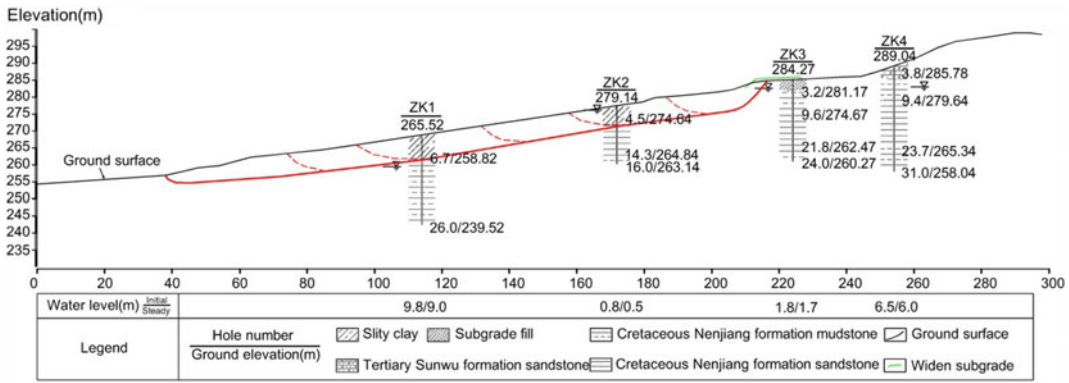


Fig. 16 The stratigraphic distribution of section K178 + 530 (the thick red dashed line shows the position of the major sliding surface, the thin red dashed lines show the secondary sliding surfaces)

permeability, forming watertight layers. Water generated from precipitation, melting snow and permafrost melting is blocked by the impermeable layer when it infiltrates downward, and the local moisture content increases sharply. Water thus infiltrates along the interface between the permeable layer and the impermeable layer, forming a slip zone. Combining the geophysical and drilling data, the position of the sliding

surface can be determined, as shown by the red line in Fig. 16.

Reference

Shan W, Hu Z, Guo Y, Zhang C, Wang C, Jiang H, Liu Y, Xiao J (2015) The impact of climate change on landslides in southeastern of high-latitude permafrost regions of china. *Front Earth Sci* 3(7):1–11

TXT-tool 4.052-1.1

Landslide Risk Perception

Irasema Alcántara-Ayala

Abstract

Derived from the establishment of the Sendai Framework for Disaster Risk Reduction (SFDRR) 2015–2030, the need and desire to prevent disasters, at global, regional, national and sub-national scales is focused on initiatives directed towards Disaster Risk Reduction (DRR) and Disaster Risk Management (DRM). There is a wide consensus on the necessity of involving community participation to achieve both DRR and DRM. To build adequate strategies for DRR, risk perception analysis are a requirement for integrated disaster risk assessments, the latter being the first step of DRM. Risk perceptions consist of the explanations people build and shape to try to understand the dynamics of the complex interactions that give rise to the humanised landscape according to experiences, beliefs, social and cultural frameworks, feelings and needs. In this paper, a general panorama of some of the aspects concerning the notions of risk and risk perception is presented, to later on deepen into the broad configuration of landslide risk perception analysis.

Keywords

Risk perception • Landslides • Sendai framework for disaster risk reduction • Disaster risk management

Contents

1	Introduction	556
2	Risk	558
3	Risk Perception	558
4	Landslide Risk Perception	560
5	Discussion	565
6	Conclusion	566
	References	566

I. Alcántara-Ayala (✉)
Institute of Geography, National Autonomous
University of Mexico (UNAM), 04510 Coyoacán,
Mexico City, Mexico
e-mail: irasema@igg.unam.mx

I. Alcántara-Ayala
Circuito Exterior, Ciudad Universitaria, 04510
Coyoacán, Mexico City, Mexico

1 Introduction

Risk is a state of uncertainty, a condition in which outcomes from specific actions or processes can be positive or negative for a person or group of people. Very often uncertainty is seen as something not desirable. When an individual falls in love with someone, for instance, but has not been able to transmit those feelings, he or she is under a state of high uncertainty. His or her mind is full of worries and questions such as: Would that person have the same feelings? Is she or he already committed to somebody else? Am I attractive for her/him? and so forth. Likewise, for example during medical or financial crises, the way forward is the personal or collective (i.e. family, business group) desire and necessity of certainty in terms of positive results. To cope with such situations a system of beliefs has been created by humankind. Beliefs can be regarded as something that individuals deem to be true. They involve different degrees of certainty, but also of confidence. According to Abelson (1979) belief systems are characterised as follows:

1. “The elements (concepts, propositions, rules, etc.) of a belief system are not consensual;
2. Belief systems are in part concerned with the existence or nonexistence of certain conceptual entities;
3. Belief systems often include representations of “alternative worlds,” typically the world as it is and the world as it should be;
4. Belief systems rely heavily on evaluative and affective components;
5. Belief systems are likely to include a substantial amount of episodic material from either personal experience or (for cultural belief systems) from folklore or (for political doctrines) from propaganda;
6. The content set to be included in a belief system is usually highly “open”;
7. Beliefs can be held with varying degrees of certitude”.

Renshon (2008) suggested that beliefs are important because people have a tendency to select or filter new information according to their

pre-existing beliefs so that they can keep a steady state or uniformity of their belief system (Jervis 1976, 2006). This represents a major issue during decision-making processes since subjectivity may shadow objectivity (Holsti 1962; Boulding 1969), or when beliefs affect behaviour and the way this takes place (Jervis 2006). Such beliefs can be also associated with traditions, cosmogony or myths.

By using a very appealing narrative, Gigerenzer (2014) made reference to the ambivalence of risk and uncertainty. He referred to the fact that *Fortune*, the goddess of chance, or luck, involves randomness and probabilities, whereas *Sapientia* or Sophia, “the calculating and vain deity of science, gazes into a hand-mirror, lost in admiration for herself”. Both are contrasting, just like sweet and sour (Fig. 1). *Fortuna* is associated with good or bad luck, according to her temper, and Sophia declares certainty. As such, the contrast has endured an evolving cherished relationship. *Sapientia* aims at replacing chances by causality, and *Fortuna* hopes to undermine *Sophia* by performing through probability and statistics (Bennis et al. 2012; in Gigerenzer 2014).

For Gigerenzer (2014) decision-making involves two series of mental tools; quite often the combination of both is required—risk and uncertainty (Fig. 2). Uncertainty cannot be measured empirically, whereas risks can be. “If risks are known, good decisions require logic and statistical thinking” ... “If some risks are unknown, good decisions also require intuition and smart rules of thumb”.

In the case of risks associated with natural hazards, such as landslides, the endeavour is not that simple either. The situation gets even more complicated as the occurrence of disasters is the crystallization of those risks. The need and desire to prevent disasters is therefore directed towards Disaster Risk Reduction (DRR) and Disaster Risk Management (DRM), which should involve community participation. To build adequate strategies for DRR, risk perception analysis are a major requirement for integrated disaster risk assessments, the latter being the first step of DRM.



Fig. 1 The wheel of Lady Fortuna, miniature from “*The casibus virorum illustrium*”, Boccaccio, Paris 1467, Glasgow University Library (*left*); and *Sophia*, Greek Goddess of Wisdom (*right*)

Fig. 2 Understanding and communicating uncertainty and risk is not an easy task (Ashes 1894, by Edvard Munch)



In this paper, reference is made to some aspects concerning the notions of risk and risk perception, to later on deepen into the broad configuration of landslide risk perception analysis.

2 Risk

Risk has been defined from a number of different perspectives. Adams (1995) for example stated that “risk, according to the definitions most commonly found in the safety literature, is the probability of an adverse future event multiplied by its magnitude”. Risk is measurable uncertainty, while uncertainty is immeasurable risk (Hillson 2004).

Uncertainty can be regarded as aleatoric and epistemic (Haines 2004). While the former is associated with the inherent haphazardness of phenomena, the latter is linked to lack of knowledge. As such, when dealing with natural hazards, aleatoric uncertainty involves the degree of unpredictability of the specific hazard, and the state of knowledge or availability of accurate data is comprised within the epistemic dimension of uncertainty.

Along the same line, risk can also be understood by two perspectives, as it involves probability and effects. The probability dimension is referred to “the likelihood of some specific negative event” characterized by amount, intensity and duration “resulting from exposure to a hazard ...” and “the extent of the detriment associated with the adverse event” relates to the sphere of the effects (Breakwell 2014). Furthermore, within the sphere of the psychometric paradigm the understanding of risk is related to the general properties of the risk object (Sjöberg 1996).

In the TACTIC report it is pointed out that there are three general notions of risk: realist, constructivist, and critical (Shreve et al. 2014). The realist conception considers risk as objective, and measurable (Rosa 1998, 2008); contrastingly, for the constructivists, risk is socially constructed and hence subjective (Jasanoff 1998; Wachinger and Renn 2010), while the quest for

identifying and understanding root causes of risk is the essential ingredient of critical risk (Shreve et al. 2014; Oliver-Smith et al. 2016).

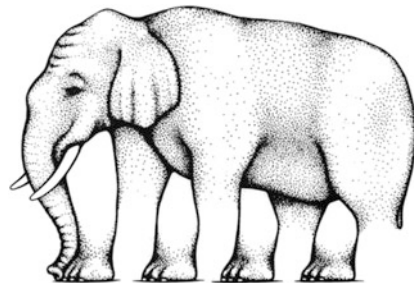
After some decades in which risk had been understood and used as a synonym for natural hazards, the frequent impact of disasters worldwide and the desire for and commitment to scientific progress by the academic community, particularly that of social scientists, have led to a paradigm shift. Disaster risk has been recognized to be a result of the relationships generated by vulnerable communities that are exposed to hazards (Blaikie et al. 1994).

More specifically, as defined by the United Nations Office for Disaster Risk Reduction (UNISDR 2016), “disaster risk is [considered to be] a function of hazard, exposure and vulnerability. It is [normally] expressed as a probability of loss of life, injury or destroyed or damaged assets which could occur to a system, society or a community in a specific period of time”. Consequently, disaster is “a serious disruption of the functioning of a community or a society due to hazardous events interacting with conditions of vulnerability and exposure, leading to widespread human, material, economic and environmental losses and impacts” (UNISDR 2016).

3 Risk Perception

We don't see things as they are; we see them as we are

Anaïs Nin



There is a large list of definitions of risk perception. They vary in principle, according to the disciplines involved and the context in which risk perception is analysed. Risk perception has been defined by Pidgeon et al. (1992), as “people’s

beliefs, attitudes, judgments and feelings, as well as the wider social or cultural values and dispositions that people adopt, towards hazards and their benefits". Risk perception refers to the types of attitudes and opinions shaped, conducted and given by experts and lay people about hazards. "People do not respond directly to the risks they are exposed to; rather they respond to the perceptions of those risks" (Etkin 2016).

Research conducted by Renn and Rohrman (2000) has indicated that risk perception is shaped by both, individual and social factors derived or associated with four horizons (Fig. 3): (1) general heuristics; (2) cognitive-affective factors; (3) social-political environment; and (4) cultural background. Heuristics of information processing include collective and individual perspectives related to common characteristics of risk (see Table 1) that have a central influence on the perceived magnitude of risks. Perception processes are linked directly or indirectly to cognitive and affective factors based on reference knowledge, stigmata, personal beliefs and

emotional affectations. People are among the main actors of social and political frameworks; as such, risk perception is shaped according to social values and trust, personal values and interest as a function of economic and political structures, socio-economic status, organizational constraints and media influence. The cultural dimension is the most intriguing, and therefore views on the specificity of prototypes within the realm of cultural factors may differ dramatically. Nonetheless, personal identity and sense of meaning, world-views, cultural institutions and political, societal and economic nature, are among the key elements that may influence risk perception of societies (Renn and Rohrman 2000).

Risk perceptions consist of the explanations people build and shape to try to understand the dynamic of the complex interactions that give rise to the humanised landscape according to their experiences, beliefs, social and cultural frameworks, feelings and needs.

The most widely used perspective to quantify risk perception involves different indicators or

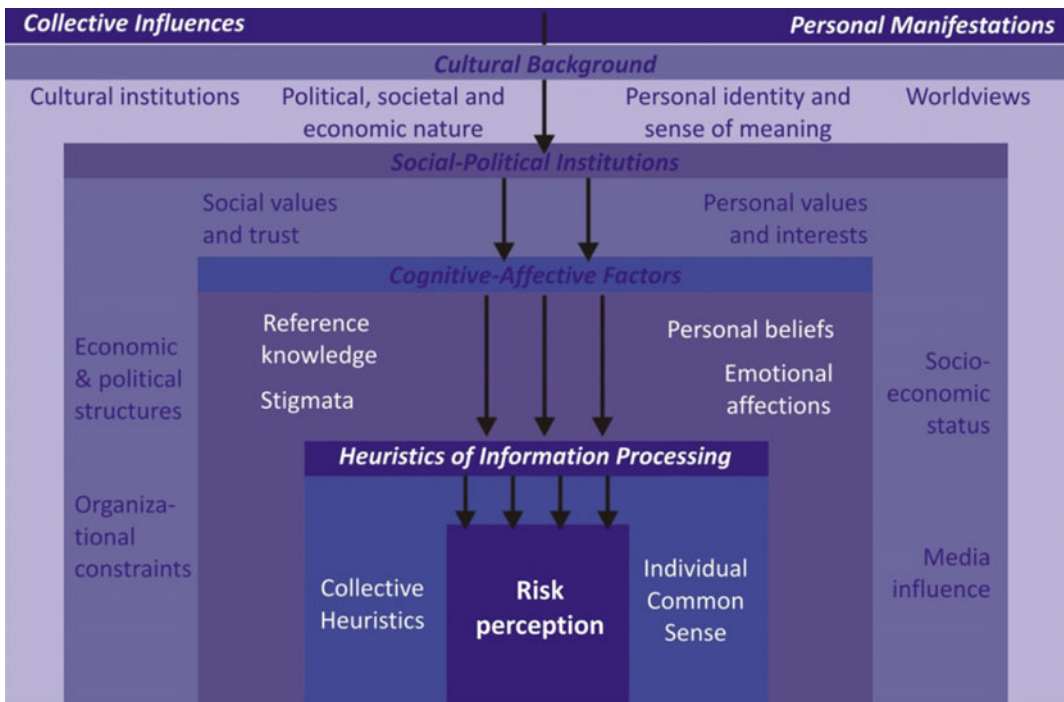


Fig. 3 Four context levels of risk perception. Source Renn and Rohrman (2000)

Table 1 Risk perception factors (Ropeik 2002)

Trust versus lack of trust	Trust in the information, strategies, actions, and responses provided or undertaken by the different stakeholders involved in risk management
Imposed versus voluntary	Exposure to risk by choice, by circumstances or imposition
Natural versus human-made	Balance between the worst scenarios of risk in terms of genesis
Catastrophic versus chronic	Spatial distribution of negative or adverse consequences of risks: concentrated or disperse
The dread factor	Worst outcome scenarios derived from specific risks
Hard to understand	Degree of difficulty to understand potential risks
Uncertainty	Lack of answers leads to greater fear
Familiar versus new	Degree of fear depending on previous experience of knowledge
Awareness	Availability of information and knowledge and updates regarding particular risks
A known victim	Acquaintance with facts and figures: specific victims
Future generations	Greater fear for the risks future generations are exposed to
Does it affect me?	Fear is greater when oneself is at risk
Risk versus benefit	Benefits overshadow risks
Control versus no control	The ability of regulating or influencing the consequences of specific risks decreases fear

socio-psychological scaling and survey techniques linked to the psychometric paradigm (Fischhoff et al. 1978; Slovic 1992; Rohrman 2003; Rohrman 2008). Special attention has been given for a long time to notions of patterns indicating that personal risk is commonly perceived as lower than the risk faced by other people (McKenna 1993; Sjöberg 2000), the existence of different perceptions when assessing risk by experts and lay people (Slovic et al. 1991) and based on diverse factors including age, gender, ethnicity, education, culture, experience, and others (Wildavsky and Douglas 1993; Flynn et al. 1994; Heine and Lehman 1995; Finucane et al. 2000; Renn and Rohrman 2000; Barnett and Breakwell 2001; Palmer et al. 2001; Silmak and Dietz 2006). The analysis of these elements and their potential association is integrated within frameworks specifically designed to evaluate risk perception towards different hazards.

4 Landslide Risk Perception

Landslides are the concrete evidence of lack of hillslope stability and can be considered as natural or socio-natural hazards. When hillslope instability is purely controlled by natural factors (geology, geomorphology) and physical processes, and people can be potentially affected by landslides, they become natural hazards. Contrastingly, they are socio-natural hazards when human activities modify the equilibrium of the slopes increasing the susceptibility to landsliding that can affect communities (Alcántara-Ayala 2016).

In addition to the natural factors linked to the properties of hillslope-forming materials and the dynamics of surface processes acting on the slopes, causes of instability are practically derived from modifications induced by human activities: development of infrastructure,

terracing, slope excavations, loading, and mining, disturbances generated by vibrations, water leaks, land-use changes, and deforestation. Many of them are direct consequence of urbanization processes and are among the most critical (Alcántara-Ayala et al. 2015).

The consequences of landslides are not only concentrated on human (casualties, wounded, people affected) and economic impacts (infrastructure, agriculture, farming, etc.), environmental degradation also can be of great significance, particularly in temperate and tropical regions.

According to Dilley et al. (2005), an area of circa 3.7 million km² of land is susceptible to sliding, and the corresponding population exposed is in the order of 300 million. What is more, approximately 66 million people live in regions of high landslide risk and occupy a land surface of 820,000 km².

Strategies and initiatives aimed at landslide disaster risk reduction and management are thus of utter importance and urgency. They should integrate, as mentioned earlier, active involvement of the exposed community and all key stakeholders.

The first stage for DRR hence needs to be directed towards a solid understanding of the perception of all actors—especially of the exposed community—regarding landslide disaster risk. Quite often that perception is shaped not only by technical or scientific knowledge. People's knowledge also can be associated with traditions or ethnicity values or beliefs, including myths, which are part of the cultural context of societies and are critical for perception and behaviour. For example, according to Msilimba and Holmes (2009) in a region located in the South of Malawi, a myth refers to a phenomenon of a sleeping snake, known by the locals as *Napolo*, which has been reported as being responsible for landslides (Chikusa 1985; Cheyo 1999; Msilimba 2002). There is a belief that when “the snake turns in its slumbers, landslides are caused by the disturbance” (Msilimba and Holmes 2009). In a similar fashion, also in Malawi, but in the North region, local inhabitants belief that spirits became angry because Vwira, a puff adder snake (*Bitis Arietans*) was killed by

someone in the Nyika National Park, resulting in the occurrence of landslides (Msilimba and Holmes 2009).

Although landslide risk perception studies are not as numerous as those related to other hazards such as earthquakes (Helweg-Larsen 1999; McClure et al. 2015), volcanic activity (Johnston et al. 1999; Bird and Gísladóttir 2012; Eiser et al. 2015), floods (Terpstra and Gutteling 2008; Bubeck et al. 2012) and tsunamis (Kurita et al. 2007), in recent years attention has been paid to the understanding of how people perceive risk to landsliding (Fig. 4). Such investigations have considered to a major extent, landslide information, hazard awareness and knowledge (Green 1992; Solana and Kilburn 2003; Ahmad and Lateh 2011; Kitutu et al. 2011; Salvati et al. 2014; Calvello et al. 2015; Moreno-Hernández and Alcántara-Ayala online); magnitude and frequency (Bjønness 1986); factors influencing perception including age, gender, education, race, culture and so forth (Bjønness 1986; Aucote et al. 2010; Kitutu et al. 2011; Damm et al. 2013; Calvello et al. 2015; Landeros-Mugica et al. 2016; Roder et al. 2016); and several aspects regarding disaster risk reduction and management (Gurung 1989; Green 1992; Finlay and Fell 1997; Wagner 2007; Ahmad and Lateh 2011; Damm et al. 2013; Misanya and Øyhus 2014; Landeros-Mugica et al. 2016).

By reviewing a series of published research papers, Wachinger and Renn (2010) identified four major groups of factors that may affect the perception of people of the risks from natural hazards, including landslides: (1) Risk factors; (2) Informational factors; (3) Personal factors; and (4) Context factors.

If these categories are applied to landsliding, investigations of landslide risk perception could be in general delineated as follows:

1. **Risk factors:** perceived likelihood of landslides; perceived or experienced (direct or indirect) frequency and magnitude of landslides.
2. **Informational factors:** source, level and clarity of landslide information, mass media



Fig. 4 Complexity of perception. The perception of a “slide area” can vary enormously according to context and individual perspective

coverage, involvement of different stakeholders, including experts in landslide risk assessment and management.

3. **Personal factors:** age, gender, educational level, profession, employment status, stakeholder membership, individual knowledge and landslide disaster experience, trust in different stakeholders—particularly trust in authorities at different levels, confidence in risk reduction measures, involvement in activities of disaster prevention and response, degree of control, spirituality.
4. **Context factors:** socio-economic factors, indicators of the different dimensions of vulnerability, homeownership, family status, time living in current residence, number of people living in the house, country, culture, area of living, traditions, size of community.

Risk perception questionnaires must be specific to the landslide context, not only in terms of the characteristics of the hazard, but based on the exposure conditions and vulnerability of different constituents of the communities at risk.

With no intention of covering all the aspects linked to landslide disaster risk, some of the main aspects that can be considered in carrying out landslide risk perception analysis are illustrated in Table 2, by using an example undertaken for Teziutlán, Puebla, Mexico, a town affected by a landslide disaster triggered by precipitation in October 1999. Here, on a single slope, more than 100 people died. Likewise, specific questions of the same undertaken survey have been included in Table 3 for further reference (Hernández-Moreno and Alcántara-Ayala 2016).

Table 2 Example of the questions and topics included in landslide risk perception in-depth interviews carried out in Mexico (Hernández-Moreno and Alcántara-Ayala 2016)

Landslide concept	<p>Have you ever heard of landslides, mudslides or debris-flows? Please tell me about landslides, slides, mudslides or debris-flows, i.e., tell me everything that comes to your mind. When the materials of a slope move down, they are called landslides, can you tell me about it?</p> <p>When a landslide (slide, mudslide or debris-flow) takes place, it may cause harm to the population living in the surrounding area. Have you heard about this? What can you tell me about this?</p>
Causes and landslide identification	<p>Why a slope falls down? What may be the role of any of the following factors?</p> <ul style="list-style-type: none"> • Natural factors: climate, vegetation, soil, rainfall • Anthropogenic causes: road construction, land-use changes, deforestation, mining <p>Why a landslide would take place in Teziutlán? Would it take place near your community? In your neighbourhood?</p> <p>What type of hillslopes “fall-down”? Why some hillslopes fall-down while others do not?</p> <p>How is the slope on which your house is built?</p>
Consequences	<p>What happens after a landslide take place?</p> <p>What type of damage can cause? In Teziutlán? In your community? To your home? To your family? To you?</p> <p>If a landslide takes place who would be affected most? What would happen in your community?</p> <p>From the type of damages you just mentioned, which one do you think would be the worst?</p> <p>Do you think that government authorities know what would it happen if a landslide take place in your community? How about the experts, researchers or scientists?</p> <p>Do you trust what the government knows about landslides and their consequences? Experts, researchers, scientists?</p>
Risk assessment	<p>Is it possible to know when a landslide would take place? How come? Which means would be used? Through a monitoring system? Observing changes in the terrain?</p> <p>What would be the best way to know if a landslide can take place?</p> <p>Under which circumstances a landslide can take place?</p> <p>Who can do the monitoring and observation? Who should do it? Who could be in charge of communicating this situation to you, to your family, to your neighbours?</p>
Risk management	<p>If a landslide is going to take place, what should it be done? When? By whom?</p> <p>What should be done during and after the landslide occurs?</p> <p>Do you think that the authorities can deal with the effects of landslides?</p>
Risk communication	<p>Have you heard about landslides (slides, mudslides, debris-flows)? Why a landslide can take place? From who have you heard it? Where?</p> <p>Have you heard, seen or read or know of something that has been made in terms of landslide mitigation (slides, mudslides, debris-flows)? Is something being done? Is something being planned? Where have you heard that? From who?</p> <p>Do you know if there is any program in your community to prevent or avoid landslides? What does it consist of? Who did/does/will do it? (Government, private sector, educational institution, international organization, NGOs, etc.)</p> <p>Do you trust the program(s) or plan(s) you mentioned?</p> <p>If you have not mentioned any,</p> <ul style="list-style-type: none"> • Who do you think should develop a program or a plan to prevent landslides? • Who should inform (give information) about programs or plans that exist or will be made to prevent the impact of landslides? <p>Who do you trust most?</p>
Landslide significance	<p>Do you get concern about the likely occurrence of landslides? Are landslides important risks for you? Your family? Your community?</p> <p>Are there any other important risks in your community? Are they more important than landslides?</p> <p>Have you are anybody you know been affected by landslides? What did you do? What happened afterwards?</p>

Table 3 Structure of a landslide risk perception questionnaire (Hernández-Moreno and Alcántara-Ayala 2016)

<p>Experience Previous experience with landslide disasters</p> <p>Q From the following sentences tell me please, what is the one that indicates best your experience with landslides?</p> <ul style="list-style-type: none"> • You have experienced landslides in this neighbourhood • You have experienced landslides in another neighbourhood • You have not personally experienced landslides, but a relative or close friend has • You have never suffered from the impact of landslides, neither a relative or a close friend • You have just heard, read or seen information related to landslides on the news 	
<p>Landslide risk awareness. Main causes of landslides</p> <p>Q. I'm going to read a series of situations that are on this card. What are the three that in your view are the main causes of landslides?</p>	
<ul style="list-style-type: none"> • Drought • The existence of a river close to slopes • Moderate rains for several days • Presence of loose or soft soil • Earthquakes • Heavy rains 	<ul style="list-style-type: none"> • Presence of drainage channels • Terracing • Negligence of the authorities • Tree removal • Houses built on slopes
<p>Exposure. Levels of landslide risk perception of exposure, based on location and nature of dwellings</p> <p>Q. Could you please indicate to me the degree of risk the following properties have to be affected by a landslide? Response options are: very low risk (VLR), low risk (LR) moderate risk (MR) and high risk (HR)</p>	
<ul style="list-style-type: none"> • Houses built on areas affected by landslides • Houses built at the top of a slope • Houses built at the foot of a slope • Houses built on the edge of a slope • Houses built very close to a river 	<ul style="list-style-type: none"> • Houses built by the government for relocation of affected settlements • Houses built of precarious materials • Houses built on the side of a road • Houses built by the government (social interest housing) • Houses built on reinforced slopes • Houses located in the City Centre
<p>Preparedness. Prioritising preventive measures to be undertaken to cope with landslide disaster events</p> <p>Q. From the following situations please let me know how necessary do you think they are for improving the safety of the inhabitants of Teziutlán</p>	
<ul style="list-style-type: none"> • Guaranteeing equality for the attention of affected people • Promoting programmes for community preparedness • Providing health programmes for people affected by disasters • Providing information on the best practices for protecting belongings during an emergency • Getting people involved in landslide risk communication programmes 	<ul style="list-style-type: none"> • Prohibiting the construction of dwellings in areas at risk • Implementing a warning system for communities at risk • Relocating people that live in areas at risk • Establishment of shelters • Promoting evacuation drills in areas at risk • Landslide instrumentation and monitoring
<p>Responsibility. Perceived accountability of actors in case of a landslide disaster</p> <p>Q. To what extent do you consider that it is responsibility of the following actors to take steps when a landslide is likely to occur, or when it already happened? Was it nothing responsible (NR), little responsible (LR), responsible (R), or very responsible (VR)</p>	
<ul style="list-style-type: none"> • Federal Government • State Government • Municipal Government • Civil Protection • Local Police • The Mexican Army 	<ul style="list-style-type: none"> • Health Institutions • The Red Cross • Lions Clubs International • The Community • Scientists

(continued)

Table 3 (continued)

<p>Response. Evaluation of the response of different actors after a landslide disaster</p> <p>Q. How was the response of these actors during or after a landslide? Was it bad (B), sufficient (S), good (G), or very good (VG)</p>	
<ul style="list-style-type: none"> • Federal Government • State Government • Municipal Government • Civil Protection • Local Police • The Mexican Army 	<ul style="list-style-type: none"> • Health Institutions • The Red Cross • Lions Clubs International • The Community
<p>Trust. Level of people’s confidence to be informed about disaster preparedness and response by different social actors</p> <p>Q. To get information on how to prevent or respond to a landslide, how much do you trust the following actors? No trust (NT), some trust (ST), regular trust (RT) always trust (AT)</p>	
<ul style="list-style-type: none"> • Federal Government • State Government • Municipal Government • Civil Protection • Local Police • People from other communities 	<ul style="list-style-type: none"> • Health Institutions • The Red Cross • The chieftain of the neighbourhood • Lions Clubs International • Scientists

5 Discussion

Looking at the perspective offered by the International Council for Science, it is stated that “The risk associated with environmental hazards depends not only on physical conditions and events but also on human actions, conditions (vulnerability factors, etc.), decisions and culture. The seriousness of the consequences of any disaster will depend also on how many people choose, or feel they have no choice but, to live and work in areas at higher risk” (ICSU 2008). It is thus clear that risk perception should play a cardinal role for disaster risk assessment, and consequently DRR and DRM.

One of the most striking examples of analysis of landslide risk perception is perhaps the case of Sarno in Southern Italy, a small town that, along with Bracigliano, Quindici, and Siano, was severely affected by rainfall-induced flow-like mass movement processes on 5–6 May 1998 involving 137 casualties out of the total regional death toll of 160 (Cascini 2004; in Calvello et al. 2015). After the disaster, structural and non-structural measures involving large financial support were undertaken. The former comprised actions directed towards the functionality of the

drainage channel network and structural control works, whereas the latter involved the establishment of a strategy for emergency management (Cascini 2004; Calvello et al. 2015). However, derived from interviews carried out in 2013 to inhabitants living inside and outside the “red zone”, that is to say the urbanised area exposed to residual risk after the 1998 landslides, it was clear that 15 years after the disaster, there is a lack of information on landslide risk. Moreover, and even though the perception of risk within the region is greater than that observed nationwide, more than 60% of interviewees did not perceive their households at risk, and circa 40% were not particularly engaged with their own risks (Calvello et al. 2015). This situation illustrates the complexity of risk perception and puts on the table the problem of delineating efficient strategies of permanent communication so that both the people at risk and all stakeholders involved properly comprehend the construction of disaster risk, and play a significant contributing role towards disaster risk reduction and management.

Landslide risk assessment should be directed towards the integration of knowledge concerning hazards, vulnerability and exposure. This has to be undertaken not only from the perspective

developed by the “experts”, but also by considering the perception of risk by all stakeholders involved in the construction, and potential reduction and mitigation of disaster risk.

Consequently, landslide disaster risk communication turns out to be a critical mode for understanding risk, and therefore, strategies must be built up according to the target population, as a function of the characteristics of the existing hazards, in this case landslides (i.e. typology, extent, magnitude, frequency, etc.), and according to the context in which the exposed community is embedded.

6 Conclusion

Investigations aiming at understanding how people perceive landslides are a major requirement for risk assessment, communication and management. Topics of wide interest to be examined by undertaking risk perception analysis include: (1) *landslide experience* (previous experience with landslide disasters, direct and/or indirect); (2) *landslide risk awareness and knowledge* (understanding of main causes of landslides and disaster risk); (3) *landslide exposure* (levels of landslide risk perception of exposure, based on location of dwellings and nature of properties); (4) *landslide preparedness* (acquaintance with preventive measures to be undertaken to confront and cope with landslide disaster events); (5) *Responsibility issues* (perceived accountability of actors in case of a landslide disaster); (6) *Disaster response* (evaluation of the response of different actors before and after a landslide disaster); (7) *Trust* (level of people’s confidence that they are being adequately informed about disaster risk, DRR and DRM by different stakeholders).

Landslide disaster risk policy making and practice should not be conceived without a proper understanding of the perception of risk by the exposed communities. As such, DRR should

be tailored as an open invitation to consider the multi-dimensions of the social construction of risk driven by the inclusion of the socio-environmental, individual and collective factors that can potentially affect behaviour and perceived risk.

Acknowledgements Special thanks are due to CONA-CyT for the financial support kindly provided through the research project 156242.

References

- Abelson RP (1979) Differences between belief and knowledge systems. *Cogn Sci* 3:355–366
- Adams J (1995) *Risk*. UCL Press, London
- Ahmad JH, Lateh HH (2011) Awareness on landslide issues in Malaysia: a review in Paya Terubong, Penang. *Asian J Environ Disaster Manag* 3(3):275–284
- Alcántara-Ayala I (2016) On the multi-dimensions of integrated research on landslide disaster risk. In: Aversa S, Cascini L, Picarelli L, Scavia C (eds) *Landslides and engineered slopes. Experience, theory and practice*. CRC Press/Balkema, Taylor & Francis Group, Leiden
- Alcántara-Ayala I, Altan O, Baker D, Briceño S, Cutter S, Gupta H, Holloway A, Ismail-Zadeh A, Jiménez-Díaz V, Johnston D, McBean G, Ogawa Y, Paton D, Porio E, Silbereisen R, Takeuchi K, Valsecchi G, Vogel C, Wu G, Zhai P (2015) Disaster risks research and assessment to promote risk reduction and management. In: Ismail-Zadeh A, Cutter S (eds) *ICSU-ISSC ad hoc group on disaster risk assessment*, Paris. http://www.icsu.org/science-for-policy/disaster-risk/documents/DRRsynthesisPaper_2015.pdf
- Aucote HM, Miner A, Dahlhaus P (2010) Rockfalls: predicting high-risk behaviours from beliefs. *Disaster Prev Manag* 19:20–31
- Barnett J, Breakwell GM (2001) Risk perception and experience: hazard personality profiles and individual differences. *Risk Anal* 21:171–178
- Bennis W, Katsikopoulos K, Goldstein D, Dieckmann A, Berg N (2012) Designed to fit minds: institutions and ecological rationality. In: Gigerenzer G, Todd PM (eds) *Ecological rationality: intelligence in the world*. Oxford University Press, New York, pp 409–427
- Bird DK, Gísladóttir G (2012) Residents’ attitudes and behaviour before and after the 2010 Eyjafjallajökull eruptions—a case study from southern Iceland. *Bull Volcanol* 74(6):1263–1279

- Bjønness IM (1986) Mountain hazard perception and risk-avoiding strategies among the Sherpas of Khumbu Himal, Nepal. *Mt Res Dev* 6(4):277–292
- Blaikie P, Cannon T, Davis I, Wisner B (1994) *At risk: natural hazards, people's vulnerability, and disasters*. Routledge, London
- Boulding K (1969) National images and international systems. In: Rosenau JN (ed) *International politics and foreign policy: a reading in research and theory*. Free Press, New York, pp 422–431
- Breakwell GM (2014) *The psychology of risk*. Cambridge University Press, Cambridge
- Bubeck P, Botzen WJW, Aerts JCIH (2012) A review of risk perceptions and other factors that influence flood mitigation behavior. *Risk Anal* 32:1481–1495
- Cascini L (2004) The flowslides of May 1998 in the Campania region, Italy: the scientific emergency management. *Riv Ital Geotec* 2:11–44
- Calvillo M, Nicolina-Papa M, Pratschke J, Nacchia-Crescenzo M (2015) Landslide risk perception: a case study in Southern Italy. *Landslides* 13 (2):349–360
- Cheyo DR (1999) Geohazards around the Michesi and Zomba areas. In: *Proceedings of the symposium on natural geological hazards in Southern Malawi, Zomba*, pp 30–42
- Chikusa CM (1985) The phenomenon of “Napolo” in Zomba with reference to the 1985 Ntonya–Ulumba Events, Zomba. Geological Survey Department, Zomba
- Damm A, Eberhard K, Sendzimir J, Patt A (2013) Perception of landslides risk and responsibility: a case study in eastern Styria, Austria. *Nat Hazards* 69:165–183
- Dilley M, Chen RS, Deichmann W, Lerner-Lam AL, Arnold M (2005) *Natural disaster hotspots: a global risk analysis*. The World Bank, Washington
- Eiser JR, Donovan A, Sparks SJ (2015) Risk perceptions and trust following the 2010 and 2011 Icelandic volcanic ash crises. *Risk Anal* 35:332–343
- Etkin D (2016) *Disaster Theory: An interdisciplinary approach to concepts and causes*. Butterworth-Heinemann, pp 386
- Finlay PJ, Fell R (1997) Landslides: risk perception and acceptance. *Can Geotech J* 34:169–188
- Finucane ML, Slovic P, Mertz CK, Flynn J, Satterfield TA (2000) Gender, race, perceived risk: the ‘white male’ effect. *Health Risk Soc* 2:159–172
- Fischhoff B, Slovic P, Lichtenstein S, Read S, Combs B (1978) How safe is safe: a psychometric study of attitudes towards technological risks and benefits. *Policy Sci* 9:127–152
- Flynn J, Slovic P, Mertz CK (1994) Gender, race, and perception of environmental health risks. *Risk Anal* 14 (6):1101–1109
- Gigerenzer G (2014) *Risk savvy: how to make good decisions*. Viking, New York
- Green JE (1992) Landslide awareness in Cincinnati, Ohio. *East Lakes Geogr* 27:30–37
- Gurung SM (1989) Human perception of mountain hazards in the Kakani-Kathmandu area: experiences from the middle mountains of Nepal. *Mt Res Dev* 9 (4):353–364
- Haimes Y (2004) *Risk modeling, assessment, and management*, 2nd revised edn. Wiley, London
- Heine SJ, Lehman DR (1995) Cultural variation in unrealistic optimism: does the west feel more invulnerable than the east? *J Pers Soc Psychol* 68:595–607
- Helweg-Larsen M (1999) (The lack of) optimistic biases in response on the Northridge earthquake: the role of personal experience. *Basic Appl Soc Psychol* 21:19–129
- Hernández-Moreno G, Alcántara-Ayala I (2016) Landslide risk perception in Mexico: a research gate into public awareness and knowledge. *Landslides*. doi:10.1007/s10346-016-0683-9
- Hillson D (2004) *Effective opportunity management for projects: exploiting positive risk*. Marcel Dekker, New York, p 316
- Holsti O (1962) The belief system and national images: a case study. *J Confl Resolut* 6(3):244–252
- ICSU (2008) *A science plan for integrated research on disaster risk: addressing the challenge of natural and human-induced environmental hazards*. ICSU, Paris
- Jasanoff S (1998) The political science of risk perception. *Reliab Eng Syst Saf* 59(1):91–99
- Jervis R (1976) *Perception and misperception in international politics*. Princeton University Press, Princeton
- Jervis R (2006) Understanding beliefs. *Polit Psychol* 27 (5):641–663
- Johnston DM, Bebbington M, Lai CD, Houghton BF, Paton D (1999) Volcanic hazard perceptions: comparative shifts in knowledge and risk. *Disaster Prev Manag* 8:118–126
- Kitutu MG, Muwanga A, Poesen J, Deckers AJ (2011) Farmers' perception on landslide occurrences in Bududa District, Eastern Uganda. *Afr J Agric Res* 6 (1):7–18
- Kurita T, Arakida M, Colombage SRN (2007) Regional characteristics of tsunami risk perception among the tsunami affected countries in the Indian Ocean. *J Nat Disaster Sci* 29(1):29–38
- Landeros-Mugica K, Urbina-Soria J, Alcántara-Ayala I (2016) The good, the bad and the ugly: on the interactions among experience, exposure and commitment with reference to landslide risk perception in México. *Nat Hazards* 80:1515–1537
- McClure J, Johnston D, Henrich L, Milfont T, Tarciano L, Becker J (2015) When a hazard occurs where it is not expected: risk judgments about different regions after

- the Christchurch earthquakes. *Nat Hazards* 75:635–652
- McKenna FP (1993) It won't happen to me: unrealistic optimism or illusion of control? *Br J Psychol* 84:39–50
- Misanya D, Øyhus AO (2014) How communities' perceptions of disasters influence disaster response: managing landslides on Mount Elgon, Uganda. *Disasters* 39:389–405
- Msilimba GG (2002) Landslides geohazard assessment of the Vunguvung/Banga Catchment Area in Rumph District. Unpublished M.Sc. dissertation, University of Malawi, Zomba
- Msilimba GG, Holmes PJ (2009) Landslides in northern and central Malawi; awareness, perceptions and coping strategies. *S Afr Geogr J* 91:38–45
- Oliver-Smith A, Alcántara-Ayala I, Burton I, Lavell A (2016) Forensic investigations of disasters (FORIN): a conceptual framework and guide to research (IRDR FORIN publication no. 2). Integrated research on disaster risk. ICSU, Beijing, p 56
- Palmer C, Carlstrom LK, Woodward JA (2001) Risk perception and ethnicity. *Risk Decis Policy* 6(3):187–206
- Pidgeon N, Hood C, Jones D, Turner B, Gibson R (1992) Risk perception. In: G. Royal Society Study (ed) *Risk: Analysis, Perception, and Management*. London, pp 89–134
- Renn O, Rohrmann B (2000) Cross-cultural risk perception research: state and challenges. In: Renn O, Rohrmann B (eds) *Cross-cultural risk perception. A survey of empirical studies*. Springer, Dordrecht, pp 211–233
- Renshon J (2008) Stability and change in belief systems: the operational code of George W. Bush. *J Confl Resolut* 52:820–849
- Roder G, Ruljigaljig T, Lin CW, Tarolli P (2016) Natural hazards knowledge and risk perception of Wujie indigenous community in Taiwan. *Nat Hazards* 81(1):641–662
- Rohrmann B (2003) Perception of risk—research overview. In: Gough J (ed) *Sharing the future—risk communication in practice*. CAE, University of Canterbury, Christchurch
- Rohrmann B (2008) Risk perception, risk attitude, risk communication, risk management: a conceptual appraisal (Keynote). In: The International Emergency Management Society (ed) *Global co-operation in emergency and disaster management - 15th TIEMS Conference booklet*
- Ropeik D (2002) Understanding factors of risk perception. *Nieman reports*. Winter 56(4):52. <http://niemanreports.org/articles/understanding-factors-of-risk-perception/>
- Rosa EA (1998) Metatheoretical foundations for post-normal risk. *J Risk Res* 1(1):15–44
- Rosa EA (2008) White, black, and gray: critical dialogue with the international risk governance council's framework for risk governance. *Glob Risk Gov*. Springer, Dordrecht, pp 101–118
- Salvati P, Bianchi C, Fiorucci F, Giostrella P, Marchesini I, Guzzetti F (2014) Perception of flood and landslide risk in Italy: a preliminary analysis. *Nat Hazards Earth Syst Sci* 14:2589–2603
- Shreve C, Fordham M, Anson S, Watson H, Hagen K, Wadhwa K, Begg C, Müller A, Kuhlicke C, Karanci N (2014) Report on risk perception and preparedness. The TACTIC project. https://www.tacticproject.eu/sites/default/files/images/resources-logo/Deliverable_DI.1_FINAL.pdf
- Silmak MW, Dietz T (2006) Personal values, beliefs and ecological risk perception. *Risk Anal* 26(6):1689–1705
- Sjöberg L (1996) A discussion of the limitations of the psychometric and cultural theory approaches to risk perception. *Radiat Prot Dosimetry* 68:219–225
- Sjöberg L (2000) Factors in risk perception. *Risk Anal* 20(1):1–11
- Slovic P, Flynn JH, Lyman M (1991) Perceived risk, trust and the politics of nuclear waste. *Science* 254(5038):1603–1607
- Slovic P (1992) Perception of risk: reflections on the psychometric paradigm. In: Golding D, Krinsky S (eds) *Theories of risk*. Praeger, London, pp 117–152
- Solana MC, Kilburn CRJ (2003) Public awareness of landslide hazards: the Barranco de Tirajana, Gran Canaria, Spain. *Geomorphology* 54:39–48
- Terpstra T, Gutteling JM (2008) Households' perceived responsibilities in flood risk management in the Netherlands. *Int J Water Resour Dev* 24(4):555–565
- UNISDR (2016) Working text on terminology. The second session of the open-ended inter-governmental expert working group on indicators and terminology relating to disaster risk reduction, Geneva, 10–11 Feb 2016
- Wachinger G, Renn OWG (2010) Risk perception and natural hazards. *CapHaz-Net WP3 report*, Stuttgart. <http://caphaz-net.org/outcomes-results>
- Wagner K (2007) Mental models of flash floods and landslides. *Risk Anal* 27:671–682
- Wildavsky A, Douglas M (1993) *Risk and culture: an essay on the selection of technological and environmental dangers*. University of California Press, Los Angeles

TXT-tool 4.886-1.1

Taiwan Typhoon Loss Assessment System (TLAS Taiwan) Web Tool

Hsin-Chi Li, Yi-Chen Chen and Mei-Chun Kuo

Abstract

The Taiwan Typhoon Loss Assessment System (TLAS Taiwan) can be used to quickly estimate flood or landslide losses and then present the results spatially. For the purpose of disaster reduction, it can be used to conduct cost-benefit analyses of regulation projects. For disaster mitigation, it can have a role in land-use planning. During phases of disaster response, it can assist governments to find potential areas with large losses and then to distribute disaster prevention equipment based on the results. Finally, for disaster recovery, it can help to formulate financial plans for different regions based on the disaster loss amounts.

Keywords

Typhoon · Flood · Slope land disaster · Loss assessment · Subaerial GIS

Contents

1 Introduction	569	3 TLAS Taiwan Operating Process	570
2 The Methodology of Loss Assessment	570	4 Case Analysis—A Debris Flow Disaster in Daniao Village	572
2.1 Land-Use Categories	570	4.1 Input Influence Area.....	572
2.2 Loss Estimate Method.....	570	4.2 Loss Calculated.....	572
		4.3 Loss Results.....	572
		References	574

H.-C. Li (✉) · Y.-C. Chen
Socio-Economic System Division, National Science and Technology Center for Disaster Reduction, New Taipei, Taiwan, ROC
e-mail: hsinchi@ncdr.nat.gov.tw

Y.-C. Chen
e-mail: ycchen@ncdr.nat.gov.tw

M.-C. Kuo
Information Division, National Science and Technology Center for Disaster Reduction, New Taipei, Taiwan, ROC
e-mail: bettyk@ncdr.nat.gov.tw

1 Introduction

The Taiwan Typhoon Loss Assessment System, also called TLAS Taiwan, utilizes different kinds of loss research and empirical survey data in Taiwan, mainly including land loss, household loss, agricultural loss, industry and commerce loss, building loss, and transportation and hydraulic losses. The system combines the

technology of geographic information systems, to build a calculating system. The purpose for this system is to quickly obtain monetized losses for a current event or estimates for a potential event.

The goal for establishing this automatic evaluating system is to estimate loss quickly after a disaster. If a numerical scheme can be used to simulate flood or landslide disasters with mitigation measures, this method can also be used to obtain the financial gain or loss from employing the mitigation measures. TLAS Taiwan can be used in any real engineering application, so that there will be a standard or reference loss value associated with future hazards.

2 The Methodology of Loss Assessment

2.1 Land-Use Categories

Base on past research, typhoon losses (due to flooding or landslides) include loss of human life and property loss. To facilitate the following computations, this study uses the land-use classification (as shown in Table 1) of Liu et al. (2009) which divides property losses into seven categories: Construction Use, Agricultural Use,

Forest Use, Tourism Use, Other Production Use, Transportation and Hydraulic Use, Other Use.

2.2 Loss Estimate Method

TLAS establish seven loss calculation models based on land law, land usage data, and the analysis report on Typhoon Morakot by the National Science Council (Li 2010). The seven models include influence population model, land loss, household loss model, agriculture loss model, industry and commerce loss model, public building model, transportation and hydraulic loss model (as show in Table 2).

3 TLAS Taiwan Operating Process

TLAS Taiwan can evaluate both flood and landslide disasters. Each includes a model of inferred population, model of land loss, model of household loss, model of agriculture, mode of industry and business, model of public building, model of transportation and hydraulic use. The following operating process uses a landslide disaster as an example. The calculation process can separated into three parts: (1) input data, (2) model calculated, and (3) output and display data, as shown in Fig. 1.

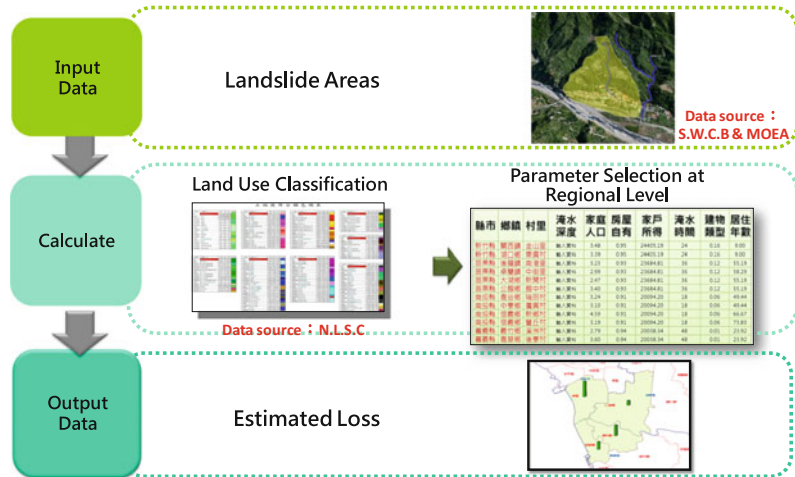
Table 1 The seven different types for of land utilization

Land class	The type of land use		Content
Type 1	Construction use		Such as houses, industry, commerce, etc.
Type 2	Agricultural use		Such as paddy fields, fruit orchards, etc.
Type 3	Forest use	Developed	Bamboo fields, logging areas, etc.
		Original	Such as broadleaf wood, coniferous wood, bush woods, wasteland, etc.
Type 4	Tourism use		Such as holiday villages
Type 5	Other production use		Such as industry use, commerce use etc.
Type 6	Transportation and hydraulic use		Such as roads, bridges, irrigation canals, dykes and weirs, watercourses, etc.
Type 7	Other use		Not included in the above-mentioned areas

Table 2 Loss formula for different types of loss

Types		Formula	Value for assessment
• Influence population		$INP = \sum_{i=1}^N PD_i \times IA_i$ <i>INP</i> : Influence population (people) <i>PD_i</i> : Population density (people/m ²) <i>IA_i</i> : Influence area (m ²)	Government’s population data
• Property loss			
Land loss		$LL = \sum_{i=1}^N LV_i \times LLA_i$ <i>LL</i> : Land loss (NT dollar) <i>LV</i> : Land value (NT dollar/m ²) <i>LLA</i> : Land value area (m ²)	Government’s bulletin
The loss on the ground	Household use (flood)	$Household\ loss = EXP[-0.421 + 1.875Ln(\text{flood depth}) - 1.06(\text{house possession}) + 0.736Ln(\text{household member}) + 0.637Ln(\text{flood duration}) - 0.834(\text{apartment/mansion}) - 0.028(\text{residential years}) + 1.159Ln(\text{income})]$	Household loss function (Li et al. 2008)
	Household use (slopedland)	$Household\ loss = EXP[9.36 + 0.736Ln(\text{landside coverage}) + 0.603Ln(\text{height of coverage}) + 0.21(\text{disaster experiecne}) + 0.092(\text{number of household people}) - 1.015(\text{house type}) - 0.231(\text{community preparedness}) + 0.451(\text{construction type})]$	Household loss function (Li and Yang 2011)
	Agriculture use	$CL = \sum_i \alpha_i [CPA_i \times CLA_i]$ <i>CL</i> : Crop loss per area (NT dollar/m ²) <i>CPA_i</i> : Crop price (NT dollar/m ²) <i>CLA_i</i> : Crop loss area (ha) α_i : Modify coefficient <i>i</i> : Different crop	Agriculture product price from government
	Industry and commerce use	$ICL = \sum_i \alpha_i [ICP_i \times ICLA_i]$ <i>ICL</i> : Industry and commerce loss (NT dollar) <i>ICP_i</i> : Industry and commerce price (NT dollar/m ²) <i>ICLA_i</i> : Industry and commerce loss area (m ²) α_i : Modify coefficient <i>i</i> : Different place (county)	Industry and commerce product price from government
	Building use (public)	$BL = \sum_{i=1}^N \sum_{j=1}^M \alpha_i [BC_{ij} \times BLA_{ij}]$ <i>BL</i> : Building loss (NT dollar) <i>BC_{ij}</i> : Building cost (NT dollar/m ²) <i>BLA_{ij}</i> : Building loss area (m ²) α_i : Modify coefficient <i>i</i> : Different place (county) <i>j</i> : Different building	Government’s bulletin (Liu et al. 2009)
	Transportation and hydraulic use	$THL = \sum_{i=1}^N \alpha_i [SUC_i \times SLN_i]$ <i>THL</i> : Traffic and hydraulic loss (NT dollar) <i>SUC</i> : Structure unit cost (NT dollar/m or NT dollar/m ²) <i>SLN</i> : Structure loss number (m or m ²)	Transportation and hydraulic loss function (Liu et al. 2009)

Fig. 1 TLAS TAIWAN calculation process



4 Case Analysis—A Debris Flow Disaster in Daniao Village

In 2009, Typhoon Morakot seriously affected Taiwan. Daniao Village, struck by a debris flow, suffered serious damage. The following section will assess the losses by choosing the real debris flow disaster of Daniao Village, using the calculation procedures of TLAS Taiwan.

4.1 Input Influence Area

According to aerial photographs taken after the disaster (see Fig. 2a) and field investigations following the disaster, we found that almost 17.2% (0.1485 km²) of the watershed was buried, the total volume of the debris flow exceeded 500,000 m³ and almost 200,000 m³ flowed out of the valley. Then, based on the data from field investigations and the results calculated by TLAS Taiwan, we can derive the influence area and the depth distribution on different land usages (show in Fig. 2b). This final debris flow

influence area including depth is typical input data for TLAS Taiwan.

4.2 Loss Calculated

Based on the input data we can calculate the losses using TLAS Taiwan; the operating interface is show in Fig. 3. Based on the analysis results, we have learnt that the total affected area is 94,964 m², of which the main land utilization type is forestry (49%); followed by farmland area (32%); construction land area (8%); transportation and hydraulic use and other production use (10 and 1% respectively).

4.3 Loss Results

According to calculation formulae in Table 2, the final direct losses are calculated as shown in Table 3. Based on the above, the total loss value caused by debris flow for Daniao Village is \$72,686,851 NTD. The greatest loss is for roads, followed by buildings, and cropland and forest

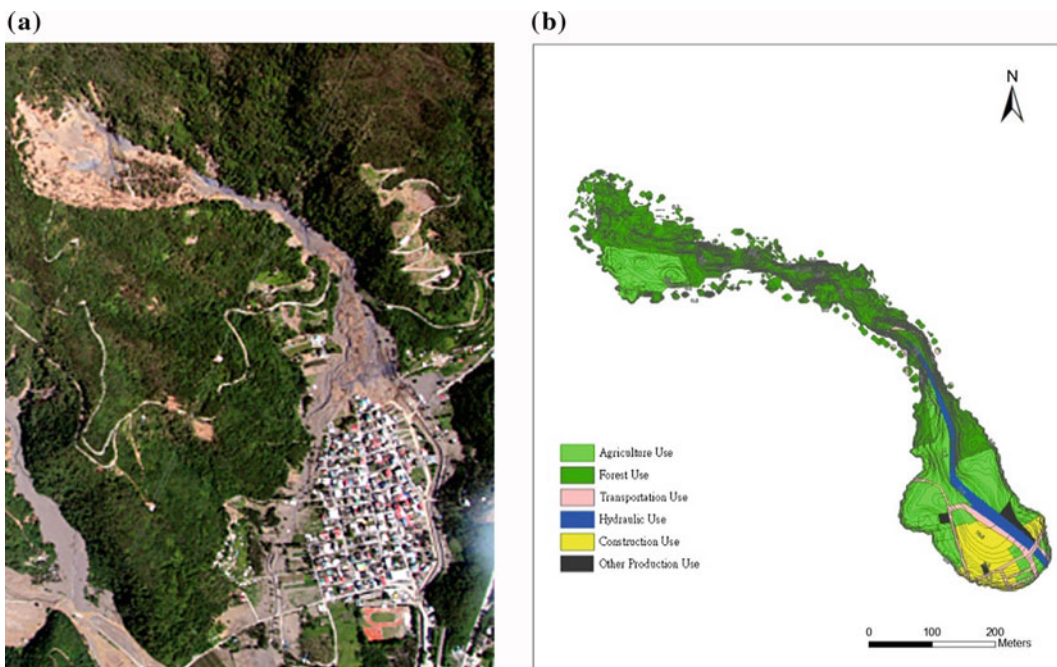


Fig. 2 a Aerial photograph taken after a debris flow disaster struck Daniao tribe. b The influence area and depth on different land usage

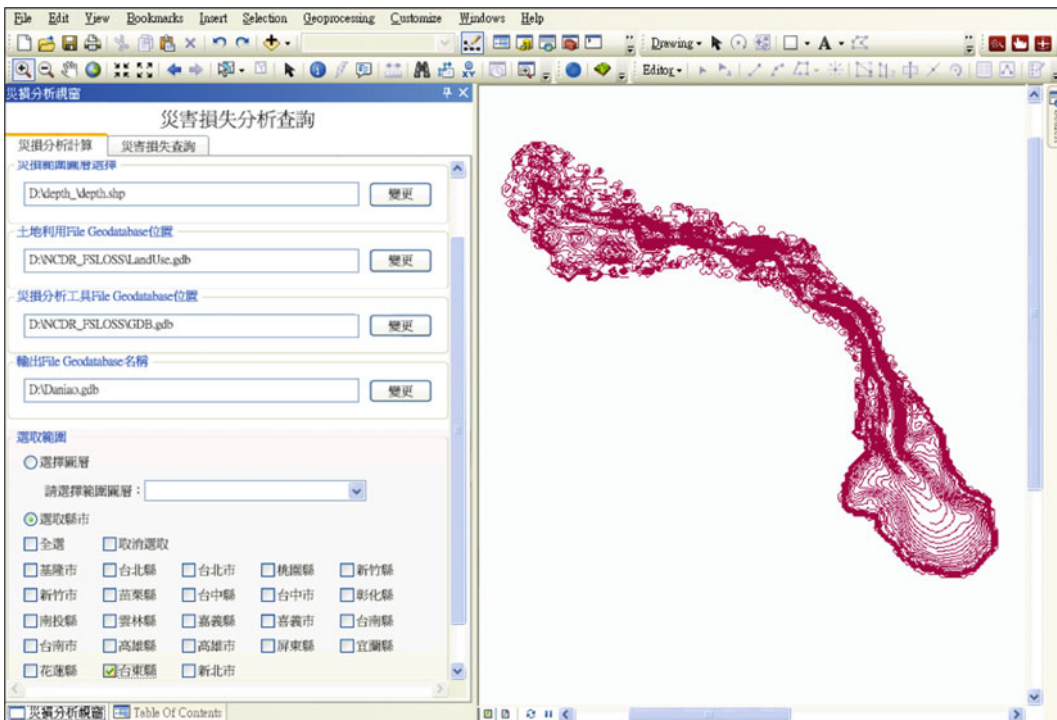


Fig. 3 TLAS calculation interface

Table 3 Calculation results for Daniao tribe losses

Loss types	Buildings	Agriculture	Forestry	Road	Hydraulic	Other	Subtotals
Loss amount	10,144,898	174,186	257,532	43,198,258	17,500,164	1,411,812	72,686,851

tree losses. This also agrees with the total financial aid to reconstruct this area in the next two years.

References

- Li HC, Kuo YL, Shaw D, Huang TH (2008) The household benefits assessment of the flood reduction plan in a flood-prone area: a case study of Sinwen, Chiayi, Taiwan. *Agric Resour Econ* 5(2):41–58
- Li H-C, Wu T, Wei H-P, Shih H-J, Chao Y-C (2017) Basinwide disaster loss assessments under extreme climate scenarios: a case study of the Kaoping River basin. *Nat Hazards* 86(3),1039–1058
- Li H-C, Yang H-H (2011) Modeling slopeland household loss and application. *J Chin Inst Eng* 23(4):437–444
- Li H-C, Chen Y-C, Guo M-J (2013) The development and application of Taiwan typhoon loss assessment system (TLAS). *J Taiwan Agric Eng* 59(4):42–55 (In Chinese)
- Liu K-F, Li H-C, Hsu Y-C (2009) Debris flow hazard assessment with numerical simulation. *Nat Hazards* 49 (1):137–161

TXT-tool 4.385-1.1

Method for Prediction of Landslide Movements Based on Random Forests

Martin Krkač, Drago Špoljarić, Sanja Bernat
and Snježana Mihalić Arbanas

Abstract

Prediction of landslide movements with practical application for landslide risk mitigation is a challenge for scientists. This study presents a methodology for prediction of landslide movements using random forests, a machine learning algorithm based on regression trees. The prediction method was established based on a time series consisting of 2 years of data on landslide movement, groundwater level and precipitation gathered from the Kostanjek landslide monitoring system and nearby meteorological stations in Zagreb (Croatia). Because of complex relations between precipitations and groundwater levels, the process of landslide movement prediction is divided into two separate models: (1) model for prediction of groundwater levels from precipitation data; and (2) model for prediction of landslide movements from groundwater level data. In a groundwater level prediction model, 75 parameters were used as predictors, calculated from precipitation and evapotranspiration data. In the landslide movement prediction model, 10 parameters calculated from groundwater level data were used as predictors. Model validation was performed through the prediction of groundwater levels and prediction of landslide movements for the periods from 10 to 90 days. The validation results show the

M. Krkač (✉) · S. Bernat · S.M. Arbanas
Faculty of Mining, Geology and Petroleum
Engineering, University of Zagreb, Pierottijeva 6,
10000 Zagreb, Croatia
e-mail: mkrkac@rgn.hr

S. Bernat
e-mail: sbernat@rgn.hr

S.M. Arbanas
e-mail: smihalic@rgn.hr

D. Špoljarić
PLIVA Croatia Ltd, Prilaz Baruna Filipovića 25,
10000 Zagreb, Croatia
e-mail: Drago.Spoljaric01@pliva.com

capability of the model to predict the evolution of daily displacements, from predicted variations of groundwater levels, for the period up to 30 days. Practical contributions of the developed method include the possibility of automated predictions, updated and improved on daily basis, which would be an important source of information for decisions related to crisis management in the case of risky landslide movements.

Keywords

Landslide · Movement prediction · Random forests
Monitoring · Groundwater level · Precipitation

Contents

1	Introduction	576
2	Study Area and Input Data	577
2.1	Kostanjek Landslide	577
2.2	Kostanjek Landslide Monitoring System.....	579
2.3	GNSS Monitoring Data.....	580
2.4	Groundwater Level Monitoring Data.....	580
2.5	Meteorological Data	581
3	Random Forests	582
4	Landslide Movements Prediction Method ...	583
4.1	Modeling of Groundwater Level Depth.....	583
5	Modeling of Landslide Velocity	590
6	Method Verification	591
7	Discussion	592
8	Conclusion	595
	References	596

1 Introduction

Prediction of landslide movements is important in the avoidance, or at least minimization, of adverse impacts on humans, property and the environment, especially when countermeasures are ineffective. Calvello et al. (2008) and Federico et al. (2012) differ physically based and phenomenological models for the prediction of landslide movements. A physically based approach attempts to predict landslide movements by considering soil/rock mechanical and/or hydraulic properties. Some examples of physically based numerical models are presented by Corominas et al. (2005), Van Asch et al. (2007) and Sassa et al. (2010). A phenomenological approach is an empirical approach, based on analyses of data series gathered by continuous

monitoring of landslide movement and eventually landslide trigger (e.g., rainfall) parameters. In a phenomenological approach, mechanical parameters of the soil/rock or boundary conditions within the slope are neglected (Federico et al. 2012), which makes it suitable for large and complex landslides in which physical parameters are not properly defined but monitoring data are available. Some examples of phenomenological models for landslide failure prediction, based on observations of landslide displacement versus time, are presented by Saito (1965), Fukuzono (1985) and Crosta and Agliardi (2003).

Landslide movements are in most cases initiated by a known landslide trigger (Wieczorek 1996), of which the most frequent is rainfall (e.g., Martelloni et al. 2011; Mansour et al. 2011). Rainfall causes multiple processes decreasing slope stability, such as positive pore pressure (e.g., Simoni et al. 2004; Matsuura et al. 2008; Hong and Wan 2011), loss of suction (e.g., Godt et al. 2009) or seepage forces (e.g., Ghassian and Ghareh 2008). The processes influencing relationship between rainfall and groundwater are various and, sometimes, extremely complex. For example, groundwater response can depend on rainfall intensity, evapotranspiration (e.g., Baird and Maddock 2005), surface runoff and slope morphology (e.g., Schilling 2009), groundwater level depth (e.g., Wu et al. 1996), thickness of unsaturated zone (e.g., Lee et al. 2006), or existence of preferred paths (e.g., Crosta and Di Prisco 1999).

Cascini et al. (2010) differ phenomenological and physically based approaches for prediction of pore water pressure and groundwater level. Unlike physically based models, phenomenological models for predicting pore water pressure do not require knowledge of hydraulic processes acting within the slope (Cascini et al. 2010). Examples of phenomenological groundwater level prediction were described by Hodgson (1978), who used multiple linear regression with rainfall and discharge data as predictors, or Yoon et al. (2011), who established models by artificial neural network and vector machine techniques based on groundwater level, precipitation and tide level data. Physically based models for prediction of pore water pressure are presented, for example, by Cascini et al. (2010).

The aim of this paper is to present a phenomenological method developed for prediction of movements of large and slow deep-seated landslides. Models that are part of the described method are established on the basis of 2-year (2013–2014) data series gathered by continuous monitoring of landslide movement, groundwater level (GWL) and precipitation. Landslide movement and GWL data were collected from the Kostanjek landslide in Zagreb (Croatia) and precipitation data from Zagreb-Grič meteorological station. The landslide movement prediction model was developed with random forests, a machine learning algorithm developed by Breiman (2001). This algorithm presents a tree-based technique, in which a large number of decision trees are grown in such a way that each tree depends on the values of a random vectors sampled independently and with the same distribution for all trees in the forest. Random forests have many interesting features, such as accurate prediction power (comparable to or even outperforming artificial neural networks and support vector machines), low tendency to overfitting, low computational cost and the ability to work with very high-dimensional data (Caruana and Niculescu-Mizil 2006; Micheletti et al. 2014). Major applications of random forests are found in medicine (e.g., Pauly 2012; Lebedev

et al. 2014), bioinformatics and genetics, environmental management (e.g., Prasad et al. 2006; Peters et al., 2007) and remote sensing (e.g., Pal 2005; Ham et al. 2005; Gislason et al. 2006). However, the random forests technique has been rarely used in landslide studies, and all applications are aimed at landslide susceptibility mapping (Brenning 2005; Stumpf and Kerle 2011; Vorpahl et al. 2012; Catani et al. 2013; Micheletti et al. 2014; Segoni et al. 2014; Goetz et al. 2015; Trigila et al. 2015; Youssef et al. 2015; Pourghasemi and Kerle 2016).

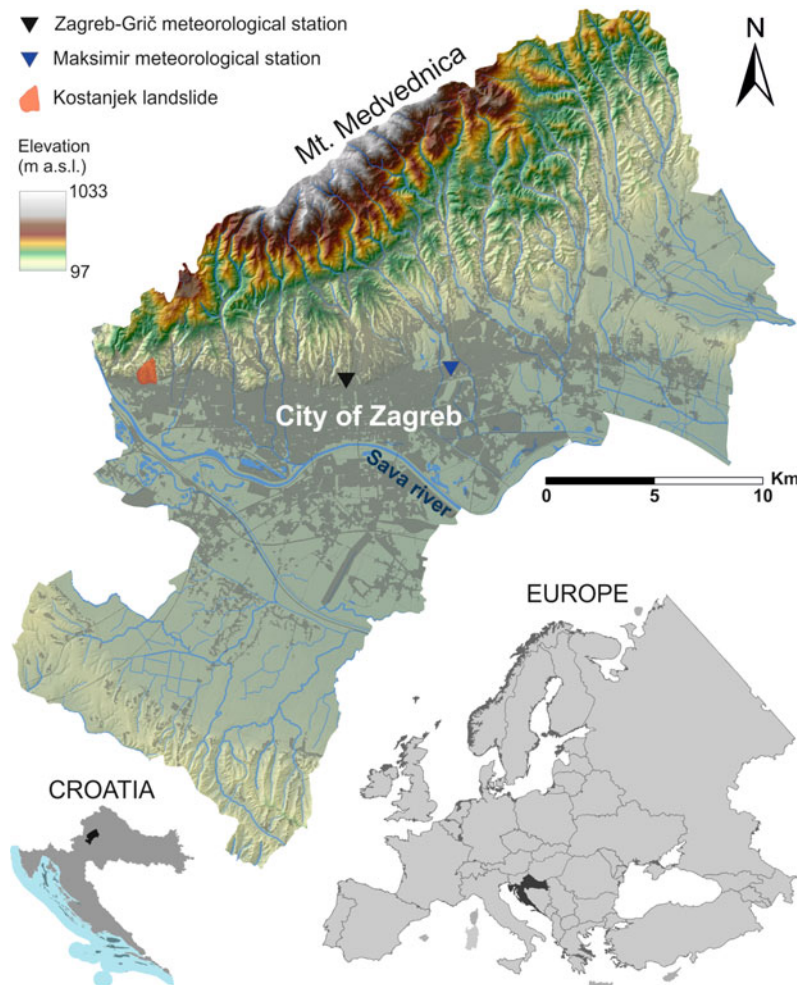
2 Study Area and Input Data

2.1 Kostanjek Landslide

The Kostanjek landslide is the largest landslide in the Republic of Croatia. It is a reactivated deep-seated translational landslide located in the urbanized area of the City of Zagreb at the base of the southwestern slopes of Medvednica Mt. (Fig. 1). The sliding surface is developed in Sarmatian laminated marl, characterized by alternation of very thin light and dark laminae known as varves (according to Weinheimer and Biondi 2003). Displaced mass above the Sarmatian sediments consist of Lower Pannonian clayey marls with thin limestone layers and Upper Pannonian massive clayey marls. The width of the displaced mass is 960 m, and the total length of the Kostanjek landslide is 1.26 km. The depth of the sliding surface is 90 m according to the landslide model interpreted by Ortolan and Pleško (1992). The total landslide area is approximately 1 km², and the volume of the sliding mass is evaluated to be 32×10^6 m³ (Stanić and Nonveiller 1996).

Since its activation in 1963, Kostanjek landslide has caused substantial damage to buildings and infrastructure in the residential and in industrial zones. The deep-seated landslide was caused by anthropogenic factors, mainly by excavations in a marl quarry placed in the toe part of the landslide (Fig. 2). Uncontrolled

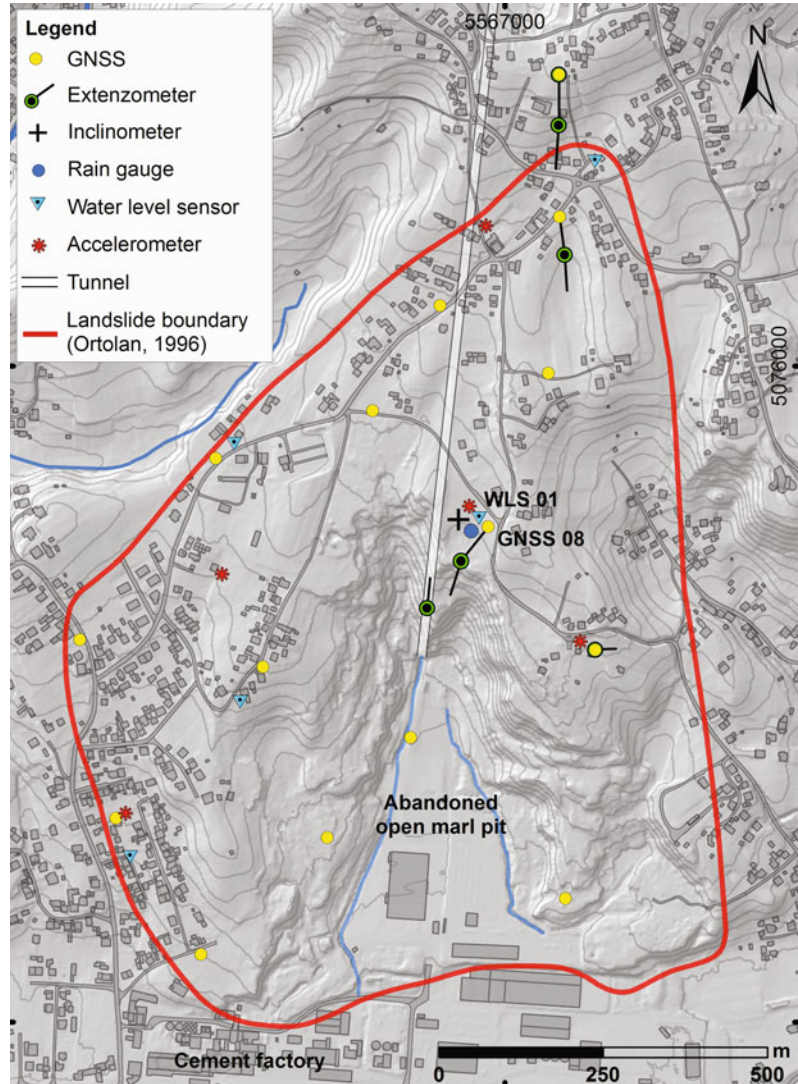
Fig. 1 Location of the Kostanjek landslide and the meteorological station Zagreb-Grič



blasting during the 1960s and 1970s in the marl quarry and the limestone quarry, placed approx. 1 km to the north from the upper part of the landslide, were also important destabilizing factors. Surface deformations are mostly expressed as ductile deformations (in the form of terrain lowering and bulging) with rare opening of cracks, even at the landslide boundaries (main scarp and landslide flanks). Despite extremely slow to slow landslide movements for 52 years, the risk in the area of the Kostanjek landslide is very high for residential properties (approx. 300 single-family houses and infrastructure networks are placed on the moving landslide mass).

The total displacement of the Kostanjek landslide is unknown because of poor temporal resolution of landslide movement observations and inconsistent measurements at stable geodetic points. Horizontal displacements of the ground surface in a range of 3–6 m were determined for the period 1963–1988 based on analysis of historical stereo-pairs of aerial photographs (Ortolan and Pleško 1992). Ortolan (1996) estimated that the maximal horizontal displacement of 44 cm/year occurred in the period 1973–1976.

Fig. 2 Locations of multiple sensor networks at the Kostanjek landslide



2.2 Kostanjek Landslide Monitoring System

The Kostanjek landslide monitoring system was established in the framework of the scientific Japanese-Croatian bilateral SATREPS FY2008 project ‘Risk Identification and Land-Use Planning for Disaster Mitigation of Landslides and Floods in Croatia’ with the main objective of landslide mitigation through the development of an early-warning system (Mihalić Arbanas et al. 2013). In the period 2011–2014, multiple sensor networks (Fig. 2) were setup for continuous

observations of (1) displacement/deformation/activity (Global Navigation Satellite System or GNSS stations, extensometers, borehole extensometers); (2) hydrological properties (pore pressure gauges and water level sensors in boreholes and domestic wells, water level sensors at outflow weirs); and (3) external triggers (rain gauge and accelerometers). The majority of monitoring equipment (GNSS station, water level sensor, accelerometers, rain gauge, inclinometer casing and extensometers) is installed at a central monitoring station, located in the central part of the Kostanjek landslide (Fig. 2). A more

detailed description of sensor networks was given by Krkač et al. (2014a, b).

Results of 2-year (2013–2014) monitoring at the central station, consisting of movement observations gathered by GNSS station (GNSS 08) and GWL depth observations gathered by water level sensor (WLS 01), together with precipitation data from Zagreb-Grič meteorological station, located 9 km east of Kostanjek (Fig. 1), were used for the establishment of the phenomenological model for the prediction of landslide movements.

2.3 GNSS Monitoring Data

The Kostanjek landslide GNSS monitoring network for continuous surface displacement measurement consists of 15 double-frequency NetR9 TI-2 GNSS reference stations with Zephyr Geodetic 2 GNSS antennas (Trimble). The 16th GNSS, reference station, is considered to be a stable GNSS and it is located approximately 7 km south of the landslide. GNSS receivers are fixed to 4 m high poles with 1 m deep reinforced foundations. Receivers collect raw GNSS data and deliver it in real-time (using routers) to Trimble 4D Control software (T4DC) installed on an application/data server in a data center. The precision of GNSS measurements, calculated as the root mean square error on the 24-h post-processing position (at 2σ , 95% confidence), was 3.2–4.6 mm in planimetry and 6.1–10.5 mm in altimetry. The highest precision was reached for GNSS 08 installed at the central monitoring station in the central part of the landslide.

In this study 7-day moving averages of 24-h post-processing data were used to reduce measurement errors. Analysis of monitoring data from all 15 permanent GNSS stations showed similar patterns of landslide movements across the entire landslide area, but with different velocities. Maximal velocities were recorded in the central part of the landslide (the area encompassing the central monitoring station, slope cuts of open marl pit and the area in their vicinity), and the lowest velocities were along the landslide boundaries. Highest precision of

measurement by GNSS 08 as well as its position inside landslide area with maximal velocities were main criteria to select GNSS 08 as the most representative for the movement analyses of the translational Kostanjek landslide.

The total temporal data coverage of GNSS 08 during 2013–2014 period was 99.9% because only one record is missing from 730 total records. The total measured surface displacement was 313 mm, the horizontal displacement was 307 mm, and the vertical displacement was –61 mm. The average annual velocity of the landslide during the monitoring period in the central part was 155.8 mm/year. Figure 3 displays the evolution of surface displacement of the GNSS 08 receiver. From Fig. 3, five periods of faster movements and five periods of slower movement can be distinguished. The patterns of faster movement are similar to patterns observed at the Utiku landslide (Massey et al. 2013) and can be considered as reactivations in which movement occurs along a fully developed sliding surface in which the material is assumed to be at residual strength (Skempton 1985). The maximal velocity observed with GNSS 08 was 3.3 mm/day, which was reached in the first period of faster movement during the first week of April 2013. The longest period of faster movement lasted from the end of January 2013 to the end of May 2013, during which the total horizontal displacement was 127.4 mm. All five periods of faster movement occurred as a consequence of rising groundwater level (Fig. 3). Periods of slower movement can be described as a periods of rest or suspended state of activity according to Cruden and Varnes (1996). During periods of slower movement, the landslide velocities measured by GNSS 08 were up to 3 mm/month (0.1 mm/day).

2.4 Groundwater Level Monitoring Data

GWL monitoring data observed at the five locations within the landslide (Fig. 2) showed similar patterns of GWL change and hydraulic connectivity throughout the landslide area. The data

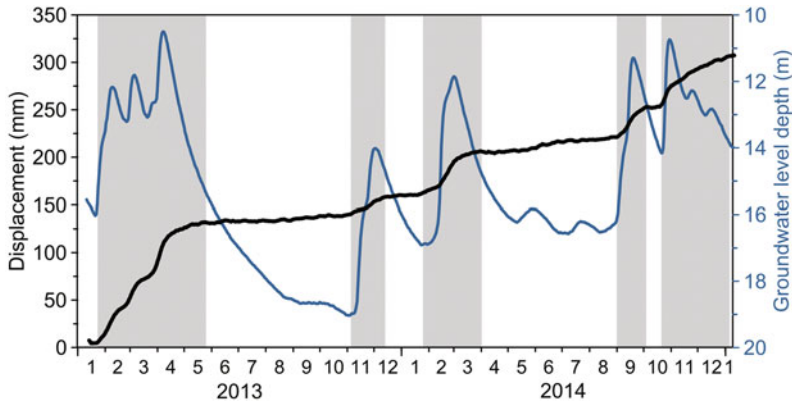


Fig. 3 Cumulative horizontal displacements and groundwater level depths measured at the central monitoring station of the Kostanjek landslide. The *gray area* depicts periods of faster movements

records from water level sensor WLS 01, installed at the central monitoring station, shows the strongest relation to the GNSS 08 data (Fig. 3). Therefore, WLS 01 sensor data as the most representative for the Kostanjek landslide behavior, in combination with GNSS 08 data, was used for landslide prediction. Data measured with other water level sensors, which are located near the landslide boundaries, generally shows higher GWL, smaller relative change between maximal and minimal GWL and greater susceptibility to short term precipitations. The data obtained from WLS 01 correspond to depths of the water table measured between the top of the borehole at the ground surface and 35 m of depth, below which the borehole is sealed. In this study, daily groundwater level data are used, calculated as 24-h average data. Figures 3 and 4a show GWL depths during the 2-year period. The minimal observed GWL depth was 10.5 m, and the maximal GWL depth was 19.03 m.

Through the monitoring period, groundwater level rise in the central part of landslide occurred during a total of 111 days, whereas groundwater level recession or stagnation occurred in 619 days. Altogether, 11 periods of groundwater level rise occurred, during which groundwater level relatively changed from 0.19 to 5.04 m. The maximal observed groundwater level rise rate was 0.87 m/day (Fig. 4a), whereas the average rate of groundwater level rise was 0.14 m/day. The maximal observed groundwater

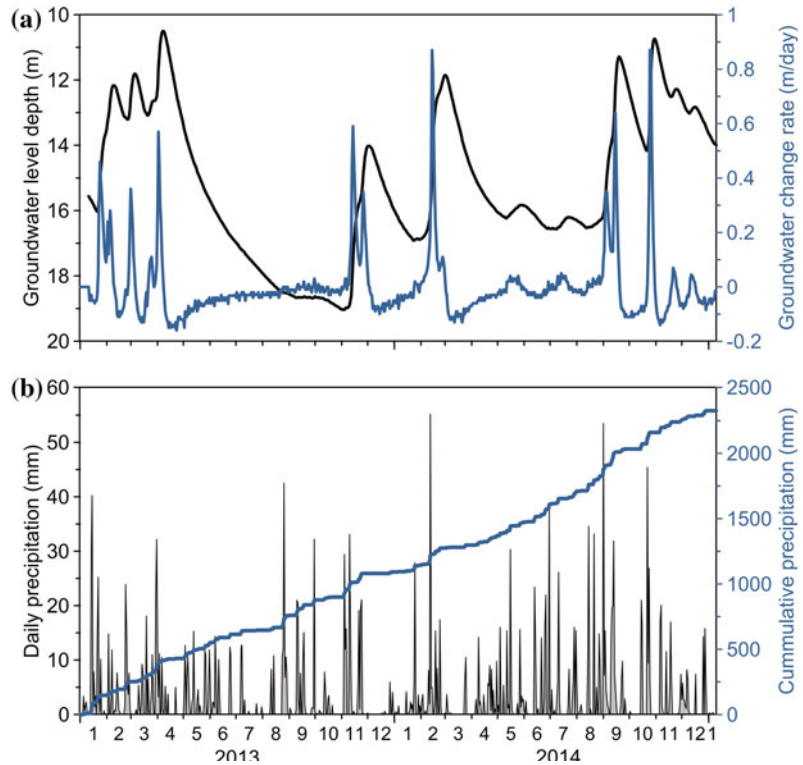
level recession rate was 0.16 m/day (Fig. 4a), whereas the average groundwater level recession rate was 0.05 m/day.

Nine of the 11 periods of groundwater level rise correspond to five periods of faster displacement (Fig. 3). The remaining two periods occurred in May and July 2014, during which the groundwater level rose 0.37 and 0.40 m from initial groundwater level depths of 16.2 and 16.6 m, respectively. Generally, it can be concluded that greater movement velocities at the Kostanjek landslide occur during the groundwater level rise periods that start at high initial groundwater levels. Additionally, lower values of landslide velocities were recorded for the same value of groundwater level during the groundwater level recession. All groundwater level rising periods occurred after periods of intensive precipitations and snowmelt.

2.5 Meteorological Data

The climate of the City of Zagreb is continental under a mild maritime influence (Gajić-Čapka and Zaninović 2008), characterized by warm summers and cold winters. The average annual precipitation measured at the Zagreb-Grič meteorological station is 887 mm for the period 1862–2012. The maximal daily precipitations and the highest monthly precipitations (Gajić-Čapka and Zaninović 2008) occur during the

Fig. 4 Cumulative horizontal displacements and groundwater level depths measured at the central monitoring station of the Kostanjek landslide. The gray area depicts periods of faster movements



summer and autumn months. The average number of days per month with precipitation is highest (an average of 12–14 days) from April to June and lowest (9–12 days) in September and October (Gajić-Čapka and Zaninović 2008).

Daily and cumulative precipitations measured at the Zagreb-Grič meteorological station for the period 2013–2014 are displayed in Fig. 4b. Generally, meteorological conditions during the monitoring period can be considered as very wet. In 2013, the total precipitation (rainfall and snow) was 1092 mm, and in 2014, it was 1234 mm. The highest daily precipitation (55.2 mm) in the two analyzed years was recorded in February 2013. The maximal monthly precipitation (208 mm) was recorded in September 2014.

The cumulative precipitations that caused GWL rise at the Kostanjek landslide ranged from 21 to 180 mm. The amount of GWL change at Kostanjek landslide depends on precipitation amount and initial groundwater level. For example, at the initial GWL depth of 18.5 m, a 91 mm precipitation during 6 days in August

2013 did not cause a groundwater level rise (causing only a slowing of the recession rate and few days of groundwater level stagnation). In contrast, at the initial GWL depth of 12.5 m, 21 mm of precipitation during 7 days in November 2014 caused a groundwater rise of 0.23 m (approximately 25 days after intensive precipitation of 125.5 mm). This phenomenon is related to the soil moisture above the groundwater level. Low groundwater level indirectly implies low soil moisture caused by long periods without significant precipitation, and vice versa.

3 Random Forests

Random forests is based on a standard machine learning technique called a *regression tree*, which is simple and useful for interpretation but typically is not competitive in terms of prediction and accuracy (James et al. 2014). The process of building a regression tree first divides the predictor space into M distinct and non-overlapping regions

R_1, \dots, R_J , and then for every observation that belongs to region R_j , the response variable is predicted by means of the response values for the testing observations in R_j (James et al. 2014). The regions R_1, \dots, R_J are divided in a way to minimize the root of sum of squares (RSS) given by:

$$\sum_{j=1}^J \sum_{i \in R_j} (y_i - \hat{y}_{R_j})^2, \quad (1)$$

where \hat{y}_{R_j} is the mean response for the training observations within the j th region.

Computationally, it is very demanding to consider every possible partition of the predictor space into J regions. For this reason, a *greedy* approach, known as *recursive binary splitting*, is used. The approach is *top-down* because it begins at the top of the tree (all observations belong to a single region) and then successively splits the predictor space of the tree (each split is indicated via two new *branches*). At each step of the tree-building process, the best split is made at that particular step (maximally reducing RSS) rather than looking ahead and picking a split that will lead to a better tree in some future step (James et al. 2014). A tree obtained in this way will probably have high variance, i.e. poor prediction capacity. For example, if the training dataset is randomly split into two and regression tree analysis is applied to both sets, the resulting trees can be very different. High variability of regression trees can be solved partly by the *bagging* procedure.

Bagging is a general-purpose procedure for reducing the variance of a statistical learning method (James et al. 2014). The procedure is to take many training sets from the population, build separate prediction models (regression trees) using each training set, and average the resulting predictions:

$$\hat{y}_{bag} = \frac{1}{B} \sum_{i=1}^B \hat{y}_i. \quad (2)$$

where $\hat{y}_1, \dots, \hat{y}_B$ are the predictions of B regression trees, and \hat{y}_{bag} is the final (average)

prediction result. Bagging can improve accuracy by combining hundreds or thousands of trees into a single procedure (James et al. 2014).

One problem related to bagging is found in the case when there is one very strong predictor in the dataset. In such a case, most or all trees will use this strong predictor in the top split. Consequently, the bagged trees will look similar, and averaging their highly correlated quantities will lead to a smaller reduction in variance than when averaging many uncorrelated quantities. The random forests model used in this study overcomes this problem. Each time when a split in a tree is considered, a random sample of m predictors is chosen from the full set of p predictors (James et al. 2014). In this way, on average, $(p - m)/p$ of the splits will not consider the strong predictor, so other predictors will have more influence on the result. Typically, the chosen m is equal to \sqrt{p} .

In contrast to regression trees, which can be easily interpreted, a collection of bagged trees and random forests is much more difficult to interpret. Some information about the importance of each predictor can be obtained by using the sum of squared residuals (SSR). The predictor is more important if the total amount of SSR, decreased owing to splits over a given predictor and averaged over all trees, is larger (for more details, see James et al. 2014).

4 Landslide Movements Prediction Method

4.1 Modeling of Groundwater Level Depth

The premise of landslide prediction in this study is that landslide movement depends on GWL depth and that GWL depth depends on precipitation. Because of the complex relationships described in previous sections, it is first necessary to predict GWL depth from the precipitation data and then separately predict landslide velocity from predicted GWL depth. The landslide movement prediction method based on the

random forests was developed using the R statistical environment version 3.1.2 (Venables and Smith 2014). The complete process of development of the landslide movement prediction method is presented in a flowchart (Fig. 5).

The prediction of GWL depth at the central part of the landslide was made using a series of variables defined and calculated from two types of monitoring data: (1) daily precipitation data measured at the Zagreb-Grič meteorological station; and (2) monthly evapotranspiration data measured at the Maksimir meteorological station. In total, 75 variables were used as predictors, belonging into six main data groups: (1) antecedent precipitation; (2) effective precipitation; (3) precipitation events; (4) modified precipitation; (5) different time periods past since a certain precipitation event; and (6) climatological indexes.

Antecedent precipitation (Table 1) presents precipitation that fell in a certain number of days preceding a period of prediction. In this study, antecedent precipitation from 1 to 100 days was analyzed. Effective precipitation (Table 2) in this paper presents antecedent (1–100 days) precipitation minus the quantity of evapotranspiration for the same antecedent period. Owing to lack of more precise measurements, daily evapotranspiration was calculated from the average monthly evapotranspiration by dividing it by the number of days in a month. Monthly evapotranspiration is measured at the Maksimir meteorological station (Gajić-Čapka and Zaninović 2008), located 14 km east of Kostanjek landslide (Fig. 1). Effective precipitation can be negative (e.g., for long dry periods) because the daily evapotranspiration amounts were subtracted from the daily precipitation for each day of the antecedent period. Precipitation event (Table 3) presents cumulative precipitation in the period limited by a particular minimum number of days without precipitation. In this study, the number of days that were used to define rainfall events ranged from one to five. The modified precipitation (Table 4) data were used to emphasize the dry and wet periods. Modified precipitation presents antecedent precipitation (1–30 days) multiplied by monthly or 3-month indexes. The monthly

index presents ratio of monthly (or 3 month) precipitation and average monthly (or 3 month) precipitation calculated for the period 1862–2012. Time periods (Table 5) since a certain precipitation event are given by number of days passed since a 30, 40 and 50 mm precipitation, falling during the 1, 2 and 3 days. Longer periods since significant precipitation indicate lower groundwater levels or lower soil moisture above the groundwater level. Another variable indicating wet or dry periods is climatological season, indexed with numbers 1 (autumn), 2 (winter), 3 (spring) and 4 (summer). According to historical data, lower climatological indexes specify wet seasons, and higher indexes indicate dryer seasons.

First, a prediction capability and variable importance of the two models (using 75 GWL depth predictors) was evaluated: (1) a model for direct prediction of GWL depth; and (2) model for indirect prediction of GWL depth from predicted GWL change rate. Both models were evaluated for whole datasets (730 days) with the same following random forest parameter values in R software: (1) number of random predictors in tree building (*mtry* parameter) of 15; and (2) number of generated trees in each analysis (*ntree* parameter) of 1000.

The result of modeling the GWL depth is presented in Fig. 6a. The coefficient of correlation between the modeled and observed results is 0.998, and the maximal difference between the modeled and observed data is 0.64 m (in November 2013). The most important 20 predictors are presented in Fig. 7a. The importance of a certain predictor is depicted with parameter *%IncMSE*, which presents the average increase of mean squared error (MSE) if a certain predictor is excluded from model building. The most important predictors are 50 and 100 days effective precipitations and the number of days since 40 or 50 mm precipitations during 1- and 3-day periods.

The result of GWL change rate modeling is presented in Fig. 6b. The coefficient of correlation between the modeled and observed data is 0.989, and the maximal difference between the modeled and observed data is 0.17 m/day (in

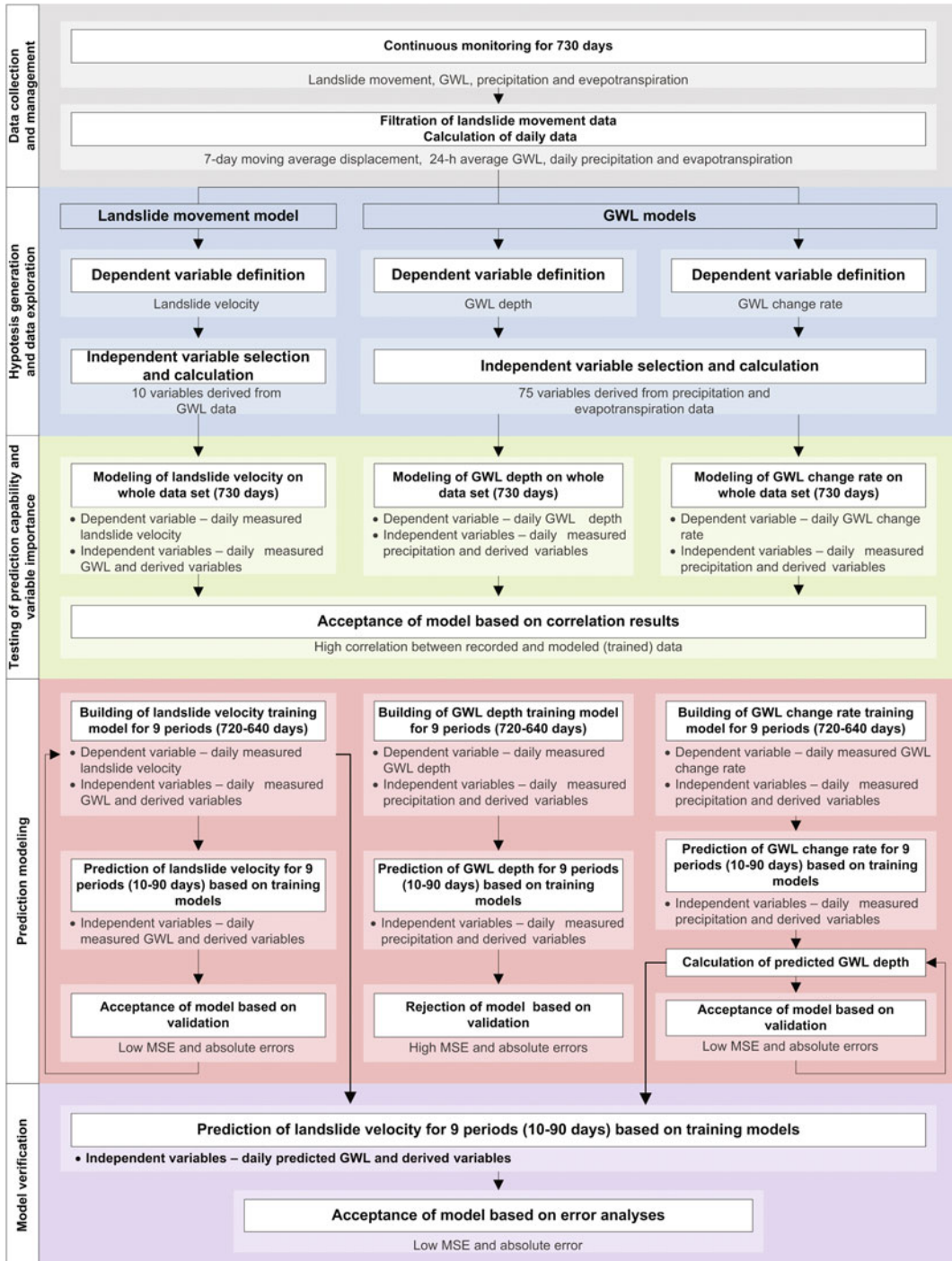


Fig. 5 Flowchart of developed methodology for prediction of landslide movement

Table 1 Antecedent precipitation used in the prediction of groundwater level depth/change rate

Label	Description
1 AP	Daily precipitation
2 AP	2-day antecedent precipitation
3 AP	3-day antecedent precipitation
4 AP	4-day antecedent precipitation
5 AP	5-day antecedent precipitation
6 AP	6-day antecedent precipitation
7 AP	7-day antecedent precipitation
8 AP	8-day antecedent precipitation
9 AP	9-day antecedent precipitation
10 AP	10-day antecedent precipitation
15 AP	15-day antecedent precipitation
20 AP	20-day antecedent precipitation
30 AP	30-day antecedent precipitation
50 AP	50-day antecedent precipitation
100 AP	100-day antecedent precipitation

Table 2 Effective precipitation used in the prediction of groundwater level depth/change rate

Label	Description
1 EP	1 AP reduced for 1-day evapotranspiration
2 EP	2 AP reduced for 2-day evapotranspiration
3 EP	3 AP reduced for 3-day evapotranspiration
4 EP	4 AP reduced for 4-day evapotranspiration
5 EP	5 AP reduced for 5-day evapotranspiration
6 EP	6 AP reduced for 6-day evapotranspiration
7 EP	7 AP reduced for 7-day evapotranspiration
8 EP	8 AP reduced for 8-day evapotranspiration
9 EP	9 AP reduced for 9-day evapotranspiration
10 EP	10 AP reduced for 10-day evapotranspiration
15 EP	15 AP reduced for 15-day evapotranspiration
20 EP	20 AP reduced for 20-day evapotranspiration
30 EP	30 AP reduced for 30-day evapotranspiration
50 EP	50 AP reduced for 50-day evapotranspiration
100 EP	100 AP reduced for 100-day evapotranspiration

Table 3 Precipitation events used in the prediction of groundwater level depth/change rate

Label	Description
1 PE	Cumulative precipitation in the period limited by minimum of one day without precipitation
2 PE	Cumulative precipitation in the period limited by minimum of two days without precipitation
3 PE	Cumulative precipitation in the period limited by minimum of three days without precipitation
4 PE	Cumulative precipitation in the period limited by minimum of four days without precipitation
5 PE	Cumulative precipitation in the period limited by minimum of five days without precipitation

Table 4 Modified precipitation used in the prediction of groundwater level depth/change rate

Label	Description
1 AP*M	1 AP multiplied by 1-month index
2 AP*M	2 AP multiplied by 1-month index
3 AP*M	3 AP multiplied by 1-month index
4 AP*M	4 AP multiplied by 1-month index
5 AP*M	5 AP multiplied by 1-month index
10 AP*M	10 AP multiplied by 1-month index
15 AP*M	15 AP multiplied by 1-month index
20 AP*M	20 AP multiplied by 1-month index
30 AP*M	30 AP multiplied by 1-month index
1 AP*3 M	1 AP multiplied by 3-month index
2 AP*3 M	2 AP multiplied by 3-month index
3 AP*3 M	3 AP multiplied by 3-month index
4 AP*3 M	4 AP multiplied by 3-month index
5 AP*3 M	5 AP multiplied by 3-month index
10 AP*3 M	10 AP multiplied by 3-month index
15 AP*3 M	15 AP multiplied by 3-month index
20 AP*3 M	20 AP multiplied by 3-month index
30 AP*3 M	30 AP multiplied by 3-month index
1 AP*3 M_Av	7-day moving average of 1 AP*3 M
2 AP*3 M_Av	7-day moving average of 2 AP*3 M
3 AP*3 M_Av	7-day moving average of 3 AP*3 M
4 AP*3 M_Av	7-day moving average of 4 AP*3 M
5 AP*3 M_Av	7-day moving average of 5 AP*3 M
10 AP*3 M_Av	7-day moving average of 10 AP*3 M
15 AP*3 M_Av	7-day moving average of 15 AP*3 M
20 AP*3 M_Av	7-day moving average of 20 AP*3 M
30 AP*3 M_Av	7-day moving average of 30 AP*3 M

February 2014). Generally, modeled groundwater level change rates are slightly lower than the observed values. The most important predictors (Fig. 7b) are 50 and 100 days effective precipitations, number of days since 50 mm precipitations during 1- and 3-day periods and 10 days antecedent precipitation multiplied by 1 month index.

The conclusion after the step of modeling with the whole dataset of 730 days was that the random forests method has a potential to predict GWL depth from selected 75 variables. The next step were direct and indirect (through GWL change rate) predictions of GWL depth for periods from 10 to 90 days. For each prediction,

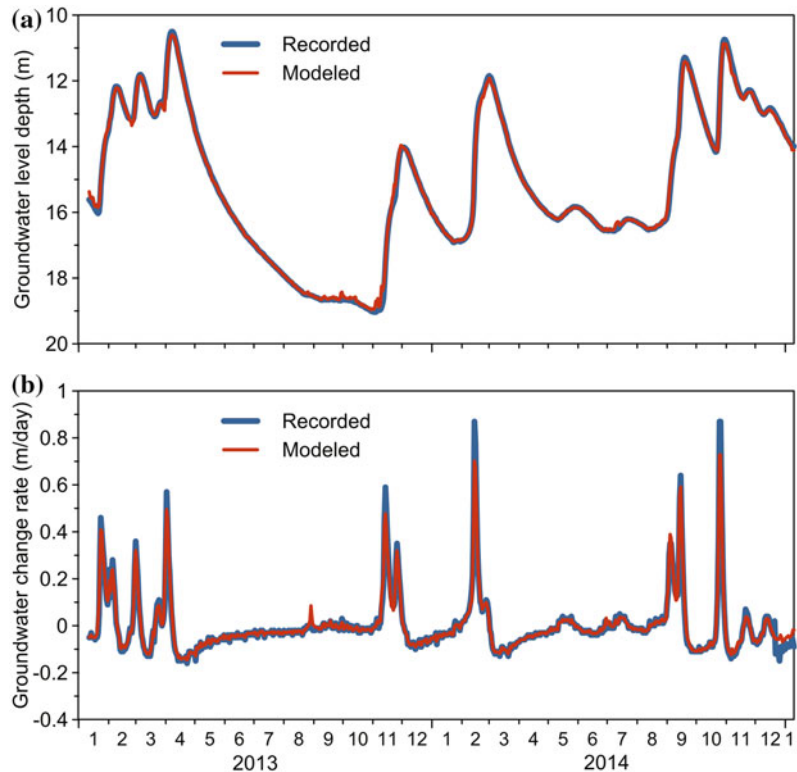
the models were trained on datasets containing 640 to 720 of 730 total daily data. The results of the predictions are presented in Fig. 8, and the mean squared error of predictions is presented in Fig. 9. In indirect prediction, GWL depth was calculated as a cumulative value of predicted GWL daily changes added to the last value of GWL depth from the training period.

The predictions of GWL change rate (indirect prediction of GWL depth) yielded significantly better results than the direct predictions of GWL depth (Figs. 8 and 9). Poor results of direct prediction of GWL depth may indicate that the model, built on a whole dataset (Fig. 6a), is overtrained. Nevertheless, there are other

Table 5 Different time periods past since a certain precipitation event and climatological indexes used in the prediction of groundwater level depth/change rate

Label	Description
1 D_20	Number of days since the last daily precipitation higher than 20 mm
1 D_30	Number of days since the last daily precipitation higher than 30 mm
1 D_40	Number of days since the last daily precipitation higher than 40 mm
1 D_50	Number of days since the last daily precipitation higher than 50 mm
3 D_20	Number of days since the last 3-day precipitation higher than 20 mm
3 D_30	Number of days since the last 3-day precipitation higher than 30 mm
3 D_40	Number of days since the last 3-day precipitation higher than 40 mm
3 D_50	Number of days since the last 3-day precipitation higher than 50 mm
5 D_20	Number of days since the last 5-day precipitation higher than 20 mm
5 D_30	Number of days since the last 5-day precipitation higher than 30 mm
5 D_40	Number of days since the last 5-day precipitation higher than 40 mm
5 D_50	Number of days since the last 5-day precipitation higher than 50 mm
Clm_I	Climatological index

Fig. 6 Recorded data and data modeled by random forests: **a** groundwater level depth; **b** groundwater level change rate



possible reasons for such a poor prediction of GWL depth. One reason for the great error is that similar combinations of precipitation events and GWL depth in the period of prediction did not occur during the training period. Another reason

is that the range of values of GWL depth is much wider than the range of GWL change rate values. Consequently, an incorrect prediction of GWL change rate is not as significant as that for a change in GWL depth. For all these reasons, the

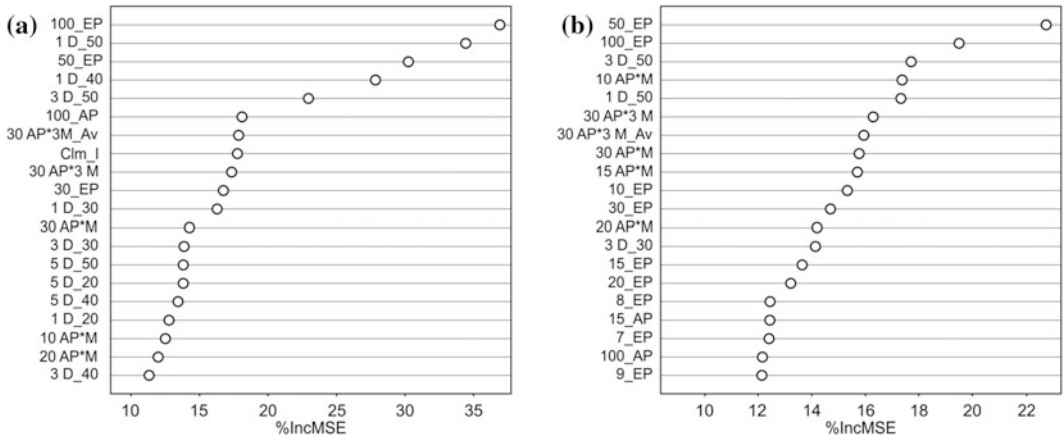


Fig. 7 Variable importance for: **a** prediction of groundwater depth level; and **b** groundwater level change rate

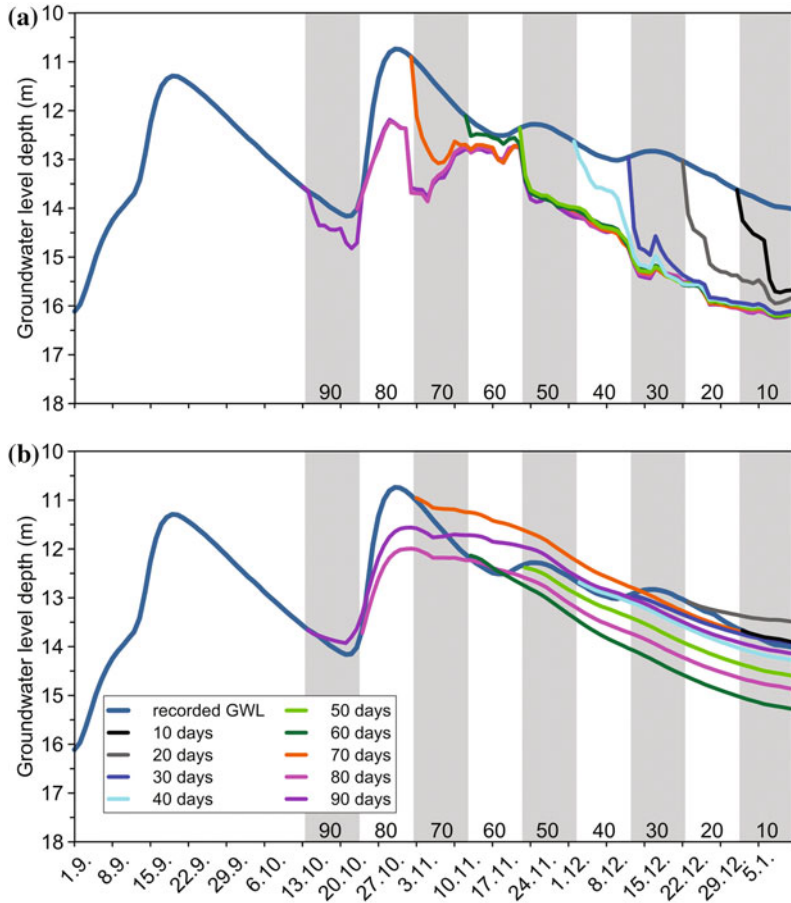
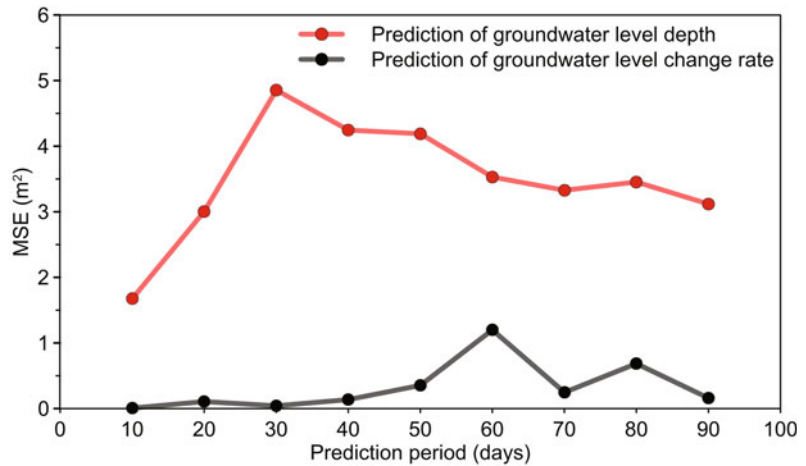


Fig. 8 Prediction of groundwater level depth by random forests technique: **a** direct prediction; and **b** indirect prediction, i.e., calculation from predicted groundwater level changes

Fig. 9 Mean squared errors for different periods and different models of groundwater level depth prediction



model for the prediction of GWL change rate was selected as an optimal prediction model in further analyses. Figure 8b demonstrates that the chosen model could not predict minor groundwater level rising periods, which generally does not significantly influence Kostanjek landslide velocity.

5 Modeling of Landslide Velocity

The velocity prediction model for the central part of the Kostanjek landslide was made using a series of variables defined and calculated from daily GWL depth monitoring data. In total, 10 variables were used as a predictors belonging to four main groups (Table 6): (1) groundwater level depth; (2) groundwater level change rate; (3) groundwater level change acceleration; (4) climatological indexes. GWL change rates were calculated for periods from 1 to 7 days prior to the day of prediction and for the day before and day after the day for which the velocity is predicted. These variables, together with acceleration of groundwater level changes, indirectly imply groundwater level trends, e.g. increasing or decreasing trends of groundwater level changes. Climatological indexes from 1 (autumn) to 4 (summer) indicate periods of higher and lower landslide velocities as a consequence of wet or dry conditions.

The prediction capability of the landslide velocity model, based on 10 predictors, was tested on the whole dataset (730 days), with random forests parameters in R software: (1) number of random predictors in tree building (*mtry* parameter) of 4; and (2) number of generated trees in each analysis (*ntree* parameter) of 1000. The results of landslide velocity modeling are presented in Fig. 10. The coefficient of correlation between the modeled and observed result is 0.974, and the maximal difference between the modeled and observed data is 0.68 mm/day (in November 2013). The most important predictors (Fig. 11) are GWL depth, GWL change rate for the period of 7 days and GWL change rate for the day after the day for which velocity is predicted.

Based on good predictive capability of the tested model on the whole dataset (730 days) using 10 variables, predictions of landslide velocity were made for periods from 10 to 90 days. For each prediction, the models were trained on datasets containing 640 to 720 of 730 total daily data. Cumulative landslide displacements were calculated as the sum of cumulative daily velocities. The resulting predicted cumulative displacements are presented in Fig. 12, and the MSE of predicted cumulative displacements are shown in Fig. 13. According to MSE analysis, the error for the periods up to 30 days is acceptable.

Table 6 Predictors used in the prediction of landslide velocity displacement

Label	Description
GWL_D	Groundwater level depth
GWL_CR	1-day groundwater level change rate
GWL_2 CR	2-day groundwater level change rate
GWL_3 CR	3-day groundwater level change rate
GWL_5 CR	5-day groundwater level change rate
GWL_7 CR	7-day groundwater level change rate
GWL_CR_DB	GWL_CR for the day before the day of prediction
GWL_CR_DA	GWL_CR for the day after the day of prediction
GWL_A	1-day groundwater level change acceleration
CIm_I	Climatological index

Fig. 10 Recorded landslide velocities and landslide velocities modeled by random forests

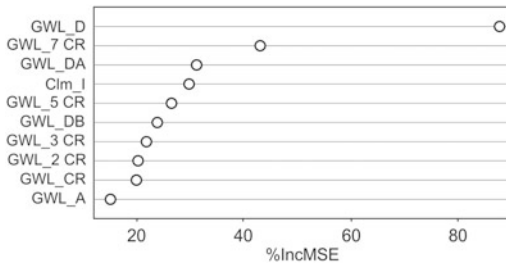
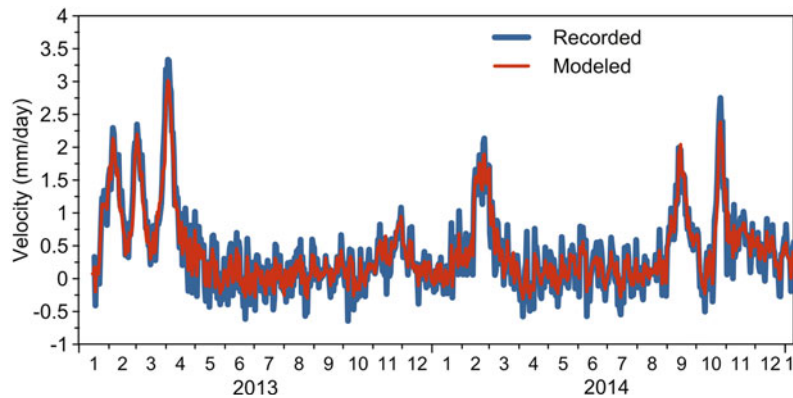


Fig. 11 Variable importance for prediction of landslide velocity

6 Method Verification

Verification of the established method was performed by comparing the predicted landslide displacements with the measured displacements. The process of verification consisted of two steps: (1) prediction of GWL change rates from

precipitation data and calculation of GWL depth; and (2) prediction of landslide velocities from predicted GWL depth. A prediction was made for the periods of the last 10–90 days of the monitoring period (total duration of 730 days) based on training periods of the first 640–720 days. The predicted GWL depths enabled the calculation of independent variables (predictors) and prediction of landslide velocities, which enabled the calculation of cumulative landslide displacements. The results of displacement predictions for 30, 60 and 90 days are presented in Fig. 14, and prediction error (MSE and absolute error) for the end of each prediction period is shown in Fig. 15.

MSE values are highest for the prediction periods of 50, 60 and 70 days (Fig. 15). The differences between the measured and predicted cumulative displacements are 0.76 mm at the end of the 10-day prediction period and 11.5 mm at

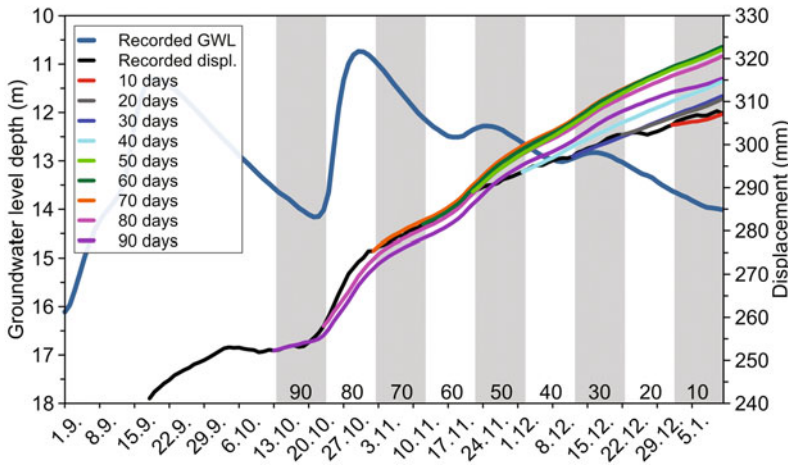


Fig. 12 Prediction of landslide displacement by random forests from groundwater level data

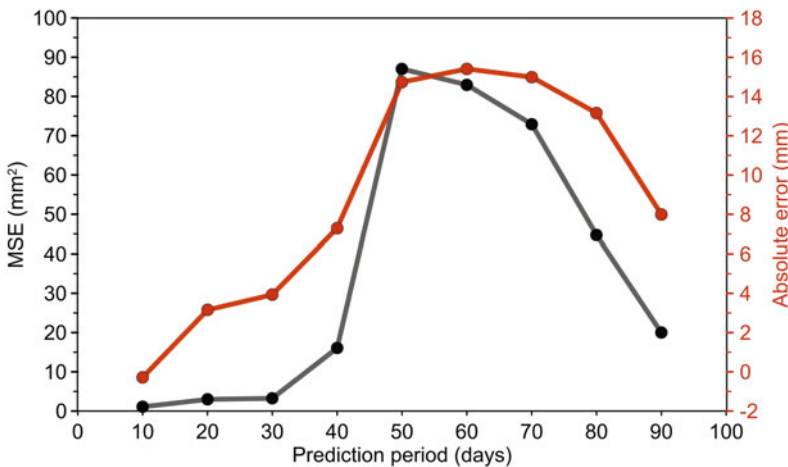


Fig. 13 Mean squared and absolute errors for different prediction periods of landslide displacement from groundwater level depth

the end of the 70-day prediction period. The average difference between the measured and predicted cumulative displacements is 5.96 mm. Based on the results shown in Fig. 15, the prediction of landslide displacements from the data on GWL depth prediction is considered to be acceptable for periods of up to 30 days.

7 Discussion

The developed model for the prediction of landslide movements using random forests, a popular statistical learning model, is a

phenomenological or black box model because only input and output parameters are known whereas the physical processes within the slope are neglected. Inputs and outputs in the model are obtained from continuous monitoring of landslide movement, groundwater level and precipitation data relevant to the central part of the large and deep-seated Kostanjek landslide. Prediction models were developed for three dependent variables (GWL depth, GWL change rate and landslide velocity) on the basis of independent variables derived from precipitation parameters (in the case of GWL depth and GWL change rate predictions) and GWL parameters (in

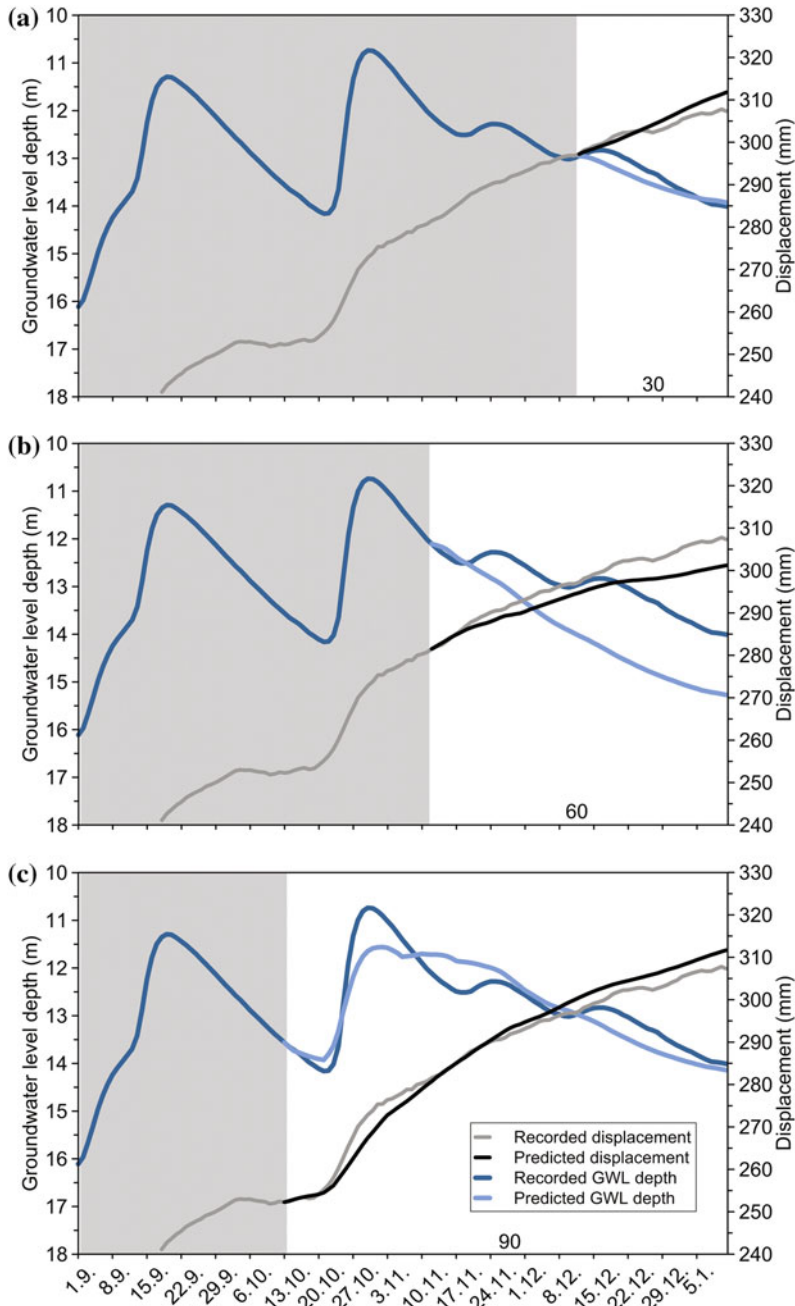


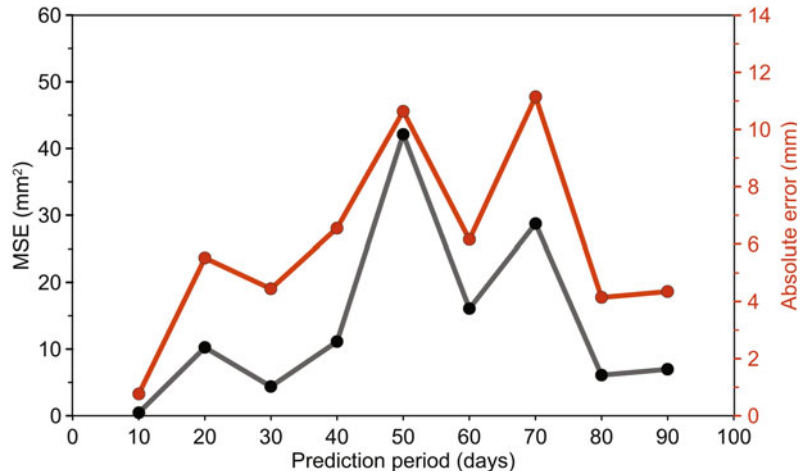
Fig. 14 Prediction of landslide displacements from predicted groundwater levels for periods of: **a** 30 days; **b** 60 days; and **c** 90 days

the case of landslide velocity prediction). The models were tested for different prediction periods (10–90 days) based on training datasets from 640 to 720 days. Acceptable models are selected on the basis of the statistical parameters such as

MSE or absolute difference between the measured and predicted values.

The landslide movement prediction model developed using the Kostanjek landslide monitoring data consist of two sub-models:

Fig. 15 Mean squared and absolute errors for different prediction periods of landslide displacement from predicted groundwater level depth



(1) precipitation–groundwater level depth model; and (2) groundwater level depth–landslide movement model. Both models were used because of limitations in the direct prediction of landslide movements from precipitation. Namely, landslide movements are directly influenced by groundwater level changes; however, groundwater level does not depend entirely on precipitation itself but also on the initial groundwater level or soil moisture. Consequently, the same amount of precipitation at different initial conditions may or may not cause a groundwater level rise and subsequent landslide movement.

The lack of data related to the soil moisture at the Kostanjek landslide was compensated in the precipitation–groundwater level depth model by use of precipitations modified by indexes that describe the prediction period as wetter or dryer than average (indicating high or low groundwater level). Other parameters to describe initial conditions are temporal parameters, which describe the period since the last “significant” precipitation, thus identifying the relative probability of high or low soil moisture. All of these parameters could be calculated from continuous precipitation data (recorded by the certain landslide monitoring system, or by the nearest meteorological station). A certain time lag between a precipitation event and groundwater level change is considered in the model by introducing various types of antecedent precipitations.

For the prediction of landslide velocities as predictors, various parameters were calculated from groundwater level depth. These parameters imply groundwater depth, groundwater level changes and trends that are important because landslide velocity is different during groundwater level rise and fall.

Although it can be seen from monitoring data that groundwater level depth reacts to precipitation during periods of 3–8 days, for the precipitation–groundwater level depth model, the most important predictors are 50- and 100-day effective precipitations and the number of days since 40 or 50 mm precipitations. Long-term precipitations are important for the model because the curve shape of long-term precipitations are more similar to the shape of groundwater depth. At the same time, the shape of the short antecedent precipitation curve has a very distinct “zig-zag” pattern, which has a very small correlation with the groundwater level depth curve and a consequently low prediction capability.

Limitations of random forests are similar to those of other statistical models as follows: (1) relatively long and continuous data time series are necessary to develop an adequate model; (2) the natural/anthropogenic conditions on which model was developed must remain unchanged during the prediction period; (3) the model will be more reliable if it describes a more deterministic system (similar inputs result in similar outputs); (4) the choice of

unrepresentative variables in the model will cause the model to have poor prediction capabilities; (5) if an event occurs during the prediction period that did not occur during the training period, there is a possibility that this event will not be predicted.

Important limitations of the random forests technique that are eliminated by the described landslide prediction model are as follows. The data time series used to develop adequate models for the Kostanjek landslide are 2 years long and continuous, and cover a wide range of landslide behavior. The total cumulative Kostanjek landslide displacement is relatively small comparing to its size, so it is expected that physical processes within the slope will not change significantly in the near future. Results of the model validation imply that the prediction variables are representative. The model can be constantly updated with new data from the monitoring system, which would enable more accurate predictions.

8 Conclusion

The established phenomenological method enabled the prediction of slow landslide movements by means of landslide velocity and displacements from the precipitation data. The described method encompasses the modeling of groundwater level change rate from the daily and historical precipitation data followed by modeling of landslide velocity from the predicted daily groundwater level depths (calculated from groundwater level change rates). The modeling was performed using random forests, which enabled the evaluation of model parameter importance and development of the prediction model. The phenomenological model was validated via comparison of the predicted data with data measured at the Kostanjek landslide (Croatia).

The model is established on 2-year monitoring data from the Kostanjek landslide, enabling the prediction of cumulative landslide displacements for periods up to 30 days. The maximal cumulative displacement during this period was 15 mm and the differences between the measured and predicted cumulative displacements were up

to 5.5 mm. The rainfall–groundwater level depth model was developed using 75 variables placed in six main groups: (1) antecedent precipitation; (2) effective precipitation; (3) precipitation events; (4) modified precipitation; (5) time periods since a certain precipitation event; and (6) climatological indexes. Among all of these, the most important predictors for groundwater level prediction are 50- and 100-day effective precipitation, number of days since 50 mm precipitation during 1- and 3-day periods and 10 days antecedent precipitation multiplied by 1 month index. The groundwater level depth–landslide movement model was developed using 10 variables belonging to four main groups: (1) groundwater level depth; (2) groundwater level change rate; (3) groundwater change acceleration; and (4) climatological indexes. The most important predictors for movement prediction are groundwater level depth, 7-day groundwater level change rate and groundwater level change rate on the day after the day for which velocity is predicted.

Input data in the form of data series, gathered by continuous monitoring of groundwater level and landslide movement in the central part of the Kostanjek landslide, were of satisfactory quality for modeling purposes because of the high data coverage of 99.9%, wide range of landslide behavior (multiple interchanges of steady states and faster movements) and mutual dependency of groundwater level and landslide movement parameters.

Random forests prove to teach different patterns of landslide behavior under various conditions, which can be described by a large number of variables. Considering the described reliability of the prediction results, simplicity and robustness, a random forests is proposed for application in the prediction of landslide movements. Automated predictions updated on a daily basis would produce improved everyday predictions, which are an important source of reliable information for decisions related to crisis management in the case of risky landslide movements.

Acknowledgements The results presented herein have been obtained with the financial support from JST/JICA's

SATREP Program. This support is gratefully acknowledged. The authors would also like to thank the Croatian Meteorological and Hydrological Service for the meteorological data. The authors are grateful to Ž. Arbanas and anonymous reviewers for their valuable advice.

References

- Baird KJ, Maddock T III (2005) Simulating riparian evapotranspiration: a new methodology and application for groundwater models. *J Hydrol* 312(1–4):176–190. doi:10.1016/j.jhydrol.2005.02.014
- Breiman L (2001) Random forests. *Mach Learn* 45:5–32
- Brenning A (2005) Spatial prediction models for landslide hazards: review, comparison and evaluation. *Nat Hazards Earth Syst Sci* 5:853–862
- Calvello M, Cascini L, Sorbino G (2008) A numerical procedure for predicting rainfall-induced movements of active landslides along pre-existing slip surfaces. *Int J Numer Anal Methods Geomech* 32(4):327–351. doi:10.1002/nag.624
- Caruana R, Niculescu-Mizil A (2006) An empirical comparison of supervised learning algorithms. In: Proceedings of the 23rd international conference on machine learning, pp 161–168. doi:10.1145/1143844.1143865
- Cascini L, Calvello M, Grimaldi G (2010) Groundwater modeling for the analysis of active slow-moving landslides. *J Geotech Geoenviron Eng* 136(9):1220–1230
- Catani F, Lagomarsino D, Segoni S, Tofani V (2013) Landslide susceptibility estimation by random forests technique: sensitivity and scaling issues. *Nat Hazards Earth Syst Sci* 13:2815–2831. doi:10.5194/nhess-13-2815-2013
- Corominas J, Moya J, Ledesma A, Lloret A, Gili JA (2005) Prediction of ground displacements and velocities from groundwater level changes at the Vallcebre landslide (Eastern Pyrenees, Spain). *Landslides* 2:83–96
- Crosta GB, Agliardi F (2003) Failure forecast for large rock slide by surface displacement measurements. *Can Geotech J* 40(1):176–191
- Crosta G, Di Prisco C (1999) On slope instability induced by seepage erosion. *Can Geotech J* 36:1056–1073
- Cruden DM, Varnes DJ (1996) Landslide types and processes. In: Turner AK, Schuster RL (eds) *Landslide investigation and mitigation* (Special Report/ Transportation Research Board, National Research Council; 247). National Academy Press, Washington DC, Chapter 3, pp 36–75
- Federico A, Popescu M, Elia G, Fidelibus C, Internò G, Murianni A (2012) Prediction of time to slope failure: a general framework. *Environ Earth Sci* 66:245–256. doi:10.1007/s12665-011-1231-5
- Fukuzono T (1985) A new method for predicting the failure time of a slope. In: Proceedings of the 4th international conference and field workshop on landslides, Tokyo (Japan), pp 145–150
- Gajić-Čapka M, Zaninović K (2008) Climate of Croatia. In: Zaninović K (ed) *Climate atlas of Croatia, 1961–1990 and 1971–2000*. Croatian Meteorological and Hydrological Service, Zagreb, pp 15–17
- Ghiassian H, Ghareh S (2008) Stability of sandy slopes under seepage conditions. *Landslides* 5:397–406. doi:10.1007/s10346-008-0132-5
- Gislason PO, Benediktsson JA, Sveinsson JR (2006) Random forests for land cover classification. *Pattern Recogn Lett* 27(4):294–300
- Godt JW, Baum RL, Lu N (2009) Landsliding in partially saturated materials. *Geophys Res Lett*. doi:10.1029/2008GL035996
- Goetz JN, Brenning A, Petschko H, Leopold P (2015) Evaluating machine learning and statistical prediction techniques for landslide susceptibility modeling. *Comput Geosci* 81:1–11. doi:10.1016/j.cageo.2015.04.007
- Ham J, Chen Y, Crawford M, Ghosh J (2005) Investigation of the random forest framework for classification of hyperspectral data. *IEEE Trans Geosci Remote Sens* 43:492–501
- Hodgson FDI (1978) The use of multiple linear regression in simulating ground-water level responses. *Ground Water* 16(4):249–253
- Hong Y-M, Wan S (2011) Forecasting groundwater level fluctuations for rainfall-induced landslide. *Nat Hazards* 57:167–184. doi:10.1007/s11069-010-9603-9
- James G, Witten D, Hastie T, Tibshirani R (2014) An introduction to statistical learning with applications in R. Springer, New York
- Krkač M, Mihalić Arbanas S, Arbanas Ž, Bernat S, Špehar K, Watanabe N, Nagai O, Sassa K, Marui H, Furuya G, Wang C, Rubinić J, Matsunami K (2014a) Review of monitoring parameters of the Kostaňek Landslide (Zagreb, Croatia). In: Sassa K, Canuti P, Yin Y (eds) *Proceedings of the 3rd World Landslide Forum ‘Landslide science for a safer geoenvironment’, vol 2. Methods of landslide studies*. Springer, Dordrecht, pp 637–645
- Krkač M, Mihalić Arbanas S, Nagai O, Arbanas Ž, Špehar K (2014b) The Kostaňek landslide—monitoring system development and sensor network. In: Mihalić Arbanas S, Arbanas Ž (eds) *Proceedings of the 1st regional symposium on landslides in the Adriatic-Balkan region: landslide and flood hazard assessment*. Croatian Landslide Group, Zagreb, pp 27–32
- Lebedev AV, Westman B, Van Westenc GJP, Kramberger MG, Lundervold A, Aarsland D, Soininen H, Kłoszewska I, Mecocci P, Tsolaki M, Vellas B, Lovestone S, Simmons A (2014) Random Forest ensembles for detection and prediction of Alzheimer’s disease with a good between-cohort robustness. *NeuroImage Clin* 6:115–125
- Lee LJE, Lawrence DSL, Price M (2006) Analysis of water-level response to rainfall and implications for recharge pathways in the Chalk aquifer, SE England. *J Hydrol* 330:604–620
- Mansour MF, Morgenstern NR, Martin CD (2011) Expected damage from displacement of slow-moving

- slides. *Landslides* 8(1):117–131. doi:[10.1007/s10346-010-0227-7](https://doi.org/10.1007/s10346-010-0227-7)
- Martelloni G, Segoni S, Fanti R, Catani F (2011) Rainfall thresholds for the forecasting of landslide occurrence at regional scale. *Landslides* 9:485–495. doi:[10.1007/s10346-011-0308-2](https://doi.org/10.1007/s10346-011-0308-2)
- Massey CI, Petley DN, McSaveney MJ (2013) Patterns of movement in reactivated landslides. *Eng Geol* 159:1–19
- Matsuura S, Asano S, Okamoto T (2008) Relationship between rain and/or meltwater, pore-water pressure and displacement of a reactivated landslide. *Eng Geol* 101:49–59
- Micheletti N, Foresti L, Robert S, Leuenberger M, Pedrazzini A, Jaboyedoff M, Kanevski M (2014) Machine learning feature selection methods for landslide susceptibility mapping. *Math Geosci* 46:33–57. doi:[10.1007/s11004-013-9511-0](https://doi.org/10.1007/s11004-013-9511-0)
- Mihalić Arbanas S, Arbanas Ž, Krkač M (2013) Comprehensive landslide monitoring system: The Kostanjek landslide case study, Croatia. In: Sassa K, He B, McSaveney M, Osamu N (eds) ICL landslide teaching tools. International Consortium on Landslides, Kyoto, pp 158–168
- Ortolan Ž, Pleško J (1992) Repeated photogrammetric measurements at shaping geotechnical models of multi-layer landslides. *Rudarsko-geološko-naftni zbornik* 4:51–58
- Ortolan Ž (1996) Development of 3D engineering geological model of deep landslide with multiple sliding surfaces (Example of the Podsused Landslide). Dissertation, University of Zagreb (in Croatian)
- Pal M (2005) Random forest classifier for remote sensing classification. *Int J Remote Sens* 26:217–222
- Pauly O (2012) Random forests for medical applications. Dissertation, Technische Universität München
- Peters J, De Baets B, Verhoest NCA, Samson R, Degroeve S, De Becker P, Huybrechts W (2007) Random forests as a tool for ecohydrological distribution modelling. *Ecol Model* 207:304–318
- Pourghasemi HR, Kerle N (2016) Random forests and evidential belief function-based landslide susceptibility assessment in Western Mazandaran Province, Iran. *Environ Earth Sci* 75(185):1–17. doi:[10.1007/s12665-015-4950-1](https://doi.org/10.1007/s12665-015-4950-1)
- Prasad AM, Iverson LR, Liaw A (2006) Newer classification and regression tree techniques: bagging and random forests for ecological prediction. *Ecosystems* 9(2):181–199
- Saito M (1965) Forecasting the time of occurrence of a slope failure. In: Proceedings of the 6th international conference on soil mechanics and foundation engineering, vol 2, Montreal, pp 573–541
- Sassa K, Osamu N, Solidum R, Yamazaki Y, Ohta H (2010) An integrated model simulating the initiation and motion of earthquake and rain induced rapid landslides and its application to the 2006 Leyte landslide. *Landslides* 7:219–236. doi:[10.1007/s10346-010-0230-z](https://doi.org/10.1007/s10346-010-0230-z)
- Schilling KE (2009) Investigating local variation in groundwater recharge along a topographic gradient, Walnut Creek, Iowa, USA. *Hydrogeol J* 17:397–407
- Segoni S, Lagomarsino D, Fanti R, Moretti S, Casagli N (2014) Integration of rainfall thresholds and susceptibility maps in the Emilia Romagna (Italy) regional-scale landslide warning system. *Landslides* 12(4):773–785. doi:[10.1007/s10346-014-0502-0](https://doi.org/10.1007/s10346-014-0502-0)
- Simoni A, Berti M, Generali M, Elmi C, Ghirotti M (2004) Preliminary result from pore pressure monitoring on an unstable clay slope. *Eng Geol* 73:117–128
- Skempton AW (1985) Residual strength of clays in landslide, folded strata and the laboratory. *Geotechnique* 35(1):3–18
- Stanić B, Nonveiller E (1996) The Kostanjek landslide in Zagreb. *Eng Geol* 42:269–283
- Stumpf A, Kerle N (2011) Object-oriented mapping of landslides using Random Forests. *Remote Sens Environ* 115:2564–2577. doi:[10.1016/j.rse.2011.05.013](https://doi.org/10.1016/j.rse.2011.05.013)
- Trigila A, Iadanza C, Esposito C, Scarascia-Mugnozza G (2015) Comparison of Logistic Regression and Random Forests techniques for shallow landslide susceptibility assessment in Giampileri (NE Sicily, Italy). *Geomorphology* 249:119–136. doi:[10.1016/j.geomorph.2015.06.001](https://doi.org/10.1016/j.geomorph.2015.06.001)
- Van Asch TWJ, Van Beek LPH, Bogaard TA (2007) Problems in predicting the mobility of slow-moving landslides. *Eng Geol* 91:46–55
- Venables W N, Smith D M (2014) An introduction to R: a programming environment for data analysis and graphics version 3.1.2. <http://www.r-project.org/>. Accessed 17 Dec 2015
- Vorpahl P, Elsenbeer H, Märker M, Schröder B (2012) How can statistical models help to determine driving factors of landslides? *Ecol Model* 239:27–39
- Weinheimer A, Biondi F (2003) Varves. In: Holton JR, Curry JA, Pyle JA (eds) Encyclopedia of atmospheric sciences, vol 4. Academic Press, Oxford, pp 1680–1685
- Wieczorek GF (1996) Landslide triggering mechanism. In: Turner AK, Schuster RL (eds) Landslides investigation and mitigation, special report, vol 247, no 4. Transportation Research Board. National Academy Press, Washington, pp 76–89
- Wu J, Zhang R, Yang J (1996) Analysis of precipitation-recharge relationships. *J Hydrol* 177:143–160
- Yoon H, Jun S-C, Hyun Y, Bae G-O, Lee K-K (2011) A comparative study of artificial neural networks and support vector machines for predicting groundwater levels in a coastal aquifer. *J Hydrol* 396:128–138
- Youssef AM, Pourghasemi HR, Pourtaghi ZS, Al-Katheeri MM (2015) Landslide susceptibility mapping using random forest, boosted regression tree, classification and regression tree, and general linear models and comparison of their performance at Wadi Tayyah Basin, Asir Region, Saudi Arabia. *Landslides*. doi:[10.1007/s10346-015-0614-1](https://doi.org/10.1007/s10346-015-0614-1)

TXT-tool 4.062-1.1

Community Hazard Maps for Landslide Risk Reduction

Dwikorita Karnawati, Teuku Faisal Fathani,
Wahyu Wilopo and Budi Andayani

Abstract

This paper highlights the importance of a non-technical approach to providing hazard maps for community-based landslide risk reduction at the village level. Such maps should be simple and user friendly, so they can be easily prepared and used effectively for mitigation actions by the village communities. Various key parameters required for such mapping are discussed, in line with standard procedures for hazard mapping. A pilot study was carried out in Tengklik Village in Karanganyar Region, Central Java, Indonesia, to test this proposed procedure for hazard mapping. It was concluded that converting the technical information in the maps into more simple terms that will address the practical needs and socio-cultural conditions in any particular village is crucial for assuring the effective employment of such maps in landslide mitigation actions. This chapter describes the achievements and the current activities of IPL-165 “Development of community-based landslide hazard mapping for landslide risk reduction at the village scale in Java, Indonesia” and IPL-158 “Development of Education Program for Sustainable Development in Landslide Vulnerable Area through Student Community Service”.

Keywords

Hazard map · Community participation · Simple procedure for mapping
Socio-cultural condition · Risk management

D. Karnawati (✉) · W. Wilopo
Department of Geological Engineering, Universitas
Gadjah Mada, Jl. Grafika No. 2, Yogyakarta 55281,
Indonesia
e-mail: dwiko@ugm.ac.id

W. Wilopo
e-mail: wwilopo@gadjahmada.edu

D. Karnawati · T.F. Fathani · W. Wilopo
Center for Disaster Mitigation and Technological
Innovation (GAMA-InaTEK), Department of Civil
and Environmental Engineering, Universitas Gadjah
Mada, Jl. Grafika No. 2, Yogyakarta 55281,
Indonesia
e-mail: tfathani@ugm.ac.id

B. Andayani
Faculty of Psychology, Universitas Gadjah Mada,
Bulaksumur, Yogyakarta 55281, Indonesia
e-mail: anikoentjoro@ugm.ac.id

Contents

1	Introduction	600
1.1	Problem Background	600
1.2	Objectives of Community Hazard Mapping ...	600
2	Mapping Approach, Methods and Parameters	600
2.1	Mapping Approach	600
2.2	Methods of Hazard and Risk Mapping	601
2.3	Parameters Affecting Slope Movement	601
2.4	Mapping Procedure	602
3	Case Example—Tengklik Village	603
3.1	Village-Based Mapping	603
3.2	Implementation of Hazard Mapping.....	604
3.3	The Challenges.....	605
4	Conclusions	605
	References	606

1 Introduction

1.1 Problem Background

Indonesia is a land with dynamic geological conditions, where landslides are a major threat and frequently cause disasters during the rainy season. Many landslides have been serious, resulting in substantial socio-economical losses, due to insufficient landslide hazard information being provided at village levels. Landslide hazard maps are a crucial tool for providing early information about potentially susceptible zones where landslides are most likely to occur. The provision of these hazard maps is urgently needed to support land-use planning, as well as landslide mitigation and early warning. Unfortunately, it is quite difficult to provide landslide hazard maps for vulnerable villages due to the limited human and financial resources of the villages. In order to reduce the risk of landslides at the villages, and thus to address the need for landslide mitigation there, a community landslide hazard map needs to be specifically developed. Admittedly, the Government has produced landslide hazard maps at a regional scale for the most vulnerable regions in Indonesia. Such regional-scale maps, however, are not useful for

landslide mitigation programs at the village level—they are not practical and are too technical to be understood by the village communities. Therefore, it is quite challenging to provide a community landslide hazard map which is both simple to prepare, and user friendly, for mitigation actions in the village.

1.2 Objectives of Community Hazard Mapping

The provision of landslide hazard maps is urgently required for appropriate landslide mitigation and early warning, and to improve community awareness and disaster risk reduction in village or rural areas. Accordingly, this proposed community-based hazard mapping needs to be undertaken in order to provide a non-technical mapping approach and method that is user friendly.

2 Mapping Approach, Methods and Parameters

2.1 Mapping Approach

Community participation should be the main approach for preparing a community-based hazard map (Andayani et al. 2008; Karnawati et al. 2008, 2009a, b, c; Aditya et al. 2010). It is important that such a map should not be too technical, but quite simple and easily understood by non-technical people. Thus, an observational or social survey to identify the level of community knowledge and understanding of landslide phenomena, as well as to determine the community's perceptions on hazard awareness and preparedness, must be carried out prior to the mapping process. All of these considerations need to be addressed, in order to guarantee the effectiveness of the map for landslide risk reduction at the vulnerable village.

2.2 Methods of Hazard and Risk Mapping

Landslide hazard mapping is conducted by observing and recording any indicators of slope movement and/or the key parameters causing the slope movement, in order to visually illustrate the levels of hazard and risk. A simple technical method is proposed for both hazard and risk mapping, as follows.

2.2.1 Hazard Mapping

A simple method of mapping is proposed to illustrate the level of hazard at a particular zone in a village. This mapping is mainly based on empirical observations to record and assess various indicators of slope movement and the key parameters that may cause landslides to occur. Due to the simplicity of such a method, the observations can be conducted by the community (often with the assistance of an adviser), and accordingly they can distinguish three different levels of landslide hazard using the following criteria.

- a. active slopes (where evidence of movement can be recorded clearly and these signs are quite persistent),
- b. non-active slopes (showing no signs of movement), and
- c. moderately active slopes (showing transitional conditions from active to non-active).

However, it is also important to re-assess the level of landslide hazard for non-active slopes where there are no signs of movement, by considering the key parameters causing landsliding discussed in Sect. 2.3. Therefore, in the regions with no signs of slope movement, the hazard level can be separated into:

- a. Zones with the most potential for landsliding (zones with the highest hazard level). These zones will have steep slopes where the inclination is more than 20° and the soil is fragile or very loose, in which soil particles can be

easily separated using simple means (such as fingers, hand or a pen).

- b. Zones with a moderate potential for landsliding (a moderate hazard level), where landslides occur but not frequently. These zones may have steep slopes but they are formed of relatively compact and firm soils, or they may have a rather gentle slope (such as 20° – 30° slopes) with fragile or sensitive soil/rock formations.
- c. Zones with low or no potential for landsliding (zones with a low hazard level). Here landslides will be rare or never occur, as the zones have gentle slopes with firm or compact soil/rock formations.

2.2.2 Risk Mapping

Afterwards, risk mapping can be conducted based on the risk perceptions empirically observed by the community. The level of risk also can be simply classified as:

- a. high,
- b. moderate, or
- c. low.

The high-risk zone is defined as the zone with most potential for landsliding and the most severe potential impacts and consequences if a landslide occurs. The zone may have quite a large number of houses and infrastructure potentially threatened by the landslide. The low risk landslide zone then is defined as the landslide hazard zone with no serious potential impacts or consequences of landslides (no houses, no people and no infrastructure will be affected by landslides). The zones which are not categorized as high risk or low risk should be considered as zones with a moderate risk level.

2.3 Parameters Affecting Slope Movement

The indicators of slope movement can be recorded empirically by observing any signs of slope

movement such as any appearance of surface deformation of the slope and the surrounding area, as well as any effects of movement on houses and infrastructure. Deformation and signs which indicate slope movements may include:

- a. the appearance of cracks with a typical “horse-shoe shape” on the slope surface, or cracks in structures and infrastructure;
- b. land subsidence or the displacement of any feature on the slope surface;
- c. bulging or deformation at the slope surface or of a retaining wall;
- d. the appearance of seepage or a spring at the toe or foot slope or a water discharge from the slope surface that is mixed with sediments or forms a slurry.
- e. the inclination of any vertical features (piles, trees, etc.) at the slope surface.

Karnawati et al. (2005) suggested several key parameters controlling landslide occurrence. Those include:

- a. Slope inclination,
- b. Slope stratigraphy, which indicates the configuration as well as the strength of the soils and rocks forming the slope,
- c. Slope hydrology, and
- d. Land-use conditions.

However, the terms in the key parameters listed above are too technical, so they should be modified or converted into more simple terms that will be easily recognized by the community. Therefore, several adjusted terms for those parameters are introduced below:

- a. Slope steepness to indicated the slope inclination
- b. Fragility and the arrangement of soils/rocks forming the slope are used to indicate the soils/rock strength and stratigraphy.
- c. Slope saturation is used to indicate the slope hydrology.
- d. Type of land-use is used to indicate the conditions of land use.

2.4 Mapping Procedure

A simple mapping procedure is suggested to enable the community to actively participate in this mapping process. The main procedure should follow these steps:

- a. Carry out a social survey (through interviews, circulating questionnaires, or some other feasible method) to identify the level of the community’s knowledge of landslide phenomena and the causes, consequences and prevention of landslides, as well as to grasp the general perceptions of the community on landslide hazard and risk, and also the importance of mapping the hazard and risk.
- b. Develop a strategy for landslide hazard and risk mapping based on community participation. For instance, it might be more effective to invite only limited numbers of people from the community, those who can carry out simple mapping by observing and recording the visual signs of landslides.
- c. Establish a community task force for mapping, which may consist of several (3–5) people in charge to conduct the mapping. The availability of at least one technical adviser to guide the mapping process is recommended, in order to assure that the process is technically correct and quite accurate.
- d. Conduct a field landslide recognition tour through the region of the village, with not only the task force but other participants from the community. It is recommended that these participants should include groups of young men and women, teachers, village leaders and key persons who should have a strong concern about landslide awareness and risk reduction. This step is mainly carried out as a part of public education and consultation. During this tour discuss the causes of landslides, how to prevent landslide disasters, how to recognize the signs of potential landslides and how to develop an appropriate landslide early warning system.
- e. The community task force should observe the existence and frequency (persistence) of

- landslide signs, as well as plotting or recording the position of such signs, and estimating the extent of potential impacts or risks of landslides..
- f. For the zones without any signs of landslides, the community task force should observe the key factors controlling landslide occurrence (slope steepness, fragility of the rocks/soils forming the slope and the land use).
 - g. Compile data by plotting all the findings from field observations and then determine the boundaries of hazard and risk (establishment of hazard and risk zones), based on community participation through a series of focus group discussions that are driven by the community task force, in order to produce a draft landslide hazard and risk map.
 - h. Enhance the draft hazard and risk maps by conducting community tours in the field under the guidance of the community task force (a process similar to that conducted in step d). The main purpose of this tour is to have the community participate in confirming the hazard boundaries established in step g above.
 - i. Revise the map, based on the community task force results from step h.
 - j. Construct the final landslide hazard and risk maps.

- k. Disseminate the hazard and risk maps through public education, focus group discussions, community tours to the field, and traditional performances conducted in any festival event in the village.

It is important that the map be regularly reviewed or enhanced, based on the ongoing landslide activity in the field. A community task force for mapping may also need to be permanently established for a given period (such as for 3–5 years), and also regularly replaced by another new task force each following period of 3–5 years. The task force may also be enlarged to include more participants from the community with a special mission to conduct disaster risk reduction program at the village level.

3 Case Example—Tengklik Village

3.1 Village-Based Mapping

Several landslides occurred in Tengklik Village, in Tawangmangu District, Karanganyar Regency, Central Java, Indonesia, in the rainy season of 2008, damaging several houses and the main road (Fig. 1). Due to the natural conditions within this mountain village and inappropriate

These positions were situated at the same level



Fig. 1 The impacts of landslide Tengklik Village, landsubside and the damage of houses and main road (Karnawati et al. 2009a)

land use management, this village region remains susceptible to landslides. Unfortunately, it was quite difficult for the community to estimate the particular sites which had a potential for landsliding. Thus, it was difficult to carry out landslide risk reduction without being able to predict the areas with a potential for landsliding. Therefore, community participation in landslide hazard mapping was carried out in order to identify the potential landslide zones, and thus reduce the risk of landslides.

The mapping was conducted by a community task force of two people for the period of two months in July to August, 2009 under the guidance of a final year student from Geological Engineering Department in Gadjah Mada University, Indonesia. The existing documentation map, illustrating the locations of houses, roads and the land uses within the village region, was used as the base map for this mapping. It is a government rule that each village should provide this village documentation map as the village base-map. Accordingly, the landslide hazard map was developed based on the observation of the

signs and controlling factors of landslides, and then those observation results were recorded and plotted on the base map, as illustrated in Fig. 2. This community hazard map, landslide mitigation efforts, evacuation procedures and other related information for public awareness can be published on an information board placed at several locations in areas vulnerable to landslides (Fig. 3).

3.2 Implementation of Hazard Mapping

The landslide hazard and risk map can be successfully developed using quite a simple procedure. This map can illustrate general conditions with respect to the potential landslide hazard in the village. From this mapping, five clusters with a high hazard level (marked in red) were identified (see Fig. 2). Most of these were located in the north part of the village. It is also obvious from the map that the village roads were potentially threatened by the landslides, and two of the

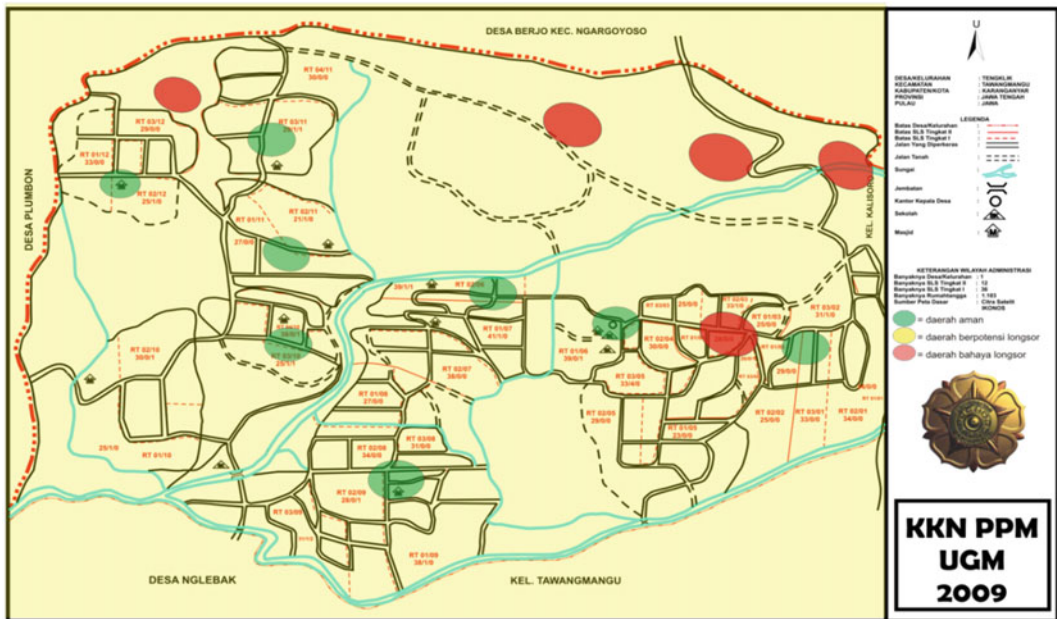


Fig. 2 Landslide hazard map for Tengkluk Village, which indicates the zones of hazard level, such as high level (in red) and low level (in green)



Fig. 3 Information board for landslide mitigation and risk reduction at Tengklik Village, Karanganyar Regency. The community hazard map and other related information are placed on the board and updated

red clusters were situated in the housing areas in the middle-east and north-west parts of the village. These two clusters were thus considered as the highest landslide risk zones, in which mitigation efforts were urgently required.

During a series of public consultations and discussions in the period of July to August 2009, the community realized that appropriate surface and subsurface drainage were required to control the rise of water pressure in the slope. The existing drainage also needed to be maintained by removing blocking sediment, to assure proper drainage. Indeed, the local Government of the Regency had established a new regulation for revegetation of the vulnerable slopes. Therefore, it was an obligation for each individual in the village to plant one tree as a part of the landslide mitigation efforts.

It is apparent that this map was also quite simple and user-friendly, and easily understood by the community. Thus, through community participation, the community can use the hazard map to decide the evacuation routes.

3.3 The Challenges

Admittedly a community hazard map can be produced using quite a simple approach and method. However, it is very challenging to stimulate community awareness and participation to provide such a map, especially when no landslides have occurred yet in the village. This map cannot be effectively developed and implemented without the strong motivation and willingness of the community. Therefore, the mapping process should be in line with an education program to improve public awareness and willingness to conduct landslide mitigation actions. That is why a social approach is strongly recommended in the mapping process.

4 Conclusions

Landslide hazard mapping developed by community participation obviously is required to assure the effective implementation of landslide

disaster risk reduction at village level. The method of mapping should be simplified (to avoid too technical a procedure), and the hazard map produced by this simple approach and method should be user-friendly. Finally, it should be highlighted that a social approach is crucial to assure effective public participation during the mapping process.

References

- Andayani B, Karnawati D, Pramumijoyo S (2008) Institutional frame work for community empowerment towards landslide mitigation and risk reduction in Indonesia. In: 1st World landslide forum; proceedings of the international symposium, Tokyo, 17–19 Nov 2008. Global Promotion Committee of the International Program on Landslide (IPL)—ISDR, pp 57–59
- Karnawati D, Ibriam I, Anderson MG, Holcombe E, Mummery G, Renaud J-P, Wang Y (2005) An initial approach to identifying slope stability controls in Southern Java and to providing community-based landslide warning information. In: Glade T, Anderson MG, Crozier MJ (eds) *Landslide hazard and risk*. Wiley, Hoboken, pp 733–763
- Karnawati D, Fathani TF, Burton P (2008) Seismic and landslide hazard mapping for community empowerment. Development of Partnership in Higher Education Program; Annual Report 2008. The British Council (unpublished)
- Karnawati D, Fathani TF, Aditya T, Suharyanto (2009a) Development of landslide early warning system based on GPS On-line at Tengkluk Village, Tawangmangu District, Karanganyar Regency, Central Java. Cluster Research; Final Project Report. Gadjah Mada University, Yogyakarta (unpublished)
- Karnawati D, Fathani TF, Sudarno I, Andayani B, Burton PW (2009b) Landslide hazard and community-based risk reduction effort in Karanganyar and the surrounding area, Central Java, Indonesia. In: 7th regional conference of IAEG (International Association of Engineering Geology); proceeding, Chengdu, Balkema, 9–12 Aug 2009
- Karnawati D, Fathani TF, Andayani B, Burton PW, Sudarno I (2009c) Strategic program for landslide disaster risk reduction; a lesson learned from Central Java, Indonesia. In: Duncan K, Brebbia CA (eds) *Disaster management and human health risk; reducing risk, improving outcomes*. WIT transactions on the built environment. WIT Press, Southampton, pp 115–126

TXT-tool 4.039-1.1

Definition and Use of Empirical Rainfall Thresholds for Possible Landslide Occurrence

Silvia Peruccacci and Maria Teresa Brunetti

Abstract

In Italy, landslides are frequent and widespread phenomena triggered chiefly by intense or prolonged rainfall. Individual rainfall events can result in single or multiple slope failures in small areas or in very large regions, causing fatalities and large economic damage. Thus, assessing the rainfall conditions responsible for landslides is important and may contribute to reducing risk. Following a review of methods for establishing the dependence of landslide occurrence on rainfall. Next, we present the statistical method used for the definition of objective cumulated event rainfall-duration (*ED*) thresholds, and we show regional, lithological and seasonal thresholds in central Italy.

Keywords

Rainfall threshold · Shallow landslide · Central Italy

Contents

1	Introduction	607
2	Types and Characteristics of Rainfall Thresholds	608
3	<i>ID</i> and <i>ED</i> Rainfall Thresholds	610
4	Study Area	612
5	Regional Rainfall Thresholds	613
6	Lithological Rainfall Thresholds	614
7	Seasonal Rainfall Thresholds	616
8	Comparison with Existing Rainfall Thresholds	618
	References	619

1 Introduction

Rainfall is a recognized trigger of landslides, and investigators have long attempted to determine the amount of precipitation needed to trigger slope failures, a problem of scientific and societal interest. Landslides triggered by rainfall are caused by the build up of water pressure into the ground (Campbell 1975; Wilson 1989). Groundwater conditions responsible for slope failures are related to rainfall through infiltration, soil characteristics, antecedent moisture content, and rainfall history (Wieczorek 1996). These phenomena are poorly understood, and prediction of rainfall-induced landslides is problematic. In the literature, two approaches have been proposed to evaluate the dependence of landslide on

S. Peruccacci (✉) · M.T. Brunetti
Istituto di Ricerca per la Protezione Idrogeologica,
Consiglio Nazionale delle Ricerche, CNR IRPI,
Perugia, Italy
e-mail: Silvia.Peruccacci@irpi.cnr.it

M.T. Brunetti
e-mail: Maria.Teresa.Brunetti@irpi.cnr.it

rainfall measurements. The first approach relies on process-based models (Montgomery and Dietrich 1994; Wilson and Wieczorek 1995; Wu and Sidle 1995; Iverson 2000; Crosta and Frattini 2003), and the second approach is based on empirical thresholds (Caine 1980; Reichenbach et al. 1998; Aleotti 2004; Wieczorek and Glade 2005; Guzzetti et al. 2007).

Here, we review the literature on rainfall thresholds for the initiation of landslides, we present a catalogue of rainfall events responsible for slope failures in central Italy, and finally we use this information to establish cumulated event rainfall-duration (*ED*) thresholds for the occurrence of landslides in the study area. To define objective and reproducible thresholds, we adopt a frequentist statistical method proposed by Brunetti et al. (2010) and refined by Peruccacci et al. (2012). The sensitivity of the thresholds to the number of (*D*, *E*) data points in the empirical data set is also assessed. We report *ED* thresholds (i) for a selected study area, and for the three individual regions included in the study area (Abruzzo, Marche, and Umbria); (ii) for three main lithological domains in the same study area (post-orogenic sediments, flysch deposits, carbonate rocks); and (iii) for two seasonal periods (May–September, October–April).

Issues reported here are published in Guzzetti et al. (2007, 2008), Brunetti et al. (2010), Peruccacci et al. (2012), and Brunetti et al. (2015).

2 Types and Characteristics of Rainfall Thresholds

A threshold is the minimum or maximum level of some quantity needed for a process to take place or a state to change (White et al. 1996). A minimum threshold defines the lowest level below which a process does not occur. A maximum threshold represents the level above which a process always occurs. For rainfall-induced landslides a threshold may define the rainfall, soil moisture, or hydrological conditions that,

when reached or exceeded, are likely to trigger landslides.

In the literature, two approaches have been proposed to evaluate the dependence of landslide occurrence (or lack of occurrence) on rainfall measurements. The first approach relies on process-based models, and the second approach is based on empirical thresholds.

Process-based models rely upon the understanding—and schematization—of the physical laws controlling slope instability. They attempt to extend spatially the simplified stability models widely adopted in geotechnical engineering. Stability conditions are evaluated chiefly by means of a static stability model where the local equilibrium of forces along a predefined slip surface is considered. Most commonly, the slip surface is assumed planar, at a fixed depth, and parallel to the topographic surface. Values for the pore fluid pressure are assumed, or obtained adopting rainfall infiltration models, coupled to surface and sub-surface runoff models.

The main problem of process-based models consists in the difficulty of obtaining reliable and accurate information necessary to construct and calibrate the distributed models. The problem is particularly severe where the models are applied to large areas. The simplest model requires eight parameters (i.e., terrain gradient, soil density, friction angle, cohesion, hydraulic conductivity, failure depth, water table depth, and rainfall history), of which only terrain gradient is known reasonably accurately over large areas through the use of digital terrain models. Although a stochastic approach may partly solve the problem of insufficient geotechnical and hydrological data, lack of distributed information constrains the applicability of process-based models to areas of limited extent, and mostly to the back analysis of individual rainfall events. This reduces the use of process-based models in operational landslide forecasting systems (Aleotti 2004). A second limitation of process-based models is that, for a given rainfall event, the models predict as unstable an area significantly larger than the area

actually affected by the triggered landslides. The overestimation of the extent of the unstable areas has multiple reasons that must be considered when the model outputs are used in landslide forecasting systems. A different method consists in using process-based models to determine the amount of rainfall (i.e., the critical rainfall) that can result in slope instability, and use this information to forecast possible landslide occurrence during a rainfall event, or using quantitative rainfall forecasts or estimates (Chang et al. 2007; Chiang and Chang 2008).

The second approach to relate landslide occurrence on rainfall measurements consists in the use of empirical thresholds. Empirical rainfall thresholds are defined through the analysis of past rainfall events that have (or have not) resulted in slope failures. The thresholds are usually obtained by drawing lower-bound lines to the rainfall conditions that resulted in landslides plotted in Cartesian, semi-logarithmic, or logarithmic coordinates.

Rainfall thresholds can be classified based on the geographical extent for which they are determined (i.e., global, national, regional, or local thresholds), and the type of rainfall information used to establish the threshold (Guzzetti et al. 2007, 2008). Based on the geographical extent, rainfall thresholds can be subdivided in global, national, regional, or local thresholds. A global threshold attempts to establish a general (“universal”) minimum level below which

landslides do not occur, independently of local morphological, lithological and land-use conditions and of local or regional rainfall pattern and history. National thresholds are similar to global thresholds, and are established using information for a single nation (e.g., Brunetti et al. 2010). Regional thresholds are defined for areas extending from a few to several thousand square kilometers of similar meteorological, climatic, physiographic, and soil characteristics. Local thresholds consider the local climatic regime and geomorphic setting, and are applicable to single landslides or to groups of landslides in areas extending from a few to some hundreds of square kilometers. Regional and local thresholds perform reasonably well in the area where they were developed, but cannot be easily exported to neighbouring areas. Global thresholds are relevant where local or regional thresholds are not available, but may result in false positives, i.e., prediction of landslides that do not occur (Table 1).

Based on the rainfall measurements, empirical rainfall thresholds can be grouped in three broad categories: (i) thresholds that combine precipitation measurements obtained for specific rainfall events (e.g., Caine 1980; Innes 1983; Cancelli and Nova 1985; Corominas and Moya 1999), (ii) thresholds that include the antecedent rainfall and soil moisture conditions (e.g., Terlien 1998; Crozier 1999; Glade 2000; Chleborad 2003; Aleotti 2004), and (iii) other thresholds (e.g.,

Table 1 Threshold types based on the extent of the study area

Type	Area	Characteristics	Pros	Cons
Global	World	Are independent of local conditions and rainfall pattern	Useful where other thresholds are not available	May result in numerous false positives
Regional	From few to several thousands of km ²	Group areas with similar meteorological, climatic, and physiographic characteristics	Suited for landslide warning systems	Cannot be easily exported to neighboring areas
Local	From few to some hundreds of km ²	Dependent on the local climatic regime and geomorphological setting	Suited for warning systems on a single or a group of landslides	Cannot be easily exported to neighboring areas

Characteristics, pros and cons are also listed

Jakob and Weatherly 2003). Thresholds using combinations of rainfall measurements can be subdivided in four subcategories: (i) rainfall mean intensity-duration (*ID*) thresholds; (ii) thresholds based on the total event rainfall; (iii) cumulated event rainfall-duration (*ED*) thresholds; and (iv) cumulated event rainfall-intensity (*EI*) thresholds (for a review see Guzzetti et al. 2007, 2008).

3 *ID* and *ED* Rainfall Thresholds

Mean intensity-duration (*ID*) thresholds are the most common type of thresholds proposed in the literature. *ID* thresholds have the general form of a negative power law.

$$I = \alpha \times D^{-\beta} \tag{1}$$

In the equation, *I* is the rainfall mean intensity, *D* is the duration of the rainfall event, α is a scaling parameter (the intercept), and β is the shape parameter that controls the slope of the threshold curve. Note, that in logarithmic coordinates the power law curve is a straight line. Cumulated event rainfall-duration (*ED*)

thresholds are also common in the literature. *ED* thresholds have also the format of a power law.

$$E = \alpha \times D^\gamma \tag{2}$$

In the equation, *E* is the cumulated event rainfall, *D* is the duration of the rainfall event, α is a scaling parameter, and γ is slope of the threshold curve. Note that $\gamma = -\beta + 1$, where β is the slope of the corresponding *ID* power law threshold.

Figure 1 shows two examples of *ID* and *ED* rainfall thresholds for Italy, which are the blue lines in the left and right graph, respectively.

Guzzetti et al. (2007, 2008) highlighted the need to adopt objective and reproducible methods to define and validate rainfall thresholds for the possible occurrence of rainfall-induced landslides. Brunetti et al. (2010) proposed a frequentist statistical method for the definition of objective and reproducible empirical rainfall thresholds, and used their method to determine rainfall thresholds of the *ID* type for Italy. Specifically, the ensemble of the rainfall *ID* conditions responsible for the known slope failures is fitted with a power law (Fig. 2a). For each event, the difference $\delta(D)$ between the rainfall intensity and the fit is calculated. The probability

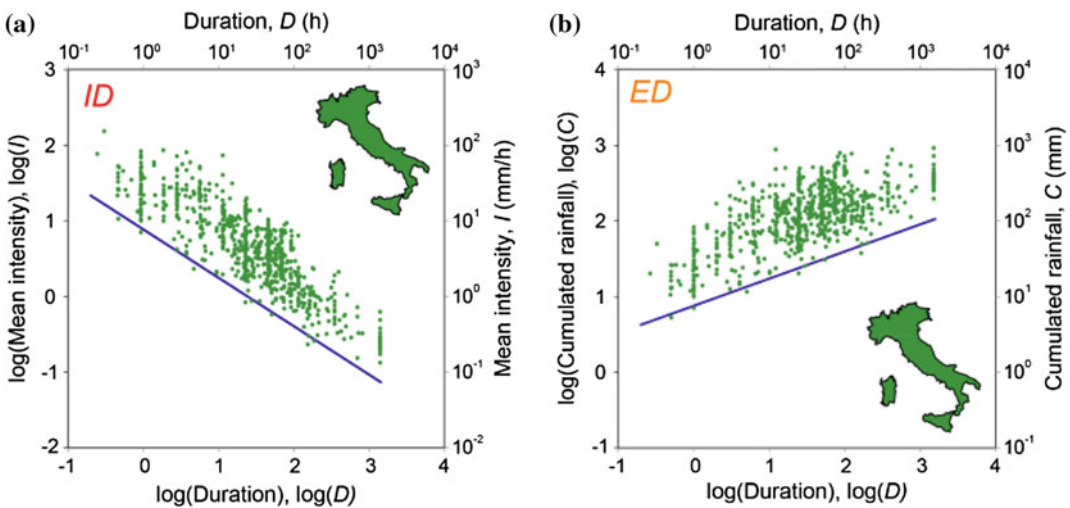


Fig. 1 a Intensity-rainfall duration (*ID*) and b cumulated event rainfall-rainfall duration (*ED*) thresholds for Italy

density of the distribution of the differences is determined through a Kernel Density approach, and the result modeled with a Gaussian function (Fig. 2b). Using the modeled distribution, thresholds corresponding to different exceedance probabilities are calculated. As an example, Fig. 2c portrays the 5% threshold as a red solid line. The distance δ between the red line and the mean of the distribution (solid grey line) is used to calculate the intercept of the 5% threshold curve. Assuming the set of the empirical (D, I) points is complete and representative of the conditions that led to slope failures in a study area, the 5% threshold is the curve that should leave 5% of the rainfall events with landslides below the threshold.

Peruccacci et al. (2012) adopted the same frequentist method, and modified it to determine

ED thresholds for possible landslide occurrence. The method assumes the threshold curve is a power law:

$$E = (\alpha \pm \Delta\alpha) \times D^{(\gamma \pm \Delta\gamma)} \tag{3}$$

where, E is the cumulated (total) event rainfall (in mm), D is the duration of the rainfall event (in h), α is the scaling parameter, γ is the slope of the power law threshold curve, and $\Delta\alpha$ and $\Delta\gamma$ are the uncertainties associated to α and γ , respectively. The mean values of the two parameters, and the associated uncertainties were estimated adopting a “bootstrap” statistical technique.

Figure 3a, b show the same threshold, and the associated uncertainty, in logarithmic coordinates (to the left) and in linear coordinates (to the right). The shaded area around the threshold line

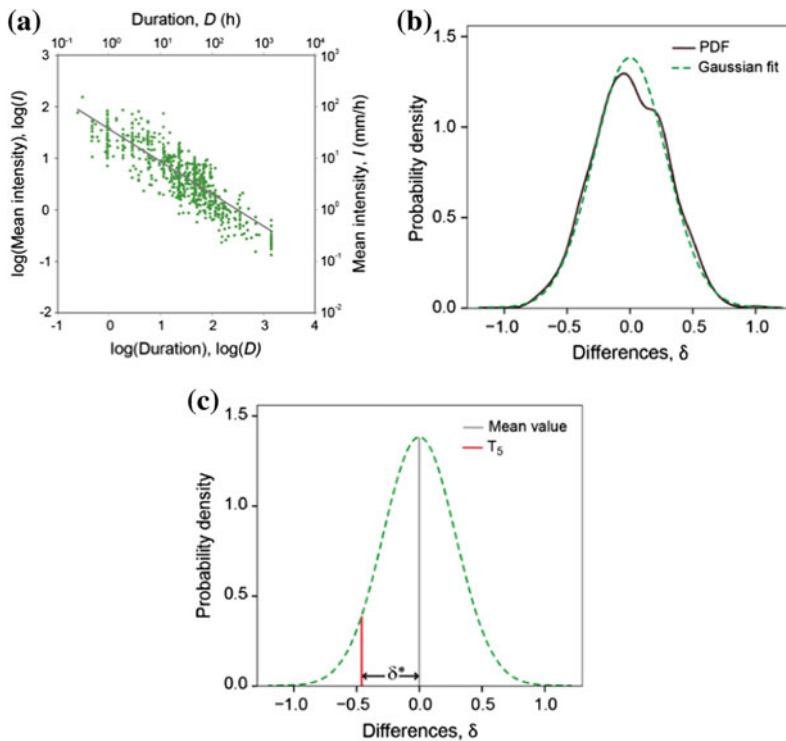


Fig. 2 **a** Rainfall events that have resulted in landslides, for which the rainfall duration D (in h) and the rainfall mean intensity I (in mm h^{-1}) are known. The *black line* is a fit (least square method) of the empirical rainfall (D, I) conditions. **b** Kernel density estimation of the

differences $\delta(D)$ (in *black*), fitted with a Gaussian function (in *green*) for the distribution of the empirical data points (D, I) . **c** Graphical representation of the threshold corresponding to the 5% exceedance probability (T_5)

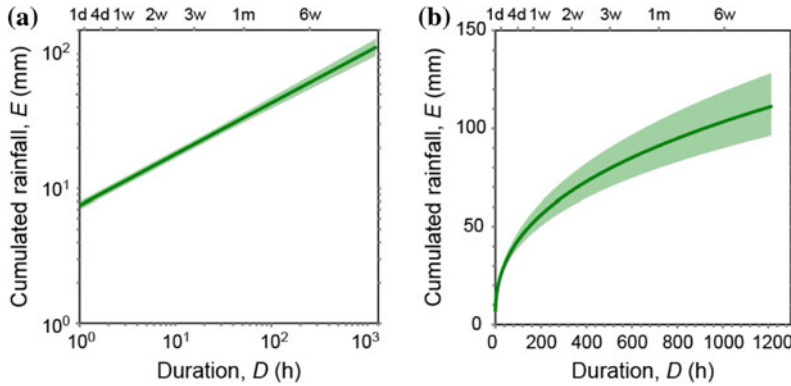


Fig. 3 ED thresholds for Italy in **a** logarithmic and **b** linear coordinates. The *shaded areas* in the two graphs represent the threshold uncertainties

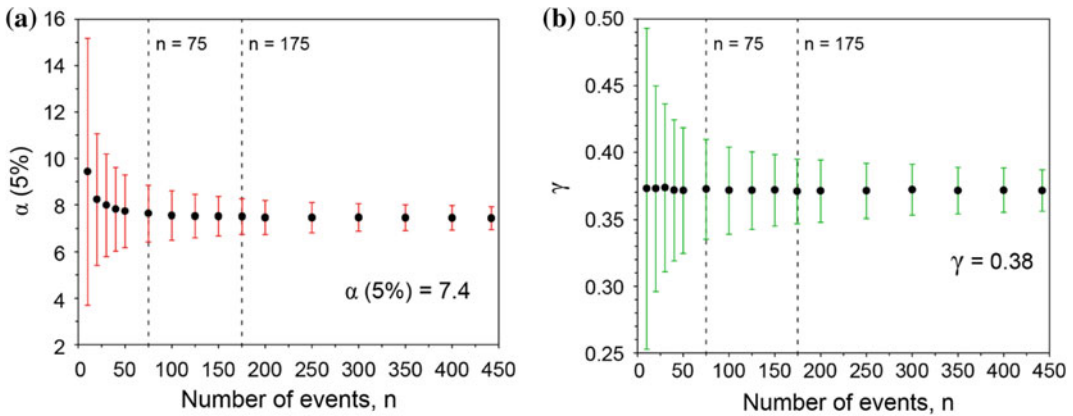


Fig. 4 Variation of the threshold model parameters α , γ , and their uncertainty $\Delta\alpha$ and $\Delta\gamma$, as a function of the number of events n for the 5% exceedance probability levels. **a** Variations of the threshold curve model

parameter α . *Red vertical bars* show range of variation of α for different n . **b** Variations of the threshold curve model parameter γ . *Green vertical bars* show range of variation of γ for different n

represents the uncertainty associated with the definition of the threshold, given the empirical data.

Small values of $\Delta\alpha$ and $\Delta\gamma$ are associated to less uncertain (more robust) thresholds, insensitive to the addition of new empirical data points (i.e. new rainfall events with landslides). With a bootstrap technique, the dependence of α and γ on the number of events was evaluated for the 5% exceedance probability level. The uncertainties associated with the model parameters, represented by the colored error bars in Fig. 4a, b, decrease as the number of events increases. For a number of events less than 75, the

uncertainties of the two parameters α and γ are high. For a number of events larger than 175, the uncertainties of the two parameters α and γ are low.

4 Study Area

Here, we present some results for an area (AMU) that includes three administrative regions in central Italy, Abruzzo, Marche and Umbria (Peruccacci et al. 2012). The study area is about 28,600 km². The study area pertains to the central Italian Apennines, elevation ranges from sea

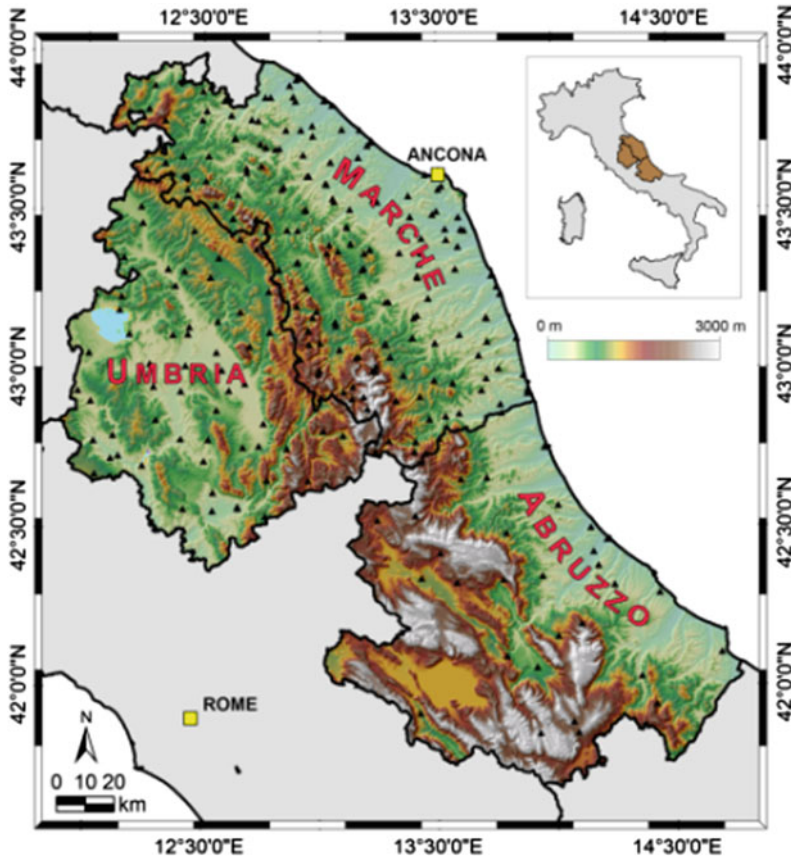


Fig. 5 Map of the study area, central Italy, including the Abruzzo, Marche, and Umbria regions. *Shades of color* show elevation, from a 90 × 90 m DEM obtained by the

NASA Shuttle Radar Topography Mission in February 2000. *Black triangles* show location of 150 rain gauges

level, along the Adriatic coast, to 2914 m at the Gran Sasso d'Italia (Corno Grande). Climate in central Italy is Mediterranean with distinct wet and dry seasons. In the area, mean annual precipitation ranges from <600 mm along the Adriatic coast, to >1400 mm along the mountain ranges. For the Abruzzo, Marche, and Umbria regions a catalogue of 442 rainfall events with 573 landslides occurred between February 2002 and August 2010 was compiled. For each event, the duration *D* (in h) and the total event rainfall *E* (in mm) was determined using rainfall measurements obtained from a dense network of 150 rain gauges, shown by black triangles in Fig. 5.

Landslides of all types are abundant in AMU, and locally cover more than 8% of the slopes. The information on rainfall induced landslides

was obtained searching: (i) national, regional and local newspapers; (ii) blogs and on-line sources; (iii) reports of local Fire Brigades; and (iv) reports of CCISS (Italian agency that provides traffic and travel information).

5 Regional Rainfall Thresholds

A preliminary *ED* threshold for the entire study area was defined. Figure 6 shows, in logarithmic coordinates, the distribution of rainfall duration and cumulated event rainfall conditions that have resulted in landslides in Abruzzo (blue dots), Marche (grey dots), and Umbria (red dots). The brown line is the 5% *ED* threshold for the entire data set and the inset shows the same threshold in

Fig. 6 Rainfall conditions that have resulted in landslides in Abruzzo (blue dots), Marche (grey dots), and Umbria (red dots), central Italy. Brown line is the 5% ED power law threshold for the entire study area ($T_{5,AMU}$). Data shown in logarithmic coordinates. Inset shows the same $T_{5,AMU}$ threshold in linear coordinates, with shaded area showing uncertainty around the threshold curve

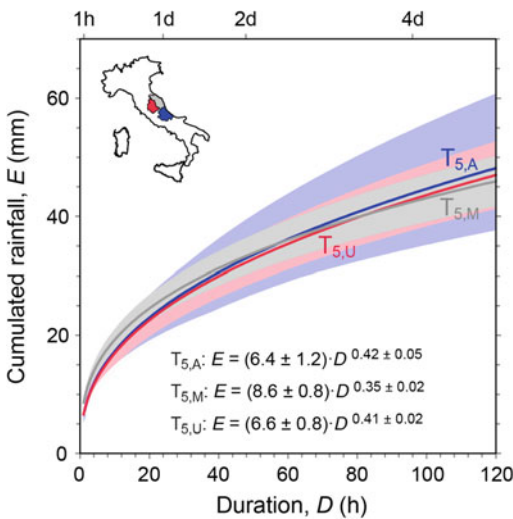
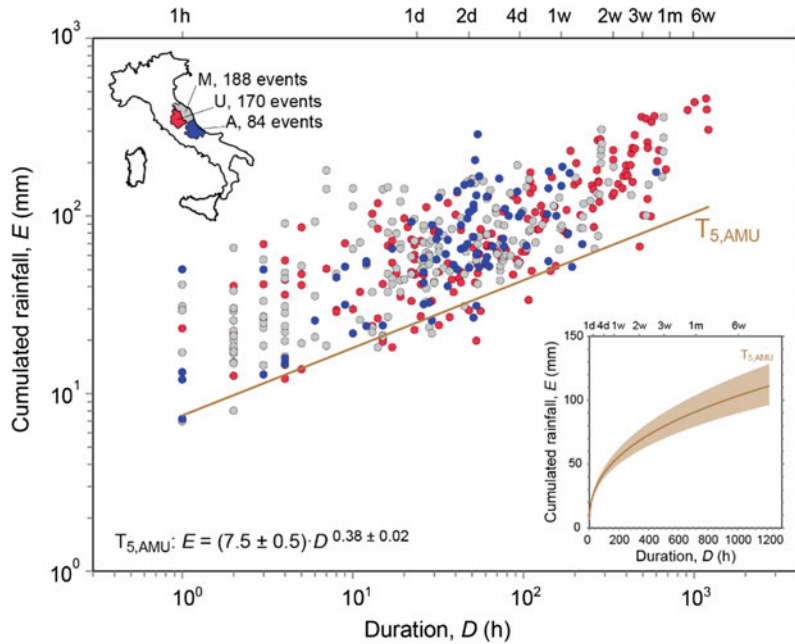


Fig. 7 ED thresholds for Abruzzo (in blue), Marche (in grey), and Umbria (in red), central Italy. Solid colored lines are 5% ($T_{5,A}$, $T_{5,M}$, $T_{5,U}$) thresholds. Shaded areas show uncertainty around the threshold curves. Data shown in linear coordinates in the range $1 \leq D \leq 120$ h

linear coordinates, with the shaded area showing the uncertainty associated to the threshold.

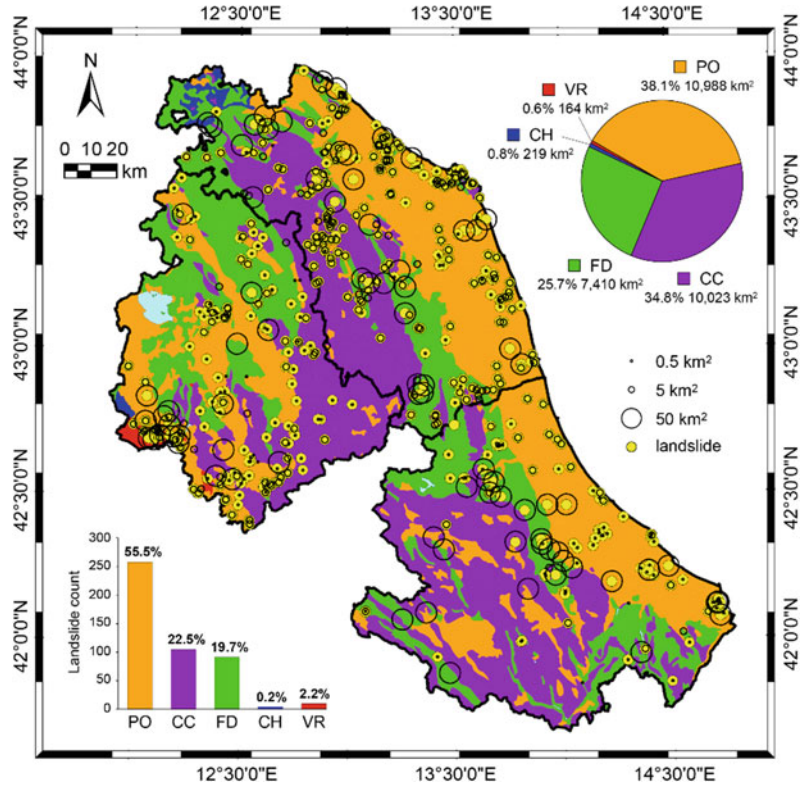
Figure 7 shows, in linear coordinates, the 5% ED thresholds and their uncertainties for the three individual regions. As shown in Fig. 4, the

uncertainty depends mainly on the size of the catalogue (for instance, compare 84 events in Abruzzo to 188 events in Marche). Due to the uncertainties, the ED thresholds for the Abruzzo, Marche, and Umbria regions are statistically indistinguishable.

6 Lithological Rainfall Thresholds

To investigate the relationships between lithology and rainfall thresholds, each landslide in the catalogue was attributed to a lithology type using a 1:500,000 scale lithological map that shows five main complexes, namely In the study area, five main lithological complexes are present, namely: (i) post-orogenic sediments (PO) including continental and marine clay, silt, sand, gravel, and travertine; (ii) flysch deposits (FD), comprising well-stratified, graded marl, sandy shale, and mud, orderly interbedded with greywacke's, coarse and fine sandstone, calcarenite, and gypsum deposits; (iii) carbonate rocks (CC), comprising massive and layered limestone, chert, marl, and shale; (iv) chaotic complex (CH), a mélange of clay, shale, marl, sandstone, and calcarenite; and (v) volcanic rocks (VR),

Fig. 8 Lithological map of the study area. *PO* post-orogenic sediments complex, *FD* flysch deposits complex, *CC* carbonate rocks complex, *CH* chaotic deposits, *VR* volcanic rocks complex. *Yellow dots* show location of rainfall-induced landslides. *Black circles* show uncertainty in the location of the landslides, in three classes. *Pie chart* shows extent and percentage of the lithological complexes. *Histogram* shows the number and proportion of landslides in each lithological complex



represented by lava flows, ignimbrites, and pyroclastic deposits (Fig. 8). The pie chart shows the extent and the percentage of the lithological complexes, and the histogram shows the number and the proportion of landslides in each lithological complex.

Landslides, mapped as single points, were attributed a level of mapping accuracy P , in three classes, i.e., $P_1 < 1 \text{ km}^2$, $P_{10} < 10 \text{ km}^2$, $P_{100} < 100 \text{ km}^2$. Each landslide was represented by a circle, with the area of the circle dependent on the mapping accuracy: P_1 , $A = 0.5 \text{ km}^2$; P_{10} , $A = 5 \text{ km}^2$; P_{100} , $A = 50 \text{ km}^2$. The values were selected heuristically, as a compromise between the landslide mapping accuracy and the scale of the lithological map. The landslide circles were then intersected with the lithological map, and a lithological type was attributed to each landslide if it covered 75% of more of the circle.

Landslides that did not satisfy this criterion were excluded from the analysis.

Using this procedure, 381 events were attributed to a specific lithological type. *ED* thresholds for three main lithological complexes (PO, FD and CC) were determined. For the other rock types, the number of events was too small to determine specific thresholds. Figure 9 shows, in logarithmic coordinates, the distribution of the rainfall conditions that have resulted in landslides in PO (orange dots), in FD (green dots), and in CC (purple dots) together with the 5% thresholds for the same three lithological complexes. Figure 10 illustrates the *ED* lithological thresholds in linear coordinates with their relative uncertainties. The green threshold for flysch terrains is systematically higher than (and statistically different from) the equivalent thresholds for the post-orogenic sediments (in orange) and the

Fig. 9 Rainfall conditions that have resulted in landslides in the post-orogenic sediments (PO, orange dots), flysch deposits (FD, green dots), and carbonate rocks (CC, purple dots), in the study area. Colored lines are 5% ($T_{5,PO}$, $T_{5,FD}$, $T_{5,CC}$) power law thresholds. Data shown in log–log coordinates. *Inset* shows distribution of lithological complexes

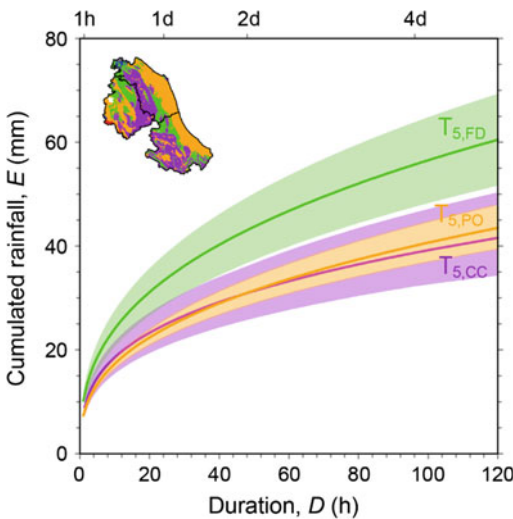
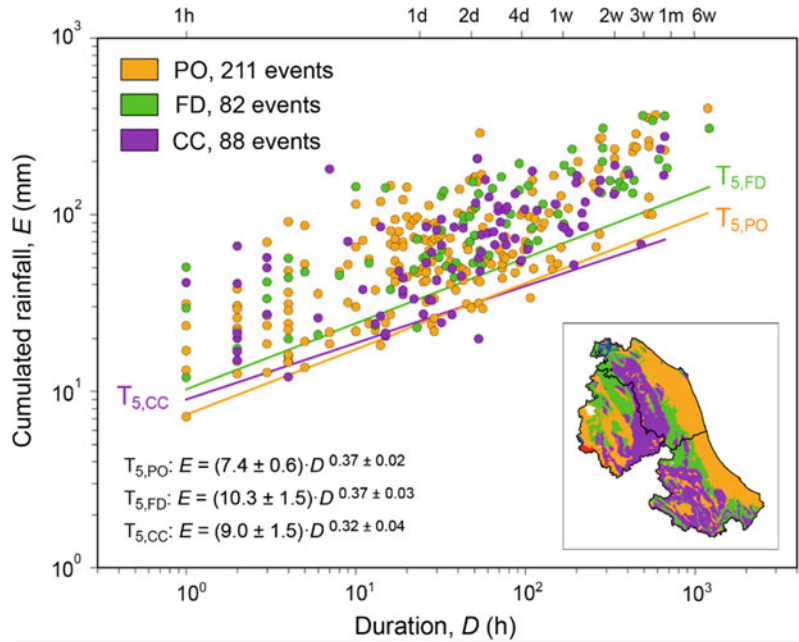


Fig. 10 ED thresholds for the post-orogenic sediments (in orange), flysch deposits (in green), and carbonate rocks (in purple). Solid colored lines are 5% ($T_{5,PO}$, $T_{5,FD}$, $T_{5,CC}$) thresholds. Shaded areas show uncertainty around the threshold curves. Data shown in linear coordinates in the range $1 \leq D \leq 120$ h

carbonate rocks (in purple). This means that the cumulated amount of rainfall necessary to trigger landslides in flysch deposits is higher than in the

other two lithological complexes. Moreover, the thresholds for the post-orogenic sediments and for the carbonate rocks are indistinguishable in the study area.

7 Seasonal Rainfall Thresholds

In AMU climate is Mediterranean, with distinct summer and winter seasons. The different seasons are characterized by different types of meteorological events. In summer, rainfall is associated primarily with convective events characterized by short duration and high intensity. In the period from autumn to spring, abundant rainfall is associated with regional frontal systems, characterized by long duration and low mean intensity. To investigate the effects of the different rainfall types on the rainfall ED thresholds, we segmented the catalogue of rainfall events with landslides by the month of occurrence, and obtained two sets of rainfall events with landslides: (i) one for the period from October to April (OA, 282 events), and (ii) a second for the period from May to September (MS, 160 events). Figure 11a, b show the

Fig. 11 **a** Proportion of rainfall events for different rainfall durations. **b** Proportion of rainfall events with landslides for different subsets. **c** Number of rainfall events with landslides in the MS months. **d** Number of rainfall events with landslides in the OA months

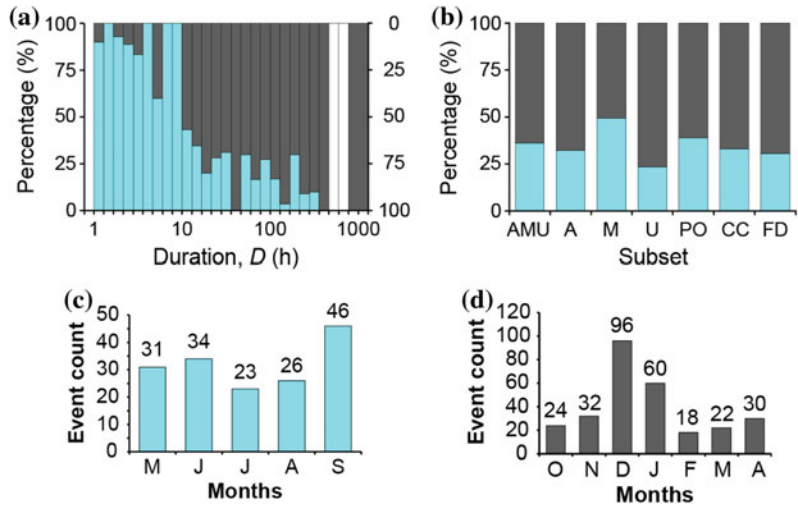
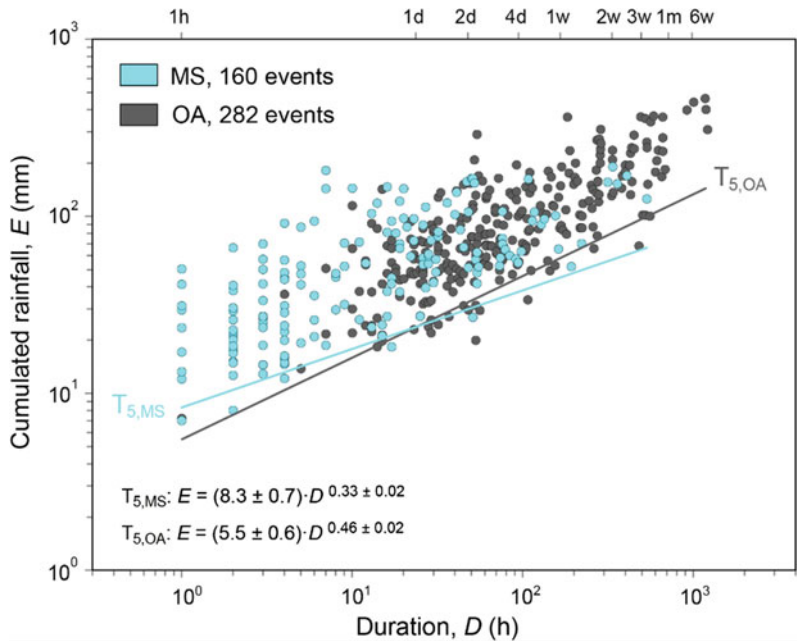


Fig. 12 Rainfall conditions that have resulted in landslides in the period May–September (MS, light blue dots), and for the period October–April (OA, dark grey dots). Colored lines are 5% ($T_{5,MS}$, $T_{5,OA}$) power law thresholds. Data shown in logarithmic coordinates



proportion of rainfall events for different rainfall durations and the proportion of rainfall events with landslides for different subsets, respectively. Figure 11c, d portrays the monthly number of rainfall events with landslides in the MS and the OA periods.

Figure 12 shows, in logarithmic coordinates, the ensemble of the rainfall conditions that have resulted in landslides in the MS (light blue dots), and OA (grey dots) periods together with the 5%

thresholds for the two seasonal periods. Light blue dots predominate for rainfall duration less than 24 h, and grey dots are more abundant for rainfall duration larger than 24 h. Figure 13 illustrates the seasonal thresholds, in linear coordinates, with the uncertainty portrayed by the shaded areas.

Due to the uncertainty, the seasonal thresholds are statistically different only for rainfall durations shorter than 12 h and longer than 4 days. In

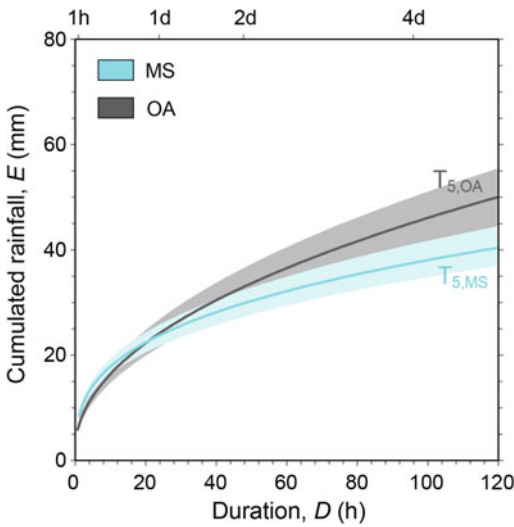


Fig. 13 *ED* thresholds for the periods **a** May–September (MS), and **b** October–April (OA). Solid colored lines are 5% ($T_{5,MS}$, $T_{5,OA}$) thresholds. Shaded areas show uncertainty around the threshold curves. Data shown in linear coordinates in the range $1 \leq D \leq 120$ h

the intermediate range of durations, the seasonal thresholds are statistically indistinguishable in AMU.

8 Comparison with Existing Rainfall Thresholds

The regional, lithological and seasonal *ED* rainfall thresholds defined in AMU are compared with similar thresholds for possible landslide occurrence in Italy and globally (Fig. 14). Thresholds for AMU are shown with an *ED* threshold derived from the 5% national ID threshold proposed for Italy by Brunetti et al. (2010) (dashed black curve), and with the global *ED* threshold for the possible occurrence of debris flows proposed by Innes (1983) (dotted black line).

The *ED* thresholds for central Italy indicate that landslides in the study area are triggered by

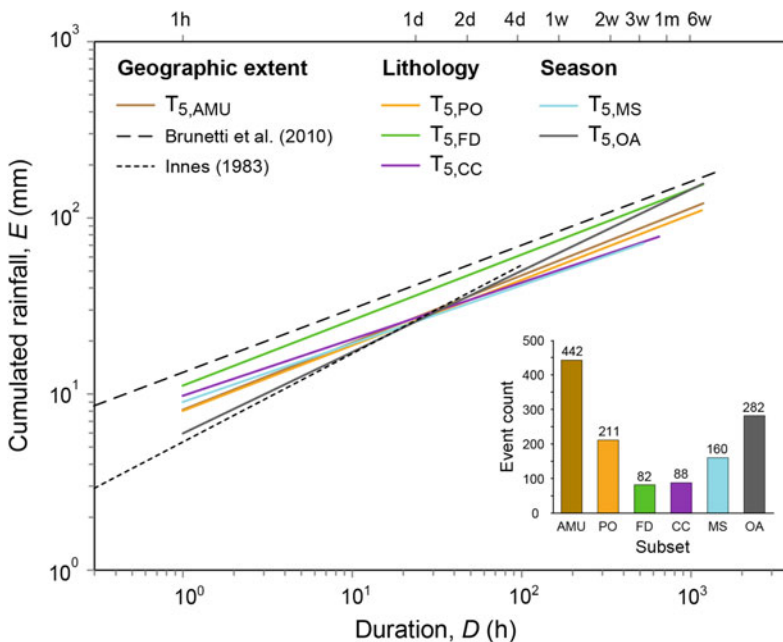


Fig. 14 Comparison of cumulated event rainfall–rainfall duration (*ED*) thresholds for possible landslide occurrence in Italy, and worldwide. Colored thresholds are 5% frequentist threshold for central Italy of Peruccacci et al. (2012). Dashed black line is derived from the 5%

frequentist threshold for Italy of Brunetti et al. (2010). Dotted black line is the global *ED* threshold for debris flows of Innes (1983). Data shown in logarithmic coordinates. Bar chart shows count of rainfall events with landslides, for different subsets

less severe rainfall conditions than previously recognized. This has consequences for landslide forecasting, and for hazard and risk assessment.

References

- Aleotti P (2004) A warning system for rainfall-induced shallow failures. *Eng Geol* 73:247–265
- Brunetti MT, Peruccacci S, Rossi M, Luciani S, Valigi D, Guzzetti F (2010) Rainfall thresholds for the possible occurrence of landslides in Italy. *Nat Hazards Earth Syst Sci* 10:447–458
- Brunetti MT, Peruccacci S, Antronico L, Bartolini D, Deganutti AM, Gariano SL, Iovine G, Luciani S, Luino F, Melillo M, Palladino MR, Parise M, Rossi M, Turconi L, Vennari C, Vessia G, Viero A, Guzzetti F (2015) Catalogue of rainfall events with shallow landslides and new rainfall thresholds in Italy. In: Lollino G et al (eds) *Engineering geology for society and territory*, vol 2: landslide processes. Springer, Berlin, pp 1575–1579
- Caine N (1980) The rainfall intensity-duration control of shallow landslides and debris flows. *Geogr Ann A* 62:23–27
- Campbell RH (1975) Soil slips, debris flows, and rainstorms in the Santa Monica Mountains and vicinity, southern California. In: *US Geological Survey Professional Paper 851*. U.S. Government Printing Office, Washington
- Cancelli A, Nova R (1985) Landslides in soil debris cover triggered by rainstorms in Valtellina (central Alps—Italy). In: *Proceedings of the 4th international conference and field workshop on landslides*. The Japan Geological Society, Tokyo, pp 267–272
- Chang K, Chiang SH, Lei F (2007) Analysing the relationship between typhoon-triggered landslides and critical rainfall conditions. *Earth Surf Process Landf* 33(8):1261–1271
- Chiang SH, Chang K (2008) Application of radar data to modelling rainfall-induced landslides. *Geomorphology* 103(3):299–309
- Chleborad AF (2003) Preliminary evaluation of a precipitation threshold for anticipating the occurrence of landslides in the Seattle, Washington, Area. *US Geological Survey Open-File Report* 03-463
- Corominas J, Moya J (1999) Reconstructing recent landslide activity in relation to rainfall in the Llobregat River Basin, Eastern Pyrenees, Spain. *Geomorphology* 30:79–93
- Crozier MJ (1999) Prediction of rainfall-triggered landslides: a test of the antecedent water status model. *Earth Surf Proc Land* 24:825–833
- Crosta GB, Frattini P (2003) Distributed modelling of shallow landslides triggered by intense rainfall. *Nat Hazards Earth Syst Sci* 3(1–2):81–93
- Glade T, Crozier MJ, Smith P (2000) Applying probability determination to refine landslide-triggering rainfall thresholds using an empirical “Antecedent Daily Rainfall Model”. *Pure Appl Geophys* 157(6/8):1059–1107
- Guzzetti F, Peruccacci S, Rossi M, Stark CP (2007) Rainfall thresholds for the initiation of landslides in Central and Southern Europe. *Meteorol Atmos Phys* 98:239–267
- Guzzetti F, Peruccacci S, Rossi M, Stark CP (2008) The rainfall intensity-duration control of shallow landslides and debris flows: an update. *Landslides* 5(1):3–17
- Innes JL (1983) Debris flows. *Prog Phys Geogr* 7:469–501
- Iverson RM (2000) Landslide triggering by rain infiltration. *Water Resour Res* 36(7):1897–1910
- Jakob M, Weatherly H (2003) A hydroclimatic threshold for landslide initiation on the North Shore Mountains of Vancouver, British Columbia. *Geomorphology* 54:137–156
- Montgomery DR, Dietrich WE (1994) A physically based model for the topographic control of shallow landsliding. *Water Resour Res* 30(4):1153–1171
- Peruccacci S, Brunetti MT, Luciani S, Vennari C, Guzzetti F (2012) Lithological and seasonal control of rainfall thresholds for the possible initiation of landslides in central Italy. *Geomorphology* 139–140:79–90
- Reichenbach P, Cardinali M, De Vita P, Guzzetti F (1998) Regional hydrological thresholds for landslides and floods in the Tiber River Basin (Central Italy). *Environ Geol* 35(2–3):146–159
- Terlien MTJ (1998) The determination of statistical and deterministic hydrological landslide-triggering thresholds. *Environ Geol* 35(2–3):124–130
- White ID, Mottershead DN, Harrison JJ (1996) *Environmental systems*, 2nd edn. Chapman & Hall, London, p 616
- Wieczorek GF (1996) Landslide triggering mechanisms. In: Turner AK, Schuster RL (eds) *Landslides: investigation and mitigation*. Transportation Research Board, National Research Council, Special Report, Washington, pp 76–90
- Wieczorek GF, Glade T (2005) Climatic factors influencing occurrence of debris flows. In: Jakob M, Hungr O (eds) *Debris flow hazards and related phenomena*. Springer, Berlin, pp 325–362
- Wilson RC (1989) Rainstorms, pore pressures, and debris flows: a theoretical framework. In: Morton DM, Sadler PM (eds) *Landslides in a semi-arid environment*, vol 2. Publications of the Inland Geological Society, California, pp 101–111
- Wilson RC, Wieczorek GF (1995) Rainfall thresholds for the initiation of debris flow at La Honda, California. *Environ Eng Geosci* 1(1):11–12
- Wu W, Sidle RC (1995) A distributed slope stability model for steep forested basins. *Water Resour Res* 31:2097–2110

TXT-tool 4.062-1.1

A Socio-Technical Approach for Landslide Mitigation and Risk Reduction

Dwikorita Karnawati, Teuku Faisal Fathani,
Wahyu Wilopo and Syamsul Maarif

Abstract

This paper highlights the importance of integrating social and technical approaches (a so called a “hybrid socio-technical approach”) as an innovative approach to landslide disaster risk reduction. Such a program is mainly based on multi-disciplinary action and research to support a community empowerment program through public education. The technical approach was developed for mainly geological and geotechnical investigations to analyse and predict susceptibility levels in landslide-prone areas, as well as to develop appropriate technology for hazard mapping and disaster early warning systems. Meanwhile, a social approach was undertaken for analysing and mapping psychological and social conditions in disaster-prone areas. An appropriate strategy and program to implement the produced technology can be thus be formulated. Moreover, it is also important to establish a “community task force” as the driving power for landslide disaster risk reduction, which can sustain the program at the village level. This paper describes the achievements and the current activities of IPL-165 “Development of community-based landslide hazard mapping for landslide risk reduction at the village scale in Java, Indonesia”.

Keywords

Hybrid socio-technical system • Indigenous technology
Life and environmental protection • Community empowerment

D. Karnawati (✉) · W. Wilopo
Center for Disaster Mitigation and Technological
Innovation (GAMA-InaTEK), Department of
Geological Engineering, Universitas Gadjah Mada,
Jl. Grafika No. 2, Yogyakarta 55281, Indonesia
e-mail: dwiko@ugm.ac.id

W. Wilopo
e-mail: wwilopo@gadjahmada.edu

T.F. Fathani
Department of Civil and Environmental
Engineering, Universitas Gadjah Mada, Jl. Grafika
No. 2, Yogyakarta 55281, Indonesia
e-mail: tfathani@ugm.ac.id

S. Maarif
National Agency for Disaster Management, Jl. Ir.
H. Juanda 36, Jakarta, Indonesia

Contents

1 Introduction	622
2 Socio-technical Challenges for Landslide Disaster Risk Reduction	622
3 Hybrid Socio-technical Concept for Landslide Disaster Risk Reduction	622
4 Implementation of the Hybrid Socio-technical System	623
5 Development of a Technical System	623
5.1 Early Warning Instruments.....	623
5.2 Smart Grid for Landslide Hazard Monitoring and Early Warning.....	625
5.3 Community-Based Hazard Map.....	626
6 Development of the Social System	627
7 Discussion	628
8 Conclusion	629
References.....	630

1 Introduction

Situated in a dynamic geological region, in which the population density is high, Indonesia is frequently struck by various types of geological disasters, which have led to substantial death tolls, casualties and socio-economic loss. According to the Indonesian National Agency for Disaster Management, Indonesia has been struck by 6632 natural disaster events (mainly geological disasters) within the period from 1997 to 2009, with a total death toll of 151,277 people. Therefore, it is urgent to develop appropriate geo-disaster mitigation processes for life protection and environmental sustainability, through the improvement of society resiliency in such disaster-prone areas.

2 Socio-technical Challenges for Landslide Disaster Risk Reduction

Landslides are among the most frequently occurring disasters in Indonesia. Because of the geological conditions and the high rainfall, more than 50% of the Indonesian region is prone to landslides. It is commonly found that soils in these regions are fertile, with abundant amounts

of water resources and beautiful scenery. This is why most of the landslide-prone areas have been developed as villages or cities with a high population density, such as in Java and Sumatera. As a result, the risk of landslide disasters seriously increases in response to the continuous growth of population and uncontrolled changes in land use. Indeed, thousands of people have died, several thousands of houses have been damaged and thousands of hectares of land have been buried due to landslide disasters. Accordingly, the improvement of community resilience in landslide-prone areas has become a critical challenge that should be tackled through appropriate approaches, technology and capacity development programs, as suggested by Karnawati et al. (2009), Anderson et al. (2010, 2011), and also Halcombe et al. (2012), in order to ensure human survivability and environmental sustainability.

The development of hazard maps and the application of appropriate technologies for early warning systems are considered to be crucial in reducing the risk of landslide disasters. Unfortunately, effectiveness in implementing the production of hazard maps and an early warning system cannot be guaranteed due to the lack of consideration of the social-cultural and socio-economical conditions in the disaster-prone areas. Accordingly, the need to integrate social considerations into technical systems should be addressed in order to assure effectiveness in the construction of hazard maps and early warning systems for disaster risk reduction.

3 Hybrid Socio-technical Concept for Landslide Disaster Risk Reduction

To ensure effectiveness in implementing any technologies for disaster risk reduction, a combined (hybrid) system, which takes into account both social and technical conditions has been developed by Karnawati et al. (2009, 2011). Such an approach mainly consists of the

development of technical systems for providing community landslide hazard/risk maps and early warning systems, and also the social systems for developing an appropriate community empowerment program.

The technical system is recommended to address the development of methods utilizing the existing indigenous or local knowledge and technology, through considering the simplicity of such systems and technologies. Moreover, the utilization of local materials should be promoted, by encouraging local knowledge (by local experts and local operators) to drive the local participation program. Indeed, it is important that the hybrid system should involve low cost and simple technology, approaches and methods, so that it can be easily understood, reproduced, operated and maintained by the local community, such as suggested by Karnawati et al. (2009, 2011). This empowerment program relies on public education and encouraging community participation in developing and implementing action plans for disaster mitigation and risk reduction. A schematic concept of this approach is illustrated in Fig. 1.

All of these approaches can be successful only if the local community has been empowered. Therefore, the process of technology development can be carried out during or as a part of the process of community empowerment.

4 Implementation of the Hybrid Socio-technical System

A hybrid socio-technical system has been implemented in one pilot area in Central Java, notably in Karanganyar Regency. This Regency is situated on the western slope of Lawu Volcano, in which 30% of the region is highly at risk from landslides (high susceptibility indicated by the red color in the map in Fig. 2) due to the geology and climate conditions, and also because of the high human vulnerability due to social and

economic conditions in the landslide-prone area (Karnawati et al. 2009, 2011).

Managing the social conditions in order to reduce vulnerability in the landslide-prone area is considered to be more feasible than changing the natural conditions, such as the geology and climate. Thus, the landslide disaster risk reduction in the pilot study area was conducted by targeting the social conditions through adaptive management, as suggested by Andayani et al. (2008), Karnawati et al. (2009, 2011), and also Halcombe et al. (2012). They emphasized improving community resilience by implementing a hybrid socio-technical approach.

5 Development of a Technical System

A technical system for landslide disaster risk reduction was developed by Karnawati et al. (2009, 2011, 2012). It consists of several technical components, such as the instruments for a landslide early warning system recommended by Fathani et al. (2008) and Fathani and Karnawati (2009), supported by a smart-grid for landslide hazard communication, monitoring and early warning developed by Karnawati et al. (2012), as well as the community-based landslide hazard map suggested by Karnawati et al. (2010).

5.1 Early Warning Instruments

The early warning instruments were designed by relying on manual extensometers connected with an alarm powered by a dry battery, as illustrated in Fig. 3a. Each of these instruments has a wire installed across the growing crack, so that the progress of crack development due to the slope movement can be monitored. The instalment of extensometers was also supplemented by a rain-gauge, as illustrated in Fig. 3b, and a solar panel; so two different warning levels can be defined. The first threshold of warning was set up

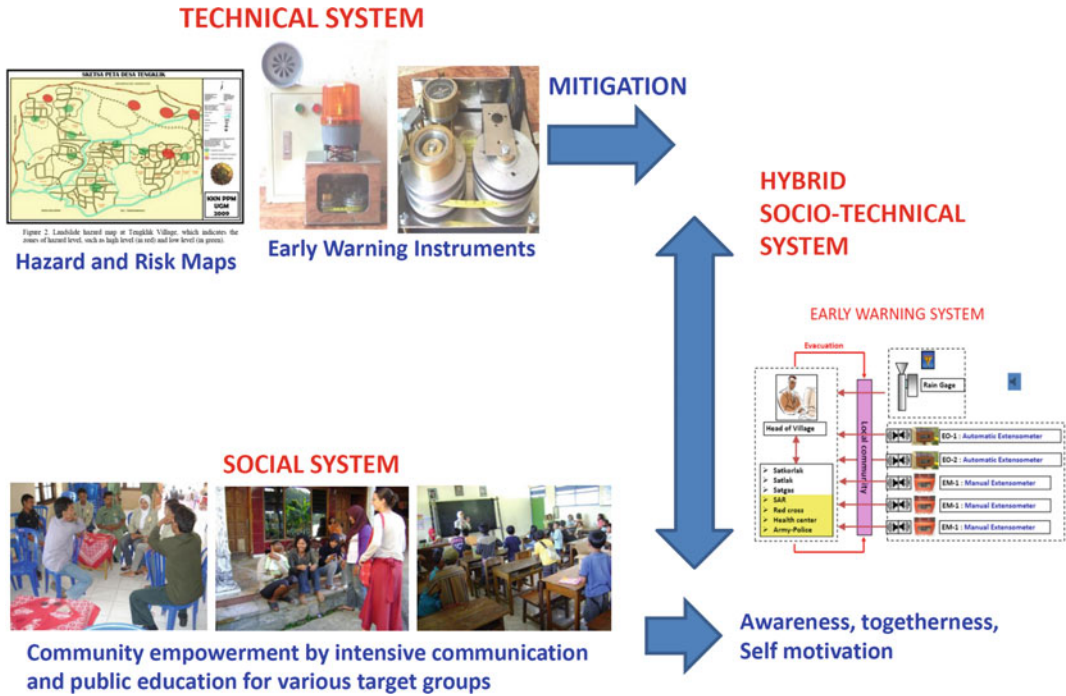


Fig. 1 The concept and key components of a hybrid socio-technical system for landslide mitigation and an early warning system (Karnawati et al. 2009, 2011)

Fig. 2 Landslide susceptibility map of Karanganyar Regency, Central Java, Indonesia, on a regional scale of 1:100,000 (Karnawati et al. 2009, 2011)

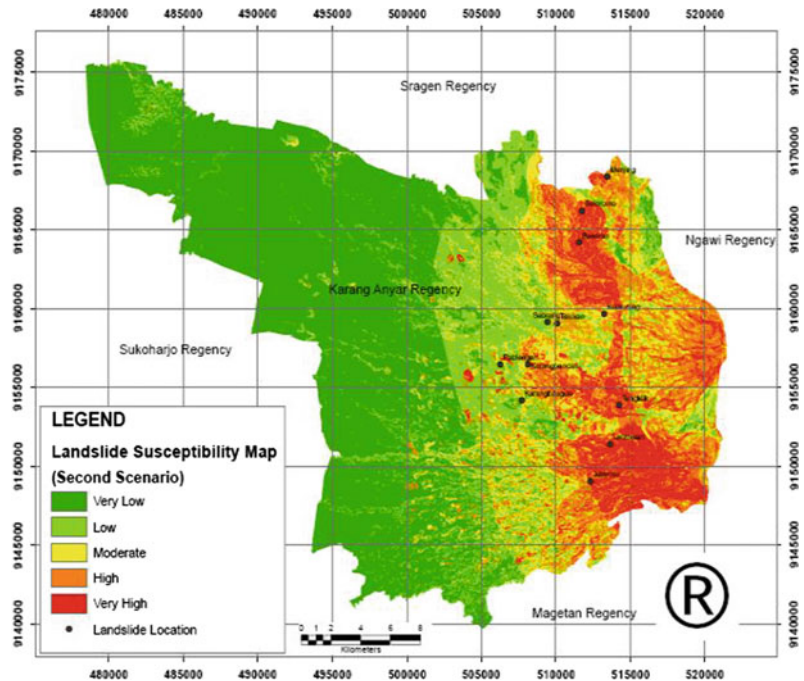


Fig. 3 Early warning instruments, consisting of (a left and right) the extensometer and (b left) the rain gauge, which also manually linked to the traditional “kentongan” (b right)



by setting the ON alarm in response to precipitation of 70 mm/h or cumulative rainfall of 100 mm, whilst the second threshold was defined when the extension of the wire crossing the crack reached the distance of 5 cm. The first alarm was used for raising a community alert, and the second alarm was set up for starting evacuation in the landslide-prone zone.

It was also crucial that all of the alarm warning instruments were also manually backed-up by a traditional tool—a “kentongan” made of bamboo or wood (Fig. 3b right). This system, which combines the developed early warning instruments and the traditional or local warning system allowed a wider spread of the warning alarm sound. Admittedly, the numbers of early warning instruments are limited, and were not sufficient to cover the large area of the landslide-prone zone. Therefore, a smart grid for landslide early warning has been developed by Karnawati et al. (2012).

5.2 Smart Grid for Landslide Hazard Monitoring and Early Warning

Smart Grid is a participatory cyber-based communication and information system, developed as a system for handling networks of information nodes consisting of local experts, local surveyors, or selected members of the local task force and the contact persons in the local communities. The information is sent to the ‘online’ web or cybersystem, with the specific functions of facilitating data reporting via the online web, mobile phone (text messages), or various other social media. The system will also store and analyse those participatory input-reports (related to the geological/geotechnical conditions and processes that are symptoms or early indications of landslides), for defining the landslide hazard and risk level in any particular site or zone.

Results of the analyses are required to provide support for emergency-decision making, which are related to information on the zone and level of landslide hazard/risk, evacuation routes and shelters, and the recommended methods or approaches for mitigation, preparedness and emergency actions. All of the information about hazard/risk and the guidance for response will be blasted/transmitted back to the respective reporting node, as well as to the other relevant registered nodes. This participatory system can also be connected to various types of social media (mobile phone call/text, Twitter, Facebook, Google+, Yahoo, etc.).

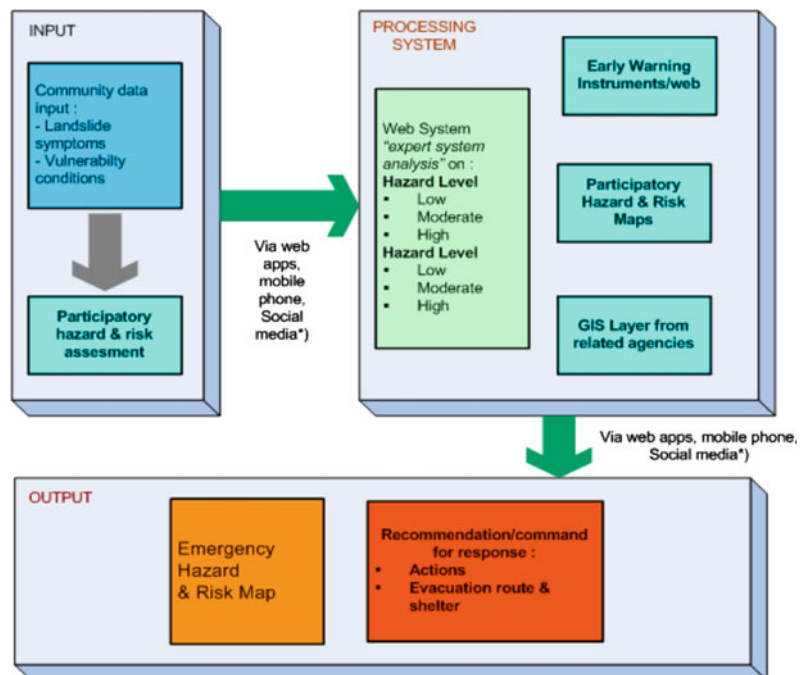
It is also important that the communication flow in this participatory smart grid system is two-way. Such a system can also be linked to the existing community-based landslide early warning instruments developed in parallel with this smart grid system. The concept of the smart grid design is illustrated in Fig. 4, whilst an example of the web performance of a smart grid is displayed in Fig. 5.

5.3 Community-Based Hazard Map

The most critical part in guaranteeing the effectiveness of the disaster risk reduction program is to produce maps that are simple and easy to understand.

Unfortunately, it is apparent that most technical landslide hazard maps were not easily understood by the local community. That is why a simple participatory hazard mapping method was developed by Karnawati et al. (2010), to expedite community landslide hazard mapping, while also addressing the Landslide Risk Assessment and Mitigation Strategy suggested by Lacasse and Nadim (2008). Therefore, the standard technical methods for landslide hazard mapping were simplified, using community participation to prepare a simple landslide hazard map that can be used by the local community and that is based on the existing village base-map (i.e. the village “situation” map). The map was presented without any contours, but mainly showed the layout of roads, rivers, houses and

Fig. 4 Concept of an expert system in the smart grid design developed by Karnawati et al. (2012)



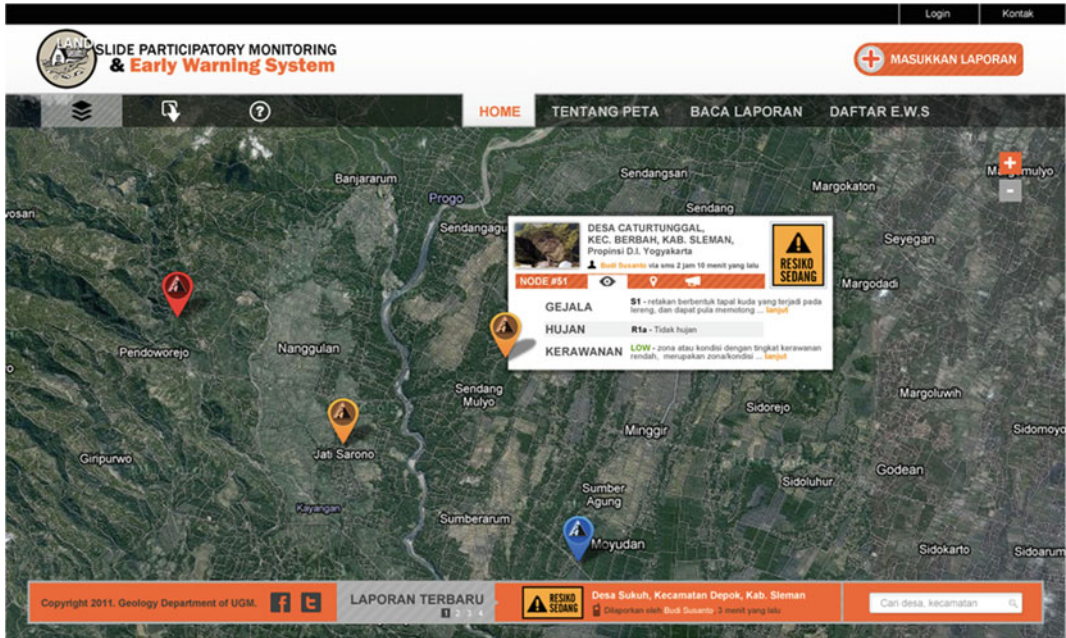


Fig. 5 Web page showing the geographical position of the reporting nodes

land farming areas which could be easily identified by the local community. High susceptible zones (red zone) and low susceptible or safe zones (green zone) for landslides were identified by the community task force through public participation, with the assistance of the local expert. Figure 6 shows the landslide hazard map and evacuation route that was developed by the local community in Koripan Village, Karanganyar Regency, Central Java.

This map is also very important for deciding where the early warning instruments should be installed and how evacuation routes should be chosen.

6 Development of the Social System

Development of the social component in the hybrid system was initiated by social survey, to identify people’s existing knowledge about the landslide hazard, which will affect their perception of the landslide risk and their expectations for the proposed technology for landslide disaster

risk reduction. Those aspects will significantly control their motivation or willingness to actively participate in any disaster risk reduction program. The results of this social survey will be crucial for formulating an appropriate and effective strategy for public education and for raising community awareness and for conducting a community empowerment program.

Various target groups were defined, consisting of the group of women (as the key person in the family), teachers, and children, as well as the younger and senior leaders. The local government of Karanganyar Regency also continuously and actively supported this social development program.

Results of the social survey indicated that most community members had been quite aware of the potential occurrence of landslides during the rainy season, because landslide disasters have quite frequently struck the area they lived in, especially during heavy or long continuous rainfall. Nevertheless, most of the community members preferred to remain living in their vulnerable region, instead of being relocated to the other areas that were safer. Obviously, the

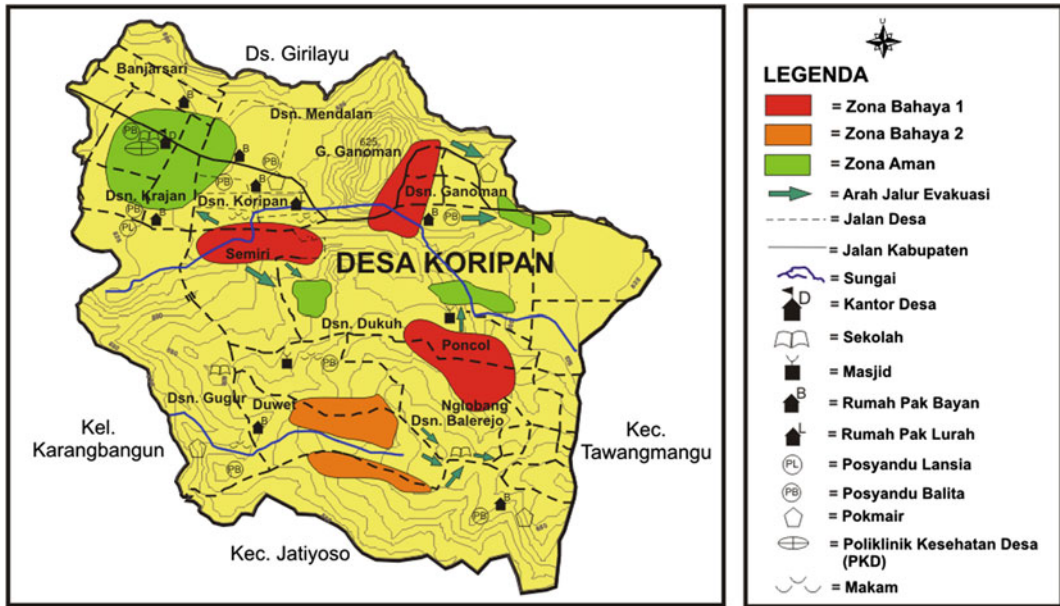


Fig. 6 Community-based landslide hazard map and evacuation route for Koripan Village, Karanganyar Regency, Central Java, indicating zones of hazard level (red is a high hazard level and green is a low level)

fertility of soil, the abundance of water resources, the beauty of the mountain scenery and the strong psychological engagement with their homeland or home-heritage strongly affected their willingness to leave their dangerous homeland. Unfortunately, they did not have enough knowledge, skill and capacity to decide about “what they should do” and “what they should not do” in case of landslides or to protect their life and environment from landslides. They were not yet capable of identifying the sites (slopes) that were susceptible to landsliding, or of recognizing the initial warning signs of possible landsliding. Therefore, the hybrid socio-technical approach for community-based landslide early warning was applied to develop their ability to carry out an appropriate landslide disaster risk reduction program. This will support the improvement of the community resiliency in this landslide-prone area.

A community task-force for disaster risk reduction at the village level was also established in coordination with the Agency for Disaster Management at the Regency level (Fig. 7). This network is also linked to the local hospital

(health centre), the local army and police, and also the Search and Rescue Team (SAR team) at the local Regency. Indeed, this task force was the driving power for the disaster risk reduction program, and also effectively implementing and sustaining the technical systems for landslide risk reduction.

7 Discussion

It was apparent that the existence of a community task force for landslide disaster risk reduction at each village level was the most important factor to ensure the effectiveness and sustainability of the landslide mitigation and risk reduction program. This task force had an important role as the driving agent in the empowerment and mitigation program. In fact, since this proposed hybrid socio-technical approach was implemented in several pilot areas in Karanganyar Regency, such as in Ledoksari Village in 2008, Tengkluk Village in 2009, Matesih Village in 2010, Koripan Village in 2010 and also Gempolan and Plosorejo Villages in 2011, community resilience



Fig. 7 Activities to develop and empower the community task force at Tengklik Village, facilitated by the student community service program conducted by UniversitasGadjahMada

for landslide disasters has gradually increased. The socio-economical losses due to landslides have been minimised and the numbers of landslide victims have dropped to zero. It seems that this approach effectively empowered the local community to mitigate the landslides. The key people, who were also the members of the community task force and were in charge of the mitigation program, were also invited to share their experiences in community empowerment actions to tackle landslide problems in another landslide disaster area in Tanjungsani Village at Agam Regency, West Sumatera.

Therefore, the Hybrid Socio-Technical approach is also very applicable to other disaster-prone areas in developing countries, although several adjustments may be required to address the social and environmental characteristics of the specific community. Moreover, the importance of the commitment and leadership of the local Agency for Disaster Management at the Regency and District levels in supporting the effectiveness of the disaster management program at the village must be highlighted.

It was also obvious that the social, cultural and economical constraints can be minimized during

the mitigation program by using the hybrid socio-technical approach. Indeed, the introduction and implementation of a new technology for early warning and disaster management system can be conducted more effectively through public participation. The enthusiastic response of the local community and local authorities to active participation in the landslide disaster risk reduction program is illustrated in Fig. 7.

8 Conclusion

One of the most critical considerations for disaster risk reduction in Indonesia is the assurance of an effective and sustainable disaster management program. It is apparent that the proposed model, the combined (hybrid) socio-technical approach, has been quite effective in improving community resilience in villages vulnerable to landslides. It is also crucial that the system should be developed through community participation, with the provision of simple and low cost technology for landslide hazard mapping and early warning. Indeed, the establishment of a community task force at the village level is very

important to ensure the effectiveness, continuity and sustainability of this proposed system. This approach may also be used to tackle similar problems of landslide risk reduction in other developing countries in Asia.

Acknowledgements Special thanks are directed to the Indonesian Agency of National Disaster Management, the British Council DelpHE Program, as well as the Directorate General of Higher Education. We are grateful to the Indonesian Ministry of National Education and the Fulbright Senior Research Program funded by US Department of State's Bureau of Education and Cultural Affairs for financial support to carry out the pilot studies. Acknowledgments are also extended to Universitas Gadjah Mada for the provision of academic facilities, as well as to the research assistant at the Laboratory of Environmental Geology and the Computing Laboratory of Civil and Environmental Engineering at Faculty of Engineering, Universitas Gadjah Mada. This research can be successfully conducted was due to the continuous and intensive assistance of Mr. Sani Tanaka Ismawanto, the student of Magister Instrumentation at the Faculty of Engineering, Universitas Gadjah Mada.

References

- Andayani B, Karnawati D, Pramumijoyo S (2008) Institutional framework for community empowerment towards landslide mitigation and risk reduction in Indonesia. In: Proceedings of the 1st world landslide forum, Tokyo, Global Promotion Committee of the International Program on Landslide (IPL)—ISDR, pp 57–59
- Anderson MG, Halcombe E, Esquivel M, Toro J, Ghesquire F (2010) The efficacy of a program of landslide risk reduction in area of unplanned housing in the eastern of caribbean. *Environ Manag* 45:807–821
- Anderson MG, Halcombe E, Blake JR, Ghesquire F, Holm-Nielsen N, Fisseha T (2011) Reducing landslide risk in communities; evidence for the Eastern Caribbean. *Appl Geogr* 31:590–599
- Fathani TF, Karnawati D, Sassa K, Fukuoka H, Honda K (2008) Landslide monitoring, prediction and early warning in Banjarnegara, Indonesia. In: Proceedings of 1st World Landslide Forum, Tokyo, pp 195–198
- Fathani TF, Karnawati D (2009) Early warning of landslide for disaster risk reduction in Central Java Indonesia. In: Proceedings of international workshop on early warning for landslide disaster risk reduction in the Eastern Asian region, Kunming, China
- Halcombe E, Smith S, Wright E, Anderson MG (2012) Integrated approach for evaluating the effectiveness of landslide risk reduction in unplanned communities in the Caribbean. *Nat Hazards* 61:351–385
- Karnawati D, Fathani TF, Andayani B, Burton PW, Sudarno I (2009) Strategic program for landslide disaster risk reduction; a lesson learned from Central Java, Indonesia. In: Duncan K, Brebbia CA (ed) Disaster management and human health risk; reducing risk, improving outcomes. WIT transactions on the built environment transaction. WIT Press, Southampton, pp 115–126
- Karnawati D, Setianto A, Wilopo W, Andayani B, Suharto (2010) Development of community landslide hazard map for landslide risk reduction. In: Proceeding of 11th international association of engineering geologist congress, Auckland, 5–10 Sept 2010. Auckland, New Zealand, pp. 1203–1208
- Karnawati D, Fathani TF, Andayani B, Legono D, Burton PW (2011) Landslide hazard and community-based risk reduction effort in Karanganyar and the Surrounding Area Central Java, Indonesia. *J Mt Sci* 8(2):149–153
- Karnawati D, Frost EG, Fathani TF, Subroto (2012) Smart grid for landslide monitoring and early warning system in Indonesia. In: Proceedings of the 10th Anniversary of ICL, Kyoto (in press)
- Lacasse S, Nadim F (2008) Landslide risk assessment and mitigation strategy. In: Sassa K, Canuti P (eds) Landslide Disaster Risk Reduction. Springer, Berlin, pp 31–61

TXT-tool 4.066-1.1

Community-Based Landslide Risk Management Approaches

Asian Disaster Preparedness Centre (ADPC)

Abstract

In recent times landslides and mass movements have become widespread events, posing great problems and serious challenges to development, especially in mountainous areas of developing nations in Asia. Landslides have increased both in frequency and intensity and have assumed catastrophic and disastrous proportions in a number of countries, causing extensive damage to life and property. Mass movements occur as a result of heavy precipitation or as a secondary hazard triggered by geological events such as earthquakes or volcanic eruptions. In addition to those triggering factors, increases in landslide occurrence have been associated with a combination of factors, including geology, topography, morphometry, climate, and human activities that directly or indirectly contribute to the phenomena of slope instability. Landslides are often triggered in areas with a past history of landslides and reducing the risk due to landslides using community-based approaches is considered as an effective measure for reducing the damage from landslides. In most areas, development activities seem to be responsible for new landslides, as well as reactivation of dormant landslides. The community members are the first responders to any disaster event at local level. Therefore they should understand the signs of impending landslides or slope destabilization, and have knowledge of potential high hazard areas, and ways of avoiding exposure. It is also appropriate to develop hazard maps for landslide-prone areas using community-based risk assessment tools and undertake preparedness planning with affected communities. They also should be warned in time through constant monitoring, and early warning of potential reactivation. In addition, slow-moving slides on hill slopes need constant monitoring, as many developing countries in Asia cannot afford to undertake mitigation measures or to resettle people to safer areas after identification of the potential threat. Hence the purpose of this training session is to create awareness of possible

community-based interventions so that local government level officials will be able to build the capacity of the local or community-level stakeholders on landslide-related issues and involve them actively in landslide risk management activities. In the same way, many landslides are triggered by inappropriate practices in construction on hill slopes, land uses such as agriculture, excavations, and mining practices. Communities living in areas with a history of landslides should understand the factors causing the landslides and mitigation measures that can be undertaken to minimize losses. This session deals with community-based interventions such as hazard, vulnerability and risk mapping, preparedness planning, mitigation interventions and community-level training to improve first responder capacity for early warning evacuation and undertaking preparedness measures at a community level.

Keywords

Participatory risk assessment • Community level early warning
 Community first responders • Risk-resource-evacuation mapping

Contents

1 Importance of Community-Based Disaster Risk Reduction 632

2 Applying Lessons in Community-Based Disaster Risk Reduction (CBDRR) to Landslide Risk Management Practice Using the Bottom-Up Approach Versus the Top-Down Approach 633

3 Conduct Awareness Programs for Different Stakeholders 642

Sources 645

Further Reading 645

impact of such disasters is spread over a larger area. Local communities need to take measures to manage landslide risk in order to ensure safety.

The international community endorsed the Hyogo Framework for Action (HFA) as a strategy that recognized the importance of community participation in disaster risk management. The Hyogo Framework for Action (HFA) is the first plan to explain, describe and detail the work that is required from all different sectors and actors to reduce disaster losses. It was developed and agreed on with the many partners needed to reduce disaster risk—governments, international agencies, disaster experts and many others—bringing them into a common system of coordination. The Hyogo Framework outlines five priorities for action, and offers guiding principles and practical means for achieving disaster resilience. Its goal is to substantially reduce disaster losses by 2015 by building the resilience of nations and communities to disasters. This means reducing loss of lives and social, economic, and environmental assets when hazards strike. As the guiding principle of the Hyogo Framework recognizes that “Preventive measures are most

1 Importance of Community-Based Disaster Risk Reduction

Whatever the scale of hazards, big or small, it is the community that either suffers devastation or survives from the effects of the hazards. The community is the first to be affected and, as such, also become the first/initial responders who manage the emergencies at the household and at the community levels. By managing emergencies well, they can prevent the escalation of these emergencies into disasters. This is true for landslide-prone areas too, as landslides are a local level emergency. Landslides differ from other type of hazards such as earthquakes and floods, in which the

effective when they involve participation at all levels, from the local community through the national government to the regional and international level.”

Madhavi Ariyabandu (at that time representing the Intermediate Technology Development Group—Sri Lanka) cited in a paper presented to the IDNDR Closing Forum in July 1999 the merits of the community-based approaches to disaster management:

- Communities are knowledgeable about their own environment and are often able to predict unfavorable events. They are rich in experience of coping both in preparedness and emergencies. The community coping methods evolve over time, and suit the local socio-economic, cultural and political environment best.
- This approach has the benefit of enabling communities to be more independent of relief during disaster periods and strengthens them to increase their capacities to support their own livelihoods.
- Interventions with community participation have the potential to positively address general socio-economic concerns. Participation will empower them with new knowledge and skills, and develop leadership skills among the community members, which will further strengthen their capacity to contribute to development initiatives.
- The impact of disaster situations on women and vulnerable groups, and also their concerns and capacities to cope and contribute, are different from others. Community-based approaches, which recognize this concern, have the potential to contribute towards the social issue of gender equity.

The empowering nature of community based approaches has the capacity to remove some of the causes of vulnerability, thereby reducing the impact of future extreme natural events.

2 Applying Lessons in Community-Based Disaster Risk Reduction (CBDRR) to Landslide Risk Management Practice Using the Bottom-Up Approach Versus the Top-Down Approach

Practical considerations

- The communities living in landslide-prone areas can understand local opportunities and constraints better.
- The local community members are more interested in understanding the ways of managing the risk, as their survival and well-being are at stake if a landslide hazard strikes.
- Local communities are a most abundant and valuable resource, which need to be mobilized, harnessed and strengthened to cope with local-level hazardous environments such as landslides.

General elements of the bottom-up approach

- Local people are capable of initiating risk reduction measures and sustaining the gains of their own community development.
- While the role of the local government, the private sector and NGOs are important, the primary requirement for sustaining the gains of grassroots development is local leadership and local responsibility.
- A successful bottom-up strategy will include broad-based local participation in comprehensive planning and decision-making, and activities that promote and motivate people to take actions for creating and sustaining a safer environment.
- Opportunities for creating awareness of local hazardous environments, ways of mitigation and preparedness should be used to create understanding based on identified local needs.

- Emphasis should be on improving the utilization and management of local resources.
- Responsible utilization of outside financial assistance is required.
- Replication of a community's success is a powerful factor in continuing local initiatives.
- Responsibility for change rests with those living in the local community.

This session presents various community-level actions that can be undertaken at the local level.

Community-level early warning

Early warning is the provision of timely and effective information, through identified institutions, that allow individuals at risk of a disaster to take action to avoid or reduce their risk and prepare for an effective response.

Early warning systems consist of three elements (UNISDR):

1. Forecasting and prediction of impending events,
2. Processing and disseminating warnings to political authorities and at-risk communities,
3. Undertaking appropriate reaction to warnings.

In designing for community-based early warning, the hazard assessment of the characteristics, nature and behavior of the hazard are specifically used. Aside from warnings from outside sources, the community, through its village officials and the community-based organizations can monitor hazard events through observation of their environment and issue precautionary action advice to other community members.

Warning is given to:

- Inform about hazards and elements at risk,
- Advise on means of protection, preparedness, mitigation, and response to the threat,
- Instruct what, when, how, who, where to do or act.

Key considerations in Early Warning Systems:

1. All stakeholders should have a common understanding of the meaning of the warning (for example, precipitation threshold), early signs of impending landslides and which actions to take when receiving such warnings (e.g., what Ready, Set, Go means; what each precipitation threshold means; what colors such as red, blue, and green mean).
2. Early warning systems should be for specific landslide-prone areas, and culture specific.
3. There should be continuous monitoring and regular updates

Sample:

Warning Level# 1: Standby Stage

Warning Level# 2: Alert Stage

Warning Level# 3: Preparatory Stage

Warning Level# 4: Evacuation Stage

4. Early warnings should include advice on precautionary and protective actions to take.
5. Assignment of personnel and/or committees and the roles and responsibilities in issuing and disseminating the warning should be clear.

Sample:

Volunteers responsible for monitoring the rainfall send their observations to the Municipality Warning Committee. The Warning Committee gives an advisory on warning level to the Head of the Community Disaster Management Committee. The Head of the Community Disaster Management Committee then gives instructions to the volunteers to relay the warning to the community.

6. There should be an early and timely relay of advisories and warnings.
7. Forms and methods to communicate and disseminate warning information are identified and there are fail-safe mechanisms in place (alternative, back-up or redundancy)

Different ways of giving warning in the community:

- Warning boards with numbers or colors to indicate different warning levels
- Putting up different colors of flags
- SMS messages using mobile phones
- House-to-house relay
- Ringing of bells, sirens
- Community sound system, so different parts of the community receive the warning at the same time.
- Vehicle with loud speaker or persons with megaphones going around the community to relay the warning
- Radio and television.

End-to-End Early Warning System Approach (ADPC, Safer Cities 18)

An early warning system (EWS) is described as an end-to-end generally considered to be safe and-end if it connects the technical (upstream) and societal (downstream) components of warning through identified institutions. The effectiveness of an early warning system will depend on the detection technology, as well as socio-economic factors that dictate the manner in which people at the local level can understand and react to disasters.

1. Technical components: The technical components of an early warning system are:
 - The understanding and mapping of hazards and vulnerabilities (risk mapping),
 - Monitoring and forecasting of impending events (technical monitoring and warning, including information and communication technology).

One of the essential components of a comprehensive early warning system is its capability for predicting and detecting hazards. The detection of hazards may require the collection of various types of data.

In the case of landslides, the community can monitor hazards by monitoring and recording rainfall using rain gauges showing the amount of precipitation over time intervals, and by constantly monitoring whether the rainfall reaches the precipitation threshold alerts established by mandated institutions of the local government.

Early and accurate detection as well is required for an efficient communication system and decision making. The lead-time for early warning (for example, the time between the detection of a potential landslide after reaching a given precipitation threshold until a decision is made for evacuation of at-risk families from the area) is limited, and may be merely a few hours, or even minutes.

2. Societal components: The societal components are:

- Processing and disseminating understandable and actionable warnings to political authorities and the population at-risk (dissemination).
- Undertaking appropriate and timely actions to prepare communities to respond to warnings (providing knowledge and procedure for preparedness to act). This will be initiated in advance by identifying and describing the flow of information from the detection of an impending landslide by instrumentation, observation, or reaching the precipitation threshold, to the distribution of the alert to the relevant authorities, identifying communities who are exposed to the potential landslide, and preparing action plans for evacuation and response, evacuation drills, and emergency response actions.

An early warning system should provide communities with timely information, enabling them to prepare for anticipated landslide hazard to minimize the impact on lives, livelihoods and property. This communication should proceed in a way that is easily understandable for people, and causes them to react appropriately to disasters. Community participation in the formation of effective early warning messages can improve the communication process.

Comprehensive early warning systems should have an “end-to-end” approach, addressing all stages of early warning from initial hazard detection and warning to community-level response to warning messages. Also, it should address multi-hazards, for example it will simultaneously

address landslide hazards and number of other critical hazards such as cyclones and floods. For example during cyclones, communities in Chittagong in Bangladesh face all three hazards.

There should be a single authority (national or regional) to originate the hazard warning or provide information on precipitation thresholds in a given area in order to avoid confusion. For example, the Disaster Management Centre is the authority responsible in Sri Lanka for issuing Early Warnings. In addition, there are specific agencies that issue warnings for landslides within their specific technical capacity, such as National Building Research Organization (NBRO).

Next, the hazard warning should be disseminated quickly to the population at risk. In order to make sure the warning is successful, the message should be easily understood and delivered on time. A good communication network/system is vital in disseminating warning messages on time, especially for a disaster that has a low lead-time, such as landslides. It is also effective to use local community warning systems such as loudspeakers and sirens. However, all these are useful only if there is constant monitoring of the alert levels, if the equipment is well maintained, and if names of contact people and the relevant telephone numbers are available and kept up-to-date. This is one area where trained community members can contribute their time and ensure that the “last mile” in the communication relay is closed.

Evacuation

Evacuation is the organized movement of people from an area of risk to a safer location. Evacuation is better as a precaution rather than as a necessity after a disaster has struck.

Phases of Evacuation:

1. Warning
2. Order to move
3. Actual evacuation
4. Evacuation Center management
5. Return to homes or resettlement

Early warning indicators

The question of early warnings of landslides, primarily arise in the following two situations:

- Early warning of a possible re-activation of old landslides or development of new landslides in areas known to be landslide prone.
- Early warning against occurrences of landslides (for the first time) in the areas which are generally considered to be safe and without any significant previous landslide history.

Early warning in areas of known hazard

1. The active monsoon seasons should be designated and declared as the months of intensive hazard patrolling, particularly in areas with a history of landslides. The “taskforce” or volunteers charged with the responsibility of patrolling will have to be trained in the art of observing slopes and gathering and collecting information on the changes in slopes. Timely processing and interpretation of such new data against the backdrop of known information will be a key to warning against impending landslides.

Some of the early symptoms of landslides are listed below to serve as examples (an elaborate check list need to be developed and communities should be trained to observe such signs)

- a. Excessive rainfall spread over long periods of time, particularly unusual or unprecedented events (related thresholds should be developed by a competent authority and provided to community members for necessary observations)
- b. Sudden opening and progressive widening of cracks on the slope surface or on the walls of buildings, houses, and other structures
- c. Progressive or sudden tilting (forward or backward) of trees, poles, towers, etc. located on the slope
- d. subsidence or bulges observed on slopes

- e. sudden oozing or appearances of water on the slope and continuous water logging due to poor slope drainage
- f. Spurts of rock fall activity on unstable upper slopes
- g. subsidence of roads and bulging of road-side retaining walls
- h. usual behavior changes in animals, birds, etc.

The actions required are;

- Establishment of a schedule of patrolling by volunteer teams, data recording and informing the authorities in time.
 - Developing a field manual and training and capacity building for volunteer monitoring teams. For example the communities should be trained to draw sketches or take photographs (mobile phones can be used for this now) and transmit the images to competent professionals.
 - Setting up an expert group who will be readily available for providing necessary advise to communities. Such expert groups can be set up under disaster management key persons or designated mandated institutions.
2. Instrumentation of selected problematic slopes and landslides in critical areas, and continuous monitoring based on observations to provide early warning to communities (this is beyond the capacity of communities or local governments and should be handled by a competent authority).

Early warning in areas generally considered to be safe

Reliable forecasting of first-time landslides has always been a big challenge and if these happen to occur in areas hitherto considered to be safe, there will be certain difficulties in predicting the landslide in advance.

The early warning against possible occurrences of first-time landslides requires a more careful scrutiny of geological, topographical and hydrological factors in relation to the past history

and current and anticipated development and construction activities. The broad indicators mentioned above will remain applicable to areas not known for landslide hazards, and community members can be trained to make periodic observations and report on the development of warning signs.

It is recommended to identify slopes associated with important public utilities, such as schools, hospitals, reservoirs, bridges, and temples, where signs of adverse geology and intensive landuse change or human intervention may have created a possibility for slope destabilization. A scheme for instrumentation and continuous monitoring the slopes should be developed. This can be included as a project activity and hence the cost estimate for instrumentation and monitoring can be included in the project budget.

But this sort of activity and monitoring is beyond the capacity of the community members and should be implemented by project authorities or mandated institutions for landslide services for the benefit of at risk communities.

Development of community-based landslide monitoring and early warning systems for selected vulnerable locations.

The system development activities should include knowing the spatial risks (through the participatory social mapping process) and increasing risk knowledge (through regular monitoring and observation of precipitation using installed community-level rain-gauges). Adequate enabling systems for coordinated dissemination and communication should be set up, with active engagement of the local communities and institutions (through community-based volunteers on behalf of community, municipality administration, etc.).

Centrality was given to the following “key principles” of the community-based early warning systems in developing the system:

- The monitoring and early warning system will be ‘based and managed’ in the community;

- It will be understandable by all the stakeholders involved in monitoring and warning dissemination in the community;
- The system will be maintained by the community themselves (with a relatively low level of support from outsider stakeholders);
- The community will be able to make themselves ‘vigilant’ to anticipated landslides within their own areas;
- The system will be effectively linked to the national Disaster Risk Management, and particularly the Disaster Response systems operating in the respective areas;
- The system would be able to be replicated by others in the future with relative ease.

In developing a Community-based Landslide Monitoring and Early Warning System, a step-wise process should be followed.

Details of this step-wise development are elaborated below:

Step 1: Development of “Landslide Hazard Zonation Mapping”

The first level for developing community-level activities is the consideration of a landslide hazard zonation mapping exercise performed by the target communities, identifying the existing hazard, exposure and vulnerabilities. The basic criteria used for identifying the most vulnerable communities are:

- i. Previous landslide record
- ii. Losses of lives
- iii. Damages of assets
- iv. Frequency of hill cutting and other man-made interventions
- v. Concentrations of vulnerable, densely spaced houses in a hilly area
- vi. Highly density of population in the target area
- vii. Underprivileged and highly vulnerable people in the community, such as the elderly, children, differently abled etc.

Step 2: Development of “Risk-Resource-Evacuation Mapping”

Apart from the hazard zonation mapping, a rigorous exercise was carried out with the communities to develop “Risk-Resource-Evacuation”. This process is a social mapping process where the landslide risk locations in the communities are identified on a social map (non-scaled) and risks are categorized by the communities through a participatory approach with demarcation colors identifying where each house in the community would fall and what is the level of risk they face on landslide for their area. The critical slopes that might be subjected to any form of landslide in the communities are marked in the risk zones as well. The major resources and assets are also identified on the map. This exercise is essentially a participatory exercise where the ‘safer evacuation sites’ and ‘evacuation routes’ for the community are marked on the map, with active consultation with the respective community members and stakeholders (Fig. 1).

Step 3: Development of a “Precipitation Threshold” and “Alerting System”

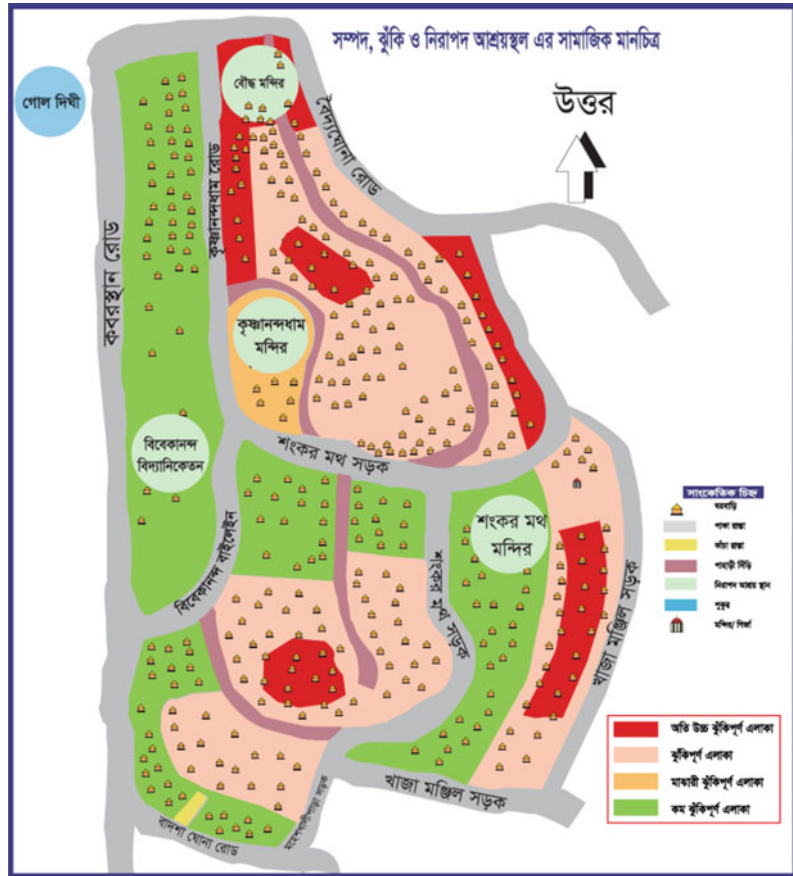
A major factor of developing the community alert procedure for this system is based on a scientific analysis and understanding of the “precipitation threshold” for the respective areas. This was carried out through a comprehensive analysis of the historical factors and observations of the precipitation. A precipitation threshold report was developed by a competent technical agency such as the Asian Disaster Preparedness Center, with details of the threshold generation process and information.

The following is an example of the recommendations that emerged for the perception threshold for the Cox’s Bazar and Teknaf municipalities in Bangladesh.

A three step alerting system was developed:

“Alert”—75 mm rainfall for 24 h—Increase vigilance and observe appearance of any critical slopes for symptoms of slope destabilization.
 “Get ready for Evacuation” to safer location from high-risk locations for 100 mm rainfall for 24 h
 “Evacuation”—200 mm rainfall for 24 h—Warning to evacuate to safer places.

Fig. 1 “Risk-resource and evacuation” map of a target community



Following the detailed recommended threshold values, the above alert system was developed for the target communities. Community volunteers were identified from each of the vulnerable communities to learn the threshold values, and

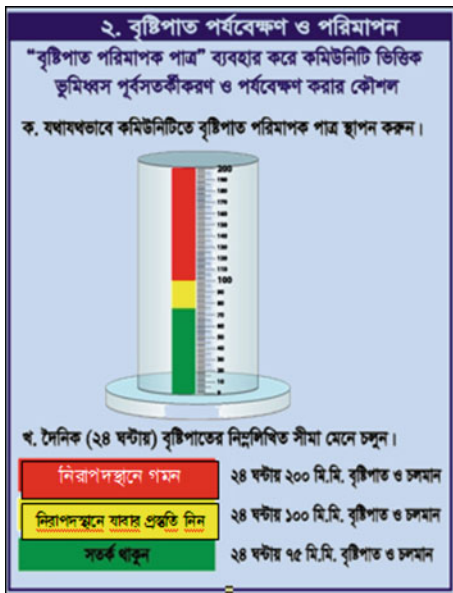
the different levels and actions to be taken for the safety and preparedness of the community.

The rain gauges installed at the target communities have three different color codes as shown below:

Color code	Level	Threshold values	Actions
	Evacuate	101–200 mm rainfall recorded within 24 h	Evacuate to safer place
	Ready	76–100 mm rainfall recorded within 24 h	Get ready for evacuation
	Alert	0–75 mm rainfall recorded within 24 h	Get alert

To communicate the alert system to the local people in an active way, the color system is further put into the local language and local patterns in following matter. The details of each of the colors and the explanation should be discussed with the community and the needed procedures for observations of the rainfall was detailed out with the community volunteers respectively.

Public awareness billboards produced under the project to show the simple issues of mapping, rainfall observation, alerting system and simple standard operating procedures for communities to remain vigilant to landslides in their communities.



Step 4: Setting up community based rainfall observation, recording and documentation process and voluntary training procedures

The community Volunteers also needed to be oriented with the reading and setting of Rain

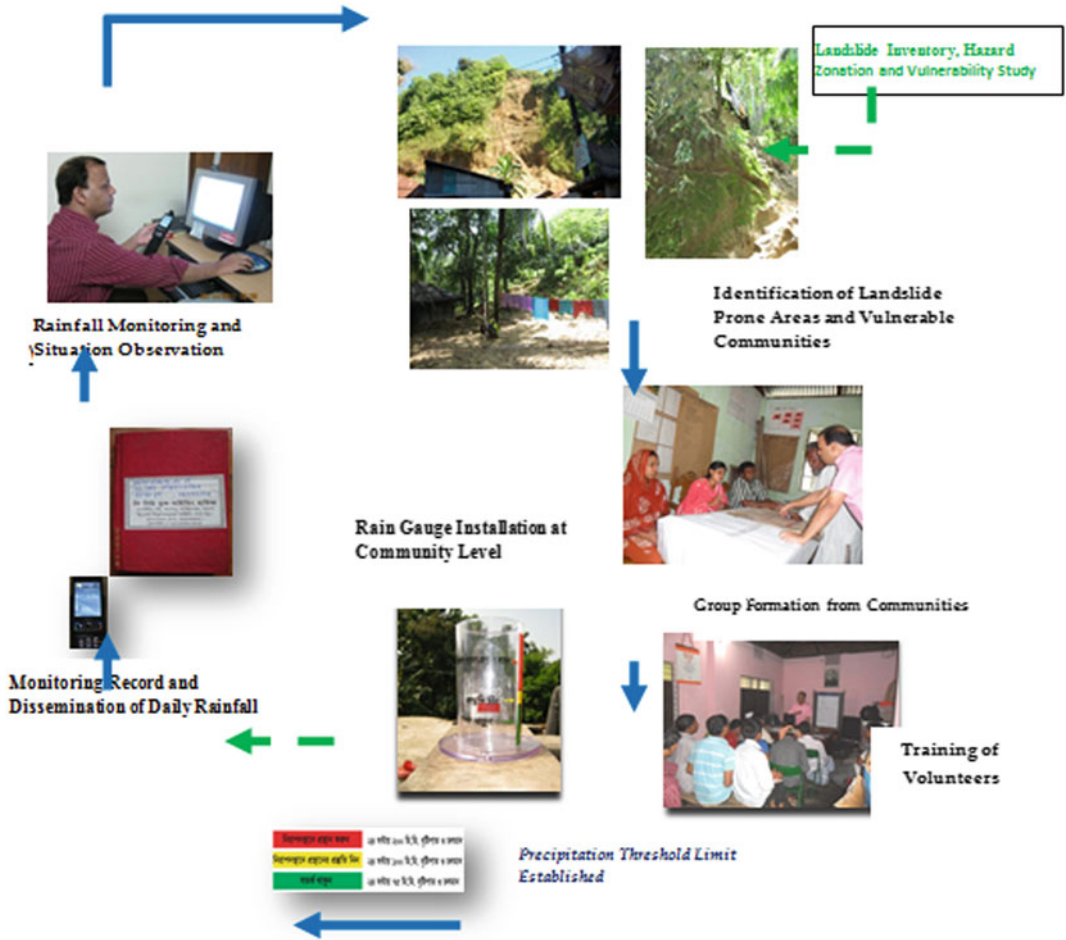
Gauges in the respective community. A total number of 43 and 15 volunteers have been selected and trained respectively in the case of Cox’s Bazar and Teknaf Municipalities in Bangladesh. In Cox’s Bazar and Teknaf respectively 5 and 3 volunteers have been assigned with Rain Gauge in their locality. Moreover, Simple Standard Operating Procedures (SOP) has been developed for Volunteers, Community and Municipality for assigning more specific responsibilities at different period of landslide hazard. Following is the SOP of different groups.

For Rain gauge observation:

- Daily observation and monitoring of rainfall through “rain-gauge” and “critical slopes” in the area;
- Daily documentation and maintenance of the observes data into a simple “log-book”;
- “Communicate” to other clusters and rain-gauge observers, community, municipality and other agencies;
- “Maintenance” and “secure” the rain-gauge;

For Community:

- Maintains “a list of socially vulnerable groups/people” (e.g. children, elderly, pregnant, disable, women etc.);
- Observes “settlements or new development on the identified critical slopes” and Operation and Maintenance of “critical slopes” in the area;
- Make enhanced use of “local knowledge” for “traditionally practiced landslide alert” measures (e.g. observe unusual behavior of dogs during heavy rainfall and in case of such event to observe the critical slopes for any changes);



4. Raising “awareness for community-based landslide monitoring and early warning” through youth, students, religious leaders, teachers, volunteer groups and others;
5. Maintaining a sustainable “Community based Landslide Discussion Forums” in each community

For Municipality:

1. Takes “decision on the evacuation and coordination” for wards and respective communities for landslide risk management;
2. Maintains the coordination between the “District Disaster Management Committee (DDMC) and related DDMC member agencies;
3. Follow the nationally approved “Standing Order on Disaster (SOD)” of the respective Government for landslide



Rain gauge installed in a community at Cox’s Bazar (Bangladesh)

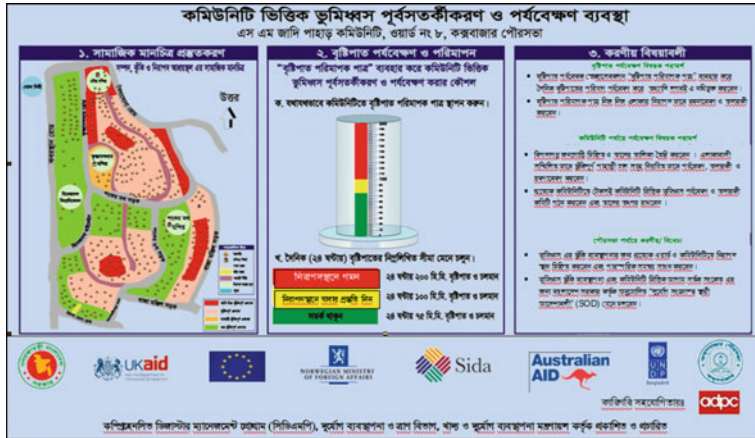


A volunteer at Teknaf municipality (Bangladesh) with his assigned Rain Gauge and log book

Recording and Documentation of Rainfall: Each of the community Volunteers need to take action for reading the daily rainfall in the rain gauge installed in their respective communities and keep record in the log-book assigned for them. At the same time each of the volunteers send the record of rainfall through mobile SMS to a central Mobile where all the records are stored and being observed for monitoring for landslide early warning.

3 Conduct Awareness Programs for Different Stakeholders

The awareness development programs can vary from place to place in line with usual cultural practices. Some of the examples are: town level stakeholder meetings, Rapport building with the vulnerable communities, arrangement of orientation and training program, community risk assessment through involving the respective communities, Simulation Exercise for Landslide Early warning and Preparedness. Following is a brief on different initiatives of awareness development in the Teknaf and Cox’s Bazar Municipalities in Bangladesh.



Billboards produced under the project to create public awareness on the system

Municipality level meetings and workshops—Municipality level workshops can be organized from the initial stage of the project. In the first orientation meeting with the municipal level stakeholder, all related town level agencies should be invited to share the objectives, activities and outcomes of the project. The town level meetings can be held with the respective municipality mayors in Chair. The other town level stakeholders that can be invited for the meetings are: the elected councilors, DMC members, representatives from metrological department, other DM projects in the area, Fire service and Civil Defense agencies, civil servants, Representatives of community organizations, Representatives of Women and Youth Organizations, etc. During the workshop, the consensus should be built to the effect that, municipality would take lead role in the implementation of the CBDRM activities in landslide prone areas with the participation of respective communities.

Necessary funding support should come from the local government or Municipality and community should be agreed to provide in-kind contributions.



Town level consultation meeting on 5th March, 2011 at Cox’s Bazar municipality



Town level consultation meeting on 5th April, 2012 at Cox's Bazar municipality

Orientation and Training Program for Volunteers and Community facilitators—With the identification of the community based facilitators and volunteers', training on early warning system can be organized to orient them in the process. In this training, the focus will be to discuss the basics of early warning components such as conducting risk assessment to provide knowledge, monitoring and warning, dissemination and communication and response capability building at community. The training usually should cover all aspects of community based disaster risk reduction (CBDRR) and the process how to mobilize vulnerable community to support such initiatives.

Community Risk Assessment (CRA)—After conducting the training, the communities can be facilitated with the process of community risk assessment. Under this activity, risk mapping, early warning action planning and implementation can be undertaken through the identified volunteers and community based facilitator. Risk and resource maps should be developed for each of the community (most vulnerable) level.

Various activities during the CRA and social mapping process in the pilot sites.

Simulation Exercise for Landslide Early warning and Preparedness.

The Community based landslide monitoring and early warning system need to be developed with the active participation of the respective targeted communities and the simple process can be demonstrated through 'simulations and drills' in the community. The simulation and drills have two major objectives:

- to identify the gaps in the developed community based landslide monitoring and early warning system,
- educate people and the community in the system and for future sustainability of the system by themselves.

In the simulation and drills the communities are engaged in a systematic way to simulate a situation of landslide and demonstration will be to explain what measures each stakeholder from the community and institutions should take in real-time situation. The timing and process should be documented for identification of the gaps and the potential review of the system for the future sustainability.



Simulation Exercise at Cox's Bazar on 28th February 2012

Case study; Community based landslide early warning system development in Cox's Bazar and Teknaf municipalities in Bangladesh

Sources

Complexities in landslide forecasting, LHMP document no. 24, National Building research Organization, Sri Lanka 1994

ADPC (2007) Safer cities 18: The boy who cried, 'Wolf' or why a community-based alert system is a good idea

ADPC (2011) CBDRR 20 participants workbook

Further Reading

ADPC, PAGASA (2006) Taking up flooding through a community-based early warning system

ADPC (2007) Safer cities 18: the boy who cried "Wolf!" or why a community-based alert system is a good idea

TXT-tool 4.039-2.1

On the Protection of Cultural Heritages from Landslides

Claudio Margottini

Abstract

Protection of cultural heritage from landslide is a science at the border between Engineering Geology and Conservation of Cultural Heritage. It needs both a highly qualified know-how and funds, due to the importance of the site to protect and the possibly additional difficulties during the works execution. Cultural Heritage protection requires also an integrated approach among different disciplines, including restoration, and very deep investigation in each different sector of knowledge. Since a limited knowledge in a single step of the process may affect the entire process. In detail, when dealing with Cultural Heritage, there is the need of a correct geological and geotechnical model and relationship with slope stability. Data collecting do have to emphasize the requested need. Simplified approach can lead to a misunderstanding of processes and then to a wrong mitigation measurement.

Keywords

Landslide · Cultural heritage · Mitigation · Monitoring
Traditional knowledge

Contents

1 Introduction	648	2.2 Traditional Knowledge in the Soil Erosion Mitigation of Akapana Pyramid in Tiwanaku (Bolivia)	653
2 Landslide Science and Science for Conservation of Cultural Heritages	652	2.3 Low Environmental Impact Consolidation and Conservation of Buddha Niches in Bamiyan (Afghanistan)	656
2.1 New Approaches and Instrumentation in Mata Ngarau, Orongo (Rapa Nui, Easter Island).....	652	2.4 Monitoring for Cultural Heritage Conservation: The Siq of Petra (Jordan)	658
		2.5 Low Environmental Impact Monitoring Systems: Machu Picchu.....	663
		3 Conclusion	665
		References	667

C. Margottini (✉)

ISPRA—Italian National Institute for Environmental Protection and Research, Geological Survey of Italy, Via V. Brancati, 60, 00144 Roma, Italy
e-mail: claudio.margottini@isprambiente.it

1 Introduction

Cultural Heritages represent the trace of human being on the Planet Earth. They are the evidence of thousand years of humanity activity, to adapt our living condition to environment.

The United Nations Educational, Scientific and Cultural Organization (UNESCO) seeks to encourage the identification, protection and preservation of cultural and natural heritage around the world considered to be of outstanding value to humanity. This is embodied in an international treaty called the Convention concerning the Protection of the World Cultural and Natural Heritage, adopted by UNESCO in 1972.

According to the Convention, the following shall be considered as “cultural heritage”: monuments (i.e. architectural works, works of monumental sculpture and painting, elements or structures of an archaeological nature, inscriptions, cave dwellings and combinations of features, which are of outstanding universal value from the point of view of history, art or science); groups of buildings (i.e. groups of separate or connected buildings which, because of their architecture, their homogeneity or their place in the landscape, are of outstanding universal value from the point of view of history, art or science); sites (i.e. works of man or the combined works of nature and man, and areas including archaeological sites which are of outstanding universal value from the historical, aesthetic, ethnological or anthropological point of view).

This broad definition can be put into a list of typologies, as in Table 1 (from World Bank 1994), where some selected types of cultural heritage are catalogued.

A great part of the above sites and remains are not in equilibrium with environment. They are continuously affected by several factors both natural and human, with rapid and slow onset. Figure 1 is describing the major disrupting factors affecting cultural heritages (courtesy of J. Hamie, modified).

Among rapid onset natural phenomena the major role in endangering cultural heritages is played by earthquake, flooding and landslide. It is difficult to evaluate the percentage of losses

caused by any kind of these phenomena. Moreover, it is significant to underline that any earthquake or flooding hit generally a very large area and a large number of monuments in the same moment whereas landslides act more locally, since the “size” of the phenomenon, making data collection more difficult. As a consequence, a reliable statistic on the worldwide impact of landslides on Cultural Heritages is currently missing.

As a matter of fact, the protection of Cultural Heritages (CH) from landslides is a border area between Science for Conservation of Cultural Heritages and Landslide Science. Conservator has to develop the proper CH restoration project taking into consideration and having understood geomorphological process acting on the cliff; in the meantime, landslide expert has to implement a mitigation plan and monitoring system that are fulfilling the request of low impact and perfect integration of solutions into the archaeological contest. In principle, most of stabilisation works of landslides affecting archaeological sites has to be investigated by landslide expert but, the final solution has to be decided jointly with CH conservation expert. Typical example of connection points between these two major categories is the usage of solution that can damage the CH or the cultural landscape, even if stabilising the mass movement; similarly the use of materials that, during time, can loose original properties, generating salts, oxides, etc., that may affect the integrity and conservation of CH. In this context also the proposed monitoring systems need to fulfil the requirement of low environmental impact and minimum interference with the archaeological remains.

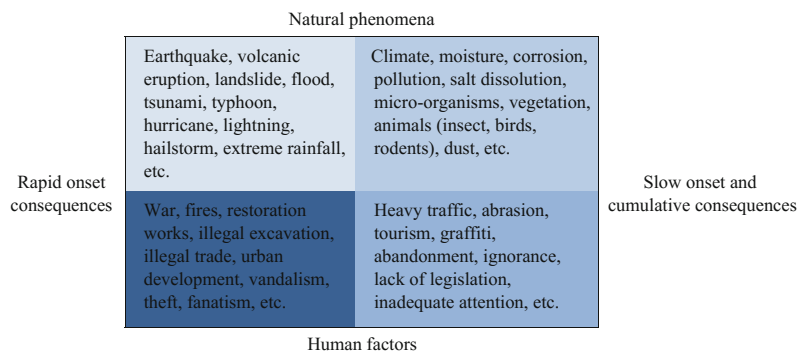
The following figure is trying to synthesize the potential interconnections among landslide science and science for cultural heritage conservation (Fig. 2).

The above reflections, without obviously being exhaustive of the problem list, clearly underline the impact that the Earth Sciences have had in the construction, development and maintenance of the cultural properties; it is evident that the same disciplines have to assume a fundamental role in all the policies that are today

Table 1 Selected types of cultural heritage (modified from World Bank 1994)

Main categories	Sub-types	Examples
Sacred sites	Burial sites	Xian, China Tomb Fields, Bahrain
	Sites of religious significance	Mecca, Saudi Arabia Jerusalem, Israel
Archaeological sites	Pre-historic sites	Altamira, Spain Lascaux, France
	Historical sites	Historic roads, bridges, dams, fortifications, and walls
	Engineering and industrial sites	Marib Dam, Yemen The Great Wall, China
	Submerged or marine sites	Alexandria, Egypt Mahabalipuram, India
	Sites within biologically diverse areas or protected reserves	Tikal, Guatemala Sacred groves, Ghana
Monumental sculpture	Cave sculpture	Indian Buddhist cave sites Chinese cave sites
	Architectural sculpture	Thebes, Egypt Petra, Jordan
Monumental painting	Cave or wall painting	Tombs in Luxor, Egypt Tassili, Algeria
Architecture and town planning	Monumental architecture	Monte Alban, Mexico Copan, Honduras
	Indigenous or vernacular architecture	M'zab Valley, Algeria Chitral, India
	Historic settlements and town centers	Quito, Ecuador San Gimignano, Italy
Historic landscapes	Cultural landscapes	Cres, Croatia Land of the Dogon, Mali
	Historic parks and gardens	Sigiriya, Sri Lanka Shalimar Gardens, Pakistan
	Trade routes monuments and remains	The Silk Route Pan-African trade routes

Fig. 1 Threats facing cultural heritage (ICCRUM 2006, modified)



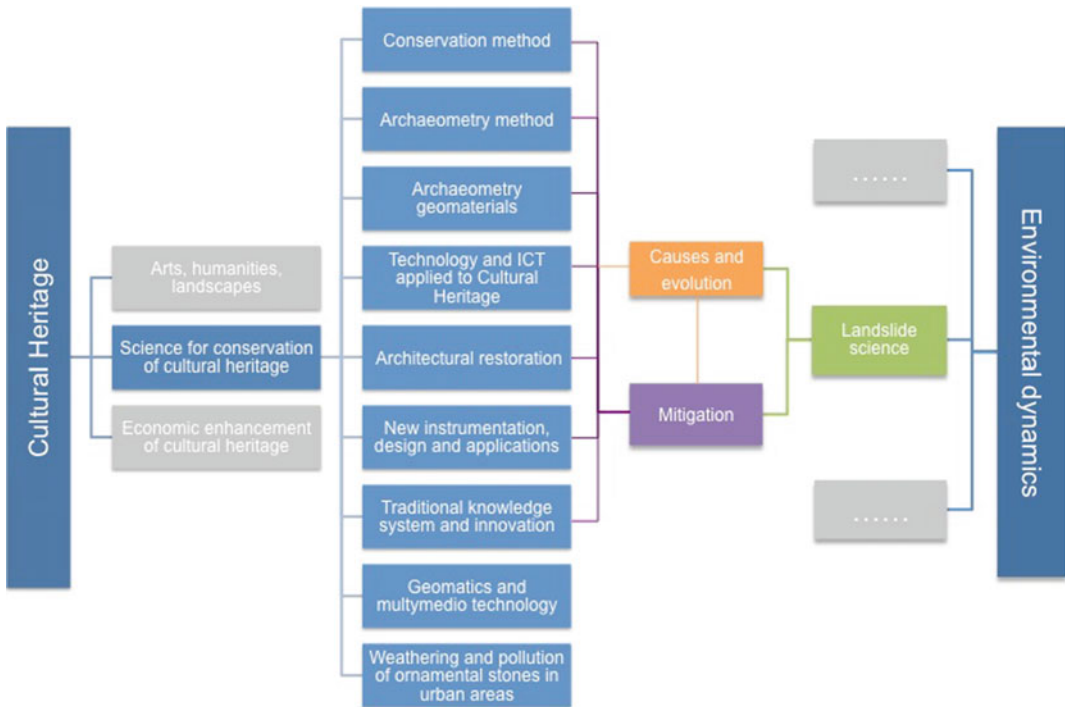


Fig. 2 Relationship between science for the conservation of cultural heritage and landslide science

necessary for the protection of the heritage. This passage has never been very clear in the past, since the archaeology and the conservation aspects had a strong centrality and autonomy. This point of view is now less evident, with more attention to the integration of different sciences. Indeed it is possible to affirm that the protection of the cultural heritage represents an interdisciplinary process (and not multi-disciplinary) to the border-line among art, history, science, policies for management and exploitation.

In general the adopted measures to conserve the cultural heritage from its destruction by the natural events and agents have been relegated in background (Canuti et al. 2008a, b); even if natural processes, especially the geological and geomorphological ones (sedimentation and erosional processes, debris and mud flows, inundations, landslides, fluvial dynamics), remarkably affect the existence of the cultural heritage sites, in this case the usually adopted tasks are emergency work.

Nevertheless, the diagnosis of geologic risk and the measures of conservation derived from

the same one are necessary if we are intentioned to recover the cultural heritage and to prolong their existence.

In this framework, the conservation “in situ” is one of the main targets; for this reason the diagnosis of risk and the elaboration of measures of risk mitigation are the most important aims to preserve cultural heritage.

From this point of view, landslides are a very interesting example: in fact, not only large and rapid movements can be constitute a menace for heritage conservation, but also low moving landslide activity or very small phenomena are able to destroy, at the end, a monuments or a site.

Besides, it should be considered some features peculiar to landslides: in fact, they can present precursory phenomena or occur slowly, and this allows the risk assessment and countermeasures planning.

In these cases, the landslides can be considered as a predictable phenomenon and a remedy can be found: however, this requires a deep knowledge about landslide hazard and

Fig. 3 Scale of the problems and involved disciplines and investigations for the conservation of cultural heritages (Fitzner 2004 modified)

Problem	Scale of the problem	Main parameters to investigate	Main typology of investigation	Main involved disciplines
Non visible deterioration	Nano-scale (<mm)	Changing of properties of the rock (composition, texture, porosity, strength, etc.)	Laboratory analysis	Earth science, material science, chemistry physics, microbiology, etc.
	Micro-scale (mm<cm)	Discoloration, loss of surface's material, micromorphology		
Visible deterioration	Meso-scale (cm < m)	Deterioration, alteration	In situ analysis	Structural engineer, Engineering geology, Architecture and conservation
	Macro-scale (entire structure or monument)	Structural stability, (also for site hazards) aesthetic appearance		

vulnerability of element at risk. This a multidisciplinary task, not easy to achieve and manage, but very important, in particular for cultural heritages.

The following Fig. 3, from Fitzner (2004, modified) underlines the articulation of the involved disciplines and the necessary investigations to the resolution of real conservation problems.

An additional complexity to the above is the nature of landslide phenomena. While earthquake and flooding are mainly dealing with a single hazard as input, e.g. seismic motion or water level or flow velocity, landslide science is dealing with different kinematic processes, depending from parent material (Cruden and Varnes 1996). As a consequence no unique approach can be proposed, but different methodologies that are depending from typology of movements (fall, topple, slide, lateral spreading, flow, complex) and involved materials (rock, engineering soil fine or coarse). Finally, also investigations and monitoring has to be planned according to the specific process they have to understand.

Among the many earth science disciplines, engineering geology (www.iaeg.info) contributes to this task, being the science devoted to the investigation, study and solution of the engineering and environmental problems which may arise as the result of the interaction between geology and the works and activities of man as well as to the prediction of and the development of measures for prevention or remediation of geological hazards.

Engineering Geology embraces:

1. the definition of the geomorphology, structure, stratigraphy, lithology and groundwater conditions of geological formations;
2. the characterisation of the mineralogical, physic-geomechanical, chemical and hydraulic properties of all earth materials involved in construction, resource recovery and environmental change;
3. the assessment of the mechanical and hydrologic behaviour of soil and rock masses;
4. the prediction of changes to the above properties with time;
5. the determination of the parameters to be considered in the stability analysis of engineering works and of earth masses;
6. the improvement and maintenance of the environmental condition and of the properties of the terrain.

From the above it is quite evident as engineering geology (in the widest sense of the term) is a major science for the protection of cultural heritages from environmental degradation and disruption, especially from landslides.

This sentence introduce the case histories that constitute part of this paper: they are examples of various problems from different countries, without the claim to offer an exhaustive view on the topic. On the contrary, the presence of sites affected by small problems testifies the peculiarity of interactions between landslides science for conservation of cultural heritage.



Fig. 4 A view of Mata Ngaroa ceremonial altar in Rapa Nui (Easter Island, Chile). Most of the visible blocks have been analysed by means of vibration analysis, to compare

response spectra, H/V spectral ratio and intensity/direction of horizontal displacement. *White arrows* indicate North

2 Landslide Science and Science for Conservation of Cultural Heritages

2.1 New Approaches and Instrumentation in Mata Ngarau, Orongo (Rapa Nui, Easter Island)

The identification of unstable rock blocks it is still unclear. In the meantime most of ancient rupestrial sites are excavated in soft rock site. Monitoring network can offer a great support but only during rupture phase. However, identifying such blocks visually is extremely difficult, so an identification method using peculiar features of unstable blocks must be developed. The method reported here uses a portable velocimeter (Micromed, TrominoTM), which is inexpensive and easy to operate. This technique, measuring environmental noise, can provide useful information about an estimate of the block resonances thickness as well as direction and intensity of ground motion (Tanaka et al. 2008).

In order to assess the feasibility of the method, a field experiment was carried out on

rock blocks composing the ceremonial center of Mata Ngarau. This site is extremely important for Rapa Nui culture due to its unique petroglyphs and dominant view of the surrounding landscape, ocean and motus. Mata Ngarau is located inside the village of Orongo, in one of the most spectacular sites within Rapa Nui National Park, on a narrow plateau between Rano Kau crater and a 300 m cliff to the waters of the Pacific Ocean.

The site is composed by individual rock blocks, hanging over 200 m of high slope cliff. Below the ceremonial site were located two small Moai, that collapsed on the sea on '90. An active landslides is located just underneath the Mata Ngarau.

The use of portable seismometer allowed the measurement of environmental noise characteristics for many as possible blocks, compared with bedrock measurements developed outside the site. The results show a clear correlation of most unstable blocks with largest intensity of ground motion and versus of it.

The analysis was carried out by means of comparing response spectra, horizontal to vertical spectral ratio and intensity/direction of horizontal motion (Fig. 4).

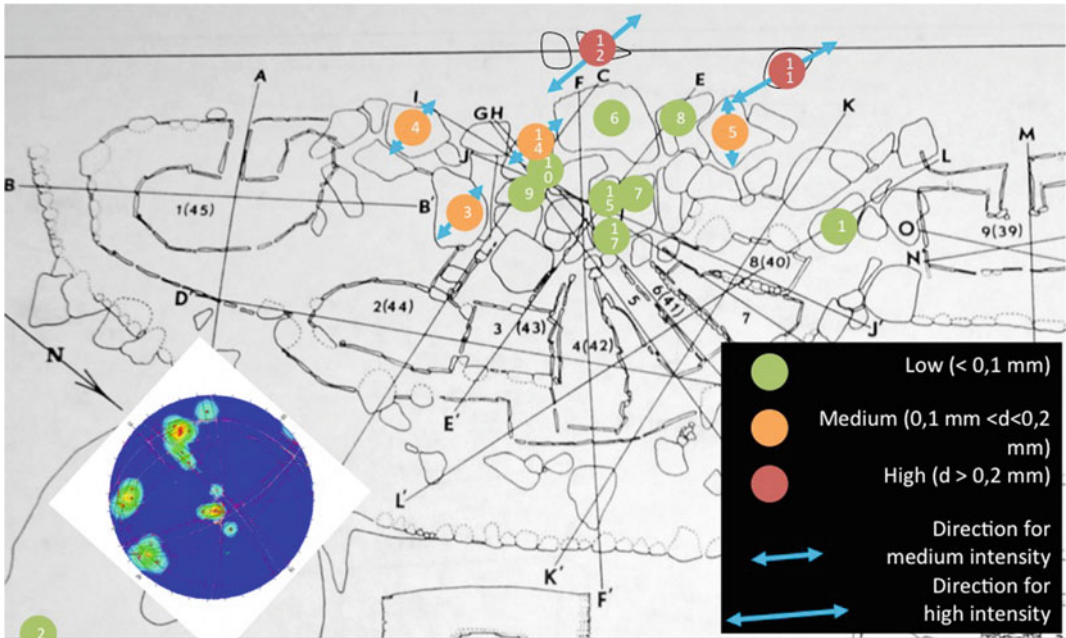


Fig. 5 Plan of Mata Ngaroa ceremonial altar in Rapa Nui (Easter Island, Chile) and intensity/direction of horizontal components of environmental noise. The single

measurement have been ranked in three categories of intensity (low, medium and high)

The result of such approach is reported in Fig. 5, as far as the analysis of intensity/direction of horizontal components of environmental noise. From this it is possible to notice:

1. major displacement (>0.2 mm) is detected in the blocks prominent to the cliff, looking at the see (top in the figures), characterised by red colour;
2. minor displacement (<0.1 mm, green) is noticed in blocks located in the inner part of the ceremonial altar, suggesting a satisfactory degree of connection among individual blocks; this concept is
3. horizontal components are almost showing the same direction, for medium and high detected values of motion;

Such techniques demonstrate a remarkable degree of maturity and the possibility to be applied in rock fall prediction. In fact, most critical blocks of the ceremonial altar are those hanging to the 200 m cliff, for which a serious

threat can be logically posed. Also the missing of scatter among single data suggests an internal consistency of the experiment.

The results of the test can now be applied in establishing a priority in mitigation measurement.

2.2 Traditional Knowledge in the Soil Erosion Mitigation of Akapana Pyramid in Tiwanaku (Bolivia)

Tiwanaku is a pre-Inca Archaeological World Heritage Site, located at an elevation of 3885 m. a.s.l., south of Lake Titicaca, in the altiplano or high plateau region of the Republic of Bolivia. It is in the province of Ingavi, department of La Paz, 60 km from the city of La Paz.

An area of 420–600 ha has been calculated for the ancient urban settlement, and 40 ha for the ceremonial center with monumental architecture, although a geophysical project refers to

100 ha. In the absence of an archaeological evaluation, there is no certainty in this respect.

The archaeological research carried out refers to several periods of occupation, to the different styles and techniques of construction, and to the different uses given to the built-up area. But systematic research is needed on the formation and the process to explain the development attained by the Tiwanaku culture.

Core of the site is the huge Akapana pyramid. The pyramidal building constituting the monument is a great mound of earth, composed of clay, gravel, and sandy materials from the alluvial deposits and river-and-lake deposits of the valley, with a large hole at the summit, some platforms, main stairways, and monoliths. It was originally covered by large block of stone, depleted in the colonial period and more recently (Fig. 6).

The pyramid is suffering for extensive erosional phenomena such as (Margottini 2013):

1. Rill erosion;
2. Mass movement;
3. Creeping;

The majority of the phenomena mentioned above are caused by the uncontrolled flow of the rainwater, which flows freely through the depressions (natural or cultural) but which, also, infiltrates and deforms the materials of the deposits and appears to be affecting the stability of the internal structures. From site inspection it is possible to note the large toe deposit originated by the erosion/dismantling of the earth mound, some potential surficial mass movement and creeping and the evidence of deformed walls, suggesting internal deformation to the mound.

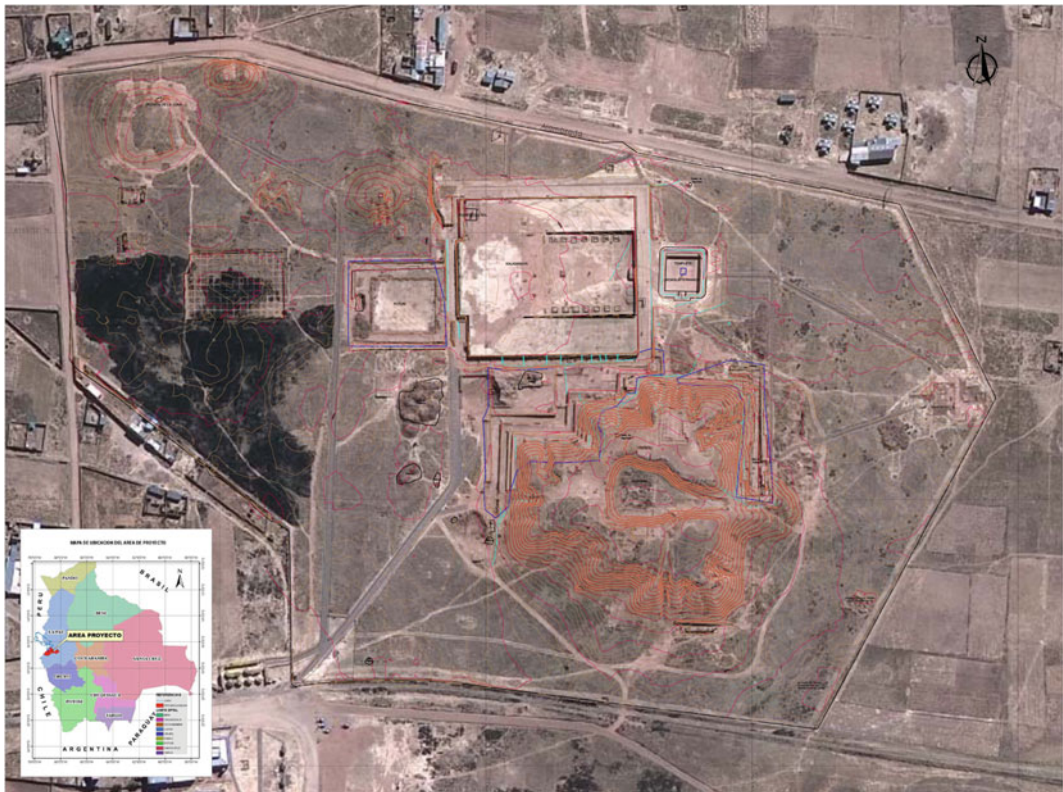


Fig. 6 The Tiwanaku, Bolivia, site and the Akapana pyramid (courtesy provided from Bolivian Ministry of Cultural Heritage to UNESCO, in Margottini and Shadis 2010)

Also, in grey is the large rubble left from the excavation of the Colonial Period.

With reference to the erosion of the mound, there is a clear evidence (rill erosion and small valleys on the mound) that a large part of the original structure has been affected by erosion and deposited at the base or foot of the pyramid; moreover, it is not possible to exclude that the stepped design in the shape of the “chacana” or Andean cross could have played some roles in such erosion.

At present it is not very clear how to prevent the soil erosion of a man made back fill, in an area of very high yearly precipitation. Some preliminary hypothesis have been provided in Margottini and Shadis (2010) considering the use of low environmental impact techniques such as traditional and biotechnical. In particular, the usage of traditional techniques seems offer an interesting approach to soil erosion control. In particular, most of Andean populations experience the use of cactus for clay stabilisation and reinforcement. Evidence of knowledge and use of the cactus by the first settlers Mexico is in the excavation of Tamaulipas and Tehuacán, Puebla, where found fossilized shells of seeds as well as cactus fiber stalks, dating back 7000 years (Flores-Valdez 2003).

The stems are succulent and articulated, botanically called cladodes and commonly penca. Penca (or Penka) is also a common name for a cactus mucilage, locally used adobe reinforcement (Ramsey 1999). Also, Due to the rheological and high-molecular-weight properties of the pectin-like polysaccharide of the *Opuntia* mucilage (penka) Gardiner et al. (1999) compared the use of cactus mucilage to polyacrylamides for use in increasing soil water infiltration on soils with low hydraulic conductivity.

In Tiwanaku the tradition to use penca is quite relevant as soil amending to reduce erosion from heavy rainfall in monumental earth mound pyramids. Cactus mucilage is firstly produced to obtain a penca (Fig. 7) which is later on added with soil, water and straw.

Indeed, according to practical use in Bolivia (Irene Delaveris, personal communication) the quality of soil is depending from its grain size distribution: clay, sand and gravel are mixed in different percentage according to final usage. In case of soil erosion reduction, the percentages are the following: clay 50%, silt 20%, sand and gravel 10%, straw, water 10%, penca about 5% and straw. The material so mixed is placed on top of earth mound cultural heritages, to protect from

Fig. 7 Preparation of cactus mucilage (penka) and amending to soil, water and straw



Fig. 8 Protecting a pyramid earth mound from soil erosion by means of penka



soil erosion. From information received the stabilisation is not permanent but need to be replaced after about 5 years. This is producing a local economy since population is continuously active to replace, periodically, old stabilisations (Fig. 8).

2.3 Low Environmental Impact Consolidation and Conservation of Buddha Niches in Bamiyan (Afghanistan)

The present chapter synthetically describes all the emergency intervention performed in Bamiyan (Central Afghanistan) for the consolidation of niches and unstable blocks resulting from the explosion, executed by Talibans in March 2001, aimed at destructing the VI c. A.D. giant statues of Buddha (Margottini 2008).

The effect of explosion was quite dramatic: the two statues totally collapsed but also some small part of the niches fall down and, mainly large part of the Eastern Giant Buddha Niche was close to the collapse. UNESCO was immediately prompt to undertake an emergency intervention for securing the remaining of such wonderful cultural heritages and, thanking to the gene rous

Government of Japan financial support, the works started in November 2003.

The activities were developed according to the following general scheme:

1. engineering geological study of the site, including laboratory testing and filed work (the first were conducted in Europe in few samples and the latter conditioned in their execution from the presence of land mine);
2. installation of a high precision monitoring system;
3. realisation of temporary support infrastructure, to maintain stable the blocks at limit equilibrium, also during the execution of works;
4. execution of the consolidation work, with professional climbers to avoid any activities below the hanging and unstable blocks, with a system of small and long passive anchors and grouting (Fig. 9);
5. minimisation of impact of anchor heads, with a mixture of special mortar, investigated in detail with the support of ICOMOS expert.

The result was quite satisfactory, in an area that is slowly coming out from decades of war, and in which it was necessary to adopt the maximum of professional judgment in

Fig. 9 Execution of anchors and nails for the stabilisation of unstable blocks



identifying weak points and limits in knowledge and, in the mean time, to adopt technologies capable to solve the problems in very short time and in safe conditions. The following Fig. 10 is reporting the anchor suitability tests for siltstone and conglomerate, in 1 m. length anchor showing, till 40 ton, the uphold of elastic domain and still the missing of any permanent deformation for the tested anchor.

As mentioned previously, high attention was posed to the methodology for consolidation. Short (16 mm) and medium (20 mm) length passive anchors (stainless steel) have been realised with rotary drilling machine, with diamond head, to avoid any possible vibration. Cooling fluid was facing the occurrence of slaking prone siltstone in presence of water: due to this, the usage of water was limited when drilling the conglomerate and a mix of compressed air and water was adopted when discontinuities were detected and when a possible level of siltstone was encountered. Pre-grouted long passive anchors, used only in the first phase 2003, (26 mm) have been realised with roto-percussion machine and use of air as flushing medium. From a temporal point of view they have been drilled only after the realisation of shorter ones and from the further part of the unstable blocks, towards

the most critical one. The purpose of small anchors is to sew all together the unstable masses and fixing them the proxy stable geological background. The long anchors have to homogenise this part to the most internal and stable geological material. Direction and inclination of anchors have been defined on site but, in any case, direction of deformation and perpendicularity to discontinuities has been taken into consideration.

Temporal execution considered the principle to start from the most stable place to the most unstable. This is to start consolidation from the part where disturbance can better be sustained. In particular, with respect to the internal side of the niche, the lowermost unstable block, has been approached from the bottom of it to the top. In fact, in the top of the niche there is a hanging block that cannot be touched without having stabilised the lower part.

Grouting was made with cement added with superplasticizer to avoid any water release, capable to interfere with the slaking siltstone as well as to get the best possible adherence between bar and rock.

After the investigations started in September 2002 and the practical intervention of October–December 2003, March 2004 and October–

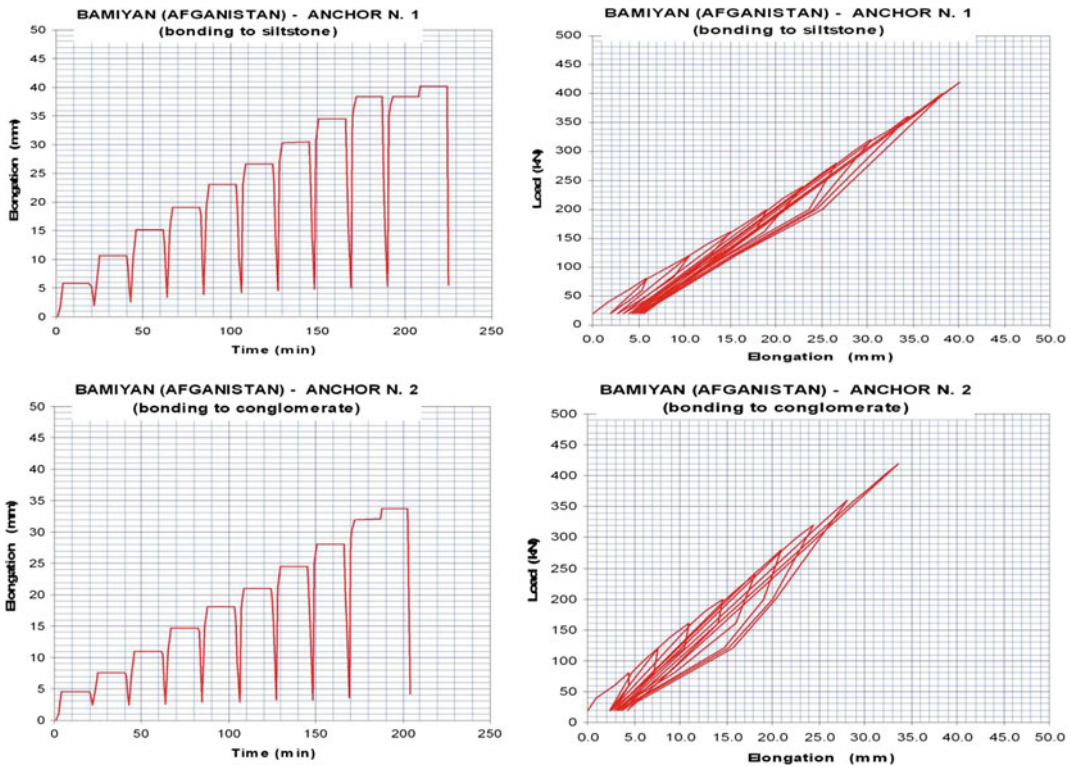


Fig. 10 Anchor suitability tests for siltstone and conglomerate, in 1 m. length anchor. The load (kN) and respective time (min) and elongation (mm) are reported

showing, till 40 ton, the uphold of elastic domain and still the missing of any permanent deformation for the tested anchor

December 2006, the cliff and niche of the Eastern Giant Buddha (the most critical part) it is now more stable and the risk of collapse almost avoided. Also, the niche of Western Giant Buddha have been protected from water infiltration. Further work are now in progress, especially in back side of both niches but, at least, the major risk to have a collapse involving also the few remains not destroyed by Talibans it is now turned away.

2.4 Monitoring for Cultural Heritage Conservation: The Siq of Petra (Jordan)

Petra is located on the eastern side of the Dead Sea-Wadi Araba tectonic depression, in SW Jordan. The Siq is a 1.2 km long natural deep gorge in the sandstone mountains that connects

the urban area of Wadi Musa with the monumental area of Petra (Fig. 11). Since Nabataean times, the Siq is the main narrow entrance for some thousands tourists that access the archaeological area every day.

Rock falls was noted by the Nabataean inhabitants of Petra (dated 550 BC to 106 AD). For example, large fallen rocks in the middle of the Siq were used in the curved water channel in the left side of the Siq. Different niches for worshiping were also carved from this rock. Ancient rock fall and rock avalanche deposits, such as those that blocked the staircase to the Deir (Monastery) are recognized at several locations.

In recent times few cases of rock falls have been documented by locals and authorities; no human life loss has been documented but accidents of complete destruction or serious damage to monuments and killing of animals were reported in 2006, 09, in 2010 especially during



Fig. 11 The SIQ (Wadi Musa canyon) of Petra, Jordan (source APAAME—David Kennedy)

heavy rainfall in the period between the months of November to April and in May 2015. Many tourist trails, roads, slopes and Wadi beds have been affected by Rock falls.

The geomorphology of the Siq (Delmonaco et al. 2014) is the result of long and short-term factors affecting this part of the Petra territory such as tectonic uplift, erosion due to runoff, differential erosion and weathering of sandstone materials. The Siq has a main E–W orientation and a meandering course, governed by intersection of faults and master/secondary joints. The slopes generally presents a rupestral aspect, mainly massive. Nevertheless, discontinuities of various types are present, mainly related to bedding (generally horizontal), tectonic activity (faults, master joints, mainly sub-vertical), geomorphological activity (from vertical to medium-inclined joints). Sub-vertical and medium-angle dipping joints intersecting horizontal bedding are quite frequent and

observed during field investigation. This situation may cause potential sliding of blocks, whose dimensions are depending on local orientation, density and persistence of discontinuities. Potential and actual rock slope failures are strictly depending on type and degree of structural control. They can be classified as: (1) planar failures, (2) wedge failures, (3) toppling failures, (4) unstable isolated blocks (toppling/sliding) (Delmonaco et al. 2013). All the above geomorphological processes have been collected and elaborated in a geo-database. An inventory map of potential unstable blocks has been implemented reporting types and magnitude of the inventoried phenomena (Fig. 12). Geostructural and landslide kinematic analysis have detected the probability of the main failure modes of the Siq slope-forming rocks.

Considering the morphological setting and slope instability processes, the following monitoring techniques have been proposed, designed, implemented and installed for the monitoring of the Siq slopes in Petra (Fig. 13) (Delmonaco et al. 2014):

1. Satellite SqueeSAR™ analysis with permanent scatters techniques, to evaluate potential regional deformation pattern of the site and possible Siq border effects;
2. automated crack-gauge network, with wireless connection, to monitor main cracks and isolated potentially unstable blocks, with a low environmental impact technology;
3. high resolution total station network measuring a prisms network, individual reflectorless points network and reflectorless grid network in the Siq slopes, for monitoring slope/blocks deformation;
4. manual crack gauge network on 25 main discontinuities.

An integrated set of direct and remote distinct monitoring systems and techniques has been implemented for the analysis of rock slope deformations in the Siq of Petra. The overall system has been designed and installed according to potential capability of the different techniques as well as cost/benefit and long-term

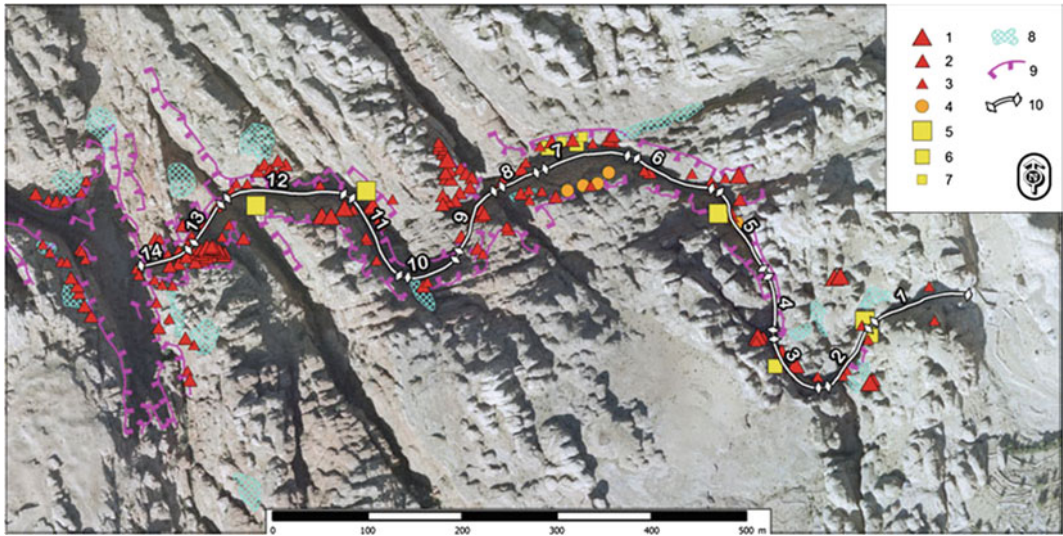


Fig. 12 Landslide inventory map of Petra area: 1 rockfall large; 2 rockfall medium; 3 rockfall small; 4 toppling large; 5 slide large; 6 slide medium; 7 slide

small; 8 unstable debris; 9 scarp; 10 Siq sector. Landslide volume: large >15 m³; medium 5–15 m³; small <5 m³ (Delmonaco et al. 2014)

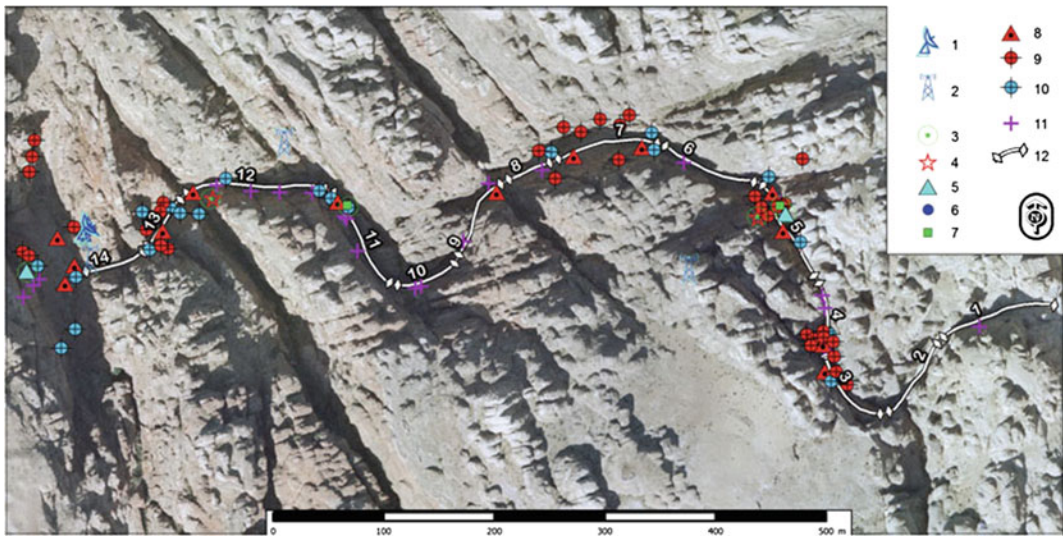


Fig. 13 Monitoring system map: 1 gateway; 2 repeater; 3 air temperature/humidity sensor; 4 crackmeter; 5 wire deformometer; 6 meteorological station; 7 tiltmeter; 8

TM30 robotized station; 9 TM30 monitoring prism; 10 TM30 reference prism; 11 Manual crack gauge, 12 Siq sector (Delmonaco et al. 2014)

sustainability, considering the specific geological and cultural environment of the Siq of Petra.

A regional scale analysis of the measurement points derived by SqueeSAR™ technique has provided evidence of a general stability of the Petra area in the time span considered (2003–

2010). The areas where some movement (>2 mm/year) occurred, are characterized by presence of incoherent material (e.g. debris, sands) removed by human activities and/or natural erosion and mostly located out of the Siq (Fig. 14).

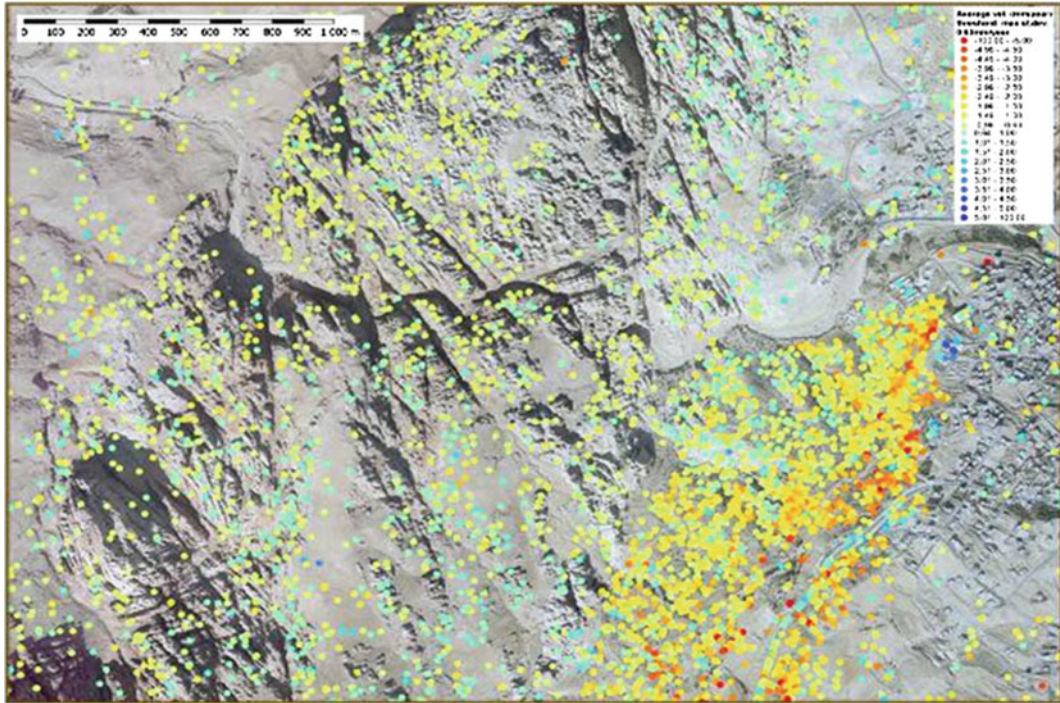


Fig. 14 Annual average velocity with 0.63 mm/year threshold (maximum standard deviation) (Delmonaco et al. 2014)

An integrated network composed by 2 wire deformometers, 2 crack deformometers and 2 tiltmeters, 6 air-temperature sensors, a meteorological station, provided by Minteos® s.r. l., with wireless technology sensors for on-time registration and transmission of data, has been installed in the Siq in June 2013 (Fig. 15). The crack and wire-gauge system, based on 18 months observation data set, has provided a generally constant trend of movements, with negligible displacements, mostly related with daily temperature and humidity fluctuations. Only one discontinuity, in a large block located in sector 5, is showing a permanent displacement, in closure, of about 5.5 mm from 10 June 2013 to 10 August 2015.

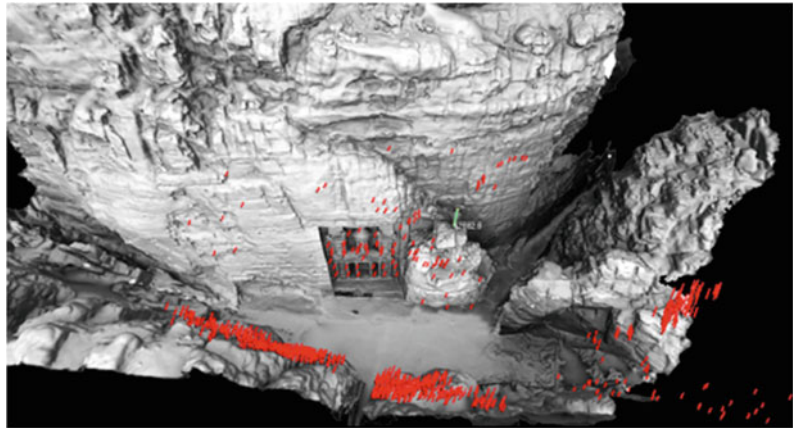
A Leica® TM30 reflectorless total station has been used to extend deformation control and analysis of the 6 potentially unstable blocks as well as provide information on movements of 15 slope faces located inside the Siq and in the Outer Siq (Treasury area, Fig. 16).

A total of 81 micro prisms, (22 prisms in stable areas as reference points and 59 as monitoring targets) properly designed to reduce visual impacts, have been installed by local climbers. The technique (acquisition and elaboration of different 3D model compared during time) will provide 3D movement of unstable blocks/slope sectors and further movement (2D analysis) of the deformation slopes through the acquisition of about 1700 reflectorless monitoring points. In detail, the TM30 monitoring system is based on a polygonal constituted by prisms located in the lower portions of the Siq, working as reference points. Bimonthly lectures with the total station along the base polygonal will provide a regular time-space acquisition of control point clouds in the slope sectors to be monitored. Point clouds are constituted by prisms, working as base monitoring points, and reflectorless points that the total station is capable to detect and measure in the field between consecutive acquisitions. The precision with such a topographic



Fig. 15 Installation of wireless instrumentation network (Delmonaco et al. 2014)

Fig. 16 Reflector-less surveyed points in the Treasury area (Petra, Jordan), superimposed on the terrestrial laser scanner (Delmonaco et al. 2014)



monitoring system is sub-millimetric. The monitoring output is given by differences between distinct lectures and 3D topographic models derived by point clouds analysis in any monitored sector of the Siq. Such differences will provide deformation of points in the slopes for further analysis of actual/potential unstable areas of the Siq. The analysis with reflectorless total station is actually in the stage of set up finalization (i.e. reference and monitoring prisms georeference, implementation of reflectorless monitoring plan, zero cycle measurement) so that no data are available. For this technique, a correct design of the network is fundamental to determine and assess relative movements of points, so that a particular attention and intense field work is being devoted to provide the highest accuracy

in the system configuration (Margottini et al. 2016a).

Measurements of the manual crack gauge network, since June 2011, has provided records that exhibit a general enlargement of the monitored discontinuities (average of ca. 1 mm) during the 2011–2012 winter seasons and a slight shrinking of the fractures apertures in the summer seasons. Nevertheless, considering the limited number of measurements taken, it is still insufficient to define a clear displacement trend versus climate-related parameters and local geomorphic conditions of the blocks/slope portions examined.

In conclusion, in the Siq of Petra, conventional geotechnical and topographic instrumentation, with innovative and powerful

components, has been installed to provide a wide set of techniques to produce evidence of displacement in the Siq slopes. These site-scale field techniques have been integrated with a satellite interferometric analysis in order to provide also a large-scale analysis of ground displacement in the Petra Park. It is expected that the adopted approach will provide in the development of the project, a discrimination of the most critical blocks/areas where to focus a geotechnical modeling for the analysis of actual slope stability conditions and suggestion of mitigation strategies for the benefit of the site managers (Margottini et al. 2016b).

2.5 Low Environmental Impact Monitoring Systems: Machu Picchu

The Geology of Machu Picchu area (Fig. 17) is characterised by granitoid bodies that had been emplaced in the axial zones of the main rift system. Deformation of the granite, caused by cooling and tectonic phases, originated 4 main joint sets, regularly spaced (few decimetres to metres). Several slope instability phenomena have been identified and classified according to mechanism, material involved and state of activity. They are mainly related to rock falls, debris flows, rock slides and debris slides. Origin of phenomena is kinematically controlled by the

structural setting and relationship with slope face (rock falls, rock slide and debris slides); the accumulated materials is the source for debris flow. Geomorphological evidences of deeper deformations are currently under investigation (Canuti et al. 2008a, b).

The geological and geomorphological investigations conducted in the area of Machu Picchu highlight the presence on many slope instabilities, mainly with low depth (Fig. 18). Several slope instability phenomena have been identified and classified according to mechanism, material involved and state of activity. They are mainly related to rock falls, debris flows, rock slides and debris slides. Origin of phenomena is kinematically controlled by structural asset and relationship with slope face (rock falls, rock slide and debris slides); the so accumulated materials is the source for debris flow.

In the area of the Carretera (road to Citadel of Machu Picchu) a precise mapping of debris deposits and past debris flows was carried out, leading to a zonation of processes within the limits of the ancient landslide detected by Sassa et al. (2001). The situation of the slope with the citadel is more complex due to the strong structural control of the master joints on the slope evolution. In this, planar rock slides are mainly affecting the NE flank while rock falls are predominant on SE cliff.

A low environmental impact monitoring system has been established on the area having the



Fig. 17 General view of Machu Picchu area

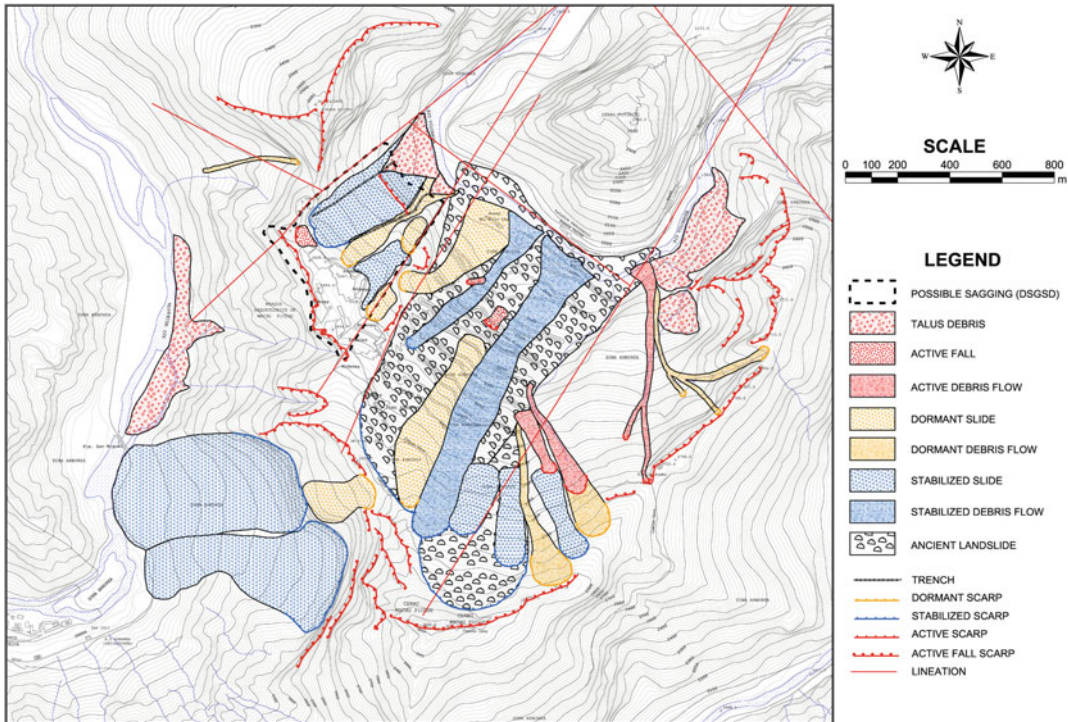


Fig. 18 Geomorphological map of the area (Canuti et al. 2008a, b)

purpose to minimize equipments usage and, in the mean time, to collect reliable data on surface deformations. The monitoring network comprise a GPS, multi temporal laser scanner survey, Ground based Radar interferometry (GB-SAR) and Satellite Interferometric Synthetic Aperture Radar (InSAR).

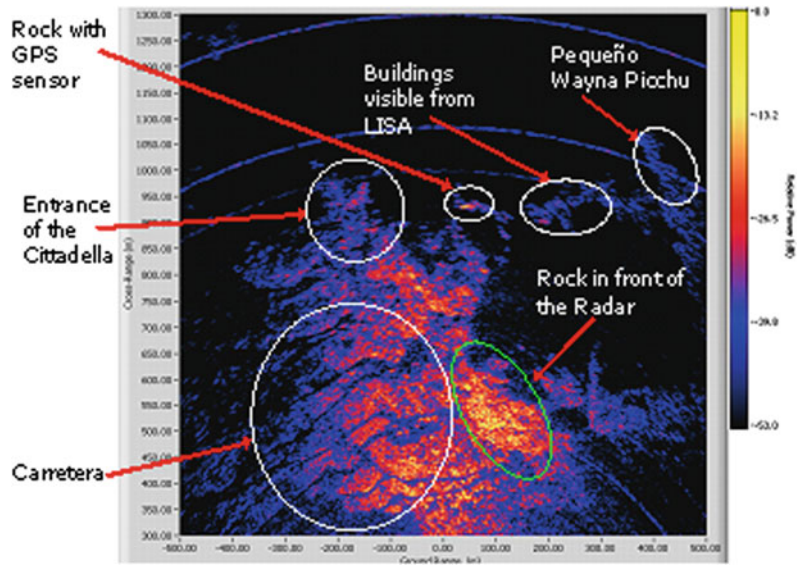
The site was one of the first worldwide case study for the application of Ground based Radar interferometry (GB-SAR). On the 3rd October 2004 the LISA Radar system was installed in a small open area which is part of the old train station in Puente Ruinas, just at the beginning of the road going up to the archaeological village (Fig. 19). From this site (Fig. 20) it is possible to see some buildings of the lower part of the “Ciudadela” entrance and to see the whole vegetated zone below, where it is expected to observe the possible sliding movement. With the data, that has been continuously acquired up until now, no significant displacements have been detected. Considering the very low displacement rate



Fig. 19 The LISA GB SAR system

measured by other monitoring systems, we expect that at least a full year of measurement is needed to get reliable data in order to see every possible small displacement affecting the Inca site.

Fig. 20 Power image with reference points



The analysis of monitoring data, integrated with field observations is suggesting (Fig. 21).

1. the stability of the upper part of the citadel were several GPS sensor do not exhibit any movements; also archaeological structures seem to be relatively undamaged;
2. the continues rock falls in the S–W side of the cliff and related citadel’s border, were also archaeological structure have been damaged by progressive lateral detensioning; this is probably the area with the highest short-term conservation problem.
3. the presence of a paleo-landslide in the North–East flank, with likely thickness of some tens meters, limited by a tension crack the discovering in 2004; in this area neither GPS nor PS nor JRC GBR-SAR detected any kind of deformation; in this area also structural geology detect some not regular pattern in the measurement.

Finally, the collected data are beginning to give a first picture of the slope evolution of the site. Nevertheless, the analysis of the monitoring data collected from the systems installed by Italian, Japanese and Czech–Slovak groups, together with data provided by Canadians and Peruvians, will allow a better evaluation of the

mechanisms of slope processes and of landslides, leading to a complete harmonization amongst the observation of the different research groups involved.

As historical consideration, the data collected suggest the possibility that the site of Machu Picchu could have been selected by Incas also because of the availability of two large block deposits, useful for constructions: one on the so called “cantera” and the second in the paleo-landslide recently discovered.

3 Conclusion

Protection of cultural heritage from landslide needs both a highly qualified know-how and funds, due to the importance of the site to protect and the possibly additional difficulties during the works execution; in some developing Countries such achievement is still difficult and international support as from International Consortium on Landslides is quite important for rising awareness. Along with the funds used to consolidate and make safer the areas at risk, additional economical efforts have to be considered for the monitoring and maintenance of such works.

Cultural heritage protection requires integrated approach among different disciplines,

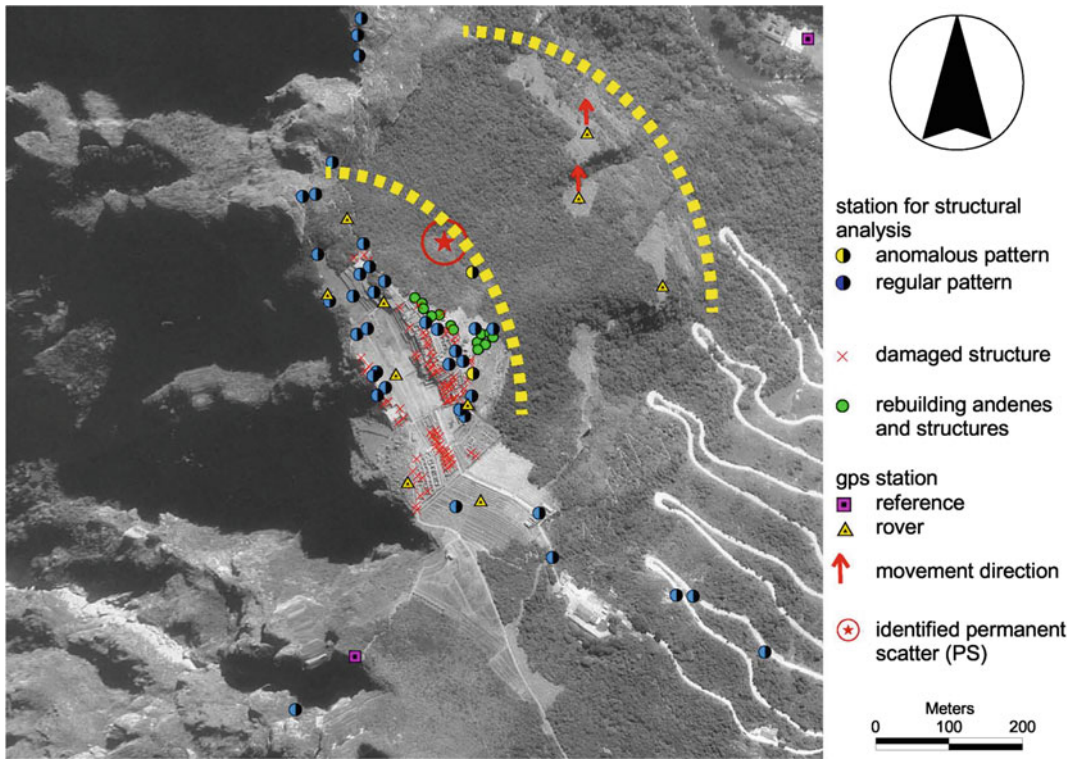


Fig. 21 Integrated map of surface deformation evidences and present monitoring data. *Yellow dashed lines* show area covered by radar interferometry monitoring (Canuti et al. 2008a, b)

including restoration, and very deep investigation in each different sector of knowledge. Even a limited knowledge in a single step of the process may affect the entire process.

The majority of damage to historic structures has been caused due to changes in the geotechnical environment (foundation ground, subgrade) resulting from both the change of the stress (re)-distribution and the change of engineering properties of the soils and rocks triggered by: groundwater effects, dynamic effects (incl. internal stresses), and static load effects, series of geohazards with different impact on the cultural heritage site occur. Very often the above changing in geotechnical environment are the consequent of not proper human intervention on the same cultural heritage site and/or in the surroundings.

Climate change is an important element for changing the geotechnical environment leading to landslides, suitable to reactivate areas with

stabilized phenomena, where cultural heritages have been settled.

In detail, when dealing with cultural heritage there is the need of a correct geological and geotechnical model and relationship with slope stability modelling. Data collecting do have to emphasize the requested need. Simplified approach can lead to a misunderstanding of processes and then to a wrong mitigation measurement.

Also there is the need to correlate properly data collection and elaboration (geological and geotechnical modelling and slope stability analysis) with mitigation measurements. Very often, in practical activities these elements are poorly connected together. Additionally, a proper maintenance plan, adequately economically supported, is essential to ensure long term stability of cultural heritage and efficiency of mitigation measurement.

Monitoring has re-affirmed to be an essential point in data collection for understanding evolutionary process, in monitoring work execution, in defining efficacy of adopted solutions.

New technologies can now provide powerful tools for better understanding mechanical properties of soil and rock, supporting strongly geological and geotechnical modelling. Namely, “in situ” laboratory are now the most promising.

Finally, it is worthwhile the importance of implementing a proper legislation and responsibility, since Cultural Heritage are a special case of exposed elements which require a special attention. This is also essential from an economical point of view since the conservation of Cultural Heritage is an essential step in the sustainable development of local communities.

References

- Canuti P, Margottini C, Fanti R, Bromhead E (2008a) Cultural heritage and landslides: research for risk prevention and conservation. In: Canuti P, Sassa K (eds) Landslides—disaster risk reduction, proceedings 1st world landslide forum. Tokyo, Springer, Nov 2008
- Canuti P, Margottini C, Casagli N, Delmonaco G, Falconi L, Fanti R, Ferretti A, Lollino G, Puglisi C, Spizzichino D, Tarchi D (2008b) Monitoring, geomorphological evolution and slope stability of Inca citadel of Machu Picchu: results from Italian INTERFRASI project. In: Canuti P, Sassa K (eds) Landslides—disaster risk reduction, proceedings 1st world landslide forum. Tokyo, Springer, Nov 2008
- Delmonaco G, Margottini C, Spizzichino D (2013) Rock fall assessment in the Siq of Petra, Jordan. In: Canuti P, Margottini C, Sassa K (eds) Landslide science and practice, volume 6: risk assessment, management and mitigation. Springer, Heidelberg, pp 441–449. ISBN 978-3-642-31312-6
- Delmonaco G, Leoni G, Margottini C, Spizzichino D (2014) Implementation of advanced monitoring system network in the Siq of Petra (Jordan). In: Lollino G et al. (ed) Engineering geology for society and territory, vol 8. Preservation of cultural heritage. Proceeding of IAEG XII CONGRESS, Torino, Springer, Sept 2014
- Fitzner B (2004) Documentation and evaluation of stone damage to monuments. In: Kwiatkowski D, Lofvendahl R (eds) Proceedings of the 10th international congress on deterioration and conservation of stone, Stockholm, vol II, pp 667–690, ICOMOS, Sweden, 27 June–2 July 2004
- Flores-Valdez C (2003) Importancia del nopal. In: Flores Valdez CA (ed) Nopalitos y tunas, producción, comercialización, poscosecha e industrialización. 1. Ed. Universidad Autónoma Chapingo, CIESTAAM. México, pp 1–18
- Gardiner D, Felker P, Carr T (1999) Cactus improves water infiltration rates in two soils. *Commun Soil Sci Plant Anal* 30:1707–1712
- ICCROM (2006) Introducing young people to the protection of heritages sites and historic cities—a practical guide for school teachers in the Arab region. Revised second edition
- Margottini C (2008) Recovery of the Buddha’s niches and cliff in Bamiyan (Central Afghanistan) after the Taliban destruction of 2001. Key note lecture. In: Landslides: disaster risk assessment. Springer, Berlin. ISBN: 978-3-540-69966-8
- Margottini C (2013). Surface erosion and mass movement constrains in the conservation of Akapana pyramid mound (Tiwanaku, Bolivia). In: (a cura di) Margottini C, Canuti P, Sassa K (eds) Landslide science in practice: risk assessment and mitigation. Springer, Berlin. ISBN: 978-3-642-31318-9
- Margottini C, Shadis R (2010) monitoring mission in Tiwanaku (Bolivia). UNESCO World Heritage Centre internal report, 8–12 Nov 2010
- Margottini C, Gigli G, Ruther H, Spizzichino D (2016a) Advances in geotechnical investigations and monitoring in rupestrian settlements inscribed in the UNESCO’s World Heritage List. In: Proceedings of the fourth Italian Workshop on Landslides, Procedia, Elsevier
- Margottini C, Gigli G, Ruther H, Spizzichino D (2016b) Advances in sustainable conservation practices in rupestrian settlements inscribed in the UNESCO’s World Heritage List. In: Proceedings of the fourth Italian workshop on landslides, Procedia, Elsevier
- Ramsey JE (1999) Evaluación del comportamiento del adobe estabilizado con cal y goma de tuna. Tesis para optar al Título de Ingeniero Agrícola. Universidad Nacional Agraria. La Molina. Lima
- Sassa K, Fukuoka H, Kamai T, Shuzui H (2001) Landslide risk at Inca’s World Heritage in Machu Picchu, Peru. In: Proceedings UNESCO/IGCP symposium on landslide risk mitigation and protection of cultural and natural heritage, Tokyo, pp 1–14
- Tanaka H, Fujisawa K, Asai K (2008) Identifying unstable rock blocks by measuring micro-tremors and vibration on cliffs. *Adv Geosci* 14:165–171
- World Bank (1994) Cultural heritage in environmental assessment. Environmental assessment sourcebook, Update, n 8 (prepared by Taboroff J). The World Bank, Environment Department, 8 p

TXT-tool 4.886-1.2

Procedures for Constructing Disaster Evacuation Maps: Guidelines and Standards

Su-Chin Chen and Lien-Kuang Chen

Abstract

How to reduce the damage and casualties from debris flows is one of the most significant studies needed to protect the public. The most pressing need, as a precaution against natural calamities, is to map out evacuation directions and refuges in debris flow disaster areas. Local residents should be trained in emergency concepts and instinctively using common sense, through teaching, evacuation training, organizing a system for warning announcements, and weather prediction information.

Keywords

Debris flow · Evacuation map · Evacuation route
Disaster prevention

Contents

1 Introduction	669
2 Fundamental Principles	670
2.1 Evacuation Map Construct Steps	670
2.2 Evacuation Map Samples	671
References	673

1 Introduction

Typhoon Herb on July 31, 1996, the Chi–Chi earthquake on September 21, 1999, and Typhoon Toraji on July 30, 2001 caused massive debris flow disasters in Taiwan. Serious damage included embankment breaches, damage to bridges, the undermining of road foundations, and collapse of buildings. There were dozens of casualties in the debris flow disasters.

The effects of global warming have changed rainfall patterns towards greater rainfall extremes. Traditional engineering countermeasures appear to be unreliable, so evacuation maps have become the one of the most effective methods for decreasing the chances of casualties in potential hazard areas. Therefore, creating evacuation maps plays an important role in

S.-C. Chen (✉)
Department of Soil and Water Conservation,
National Chung Hsing University, Taichung 402,
Taiwan, ROC
e-mail: scchen@dragon.nchu.edu.tw

L.-K. Chen
National Science and Technology Center for Disaster
Reduction (NCDR), New Taipei 23143, Taiwan,
ROC
e-mail: steven_chen@ncdr.nat.gov.tw

disaster management, reaction and recovery. The map is also an important tool in decision-making during disaster response.

Evacuation maps can provide information for the disaster response decision-maker about evacuation routes, the locations of rescue manpower and machinery, and all necessary infrastructure information within the disaster area. The map may also provide information on the potential hazard area, preparation for hazards, warning signs of potential disasters, response procedures during the disaster, and resources for recovery from the disaster. All of this information can raise overall self-defense capability with respect to disasters in the society and reduce the possibilities of loss of lives and property.

This guide will explain the principles and steps for producing an evacuation map. Both residents and rescue units can learn from the map. This guide includes

1. Understanding the information needed to construct the map.
2. Flow chart for producing the map.
3. Simple guide to identifying potential disasters in a neighborhood.
4. Principles for finding the best evacuation routes and shelter.
5. Simple methods for evaluating defense capacity.
6. Disaster prevention knowledge.
7. Other useful knowledge for management.

2 Fundamental Principles

Evacuation maps are produced based on the current understanding of the possible disaster locations and affected areas. The impact on

society and social vulnerability must be evaluated first. When the impact of a disaster exceeds the defense capabilities of the society, residents must be evacuated before the disaster. Shelters must be located in a safe area or in a location that has easy access to all rescue resources. This can dramatically reduce casualties and possible property loss.

2.1 Evacuation Map Construct Steps

The procedure for constructing an evacuation map is shown in Fig. 1.

1. Making a draft plan: Produce a plan according to the probable disaster type and area. This plan should consider the objects, targets, area, information, mission, budget and schedule.

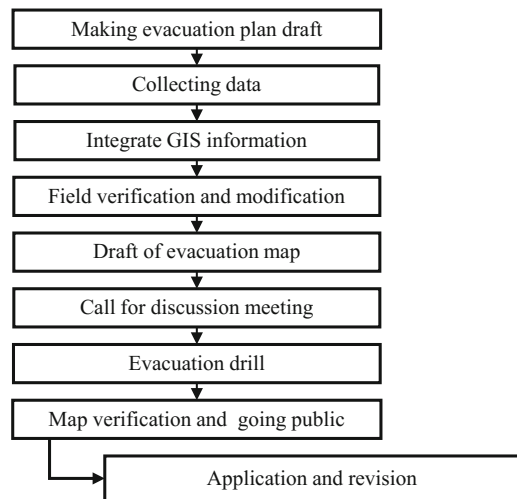


Fig. 1 Map construction procedure

2. Collecting data: The data collected should include the following:
 - i. Potential disaster types (earthquakes, floods, landslides, debris flows, etc.)
 - ii. Influence area (direct and indirect influence area, such as houses, roads, infrastructure, etc.)
 - iii. Evacuation and transportation routes (route distance, direction, transport capacity, etc.)
 - iv. Shelter (photos of buildings, their capacity, location, managers, etc.)
 - v. Rescue resources (police, firefighters, rescue teams, medical, transportation, volunteers, etc.)
 - vi. Emergency contact information (the phone numbers and addresses of police stations, fire brigades, public health centers, officers, etc.)
 - vii. Common knowledge (signs for debris flows)
 - viii. Landmarks (name, location, photo, etc.)
 - ix. Indicators for evacuation (warning criterion of rainfall or water level)
 - x. Other useful information (useful resources, maps, indices, etc.).
3. Data integration: Overlap all information on the map using the same scale in a GIS system.
4. Field verification and modification: Invite experts and local residents to examine the map information. This examination must be done through field investigation so that all potential hazards can be identified.
5. Draft of evacuation map: Combine all the above information, producing the evacuation map.
6. Call for discussion meetings: Invite all officers from responsible agencies, bureaus, cities and administrative units to check the information on the map, and call for a discussion meeting. Confirm that all the figures, text, symbols, etc. are correct, readable, and easy to understand.
7. Drills: Local residents must carry out practice drills to find all potential problems and application difficulties.
8. Map verification and going public: The final map must be verified by a meeting of experts. Then the map should be sent to all related agencies, bureaus, administrative units and people within the potential hazard area.
9. Application and revision: To reflect the changes in local conditions over time, drills should be held at a regular frequency and may require modification after a disaster. Revisions can guarantee that the map is still applicable for any future disasters.

2.2 Evacuation Map Samples

Different types of disasters require different types of maps. A version for ordinary people should list only simple and necessary information. The professional version should have more detailed information. These kinds of maps usually are prepared for the smallest administrative units such as a village. Figure 2 shows a simple

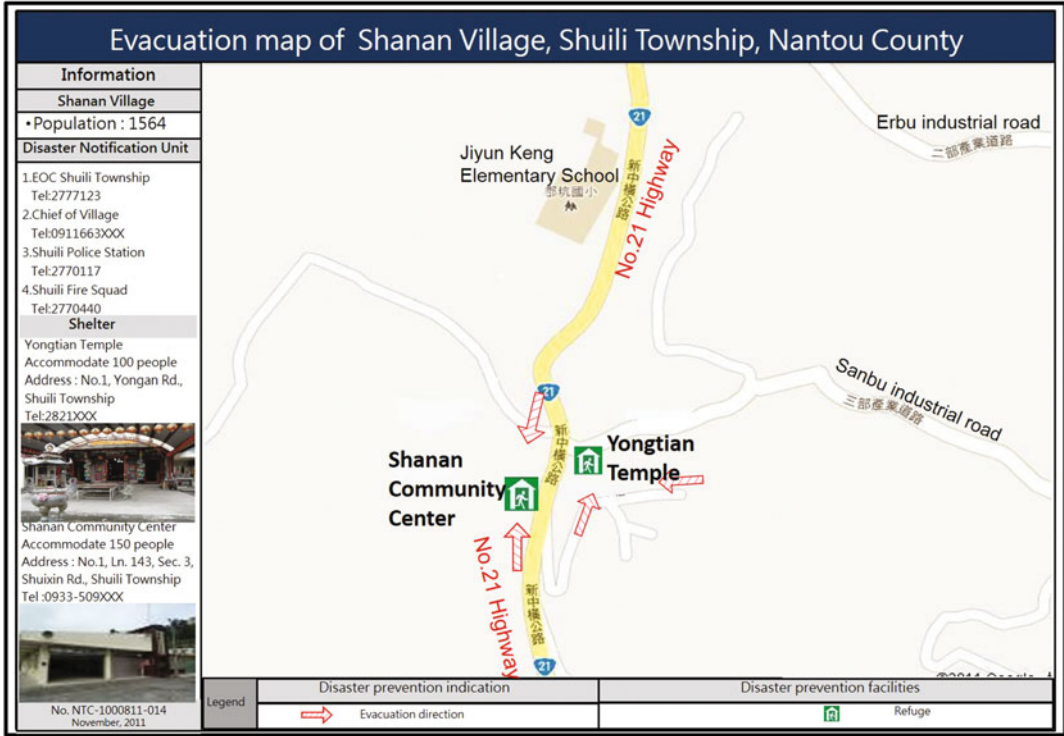


Fig. 2 Simple version of an evacuation map for residents. Source National Fire Agency

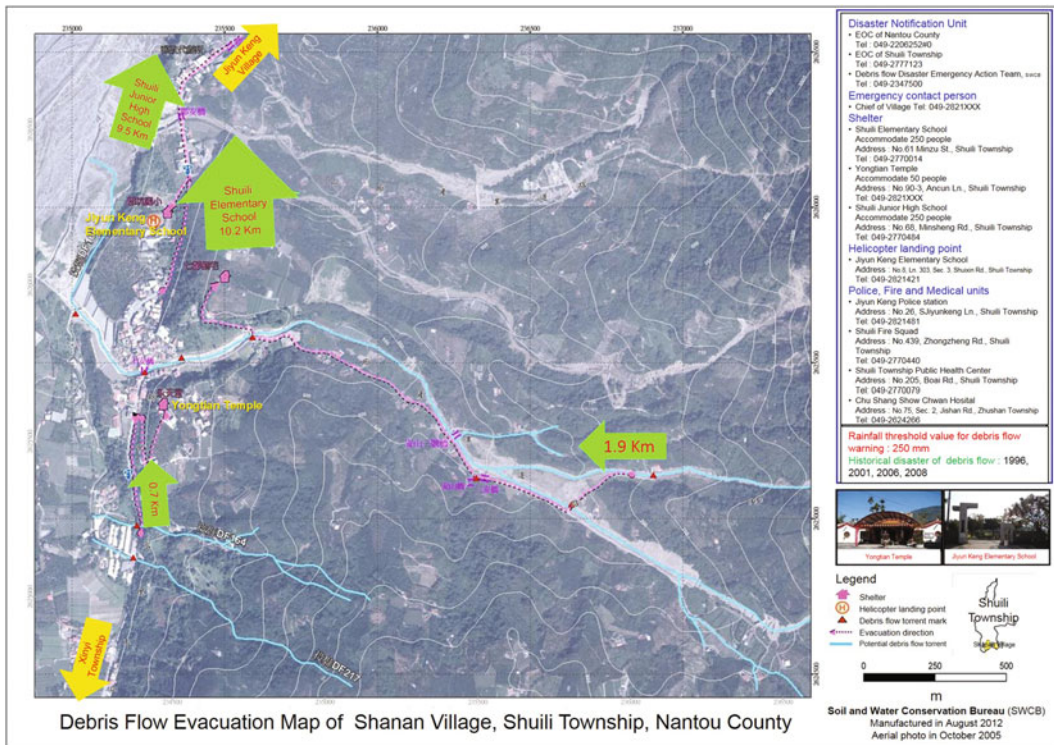


Fig. 3 Debris flow evacuation map. Source Soil and Water Conservation Bureau



Fig. 4 Earthquake evacuation map. Source Tainan City

version of a disaster evacuation map. Figure 3 shows a professional version of a debris flow evacuation map. Figure 4 shows the professional version of an earthquake evacuation map. The simple version focuses on providing correct and clear information on evacuation routes, shelters, and related emergency contact information.

References

Debris flow disaster prevention information web. <http://246.swcb.gov.tw>
 Disaster prevention information web of Tainan City. <http://210.59.250.229/TNDS/>
 National fire agency disaster information service web. <http://www.nfa.gov.tw>

TXT-tool 4.886-1.3

Emergency Post-landslide Disaster Documentation

Lien-Kuang Chen

Abstract

Learning from disaster is the motto for all disaster prevention workers. Not everyone has the chance to experience a disaster and to learn from the experience. Therefore, recording all the details of a disaster for people to learn becomes very important. Based on the report of a disaster investigation can provide rescuer reference for danger evaluation, immediate hazard mitigation and recovery process. Emergency post-landslide documentation guides the investigating officers on the application of the survey form. Combining multiple hazard record, we can learn about the social vulnerability influence and future policy making reference.

Keywords

Landslide · Disaster investigation · Survey form · Hazard mitigation

Contents

1 Introduction	675
2 Investigation Procedure	676
3 Sample Result	676
4 Investigation Form	678
References	682

1 Introduction

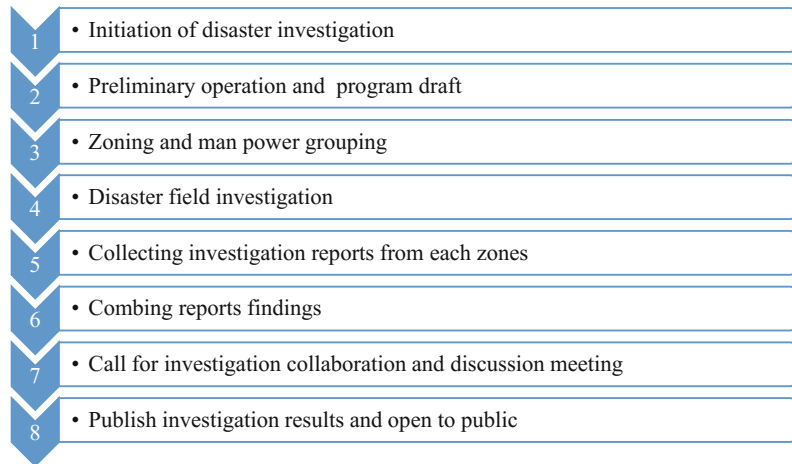
Emergency post-landslide investigation guide are composed of:

1. Disaster investigation method
2. Disaster investigation procedure
3. Determine input for investigation form
4. Preliminary disaster evaluation
5. Writing of investigation report
6. Other investigation skill.

According to the users or purposes of the investigation report, it can be for general purpose or professional use. General investigation emphasizes on the locations, the type of disaster,

L.-K. Chen (✉)
National Science and Technology Center for Disaster
Reduction (NCDR), New Taipei 23143, Taiwan,
ROC
e-mail: steven_chen@ncdr.nat.gov.tw

Fig. 1 Natural disaster investigation operation procedure



loss, casualties, qualitative description of disaster and emergence response and immediate mitigation measures. Usually there is no information for scale of disaster, detailed cause or quantitative description of disaster in general investigation and it is meant for general public or quick statistics. Professional investigation includes all information above and detailed geographical location, scale of disaster (type, depth, volume, etc) and original land usage (vegetation, land cover and land use). Combining with river elevation, precipitation and earthquake information, one can analyze the mechanics for the disaster, disaster process and disaster causing parameters. Professional investigation usually is the base for long term recovery and mitigation measures.

2 Investigation Procedure

Disaster information can be obtained through the following sources:

1. Disaster reported from residents
2. Disaster investigator
3. Remote sensing photos
4. Interview with local residents
5. Historical observation data
6. Disaster field measurements
7. Other information.

Therefore, disaster investigation can be done through different approaches. Voice, photos, maps, images and videos can be used to describe the location, cause, scale, type and mitigation of the disaster. Hence a standardized investigation form can enforce the uniform standard between investigators or events. This is essential for large-scale events.

For single event investigation, Fig. 1 shows the standard procedure.

3 Sample Result

Disaster investigation is based on single event (from typhoon, heavy rainfall, and earthquake). In the investigation report, tables and figures should be separated according to the type of disaster and locations. The investigation results can be shown at a global scale (Fig. 2 for a large watershed) or at a single location scale (Fig. 3 a single landslide). The content should include:

- (1) Introduction: rough description, investigation purpose, man power organization and structure, investigation schedule
- (2) Basic information: administrative information, disaster locations, critical time frame and type of disasters

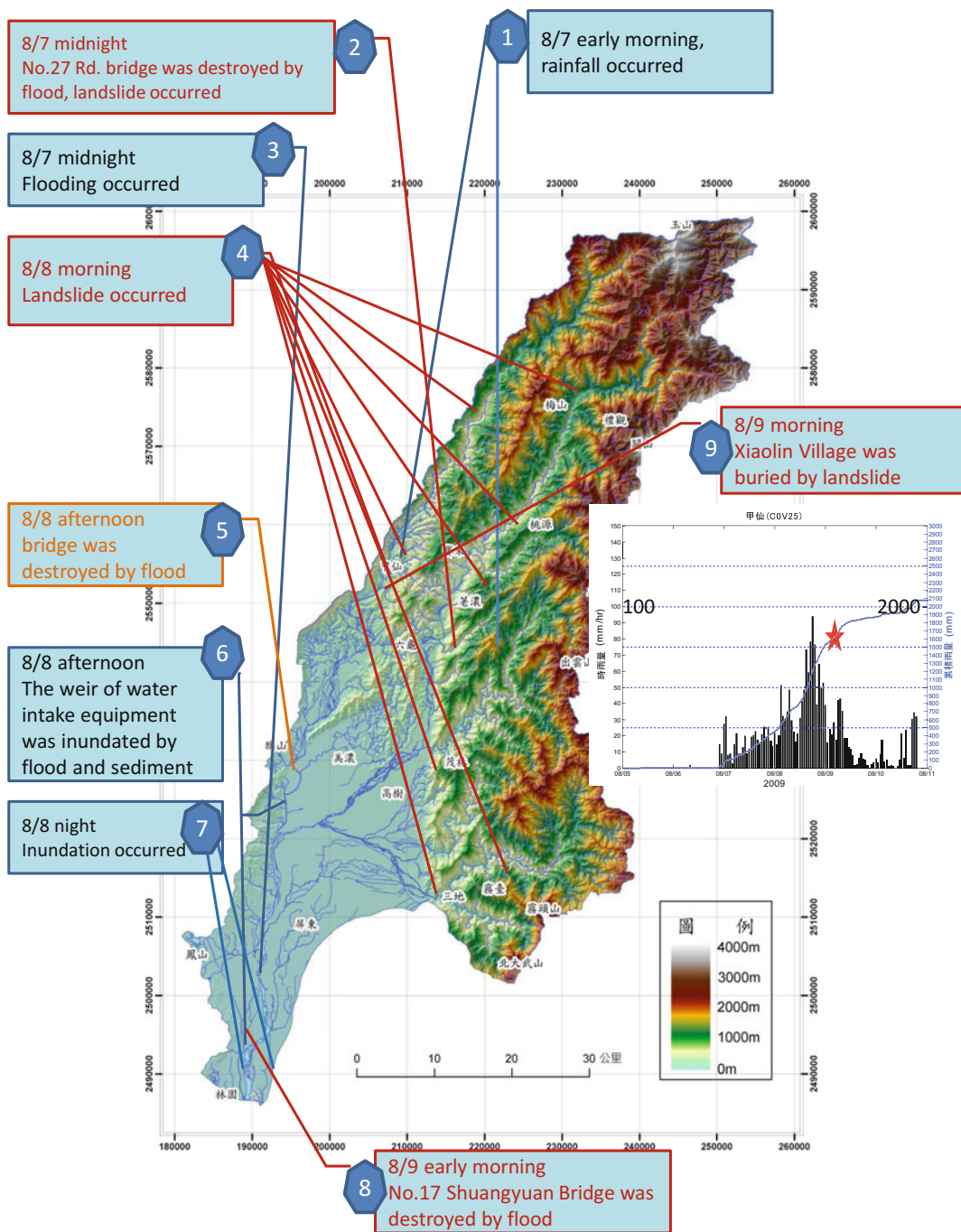


Fig. 2 Disaster relation in KaoPing watershed from Typhoon Morakot. *Source* National Science and Technology Center for Disaster Reduction (2010)

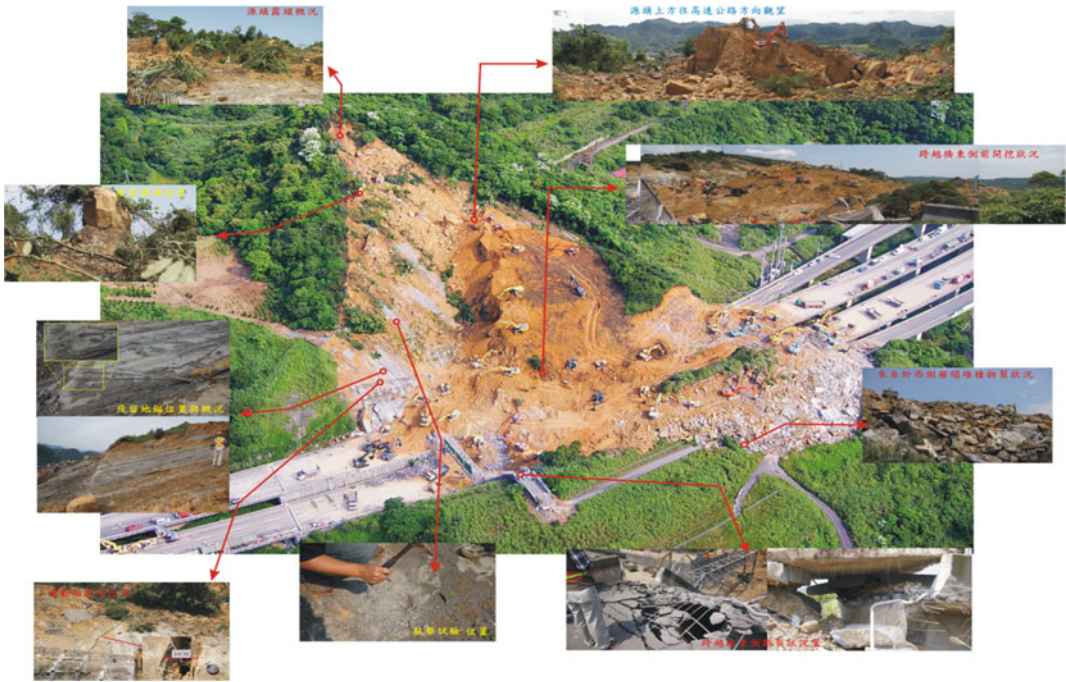


Fig. 3 Field investigation for landslide besides Highway. *Source* National Science and Technology Center for Disaster Reduction (2010)

- (3) Collected information: disaster details, surrounding conditions, historical data, structure condition within disaster area
- (4) Investigation: statistics, loss, interviews
- (5) Discussion: cause of disaster and possibility for immediate second disaster
- (6) Mitigation strategy: short, medium and long term strategy for disaster mitigation
- (7) Suggestion and conclusion
- (8) Other information: meeting record, other reports.

4 Investigation Form

Apply systematic disaster record and institutionalized disaster investigation forms can help us to understand the different temporal and spatial disaster events, in particular the often occur disaster areas. The disaster investigation records just as the hospital patient’s chart-record, that are useful for the officer to assess the disaster potential and land use management. As shown in

Table 1 Landslide investigation form

(I) Basic Information Investigation time: _____ Investigator: _____

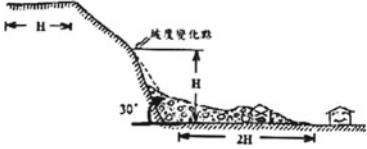
Landslide No.	Province	Town	Village	Watershed	Sub-watershed	GPS coordinate		Land mark
						Lat.	Lon.	

Type of landslide Bed erosion Major slide Side slides

(II) Field condition

Landslide reason (Multiple choice)	<input type="checkbox"/> Rainfall <input type="checkbox"/> Earthquake <input type="checkbox"/> Bed erosion <input type="checkbox"/> Other: _____
Type of slide (Multiple choice)	<input type="checkbox"/> Rock fall <input type="checkbox"/> Turning <input type="checkbox"/> Wedge Failure <input type="checkbox"/> Plain Failure <input type="checkbox"/> Arc Failure <input type="checkbox"/> Debris slide <input type="checkbox"/> Creep <input type="checkbox"/> Erosion <input type="checkbox"/> Road foundation break <input type="checkbox"/> Others: _____
Rock Strata	<input type="checkbox"/> Stratified <input type="checkbox"/> Block <input type="checkbox"/> Sandstone-Shale Interface <input type="checkbox"/> Conglomerate <input type="checkbox"/> Decomposed
Material for rock (Multiple choice)	<input type="checkbox"/> Volcanic rock (<input type="checkbox"/> Felds path <input type="checkbox"/> Quartz <input type="checkbox"/> Pyroxene) <input type="checkbox"/> Metamorphic rock (<input type="checkbox"/> Slab <input type="checkbox"/> Schist <input type="checkbox"/> Gneiss <input type="checkbox"/> Meta-Sandstone <input type="checkbox"/> Marble) <input type="checkbox"/> Sedimentary rocks (<input type="checkbox"/> Sandstone <input type="checkbox"/> Shale <input type="checkbox"/> Conglomerate <input type="checkbox"/> Lime) <input type="checkbox"/> Others (<input type="checkbox"/> Colluvial soil <input type="checkbox"/> Other: _____)
Scale(m)	<input type="checkbox"/> Measured with device <input type="checkbox"/> Estimation Average length: _____m, Average width: _____m, Average depth: _____m
Remaining	<input type="checkbox"/> None <input type="checkbox"/> Width: _____m, Length: _____m, Average depth: _____m Max rock diameter: _____cm
Description for landslide material	
Vegetation	<input type="checkbox"/> Bare <input type="checkbox"/> Grass <input type="checkbox"/> Man made forest <input type="checkbox"/> Natural Forest
Vegetation on slide	<input type="checkbox"/> Bare rock <input type="checkbox"/> Rock pile (Vegetation area<10%) <input type="checkbox"/> Loose vegetation (10%<vegetation area<30%) <input type="checkbox"/> Medium vegetation (30%<area<80%) <input type="checkbox"/> Dense vegetation (area>80%)
Land use (Multiple choice)	Upper <input type="checkbox"/> Construction <input type="checkbox"/> Wet paddy field <input type="checkbox"/> Dry paddy field <input type="checkbox"/> Orchard <input type="checkbox"/> Beetle But <input type="checkbox"/> Bamboo <input type="checkbox"/> Man made forest <input type="checkbox"/> Road <input type="checkbox"/> Scenic area <input type="checkbox"/> Other: _____
	Lower <input type="checkbox"/> Construction <input type="checkbox"/> Wet paddy field <input type="checkbox"/> Dry paddy field <input type="checkbox"/> Orchard <input type="checkbox"/> Beetle But <input type="checkbox"/> Bamboo <input type="checkbox"/> Man made forest <input type="checkbox"/> Road <input type="checkbox"/> Scenic area <input type="checkbox"/> Other: _____
Position	_____ Landslide photo
Remarks	

(III) Protected target

Buildings	<input type="checkbox"/> None <input type="checkbox"/> No. of Public building (School, Hospital, Assembly Pt) <input type="checkbox"/> No of Houses: _____ (5 or more is considered as village)				
Public construction	<input type="checkbox"/> None <input type="checkbox"/> Road _____ Possible damage: _____ m <input type="checkbox"/> No. of Bridge _____ (Name: _____) <input type="checkbox"/> Retaining Wall, Possible damage: _____ m				
Other	<input type="checkbox"/> None <input type="checkbox"/> Agriculture land <input type="checkbox"/> Others: _____				
Protected target address					
History of hazard	Time	Type	Reason	Loss(Casualty, Property)	Countermeasure
<input type="checkbox"/> Yes					
<input type="checkbox"/> No					
Danger level	Upper slope <input type="checkbox"/> A <input type="checkbox"/> B <input type="checkbox"/> C <input type="checkbox"/> D Lower slope <input type="checkbox"/> A <input type="checkbox"/> B <input type="checkbox"/> C <input type="checkbox"/> D				
Description of danger level and suggestion					
Object danger level from landslide					Level of treatment
Distance from the landslide		Protected target			A: immediate
Lower slope	Upper slope	Public facilities or housing	General structure	Other	B: necessary
<2H	<1H	A B	C	D	C: can wait
2H~5H	1H~3H	C	D		D: no need

(IV) Suggested mitigation and cost

Necessity of mitigation	Suggested mitigation	Estimate cost

(V) Landslide location and photo

Location Map	Use 1/5,000 Photo map or 1/25,000 Geological Map, mark any mitigation structures with color pen, and write down GPS coordinates.
Draft map for landslide	

No. of Photo		Photo-01
Location	X: Y:	
Description		
No. of Photo		Photo-02
Location	X: Y:	
Description		

Remarks : Please add more columns for more photos

Table 1 for the investigation of landslide disaster. Fill in all the information in the table, also provide investigator to understand landslide or debris flow disaster response required survey work items and content.

References

- Ministry of Economic Affairs—Standard procedure for flood and draught disaster investigation
- Ministry of the Interior—Standard procedure for typhoon and earthquake disaster investigation
- National Science and Technology Center for Disaster Reduction (NCDR) (2010) 2010 disasters investigation and comprehensive database building project report
- Public Construction Commission—Standard procedure for typhoon disaster investigation
- Council of Agriculture—Standard procedure for major debris flow disaster investigation

TXT-tool 4.386-1.1

State-of-the-Art Overview on Landslide Disaster Risk Reduction in Slovenia

Matjaž Mikoš, Magda Čarman, Jože Papež
and Jernej Jež

Abstract

This paper is a state-of-the-art review of the present status of the Slovenian national legislation and procedures for the hazard and risk assessment of landslides (including rock falls and debris flows). The relevant governing act is the 2002 Waters Act that foresees several legislation documents to be accepted by the ministry in charge of waters in Slovenia. Thanks to the European Flood Directive, procedures have already been regulated in the field of floods, but have still to be regulated in the field of other water-related natural hazards and geo-hazards, such as landslides. In the last decade, several methodologies and different hazard maps have been prepared, but no legal acts (such as decrees, regulations, recommendations or similar acts, let alone standards) have been accepted so far on their basis. Generally, state legislation in the sectors of spatial planning and water management in the form of acts is up-to-date in Slovenia, but much more should be done for its direct implementation for a modern landslide disaster risk reduction.

M. Mikoš (✉)
Faculty of Civil and Geodetic Engineering,
University of Ljubljana, Jamova c. 2, 1000
Ljubljana, Slovenia
e-mail: matjaz.mikos@fgg.uni-lj.si

M. Čarman
SIIPS AD d.o.o., Potočka vas 20, 1410 Zagorje ob
Savi, Slovenia
e-mail: magda.carman@siips-ad.si

J. Papež
Hidrotehnik Vodnogospodarsko podjetje d.d.,
Slovenčeva ul. 97, 1000 Ljubljana, Slovenia
e-mail: joze.papez@hidrotehnik.si

J. Jež
Geological Survey of Slovenia, Dimičeva ul. 14,
1000 Ljubljana, Slovenia
e-mail: jernej.jez@geo-zs.si

Keywords

Hazard assessment · Legislation · Risk assessment
Slovenia · Landslide

Contents

1 Introduction	684
2 Review of Legislation in Slovenia	684
2.1 Protection Against Natural and Other Disasters Act (2006).....	685
2.2 National Programme for the Protection Against Natural and Other Disasters (2009).....	685
2.3 Waters Act (2002).....	685
2.4 Spatial Management Act (2002) and Spatial Planning Act (2007).....	687
2.5 Construction Act (2002).....	688
2.6 Other Acts (Since 2000).....	688
3 Emergency Acts in Slovenia	688
4 Conclusions	689
References.....	690

1 Introduction

Effective protection against landslides (the term landslides includes all types of slope mass movements), i.e., by directing settlements outside landslide-prone areas, must be provided for by the joint efforts of landslide experts and by the state and regional authorities. The most cost effective and therefore financially sustainable form of long-term landslide protection is prevention, especially the appropriate land use in landslide-prone areas. Therefore, it is crucial that spatial planning takes account of the technical knowledge of landslide occurrences. Such knowledge on landslide phenomena (i.e., causes, trigger factors) makes it possible to predict the possibilities of future landslides in selected areas.

In Slovenia, several studies have been made in the last two decades on predicting the occurrence of landslides. Initial estimates of the probability of the occurrence of landslides were preliminary and/or regional, but with technological advancements they have become ever more precise, i.e., local. More accurate assessments were made possible by developing and extending a comprehensive database of active landslides (called GIS_UJME), which was upgraded and modernized in 2005 (MORS 2005), but is not fully in the public domain. Nowadays in Slovenia, we have

three detailed hazard assessments of geo-hazards, namely the *Landslide susceptibility map* of Slovenia (Komac and Ribičič 2006), the *Debris-flow susceptibility map* of Slovenia (Komac et al. 2009), and the *Rock-fall susceptibility map* of Slovenia (Čarman et al. 2011), all of them at the scale 1:250,000—an overview of mass movement susceptibility maps in Slovenia was prepared by Zorn et al. (2012). The rock-fall susceptibility map was prepared by the Geological Survey of Slovenia, but it still lacks the proper validation. The methodology used to prepare these former two susceptibility maps (landslides & debris flows) can also be adopted for use at large scales for local hazard assessments (i.e., of the order 1:1000 to 1:50,000) (Jemec Auflič and Komac 2011). A similar methodology and susceptibility map of Slovenia are still needed for rock falls.

Such hazard assessments at the Slovenian national level are a good basis for directing human spatial activities (land use) at the local level and for further creating more precise local hazard maps in areas already identified for their high landslide hazard. Despite the developed methodologies, the estimates of geo-hazards are still rarely used in spatial planning, mainly due to the lack of legislation in landslide protection, and to a lesser degree due to inconsistencies and lack of supervision in the implementation of existing regulations. In all recent national regulations, prevention is stressed over intervention during natural disasters; yet how to act upon and after hazardous (e.g., landslide) events is more precisely defined than how to prevent them.

2 Review of Legislation in Slovenia

In 2005, the *Resolution on a National Programme for Mitigation of Instability Phenomena* was announced in the *Execution Plan of National Prevention Programme of Protection Against Natural and Other Disasters* in 2006, but it was not confirmed by the Government and therefore

not accepted in the National Assembly. The Slovenian national legislation documents that are important for the field of mass movements are as follows (Ribičič 2007; the date of acceptance of the original act is given; each has been changed several times afterwards, the list was updated for the current situation in 2014):

2.1 Protection Against Natural and Other Disasters Act (2006)

This act regulates the protection of people, animals, property, cultural heritage and the environment against natural and other disasters (ZVNDN 2006). Landslides are regarded as a natural disaster. The aim of protection against disasters is to reduce the number of disasters and mitigate their consequences. The act gives priority to preventive measures over intervention, but mainly regulates protection, rescue and relief during a disaster. Preventive measures in this act are defined as all measures that are undertaken in order to avoid the risk of a disaster, and respectively, measures to reduce the adverse consequences of a disaster.

The state and the municipalities are competent for the protection against natural and other disasters and for the implementation of protection, rescue and relief actions when such disasters occur. By law, it is necessary to prepare both corresponding risk assessments and, furthermore, on the basis of these assessments, emergency response plans for each type of natural and other disaster separately. The risk assessment is an analysis of the favorable conditions for a natural and other disaster to happen with an estimate of the possible course and consequences of the disaster, the proposed level of protection against hazards, and the proposal of preventive and other measures for protection, rescue and relief. The methodology for preparation is defined by the Decree on the contents and elaboration of protection and rescue plans (Decree 2012). The competent local and national authorities are liable for damages if these risk assessments and emergency response plans for municipalities are not prepared (the penalty is at least 1000 €).

Municipalities must use appropriate protective measures against disasters prescribed by this act; among others, spatial and urban planning measures (non-structural) and construction (structural) measures, mainly of a preventive nature, which shall be taken into account in spatial planning. An important complement to this act was accepted in 2010 that gives the Administration of the Republic of Slovenia for Civil Protection and Disaster Relief (URSZR) the right to accept guidelines and give opinions on disaster protection which has to be taken into account in national and municipal spatial planning documents (Guidelines 2013a, b). The administration (URSZR) also collects data on natural phenomena, disasters, their sources and the damages caused.

2.2 National Programme for the Protection Against Natural and Other Disasters (2009)

The *Resolution on National Programme for the Protection Against Natural and Other Disasters* gives priority to prevention (ReNPVNDN 2009). Provides for the preparation of a specific strategy and a specific program for protection against landslides, with the fundamental objective of mitigating the consequences of landslides, as well as the preparation of technical bases for deciding on conditions for a specific land use and for protection of areas threatened by landslides.

2.3 Waters Act (2002)

This act most directly treats the questions of landslide-prone areas and active landslides (ZV-1 2002). One of the objectives of this act is to provide protection for mankind and human property against the adverse effects of waters. The protection encompasses the implementation of measures to reduce or prevent risks from the adverse effects of waters and to eliminate consequences of such adverse actions. This law provides preventive and curative measures. The *Forest Act* (ZG 1993) is of lesser importance;

torrent watersheds management and the mitigation of torrential floods, landslides, rock falls and avalanches are part of integrated watershed management (Mikoš 2012) and therefore covered by the *Waters Act*.

The *Waters Act* foresees the determination of risk areas due to the adverse action of waters: i.e., flood, erosion, avalanche and landslide areas; the former being threatened by any form of mass wasting phenomena respectively mass movements (slides and slips, debris slides, debris flows, mud flows, rock falls, bergstürzes, rock avalanches, etc.). Risk areas are determined by the Slovenian Government; the methodology for their determination and classification into risk classes is to be prepared by the ministry responsible for waters (this is nowadays again the Ministry of the Environment and Spatial Planning—MOP). The risk areas should be displayed in spatial planning documents and in sectorial plans.

The first hazard map (not susceptibility map) and risk map was prepared for the devastated area after the large debris flow in the village of Log pod Mangartom that was triggered in November 2000 (Mikoš 2011). The debris-flow risk map of the area (Mikoš et al. 2007) that was prepared under the *Decree on the location plan for the impact area of the Stovže landslide in Bovec Municipality* (Decree 2003b) was used by the Government of the Republic of Slovenia to accept the *Decree on the conditions and limitations of construction in the area of Log pod Mangartom under threat from debris flows* (Decree 2004); the first decree of such art in Slovenia.

In accordance with the *European Flood Directive*, the corresponding methodology for flood areas has already been accepted in Slovenia: the *Rules on methodology to define flood risk areas and erosion areas connected to floods and classification of plots into risk classes* (Rules 2007), and the *Decree on conditions and limitations for constructions and activities on flood risk areas* (Decree 2008). The *Rules* lays down the method and criteria for the classification of land into flood and erosion risk classes, and the *Decree* specifies which spatial interventions are permitted or prohibited, depending on corresponding hazard classes in flood-prone areas.

Similar regulations for landslide-prone areas are still missing. In order to be able to accept such regulations, a methodology for determining risk areas and classifying land into risk classes due to landslides has been prepared (MORS 2004); official executive legal acts, such as rules and/or decrees are still missing. The same is true for debris flows, since a methodology for debris flow risk assessment has been prepared (MORS 2008) with no legal consequences.

Protection against the adverse effects of waters in risk areas should be provided by state and local authorities (municipalities). The state is responsible for the protection of people, the environment, economic activities and cultural heritage, and in periods of increased risk it should ensure the implementation of emergency measures. Landowners in landslide-prone areas are limited in their property owners' rights and are not allowed to freely intervene in such risk areas. The *Waters Act* defines the conditions under which landowners may intervene in the risk areas, but the detailed conditions and restrictions are set by the government in a water approval. A water approval is also issued for interventions in risk areas and must be issued prior to the issuing of a building permit. The applications for a water approval for interventions in landslide areas must contain a geological report on the terrain stability and propose mitigation measures. The same is true for interventions in an area that is landslide-prone as determined from a preliminary landslide hazard map. Such a warning hazard map must be published on the website of the ministry responsible for waters. Since there is not yet an officially accepted preliminary landslide hazard map, for informational purposes we use the Landslide susceptibility map of Slovenia at scale 1:250,000 (Komac and Ribičič 2006), prepared by the Geological Survey of Slovenia and which is available on the website of the Slovenian Environment Agency (ARSO). Thus the *Waters Act* prohibits the following in landslide-prone areas (Waters Act 2002, § 88):

- the retention of water, especially through the construction of terraces, and other

- encroachments that could accelerate saturation of the land;
- encroachments that could cause additional saturation of land and a rise in ground water levels;
- implementation of earthworks that additionally burden the land or remove burden from the base of the land;
- deforestation and major rehabilitation of forest structures and shrubbery that accelerate the sliding of land.

2.4 Spatial Management Act (2002) and Spatial Planning Act (2007)

This act (ZUreP-1 2002) defines that spatial planning in Slovenia should among other things take into account protection against natural and other disasters, and accordingly plan the appropriate spatial interventions, as defined by a stand alone Spatial Planning Act (ZPNačrt 2007). Under the current principles of spatial development for settlements, areas at risk to natural hazards are currently not exposed as less suitable for new settlements, since if flood alleviation measures for an existing settlement area are executed, new buildings are allowed to be built. If the spatial documents for a piece of land have settlements as a proposed land use, this use can be changed only by changing the spatial documents themselves. This act defines the types of spatial planning documents, their contents and preparation processes. Spatial planning documents allow for planning spatial arrangements and determining the guidelines, requirements and criteria related to land development. These documents should be based on expert knowledge of features and capacities of space; in their preparation it is necessary to consider the documents from the water management sector and from the protection against natural and other disasters. Spatial documents are the basis for developing projects for obtaining building permits, which are a prerequisite to starting the construction process.

The basis for developing spatial planning documents is information on the status of spatial conditions. The ministry in charge for spatial planning must establish and maintain a spatial information system, which encompasses data on the legal and factual situation in space, including information on risk areas. In Slovenia, a complete and fully updated spatial information system is not yet fully in place.

In Slovenia, we distinguish between government, municipal and inter-municipal spatial planning documents. The *National spatial plans* (NSPs) are the spatial arrangements of national importance, which include arrangements in the field of protection against natural and other disasters. Prior to the adoption of the *Act regarding the siting of spatial arrangements of national significance in physical space* (ZUPUPDD 2010), the NSP was used as a tool to plan spatial arrangements that were necessary due to the mitigation of the consequences of natural disasters. On the basis of the policies and guidelines established by the state, the municipalities are responsible for determining land use and conditions for the placement of interventions in space. The *Municipal spatial plans* (MSPs) govern spatial arrangements of local importance and provide land use and conditions for the placement of objects in space, i.e., the so-called *Spatial implementation conditions* (SICs) for both the entire territory of the municipality and specifically for each individual planning unit. But those plans have not yet been produced, because the regions have not been formally established. At present only the MSPs are valid for procedures related to building. The SICs are determined on the basis of development policy and land use, and also determine, inter alia, measures to protect people and property from natural disasters. The flood, erosion and fire safety are specifically exposed, but not so for landslide risk areas. Land use and SICs may also be provided by *Regional spatial plans* (RSPs). The operative part of MSPs should come out of natural conditions (e.g., soil bearing capacity, depth of groundwater table, effects on ground water regime ...), but in reality, it is not always

consistently considered. Also the regulation that a new object should not affect an existing one is not implemented strictly on landslide-prone areas.

2.5 Construction Act (2002)

This act prescribes the procedures for obtaining a building permit (ZGO-1 2002); it is directly associated with the *Spatial Planning Act*, because in the process of issuing a building permit the location and use of the planned object are assessed (if allowed) according to the prescribed conditions in the spatial planning act. The *Construction Act* stems from the assumption that the adopted spatial planning documents are clear, accurate, reliable, and render it possible to figure out the location's conditions, which are the starting point for construction. So any commencement of construction works, whose conditions are in detail prescribed by the *Construction Act* is also in its substance associated with the conditions laid down by the regulations on spatial planning and other legislation (i.e., *Environment Protection Act*, *Waters Act*, *Nature Protection Act*). Recently, the Ministry of the Environment and Spatial Planning started the procedure to update the *Construction Act*—together with the *Spatial Management Act* and a new *Act on Certified Architects and Engineers*; on one hand to make issuing a building permit a faster and an easy task to stimulate more new construction works in Slovenia and help stopping the crisis in the construction sector in Slovenia being there since 2009 (Sodnik et al. 2016), and on the other hand to de-regulate this profession.

2.6 Other Acts (Since 2000)

Other recently accepted acts related to landslide risk reduction in Slovenia are the following ones:

- *Ordinance on Spatial Planning Strategy of Slovenia* (OdSPRS 2004)
- *Resolution on National Environmental Action Plan 2005–2012* (ReNPVO 2006)

- *Natural Disaster Recovery Act* (ZOPNN-UPB1 2005)
- *Environment Protection Act* (ZVO-1-UPB1 2006).

3 Emergency Acts in Slovenia

In the last decades, the Slovenian National Assembly adopted a series of emergency acts, which provided the (financial) resources for the mitigation of large landslides triggered during heavy rainfalls. The best known such act was the *Act on the Measures to be Taken to Repair the Damage Caused by Landslide Stože in Bovec Municipality and by Large-Scale Landslides in the Territory of the Republic of Slovenia Occurring after 15 October 2000* (ZUPSB 2000), followed by the *Measures to Repair the Damage Caused by Certain Large-Scale Landslides in 2000 and 2001 Act* (ZUOPZ 2002). The conditions and modalities of funding—the acquisition and allocation is defined by the *Natural Disaster Recovery Act* (ZOPNN-UPB1 2005).

The Treaty on European Union allows the Republic of Slovenia as an EU Member State the use of state aid in mitigating natural disasters (including landslides). The awarding of state aid that applies only to the elimination of material damage is defined in the provisions of the Constitutional Treaty of the European Community. An overview of the legal regimes of neighboring countries which are EU members shows that they generally do not have a system act that regulates this area. Much emphasis is therefore placed on the role of insurance companies and state budget funds are drawn upon only after large natural disasters. Some countries (Austria, the Netherlands) also have special financial catastrophe funds, activated after natural disasters. Furthermore, a kind of an obligatory insurance against natural disasters exists in Spain, France and in the majority of Swiss cantons with a somewhat different role of the state among those countries.

Financing preventive activities, such as the preparation of hazard and risk maps, is not

regulated in Slovenia so they are not prepared for spatial planning documentation. The situation of financing the mitigation of large landslides is somewhat better; in such cases the Slovenian National Assembly adopts a special law for the mitigation of a local but large landslide or for the mitigation of numerous landslides triggered in large areas during heavy rainfalls. According to the *Public Finance Act* (ZJF-UPB4 2011) and the *Financing of Municipalities Act* (ZFO-1 2006), financial resources, from which funds for the mitigation of natural and other disasters can be drawn, are state and municipal annual financial reserves, which must, according to the *Public Finance Act* (ZJF-UPB4 2011), be 1.5% of the annual budget. For the state financial funds to be activated, the estimation of mitigation costs for all landslides triggered within a period of 90 days must be at least 0.3% of the annual budget of the Republic of Slovenia. This also means that the first landslides cannot be mitigated using the state funds, since a period of 90 days must be awaited in order to sum up the estimated costs of all the triggered landslides—in many cases it takes too much time for this system to work. The *Decree on damage evaluation methodology* (Decree 2003a) is an additional limitation factor since it defines the mitigation of which landslides count for the state financial support: only landslides that threaten settlements or engineering structures, particularly infrastructure. Thus, all smaller slips and slides or smaller rock falls not of large dimensions are not taken into account for state financing and are left to the municipalities to mitigate them as best they can.

4 Conclusions

The 2002 *Water Act* (ZV-1 2002) precisely defines the prohibitions and restrictions in activities in landslide areas, which have to also be taken into account when planning and constructing buildings, but an officially prescribed methodology for hazard and risk assessment for landslide-prone areas has not yet been laid out. As a result, landslide-prone areas are not

adequately represented in spatial planning legislative acts, and studies of geo-hazards are not a compulsory element of spatial planning documents. Therefore, the municipalities include the results of geo-hazard studies in their local spatial regulations at free will. Since the law does not oblige municipalities to estimate geo-hazards, they prefer to invest funds into other emergency or mandatory measures and research in the field of natural disaster protection. Existing knowledge in the field of forecasting the probability of the occurrence of landslides in Slovenia is sufficient to direct new settlements outside landslide-prone areas. Therefore, the implementation of preventive protection against landslides, rock falls and debris flows to the same level as floods is long overdue. The basis for such steps are already present in the existing legislation, but there has been a lack of interest and energy to prepare and also finally to accept the adequate legislative acts, such as methodologies, decrees, regulations and/or recommendations.

Inadequate implementation of preventive measures, i.e., preparing hazard and risk assessments for different areas, avoiding new construction in critical (risk) areas and carrying out preventive mitigation works (such as works to prevent the increase of landslide-active and erosion areas, and mitigation works on unstable slopes and in torrential watersheds), are reflected during heavy rainfalls in the unprecedented damage that is several times larger than the funds invested in prevention. There are still lessons to be learned in Slovenia from recent heavy rainfalls causing wide-spread catastrophic floods and triggering numerous landslides.

The situation in Slovenia in the field of legislation, planning and implementation of prevention activities against different kinds of mass movements is unsatisfactory. To a large extent the legislation has been modernized since 2000, but it remains too general and does not prescribe the mandatory mapping of hazard and risk areas due to mass movements as a part of spatial plans at different levels. Furthermore, funds that are invested in preventive measures are far too small for a decisive step forward.

Acknowledgements The overview presented in this paper was prepared within the framework of the European Alpine Space project START_it_up (State-of-the-Art in Risk Management Technology: Implementation and Trial for Usability in Engineering Practice and Policy), financed by the European Commission. Some of the Slovenian legislation documentation (especially acts) is made available in English in the new database called “Risk Technology Platform and Database” that is a web portal for hazard engineers and risk managers, offering them selected norms, standards and best practices (http://www.interpraevent.at/start_it_up/). The authors would like to thank Ivan Stanič for comments on spatial planning issues.

References

- Čarman M, Kumelj Š, Komac M, Ribičič M (2011) Rockfall susceptibility map of Slovenia. In: Proceedings Rocexs2011, interdisciplinary rockfall workshop, Innsbruck, May 16–19, 2011. Austrian Service for Torrent and Avalanche Control, Geological Service, Innsbruck, p. 3
- Decree (2003a) Decree on damage evaluation methodology (Uredba o metodologiji za ocenjevanje škode). Official Gazette RS, No 67/2003
- Decree (2003b) Decree on the location plan for the impact area of the Stovže landslide in Bovec Municipality (Uredba o lokacijskem načrtu za vplivno območje plazu Stovže v Občini Bovec). Official Gazette RS, No 127/2003
- Decree (2004) Decree on the conditions and limitations of construction in the area of Log pod Mangartom under threat from debris flows (Uredba o pogojih in omejitvah gradnje na območju Loga pod Mangartom, ogroženem zaradi pojava drobirskih tokov). Official Gazette RS, No 87/2004
- Decree (2008) Decree on conditions and limitations for constructions and activities on flood risk areas (Uredba o pogojih in omejitvah za izvajanje dejavnosti in posegov v prostor na območjih, ogroženih zaradi poplav in z njimi povezane erozije celinskih voda in morja). Official Gazette RS, No 89/2008
- Decree (2012) Decree on the contents and elaboration of protection and rescue plans (Uredba o vsebini in izdelavi načrtov zaščite in reševanja). Official Gazette RS, No 24/2012
- Guidelines (2013a) General guidelines for the preparation of the National spatial plan (Splošne smernice za pripravo državnega prostorskega načrta). Administration for Civil Protection and Disaster Relief, Ministry of Defence of the Republic of Slovenia, No 350-17/2013-6-DGZR. <http://www.sos112.si/slo/download.php?id=16167>
- Guidelines (2013b) General guidelines for the preparation of Municipal spatial plan or Inter-municipal spatial plan (Splošne smernice za pripravo občinskega prostorskega načrta ali medobčinskega prostorskega načrta). Administration for Civil Protection and Disaster Relief, Ministry of Defence of the Republic of Slovenia, No 350-17/2013-5-DGZR. <http://www.sos112.si/slo/download.php?id=16169>
- Jemec Auflič M, Komac M (2011) Standards und methoden der Gefährdungsanalyse für schnelle Massenbewegungen in Slowenien (Standards and methods for hazard assessment for rapid mass movements in Slovenia). WLF Zeitung 74(166):54–69
- Komac M, Ribičič M (2006) Landslide susceptibility map of Slovenia at scale 1:250,000 (Karta verjetnosti pojavljanja plazov v Sloveniji v merilu 1:250,000). Geologija 49(2):295–309
- Komac M, Kumelj Š, Ribičič M (2009) Debris-flow susceptibility model of Slovenia at scale 1: 250,000 (Model dovzetnosti za pojavljanje drobirskih tokov v Sloveniji v merilu 1: 250,000). Geologija 52(1):87–104
- Mikoš M (2011) Public perception and stakeholder involvement in the crisis management of sediment-related disasters and their mitigation: the case of the Stože Debris flow in NW Slovenia. Integr Environ Assess Manage 7(2):216–227. doi:10.1002/ieam.140
- Mikoš M (2012) Prispevek k zgodovinskemu pregledu razvoja hudournišva in hudourničarstva v Sloveniji (A contribution to history of torrent control theory and practice in Slovenia). Gozdarski vestnik 70(10):429–439
- Mikoš M, Fazarinc R, Majes B (2007) Delineation of risk area in Log pod Mangartom due to debris flows from the Stože landslide (Določitev ogroženega območja v Logu pod Mangartom zaradi drobirskih tokov s plazu Stože). Acta geographica Slovenica 47(2):171–198. <http://giam.zrc-sazu.si/zbornik/02-Ags47-2-171-198-Mikos-Fazarinc-Majes.pdf>
- MORS (2004) Metodologija za določanje ogroženih območij in način razvrščanja zemljišč v razrede ogroženosti zaradi dolovanja zemeljskih plazov – končno poročilo (Methodology for determining risk areas and classifying land into risk classes due to landslides—final report). Ministry of Defence of the Republic of Slovenia, Ljubljana. http://www.sos112.si/slo/tdocs/met_zemeljski_1.pdf, http://www.sos112.si/slo/tdocs/met_zemeljski_2.pdf
- MORS (2005) Novelacija in nadgradnja informacijskega sistema o zemeljskih plazovih in vključitev v bazo GIS_UJME – končno poročilo (Updating and upgrading the information system on landslides and inclusion in the database GIS_UJME—final report). Ministry of Defence of the Republic of Slovenia, Ljubljana. http://www.sos112.si/slo/tdocs/zem_plaz_gis_ujme.pdf
- MORS (2008) Ocena ogroženosti zaradi drobirskih tokov – končno poročilo (Debris-flow risk assessment—final report). Ministry of Defence of the Republic of Slovenia, Ljubljana. http://www.sos112.si/slo/tdocs/naloga_76.pdf
- OdSPRS (2004) Ordinance on spatial planning strategy of Slovenia (Odlok o Strategiji prostorskega razvoja Slovenije). Official Gazette RS, No 76/2004

- ReNPVNDN (2009) Resolution on national programme for the protection against natural and other disasters (Resolucija o Nacionalnem programu varstva pred naravnimi in drugimi nesrečami v letih 2009 do 2015). Official Gazette RS, No 57/2009
- ReNPVO (2006) Resolution on National Environmental Action Plan 2005–2012 (Resolucija o Nacionalnem programu varstva okolja 2005–2012). Official Gazette RS, No 2/2006
- Ribičič M (2007) Stanje in zakonodaja na področju plazenja in erozije tal v Sloveniji (Status and legislation in the field of landsliding and soil erosion in Slovenia). In: Zbornik konference Strategija varovanja tal (Proceedings of the conference on the soil protection strategy), Ljubljana. http://www.pds.si/uploads/doc/SVTS_51207_10.pdf
- Rules (2007) Rules on methodology to define flood risk areas and erosion areas connected to floods and classification of plots into risk classes (Pravilnik o metodologiji za določanje območij, ogroženih zaradi poplav in z njimi povezane erozije celinskih voda in morja ter o načinu razvrščanja zemljišč v razrede ogroženosti). Official Gazette RS, No 60/2007
- Sodnik J, Kogovšek B, Mikoš M (2016) Water management as a part of civil engineering sector in Slovenia. In: INTERPRAEVENT 2016—Conference Proceedings 141–149. http://www.interpraevent.at/palm-cms/upload_files/Publikationen/Tagungsbeitraege/2016_1_141.pdf
- TXT-tool 1.386-2.1 (2016) Landslide susceptibility model development and evaluation—from regional to local scale (this book)
- TXT-tool 1.386-2.2 (2016) Geohazard methodology—from mapping of mass wasting to producing a hazard maps (this book)
- TXT-tool 2.386-2.1 (2016) SAR interferometry as a tool for detection of landslides in early phases. pp. 275–285
- TXT-tool 2.386-2.2 (2016) A system to forecast rainfall induced landslides in Slovenia. pp. 391–404
- ZFO-1 (2006) Financing of Municipalities Act (Zakon o financiranju občin). Official Gazette RS, No 123/2006
- ZG (1993) Forest Act (Zakon o gozdovih). Official Gazette RS, No 30/1993
- ZGO-1 (2002) Construction Act (Zakon o graditvi objektov). Official Gazette RS, No 110/2002
- ZJF-UPB4 (2011) Public Finance Act (Zakon o javnih financah – uradno prečiščeno besedilo). Official Gazette RS, No 11/2011
- ZOPNN-UPB1 (2005) Natural disaster recovery act (Zakon o odpravi posledic naravnih nesreč - uradno prečiščeno besedilo). Official Gazette RS, No 114/2005
- Zorn M, Komac B, Kumelj Š (2012) Mass movement susceptibility maps in Slovenia: the current state. Geografski vestnik 81(1):99–112. http://zgs.zrc-sazu.si/Portals/8/Geografski_vestnik/vestnik-84-1-zorn-komac-kumelj.pdf
- ZPNAČRT (2007) Spatial Planning Act (Zakon o prostorskem načrtovanju). Official Gazette RS, No 33/2007
- ZUOPZ (2002) Measures to repair the damage caused by certain large-scale landslides in 2000 and 2001 act (Zakon o ukrepih za odpravo posledic določenih zemeljskih plazov večjega obsega iz let 2000 in 2001). Official Gazette RS, No 21/2002
- ZUPSB (2000) Act on the measures to be taken to repair the damage caused by landslide Stože in Bovec municipality and by large-scale landslides in the territory of the Republic of Slovenia occurring after 15 October 2000 (Zakon o odpravi posledic plazu Stovže v Občini Bovec in plazov večjega obsega nastalih na območju Republike Slovenije po 15. oktobru 2000). Official Gazette RS, No 124/2000
- ZUPUDPP (2010) Act regarding the siting of spatial arrangements of national significance in physical space (Zakon o umeščanju prostorskih ureditev državnega pomena v prostor). Official Gazette RS, No 80/2010
- ZUreP-1 (2002) Spatial Management Act (Zakon o urejanju prostora). Official Gazette RS, No 110/2002
- ZV-1 (2002) Waters Act (Zakon o vodah). Official Gazette RS, No 67/2002
- ZVNDN (2006) Act on protection against natural and other disasters (Zakon o varstvu pred naravnimi in drugimi nesrečami). Official Gazette RS, No 51/2006
- ZVO-1-UPB1 (2006) Environment Protection Act (Zakon o varstvu okolja—uradno prečiščeno besedilo). Official Gazette RS, No 39/2006

TXT-tool 4.086-1.2

Shallow Landslides and Plant Protection in Seasonal Frozen Regions

Ying Guo, Wei Shan, Yuying Sun
and Chengcheng Zhang

Abstract

In high-latitude frozen regions of Northeast China, soil cutting slopes often trigger shallow landslides. These shallow landslides are of a unique type and the root cause of it is the seasonal freeze-thaw behavior. In autumn, shallow slopes have high moisture content and get frozen quickly. In spring these layers thaw slowly and become impermeable layer, so thawing water was hampered by frozen layer, resulting in the water content increasing rapidly in the interface between thawed layer and impermeable layer, and then causing the partial or complete sliding of the shallow layer of the slope along the slip band due to gravity. Traditional geotechnical countermeasure approach often may not be effective for the slope protection. We select the method of planting shrubs. Plant roots could reduce soil moisture by absorbing water and increasing transpiration, as well as roots into the slope form anchor system and strengthen the shear strength of soil body, preventing the shallow landslides.

Y. Guo · W. Shan (✉) · C. Zhang
Institute of Cold Regions Science and Engineering,
Northeast Forestry University, Harbin 150040,
China
e-mail: shanwei456@163.com

Y. Guo
e-mail: samesongs@163.com

C. Zhang
e-mail: 93038478@qq.com

Y. Sun
Heilongjiang Institute of Technology, Harbin
150090, China
e-mail: sunyuying790229@163.com

Keywords

Shallow landslides · Freeze-thaw · Planting shrubs

Contents

1	Introduction.....	694
2	Geography and Climate.....	694
3	Laboratory Test and In-Site Monitoring.....	695
4	The Reason of Shallow Cutting Slope Landslide.....	698
5	Protection Methods for Seasonal Shallow Landslide.....	699
6	Conclusion.....	701
	References.....	702

of the highway. Traditional geotechnical countermeasure approach such as hollow blocks, brick masonry, even reinforced concrete frame etc. are not effective for the slope protection (Fig. 2). Such shallow landslide is of a unique type in seasonal frozen regions in Northeast of China. This paper will discuss its occurrence causes and protection measures.

1 Introduction

In high-latitude frozen regions of Northeast China, soil cutting slopes frequently trigger shallow landslides (Wu et al. 2006; Liu and Wang 2006). Figure 1 is a typical case of this kind of slope failure, which often occurs on the southern slope in April and May during the first several years after the highway opening. The thickness of the displaced soil mass is at the order of about 1 m, but the sliding mass moves for a long distance, generally 3–5 m. Such shallow landslides not only damage the highway scenery and increase the maintenance cost every year, but also hinder the drainage at roadside of the highway and even encroach the driving path

2 Geography and Climate

We selected “Ha-Tong” highway K560+090-K565+690 as the study section. The highway passes through mostly mountainous and hilly areas, which is higher at south and lower at north and the altitude ranges between 150 and 250 m. Surface drainage mostly is unobstructed with exception in some low-lying sections. The surface deposits along the highway are mostly Quaternary alluvium. No activities were found in fault zone, and the geological stability is good. Climate of this region belongs to continental seasonal windy climate of the North Temperate



Fig. 1 Typical failure of cutting slope

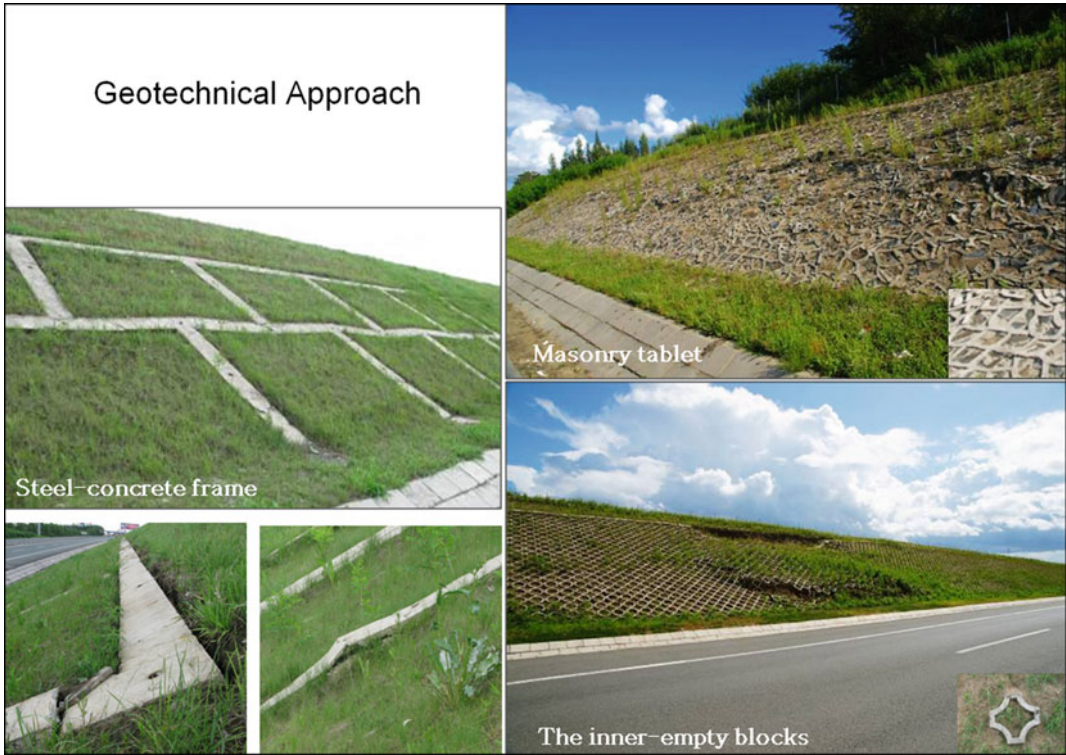


Fig. 2 Traditional geotechnical countermeasure approach

Zone. It is characterized by hot and rainy summer, cold and dry winter, windy and drought spring, and cool autumn with early frost. The average annual temperature is 3.2 °C, with a high record of 36.4 °C, low record of -41.1 °C. The average annual rainfall is 542.6 mm. The maximum thickness of snow accumulation is 500 mm and the maximum depth of frozen soil ranges from 1.8 to 2.2 m. The stable ground freezing starts at late November, and the stable ground melting is from mid-April of the next year. The average annual evaporation is 1418.8 mm, prevailing wind is southwest wind, with maximum wind speed of 30 m/s and average wind speed of 4.3 m/s.

The soil of cutting slope is sandy clay, its natural density is 1.8–2.1 g/cm³, the average height of the slope is 5–15 m, and the average ratio of it is 1.5–1.75. According to the on-site investigation, the depth of sliding surface of the cutting slope landslide is about 1–1.5 m, and its thickness is 10–25 cm.

3 Laboratory Test and In-Site Monitoring

The Impact of Freeze-Thaw and Soil Moisture on Shear Strength of Slope Soil

In order to understand the impact of freeze-thaw cycles, soil moisture on the shear strength of slope soil, the silty clay from cutting slope was subjected to various laboratory tests to evaluate basic physical properties; the results are shown in Table 1. Triaxial test was conducted under various test conditions. Specific testing condition is as follows—dry density of 1.615 g/cm³, moisture contents of 9, 14, 19, 22, and freeze-thaw cycles of non, one, and five. The test results are shown in Figs. 3 and 4.

It could be seen that, when soil moisture is close to the optimum moisture content (13%), soil cohesion reaches its peak. Soil cohesion decreases gradually with the increasing of

Table 1 Basic physical properties of the silty clay

Liquid limit (%)	Plastic limit (%)	Plasticity index	Maximum dry density (g/cm ³)	Optimum water content (%)
32.5	18.7	13.8	1.90	13

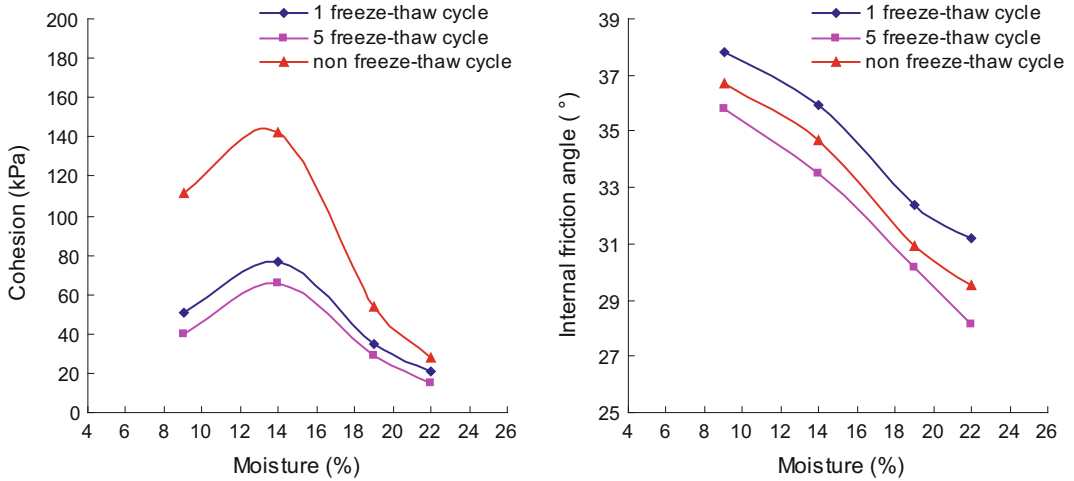


Fig. 3 The relationship curve between soil shear strength and soil moisture content before and after Freeze-thaw cycles

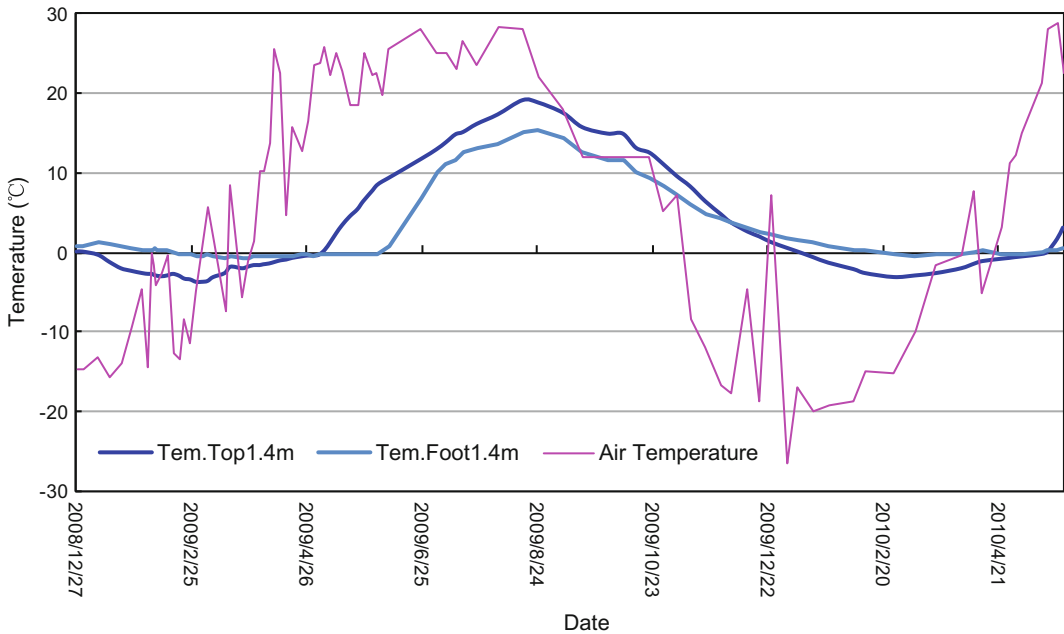


Fig. 4 The temperature curve of air and soil body in 1.4 m depth in K560+700 section

freeze-thaw cycles. At the same time, the soil friction angle decreased with increasing soil moisture content; it increased after the first freeze-thaw cycle, and then decreased gradually in later freeze-thaw cycles.

According to Mohr-Coulomb envelopes obtained from this study, soil shear strength decreased linearly when its soil moisture exceeds optimum moisture, and soil shear strength also decreased greatly after the first freeze-thaw cycle.

Seasonal Changes of Soil Moisture in Shallow Slope Body

We selected K560+700 section as the monitoring section, in different place of the monitoring section (top-slope, foot-slope), we installed temperature and moisture sensors at 1.4 m depth, from January 2009 to June 2010 and monitored the temperature and moisture regularly.

A. Soil temperature in the slope (Fig. 4)

It could be seen from temperature curve distribution that: The variation of air temperature

was much higher than soil body temperature (1.4 m), and there was obvious lagging phase between them. In autumn and spring, there was significant difference in ground temperature curve: the ground temperature curve slowly declining in fall, and increased upward after a long period wandering in spring. In seasonal frozen areas, the differences in ground temperature is a unique phenomenon, and also is one of potential causes for landslides formation.

B. Soil moisture in the slope (Fig. 5)

Figure 5 is the soil temperature and soil moisture curve of K560+700 section at 1.4 m depths. It should be noted that: the data in the monitoring curve is the value of moisture content, which is obtained through the dielectric constant measured with the moisture sensor. When the soil come into the frozen state, part of the water in the soil became ice (segregate), so the moisture measured is the mixture of ice and water. When the soil is in the non-frozen state, the moisture measured is the actual soil moisture.

In the curve, combining with the soil temperature cycle, the freeze-thaw process of the soil

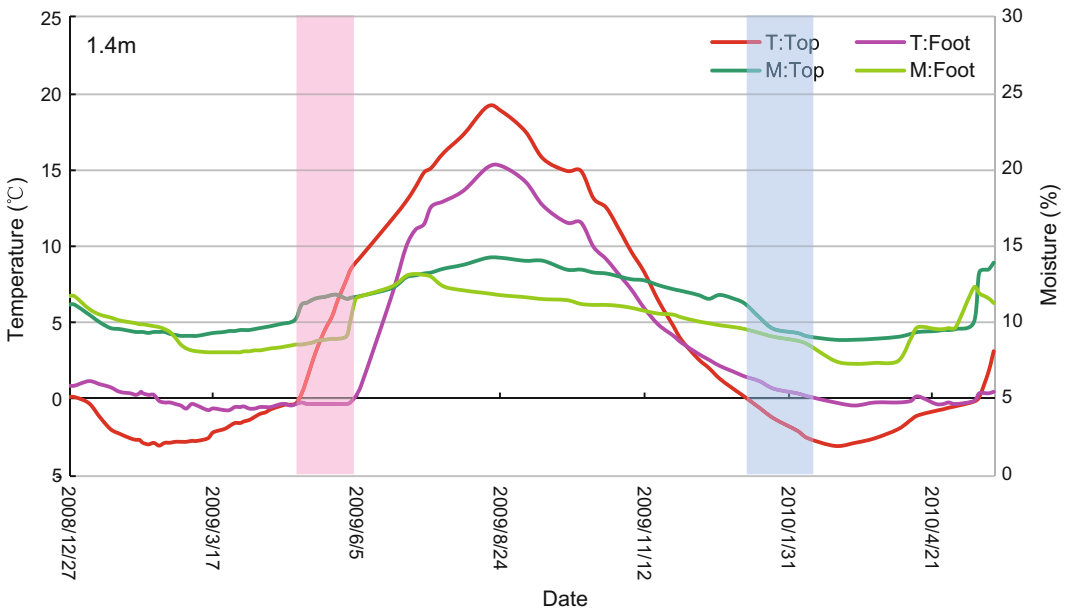


Fig. 5 The temperature and moisture curve of soil body in 1.4 m depth in K560+700 section

could be divided into five stages (Guo et al. 2014): Non-frozen, Early-freezing (blue range), Frozen, Early-thawing, Ongoing-thawing (pink range). The soil temperature and moisture in five stage will be analyzed as follows.

Soil moisture migration in stage of Early-freezing: The stage of early-freezing refers to the period that is from soil temperature coming into 0 °C to soil temperature keeping a certain stable negative temperature (blue area). The sign of this process was moisture curve measured having a drop. The reason for it is: During freezing process, the temperature of soil particle decreased firstly, then the pore water near the soil particle crystallized by releasing the heat, finally soil temperature decreased continually.

Moisture and temperature in stable Frozen stage: In stable frozen period, with a further decline in soil temperature, the soil moisture curve decreased further, but slightly. This is because the stable temperature field could made temporary balance between frozen water and unfrozen water.

Moisture and temperature in stage of Early-thawing: The stage of Early-thawing refers to the period that soil negative temperature rise from the lowest negative temperature to -0.3 °C. During this period, with the stable ascent of soil temperature, at the beginning, soil moisture curve uplifted slowly firstly, then kept constant. This is because crystallization thawing needs enough hydration heat, so the soil moisture would be constant until the energy gathering from soil particle was bigger than the heat of hydration. This process is the energy reserves for the next stage of Ongoing-thawing.

Moisture and temperature in Ongoing-thawing stage: The stage of Ongoing-thawing stage refers to the period that the soil temperature rises from -0.3 to 0 °C (pink areas). During this period, in frozen soil layer, the temperature rose from -0.3 to 0 °C and lingered near 0 °C. But, the soil moisture had a steep uplift at a certain moment. After steep uplift of soil moisture, soil temperature rose to 5–10 °C rapidly. The reasons for this phenomenon are: because there was a ice thawing layer over the non-frozen soil body, which made the moisture in non-frozen soil

migrating to the interface of ice thawing, so the rich moisture layer formed in fall continue grow up, which need a period of accumulating hydration heat energy, so the soil temperature both in frozen soil and in non-frozen soil remained relatively constant. When the crystallization in soil voids thawed completely, and interface of ice thawing disappeared, so the soil moisture have a steep uplift.

Moisture and temperature in Non-frozen stage: The stage of Non-frozen refers to the period that soil temperature is all in positive value. In this period, the soil temperature varies with air temperature, and is mainly affected by rainfall, evapotranspiration and penetration.

4 The Reason of Shallow Cutting Slope Landslide

Through above results of indoor and outdoor tests, we can find the reasons for shallow cutting slope Landslide.

The first freeze-thaw cycle could reduce the soil shear strength. Cutting Slope is artificial slope, soil shear strength of the slope will be significantly decreased after the first freeze-thaw cycle, which was proved in indoor test. That's the reason for landslide occurrence often in the first several years after the highway opening.

In autumn, shallow slope has rich moisture and is frozen quickly. In outdoor monitoring tests, the soil moisture curve drops steeply in freezing process that indicated that the local air temperature drops quickly and the water is frozen and cannot be penetrated, especially in the year having more rainfall and deep drop of air temperature, the situation is more obvious.

In spring, shallow slope has impermeable layer forming a sliding band. In outdoor monitoring tests also it can be found that the moisture curve have a nearly a month of lingering near 0 °C, that indicated that the rich ice layer formed in fall and grow (by moisture migration) in spring when this layer thawed slowly and became impermeable layer, so thawing water was hampered by frozen layer, resulting in the water content increasing rapidly in the interface

between thawed layer and impermeable layer, and reaching saturation or super saturation state, then the effective stress of the soil in the cutting slope reduced. Gradually, slip band formed along the interface between thawed layer and the impermeable layer, and then the partial or entire shallow layer of the slope slide down along the slip band due to gravity.

In summary, the seasonal freeze-thaw is the root cause of shallow slope landslide. Soil moisture migration in freezing and thawing period is an internal factor. Concentrated precipitation in spring and autumn as well as sharp temperature changes promote landslide formation.

adding slope load instead of protecting the slope, so we need to find out a new method to protect the slope according to appropriate slope stabilization measures.

Planting Local Shrubs

According to the causes of shallow landslides, protection method should begin with reducing water content in the shallow slope, especially in autumn and spring. In this case, the method of planting shrubs comes first. Following are the three common shrubs, which have better protection performance (Fig. 6).

5 Protection Methods for Seasonal Shallow Landslide

The Traditional Geotechnical Methods

As can be seen from Fig. 2, traditional geotechnical methods aggravated landslide because of

- A. Longer plant roots into the slope formed anchor system, which strengthen the shear strength of soil body. In order to evaluate the function of plant roots system, in situ direct shear tests were conducted on the shallow slope with the roots of *Amorpha fruticosa* (AF) and *Lespedeza* (LP) and the test result is as follows (Fig. 7).

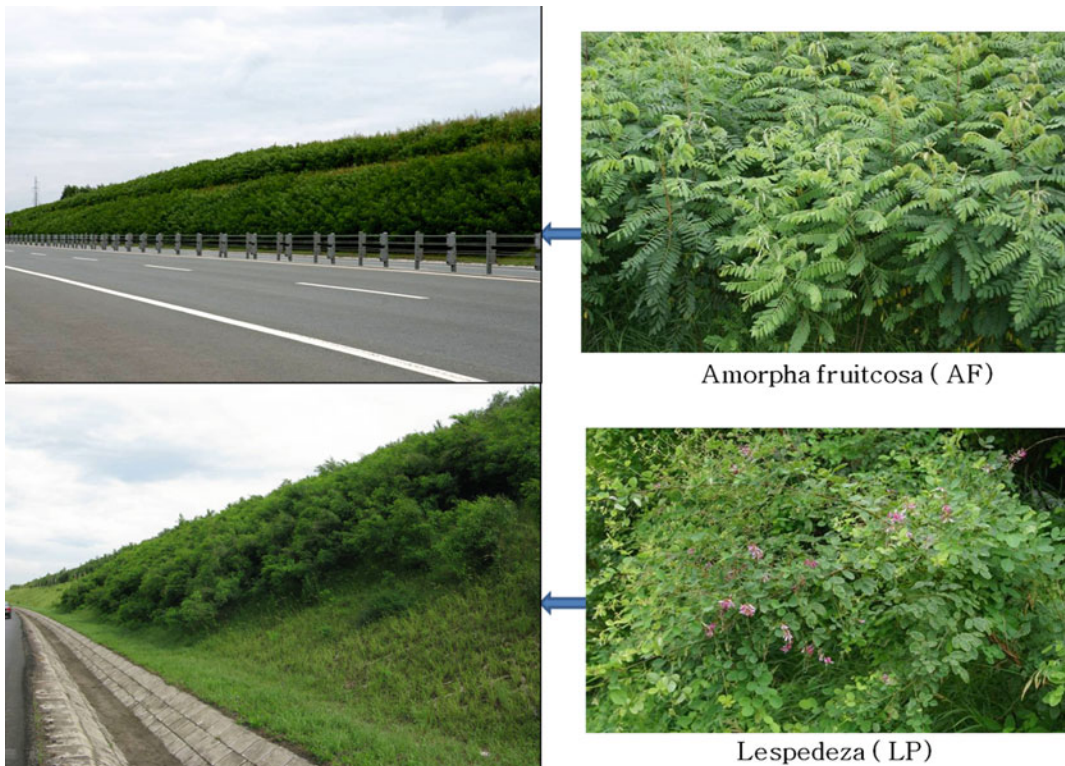


Fig. 6 Two shrubs for slope protection

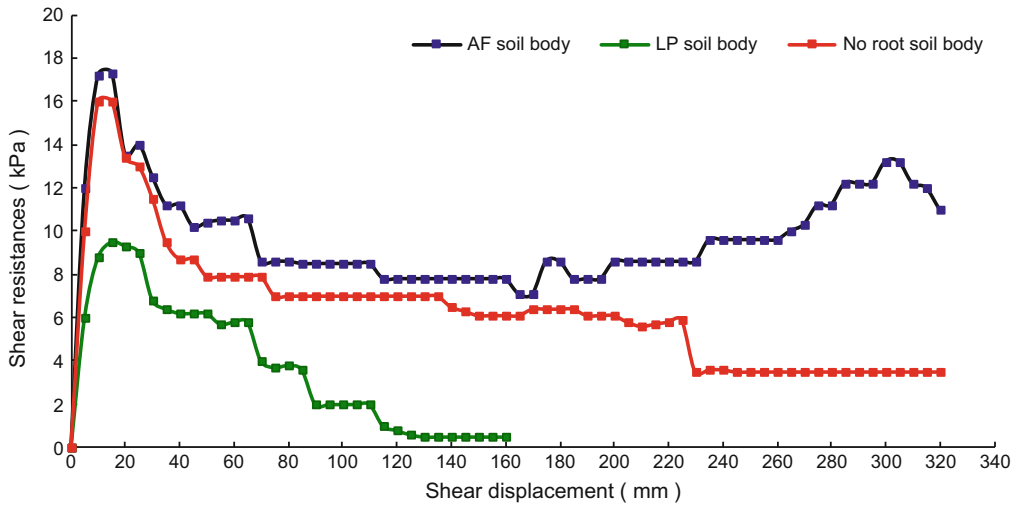


Fig. 7 In-situ direct shear tests on the surface soil with AF root, with LP root, and without tree roots

It can be seen that the soil body with roots can improve soil shearing resistance, increase soil shear displacement, by more than two times of the soil without any roots. The shear displacement curve of AF has two peaks, because its root system has no main root.

B. Absorbing water and transpiration by plant root system could decrease soil moisture in

the slope. From February to May 2008, we measured the soil moisture in the slope with different plant (Fig. 8).

It can be seen from the figure that under the same conditions, shrub can more effectively reduce the soil moisture of the slope compared to grass, especially within 0–100 cm depth.

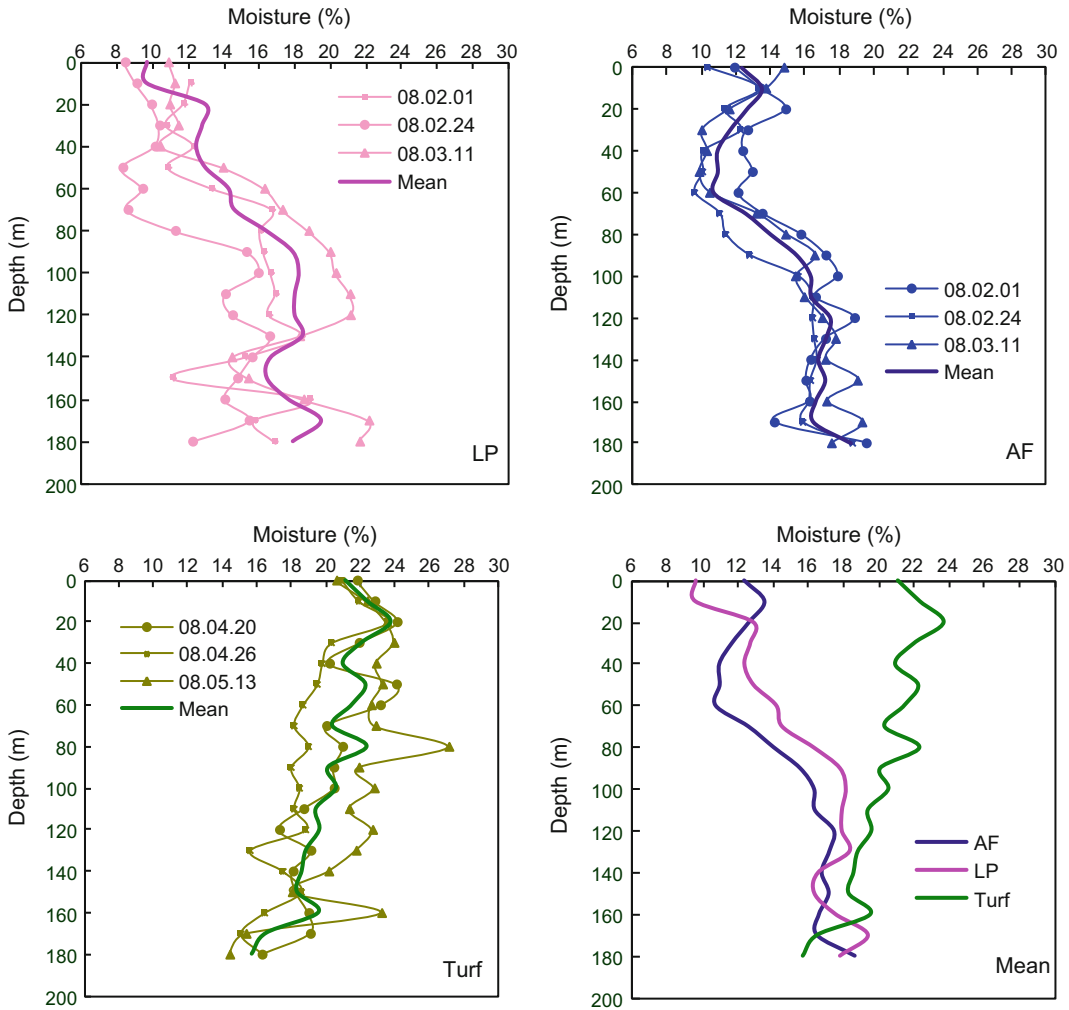


Fig. 8 The moisture curve of the slope with different plant (AF, LP and Turf)

6 Conclusion

In high-latitude frozen regions of Northeast China, soil cutting slope often trigger shallow landslide. Such shallow landslides are of unique types and the root cause of it is the seasonal freeze-thaw behavior. In autumn, shallow slope has high moisture and is frozen quickly. In spring this layer thaws slowly and become impermeable layer, so thawing water is hampered by frozen layer, resulting in the water content increasing rapidly in the interface between thawed layer and

impermeable layer, and then the partial or entire shallow layer of the slope slide down along the slip band due to gravity.

According to the causes of shallow landslides occurrence, protection method should begin with reducing water content in the shallow slope, especially in autumn and spring. We selected the method of planting shrubs. Plant roots could reduce soil moisture by absorbing water and transpiration, as well as roots into the slope and form anchor system, which then could strengthen the shear strength of soil body and prevent the shallow landslides.

Acknowledgements The authors would like to express their thanks for the support provided by the science and technology research project of Heilongjiang provincial Education Department (12533017).

References

- Guo Y, Shan W et al (2014) The impact of freeze-thaw on the stability of soil cutting slope in high-latitude frozen regions. In: Landslides in cold regions in the context of climate change. Springer, Berlin, ISBN 978-3-319-00867-7, pp 85–98
- Liu H, Wang P (2006) Stability analysis of loss of stability caused by freeze and melt of earthen side slopes of highways. *J Harbin Inst Technol* 38(5):764–766 (in Chinese)
- Wu H, Gao W, Wang G et al (2006) Cause and control of soil-cutting's sliding collapse in frigid zone. *J Nat Disasters* 15(3):66–70 (in Chinese)

TXT-tool 4.886-1.4

Ecological: Countermeasure Guidelines and Case Histories in Taiwan

Chia-Chun Ho, Jen-Yang Lin and Yi Wen Chiu

Abstract

Over the past decade, the ecological engineering method in Taiwan has been concentrated principally in river restoration and slope protection. In September, 1999, Taiwan was severely affected by the Chi-Chi earthquake. The Public Construction Committee of Executive Yuan decided to rebuild the disaster area using ecologically sound measures and since 1999 has become the leading governmental agency promoting ecological engineering. In 2000–2004, more than 90% of so-called ecological engineering projects in Taiwan were associated with river stabilization, river reconstruction, and slope stabilization conducted by the Water Resource Agency, Water and Soil Conservation Agency, and local public sectors governed by these two agencies. This paper describes two typical case histories in Taiwan, Chichawan Creek Stabilization Project and Dahgo Creek Reconstruction Project.

Keywords

Ecological engineering method • River restoration
Slope protection • Chi-Chi earthquake

C.-C. Ho (✉) · J.-Y. Lin
Water Environment Research Center, National
Taipei University of Technology, 1, Sec. 3,
Chung-Hsiao E. Rd., Taipei 106, Taiwan
e-mail: ccho@ntut.edu.tw

J.-Y. Lin
e-mail: jylin@ntut.edu.tw

Y.W. Chiu
Energy Systems Division Argonne National
Laboratory, 9700 S Cass Ave Bldg 362, Rm E313,
Lemont, IL 60439, USA
e-mail: ychiu@anl.gov

Contents

1	Introduction	704
2	Development History	704
2.1	Background.....	704
2.2	Application.....	706
2.3	Course Description.....	707
3	Case Histories	707
3.1	Chichawan Creek Stabilization Project.....	707
3.2	Dahgo Creek Reconstruction Project.....	709
	References.....	713

1 Introduction

Due to an increase in ecological awareness, Taiwan started to seek advanced technology from other countries in order to modify traditional civil engineering practices that had placed priority on development and human demands. In the late 1990s, research in the fields associated with environment beautification was launched. The new philosophy of ecological engineering gradually began to attract the attention of academic institutes. The Government also initiated substantial funding for (a) understanding the application of ecological engineering and its results in Japan, Europe and the United States; (b) the possible limitations of applying it in Taiwan, and (c) establishing localized methods applicable to river reconstruction. Shortly after this work by water-resources-related agencies, this new trend started to affect soil conservation practices through the introduction of river bank stabilization methods. In addition to its value in improving water quality control, ecological engineering has also contributed to Taiwan's environmental engineering since 2003. This is intended as brief introduction to the subject of ecological engineering methods, which is a whole new concept in the field of civil engineering. The advantages of these methods is not only satisfying the demands for increased safety (i.e., natural hazards control) but also in protecting ecosystem and landscape aesthetics.

2 Development History

2.1 Background

In Taiwan, related government agencies are trying to promote the application of ecological engineering methods, and attempting to adopt their specific measures. These two steps (applying the methods to regulating water quantity and to water quality treatment) are introduced below.

Taiwan was mostly influenced in the beginning by two aspects of ecological engineering: channels and soil and water conservation. However, with academic and governmental efforts,

the study of the topic has blossomed since the late 1990s. Nearly 30 recognized related conferences, workshops or forums (announced nation-wide and open to the public) took place within 7 years (1998–2004). This evolution can be illustrated by a brief history of introducing ecological engineering to Taiwan.

In the early 1980s people started being aware of the importance of environmental aesthetics. Although ecological considerations were associated with this, it was limited to a conceptual level.

In 1992–1998, a series of soil and water conservation sites were constructed, based on a broader vision including providing recreational and aesthetic values.

In 1999, Lin et al. conducted the first of successive research projects sponsored by the Water Resource Agency, and focused on the study of ecological engineering and evaluating the possibility of its application in river reconstruction.

In September, 1999, Taiwan was severely affected by the Chi-Chi earthquake (or 921 earthquake). The Public Construction Committee of Executive Yuan (PCC) decided to rebuild the disaster area using ecologically sound measures and since 1999 has become the leading governmental agency promoting ecological engineering.

In 2001, the PCC requested the Soil and Water Conservation Bureau to jointly make efforts to introduce ecological engineering into related projects. Grants were offered to study related slope stabilization issues. Meanwhile, the Construction and Planning Agency of the Ministry of the Interior also became part of promoting ecological aspects.

In 2002, in order to establish localized ecological engineering systematically, the PCC started by forming the Ecotechnology Advisory Board (EAB) and hosted a series of meetings, concluding with an official definition of ecological engineering to suit Taiwan's circumstances. The Ecotechnology Advisory Board also plays an important rule in assisting the PCC in making decisions to develop strategies for promoting ecotechnology.

In 2003, in order to educate the public in ecotechnology concepts, the PCC hosted the National Ecotechnology Expo, which took place

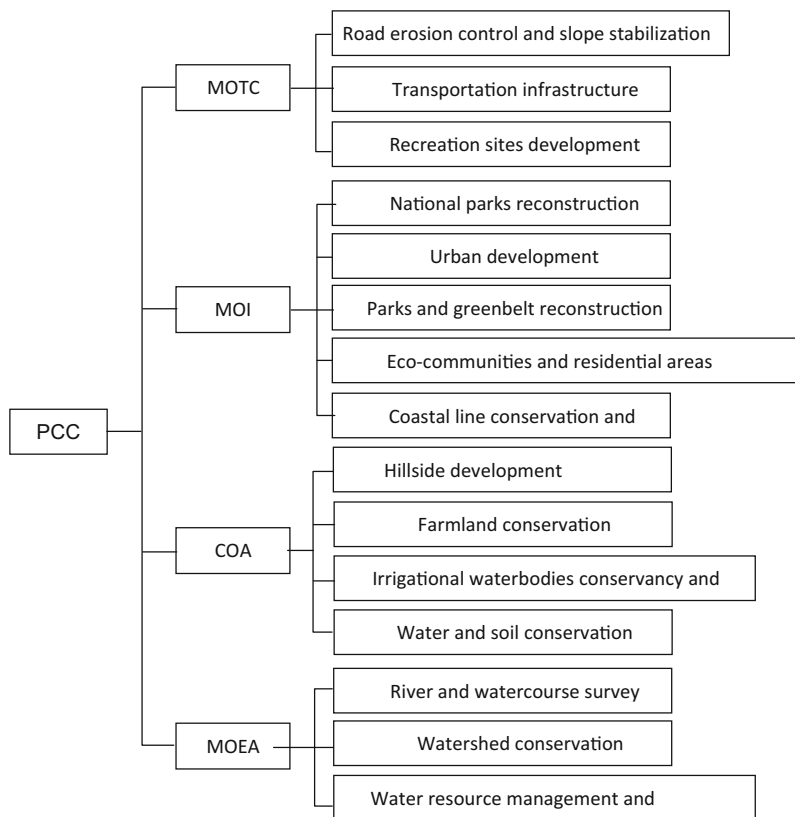
nation-wide. The total expense, including construction costs, was estimated at 251,000,000 NTD (approximately 7 million USD). Simultaneously, the Executive Yuan subsumed ecological engineering as one of the key issues in the “2008 National Development Plan” and it was addressed as a guideline in the subplan “Water and Green Development”. This ensured the status of ecological engineering as one of the national key policies.

The second step of ecological engineering development in Taiwan has been water-quality oriented since 2003. It includes its application in water quality treatment, with wetland and riparian buffer zones being launched.

As mentioned previously, the Council for Economic Planning and Development (CEPD) Executive Yuan of Taiwan (2001) promulgated “The Planning and Implementation of the Chal-

lenge 2008 National Development Plan”. The Plan emphasized water resources planning and landscape remediation in the section “Water and Green Construction Plan”. This section was aimed at gradually restoring Taiwan’s natural ecology and creating a model for subtropical island ecologies. To accomplish this goal, the highest central infrastructure advisory and supervisory agency, the Public Construction Commission (PCC), invited the Ministry of Transportation and Communication (MOTC), the Ministry of the Interior (MOI), the Council of Agriculture (COA), and the Ministry of Economic Affairs (MOEA) to organize an ecological engineering impetus team for establishing a unique plan, strategy, and timetable for implementing ecological engineering. The participative agencies and the main issues addressed within each of them are listed in Fig. 1.

Fig. 1 Public sectors and individual major realms participating in ecological engineering promotion. *PCC* Public Construction Commission, *MOTC* Ministry of Transportation and Communication, *MOI* Ministry of the Interior, *COA* Council of Agriculture, *MOEA* Ministry of Economic Affairs



2.2 Application

In 2000–2004, more than 90% of so-called ecological engineering projects in Taiwan were associated with river stabilization, river reconstruction, and slope stabilization conducted by the Water Resource Agency, Water and Soil

Conservation Agency, and local public sectors governed by these two agencies. For general projects emphasizing ecological engineering, principles are advised to follow the following procedure for planning and implementation (Fig. 2). The standardized procedure is to ensure the specific issues related to ecological and safety

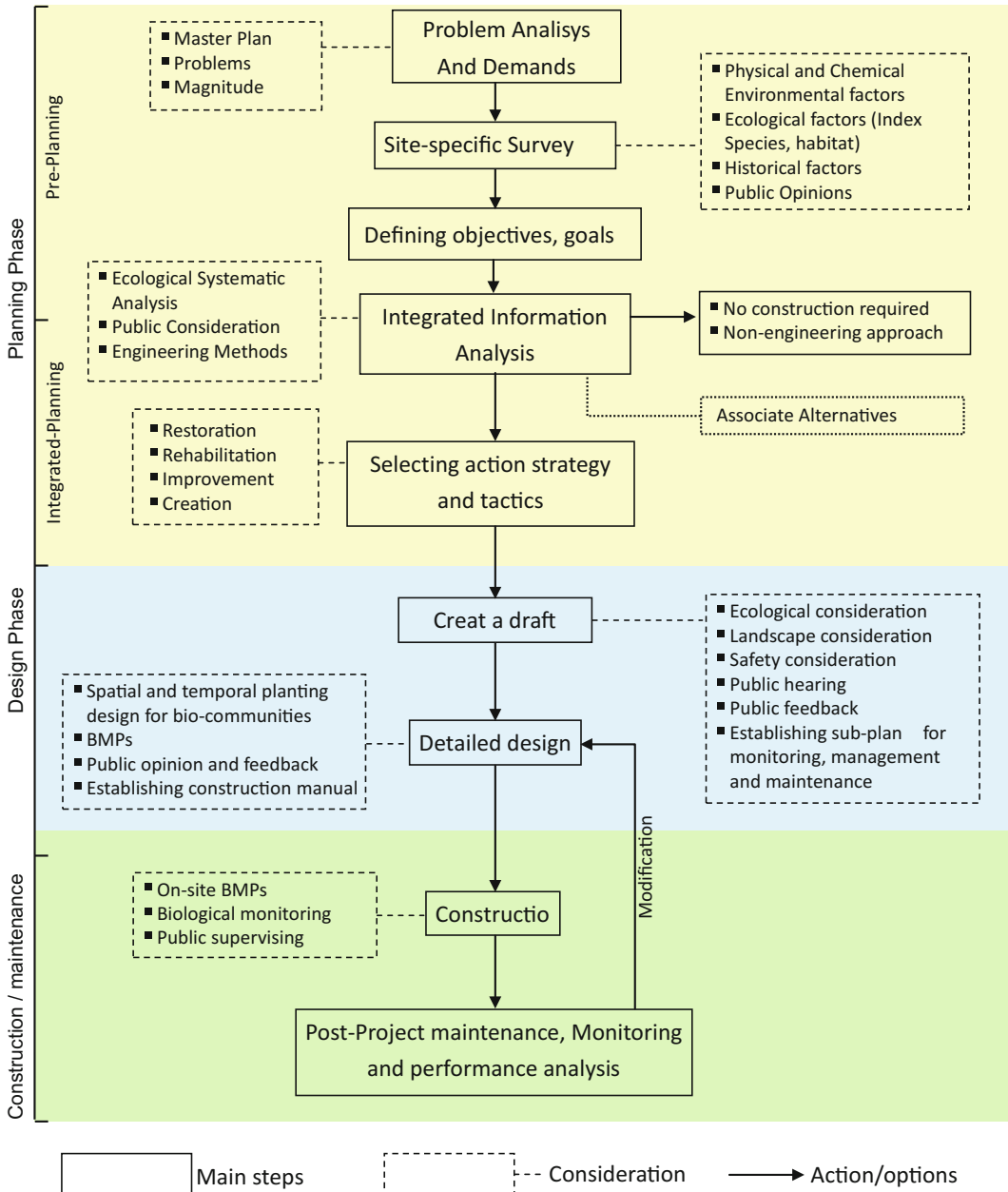


Fig. 2 Diagram of standardized project procedures in ecological engineering

concerns for each location are properly addressed.

2.3 Course Description

A lack of basic understanding and knowledge has been the main reason why engineers are struggling in introducing ecological engineering methods into their work. Therefore, fundamental theories, cases studies, and practical aspects of application will be taught in this course. The optimal goal is to inspire students to learn more about this new philosophy and new techniques in the world of civil engineering. The main issues of ecological engineering involve:

1. River and watercourse surveys,
2. Watershed conservation and water resource management,
3. Biotechnical and soil bioengineering slope stabilization,
4. Transportation infrastructure, and
5. Eco-communities and residential areas development.

3 Case Histories

3.1 Chichawan Creek Stabilization Project

Chichawan Creek, 14 km long, is located in Taichung County and is best known for being the only habitat of Formosan Landlocked Salmon (or Taiwan Trout, *Oncorhynchus masou formosanum*), an species endemic to Taiwan that has been officially labeled as Critically Endangered in the IUCN Red List since 1996. The Chichawan Creek watershed is part of the district of Shei-Pa National Park headquarters and is protected strictly in order to preserve the population of Formosan Landlocked Salmon. However, like the rest of Taiwan's streams, erosion is severe along the Chichawan Creek due to intensive rainfall and rapid flows, and the erosion had increased as a result of reduced stability of

banks due to frequent earthquakes after 1999 (Fig. 3).

It has been observed that the hydrological patterns and aquatic habitat have gradually altered, which has caused a noticeable decrease in the salmon population. Moreover, severe erosion has also increased the turbidity of the Creek, and consequently increased deposition in the Derjee Reservoir downstream and affected the reservoir water quality.

Because of the importance of the Chichawan Creek and the effects of losing habitat, Shei-Pa National Park headquarters carried out various evaluations and field surveys and was funded by Taiwan Water Resource Bureau (current Water Resource Agency) in 2000.

3.1.1 Project Emphasis

The right bank of Chichawan Creek from station 0 + 133 to 0 + 400 m was restored in the winter of 2000. At this section the stream has an average width of 20–30 m and a depth of 0.3–0.6 m, with a 1.8% gradient. It is a rapid 4th-order stream typical of those located at 1500 m of elevation or above. Its mean velocity is 0.54 m/s (0.4–1.3 m/s), with an average flow of 7 cm.

To ensure the newly installed stream bank structure would have little impact on altering the flow regime, yet improve habitat quality, the streams's ideal vegetation communities, stream bank features, and stream bed characteristics (including rock diameter and profile diversity) were taken into account. This required detailed ecological and hydrological information to determine the right habitat components for all aspects. Due to the existing long-term research funded by related governmental agencies on Formosan Landlocked Salmon, ecological and biological information was sufficient and required little additional surveying.

The main emphasis in the ecological conservation aspect included: (a) Water quality control during construction; (b) Maintaining the diversity of aquatic habitat favored by the Salmon and associated species; (c) Ensuring riparian aesthetics; (d) Introducing native vegetation communities and utilizing them as a factor for providing proper habitat, and (e) Using the restored bank to

Fig. 3 Unstable river bank and severely scoured road bed along Chichawan Creek (Lin et al. 2001)



(a) Habitat destruction



(b) Riverbank landslide



(c) Soil erosion

bridge foodweb and ecological functions by creating a stairway of ecotones required by key species in this unique ecosystem.

The new stream bank was designed resist deterioration due to erosion. The best alternative was selected based on the principle of reducing the amount of concrete and thus the area of impervious surface. Although traditional hydraulic engineering still played the most important role, this project was meant to challenge the limitations of reducing well-adopted solid materials, including reinforced concrete.

During the construction, water quality, quantity, engineering materials, and live materials were held under strict control, and construction guidelines were clearly outlined to guide the construction crew. The construction period was set to avoid fish reproduction season.

3.1.2 Implementation

The entire project was completed in the spring of 2001, and is maintained by the Shei-Pa National Park headquarters. The abiotic structures have remained stable after three consecutive typhoon seasons. Biotic structures, on the other hand, consisting of the live materials that played a role as pioneer species in the succession process, have developed into more mature community layers as expected (Fig. 4). Therefore, the constructed

stream bank shows little difference from a natural one in its vegetation community and formation (Fig. 5). The percent survival of planted vegetation reached the project goal in the winter of 2002. However, there is no official report published to address the monitoring and evaluation associated with ecological succession. No biological indicators or environmental criteria were selected to measure the effectiveness of this project. Most of the description related to current status was primarily by visual identification.

3.2 Dahgo Creek Reconstruction Project

Running into a high-density residential area, the 3500-m long Dahgo Creek has important hydraulic, recreational and educational values. With a 330-ha watershed area, the Creek represents a typical second-order stream that is highly altered by adjacent development. It was once a natural stream surrounded by dense riparian forests, but the population has increased over five times in the past two decades, and the downstream section of Dahgo Creek was channelized and covered up in order to create more residential space.

In 1997, Typhoon Winnie (No. 9714) produced heavy precipitation over a short period of

Fig. 4 Constructed bank formed of natural abiotic and live material



Fig. 5 Constructed stream bank (*right*) versus a natural bank (*left*)



time, and many climate stations recorded precipitation of 500–600 mm during the storm event. A flash flood occurred along Dahgo Creek and several other tributary streams in the area. The excessive amount of rainfall scoured farmlands along the Creek, and the downstream area, including the residential area which used to be floodplain, was severely flooded due to the limited cross section. Two lives were lost as a direct result of the flooding. Roads, bridges, water

lines, and other utility lines were damaged or destroyed. A large quantity of sediment and debris was carried from the watershed and deposited along the affected stream reaches (Fig. 6.). In response to the disastrous loss from the flood, the Taipei Municipal Government urgently launched a reconstruction project, and sought possible alternatives to provide balance among the dimensions of hydrology, ecology, recreation, and esthetics.

Fig. 6 Debris flow of Dahgo Creek



3.2.1 Project Emphasis

The degradation and inappropriate development of Dahgo Creek were brought to public attention due to the losses caused by the flood. How to regulate the hydrology regime and fulfill the goal of providing safety to the public from further storms became the priority of the entire project. Moreover, Taipei Municipal Government also expected this reconstruction project would benefit the adjacent neighborhood more than just serving as flood prevention. Engineers therefore attempted to integrate multiple functions in the project and took various interests into account.

The project manager was expected to hold to the value of “respecting the power of nature” by addressing several ecological and morphological criteria, along with hydrological considerations. Thus, the objectives of this project were clear and are listed below:

1. Bridge “blue and green belts” by reserving a stormwater detention area that can serve as recreation space during low water levels or dry season.
2. Minimize construction and create diverse habitat.
3. Install fish paths to ensure the in-stream accessibility for fish.

4. Employ shelters and platforms for educational purposes.
5. Naturalize the channel profile and stream banks.
6. Increase the ecological and landscape integrity in both the vertical and horizontal dimensions.
7. Increase the diversity of flow patterns, aquatic habitat, and riparian characteristics.

3.2.2 Implementation

The design of the Dahgo Creek reconstruction project aimed to satisfy various demands using a new approach that differs from Taiwan’s traditional hydrological infrastructure. The project site remained a near-natural meandering channel with little alteration of the original cross-section profile. A recreational path was built along the stream which may be inundated during storms or the rainy season. In terms of biotic aspects, most of the construction materials, including rocks and logs, were selected and prepared onsite. However, to counter the stream’s flow power, a concrete base was implanted behind the rocky bank surface (Fig. 7).

The pervious bank surface allowed sediment accumulation, and eventually, supporting vegetation. The combination of plants and natural

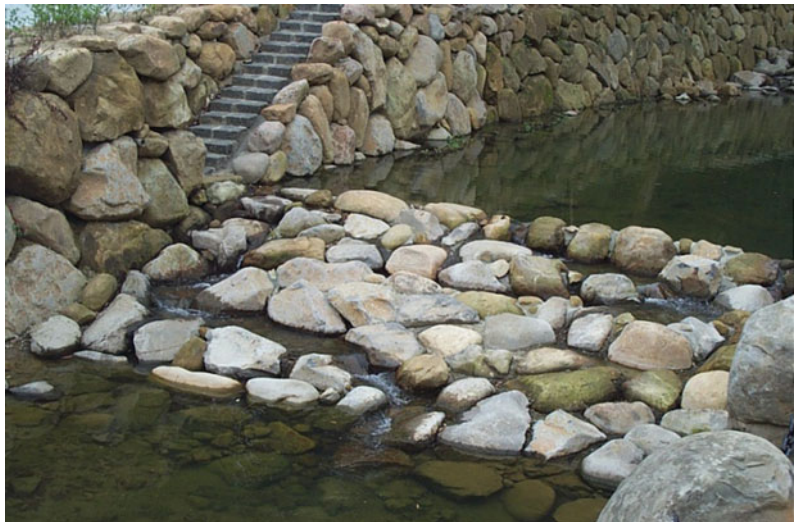
Fig. 7 The constructed stream banks and recreational path



Fig. 8 Vegetation invasion on revetment



Fig. 9 The fish path at a period of low water level



rocks generated a soft image and reduced the visual impact from the constructed structure (Fig. 8). Evidence showed that the pre-installed fish path (Fig. 9) appeared to be functional, and the fish population started to immigrate from upstream after the project was completed.

Although this project was proposed to be a nature-friendly infrastructure, there was no pre-project ecological survey and it also lacked the participation of ecologists and conservation

specialists. The entire project was designed and completed by a hydrological engineering team. Natural considerations were fulfilled without any estimated ecological expectations; therefore, the ecological function is limited and not restored. Several disadvantages of the design have been observed. For instance, the open riparian forest canopy led to the negative result of increasing water temperature and reducing food sources from plant debris. The lack of a buffer zone as a

water quality control mechanism caused eutrophication during warm seasons. Exact ecological side effects are still unknown because a lack of post-project monitoring due to insufficient funding.

References

- Allen TFH, Giampietro M, Little A (2003) Distinguishing ecological engineering from environmental engineering. *Ecol Eng* 20:389–407
- Bergen SD, Bolton SM, Fridley JL (2001) Design principles for ecological engineering. *Ecol Eng* 18:201–210
- Brick C, Watson V (2002) Watershed restoration planning information system—final report. For Montana Natural Resource Damage Program
- Chen JC (2002) Civil engineers: the engineers of sustainable development. *J Hydrol Civ Eng* 39:10–11
- Chen, SC (2003) Sustaining eco-communities and public participation. In: Proceeding of international workshop on ecohydraulics and eco-rivers engineering, Taipei, Taiwan
- Chiu YW, Lin JY (2002) The outreach strategies of ecological engineering methods. *Constr News Rec* 238:32–43
- Council for Economic Planning and Development (2005) Challenge 2008 national development plan (final report). Executive Yuan, Taipei, Taiwan
- Dale VH, Brown S, Haeuber RA, Hobbs NT, Huntly N, Naiman RJ, Riebsame WE, Turner MG, Valone TJ (2000) Ecological principles and guidelines for managing the use of land. *Ecol Appl* 10(3):639–670
- Foundation of River and Watershed Environment Management (1992) The consideration and methods for restoring diverse river forms. FRWEM, Tokyo, Japan
- Foundation of River and Watershed Environment Management (1996) The accomplishment and case study of restoring near-nature river forms. FRWEM, Tokyo, Japan
- Herricks E (2000) An ecological design paradigm for watershed management. In: Proceedings of the international workshop on watershed management in the 21st century, Taipei, Taiwan
- Jackson L, Lopoukhine N, Hillyard D (1995) Ecological restoration: a definition and comments. *Restor Ecol* 3:71–75
- Lewis III RR (1989) Wetland restoration/creation/enhancement terminology: Suggestions for standardization. Wetland creation and restoration: the status of the science, vol II. EPA 600/3/89/038B. U.S. Environmental Protection Agency, Washington, DC
- Lin JY, Chiu YW (2002) Ecological technology and constructional infrastructure. *Landsc Archit Q* 44–45:43–58
- Mitsch WJ, Cronk JK (1992) Creation and restoration of wetlands: some design consideration for ecological engineering. In: Lal R, Stewart BA (eds) *Advances in soil science*, vol 7, Soil restoration. Springer, New York, pp 217–259
- Mitsch WJ, Jørgensen SE (2003) Ecological engineering: a field whose time has come. *Ecol Eng* 20:363–377
- Odum HT (1962) Man in the ecosystem. In: Proceedings Lockwood conference on the suburban forest and ecology. Bulletin of the Connecticut agricultural station 652, Storrs, CT, pp 57–75
- Schiechl H, Stern R (1997) Water bioengineering techniques: for watercourse bank and shoreline protection. Blackwell Science Ltd., Oxford
- Sue YM (2002) A study on enhancement and management plan of river environment (final report). Water Resource Bureau, Taipei, Taiwan
- Tonn B, English M, Travis C (2000) A framework for understanding and improving environmental decision making. *J Environ Plan Manage* 43(2):163–183
- Tsai JH (2001) Public participation in ecological engineering: the case study. In: Conference on ecological engineering and new Taiwan urban planning, Taipei, Taiwan
- Wang RS, Yan JS (1998) Integrating hardware, software and mindware for sustainable ecosystem development: principles and method of ecological engineering in China. *Ecol Eng* 11:277–289
- Wang R, Yan Y, Mitsch WJ (1998) Editorial-ecological engineering: a promising approach towards sustainable development in developing countries. *Ecol Eng* 11:1–16
- Weber C (2002) The planning and design practices in river restoration. In: International ecological engineering methods workshop, Taipei, Taiwan
- Wetzel V (2002) The experience of Germany: applying ecotechnology in watershed management. International Forum on Water & Ecology, Taipei

TXT-tool 4.086-1.3

The Impact of Climate Change on Landslides in Southeastern of High-Latitude Permafrost Regions of China

Wei Shan, Zhaoguang Hu and Ying Guo

Abstract

Climate warming leads to permafrost degradation and permafrost melting phase transition, resulting in an increasing number of landslides. This study uses the road segments and road area at the intersection between Bei'an-Heihe Highway and the northwest section of the Lesser Khingan Range in north China as the study area. By means of geological survey combined with meteorological data, we analyzed the impact of climate change on landslide movement in the permafrost zone. Over a 60 year period, the average annual temperature of the study area has increased by 3.2 °C, and permafrost degradation is severe. Loose soil on the hillside surface provides appropriate conditions for the infiltration of atmospheric precipitation and snowmelt, and seepage from thawing permafrost. As it infiltrates downwards, water is blocked by the underlying permafrost or dense soil, and infiltrates along this barrier layer toward lower positions, forming a potential sliding zone. The representative Landslide in the study area was examined in detail. Displacement monitoring points were set up on the surface of the landslide mass, and at the trailing edge of the landslide mass. The data collected were used to investigate the relationship between landslide movement and pore water pressure at the tailing edge as well as the ground temperature. The results show that the landslide movement process changes with the season, showing a notable annual cyclical characteristic and seasonal activity. Landslide movement is characterized by low angles and intermittence. The time of slide

W. Shan (✉) · Z. Hu · Y. Guo
Institute of Cold Regions Science and Engineering,
Northeast Forestry University, Harbin 150040,
China
e-mail: shanwei456@163.com

Z. Hu
e-mail: huzhaoguang008@163.com

Y. Guo
e-mail: samesongs@163.com

occurrence and the slip rate show a corresponding relationship with the pore water pressure at the tailing edge of the landslide mass. The seepage of water from thawing into the landslide mass will influence the pore water pressure at the tailing edge of the landslide mass, and is the main cause of landslide movement.

Keywords

Climate change · High-latitude permafrost · Permafrost degeneration · Landslide movement · Pore water pressure

Contents

1	Introduction	716
2	Background	717
3	Climate Change and Landslides	721
4	Monitoring of Landslide Movement	722
5	Results, Analysis, and Discussion	725
6	Conclusion	728
	References.....	729

1 Introduction

In northeast China, the area north of 47°N contains widespread permafrost. This is China's only high-latitude permafrost region, and is also China's second largest permafrost region (Guo et al. 1981; Zhou et al. 1996; Sun et al. 2007). In recent years, due to the effects of climate change, the southern boundary of China's northeast high-latitude permafrost region gradually moved northward. Permafrost near the southern boundary shows discontinuous island-like distribution and accelerated degradation (Jin et al. 2000; Wei et al. 2010; He et al. 2009a).

Climate is the long-term average state of atmospheric physical characteristics. Climate change refers to the change in the mean state of climate over time. In the last century, the average global surface temperature has been continuously increasing, which shows a consistent warming trend worldwide. The rate of warming during the past 50 years is almost twice that of the past

100 years (IPCC 2007). Since the early 1980s, in most of the permafrost regions in the world, the temperature has increased. In some regions in northern Alaska, the observed temperature increase has reached 3 °C, in the northern European region and Russia, the increase has reached 2 °C. In the latter region, during the 1975–2005 period substantial reduction in the thickness and range of the permafrost layer was observed (IPCC 2013). Climate change and its impact are an important research issue receiving extensive global attention.

Numerous studies have shown that the climate change in China exhibits the same trend as the global climate change (Ding et al. 2006). In the last 54 years, the rate of temperature increase in China was about 0.25 °C/10a, far higher than the global or hemispheric average rate of warming. Northeast China is one of the areas showing the most significant warming and permafrost degradation in the country (Shi et al. 2014).

Forest and accumulated snow have a very important influence on the temperature change and the thawing process of the underlying seasonal frozen ground and permafrost (Chang et al. 2011). In the Great and Lesser Khingan Ranges of northeast China and the Outer Baikal region of Russia, temperature shifts caused by snow, vegetation, water, topography, atmospheric inversion, and other local factors are substantial, forming the “Khimgan–Baikal type” that is permafrost distinctly from polar and high-altitude

permafrost distribution (Zhou and Guo 1982; Chang et al. 2013). Affected by the occurrence conditions, the process and form of high-latitude permafrost degradation in northeast China are also different from that of polar and high-altitude permafrost (Jin et al. 2009).

In recent years, landslide incidents triggered by climate change and extreme weather have increased (Blunden and Arndt 2011), and have gradually received attention from national governments and relevant international academic organizations (EU/FP7 2008; ICL 2014). In particular, landslides in cold areas are becoming a hot issue in landslide research (ICL 2012; Guo et al. 2013).

Landslides are a natural geological phenomenon in mountainous areas. Their mechanism and evolution are closely related to the geological conditions and environmental factors, and are controlled not only by geological forces, lithologic structure, and other crustal internal factors; but also by topography, land cover, precipitation, changes in human activities, and environmental conditions. The spatial and temporal distribution of landslides has characteristics of uncertainty, sporadic nature, continuation, and irreversibility. Landslides are the result of geological and environmental changes and in turn also drastically change the geological environment (Shan et al. 2014b). Scientists have applied different methods in order to analyze the relationship between climate change and landslide mechanisms and evolution in cold areas (Shan et al. 2014a). The impact of landslides induced by glacier and permafrost degradation in cold regions; on the topography, geological environment, water resources, and biodiversity has been examined; and the role of climate, a main factor influencing the landslide movement, in the evolution of landslides in cold areas has been discussed (Grab and Linde 2014; Ballantyne et al. 2014; Nussbaumer et al. 2014; Haeberli 2013; Kliem et al. 2013; Fischer et al. 2013; Starnberger et al. 2013). However, due to lack of monitoring data, the majority of these studies were large-scale (Stoffel et al. 2014). Currently, there has been no report on the mechanisms, movement characteristics, and patterns of landslides induced by the combined effect of

permafrost thawing and extreme weather events due to climate change and geological conditions.

In the present study, the road area where the Bei'an to Heihe Highway crosses the northwest section of the Lesser Khingan Range is used as the study area. We performed a geological survey, an engineering survey, and field measurements which were plotted on the topographic map of the landslide area and a relevant geological cross section. Using the meteorological data of Sunwu County (30 km from the study area), which was released by the China Meteorological Data Sharing Service System (<http://cdc.cma.gov.cn/home>), we analyzed the impact of climate change on permafrost thaw, geological environment, and landslide mechanisms in the study area. Using Landslide K178+530 in the landslide area as an example, we used monitoring data of point displacement on the landslide mass, ground temperature at the trailing edge, and pore water pressure to perform a comprehensive analysis of the impact of climate change on the pore water pressure at the measuring points and the landslide movement process.

2 Background

China's Bei'an-Heihe Highway intersects the northwest section of the Lesser Khingan Range at the junction between Sunwu County and the Aihui District. The study area lies between east longitude 127° 17' 31"–127° 21' 24" and north latitude 49° 30' 57"–49° 41' 50" (Fig. 1). The area is located on the southern fringe of China's high-latitude permafrost region and has typical periglacial landforms. The island-like permafrost in this region is the result of residual paleo-glacial deposition and is currently in the degradation stage. The geological conditions are extremely unstable.

Topography and Geological Structure

The study area is located in the northwest section of the Lesser Khingan Range. It has a hilly landscape with undulating terrain. The slope of the ground is generally 10°–20°, and the upper

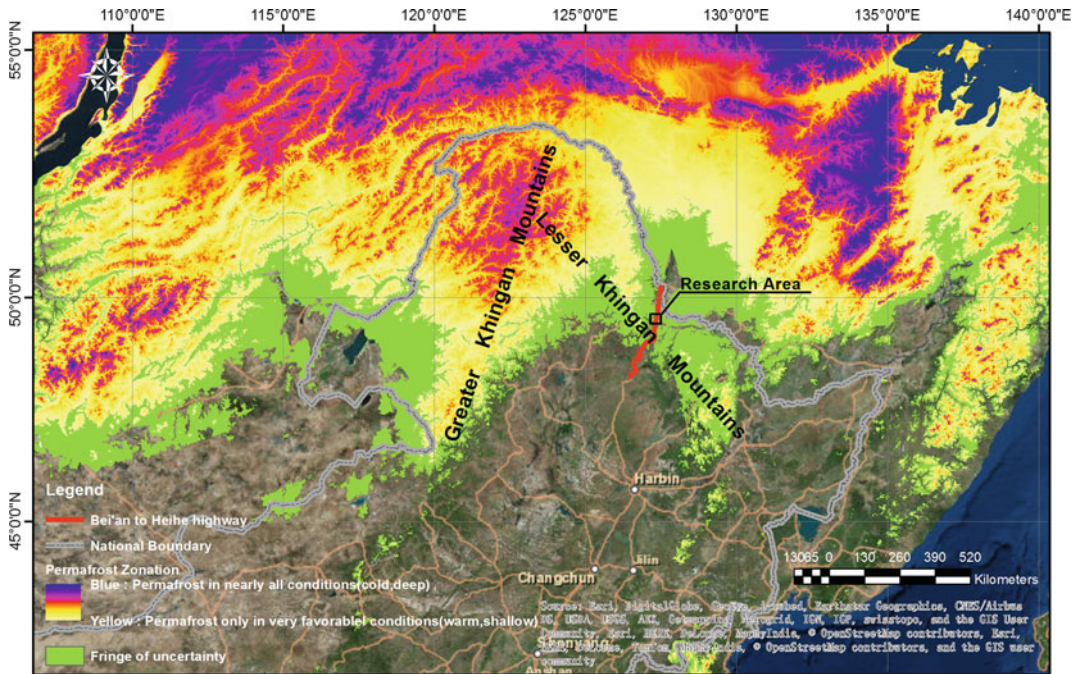


Fig. 1 High-latitude permafrost distribution in Northeast China (data from Zurich University, Switzerland), and the location of study area

part of the slopes are relatively steep, about 25° – 30° , but locally can be up to 40° . The area can be further divided into the valley bottomland and hills. The altitude of the entire area ranges from 210 to 330 m.

The geological structure of the study area belongs to the Khingan–Haixi fold belt. From the bottom up, the stratigraphy is composed by Cretaceous mudstone, Tertiary pebbly sandstone, silty mudstone, and powdery sandstone. From the late Tertiary to the early Quaternary, the Lesser Khingan Range experienced block uplift. Due to long-term erosion and leveling, loose sediments on the summit and the slope of the hills have gradually thinned, and the thickness of the current residual layer is generally only 1–2 m. The loose deposits accumulate mainly in the basin and valley areas between mountains, with a thickness of about 10 m. The soil is mainly composed of clayey silt, mild clay, and gravelly sand, and the surface is covered with a relatively thick layer of grass peat and turf. The

surface vegetation is that of grassland and woodland, and there are inverted trees in the woodlands. Figure 2 shows the geological map of the landside road area of the study area plotted from the field survey conducted in June 2010.

Climate Conditions

The study area is located in the transition zone between the north part of the middle-temperate zone and the cold-temperate zone. The area is affected by alternating influences of high and low pressures from inland and the sea as well as by monsoons. Overall the climate is characterized by long, dry and cold winters and short, hot and humid summers. In other words, it belongs to the continental monsoon climate zone.

The average annual temperature in this area ranges -2 to 1°C , with an extreme maximum of 38.6°C , and an extreme minimum of -48.1°C . The annual average wind speed is 2.7–4.0 m/s. The average annual precipitation is 530–552 mm,

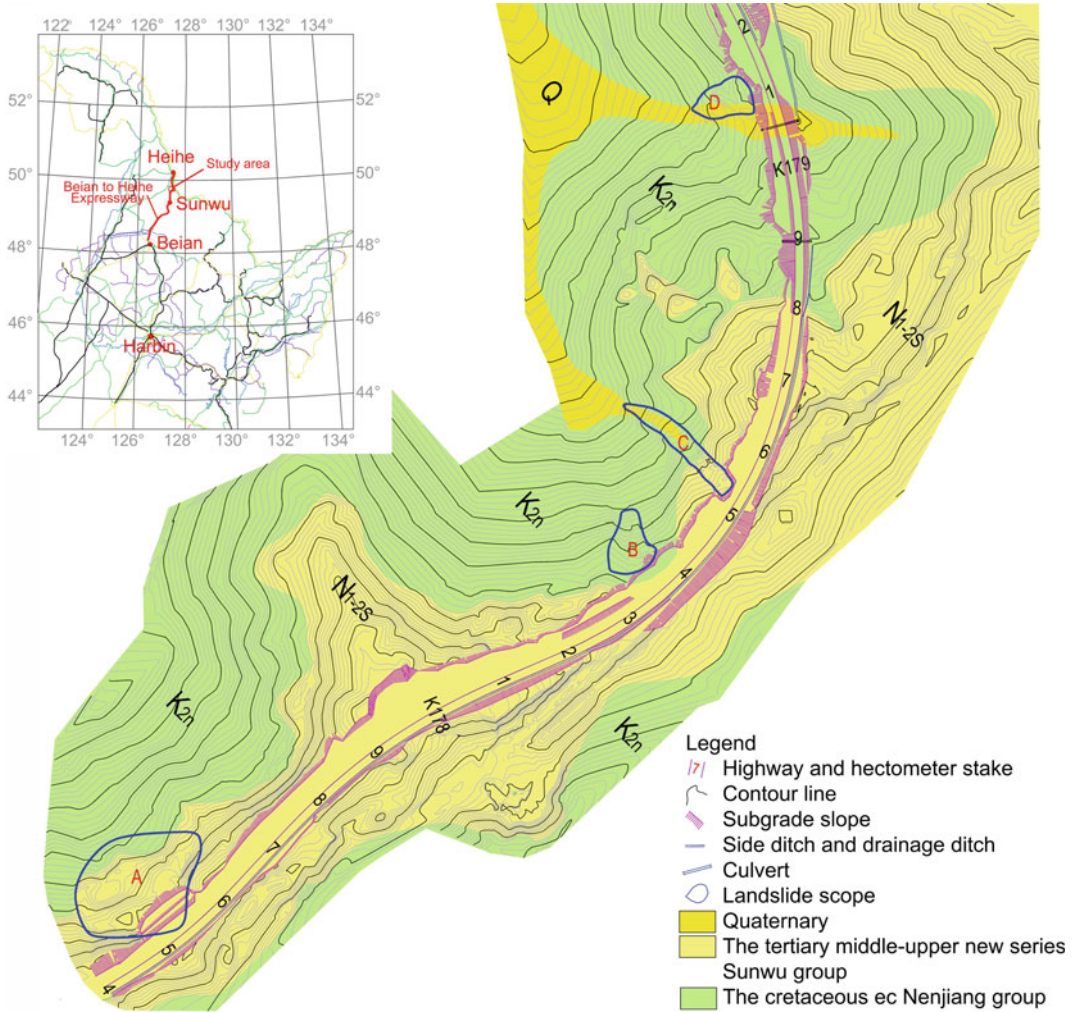


Fig. 2 Geological map of K177+400-K179+200 section of Bei'an-Heihe Highway

with a maximum of 800 mm. Precipitation is mostly concentrated in the summer, from July to September, accounting for 61–67% of the total annual precipitation. The first snow fall is typically in mid-October, and the final snow fall is often in late March or early April of the following year. The maximum annual evaporation is greater than 1000 mm, whereas the minimum is 850 mm. The average annual sunshine is 2500 h, with a maximum of 2800 h and a minimum of 2200 h. The total amount of annual radiation averages 1148 kcal/cm², with a maximum of 1229 kcal/cm², and a minimum of 1039 kcal/cm².

Permafrost Distribution

The climate in Northeast China is controlled by the Siberia–Mongolia high-pressure control. The inversion layer is widely distributed in this region and has an important impact on the development process and regional distribution of permafrost. Meanwhile, the northeast region of China is China's main forest distribution area, where the ecological environments of wetlands, grasslands, and forests coexist with permafrost mutually restraining and influencing each other. Forests, bushes, mosses, and other ground covers reduce solar radiation, hindering the increase of

air and ground temperatures. The low-lying river terraces, valleys, wetlands, and shady slopes provide good conditions for the development and preservation of island-like permafrost and slow permafrost degradation.

The seasonal ground freezing in the study area reaches maximum depth at the end of May, and the observed maximum depth is 2.26–2.67 m. In the mountains, the maximum seasonal freezing depth exceeds this value. April to September is the thawing period of seasonal frost; in dry areas all the seasonal frost thaws in early July, whereas in swamped thick peat and humus zones, seasonal frosts do not completely thaw until the end of October. On shady slopes and in valley areas, island-like permafrost is distributed.

Because there is no long-term meteorological data for the study area obtained from field measurements, meteorological data from Sunwu County (30 km from the study area), published by the China Meteorological Data Sharing Service System, was used for the analysis of climate change. Figure 3 plots the monthly average temperatures, soil temperatures in 40 cm depth, atmospheric precipitations, and maximum

permafrost thicknesses from 1971 to 2000 using meteorological data of Sunwu County.

Climate Change of the Study Area

Affected by global climate change, the study area has become one of the regions in northeast China with the largest temperature increase in the past 50 years. Meteorological data of Sunwu County show that in the past 60 years, among all climate indicators, change in temperature was the most significant. Figure 4 shows the annual average maximum temperatures, average temperatures, average minimum temperatures, and average precipitation from 1954 to 2013 using meteorological data of Sunwu County. By applying linear regression, we found that, over the 60 year period from 1954 to 2013, the annual average temperature in the study area increased by 3.2 °C; the average annual maximum temperature increased by 1.5 °C, or 21.99%; the average annual minimum temperature increased by 5.2 °C, or 69.04%; and the average annual precipitation decreased by 4.85 cm, or 8.93%. The increase in the average annual minimum

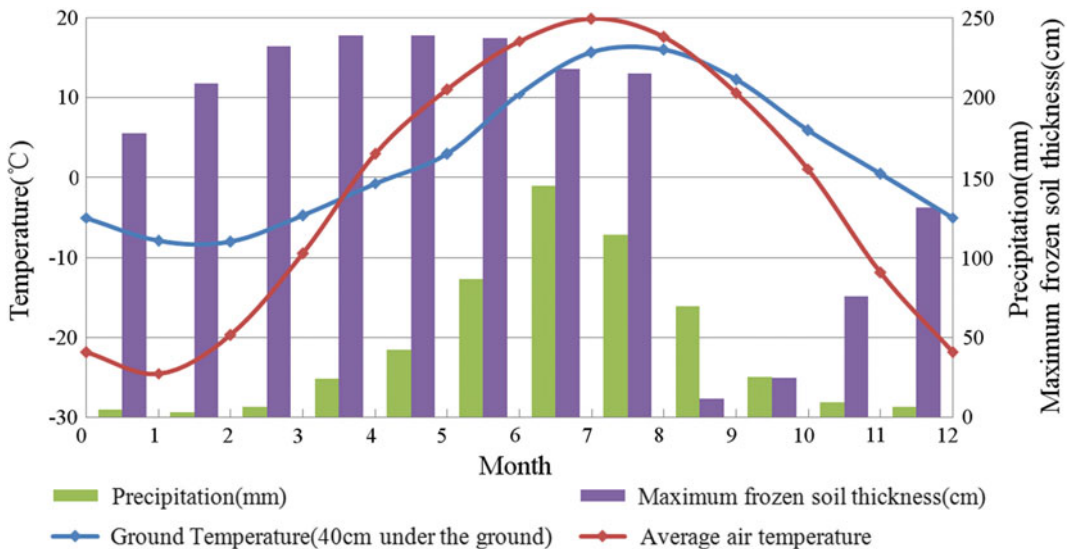


Fig. 3 Monthly average temperature/soil temperature in 40 cm depth/permafrost thickness/precipitation in Sunwu County (1971–2000, Data: China Meteorological Data Sharing Service System)

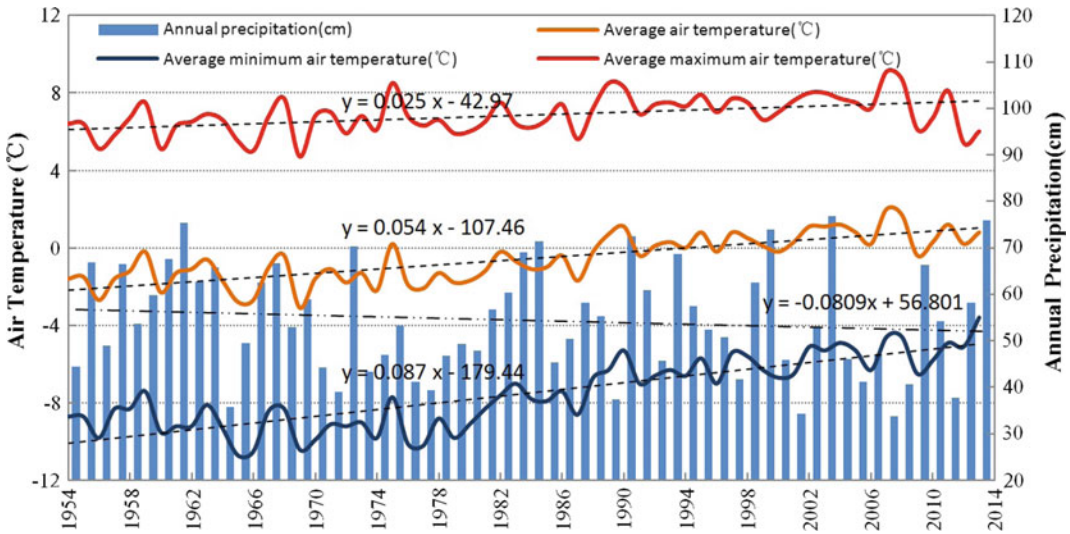


Fig. 4 Annual average maximum temperatures, average temperatures, average minimum temperatures and average precipitation in Sunwu County (1954–2013)

temperature was 3.45 times that of the average annual maximum temperature.

3 Climate Change and Landslides

Climate change leads to permafrost degradation in the study area, and human engineering projects further accelerate the process of permafrost degradation (He et al. 2009b). In 1999, a survey conducted for constructing the secondary road from Bei'an to Heihe showed that there were 17 permafrost road segments along the entire road length (Zhang et al. 2001; Wang et al. 2001). Yet in 2009, a survey conducted right before the construction of the Bei'an-Heihe Highway showed that there were only six permafrost road segments remaining; the other 11 segments had been completely degraded.

During the thawing of permafrost, the phase change of water has a severe impact on the mechanical properties of the soil (Wang et al. 2014b). Permafrost degradation causes a lot of geological engineering problems in the construction of roads. The construction of the Bei'an-Heihe secondary road started in 1999, and

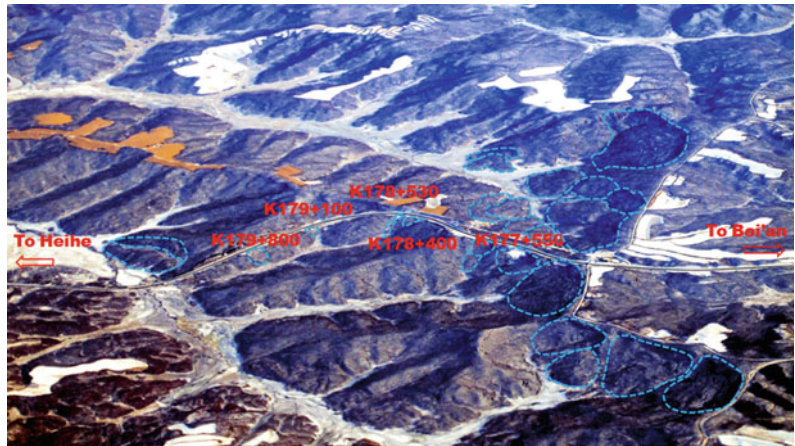
in August 2000 on the K176+900-178+200 section a landslide was induced by thawing of permafrost in the roadbed. This caused instability of the entire roadbed in this section, which had to be completely abandoned. The road was then redirected toward the left along the ridge, as shown in Fig. 5a.

The survey conducted before the 2009 project of widening the Bei'an-Heihe road and constructing the Bei'an-Heihe Highway also showed that, in the K177+400-K179+200 section, within 10 m of the left of the roadbed there were four landslides with a volume of over 20,000 m³, as illustrated in Fig. 2. In addition, a number of landslides were found within 3 km of this road area (Fig. 6), thus forming the landslide group at the intersection where the Bei'an-Heihe Highway crosses the northwest section of the Lesser Khingan Range. When compared with the permafrost distribution map obtained from the Enhanced Thematic Mapper (ETM+) imaging data collected from satellite Landsat7 in 2009 (Fig. 7) (Wang et al. 2014a), it can be seen that the locations of the landslides fit the permafrost distribution very well. Thus, we deduced that these landslides were induced by the thawing of permafrost.



Fig. 5 Satellite photos of K176+500-K179+900 section of Bei'an-Heihe Highway (Google earth). **a** Landslide in K178+530 section (in 2000). **b** Satellite photos of K178+530 (2004.6). **c** Satellite photos of K178+530 (2010.9)

Fig. 6 Full view of K175+500-K180+200 section of Bei'an-Heihe Highway (*Blue line* is the boundary of the landslides, the *orange area* is corn field)



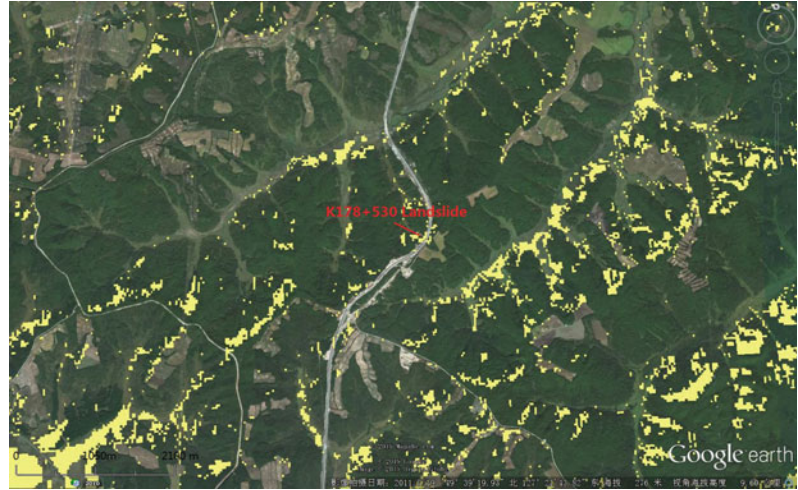
4 Monitoring of Landslide Movement

In June 2010, on the basis of geological survey and topographic measurements of the study area, comprehensive examination and dynamic monitoring of the slip movement were performed on a representative landslide that may threaten the

roadbed in order to investigate the impact of permafrost thaw on landslide movement.

Landslide K178+530 on the Bei'an-Heihe Highway (Fig. 2c) is one of the landslides that is closest to the roadbed and has the fastest slip rate. Because survey and monitoring data prior to 2009 are not available, the time of the initial slip could not be determined. From the satellite photo taken on June 15, 2004, it can be seen that at that

Fig. 7 Permafrost distribution map in K176 +500-K180+000 section of Bei'an-Heihe Highway



time the straight-line distance between the leading edge and the tailing edge of the landslide mass was 101.26 m (Fig. 5b). The satellite photo taken on September 12, 2010 showed that the straight-line distance between the leading and tailing edges of the landslide mass had increased to 145.05 m (Fig. 5c). Over this six year period, the leading edge of the landslide moved forward 43.79 m, whereas the position of the trailing edge basically did not change.

Figure 8 shows the distribution of the drillings, the geophysical measurement lines and points for monitoring displacement, ground temperature, and pore water pressure for Landslide K178+530. The points A, B, C, D, E, and F in the figure denote the positions of the drilling, and lines G and H denote the high-density resistivity measurement line and the ground-penetrating radar (GPR) measurement line, respectively. During the drilling in holes E and F, permafrost was found at a depth 2.2 m below the ground surface, and the permafrost thicknesses at points E and F were 3.7 and 2.4 m, respectively. The area of permafrost distribution in Fig. 8 is inferred according to Fig. 7.

Through drilling, GPR, and high-density resistivity prospecting; the profiles of Landslide K178+530 in cross section H along the sliding direction and in cross section G perpendicular to the slide direction were obtained (Figs. 9 and 10).

In boreholes A and B shown in Fig. 8, plastic displacement measurement piles with a length of 400 cm and an above-ground height of 30 cm were buried; the top of the pile was used to monitor the slope displacement of the landslide mass at points A and B. C served as the monitoring point of the ground temperature; in the borehole, thermistor soil temperature sensors were set up at every 0.5 m from 0.5 to 2.5 m below the ground surface. D served as the monitoring point of pore water pressure; in the borehole, steel-wire soil pore water pressure sensors were set up at 3.8, 9.4, 19.4, and 23.7 m below the ground surface. Regular monitoring of relevant parameters started in July 2010.

The real-time dynamic deformation monitoring system, a Real Time Kinematic-Global Positioning System (RTK-GPS), was used to monitor the displacements of the measuring points on the landslide surface. From July 2010 to August 2014, point A slid horizontally by 69.03 m, and its elevation dropped by 7.95 m; point B slid horizontally by 113.97 m, and its elevation dropped by 17.37 m. Based on these values, it can be deduced that the angle between the slope and the horizontal plane decreased from 8.07° to 6.02° . Points A' and B' in Figs. 8 and 9 show the positions of points A and B, respectively, in August 2014 after sliding.

Figure 11 shows the average daily ground temperatures and atmospheric precipitations over

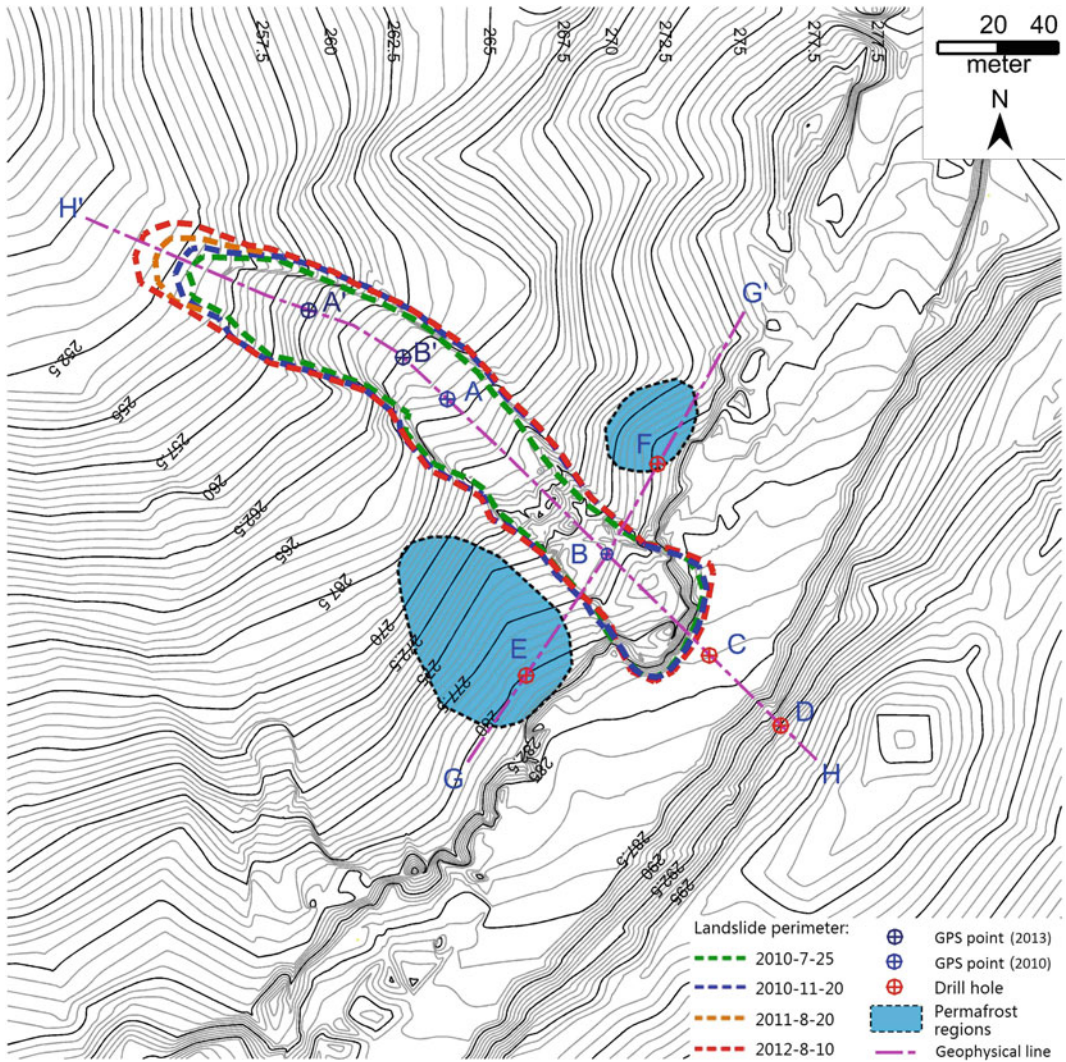


Fig. 8 Distribution of the drillings, the geophysical measurement lines and points for monitoring displacement, ground temperature, and pore water pressure in Landslide K178+530

time at point C on Landslide K178+530 at depths of 0.5 and 2.0 m. The ground temperature data is on-site monitoring data; the average daily atmospheric temperatures and precipitations are meteorological data collected at Sunwu County weather station.

To facilitate data analysis, the soil freeze period was defined as the period from the time when the thermistor sensor at 0.5 m below ground surface detected temperature below zero degree Celsius in the autumn to the time when the thermistor sensor at 2.0 m below ground

surface detected temperature changing from below to above zero degree Celsius in the spring. This period is displayed in light blue in Fig. 11. The sums of atmospheric precipitation over the soil freeze period and non-freeze period were calculated, and are denoted by the dark blue bars in Fig. 11. During the soil freeze period, atmospheric precipitation and snowmelt water are blocked by the seasonal frozen soil layer and cannot normally infiltrate downward to deep soil.

Figure 12 shows the pore water pressure measured at point D, 19.4 m below the ground

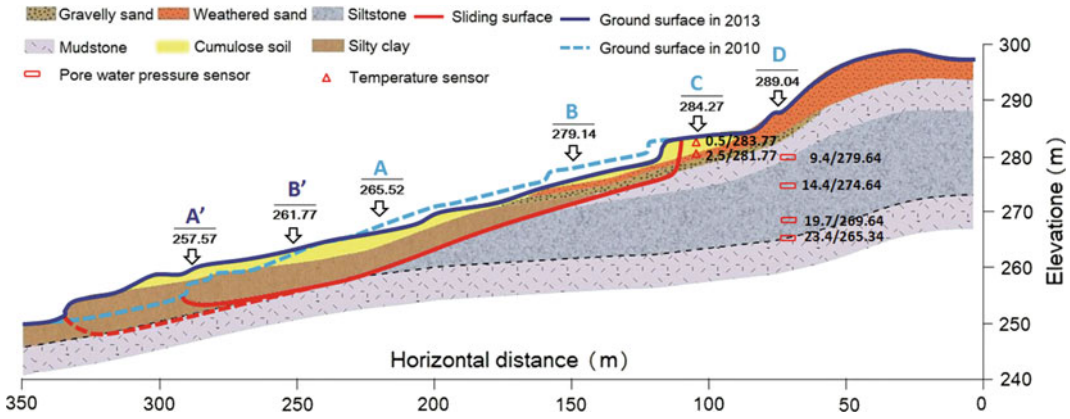


Fig. 9 The profiles of Landslide K178+530 along the sliding direction

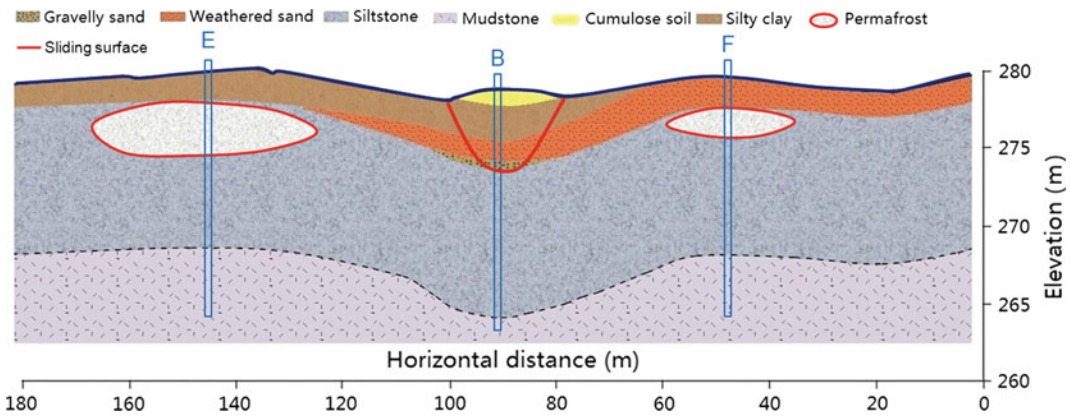


Fig. 10 The profiles of Landslide K178+530 perpendicular to the slide direction

surface. At point D at the time of drilling, water was first observed at a depth of 3.8 m below the ground surface, but the stable water level measured during the monitoring period ranged from 15.8 to 16.6 m. Soil at 3.8 and 9.4 m below the ground surface was found to be unsaturated during the monitoring period. Readings from the pore water pressure sensor placed at 23.7 m below the ground surface were unstable during the late stage of monitoring, and thus data collected from the sensor placed at 19.4 m below the ground surface are used to represent pore water pressure at point D.

Figure 13 illustrates changes in the displacement rates at point A and point B on the landslide mass, and in pore water pressure at point D over time. To obtain the displacement rate,

displacement data collected using the RTK-GPS real-time dynamic deformation monitoring system were divided by the monitoring interval.

5 Results, Analysis, and Discussion

The permafrost distribution determined by the present study is consistent with previous investigations (Wang et al. 2014a, 2015). In the current study, meteorological data of Sunwu County, 30 km south of the study area, was analyzed to examine the climate change in the study area. The causes of landslide in the study area were evaluated preliminarily by means of permafrost distribution, topography, geological survey of the study area, and investigation on the

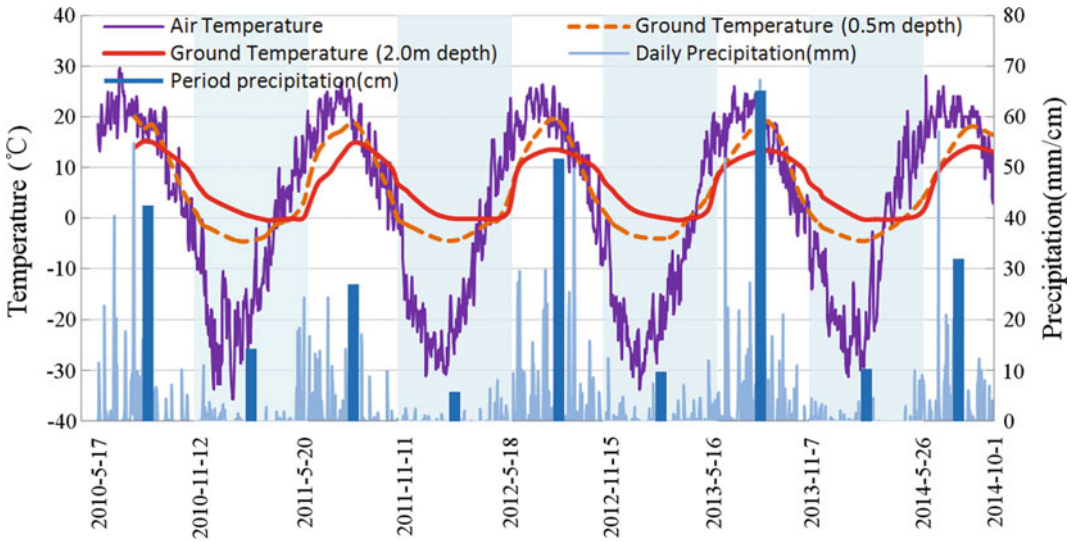


Fig. 11 Daily average air temperature/precipitation/soil temperature in the depth of 50, 200 cm in K178+530 section of Bei'an-Heihe Highway

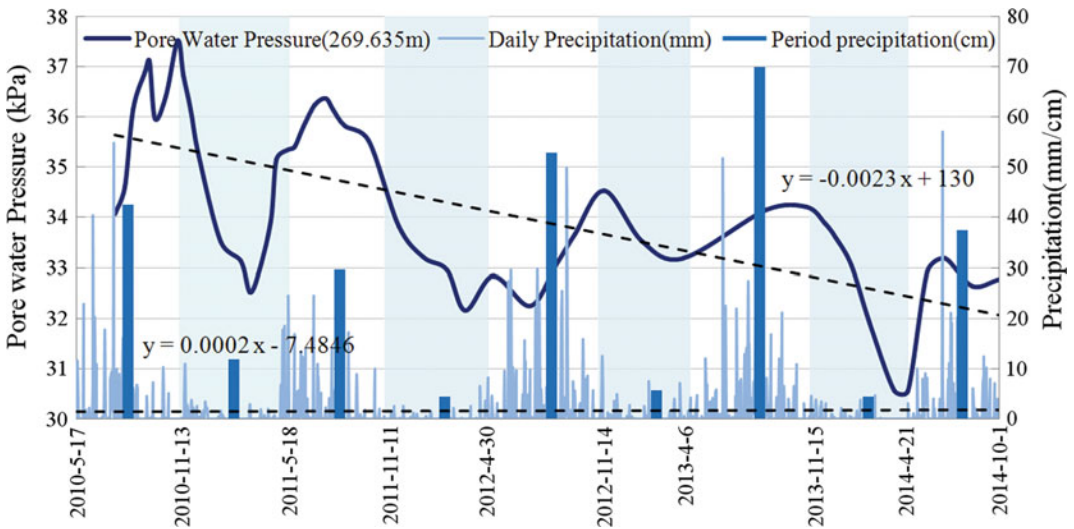


Fig. 12 Daily precipitation & pore water pressure in the depth of 19.4 cm of D point in K178+530 section of Bei'an-Heihe Highway

specific case of roadbed instability occurring in section K176+900-178+200 on a Bei'an-Heihe secondary road in August 2000.

The Sunwu County meteorological data show that, over the 60 year period from 1954 to 2013, the variation in atmospheric precipitation was 8.93%, and that this had little long-term effect on the thermal state of the soil in the study area. As

shown in Fig. 4, the increase in the average annual minimum temperature was substantially higher than the increase in the average annual maximum temperature. This suggests that the main cause of the temperature rising was not the increase in the amount of direct radiation, but rather the decrease in the heat demand of the soil from the atmosphere and the increase in the

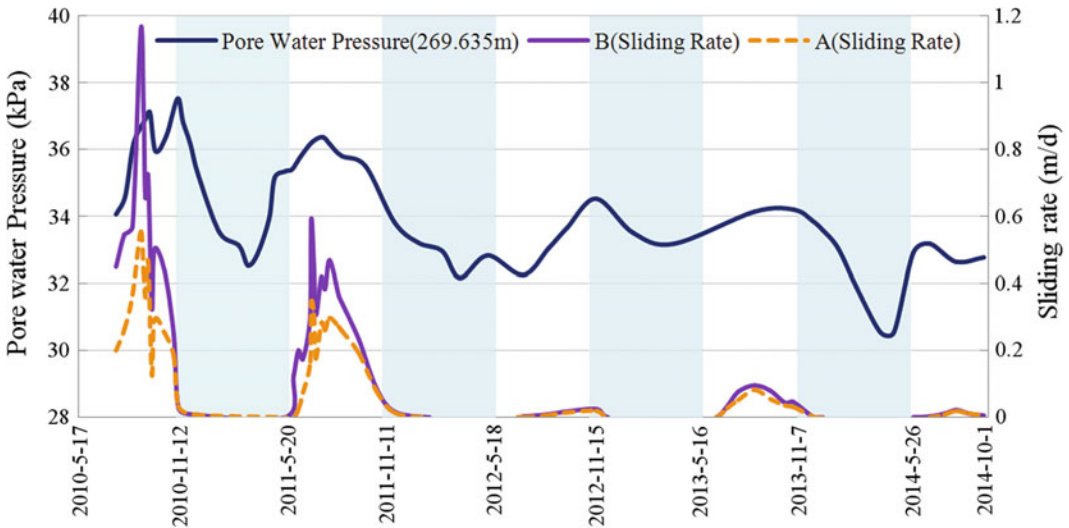


Fig. 13 Horizontal displacement rates at point A and point B on the landslide mass and pore water pressure at point D (19.4 m depth) in K178+530 section of Bei'an-Heihe Highway

ability of the soil to radiate heat into the atmosphere (Chen et al. 2006). The difference in the amplitude of temperature increase between the average annual maximum temperature and the average annual minimum temperature was caused by the latent heat of permafrost thaw. The fact that the amplitude of temperature increase in the average annual maximum temperature and in the average annual minimum temperature differed by 47.05% over a 60 year period demonstrates that the permafrost in the study area is decreasing in amount, going through rapid degeneration.

In Fig. 7, permafrost is not found in section K176+900-178+200 (where overall roadbed instability occurred) of the previous Bei'an-Heihe secondary road. This is because the ground temperature data used to plot Fig. 7 are the ETM+ data collected by satellite Landsat7 in 2009, whereas the roadbed instability occurred in August 2000. After nine years, the permafrost in this road section had degraded entirely. In Fig. 7, along the road direction on both sides of point B, which is to the right of the road section K178+530, there are permafrost distributions. Yet in Fig. 8e, in borehole B no permafrost was found; in addition, in the exploration of line G using a high-density resistivity method and GPR, no data

abnormality was detected below point B within 15 m along line G, demonstrating that there was no permafrost distribution. This may be because permafrost in this location was at a stage of severe degradation; and although the soil temperature was low, the phase transition of soil moisture had already taken place and had transitioned to warm permafrost or melting permafrost. It may also be related to the resolution of the Landsat7 satellite ETM+ data.

From Fig. 11, it can be seen that each year the initial soil freezing in the study area occurred in a relatively concentrated time period, between 11 November and 15 November. But for the same measurement point, the time needed for seasonal frost to complete thawing varied rather largely from year to year. This may be related to the amount of autumn precipitation and winter snowfall in the previous year, as well as the thermal condition of soil water near the maximum seasonal frost depth, but needs to be further investigated.

As shown in Fig. 12, at point D the pore water pressure started to rise in the spring of each year, reached the peak value in the summer, and then fell, thus showing annual periodic changes. But on an interannual time scale, pore water pressure showed an overall downward trend. This change

was not correlated with atmospheric precipitation. Linear analysis showed that, over the monitoring period, the atmospheric precipitation in the study area increased by 0.318 mm, whereas the pore water pressure at point D decreased by 3.675 kPa. In other words, the groundwater level dropped by 36.75 cm, and the amount of groundwater reduction was 1155 times the increase in the atmospheric precipitation over the same period.

From Fig. 13, it can be seen that the slip rates at measurement points A and B on the landslide mass correspond well to pore water pressure at point D. During the monitoring period, with the snowmelt and thawing of seasonal frost each spring, the pore water pressure in the hillside soil gradually increased, and the landslide mass started to slip. During the concentrated rainfall in the summer, the pore water pressure reached the peak for the year, and the slip rate of the landslide reached the peak value simultaneously. Along with the landslide movement, the soil pore water pressure gradually decreased, and the slope sliding gradually stagnated. The landslide movement had notable characteristics of annual periodicity and seasonal activity.

Figures 9 and 13 reveal that changes in the slip rates of points A and B on the landslide mass were consistent. Over the monitoring period, the displacement of point B was 1.65 times that of point A. We deduced that the movement of point A might be occurring due to the force coming from the rear part of the landslide mass. From Fig. 13, it can also be seen that the annual maximum pore water pressures at point D from 2010 to 2014 were 37.52, 36.37, 34.53, 34.14, and 33.19 kPa, respectively, declining year by year, and the decline in amplitude was relatively large in 2012. The maximum slip rates of point B from 2010 to 2014 were 115.7, 59, 2.55, 9.63, and 2.2 cm/d, respectively. Rapid sliding mainly occurred in 2010 and the summer of 2011. The slip rate decreased year by year, and the largest decline occurred in 2012. But in the summer of 2013, there was a slight increase in the slip rate. The reason behind these phenomena might be related to the fact that at points E and F (Fig. 8), which are located outside the lateral edge of the

slope at point B, permafrost thawed and supplemented water to the landslide mass. In addition, this might be related to the amount of summer precipitation. As shown in Fig. 12, in 2013 the summer atmospheric precipitation reached the highest value over the entire monitoring period, 672 mm; this was 14.33 mm higher than the second highest summer precipitation (occurring in 2012) and 1.46 times the mean summer atmospheric precipitation over the monitoring period. We thus concluded that, in the monitoring period, the slip rate of Landslide K178+530 was mainly controlled by pore water pressure at the tailing edge of the landslide mass, and meanwhile it was also affected by the amount of summer precipitation in the study area. The pore water pressure at the tailing edge of the landslide mass was related to the thawing of permafrost at the lateral edge of the slope. As permafrost thawed year by year, its volume was reduced, which gradually reduced the pore water pressure at the tailing edge of the slope. As a result, the slip rate of the landslide mass was gradually reduced year by year.

6 Conclusion

In this study, we performed a comprehensive analysis of climate change data in the study area and data on the displacement, ground temperature, and pore water pressure at measurement points on Landslide K178+530 in Bei'an-Heihe Highway, and from this analysis we obtained the following main conclusions.

First, affected by the global climate change, the northwest section of the Lesser Khingan Range located at the southern boundary of the high-latitude permafrost region in northeast China experiences temperature increase, and the amplitude of the increase in average annual minimum temperature is 3.45 times that in average annual maximum temperature. Permafrost degradation is severe. Permafrost degradation will lead to further temperature rise in this region, and the northward movement of the southern boundary of the permafrost region will also accelerate.

Second, permafrost thaw causes the number of landslides in the northwest section of China's Lesser Khingan Range to increase, which results in topographical changes in this region. Human construction activity accelerates the thawing of permafrost.

Third, water seepage from thawing permafrost and infiltration of concentrated summer precipitation together increase the local moisture content in hillside soil. This is the main cause of landslides in the northwest section of the Lesser Khingan Range in China.

Fourth, in the northwest section of China's Lesser Khingan Range, landslide movement begins in the summer season with concentrated precipitation each year, and gradually stops in the autumn when the soil freezes. The landslide movement clearly has characteristics of seasonal and annual periodicity.

Fifth, the slip rate and movement process of landslides in the northwest section of China's Lesser Khingan Range are controlled by the thawing process of permafrost on and near the landslide mass. As the permafrost thaws year by year, its volume is reduced, and its ability to supplement water to the landslide mass is also reduced. This causes the slip rate of the landslides to decrease year by year until it reaches zero, and then the landslides tend to become stable.

Acknowledgements We thank the Science and Technology Project of the Chinese Ministry of Transport (2011318223630) and the International Landslide Research Program (IPL-167) for funding support. We are also grateful to an anonymous referee who helped improve the manuscript.

References

- Ballantyne CK, Sandeman GF, Stone JO, Wilson P (2014) Rock-slope failure following Late Pleistocene deglaciation on tectonically stable mountainous terrain. *Quat Sci Rev* 86:144–157
- Blunden J, Arndt DS (2011) State of the climate in 2011. In: American Meteorological Society. <http://www.ncdc.noaa.gov/bams-state-of-the-climate/>
- Chang XL, Jin HJ, Yu SP, Sun HB, He RX, Luo DL, Sun GY, Lu LZ (2011) Influence of vegetation on frozen ground temperatures the forested area in the Da Xing'anling Mountains, Northeastern China. *Acta Ecol Sin* 31:5138–5147
- Chang XL, Jin HJ, He RX (2013) Review of permafrost monitoring in the northern Da Hinggan Mountains, Northeast China. *J Glaciol Geocryol* 35:93–100
- Chen J, Sheng Y, Cheng GD (2006) Discussion on protection measures of permafrost under the action of engineering from the point of earth surface energy balance equation in Qinghai Tibetan Plateau. *J Glaciol Geocryol* 28:223–228
- Ding YH, Ren GY, Shi G (2006) National assessment report of climate change (I): climate change in China and its future trend. *Adv Clim Change Res* 2:3–8
- Eu-Fp7 (2008) ACQWA: assessing climate impacts on the quantity and quality of water a large integrating project under EU framework programme 7 (FP7): a summary for policymakers. www.acqwa.ch
- Fischer L, Hugge C, Kääh A, Haerberli W (2013) Slope failures and erosion rates on a glacierized high-mountain face under climatic changes. *Earth Surf Process Land* 38:836–846. doi:10.1002/esp.3355
- Grab SW, Linde JH (2014) Mapping exposure to snow in a developing African context: implications for human and livestock vulnerability in Lesotho. *Nat Hazards* 71:1537–1560. doi:10.1007/s11069-013-0964-8
- Guo DX, Wang SL, Lu G, Dai JB, Li EY (1981) Regionalization of permafrost in the Da and XiaoXing'anling Mountains in northeastern China. *J Glaciol Geocryol* 3:1–9
- Guo Y, Canuti P, Strom A, Hideaki M, Shan W (2013) The first meeting of ICL landslides in cold regions network, Harbin, 2012. *Landslides* 10:99–102. doi:10.1007/s10346-012-0369-x
- Haerberli W (2013) Mountain permafrost—research frontiers and a special long-term challenge. *Cold Reg Sci Technol* 96:71–76
- He RX, Jin HJ, Lv LZ, Yu SP, Chang XL, Yang SZ, Wang S-L, Sun GY (2009a) Recent changes of permafrost and cold regions environments in the northern part of northeastern China. *J Glaciol Geocryol* 31:525–531
- He RX, Jin HJ, Chang XL, Lv LZ, Yu SP, Yang SZ, Wang SL, Sun GY (2009b) Degradation of permafrost in the northern part of northeastern China: present state and causal analysis. *J Glaciol Geocryol* 31: 829–834
- ICL (International Consortium on Landslides) (2012) International consortium on landslides strategic plan 2012–2021—to create a safer geo-environment. <http://iplhq.org/category/home/>
- ICL (2014) The 2014 Beijing declaration landslide risk mitigation: toward a safer geo-environment. <http://iplhq.org/category/home/>
- IPCC (Intergovernmental Panel on Climate Change) (2007) Summary for policymakers. Climate change 2007: the physical science basis. Contribution of working group I to the fourth assessment report of the intergovernmental panel on climate change. Cambridge University Press, Cambridge

- IPCC (2013) Summary for policymakers. Working group I contribution to the IPCC fifth assessment report climate change 2013: the physical science basis. Cambridge University Press, Cambridge
- Jin HJ, Li SX, Wang SL, Zhao L (2000) Impacts of climatic change on permafrost and cold regions environments in China. *Acta Geogr Sin* 55:161–173
- Jin HJ, Wang SL, Lv LZ (2009) Features of permafrost degradation in Hinggan Mountains, northeastern China. *Sci Geogr Sin* 2:223–228
- Kliem P, Buylaert JP, Hahn A, Mayrd C, Murray AS, Ohlendorf C, Veres D, Wastegård S, Zolitschka B, Team TPS (2013) Magnitude, geomorphologic response and climate links of lake level oscillations at Laguna Potrok Aike, Patagonian steppe. *Q Sci Rev* 71:131–146
- Nussbaumer S, Schaub Y, Huggel C, Nat AW (2014) Risk estimation for future glacier lake outburst floods based on local land-use changes. *Hazards Earth Syst Sci* 14:1611–1624. doi:10.5194/nhess-14-1611-2014
- Shan W, Guo Y, Wang F, Marui H, Strom A (2014a) Landslides in cold regions in the context of climate change. *Environmental science and engineering*, Springer. doi:10.1007/978-3-319-00867-7. ISBN 978-3-319-00866-0. ISBN 978-3-319-00867-7 (eBook)
- Shan W, Guo Y, Zhang C, Hu Z, Jiang H, Wang C (2014b) Climate-change impacts on embankments and slope stability in permafrost regions of Bei'an-Heihe highway. *Landslide Sci Safer Geoenviron* 1:155–160. doi:10.1007/978-3-319-04999-1_18
- Shi PJ, Sun S, Wang M (2014) Climate change regionalization in China (1961–2010). *Sci China Earth Sci* 44:2294–2306. doi:10.1007/s11430-014-4889-1
- Starnberger R, Drescher SR, Reitner JM, Rodnight H, Reimer PJ, Spötl C (2013) Late Pleistocene climate change and landscape dynamics in the Eastern Alps: the inner-alpine Unterangerberg record (Austria). *Quatern Sci Rev* 68:17–42
- Stoffel M, Tiranti D, Huggel C (2014) Climate change impacts on mass movements—case studies from the European Alps. *Sci Total Environ* 2014:1255–1266
- Sun GY, Yu SP, Wang HX (2007) Causes south borderline and subareas of permafrost in Da Hinggan Mountains and Xiao Hinggan Mountains. *Sci Geogr Sin* 27:68–74
- Wang B, Sheng Y, Liu JP (2001) Distribution and degradation of permafrost in Xiao Hinggan Mountains along the Heihe-Dalian highway. *J Glaciol Geocryol* 23:302–306
- Wang C, Shan W, Guo Y, Hu Z, Jiang H (2014a) Permafrost distribution study based on landsat ETM+ imagery of the northwest section of the Lesser Khingan Range. *Landslide Sci Safer Geoenviron* 3:529–534. doi:10.1007/978-3-319-04996-0_81
- Wang SH, Qi JL, Yin ZY, Zhang JM, Ma W (2014b) A simple rheological element based creep model for frozen soils. *Cold Reg Sci Technol* 106:47–54. doi:10.1016/j.coldregions.2014.06.007
- Wang C, Shan W, Guo Y, Hu Z, Jiang H (2015) Permafrost distribution research based on remote sensing technology in northwest section of Lesser Khingan Range in China. *Eng Geol Soc Territ* 1:285–290. doi:10.1007/978-3-319-09300-0_53
- Wei Z, Jin HJ, Zhang JM (2010) Prediction of permafrost changes in northeastern China under a changing climate. *Sci China Earth Sci* 41:74–84. doi:10.1007/s11430-010-4109-6
- Zhang Y, Wu QB, Liu JP (2001) Distribution characteristics of the permafrost in the section from Heihe to Bei'an in the Xiao Hinggan Mountains. *J Glaciol Geocryol* 23:312–317
- Zhou Y-W, Guo D-X (1982) Principal characteristics of permafrost in China. *J Glaciol Geocryol* 4:1–19
- Zhou YW, Wang YX, Gao XW, Yue HS (1996) Ground temperature, permafrost distribution and climate warming in northeastern China. *J Glaciol Geocryol* 18:139–147

TXT-tool 4.052-1.2 Landslide Risk Communication

Irasema Alcántara-Ayala

Abstract

Risk communication is a central key for Disaster Risk Reduction (DRR) and Disaster Risk Management (DRM). While a number of strategies of risk communication are focused on confronting and responding to disaster events, there is an increasing need to establish schemes or initiatives dealing with prevention and disaster risk reduction. In this paper, the significance of effective landslide risk communication is highlighted by looking at four specific elements. On one hand, it is argued that risk perception analysis should be a requirement for any strategy to communicate risk, as awareness, preparedness, knowledge, experience, trust, and other multi-factorial aspects of social, economic, cultural, political and institutional character influence decision-making and behavior at both individual and collective levels. On the other, and in addition to the particular targets specified by each program or initiative, understanding disaster risk should be a baseline for shaping any tactic or approach aiming at communicating risk. Likewise, regardless of the structure, the specific purposes and means selected for risk communication, a critical and intentional line of information exchange and knowledge sharing should be permanently offered to favor a social and institutional behavior on which avoidance of the creation of new risks is an imperative. Finally, the idea of incorporating an observer or advisor into the risk communication process to foresee potential obstacles or requirements associated with the appropriate understanding of disaster risk, and the need to avoid the construction of new risks, in addition to other particular objectives linked to the specific scheme per se, is also pointed out.

Keywords

Landslides · Risk communication · Effective · Risk perception
Risk understanding · Avoiding the construction of new risks

I. Alcántara-Ayala (✉)
Institute of Geography, National Autonomous
University of Mexico (UNAM), 04510 Coyoacán,
Mexico City, Mexico
e-mail: irasema@igg.unam.mx

I. Alcántara-Ayala
Circuito Exterior, Ciudad Universitaria, 04510
Coyoacán, Mexico City, Mexico

Contents

1	Introduction	732
2	Disaster Risk and Communication	732
2.1	Disaster Risk.....	732
2.2	Communication.....	733
3	Risk Communication	735
4	Effective Risk Communication	737
5	Landslide Risk Communication	739
6	Discussion	740
7	Conclusion	741
	References.....	742

1 Introduction

The story of the three wise monkeys makes reference to the proverbial principle “see no evil, hear no evil, speak no evil”; however, it can be also related to an expression of lack of interest in becoming involved in or committed to a communication process (Fig. 1).

Communication is defined by the Merriam-Webster dictionary as “the act or process of using words, sounds, signs, or behaviors to express or exchange information, or to express your ideas, thoughts, feelings, etc., to someone else”. The origin of this process in which expressing, exchanging or sharing ideas, experience, knowledge or/and concerns is involved, goes back perhaps to 5000 years ago, when the first records of human language were found. Communication, no doubt, has evolved through time and along with the progress of civilizations, and although it takes place on a daily basis, it becomes very complicated when the subject of communication is *Risk*.

Disaster Risk Reduction (DRR) and Disaster Risk Management (DRM) cannot be achieved when risk communication strategies lack adequate approaches to target the hazard or series of hazards involved, the specific needs of people exposed to understand such hazards and their impact as a function of the vulnerability dimensions of the specific communities, including risk perception. The effectiveness of such approaches is also related to the clarity and purposes of the messages that

are going to be transmitted, the means to do so, and to the definition of a time-frame to develop the communication process.

2 Disaster Risk and Communication

2.1 Disaster Risk

Since the impact of disasters, including those associated with landslides, are increasing considerably in both the developed and developing worlds, communicating risk has become a major endeavor. Therefore, a solid, scientifically based and widely accepted conceptual ground should be provided, aimed at the thoughtful understanding of disaster risk.

While there are a series of definitions concerning risk in the scientific literature, whose review and discussion is beyond the scope of this work, the definition provided by the United Nations Office for Disaster Risk Reduction (UNISDR 2016) has been adopted for this paper: “disaster risk is [considered to be] a function of hazard, exposure and vulnerability (Fig. 2). It is [normally] expressed as a probability of loss of life, injury or destroyed or damaged assets which could occur to a system, society or a community in a specific period of time”. Bearing that concept in mind, therefore, disaster can be regarded as “a serious disruption of the functioning of a community or a society due to hazardous events interacting with conditions of vulnerability and exposure, leading to widespread human, material, economic and environmental losses and impacts” (UNISDR 2016).

Vulnerability and exposure however, should not be seen as set circumstances or produced out of the blue; a more comprehensive explanation of why and how such conditions or contexts exist in the first place and are transformed would allow a causal analysis to understand the root or underlying causes of risk. We should not fail to recognize that social processes have led to the generation of risk drivers and unsafe conditions



Fig. 1 The three wise monkeys: “hear no evil, speak no evil, see no evil” (Tōshō-gū shrine, Nikkō, Japan)



Fig. 2 Exposure of dwellings and their vulnerable inhabitants to landsliding in the municipality of Teziutlán, Puebla, México

throughout time that exacerbate existing or generate new forms of risk. Population growth, environmental degradation, land-use changes, inadequate water management practices, and lack of planning, are some of the most common processes that determine exposure and vulnerability, risk and disaster; all these interactions are the baseline of the social construction of risk (Blaikie

et al. 1994; Wisner et al. 2004, 2011; Oliver-Smith et al. 2016) (Fig. 3).

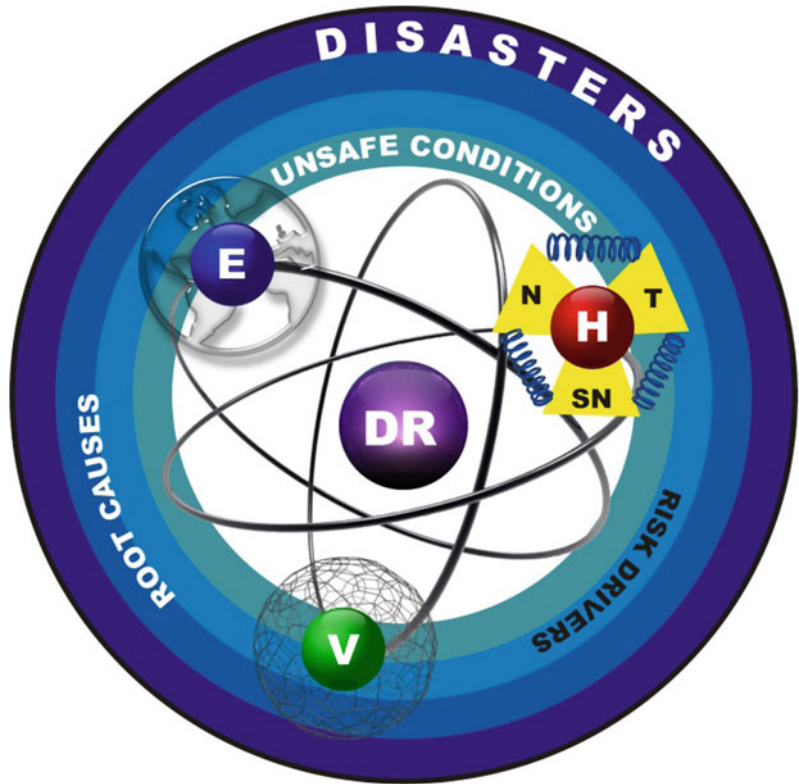
2.2 Communication

Etymologically, the word communication derives from old French *comunicacion*, from Latin *communicationem*, from the past participle stem of *communicare* “to share, divide out; communicate, impart, inform; join, unite, participate in”. Additionally, it also derives from *communis*, which means “to make common” (Online Etymology Dictionary). Although communication in terms of formal dialogue is credited with originating in ancient Greece with Aristotle, human communication began well before that era and can be easily understood as an intrinsic social phenomenon that has evolved through time. Since the first human groups were formed, interaction and communication were vital for learning from and transforming the environment in pursuit of survival and later on for achieving progress.

One of the most influential works in literature concerning information theory is that of Shannon (1948), on which the five basic elements of a communication system were identified: “(1) an information source which produces a message or sequence of messages to be communicated to the receiving terminal; (2) a transmitter which operates on the message in some way to produce a signal suitable for transmission over the channel;

Fig. 3 Major relationships and processes in the social construction of risk.

E indicates exposure; *V* indicates vulnerability; *H* indicates hazard and involves the categories *N* (natural), *T* (technological) and *SN* (socio-natural); *DR* stands for disaster risk.
 Source Oliver-Smith et al. (2016)



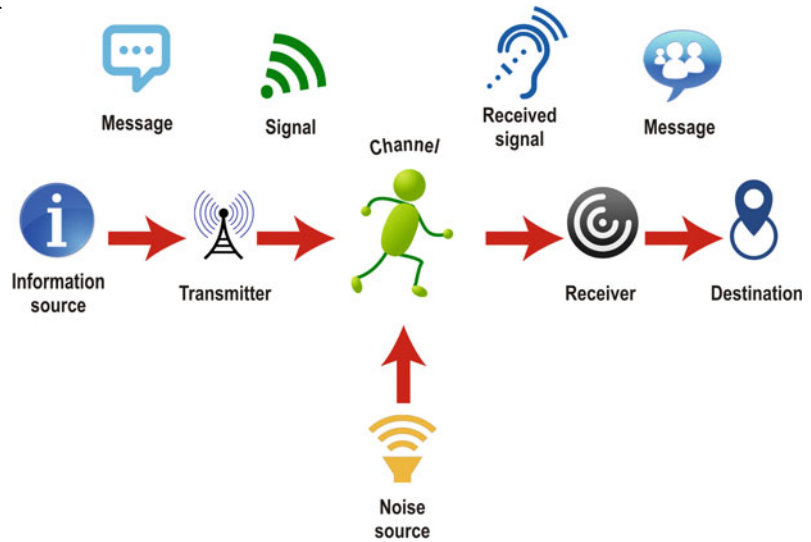
(3) the channel is merely the medium used to transmit the signal from transmitter to receiver; (4) the receiver ordinarily performs the inverse operation of that done by the transmitter, reconstructing the message from the signal; and (5) the destination is the person (or thing) for whom the message is intended” (see Fig. 4). For Shannon the elemental problem of communication was that of “reproducing at one point either exactly or approximately a message selected at another point” (Shannon 1948).

In a similar fashion and perhaps based on Shannon’s view, DeVito (1986) defined communication as the process or act of transmitting a message from a sender to a receiver, through a channel and with the interference of noise, while Anderson (1987) pointed out that the process would involve a time dimension, from which it is possible to infer that characteristics, causes, and consequences of communication are dynamic and not mere facts.

Communication should not involve exclusively a one-way message. Communicating is a process in which exchange of information, experiences, necessities, constraints and ideals takes place among groups. Communication therefore does not imply a single action or connection between two individuals or parties, as daily life depends on a series of exchanges, dialogues and permanent connectivity.

There are four main types of communication: non-verbal, verbal, writing, and listening; all of them are complementary to each other. Body language is used when non-verbal communication takes place; as such, it is limited but when combined with verbal communication it increases the transmissibility of messages. Writing is a good manner to reach several potential recipients, whereas listening is a key for communication, since effectiveness of verbal or oral communication relies on the interest and skills of the final destination.

Fig. 4 Schematic diagram of a general communication system. Adapted from Shannon (1948)



New technologies have increased considerably the availability of communication channels and, what is more, they have also decreased the timing involved for the transmission of messages as velocity increases—*Internet, Facebook, Twitter, WhatsApp* and a number of other applications are used on daily basis across the globe. It is important however, not to forget the barriers to communication that can be caused by the source, the transmitter, the functionality of the channel, the receiver and the understanding or comprehension of the final destination. Consequently, the message to be delivered should be clear to the transmitter, but also acquaintance or knowledge regarding the background of the final recipient would be helpful in building up an adequate structure for the message to be transmitted.

3 Risk Communication

Although communication can be regarded as a common process that takes place at all scales day by day, communicating risk is not an easy endeavour (Fig. 5). On one hand, risk is linked to uncertainty, and therefore to unpredictability or aleatoric uncertainty (Haimes 2004); it turns into something not desirable for people as outcomes can be either positive or negative (see *Landslides Risk Perception* in this volume), but also, on the

other hand, risk is embedded within the epistemic dimension of uncertainty by its association with availability of accurate data or state of knowledge about the specific hazards (Haimes 2004).

Risk communication, as defined by the National Research Council (1989) “is an interactive process of exchange of information and opinion among individuals, groups, and institutions. It involves multiple messages about the nature of risk and other messages, not strictly about risk, that express concerns, opinions, or reactions to risk messages or to legal and institutional arrangements for risk management”. Nonetheless, in real life, very often risk communication is focused on one way-single actions, on which people are informed about an imminent episode involving risk (i.e. volcanic eruption) and in addition requested (in the best of the cases) or instructed to evacuate their houses.

As inhabitants often lack knowledge regarding hazards, and evidently lack even more on disaster risk, as that is not provided to them on a regular basis and/or as a part of the educational curricula, the degree of disaster risk awareness and preparedness of the exposed communities is rather low. Additionally, the nature of scientific uncertainty about the dynamics of hazards is not well understood by non-experts, and therefore, the duty of achieving risk communication repeatedly remains incomplete. Not to mention



Fig. 5 “The risks that kill people and the risks that upset them are completely different” (Sandman 2012) (*Anxiety*, 1894, by Edvard Munch)

the issue of trust or social distrust, this is perhaps one of the most delicate issues, not only for disaster perception and communication, but for practice and hence disaster risk management.

As suggested by Höppner et al. (2010), actors, purposes, modes, tools and messages together have been considered as the pillars of risk communication. Government (local and central) and regulatory agencies, politicians, scientists and experts, industry, trade unions, Non-Governmental Organizations and groups, the exposed/concerned/affected community, the general public, and the mass media such as local and national television, radio and newspapers, are among the main actors for risk communication. Likewise, the major purposes and functions of communicating risk have previously been identified by analysing a series of applied reported strategies. These include raising awareness and preparedness, encouraging protective behaviour, providing the information to build up knowledge on hazards and risks, promoting the acceptance of risks and specific management

measures, informing on how to behave or respond during and after events, warning of and triggering action to impending and current events, reassuring the audience (to reduce anxiety or ‘manage’ outrage), improving relationships (such as building trust, cooperation, networks), enabling mutual dialogue and understanding, and involving actors in decision-making (Höppner et al. 2010).

In addition to those very valuable common objectives to communicate risk, achieving disaster risk reduction would require a major commitment to two essential insights. The first one is related to the priority for action number one of the recent adopted Sendai Framework for Disaster Risk Reduction (SFDRR): “Understanding disaster risk” (Fig. 6). Notwithstanding the contribution of the existing strategies of risk communication in different contexts at local, national, regional and global scales, there seems to be a gap between providing information of the likely specific impact of a hazard, and communicating how disaster risk is constructed. In the evolving perspectives of disaster risk research, there is still a tendency to focus on the hazard as the main controller of the impact of disasters. The profound understanding of disaster risk aspects of vulnerability and exposure is neglected, and in consequence root causes and risk drivers are not considered as key issues for communicating risk.

The second insight that is still missing is related to communicating the necessity of avoiding the construction of new risks. Very rarely, aspects such as lack of planning, inadequate water management, land-use changes, urbanization processes, deficient health systems, inequality and poverty, among others, are view as unsafe conditions and drivers of disaster risk. It is important therefore, not only to get messages across regarding how to cope or respond to disasters, but to avoid actions that generate exposure and the configuration of new risks (Fig. 6).

Different ways have been put forward to examine the contributions and potential developments of the processes and actors involved in effectively communicating risk (Árvai and Rivers 2014). Perhaps this resulted, among other issues,



Fig. 6 Common purposes and functions of risk communication. Adapted from Höppner et al. (2010)

from the type of concerns raised by Bostrom and Lofstedt (2003) regarding a perspective on which risk communication is perceived as “small, immature, incredibly interdisciplinary, and—in the eyes of some—still more art than science, relying as it often does in practice on good intuition rather than well-researched principles”. Because of the particular contexts in which disaster risk is embedded, and in addition to a series of intuitive heuristics, social, economic, cultural, political and institutional conditions should constitute the foundation of any risk communication strategy. All of them no doubt would offer

valuable insights in understanding how disaster risk is shaped, and therefore the task of disaster risk reduction could be more easily enhanced.

4 Effective Risk Communication

To generate positive outcomes, effectiveness should be regarded as an intrinsic characteristic of any risk communication process. Árvai and Rivers (2014), for instance, foresee an effective communication as that process in which the dimensions of *what*, *how*, and *why* are considered

as fundamental and are incorporated. “*What*” implies the information provided, while the “*how*” refers to the means through which information is transferred and shared, and “*why*” represents the pursued objective and the reason for risk communication engagement. Perhaps meaningful and successful strategies for communicating risk are those in which the first step concentrates on the “*why*”, and this is consciously, scientifically based and accurately defined. The “*how*” is very much related to resources, skills, capabilities, vision, sagacity, and timeframes, whereas the “*what*” is based on information, knowledge, accuracy and, at the same time, degree of uncertainty of that knowledge. All of them are inevitably embedded into a trust—no trust social dimension that is not easy to handle.

Along the line of the perspective offered by Árvai and Rivers (2014), by analysing the difficulties encountered in the initiatives and practices undertaken in the last three decades, Kaspersen (2014) published his interesting, debatable and challenging “*Four questions for risk communication*”, and suggested four principles for improving and conducting risk communication that can contribute to the assessment and management of risk:

Principle 1. Risk communication programs need to be more sustained over time, better funded, and more ambitious in the goals adopted and the outcomes sought;

Principle 2. The scope of risk communication should be broadened to internalize conflicting issues of concern and decision-makers should deepen their analysis to address the embedding of risk issues in value and lifestyle structures;

Principle 3. If uncertainties are large and deeply embedded, more communication will be needed, particularly that regarding those uncertainties that really matter in risk terms and not the full catalogue of uncertainties that scientists uncover. Attention will also be needed to identify which uncertainties can and cannot be reduced over time and within what time frames;

Principle 4. In situations where high social distrust prevails, and this is increasingly common, a thorough revamping of the goals, structure, and conduct of risk communication will be needed.

These principles offer a valuable synthesis of lessons learnt and yet to be learnt that are

important to consider when delineating and implementing a strategy of disaster risk communication.

Similarly, for Fischhoff (2013), successful science communication should accomplish four tasks: (1) identifying the science most relevant to the decisions that people face; (2) determining what people already know; (3) designing communications to fill the significant gaps between what people know and need to know; and (4) evaluating the competence of those communications (“*Repeat as necessary*”).

As early as in the decades of the forties, Shannon (1948) had already envisaged a problem related to the reliability of the communication system. Therefore, he also proposed the inclusion of an observer—or auxiliary device—who could see what was sent and received. This enabled the observer to identify the errors in the recovered or received message and to send out data to the final destination throughout a correction channel, so that errors could be amended. The application of that notion in a revised manner—in which the participation of varied and not just a single channel could be acknowledged—to disaster risk communication would be advisable. The fact is that even though outcomes of specific strategies of risk communication are often examined from a research perspective, this is usually undertaken after the full scheme is applied. Integrating an observer or advisor as part of the risk communication process, who can interact on continuous basis from outside to foresee potential barriers or to identify lack of suitable configurations to accomplish specific targets, bearing in mind the necessity of an appropriate understanding of disaster risk and avoiding the construction of new risks, could provide a way to improve the efficiency of the process of disaster risk communication (Fig. 7).

All these ideas are provided as a possibilities to improve the process of disaster risk communication. Nonetheless, strategies should be locally or site specific, and in addition to being attractive, they also need to be realistic. They would hopefully aid in conceiving and enhancing changes useful not only for response and coping actions, but directed towards sharing



Fig. 7 Schematic diagram of a correction communication system. Adapted from Shannon (1948)

responsibilities and commitments to understanding the social construction of risk and to lessening the generation of unsafe conditions and practices leading to the generation of new risks.

5 Landslide Risk Communication

Understanding landslides requires the comprehension of natural phenomena, together with the awareness of some conditions of the landscape influenced by human activities that affect its equilibrium. Landslides take place when hillslopes are unstable. Such instability can be entirely controlled by natural causes, including geology, geomorphology, and physical processes, but also result from the combination of natural and human-induced factors. In both cases, they can be regarded as hazards when societies can be potentially affected by them: the former are known as natural hazards, while the latter as socio-natural hazards (Alcántara-Ayala 2016).

Of great significance for slope instability are different practices leading to modifications of the hillsides: infrastructure construction, terracing, slope excavations, mining, vibrations, land-use

changes, and deforestation. Many of them are related to processes of urbanization and are among the most important factors influencing the stability of the slopes (Alcántara-Ayala et al. 2015).

Additionally, in many parts of the world, the establishment of human settlements in areas highly susceptible to mass movements increase the exposure of people to landsliding. This is becoming more frequent, as urbanization processes often lack adequate planning and territorial management. What is more, substandard living conditions of human groups also add a dimension of vulnerability, enhancing risk. Consequently, if landslide disasters are to be prevented and landslide disaster risk reduced, strategies to communicate risk have to take into account all these interrelationships. General targets would involve therefore landslide (hazard) awareness and preparedness, landslide (hazard) mitigation, reducing vulnerability and understanding landslide disaster risk (Fig. 8).

Increasing or preventing potential impacts of landslide hazards can be achieved by implementing structural and non-structural measures. The former involves the application of engineering techniques to improve the resistance of

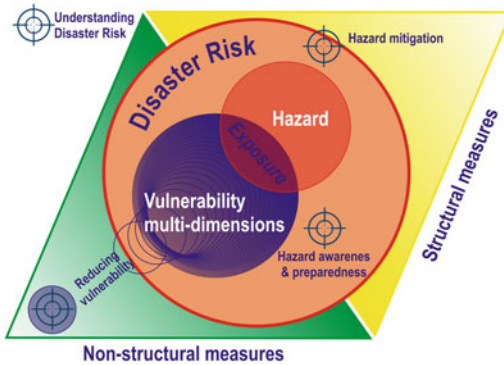


Fig. 8 General scheme of the major targets to be addressed by landslide risk communication strategies to reduce landslide disaster risk

structures or infrastructure systems, whereas the latter do not entail physical construction but knowledge, and adequate practice to minimize risks and impacts (UNISDR 2009) (see Fig. 8). Both are complementary to each other, however, in some cases where remedial works on unstable slopes can be afforded, the degree of confidence of people becomes so high that it is mistakenly believed that infrastructure can support any kind of external impact. Overconfidence is transformed into vulnerability as there is a wrong perception of risk avoidance. Moreover, structural measures are very expensive, not only for setting-up, but for maintenance, and perhaps only in countries such as Japan can enough resources be directed towards their implementation.

Non-structural measures, on the contrary, are less expensive, and of greater benefit and positive impact through time. Awareness and preparedness, education, knowledge, community participation and mapping, early warning systems, establishment of legal frameworks and policy making are indeed among the indispensable measures to be undertaken, especially at local scale.

As suggested by Hernández-Moreno and Alcántara-Ayala (in press), landslide communication strategies can best serve Disaster Risk Reduction and Management when incentives and engagement are focused on the understanding of the hazard, the multi-dimensions of vulnerability,

the social construction of landslide risk, the recognition of the need to undertake integrated approaches, and moving from a disaster response perspective to managing disaster risk.

Based on an extensive review of literature, Renn and Levine (1991) provided a list of specificities related to the intentions and objectives of risk communication. Some insights regarded landslides have been added to that list and are shown in Table 1.

6 Discussion

Even after some decades aiming at disaster prevention, it is still an aspiration to think of a societal level of awareness, preparedness and knowledge at which disaster risk is properly understood. If best practices for landslide disaster risk communication are sought, it is rather difficult to stand on a platform on which disasters are seen as natural events or acts of God. Landslides, in contrast to other hazards, such as seismic and volcanic activity, can be regarded not only as natural, but also as socio-natural. The task therefore becomes more complex. On the other side of the coin, the comprehension of vulnerability and exposure requires a deep analysis of root or underlying causes, unsafe conditions and drivers of risk (see Fig. 3), elements often neglected by risk communication strategies. As indicated by Renn and Levine (1991), there are series of key functions and goals that have been considered over time to communicate risk (Table 1). Nonetheless, focussing on disaster response has less complicated results, and that is why there is still an urgent need to work towards understanding risk and avoiding the configuration of new ones. This endeavour would involve enormous challenges, as critical issues, including trust, governance, political and economic interests, and legal frameworks, among other, are embedded in the sphere of Disaster Risk Reduction, and there is a need to draw the line among sustainability, territorial management and the generation of greater exposure.

Table 1 Functions and objectives of risk communication and landslide risk communication

Goals	Function (Renn and Levine 1991)	Landslide risk communication
Enlightenment function	Improving risk understanding among target groups	<ul style="list-style-type: none"> • Enabling the availability of means for all stakeholders to acquire knowledge of landslide hazards, vulnerability and exposure
Right-to-know-function	Disclosure of information about hazards to potential victims	<ul style="list-style-type: none"> • Making available the necessary elements to fully understand the social construction of landslide disaster risk • Providing maps on which zones at risk of landsliding are identified
Attitude change function	To legitimate risk-related decisions, to improve the acceptance of a specific risk source, or to challenge such decisions and reject specific risk sources	<ul style="list-style-type: none"> • Conveying the appropriate information to be aware of the root causes and drivers of exposure and risk, so that such conditions are not reproduced, but attended and/or reduced • Avoiding the transference of landslide disaster risk to other people
Legitimation function	Explaining and justify risk management routines and to enhance the trust in the competence and fairness of the management process	<ul style="list-style-type: none"> • Generating dynamic modes of community involvement in landslide disaster risk management • Improving the social dimension of trust
Risk reduction function	Enhancing public protection through information about individual risk reduction measures	<ul style="list-style-type: none"> • Building up integrated and inclusive strategies for coordinated actions aiming at reducing the vulnerability, particularly of social and institutional types
Behavioral change function	Encouraging protective behavior or supportive actions toward the communicating agency	<ul style="list-style-type: none"> • Supporting the establishment of programmes to reduce unsafe conditions • Promoting exposure lessening and the avoiding the creation of new risks
Emergency preparedness function	Providing guidelines for emergencies or behavioral advice during emergencies	<ul style="list-style-type: none"> • Elaborating guidelines of community co-responsibility and practice to confront disaster episodes
Public involvement function	Educating decision makers about public concerns and perceptions	<ul style="list-style-type: none"> • Undertaking analysis of public perception of risk as a baseline for educational strategies and initiatives, decision-making and practice
Participation function	Assisting in reconciling conflicts about risk-related controversies	<ul style="list-style-type: none"> • Promoting participatory processes for disaster risk reduction regardless of political position, religion or any other affiliations

Adapted from Renn and Levine (1991)

7 Conclusion

Improving risk communication will be a permanent challenge, in which scientist are in the position to bridge the gap between science, society, decision-making and practice. It is not only a matter of disseminating or exchanging

information and experience regarding the impact of hazards on vulnerable communities exposed to risk. It is a matter of comprehending why and how disaster risk is shaped and how human actions and their perceptions are strongly linked to the social construction of risks. We need to reach an state in which, aided by solid risk communication processes, human beings can

thoroughly reflect on the urgency of avoiding the construction of new risks.

Acknowledgements Special thanks are due to CONA-CyT for the financial support kindly provided through the research project 156242.

References

- Alcántara-Ayala I, Altan O, Baker D, Briceño S, Cutter S, Gupta H, Holloway A, Ismail-Zadeh A, Jiménez Díaz V, Johnston D, McBean G, Ogawa Y, Paton D, Porio E, Silbereisen R, Takeuchi K, Valsecchi G, Vogel C, Wu G and Zhai P (2015) Disaster Risks Research and Assessment to Promote Risk Reduction and Management. In: Ismail-Zadeh A, and Cutter S (eds) ICSU-ISSC Ad Hoc Group on Disaster Risk Assessment. ICSU, Paris, March 12, 2015. Available at: http://www.icsu.org/science-for-policy/disaster-risk/documents/DRRsynthesisPaper_2015.pdf
- Alcántara-Ayala I (2016) On the multi-dimensions of integrated research on landslide disaster risk. In: Aversa S, Cascini L, Picarelli L, and Scavia C (eds) Landslides and engineered slopes. Experience, theory and practice, CRC Press/Balkema, Taylor & Francis Group, The Netherlands
- Anderson JA (1987) Communication research: issues and methods. McGraw-Hill Book Company, New York
- Árvai J, Rivers L III (2014) Effective risk communication. Earthscan, London
- Blaikie P, Cannon T, Davis I, Wisner B (1994) At risk: natural hazards, people's vulnerability and disasters. Routledge, New York
- Bostrom A, Lofstedt RE (2003) Communicating risk: wireless and hardwired. *Risk Anal* 23(2):241–248
- DeVito JA (1986) The communication handbook: a dictionary. Harper & Row, New York
- Fischhoff B (2013) The sciences of science communication. *Proc Natl Acad Sci* 110(Supplement 3):14033
- Haines Y (2004) Risk modeling, assessment, and management, 2nd revised edn. Wiley, Hoboken
- Hernández-Moreno G, Alcántara-Ayala I (online) Landslide risk perception in Mexico: a research gate into public awareness and knowledge. Landslides. doi:10.1007/s10346-016-0683-9 (in press)
- Höppner C, Buchecker M, Bründl M (2010) Risk communication and natural hazards. CapHaz-Net WP5 report. WSL, Birmensdorf. Available via: <http://caphaz-net.org/outcomes-results>. Accessed 03.06.16
- Kasperson RE (2014) Four questions for risk communication. *J Risk Res* 17(10):1233–1239
- National Research Council (1989) Improving risk communication. Committee on Risk Perception and Communication, Commission on Physical Sciences, Mathematics, and Resources, Commission on Behavioral and Social Sciences and Education. National Research Council, National Academy of Sciences, USA
- Oliver-Smith A, Alcántara-Ayala I, Burton I, Lavell A (2016) Forensic investigations of disasters (FORIN): a conceptual framework and guide to research. (IRDR FORIN Publication No. 2). Integrated research on disaster risk, ICSU, Beijing, 56 pp
- Renn O, Levine D (1991) Credibility and trust in risk communication. In: Kasperson RE, Stallen PJ (eds) Communicating risks to the public. Kluwer, Dordrecht
- Sandman PM (2012) Responding to community outrage: strategies for effective risk communication. American Industrial Hygiene Association, Fairfax. <http://psandman.com/media/RespondingtoCommunityOutrage.pdf>
- Shannon CE (1948) A mathematical theory of communication. *Bell Syst Tech J* 27:623–656
- UNISDR (2009) Terminology on disaster risk reduction. http://www.unisdr.org/files/7817_UNISDRTerminologyEnglish.pdf
- UNISDR (2016) Working text on terminology. The second session of the open-ended inter-governmental expert working group on indicators and terminology relating to disaster risk reduction, Geneva. 10–11 Feb
- Wisner B, Blaikie P, Cannon T, Davis I (2004) At risk: natural hazards, people's vulnerability and disasters, 2nd edn. Routledge, New York
- Wisner B, Gaillard JC, Kelman I (2011) Routledge handbook of hazards and disaster risk reduction. Routledge, New York

TXT-tool 4.504-1.1

How to Make a Database of Landslides in Tegucigalpa, Honduras

Lidia Torres Bernhard, Nelson Sevilla, Kiyoharu Hirota, Hiromitsu Yamagishi and Tsukamoto Satoru

Abstract

This article aims first to highlight the importance of integrating new divulgation systems for the application of analytical tools in evaluating landslides, also it aims to inform the reader interested; the basic process for creating a map of susceptibility to landslides through photo interpretation in conjunction with basic elements such as geological field surveys and use of geographic information systems GIS. This tool is the result of the Project: Assistance for Strengthening and Building of Professional Techniques for the Control and Mitigation of Landslide Capacity in Tegucigalpa-Honduras Metropolitan Area; which it was conducted with the support of the Japan International Cooperation Agency (JICA) to strengthen Honduras Researchers and to strengthen action framework between academia and decision makers at the local level.

Keywords

Landslides · Aerial photographs · Photointerpretation
Geographic information system (GIS) · Susceptibility maps
Database · Layers · Analytical hierarchy process (AHP)

L.T. Bernhard (✉) · N. Sevilla
Honduras Earth Science Institute, National
Autonomous University of Honduras, Boulevard
Suyapa E-1, Tegucigalpa, Honduras
e-mail: torres.lidia@unah.edu.hn

N. Sevilla
e-mail: nelson.sevilla@unah.edu.hn

K. Hirota
International Consortium on Landslides, Private
home: 1-28, Minami-machi 2choume, Matsuyama,
Ehime 790-0856, Japan
e-mail: sbhirota@gmail.com

H. Yamagishi
Shin Engineering Consultant Co.Ltd., 2-8-30,
Sakaedori, Shiroishi-ku, Sapporo 003-0021, Japan
e-mail: hiromitsuyamagishi88@gmail.com

T. Satoru
Kokusai Kogyo Co., Ltd., Tokyo, Japan
e-mail: satoru_tsukamoto@jcom.home.ne.jp

Contents

1 Introduction	744
2 The History of Landslides in Honduras and Specifically in the Metropolitan Area of Tegucigalpa	745
3 Landslide Susceptibility Map Development in Tegucigalpa (Basics Processes)	747
3.1 Methodology.....	747
4 Technical Development of the Database for Landslide in Tegucigalpa	753
4.1 Technical Requirements.....	753
4.2 New Web System: Designing, Creating and Feeding the Database.....	754
4.3 How and Who Can Access the Database	755
5 A Tool of Social Contribution (Point of View of the Creators)	756
6 Discussion	757
7 Conclusion	757
Appendix: Acronyms of Related Subjects	758
References.....	758

1 Introduction

Honduras, a country located in the central part of Central America, with coastlines open to both the Atlantic Ocean and the Pacific; it is geographically located in a region that increases the level of risk to be affected by natural hazards, as it is positioned in the forced route of tropical storms and hurricanes; it has also been listed as one of the 20 countries with the highest risk of damage from flooding and landslides caused by hydro-meteorological threat, and also the degree of exposure and vulnerability of communities living in risk areas. In Honduras are also seen, different factors that increase the level of risk such as indiscriminate development, land and agro-ecological condition of the country, as well as mismanagement and destruction of watersheds, uncontrolled population growth and migration from the rural areas to the city, etc.

Hurricane Mitch in 1998, let see not only the high level of country's exposure to natural hazards stemming from its geographical position, but also its high degree of vulnerability, resulting from the interaction of natural hazards with inadequate systems of the environmental/land

resources and a number of human factors causing alarming risk conditions.

The Republic of Honduras has a population of 8.6 million people of which 54% live in the major cities; it has an area of 112,000 km². In Honduras the population is unevenly distributed; migration from the countryside to major cities increases poverty in them, forcing residents to settle in high risk areas in precarious conditions. During the second half of the twentieth century, there was an accelerated process of urbanization in Honduras. The population living in cities increased from 30.3% of the total in 1950 to 46% in 2001. Between 1988 and 2001, the urban population grew at an average annual rate of 3.4%, higher than the population growth of the country a whole, which was 2.6%. According to the National Institute of Statistics (INE) estimates this trend has continued in the period 2001–2008, with a growth rate of urban population of 3.6% compared to 2.4% of the total population, increasing urban population to 50% of the total (INE 2007).

Tegucigalpa is a city with an area of 150 km² approximately; and hosts about 14% of the country total population, and according to the Municipal Emergency Committee of the Central District of Tegucigalpa (CODEM-DC) in 2010, about 150 neighbourhoods has some problem with landslides.

All the above, reveals the urgent need to study landslide risk in Tegucigalpa, promote joint actions among relevant institutions such as National Autonomous University (UNAH), local government offices, the municipal emergency committee (CODEM) supported by the Honduran Permanent Commission of Contingencies (COPECO); these institutions should be kept permanently researching for vulnerability and risk reduction, control and mitigation of landslides. That is why the focus of the Cooperation Agency of Japan (JICA) suggested and urged capacity building for the National Autonomous University of Honduras (UNAH) through the Honduran Institute of Earth Sciences to jointly with the Local Government in the developing of landslide

evaluation projects to promote the control and mitigation from landslide. That’s why a pilot intervention had development in two critical sites in the capital city and have resulted in Maps of Landslide Susceptibility. This landslide teaching tool is, seeking to create an interactive and dynamic way to socialize results through a database or web tool based on our experiences from landslide interpretation by aerial photographs to landslide mapping using GIS.

2 The History of Landslides in Honduras and Specifically in the Metropolitan Area of Tegucigalpa

Throughout history, Honduras has been hit by severe hurricanes and tropical storms, which have caused huge economic losses but even more importantly loss of life. Among the hurricanes that more damage caused can mention Hurricane Alma in 1966, Hurricane Marco occurred in 1969, Edith in September 1971, Hurricane Fifi in 1974, Mitch in October 1998, Katrina in 1999, most recently we have Michelle and Beta in 2001, Hurricane Wilma in 2005 and Felix in 2007. The most devastating of all were the Fifi and Mitch, as we can see in the Table 1.

Hurricane Mitch, a Category 5, considered one of the most powerful and deadly of the modern era Tropical Cyclones. According to the evaluation report of damages and losses presented by the United Nations Economic

Commission for Latin America and the Caribbean, Hurricane Mitch affected in practice to the entire Honduran population, leaving 7007 dead, 11,998 wounded and 8052 missing. In addition to these irreparable losses, a huge number of families—about 10% of the country lost their homes or had to abandon them, to take refuge with relatives or friends or in shelters that had to be improvised as immediate emergency measures taken by government. It is estimated that more than 600,000 people—and may even have exceeded 700,000 according to other estimates—had to move or shelter (CEPAL 1999).

JICA have undertaken five projects involving Japanese scientific methods and technologies to reduce hazards on slope disaster in this region, which are 1) Metropolitan landslide prevention plan in the Republic of Honduras, 2) Project on landslide prevention in the Tegucigalpa Metropolitanarea, 3) Project on capacity development for disaster risk management in Central America “BOSAI”, 4) Hazard geology focusing on the landslides in Tegucigalpa (Yamagishi 2014), and 5) Technical support for landslide studies by Senior Volunteer (Hirota 2015). These projects are thematically consistent, and have been effectual in transferring knowledge of technological models in the areas (Sato et al. 2015).

Landslide Disasters by Hurricane Mitch in 1998

The intense rainfall caused by Hurricane Mitch from 27 to 31 October 1998 in parts of Honduras

Table 1 The Hurricane that damaged the most in the past 35 years in Honduras

Hurricanes cause more damage in the last 35 years in the Honduran Territory		
Year	Hurricane	Caused impact
1974	Fifi	Approximately 8000 deaths, 80% of the road network destroyed, half of crops devastated, total damages around 900 million USD in 1974 (about 3700 million of actual USD)
1998	Mitch	Around 5657 dead, 8058 missing, 12,272 injured, 285,000 houses affected or destroyed, 60% of road infrastructure seriously damaged with a total of 531 tracks communication unutilized, 189 bridges destroyed, 81 uncommunicated cities, 25 villages devastated, 70% of crops destroyed or severely affected, damage around of 3800 million USD
2001	Michelle	6 deaths, 14 missing, 27,719 victims
2001	Beta	60,483 victims, 237 homes destroyed and 954 damaged, 11,000 people without home, 41 bridges destroyed or damaged, 30 unutilized roads around 3000 has of arable land destroyed

Translated from the report: En Tierra Segura. Desastres Naturales y Tenencia de la Tierra-Honduras: La Amenaza Hidrometeorologica en Honduras. (FAO)

came to exceed 900 mm and caused more than 500,000 landslides throughout the country. Based on calculations of the Corps of Engineers US Army, it is estimated that landslides damaged 70% of the road network in Honduras. It is not known precisely the number of deaths caused by landslides because in many of the Honduran communities the number of people missing as a result of landslides were not recorded. A conservative estimate this number to 1000. More than 95% of landslides consisted debris flows. These thicknesses ranged from 1 to 15 m; path length of the flow was from several meters to 7.5 km (Harp et al. 2002). The highest concentration of debris flows occurred in the mountains near the town of Choluteca at the south part of the country, where a rainfall of 900 mm was recorded within three days. While there were few slides other than debris flows, landslides with several meters deep scars that occurred in the city of Tegucigalpa seriously affected people and property in this city. The collapse of rotation type of slide (Berrinche slide), followed with a volume of approximately six million cubic meters, completely destroyed the neighbourhood of Colonia Soto, near the downtown. The landslide caused the damming of the Río Choluteca (hereinafter Choluteca River), which resulted in the formation of a lake; brought about a serious health problem for the city, due to the discharge of untreated sewage in the Choluteca River.

The characteristics of the risks in Tegucigalpa can be summarized as follows:

- A high rate of pollution of rivers.
- Invasion of land over the banks of rivers.
- Insufficient solid waste collection system.
- Soil erosion, including reducing Natural riverbeds generating floods in the lower basin.
- The city of Tegucigalpa is surrounded by sedimentary overlaid by volcanic rocks, the latter of which are highly susceptible to fail in the presence of water.
- Lack of urban water channelling.
- Inadequate management of surface water and lack of sewerage system in some sectors. This

causes inadequate water management saturation on the soils (with materials likely to fail) loose.

- There are approximately 54 critical sectors, the risk conditions are exacerbated by steep terrain, or the road constructions in inadequate forms.

According to UNDP, (Orrego, 2013) there are some factors influencing the risk construction in Tegucigalpa, as shown in Fig. 1.

These factors have conditioned the occurrence of landslides; mainly in the rainy season where we can observe a large number of emergencies, damages and losses due to landslides.

Landslides give a serious impact on people and property if they occurred in densely populated areas. The largest Landslides caused by Hurricane Mitch was held in Tegucigalpa in 1998. It destroyed part of the downtown known as Colonia Soto and dammed up the Cholulteca River; this damming up resulted in a sewage lagoon upstream of the dam created (Fig. 2). This subsidence/complex flow of land had a volume of about 6 million m³. Due to the slow movement of the earth it was possible to evacuate residents who lived in the mass of the landslide however the rapid displacement of slide began and culminating in the damming of the river. The river was blocked at approximately



Fig. 1 Factors affecting the risk construction in Tegucigalpa, Honduras. *Source* UNDP-Honduras. Orrego (2013). Systematizaion UNDP-SDC Project



Fig. 2 Aerial view of the land called The Berrinche, followed by subsidence/rotational flow. The *arrow* indicates the direction of displacement of the whole landslide

body. *T* denotes the sliding to the river; the *L* indicates the lake dammed by the landslide (Harp et al. 2002)

12:30 am of October 31, about an hour after the maximum flood flow (*Q*) occurs in the Choluteca River.

evaluation to finally obtain the two susceptibility maps and also the database through the Project Cloud System. Figure 3 summarizes whole main activities for the landslide susceptibility mapping.

3 Landslide Susceptibility Map Development in Tegucigalpa (Basics Processes)

This section summarizes the most important points during the construction of landslide susceptibility maps. This requires the generation of an inventory maps of landslides in the study sites (Nueva Santa Rosa and El Edén, in Tegucigalpa). In this project landslide susceptibility mapping is analysed through the methodology known as Analytic Hierarchical Process (AHP) method (Yagi et al. 2009); managing to give a quantitative value to each slide block; this allows classified interpretation through the use of geographic information systems (GIS). Many different activities were taken place during this

3.1 Methodology

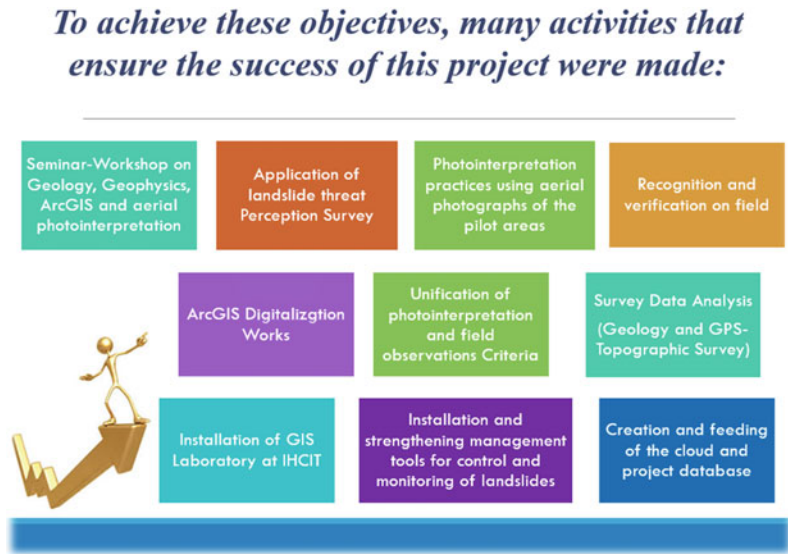
3.1.1 Preparative Phase

- a. JICA phase preparative:

As JICA project was in charge of initial preparations, the agenda and organization of the relevant national authorities. It continued with the organization itself by all the initial participating entities.
- b. Workshops and training:

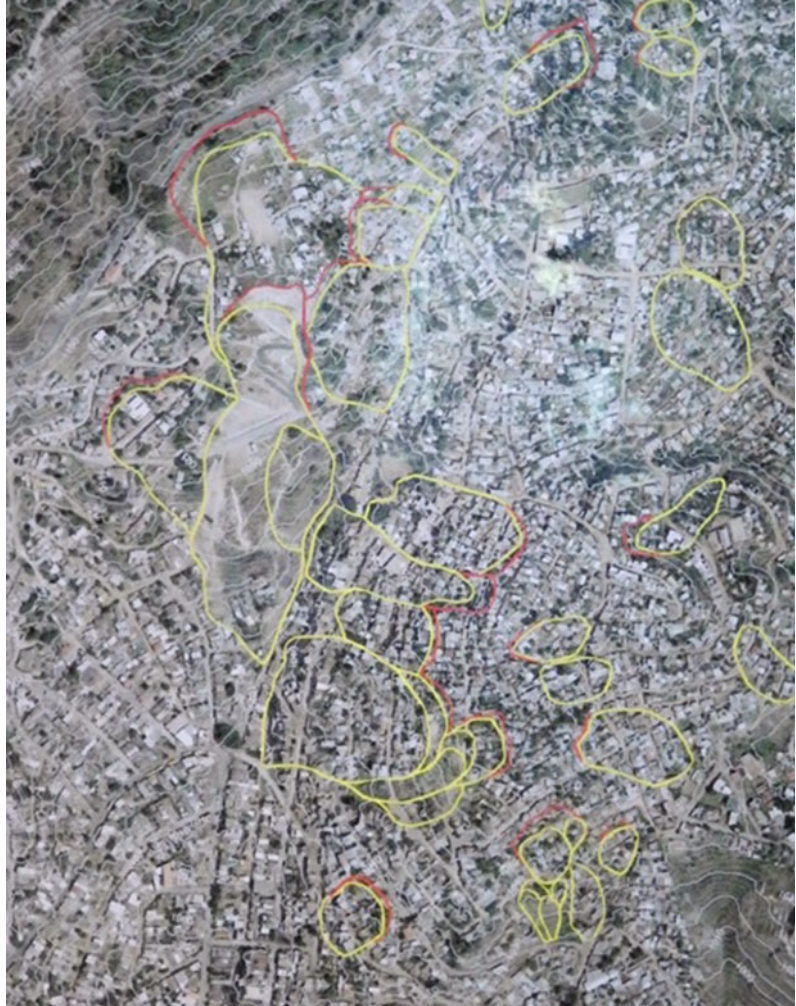
Several workshops of technical transfer and training focused on different landslides topics were organized, among which can be mentioned:

Fig. 3 Summary of main activities development during this project to achieve the objectives and also the landslides teaching tool



- Training of GIS
 - Basic study on geology
 - Landslides typology and its triggered factors
 - Photointerpretation
 - Process of project and technical procedure.
- c. Preparation of field visits:
Field reconnaissance workshops which were managed and handled by Japanese experts and honduran participants what they learned in the workshops and were given the initial training. The identification and mapping of landslides are the main mission of the visiting the sites.
- d. Initial phase identification and mapping of landslide bodies:
After receiving the workshops with the use of stereoscope and ortho-photos provided by JICA, the photointerpretation works began; initial drafts of landslide mapping of the two modelled sites to proceed to the verification field phase on the chosen sites as shown in Figs. 4 and 5.
- ### 3.1.2 Field Works Phase
- Different field researching has been done for the recognition of field data needed to creating a map of susceptibility (Fig. 6).
- a. Perception surveys:
Perception surveys were conducted to investigate the level of perceived risk against different threats such as floods, landslides, heavy rain etc.
 - b. Geological mapping:
The geological field surveys were guided by Japanese experts, who were helping for the identification of the geological conditions of landslides; offering practical training Honduran participants.
 - c. Public and Private Facilities Georeferencing:
Through GPS use there were located and identified all public and private institutional centers in the two sites as well as schools, police stations, churches etc.
 - d. Topographic Survey:
Field topographic surveys were organized using a differential GPS System in the two pilot sites.
 - e. Hydrological mapping:
In recognition of field survey there were recognized as hydrological characteristics recognition; identifying: permanent and intermittent rivers, streams, springs, wells, winter runoff, gutters etc. After, those data were transferred into a Map using ArcGIS
 - f. Morphological indicators of activity:

Fig. 4 Represents the early stages of photo interpretation with which they proceeded to field testing. Distribution of landslide bodies created by photo-interpretation. Site: Nueva Santa Rosa



Field surveys were also done for the recognition of morphological indicators of activity as well as cracks, joints, subsidence, faults and other evidence of displacement in both sites.

g. Identification of landslides:

Site visits for identification and verification of landslides were done in study sites. The main purpose of these visits was to check using mirror stereoscopes during the laboratory works and confirm the interpreted aerial photos. We make sure of the characteristics of landslides in the field and the presence of

scarps, identification and delimitation of bodies, location of fault lines and the other features of displacement.

3.1.3 Data Processing Work Phase

The data processing work phase continues from the field phase. In this project, the following steps were performed:

a. Photointerpretation correction:

In these phase, some corrections from the initial photointerpretation was needed repeatedly. This point has been solved by

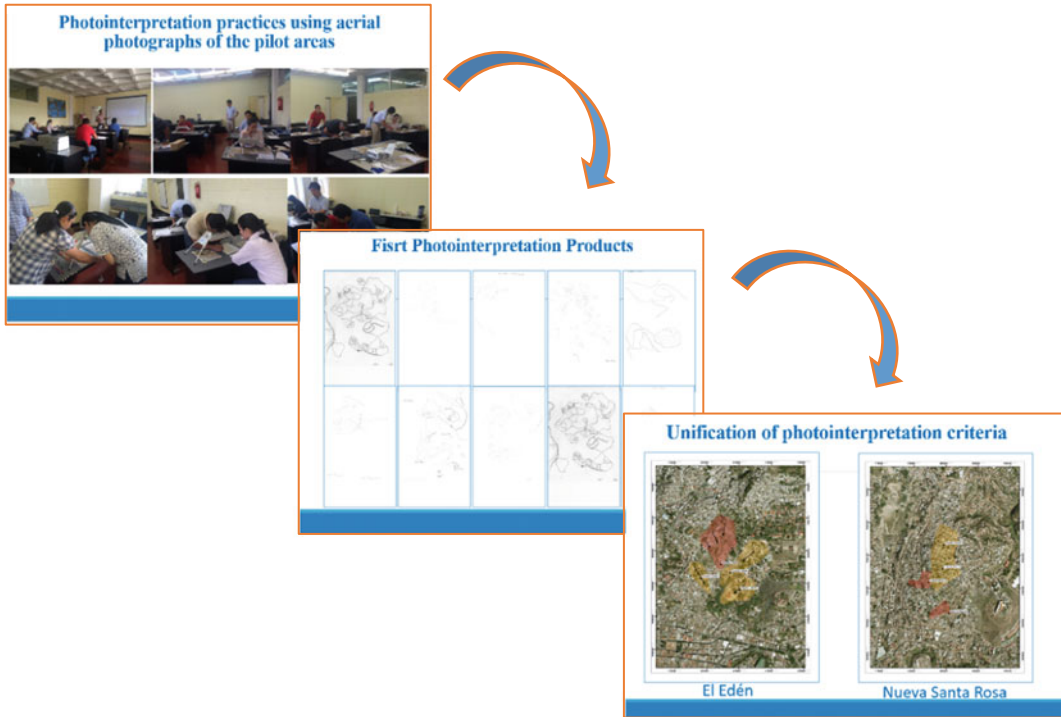


Fig. 5 Shows the basic sequential process for photo interpretation and field verification. Finally getting a map verified and improved through the field recognition

updating the recognition in the field of identification and delimitation of landslides bodies, scarps, cracks etc.

b. Digitization of field data:

Data collected in the field using GPS instruments, geological and geomorphological surveys, photographs, etc. were digitized using Geographical Information Systems GIS; (ArcGIS 10.0).

c. Mapping through Geographic Information Systems (GIS)

Different maps were created based on the digitization of field data. They were created using ArcGIS 10.0 software. The following layers or maps were created and integrated:

- Geological
- Hydrographic
- Topographical
- Location of Public and Private Facilities
- Morphological indicators
- Landslide scarps and Bodies.

d. Development of Susceptibility Map:

Once we have the distribution of landslide susceptibility assessment matrix, the susceptibility of each landslide body has been analysed. We use the AHP Method (Yagi et al. 2009) to evaluate the susceptibility of the landslides blocks in each site. The AHP method is one of the hazard evaluation different methods. AHP has been used worldwide for over four decades now for decision making processes in various disciplines; there are a number of factors which influence landslides depending on the study area such as rainfall, slope, aspect, geology, soil, land use etc. This method requires multi-criteria decision based on the knowledge and experiences of the experts. For this reason a group of participants involves in this project were divided into two separately groups; one for each site. This multi-disciplinary groups has to revise the methodology and to be recommended some adjustments to our current situation in the sites. This method has been developed and applied in several landslide project handled by JICA experts.

Fig. 6 Shows a photographic overview of the different field activities done for obtaining susceptibility maps



Finally, a score into 1–100 susceptibility has been given to each block and it depends on the value of each factor that were evaluated by the expert criteria.

Ranges were established as follow:

- 0–49 Low Susceptibility Level (green colour), Latent behaviour Landslide (with no perceived activity)
- 50–74 Medium Susceptibility Level (yellow colour), No very Active behaviour (with little perceived activity)
- 75–100 High Susceptibility Level (red colour), Active Behaviour (with remarkable perceive activity).

An example of evaluation results obtained are shown in Table 2. The different criteria evaluated as well as the scores for each of the sliding

blocks in the case of Nueva Santa Rosa are observed. The main indicators evaluated are: micro topography, slope profile, geological conditions, water conditions, land use. Each of this factors has its own series of criteria evaluation and the maximum average possible to assign for each criteria as shown in Table 2.

e. Landslide Inventory Sheets:

The Landslide Inventory sheets are the product of all the work data collection for each landslide block; with the information contents in those sheets the final maps were elaborated. The sheets summarized all the characteristics data for each landslide body, as shown in Table 3

- The number of body and its location, given for the experts and its location.

Table 2 shows the results obtained for the criteria and evaluation of the landslide blocks susceptibility identified in Nueva Santa Rosa (Fig. 7); using the method AHP (Data published in Spanish)

Evaluación de Susceptibilidad de los Cuerpos de Deslizamientos de Nueva Santa Rosa																										
Indicador	Criterio de Evaluación	Puntaje Asignado	Puntaje Obtenido																							
			1	2	3	4	5	6	7	8	9	10	11	12	13	14	15	16	17	18	19	20	21	22	23	
Microtopografía	Inclinación (Postes, arboles, muros)	20				20			20									20	20							
	Gradas de Fragmentación	15				15														15	15	15				
	Grietas	10	10									10	10		10	10						10				
	Fisuras	5																								
	No	0			0			0		0	0							0								
Perfil de la Pendiente	Falla De pendiente	20																20						15	15	
	Punto de quiebre	15							15										15	15	15	15				
	Pendiente Convexa	7						7																		
	Pendiente con inclinación lineal	3	3	3		3				3	3	3	3	3	3	3	3									
	Pendiente concava	0			0		0																			
Condiciones Geológicas	Coluvial (detritos del cuerpo deslizamiento)	20	20			20												20	20		20	20				
	Sedimentos Terciarios	15		15	15	15		15	15	15	15	15	15	15	15	15	15			15			15	15	15	
	Roca Sólida	0																								
Condición de Agua	Manantial en el pie	20																								
	Filtración de agua en la parte del pie	15																								
	Filtración o manantial o Presencia de aguas servidas en el cuerpo deslizante	12																12	12							
	Escorrentía natural o de invierno	10	10	10	10	10	0	0	10	0	0	10	10	10	10	10	10			10	10	10	10	10	10	
Uso del Suelo	Urbanización densa	20		20	20							20	20	20	20	20	20						20			
	Viviendas dispersas	10	10			10				10	10	10						10	10	10	10			10	10	
	Vegetación o bosque	5					5	5															5			
Puntaje Total =		100	53	48	45	58	40	27	70	28	28	58	58	48	58	58	48	82	77	65	70	65	55	50	50	
¿Existen Obras de Mitigación? =			No	No	No	No	Si	Si	No	No	No	No	No	Si	No	No	No	No	No	No	No	No	No	No	No	
¿Son Adecuadas las Obras de Mitigación? =			No	No	No	No	Si	Si	No	No	No	No	No	No	No	No	No	No	No	No	No	No	No	No	No	
Susceptibilidad al Deslizamiento =			Med	Bajo	Bajo	Med	Bajo	Bajo	Med	Bajo	Bajo	Med	Bajo	Med	Bajo	Med	Bajo	Med	Bajo	Alto	Alto	Med	Med	Med	Med	
Susceptibilidad al Deslizamiento =			Medio	Bajo	Bajo	Medio	Bajo	Bajo	Medio	Bajo	Bajo	Medio	Bajo	Medio	Bajo	Medio	Bajo	Medio	Bajo	Alto	Alto	Medio	Medio	Medio	Medio	
Criterio de Susceptibilidad			Bajo = 0 - 49 Puntos Medio = 50 - 74 Puntos Alto = 75 - 100 Puntos																							

- Landslide body dimensions (Maximum and minimum elevation, coordinates, length, width, depth, surface, structures etc.).
- Type of landslide.
- Susceptibility level.
- Topographic characteristics.
- Geology and hydrogeology.
- Social conditions.
- Disaster history registration.
- Counter measures (in case of existing).
- Monitoring systems (in case).
- Other relevant information.

f. Susceptibility Map:

The susceptibility map is the final product by all the above activities. Field work, laboratory, data processing work and multi-criteria analysis are summarized in a single product. Finally this is the product that can be use by the decision makers to prioritize areas of intervention, monitoring work, evacuation, control and mitigation; as well as community education. Figures 7 and 8

Table 3 Landslide Inventory Sheets summarizing all the characteristics data for each landslide body

Inventario de Deslizamiento		Día: Investigador:	
Número de deslizamiento		Característica Topografica	Obras de Mitigacion
8			
Lugar			
CANTON: El Reparto			
Elevación Max:			
Elevación Min:		Geología y hidrogeología	Monitoreo
GPS coordinación:			
Tamaño			
Longitud: m			
Ancho: m			
Profundidad: m			
Superficie: m2			
Geología		Condición Social	Riesgo de deslizamiento
Tipo de movimiento de ladera		Registro de Desastre	Información de CODEL
<input type="checkbox"/> Deslizamiento <input type="checkbox"/> Derrumbe <input type="checkbox"/> Caída de rocas <input type="checkbox"/> Flujo de detritos <input type="checkbox"/> Flujo de lodos			
Susceptibilidad y Amenaza			

show the preliminary results of two examples of the pilot cases operated during this project.

colonies of the Central District of Honduras, formed by the cities of Tegucigalpa and Comayagüela.

4 Technical Development of the Database for Landslide in Tegucigalpa

This process is discussed among a group of specialists on the systems, data management, geographic information systems and networks; trying to find a friendly way to integrate, store and view reports, data, surveys and Landslide Characterization Maps for each of the two pilot sites: Nueva Santa Rosa and El Edén, both

4.1 Technical Requirements

Technical requirements can be summarized as follows:

- Server Open Source operating system, data-base manager MS SQL.
- Server Geographic Information Systems.
- Server/Application Image Viewer.

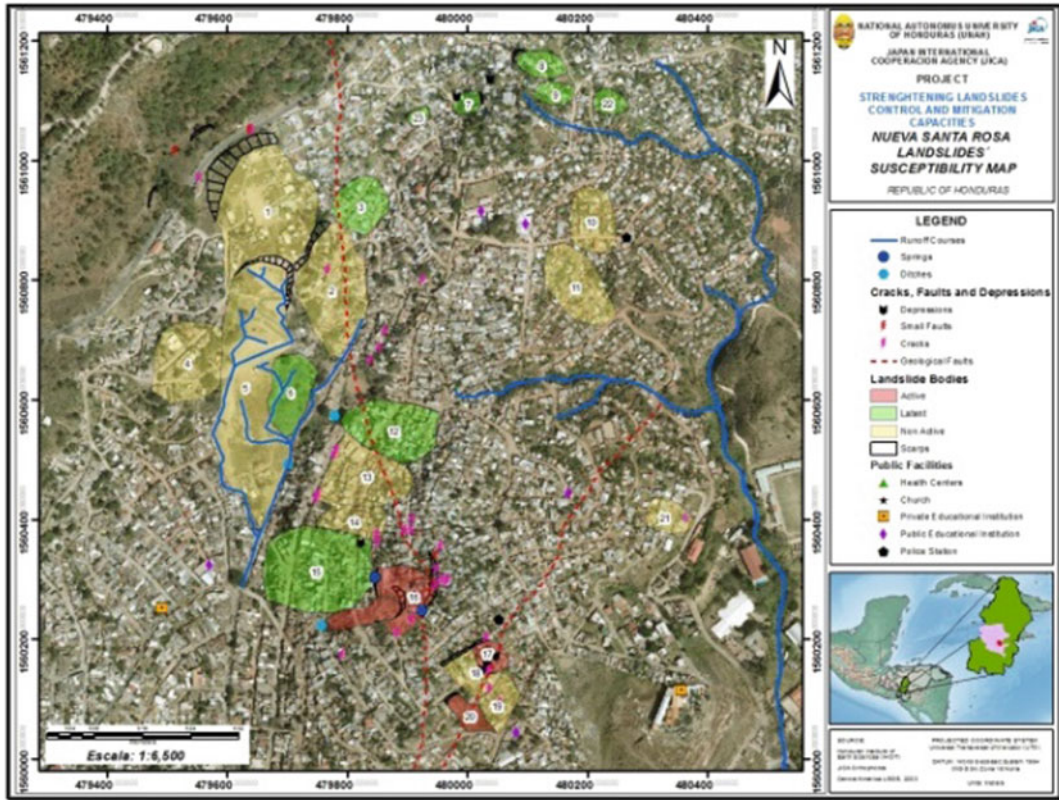


Fig. 7 Landslide susceptibility map of Nueva Santa Rosa (based on Table 2)

4.2 New Web System: Designing, Creating and Feeding the Database

The operation of this tool is based on client—server; where the administration of the layers and information is stored and processed on a network server with restricted access, but the publication is free access to specialized users, academics and the general public. Figure 9 shows the structure of the system, which is explained in detail by component as below:

- a. Data Server Layers: Will store finished products like layers, images, reports, documents and others.
- b. Data Server: Stores, manages data in tables for easy reference and access.
- c. GIS Server: Server where final landslides mapping is generated and converted into publishable images.
- d. Work station: By the equipment specialists and other researchers make their own calculations, studies, topographic maps, documents, etc.
- e. System Security: Access control system to provide products according to the permissions granted to each user.
- f. Viewer: Public Access to server images, layers, documents, etc. The user can access to all published information located on the server. But, through the viewer we do not allow that consultations access directly to the server for security reasons.

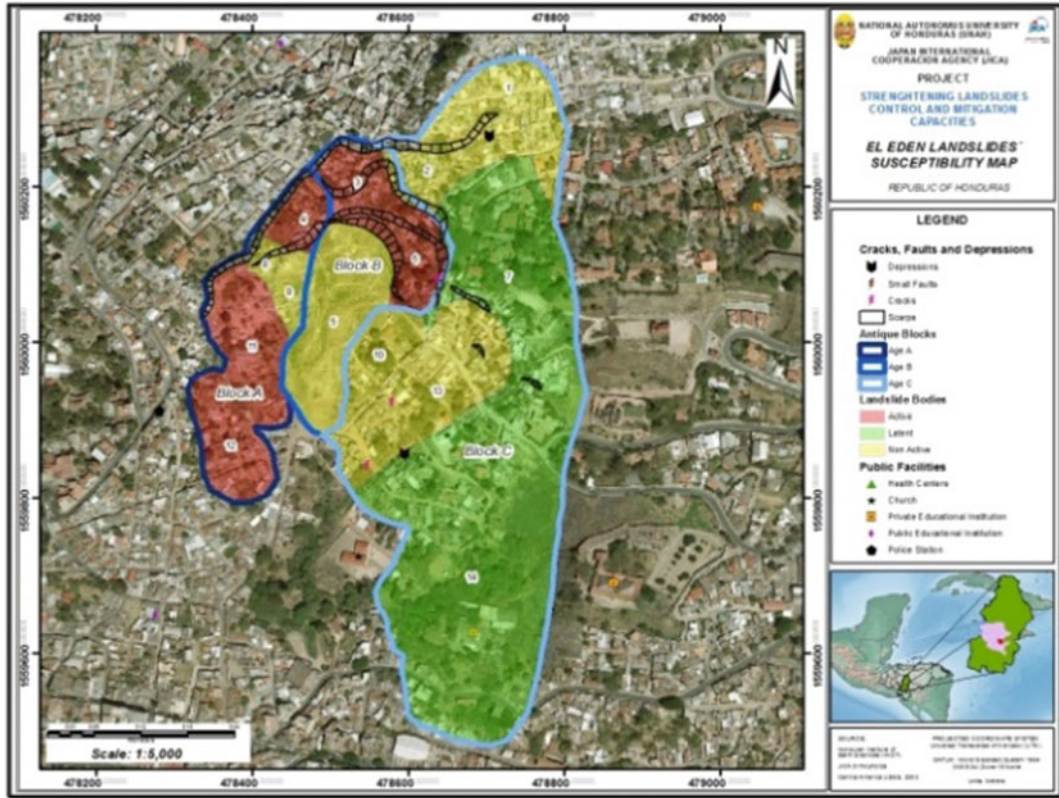


Fig. 8 Landslide susceptibility map of El Edén

- g. Network:
Network system that enables communication between process equipment, storage and display of information.
- h. General User:
Group of users who can access information in their computers, mobile devices such as iPad, smartphones, PDAs, etc.

- Level 1 users and the general public.
- Level 2 users with editing faculty.
- System administrators.

4.3 How and Who Can Access the Database

Management services, consultation and feeding the database are performed via web through the HTTPS protocol, this according to the roles assigned to each user created for different authors.

User roles are defined as follows:

On the basis that user’s level 1 could be students, teachers and the general public, and they can access only to layers in image format and to documents and reports in txt or pdf etc. Clarifying that at any time they need data for non-profit purposes, through formal request they will be able to offer the raw data. In the case of Level 2 users; these will have editor faculties, this means that they can upload information, which will be reviewed by specialists in charge; who grant permission to publish any new information that has been charged by these users and can also generate a change in layers, adding or removing relevant information. Managers are responsible for reviewing each of the information (surveys, data, images, etc.) received by level 2

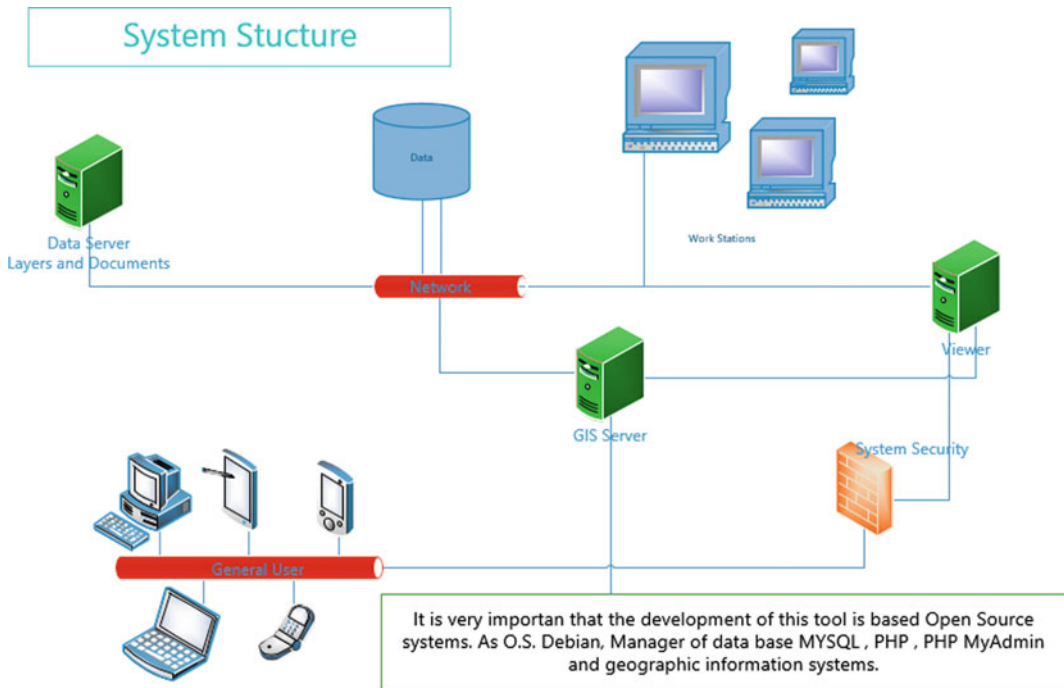


Fig. 9 Informatics system structure containing and displays the database through the Project Cloud

users, for analysis and subsequent publication or removal from the system.

5 A Tool of Social Contribution (Point of View of the Creators)

The Autonomous National University of Honduras, through the Honduran Institute of Earth Sciences who were in charge of design, development and implementation of this Teaching Tool, believes that this tool is an innovative proposal for communication with the general public regarding to the issue of landslides. This Teaching Tool is intended to publicize the results of the pilot project in the colonies El Edén and Nueva Santa Rosa with support and funding from the International Cooperation Agency of Japan (JICA) through Kokusai Kogyo Co. LTD, in collaboration with the Central District Municipality (AMDC) and the Municipal

Emergency Committee (CODEM); but at the same time, this teaching tool seeks to integrate other actions, to create a database that offers quality information and serve to document the efforts of both the Academy, the Local Government, NGOs, international cooperation and any other interested party. It is noteworthy that the development of this action marks an starting point for multi-sectoral integration; since it involved the participation and collaboration of other universities in the public sector such as the National Pedagogical University Francisco Morazán (UPNFM) and the Polytechnic University of Engineering (UPI) from the private sector; also managed to establish joint collaboration agreements with AMDC, CODEM, Secretary of Infrastructure and Public Services among others; therefore, we believe that the tool has a social value to improve knowledge of risk and disaster risk reduction and is offering a significant contribution to the Honduran society.

6 Discussion

It is important to note that the scope of this Teaching Tool would not have been possible without the prior existence of the JICA Project for Assistance Strengthening and Capacity Building of Professional Techniques for the Control and Mitigation of Landslide in Tegucigalpa Metropolitan Area; through which all capacity building activities in IHCIT/UNAH researchers and technicians of AMDC and CODEM-DC were strengthened; this results had not been achieved without good manual such as GMDTT (2014) and Carlos et al (2001), and without support of Japanese expert of JICA (Hirota, 2015; Sato et al., 2015; Yamagishi, 2014). It has been observed that the hybrid resulting from this multidisciplinary interaction between specialists, technical personnel and the support of the Cooperation Agency gave the best results, so it is to rescue this trinomial must continue to be empowered in order to ensure the sustainability of the results of this or any other execution in the near future.

The main objective of the aforementioned project, aims to build the landslide management capacity of UNAH researchers and Tegucigalpa City Engineers and to support UNAH and Tegucigalpa City to establish organizations to implement landslide countermeasures, thereby contributing to the country's landslide disaster mitigation. The project intends to establish:

- A research organization to survey and analyse small- and medium-scale landslides and the design of countermeasures at UNAH.
- An organization within the Tegucigalpa City government to plan landslide countermeasures, contract out small- and medium-scale countermeasures, and supervise, maintain, and manage such countermeasures by using the landslide inventory and risk maps.

However, it should be noted that the objectives were exceeded; proof of this is the generation of this Learning Tool. Among the main achievements include the following:

- Support for the creation of Geological Program in UNAH.
- Strengthening research capacity in terms of IHCIT of landslides.
- Strengthening Capacities of evaluation and monitoring of AMDC (UMGIR, CODEM and GER).
- Strengthening the Civil Engineering Department.
- Promotion of links With other universities (UPNFM), government agencies, NGOs (GOAL) and Private Enterprise (ACI, Hazama).
- Adhesion of IHCIT to the ICL.
- Development of the Second Central American and Caribbean Congress of Landslides (15 Lat. America, 1 German, 4 Japanese Experts and around 19 Honduran will participate as presenters).
- Signing of MOU Between IHCIT, DIC and AMDC.
- Signing of MOU Between IHCIT-JICA and others involved in the study of landslides in the country.
- Training of personnel IHCIT and AMDC in Japan.
- Proposal of a Landslides Interactive Teaching Tools (LITT) on Landslide Dynamics: ISDR-ICL.

Through this document and the database represented in the Project Cloud, there are available to the general public the results obtained, as a contribution to Honduran society and specific to neighbourhoods of the Central District; seeking to promote the strengthening of this initiative and any other that is generated in the near future.

7 Conclusion

One of the main factors of weakness in Honduras to cope with risk and vulnerability, is the lack of knowledge of our hazards and the risk situation, lack of socialization and awareness to communities at risk; as well as the lack of economic

resources permanently assigned to disaster risk reduction with a focus on prevention and mitigation.

Therefore, certain considerations must be taken into account, especially social education in terms of the threats we face; it is necessary to promote the analysis and scientific research of natural hazards over the country so that these studies become an instrument for the decision makers and also can be used as tools for teaching/learning to the public and private sectors; but specially for communities at risk.

For these reasons, we believe that this Teaching Tool provides useful information, certified by international and national experts; technically supported by the local government and supported by other relevant institutions. It also offers a new proposal for mass communication of understanding of the threats against landslides through the virtual accessibility.

This Teaching Tool aims at a significant contribution to the Honduran society in promoting Risk Management and Disaster Reduction caused by landslides specially in the Central District Metropolitan Area.

Acknowledgements Special thanks to the Japanese International Cooperation Agency (JICA), to the International Consortium on Landslides (ICL), to Kokusai Kogyo Corporation from Japan, and each one of the Japanese experts who gave us their experience, knowledge and confidence as its unconditional support to move forward with this project. Extend our thanks to the Dean of the Faculty of Sciences, to all the technical and scientific personnel in different units of the Honduran Institute of Earth Sciences (IHCIT), special thanks to the PhD. Elías Urquía from the Civil Engineering Department and to the Dean of the Engineering Faculty at our National Autonomous University of Honduras (UNAH). We also want to thank to all specialists of institutions who supported this process: to the Central District Municipality (AMDC), Municipal Emergency Committee (CODEM), Ministry of Infrastructure and Utilities (INSEP), Polytechnic University of Engineering (UPI). Special thanks to the National Pedagogical University Francisco Morazán for all the support and demonstrate their interest in getting involved throughout the process. We want to thank in a special way, to the families of the authors of this document as to all those involved in the development of activities in the framework of this project and the creation of this tool; who has wholeheartedly supported our efforts and those who have sacrificed time that has been designed with dedication to perform assigned tasks.

Appendix: Acronyms of Related Subjects

Acronym	Description
ACI	Engineering Consultants Association S. de RL
AHP	Analytic Hierarchical Process
AMDC	Central District Municipality
CEPAL	Economic Commission for Latin America and the Caribbean
CODEM-DC	Municipal Emergency Committee of the Central District
COPECO	Permanent Commission if Contingencies
DIC	Department of Civil Engineering of UNAH
GER	Risk Management Assessment
GOAL	International Ireland NGO
HAZAMA	Hazama Ando Co. Japan Consultant Enterprise
ICL	International Consortium on Landslides
IHCIT	Honduran Institute of Earth Sciences
ISDR-ICL	International Strategy for Disaster Reduction-International consortium on Landslides
JICA	Japan International Cooperation Agency
LITT	Landslides Teaching Tool
MOU	Memorandum of Understanding
UMGIR	Municipal Risk Management Unit
UNAH	National Autonomous University of Honduras
UNDP	United Nations Development Programme
UPI	Polytechnic Engineering University
UPNFM	National Pedagogical University Francisco Morazán
USGS	United State Geological Survey

References

- Carlos E, Pacheco A, Ennion N, Pozzobon B (2011) Manual de ejercicios de laboratorio. Fotogrametría y fotointerpretación

- CEPAL (1999) Honduras: evaluación de los daños ocasionados por el huracán mitch, 1998. Sus implicaciones para el desarrollo económico y social y el medio ambiente
- Grupo de Mapeo de Deslizamientos de Tierra de Tegucigalpa (GMDTT; 2014) Manual para elaboración de mapa de inventario de deslizamientos de tierra. Caso de aplicación ciudad de Tegucigalpa. Agencia de Cooperación Internacional del Japón (JICA). ISBN: 978-99926-701-1-8
- Harp EL, Hagaman KW, Held MD, McKenna JP (2002) Landslides triggered by Hurricane Mitch in Tegucigalpa, Honduras. USGS open-file report 2-33, p18
- Hirota K (2015) Landslide and geology education in Honduras, as activities of Japan International Cooperation Agency senior volunteer. J Jpn Landslide Soc 52(4):36-42
- INE (2007) Honduras: Proyecciones de Población 2001-2050. Tegucigalpa 2007. Instituto Nacional de Estadística
- Orrego JC (2013) UNDP-Honduras. Sistematización de Proyecto UNDP-COSUDE
- Sato G, Kamiya S, Hirota K (2015) Investigation and mitigation of landslides in Republic of Honduras as Japan's International cooperation program. J Jpn Landslide Soc 52(4):1-7
- Yagi H, Higaki D, Japan Landslide Society Research Committee for Detection of Landslide Hazardous Sites in Tertiary Distributed Area (2009) Methodological study on landslide hazard assessment by interpretation of aerial photographs combined with AHP in the middle course area of Agano River, central Japan. J Jpn Landslide Soc 45(5):358-366
- Yamagishi H (2014) Integrated disaster prevention maps and landslide hazard maps using GIS—examples of Shikoku and Central America Honduras. J Jpn Landslide Soc 51(2):24-29

TXT-tool 4.039-3.3

Debris Flows Modeling for Hazard Mapping

Massimiliano Nocentini, Veronica Tofani, Giovanni Gigli,
Francesco Fidolini and Nicola Casagli

Abstract

The Island of Ischia is located in the Tyrrhenian Sea, approximately 30 km WSW from the city of Naples in Southern Italy. The Island is a debris-flow prone area due to its steep slopes covered by loose volcanic lithologies. On April 30th 2006, following several hours of rainfall, four soil slips were triggered on the slopes of Mt. Vezzi (about 400 m a.s.l.) in the SE portion of the island. The soil slips changed quickly into debris flows that reached the inhabited at the foot of the hill, causing four victims, destroying several buildings and forcing the evacuation of 250 inhabitants. This work presents the analysis of the triggering and propagation phase of the phenomena. In particular, to model the triggering conditions, a finite element analysis was used to reconstruct the variations in pore water pressure during the event in transient conditions. The limit equilibrium slope-stability method was then applied using the temporal pore water pressure distributions derived from the seepage analysis. The dynamic modeling of the propagation phase was carried out by means of two dynamic codes DAN-W and FLO2D, with the aim of evaluating the residual hazard linked to other potential debris flows recognized in the same area. Once the DAN-W and FLO2D models satisfactorily reproduced the 30th April events, the simulations were extended to a larger area, whose susceptibility to future landslide events has been determined through a detailed geomorphological survey and a following GIS analysis.

M. Nocentini · V. Tofani (✉) · G. Gigli · F. Fidolini ·
N. Casagli
Department of Earth Sciences, University of Firenze,
Via La Pira 4, 50121 Florence, Italy
e-mail: veronica.tofani@unifi.it

M. Nocentini
e-mail: massimiliano.nocentini@unifi.it

G. Gigli
e-mail: giovanni.gigli@unifi.it
N. Casagli
e-mail: nicola.casagli@unifi.it

Keywords

Southern Italy · Debris flows · Landslide modeling · Hazard mapping

Contents

1	Introduction	762
2	Study Area, Landslide Event and Geotechnical Characterization	762
3	Landslide Modeling	764
3.1	Seepage-Stability Analysis	764
3.2	Dynamic Back Analysis	766
4	Residual Hazard	766
5	Conclusion	769
	References	769

1 Introduction

Debris flows represent one of the most dangerous natural hazards and are amongst the most frequent and serious natural disaster in many mountainous areas of Italy and worldwide. Guzzetti (2000) reports that more than 80% of deaths and injuries due to landslides in Italy are linked to fast-moving failures, including debris flows, rockfalls, rockslides, and soilslips. The occurrence of debris flows is very frequent on those areas characterized by steep slopes and loose cover. Heavy rainfalls, even if discontinuous, can trigger slope movements (Hungri et al. 2001) that, despite their commonly small volumes, can produce disastrous consequences when they involve areas characterized by unregulated urbanization. The forecasting of paths, volumes, and kinematic parameters of potential debris flows is fundamental to assess the areas at highest risk and to settle the most appropriate countermeasures.

In this work, the modeling of the triggering and subsequent propagation phase of the debris flows occurred on April 30th, 2006 in Ischia Island (Italy) has been performed, with the aim of evaluating the residual risk of the area where the debris flows occurred.

The adopted approach is based on the integration of four different numerical models, which were selected in order to perform complete back analyses of the April 30, 2006 events and to define reliable hazard scenarios associated to possible new debris flows.

First of all, a detailed geotechnical characterization of the soil through laboratory and in situ tests was performed. The subsequent modeling of the triggering and dynamic phases of the landslides is then performed based on the material properties obtained. Thus, in order to reconstruct the triggering conditions of the debris flow phenomena, a coupled seepage-stability analysis has to be carried out.

Concerning the dynamic analysis, the path and the debris flow deposits of already occurred events can be back analysed with the aim of identifying the most proper dynamic model and associated properties to be used for possible new landslides. In this study, the dynamic back analyses of the events were carried out both in 2D and in 3D, by using respectively the codes DAN-W (Hungri 1995, 2002) and FLO2D (O'Brien et al. 1993; O'Brien and Julien 1985). Finally, the back analysis results can be used to evaluate the possible propagation phase of new potential debris flows recognized in the same hydrographic basin based on geomorphological evidences and critical slopes arising from the aforementioned numerical modeling. The definition of debris flow possible runout distances and deposition areas, of the thickness distribution and of the principal dynamic characteristics is a fundamental step for future risk strategy assessments.

2 Study Area, Landslide Event and Geotechnical Characterization

The Ischia Island, located in the NW part of the Naples Gulf, is one of the nine active volcanoes existing in Italy. The island, whose highest peak is the Mt. Epomeo (787 m a.s.l.), is the remnant of a wider and older volcanic complex extending to the west and under the sea level by more than 200 m (Orsi et al. 2003; Bruno et al. 2002). The terrains exposed in the Mt. Vezzi area, where the landslides occurred, belong to the most recent

volcanic deposits (younger than 10 ka). The related phase in volcanic activity was characterized by almost 45 phases of both effusive and explosive phenomena in the last 5.5 ka (Sansivero 1999). Several landslide deposits occur at different stratigraphic levels within this volcanic sequence (de Vita et al. 2006).

The landslides originated in the northern flank of Mt. Vezzi, where the stratigraphy is composed of a 1–2 m thick layer of surficial pyroclastic deposits very loose and permeable, overlying a fine ash pyroclastic soil of higher compaction degree and lower permeability (de Vita et al. 2006). The sector of Mt. Vezzi involved in landslides shows variable slope angles, up to 35° in the triggering area. The main triggering factor for the landslides was represented by a strong rainfall event that focused on the northern slope of Mt. Vezzi. The Ischia Porto rain gauge, located about 5 km north of Mt. Vezzi, recorded 113 mm of rainfall from 9.00 am on 29th April 2006 to 9.00 am on 30th April 2006. In the area of Mt. Vezzi, a cumulative rainfall of 164 mm has been recorded.

The storm event triggered four soil slips, which evolved into debris flows. These four soil slips originated at an elevation ranging between 310 and 350 m a.s.l. and affected the surficial layer of soil or a depth of 0.5–1 m. The involved material can be classified as silty sand and it lays over a more consistent and impermeable substrate.

The landslides originated as soil slips and after several meters changed into debris flows (Fig. 1). This change in rheology was imputable to the liquefaction of the material involved in the soil slip, due to the interaction between the slope break and a contractive behaviour of the material following the shear deformation (Sassa and Wang 2005). Then, the debris flows moved downward dragging trees, rock boulders, and other materials along the path, and they stopped in correspondence of some buildings which have been destroyed, killing four people.

All the debris flows were not channeled, except for landslide 4 that partially channeled within an existing impluvium (Fig. 1), consequently, according to the flow-like landslide classification proposed by Hungr et al. (2001),



Fig. 1 The four landslides occurred in Mt. Vezzi on 30th April 2006

the events are classifiable as debris avalanches except for landslide 4 that is a debris flow.

The debris flows covered vertical drops ranging from almost 190–260 m. The mean elevation of the source areas is about of 335 m a. s. l., and the distal portion of the debris flows reach the elevation of 80 m a. s. l.

The *fahrboschung* (Heim 1932) is defined by the ratio between the start–stop point elevation difference of the debris (H) and the corresponding horizontal traveled distance ($L0$).

$$\tan \alpha = \frac{H}{L0}$$

The *fahrboschung* angles range from 21 to 24° for the coarse portion of the debris and from 11 to 14° for the respective fluid portions.

To evaluate the total volume involved in the debris flows, we splitted the flows in three zones according to both field surveys and observations of satellite and aerial images taken after the landslide events (Fig. 2): (1) triggering area, where the landslides initiated as soil slips; (2) transport area, characterized by debris transport and substrate erosion; (3) deposition area from the beginning of the deposition to the terminal portion of coarse deposits.

The total detach area was about 7000 m² divided as follows: 1100 m² for landslide 1; 3100 m² for landslide 2; 1500 m² for landslide 3; and 1350 m² for the landslide 4. The debris thickness observed immediately after the landslide events ranges from 0.5 to 1.5 m for landslides 1 and 2. Considering an average thickness of 1 m, the estimated total volume for landslides 1 and 2 is approximately 9150 m³. Deposits of flow number 3 showed a more variable thickness, ranging from 0.2 m in the uppermost part to 1.2 m in its terminal portion. Landslide 4 showed an average thickness of 2 m relating to the bouldery front of the debris flow, which resulted in a confinement of the deposition similarly to a dam structure. The volumes of landslides 3 and 4 were estimated in 2700 and 2000 m³ respectively.

Two field campaigns carried out immediately following the events were focused on collecting geotechnical data in the source area. Laboratory

tests as grain size analysis, measurement of Atterberg limits, phase relationship analysis were carried out on three soil samples taken in proximity of the exposed slip surface of the landslides. Material shear strength was determined both in the laboratory on reconstituted samples by means of a direct shear test and in situ by means of borehole shear tests (BST), coupled with a tensiometer for the measurement of matric suction (Casagli et al. 2006; Tofani et al. 2006). Saturated hydraulic conductivity (k_s) within the unsaturated zone was measured in situ using the Amoozometer or Compact Constant Head Permeameter (CCHP).

3 Landslide Modeling

3.1 Seepage-Stability Analysis

The seepage modeling has been carried out through a finite element analysis in transient conditions by using the software SEEP/W (Geo-Slope Int.), while the stability analysis has been realized through the SLOPE/W software, that applies the limit equilibrium method. In order to carry out the modeling, a simplified geological model with two layers, has been adopted; layer 1: pyroclastic soil, layer 2: pumice.

For each layer, hydrological and geotechnical properties have been defined according to the outcomes of the soil geotechnical characterization.

Rainfall intensity has been assigned as surface boundary condition to the nodes along the ground surface. All the nodes within the slopes were given an initial matric suction of 20 kPa. This value is equal to one measured during the field survey in the pyroclastic soil, and it can be considered representative of the initial pore water conditions prior to the storm event. Positive and negative pore pressure distributions obtained from the seepage analysis were used as input data for the stability analysis. This was performed with SLOPE/W, applying the limit equilibrium method (Morgenstern-Price) for each of the time steps used in the seepage analysis. The Mohr-Coulomb criterion in terms of effective stress was used in the case of positive pore

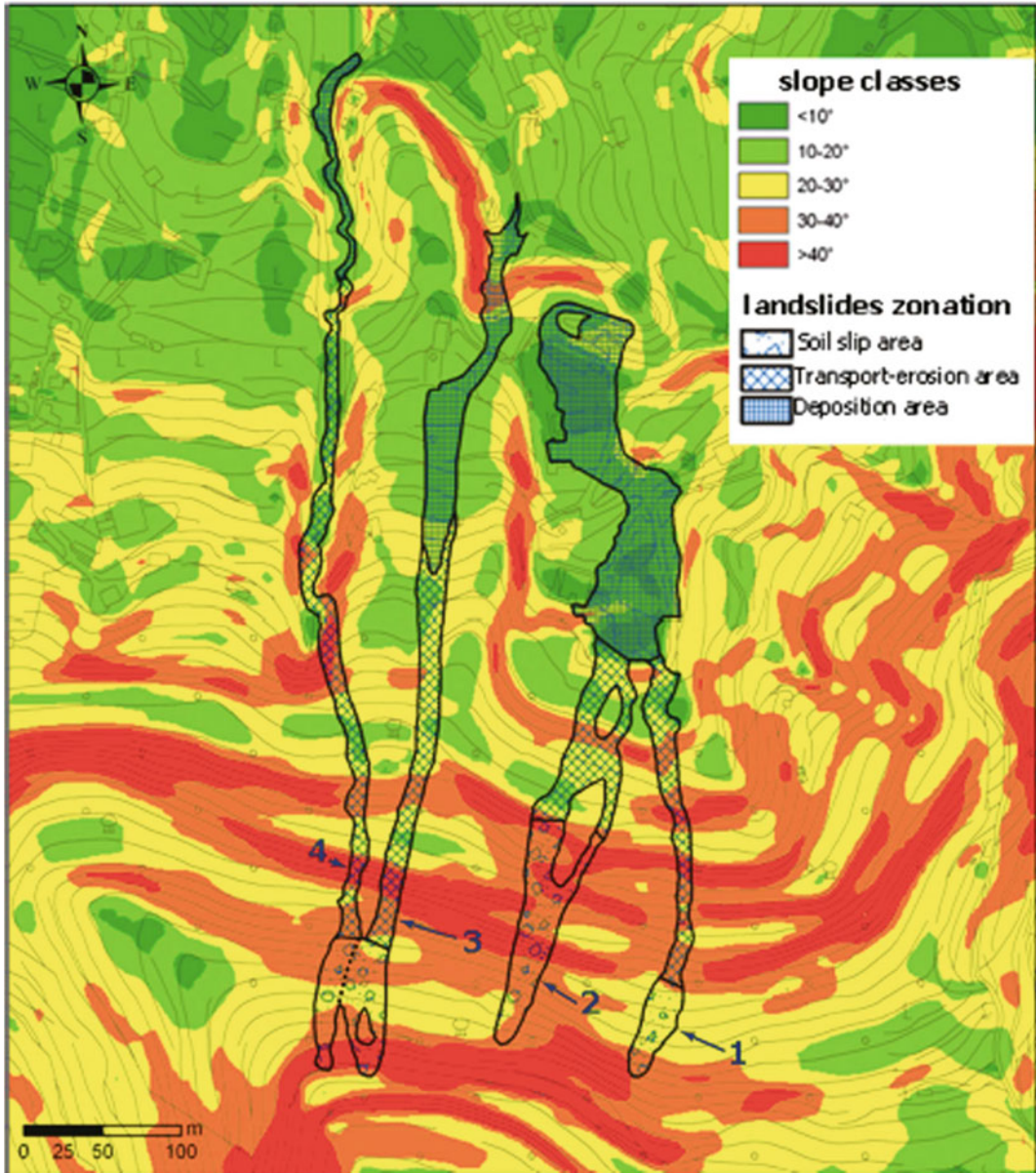


Fig. 2 Comparison between the areas of feeding, transport, and deposition of the debris flows and the map of slopes; the *broken line* describe the division of the flow 3

and 4 used for the evaluation of the areas of detachment (Nocentini et al. 2015)

pressures, while the Fredlund et al. (1978) criterion was applied in the case of negative pore pressures.

The results show that the distribution of pore pressure conditions is largely influenced by the high permeability contrast between the soil

pyroclastic cover and the underlying pumice layer, by the soil type and by the limited thickness of the cover. The factor of safety goes below 1 around 5:30 am of 30 April 2006 with a value of pore water pressure over the shear surface of about 7 kPa and a complete saturation of the soil

layer. This result is in agreement with the real time failure as reported by witnesses of the event.

3.2 Dynamic Back Analysis

Both 2D and 3D numerical modeling of the debris flows have been carried out using respectively the codes DAN-W and FLO2D.

Concerning the 2D DAN-W analysis the back analysis of the rheological parameters was carried out for the four landslides using a topographic map at scale 1:2.000 drawn before the event. The simulation results were tested by comparing runout distances, volume and thickness of deposits, and flow velocities at control points.

The best results were obtained using the two parameters Voellmy rheological model (Voellmy 1955). There is good agreement between the main parameters obtained from the 2D simulations and the real parameters of the flows except for the runout distance of landslide 4. We suppose that this difference is linked to the bouldery front formation, which reduced the maximum potential runout.

The FLO2D code (O'Brien and Julien 1985; O'Brien et al. 1993) models the flow distributions on a topographic surface, converted in a grid with square cells. The flow is dealt as a continuum fluid, composed by water and sediment, where the viscosity (η) and the yield strength (τ_y) are linked to the solid concentration of the flow.

To model the 3D debris deposition, the relative flow hydrogram at the upstream reach of the deposition zone has to be defined for each landslide. We obtained these values from control points in the 2D numerical simulation, multiplying the cross section for the flow velocity. Due to the joint depositional area of landslides 1 and 2, we modeled these phenomena together, considering, on the base of eye-witness, that flow 2 happened almost 1 h after flow 1. The calibration of the rheological

simulation parameters has been obtained on the basis of the following: (1) maximum runout distance, (2) areal and volumetric distribution of the deposits, and (3) velocities at control points.

Figure 3 shows the simulation results superimposed to the orthophoto of the area just after the landside events. There is good agreement both in the average thickness and in the planar extension of the deposits. Flow velocities obtained with FLO2D result a little lower than the real and 2D simulation values.

4 Residual Hazard

The residual hazard in the area affected by the debris flows of the 30th April is still very high. Other zones of possible debris flow alimentation were observed on the same flank of Mt. Vezzi on the base of instability evidences and similar morphological and lithological aspects. This hypothesis is supported by the recurrent character of these events, as attested by the presence of debris flow deposits in many pyroclastic sequences (de Vita et al. 2006).

To evaluate the kinematical characteristics and the depositional areas of new potential debris flows, both 2D and 3D numerical models were performed, using the rheological parameters obtained through the back analyses of the April 2006 events. The potential path of the 2D models was established on the basis of the main ephemeral creek valleys and roads within the investigated area.

The results showed maximum deposition depths of 0.6–3 m and maximum flow velocities of 12.1–15.5 m/s, in good agreement with the back analyses results. The total potential volume of the debris flow deposits amounts to 21,000 m³.

In the FLO2D numerical modeling, we used the reological parameters obtained for the landslide 4 for the potential debris flows named b and c, while for the other potential debris flows, we

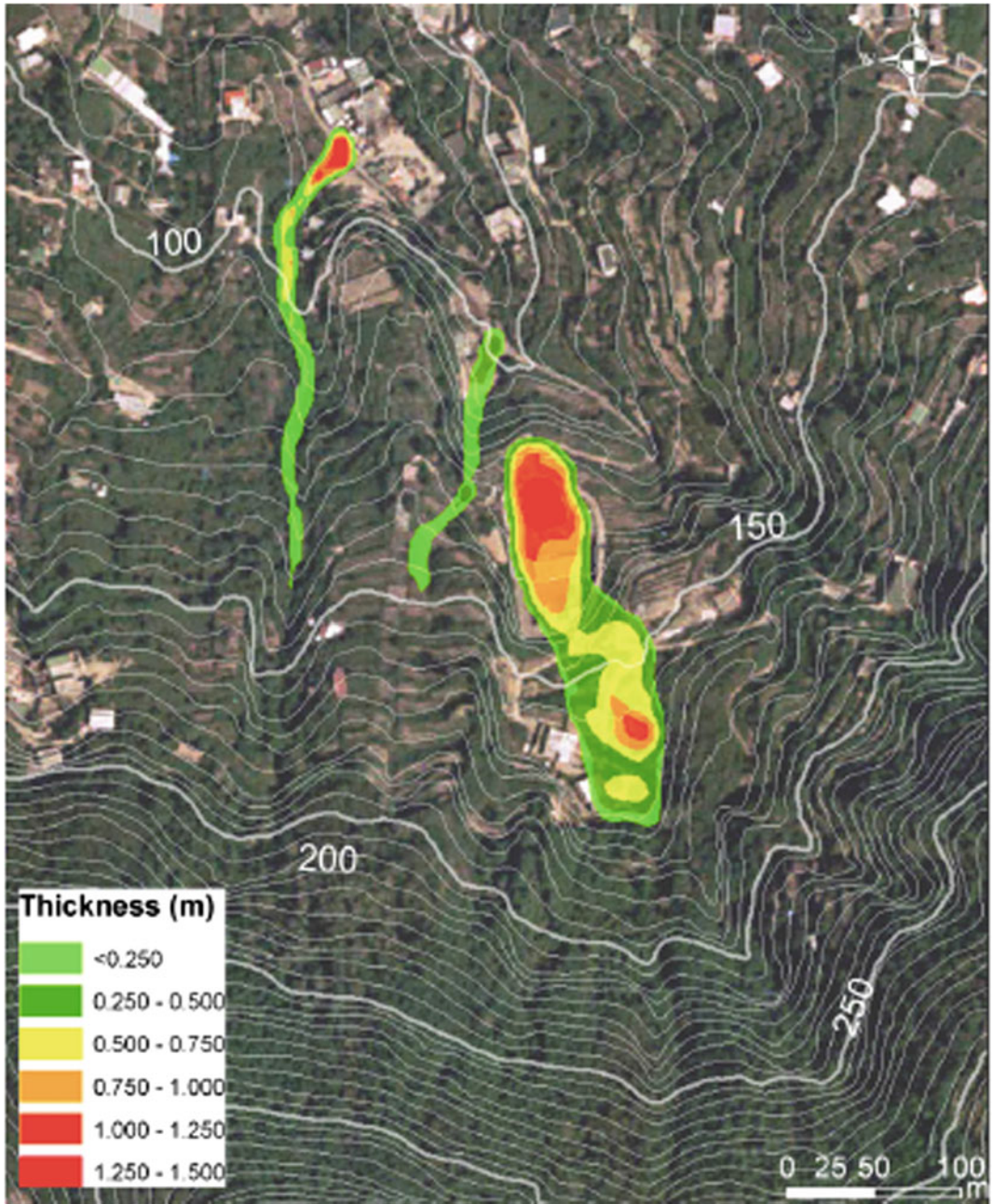


Fig. 3 Deposits flow thicknesses from the FLO2D simulation (Nocentini et al. 2015)

used the reological parameters obtained for the landslides 1 and 2.

The 3D modeling (Fig. 4) confirmed the choice of the paths of the 2D analyses and

showed that the material could mostly be deposited in the same area damaged from the debris flows of the 30th April 2006.

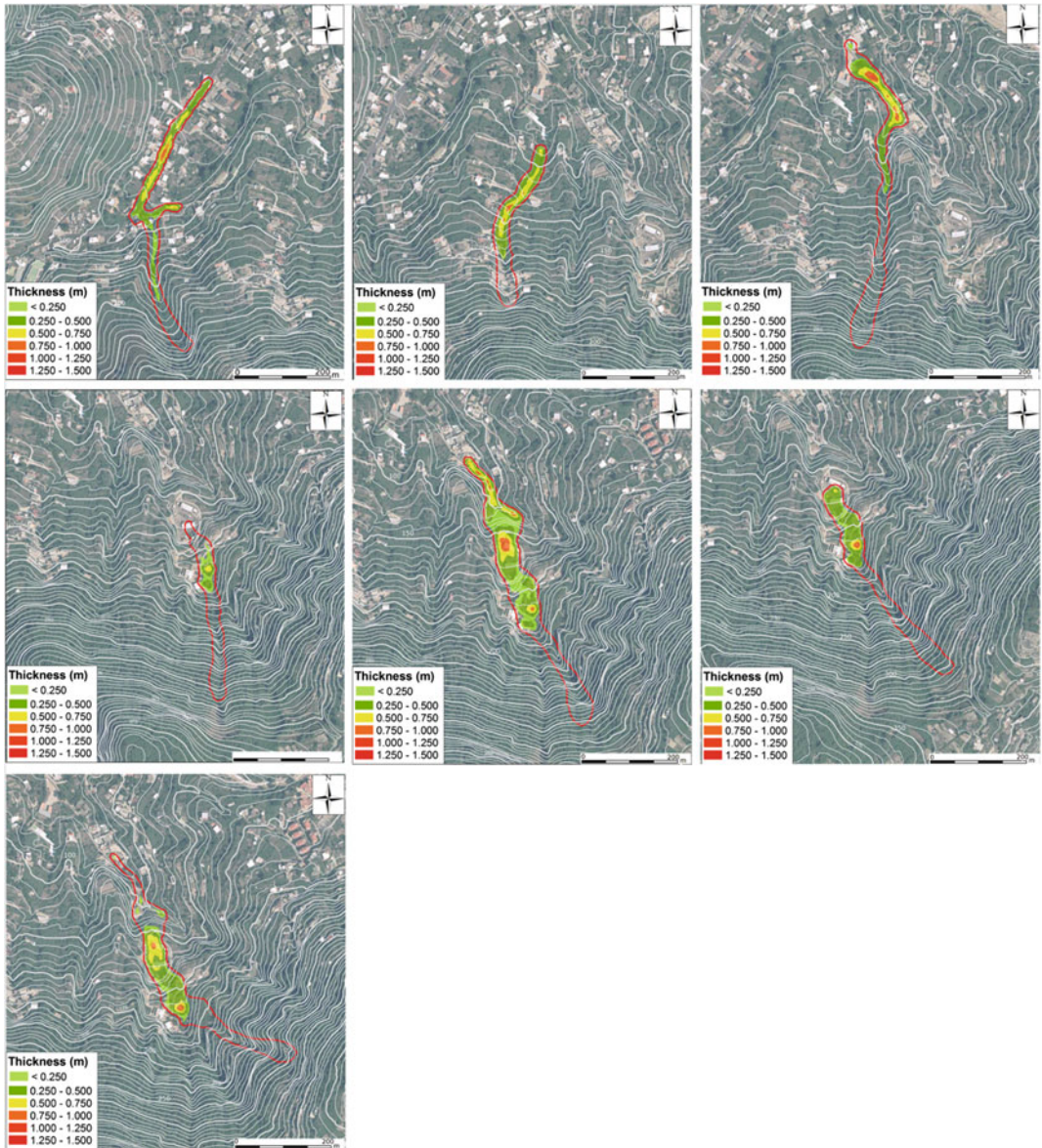


Fig. 4 Potential debris flow runout (a–g) obtained with FLO2D model. In this image are labeled the final thickness of the deposits and the affected area (red) (Nocentini et al. 2015)

5 Conclusion

The debris flows occurred on April 30th 2006 in the Ischia Island highlighted the high risk linked to these phenomena, since they killed four people, destroyed two buildings, and damaged other structures, forcing moreover the Italian Department of Civil Protection to evacuate about 250 people for several days.

The debris flows showed travel angles ranging from 21° to 24° for the coarse portion of the debris and from 11° to 14° for the respective finer portions. The analyses of the deposits and debris paths allowed to identify three zones in the flows linked to the average slope of the mountainside: triggering zones, transport zones, and deposition zones.

The seepage-stability analysis has simulated the triggering conditions of the soil slips during the rainfall event. The results has shown that the landslides have occurred due to sudden built-up of the high pore water pressures caused by the impermeable contact between the soil pyroclastic layer and the underlying pumice layer. For the simulation of the debris flows carried out with DAN-W the best results were obtained by using a Voellmy reological model with turbulence parameter (ξ) comprised between 210 and 300 m/s² and friction parameter (μ) between 0.063 and 0.11.

The flow events were also simulated with FLO2D code using the input discharge parameters deriving from the DAN-W simulation. The dynamic models of the debris flows carried out with FLO2D showed good agreement with the real thickness and spreading of debris. The rheological parameters obtained through both dynamic back analyses were used to evaluate the kinematical parameters and the deposition areas of new potential debris flows, recognized in the same area affected by the 30th April 2006 events. The dynamic modeling of these potential debris flows suggests that more than 21,000 m³ of

debris material would be able to deposit almost in the same area of the 30th April events.

The seepage-stability analysis has allowed evaluating that in the geological context like the Ischia Island where there is various types of pyroclastic deposits the landslide occurrence is mainly related to the contrast in permeability values. This consideration can help to define the potentially future prone landslide areas in similar geological context.

At the same time, the dynamic modeling calibrated on similar landslide events allows to define the propagation zones. The combination of these two kinds of analyses allows a complete identification of the hazard, including both the triggering and propagation zones.

References

- Bruno P, de Alteriis G, Florio G (2002) The western undersea section of the Ischia volcanic complex (Italy, Tyrrhenian Sea) inferred by marine geophysical data. *Geophys Res Let* 29(9):1–4. Art no. 1343
- Casagli N, Dapporto S, Ibsen ML, Tofani V, Vannocci P (2006) Analysis of the landslide triggering mechanism during the storm of 20th–21th November 2000, in Northern Tuscany. *Landslides* 3:13–21
- De Vita S, Sansivero F, Orsi G, Marotta E (2006) Cyclical slope instability and volcano tectonism in resurgent calderas: the Ischia island (Italy) case study. *Eng Geol* 86:148–165
- Fredlund DG, Morgenstern NR, Widger RA (1978) The shear strength of unsaturated soil. *Can Geotech J* 15 (3):312–321
- Guzzetti F (2000) Landslide fatalities and evaluation of landslide risk in Italy. *Eng Geol* 58:89–107
- Heim A (1932) *Bergstruz und Menschenleben*. Fretz und Wasmuth, Zürich, p 218
- Hungri O (1995) A model for the runout analysis of rapid flow slides, debris flows, and avalanches. *Can Geotech J* 32:610–623
- Hungri O (2002) Analytical models for slides and flows. In: *Proceeding international symposium on landslide risk mitigation and protection of cultural and natural heritage*, Kyoto, 21–25 Jan 2002, pp 559–586
- Hungri O, Evans SG, Bovis MJ, Hutchinson JN (2001) A review of the classification of landslides of the flow type. *Environ Eng Geosci* VII(3):221–238

- Nocentini M, Tofani V, Gigli G, Fidolini F, Casagli N (2015) Modeling debris flows in volcanic terrains for hazard mapping: the case study of Ischia Island (Italy). *Landslides* 12(5):831–846
- O'Brien JS, Julien PY (1985) Physical processes of hyperconcentrated sediment flows. In: Utah Water Research Laboratory (ed) Proceeding of the ASCE specialty conference on the delineation of landslides, floods, and debris flow hazards in Utah, series UWRL/g-85/03, pp 260–279
- O'Brien JS, Julien PY, Fullerton WT (1993) Two-dimensional water flood and mudflow simulation. *J Hydraul Div ASCE* 119(HY2):244–261
- Orsi G, de Vita S, Di Vito M, Isaia R, Nave R, Heiken G (2003) Facing volcanic and related hazards in the Neapolitan area. In: Heiken G, Fakundiny R, Sutter J (eds) *Earth sciences in cities*. American Geophysical Union (Special Publication), Washington, pp 121–170
- Pareschi MT, Favalli M, Giannini F, Sulpizio R, Zanchetta G, Santacroce R (2000) May 5, 1998, debris flows in circum-Vesuvian areas (southern Italy): insights for hazard assessment. *Geology* 28:639–642
- Sansivero F (1999) *Assetto stratigrafico ed evoluzione vulcanologica del settore orientale dell'isola d'Ischia negli ultimi 10 Ka*. Ph.D. Thesis. University of Naples, Italy, 203 pp
- Sassa K, Wang G (2005) Mechanism of landslide-triggered debris flows: liquefaction phenomena due to the undrained loading of torrent deposit. In: Jakob M, Hungr O (eds) *Debris-flow hazard and related phenomena*. Springer, Berlin, pp 81–104
- Tofani V, Dapporto S, Vannocci P, Casagli N (2006) Infiltration, seepage and slope instability mechanisms during the 20–21 November 2000 rainstorm in Tuscany, central Italy. *Nat Hazards Earth Syst Sci* 6:1025–1033
- Voellmy A (1955) Über die Zerstörungskraft von Lawinen *Schweiz Bauzeitung* 73:212–285

TXT-tool 4.039-4.1

Landslide Investigations and Risk Mitigation: The Sarno, Italy, Case

Giovanna Capparelli, Luciano Picarelli
and Pasquale Versace

Abstract

Recently, a number of catastrophic debris flows revealed the high risk in an extensive area of the Campania Region, Southern Italy. Following intense rainfall, on May 5th 1998, over 100 flow slides occurred on Pizzo d'Alvano mountain and hit the urban areas of Sarno and neighboring hills and mountains of this area are covered by air-fall pyroclastic soils deposited during volcanic eruptions occurred in the last tens of thousands years. In order to reduce the risk a lot of studies and investigations have been carried out and big and meaningful structural measures have been achieved, described in this paper.

Keywords

Debris flows triggered by rainfall · Pyroclastic soils
Event scenarios structural mitigation works

Contents

1	Introduction.....	771	3	General Description of the Debris Flow Events.....	773
2	Geological and Geomorphological Setting	772	4	General Solutions on Risk Reduction	776
			5	Protection Works in the Sarno Area	776
			6	Conclusion	783
				References	784

G. Capparelli (✉) · P. Versace
Department of Computer Engineering, Modeling,
Electronics and Systems Science (DIMES),
Università della Calabria Ponte Pietro Bucci, Cubo
41/b, 87036 Rende, CS, Italy
e-mail: giovanna.capparelli@unical.it

P. Versace
e-mail: pasquale.versace@unical.it

L. Picarelli
Department of Civil Engineering, Design,
Construction and Environment (DICDEA), Seconda
Università di Napoli, Real Casa dell'Annunziata-Via
Roma, 9, 81031 Aversa, CE, Italy
e-mail: luciano.picarelli@unina2.it

1 Introduction

On May 5th 1998 more than 100 slides were triggered on Pizzo d'Alvano mountain, due to heavy and prolonged rainfall. Many slides developed into debris flows hitting the urban areas of four small towns, Sarno, Siano, Quindici and Bracigliano; 159 people died, over 300 houses were destroyed or highly damaged.

It was one of the most serious events among those happened in Italy and it has deeply modified the way of planning risk mitigation measures and civil protection activities.

After these events the Governor of the Campania region was designated Commissioner to plan and manage structural and non structural measures in the area affected by debris flows. A technical office has been set up to carry out studies, in situ surveys and investigations, and then to design measures for achieving population safety.

In collaboration with many Italian Universities, different mathematical models were performed to support field observations and, also, to improve the knowledge of phenomena. A lot of protection works have been realized with a cost of over 285 million of euro. This paper describes some outstanding aspects. In particular, after a brief discussion on the geological context and event dynamics, the paper illustrates some of the most meaningful works realized in Sarno and its surroundings. Information about the non structural measures, adopted in this area, can be found in Picarelli et al. (2007).

2 Geological and Geomorphological Setting

The area in which the landslides took place has an extension of around 60 km² and includes the Pizzo d'Alvano massif, a NW–SE oriented morphological structure, consisting of a sequence of limestone, dolomitic limestone and, subordinatedly, marly limestone dating from the Lower to Upper Cretaceous age and reaching a thickness of several hundred meters. Elevation ranges from 30 to 1133 m a.s.l. Figure 1 reports an overview of Pizzo d'Alvano massif and the shapes of the mudflows occurred on May 5th. The average slope angle is 34° whereas subvertical limestone cliffs interrupt their morphological continuity. In particular, the slopes are generally higher than 30°, with maximum values around 50°, those at the piedmont areas are, generally, less than 20° (Fig. 2). The slopes are mantled by very loose pyroclastic soils, produced from the explosive

phases of the Somma-Vesuvius volcanic activity, both as primary air-fall deposits and re-worked deposits (volcanoclastic deposits). Pumiceous and ashy deposits belonging to at least 5 different eruptions were recognized. From the oldest to the youngest, they are: Ottaviano Pumice (8000 years b.p.), Avellino Pumice (3800 years b.p.), 79 A.D. Pumice, 472 A.D. Pumice, 1631 A.D. Pumice.

The deposits are affected by pedogenetic processes determining paleosol horizons during rest phases of the volcanic activity, then the primary deposits consist of alternating layers of ash and pumice, with interbedded paleosols.

Secondary deposits, re-worked by sheet wash waters and by mass-wasting processes, are mainly found as debris and colluvium at the toe of the valleys in the lower part of the belt, and also in the morphological concavities on the slopes and in the karstic depressions at the top of the limestone ridge, so forming the so-called “Zero Order Basins” (ZOB) (Guida 2003). The term “Zero Order Basins” was introduced by Tsukamoto (1973) to indicate unchanneled convergent slope located above ephemeral, intermittent or perennial first-order streams.

The total thickness of the pyroclastic covers in these areas ranges between few decimetres to 10 m, near to the uppermost flat areas.

The general structure of the soil progressively adapts itself to the morphology of the calcareous substratum showing, therefore, complex and variable geometries. Field surveys and in situ investigations showed that the total thickness of the pyroclastic cover increases to the foot of slopes (several meters), in agreement with observations in similar geomorphologic settings. Wide coalescing alluvial fans form the transition from alluvial plains to calcareous slopes. The considerable area and volumetric extent of the alluvial fans, as well as the sedimentologic evidence suggests that, besides a consistent primary volcanic sedimentation, a great sediment supply from upslope took place, both as post-eruption remobilization of unstable air-fall volcanoclastic deposits and as debris flow activity. Karstic springs are located at the foot of the slopes. Water supplies to the deep karstic aquifer is

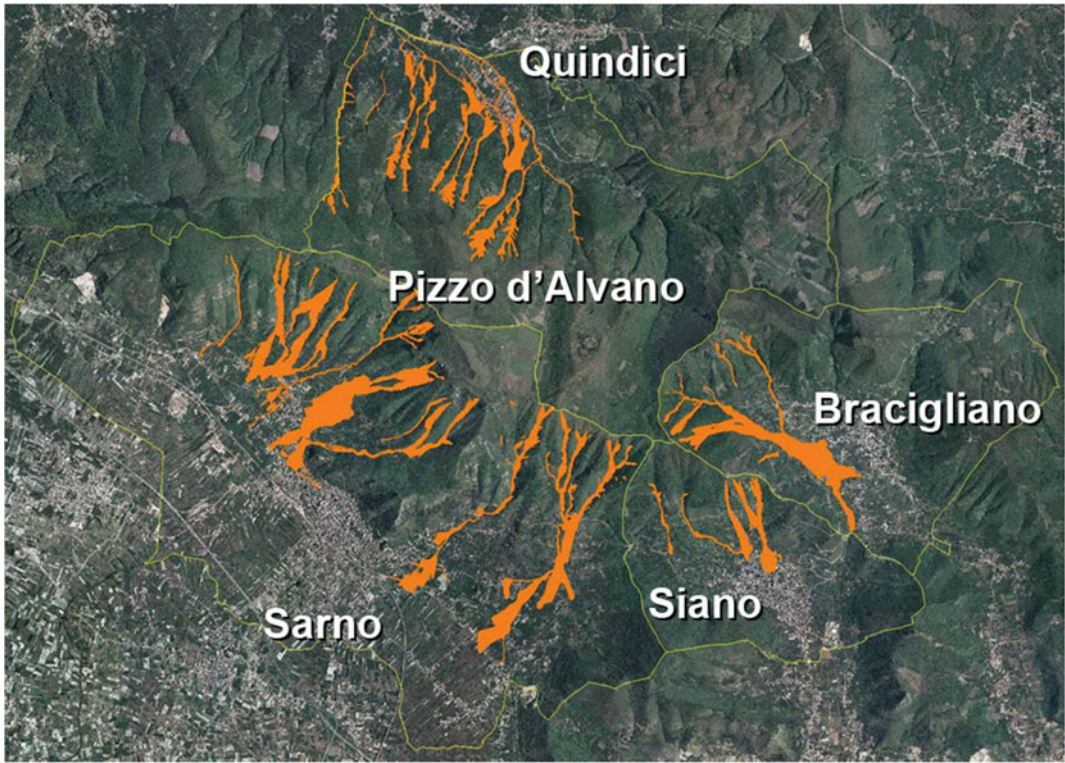


Fig. 1 Overview of Pizzo d'Alvano massif and shapes of the mudflows occurred on May 5th

modulated by the overlying pyroclastic aquifer. At higher elevation, the bedrock is shaped by the joint superficial system, which allows the ground water circulation and the forming of local weak springs.

Deep gullies, along the Pizzo d'Alvano slopes, are scoured by ephemeral creeks that are active during intense rainfall and rill erosion is evident along the slopes.

The upper flat areas and the toe of the slopes have been terraced for prevalent hazelnut cultivation. In relation to this activity an extended road network has been realized. From analysis of aerial photos a great increase in road density can be recognised in the last 30 years. A detailed analysis of geomorphological elements led to the definition of a geomorphological model referred to the Sarno slopes.

From upslope to downslope, the geomorphological system reveals:

- summit tablelands;
- basin areas, divided by the morphological frame into one upper zone, where the paleo-drainage network of the limestone slopes are mainly filled with air-fall deposits or with debris colluvial material coming from upstream slopes (ZOB) and one lower zone, or lower catchment drain, where owing to the steeper slope angle, erosional and transportational processes take place on barren slopes, and shaped them by gullies;
- area with the ancient and recent alluvial fans.

3 General Description of the Debris Flow Events

Landslides that occurred in the 1998 are classified as very rapid to extremely rapid soil slip/debris flows, and attained volumes up to 180,000 m³.

Fig. 2 The presence of rocky cliffs interrupting the morphological continuity of the slopes



They occurred in most of the basins of the mountain, with the triggering zones located primarily in the uppermost parts of the slopes or near to the morphological frame, and also above and below track ways. The size of landslides increased along their path down slope, digging and moving the debris which fill the gullies. The debris flows reached the broadly urbanized piedmont areas, releasing their huge destructive power, with high velocity (more than 10 m/s).

Figure 3a reports a scheme of most of the debris flows, based on eyewitness and accurate site surveying, Fig. 3b a some of landslide shapes occurred in Sarno area, where the different colors highlight respectively source area, run-out zone and deposition zone.

Every debris flow had a typical evolution:

- along the gentle slopes, with limited coverage of sediments, the shallow phenomena develop and become wide, sliding toward the valley;
- in strongly shaped slopes, with remarkable thickness of sediments, the debris flows tend to make deeper and canalize.

Concerning the dynamics of the collapses, with reference to the role of rainfall, an univocal and shared opinion doesn't exist (Capparelli and Versace 2014).

Soil water circulation is important due to the typical stratification of the pyroclastic covers involved, where one or more layers of pumice are present, with high permeability at saturation and layers of paleosoils, with lower saturated permeability. When persistent rainfall events occur, it

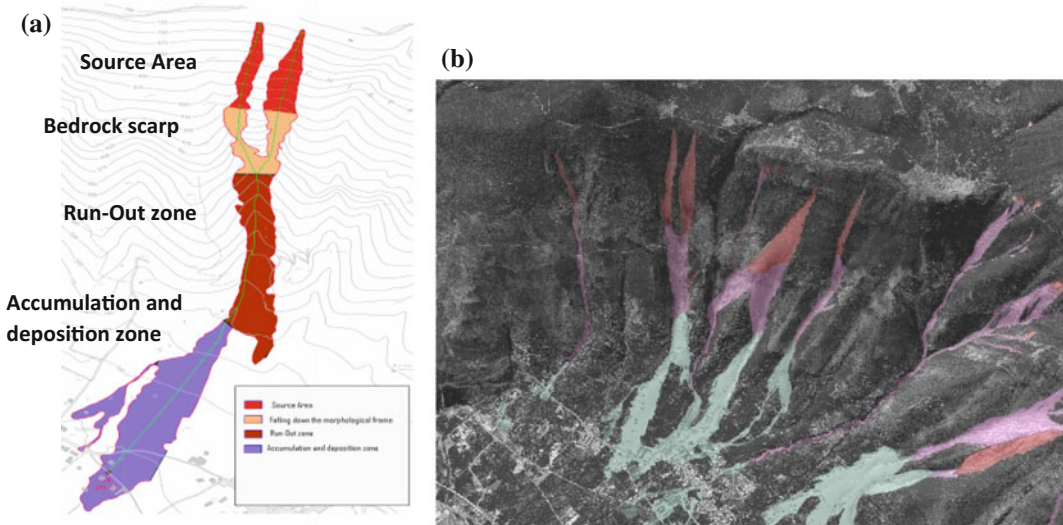


Fig. 3 **a** Sketch indicating the prevalent phenomena in the different morphological zones; **b** particular of mudflow shapes recorded on May, 5th in Sarno area

encourages subsurface runoff, which may predispose the slope to instability in limited areas. The role played by the possible interaction of the unsaturated cover with the underlying groundwater, through an impervious soil-bedrock interface, has been analyzed by Capparelli and Versace (2014), Cascini et al. (2008) and for a slope similar to those in Sarno, by Greco et al. (2013).

What appears more debatable is the identification of the phenomena that, activated by the rains, led to the development of the debris flows.

Slope failure was a result of shear rupture, provoked by decreasing shear strength of soil, as a consequence of variations in water pressure distribution. This variation could have been caused by two different mechanisms:

- water content increase, as a consequence of infiltration, and following suction decrease;
- upward water flow from the underlying fractured limestone and saturation of the lowermost layer. For many days after the May, 1998, event, a continuous flow of water was observed, in some cases, from the uncovered limestone. Nevertheless, the occurrence of this last mechanism requires a unlikely water

supply directly from the ground surface, through the complex network of joints within the rock mass.

The post-failure mechanism of the mobilized soil mass is liquefaction, which is a fundamental process responsible for the flow mechanism. Such a mechanism has been suggested for landslides involving wasted saturated coarse grained materials (Bishop 1973; Dawson et al. 1998; Blight et al. 2000), and natural slopes (Sassa 2000).

Hutchinson (1986) has proposed a new model, the so-called consolidation model, to analyse the post-failure kinematics and the run-out of debris flows. According to this model, the post-failure soil behaviour is governed by dissipation of excess pore pressure and following friction increase.

The occurrence of liquefaction in loose saturated volcanic ash has been demonstrated by Olivares and Picarelli (2006). This phenomenon develops when induced deformation is so rapid to provoke a sudden increase of the pore pressures. Deformations like these spread a chain from the upper sector, starting from the failure zones, toward the areas below, because of the

pressure induced downstream by the mobilized volumes. Deformations also increase owing to the dynamic effect of material that, falling from the morphological frames, or quickly crossing steep paths, stress underlying gullies. It is possible to observe this phenomenon only in saturated soils, relatively thin, permeable, loose and cohesionless. Moreover, the velocity of evolution of the phenomenon must be so fast as to preserve the undrained conditions, avoiding the dissipation of the induced pore pressure. When these conditions are not present, the failure does not evolve into debris flow. This incomplete evolution characterized a lot of movements in May 1998.

4 General Solutions on Risk Reduction

Structural measures for risk mitigation in the Sarno area follow a complex and articulated strategy, which intends:

- to reduce proneness to failure in source areas;
- to restrain bed and slope erosion along gullies and then to control the increase of debris flow volume along its path;
- to control rainfall water runoff toward the major rivers, i.e. the Sarno River or Regi Lagni channel, whose beds are not adequate to contain floods even with a low return period;
- to create storage area for debris flows;
- to canalize debris flows to this area.

To attain these objectives the following works have been carried out:

- slope erosion reduction works based on bio-engineering techniques;
- check dams in the upper part of the gullies, for bed erosion control and slope stabilization;
- channel for collecting rainfall water;
- retarding reservoir for flood routing;
- control structures, like sediment basins, diversion structures, transverse walls, that

bound the debris flow prone area and protect the inhabited ones.

Different kinds of work have been combined in order to obtain an articulated risk mitigation systems. In the Sarno area debris flow control has been obtained with slope stabilization, check dams, and three large deposition basins (Episcopio, Curti, Mare), located in the piedmont area above the town. In each basin more than one gully flows. The rainfall water drainage has been allowed by the channel network which cross the deposition basin and reach retarding reservoirs, located below the town, which reduce the peak flow toward the Sarno River. The Episcopio system will be described later on in this paper.

5 Protection Works in the Sarno Area

To identify the most correct strategy, some basic criteria have been adopted. The first one concerns the option, perhaps only theoretical, between active works, like bioengineering slope medications, and passive works, like check dams, channels, basins, etc. It is not a real question, because it is impossible to entrust people's safety only to bioengineering techniques, in cases like Sarno. Flowslides and debris flows can be triggered in all the areas characterized by slope angle higher than 30° and significant pyroclastic cover. This phenomenon is mainly possible in areas where ZOBs or buried channels or undrained trackways which concentrate water in impluvium, are present. Identification of all the areas with similar characteristics, often located on not easily accessible hill slopes, is difficult. Moreover, collapse may occur also in areas where these risk factors are not so evident or are even apparently lacking. Other aspects have also to be considered: the very high cost of such works extended over all the hill slope; technical difficulties in reaching the impervious area, where the marking out of new paths could generate further landslides and change the small-scale drainage network of rainfall water; very high vulnerability of wooden works in fire risk prone areas.

On the other hand, bioengineering works are beautiful (Fig. 4), they can be pleasantly inserted into the natural environment, and can be very effective if they are properly designed and located. Therefore the right choice is the integration of both types of works. The active ones reduce the probability of failure in the upper part of the hill slope, where the risk of collapse seems higher.

The passive ones mitigate and drastically reduce damage induced by debris flow that could be activated despite the presence of active works.

The location of the debris flow mitigation structures is another important issue. The chaotic development of many urban areas, in Sarno and in other towns, has produced the loss of natural courses which debris flows followed in the past.

The random growth of the town toward the mountain and the upsetting of both the natural drainage network and existing hydraulic works, produce a tangle of natural and manmade systems. Sedimentation basins built in the past above the town are now included in it and are used for different purposes: such as a football ground. Many channels disappear in long culvert with unknown pattern and unable to guarantee

hydraulic linkage. In such cases the main target is to separate natural and manmade functions, to free water and debris flow courses and to minimize meddling with built-up areas. This goal may be achieved also by existing houses delocalization, natural drainage network restoration, and a green belt boundary. In practice this latter is unlikely, as it requires a long time, large investment, and social conflict. When risk is pending, mitigation works are needed immediately. The better choice is to disconnect and separate the upstream natural system and the downstream artificial system, i.e. the built-up areas. So risk mitigation is quickly achieved and future land restoration is still possible and even easier.

Different works have been carried out, in Sarno, to disconnect the downstream and upstream areas. In many cases large basins with deposition areas have been adopted, which allow the debris flow to spread and to slow down owing to sudden gradient decrease, breakers, discharge control orifices at basin outlet. The basin volume is equal to the predicted one, as the routing effect is disregarded because outlet orifices occlusion is always possible during debris



Fig. 4 Example of bioengineering works along Pizzo d'Alvano side. Down in particular, a *top view* of the work during the construction phase

flow. This hypothesis, otherwise, leads to an increase of the safety factor. However, the routing effect is considered for downstream channel design, when runoff is only produced by rainfall and no debris flow is expected to occur. More than one gully often ends into one single basin, which can collect debris flow from all of them but also from the inter-gullies areas, so greatly increasing the safety of the downstream area. *This single basin system* allows the total volume for debris flow storage to be reduced by a proper reduction factor, as a simultaneous flow from all the confluent gullies has a very low probability of occurrence. A single basin system of Episcopio, in Sarno, is described in Fig. 5.

The system includes slope stabilization in mountain zone along main tracks; a large basin with capacity of more than 170,000 m³; two deep channels, with walls or levees on the outer side, which bound the debris flow prone areas. The basin was realized by digging, so its visual impact is very low. Lateral channels

present a top protection to prevent avulsion in the bend.

Episcopio is the most stricken district of Sarno with 90 victims and more than 120 houses destroyed or damaged. Downstream of the basin system many houses have been reconstructed with some extra precautions, that is with special technical rules. The ground floor cannot be used for residence. The structural frame is adequately reinforced. Each family was free to choose between rebuilding its own house in the same place or buying a new one in another part of Sarno or also in another town. In both cases the Italian Government bore the cost.

In some cases slope morphology does not allow a single basin system, so one sediment basin for each gully is needed, and more basins are present at slope bottom (*multiple basin system*). If both systems are possible the single one seems better, as it can contain inter-gullies debris flow and it is safer in the case of debris flow produced only from a single gully.



Fig. 5 In the *upper picture* a large view of the single basin system, in Episcopio (Sarno). *Down-left* the drawing shows the area of potential flows from the slopes which converge in the tank; *down-right* a photographic detail inside the tank



Fig. 6 Basin system, in Quindici

Figures 6 and 7 show a multiple system in Quindici and details of one of the basins (Connola basin).

These have to be filled only when debris flow occurs, i.e. once in many years. During normal periods, the clear water must be diverted and cannot reach the basin, because sediments could reduce the available capacity. So clear water must follow a different course to reach the downstream drainage system.

The debris, on the contrary, has to come into the basin and only a very small part of it can flow downstream. Then an appropriate diversion structure has to be designed, taking into account the fast flow regime. Usually this kind of basin is blind, i.e. there is no outlet, then its capacity needs to be large enough to contain all the design volume.

Of course when the basin is filled by mud, it has to be cleaned rapidly.

Figure 7 shows the diversion system of the Connola basin. An orthogonal channel receives clear water up to a discharge of about $30 \text{ m}^3/\text{s}$. For larger values, i.e. when the debris flow occurs, the flow passes over the channel and reaches the basin.

The discharge in the orthogonal channel changes a little. This device may exhibit some problems owing to both high flow velocity and conspicuous sediment transport. So it seems better to allow diversion inside the basin than to do it upstream. This choice drastically reduces the risk of exceeding the designed downstream discharge. Moreover the diversion occurs in the basin with slow flow or in any case with low Froude numbers, so the risk of outflow is highly reduced. A low flow channel is built along the basin with proper outlet for clear water runoff.

If the basin length or slope change between the upstream reach and the basin bed are not



Fig. 7 a On the *left side*, a large view of one tank located in upper area. *Down-right side* a photographic detail inside the tank (Basin system in Quindici), **b** On the *left*

side, a large view of one tank located in down area. *Down-right side* a photographic detail inside the tank (Basin system in Quindici)

(a)



Fig. 8 a Diversion structure in Siano area. The picture shows the area of potential flows which converge into the channel. **b** The *colored lines* indicate the channels which

convey the flow in the diversion structure. Then the containment tanks (System in Siano)

large enough, breakers have to be inserted into the basin, otherwise only riprap protection in the inlet area is achieved. Separation between upstream area, where debris sources are located and downstream urbanized area, which must be protected, can be also performed by diversion structure, which deviate water and debris flow into a not vulnerable area (Fig. 8). The structure is formed by (1) a large and deep channel, with high slope, not less than 6–7%, so no debris deposition may occur inside, and (2) a wall in the downstream side so avulsion may be avoided.

In some cases an embankment effect is obtained by increasing the downstream channel

edge, which is built higher and stronger, and can be integrated within the channel or not.

In the Episcopio system there are both basin and diversion structure. In this case the latter deviates the flows into the basin area.

One of the most important works is the first upstream check dam, which is the one that withstands the highest stress. It closes the whole system upward, breaks and slows down debris flows, stabilizes both the bed and banks, traps and stores sediment transport. Moreover, it directs flows towards the canalized reach.

Open check dams, like that in Fig. 9 can also select transported sediment, trapping the largest

(b)



Fig. 8 (continued)

one. When the opening is very high, these dams can work for a long time, as occlusion gradually increases upwards. Periodic cleaning of course is needed.

The breaking and slowing down effect are only transient owing to the very steep gradient

which allows velocity and sediment loading capacity to increase over a short distance. Then other check dams downstream of the first one are needed.

Figure 10 shows a series of check dams in the Cantariello gully in Sarno.



Fig. 9 Upstream open check dam in the Cantariello gully in Sarno

Fig. 10 Check dams in the Cantariello gully in Sarno



6 Conclusion

The tragedy that happened in Sarno caught our defence systems unprepared, incapable of assuring acceptable safety conditions. The event shook people's consciences and gave new impulse to the management of soil defence and civil protection systems. A lot of resources were allocated to these sectors and the situation has certainly improved, but there is still much work to do. Since Sarno and its neighbourhood was hit hard by the debris flows, to better support the operative management of the emergency,

numerous investigations and studies were set up that allowed, also, to deepen the knowledge of these phenomena and perform useful simulation models. Huge funding has been devoted to building of the structural systems that have been, mostly, successfully completed, even if with some mistakes. Nevertheless, an acceptable defence strategy from the debris flows has been focused, which provides the correct integration of active and passive works. As regards the containment structures, the single basin system, which can receive debris from more than one gully, greatly increases downstream area safety,

as it can intercept material also from the inter-gully areas. When the slope morphology requires a multiple basin system, that is, one basin for each gully, the better choice is to allow diversion from the clear water and debris flow into the basin instead of building this diversion upstream. However, even if it has not been discussed in this memory, the events of Sarno have also allowed a turning point in the management of civil protection. In fact, a control scheme has been carried out that assembles real time monitoring systems, forecasting models, and above all, the Territorial Survey composed of technical staff, engineers and geologists, who look after the territory during the emergency phases, when the models suggest the threshold values have been exceeded (Picarelli et al. 2007).

Acknowledgements Special thanks are directed to the technical staff of the Territorial Survey, i.e. engineers and geologists that during the emergency phases, the days after the events, and during the phases of the planning and construction of the protection works have collected and stored data, pictures, drawing here presented.

References

- Bishop AW (1973) The stability of tips and spoil heaps. *Quat J Eng Geol* 6:335–376
- Blight GE, Troncoso JH, Fourie AB, Wolski W (2000) Issue in the geotechnics of mining wastes and tailings. In: International conference on geotechnical and geological engineering GEOENG2000, pp 1253–1285
- Capparelli G, Versace P (2014) Analysis of landslide triggering conditions in the Sarno area using a physically based model. *Hydrol Earth Syst Sci* 18:3225–3237. doi:10.5194/hess-18-3225-2014
- Cascini L, Cuomo S, Guida D (2008) Typical source areas of May 1998 flow-like mass movements in the Campania region, Southern Italy. *Eng Geol* 96: 107–125
- Dawson RF, Morgenstern NR, Stokes AW (1998) Liquefaction flowslides in Rocky Mountain coal mine waste dumps. *Can Geotech J* 35:328–343
- Greco R, Comegna L, Damiano E, Guida A, Olivares L, Picarelli L (2013) Hydrological modelling of a slope covered with shallow pyroclastic deposits from field monitoring data. *Hydrol Earth Syst Sci* 17:4001–4013. doi:10.5194/hess-17-4001-2013
- Guida D (2003) The role of the Zero-Order Basins in flowslide-debris flow occurrence and recurrence in Campania (Italy). In: Picarelli L (ed) International conference on fast slope movements prediction and prevention for risk mitigation, vol 1, pp 255–262
- Hutchinson JN (1986) A sliding consolidation model for debrisflow-slides. *Can GeotechJ* (23):115–126.
- Olivares L, Picarelli L (2006) Modelling of flowslides behaviour for risk mitigation. In: Proceedings of the international conference on physical modeling in geotechnics, proceedings of the 6th international conference on physical modelling in geotechnics, Hong Kong, vol 1. Taylor & Francis, London, pp 99–112
- Picarelli L, Versace P, de Riso R (2007) Landslide disaster management in Italy. In: 2007 International forum on landslide disaster management, Hong Kong
- Sassa K (2000) Mechanism of flows in granular soils. In: International conference on geotechnical and geological engineering GEOENG2000, pp 1671–1702
- Tzukamoto Y (1973) Study on the growth of stream channel, (I) relation between stream channel growth and landslides occurring during heavy storm. *Shin-Sabo* 25:4–13

TXT-tool 4.081-8.1

Landslide Monitoring for Early Warning in the Hai Van Station Landslide in Vietnam

Shiho Asano, Hirotaka Ochiai and Huynh Dang Vinh

Abstract

Landslide monitoring system is important for early warning for landslide prevention. In this study, the monitoring system was developed for landslide prone slope in Vietnam. The system monitored landslide phenomena as like displacement of mass and hydraulic condition to clarify the specific landslide mechanism. It also has function of landslide prediction for early warning of the monitored landslide. Prediction based on displacement velocity is useful in this system. And it will be improved the landslide flume test in the future.

Keywords

Landslide monitoring · Hai van station landslide · Landslide displacement
Tropical heavy rainfall

S. Asano (✉)
Department of Disaster Prevention, Meteorology and Hydrology, Forestry and Forest Products Research Institute, 1 Matsunosato, Tsukuba, Ibaraki 305-8687, Japan
e-mail: shiho03@ffpri.affrc.go.jp

H. Ochiai
Forestry and Forest Products Research Institute, Japan Forest Technology Association, 7 Rokuban-cho, Chiyoda-ku, Tokyo 102-0085, Japan
e-mail: hirotaka_ochiai@jafta.or.jp

H.D. Vinh
Centre of Geotechnical Science and Technology, Institute of Transport Science and Technology, 1252 Lang Road, Dong Da District, Hanoi, Vietnam

Contents

1	Introduction	786
2	Study Area	786
3	Development of Monitoring System	786
3.1	Purpose of the Monitoring System	786
3.2	Functions of Developed Monitoring System ...	786
4	Characteristics of Monitoring System	787
4.1	Robotic Total Station	787
4.2	Global Navigation Satellite System (GNSS) ...	788
4.3	Wire Extensometer	789
4.4	Borehole Inclinator for Underground Displacement.....	789
4.5	Borehole Wire Extension Meter.....	790
4.6	Rainfall, Groundwater Observation and Others	790
4.7	Data Collecting System.....	790
4.8	Improvement of Landslide Prediction.....	792

5 Concluding Remarks	792
References	792

1 Introduction

For landslide risk reduction, landslide monitoring system is effective tool. It is useful for clarification Landslide disaster is often affected by their environmental condition, therefore landslide monitoring system need to adapt to geological, environmental and social condition each other. There are few case of the landslide prevention using a large-scaled monitoring system in Vietnam. Therefore the prototype model which is adapted for natural and social condition in Vietnam has been needed to develop.

In JST-JICA SATREPS project “Development of landslide risk assessment technology along transport arteries in Vietnam”, the prototype model of landslide monitoring system for early warning is developed for the landslide risk reduction in the mountainous area in middle part of Vietnam. In this paper, we explain this system which tuned up for actual landslide as case study.

2 Study Area

This study was conducted in Hai van station landslide area (Asano et al. 2014). The landslide is located on Hai van mountain slope near Danang city in the centre part of Vietnam. The important transport system as like national railway and national road run through the mountain. The granite rock and its weathered sand are distributed in this area. The railway runs through the middle area of slope and landslides-prone slope is located at the upper slope of railway (Fig. 1).

Size of recent landslide active area is not clearly. But deformation of gabion slope and concrete drainage channel on slope can be found

and small-scale slope failure occurred nearby railway.

3 Development of Monitoring System

3.1 Purpose of the Monitoring System

The purpose of this developed monitoring system is the prevention of the landslide disaster along the transportation system. In order to prevention landslide in specific slope, it is important to clarify the landslide mechanism and to predict of landslide occurrence for early warning. Rainfall and groundwater which causes landslide change with time. Therefore the characteristics of change of rainfall, groundwater and landslide movement by the observation is important for the elucidation of landslide mechanism and early warning.

3.2 Functions of Developed Monitoring System

Main functions of the developed monitoring system are the clarification of the range and movement vector of landslide displacement and the relationship between landslide displacement and rainfall and groundwater. And using this system, the time change of data can be observed successively and the final failure time of landslide can be estimated based on observed data in emergency condition.

The information for the early warning should be shared in all parties concerned. And the way to use it for warning and taking any measures should be decided in the related organization beforehand.

In case of landslide risk management in wide area which isn't covered by observation system, other type of system needs to be considered. For

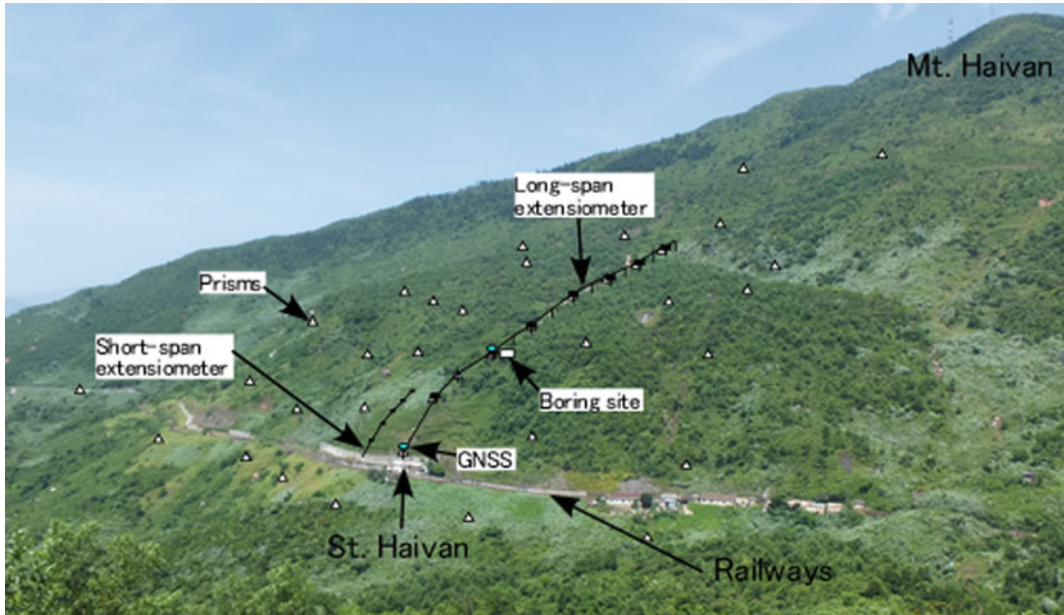


Fig. 1 The study area and sensor location on the landslide-prone slope

example, relationship between landslide characteristics as like location, scale and timing and weather condition as like rainfall and snow will be clarified by collecting cases of past landslide disaster in the area.

4 Characteristics of Monitoring System

The monitoring items of this system are the ground surface displacement, the underground displacement and hydrological condition in landslide area. The ground surface displacement is measured by the wire extension meter and the moving pole survey with the total station and GNSS. The underground displacement is measured by the borehole inclinometer and multi-depth borehole wire extension meter. The hydrological condition is measured by rainfall gauge, groundwater pressure gauge, air temperature gauge and air pressure gauge. Sensor location is shown in Fig. 2. Characteristics of each sensor are shown as bellow.

4.1 Robotic Total Station

Landslide mass shows three-dimensional displacement. The three-dimensional moving direction and size of active area need to be measured. It can be measured by total station surveying of moving pole which set on the slope repeatedly. The robotic total station can collimate and survey the target prism position automatically from a stable place by contactless. It measures displacement of target position by a repeat surveying.

In this study area, monitoring station (TSH) was constructed on opposite slope of landslide, and total station surveys the landslide displacement automatically from TSH. The 37 target poles are arranged on the landslide slope and 3 target poles are set on the outside of landslide slope for stable point. Relative displacement each point from stable point is analysed.

The displacement observation by total station can monitor the displacement vector of a lot of targets which are simple pole. On the other hand,



Fig. 2 Total station setting condition in TSH and target prism on slope

target which is at blind place by the topology, vegetation and weather condition cannot be measured. Surveying by total station is difficult in at short time, because it need to take a time each target.

4.2 Global Navigation Satellite System (GNSS)

GNSS measures the position using the signal from the satellite. Enough canopy openness over

the antenna is needed, but the visibility from other place isn't need to be worried. Measurement data is global coordination and it can be compared in wide area. Baseline analysis computing is need to be carried out for high accuracy positioning each point. Enough amount of data is necessary to improve accuracy because the variation of data is large. Real time monitoring for rapid landslide isn't easy using GNSS. In this landslide, three GNSS are installed; near railway, boring site and on the monitoring station (TSH) (Fig. 3).

Fig. 3 GNSS setting condition on TSH



4.3 Wire Extensometer

The wire extensometer is used for measuring the change of the distance between two points. It is usually used for measurement of crack openness. It can measure the landslide displacement of each part of slope by arranging the multiple extension meter in the series. Continuous maintenance for reducing noise such as contact to the wire is necessary to obtain good quality measurement data. However, the small displacement can be continuously measured in many point with small battery.

The maximum wire length of the extension meter which we use is 20 m. It is short to use large-scale landslide. The developed extension meter which can measure 50 m distance was installed. In this study, it was called “Long-span extension meter”, and normal type extension meter was called “Short-span extension meter”.

The wire of Short-span extension meter was protected using PVC pipe from noise. The long-span extension meter was set on the poles which is 3 m height. And the long-span extension meter isn't high accuracy because of wire slack of long and heavy wire. Five short-span extension meters were arranged in the series near

railway. 14 long-span extension meters were arranged in the series (Fig. 4).

4.4 Borehole Inclinometer for Underground Displacement

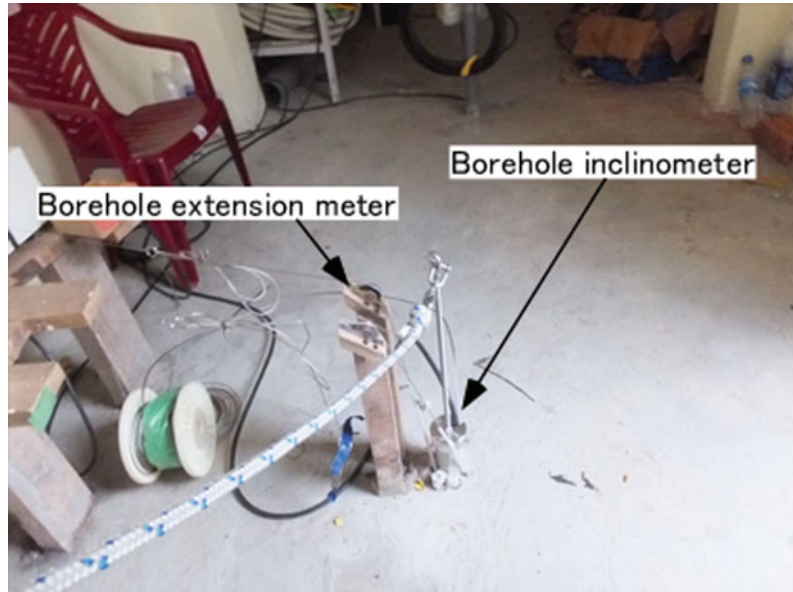
The direct measurement of displacement of the slip surface is also the necessary in order to clarify the mechanism of the landslide. In this landslide, the monitoring hut (BHH) in which boreholes for monitoring were covered was constructed for underground measurement. The displacement of the slip surface can be observed by the borehole inclinometer and vertical extension meter in borehole.

Borehole inclinometer can measure the small displacement at specific depth of landslide moving body. It measures the deformation of borehole casing and the small displacement sometimes show early stage of landslide activity. The amount of the inclination at the position is continuously observed by installing the sensor in specific depth. It is necessary to install the sensor on the depth in which the transformation of borehole



Fig. 4 Short-span extension meter (*left side*) and long-span extension meter (*right side*)

Fig. 5 Borehole inclinometer and Borehole wire extension meter setting condition



accumulates. In order to decide the installation depth of each sensor, measurement the deformation of borehole at each depth by manual (Fig. 5).

4.5 Borehole Wire Extension Meter

The borehole inclinometer is useful to measure the small deformation, but it becomes impossible to measure when the accumulated deformation exceed the range of sensor. The large displacement can be measured by the borehole extension meter which is installed previously. The borehole extension meter measures the distance between ground surface and anchor which was attached borehole casing at underground. In this landslide, the two anchors were attached on 30 m depth and 80 m depth and the underground displacement was measured.

4.6 Rainfall, Groundwater Observation and Others

Rainfall and groundwater observation is important for landslide induced heavy rain. The tipping-bucket rain gauge is installed on BHH. The groundwater condition is monitored using

pressure gauge at two depth in the borehole. The groundwater at bottom of weathered soil layer (GL-47.4–GL-51.4 m) and shallow part of soil layer (from GL-4 to GL-30 m depth) are monitored.

IP cameras were installed on the area in order to observe the slope situation from far site when the sensor data show the indication of landslide phenomena (Fig. 6).

4.7 Data Collecting System

The information of observed data is needed to share by the authorities concerned the landslide risk in short time. The data collection system was developed (Takimoto et al. 2014). The output of each sensor with different communication type was converted into TCP/IP communication protocol. Therefore, all sensors were able to be controlled from one PC. All sensor data is collected observation station (TSH), it is sent to the database server at ITST office in Hanoi.

Web-based monitoring software is developed to observe and analyse the data of the database. The users who has permission can access to observe and analyse from anywhere. The system has functions which is the observation of data

Fig. 6 Groundwater pressure gauge setting condition



and snapshot of landslide, status for maintenance of system and prediction of final slope failure by landslide activity for the early warning (Fig. 7).

The timing of final slope failure by landslide activity on this system is predicted with slope displacement. It is estimated by inversion index

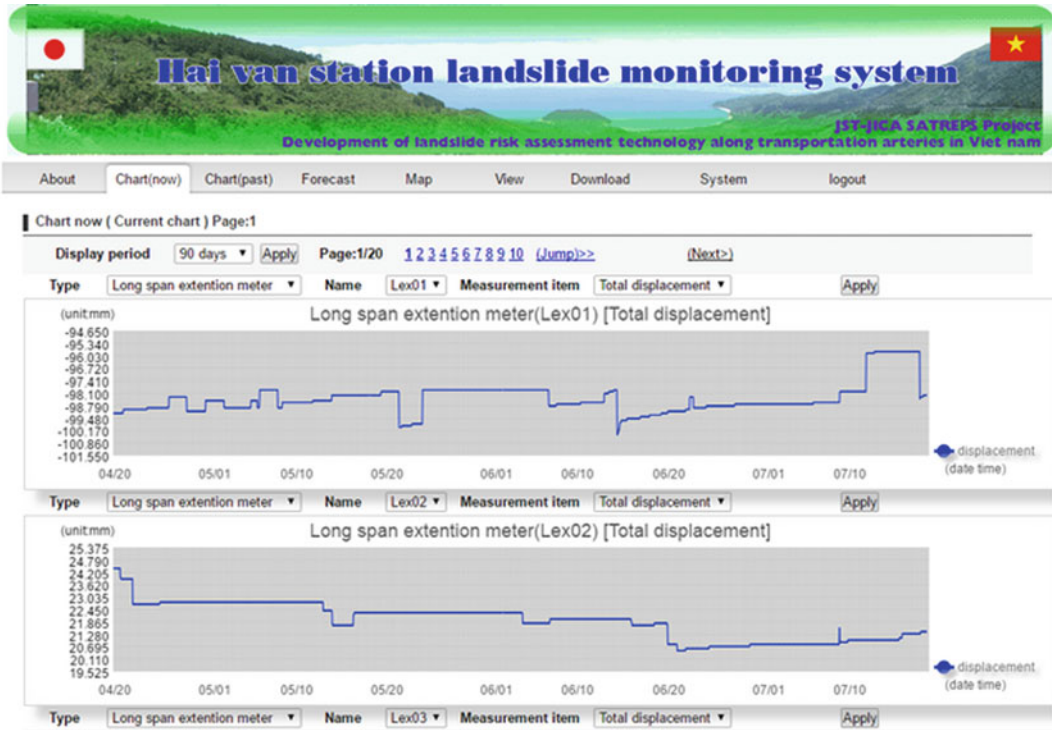


Fig. 7 Web-based monitoring software

of observed displacement velocity (Fukuzono 1985). It is simple way and easy to understanding. But it is needed that direct measured data of displacement can be collected and the tendency of increase at velocity is clearly for long time. Therefore, this prediction method in this system can be applied to the large-scale landslide which moves gradually for long time. The prediction of small and suddenly occurred landslide is difficult for early warning.

4.8 Improvement of Landslide Prediction

This monitoring system for early warning is initial system focused on the observation and clarification of landslide mechanism. It is needed to improve prediction accuracy of early warning of landslide disaster. It is need to consider about the influence of topology, geology and hydraulic condition on each landslide. In order to clarify the mechanism of each landslide, the equipment of landslide flume test was installed in ITST office in Hanoi (Ochiai et al. 2014). Using this flume test, the effect of topology, geology and hydraulic condition on the specific landslide will be clarified and the accuracy of landslide prediction will be improved. The monitoring system for early warning will be improved in the future.

5 Concluding Remarks

The monitoring system for early warning of landslide induced by heavy rain was developed. This system can be used for the landslide risk assessment of the specific landslide-prone slope which is large-scale and shows long-time landslide displacement. The surface and underground displacement and hydraulic condition in landslide-prone slope are observed and stored on database. All data can be monitored by related

organization using web. And it also has a function that the timing of final slope failure by landslide activity can be predicted with the slope displacement velocity. But the prediction is primary method and it need to improve by continuous studying as like considering the effect of the other item though the landslide flume test.

Acknowledgements This study have been obtained with the financial support from JST (Japan Science and Technology Agency)—JICA (Japan International Cooperation Agency) SATREPS (Science and Technology Research Partnership for Sustainable Development) program. We are grateful to the Ministry of Transport in Vietnam and local committee in Danang city for supporting. We want to express our appreciation to the Vietnam-Japan Engineering Consultants Co. Ltd. (VJEC) and Indochina Geotek Co. for installation work of the system. Authors want to thank for the kindness supporting of Mr. Do Ngoc Ha, Mr. Phan Duy Tho, Mr. Huynh Thanh Binh and other stuff in Institute of Transport Science and Technology (ITST) of Ministry of Transport in Vietnam and Japanese experts in this project; Dr. Osamu Nagai, Dr. Shinro Abe, Mr. Keisuke Takimoto, Dr. Masao Yamada, Mr. Akio Sato, Mr. Tatsuji Itayama, Mr. Ryo Miyazaki and Dr. Mitsuru Yamamura.

References

- Asano S, Abe S, Nagai O (2014) Development of landslide monitoring and data transfer system in the Hai van station landslide and the initial extensometer monitoring result behind the station. *Landslide risk assessment technology*. In: *Proceedings of SATREPS workshop on landslides*, pp 190–194
- Fukuzono T (1985) A method to predict the time of slope failure caused by rainfall using the inverse number of velocity of slope displacement. *J Jpn Landslide Soc* 22 (2):8–13 (In Japanese with English abstract)
- Ochiai H, Okada Y, Read ME, Sassa K (2014) Landslide experiments on natural slopes and indoor landslide flume tests by artificial rainfall. *Landslide risk assessment technology*. In: *Proceedings of SATREPS workshop on landslides*, pp 179–184
- Takimoto K, Asano S, Nagai O, Fukuoka H, Sassa K (2014) Development of integrated data and web-based analysis software for Vietnam. *Landslide risk assessment technology*. In: *Proceedings of SATREPS workshop on landslides*, pp 82–86

TXT-tool 4.081-1.1 Mechanism of Large-Scale Deep-Seated Landslides Induced by Rainfall on Gravitationally Deformed Slopes: A Case Study of the Kuridaira Landslide in the Kii Peninsula, Japan

Pham Van Tien, Kyoji Sassa, Kaoru Takara,
Hiroshi Fukuoka, Khang Dang, Tatsuya Shibasaki,
Hendy Setiawan, Nguyen Duc Ha and Le Hong Luong

Abstract

In September 2011, heavy rainfall brought by Typhoon Talas triggered 72 large-scale deep-seated landslides in Nara and Wakayama Prefectures, the Kii Peninsula, Japan. Most investigated landslides on the gravitationally deformed slopes were preceded by pre-existing small scarps along or near the head of the slopes. This study seeks to clarify the mechanism of the huge rainfall-induced Kuridaira landslide by simulating the increasing of pore water pressure with undrained high-stress dynamic loading ring shear apparatus. The authors also examined how gravitational deformations of upland slopes contribute to the mass movement under shear deformation. Laboratory experiments were conducted on two samples of the sliding plane taken in a site investigation, namely sandstone-dominated materials and shale materials. The pore water pressure control tests and shear

P. Van Tien (✉) · K. Takara · T. Shibasaki ·
H. Setiawan · N.D. Ha
Graduate School of Engineering, Disaster Prevention
Research Institute, Kyoto University, Kyoto, Japan
e-mail: phamtiengtvt@gmail.com

P. Van Tien · L.H. Luong
Institute of Transport Science and Technology,
Ministry of Transport, Hanoi, Vietnam

K. Sassa · K. Dang
International Consortium on Landslides, Kyoto,
Japan

K. Dang
VNU University of Science, Hanoi, Vietnam

H. Fukuoka
Research Institute for Natural Hazards and Disaster
Recovery, Niigata University, Niigata, Japan

displacement control tests clearly indicated that the rapid landslide was initiated due to high excess pore pressure generation and significantly shear strength reduction in the progress of shear displacement. The critical pore pressure ratio (r_u) was about from 0.33 to 0.36 while shear displacement at the starting point of failure (DL) had a threshold value ranging only from 2 to 6 mm. More specifically, the high mobility of the landslide was in tests on shale sample due to a significant loss of shear strength. In addition, the authors observed the landslide occurrence associated with the sliding surface liquefaction behavior for both samples. The evidence of liquefaction phenomena in the tests was in accordance with the findings in the field survey and previous studies.

Keywords

Deep-seated landslides • Gravitational deformed slopes
Ring shear apparatus • Rainfall • Kuridaira landslide • Kii peninsula

Contents

1	Introduction	794
1.1	Sediment-Related Disasters Induced by Typhoon Talas.....	794
1.2	A Literature Review of Research on the 2011 Disaster.....	795
2	Study Area	797
3	Site Survey and Soil Sampling	798
4	Results of Ring Shear Test and Discussions	800
4.1	Un-drained Monotonic Shear Stress Control Tests.....	800
4.2	Rainfall-Induced Landslide Simulation by Pore Water Pressure Control Tests.....	801
4.3	Undrained Shear Displacement Control Test...	803
4.4	Shear Strength Reduction in Progress of Shear Displacement and Sliding Surface Liquefaction	804
5	Conclusion	804
	References.....	805

1 Introduction

1.1 Sediment-Related Disasters Induced by Typhoon Talas

The Kii peninsula was extensively devastated by Typhoon Talas and sediment-related disasters in the period of 5 days from August 31 to September 4 in 2011. According to the Fire and Disaster Management Agency (FDMA 2012), the disasters not only claimed 98 casualties but

also led to 379 houses completely destroyed and 3159 houses partially destroyed. Slope failures occurred in 3000 locations with a total collapsed sediment volume estimated to be 100 million m³. There were 55 large deep-seated landslides and 17 landslide dam lakes were formed as the result of the blockages of river channels caused by slope movements in mountainous areas of Wakayama, Nara and Mie Prefectures. The Ministry of Land, Infrastructure, Transport and Tourism (MLIT) selected the five most hazardous landslide dams to take into account urgent measures due to a high risk of overflow and its failure, namely Kuridaira, Akatani, Kitamata and Nagatono reservoirs in the basin of Kumano river and Iya reservoir in the basin of Hiki river as seen in Fig. 1 (Hayashi et al. 2013; SABO 2013). In the 2011 event, heavy rainfall migrated from western to northern Japan that exceeded 1000 mm hit over a wide area the Kii Peninsula. The Japan Meteorological Agency (JMA) recorded a record-breaking heavy rainfall event of 1812.5 mm monitored at the rain gauge station of Kamikitayama village in Nara Prefecture between August 31 and September 4 (Fig. 2). The maximum 72 h rainfall was about 1600 mm and the maximum daily rainfall reached 661 mm on September 3.

Fig. 1 Location of the five biggest landslide dams in the Kii Peninsula

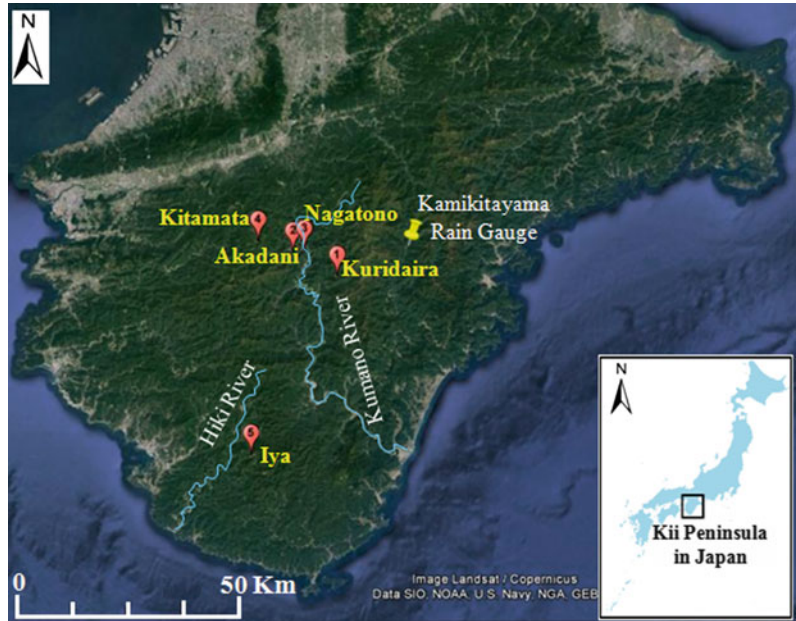
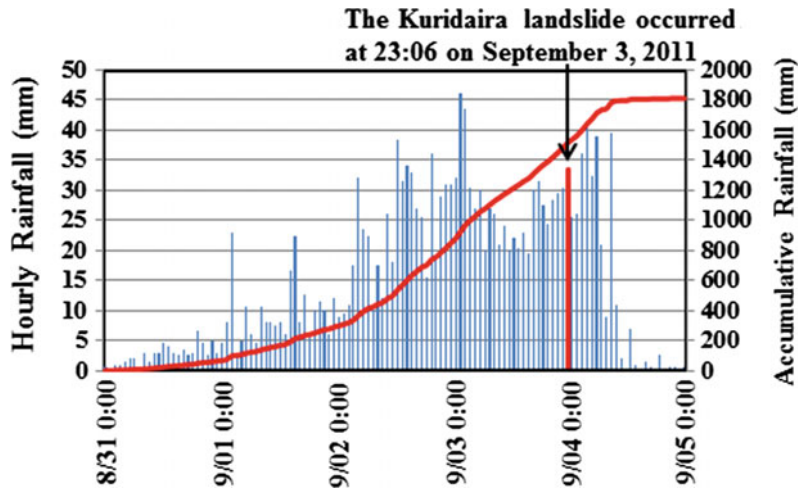


Fig. 2 Rainfall data at Kitayama Station during the period from 31 August to 4 September 2011 (Data by JMA)



1.2 A Literature Review of Research on the 2011 Disaster

The severe destruction caused by deep-seated catastrophic landslides in the Kii Peninsula attracted much attention to the society. In order to mitigate impacts induced by such disaster, researchers studied the involved processes and the mechanism of slope failures while others

carried out a risk assessment of secondary hazards such as upstream inundation, downstream flood, dam breach and overflow. Chigira et al. (2013) analyzed geological and geomorphological characteristics of the 14 deep-seated landslides through doing site observations and investigating aerial photos and DEM data in detail. The authors highlighted that the geologic factor and topographic setting have a significant

role in the formation of gravitational slope deformations that preceded the events. All identified landslides have either small scarps or linear depressions near the head of slopes prior to the events. These geological features created favourable conditions for a build-up of ground water table in the slopes. The precursor of deformed slopes gave an important marker to predict potential sites or future events. The geological and topographic features and its relation with large deep-seated landslides were reported in many case studies worldwide, namely the 2006 Leyte landslide in Philippines, the 2011 Shiaolin landslide in Taiwan, the 2005 catastrophic landslides induced by Typhoon NABI in Japan and destructive landslides in Canada (Chigira et al. 2013). Another geologic structure characteristic of deep-seated landslides in the Kii Peninsula is that almost landslides occurred on dip slopes along the north-dipping bedding/cleavage/fault planes, but it does not include a case of Kasugadani area (Kojima et al. 2015). In this research, 269 landslides were investigated to identify the movement direction as N-NNE, the study's findings inferred that future landslides are thus likely to occur on north-facing slopes. With reference to past events and basing on micro-topography and other topography-related factors as well as geological and topographical features of slopes, a map for evaluating the susceptibility and potential sites of deep-seated landslides in the Kii Peninsula was created for disaster mitigation and preparedness (SABO 2012).

Debris flows and landslides temporarily or permanently blocking river courses by mass movements continuously pose secondary hazards of overtopping or dam failures. Taking into account these issues Wang et al. (2014) and Okeke et al. (2016) have, studied the mechanism of piping-induced collapse and hydro-mechanical behavior of the Akatani and Kuridaira dams. The authors conducted both on-site behavior measurements of the dams using the micro-tremor chain array survey method and an experimental investigation in the laboratory by building dam models using different samples taken at landslide

sites. Results from those research represented that (1) there was an underground movement of water in the drainage pipe installed after dam formations by detecting some concentric holes beneath ground surface of the Akatani dam; (2) an increment in soil density and homogeneity of the dam materials might reduce the potential to form a successive piping hole through the dams; (3) and the probability for piping and progressive formation of the piping hole through the earth dams would be increased with a percentage growth of fines and a decrease in hydraulic conductivity. These studies brought an in-depth awareness to propose appropriate measures to disaster mitigation and prevention.

In order to investigate the mechanism and physically soil properties of Kii landslides, Kinoshita et al. (2013) conducted some laboratory experiments under small stress conditions on samples of the slickenside coupled with geological investigation on sites. These study results expressed that excess pore water pressure generated under a shear displacement has a significant role to initiate the landslide. Besides, the strata of the large deep-seated landslides consisting of heavily weathered cracked bedrock and their sliding surface in subparallel to the bedding planes was recognized in the research.

Taking a look at previous studies, most of them emphasize on geological, morphological and hydrological viewpoints on which mechanism of deep-seated catastrophic landslides quite depends. The studies mentioned above have significant contributions to the prediction of areas prone to deep-seated landslides based the evidences or precursors of its geology and topography. Although Kinoshita et al. (2013) carried out testing to measure physical and mechanical properties of materials constituting the sliding zone, the research still has a lack of understanding in the processes involved rainfall-induced landslides and the mechanism of the deep-seated landslides. Because the capacity of the simulation devices has some limitations, laboratory experiments for studying Kii landslides have only conducted at shallow depths and the reproduction of rainfall-induced landslides

have not carried out as well. Therefore, this study aims to investigate and interpret the mechanism of the deep-seated Kuridaira landslide through a series of tests by using the undrained high-stress dynamic loading ring shear apparatus. The study findings will give an insight into the failure mechanism of landslides on the gravitationally deformed slopes such as in the Kii Peninsula.

2 Study Area

This study solves the mechanism of the deep-seated landslide induced by Typhoon Talas in Kuridaira valley, Totsukawa Village, Nara Prefecture where the geology setting is located in the Miyama Formation, Hidakagawa Group of the Cretaceous Accretionary Complex (Geological Survey of Japan 1998). The landslide

occurred on September 3, 2011, which formed the largest dam of 100 m in height with a water storage capacity of 7.5 million m³ in a large basin area approximately 8.7 km² (SABO 2013). The landslide was about 800 m in length and 600 m in width. The collapsed sediment calculated from DEM data of the ground surface before 2011 and the sliding surface after the failure in September 2011 was 23.0 million m³ approximately. The landslide occurred from the crest of the steep slope and the debris flow rushed the opposite valley, and then dammed the river course and formed a natural reservoir in the upstream region. Figure 3a, b present a google earth's image and an aerial photo of the Kuridaira slope before and after the sliding, respectively. The geological plan and a cross section (A–A) of the landslide created by the Kii Mountain District Sabo Office in 2014 were redrawn as shown in Fig. 3c, d

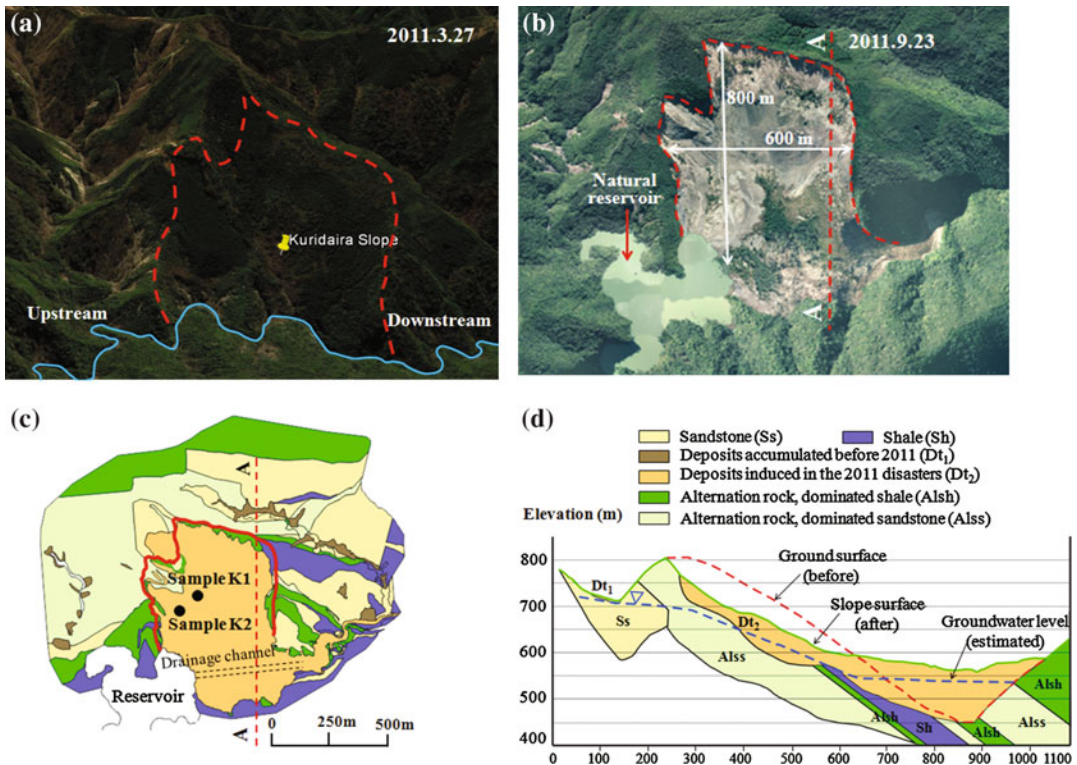


Fig. 3 Kuridaira area before the event by the Google Earth (a), an aerial photo of the landslide (b), and the geological plan (c) and a cross section A–A (d) of the landslide (created by the Kii Mountain District Sabo Office)

(SABO 2014). The geology of the landslide mainly consists of alternative layers of sandstone and shale (Fig. 3c). The maximum depth of the sliding surface that was estimated from DEM data before and after the sliding) reached over 100 m (Fig. 3d).

3 Site Survey and Soil Sampling

In this study, a site survey was carried out in the some large deep-seated landslides around Totukawa village, the Kii Peninsula, Nara Prefecture, namely landslide dams of Nagatono, Shimizu, Kuridaira and Akatani. The geological structure characteristics formed in the accretionary

processes in the Kii Peninsula reported by Chigira et al. (2013) were observed in the landslide sites, including interbedded structures, northwest dip-slip faults, wedge-shaped discontinuities, and broken formations and mixed blocks as well. The collapsed materials of these clastic sedimentary rocks consist of siliceous shale, sandstone, mudstone, alternation of sandstone and shale dominantly (Fig. 3c). The Kuridaira landslide occurred on northwest-facing slope with the undulatory sliding surface being subparallel to the bedding plane. The fractured wedge-shaped blocks (Fig. 4a) exposed at many outcrops within the landslide body, which dominantly controlled the failure pattern and the shape of the sliding surface (Fig. 4b). Under a high stress of the sliding mass,

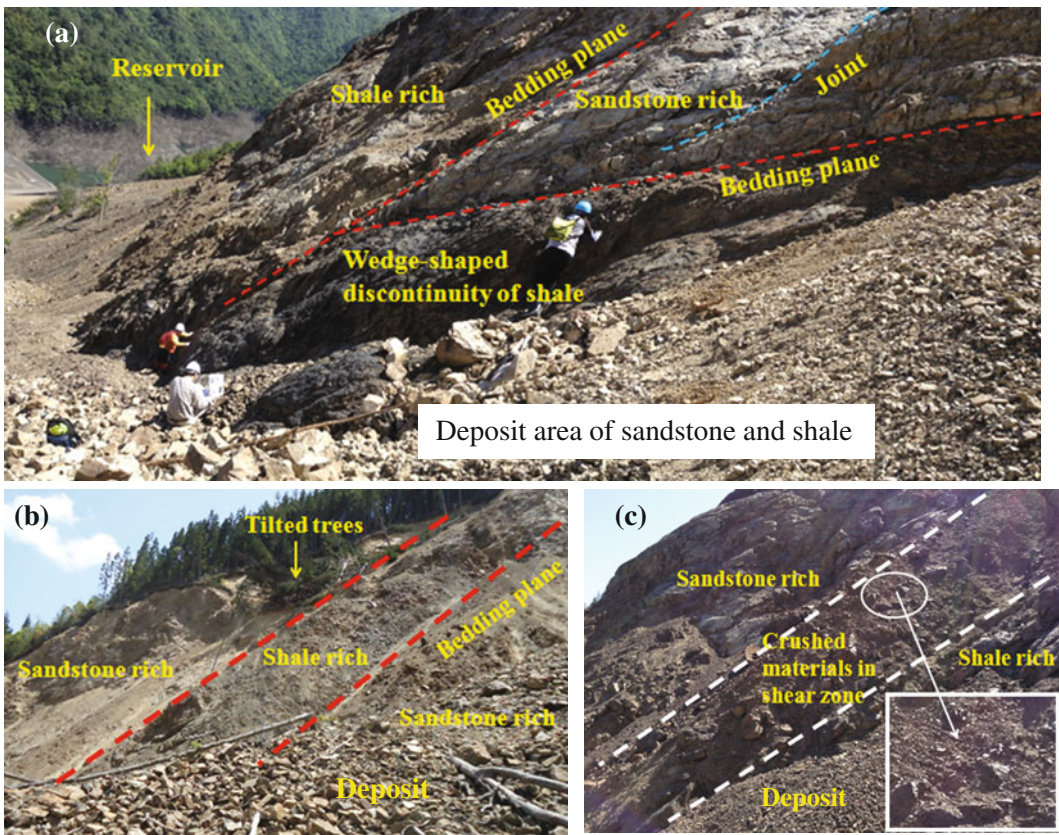


Fig. 4 Undulatory sliding surface and fractured wedge-shaped discontinuities near to the head scarp (a), the interbedded layer of shale and sandstone on the right flank of the landslide (b), and crushed materials at the sliding zone closed to the head scarp (c)

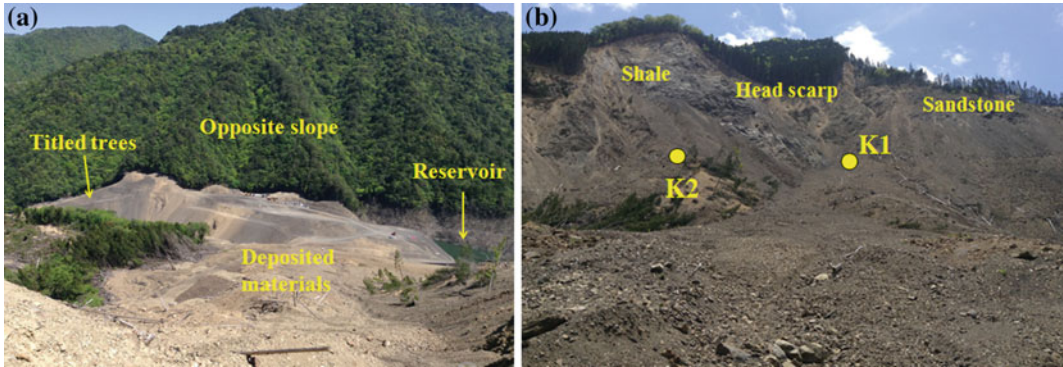


Fig. 5 The toe of the landslide viewed from the main head scarp (a) and locations of soil sampling (b)

materials along the sliding surface were subjected to grain crushing and liquefaction phenomena during motion (Fig. 4c). The wedge-shaped blocks and fractured fault zones existed beneath the slope are a potential condition for the build-up of pore water pressure that was the main trigger of the landslides (Chigira et al. 2013). Since rain-water could easily percolate deeply into the slope through fractured formations and fissures and this process resulted in increasing of groundwater level. The collapsed sediments moved from the upper slope and deposited at the opposite valley (Fig. 5a).

The landslide mechanism is mainly controlled by the nature of the materials of the

potential sliding surface. In the survey, the mixed sample of sandstone and shale materials and the shale sample of the sliding zone were taken to further study the landslide mechanism, namely sandstone-dominated material sample (henceforth Sample K1) and fractured shale rock sample (Sample K2). Sample K1 contains a small part of clay-size materials and it is finer than Sample K2. Sample K2 is produced from broken and fragmented rocks of shale of which grain sizes are small and much angular. Locations of soil sampling are depicted on Figs. 3c and 5b. The photo of soil samples and its grain-sized distribution are denoted in Fig. 6.

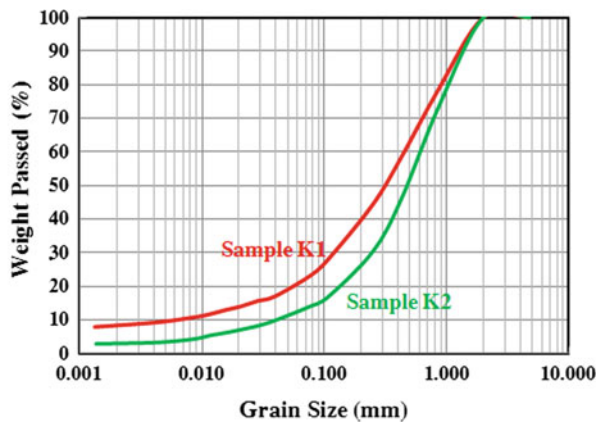
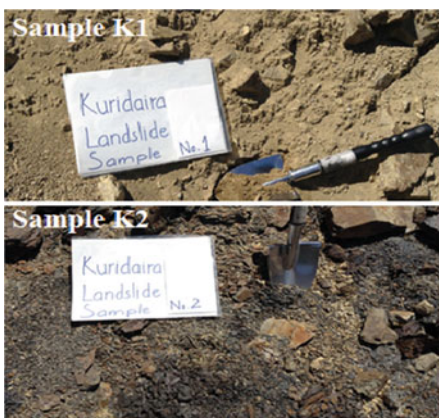


Fig. 6 Photos of two samples (left) and its grain-size distribution (right)

4 Results of Ring Shear Test and Discussions

The undrained high-stress dynamic loading ring shear apparatus ICL-2 with a high capability to keep the undrained condition up to 3.0 Mpa was employed for doing tests on two samples. Testing procedure mainly consists of the following steps: sample saturating, sample setting; saturation checking by measurement of the pore pressure parameter ($B_D = \Delta u / \Delta \sigma$), sample consolidation and shearing (Sassa et al. 2014). For laboratory experiments, the most important thing is that all undrained tests were usually performed on fully saturated samples with the degree of saturation $B_D \geq 0.95$ (Sassa et al. 2004).

In this study, we conducted three types of tests: undrained shear stress control tests (USCT), pore water pressure control tests, and undrained shear displacement control tests (USDT). The initial stress state of samples due to gravity is calculated from the depth of the sliding surface, slope angle and unit weight of the samples. The unit weight of the soil samples calculated from laboratory tests is 20.1 kN/m^3 approximately. The angle of the Kuridaira slope is 31° . Considering to the sliding depth, we used initial normal stress of 1000 kPa for all tests, it corresponds to about 60 m depth of the sliding surface. After the consolidation, shearing was

applied by operating stress control modes. The initiation and motion mechanism of the landslide was observed while pore water pressure generation and shear strength reduction were monitored during the test.

4.1 Un-drained Monotonic Shear Stress Control Tests

Firstly, undrained shear stress control tests are performed to measure some basic parameters of soil samples such as the friction angle at peak and during motion, shear resistance at the steady state or apparent friction angle. In these tests, saturated samples to $B_D = 0.96$ were consolidated to 1000 kPa and then sheared by monotonic shear stress control with an increment of 2 kPa/s. The shearing was stopped when shear displacement reached 10 m for all tests. Figures 7a and 8a present the effective stress path in red color and the total stress path in black color. In these tests, pore water pressure generation, shear strength reduction in progress with shear displacement and time series data are plotted in Figs. 7b and 8b.

As can be seen in Figs. 7 and 8, the failures appeared at a point where stress path reached the failure line and then it moved down along the failure line to the steady state stress point. The peak friction angle (φ_p) of Sample K1 and

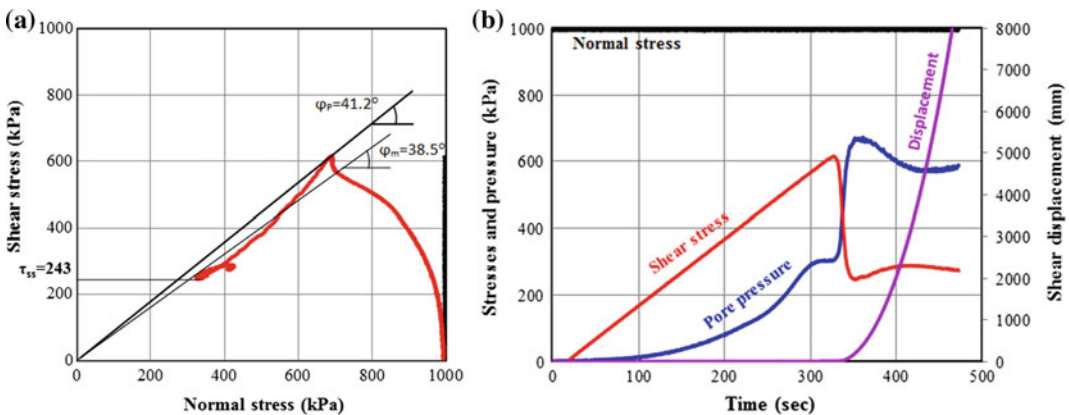


Fig. 7 Effective stress path (a) and time series data (b) of shear stress control test of Sample K1

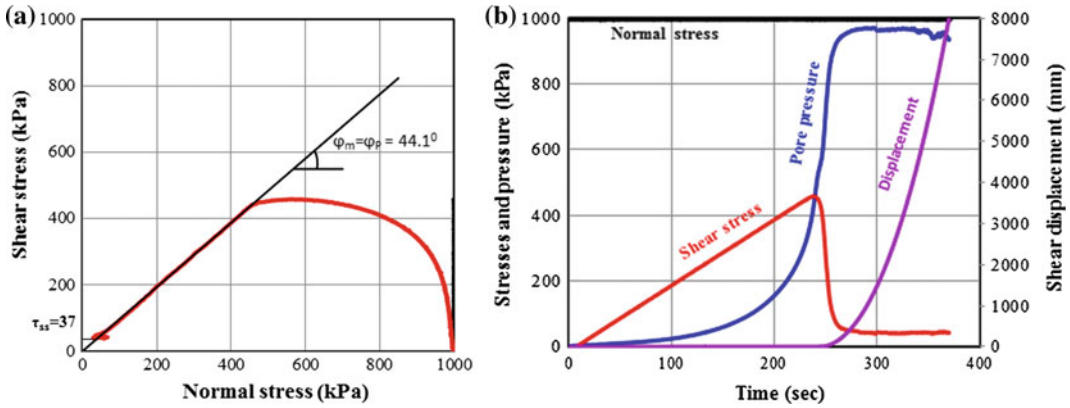


Fig. 8 Effective stress path (a) and time series data (b) of shear stress control test of Sample K2

Sample K2 are 41.2° and 44.1° , respectively. Since the generation of pore pressure strongly depends on characteristics and type of soil samples, the pore pressure monitored at shear zone of two samples is very different with more excess pore water pressure produced in Sample K2 than that in Sample K1 during shearing. This led to a large reduction of shear resistance of Sample K2 than that of Sample K1. Consequently, the residual strength of Sample K2 is quite low at 37 kPa while the figure for Sample K1 is 243 kPa. Besides, a less pore water pressure from Sample K1 is possibly due to an insufficient monitoring of pore water pressure by transducers of the apparatus. The reason is that during shearing at a high stress, Sample K1 at shear zone became stiff materials with a low permeability (like mud or clay) which mostly filled up two annular metal filters inside the gutter where pore pressure transducers are installed. As a result, pore pressure monitoring that depends on the permeability of the sample and the equipment capability was not well in the test of such low permeable samples. In addition, there was a small amount of negative pore water pressure generated at post-failure stage of the test on Sample K1. This phenomenon is explained by the dilatant characteristic of dense samples along shearing zone due to landslide movement at a very high velocity. When the sample dilated, a small amount of pore water pressure dissipated in the shear zone.

4.2 Rainfall-Induced Landslide Simulation by Pore Water Pressure Control Tests

The deep-seated catastrophic Kuridaira landslide was induced by heavy rainfall derived from Typhoon Talas. The triggering mechanism of the landslide is explained as follows: The increment of groundwater level above the impermeable layer (bedrock) during rainstorms resulted in increasing of pore water pressure. This process gave a simultaneous rise in driving shear stress of the sliding surface materials, and the failure then occurred at a critical value of pore water pressure due to a significant decrease in the effective stress. In this research, pore pressure control tests were conducted to simulate the failure and post-failure behaviour of the Kuridaira landslide corresponding to the rise of groundwater level during rainfall in the drained condition. To do this, both samples of the sliding surface were saturated ($B_D = 0.95$) and consolidated to 1000 kPa of normal stress and 600 kPa of shear stress corresponding to the initial stress condition of the slope in the drained condition. Then, in order to replicate pore pressure acting on a soil mass at the sliding surface, pore water pressure was increased gradually at the rate of 1 kPa/s until the failure for all tests. Test results of the Kuridaira samples are depicted in Figs. 9 and 10 with time series data (a) and the stress path (b) including the effective stress path in red color

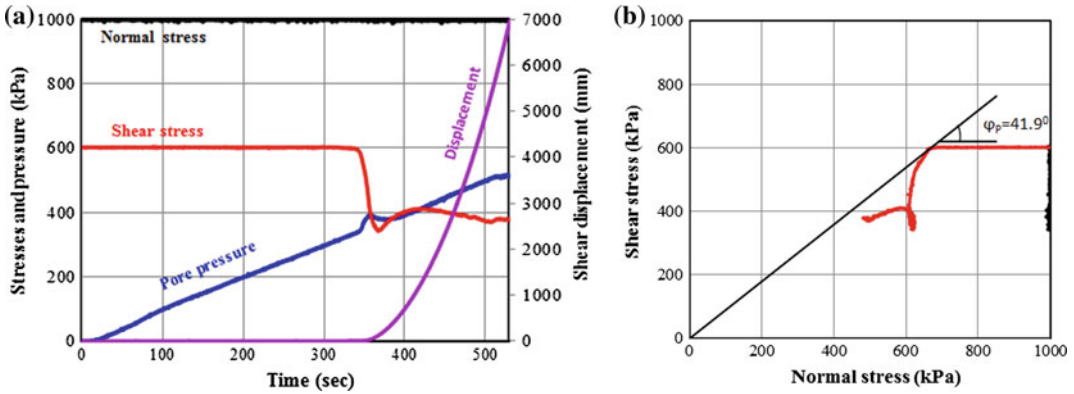


Fig. 9 Test results of rainfall-induced landslide conducted on Sample K1

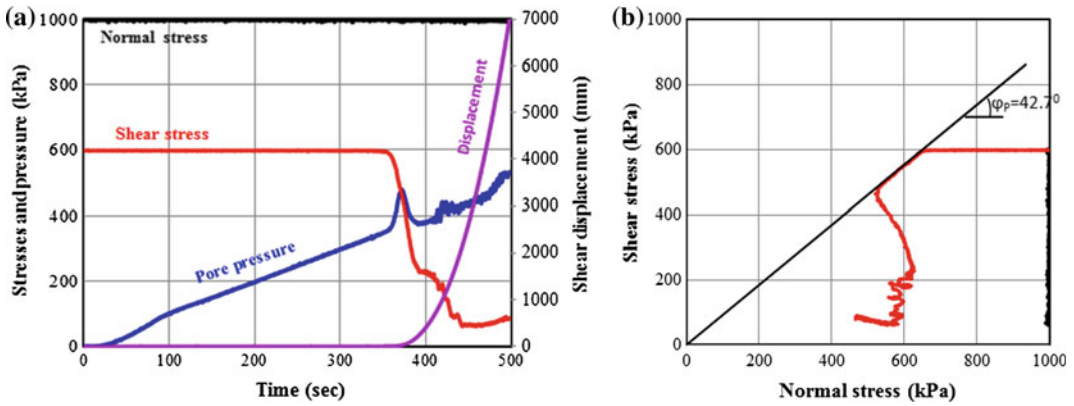


Fig. 10 Test results of rainfall-induced landslide conducted on Sample K2

and the total stress path in black color, respectively. In Figs. 9a and 10a, pore water pressure control signals are presented by blue color lines.

Landslides occurred when the effective stress path reached the failure line at the peak, i.e. 41.9° for Sample K1 and 42.7° for Sample K2. In detail, failures were triggered at a pore water pressure of 330 kPa for Sample K1 and about 360 kPa for Sample K2 that correspond to critical pore pressure ratios of $r_u = 0.33$ and $r_u = 0.36$ (r_u defines as a ratio of pore water pressure increment triggering failures and its normal stress). Soon after failures initiated, the sliding surface was formed due to shear displacement and grain crushing resulting in excess pore water pressure generation. At a large shear displacement, sliding surface liquefaction behaviour and

the post-failure motion were observed in all tests. Consequently, rapid landslides induced by rainfall taken place along the sliding plane at a large displacement. Sliding surface liquefaction (Sassa 2000) presents the behavior of shearing zone account of grain crushing of samples resulting in volume reduction. In this progressive failure process, a much pore water pressure generated while shear resistance quickly reduced in the progress of shear displacement. One thing noted in these simulations is that there was also the occurrence of negative pore water pressure after failures because of both dilatant and contractive behaviour of two samples under high stress conditions. This is one of a typical feature of sliding surface liquefaction of the Kuridaira samples.

4.3 Undrained Shear Displacement Control Test

In this study, a shear displacement control test was conducted on Sample K1 for understanding the mechanism of landslide induced under a given shear displacement. After the saturated sample was consolidated to 1000 kPa of normal stress in the drained condition, the test by shearing was started under a constant velocity of shear displacement of 0.01 cm/s in the undrained condition. During the simulation, pore pressure change, shear strength reduction in progress of shear displacement increase during motion and post-failure were monitored in Fig. 11. As seen from the result, a rapid motion of the landslide was reproduced as so high pore water pressure generation. Similarly, the effective stress path (ESP) in red color and the total stress path (TSP) in blue color are depicted in Fig. 11a, while Fig. 11b describes the monitored test with time series data consisting of normal stress (a black color line), shear resistance mobilized on the sliding surface (a red color line), monitored pore pressure (a blue color line) and shear displacement (a green color line). In this test, the friction angle of the sample at peak friction angle

is 41.6° . The sample was sheared until 1000 mm of shear displacement at the steady state.

As mentioned in the introduction, the deep-seated Kuridaira landslide was preceded by a small gravitational deformation in several meters on the crest of the slope before failure. This important precursor was one of main contributing factors causing the disaster. On this point of view, the deformed slope allowed rainwaters to deeply infiltrate into the slope leading to groundwater level rise, so this make a suddenly reduction of the shear strength of slope materials. Besides, it is high possible that the gravitational deformation could act on the lower slope and/or certain areas of the potential sliding plane, which might create a small shear displacement along the sliding surface. Under the latter circumstance, as shear displacement reached a critical value (DL), excess pore water pressure was immediately generated and mainly responsible for the landslide. In short, it means that gravitational deformation of the crest of slopes did not only facilitate the build-up of pore water pressure triggering the landslide, but it could also create a small deformation and shear displacement at the potential sliding surface to provoke the progressive failure.

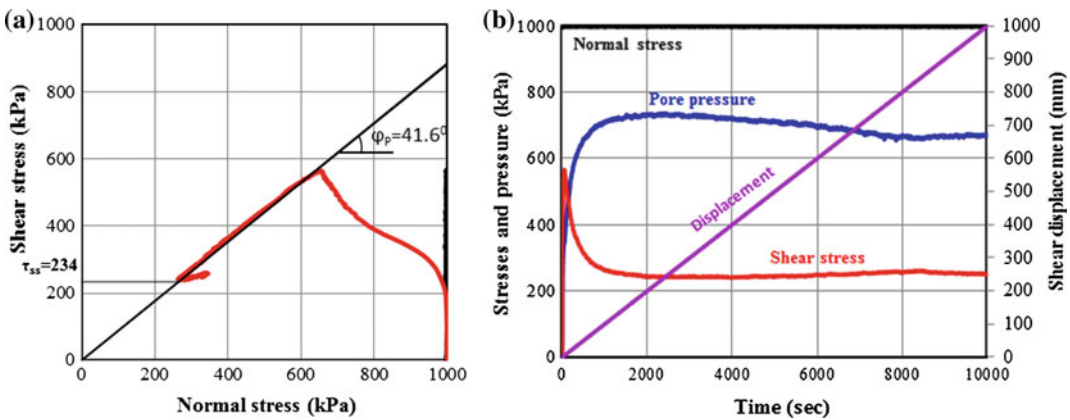


Fig. 11 Effective stress path (a) and time series data (b) of undrained shear displacement control test on saturated Sample K1 ($B_D = 0.96$)

4.4 Shear Strength Reduction in Progress of Shear Displacement and Sliding Surface Liquefaction

Shear strength reduction in progress of shear displacement is observed through undrained monotonic shear stress control tests for two samples and a shear displacement control test for Sample K1 (Fig. 12). In detail, ring shear tests indicated that landslides were triggered at a critical shear displacement (DL) at peak strength from 2 to 6 mm. To be specific, Sample K2 was weaker than Sample K1 in shear strength behaviour due to the fact that DL value of Sample K2 is only about 2 mm. Consequently, the residual strength at the steady state of Sample K2 is smaller than that value of Sample K1. So Sample K2 might be vulnerable to mobilize in a long traveling shear displacement. For Sample K1, shear resistance has a small increase during motion, but it decreased soon after the failure proceeded to the steady state.

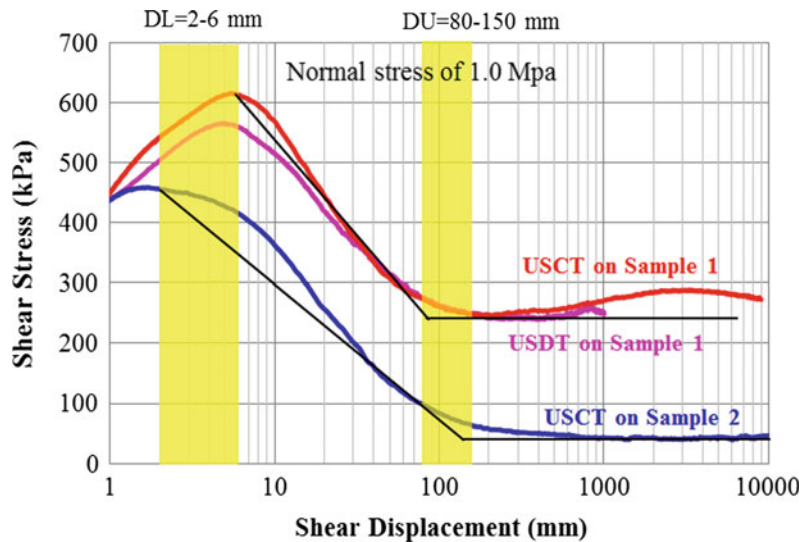
In all tests, liquefaction behavior along the sliding plane within shear zone was manifested as a key important characteristic of the Kuridaira landslide. This phenomenon was formed in shear

zone as the following explanation. First, grain crushing within the shear zone resulted in volume reduction of the samples. Immediately a high pore pressure and shear strength reduction occurred at which a rapid motion of landslide was produced in progressive shear displacement. Finally, a small negative pore water pressure was measured just after failure reached the steady state due to a dilative behavior of dense samples. The liquefaction phenomena led to a drop of the effective stress and the mobilized shear resistance. This is a typical sliding surface liquefaction characteristic for the Kuridaira landslide. The evidence of sliding surface liquefaction and crushed materials during tests of Sample K1 and Sample K2 is illustrated in Fig. 13a, b, respectively. This was agreed with findings in a site observation (Fig. 4b) and previous studies as well.

5 Conclusion

We carried out a detailed site investigation in the area of the Kuridaira dam to clarify the features of slope failures, especially to observe the sliding surface zone. All surveyed landslides have an

Fig. 12 Shear strength reduction in progress of shear displacement at 1000 kPa of normal stress



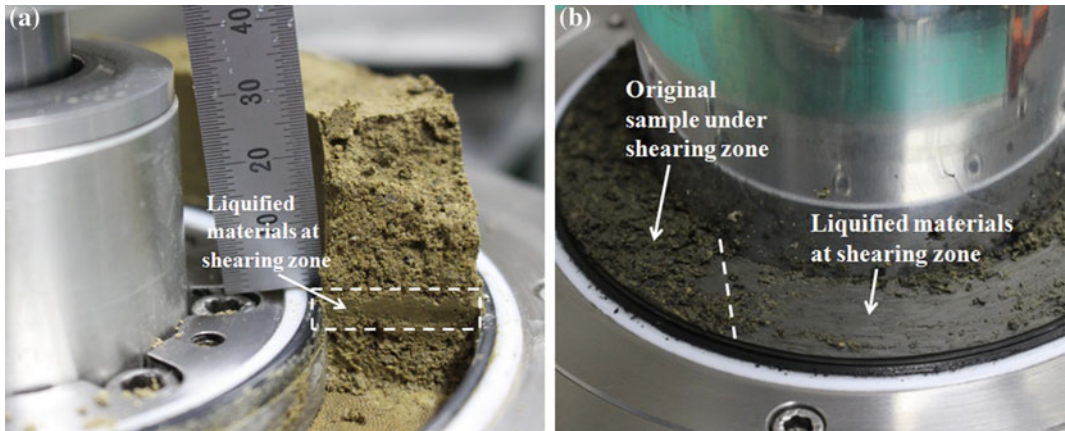


Fig. 13 Photographs show liquefied materials of Sample K1 (a) and Sample K2 (b) at the shear zone after testing

undulating sliding plane within layers of wedge-shaped blocks and fractured discontinuities of sandstone and shale. This geologic condition also characterizes the entire of the study area, which allows the groundwater and rainwater penetrate easily into slopes leading the build-up of pore water pressure as the main trigger of the events. Basically, failure characteristics of two different samples of the sliding surface are quite the same in undrained ring shear tests. Both samples were prone to a rapid landslide due to a liquefaction behavior at the sliding surface during shearing. On this feature, landslides were triggered due to a excess pore water pressure generation and a high shear resistance reduction of sliding surface materials in progress of progressive shear displacement. The high mobility of the rapid Kuridaira landslide was governed by the shear behavior of Sample K2 (shale materials) due to a significant shear strength reduction. Particularly, ring shear tests pointed out that landslides induced by rainfall with the critical pore pressure ratio of r_u from 0.33 to 0.36. Meantime, a shear displacement control test on Sample K1 described an excess pore water pressure generation in shear zone during motion and at post-failure. This important test interpreted the landslide mechanism due to excess pore water pressure resulted from a small amount of shear deformation along the sliding plane as gravitational slope deformation might

act on the sliding surface. Besides, test results revealed that the critical shear displacement (DL) of the sliding surface ranges from 2 to 6 mm under which the landslide initiated to move down. Understanding of the landslide mechanism of gravitationally deformed slopes through physical simulations has a significant importance for disaster mitigation and preparation in the future.

Acknowledgements Authors thank the Kii Mountain District Sabo Office, Ministry of Land, Infrastructure, Transport and Tourism (MLIT) for their assistance in doing the site survey. We specially thank Mr. HAYASHI, vice-director of the Kii Mountain District Sabo Office for offering us a number of relevant data including DEM data, drawings and reports. Furthermore, the authors are greatly grateful to Mr. OGAWAUCHI (senior engineers at Japan Conservation Engineers & CO., LTD.) for his cooperation and kindly supports during the field investigation and data collection. This research was financially supported by the research grant from a Leading Graduate School Program on Global Survivability Studies (GSS Program) in Kyoto University. We deeply acknowledge all these important supports during this study.

References

- Chigira M, Tsou C, Matsushi Y, Hiraishi N, Matsuzawa M (2013) Topographic precursors and geological structures of deep-seated catastrophic landslides caused by Typhoon Talas. *Geomorphology* 201:479–493
- FDMA (2012) Report No. 20 dated September 28, 2012 on the damage situation by Typhoon No. 12 in

- September, 2011. The Fire and Disaster Management Agency. Ministry of Internal Affairs and Communications, p 10 (in Japanese)
- Geological Survey of Japan (1998) Geological map of Wakayama NI-53-15 at the scale 1:200,000. <https://gbank.gsj.jp/geonavi/geonavi.php#9,34.312,136.006>
- Geospatial Information Authority of Japan (GSI) Website for DEM data before the landslide. <http://www.gsi.go.jp/>
- Hayashi SI, Uchida T, Okamoto A, Ishizuka T, Yamakoshi, T, Morita K (2013) Countermeasures against landslide dams caused by Typhoon Talas 2011. *Tech Monitor* 20–26
- Japan Meteorological Agency (JMA) Website for Rainfall data. <http://www.data.jma.go.jp/gmd/risk/obsdl/index.php>
- Kinoshita A, Ogawauchi Y, Mayumi T, Shibasaki T (2013) Geological factors of deep-seated catastrophic landslide and physical and mechanical properties of its sliding layer triggered by the heavy rainfall associated with Typhoon Talas T1112 in the Kii Peninsula. *J SABO* 66(3):3–12
- Kojima S, Nagata H, Yamashiroya S, Iwamoto N, Ohtan T (2015) Large deep-seated landslides controlled by geologic structures: prehistoric and modern examples in a jurassic subduction–accretion complex on the Kii Peninsula, central Japan. *Eng Geol* 186:44–56
- Okeke AC, Wang F (2016) Hydro-mechanical constraints on piping failure of landslide dams: an experimental investigation. *Geoenviron Disasters* 3:4
- SABO (2012) Press release dated September 10, 2012, on survey of deep catastrophic landslides at the stream (small watershed) level. Division of the River Bureau, The Ministry of Land, Infrastructure, Transport and Tourism, and the Public Works Research Institute. http://www.mlit.go.jp/report/press/mizukokudo03_hh_000552.html (in Japanese)
- SABO (2013) A Pamphlet released in October, 2013 on overview of the 2011 disaster induced by Typhoon No. 12, implementation of an urgent investigation and countermeasures to disaster areas. Kii Mountain District SABO Office, Kinki Regional Development Bureau. The Ministry of Land, Infrastructure, Transport and Tourism (MLIT). <http://www.kkr.mlit.go.jp/kiisanchi/outline/> (in Japanese)
- SABO (2014) A PDF document dated in July, 2014 on Deep-seated landslides occurred during Typhoon No. 12 in September 2011 in Kuridaira area. The Kii Mountain District SABO Office, Kinki Regional Development Bureau. The Ministry of Land, Infrastructure, Transport and Tourism, p 8 (in Japanese)
- Sassa K (2000) Mechanism of flows in granular soils. In: *Proceedings of GeoEng2000*, Melbourne, vol 1, pp 1671–1702
- Sassa K, Fukuoka H, Wang G, Ishikawa N (2004) Un-drained dynamic loading ring shear apparatus and its application to landslide dynamics. *Landslides* 1 (1):7–19
- Sassa K, He B, Khang D, Nagai O, Takara K (2014) Plenary: progress in landslide dynamic. In: *Landslide science for a safer geoenvironment*, vol 1, pp 37–67
- Wang F, Hayashi H, Okeke AC, Mitani Y, Yang H, Kuwada Y, Baba S (2014) Using microtremor array survey to evaluate the possibility of piping-induced landslide dam failure. *Landslide Sci Safer Geoenviron* 3:649–657

TXT-tool 4.081-9.1

Rotary Sampling Drilling Technology to Extract High-Quality Cores Using a Sleeve-Incorporating Core Barrel and Polymer Mud in Landslide Areas of Japan and Vietnam

Shinro Abe, Norio Sato, Dinh Van Tien, Do Ngoc Ha,
Le Ngoc An and Luu Xuan Khoat

Abstract

In many cases, cores that are extracted from landslide areas contain loose, moving land blocks and crushed rock that differ from their in situ state because of disturbance at the time of drilling. Therefore, it is difficult to obtain much of the information required for analysis of landslide mechanisms. In recent years, a rotary drilling technology in which a core barrel incorporating a plastic film and diamond bit has been used in Japanese landslide areas, along with polymer mud as the drilling fluid. This drilling technology is effective in maintaining the core hole wall in soft layers, such as gravel mixed with soil, and has made it possible to eliminate cutting in many cases. As a result, it has become possible to extract high-quality cores from depths of 200 m or more in landslide areas and to obtain the information needed to analyze landslide mechanisms, such as the slide surface and the record of landslide movements and activity, as well as the geological features, during the initial stage of investigation. We studied the feasibility of this drilling method, which is highly dependent on the experience and judgment of veteran drilling engineers, the adaptability of the method to landslide areas other than those in Japan, and the economic efficiency of the method in comparison to the conventional drilling method.

Keywords

Landslide research drilling · Drilling method · High-quality drilling core · Core barrel · Polymer mud

S. Abe (✉)
Okuyama Boring Co., Ltd., Yokote-shi, Akita, Japan
e-mail: abeshinro@gmail.com

N. Sato
Nasu Construction Co., Ltd., Yamagata, Japan

D. Van Tien · D.N. Ha
Ministry of Transport, Institute of Transport Science
and Technology, Hanoi, Vietnam

L.N. An
Vietnam Japan Engineering Consultants Co., Ltd.,
Hanoi, Vietnam

L.X. Khoat
Indochina Geotechnics JSC, Hanoi, Vietnam

Contents

1	Introduction	808
2	Outline of Rotary Sampling Drilling Method Using a Sleeve-Incorporating Core Barrel, Diamond Bit, and Polymer Mud (SP Method)	808
2.1	Sleeve-Incorporating Core Barrel.....	808
2.2	Polymer Mud as Drilling Fluids	809
2.3	Comparison of Cores Obtained by SP Method and Conventional Drilling Method	810
3	Drilling Cases by SP Method in Hai Van Landslide of Vietnam	812
4	Discussion	813
5	Conclusions	816
	References.....	817

1 Introduction

Cores obtained by research drilling in landslide areas are important sources of information on landslide movement, landslide activity, and groundwater behavior, in addition to information on the geological features and slide surfaces of landslide areas. This information is important at the initial stage of landslide research. Landslide disasters in particular create pressing needs for emergency response measures that need to be taken without waiting for measurements by various types of instruments, and in such situations, assessments based on cores become especially important. However, research drilling in landslide areas involves considerable work that is inconvenient to perform, including transporting equipment on mountainous slopes. In many cases, researchers have no choice but to drill through mixed gravel–sand layers, clay layers, and crushed rock that are specific to the landslide area using compact drilling machines. As drilling through such layers is prone to problems, such as collapse of borehole walls, falling of cores, and difficulties in inserting casing, large quantities of cutting deposits and advanced technologies are required (Eugene and Warren 1989; Austin 1983). Additionally, in many cases, as research drilling for landslides is conducted in

combination with groundwater surveying, it is subject to more restrictions than typical survey drilling, due to the necessity to refrain from using bentonite mud as the drilling fluid. As cores are extracted in a disturbed state under such conditions, in many cases, it is difficult to obtain the required landslide information.

In recent years, along with the development of core barrels and drilling fluids, rotary sampling drilling technologies have been drawing attention for use in research on landslide and active faults. Drilling methods in which sleeve-incorporating double core barrels (hereinafter referred to as sleeve-incorporating core barrels) and diamond bits, in combination with the use of polymer mud as the drilling fluid (referred to hereinafter as SP methods), have been developed and improved since the 1980s and have become known for being able to obtain high-quality cores comparatively economically and without any special equipment. In this paper, we describe the characteristics of this method, such as its feasibility, economic efficiency, adaptability to other regions, and associated problems, based on application in drilling cases and comparison with conventional drilling methods.

2 Outline of Rotary Sampling Drilling Method Using a Sleeve-Incorporating Core Barrel, Diamond Bit, and Polymer Mud (SP Method)

2.1 Sleeve-Incorporating Core Barrel

Drilling through gravel–sand mixtures and crushed rock tends to cause various types of problems that require relatively more sophisticated drilling and sampling methods than those used for hard bedrock. In recent years, development of core barrels has advanced to facilitate extraction of high-quality loose cores in less disturbed states (Tani et al. 2004). One such type of barrel is a sleeve-incorporating core barrel that is equipped with a thin bag-shaped plastic film within an inner tube in a double core barrel that extracts a core while wrapping it. This type of

core barrel has been developed since approximately 1980 (Fig. 1) and has come to be used in landslide areas. Figure 2 shows a comparison of cores obtained using different types of core barrels, including a sleeve-incorporating core barrel, during drilling in the landslide area of Ha Long in the northern part of Vietnam. Among the core barrel types compared were the types of single-tube and double-tube core barrels that are commonly used, sleeve-incorporating core barrels that are made in China and used in Vietnam, and sleeve-incorporating core barrels that are made in Japan. The drilling machine was made in China, and the sleeve-incorporating core barrel was attached by a reducer. The same operator conducted three drillings on the same slope over a distance of approximately 50 m using fresh water as the drilling fluid. The site was characterized by alternating beds of sandstone and mudstone formed during the Mesozoic Era. The drilling results clearly show that the core

recovery rate was highest for the sleeve-incorporating core barrels, followed by the double-tube core barrel and the single-tube core barrel. In Japan, most landslide research drilling is currently conducted using this type of sleeve-incorporating core barrel with fresh water as the drilling fluid. This method is referred to hereinafter as the “conventional drilling method”.

2.2 Polymer Mud as Drilling Fluids

In most survey drilling in landslide areas in Japan, fresh water has been used as the drilling fluid. The use of polymer mud has developed in association with oil drilling in the USA and Canada since the late 1970s to maintain borehole walls through elimination of cutting and retention of hole walls, coating of core surfaces, and reduction of friction between samplers and cores (Chilingarian and Vorabutr 1983; Okino 1981,

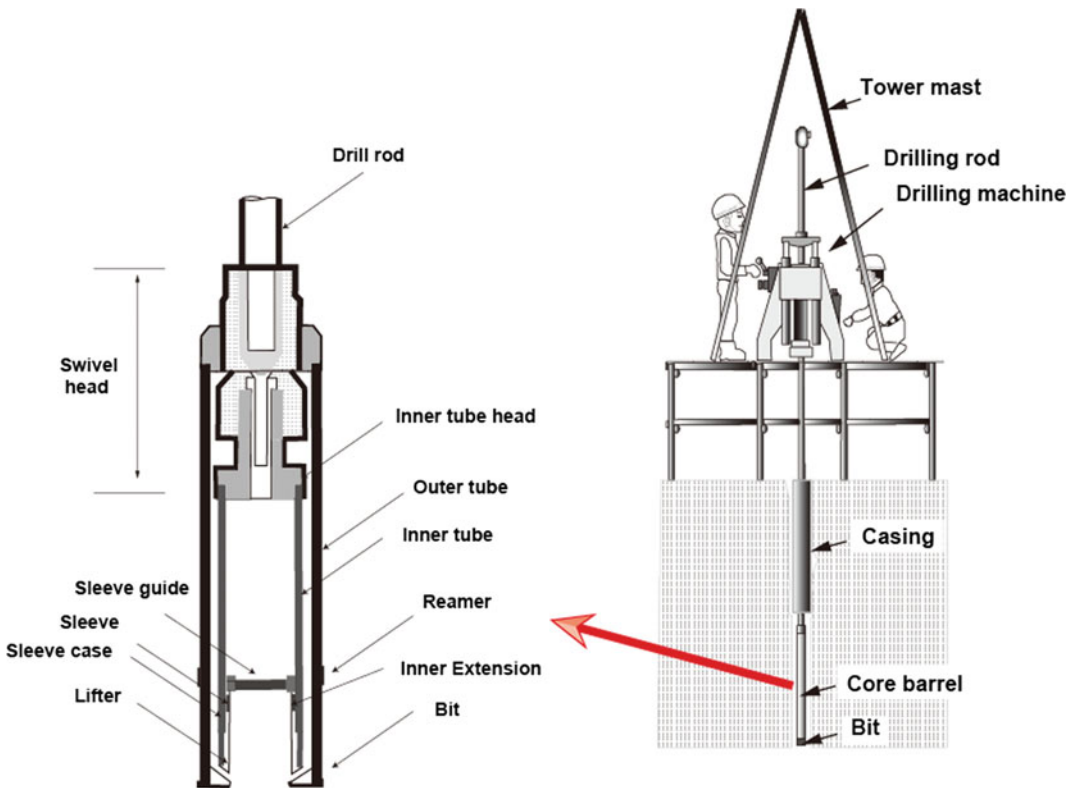


Fig. 1 Sleeve-incorporating core barrel

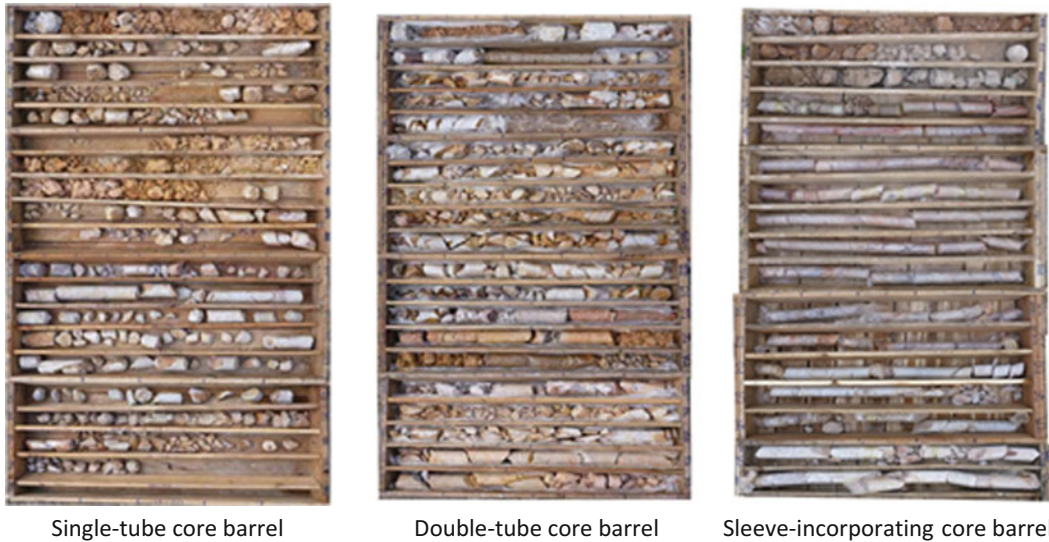


Fig. 2 Comparison of cores obtained with different types of core barrels. All the partitions are 1 m, and the overall length is 20 m

1989; Steiger 1982). Air bubble generation by mixing of surface-active agents, water, and air has also been used (Takeda and Komiya 2005; Chilingarian and Vorabutr 1983). This latter method requires an air bubble generation apparatus and a device for drilling at or below the groundwater level. The drilling core diameter used with this method is slightly larger than that used with polymer mud. On the other hand, when the SP method is used with polymer mud as the drilling fluid, although the success of the drilling depends on the experience and judgment of the drilling operator with respect to the geological features of the site, no special equipment is required.

2.3 Comparison of Cores Obtained by SP Method and Conventional Drilling Method

Figure 3 shows a comparison of drilling core obtained by the conventional drilling method and the SP method within a large-scale landslide area within a Quaternary volcanic area in Japan.

Both borehole depths were approximately 150 m. While there are some differences between the cores in the location of the boundary between Quaternary volcanic detritus and Neogene sedimentary rock, the cores reflect almost the same geological features. It is clear that in the DH-B core hole there are fewer mixtures than in the DH-A hole. In particular, andesite gravel, sand, and clay from Quaternary volcanic detritus were extracted without separation and with their underground deposition characteristics retained in a high-quality state. Most of the other drilling cores obtained from this landslide area exhibited clear differences in quality due to the differences between the drilling methods used. Approximately 100 drillings have been conducted in this landslide area for research purposes between approximately 2005 and the present, of which 40 have been to depths of 100 m and the deepest has been to a depth of 250 m. Until approximately 2008, the conventional drilling method was used as the main drilling method. Since approximately 2013, most of the drilling in this area has been conducted using the SP method.

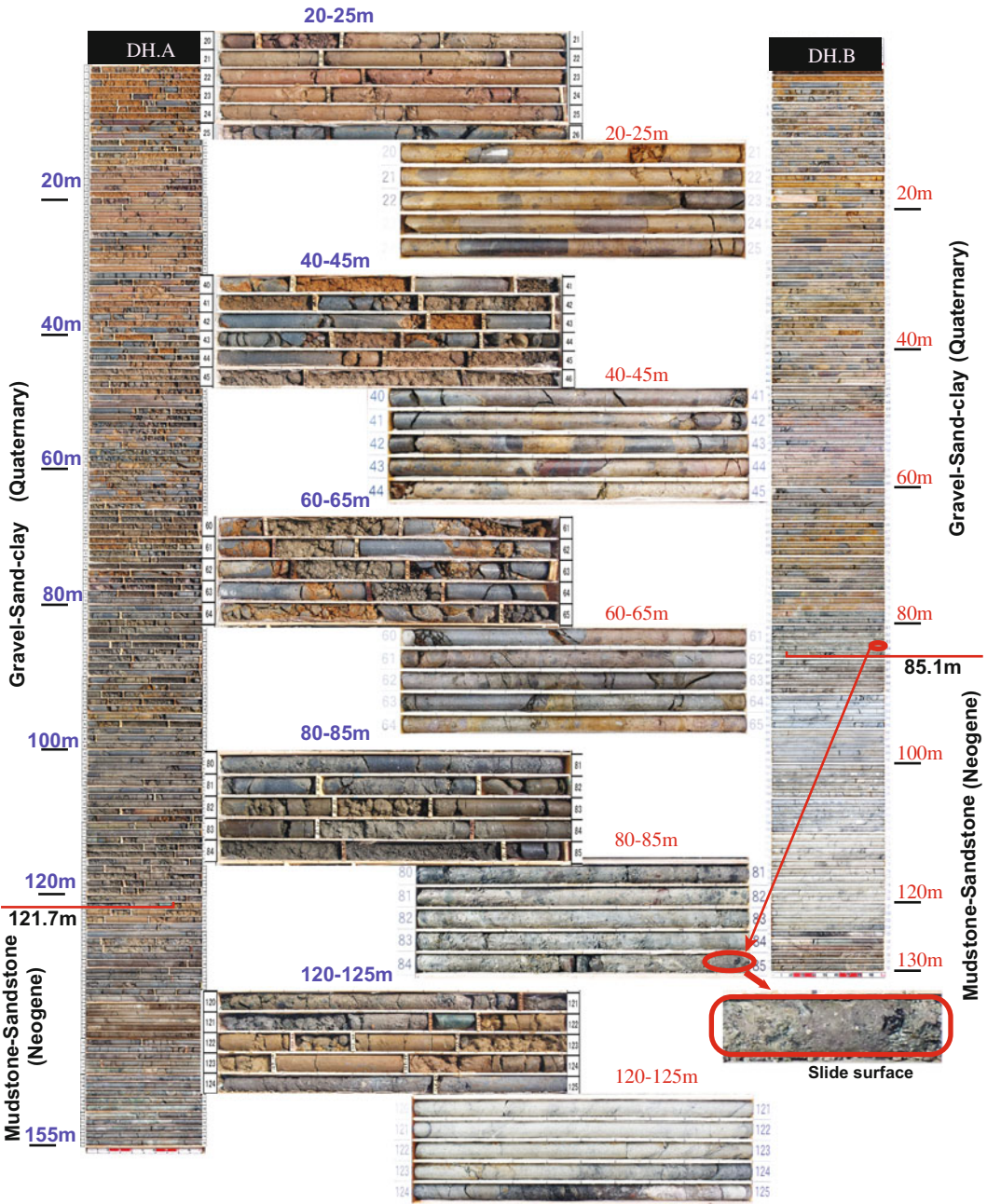


Fig. 3 Comparison of drilling cores obtained by conventional drilling method (DH.A) and SP method (DH.B). Photos of the cores in the center are the ones partly picked up

3 Drilling Cases by SP Method in Hai Van Landslide of Vietnam

In the JICA/JST/ITST project “Development of landslide risk assessment technology along transport arteries in Viet Nam,” which is a research project being conducted jointly by Japan and Vietnam, the Hai Van landslide was selected as the study area, and one hole was drilled in the area for research purposes.

The Hai Van landslide area is located on the back slope of the Hai Van station of the national railway, in a steeply mountainous seashore area 10 km north of the city of Da Nang in central Vietnam. The main objectives of the research drilling were to confirm the geology, slide surface, and record of landslide movement and landslide activity through observation of cores, to conduct soil testing to obtain information needed to implement landslide movement simulation, and to install instruments for groundwater and ground movement observation in the borehole after drilling. Because the loose layer of sandy soil in this area contains granitic gravel and clayey soil to a considerable depth, extraction of high-quality cores using the conventional drilling method was expected to be difficult. Therefore, the SP method was adopted for the drilling and

was performed by a team consisting of a Japanese lead engineer and three Vietnamese drilling engineers.

The drilling machine used was a YSO-1H (horsepower: 7.5 HP, excavation performance: 150 m, weight: 470 kg, YBM Co., Ltd.), and the core barrel was a sleeve-incorporating core barrel with a diameter of 86 mm (GWS core barrel, Christensen Maikai Co., Ltd.). On the upper part of the core barrel, a mud tube was connected to eliminate cutting. An 86-mm diamond-impregnated bit was used for both the rudaceous soil part and the bedrock part. The polymer mud products used were TEL-POLYMER, TK60B (Telnite Co., Ltd.) and LIQUI-POL (Imdex Co., Ltd.). These muddy water modifiers served as both thickeners and dehydration-reducing agents and were effective in maintaining the borehole wall through strong weathered granite that was crushed into sand and gravel and in eliminating cutting (Fig. 4).

After confirmation that the boundary between the strong weathered granite that was crushed into sand and gravel and the hard granite bedrock was 51 m deep and that fresh granite was present to an additional depth of approximately 30 m, the drilling was conducted to a depth of 80 m. The rate of drilling fluid use during excavation

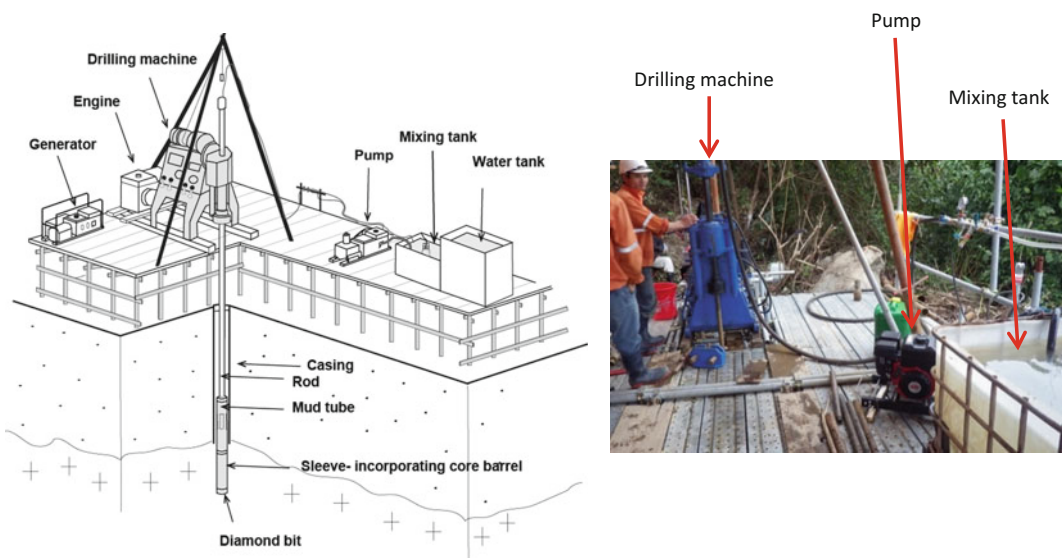


Fig. 4 Instruments and materials for use of SP method in Hai Van landslide area of Vietnam

was 5–6 L/min, which is 20–30% of the rate for the conventional drilling method. The excavation was conducted at a bit pressure of approximately 2000–3000 N. Polymer mud was used based on the experience of the engineers, in light of the geological conditions of the site. Approximately 250 cc of polymer mud was introduced to 200 L of water, and a casing 100 mm in diameter was inserted to the rock contact depth of 51 m. It took 19 days to reach a depth of 51 m in the weathered rock (corresponding to a drilling rate of approximately 2.7 m/day) and an additional 11 days after reaching the bedrock at a depth of 51 m to reach a depth of 80 m (a rate of approximately 2.6 m/day). During the drilling operation, when the clogging situation was severe, a core barrel of 1 m length was used. After the cores were carefully extracted from the sleeve tube (Fig. 5), the thin clay layer on the core surfaces was washed away (Fig. 6), and the cores were arranged in core boxes.

Figure 7 shows the cores and the geologic column. The core recovery rate was low for the first 10 m, partly because of the presence of loose gravel–sand mixtures, but once the drilling team becoming accustomed to the drilling method, the core recovery rate was almost 100% beyond a depth of 10 m. Beyond a depth of 51 m, hard

fresh granitic rock was almost perfectly extracted. Although the cores obtained at depths of up to 51 m consisted of soft sand that was easily crushed when acupressure forces in the range of 1–50 kgf/cm² was applied in needle penetration tests, the cores were continuously extracted in a state that retained the composition of the rock. As a result, the weathering of the granitic rock in the form of gradations from fresh blue–gray to dark brown sand could be continuously observed (Fig. 7). Furthermore, neither a slide surface nor any mixtures of gravel and organic soil could be observed. Therefore, it was presumed that the loose geological features within the depth of 51 m were caused by weathering of the material in its original position.

4 Discussion

The SP method makes it possible to extract high-quality cores at depths of up to approximately 200 m with less disturbance than is caused by the type of drilling equipment that has conventionally been used on landslide slopes. As a result, through observation of cores obtained using the SP method, it is possible to obtain valuable information more quickly easily and

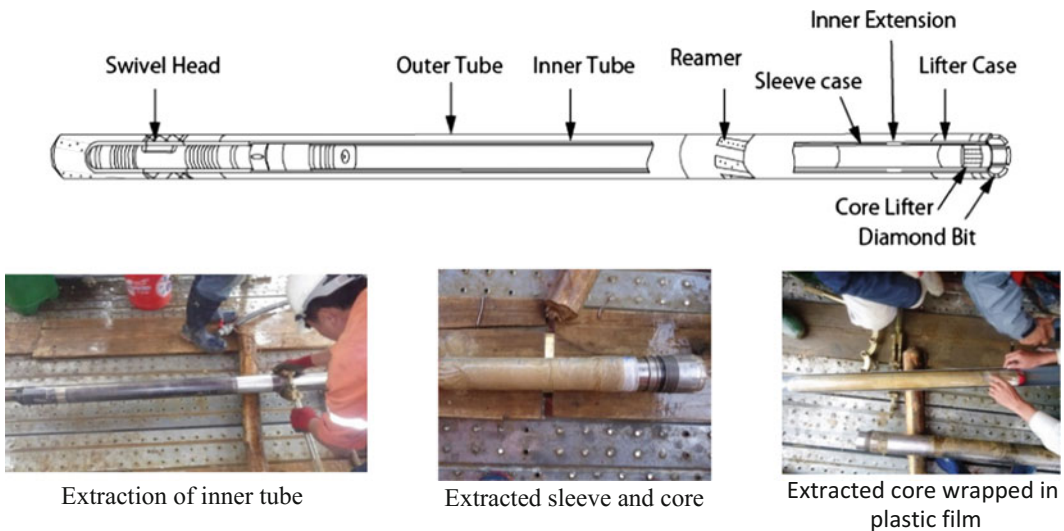


Fig. 5 Sleeve-incorporating core barrel and drilling core

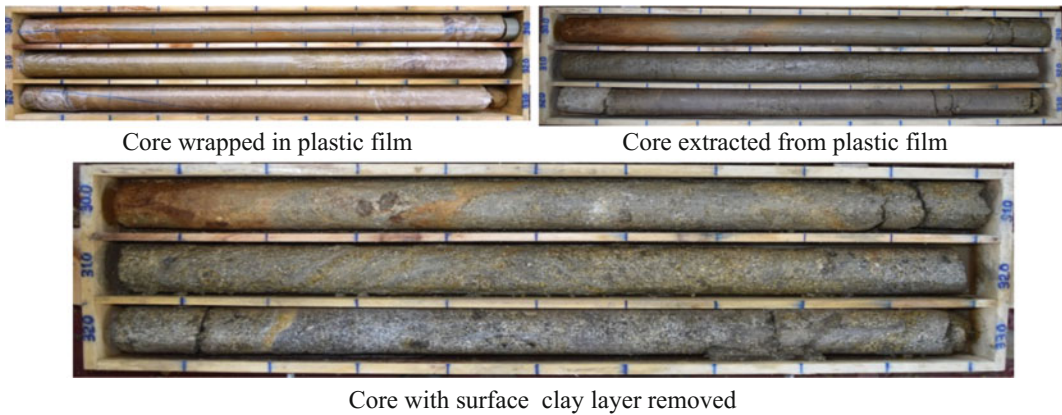


Fig. 6 Sampling and processing states of cores obtained by SP method (30–33 m)

particularly to confirm the slide surface accurately, which is the most important piece of information in landslide analysis (Fig. 3). In the case of the Hai Van landslide area, through observation of successive cores of high quality, we were able to disprove the existence of a present slide surface and a history of past landslides, and at the same time, we were able to show that a weathered layer of extremely loose granite with a thickness of approximately 50 m exists on the slope in an unstable state. If the conventional drilling method had been adopted, we would not have been able to draw these conclusions, because the cores would very probably have been extracted in such a state of disturbance to the gravel and sand that we could not have made such judgments. In fact, in the Hai Van landslide area, 12 research drillings were conducted in 2007 after the landslide disaster, but the maximum possible drilling depth was only 30 m, and only a few cores could be extracted.

The drilling speed of research drilling is important from the perspectives of safety and cost when working within a hazardous disaster-affected area. A comparison of the drilling speeds for various drilling methods at three landslide areas in the Tohoku region of Japan, where the landslide movement thickness is approximately 100 m or more, showed that for all of the drilling methods considered, the variation in speed becomes large at depths in the range of approximately 100–150 m and becomes

relatively stable at depths of 150 m and more (Fig. 8). Because many difficulties encountered in drilling, such as hole wall collapse and difficulties insert casing, occur at depths of 100–150 m, it can be concluded that drilling difficulties decrease in hard bedrock at depths greater than 150 m. At depths of 100–150 m, the speed of the SP method tends to be slower than the speed of the conventional method. However, at two drilling points 30 m apart in landslide area B, there was little difference in the drilling speeds of the two methods (Fig. 9). Thirty days were required to conduct the drilling in the Hai Van landslide in Vietnam, with the SP method requiring approximately 5–10 more days than the conventional drilling method, as shown in Figs. 8 and 9. This was because the geological conditions made drilling difficult, the equipment and materials available for use were limited, and the drilling operation required technical instructions. As the operator's technical skills have a great impact on the drilling speed for the SP method, with increasingly widespread use of the SP method in the future, it is likely to come to be conducted at almost the same speed as the conventional drilling method.

With respect to the impact on the groundwater survey of the use of polymer mud as the drilling fluid, it is reported that potassium (K) is deposited around the inside of the borehole (Tomioka et al. 2013). Care should therefore be taken in using this method for water quality testing of

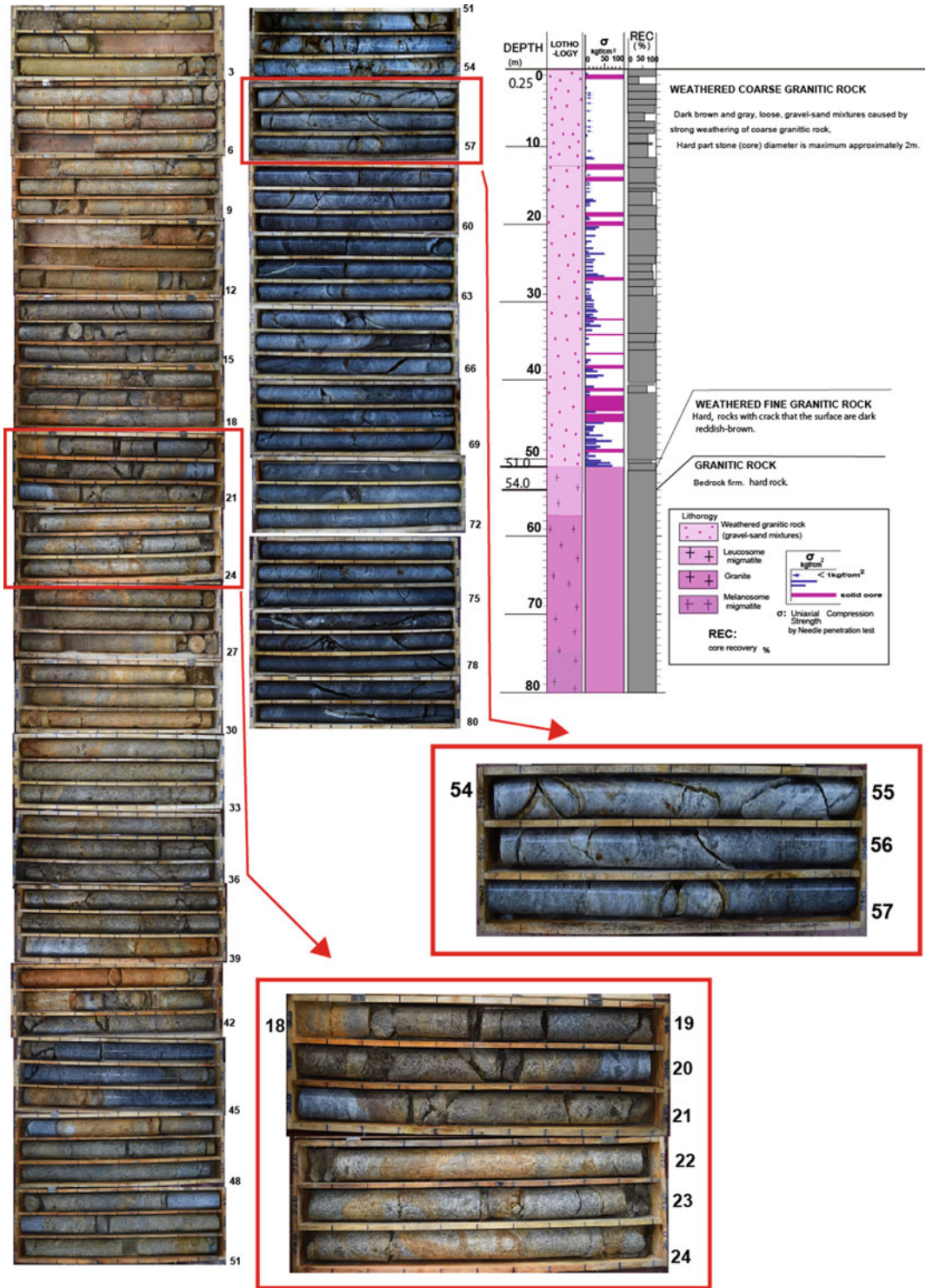


Fig. 7 Drilling cores obtained by SP method and geologic column in Hai Van landslide

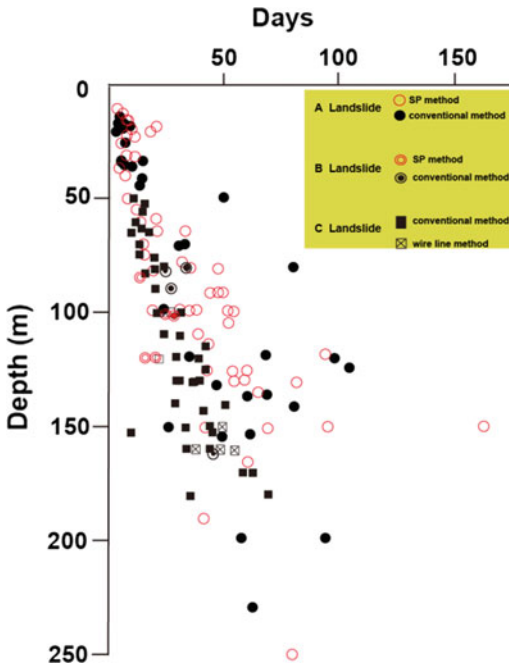


Fig. 8 Drilling method and drilling speed at three large-scale landslides in Japan—Main Geology of *A*, *B* and *C* landslides—*A* quaternary volcanic detritus and neogene sedimentary rock, *B* neogene sedimentary rock and rhyolite, *C* neogene sedimentary rock and andesite

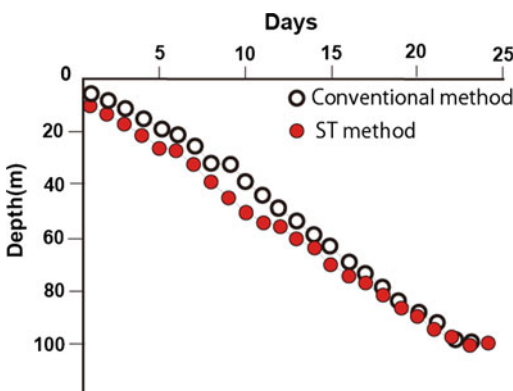


Fig. 9 Comparison of drilling speeds for conventional and SP drilling methods for two adjacent boreholes in *B* landslide area (see Fig. 8)

groundwater. The method has been reported to have little impact on groundwater logging (Igarashi et al. 2013).

The disadvantage of the SP method is that its success is highly dependent on the experience

and judgment of drilling engineers in matters such as the selection and application of a polymer mud that corresponds to the geology of the site, the selection of the diamond bit, the casing method applied. Incidentally, at the Hai Van landslide site in Vietnam, the operator, who was skilled in the conventional drilling method, gained competence with the basic techniques of the SP method through technical training for approximately 4 months. Thus, while it requires time to obtain skill with the SP method, it is possible to extract cores of high quality at depths of up to approximately 200 m without preparing special equipment, other than the sleeve-incorporating core barrel and commercially available diamond bits and polymer mud. Although, the drilling costs of the SP method are not well established yet, they are estimated to be approximately 1.5 times greater than for the conventional drilling method.

In the future, it is expected that this drilling method, which is economically efficient and effective for use in the analysis of landslides, will be increasingly used to study landslide areas in various countries.

5 Conclusions

Drilling of high-quality cores from landslide areas provides valuable information for use in the initial stage of landslide analysis, such as information on the geological features of the landslide area, the weathering and crushing of underground bedrock, the record and activity of landslides, slide surfaces, and cracks in the bedrock. The development in recent year of the SP method described in this paper has made it possible to extract high-quality cores with minimal mixing of materials at depths of up to approximately 200 m.

In contrast to the conventional core drilling method used in landslide research, this core drilling method does not require as much special equipment and so is suitable for use in landslide exploration in various regions. However, at present, the successful use of this drilling method is highly dependent on several factors, such as the

selection of operating techniques corresponding to the specific geological features of the site, the use of appropriate amounts of polymer mud, the selection of appropriate diamond bits and bit pressures, and thus is highly dependent on the experience and judgment of the drilling operator. In the future, a technical manual based on quantitative analysis should be developed to provide guidance on the use of this core drilling method.

Acknowledgements Data from the Hai Van landslide in Vietnam obtained in the Japanese and Vietnamese joint JICA/JST/ITST research project “Development of landslide risk assessment technology along transport arteries in Viet Nam” was used in this study. I would like to express my appreciation to those who collected the data and made it available for use. I am also grateful for information and advice concerning polymer mud received from Mr. Kazuhiro Kodama of the Telnite Co., Ltd. and for information and advice concerning the sleeve-incorporating core barrel received from Mr. Hiroshi Tanaka of the K. Maikai Co., Ltd.

References

- Austin EH (1983) *Drilling engineering handbook*. International Human Resources Development Corporation, Boston, p 301
- Chilingarian GV, Vorabutr P (1983) *Drilling and drilling fluids*. Developments in petroleum science II. Elsevier, Amsterdam, p 801
- Eugene S, Warren ET (1989) *Application of drilling, coring, and sampling techniques to test holes and wells. Techniques of water-resource investigations of the United States Geological Survey*, United States Government Printing Office, Washington, p 97
- Igarashi N, Sakurai M, Takeuchi A, Kuroki K (2013) Example cases of field experiments of boreholes for ground survey. In: Japan geotechnical consultants association, proceedings of the geotechnology forum 2013, Nagano, Japan
- Okino B (1981) *Drilling fluids*. Gihodo Shuppan, Chiyoda-ku, p 398
- Okino B (1989) *Manual of drilling fluid technology*. Telnite Co. Ltd, Shibuya-ku
- Steiger RP (1982) Fundamentals and use of potassium/polymer drilling fluids to minimize drilling and completion problems associated with hydratable clays. *Soc Pet Eng J Pet Technol* 34(08):1661–1670
- Takeda S, Komiya K (2005) From air bubble boring: the hybrid method to a core sampling of high-quality, Tsuchi-to-kiso. *Jpn Geotech Soc* 54–4(579):16–18
- Tani K, Kaneko S, Oshida Y, Ikemi M (2004) Development of instrumented drilling technology for geotechnical investigation of rock mass. In: Proceedings of the 3rd Asian Rock mechanics symposium, Kyoto, pp 1181–1186
- Tomioka Y, Kondo H, Goto K, Goto K, Yoshimura K, Muramoto S (2013) Evaluation of chemical properties of groundwater affected by fluids and cementing used in a borehole drilling. *Civil Engineering Research Laboratory, Rep. No. N12012*, Central Research Institute of Electric Power Industry, p 34

TXT-tool 4.081-1.2

Mechanism of the Aratozawa Large-Scale Landslide Induced by the 2008 Iwate-Miyagi Earthquake

Hendy Setiawan, Kyoji Sassa, Kaoru Takara, Maja Ostric, Toyohiko Miyagi and Hiroshi Fukuoka

Abstract

A large-scale landslide near the Aratozawa dam reservoir was occurred when the 2008 Iwate-Miyagi Nairiku earthquake with magnitude of 7.2 hit the area of Mount Kurikoma in Miyagi Prefecture of Japan. The epicenter of the earthquake was located about 10 km northeast part of Mount Kurikoma, at the border between Miyagi Prefecture and Iwate Prefecture. This paper highlights site investigation and sampling of the Aratozawa landslide, following with the laboratory experiment by means of undrained dynamic loading ring shear apparatus. In addition, to understand the initiation mechanism, landslide simulation using the LS-RAPID model was carried out. By combining the ring shear test results and LS-RAPID, the Aratozawa landslide process from pre-failure state, failure initiation, post-failure motion up to deposition stage are well described. The result of this study contributes to the landslide hazard assessment, particularly for the case of landslides near reservoir where earthquake, rainfall and or reservoir impoundment are considered as single or combined triggering factors.

Keywords

Earthquake-triggered landslide • Aratozawa reservoir • Ring shear tests • LS-RAPID model

H. Setiawan (✉) · K. Takara
Disaster Prevention Research Institute, Kyoto
University, Uji 611-0011, Japan
e-mail: hendy@flood.dpri.kyoto-u.ac.jp

K. Takara
e-mail: takara.kaoru.7v@kyoto-u.ac.jp

K. Sassa
International Consortium on Landslides, 138-1,
Tanaka Asukaicho, Sakyo-ku, Kyoto 606-8226,
Japan
e-mail: sassa@iclhq.org

M. Ostric
Croatian Waters, Rijeka, Croatia
e-mail: ostric.maja@gmail.com

T. Miyagi
Tohoku Gakuin University, Sendai, Miyagi
981-3193, Japan
e-mail: miyagi@izcc.tohoku-gakuin.ac.jp

H. Fukuoka
Research Institute for Natural Hazards and Disaster
Recovery, Niigata University, Niigata 950-2181,
Japan
e-mail: fukuoka@cc.niigata-u.ac.jp

Contents

1	Introduction	820
2	Site Investigation and Sampling of the Aratozawa Landslide	820
3	A High Stress Undrained Dynamic Loading Ring Shear Apparatus ICL-2	822
4	The Integrated Landslide Simulation Model (LS-RAPID)	824
5	Experiment and Landslide Modeling Results	825
5.1	Ring Shear Tests Results.....	825
5.2	LS-RAPID Simulation Model Results.....	827
6	Conclusion	830
	References.....	830

1 Introduction

Aratozawa Dam is located southeastern part of Mount Kurikoma, where the area is mainly consists of Tertiary to Quaternary pyroclastic rocks, e.g. sedimentary and welded tuff (Kazama et al. 2012). A reverse fault earthquake was occurred on 14 June 2008, with the epicentre about 10 km northeastern part of Mount Kurikoma, the depth of 8 m and magnitude of 7.2, causing large-scale and deep landslide near the Aratozawa Dam (Fig. 1). The earthquake epicentre was located at 39°01.7' of north latitude and 140.9°52.8' of east longitude (Yamashina et al. 2009).

According to Kazama et al. (2012), the surface fault was found very close to the Aratozawa landslide and other concentrated slope failures. The huge dimension of Aratozawa landslide in overall reached 1300 m in length, 900 m in width and the thickness varied of about 70–150 m. The total volume of landslide was estimated of about 67 million m³ and it was stated at that time as the largest landslide in the last 100 years in Japan (Miyagi et al. 2008, 2011). This paper describes briefly of several findings that we had during site investigation and sampling of Aratozawa landslide. The samples were tested by using the undrained dynamic loading ring shear apparatus ICL-2 version. Soil parameters from the tests results were used in the

LS-RAPID model to simulate the initiation mechanism and motion of the large-scale Aratozawa landslide induced by the 2008 Iwate-Miyagi Nairiku earthquake.

2 Site Investigation and Sampling of the Aratozawa Landslide

The Aratozawa landslide consists of massive blocks, several ridges, depression zones and debris material (Fig. 2). The slicken-sided slip surface has a gradient of only 2–4, with the blocks were moved of about 320 m that makes this landslide identified as the translational block glide of a deep slide (Kazama et al. 2012; Miyagi et al. 2011).

Based on the DEM data interpretation and landslides distribution in the earthquake-affected area, the Aratozawa landslide was occurred right on the landslide topography zone, where several deep landslides were formed in the past (Yagi et al. 2009; Miyagi et al. 2011; Kazama et al. 2012). We carried out site investigations two times in different seasons, late of autumn in November 2012 and early summer of June 2013. During observation, several natural reservoirs (lakes) were formed in the cavities between ridges and depression zones (Setiawan et al. 2014). This finding is obvious since the landslide blocks had changed the watershed geomorphology of Nihasama River as the main surface discharge to the Aratozawa reservoir.

According to Moriya et al. (2010), the geological structure at the upstream area of Aratozawa Dam in descending order is composed of volcano debris deposit, welded tuff, thin layers of sandy clay, silty clay and mudstone, massive and thick pumice tuff, alternating beds of sandstone and silty mudstone, and lapilli tuff. Most of the soil structure in Aratozawa area was formed in a Quaternary period, where the pyroclastic flows are resulted from volcanic activities of Mount Kurikoma. In the late autumn of our investigation (in the snowy rainy day), we found at the collapse zone that the volcanic tuff

Fig. 1 Large-scale landslide near the Aratozawa dam reservoir, Miyagi Prefecture, Japan (photo was taken at the site board during investigation)



materials are very fine (like talc powder), loose, weathered and very crushable when it is in wet condition (almost saturated) (Fig. 3). In addition, the gullies were formed at the toe part of the landslide blocks, where the surface water drained and make the materials eroded easily. Based on these investigations, the very fine materials in the Aratozawa area are the key to understand the initiation mechanism of Aratozawa landslide.

We took samples of Aratozawa landslide basically from 5 locations: (1) very fine tuff that squeezed out along cracks within landslide

blocks in a collapse zone (further called collapse zone), (2) Small depression at the toe part of run up body (toe part), (3) the exposed wall ridge near the upper depression zone (wall ridge), (4) the opposite fraction layer on the toe part of run up body (opposite toe part), and (5) exposed pumice tuff mound on the flank side (flank side) (Fig. 4). The grain size distribution and soil properties of all five samples are given in Table 1.

To understand the initiation mechanism and motion of Aratozawa landslide, we focused the



Fig. 2 Edge of the landslide massive block faces to the lower ridge and a head scarp



Fig. 3 Observing landslide debris material within block (*top*) and at the toe part (*bottom*)

samples from collapse zone and flank side to be tested by using a high stress undrained dynamic loading ring shear apparatus (ICL-2).

3 A High Stress Undrained Dynamic Loading Ring Shear Apparatus ICL-2

Samples from the Aratozawa landslides were tested in laboratory by means of ring shear apparatus. The ring shear apparatus was developed

since 1984 by Professor Sassa and his colleagues at the Disaster Prevention Research Institute (DPRI) of Kyoto University. The main aims of the soil tests in ring shear apparatus is to observe pore pressure generation within samples in a failure condition, where the sliding surface is reproduced at a large shear displacement (Sassa et al. 2004). In such tests, the mobilized shear resistance and post-failure rapid motion can be monitored (Sassa et al. 2010, 2012). A high stress undrained dynamic loading ring shear apparatus of ICL-2 was developed by Professor Sassa and his

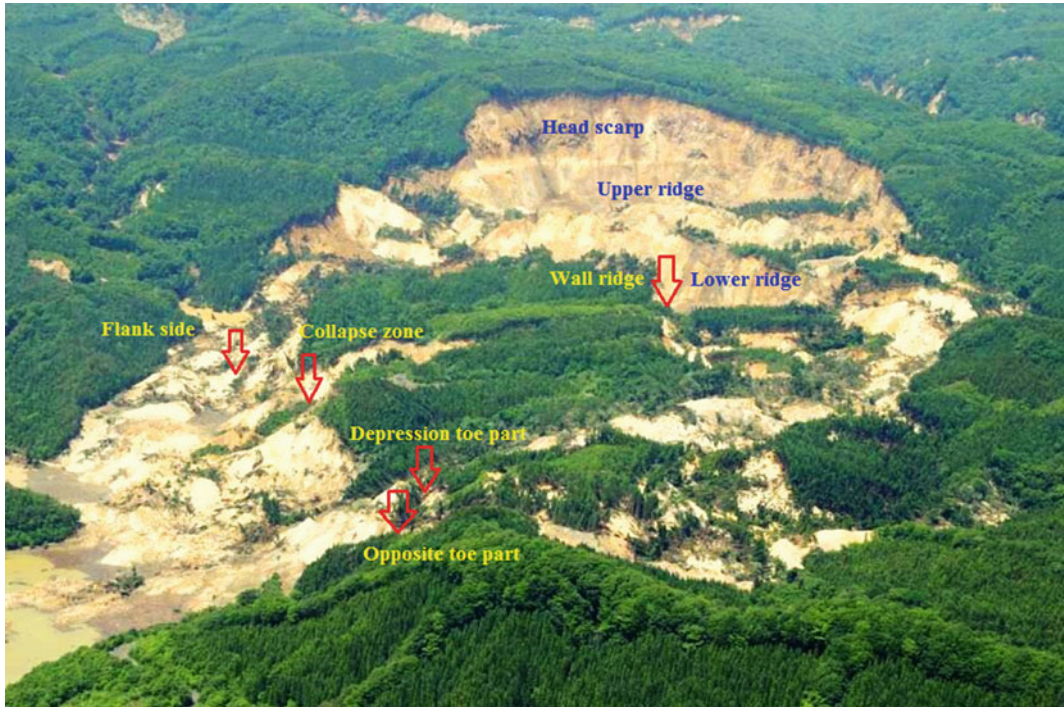


Fig. 4 All sampling locations of the Aratozawa large-scale landslide (photo was taken by H. Fukuoka on his site investigation)

Table 1 Grain size distribution of samples from the Aratozawa landslide

Specification	Collapse zone	Depression toe part	Opposite toe part	Wall ridge	Flank side
Average particle size, D50 (mm)	0.022	0.008	0.035	0.267	0.070
Effective particle size, D10 (mm)	0.0038	0.0023	0.0078	0.011	0.0131
Particle size of D30 (mm)	0.014	0.0054	0.024	0.096	0.044
Coefficient of uniformity (Cu)	6.61	4.57	5.17	33.88	6.35
Coefficient of curvature (Cc)	2.16	1.20	1.78	2.17	1.85

colleagues at the International Consortium on Landslides as the second upgrade version of the apparatus (after ICL-1). The ICL-2 (ICL stands for International Consortium on Landslides), with the single central axis for normal loading system, has capability to give the maximum normal stress of up to 3000 kPa in undrained condition (Fig. 5). Thus, the pore water pressure of 3000 kPa can be observed, while the maximum frequency of loading reached 20 Hz in maximum with the shear speed capacity of 50 cm/s (Sassa et al. 2014). The

ICL-2 is very suitable for the case of a deep landslide. The detail explanation of the apparatus working processes was reported in Sassa et al. (2014) and other part of this text tool (e.g. Manual for the undrained dynamic-loading ring-shear apparatus).

The Aratozawa samples were prepared in fully saturated conditions by immersing it into the de-aired water and left in a vacuum tank for 2 days. The gap adjustment and rubber edge friction in the apparatus were adjusted to prevent

Fig. 5 Overview of the ICL-2: main control unit and the ring shear apparatus



water leakage during the tests with high stress loading. The CO₂ and de-aired water circulation were given to the installed shear box before placing the saturated samples. After placing the samples, circulation of de-aired water was conducted once more before checking the saturation condition. The degree of saturation was measured through BD value as the pore pressure parameter in the direct shear state, formulated as $BD = u/\Delta s$. The tests for Aratozawa samples in ring shear apparatus of ICL-2 consists of undrained speed control test, cyclic shear test, pore pressure control and earthquake loading test.

4 The Integrated Landslide Simulation Model (LS-RAPID)

The LS-RAPID is a computer simulation code that integrating the initiation and motion of landslides which are triggered either by

earthquakes, rainfall or both of combined factors. By considering a vertical imaginary column with the acting forces within a moving landslide mass, the LS-RAPID aims to simulate landslide processes from its failure initiation, pore pressure increase, seismic loading, moving process and up to the deposition stage (Sassa et al. 2010, 2012). As shown in Fig. 6, the landslide mass (m) will be accelerated (a) with the total forces as the sum of driving force (self-weight and seismic force), lateral pressure and shear resistance, which denoted as:

$$a.m = (W + F_v + F_x + F_y) + \left(\frac{\partial P_x}{\partial x} \Delta x + \frac{\partial P_y}{\partial y} \Delta y \right) + R \quad (1)$$

The R indicates the effects of normal force (N) and pore pressure (U) that works in the upward direction of the maximum slope line before motion and in the opposite direction of

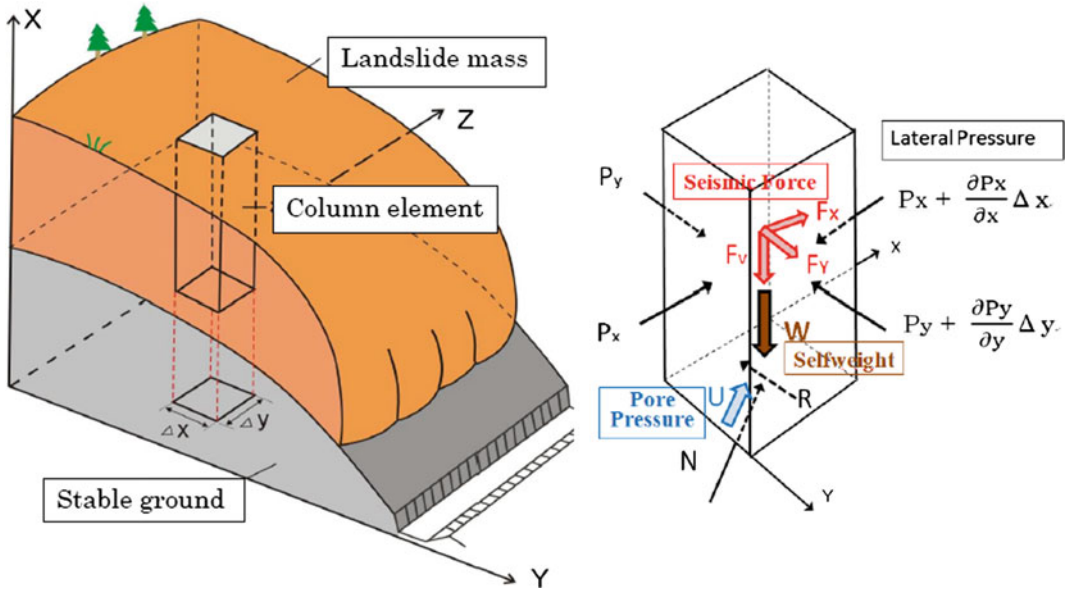


Fig. 6 Vertical imaginary column within a moving landslide mass in the LS-RAPID model

landslide during motion. Equation (1) expressed into x and y directions as follows:

$$\begin{aligned} & \frac{\partial M}{\partial t} + \frac{\partial}{\partial x}(u_o M) + \frac{\partial}{\partial y}(v_o M) \\ &= gh \left\{ \frac{\tan \alpha}{q+1} (1 + Kv) + Kx \cos^2 \alpha \right\} \\ & - (1 + Kv) kgh \frac{\partial h}{\partial x} - \frac{g}{(q+1)^{1/2}} \cdot \frac{u_o}{(u_o^2 + v_o^2 + w_o^2)^{1/2}} \\ & \{ h_c(q+1) + (1 - r_u)h \tan \phi_a \} \end{aligned} \quad (2)$$

$$\begin{aligned} & \frac{\partial N}{\partial t} + \frac{\partial}{\partial x}(u_o N) + \frac{\partial}{\partial y}(v_o N) \\ &= gh \left\{ \frac{\tan \beta}{q+1} (1 + Kv) + Ky \cos^2 \beta \right\} \\ & - (1 + Kv) kgh \frac{\partial h}{\partial y} - \frac{g}{(q+1)^{1/2}} \cdot \frac{v_o}{(u_o^2 + v_o^2 + w_o^2)^{1/2}} \\ & \{ h_c(q+1) + (1 - r_u)h \tan \phi_a \} \end{aligned} \quad (3)$$

$$\frac{\partial h}{\partial t} + \frac{\partial M}{\partial x} + \frac{\partial N}{\partial y} = 0 \quad (4)$$

From the derived equations above, the cohesion expressed in the unit weight (h_c), the pore pressure ratio (r_u), the lateral pressure ratio (k) and the apparent friction coefficient mobilized at the sliding surface of landslide (ϕ_a) are the key

dependent parameters that could be determined based on the ring shear tests. In previous research, the LS RAPID model were successfully simulated for the cases of Leyte landslide in the Philippines (reported in Sassa et al. 2010), the Senoumi submarine megaslide in Suruga Bay of Japan (Sassa et al. 2012) and the past megaslide of Unzen Mayuyama, Shimabara city, Nagasaki, Japan (Sassa et al. 2014). Simulation of the Aratozawa landslide is carried out by LS-RAPID, based on the ring shear test results of samples from the collapse zone and flank side of the Aratozawa landslide area.

5 Experiment and Landslide Modeling Results

5.1 Ring Shear Tests Results

All samples were conditioned in a normal consolidation, means before shearing we performed the normal stress in the ICL-2 through vertical loading plate which was pulled by the central axis. The value of 3000 kPa of normal stress is the maximum capacity of the ICL-2 that we applied to the samples, and represent the deep

landslide of more than 100 m. The normal stress was applied with rate of 2.0 kPa/s and loaded up to 3000 kPa in a drained condition. We conducted undrained speed control test for samples from collapse zone and flank side to obtain briefly the values of shear resistance, the peak friction angle, mobilized friction angle as well as apparent friction angle (Fig. 7).

In addition, a cyclic shear tests in undrained condition were also carried out to observe pore pressure generation and the imitation of failure motion. Since the Aratozawa landslide was occurred due to the earthquake event, the cyclic shear test is suitable as the manifestation and simplification of the earthquake-pattern in a slow speed. We performed cyclic shear test with the initial normal stress of 2000 kPa and static shear stress of 1200 kPa with rate of 2 kPa/s. The initial amplitude was 300 kPa, with the amplification of 4 cycles and 5 constant cycles (Fig. 8). The pore water pressure was generated of more than 1000 kPa where shear resistance rapidly lost its strength and shear displacement was accelerated.

In further, the earthquake loading test was performed directly to the Aratozawa samples in the ICL-2 after the normal consolidation. The 2008 Iwate-Miyagi Nairiku earthquake record of NS direction on MYG004 at Tsukidate measurement station was used with the maximum

acceleration of 740 gal. According to Setiawan et al. (2016), by directly applying earthquake loading to the samples in the ring shear tests, the pore pressure was generated of only 270 kPa with a very small shear displacements (no moving failure). Through this result, the pore pressure control tests were conducted for the Aratozawa samples from the collapse zone and the flank side, and it gives the critical pore pressure ratio of 0.61–0.63 in the normal stress of 3000 kPa (Setiawan et al. 2016). Thus, the combined loading of initial pore pressure and the earthquake test was carried out for the sample from collapse zone as the initiation mechanism of Aratozawa landslide, and the undrained dynamic loading test was conducted to explain the movement of landslide blocks in a gentle slope (Fig. 9).

The values of shear resistance in the results above are including the rubber edge friction that appears during the shearing process. The rubber edge friction tests were conducted in advance before the main tests were performed. For normal stress of 3000 kPa, the rubber edge friction in a stable condition when the shear displacement reached more than 2 meters was about 101 kPa. Based on Fig. 9 and the rubber edge friction, we generalized the value of steady state shear resistance (τ_{ss}) of 80 kPa in a whole landslide area for the LS-RAPID simulation.

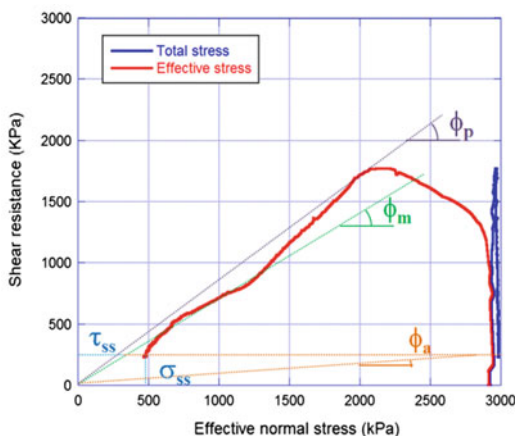


Fig. 7 Example of the undrained speed control test to the sample from collapse zone (ϕ_m is the friction angle during motion, ϕ_p is the friction angle at peak, ϕ_a is the apparent friction angle in a residual/steady state, ϕ_{ss} and τ_{ss} are the shear and normal of steady state resistance)

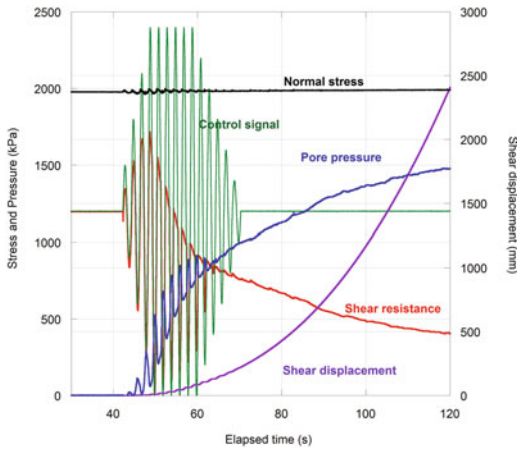


Fig. 8 Overview graph of the cyclic shear test time series of sample from collapse zone

5.2 LS-RAPID Simulation Model Results

After conducting experiment for the Aratozawa samples, we performed landslide simulation model using LS-RAPID. Since the ring shear tests results already explained briefly in the section above, the parameters used in the LS-RAPID for Aratozawa landslide are generally shown in Table 2. In this paper, we generalized the shear

strength parameters of the landslide area for the LS-RAPID simulation based on the ring shear tests results. The detail delineation of the shear strength parameters of each landslide area e.g. initiation blocks area and moving blocks area are still on going. Therefore, we define the same value of parameters in a whole landslide area. For example, the friction angle during motion (ϕ_m) is 33.4° , the peak friction coefficient at sliding surface ($\tan \phi_p$) is 0.78, the lateral

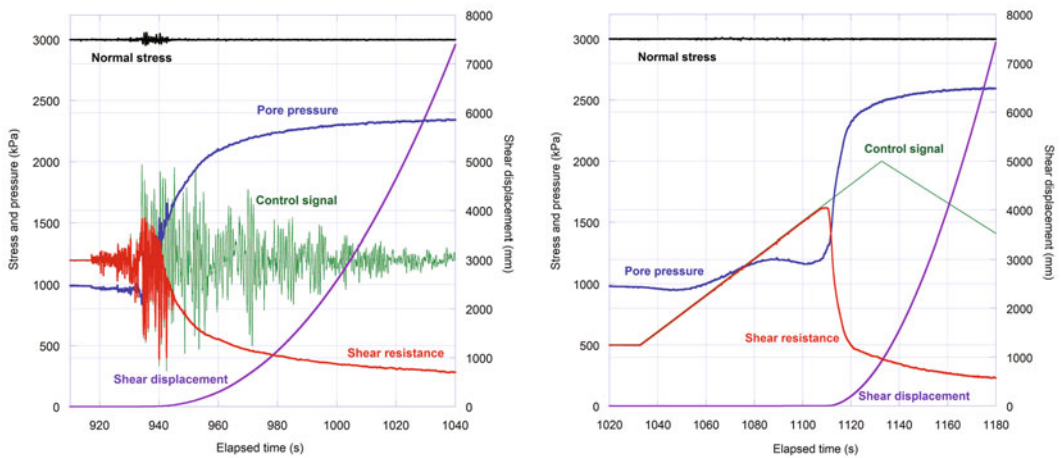


Fig. 9 The earthquake loading test for the sample from collapse zone (left) (Setiawan et al. 2016) and the undrained dynamic loading test (right) of the Aratozawa samples with predefined pore pressure using the ICL-2 ring shear apparatus

Table 2 Generalized parameters used in the LS-RAPID simulation for the Aratozawa landslide

Parameter	Value	Remarks
<i>Shear strength parameters</i>		
Steady-state shear resistance (τ_{ss})—kPa	80	In the condition of 3 MPa of normal stress
Lateral pressure ratio ($k = \sigma_h/\sigma_v$)	0.50	Applied in a whole landslide area
Friction coefficient inside landslide mass ($\tan \phi_i$)	0.5	Based on 26.6° degree of average slope
Friction coefficient during motion at sliding surface ($\tan \phi_m$)	0.66	Based on 33.4° of angle from ring shear test results, applied in a whole landslide area
Peak friction coefficient at sliding surface ($\tan \phi_p$)	0.78	Based on 37.95° of peak angle from ring shear test results, applied in a whole landslide area
Cohesion at peak (c_p)—kPa	80	Assumption
Friction angle during motion (ϕ_m)	33.4°	From ring shear test results
Shear displacement at the start of strength reduction (D_L)—mm	3	Based on analysis of shear strength reduction from ring shear test results
Shear displacement at the start of steady state (D_U)—mm	3000	Based on analysis of shear strength reduction from ring shear test results
Rate of excess pore pressure generation (B_{ss})	0.60–0.95	0.60 for the area near head scarp 0.95 for the toe near reservoir
Total unit weight of the mass (γ_t)—kN/m ³	20	Assumption
<i>Parameters of the function for non-frictional energy consumption</i>		
Coefficient for non-frictional energy consumption	1.00	Assumption
Threshold value of velocity—m/s	100	Assumption
Threshold value of soil height (H)—m	200	Based on max height of landslide depth
<i>Triggering factors and other factors</i>		
Excess pore pressure ratio in the fractured zone (r_u)	0.33	Based on pore pressure control test combined with earthquake loading in ring shear test results
Slope angle (θ , degree)	10°	Calculated from top elevation of head scarp to the toe elevation in average
Unit weight of water (γ_w)—kN/m ³	9.8	

pressure ratio (k) is 0.50 and the steady state shear resistance (τ_{ss}) is 80 kPa. We generate the topography setting in the LS-RAPID based on the DEM data with resolution of 10 m (Fig. 10).

By setting all the parameters in Table 2 inside the LS-RAPID, we conducted Aratozawa landslide simulation with the condition of initial pore pressure of 0.33, followed by the Iwate-Miyagi earthquake loading (Fig. 11).

According to the LS-RAPID simulation results for the Aratozawa landslide, the initial slope failure was occurred soon when the main shock of the earthquake takes place (Fig. 11-2). The progressive motion was appeared when the earthquake has decelerated and causing the

undulated forms of the main landslide blocks (Fig. 11-3). At the final stage, the main landslide block was remained near the toe part and some of them are facing to the reservoir. Such different elevation between the formed landslide block (as unstable hill) and surrounding topography might cause the second failure of the block down to the reservoir, as reported by Miyagi et al. (2008). In addition, the crescent shaped that left at the upper part indicates the forming of the upper ridge (orange colour) and lower ridge (red color), while between them formed as the depression area that consists of debris material (Fig. 11-4). The simulation by LS-RAPID implied that the results are in a good agreement with site

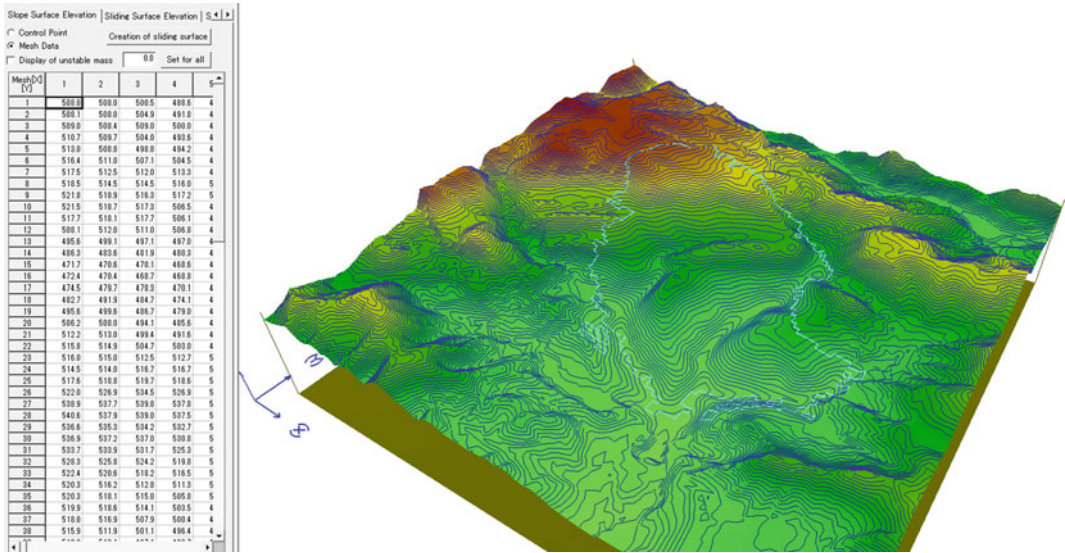


Fig. 10 Topography setting for the Aratozawa landslide simulation in the LS-RAPID (the blue light line color indicates the border of the unstable area)

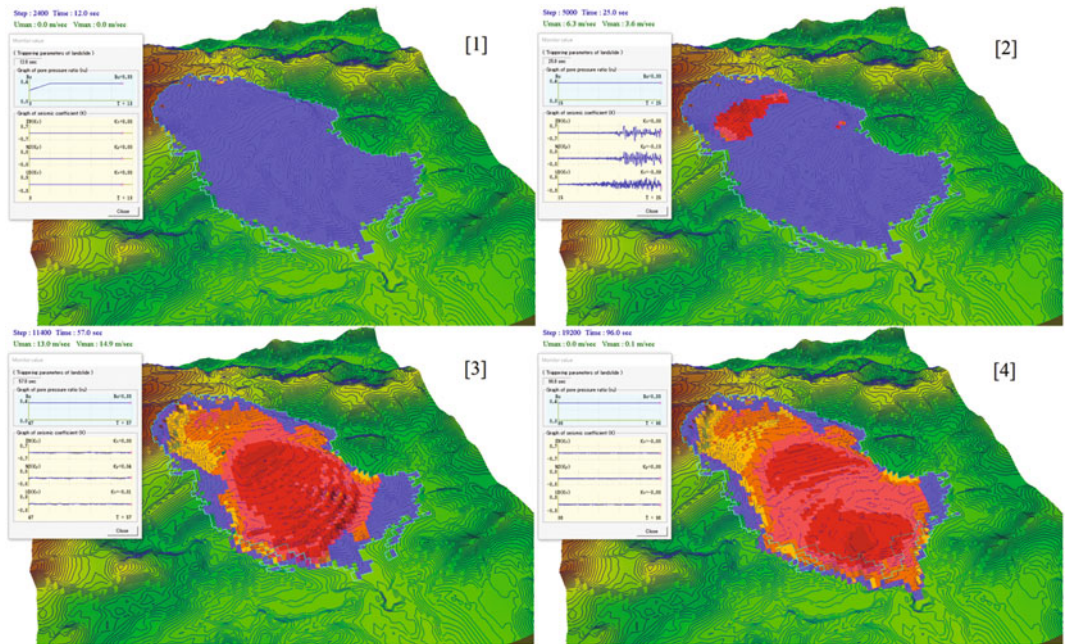


Fig. 11 The Aratozawa landslide simulation using LS-RAPID model: (1) initial stage, when the pore pressure ratio increased up to 0.33, (2) initial slope failure, when earthquake wave applied, (3) the progressive motion after earthquake wave was decelerated, (4) final deposition stage

investigation and geomorphology analysis that reported by Miyagi et al. (2011).

6 Conclusion

The very fine materials that were found during site investigations are the key to understand the initiation mechanism of a deep and large-scale of the Aratozawa landslide. A high stress undrained dynamic loading ring shear apparatus of ICL-2 was used to test the samples of Aratozawa landslide, particularly for the samples taken from the collapse zone and the flank side. The tests include undrained speed control test, cyclic shear test, earthquake loading test and pore pressure control test. The ring shear tests results indicated that the failure was triggered by the combination of initial pore water pressure and the 2008 Iwate-Miyagi Nairiku earthquake. Generalizing the results from ring shear tests, we conducted landslide simulation using the LS-RAPID model. The simulation results presents that the initial slope failure was came when the main shock of the earthquake occurred, after the landslide area experienced an initial pore pressure of about 0.33. The post-failure motion was shown in a progressive deformation when the earthquake has decelerated, that interpreted as the undrained dynamic shear process in a very gentle slip surface. The final stage of the LS-RAPID simulation shows quite similar with the real condition after the landslide that reported by previous researcher. The result of this study has shown that the integrated methods of laboratory experiment and computer simulation are very important to support the landslide hazard assessment. The combined triggering factors have to be considered when we deal with the case of landslides near the reservoir, when prolonged rainfall, reservoir impoundment and or earthquake (at an active fault area) are obviously takes place.

Acknowledgements The assistance from Japan Conservation Engineering and Japan Forestry Agency is gratefully acknowledged. The authors would like to thank Kawanami Akiko from Ministry of Agriculture, Forestry and Fisheries of Japan for her kind assistance during site

investigation. This landslide research is supported by the Global Survivability Studies Program of Kyoto University (A Leading Graduate School Program of MEXT). The undrained ring shear apparatus ICL-2 version is developed by the International Consortium on Landslides (ICL) as a part of SATREPS (Science and Technology Research Partnership for Sustainable Development Program of the Government of Japan) for Vietnam project in 2012–2017.

References

- Kazama M, Kataoka S, Uzuoka R (2012) Volcanic mountain area disaster caused by the Iwate-Miyagi Nairiku earthquake of 2008, Japan. *Soils Found* 52 (1):168–184
- Miyagi T, Kasai F, Yamashina S (2008) Huge landslide triggered by earthquake at the Aratozawa Dam Area, Tohoku, Japan. In: *Proceedings of the first world landslide forum*. ICL, ISDR, Tokyo, pp 421–424
- Miyagi T, Yamashina S, Esaka F, Abe S (2011) Massive landslide triggered by 2008 Iwate-Miyagi inland earthquake in the Aratozawa Dam area, Tohoku, Japan. *Landslides* 8:99–108
- Moriya H, Abe S, Ogita S, Higaki D (2010) Structure of the large-scale landslide at the upstream area of Aratozawa dam induced by the Iwate-Miyagi earthquake in 2008. *J Jpn Landslide Soc* 47(2):77–83 (in Japanese)
- Sassa K, Fukuoka H, Wang GH, Ishikawa N (2004) Undrained dynamic-loading ring shear apparatus and its application to landslide dynamics. *Landslides* 1:7–19
- Sassa K, Nagai O, Solidum R, Yamazaki Y, Ohta H (2010) An integrated model simulating the initiation and motion of earthquake and rain induced rapid landslides and its application to the 2006 Leyte landslide. *Landslides* 7:219–236
- Sassa K, He B, Miyagi T, Strasser M, Konagai K, Ostric M, Setiawan H, Takara K, Nagai O, Yamashiki Y, Tutumi S (2012) A hypothesis of the Senoumi submarine megaslide in Suruga Bay in Japan—based on the undrained dynamic-loading ring shear tests and computer simulation. *Landslides* 9:439–455
- Sassa K, Dang K, He B, Takara K, Inoue K, Nagai O (2014) A new high-stress undrained ring-shear apparatus and its application to the 1792 Unzen-Mayuyama megaslide in Japan. *Landslides* 11:827–842
- Setiawan H, Sassa K, Takara K, Miyagi T, Fukuoka H, He B (2014) The simulation of a deep large-scale landslide near Aratozawa dam using a 3.0 MPa undrained dynamic loading ring shear apparatus. In: Sassa et al (eds) *Landslide science for a safer geoenvironment*, vol 1. Springer International Publishing, Basel, pp 459–465
- Setiawan H, Sassa K, Takara K, Miyagi T, Fukuoka H (2016) Initial pore pressure ratio in the earthquake

- triggered large-scale landslide near Aratozawa dam in Miyagi Prefecture, Japan. *Procedia Earth and Planetary Science* 16:61–70.
- Yagi H, Sato G, Higaki D, Yamamoto M, Yamasaki T (2009) Distribution and characteristics of landslides induced by the Iwate-Miyagi earthquake in 2008 in Tohoku district, Northeast Japan. *Landslides* 6:335–344
- Yamashina S, Yamazaki T, Hashimoto J, Kasai S, Agatsuma T, Shibuya K (2009) Aratozawa landslide triggered by the Iwate-Miyagi Nairiku earthquake in 2008. *J Jpn Landslide Soc* 45(5):392–397 (in Japanese)

List of PPT-tools and PDF-tools

List of PPT-tools & video tools

No.	Identifier	Title	Author	Email/website	Slides
1	PPT-tool 1.039-1.1	Remote Sensing Data and Methodology for Event Landslide Recognition and Mapping	Alessandro Mondini	alessandro.mondini@irpi.cnr.it	30
2	PPT-Tool 1.052-1.1	Logisnet Manual and Quick-start Tutorial	Gabriel Legorreta Paulín, Marcus I. Bursik	legorretag@hotmail.com	127
3	PPT-tool 2.039-1.1	Italian National Landslide Warning System	Mauro Rossi et. al.	mauro.rossi@irpi.cnr.it	29
4	PPT-tool 2.062-1.1	Landslide Monitoring and Early Warning System	Teuku Faisal Fathani, Dwikorita Karnawati	tfathani@ugm.ac.id, dwiko@ugm.ac.id	31
5	PPT-tool 2.062-1.2	Monitoring and Early Warning System for Debris Flows in Rivers on Volcanoes	Teuku Faisal Fathani, Djoko Legono	tfathani@ugm.ac.id, djokolegono@yahoo.com	37
6	PPT-tool 2.385-1.2	Landslide Comprehensive Monitoring System: The Grohovo Landslide Case Study, Croatia	Željko Arbanas, Snježana Mihalić Arbanas, Martina Vivoda Prodan, Josip Peranić, Sanja Dugonjić Jovančević, Vedran Jagodnik	zeljko.arbanas@gradri.uniri.hr	28
7	PPT-Tool 3.385-1.3	Landslide Occurrence Prediction in the Rječina River Valley as a Base for an Early Warning System	Martina Vivoda Prodan, Sanja Dugonjić Jovančević, Željko Arbanas	martina.vivoda@gradri.uniri.hr	24
8	PPT-tool 2.886-1.2	Landslide Monitoring and Warning	An-Bin Huang, Wen-Jong Chang	huanganbin283@gmail.com	69
9	PPT-tool 3.039-1.1	Landslide Hazards and Risk Assessment	Fausto Guzzetti	F.Guzzetti@irpi.cnr.it	52
10	PPT-tool 3.039-1.2	Landslide-Related WPS Services	Ivan Marchesini	I.Marchesini@irpi.cnr.it	46

(continued)

No.	Identifier	Title	Author	Email/website	Slides
11	PPT-tool 3.039-1.3	Probabilistic Approach to Physically Based Landslide Modeling	Massimiliano Alvioli, Mauro Rossi, Fausto guzzetti	Massimiliano.Alvioli@irpi.cnr.it	29
12	PPT-tool 3.039-1.4	Advanced 2D Slope Stability Analysis by LEM by SSAP Software: a Full Freeware Tool for Teaching and Scientific Community	Lorenzo Borselli	lborselli@gmail.com	52
13	PPT-tool 3.886-1.1	Debris-2D Tutorial	Ko-Fei Liu, Ying-Hsin Wu	kfliu@ntu.edu.tw, wu.ahsin@gmail.com	43
14	PPT-tool 4.039-1.1	Definition and Use of Empirical Rainfall Thresholds for Possible Landslide Occurrence	Maria Teresa Brunetti, Silvia Peruccacci	Maria.Teresa.Brunetti@irpi.cnr.it, Silvia.Peruccacci@irpi.cnr.it	39
15	PPT-tool 4.039-1.2	Landslide Risk to the Population of Italy	Paola Salvati, Cinzia Bianchi	P.Salvati@irpi.cnr.it	37
16	PPT-tool 4.062-1.1	Socio-Technical Approach for Landslide Mitigation and Risk Reduction	Dwikorita Karnawati, Teuku Faisal Fathani, Wahyu Wilopo, Budi Andayani	dwiko@ugm.ac.id	10
17	PPT-tool 4.062-1.2	Community Hazard Maps for Landslide Risk Reduction	Dwikorita Karnawati, Teuku Faisal Fathani, Wahyu Wilopo, Budi Andayani	dwiko@ugm.ac.id	10
18	PPT-tool 4.066-1.1	Course on Landslide Disaster Risk Reduction for Local Government Level Stakeholders	Asian Disaster Preparedness Centre	peeranan@adpc.net	416
19	PPT-tool 4.886-1.1	Typhoon Loss Assessment System (TLAS) Taiwan Web Tool	Hsin-Chi Li, Yi-Chen Chen, Mei-Chun Kuo	hsinchi@ncdr.nat.gov.tw	8
20	PPT-tool 4.886-1.2	Assessment Social Impact of Debris Flow Disaster by Social Vulnerability Index (17 pages)	Ko-Fei Liu, Hsin-Chi Li, Mei-Chun Kuo, Hui-Hsuan Yang	kfliu@ntu.edu.tw, hsinchi@ncdr.nat.gov.tw	17
21	PPT-tool 4.886-1.3	Tutorial: Procedures for Constructing Disaster Evacuation Maps	Su-Chin Chen, Lien-Kuang Chen	scchen@dragon.nchu.edu.tw, steven_chen@ncdr.nat.gov.tw	56
22	Video-tool 3.084-2.1	Manual for Undrained Dynamic-Loading Ring Shear Apparatus	Lam Huu Quang	lhqlinh@yahoo.com	20 minutes

List of PDF tools

No.	Identifier	Title	Author	Email	Pages
1	PDF-tool 1.064-1.1	Field Guide for the Identification and Assessment of Landslide and Erosion Features and Hazards Affecting Pipelines	Chris Massey, Graham Hancox, Mike Page	c.massey@gns.cri.nz	88
2	PDF-tool 3.081-1.1	An Integrated Model Simulating the Initiation and Motion of Earthquake and Rain Induced Rapid Landslides and Its Application to the 2006 Leyte Landslide	Kyoji Sassa	sassa@iclhq.org	18
3	PDF-tool 3.081-1.3	A Hypothesis of the Senoumi Submarine Megalide in Suruga Bay in Japan—Based on the Undrained Dynamic-Loading Ring Shear Tests and Computer Simulation	Kyoji SASSA, Bin HE	sassa@iclhq.org	17
4	PDF-tool 3.081-1.5	Manual for the LS-RAPID Software	Kyoji Sassa, Hendy Setiawan, Bin He, Karolina Gradiški, Khang Dang	sassa@iclhq.org	80
5	PDF-tool 3.081-1.6	Manual for Undrained Dynamic-Loading Ring Shear Apparatus	Hendy Setiawan et al.	sassa@iclhq.org	32
6	PDF-tool 3.081-1.7	Undrained Dynamic—Loading Ring Shear Apparatus and Its Application to landslide Dynamics	Kyoji Sassa, Hiroshi Fukuoka, Gonghui Wang and Naohide Ishikawa	sassa@iclhq.org	13
7	PDF-tool 3.081-1.9	Dynamic Properties of Earthquake Induced Large-Scale Rapid Landslides Within Past Landslide Masses	Kyoji Sassa	sassa@iclhq.org	10
8	PDF-tool 4.091-1.2	Training Module on Comprehensive Landslide Risk Management	Surya Parkash	suryanidm@gmail.com	304
9	PDF-tool 4.064-1.1	Guidelines for Assessing Planning Policy and Consent Requirements for Landslide Prone Land	Wendy Saunders and Phillip J. Glassey	https://www.gns.cri.nz/	78
10	PDF-tool 4.064-1.2	Shut Happens—Building Hazard Resilience for Businesses in NZ	Resilient Organisations	www.resorgs.org.nz	9
11	PDF-tool 4.064-1.3	Working from the Same Page Consistent Messages for CDEM: PART B: Hazard-Specific Information—Landslides	Ministry of Civil Defence & Emergency Management	www.civildefence.govt.nz	14
12	PDF-tool 4.007-2-1	Summer School Guidebook	Alexander Strom	strom. alexandr@yandex.ru	131



International Consortium on Landslides

An international non-government and non-profit scientific organization
promoting landslide research and capacity building for the benefit of society and the environment

President: Yueping Yin (China Geological Survey)

**Vice Presidents: Irasema Alcantara-Ayara (UNAM), Mexico, Matjaz Mikos (University of Ljubljana), Slovenia
Dwikorita Karnawati (Gadjah Mada University, Indonesia)**

Executive Director: Kyoji Sassa (Prof. Emeritus, Kyoto University, Japan), Treasurer: Kaoru Takara (Kyoto University, Japan)

ICL Supporting Organizations:

The United Nations Educational, Scientific and Cultural Organization (UNESCO) / The World Meteorological Organization (WMO) / The Food and Agriculture Organization of the United Nations (FAO) / The United Nations International Strategy for Disaster Reduction Secretariat (UNISDR) / The United Nations University (UNU) / International Council for Science (ICSU) / World Federation of Engineering Organizations (WFEO) / International Union of Geological Sciences (IUGS) / International Union of Geodesy and Geophysics (IUGG) / Government of Japan

ICL Members:

Albania Geological Survey / The Geotechnical Society of Bosnia and Herzegovina / Geological Survey of Canada / Chinese Academy of Sciences, Institute of Mountain Hazards and Environment / Northeast Forestry University, Institute of Cold Regions Science and Engineering, China / China Geological Survey / Nanjing Institute of Geography and Limnology, Chinese Academy of Sciences / Tongji University, College of Surveying and Geo-Informatics, China / Universidad Nacional de Columbia, Columbia / City of Zagreb, Emergency Management Office, Croatia / Croatian Landslide Group (Faculty of Civil Engineering, University of Rijeka and Faculty of Mining, Geology and Petroleum Engineering, University of Zagreb) / Charles University, Faculty of Science, Czech Republic / Institute of Rock Structure and Mechanics, Department of Engineering Geology, Czech Republic / Cairo University, Egypt / Joint Research Centre (JRC), European Commission / Technische Universität Darmstadt, Institute and Laboratory of Geotechnics, Germany / National Environmental Agency, Department of Geology, Georgia / Universidad Nacional Autónoma de Honduras, UNAH, Honduras / Amrita Vishwa Vidyapeetham, Amrita University / National Institute of Disaster Management, India / University of Gadjah Mada, Indonesia / Parahyangan Catholic University, Indonesia / Research Center for Geotechnology, Indonesian Institute of Sciences, Indonesia / Agricultural Research and Education organization (AREO) Iran / Building & Housing Research Center, Iran / University of Calabria, DIMES, CAMILAB, Italy / University of Firenze, Earth Sciences Department, Italy / Istituto de Ricerca per la Protezione Idrogeologica (IRPI), CNR, Italy / Italian Institute for Environmental Protection and Research (ISPRA) - Dept. Geological Survey, Italy / Forestry and Forest Product Research Institute, Japan / Japan Landslide Society / Kyoto University, Disaster Prevention Research Institute, Japan / Korea Forest Research Institute, Korea / Korea Infrastructure Safety & Technology Corporation, Korea / Korea Institute of Civil Engineering and Building Technology / Korea Institute of Geoscience and Mineral Resources (KIGAM) / Korean Society of Forest Engineering / Slope Engineering Branch, Public Works Department of Malaysia / Institute of Geography, National Autonomous University of Mexico (UNAM) / International Centre for Integrated Mountain Development (ICIMOD), Nepal / University of Nigeria, Department of Geology, Nigeria / International Centre for Geohazards (ICG) in Oslo, Norway / Grudec Ayar, Peru / Moscow State University, Department of Engineering and Ecological Geology, Russia / JSC "Hydroproject Institute", Russia / University of Belgrade, Faculty of Mining and Geology, Serbia / Comenius University, Faculty of Natural Sciences, Department of Engineering Geology, Slovakia / University of Ljubljana, Faculty of Civil and Geodetic Engineering (UL FGG), Slovenia / University of Ljubljana, Faculty of Natural Sciences and Engineering (UL NTF), Slovenia / Geological Survey of Slovenia / Central Engineering Consultancy Bureau (CECB), Sri Lanka / National Building Research National Organization, Sri Lanka / Taiwan University, Department of Civil Engineering, Chinese Taipei / Landslide group in National Central University from Graduate Institute of Applied Geology, Department of Civil Engineering, Center for Environmental Studies, Chinese Taipei / Asian Disaster Preparedness Center, Thailand / Ministry of Agriculture and Cooperative, Land Development Department, Thailand / Institute of Telecommunication and Global Information Space, Ukraine / California State University, Fullerton & Tribhuvan University, Institute of Engineering, USA & Nepal / Institute of Transport Science and Technology, Vietnam / Vietnam Institute of Geosciences and Mineral Resources (VIGMR), Vietnam

ICL Supporters:

Marui & Co., Ltd., Osaka, Japan / Okuyama Boring Co., Ltd., Yokote, Japan / GODAI Development Corp., Kanazawa, Japan / Japan Conservation Engineers & Co., Ltd, Tokyo / Kokusai Kogyo Co., Ltd., Tokyo, Japan / Ohta Geo-Research Co., Ltd., Nishinomiya, Japan / OSASI Technos Inc., Kochi, Japan / OYO Corporation, Tokyo, Japan / Sabo Technical Center, Tokyo, Japan / Sakata Denki Co., Ltd., Tokyo, Japan

Contact:

International Consortium on Landslides, 138-1 Tanaka Asukai-cho, Sakyo-ku, Kyoto 606-8226, Japan

Web: <http://icl.iplhq.org/>, E-mail: secretariat@iclhq.org

Tel: +81-774-38-4834, +81-75-723-0640, Fax: +81-774-38-4019, +81-75-950-0910